Laser-Tissue Interaction XII: Photochemical, Photothermal, and Photomechanical

Donald D. Duncan
Steven L. Jacques
Peter C. Johnson
Chairs/Editors

21–24 January 2001
San Jose, USA

20030106 123

REPORT DOCUMENTATION PAGE

AFRL-SR-AR-TR-02-

0426

1. REPORT DATE (DD-MM-YYYY)	2. REPORT DATE	3. DATES COVERED (From - To)
17-07-2002	Final Technical Report	18-01-2001 – 17-01-2002

4. TITLE AND SUBTITLE

Laser-Tissue Interaction XII: Photochemical, Photothermal, and Photomechanical

5a. CONTRACT NUMBER

5b. GRANT NUMBER

F49620-01-1-0153

5c. PROGRAM ELEMENT NUMBER

6. AUTHOR(S)

Donald D. Duncan
Steven L. Jacques
Peter C. Johnson

5d. PROJECT NUMBER

5e. TASK NUMBER

5f. WORK UNIT NUMBER

7. PERFORMING ORGANIZATION NAME(S) AND ADDRESS(ES)

Society of Photo-Optical Instrumentation Engineers
PO Box 10
Bellingham, WA 98227-0010

8. PERFORMING ORGANIZATION REPORT NUMBER

Volume 4257

9. SPONSORING/MONITORING AGENCY NAME(S) AND ADDRESS(ES)

Air Force Office of Scientific Research
801 N. Randolph Street, Room 732
Arlington, VA 22203-1977

10. SPONSOR/MONITOR'S ACRONYM(S)

AFOSR/NL

11. SPONSORING/MONITORING AGENCY REPORT NUMBER

12. DISTRIBUTION AVAILABILITY STATEMENT

Approved for Public Release

13. SUPPLEMENTARY NOTES

ISBN 0-8194-3935-5

14. ABSTRACT

This proceedings contains papers on the following topics: photodynamic therapy, immunotherapy, pulsed laser effects, polarized light interactions, photochemical interactions, occular laser effects, thermal interactions, laser shaping of cartilage.

15. SUBJECT TERMS

biomedical optics

16. SECURITY CLASSIFICATION OF:			17. LIMITATION OF ABSTRACT	18. NUMBER OF PAGES	19a. NAME OF RESPONSIBLE PERSON
a. REPORT	b. ABSTRACT	c. THIS PAGE			Janice Gaines Walker
Non-classsfied			SAR	486	19b. TELEPONE NUMBER (Include area code) (360)676-3290

Standard Form 298 (Rev. 8-98)
Prescribed by ANSI-Std Z39-18

106 123

Laser-Tissue Interaction XII: Photochemical, Photothermal, and Photomechanical

Donald D. Duncan
Steven L. Jacques
Peter C. Johnson
Chairs/Editors

21–24 January 2001
San Jose, USA

SPIE is an international technical society dedicated to advancing engineering and scientific
applications of optical, photonic, imaging, electronic, and optoelectronic technologies.

Printed in the United States of America.

Contents

PART A   *Laser-Tissue Interaction XII: Photochemical, Photothermal, and Photomechanical*

PDT AND IMMUNOTHERAPY

PDT

PHOTOCHEMICAL INTERACTIONS

POLARIZED LIGHT INTERACTIONS

OCULAR LASER EFFECTS

PART B   *Optical Technologies to Solve Problems in Tissue Engineering*

Conference Committees

Part A   Laser-Tissue Interaction XII: Photochemical, Photothermal, and Photomechanical

Conference Chair

Steven L. Jacques, Oregon Medical Laser Center/Providence St. Vincent Medical Center (USA)

Program Committee

Wei R. Chen, University of Central Oklahoma (USA)
Bernard S. Gerstman, Florida International University (USA)
Randolph D. Glickman, University of Texas Health Science Center at San Antonio (USA)
E. Duco Jansen, Vanderbilt University (USA)
W. Pat Roach, Uniformed Services University of the Health Sciences (USA)
Alfred Vogel, Medical Laser Center Lübeck GmbH (Germany)
Lihong V. Wang, Texas A&M University (USA)
Brian J. F. Wong, Beckman Laser Institute and Medical Clinic (USA) and University of California/Irvine (USA)

Session Chairs

PDT and Immunotherapy
Wei R. Chen, University of Central Oklahoma (USA)

PDT
Wei R. Chen, University of Central Oklahoma (USA)

Photochemical Interactions
Steven L. Jacques, Oregon Medical Laser Center/Providence St. Vincent Medical Center (USA)

Polarized Light Interactions
Lihong V. Wang, Texas A&M University (USA)

Ocular Laser Effects
Randolph D. Glickman, University of Texas Health Science Center at San Antonio (USA)

Pulsed Laser Effects
W. Pat Roach, Uniformed Services University of the Health Sciences (USA)

Laser Shaping of Cartilage
Brian J. F. Wong, Beckman Laser Institute and Medical Clinic (USA) and University of
California/Irvine (USA

Ablation
Kester Nahen, Medical Laser Center Lübeck GmbH (Germany)
Alfred Vogel, Medical Laser Center Lübeck (Germany)

Thermal Interactions
E. Duco Jansen, Vanderbilt University (USA)

Thermal Interactions and Cavitation Effects
Steven L. Jacques, Oregon Medical Laser Center/Providence St. Vincent Medical
Center (USA)

Optics
Steven L. Jacques, Oregon Medical Laser Center/Providence St. Vincent Medical
Center (USA)

Part B   Optical Technologies to Solve Problems in Tissue Engineering

Conference Chairs

Donald D. Duncan, Johns Hopkins University (USA)
Peter C. Johnson, Tissue Informatics, Inc. (USA)

Immunoadjuvants in treatment of metastatic breast tumors using selective laser photothermal interaction

Wei R. Chen[*a, b], Michael D. Lucroy[c], Hong Liu[d], Kenneth E. Bartels[c], Baha Jassemnejad[a], Shawn L. Barker[a], Punit Gandhi[e], and Robert E. Nordquist[f, g]

[a] Department of Physics and Engineering, University of Central Oklahoma, Edmond, OK 73034
[b] Department of Physics and Astronomy, University of Oklahoma, Norman, Oklahoma 73109
[c] Department of Veterinary Clinical Sciences, College of Veterinary Medicine and Center for Laser Research, Oklahoma State University, Stillwater, OK 74078
[d] School of Electrical Engineering, University of Oklahoma, Norman, OK 73019
[e] Oklahoma School of Science and Mathematics, 1141 N. Lincoln Blvd., Oklahoma City, OK 73014
[f] Wound Healing of Oklahoma, 3945 N. Walnut Street, Oklahoma City, OK 73105
[g] Department of Ophthalmology, University of Oklahoma, Oklahoma City, OK 73104

ABSTRACT

A novel immunoadjuvant, glycated chitosan, has been used in combination with a near-infrared laser and a laser-absorbing dye to treat metastatic tumors in rats. The laser-dye combination provides selective photothermal tumor destruction. The addition of the *in situ* immunoadjuvant works in tandem with the photothermal interaction to induce a host antitumor immunity. Our previous experiments have shown the efficacy of this novel modality against a metastatic breast cancer in rat model, using the three components. The current study is to investigate the roles of different components, namely, the laser, the dye and the immunoadjuvant. First, the selective photothermal laser-tissue interactions are studied *in vivo* using rat leg muscles and rat tumors. Our results showed that with appropriate combination of laser parameter and dye dose, an optimal selective photothermal tissue interaction could be achieved. The immune response is crucial in control of tumor metastasis and the immunoadjuvant has played pivotal role in the induction of the immunity in our experiment. Therefore, the role of immunoadjuvants in the laser cancer treatment is also investigated in the current study. Specifically, three different concentrations of glycated chitosan solutions – 0.5%, 1% and 2% – were used. In comparison, the 1% solution provided the best treatment outcome. Two additional immunoadjuvants, incomplete Freund's adjuvant and complete Freund's adjuvant were also used in the same laser-dye-adjuvant treatment protocol. The functions of different adjuvants are compared.

Keywords: 805-nm laser, indocyanine green, glycated chitosan, Freund's adjuvants, selective photothermal tissue interaction, laser immunotherapy, treatment of metastatic tumors

---

[*] Correspondence: Email: wchen@ucok.edu; Telephone: 405/974-5198; Fax: 405/974-3812

1. INTRODUCTION

It has been well established that organized tissue responds strongly to temperature increase. When the tissue temperature is approaching and exceeding 40^0C, there is an increase in blood flow in both tumor and normal tissues [1-2]. As temperature reaches 41.5^0C, cellular cytotoxicity occurs [3]. Temperatures above 42.5^0C can result in vascular destruction within tumor tissue [4]. The thermal impact on tissue changes drastically when temperature exceeds 43^0C; the rate of "cell kill" doubles for every 1^0C increase beyond 43^0C and decreases by a factor of 4 to 6 for every 1^0C drop below 43^0C [5-6]. It has been noted that tumor tissue is more sensitive to temperature increase than normal tissue [7]. An important reason for the observed cytotoxicity associated with temperature increase is that thermal effects are more profound in the acidotic (low pH) conditions present in poorly oxygenated human tumors. Therefore, heat has a greater cytotoxic effect in tumors than in normal tissues [3]. However, heat alone has only limited effect in cancer treatment, with a small portion of complete responses and short response duration [8-14]. Furthermore, when heat is used, damage to surrounding normal tissue is often unavoidable.

Lasers, with precise energy delivery mechanism, can be an effective tool in photothermal treatment of cancer. However, selectivity has been a major obstacle in non-invasive treatment of deep tumors. Absorption of laser energy by tissue depends on the light wavelength. Strong absorption can cause thermal injury mainly on the surface tissue being treated, which in turn limits the scope of the thermal effect in deeper tissue. Weak absorption by tissue does not sufficiently raise the tissue temperature. To solve this problem, dye-enhanced laser-tissue interaction was proposed. Using a near-infrared laser and an *in situ* dye with corresponding absorption peak, selective tissue destruction can be achieved. Such laser beam can penetrate tissue with little tissue absorption. However, when a laser-absorbing dye is present in target tissue, the laser energy is strongly absorbed by the dye molecules. Upon returning to ground states, those molecules release the absorbed energy in the form of heat, hence causing cell destruction in the surrounding tissue. Specifically, by injecting indocyanine green solution into target tissue, an 805-nm diode laser can non-invasively raise target tissue temperature significantly, while maintaining the surface temperature below the 40^0C damage threshold [15-16].

Studies using Monte Carlo simulation also indicated that with appropriate absorption enhancement, a tumor deep inside normal tissue could absorb more laser energy than the surface tissue [17-18]. The theoretical studies showed the feasibility of treating deep tumors using the dye enhanced laser photothermal interaction, particularly with the use of multiple converging laser beams [17-18].

However, our early studies have shown that photothermal interaction alone could not provide cure for the rats bearing metastatic mammary tumors. To enhance the treatment, a novel treatment modality has been proposed using a combination of laser energy, a laser-absorbing dye and an immunoadjuvant [19-23]. It employed an immunoadjuvant, working in tandem with the selective photothermal interactions. Our preliminary studies have shown a systemic, long-term, anti-tumor immunity induced by the combination of the laser, laser-absorbing dye and the immunoadjuvant [19-23, 24-25].

In the current study, functions of different components of the novel method are investigated and our experimental results are presented. Specifically, the laser-dye combination and its photothermal effect on tissue were investigated in terms of temperature increase in tissue. Functions of different immunoadjuvants were also investigated. The objective of the study is to pave the way for determining the optimal treatment protocol for metastatic tumors.

2. MATERIALS AND METHODS

2.1. Tumor Model

DMBA-4 transplantable, metastatic mammary tumor model [26-30] in female Wistar Furth rats (Harlan Sprague-Dawley, Indianapolis, Indiana) was used in the experiments. The tumor cells were harvested from

live tumor-bearing rats and naïve rats were inoculated subcutaneously in one of the inguinal fat pads, seven to ten days before laser immunotherapy treatment. The usual inoculation dose is 10^5 viable tumor cells per rat.

2.2. Laser Immunotherapy

This novel method uses a near-infrared diode laser, indocyanine green (ICG), and an immunoadjuvant. The solution of ICG, serving as the laser absorbing dye, and immunoadjuvant, serving as the immune stimulant, was directly injected into the center of the tumor before the non-invasive laser irradiation. The dye and adjuvant was admixed with certain dye and adjuvant concentrations, used in a dose of 200 µl per tumor. The standard ICG concentration was chosen as 0.25%. The tumor was irradiated with an 805-nm laser at 2 watts (CW) for 10 minutes two hours after the dye-adjuvant administration.

2.3. Immunoadjuvants in Laser Immunotherapy

A novel immunoadjuvant, glycated chitosan (GC), was used in our experiments with three different concentrations: 0.5%, 1% and 2%. Two other immunoadjuvants were also used. Incomplete Freund's adjuvant (Sigma Co., St. Louis) was used with an 88% concentration and complete Freund's adjuvant (Sigma Co.) was used with a 50% concentration.

2.4. Tissue Temperature Measurement

The OM-700 Omega Engineering Data Acquisition and Control Unit (OMEGA, Stamford, CT) multiple-channel temperature probe was used to measure tissue temperature during laser irradiation. Nine needle probes of this unit can be placed in different locations for a detailed temperature profile in tissue. The Omega OM-700 software was used to monitor the temperature changes. In this study, several needles were inserted into the tissue injected with laser-absorbing dye and into the surrounding normal tissue. The temperature profiles were measured using different laser power densities and different concentrations of indocyanine green. The laser energy was delivered through an optical fiber with a microlens to achieve uniform energy distribution on the treatment surface. The laser power density delivered to the tissue can be controlled by changing the distance between fiber tip and the tissue surface. Both rat leg muscle and rat tumor were used as the target tissue.

3. RESULTS

3.1. Tissue temperature increase using 805-nm laser and ICG

Rat leg muscle was used to test the selectivity of the laser-dye combination. Figure 1 shows the results using different power densities. ICG solution (500 µl at 0.5%) was injected to the rat leg muscle 4 mm beneath the skin and treated with power densities from 0.8 W/cm^2 to 7.3 W/cm^2 for 5 minutes. Multiple temperature probes were placed throughout the target tissue. As shown in Figure 1, there is a thirty-degree difference between the temperature increases caused by the lowest power density and the highest power density 4 mm below the skin. At the same time, with the help of water spray and compressed air, the skin temperature was kept below that of the target tissue. The effect of different dye concentrations was also evaluated. Figure 2 shows the temperature of muscle tissue 4 mm beneath the skin during the laser treatment at 3.34 W/cm^2 with different ICG doses (500 µl at 0.25%, 0.5% and 1%).

The results in Figures 1 and 2 clearly demonstrate that the internal temperature can be controlled by manipulating laser power density and ICG concentration and dose. Furthermore, these results show that a thermal equilibrium is reached a few minutes after the treatment begins. Results in Figure 1 show a close relationship between the laser power density and the temperature increase. Similarly, results in Figure 2 clearly demonstrated the relationship between the dye concentration and the temperature increase in tissue, although the exact distribution of dye in the rat leg muscle is unknown.
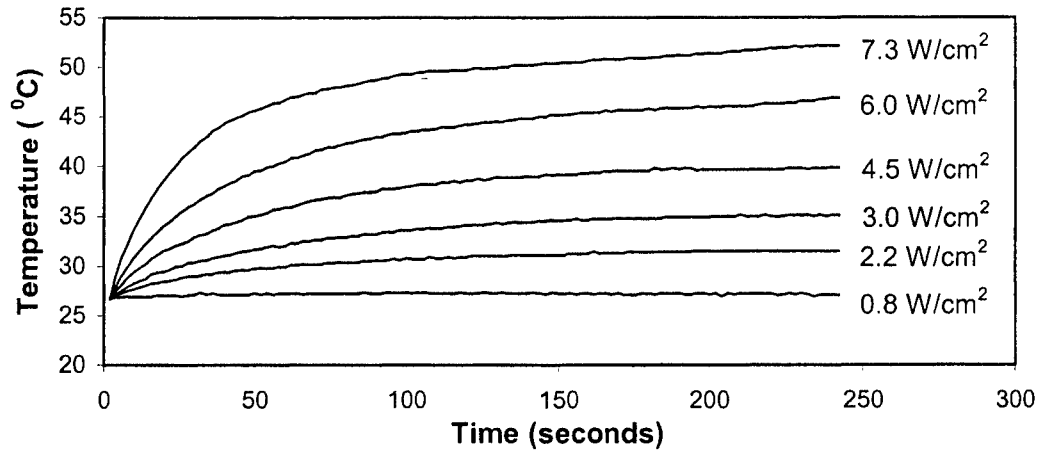
Figure 1. The temperature in rat leg muscle treated with different laser power densities and a constant ICG dose (500 μl at 0.5%). The temperature probe was placed 4 mm underneath the skin. The skin was cooled to a temperature well below the target tissue with water spray and compressed air (data not shown).
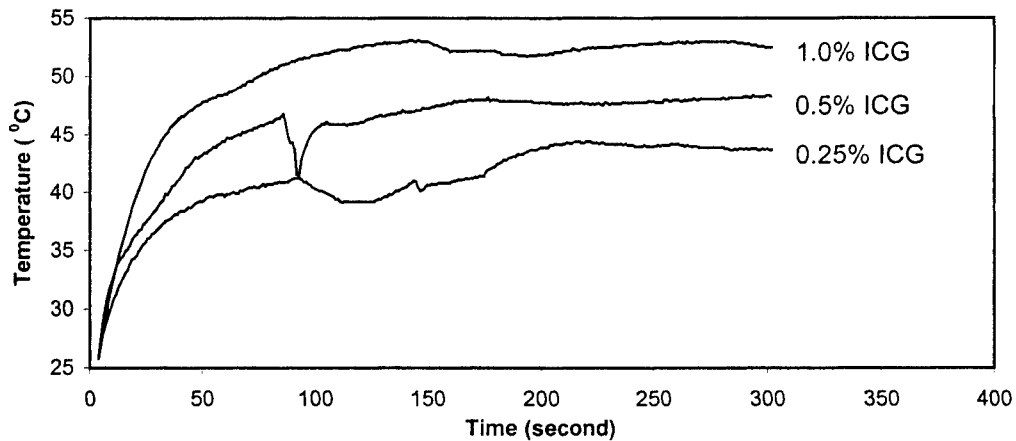
Figure 2. The temperature in rat leg muscle treated by laser with a constant laser power density (3.34 W/cm^2) and different ICG concentrations. ICG solution (500 μl at 0.25%, 0.5% and 1%) was injected to different leg muscles. The temperature probe was placed at a depth 4mm underneath the skin. The skin was cooled to a temperature well below the target tissue with water spray and compressed air (data not shown).

Figure 3 shows the temperature measured inside a rat tumor treated by the laser-dye combination. ICG solution (300 μl and 0.25%) was injected to the center of the tumor and the tumor was treated by the 805-nm laser with a power density of 2 W/cm^2. With the surface cooling, the temperature at the center of a rat tumor reached above 43^{0}C (thick solid curve in Figure 3) while the skin temperature was maintained below 40^{0}C (thin solid curve in Figure 3). The temperature of muscle tissue below the tumor is also measured. Without dye, the temperature of muscle tissue remained unchanged during the laser treatment procedure (thick gray curve in Figure 3).

3.2. Functions of laser, laser-absorbing dye, and immunoadjuvant

Tumor-bearing rats were treated with different components in laser immunotherapy, including each individual component (laser, ICG, or GC), combination of two components (laser-ICG, Laser-GC, and ICG-GC), as well as the triple components (laser-ICG-GC). The long-term survival data are given in Table I, with data of control rats.
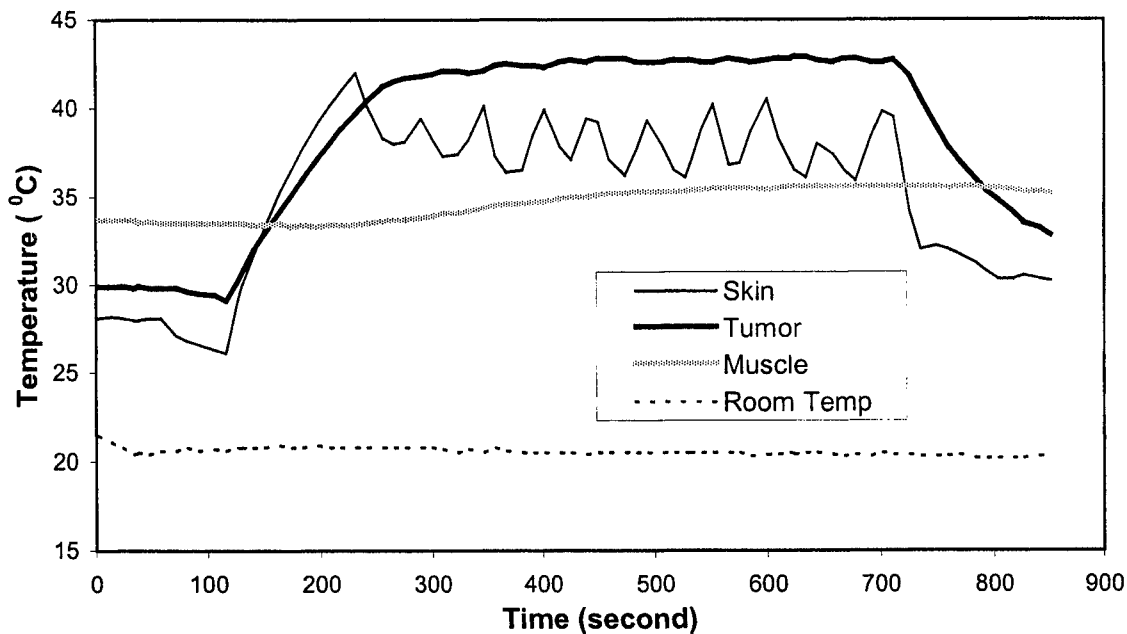
Figure 3. Temperatures of ICG injected tumor and surrounding normal tissues (skin and muscle) during laser treatment (2 W/cm^2). The ICG solution (300 μl at 0.25%) was injected to the center of the tumor. The temperature at the center of the tumor exceeded 43^{0}C while the temperature of deep muscle remained unchanged. The skin temperature was kept below 40^{0}C with compressed air and water spray. Each sharp decrease of the skin temperature (the thin solid curve) coincided with the application of water spray. The laser treatment started at 100 seconds and stopped at 700 seconds.

TABLE 1

Long-term survival of rats treated by different combinations of the laser immunotherapy

Treatment Method	Number of Treated rats	Number of Long-Term Survivors **	% of Long-Term Survival
Control Rats	35*	0	0%
Laser treatment only	12	0	0%
ICG Injection only	12	0	0%
GC Injection only	12	1	8.3%
Laser-ICG treatment	12	0	0%
Laser-GC treatment	12	1	8.3%
ICG-GC treatment	12	2	16.7%
Laser-ICG-GC treatment	31*	9	29.0%

* The data of control rats and the laser + ICG + GC treatment were from two separate experiments.
** Long-term survivor refers to a rat that survived at least 120 days after tumor cell implantation.

3.3. Functions of immunoadjuvants

To understand the impact of immunoadjuvant on the treatment of metastatic tumors, different concentrations of glycated chitosan was used and the long-term rat survival data are given in Table 2, in comparison with that of control rats.

TABLE 2

Long-term survival of rats treated by the laser immunotherapy with different concentrations of glycated chitosan

Treatment Method	Number of Treated rats	Number of Long-Term Survivors [*]	% of Long-Term Survival
Control Rats	35	0	0%
Laser-ICG-GC (GC 0.5%)	16	1	6.3%
Laser-ICG-GC (GC 1%)	16	6	37.5%
Laser-ICG-GC (GC 2%)	16	2	12.5%

[*] Long-term survivor refers to a rat that survived at least 120 days after tumor cell implantation.

Two additional immunoadjuvants, incomplete Freund's adjuvant and complete Freund's adjuvant, were used in treatment of the DMBA-4 rat tumors. As shown in Figure 4, the glycated chitosan (GC) and complete Freund's (CF) adjuvant showed similar effect, while the incomplete Freund's (IF) adjuvant showed much less impact on the survivability of the treated rats.
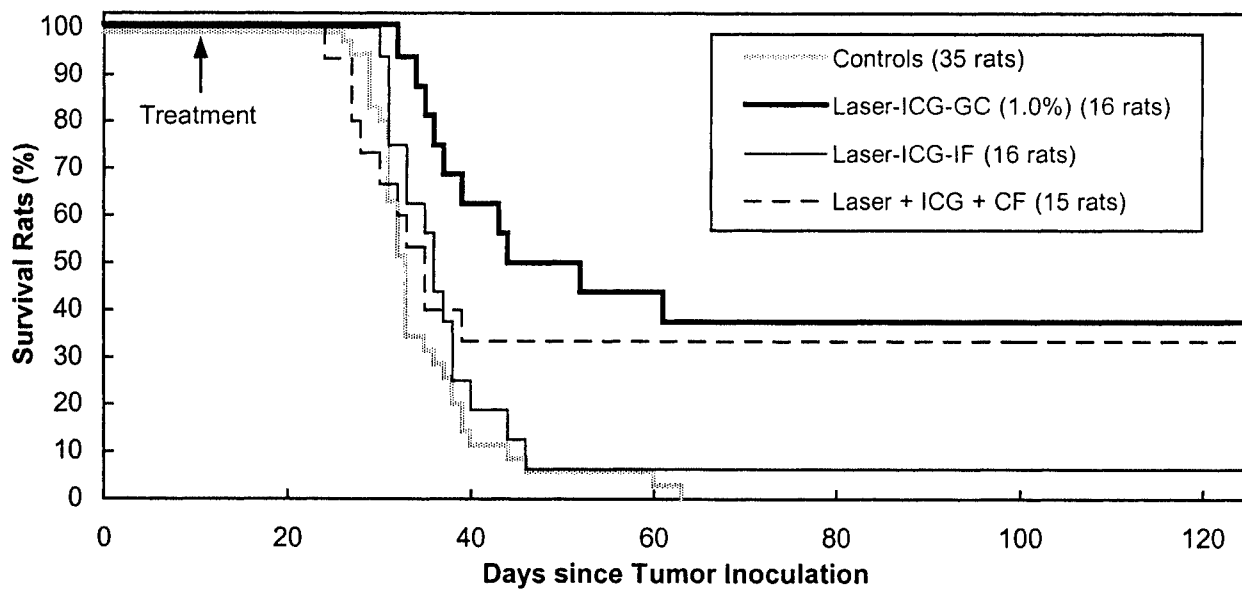
Figure 4. Rat survival data after laser immunotherapy treatment using different immunoadjuvants. The Thick solid curve represents 16 rats treated with 1% glycated chitosan. The thin solid line represents 16 rats treated with incomplete Freund's adjuvant (88%) and the thin dashed line represents 15 rats treated with complete Freund's adjuvant (50%). The treatment protocol was the same for all three groups: 200 μl ICG+adjuvant solution (0.25% ICG) followed by 10 minutes laser irradiation at 2 watts.

4. DISCUSSION

Based on our experimental results, a selective photothermal laser-tissue interaction using an infrared laser and an *in situ* laser-absorbing dye can be controlled with appropriate laser settings and dye doses. With ICG in tissue, the temperature in deep tissue can be raised above damage threshold, as shown in Figure 1, with a non-invasive laser irradiation. The temperature change in tissue can be controlled by the laser densities. Furthermore, the temperature change in tissue can also be controlled by the dye concentration, as shown by the

results in Figure 2. In most cases, the temperature in tissue reached a stable level due to the balance of heat absorption by the tissue and the heat diffusion in the tissue.

With appropriate combination of laser power and dye dose, as well as certain surface cooling measures, the temperature of the tissue surface directly under the laser fiber can be maintained below 40^0C. At the same time, the tissue below the surface can experience significant temperature increase (above the 43^0C threshold), as shown in Figure 3.

The importance of immunoadjuvant in laser immunotherapy is demonstrated by the long-term survival data. No rat in the treatment groups without using immunoadjuvant had long-term survival (see Table I). In comparison, the laser-ICG-GC treatment yielded the best treatment results. The dosage of the adjuvant could play an additional role. As shown in Table 2, 1%-GC yielded the better survival results than 0.5% and 2%. Therefore, the optimal dose of immunoadjuvant should be pursued in order to improve the efficacy of the novel treatment modality.

The results of different immunoadjuvants, shown in Figure 4, indicated the working mechanism of laser immunotherapy (with successful treatment outcome from each of the three immunoadjuvants). On the other hand, these results also indicated that other immunoadjuvant(s) could also work in the same protocol. The search for optimal adjuvants and for optimal adjuvant doses is currently in progress.

5. ACKNOWLEDGMENTS

6. REFERENCES

1. C.W. Song, A. Lokshina, J.G. Rhee, M. Patten and S.H. Levitt, Implication of blood flow in hyperthermic treatment of tumors. IEEE Trans. Biomed. Eng., 31, 9-16, 1984.
2. H.S. Reinhold and B. Endrich, Tumor microcirculation as a target for hyperthermia: A review. Int. J. Hyperthermia, 2, 111-137, 1986.
3. A.J. Thistlethwaite, D.B. Leeper, D.J. Moylan and R.E. Nerlinger, pH distribution in human tumors. Int. J. Radiat. Oncol. Biol. Phys., 11, 1647-1652, 1986.
4. W.C. Dewey, L.E. Hopwood, S.A. Sapareto and L.E. Gerweck, Cellular responses to combinations of hyperthermia and radiation. Radiology, 123, 463-474, 1977.
5. S.A. Sapareto and W.C. Dewey, Thermal dose determination in cancer therapy. Int. J. Radiat. Oncol. Biol. Phys., 10, 787-800, 1984.
6. S.B. Field and C.C. Morris, The relationship between heating time and temperature: Its relevance to clinical hyperthermia. Radiother. Oncol., 1, 179-186, 1983.
7. L.J. Anghileri and J. Robert, Hyperthermia in Cancer Treatment. CRC Press, Boca Raton, FL, 1986.
8. M.W. Dewhirst, W.G. Conner, T.E. Moon and H.B. Roth, Response of spontaneous animal tumors to heat and/or radiation: preliminary results of a phase III trial. J. Natl. Cancer Inst. 61, 395-397, 1982.
9. M.W. Dewhirst, W.G. Conner and D.A. Sim, Preliminary results of a phase III trial of spontaneous animal tumors to heat and/or radiation: early normal tissue response and tumor volume influence on initial response. Int. J. Radiat. Oncol. Biol. Phys., 8, 1951-1962, 1982.
10. J.H. Kim, E.W. Hahn and N. Tokita, Combination hyperthermia and radiation therapy for cutaneous malignant melanoma. Cancer, 41, 2143-2148, 1978.
11. H.H. Leveen, S. Wapnick, V. Riccone, G. Falk and N. Ahmed, Tumor eradication by radio-frequency therapy. J. Am. Med. Assoc., 235, 2198-2200, 1976.

12. M.R. Manning, T.C. Cetas, R.C. Miller, J.R. Oleson, W.G. Conner and E.W. Gerner, Results of a phase I trial employing hyperthermia alone or in combination with external beam or interstitial radiotherapy, Cancer, 49, 205-216, 1982

13. J.B. Marmor, D. Pounds, N. Hahn and G.M. Hahn, Treating spontaneous tumors in dogs and cats by ultrasound induced hyperthermia. Int. J. Radiat. Oncol. Biol. Phys., 4, 967-973, 1978.

14. J.B. Marmor, D. Pounds, D.B. Postic and G.M. Hahn, Treatment of superficial human neoplasms by local hyperthermia induced by ultrasound. Cancer, 43, 196-205, 1979.

15. M.D. Lucroy, W.R. Chen, D. Sensney-Sears, R.G. Higbee and K.E. Bartels, Improved light delivery for chromophore-enhanced laser-induced hyperthermia in a subcutaneous murine breast cancer model. Proceedings of Photonics West, BiOS 2001,San Jose, CA, 2001 (in press).

16. M.D. Lucroy, W.R. Chen, D. Sensney-Sears, R.G. Higbee and K.E. Bartels, Developing a subcutaneous murine breast cancer model for the evaluation of laser-induced hyperthermia. Proceeding of Vet Cancer Society 20th Annual Conference, Monterey, CA, 2000 (in press).

17. L-H. Wang, R.E. Nordquist and W.R. Chen, Optimal beam size for light delivery to absorption-enhanced tumors buried in biological tissues and effect of multiple beam delivery: a Monte Carlo study. Applied Optics Vol. 36, 8286-8291, 1997.

18. L-H. Wang, G. Marquez, R.E. Nordquist and W.R. Chen, Propagation and absorption of near-infrared laser light in photosensitizer-enhanced biological tissues. SPIE Vol. 3254, 332-339, 1998.

19. W.R. Chen, R.L. Adams, R. Carubelli and R.E. Nordquist, Laser-photosensitizer assisted immunotherapy: a novel modality for cancer treatment. Cancer Lett., 115, 25-30, 1997.

20. W.R. Chen, D.A. Okrongly, R.L. Adams and R.E. Nordquist, Laser-tissue photobiological interaction: a new mechanism for laser-sensitizer-immunoadjuvant treatment of metastatic cancers. SPIE, Vol. 2975, 290-297, 1997.

21. W.R. Chen, K. Robinson, R.L. Adams, A.K. Singhal and R.E. Nordquist, Anti-tumor immune responses induced by the treatment of photodynamic immunotherapy. SPIE Vol. 3254, 27-34, 1998.

22. W.R. Chen, W.-G. Zhu, J.R. Dynlacht, H. Liu and R.E. Nordquist, Long-term tumor resistance induced by laser photoimmunotherapy. International Journal of Cancer 81, 808-812, 1999

23. W.R. Chen, H. Liu, J.A. Nordquist and R.E. Nordquist, Tumor cell damage and leukocyte infiltration after laser immunotherapy treatment. Lasers in Medical Science, 15, 43-48, 2000.

24. W.R. Chen, A.K. Singhal, H. Liu, and R.E. Nordquist, Laser immunotherapy induced antitumor immunity and its adoptive transfer. Cancer Research (*Advances in Brief*), 2000, (in press).

25. W.R. Chen, H. Liu, A.K. Singhal, R.E. Nordquist, Passive adoptive transfer of antitumor immunity induced by laser-dye-immunoadjuvant treatment in a rat metastatic breast cancer model. SPIE Proceedings, Vol. 3914, 2000 (in press).

26. U. Kim, Metastasizing mammary carcinomas in rats: Induction and study of their immunogenicity. Science, 167, 72-74, 1970.

27. U. Kim, Characteristics of metastasizing and nonmetastasizing tumors and their interactions with the host immune system in the development of metastasis. Proc. European Organization for Research on Treatment of Cancer Metastasis Group international Conference on Clinical and Experimental Aspects of Metastasis, Editors: Hellman, K., Hilgard, P., and Eccles, S. Nijhoff, The Hague, The Netherlands, 210-214, 1981.

28. S.K. Chatterjee and U. Kim, Fucosyltransferase activity in metastasizing and nonmetastasizing rat mammary carcinomas. Journal of the National Cancer Institute. 61, 151-62, 1978.

29. S.K. Chatterjee and U. Kim, Galactosyltransferase activity in metastasizing and nonmetastasizing rat mammary carcinomas and its possible relationship with tumor cell surface antigen shedding. Journal of the National Cancer Institute, 58, 273-80, 1977.

30. S.K. Chatterjee and U. Kim, Biochemical properties of cyclic nucleotide phosphodiesterase in metastasizing and nonmetastasizing rat mammary carcinomas. Journal of the National Cancer Institute, 56, 105-10, 1976.

Augmentation of tumor immunity with ENHANZYN™ adjuvant following verteporfin PDT: photodynamic vaccination (PDV)

P.M. Curry*, A.J. Stewart, L. Hardwicke, C. Smits, J.R. North

QLT Inc., Vancouver, British Columbia, Canada

ABSTRACT

The immune system is implicated in the mechanism of tumor destruction following photodynamic therapy (PDT). Several investigators have shown that immune stimulation can augment PDT. In this study, a single intratumoral injection of ENHANZYN™ adjuvant was administered to tumor-bearing mice immediately following verteporfin PDT in a therapeutic modality referred to as Photodynamic Vaccination (PDV). After optimal PDT, little difference in the rate of tumor re-growth or time to tumor reappearance was seen upon addition of the adjuvant. This may be as expected as this treatment regimen results in effective long-term tumor cure in mice. The effect of adjuvant and sub-optimal PDT was less clear as both groups treated with either a high or low dose of adjuvant showed tumor re-growth earlier than those animals treated with PDT alone. However, tumors of mice receiving sub-optimal PDT followed by high dose immune adjuvant did not show the rapid, uncontrolled growth seen in other groups and, in the majority of cases, tumor volume decreased steadily with time. This resulted in a superior period of survival despite the animals being tumor-bearing. Interestingly, the data obtained in this study clearly demonstrate the ability of PDT to protect against re-challenge with a second round of tumor implantation. This was seen in all groups and stresses the importance of the immune response in PDT tumor control. Addition of the high immune adjuvant dose to sub-optimal PDT appeared to be the most effective treatment group in this respect, giving complete protection against tumor re-implantation.

1. INTRODUCTION

In addition to the cytotoxic action of PDT, there is growing evidence that the immune system plays an essential role in tumor destruction and vascular shutdown. Following PDT, immune responses are initiated with the rapid induction of an inflammatory reaction[1,2] involving the release of cytokines[3,4,5], eicosanoids[6,7], and clotting factors[8,9]. This progresses to the activation of immune cells[10,11,12] and infiltration of immune cells into PDT-treated tissue[13]. PDT has been shown to enhance both phagocytosis and tumor cytotoxicity when normal mouse peritoneal macrophages were treated in vitro[11,12] and similar treatments caused the secretion of tumor necrosis factor (TNF)[3]. In the clinical setting, treating bladder cancer with PDT

resulted in detectable levels of interleukin (IL)-1 and TNF-α in the urine of patients within 3 h of treatment and IL-2 within 24 h in a profile that resembled treatment of bladder cancer with Bacille Calmette Guérin (BCG). In BCG therapy, elevated cytokine levels were associated with improvement[3].

The role of the host immune system in PDT-mediated tumor eradication has recently been examined by several investigators. In one study, PHOTOFRIN® PDT cured all normal tumor-bearing mice; however, using the same treatment protocol with immune-compromised mice, the initial tumor ablation following PDT was followed by re-growth of all of the tumours[14]. Specific, cellular tumor immunity that developed following PHOTOFRIN® PDT would be adoptively transferred to naïve recipients: cytotoxic T cells were the main effector of the anti-tumor activity with helper T cells and natural killer cells playing a supportive role[15,16]. Similar results were observed when subcutaneous tumors were treated with benzophenothiazine PDT[17]. Tumors treated with PDT are associated with a rapid, transient influx of neutrophils and mast cells. Approximately 10% of the total number of cells in the tumor at 2 h after PDT with PHOTOFRIN® were characterized as monocytes that had invaded the tumor from the circulation and these cells were shown to be cytotoxic against tumor cell targets[18]. In contrast, immune cell infiltrates have not been detected in subcutaneous tumors treated with ALA[19].

The effectiveness of PDT combined with immune stimulation has been evaluated in a number of published studies in animals. Intratumoral injection of formalin-killed *Corynebacterium parvum* into experimental tumors 24 hours prior to PDT with hematoporphyrin derivative (Hpd) resulted in a greater tumor response and prolonged survival compared to PDT alone[20]. Similar results were obtained with PDT combined with intratumoral BCG in a murine transitional cell carcinoma model[21]. PHOTOFRIN® PDT was combined with repeated injections of the immune stimulant schizophyllan (SPG), a glucan derived from *Schizophyllum communae*, to mice bearing a squamous cell carcinoma. When PDT was administered 48 hours after the last SPG treatment, tumor responses were enhanced whereas SPG had no effect when it was administered after PDT[22]. Administration of vitamin D₃ binding protein macrophage activating factor (DBPMAF) immediately after PHOTOFRIN® PDT enhanced the tumor response[23].

The beneficial effects of adjuvant administration appear to be independent of the photosensitizer used. The adjuvants BCG and a purified and de-proteinized preparation of the mycobacterium cell wall extract (MCWE) were used with various photosensitizers including PHOTOFRIN®, verteporfin, zinc(II)-phthalocyanine (ZnPC), and *meta*tetrahydroxyphenyl-chlorin (mThPC). A single injection of either BCG or MCWE directly under the tumor mass immediately after PDT produced a greater tumor response rate[24]. Peritumoral injection of BCG immediately after PDT with photosensitizers such as Lutetium Texaphyrin (Lu-Tex) and mono-L-aspartyl-chlorin e6 (NPe6) produced the optimum tumor responses. Administration of BCG 7 days after PDT resulted in better tumor responses compared to PDT alone (Korbelik, M. et. al unpublished data). Intratumoral injection of glycated chitosan gel (GCG) prepared from crabshell chitin combined with the photosensitizer indocyanine green (ICG) produced tumor responses in rats and resulted in the development of tumor immunity[25,26]. Colony stimulating factors, delivered via genetically modified tumor cells[18], or direct intratumor injection[27], potentiates the anti-tumor effects of PDT.

The present study was designed to examine the interaction of verteporfin-sensitized PDT and intratumoral injection of the ENHANZYN™ adjuvant in a standard murine tumor model. Animals were observed for tumor responses to assess the efficacy of the combination relative to PDT alone, and the ability of these treatments to protect against tumor re-growth was assessed by re-implanting tumor-free mice 20 days after the initial treatment. Furthermore, in order to demonstrate that this combination did not worsen the photosensitivity seen with PDT alone, mice were scored for edema, erythema, eschar formation, weight-bearing abilities, size of eschar, size of tumor, and size of affected area.

2. METHODOLOGY

2.1 Tumor model

Male DBA/2 mice (7 – 16 weeks old, Charles River Canada) were implanted intradermally with a suspension of 2×10^4 3-methylcholanthrene-induced rhabdomyosarcoma (M1) cells on the right flank according to established procedures[28,29,30]. Approximately six to ten days after implantation, the site was shaved and tumor growth measured using vernier calipers. Only mice bearing tumors 4 - 6 mm in diameter were selected for inclusion into one of the treatment groups consisting of ten mice.

2.2 Photosensitizer

Verteporfin (QLT Inc.) was prepared as a 2.0 mg/ml solution from 15 mg vials by aseptically adding 7.0 ml of sterile water for injection to each vial and was stored at 4°C for a maximum of 14 days. For PDT and PDV, verteporfin was further diluted to 0.1 mg/ml using 5% dextrose in water (5DW, Baxter Corp).

2.3 Immune adjuvant

ENHANZYN™ adjuvant (Corixa Inc.) is a 1.0% squalane oil-in-water emulsion containing 1450 µg/ml cell wall skeleton from *Mycobacterium phlei* and 250 µg/ml monophosphoryl lipid A from *Salmonella minnesota* R595 and was used according to the manufacturer's recommendations. Two concentrations were prepared by diluting the adjuvant in sterile PBS: 1:10 (145 µg/ml cell wall skeleton, 25 µg/ml monophosphoryl lipid A) or 1:2.5 (580 µg/ml cell wall skeleton, 100 µg/ml monophosphoryl lipid A). Aliquots (50 µL) were drawn into a tuberculin syringe with a 27 gauge needle prior to intratumoral injection.

2.4 Laser

The argon pump dye laser was set to an output wavelength of 690 ± 3 nm. Before each mouse was exposed to laser light, the power output of the delivery fiber was verified. The microlens fiber optic was positioned to illuminate a 1.0 cm diameter circular area on the flank of the mouse. Power output was set to 70 mW for a light intensity of 89.2 mW/cm² at the target area.

2.5 Photodynamic vaccination

Mice received 1.0 mg/kg of verteporfin administered intravenously by tail vein injection. Immediately after injection, the mice were placed in a darkened row of an enclosed, ventilated animal racks for 30 minutes, after which each mouse was secured in a metal holder so that the tumor was centered in a 1.0 cm diameter exposure area. The tumor site was exposed to light for either 14 minutes to deliver 75 J/cm², or 4 minutes and 40 seconds to deliver 25 J/cm². Immediately following illumination and while still

immobilized in the metal holder, mice treated with PDV received a single intratumoral injection of 50 µL of the adjuvant, designed to deliver the adjuvant to the center of the tumor mass.

2.6 Treatment assessment

After treatment, mice were monitored on Days 3, 7, 14, and 20 for the presence of palpable tumor. Edema, erythema, and eschar formation were observed and scored on Days 3, 7, 14 and 20 using the scales described in Table 1. Mice monitored for tumor growth were euthenized when their tumor reached 1.0 cm in diameter.

Table I. Scoring parameters

Erythema	Value
None	0
Slight (no broken vessels)	1
Definite erythema	2
Blanching	3
Severe (broken vessels, restricted to treated area)	4
Severe (broken vessels, outside of treated area)	5
Edema	
None	0
Slight (within the exposure area)	1
Mild (skin fold < 1mm)	2
Moderate (skin fold 1-2 mm)	3
Severe (> 2mm thick)	4
Extended to the forelimb	5
Eschar	
None	0
Yellow/pale brown	3
Red-brown	4
Black	5
Weight-bearing Abilities	
Yes	0
Favoring leg	3
Non weight-bearing	5

3. RESULTS

3.1 Antitumor Efficacy

Optimal PDT gave virtually complete tumor cure, with 90% of animals being free of tumor after 20 days (Figure 1A). The inclusion of adjuvant (high and low dose) appeared to give a slight reduction in the number of tumor-free animals with this PDT regime, although the survival at the end of 20 days was identical (Figure 1B).
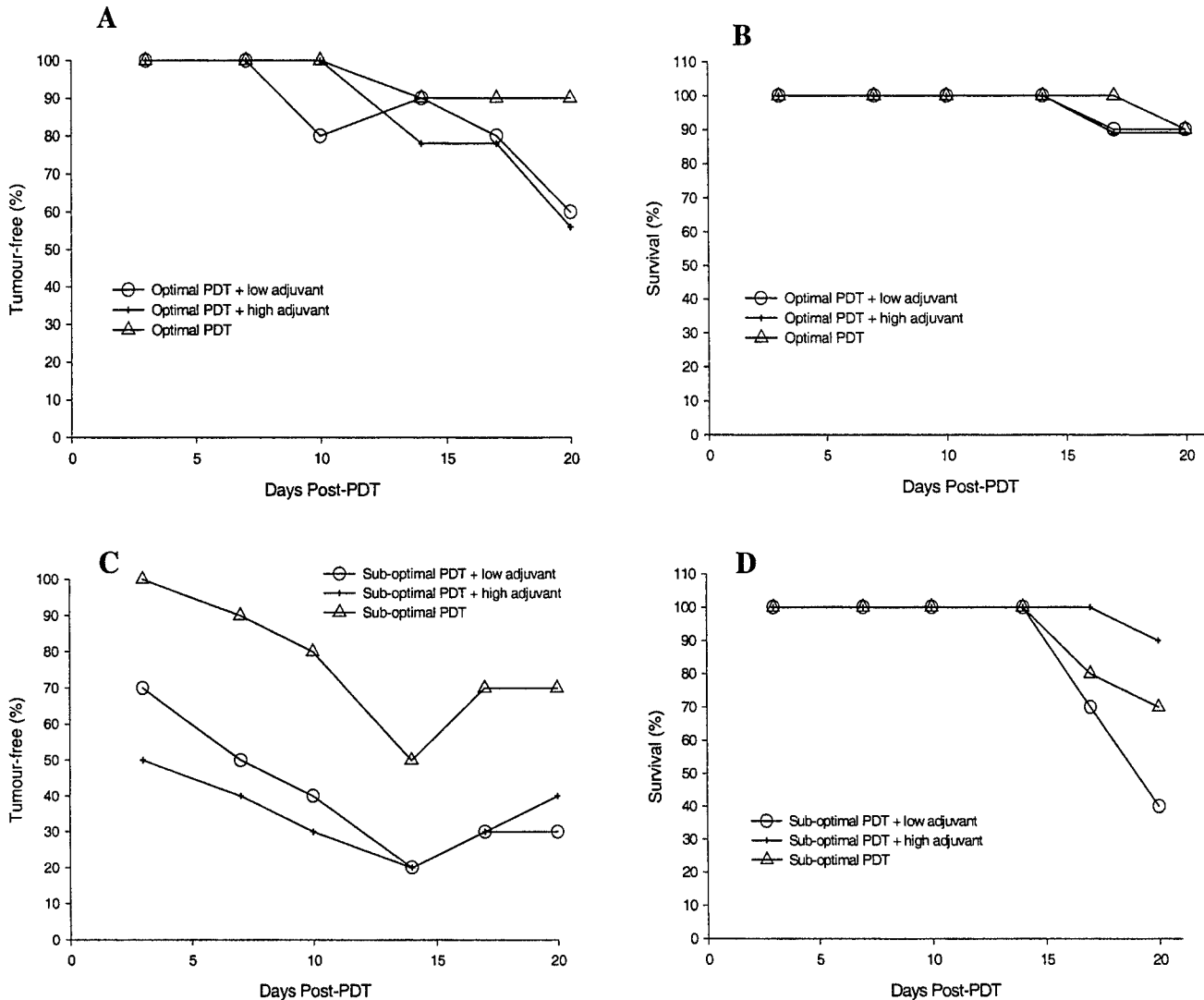
Figure 1. Tumor responses. Mice were monitored for the presence or absence of a palpable tumor and were sacrificed when tumors reached 1.0 cm in diameter. Graphed values represent the percentage of mice with no evidence of palpable tumors following treatment (A-B) and the percentage of surviving mice whose tumors have not yet reached 1.0 cm in diameter (C-D).. Each group contained 10 mice at treatment.

Sub-optimal PDT also gave effective tumor control with 70% of animals being tumor-free 20 days after treatment (Figure 1C). Again, addition of the adjuvant resulted in a slightly lower number of tumor-free animals. Importantly, the high dose immune adjuvant resulted in a longer survival time relative to sub-optimal PDT alone (Figure 1D) indicating that this therapy is apparently able to prolong the life-span of tumor-bearing animals. Tumor measurements from individual animals indicated that 8 out of 10 animals in this group had tumors that were regressing or had regressed completely by Day 20 (data not shown).

Upon re-challenge of tumor-free mice on Day 20, the tumor-take rate (percentage of re-implanted animals that showed palpable tumor) of mice treated with PDT, with or without immune adjuvant, was compared with the tumor-take rate in untreated naïve mice. Implantation of naïve mice resulted in 100% tumor take within 10 days (Figure 2A). Optimal PDT gave approximately 60% fewer tumors (n=9), and this was not changed by the addition of high dose adjuvant (n=5). The lower dose of adjuvant combined with optimal PDT gave more protection against re-challenge (20% take rate, n=6). A similar trend was seen in survival to 30 days past re-implantation, where high dose adjuvant had little or no effect in addition to optimal PDT alone (data not shown). The lower adjuvant dose gave prolonged survival.

Upon re-challenge of mice treated with sub-optimal PDT, the higher dose of the adjuvant gave the greatest degree of protection (0% take rate at 30 days, n=4). The two other treatment groups allowed approximately 30-40% tumor take (Figure 2B). The higher dose of the adjuvant also gave the longest survival with all re-implanted mice surviving for 30 days past re-implantation (data not shown). Sub-optimal PDT alone also gave substantial protection relative to controls.
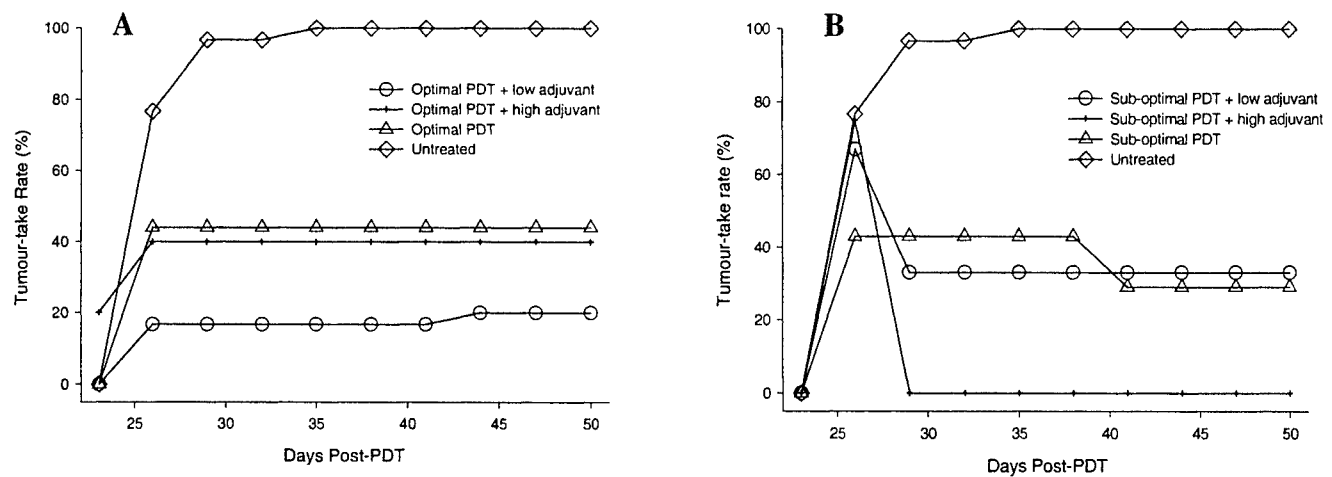
Figure 2. Tumor growth after re-implantation. Mice were monitored for the presence or absence of a palpable tumor after re-implantation of tumor-free mice and were sacrificed when tumors reached 1.0 cm in diameter. Graphed values represent the percentage of mice with evidence of palpable tumors (Tumor-take rate) following re-implantation. Each group contained 10 mice at treatment.

3.2

Safety parameters (severity of eschar, edema, erythema, weight-bearing abilities, size of eschar and size of affected area) all indicated that addition of the adjuvant to PDT with verteporfin did not change the tolerability of this therapy (Figures 3-4). As expected, eschar, edema and erythema were noted in all PDT-treated animals and optimal PDT gave higher scores that sub-optimal PDT. However, the adjuvant did not worsen the scores in any of the measured parameters at either dose of adjuvant. The local effects of PDT had generally resolved themselves within 14 days with the exception of eschar, which did not disappear from all mice until day 20. All toxicities were local and did not lead to a drop in body weight (Figure 4D), indicating that these therapeutic regimens were well tolerated.
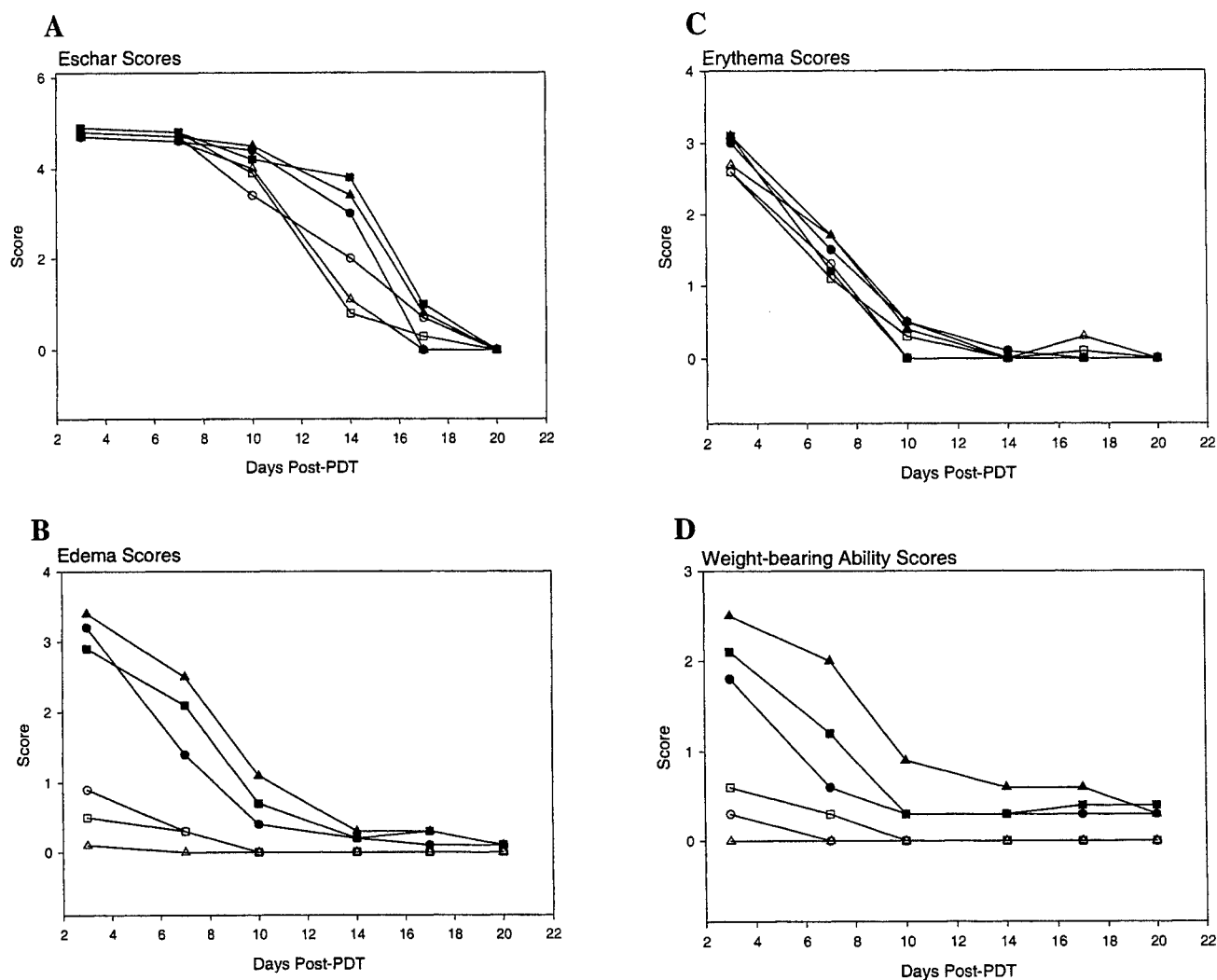
Figure 3. Eschar, edema, erythema, and weight-bearing ability scores. Tumor-bearing mice were treated with: Optimal PDT + low adjuvant (●); Optimal PDT + high adjuvant (■);Optimal PDT (▲); Sub-optimal PDT + low adjuvant (○); Optimal PDT + high adjuvant (□);Optimal PDT (△). Mice were monitored and scored for the degree of eschar (A), edema (B), erythema (C) and weight-bearing abilities (D) according to the scales in Table I. Each group contained 10 mice at treatment.

A

C

B

D
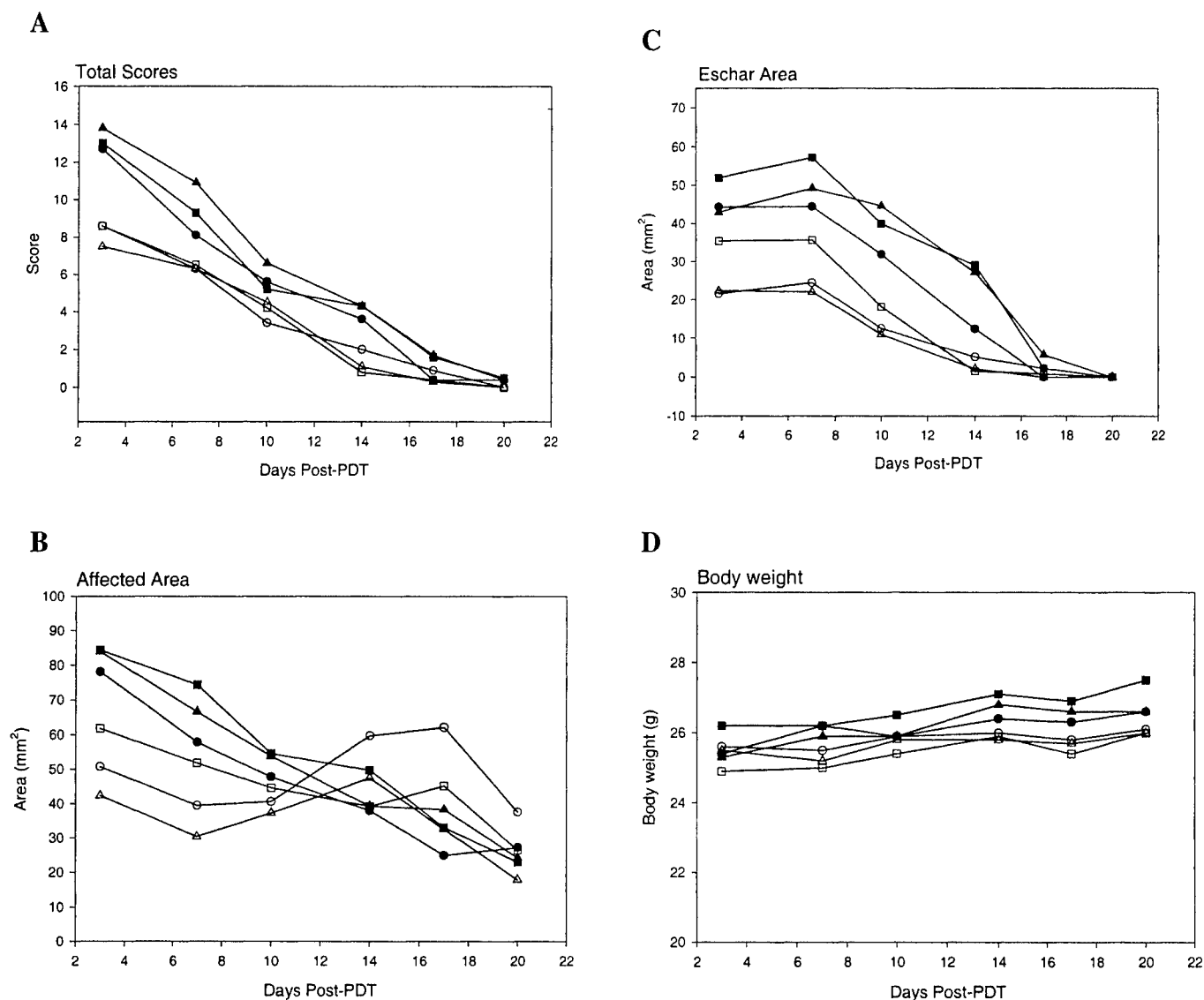
Figure 4. Total score (define in Table I), size of affected area, size of eschar and body weights. Tumor-bearing mice were treated with: Optimal PDT + low adjuvant (●); Optimal PDT + high adjuvant (■);Optimal PDT (▲); Sub-optimal PDT + low adjuvant (○); Optimal PDT + high adjuvant (□);Optimal PDT (△). Mice were monitored and scored for total score (A), size of affected area (B), size of eschar (C) and body weight (D) according to the scales in Table I. Each group contained 10 mice at treatment.

4. CONCLUSIONS

There were no adverse reactions associated with administration of the adjuvant following PDT. All safety parameter scores for PDV-treated animals were equivalent to the scores of animals treated with PDT throughout the observation periods. These data clearly demonstrate that ENHANZYN™ adjuvant can be combined safely with PDT.

The results of these experiments indicate that the efficacy of PDT has the potential to be improved with the use of the adjuvant. After optimal PDT, little difference in the rate of tumor re-growth or time to tumor reappearance was seen upon addition of the immune adjuvant. This was expected since this treatment regimen results in effective long-term tumor cure in mice.

The effect of adjuvant and sub-optimal PDT was less clear as both groups treated with adjuvant showed tumor re-growth earlier than those animals treated with PDT alone. However, tumors of mice receiving sub-optimal PDT followed by high dose immune adjuvant did not show the rapid, uncontrolled growth seen in other groups and, in the majority of cases, tumor volume decreased steadily with time. This resulted in a superior period of survival despite the animals being tumor-bearing.

Interestingly, the data obtained in this study clearly demonstrate the ability of PDT to protect against re-challenge with a second round of tumor implantation. This was seen in all groups and stresses the importance of the immune response in PDT tumor control. Addition of the high adjuvant dose to sub-optimal PDT appeared to be the most effective treatment group in this respect, giving complete inhibition of tumor re-implantation. However, some caution should be used interpreting these results, given the low numbers of animals available for re-challenge.

PDV is a safe variation of the PDT modality. In addition, ENHANZYN™ adjuvant may be able to augment the efficacy of PDT, particularly with regard to re-challenge at a second site. This may have implications for the control of metastases at sites distant from the treated primary tumor.

5. ACKNOWLEDGEMENTS

REFERENCES

1.   Henderson BW, Dougherty TJ. "How does photodynamic therapy work?" *Photochemistry and Photobiology.* **55**(1):145-157,1992.
2.   Ochsner M. "Photophysical and photobiological processes in the photodynamic therapy of tumours." *Journal of Photochemistry and Photobiology. B, Biology.* **39**(1):1-18,1997.
3.   Evans S, Matthews W, Perry R, Fraker D, Norton J, Pass HI. "Effect of photodynamic therapy on tumor necrosis factor production by murine macrophages." *Journal of the National Cancer Institute.* **82**:34-39,1990.
4.   Gollnick SO, Liu X, Owczarczak B, Musser DA, Henderson BW. "Altered expression of interleukin 6 and interleukin 10 as a result of photodynamic therapy in vivo." *Cancer Research.* **57**(18):3904-3909,1997.
5.   Nseyo UO, Whalen RK, Duncan MR, Berman B, Lundahl S. "Immune response following photodynamic therapy for bladder cancer." *Proceedings of the Society of Photo-Optical Instrumentation Engineers.* **1065**:66-72,1989.
6.   Fingar VH, Wieman TJ, Doak KW. "Mechanistic studies of PDT-induced vascular damage: evidence that eicosanoids mediate this process." *International Journal of Radiation Biology.* **60**(1-2):303-309,1991.
7.   Henderson BW, Donovan JM. "Release of prostaglandin E2 from cells by photodynamic treatment in vitro." *Cancer Research.* **49**(24 Pt 1):6896-6900,1989.
8.   Fingar VH, Wieman TJ, Doak KW. "Role of thromboxane and prostacyclin release on photodynamic therapy-induced tumor destruction." *Cancer Research.* **50**(9):2599-2603,1990.
9.   Foster TH, Primavera MC, Marder VJ, Hilf R, Sporn LA. "Photosensitized release of von Willebrand factor from cultured human endothelial cells." *Cancer Research.* **51**(12):3261-3266,1991.
10.   Qin B, Selman SH, Payne KM, Keck RW, Metzger DW. "Enhanced skin allograft survival after photodynamic therapy. Association with lymphocyte inactivation and macrophage stimulation." *Transplantation.* **56**(6):1481-1486,1993.
11.   Yamamoto N, Hoober JK, Yamamoto S. "Tumoricidal capacities of macrophages photodynamically activated with hematoporphyrin derivative." *Photochemistry and Photobiology.* **56**(2):245-250,1992.

12.   Yamamoto N, Sery TW, Hoober JK, Willett NP, Lindsay DD. "Effectiveness of photofrin II in activation of macrophages and in vitro killing of retinoblastoma cells." *Photochemistry and Photobiology.* **60**(2):160-164,1994.

13.   Korbelik M. "Induction of tumor immunity by photodynamic therapy." *Journal of Clinical Laser Medicine and Surgery.* **14**(5):329-334,1996.

14.   Korbelik M, Krosl G, Krosl J, Dougherty GJ. "The role of host lymphoid populations in the response of mouse EMT6 tumor to photodynamic therapy." *Cancer Research.* **56**(24):5647-5652,1996.

15.   Korbelik M, Dougherty GJ. "Photodynamic therapy-mediated immune response against subcutaneous mouse tumors." *Cancer Research.* **59**(8):1941-1946,1999.

16.   Korbelik M, Cecic I. "Contribution of myeloid and lymphoid host cells to the curative outcome of mouse sarcoma treatment by photodynamic therapy." *Cancer Letters.* **137**(1):91-98,1999.

17.   Hendrzak-Henion JA, Knisely TL, Cincotta L, Cincotta E, Cincotta AH. "Role of the immune system in mediating the antitumor effect of benzophenothiazine photodynamic therapy." *Photochemistry and Photobiology.* **69**(5):575-581,1999.

18.   Krosl G, Korbelik M, Krosl J, Dougherty GJ. "Potentiation of photodynamic therapy-elicited antitumor response by localized treatment with granulocyte-macrophage colony-stimulating factor." *Cancer Research.* **56**(14):3281-3286,1996.

19.   Casas A, Fukuda H, Meiss R, Batlle AM. "Topical and intratumoral photodynamic therapy with 5-aminolevulinic acid in a subcutaneous murine mammary adenocarcinoma." *Cancer Letters.* **141**(1-2):29-38, 1999.

20.   Myers RC, Lau BH, Kunihira DY, Torrey RR, Woolley JL, Tosk J. "Modulation of hematoporphyrin derivative-sensitized phototherapy with corynebacterium parvum in murine transitional cell carcinoma." *Urology.* **33**(3):230-235,1989.

21.   Cho YH, Straight RC, Smith JA, Jr. "Effects of photodynamic therapy in combination with intravesical drugs in a murine bladder tumor model." *Journal of Urology.* **147**(3):743-746, 1992.

22.   Krosl G, Korbelik M. "Potentiation of photodynamic therapy by immunotherapy: the effect of schizophyllan (SPG)." *Cancer Letters.* **84**(1):43-49, 1994.

23.   Korbelik M, Naraparaju VR, Yamamoto N. "Macrophage-directed immunotherapy as adjuvant to photodynamic therapy of cancer." *British Journal of Cancer.* **75**(2):202-207,1997.

24.   Korbelik M, Cecic I. "Enhancement of tumour response to photodynamic therapy by adjuvant mycobacterium cell-wall treatment." *Journal of Photochemistry and Photobiology. B, Biology.* **44**(2):151-158,1998.

25.   Chen WR, Adams RL, Carubelli R, Nordquist RE. "Laser-photosensitizer assisted immunotherapy: a novel modality for cancer treatment." *Cancer Letters.***115**(1):25-30,1997.

26.   Chen WR, Zhu WG, Dynlacht JR, Liu H, Nordquist RE. "Long-term tumor resistance induced by laser photo-immunotherapy." *International Journal of Cancer.* **81**(5):808-812,1998.

27.   Golab J, Wilczynski G, Zagozdzon R, Stoklosa T, Dabrowska A, Rybczynska J, et al. "Potentiation of the anti-tumour effects of Photofrin-based photodynamic therapy by localized treatment with G-CSF." *British Journal of Cancer.* **82**(8):1485-1491,2000.

28.   Richter AM, Sternberg E, Waterfield E, Dolphin D, Levy JG. "Characterization of benzoporphyrin derivative, a new photosensitizer." *Proceedings of the Society of Photo-Optical Instrumentation Engineers.* **997**:132-138,1998.

29.   Richter AM, Yip S, Waterfield E, Logan PM, Slonecker CE, Levy JG. "Mouse skin photosensitization with benzoporphyrin derivatives and Photofrin: macroscopic and microscopic evaluation." *Photochemistry and Photobiology.* **53**:281-286,1991.

30.   Richter AM, Kelly B, Chow J, Liu DJ, Towers GHN, Dolphin D, et al. "Preliminary studies on a more effective phototoxic agent than hematoporphyrin." *Journal of the National Cancer Institute.* **79**:1327-1332,1987.

Relevance of PDT-induced inflammatory response for the outcome of photodynamic therapy

Mladen Korbelik[*], Ivana Cecic[*], Jinghai Sun[*],

Cancer Imaging Department, British Columbia Cancer Agency, Vancouver, B.C., Canada

ABSTRACT

The treatment of solid cancerous lesions by photodynamic therapy (PDT) elicits an acute host reaction primarily manifested as a strong, rapidly developing inflammatory response. It is becoming increasingly clear that the destructive impact of the inflammatory process is directly responsible for the so-called indirect damage in PDT-treated tumors. The loss of vascular homeostasis followed by massive damage to vascular and perivascular regions in PDT-treated tumors and the ensuing tumor antigen-specific immunity, are direct consequences of critical initiating events including the action of complement, activation of poly(ADP-ribose)polymerase (PARP) and ischemia/reperfusion insult, and the associated cascades of tissue-destructive responses. Hence, the effectiveness of PDT as an anti-cancer modality is largely owed to the fact that it instigates a comprehensive engagement of powerful innate host defense mechanisms.

1. INTRODUCTION

While considerable progress has been made in the understanding of the antitumor immune response elicited by photodynamic therapy (PDT)[1-4], the impact of the PDT-induced host response that precedes this immune development has remained incompletely characterized. The early events, most of which are instigated already during photodynamic light treatment, include[5]:

1. Complement activation
2. Release of various potent mediators:
   - Degradation products of membrane phospholipids
   - Degradation products of extracellular matrix
   - Inflammatory chemokines and other cytokines
   - Platelet activators
   - Vasoactive mediators (arachidonic acid metabolites, histamine)
3. Coagulation cascade activation
4. Induction of vascular leakage
5. Development of ischemia/reperfusion insult
6. Activation of poly(ADP-ribose)polymerase (PARP)
7. Invasion of activated neutrophils, mast cells and monocytes/macrophages

Most of these events are mutually interrelated and, together with visibly manifested pronounced edema localized at the treatment site[6], they attest that the PDT treatment elicits a strong acute inflammatory reaction. It is becoming increasingly clear that this inflammatory cascade engages powerful innate host defense mechanisms, which make a major contribution to the effectiveness of PDT. An important role in this phenomenon have activated inflammatory cells (neutrophils, mast cells, monocytes/macrophages) that accumulate rapidly and in large numbers in PDT-treated tumors[1,3,7-9]. Contrary to a frequently held view, they are not innocent bystanders amassing as a consequence of PDT-generated necrosis. Blocking the activity of these cells dramatically reduces PDT-mediated tumor cures[10,11], which demonstrates that they are active participants in the destruction of targeted tumor tissue[1,3]. This work examines three other elements associated with the PDT-induced inflammatory reaction that have been largely neglected despite their uniquely powerful tissue-destructive capacities: complement activity, ischemia/reperfusion (I/R) insult and PARP activation.

[*] mkorbeli@bccancer.bc.ca; jsun@bccancer.bc.ca; icecic@bccancer.bc.ca; phone 1 604 877-6098; fax 1 604 877-6077; http://www.bccancer.bc.ca; Cancer Imaging Department, British Columbia Cancer Research Centre, 601 West 10th Avenue, Vancouver, B.C., Canada V5Z 1L3

2. ROLE OF COMPLEMENT IN PDT-INDUCED TUMOR DESTRUCTION

The multifactorial plasma protein cascade system called complement is the major noncellular system of innate immunity in humans[12]. Complement has the ability to kill directly, to mark the target with ligands for receptors of the cellular innate immune system and to elicit cellular and humoral responses from systems of acquired immunity. Due to its effective cytotoxic properties, overwhelming activation of the complement cascade can induce life threatening tissue damage. Aberrant regulation of complement activity is responsible for various autoimmune diseases, and is involved in other clinical conditions such as stroke[13], heart attack[14], adult respiratory syndrome[15], burn injuries[16], rejection following xenotransplantation[17], as well as in injury from bioincompatibility situations in patients undergoing dialysis[18] or cardiopulmonary bypass[19]. The complement system becomes activated not only in the presence of foreign cells and particles but also in cases of sudden tissue trauma, and this explains its involvement in the response of tumors to cancer treatments such as cryotherapy[20], hyperthermia[21], and PDT[22-24].

The role of complement in the PDT response was first documented by Lim and co-workers[22,23*], who showed that blocking complement by cobra venom factor treatment diminished the phototoxic effect of PDT on normal skin. Using immunohistochemistry, Liaw et al. demonstrated the deposition of complement in PDT-treated rabbit tumors[24]. Our studies of PDT-induced acute phase response, manifested prominently as a pronounced and protracted elevation in neutrophil blood levels, have identified complement as a key mediator of this phenomenon[5]. Complement depletion in mice prior to PDT by treatment with the C3 convertase inhibitor N-acetyl-L-aspartyl-glutamic acid (NAAGA), resulted in the reduced cure rate of subcutaneous EMT6 tumors (Cecic and Korbelik, unpublished).

The exact mechanism underlying the induction of complement activation by PDT deserves detailed examination. Judging from the available general knowledge on complement activation, there are at least several possible scenarios or even their combination:

⇒ Since various forms of oxidative stress have been shown to directly trigger complement deposition on cultured endothelial cells[25], this could also include the PDT-induced oxidative stress, either by primary-generated oxidative radicals or by secondary-generated oxidative species associated with I/R injury (see below);

⇒ The exposure of basement membrane in the endothelial wall following the retraction of injured endothelial cells (reported to occur also in the vascular endothelium of PDT-treated tumors[26]) is known to prompt complement fixation[27];

⇒ Some of the events initiated by PDT treatment may promote on endothelial and other cells the downregulation of membrane-bound complement regulatory proteins (mCRPs) that are responsible for the resistance of these cells to complement-mediated damage[28]. Among such PDT-associated events that are known to reduce the expression of mCRPs are ischemia[29], apoptosis[30] and cytokine activity[28].

⇒ PDT-induced apoptosis may activate complement not just by downregulating mCRPs, but because of the expression of molecules on apoptotic cell membranes such as the elongation factor-1α, which activate homologous complement and accept complement fragments[31,32].

The activation of complement cascade in PDT-treated tumors is most likely responsible for many inflammatory and immune events essential for the therapeutic outcome with this cancer treatment modality. Based on the available evidence and general knowledge of complement, its activation triggered by binding of the recognition component to PDT-affected tumor cells or acellular fragments will prompt a complex series of events that include:

❖ Advancement of complement cascade (by sequential activation through the proteolytic cleavage and association of precursor molecules[12]) leading to formation of its biologically most active components, anaphylatoxins and membrane attack complex (C5b-9, MAC);

❖ Release of arachidonic acid from cellular membranes and formation of its metabolites (thromboxane, leukotrienes, prostaglandins);

❖ Release of chemokines attracting the influx of neutrophils and other inflammatory cells;

❖ Mast cell activation followed by histamine release from these cells;

❖ Release of cytokines, in particular TNF-α, IL-1β, IFN-γ, IL-6, and IL-10;

❖ Increased expression of adhesion molecules on endothelial cells and invading inflammatory cells;

❖ Release of platelet activating factor, platelet activation;

❖ Activation of the coagulation cascade;

❖ Anaphylatoxin-mediated induction of acute phase response (distant reactions including the elevation in serum levels of acute phase proteins, adrenal hormone release, pronounced neutrophilia with depletion of bone marrow pools of these cells);

❖ Direct killing of cancer cells by the MAC component;

❖ Advancement of I/R injury;

❖ Vascular collapse and damage to perivascular tumor regions;

❖ Rapid clearance of tumor cell debris by massively mobilized phagocytes;

❖ Promotion of immune recognition of tumor antigens and further development of antigen-specific immune response.

Further research of the above mentioned complement activities in PDT-treated tumors will improve the understanding of the mechanism of action of PDT. Appreciation for the importance of the complement system's participation in the antitumor effect of PDT has prompted us to extend our research into testing approaches for boosting the extent and duration of complement activation within PDT-treated tumors. These ongoing studies will show whether combining PDT and treatment for improved complement activation could be of therapeutic benefit. This happens to be in tune with current developments in the research for novel anti-cancer modalities, where strategies for cancer destruction by activated complement have a prominent role.

3. ISCHEMIA/REPERFUSION INJURY IN PDT-TREATED TUMORS

Ischemia/reperfusion (I/R) injury is a classical physiological insult responsible for severe tissue damage in a variety of common pathological conditions (including myocardial infarction, stroke, acute kidney and liver failure, pulmonary and hemorrhagic shock, and organ transplant rejection)[33-35]. During tissue ischemia, xanthine dehydrogenase is converted into the oxidant-producing xanthine oxidase while the breakdown of ATP leads to the accumulation of hypoxanthine. Sudden re-introduction of oxygen at the time of reperfusion will then lead to the conversion of hypoxanthine into xanthine by xanthine oxidase, which is associated with massive generation of reactive oxygen species, primarily superoxide anion[33]. This results in the induction of oxidative stress at the level of vascular epithelium that promotes complement activation leading to the formation of inflammatory agents which recruit and activate host neutrophils[36]. As a result, I/R injury is manifested as microvascular and perivascular cell disfunction in the affected tissues.

We have suggested that the induction of I/R injury is one of the elements of the response of tumors to PDT[37-39]. Basic events associated with the induction of I/R injury following PDT treatment can be outlined as follows:

● Generation of ischemia due to
  - depletion of oxygen through its consumption by the photodynamic process
  - reduced tumor blood flow consequent to the vasoconstriction produced by thromboxane (formed via induced arachidonic acid metabolism);

● Buildup of xanthine oxidase and hypoxanthine in the ischemic tissue;

● Reperfusion of PDT-treated tumor tissue due to vasodilatation coming from the action of histamine (result of complement-mediated mast cell activation) and prostaglandins (additional arachidonic acid metabolites);

● Intense generation of superoxide, particularly in the vascular endothelium of PDT-treated tumors brought about by sudden oxygen re-introduction;

● Massive damage in the affected endothelium provoking the activation of PARP and complement deposition;

● Pervasive injury in the vascular and perivascular regions of PDT-treated tumors inflicted through the contribution of massively recruited neutrophils and other inflammatory cells and by the cytolysis mediated by MAC.

Evidence that supports the suggestion that I/R injury contributes to the therapeutic outcome of PDT has been obtained with several types of treatment that blocks/inhibits this insult. The i.v. administration of superoxide dismutase (SOD) to EMT6 or FsaR tumor bearing mice immediately after PDT decreased the cure rates of these tumors, which indicates that superoxide formation occurs at the level of vascular endothelium during that treatment interval and contributes to the antitumor effect[37]. A more direct demonstration was provided by treatment with the xanthine oxidase inhibitor oxypurinol, which showed that blocking the activity of this key enzyme in I/R injury diminished the cures of PDT-treated mouse tumors[5]. Interestingly, an enhancement in the cure rate of PDT-treated tumors was obtained with the antihistamine agent pyrilamine (Korbelik and Sun, unpublished). This latter result may reflect the impairment of histamine-mediated vasodilatation causing the prolongation of the initial ischemic episode in PDT-treated tumors.

4. INVOLVEMENT OF PARP IN PDT-MEDIATED TISSUE INJURY

This nuclear nick sensor enzyme plays an important role in the induction of cellular damage following I/R, and its involvement is also implicated in other inflammatory responses[40-42]. The induction of DNA damage initiated by reactive species such as superoxide anion activates PARP, which catalyzes the attachment of ADP ribose units from NAD to nuclear proteins and temporarily protects the damaged site. Excessive activation of PARP results in rapid depletion of intracellular pools of NAD^+, as well as ATP that is consumed in NAD regeneration, which slows the rate of glycolysis and mitochondrial respiration leading to cellular energy depletion and necrosis[43]. In addition, the inhibition of PARP was shown to attenuate the recruitment of neutrophils to the affected site and exert other anti-inflammatory effects[42]. The mechanism of this pro-inflammatory action of PARP has not been characterized, but it may simply reflect the participation of PARP in the induction of pro-inflammatory damage, possibly by promotion of complement activation.

As mentioned above, the evidence on secondary superoxide induction during I/R episodes in PDT-treated tumors implicates its role in the damage induced in the cells of vascular endothelium, and this may cause the activation of PARP. While the activation of this enzyme in PDT-treated tumors still remains to be directly verified, using the PARP inhibitor 3-aminobenzamide[42] we have obtained evidence on its participation in the PDT response. Our results show that the administration of this inhibitor reduced the rise in peripheral blood neutrophil levels in the mice bearing PDT-treated tumors. Furthermore, pretreatment of mice with 3-aminobenzamide before PDT markedly reduced the cure rate of treated tumors[5].

The relationship between the PARP-mediated necrosis and the apoptotic process triggered by direct phototoxic injury could be of a particular value for better understanding of the antitumor effect of PDT. During apoptosis, caspases cleave PARP, presumably as an energy-conserving step needed for the completion of the apopototic process[44]. It remains to be determined whether the modulation of PARP activity in PDT-treated tumors shifts the balance between the necrotic and apoptotic death and how this balance is relevant for the therapeutic outcome.

4. CONCLUSIONS

The insult mediated by PDT-mediated oxidative stress has a strong pro-inflammatory character. This attribute is owed to a large extent to its ability to initiate key events including the activation of complement cascade and PARP, and the generation of I/R injury. These events are responsible for drastic perturbation in normal homeostasis of the treated tissue, which triggers inherent mechanisms for signaling injury through a massive release of various potent pro-inflammatory mediators. The host usually tolerates progressively growing cancerous tumors because they have evaded its surveillance mechanisms. Following PDT treatment of these lesions, the host is compelled to recognize their injurious potential and responds by engaging the inflammatory process in order to contain and destroy this threat. It is becoming increasingly clear that this engagement of powerful innate host defense mechanisms makes a major contribution to the effectiveness of PDT. Both noncellular (complement) and cellular (inflammatory cells) arms of the efferent limb of innate immunity not only actively contribute to the destruction of PDT-treated tumors but also orchestrate the development of adaptive (acquired) immune response. This results in the immune recognition of even poorly immunogenic tumors following PDT and the generation of antitumor immunity that contributes to diminished recurrence of these lesions.

ACKNOWLEDGEMENTS

REFERENCES

1. T. J. Dougherty, C. J. Gomer, B. W. Henderson, G. Jori, D. Kessel, M. Korbelik, J. Moan, Q. Peng, "Photodynamic therapy," *J. Natl. Cancer Inst.* **90**, pp. 889-905, 1998.
2. B. W. Henderson, and T. J. Dougherty, "How does photodynamic therapy work?," *Photochem. Photobiol.* **55**, pp. 145-157, 1992.
3. M. Korbelik, "Induction of tumor immunity by photodynamic therapy," *J. Clin. Med. Lasers Surg.* **17**, pp. 329-334, 1996.
4. M. Korbelik, "Antitumor immune reaction elicited by photodynamic therapy," *Proc. SPIE* **3601**, pp. 68-74, 1999.

5. M. Korbelik, "The role of immune cells in PDT-induced death of cancer cells," *13th Internat. Congress on Photobiology*, San Francisco, July 1-6, 2000.

6. V.H. Fingar, "Vascular effects of photodynamic therapy," *J. Clin. Med. Lasers Surg.* **17**, pp. 323-328, 1966.

7. S. O. Gollnick, X. Liu, B. Owczarczak, D. A. Musser, and B. W. Henderson, "Altered expression of interleukin 6 and interleukin 10 as a result of photodynamic therapy *in vivo*," *Cancer Res.* **57**, pp. 3904-3909, 1997.

8. G. Krosl, M. Korbelik, and G. J. Dougherty, "Induction of immune cell infiltration into murine SCCVII tumour by Photofrin-based photodynamic therapy," *Br. J. Cancer* **71**, pp. 549-555, 1995.

9. M. Korbelik and I. Cecic, "Enhancement of tumor response to photodynamic therapy by adjuvant mycobacterium cell wall treatment," *J. Photochem. Photobiol. B: Biol.* **44**, pp. 151-158, 1998.

10. M. Korbelik, and I. Cecic, "Contribution of myeloid and lymphoid host cells to the curative outcome of mouse sarcoma treatment by photodynamic therapy," *Cancer Lett.* **137**, pp. 91-98, 1999.

11. W.J.A. de Vree, M.C. Essers, H.S. de Brujin, W.M. Star, J.F. Koster, and W. Sluiter, "Evidence for an important role of neutrophils in the eficacy of photodynamic therapy *in vivo*," *Cancer Res.* **56**, pp. 2908-2911, 1996.

12. N.R. Cooper, "Biology of the complement system," *Inflammation: Basic Principles and Clinical Correlations*, J.I. Galin and R. Snyderman editors, pp. 281-315, Lippincott Williams & Wilkins, Philadelphia, 1999.

13. U.S. Vasthare, R.H. Rosenwasser, F.C. Barone, and R.F. Tuma, "Involvement of the complement system in cerebral ischemic and reperfusion injury," *FASEB J.* **7**, pp. A424, 1993.

14. K.S. Kilgore, G.S. Friedrichs, J.W. Homeister, and B.R. Lucchesi, "The complement system in myocardial ischemia/reperfusion injury," *Cardiovasc. Res.* **28**, pp. 437-444, 1994.

15. R.A. Robbins, W.D. Russ, J.K. Rassmusen, and M.M. Clayton, "Activation of the complement system in the adult respiratory distress syndrome," *Am. Rev. Respir. Dis.* **135**, pp. 651-658, 1987.

16. R. Gallinaro, W.G. Cheadle, K. Applegate, and H.C.J. Polk, "The role of the complement system in trauma and infection," *Surg. Gynecol. Obster.* **174**, pp. 435-440, 1992.

17. M.W. Wang, P.S. Johnston, L.J. Wright, S.M.L. Lim, and D.J.G. White, "Immunofluorescent localization of pig complement component-3, regardless of the presence or absence of detectable immunoglobulins, in hyperacutely rejected heart xenografts," *Histochem. J.* **24**, pp. 102-109, 1992.

18. M. Pekna, L. Nilsson, K. Nilssonekdahl, U.R. Nilsson, and B. Nilsson, "Evidence for iC3 generation during cardiopulmonary bypass as the result of blood-gas interaction," *Clin. Exp. Immunol.* **91**, pp. 404-409, 1993.

19. A.M. Gillinov, J.M. Redmond, J.A. Winkelstein, K.J. Zehr, A. Herskowitz, W.A. Baumgartner, and D.E. Cameron," Complement and neutrophil activation during cardiopulmonary bypass: A study in the complement-deficient dog," *Ann. Thorac. Surg.* **57**, pp. 345-352, 1994.

20. R.J. Ablin, "An appreciation and realization of the concept of cryoimmunology," *Percutaneous Prostate Cryoablation*, G.M. Onik, R.J. Ablin and B. Rubinsky editors, pp. 136-154, Quality Medical Publishing, Inc., St. Louis, 1995.

21. J.P. Arnestad, A. Bengston, J.P. Bengston, B.A. Henriksson, O. Stenqvist, P. Naredi, and L. Hafstrom, "Isolated hyperthermic liver perfusion with cytostatic-containing perfusate activates the complement cascade," *Br. J. Surg.* **79**, pp. 948-951, 1992.

22. R. Kamide, I. Gigli, and H.W. Lim, "Participation of mast cells and complement in the immediate phase of hematoporphyrin-induced phototoxicity," *J. Invest. Dermatol.* **82**, pp. 485-490, 1984.

23. H.W. Lim, L. Young, M. Hagan, and I. Gigli, "Delayed phase of hematoporphyrin-induced phototoxicity: modulation by complement, leukocytes, and antihistamines," *J. Invest. Dermatol.* **84**, pp. 114-117, 1985.

24. L.-H.L. Liaw, J.S. Nelson, R.S. Steubing, G.P. Lim, and M.W. Berns, "Complement activation during tumor photodynamic therapy," *Internat. Conf. On Photodynamic Therapy and Laser Medicine*, Abstract L100, Beijing, October 15-17, 1991.

25. C.D. Collard, R. Lekowski, J.E. Jordan, A. Agah, and G.L. Stahl, "Complement activation following oxidative stress," *Molec. Immunol.* **36**, pp. 941-948, 1999.

26. V.H. Fingar, "Vascular effects of photodynamic therapy," *J. Clin. Laser Med. Surg.* **14**, pp. 323-328, 1996.

27. E.J. Hindmarsh, and R.M. Marks, "Complement activation occurs on subendothelial extracellular matrix *in vitro* and is initiated by retraction or removal of overlying endothelial cells," *J. Immunol.* **160**, pp. 6128-6136, 1998.

28. A. Gorter, and S. Meri, "Immune evasion of tumor cells using membrane-bound complement regulatory proteins," Immunol. Today 20, pp. 576-582, 1999.

29. A. Väkevä, and S. Meri, "Complement activation and regulator expression after anoxic injury of human endothelial cells," *APMIS* **106**, pp. 1149-1156, 1998.

30. T. Hara, M. Marsumoto, S. Tsuji, S. Nagasawa, A. Hiraoka, T. Masaoka, K. Kodama, T. Horai, T. Sakuma, and T. Seya, "Homologous complement activation on drug-induced apoptotic cells from a human lung adenocarcinoma cell line," *Immunobiology* **196**, pp. 491-503, 1996-97.

31. H. Aoki, F. Takizawa, S. Tsuji, and S. Nagasawa, "Elongation factor-1α as a homologous complement activator of Jurkat cells," *Int. J. Mol. Med.* **6**, pp. 87-92, 2000.

32. S. Tsuji, K. Kaji, and S. Nagasawa, "Activation of the alternative pathway of human complement by apoptotic human umbilical vein endothelial cells," *J. Biochem. (Tokyo)* **116**, pp. 794-800, 1994.

33. B.J. Zimmerman, and D.N Granger, "Mechanisms of reperfusion injury," *Am. J. Med. Sci.* **307**, pp. 284-292, 1994.

34. K.E de Greef, D.K. Ysebaert, M. Ghielli, S. Vercauteren, E.J. Nouwen, E.J. Eyskens, and M.E. de Broe, "Neutrophils and acute ischemia-reperfusion injury," *J. Nephrol.* **11**, pp. 110-122, 1998.

35. L.A. Hernandez, M.B. Grisham, B. Twohig, K.E. Arfors, J.M. Harlan, and D.N. Granger, "Role of neutrophils in ischemia-/reperfusion-induced microvascular injury," *Am. J. Physiol.* **253**, pp. H699-H703, 1987.

36. K.S. Kilgore, R.F. Todd III, and B.R. Lucchesi, "Reperfusion injury," *Inflammation: Basic Principles and Clinical Correlations*, J.I. Galin and R. Snyderman editors, pp. 1047-1060, Lippincott Williams & Wilkins, Philadelphia, 1999.

37. M. Korbelik, C.S. Parkins, H. Shibuya, I. Cecic, M.R.L. Stratford, and D.J. Chaplin, "Nitric oxide production by tumour tissue: impact on the response to photodynamic therapy," *Br. J. Cancer* **82**, pp. 1835-1843, 2000.

38. M. Korbelik, I. Cecic, and H. Shibuya, "The role of nitric oxide in the response of cancerous lesions to photodynamic therapy," *Recent Research Developments in Photochemistry and Photobiology*, S.G. Pandalai editor, Vol. 1, pp. 267-276, Transworld Research Network, Trivandrum, India, 1997.

39. M. Korbelik, H. Shibuya, and I. Cecic, "Relevance of nitric oxide to the response of tumors to photodynamic therapy," *Proc. SPIE* **3247**, pp. 98-105, 1998.

40. Y. Le Rhun, J.B. Kirkland, and G.M. Shah, "Cellular responses to DNA damage in the absence of poly(ADP-ribose)polymerase," *Biochem. Biophys. Res. Commun.* **245**, pp. 1-10, 1998.

41. Z. Yang, B. Zingarelli, and C. Szabo, "Effect of genetic disruption of poly (ADP-ribose)synthetase on delayed production of inflammatory mediators and delayed necrosis during myocardial ischemia-reperfusion injury," *Shock* **13**, pp. 60-66, 2000.

42. C. Szabo, L.H.K. Lim, S. Cuzzocrea, S.J. Getting, B. Zingarelli, R.J. Flower, A.L. Salzman, and M. Perreti, "Inhibition of poly(ADP-ribose)synthetase attenuates neutrophil recruitment and exerts antiinflammatory effects," *J. Exp. Med.* **186**, pp. 1041-1049, 1997.

43. C. Szabo, and V.L. Dawson, "Role of poly (ADP-ribose) synthetase activation in inflammation and reperfusion injury," *Trends Pharmacol. Sci.* **19**, pp. 287-298, 1998.

44. L. Virag, G.S. Scott, S. Cuzzocrea, D. Marmer, A.L. Salzman and C. Szabo, "Peroxynitrite-induced thymocyte apoptosis: the role of caspases and poly (ADP-ribose) synthetase (PARS) activation," *Immunology* **94**, pp. 345-355, 1998.

Photodynamic therapy (PDT) treatment enhances tumor cell antigenicity

Sandra O. Gollnick[*], Andrea Mazzacua, Lurine Vaughan, Barbara Owczarczak, Patricia Maier and
Barbara W. Henderson

PDT Center, Roswell Park Cancer Institute

ABSTRACT

Several groups, including our own, have reported that PDT enhances the host anti-tumor immune response and it is known that the enhanced immune response plays a role in the overall tumor response to PDT. The mechanism behind this enhancement is unknown, however it has been shown that the initiation of an inflammatory response and the infiltration of neutrophils into the tumor bed is critical to the tumor response. We have shown that PDT induces the expression of chemokines that play a critical role in neutrophil infiltration. Recent studies in our laboratory have shown that in addition to affecting the inflammatory and chemokine/cytokine response, PDT also alters the immunogenicity of the tumor, either through changes in antigen structure or enhancement of presentation of tumor associated antigens by host antigen presenting cells to tumor specific T cells. These recent studies and the underlying mechanisms will be discussed.

1. INTRODUCTION

Photodynamic therapy (PDT) refers to the use of a photoreactive drug or photosensitizer in combination with a specific wavelength of light to kill tumor tissue (reviewed in (7)). Results from worldwide studies using the clinically approved photosensitizer Photofrin® have shown that PDT leads to palliation of advanced disease and long-term tumor control of early disease. Numerous pre-clinical studies have demonstrated that PDT enhances host anti-tumor immunity. Korbelik et al (17) demonstrated that PDT treatment of tumor-bearing immuno-compromised mice was not effective at inducing long-term tumor cure; however treatment of the same tumors in immuno-competent mice did result in long-term tumor cures and adoptive transfer of bone marrow from immuno-competent mice to immuno-compromised mice restored the ability of PDT to induce long-term tumor cures. In addition several groups including our own have shown that tumor draining lymph node cells isolated from PDT-treated animals suppress tumor growth when co-injected into naïve animals with a tumorigenic dose of tumor cells (3,5).

The mechanism(s) leading to the enhancement of the anti-tumor immune response by PDT is unknown, although several possibilities have been proposed (7,14,16,9). These hypotheses include enhanced release of tumor-associated antigens (TAA) following PDT, as well as activation of the inflammatory response and stimulation of the expression of immuno-enhancing cytokines by PDT. In the following report we will present evidence that PDT induces chemokines critical for neutrophil activation, thus enhancing the inflammatory response and that PDT can directly enhance tumor cell antigenicity.

2. MATERIALS AND METHODS

2.1 Animals.

BALB/cJ mice, obtained pathogen-free from the Jackson Laboratories (Bar Harbor, ME), were used for all experiments, either tumor free of carrying the EMT6 mammary tumor (12). Animals were housed in microisolator cages in a laminar flow unit under ambient light. Six to 12 week old animals were inoculated intradermally on the shoulder with 2×10^5 tumor cells harvested from exponentially growing cultures. Prior to tumor inoculation and/or light treatment, all hair was removed from the prospective treatment site by shaving and depilation. Tumors were used for experimentation about 10 days after inoculation when they had reached a size of 6-8 mm in diameter.

2.2 Reagents.

Clinical-grade, pyrogen-free hexa-pyropheophorbide (HPPH) was obtained from the Roswell Park Pharmacy and reconstituted to 0.4mM in pyrogen-free 5% dextrose (D5W; Baxter Corp., Deerfield, IL) containing 2% ethanol and 0.1% Tween. Photofrin® was obtained from QLT PhotoTherapeutics Inc., Vancouver, B.C.

2.3 *In vivo* PDT Treatment.

Animals were given intravenous injections via tail vein of 0.4µM/kg HPPH, followed 24 h later with illumination at 665 nm light using an argon-dye laser system (Spectra Physics, Mt. View, CA). A treatment field 1 cm in diameter,

---

[*] Sandra.Gollnick@roswellpark.org; phone 1 716 845 8877 fax 1 716 845 8920; PDT Center, Roswell Park Cancer Institute, Elm and Carlton Sts. Buffalo, NY 14263

containing the tumor, was illuminated at 75 mW/cm^2 for a total light dose of 100 J/cm^2. At selected time intervals following light exposure, treated and control animals were sacrificed and tumors were harvested and processed immediately for reverse-transcriptase polymerase chain reaction RT-PCR as described (9). All experiments included control animals without treatment and animals with photosensitizer only.

2.4 RNA Isolation and RT-PCR.

Total RNA was isolated from either cells or tissue with STAT-60 (Tel-Test, Inc., Friendswood, TX). RNA was quantified spectrophotometrically and diluted to a final concentration of 2 µg/ml. Reverse transcriptase-PCR (RT-PCR) was done as previously described (9) using KC, MIP-1α and MIP-1β (30 PCR cycles) specific primers (22). Amplification using actin (25 PCR cycles) specific primers (Stratagene, La Jolla, CA) was used as a control. The reaction products were separated on a 2% agarose gel, stained with ethidium bromide, examined under UV light and subjected to densiotometry. Control PCR reactions were performed with "cDNA" synthesized in the absence of reverse transcriptase. Reagents were routinely checked for contamination and results were confirmed in three replicate experiments.

2.5 *In vitro* PDT Treatment.

EMT6 cells were grown in DMEM supplemented with 10% FBS, sodium pyruvate, L-glutamine and antibiotics; cells were cultured in a humidified atmosphere of 5% CO$_2$ in air at 37°C. For PDT-generated lysates, exponentially growing cells were exposed to 10µg/ml Photofrin® (QLT PhotoTherapeutics Inc., Vancouver, B.C.) in complete medium for 24h, followed by exposure to drug-free complete medium for 3 h. Cells were then transferred to serum free medium (Ham's F12; GIBCO) at 1 x 10^7 cells/ml and illuminated with 630 nm light via an argon-dye laser system (Spectra Physics, Mt. View, CA) with a dose equivalent to the lethal dose$_{99}$ (LD$_{99}$) (P815 ~0.8 J/cm^2). Treated cells were incubated in a humidified atmosphere of 5% CO$_2$ at 37°C for 48 h.

2.6 Tumor Response Determinations.

Tumor growth was monitored every other day in animals treated with PDT or photosensitizer alone beginning two days post-treatment and continuing until the tumors reached 400 mm^3 or 30 d, which ever occurred first, at which point the animals were euthanized.

3. RESULTS

3.1 PDT enhances inflammatory chemokine mRNA expression

One of the earliest events following PDT treatment is the initiation of an inflammatory response that is characterized by the rapid accumulation of neutrophils, mast cells and macrophages into the tumor bed (18,9). The infiltrating cells rapidly outnumber the tumor cells and are predominated by neutrophils, which appear to play a critical role in the PDT response (17,6,14,15). In order to determine a potential mechanism behind the PDT-induced neutrophil migration into the treated tissue, we examined the effect of PDT on expression of mRNA of chemokines critical to neutrophil extravasation. One of the chemokines involved in murine neutrophil recruitment is the cytokine-induced neutrophil chemoattractant (KC), a homologue of the human chemokine growth-related oncogene (GRO) (23,21,2). The chemokines MIP-1α and MIP-1β are macrophage attractants (19,1). PDT induced a 2.6 ± 0.2 fold increase in KC mRNA as compared to HPPH only controls (p<0.0013), peaking at 3 h post-PDT. KC mRNA levels remained elevated for 24 h post-treatment (Figure 1A). PDT also resulted in a 2.3 ± 0.9 fold increase in macrophage inflammatory protein (MIP)-1α mRNA levels, peaking 24 h post-treatment and returning to baseline levels by 48 h post PDT. The increase in MIP-1α levels was not significant when compared to HPPH only control levels (p<0.101). No increase was observed in MIP-1β mRNA levels. EMT6 cells express low levels of KC mRNA *in* vitro, however *in vitro* PDT treatment of EMT6 cells did not alter the expression of KC or MIP-1α (data not shown). Thus PDT alters the mRNA expression of a chemokine involved in neutrophil migration.

3.2 PDT enhances tumor cell antigenicity.

To determine if PDT enhancement of tumor immunity is due in part to the direct effects of PDT on tumor cells, we tested the protective ability of tumor cell lysates generated by *in vitro* PDT treatment at a LD$_{99}$. Naïve animals were vaccinated once a week in the right shoulder with 30 µl (3 x 10^5 cell equivalents) of lysate or 30 µl of Ham's F12 media. The animals were rested one week and inoculated with a tumorigenic dose of exponentially growing tumor cells. As shown in Table 1, animals vaccinated with PDT-generated tumor cell lysate provided protection against subsequent tumor challenge that was better than protection provided by tumor cell lysates generated by three freeze thaw cycles. These results suggest that PDT enhances tumor cell antigenicity.

Table 1: PDT Enhances Tumor Cell Antigenicity

Vaccination	Challenge	Tumor Take
None	EMT6	5/5
PDT-generated Lysate	EMT6	2/5
Freeze/Thaw-generated Lysate	EMT6	3/3
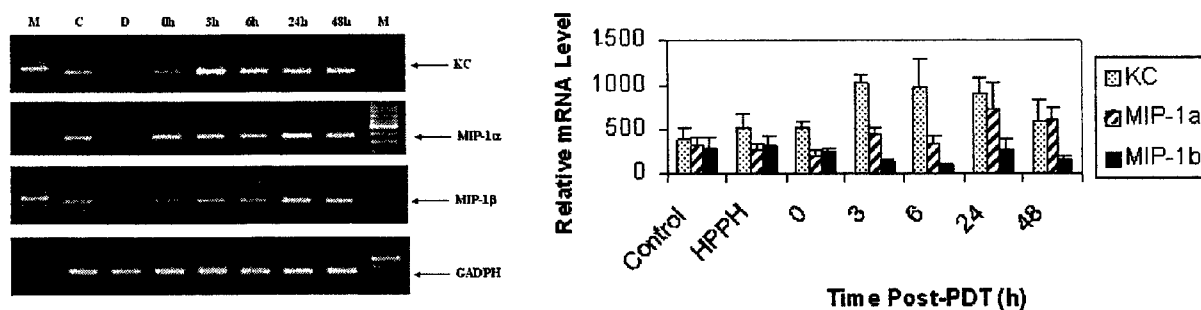
Figure 1: PDT Induces Chemokine mRNA Expression. (A) Total RNA was isolated from EMT6 tumors harvested at various times post-PDT and 2 μg from each sample were subjected to RT-PCR analysis as described in Materials and Methods. HPPH only (D) and untreated controls (C) were harvested 6 h "post-PDT". A representative experiment is shown. (B) Total RNA was isolated from tumors at various times post-PDT and 2 μg from each sample were subjected to RT-PCR analysis as described in Materials and Methods. Results are presented as in relative chemokine mRNA levels ± SEM following normalization to the GADPH mRNA levels. A minimum of three independent experiments is shown for each time point. HPPH only (D) and untreated controls (C) were harvested 6 h "post-PDT".

4. DISCUSSION

The mechanism behind PDT enhancement of the host anti-tumor immune response is unknown. However several potential mechanisms have been hypothesized including release of previously sequestered tumor antigens and activation of the immune response via induction of immuno-stimulatory cytokines (7). We have previously shown that PDT induces alterations in the cytokine expression in the tumor bed (9) resulting in an increase in IL-6 expression. IL-6 is an inflammatory cytokine and has been shown to be important in the amplification of the inflammatory response and in the generation on cytotoxic T lymphocytes (13). In the current report we have examined the effect of PDT on the expression of inflammatory chemokines, KC and MIP-1. KC is the murine homologue of the human chemokine growth-related oncogene (GRO) (2) and has been shown to play a role in neutrophil migration. Several studies have shown that neutrophils play a critical role in long-term tumor control by PDT (6,15). Neutrophils have been implicated in tumor control in several model systems (11,4,20) and have the capability of triggering the host immune response (8,10). Thus increased expression of inflammatory cytokines following PDT may be a mechanism by which PDT enhances the host anti-tumor immune system.

We have also examined the ability of PDT to enhance tumor antigenicity directly. Our studies demonstrating that vaccination with PDT-generated tumor cell lysates provide better protection than does vaccination freeze/thaw-generated tumor cell lysates, suggest that PDT is altering the immunogenicity of the tumor cell directly. Singlet oxygen is released following illumination of the photosensitizer and has the potential to react with proteins within the cell to generate new antigens. Therefore PDT may also be increasing the host anti-tumor immune response through its ability to generate novel tumor antigens.

Induction of inflammatory mediators and generation of novel tumor antigen are two possible means by which PDT enhances the host response to tumors. It is unlikely that these are the sole mechanisms or that any of the mechanisms will be sufficient alone. PDT tumor control is the result of a complex array of primary effects on the tumor cell itself and secondary effects tumor vasculature and host inflammatory response. Each of these effects is inter-related and thus it is likely that the mechanisms behind the generation of an anti-tumor immune response following PDT will also be complex and dependent upon a number of factors. However, the understanding of the mechanisms will allow manipulation of the PDT effect on host immune response, potentially allowing for further amplification of the host immune response.

ACKNOWLEDGMENTS

REFERENCES

1. M. Baggiolini, "Chemokines and leukocyte traffic." *Nature* **392**, pp. 565-568, 1998.

2. C. R. Bozic, L. F. Kolakowski, N. P. Gerard, C. Garcia-Rodriguez, C. Von Uexkull-Guldenbanc, M. J. Conklyn, R. Breslow, H. J. Showell, and C. Gerard, "Expression and biologic characterization of the murine chemokine KC." *J.Immunol.* **154**, pp. 6048-6057, 1995.

3. G. Canti, D. Lattuada, A. Nicolin, P. Taroni, G. Valentini, and R. Cubeddu, "Immunopharmacology studies on photosensitizers used in photodynamic therapy (PDT)" *SPIE* **2078**, pp. 268-275, 1994.

4. M. P. Colombo, L. Lombardi, A. Stoppacciaro, C. Melani, M. Parenza, B. Bottazzi, and G. Parminani, "Granulocyte colony-stimulating factor (G-CSF) gene transduction in murine adenocarcinoma drives neutrophil-mediated tummor inhibition in vivo: neutrophils discriminate between G-CSF-producing and G-CSF non-producing tumor cells." *J.Immunol.* **149**, pp. 113-119, 1992.

5. P. M. Curry and J. G. Levy, "Tumor inhibitory lymphocytes derived from the lymph nodes of mice treated with photodynamic therapy" *Photochemistry and Photobiology* **61S** , pp. 72S-1995.

6. W. J. de Vree, M. C. Essers, H. S. De Bruijn, W. M. Star, J. F. Koster, and W. Sluiter, "Evidence for an important role of neutrophils in the efficacy of photodynamic therapy *in vivo.*" *Cancer Res* **56**, pp. 2908-2911, 1996.

7. T. J. Dougherty, C. J. Gomer, B. W. Henderson, G. Jori, D. Kessel, M. Korbelik, J. Moan, and Q. Peng, "Photodynamic Therapy" *J.Natl.Cancer Inst.* **90**, pp. 889-905, 1998.

8. N. A. Fanger, C. L. Liu, P. M. Guyre, K. Wardwell, J. Oneil, T. L. Guo, T. P. Christian, S. P. Mudzinski, and E. J. Gosselin, "Activation of human T cells by major histocompatibility complex class II expressing neutrophils-proliferation in the presence of superantigen, but not tetanus toxiod." *Blood* **89**, pp. 4128-4135, 2000.

9. S. O. Gollnick, X. Liu, B. Owczarczak, D. A. Musser, and B. W. Henderson, "Altered expression of interleukin 6 and interleukin 10 as a result of photodynamic therapy *in vivo*" *Cancer Research* **57**, pp. 3904-3909, 1997.

10. E. J. Gosselin, K. Wardwell, W. F. C. Rigby, and P. M. Guyre, "Induction of MHC class-II on human polymorphonuclear neutrophils by granulocyte macrophage colony-stimulating factor, IFN-γ and IL-3." *J.Immunol.* **151**, pp. 1482-1490, 1995.

11. M. R. Graf, R. M. Prins, and R. E. Merchant, "IL-6 secretion by a rat T9 glioma clone induces a neutrophil-dependent antitumor response with resultant cellular, antiglioma immunity." *J.Immunol.* **166**, pp. 121-129, 2001.

12. B. W. Henderson, S. M. Waldow, T. S. Mang, W. R. Potter, P. B. Malone, and T. J. Dougherty, "Tumor destruction and kinetics of tumor cell death in two experimental mouse tumors following Photodynamic Therapy" *Cancer Research* **45**, pp. 572-576, 1985.

13. M. Kopf, G. Le Gros, A. J. Coyle, M. Kosco-Vilbois, and F. Brombacher, "Immune responses of IL-4, IL-5, IL-6 deficient mice." *Immunol.Rev.* **48**, pp. 45-69, 1995.

14. M. Korbelik, "Induction of tumor immunity by photodynamic therapy" *J.Clin.Laser Med.&Surg.* **14**, pp. 329-334, 1996.

15. M. Korbelik and I. Cecic, "Contribution of myeloid and lymphoid host cells to the curative outcome of mouse sarcoma treatment by photodynamic therapy." *Cancer Lett.* **137**, pp. 91-98, 1999.

16. M. Korbelik and G. J. Dougherty, "Photodynamic therapy-mediated immune response against subcutaneous mouse tumors." *Cancer Research* **59**, pp. 1941-1946, 1999.

17. M. Korbelik, G. Krosl, J. Krosl, and G. J. Dougherty, "The role of host lymphoid populations in the response of mouse EMT6 tumor to photodynamic therapy." *Cancer Research* **56**, pp. 5647-5652, 1996.

18. G. Krosl, M. Korbelik, and G. J. Dougherty, "Induction of immune cell infiltration into murine SCCBII tumor by photofrim-based photodynamic therapy." *British Journal of Cancer* **71**, pp. 549-555, 1995.

19. C. R. Mackay, "Chemokines: immunology's high impact factors." *Nature Immunol.* **2**, pp. 95-101, 2001.

20. F. Pericle, R. A. Kirken, P. K. Epling-Burnette, B Blanchard, and J. Y. Djeu, "Direct killing of interleukin-2-transfected tumor cells by human neutrophils." *Int.J.Cancer* **66**, pp. 367-373, 1996.

21. B. J. Rollins, "Chemokines" *Blood* **90**, pp. 909-928, 1997.

22. Y.-H. Su, X.-T. Yan, J. E. Oakes, and R. N. Lausch, "Protective antibody therapy is associated with reduced chemokine transcripts in herpes simplex virus type 1 corneal infection." *J.Virol.* **70**, pp. 1277-1281, 1996.

23. A. Zlotnik and O. Yoshie, "Chemokines: a new classification system and their role in immunity." *Immunity* **12**, pp. 121-127, 2000.

Photo-pharmaceutical therapy: features and prospects

Vladimir P. Zharov[a], Alexander Ya. Potapenko[b], Alexander A. Minenkov[c]

[a] Phillips Classic Laser Biomedical Laboratory, University of Arkansas for Medical Sciences, Little Rock AR 72205-7199; [b] Department of Medical and Biological Physics, Russian State Medical University, Moscow 117997, Russia; [c] State Research Center of Rehabilitation and Physiotherapy, Moscow 121099, Russia

ABSTRACT

This article is an attempt to analyze the concept, distinguishing features and possible application of photo-pharmaceutical therapy (PPT). Besides photopheresis, PUVA, and photodynamic therapy, PPT also embraces a broad spectrum of various combinations of light and drugs. PPT techniques can be classified according to the role of light in drug therapy into several groups: *1)* light activation of drugs before, during or after their administration, *2)* light activation of cells or biotissue to potentiate the pharmaceutical effect of drugs, *3)* light-assisted drug delivery, *4)* optical sensing of drug action at cellular and subcellular levels, and *5)* selective photochemistry of drugs during their manufacturing. PPT seeks to describe the mechanisms of light-drug interaction, to time and sequence light-drug action, and to verify their synergetic effect. This article yields the results of developing new PPT modifications created in collaboration with some Russian scientific institutes and medical centers. The developed modifications are as follows: *1)* drug pre-administration photoactivation, *2)* antibody-photoconformation photoimmunotherapy, *3)* photophonophoresis with a blend of photosensitizers and antibiotics, *4)* photoelectrophoresis, *5)* drug effect enhancement due to laser-induced blood circulation activation, *6)* "photoimmunization" with alpha-fetoprotein, *7)* photo-pharmaceutical dosimetry, and *8)* a rapid drug toxicity photoassay.

Keywords: drug, phototherapy, light-activated drug, laser drug delivery, pharmacy,

1. INTRODUCTION

Very frequently, drug therapy and physiotherapy (such as laser irradiation, ultrasonic treatment, and electrostimulation) are used separately from each other. Sometimes, they are combined with each other. However, their combination is frequently sequenced in time. Only a few procedures employ these therapeutic techniques concurrently.

This notwithstanding, the last several years have seen a rapidly growing number of laser methods based on the photoactivation of light-sensitive drugs and compounds. Moreover, one may state nowadays that photo-pharmaceutical therapy (PPT) has developed into an individual photomedical trend. The distinguishing feature of this trend is that PPT uses various combinations of the above-mentioned factors that act simultaneously. Besides the well-known methods, such as photopheresis, PUVA, and photodynamic therapy, PPT comprises a broad spectrum of possible methods based on various combinations of light and drugs. Bearing in mind that light may play different roles in drug therapy, PPT techniques can fall into six groups.

1. *Light activation of drugs after their administration.* This group of methods includes malignant and non-malignant PDT methods, PUVA therapy, and photopheresis. For example, it comprises psoriasis PUVA treatment.
2. *Light activation of drugs before their administration.* This group of methods is intended to potentiate pharmaceutical effects, to decrease possible side effects, as well as to obtain new transient properties. For example, methods for potentiating psoralen-related immunomodulation effects can be attributed to this group.
3. *Light activation of cells or biotissue to potentiate pharmaceutical effects.* This group of methods makes use of photomodulation effects. For example, it embraces antibody-conformation photoactivation techniques.
4. *Light-assisted drug delivery.* This group of methods is intended to deliver drug compounds to various regions of human beings. This especially concerns drug delivery to the internal regions of human beings. This group may comprise the following methods: photothermal blood microcirculation enhancement,

Correspondence: e-mail <zharovvladimirp@uams.edu>

5. stratum corneum laser ablation, laser-acoustic and laser-hydrodynamic drug delivery (such as laser impregnation and laser injection), photophonophoresis, and photoelectrophoresis.

6. *Optical sensing of drug action at cellular and subcellular levels.* This group includes such methods as laser photothermal phase contrast imaging of drug-tissue interaction.

7. *Selective photochemistry of drugs during their manufacturing.*

Thus, the application of light and especially of laser radiation makes it possible to improve the therapeutic efficiency of drug compounds. However, PPT faces a number of challenges. First, one needs to understand the mechanisms of light-drug interactions. Second, it is essential to time and sequence light and drug action. Finally, one must verify the synergetic effect of such a combined application.

Below, we shall analyze the PPT concept, its distinguishing features, and possible applications. The analysis of this problem will be based on the experience we gained during our work in this field. It should be mentioned that this study was carried out in close collaboration with some Moscow scientific institutions and medical centers. They include the Institute of General Physics of the Russian Academy of Sciences, Shemyakin & Ovchinnikov Institute of Bioorganic Chemistry of the Russian Academy of Sciences, the Russian State Medical University, Sechenov Moscow Medical Academy, and the Russian Center of Molecular Diagnostics and Treatment.

2. LIGHT ACTIVATION OF DRUGS BEFORE THEIR ADMINISTRATION

As an example of this group of methods, we shall consider the biomedical application of prephotooxidized psoralens. It is known that psoralens (furocoumarins [FC]) belong to the family of tricyclic heteroaromatic compounds (Figure 1). In nature, these compounds are encountered in plants. However, they can also be chemically synthesized.

| **Psoralen** | **8-methoxypsoralen** | **8-methoxyalloimperatorin** |
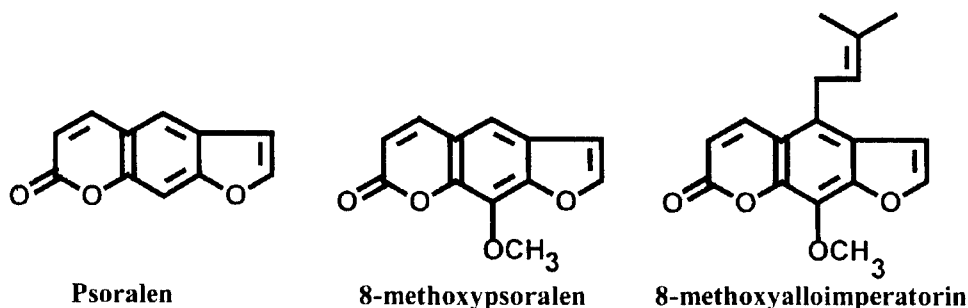
Figure 1. Structures of some furocoumarins

When FCs are combined with UVA radiation, they are used to treat numerous autoimmune and skin diseases[1]. The FC photosensitizing effect on biological systems proceeds by both oxygen-independent and oxygen-dependent pathways. The former involves sensitizer photoaddition to nucleic acids[2, 3], lipids[4], and DNA-protein crosslinks[5], whereas the latter involves photodynamic sensitization[6]. The substrates of photooxidative reactions of FCs are nucleic acids[7], proteins[8], amino acids[6], lipids[9], and other biomolecules. FC photosensitized reactions can be classified into four types (Figure 2).

Type I includes free radical reactions[10] and the production of charge transfer complexes between excited FCs and the substrate[11]. Type II comprises reactions that involve singlet oxygen[7, 8, 12]. Type III includes photoaddition to DNA and unsaturated fatty acids (the only reactions that do not require the presence of oxygen)[2, 4]. Type IV involves the formation of photooxidized FC derivatives, which can react in the dark with biomolecules and cells[13-16]. Preliminarily photooxidized psoralens (POP) can react with biosubstrates when mixed with the latter in the dark.

When psoralen + UVA (PUVA) is applied to the skin, it brings about all the above-mentioned reactions. The latter produce multiple photobiological effects, such as erythema, hyperpigmentation, immunosuppression, carcinogenesis, treatment of skin, and autoimmune diseases. PUVA therapy and photopheresis can initiate both positive and negative processes. Despite numerous controversial discussions, the photochemical mechanisms of these processes have not been established unequivocally yet. In order to relate the type of a psoralen-induced photochemical reaction to a corresponding photobiological effect, one needs either to reveal the specific inhibitors of a particular reaction or to make such an experiment in which only a limited number of reactions will take place. It was found that antioxidants[17], beta-carotene[18], and aromatic retinoids[19] reduced PUVA erythema and hyperpigmentation, not affecting therapeutic

efficiency. From these facts as well as from model experiments, it was concluded that Type-I and Type-II mechanisms were mainly responsible for side effects of PUVA therapy. Presently, there are no approaches that would allow one to inhibit specifically psoralen photoaddition to DNA in the patient's skin. It is therefore difficult to estimate the contribution of these reactions to therapeutic and side effects. The reactions of Types I, II, and III may take place only when the substrate is irradiated in the presence of a sensitizer. The role of a Type-IV mechanism can be revealed experimentally. To this end, a preirradiated sensitizer should be added to the substrate in the dark. In this case, the reactions of Types I, II, and III cannot contribute to biological psoralen-induced effects. Many photobiological effects of psoralens proceed by the Type-IV mechanism. This was proven by the following observation. When a previously photooxidized psoralen (POP) was added to a suspension of erythrocytes, it caused hemolysis[16].

Photooxidation

Reactions without participation of oxygen
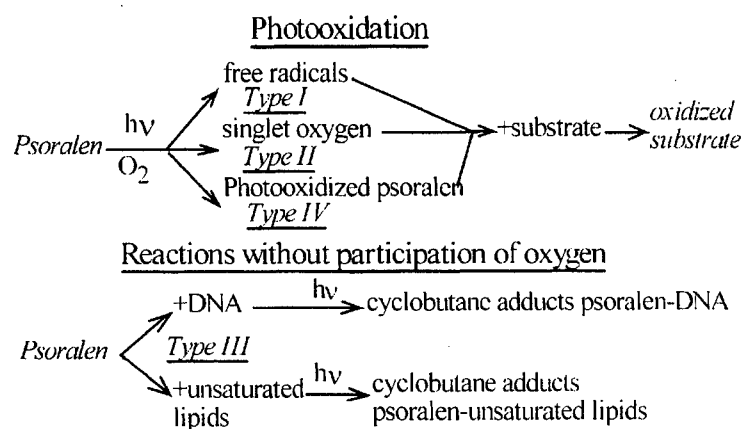
Figure 2. Psoralen-photosensitized reaction types

Psoralen photochemotherapy is efficient in respect of diseases caused by immunological imbalance. This imbalance manifests itself as T-cell-immune system hyperreactivity. A delayed-type hypersensitivity (DTH) reaction can serve as a typical example of the T-cell-mediated immune response. It is known that PUVA therapy suppresses the DTH reaction. For that reason, we investigated POP effects on the DTH reaction. These investigations were made on mice according to an experimental procedure given in Figure 3.
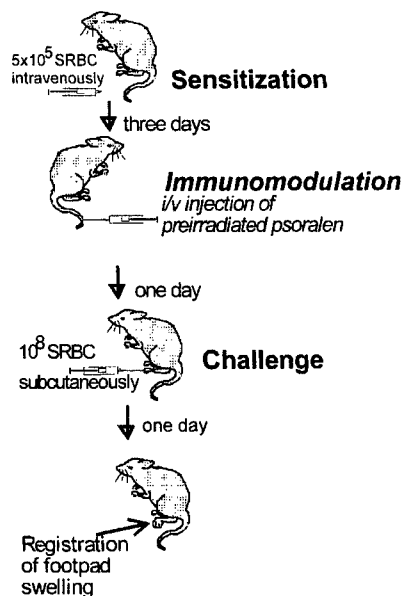
Figure 3. Experimental procedure to investigate photooxidized psoralen-induced effects on the DTH reaction in mice. Mice were immunologically sensitized to sheep red blood cells (SRBC). A POP intravenous injection was administered three days later. An SRBC challenge injection was given into mouse footpads on the fourth day. Footpad swelling was examined one day after the challenge injection.

Figure 4 shows the effect of POP treatment on the DTH reaction in mice. It was found that, when the psoralen was subjected to preliminary UVA irradiation for a short time span (from 1 to 3 minutes), the mice exhibited an activated DTH reaction to sheep red blood cells. Conversely, when the psoralen was subjected to preliminary UVA irradiation for a long time span (from 10 to 30 minutes), the mice revealed a suppressed DTH reaction. Hence, it can be concluded that the POP is a powerful T-cell-mediated immune modulator. This result demonstrates that the Type-IV psoralen-induced reactions are of special importance for psoralen photochemotherapy. Indeed, when the POP was administered to mice with a grafted EL-4 lymphoma, it inhibited tumor growth[20]. This tumor is a human cutaneous T-cell lymphoma model, and this malady turned out to be very susceptible to psoralen photochemotherapy. It is of interest to note that the POP retarded the growth of a murine EL-4 lymphoma irrespective of the POP application mode (Table 1).

Table 1. POP-related inhibition of murine EL-4 lymphoma growth for various POP application modes in mice. Psoralen (10^{-4} M in PBS) was UVA-irradiated (10 kJ m^{-2}) and administered to the mice on the third day after tumor grafting. The procedure was repeated on the first, second, or third days (altogether 9 times in the course of 18 days).

Groups	Tumor area, mean ± SEM (cm^2)	Tumor mass, mean ± SEM (g)
Control (without POP treatment), n=7	17.2±1.4	5.6±0.5
Intravenous POP injection (0.5 ml), n=9	11.0±1.5	3.9±0.2
Subcutaneous POP injection (0.5 ml), n=9	6.8±1.3	3.8±0.5
POP, oral (0.5 ml), n=6	6.5±1.4	3.9±0.6
POP, nasal (80 μl), n=7	10.1±1.8	3.8±0.6

It was established that hemolysis and immunosuppression were governed by different psoralen photooxidation products. The reciprocity law was inapplicable to these photoproducts. It was also found that the yield of immunomodulative psoralen photoproducts decreased, whereas the yield of hemolysins increased with an increase in the UVA radiation fluence rate density and/or in psoralen concentration during preirradiation[21]. When the POP was administered to eczematous patients, it produced a therapeutic effect, with the remission covering more than half a year[22]. Hence, a new psoralen photochemotherapy method based on POP application (POP therapy) can be proposed.

Psoralen photochemotherapy is a very ancient therapeutic technique. It has been in use for more than 4,000 years[23]. In the ancient world, physicians and herbalists practiced photochemotherapy to treat common disfiguring diseases and vitiligo. They used the boiled fruit extracts of certain umbelliferous plants (like tea). For example, these extracts included *Ammi majus* Linnaeus in Egypt or the leguminous plant *Psoralea corylifolia* Linnaeus in India. According to Fitzpatrick and Pathak[23], these preparations were either applied to the skin or injected as an "infusion". After that, the patients exposed their skin to the baking Egyptian or Indian sun.

Psoralens exhibit low water solubility. A saturated solution of 8-methoxypsoralen contains approximately 2 mg of a sensitizer per 100 ml. It is known that photochemotherapy efficiency depends on sensitizer concentration in plasma. For 8-methoxypsoralen, the breakthrough dose is 0.23 mg per 1 kg of the body weight. When the administered dose is less than this value, the sensitizer is absent in plasma. As a result of this, the patient's photosensitivity does not change[24]. When a saturated 8-methoxypsoralen (8-MOP) solution is administered orally, and when the body weight is approximately 70 kg, the minimal (breakthrough) extract volume should be 800 ml. To achieve the optimal therapeutic concentration of 0.6 mg kg^{-1}, this volume should amount to approximately 2,100 ml, which is improbable. It is therefore unlikely that the 8-MOP photoreactions of Types I, II, and III should take place when the extracts are administered orally. Nevertheless, this therapy appeared to be successful. This can be ascribed to the fact that the extracts were exposed to sunlight before the treatment, which caused the production of psoralen photooxidation products in them. In this case, in order to produce a therapeutic effect, it is sufficient to apply a small volume of an aqueous solution of a photooxidized sensitizer. Bearing this in mind, in our experiments on POP therapy in eczematous patients, the dose of a saturated preirradiated psoralen solution was 50 ml[22].
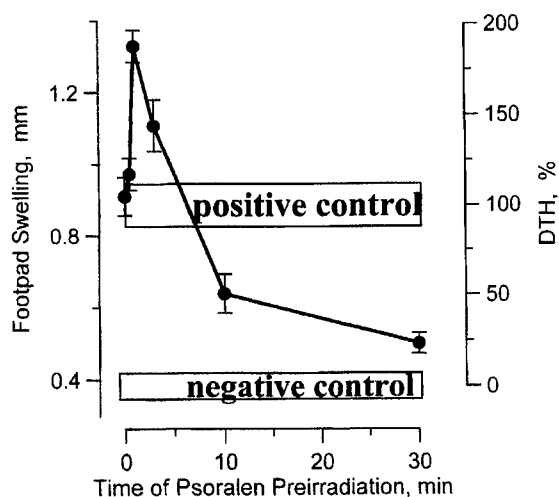
Figure 4. DTH reaction modulation in mice by using a previously photooxidized psoralen. The UVA radiation fluence rate as 6 W m^{-2}. 0.5 ml of a POP aqueous solution was injected intravenously into mice 72 h after SRBC sensitization. As a positive control, mice were sensitized and challenged without POP treatment (100% DTH reaction). As a negative control, mice were challenged without sensitization and POP treatment (0 % DTH reaction).

Presently, two psoralen photochemotherapy methods are in use, namely PUVA therapy and photopheresis. In PUVA therapy, psoralens are usually administered orally. In rare cases, however, they can be administered topically. After psoralen administration, the patient's skin is exposed to UVA radiation[25]. In the case of photopheresis, the patient's blood is subjected to extracorporeal UVA irradiation after oral administration of psoralens[26]. During PUVA treatment, all possible psoralen photoreactions take place in skin (Scheme 2) or in blood.
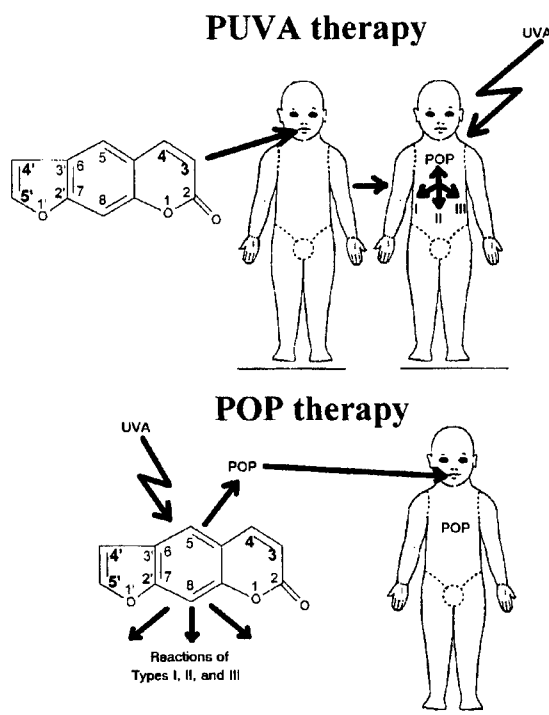
Figure 5 . PUVA therapy and POP therapy.

The results obtained demonstrated that it is feasible to create a new POP therapy (Scheme 2). This therapy does not rely on UVA irradiation of the patient's skin or blood. Thus, the deleterious effects of UVA/PUVA can be avoided.

3. LIGHT ACTIVATION OF DRUGS AFTER THEIR ADMINISTRATION

We present this group of methods on the example of a so-called photoimmunization influence on tumor growth. It is known that a number of serious diseases are accompanied by specific immunity deterioration. For example, some malignant tumors may give rise to the appearance of specific antibodies. In this connection, it is essential for modern immunology to have a tool for enhancing the immune response to specific tumor antigens. This is of special importance for preventing and treating malignant diseases.

Experiments were carried out to determine the immune reaction enhancement in animals affected by a malignant tumor[27]. The animals were preliminarily vaccinated with an oncofetal antigen (such as an alphafetoprotein receptor [AFPR]) and subjected to light irradiation. The latter was performed with the aid of an LED photomatrix array[28].

We used 12 mice of the DBA/2 line. The animals weighed from 18 to 20 g. The mice were divided into two groups: control and experimental. The control group included 3 mice. These mice remained without irradiation and immunization. The experimental group consisted of 9 mice. The AFPR was obtained in accordance with a traditional chromatographic technique using an AFP-sepharose column. An LED matrix array emitted incoherent light at a wavelength of 660±10 nm. This array produced a uniform illumination of the bioobject's surface[28]. The mice were vaccinated subcutaneously into each leg with 25 µl of the receptor solution mixed with 25 µl of Freind Adjuvant. Each animal was once vaccinated with 50 µg of the receptor. Vaccination was made 4 days before the tumor grafting (mieloleucosis P388, expressing AFPR). Immediately after immunization, all the animals were subjected to irradiation. To this end, they were placed into a special transparent cylindrical box with an internal diameter of 64 mm. The animals could move rather freely there. The capture was fixed inside the LED photomatrix array so that their axes of symmetry were parallel. This experimental pattern made it possible to maintain illumination inside the box at a constant level. Ignoring losses caused by light passage through the walls, the fluence rate was 1 mW cm^{-2}. The irradiation procedure lasted for 60 min. The tumor was introduced by means of a subcutaneous injection of 4×10^5 malignant cells. In our experiments, we measured the average tumor volume (ATV) and mouse life expectancy (MLE). The ATV was calculated as $V = a2 \cdot b \cdot \pi/6$, where a is the minor tumor's diameter and b is the major tumor's diameter. The statistical treatment of measured parameters was carried out according to the Student t test. The results obtained are shown in Figures 6 and 7.
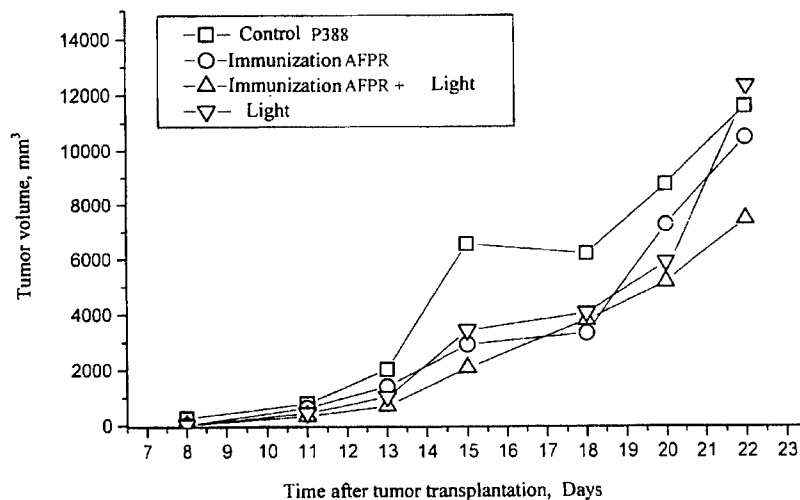
Figure 6. Average tumor volume as a function of time
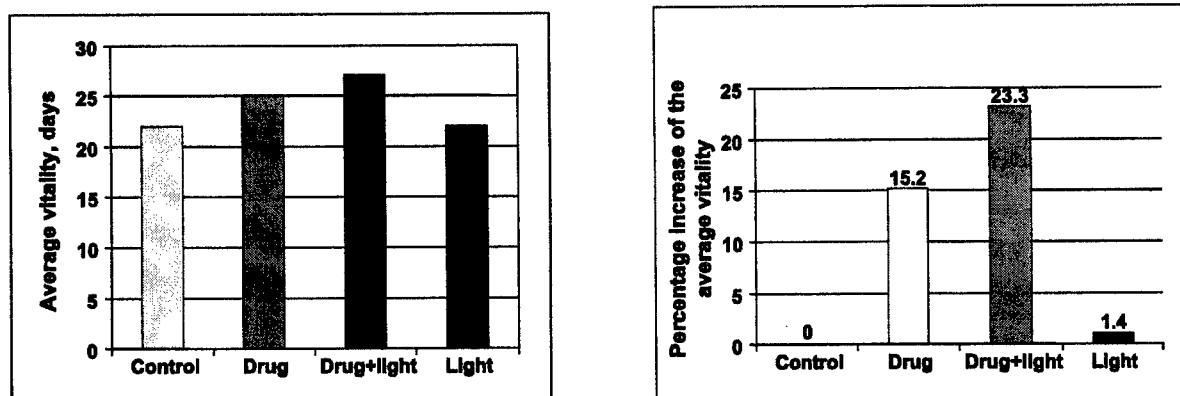
Figure 7. Mouse life expectancy for different treatment modes

In all the cases, the ATV was noticed to increase during the observation period (18 days after tumor grafting). It was found that the tumor growth in the control animals was approximately 1.5 times greater as compared to that in the experimental animals. The maximal difference in the tumor growth was observed on the fifteenth day. It was also found that photoimmunization produced a significant increase in the MLE of experimental animals (by 23,3%), whereas AFPR vaccination produced a less pronounced increase in the MLE (by 15,2% only). It should also be noted that mice receiving irradiation alone (without AFPR vaccination) exhibited an increase in the tumor growth 22 days after tumor grafting.

Hence, this combined therapy enhanced the immune reaction and produced a mediated effect on the increase in the life expectancy of immunized animals as compared to the control animals. In addition, this treatment retarded the tumor growth. Although these experiments were tentative, and although they were made on a relatively small number of animals, the results obtained were evidence of a bright outlook for this combined photoimmunization technique. This method can find application in preventing and treating malignant diseases.

In the future, it will be necessary to investigate more carefully the mechanisms of the immune response to light action. For example, our recent studies demonstrated that one of possible mechanisms may involve the conformational transition of antibodies from a low-avid state to a high-avid state[29].

4. LASER DRUG DELIVERY METHODS

Another promising group of methods employs optical radiation to deliver drugs to various regions of human beings. The last several years have seen a growing interest in applying laser radiation for transcutaneous drug delivery. In order to overcome the barrier functions of stratum corneum, researchers developed a number of techniques. The latter include stratum corneum laser ablation performed with the aid of pulsed lasers[30], photomechanical and acoustic wave generation[31, 32], forced laser drug injection based on skin perforation[32], and combined laser-ultrasound treatment[33]. In carrying out these investigations, a spectro-chromatographic technique was developed to study possible effects of radiation on drug properties[32, 34].

In this section, we shall consider a number of unpublished results obtained earlier. These results deal with laser-related transcutaneous drug delivery enhancement. They were obtained for the combined application of laser radiation and electrophoresis.

It is known that ultrasonic and electric drug delivery methods, such as phonophoresis and electrophoresis, have found broad application in medical practice. However, both methods suffer from a number of drawbacks. For example, deleterious effects of electrophoresis include the initiation of electrolytic reactions in the sub-electrode area, the irritation of skin by an electric current, and the alteration of drug properties due to oxidizing processes. Moreover, electrophoresis is contraindicated to patients affected by some skin diseases. Phonophoresis also suffers from certain drawbacks. The most serious of them is that the number of drug compounds used for phonophoresis is limited. This is related to the fact that ultrasound may destroy some drugs. In particular, many hormones, enzymes, and vitamins can be destroyed under the action of ultrasonic waves.

These limitations motivated the development of many new methods, some of which made use of laser radiation. While developing a new drug delivery technique, one needs to study the following aspects: *1*) the effect of a physical factor on drug properties, *2*) the amount of drug delivered, and *3*) the efficiency of combined application as compared to their separate action and to other existing drug delivery techniques.

The effect of various physical factors was investigated on photoconductive models by estimating the penetration rate of drug compounds. The latter passed through a semipermeable membrane under the action of physical factors. These experiments were performed with the aid of spectral and chromatographic methods. In addition, an analysis was made of the structural stability of exposed drug preparations. As physical factors, we used an electric current, ultrasound, laser radiation, and their combinations.

As an example, we shall consider the results of studies made earlier. They were performed with the aid of a He-Ne laser. Laser radiation parameters were as follows: $\lambda = 628$ nm and $P = 30$ mW. Numerous physiochemical investigations (up to 400) were carried out. In these experiments, we made use of several drug compounds having different chemical structures. These drugs included apressin, gangleron, carbochromen, inosine, and nicotinic acid. These drug preparations were tested for their structural stability and mobility under the influence of a direct electric current, laser radiation, and their combination. On the basis of these investigations, it was established that, when laser radiation was emitted at therapeutic doses (from 1.5 to 37.5 J), it did not destroy these pharmaceutical compounds.

In another experiment, we investigated the effect of physical factors on drug penetration through biological tissues. This study was made on experimental rabbits by using fluorescence analysis. The permeability of various biological structures, such as skin and capillaries, was assessed by the rate of a decrease in fluorescence intensity. To this end, symmetrical loci were sheared on the rabbits' back. After that, 0.1 ml of a fluoresceine solution was either applied topically or introduced intracutaneously. Fluorescence strength was measured periodically over a long time span (one hour and more). The measurements were made until fluorescence disappeared completely. Apart from that, blood tests were taken periodically from various regions (first of all, from the auricular vein). After centrifuging the blood, we determined fluoresceine content by using spectrophotometric analysis. The sensitivity of this method allowed us to detect fluoresceine in blood within 1 to 2 min after its control injection into the femoral muscle. Experiments were made on 36 rabbits. It was found that, when the animals' skin was subjected to preliminary He-Ne laser irradiation at a dose of up to 14.4 J, the rate of fluoresceine penetration into blood increased by a factor of 1.5 ($p < 0.01$) (Figure 8). The photometric test allowed us to detect fluoresceine in blood 2 min after its introduction. The maximal fluoresceine concentration was detected within 15 min. Thereafter, its concentration showed a tendency to decrease. Similar results were obtained when an apressin solution was exposed to laser radiation. An optimal solution concentration was below 1%. Laser radiation fluence rate was 10 mW cm^{-2}, and irradiation lasted for 10 min.
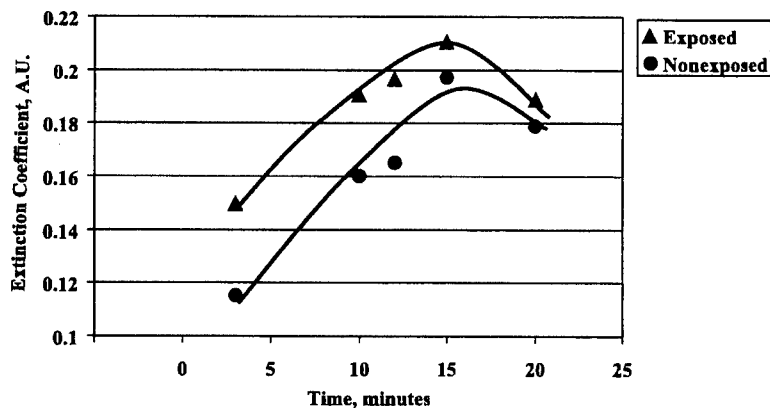
Figure 8. Dynamics of the ingress of fluoresceine into blood for nonexposed animals and after their preliminary 20-min irradiation.

Apart from that, we carried out preliminary experiments on 30 volunteers suffering from essential hypertension. They were separated into four groups. In the first group, the effect was estimated by analyzing the response of peripheral and central hemodynamics to laser radiation. The latter was incident on the skin of the neck. The exposed area was approximately 80 cm^2. Irradiation lasted for 15 min, and the administered dose was 10.8 J. Volunteers of the second group received topical application of 1 ml of 1% apressin. The drug compound diffused through the skin in these human subjects. Volunteers of the third group received the combined application of laser radiation and apressin, whereas those of the fourth group were administered to a placebo treatment.

It was found that neither the placebo treatment, nor apressin application alone produced significant hemodynamic changes. However, the combined application of laser radiation and apressin produced pronounced changes in hemodynamic parameters. Their combined application activated either peripheral or central hemodynamics and decreased systolic pressure by approximately 15%.

The results obtained thus demonstrated that, when drug compounds were exposed to laser radiation, the latter potentiated their pharmaceutical effect. Although these findings are interesting and promising, further thorough investigations

are needed to understand the mechanisms of these effects. The mechanism of blood circulation enhancement also remains to be investigated.

A comparison was made of the efficiency of combining various physical factors with pharmaceutical techniques, such as electrophoresis. This study was made on conductive and photoconductive models. To perform experiments on volunteers, a combined device was developed. This device enabled us to expose volunteers simultaneously to three physical factors, such as a direct electric current, drug preparation, and laser radiation (Figure 9). It is worth noting that this device can be used for investigating various photochemical reactions that take place in drug compounds. For example, it can be employed to study photodissociation, photolysis, electrolysis, and photoelectron electrode emission when lasers of various durations and intensities are used. The combined influence may increase the electrophoretic mobility of pharmaceutical preparations not only in model electrode-electrolyte structures but also in live biological tissues. In experiments *in vivo*, the device was attached to the human body by means of a vacuum suction cup equipped with an elastic pear. After that, it was filled with a drug solution. The solution was conveyed by a channel in the upper part of the system. An electric current source and laser were then switched on. As drug compounds, we used carbochromen and inosine. The structural stability of these preparations to a combined influence was verified by various chemical tests. The latter included fluorescence from separate groups, chemical reactions with other compounds, spectroscopy, and thin-layer chromatography.
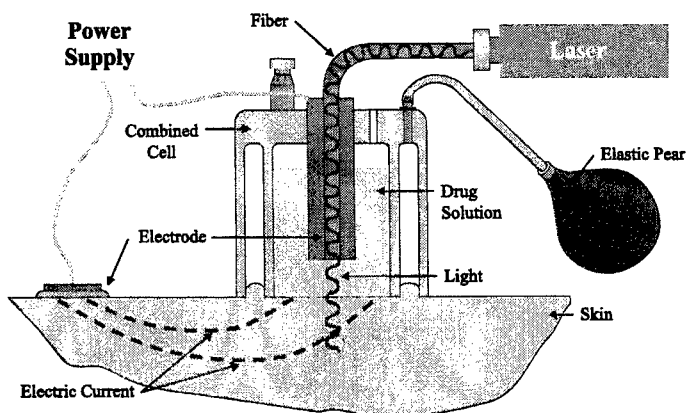
Figure 9. Schematic diagram of the device for photoelectrophoresis

An investigation was also made of the quantitative characteristics of drug mass transfer under the action of an electric current (0.05 mA cm^{-2}), laser radiation (628 nm, 20 mW), ultraviolet radiation (254 nm, 220 W), ultrasound (880 kHz, 0.6 W cm^{-2}), decimetric waves (460 MHz, 2 W), ultrahigh frequencies (40.7 MHz, 15 W), variable magnetic field (50 Hz, 35 mTl), and magnetostatic field (40 mTl). For example, 80 physiochemical investigations were performed by using an 0.1% carbochromen solution. It was found that, when exposed for 20 min, all the physical factors increased the electrophoretic mobility of this pharmaceutical compound (Figure 10). However, it was established that laser radiation produced the most pronounced increase. It increased electrophoretic mobility by a factor of approximately 1.5 as compared to electrophoresis alone.

Drug Concentration After Membrane A.U.
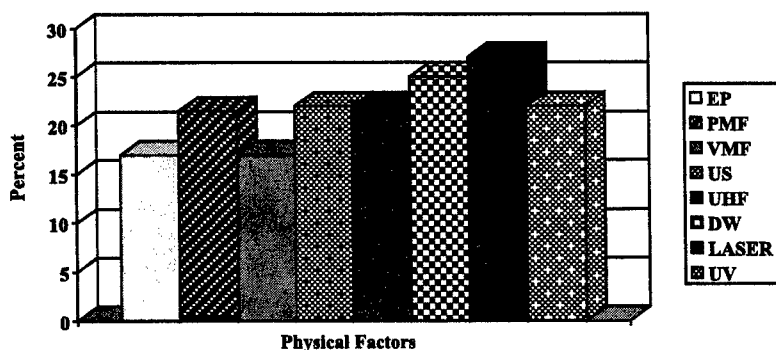
Figure 10. Effect of various physical factors on the electrophoretic mobility of an 0.1% carbochromen solution under the action of a direct electric current influencing a conductive model for 5 min.

Iontophoresometric investigations were conducted on volunteers by using a nicotinic acid solution. In these experiments, drug electrophoresis was used alone and in combination with laser radiation. The current density, exposure time, and laser radiation intensity were, respectively, 0.05 mA cm^{-2}, 20 min, and 10 mW cm^{-2}. It was found that electrophoresis alone introduced 3.7±1.1 mg, whereas its combination with laser radiation made it possible to deliver 8.2±1.6 mg (P<0.05) (Figure 11). The drug quantity that penetrated the human being's body was calculated as the difference between initial and final solution concentrations in the device. In our calculations, we took into account the adsorption properties of the skin and of the device surface. It should be pointed out that the net effect of this combined influence cannot be represented by an additive summation of effects produced by separate physical factors. This effect resulted from the synergetic enhancement produced by separate physical factors. As a result of this, the quantity of drug compounds (in our case, the quantity of a nicotinic acid) penetrating the human being's body was greater during a combined influence. Hence, the human being produces a more pronounced response to combined photoelectrophoresis than to conventional electrophoresis.
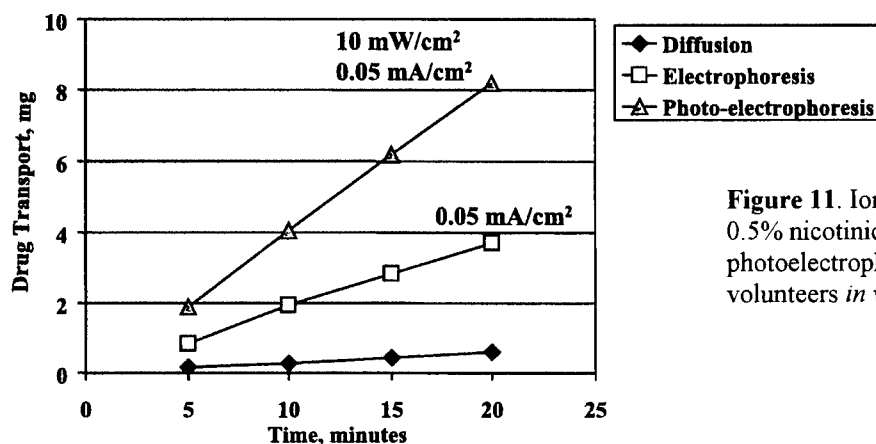
Figure 11. Iontophoresometric indices obtained for 0.5% nicotinic acid electrophoresis, photoelectrophoresis, and pure diffusion in volunteers *in vivo*.

The same results were obtained in 20 atherosclerotic patients with a subcompensated peripheral circulation. The regional shank hemodynamics was investigated with the aid of rheovasography (RVG). The RVG index of these patients was 0.56±0.11 Ohm before electrophoresis and 0.67±0.16 Ohm after electrophoresis (P>0.05), 0.89±0.01 Ohm before photoelectrophoresis and 1.31±0.18 Ohm after photoelectrophoresis (P<0.05). Thus, photoelectrophoresis produced a considerable increase in the blood engorgement of shank vessels.

CONCLUSIONS

The experimental results obtained thus demonstrated that relatively low-power laser radiation was capable of increasing the efficiency of pharmaceutical methods. It is evident that the application of high-power pulsed lasers will significantly potentiate these effects. This especially concerns the combination of pharmaceutical methods with laser perforation of skin structures[32] and ultrasonic treatment[33]. It seems very promising to combine ultrasonic and photodynamic therapies[33]. Recently, we demonstrated that, when the prostate gland was subjected to intraurethral irradiation with the aid of a semiconductor laser, the efficiency of drug delivery to internal organs increased due to local blood circulation enhancement stimulated by a photothermal effect[35]. To control laser drug delivery *in vivo*, one may employ not only the above-described methods but also optical absorption tomography[36], radioactive tracer techniques[36], as well as rheographic and photoplethysmographic methods with ring electrodes to monitor both venous and arterial blood circulation[37]. It is also feasible to combine a laser with capillary electrophoresis[38]. It is of interest to note that these methods can also be used to deliver photosensitizers in the photodynamic therapy of infectious processes[39–41]. In this case, the possible laser-induced photosensitizer destruction, which may occur under certain conditions, will play a positive role, and it can be used as the first stage of photodynamic therapy due to the bactericidal effect of toxic radicals.

PPT is a rapidly developing photomedical trend, and we touched upon only some groups of PPT methods. For example, we left out of account its promising applications in monitoring the effect of drug compounds on human beings. However, recent studies demonstrated that the high sensitivity and resolution of laser photothermal phase contrast imaging enabled the express-evaluation of the effect of drug compounds on single cells, toxicology analysis included[42–43]. One of the main PPT problem is to investigate the mechanisms of combined treatment. This is because many factors of monotherapy when laser radiation and drug compounds are used separately also remain to be investigated.

ACKNOWLEDGEMENTS

REFERENCES

1. D. Bethea, B. Fullmer, S. Syed, G. Seltzer, J. Tiano, C. Rischko, L. Gillespie, D. Brown, and F.P.Gasparro, "Psoralen photobiology and photochemotherapy: 50 years of science and medicine", *J. Dermatol. Sci.* 19, No. 2, pp. 78-88, 1999.

2. L. Musajo, G. Rodighiero, and F. Dall'Acqua, "Evidences of a photoreaction of the photosensitizing furocoumarins with DNA and with pyrimidine nucleosides and nucleotides", *Experientia.* 21, pp. 24-25, 1965.

3. F. Dall'Acqua, S. Caffieri, and G. Rodighiero, "Fluorimetric determination of 4',5'-cycloadducts in the DNA-psoralen photoreactions", *Photochem. Photobiol.* 27, pp. 77-79, 1978.

4. S. Caffieri, M. Ruzzene, B. Guerra, S. Frank, D. Vedaldi, and F. Dall'Acqua, "Psoralen fatty acid cycloadducts activate protein kinase C (PKC) in human platelets", *J. Photochem. Photobiol. B-Biol.* 22, No. 3, pp. 253-256, 1994.

5. C. Marzano, F. Baccichetti, F. Carlassare, A. Chilin, S. Lora, and F. Bordin, "DNA damage induced by 4,6,8,9-tetramethyl-2H-furo[2,3-h]quinolin-2-one, a new furocoumarin analog: biological consequences", *Photochem. Photobiol.* 71, No. 3, pp. 263-272, 2000.

6. A.Ya. Potapenko, "Mechanisms of photodynamic effects of furocoumarins", *J. Photochem. Photobiol. B-Biol.* 9, pp. 1-33, 1991.

7. G.M.J. Beijersbergen van Henegouwen, E.T. Wijn, S.A. Schoonderwoerd, H. de Vries, and F. Dall'Acqua, "Singlet oxygen mediated photobinding of 8-methoxypsoralen to DNA and genotoxicity in *E. coli*", *Z. Naturforsch.* 44c, pp. 819-823, 1989.

8. W. Poppe and L.I. Grossweiner, "Photodynamic sensitization by 8-methoxypsoralen via the singlet oxygen mechanism", *Photochem. Photobiol.* 22 pp. 217-219, 1975.

9. K. Glass, F. Pliquett, E. Grimm, A.Ja. Potapenko, G.A. Abijev, D.I. Roscupkin, and Ju.A. Vladimirov, "UV-Sensibilisierung von Lipidmembranen durch 8-Methoxypsoralen", *Wiss. Z. Karl-Marx-Univ. Leipzig, Math.-Naturwiss. Reiche* 28, pp. 148-152, 1979.

10. S. Cannistraro and A. Van de Vorst, "ESR and optical absorption evidence for free radical involvement in the photosensitizing action of furocoumarin derivatives and for their singlet oxygen production", *Biochim. Biophys. Acta* 476, pp. 166-177, 1977.

11. M. Craw, M.R. Chedekel, T.G. Truscott, and E.J. Land, "The photochemical interaction between the triplet state of 8-methoxypsoralen and the melanin precursor L-3,4-dihydroxyphenylalanine", *Photochem. Photobiol.* 39, pp. 155-159, 1984.

12. A.A. Krasnovsky, Jr., V.L. Sukhorukov, S.Yu. Egorov, and A.Ya. Potapenko, "Generation and quenching of singlet molecular oxygen by furocoumarins: Direct measurements", *Studia Biophys.* 114, pp. 149-158, 1986.

13. R. Ali and S.C. Agarwala, "In vitro and in vivo effect of normal and irradiated psoralen on glucose oxidation of brain and liver", *Enzyme*, 18, No. 6, pp. 321-326, 1974.

14. K. Yoshikawa, N. Mori, S. Sakakibara, N. Mizuno, and P.-S. Song, "Photo-conjugation of 8-methoxypsoralen with proteins", *Photochem. Photobiol.* 29, pp. 1127-1133, 1979.

15. A.Ya. Potapenko, M.V. Moshnin, A.A. Krasnovsky, Jr., and V.L. Sukhorukov, "Dark oxidation of unsaturated lipids by the photooxidized 8-methoxypsoralen", *Z. Naturforsch.* 37c, pp. 70-74, 1982.

16. A.Ya. Potapenko, L.N. Bezdetnaya, E.P. Lysenko, V.L. Sukhorukov, A.N. Remisov, and Yu.A. Vladimirov, "Mechanisms of furocoumarin-sensitized damage to biological membranes", *Studia Biophys.* 114, pp. 159-170, 1986.

17. A.Ya. Potapenko, G.A. Abijev, M.Yu. Pistsov, D.I. Roshchupkin, Yu.A. Vladimirov, F. Pliquett, A.V. Ermolayev, I.K. Sarycheva, and R.P. Evstigneeva, "PUVA-induced erythema and changes in mechanoelectrical properties of skin: Inhibition by tocopherols", *Arch. Dermatol. Res.*, 276, No. 1, pp. 12-16, 1984.

18. A. Giles, Jr., W. Warner, and A. Kornhauser, "In vivo protective effect of beta-carotene against psoralen phototoxicity", *Photochem. Photobiol.* 41, pp. 661-666, 1985.

19. S.N. Akhtyamov, A.A. Kalamkaryan, E.V. Sabanova, I.S. Persina, M.M. Kirsanova, and A.Ya. Potapenko, "Influence of prospidine om phototoxic and therapeutic effects of psoralens applied in treatment of Mycosis fungoides. Comparison with the effects of the retinoid tigason", *Studia Biophys.* 124, pp. 259-273, 1988.

20. A.Y. Potapenko, A.A. Kyagova, L.N. Bezdetnaya, E.P. Lysenko, I.Y. Chernyakhovskaya, V.A. Bekhalo, E.V. Nagurskaya, V.A. Nesterenko, N.G. Korotky, S.N. Akhtyamov, and T.M. Lanshchikova, "Products of psoralen photooxidation possess immunomodulative and antileukemic effects", *Photochem. Photobiol.* 60, pp. 171-174, 1994.

21. A.A. Kyagova, N.N. Zhuravel, M.M. Malakhov, E.P. Lysenko, W. Adam, C.R. Saha-Möller, and A.Ya. Potapenko, "Suppression of delayed-type hypersensitivity and hemolysis induced by previously photooxidized psoralen: effect of fluence rate and psoralen concentration", *Photochem. Photobiol.* 65, No. 4, pp. 694-700, 1997.

22. A.Ya. Potapenko, Yu.S. Butov, E.S. Levinzon, I.S. Mamedov, A.A. Kyagova, B.V. Nikonenko, and A.S. Apt, "Treatment of eczema with photooxidized psoralen", *Br. J. Dermatol.* 143, Suppl. 57, pp. 35-36, 2000.

23. T.B. Fitzpatrick and M.A. Pathak, "Research and development of oral psoralen and longwave radiation photochemotherapy: 2000 B.C.-1982 A.D.", *Natl. Cancer Inst. Monogr.* 66, pp. 3-11, 1984.

24. L.M.L. Stolk, A.H. Siddiqui, R.H. Cormane, and P.A. van Zwieten, "Pharmacokinetics and biopharmaceutics of psoralens", *Pharmacol. Intern.* 7, No. 10, pp. 259-262, 1986.

25. J.A. Parrish, T.B. Fitzpatrick, L. Tannenbaum, and M.A. Pathak, "Photochemotherapy of psoriasis with oral methoxsalen and longwave ultraviolet light", *N. Engl. J. Med.* 291, pp. 1207-1211, 1974.

26. R.L. Edelson, "Photopheresis: present and future aspects", *J. Photochem. Photobiol. B-Biol.* 10, No. 1-2, pp. 165-171, 1991.

27. V.P. Zharov, N.A. Kovalenko, N.B. Feldman, S.A. Ermilov, D. V. Astahov, S. V. Lucenko, S.E. Severin, and E.S. Severin, "Study of photoimmunization influence on tumor growth". Proceedings of Conference on *Biomedical Technologies for Public Health.* pp. 144-145, Gelendzik, Russia, 1999.

28. V. P. Zharov, Y. A. Menyaev, I. Z. Zharova, D. O. Leviev, V. N. Tsarev, V. P. Sarantsev, J. Krusic, "Photomatrix LED therapy of extensive cutaneous pathology", *Proceedings of SPIE*, 3907, pp. 169-177, 2000.

29. V.P. Zharov, V.S. Gevondyan, N.M. Gevondyan, S.A. Ermilov, A.M. Volynskya. "Light activation of the immune system. Influence on G-class antibodies", *Proceedings of SPIE*, 3914, pp. 324-333, 2000.

30. J.S. Nelson, J.L. McCullough, T.C. Glenn, W.H. Wright, L.L. Liaw, S.L. Jacques, "Mid-infrared laser ablation of stratum corneum enhances in vitro percutaneous transport of drugs", *The Journal of Investigative Dermatology*, 97, No. 5, pp. 874-879, 1991.

31. S. Lee, D.J. McAuliffe, T.J. Flotte, N. Kollias, and A.G. Doukas, "Photomechanical transcutaneous delivery of macromolecules", *The Journal of Investigative Dermatology*, 111, No. 6, pp. 925-929, 1998.

32. V.P. Zharov and A.S. Latyshev, "Role of photoacoustic effects occurring at laser perforation of skin and laser transcutaneous drug delivery", *In:* Biomedical Optoacoustics, *Proceedings of SPIE*, 3916, pp. 198-209, 2000.

33. V.P. Zharov and A.S. Latyshev, "Laser-ultrasonic technologies for medicine", *Proceedings of SPIE*, 3590, pp. 66-77, 1999.

34. A.A. Minenkov, *Application of Low-intensity Red and Infrared Laser Radiation in Combined Physiotherapeutic Methods.* Doctor of Medical Science's Theses. Institute of Therapy, Moscow, 1989.

35. V.P. Zharov, "Transurethral electrolaser complex therapy to treat chronic prostatitis", *In:* Lasers in Surgery: Advanced Characterization, Therapeutics, and Systems, *Proceedings of SPIE*, 3907, pp. 262-273, 2000.

36. V.P. Zharov and A.S. Latyshev, "Laser combined medical technologies from Russia". *Journal of Laser Applications*, April 1999, Vol.11, #2, p.80-90.

37. V. Zharov, Y. Menyaev, R. Kabisov, S. Alkov, A. Nesterov, V. Loshchilov, J. Suen, "Comparison of possibilities of ultrasound and its combination with laser in surgery and therapy", *In:* Biomedical Optoacoustics, *Proceedings of SPIE*, 3916, pp. 331-339, 2000.

38. A.N. Zhitov, V.P. Zharov, D.V. Vlasov, A.S. Latyshev, V.V. Markovets, and I.P. Suprun, "Detection of drug preparations using the micro-capillary electrophoresis method with photoacoustic and emission-luminescent detection at laser transcutaneous drug delivery", Technical Digest of The Tenth Scientific and Technological International Conference on *Lasers in Science, Engineering, and Medicine*, pp. 122-124. Sochi, Russia, 1999.

39. V.P. Zharov, A.M. Shoshenskii, D.O. Leviev, A.V. Lyutikov, and V.N. Tsarev, "Photo-drug therapy of inflammatory processes". Technical Digest of The Eight International Conference on Lasers in *Science, Engineering, and Medicine*, Moscow, pp. 99-100, 1997.

40. V.P. Zharov, A.S. Latyshev, and D.O. Leviev, "Photomedicine with laser drug delivery technologies". *Proceedings of SPIE*, 3829, pp. 141-155, 1999.

41. V.P. Zharov and A.M. Shoshenskii, "New achievements of laser medicine: Laser pills", Proceedings of The Fourth International Congress on *Problems of Laser Medicine*, Moscow-Vidnoye, p. 330, 1997.

42. D. Lapotko, T. Romanovskaya, G. Kutchinskii, and V. Zharov, "Photothermal studies of modulating effect of photoactivated chlorin on the interaction of blood cells with bacteria", *Cytometry*, 37, pp.320-326, 1999.

43. D. Lapotko, V. Zharov, T. Romanovskaya, G. Kutchinsky, and G. Vorojtsov, "Photothermal microscopy study of photodynamic inactivation of bacteria in the presence of living blood cells", *Proceedings of SPIE*, 3592, pp. 101-109, 1999.

Characterization of optical and thermal distributions from an intracranial balloon applicator for photodynamic therapy

Steen J. Madsen[*a], Lars O. Svaasand[b], Bruce J. Tromberg[c] and Henry Hirschberg[d]

[a]Dept. of Health Physics, University of Nevada, Las Vegas, 4505 Maryland Pkwy., Box 453037, Las Vegas, NV 89154

[b]Norwegian University of Science and Technology, Trondheim, Norway

[c]Beckman Laser Institute and Medical Clinic, University of California, Irvine, CA 92715

[d]Dept. of Neurosurgery, Rikshospitalet, Oslo, Norway

ABSTRACT

An indwelling balloon applicator developed for postoperative intracavity brachytherapy was evaluated for photodynamic therapy. Measurements of light distributions in a brain phantom show that the applicator can be used to deliver sufficiently uniform light doses during PDT. The light distribution is uniform to within 5% when the balloon is filled with a scattering medium. Based on simple assumptions, it is shown that the applicator can be used to deliver a threshold optical dose to brain tissue at depths of 1.4 cm in less than 90 minutes. A mathematical model of the thermal distribution around the applicator suggests that tissue temperatures will be below the hyperthermic threshold at the input powers required for treatments to depths of 1.4 cm in the resection cavity. The delivery of threshold light doses to depths exceeding 1.4 cm is likely to result in hyperthermic effects to tissues near the applicator surface.

Keywords: Photodynamic therapy, balloon applicator, light distribution, thermal distribution, brain tumor

1. INTRODUCTION

The prognosis for patients with high grade gliomas has not improved significantly over the past four decades. Even with the best available treatments using surgery, radiation and chemotherapy, median survival is less than one year[1]. Although gliomas are considered to be disseminated tumors in the brain, most recur at the site of the previous tumor resection – approximately 80 % of tumors recur within 2 cm of the resected margin[2]. Improved local control would therefore be of clear benefit. Intracavity therapy offers the possibility of applying various treatment modalities (brachy, photodynamic and thermal therapies) aimed at the nests of tumor cells left in the resection border while minimizing damage to normal tissue[3-5].

Although photodynamic therapy (PDT) has been used in the treatment of brain tumors for the past 20 years[6], results of clinical trials have been ambiguous due, in part, to their limited scope. In almost all cases, PDT had been given single-shot, immediately following surgery. Due to the complicated nature of PDT dosimetry, there have been relatively few attempts to optimize PDT dose.

Delivery of sufficient light doses to tumor cells residing at cm depths in the resection cavity requires long treatment times due to the highly attenuating nature of brain tissue. Due to time limitations, the delivery of adequate light doses is not feasible using traditional one-shot intraoperative techniques. Furthermore, there is reason to believe that multi-fractionated PDT treatments over long time periods are more effective than one-shot procedures[7]. Protracted multi-fractionated PDT treatments are possible using indwelling balloon

• Correspondence: Email: steenm@ccmail.nevada.edu; Telephone: 702.895.1805; Fax: 702.895.4819

applicators such as the ones currently used in afterloading brachytherapy at the Rikshospital in Oslo, Norway[4].

The goals of this paper may be summarized as follows: (1) to determine the light distribution surrounding an indwelling balloon applicator to be used in postoperative PDT of malignant brain neoplasms; (2) to estimate typical treatment times based on very simple assumptions of light propagation in brain tissues, and; (3) to estimate thermal distributions in brain tissues during PDT.

2. THEORY

2.1. Optical distribution

In scattering media, such as biological tissue, the light distribution can be adequately described by diffusion theory. In the case of a spherical applicator positioned centrally in a spherical cavity, the fluence rate (W cm^{-2}) is given by[8]:

$$\varphi = \frac{\varphi_o e^{-r/\delta}}{r},$$ (1)

where φ_o is the fluence rate at the inner surface of the cavity, r is the distance from the center of the cavity, and δ is the optical penetration depth.

Multiple reflections will build up the fluence rate in the cavity until the radiation transmitted through the cavity wall is equal to the light coupled into the cavity – the so-called integrating sphere effect. It is important to account for this effect as it reduces treatment times due to the fluence build-up. Furthermore, in a true integrating sphere effect, the irradiance is independent of source position in the applicator[9]. In the presence of the integrating sphere effect, the fluence rate is given by[8]:

$$\varphi = \left[\frac{P_t c}{4\pi a D r \left(\frac{1}{a} + \frac{1}{\delta} \right)} \right] e^{-(r-a)/\delta},$$ (2)

where P_t is the total optical power from the applicator, c is the velocity of light in tissue, a is the radius of the spherical cavity, and D is the diffusion constant. The total optical dose (Ψ) at a particular depth is given by:

$$\Psi = \varphi \cdot t,$$ (3)

where t is the irradiation time. Since decomposition of the photosensitizer (photobleaching) is common during PDT, an effective dose (Ψ_{eff}) is specified:

$$\Psi_{eff} = \Theta \left(1 - e^{-\Psi/\Theta} \right),$$ (4)

where Θ is the photobleaching parameter.

2.2. Thermal distribution

During PDT, a predominant part of the optical energy is converted to heat through tissue absorption. The thermal distribution in tissue can be expressed as[10]:

$$divgradT - \frac{1}{\chi}\frac{\partial T}{\partial t} - \frac{Q}{\chi}T = -\frac{P_t\alpha^2}{4\pi a\kappa(1+\alpha a)}\left(\frac{a}{r}\right)e^{-\alpha(r-a)}, \tag{5}$$

where T is the temperature rise, Q is the blood flow, α is the optical attenuation coefficient $(= 1/\delta)$, κ is the thermal conductivity and χ is the thermal diffusivity given by:

$$\chi = \frac{\kappa}{\rho c}, \tag{6}$$

where ρ and c are the mass density and specific heat of blood, respectively.

Since the thermal relaxation time (ca. 5 – 15 min.) is typically an order of magnitude less than the total treatment time, the temperature distribution will be close to the steady-state values for most of the exposure period[10]. Furthermore, since the dimensions of the tissue are much larger than the optical and thermal penetration depths, the medium can be considered as infinitely large in extent. The boundary conditions can thus be specified as zero heat flow at the surface of the applicator and as a finite temperature at infinity. In an infinite medium, the general steady-state solution for a spherical applicator can be written[10]:

$$T = \frac{P_t}{4\pi\kappa\left[1-(\alpha_v/\alpha)^2\right]}\times\frac{1}{r}\left\{\frac{1}{1+\alpha_v a}e^{-\alpha_v(r-a)} - \frac{1}{1+\alpha a}e^{-\alpha(r-a)}\right\}, \tag{7}$$

where α_v is the thermal attenuation coefficient given by:

$$\alpha_v = \frac{1}{\delta_v}, \tag{8}$$

where δ_v is the thermal penetration depth.

3. MATERIALS AND METHODS

3.1 Applicator construction

The applicator was constructed by modifying a standard silicon Foley urine catheter as shown in Figure 1. The distal end was removed and sealed just below the end of the balloon by a transparent silicon plug. The end of the balloon-filling channel, residing in the catheter wall, was also sealed to prevent leakage and balloon deflation. The applicators were gamma sterilized and packaged in two sizes depending on the dimensions of the cavity following tumor resection. The inner diameter of the applicator catheter was 3 or 4 mm depending on the size of the balloon chosen. The balloons could be inflated up to 5 cm in diameter.

3.2 Light Distribution Measurements

Light ($\lambda = 630$ nm) from an argon-ion-pumped dye laser was coupled into an optical fiber which was inserted into the balloon applicator. The light delivery fiber has a core diameter of 200 μm and its distal end consists of a 1.4 mm spherical diameter diffuser. The balloon was filled to a diameter of 3 cm with either saline or a 0.1 % Intralipid™ (Kabivitrum, Inc., Clayton, NC) scattering solution. The balloon was immersed in a 2 % Intralipid-filled phantom which simulated the optical scattering characteristics of human brain tissue. Light levels were measured with a 0.8 mm diameter spherical tipped optical detector fiber positioned in contact with the applicator balloon surface. A lock-in detection technique was used to minimize the effect of background noise. Prior to each measurement, light output fluctuations of the laser were monitored and found to be within 3 %.
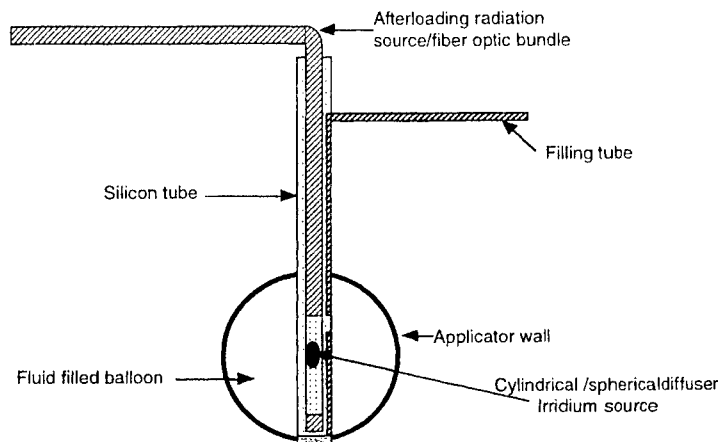
Figure 1. Cross-section illustration of the balloon applicator.
It consists of a 6 mm blind ending silicon balloon catheter. The
balloon can be inflated through a separate filling channel. Either
an ionizing radiation or laser light source can be afterloaded.

4. RESULTS AND DISCUSSION

4.1 Light distribution measurements

Results of the uniformity measurements are shown in Figs. 2a and b. Irradiance was measured as functions
of position along the balloon catheter (45° intervals from pole-to-pole), type of catheter-filling fluid (saline,
or 0.1% Inrtralipid), and position of source fiber in the applicator (geometric center, or lower pole). Each
data point represents the mean of measurements from two applicators.
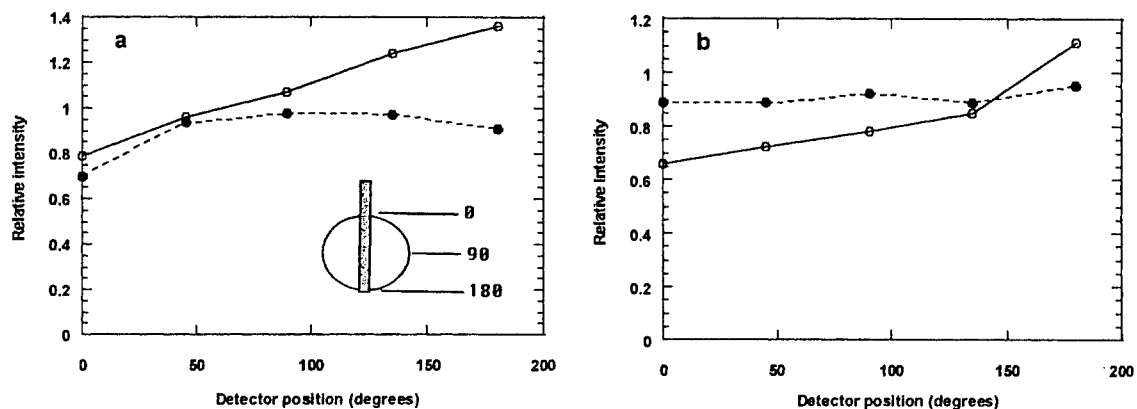
Figure 2. Normalized light output at selected positions along the balloon applicator. The applicator was
submerged in a 2% Intralipid scattering solution and measurements were made from pole-to-pole at 45°
intervals as shown in the inset. The balloon was filled with saline (a), or a 0.1% Intralipid solution (b).
●: spherical diffuser at balloon center, O: spherical diffuser at bottom of balloon. Data is normalized to
the value obtained with the spherical diffusing fiber in the center of the saline-filled balloon, and the
detector at the 90° position.

In the case of the saline-filled balloon with the spherical diffuser at the center, the irradiance is uniform to
within 5 % except at an angle of 0°. The 30 % decrease in irradiance at this angle is probably due to the
inhomogeneity of the irradiance emanating from the spherical diffuser tip. The presence of the fiber
prevents emission of light from the diffuser in the backward direction, hence, the amount of light reaching
the detector at 0° will be reduced. As shown in Figure 2b, the addition of a scattering solution to the

applicator improves significantly the uniformity of the irradiance. In this case, the irradiance is uniform to within 5 % at all measured locations when the spherical diffuser is positioned in the center of the applicator.

The results suggest that a saline-filled applicator might result in an unacceptable underdose to tissues surrounding the superior aspect of the applicator. Although far from ideal, it is conceivable that the characteristic irradiance from a saline-filled applicator may suit the required light distribution in some patients.

Variations in measured intensity, as a function of source fiber position in the applicator, can be explained in terms of the distance between the spherical source and detector. When the source is placed at the center of the applicator, measured irradiances are independent of detector position since the distance between source and detector is always the same. Conversely, when the source is placed at the bottom of the applicator, measured irradiances increase as the detector is moved towards the bottom of the applicator. The observation of irradiances greater than 100 % for angles in excess of 90° is due simply to the fact that all signals are normalized to the signal obtained for the spherical source fiber located in the center of the saline-filled balloon (detector fiber at 90°). Of clinical relevance is the finding that it is possible to change the light distribution in the resected cavity simply by changing the position of the source within the applicator.

4.2 Treatment time calculations

The time required to deliver a sufficient optical dose to tissues can be determined from knowledge of the fluence rate at the point of interest. Equation (2) was used to estimate fluence rates in brain tissue for three commonly used applicators (Figure 3). The following variables were used in the calculation: a 1 W input power (λ = 630 nm), an optical penetration depth of 3.2 mm[11-13], and a diffusion constant of 5.4 x 10^{10} mm^2s^{-1} [11-13]. Figure 3 illustrates one of the fundamental limitations of PDT, namely the poor penetration of light in biological tissues. For example, the calculations show a decrease in fluence rates of between 3 and 4 orders of magnitude over a tissue depth of 2 cm. Based on the data in Figure 3, treatment times required to deliver a PDT threshold dose of 50 J cm^{-2} are summarized in Table I for three applicator radii (denoted by a). In all cases, an input power of 1 W is assumed.
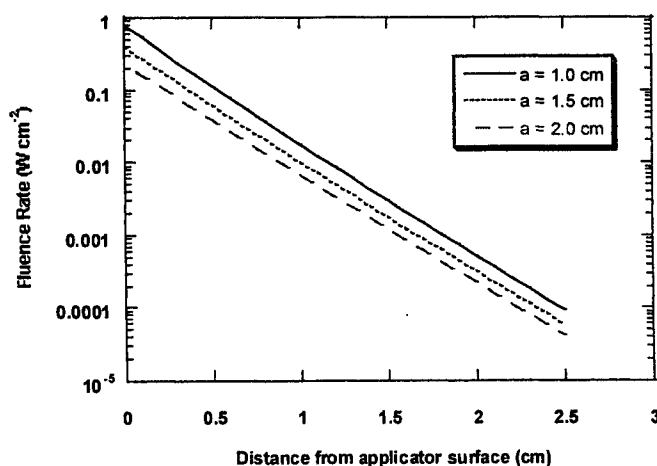
Figure 3. Calculated fluence rates in brain tissue for three different applicators (radii = 1.0, 1.5, and 2.0 cm).

Table I. Time (hours) required to deliver a dose of 50 J cm^{-2}

Depth (cm)	Time (h)		
	a=1.0 cm	a=1.5 cm	a=2.0 cm
1.0	0.8	1.4	2.1
1.5	4.7	7.7	11.5
2.0	26.7	43.0	62.6

The clinical feasibility of treatments lasting for tens of hours must be questioned, even with the use of an indwelling balloon applicator. Furthermore, for realistic input powers of a few Watts, the fluence rates at cm depths in brain tissue are likely too low to evoke a PDT response. For example, it is shown in Figure 3 that, for an input power of 1 W, fluence rates at depths of 2 cm in brain tissue range from 0.2 to 0.5 mW cm^{-2} depending on the applicator diameter. The results of *in vitro* studies in a human glioma spheroid system suggest that a fluence rate of approximately 10 mW cm^{-2} is required for significant PDT response[14]. The input power required for a fluence rate of 10 mW cm^{-2} as a function of depth, is illustrated in Figure 4. Results at specified depths are summarized in Table II.
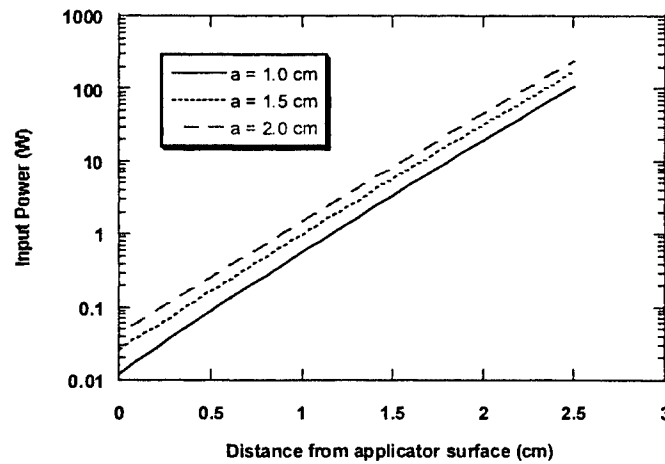
Figure 4. Calculated input powers required for a fluence rate of 10 mW cm^{-2} at various depths in brain tissue.

Table II. Input power required for a fluence rate of 10 mW cm^{-2}

Depth (cm)	Input power (W)		
	a=1.0 cm	a=1.5 cm	a=2.0 cm
1.0	0.6	1.0	1.5
1.5	3.4	5.6	8.3
2.0	19.3	31.0	45.1

The results in Figure 4 (and Table II) show that large input powers are required to obtain threshold fluence rates at cm depths in brain tissue. Although input powers of tens of watts may be possible, the maximum power, and hence the effective treatment depth, will be governed by the thermal damage threshold of brain tissue.

4.3 Thermal distribution calculations

The temperature rise during PDT is dependent on a number of parameters, such as optical absorption and scattering, exposure time, specific heat, thermal conduction, and blood perfusion. The temperature increases rapidly during irradiation and typically reaches a steady-state value after about five minutes of

exposure[15]. This steady-state temperature should be kept below about 45° C in order to avoid hyperthermic reactions[8].

Temperature distributions from various spherical applicators are illustrated in Figure 5. The curves in Figure 5 were calculated from equation (7) using the following values: thermal conductivity of 0.6 W m^{-1}K^{-1} [16], optical penetration depth of 3.2 mm, and thermal penetration depth (white matter) of 10 mm[16]. As expected, the maximum temperature (T_{max}) occurs at the surface of the applicator. Furthermore, for a given input power, T_{max} increases with decreasing applicator diameter. Since T_{max} scales linearly with input power, the input power required for a rise in T_{max} of 8° K (the hyperthermic threshold) can be determined in a relatively straightforward manner. It should be noted that higher input powers are possible if the cavity is cooled, i.e., by the circulation of water through the applicator. For example, calculations show that, for a given input power, a four-fold reduction in T_{max} is possible if the cavity is maintained at ambient temperature, i.e., 37° C[17]. As a result, input powers may be increased by a factor of four simply by cooling the applicator. The input powers resulting in a rise in T_{max} of 8 K, in the presence and absence of cooling, are shown in Table III.
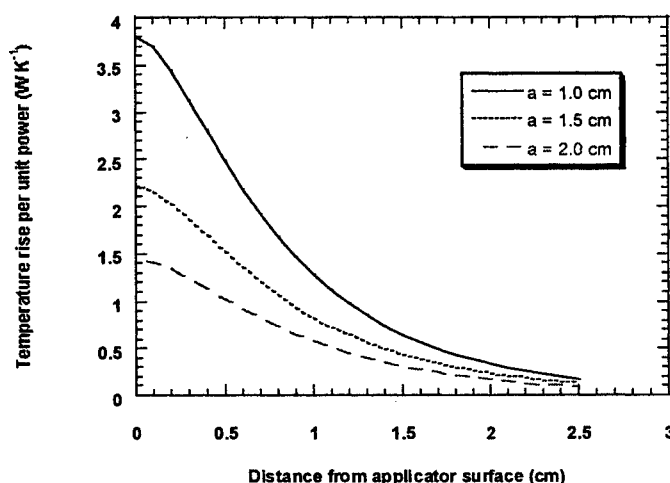
Figure 5. Temperature rise in brain tissue for a 1 W input power.
Thermal distributions are shown for three different applicator sizes.

Table III. Input power resulting in a T_{max} rise of 8 K

Applicator Radius (cm)	Input Power (W)	
	No cooling	Cooling
1.0	2.1	8.4
1.5	3.6	14.4
2.0	5.7	22.8

From the curves in Fig. 4, the input powers in Table III correspond to maximum treatment depths of 1.4 and 1.8 cm for the case of no cooling and cooling, respectively. Although it is possible to use very high optical powers if the applicator is cooled, such treatments are not clinically feasible with current laser systems. It should, however, be possible to treat with input powers of a few watts using current state-of-the-art PDT laser systems. It would thus be possible to treat to depths approaching 1.5 cm without cooling the applicator.

This paper addressed only issues related to light delivery in PDT. It is important to realize that, in addition to the light distribution, the overall efficacy of PDT depends in a complex way on factors such as the kinetics of drug uptake, type of drug, cellular localization of the photosensitizer, and tissue oxygenation status. Although, in theory, it may be possible to treat to depths approaching 1.5 cm in brain tissue, the high

fluences associated with such treatments may cause unacceptable normal tissue damage. This is especially true in the case of poorly localizing photosensitizers. It is important to note, however, that, in the high fluence region near the applicator, the optical dose is reduced drastically due to the effects of photobleaching. The effect of photobleaching is illustrated in Fig. 6. The "no-bleaching" and "bleaching" curves were calculated from equations (3) and (4), respectively. An input power of 3.6 W was chosen as this represents the hyperthermic threshold for the 1.5 cm applicator (Table III). A 5000 s radiation time was chosen since this is the time required to deliver a threshold dose of 50 J cm^{-2}, at a dose rate of 10 mW cm^{-2}. It is shown that, in the region close to the applicator where Ψ is much greater than Θ, the bleaching process limits the effective dose to $\Psi_{eff} \cong \Theta$. A bleaching parameter of 50 J cm^{-2} was chosen as this is representative of 5-Aminolevulinic acid[18]. For tissues immediately adjacent to the applicator, photobleaching lowers the optical dose by approximately 2.5 orders of magnitude.
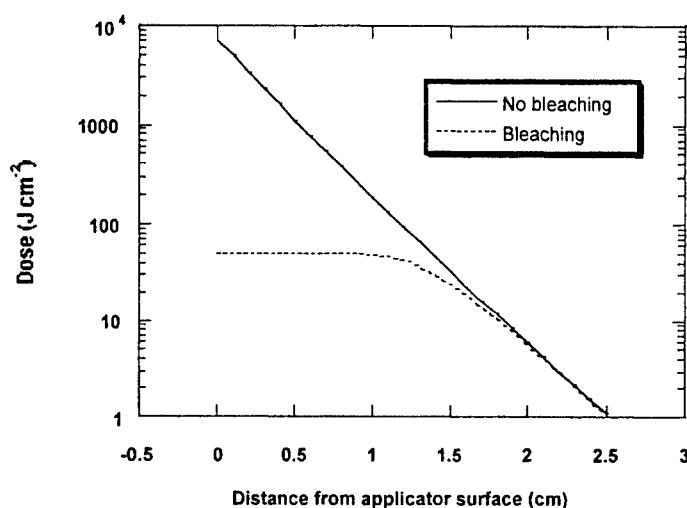
Figure 6. Calculated optical dose and effective optical dose (bleaching) versus distance from the applicator axis. Power = 3.6 W, applicator radius = 1.5 cm, exposure time = 5000 s, bleaching parameter = 50 J cm^{-2}.

The use of a balloon applicator allows for optimization of light delivery in PDT treatments. Since longer treatment times are possible, greater volumes can be irradiated than are currently possible with one-shot intraoperative procedures. Furthermore, since the applicator can be left in the resection cavity for long periods of time (weeks to months), other types of irradiation schemes are possible. This is important in view of recent *in vitro* findings suggesting that light dose fractionation and repeated PDT treatments may be more effective than one-shot procedures[7]. Finally, a vast amount of clinical experience with the applicator suggests that it can be used in PDT treatments over extended periods of time. The balloon applicator is well tolerated by patients – it has already been used for brachytherapy in over 100 patients with few complications.

5. CONCLUSIONS

Measurements of light distribution form a balloon applicator immersed in a brain-simulating phantom, show that it may be used to deliver sufficiently uniform light doses during PDT. The light distribution is uniform to within 5 % when the balloon is filled with a scattering medium. The applicator allows great flexibility in terms of light delivery: treatments are not limited by irradiation times, nor are they limited by thermal damage, especially if the applicator is cooled. Calculations show that it may be possible to deliver threshold light doses to depths of approximately 1.4 cm using balloon applicators of 1.5 cm radius or less. The main drawback of using large applicators is the significant volume of normal brain tissue irradiated. Thus, as is the case with one-shot intraoperative procedures, these types of treatments may be limited by normal tissue complications.

ACKNOWLEDGEMENTS

REFERENCES

1. M. Salcman, "Epidemiology and factors affecting survival,"in Malignant Cerebral Glioma, M.L.J. Apuzzo, Ed. Amercian Association of Neurological Surgeons, pp. 95-109, 1990.

2. K.E. Wallner, J.H. Galicich, G. Krol, E. Arbit and M.G. Malkin, "Patterns of failure following treatments for glioblastoma multiforme and anaplastic astrocytoma," Int. J. Radiat. Oncol. Biol. Phys. 16, pp. 1405-09, 1989.

3. R. Ashpole, H. Syndman and A. Bullimore, "A new technique of brachytherapy for malignant glioma with cesium-137," Clin. Oncol. 2, pp. 333-7, 1990.

4. T.B. Johannesen, K. Watne, K. Lote, J. Norum, R. Hennig, K. Tveraa and H. Hirschberg, "Intracavity fractionated balloon brachytherapy in glioblastoma," Act. Neurochir. (Wien) 141, pp. 127-33, 1999.

5. P.J. Muller and B.C. Wilson, "Photodynamic therapy: cavitary photoillumination of malignant cerebral tumours using a laser coupled inflatable balloon," Can. J. Neurol. Sci. 12(4), pp. 371-81, 1985.

6. H. Kostron, A. Obwegeser and R. Jakober, "Photodynamic therapy in neurosurgery: a review," J. Photochem. Photobiol. B: Biol. 36, pp.157-68, 1996.

7. S. J. Madsen, C.-H. Sun, B.J. Tromberg and H. Hirschberg, "Development of a novel balloon applicator for optimizing light delivery in photodynamic therapy," In preparation.

8. B.J. Tromberg, L.O. Svaasand, M.K. Fehr, S.J. Madsen, P. Wyss, B. Sansone and Y. Tadir, "A mathematical model for light dosimetry in photodynamic destruction of human endometrium," Phys. Med. Biol. 41, pp. 223-37, 1996.

9. H.J. van Staveren, J.F. Beek, J.W.H. Ramackers, M. Keijzer and W.M. Starr, "Integrating sphere effect in whole bladder wall photodynamic therapy: I. 532 nm vs. 630 nm optical irradiation,"Phys. Med. Biol. 39, pp. 947-59, 1994.

10. L.O. Svaasand, "Temperature rise during photoirradiation therapy of malignant tumors," Med. Phys. 10(1), pp. 10-17, 1983.

11. B.C. Wilson and P.J. Muller, "An update on the penetration depth of 630 nm light in normal and malignant human brain tissue in vivo," Phys. Med. Biol. 31, pp. 1295-97, 1986.

12. L.O. Svaasand and R. Ellingson, "Optical properties of human brain," Photochem. Photobiol. 38, pp. 293-99, 1983.

13. L.O. Svaasand and R. Ellingson, "Optical penetration in human intracranial tumors," Photochem. Photobiol. 41, 73-76, 1985.

14. S.J. Madsen, C.-H. Sun, B.J. Tromberg, V.P. Wallace and H. Hirschberg, "Photodynamic therapy of human glioma spheroids using 5-aminolevulinic acid," Photochem. Photobiol. 72(1), pp. 128-34, 2000.

15. L.O. Svaasand, C.J. Gomer and A.E. Profio, "Laser induced hyperthermia of ocular tumors," Appl. Opt. 28, pp. 2280-7, 1989.

16. L.O. Svaasand, "Thermal distribution from inserted optical fibers," in Optoelectronics in Medicine:Proceedings of the 2nd International Nd:YAG Laser Conference, W. Waidelich and P. Kiefhaber, Eds. Springer-Verlag, pp. 294-301, 1985.

17. L.O. Svaasand, personal communication.

18. E. Hoeydalsvik, "Characterization of the distribution of porphyrins in malignant tumors by fluorescence," M.Sc. Thesis, Division of Physical Electronics, Norwegian Institute of Technology, 1994.

Clinical study assessing the photosensitizer accumulation and light penetration for esophageal cancer prior to treatment by PDT

Paulo R. Bargo and Steven L. Jacques
Oregon Medical Laser Center
Oregon Graduate Institute of Science and Technology
Portland, Oregon 97225 USA

ABSTRACT

The FDA has approved PDT using Photofrin for certain esophageal and lung cancers, specifying an approved prescription of administered drug (mg/kg body weight) and administered light (J/linear cm of cylindrical fiber). This paper describes our development of a multi-optical fiber catheter for endoscopic use which documents the drug accumulated in the target tissues and the light penetration into the target tissues. The catheter uses reflectance to specify the light penetration depth and uses reflectance-corrected fluorescence to document drug accumulation. The goal is to document the variation in drug and light received by patients who are administered the FDA-approved prescription.

Keywords: photodynamic therapy, PDT, dosimetry, optics, fluorescence, reflectance

1. Introduction

PhotoDynamic Therapy (PDT) has been approved by the FDA for certain esophageal and lung cancers. Treatment success depends on three major factors: accumulation of photosensitizing drug, light penetration and oxygen concentration The FDA specifies an approved prescription of administered drug (mg/kg body weight) and administered light (J/linear cm of cylindrical fiber). But the administered dose of drug and light is not necessarily the same as the received dose of drug and light. Each patient may have variable pharmacokinetics which affect the amount of drug uptake into the target cancer tissue. Each patient may have variable inflammation which modulates the blood content of the tissue, a factor known to greatly impact the penetration of treatment light into a target tissue. This work describes a system and method being used to document the variation in drug and light received by patients who are administered the FDA-approved prescription.

2. Material and Methods

Patients

Patients with esophageal and bronchial tumors undergoing standard FDA PDT treatment protocols were recruited for these measurements. All were intravenously injected with 2mg/kg body weight of Photofrin II. Light dose was 288 J/cm of diffuser. Measurements were taken immediately prior to light activation of the drug, two days after injection.

Consent to take part at the dosimetry study was obtained from all patients. A study protocol was defined and approved by the Hospital IRB Committee. Detailed written and oral information on the dosimetry protocol was given to the patients prior to enrollment. The measurements extended the PDT procedure an average of 10 minutes.

Fluorescence measurements

A nitrogen-dye laser operating at 440nm wavelength, 4ns pulse duration, 20μJ/pulse energy (Laser Science) was used to excite the fluorescence (figure 1). Excitation and collection were made through a single 600μm-core-diameter disposable optical fiber (Ceramoptec) using the biopsy channel of an endoscope. The proximal end of the fiber was connected to a fiber bundle with a central 300μm optical fiber (which guided the excitation light from the laser) surrounded by twelve 100μm optical fibers that routed the fluorescence signal to an optical multichannel analyzer (OMA, Princeton Instrument) gated detector. Stray light was rejected with a 530nm cut-off colored glass filter (Schott). Data was stored in a computer trough a GPIB port. Collection time was set for 100ms and 20 accumulations were typically used, making an average collection time of 2s per measurement. The use of 4ns pulse duration and a gated detector allowed fluorescence measurements to be made in the presence of the white illumination of the endoscope, such that the doctor could observe the placement of the optical fiber during the procedure. Three normal sites and three tumor sites, judged visually by the doctor, were measured. Total fluorescence measurement procedure took about 3 minutes. A measurement of a standard Rhodamine 6G solution (1.25mg/ml in ethanol, Exciton) in a cuvette was taken before data collection to correct for day-to-day variations on the system.
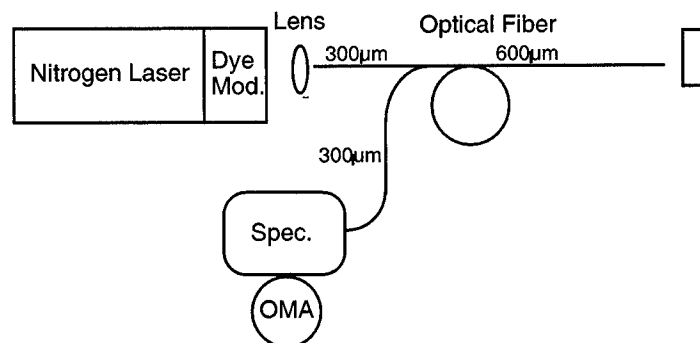
Figure 1. Fluorescence system setup. A nitrogen pumped dye laser (400nm, 4ns pulse duration, 20µJ/pulse) excites tissue fluorescence, which is collected through the same optical fiber and detected with an OMA system.

Reflectance measurements

Reflectance measurements were taken immediately after fluorescence measurements. White light from a tungsten lamp (Oriel) was used as source to collect reflectance spectra from tissue. The signal was detected with a spectrophotometer (Ocean Optics). Two different optical probes were used. The first was a single 600µm-core-diameter optical fiber used in the first 5 patients. Since the volume probed by the single fiber is very small there was very low resolution on retrieving the absorption coefficient from this data (not shown). A second-generation optical probe was designed. This probe has two optical fibers displaced 2.5mm apart at the distal end (described later). Light from the white lamp is guided through one fiber and collected by the other. Three normal and three tumor sites were collected per patient, and reflectance spectra was later analyzed with diffusion theory to extract tissue optical properties. The probe was calibrated using an epoxy/titanium-dioxide solid phantom and Intralipid phantoms. The solid epoxy standard was previously calibrated with integrating sphere measurements and Inverse Adding Doubling modeling was used to extract its optical properties. Liquid phantoms were prepared mixing 2% Intralipid and India ink, and were calibrated with adding absorber techniques.
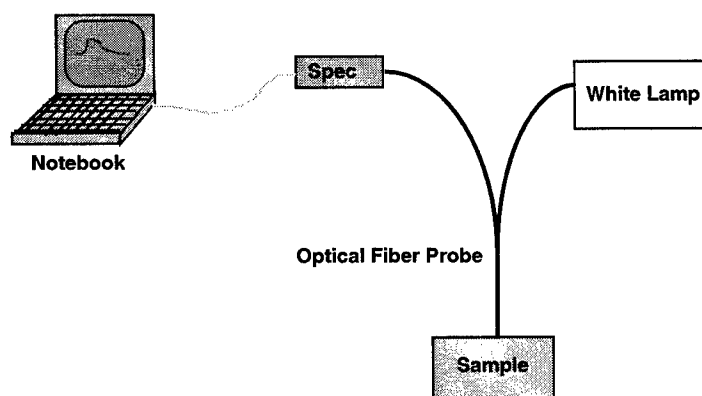
Figure 2. Reflectance system setup. Light from a tungsten lamp is guided through an optical probe (see probe preparation). Reflectance spectra is acquired with a spectrophotometer and recorded in a laptop.

Probe preparation

Two pieces of stainless steel rod (0.025 dia.) were cut 12-mm long and one end of each was polished at a 45¡ angle. Two pieces of stainless steel tubing (I.D. = 660 µm, O.D. = 830 µm) were cut 8-mm long and a hole was made in each tubing spaced 2 mm and 4.5 mm from the end, respectively, using a 0.025 end mill. The polished steel rod was aligned inside each tubing such that the mirror (45¡ polished surface) would send light through the hole. An optical fiber (silica-silica, 600 µm core diameter, 3-m long; Ceramoptec) was polished flat and inserted through the other end of the tubing. The set was fixed by filling the internal spaces of the tubing with clear epoxy (Epo-Tek 301; Epoxy Technology), cured at 60 ¡C for 4 hr. The excess rod was trimmed and filed to remove sharpen edges. The two side-viewing optical fibers were bonded together by epoxy with the two holes aligned toward the same side. The 3-m extension of the optical fibers was inserted into Teflon tubing (PTFE 17LW; Zeus) and the tip of the probe was sealed with silicone glue (between the Teflon tubing and the steel rods) and a 2-cm piece of heat-shrink Teflon tubing (14HS; Zeus).
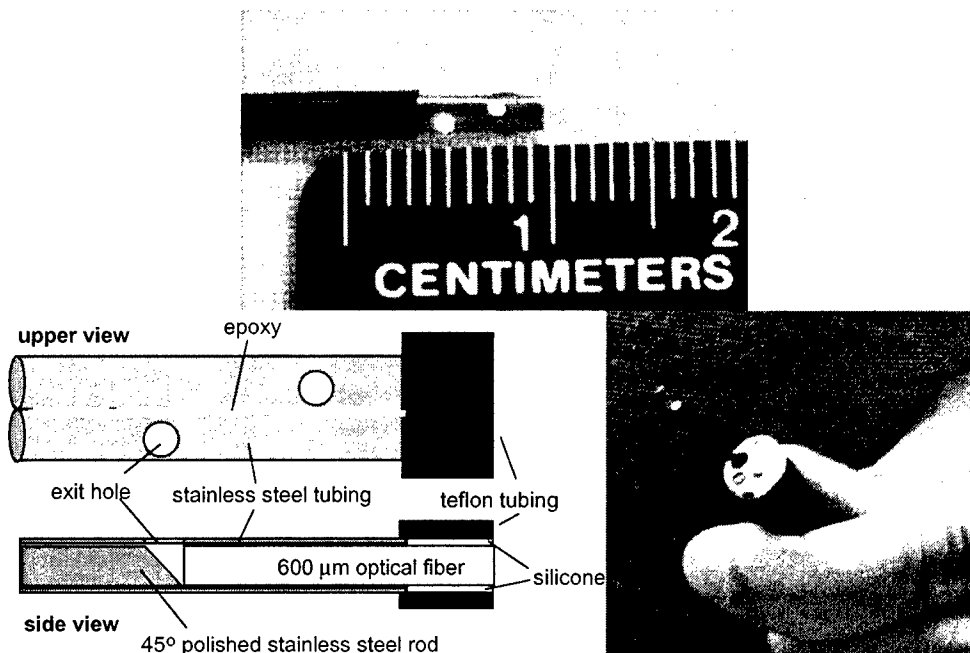
Figure 3. Two-fiber probe for reflectance measurements. A 45¡ polished steel mirror directs source light from one 600 m optical fiber 90¡ out the side of the fiber and a second mirror and fiber collect light for detection. Source-collector separation is 2.5 mm. Probe is passed through working channel of endoscope.

3. Results and Discussion

Fluorescence measurements

Analysis of fluorescence data were made after normalization of the spectra by the peak fluorescence of the rhodamine standard to correct for day-to-day variation in the system response. Background tissue autofluorescence was fitted with part of a Gaussian curve, which was subtracted from the original spectrum to yield a difference spectrum due to photosensitizer. The photosensitizer spectrum was integrated over the 620-720 nm range and divided by 100 nm to yield a fluorescence score in units of [counts/nm]. Figure 4 illustrates the procedure for tipical normal and tumor spectra.
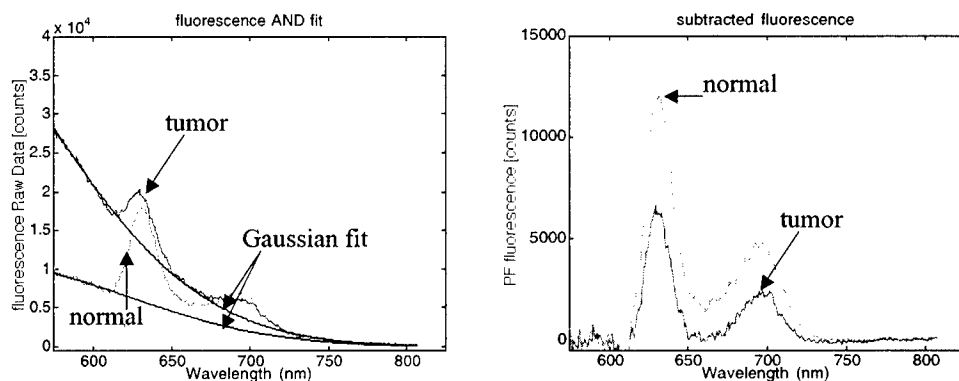
Figure 4. Fluorescence measurement of one tumor and one normal site of a patient prior to PDT treatment. (Left) Raw data and background Gaussian fit. (Right) Raw data minus Gaussian fit.

The integrated fluorescence scores for seven patients are shown in Fig. 5. Little difference between normal and tumor tissues is observed, however this data points should be corrected by a factor proportional to the optical properties of the tissue. Patient #6 was the only one that showed great distinction between normal and tumor sites. This was the only bronchial cancer patient measured so far. Although the remmarcable distinction no conclusions can be drawn at this point. The histogram in Fig. 5 shows the distribution over all measurements on all patients and all sites, both normal and tumor. A coefficient of variation (standard deviation/mean) of ~0.33 is observed.
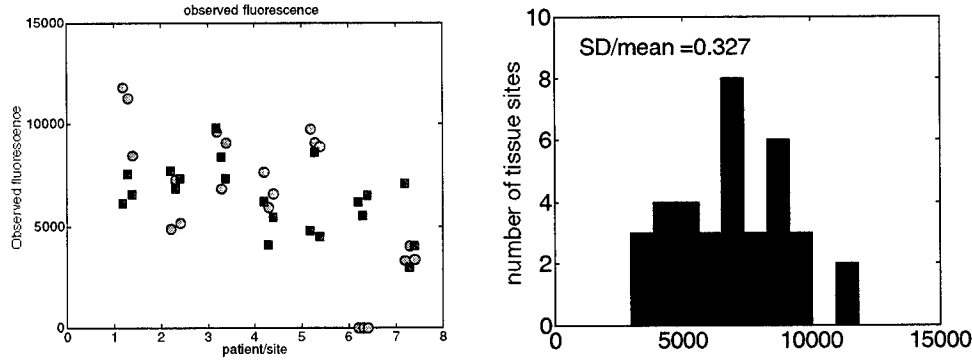
Figure 5. (Left) Fluorescence score for 7 patients (■) normal (o) tumor.
(Right) Histogram of all sites (normal and tumor) for all patients.

Reflectance Measurements

Immediately after the fluorescence measurements, the reflectance probe was passed through the biopsy channel of the endoscope and placed on the tissue under doctor visualization. The endoscope illumination was turned off for a few seconds while the spectrum was acquired (200-ms acquisition time) and the probe was than repositioned. Three normal and three tumor sites were measured at sites close to where the fluorescence data was collected. After the data collection was completed the probe was calibrated with standards. Figure 6 shows the raw reflectance spectra for patient #7. Lower intensities at the 500-600nm range are due to blood absorption.
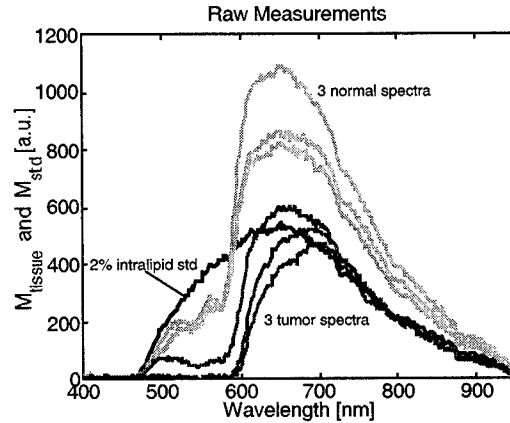
Figure 6. Reflectance raw data for 3 normal sites, 3 tumor sites of patient #7 and intraqlipid standard. Lower intensities at the 500-600nm range are due to blood absorption. Two tumor sites had zero intensities below 600nm.

The spectra were analyzed using a diffusion theory based model with the tissue been assumed to be homogeneous. The air/tissue boundary was included in the model using the method of Farrel et al[1].
Reflectance measurements on tissue (M_{tissue}) were first normalized by the measurements (M_{std}) within the standard lipid emulsion phantom (2% Intralipid", 2 grams lipid per 100 ml total volume). The final spectrum was the ratio M:

$$M = \frac{M_{tissue}}{M_{std}} = \frac{So \cdot R_{tissue} \cdot f \cdot D}{So \cdot R_{std} \cdot f_{std} \cdot D} = \frac{R_{tissue} \cdot f}{R_{std} \cdot f_{std}} \approx const \cdot \frac{R_{tissue}}{R_{std}} \qquad (Eq.1)$$

where

So   the wavelength dependent light source power [W]

D   the wavelength dependent detector sensitivity [counts/W]

R_{tissue} and R_{std} total amount of light from the source escaping to the surroundings. [1/cm^2]

f_{tissue} and f_{std} the fiber collection efficiency equal to the area of the probe, A = $\pi(0.0300cm)^2$, times the fraction of diffuse light that successfully enters the fiber, f ¯ 0.05 (from Monte Carlo simulations and experimental data). f_{std} = Af [cm^2]

The terms So (the source spectral response) and D (the detector spectral response) are the same for tissue and standard measurements and don t vary within a measurement procedure and thus can be canceled. f_{tissue} and f_{std} are constant throughout the measurements and assumed to be equal for a wide range of optical properties when the separation between source and detector fibers is larger than several mean free paths. The constant term (const) is introduced to account for variations in the fiber placement on the tissue.

Tissue absorption was modeled as 85% water content ($\mu_{a\ water}$), a background spectrum for dry bloodless tissue ($\mu_{a\ dry}$), and a variable volume fraction (f_v) of blood ($\mu_{a\ oxy}$, $\mu_{a\ deoxy}$) at a variable oxygen saturation (S). The scattering properties were represented by a simple expression that mimics the combination of Mie scattering from larger tissues structures such as mitochondria, nuclei and cells and Rayleigh scattering from the ultrastructure on the 10-100 nm scale[2]. Absorption coefficient (μ_a) and reduced scattering coefficient (μ_s) were specified as:

$$\mu_a = \mu_a^{dry} + 0.85\mu_a^{water} + f_v\left(S \cdot \mu_a^{oxy} + (1-S)\mu_a^{deoxy}\right)$$

(Eq. 2)

$$\mu_s' = a \cdot \lambda^{-b}$$

(Eq. 3)

where

μ_a	total absorption coefficient of tissue in vivo [cm^{-1}]
$\mu_{a\ dry}$	absorption coeff. of dry bloodless tissue = Aexp(-B) , [cm^{-1}] (from library)
$\mu_{a\ water}$	absorption coeff. of pure water [cm^{-1}] (from library)
f_v	volume fraction of 45%-hematocrit blood in tissue [dimensionless]
S	oxygen saturation [dimensionless]
$\mu_{a\ oxy}$	absorption coeff. of oxygenated blood (45% hematocrit) [cm^{-1}] (from library)
$\mu_{a\ deoxy}$	absorption coeff. of deoxygenated blood (45% hematocrit) [cm^{-1}] (from library)
μ_s	reduced scattering coefficient of tissue in vivo [cm^{-1}]
a	factor that characterizes magnitude of scattering [cm^{-1}]
b	factor that characterizes wavelength dependence of scattering [dimensionless]
λ	wavelength [nm]

Typical spectra for $\mu_{a\ dry}$, $\mu_{a\ water}$, $\mu_{a\ oxy}$ and $\mu_{a\ deoxy}$ are shown in figure 7.
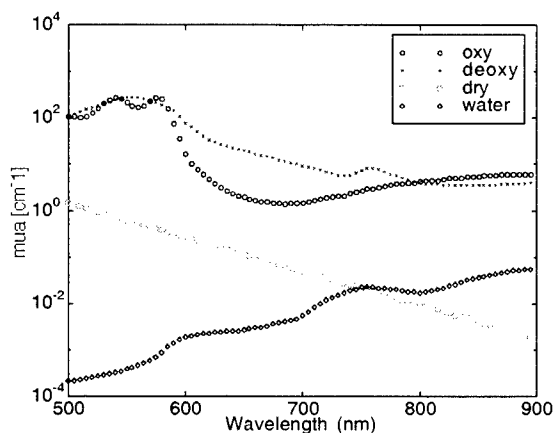
Figure 7. Spectra of blood (($\mu_{a\ oxy}$, $\mu_{a\ deoxy}$), water and dry tissue used as an input library for the modeling.

The experimental spectrum (M) was fitted by the predicted spectrum (constM$_{tissue}$/M$_{std}$) yielding five values: a, b, f_v, S and const. This fitting is sensitive to the shape of the spectrum rather than the magnitude of the experimental spectrum.

Figure 8 shows a typical outcome of the model with the experimental spectrum (o) and the predicted spectrum (-) for a normal site and for a tumor site. The values of a, b, f_v, S, and const are specified in the graph. To obtain the optical properties one must use these numbers with equations 2 and 3.
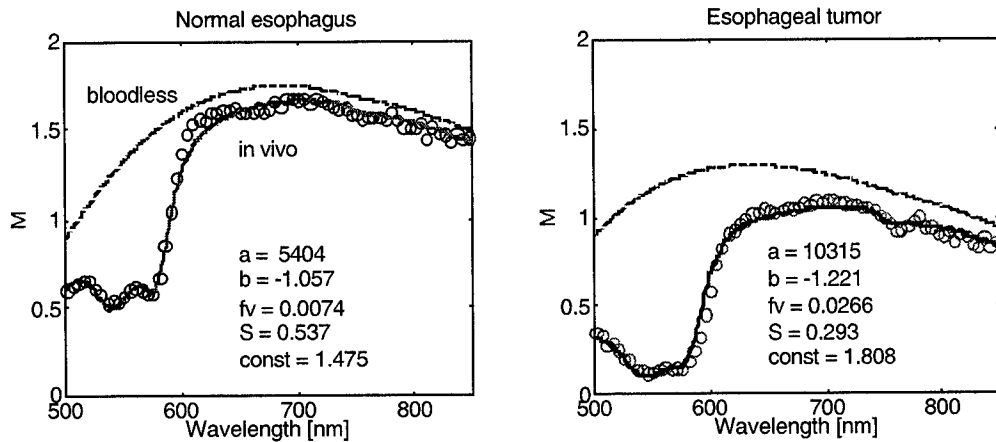
Figure 8. Blood content of normal and tumor tissue in one tissue site (patient #7). (Left) Experimental measurement of NORMAL TISSUE normalized by measurement of Intralipid standard. (Right) Same for TUMOR TISSUE. Circles are experimental measurements. Solid lines are predicted measurements based on light transport theory. Dashed lines are predicted measurements if tissue were bloodless.

Reduced scattering coefficients for the normal and tumor sites based on the values of a and b are shown in figure 10 (LEFT). Tumor sites appear to have an average lower reduced scattering coefficient than normal tissue. Average absorption coefficients for normal and tumor tissues are shown in figure 10 (RIGHT). Water and dry tissue spectra are also shown. Tumor tissue consistently had a higher blood content than the normal tissue making the average tumor absorption coefficient higher than that of normal tissue for patient #7.
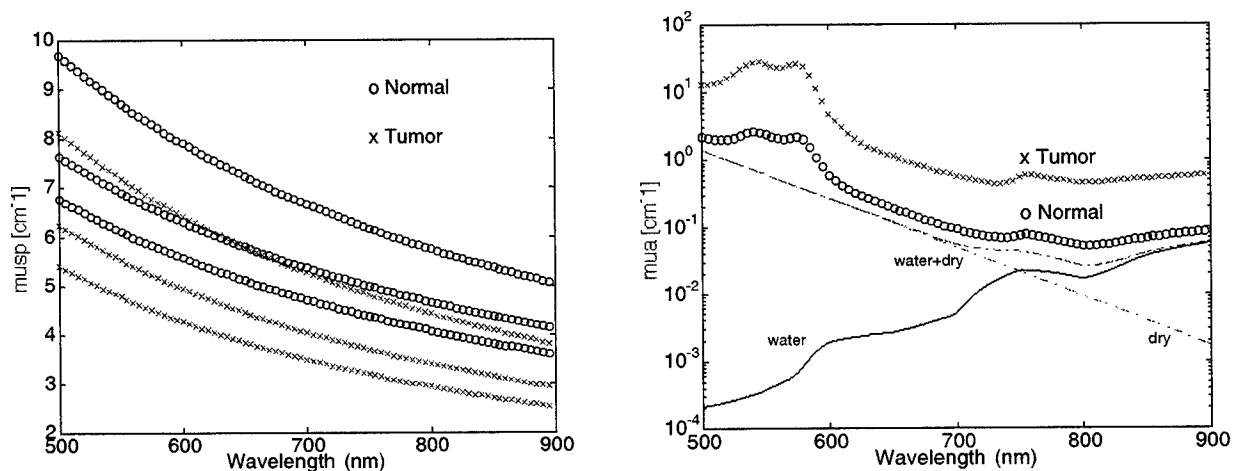
Figure 10: Optical properties of normal and tumor tissue from patient #7. (Left) Reduced scattering coefficient. (Right) Absorption coefficient. The tumor had an average 20% lower scattering coefficient and an average 3.6-fold higher blood content than the normal tissue.

4.Conclusions

We developed a system and model to acquire relative fluorescence and optical penetration depth (optical properties) in tissue, prior to endoscpic PDT. The results show that there is a great variation in the fluorescence data, which shows our first attempt to map the distribution of drug concentration in normal and tumor tissue. We are working on calibration methods to convert the fluorescence data into true drug concentration data. Light transport in the tissue and the collection efficiency of the optical fiber (both vary with the tissue optical properties) will have to be taken into account. Diffuse reflectance measurements proved to be a simple way to retrieve the tissue optical properties. Tumor had an average 20% lower scattering

coefficient than normal tissue. An average 3.6-fold higher blood content was observed in the tumor tissue representing up to 100% higher absorption coefficient in comparison to normal tissue.

ACKNOWLEDGEMENTS

REFERENCES

1. T.J. Farrell, M.S. Patterson, B. Wilson: A diffusion theory model of spatially resolved, steady-state diffuse reflectance for the noninvasive determination of tissue optical properties in vivo, Med. Phys. 19:881-888, 1992.

2. I.S. Saidi, S.L. Jacques, F.K. Tittel: Mie and Rayleigh modeling of visible-light scattering in neonatal skin. Appl. Opt. 34:7410-7418, 1995.

Influence of Red Laser Irradiation on Hemoglobin Oxygen Saturation and Blood Volume in Human Skin in vivo

Alexander A. Stratonnikov[*], Natalia V. Ermishova and Victor B. Loschenov

Laser Biospectroscopy Lab, General Physics Institute, 38, Vavilov street, Moscow, 117942, Russia.

ABSTRACT

The aim of the present work was to study the response of hemoglobin oxygen saturation and relative blood volume in human skin in vivo to laser irradiation. The hemoglobin oxygen saturation and relative hemoglobin concentration in skin were evaluated from diffuse reflectance spectra in visible wavelength range. The skin spot at human hand was irradiated with laser beam and hemoglobin oxygen saturation and relative hemoglobin concentration were sampled every two second from the center of irradiated spot. It was evidently observed that hemoglobin oxygen saturation is increased after starting irradiation. During occlusion the oxygen consumption rate was higher in the presence of laser irradiation. However these effects were observed only at sufficiently high laser fluence rates. The most probable reason is that it is due to thermal effects.

Keywords: Photo-thermal effects, Oxygenation, Laser-tissue interaction, Laser therapy.

1. INTRODUCTION

The influence of laser irradiation on biological tissues in vivo may induce different effects depending mainly on parameters of laser light (wavelength, power density, pulse duration etc.) and chromophores in tissues absorbing this light. Figure 1 demonstrates the effects induced by light absorption in tissues and corresponding applications of lasers in medicine.
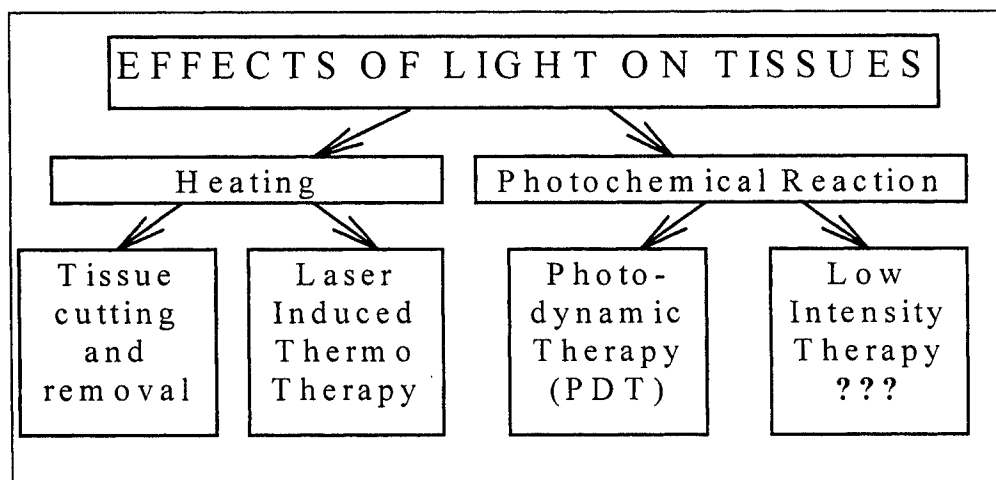
Figure 1. The effects of light in tissues and its application in medicine

The main tissue absorber in visible range is hemoglobin in oxygenated and deoxygenated form. Present work deals with the study of hemoglobin oxygen saturation changes in microcirculatory vessels of human skin in vivo under influence of laser irradiation at 675 nm. We would like to clarify the following questions. How blood oxygen saturation changes are induced by laser irradiation. In other words whether vessel response to laser irradiation is related to low intensity therapy and photodynamic therapy (PDT). It was found out that control of vessel response by measuring blood oxygen saturation may be very useful in estimating and monitoring in real time the PDT effect to tissues [1,2]. Here we apply the same method of monitoring blood oxygen saturation in skin of healthy volunteers under influence of laser irradiation alone.

---

[*] Correspondence: Email: biospec@online.ru , http://biospec.da.ru, Fax/Tel 7-095-3246363.

2. MATERIALS AND METHODS

For the measurements of diffuse reflectance spectra of tissue in vivo we applied a fiber optic spectrometer LESA-5 (Biospec, Russia). An experimental setup is shown in Figure 2. Light from a stabilized light source (halogen lamp) was delivered to the tissue by means of a 600 μm quartz fiber. After passing through the tissue the light was collected by a receiving quartz fiber 200 μm in diameter. The output end of the receiving fiber was the input slit of the spectrometer. We applied the spectrometer with a fixed grating and CCD type detector. The total spectrum range (400-1000 nm) can be acquired for 0.1 second. The spectrometer was controlled by a personal computer. A special program operating in the MS Windows environment allows one to acquire and display spectra and calculate oxygen hemoglobin saturation and relative hemoglobin concentration in real time from diffuse reflectance spectrum. For calculation of hemoglobin oxygen saturation we exploited only part of the spectral range acquired by the spectrometer between 510 nm and 590 nm.
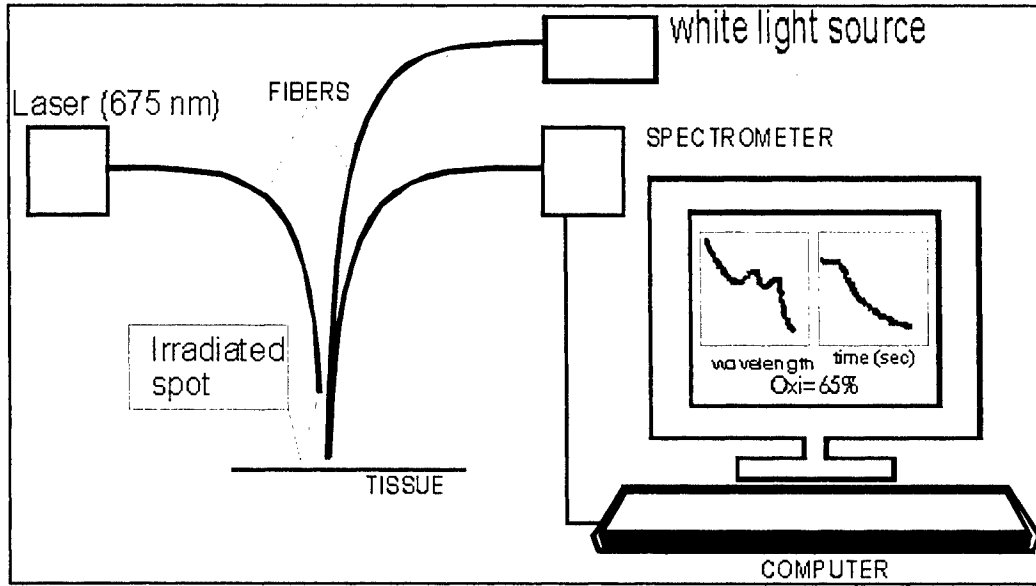
Figure 2. Experimental setup for monitoring blood oxygen saturation in skin during laser irradiation.

The distance, d, between delivery and receiving fibers was set to 2 mm. During the measurements the fibers were fixed parallel to each other at the distance less than a millimeter from the tissue and at 30 degrees angle from the normal to the tissue. This configuration allowed only diffuse reflected photons enter into the receiving fiber. There was no contact between fibers and tissue to avoid the influence of fiber pressure on blood circulation.

We used semiconductor laser (3 W, 675 nm) to induce blood oxygen saturation changes. This laser is applied in clinics for PDT with sulphonated aluminum phthalocyanines as photosensitizer. The laser light was delivered to the tissue with the use of 600 μm quartz fiber, the diameter of irradiated spot being 5-6 mm allowing to get fluence rates at the tissue surface up to 8 W/cm^2. The fiber was positioned so that blood oxygen saturation was measured in the center of irradiated spot and sampling fibers did not give a shadow to laser irradiation in the measurement region.

The experimentally measured spectral dependence of light attenuation was evaluated with the use of the following relation:

$$A_{exp}(\lambda) = \ln\left(\frac{I_{ref} - I_{dark}}{I - I_{dark}}\right), \tag{1}$$

where I_{ref} is the measured reflectance signal from the reference sample (BaSO$_4$) which has the uniform diffuse reflectance near unity in the spectral range under consideration (400-1000 nm), I_{dark} is the signal in the absence of any light (dark current of CCD) and I is the diffuse reflectance signal from the tissue. Equation (1) takes into account the spectral non uniformity of light source, fiber transmission and detector sensitivity. It should be noted that $A_{exp}(\lambda)$ as given by Eq. (1) is defined to within some constant value. However, the exact value of the constant in $A_{exp}(\lambda)$ is not important for our algorithm as only its wavelength dependence does matter.

The experimental dependence of attenuation was fitted by the following approximate model function:

$$A_{\text{model}}(\lambda) = c_0 + c_1 \cdot \lambda + <L> \cdot \left\{ c_{Hb} \cdot \varepsilon_{Hb}(\lambda) + c_{HbO2} \cdot \varepsilon_{HbO2}(\lambda) \right\} \cdot \ln(10), \tag{2}$$

where c_0 and c_1 are coefficients taking into account the contributions of scattering and background absorption, ε and c are the extinction coefficients and concentrations respectively of deoxygenated (Hb) and oxygenated (HbO$_2$) hemoglobin, $<L>$ is the averaged photon path length through the tissue. The c_0 coefficient also takes into account the uncertain constant additive entering into experimental attenuation curve (see Eq. (1) and argumentation to it). The values of these coefficients as well as the values of $<L>c_{Hb}$ and $<L>c_{HbO2}$ are obtained by minimizing the difference between model and experimental spectra with the least square method in the spectral range between 510 nm and 590 nm.

The blood oxygen saturation degree SO2 and relative hemoglobin concentration HbT are calculated from the above-determined coefficients as follows:

$$SO2 = \frac{<L>c_{HbO2}}{<L>c_{HbO2} + <L>c_{Hb}} = \frac{c_{HbO2}}{c_{HbO2} + c_{Hb}}, \qquad HbT = <L> \cdot (c_{Hb} + c_{HbO2}). \tag{3}$$

The relative hemoglobin concentration values depend on measurement geometry (through the $<L>$ value), so only the relative changes taken during the measurements at the same geometry are meaningful. It should be also mentioned that for in vivo measurements the movement of the object (the change of distance between fiber probe and tissue for non contact measurements) might result to the small random changes in $<L>$ and consequently the errors in relative hemoglobin concentration monitoring, while the oxygen saturation value is less receptive to these changes.

3. RESULTS AND DISCUSSION

To demonstrate applicability of the above described algorithm we present here the results of deoxygenating observed during artery occlusion. The measurements were done on the outer surface of upper finger phalanx. Figure 3 demonstrates the attenuation spectra $A_{exp}(\lambda)$ at different time after starting arterial occlusion. The spectra are shifted along y-axis on arbitrary values for convenient observation, the amount of shift being not important for calculations. We see that the spectral line shapes strongly correlate with blood oxygen saturation. The modeled spectra in the range of 510-590 nm calculated using Eq. (2) are shown in Figure 3 by a black thin lines and corresponding blood oxygen saturation values calculated from the model are given. The closeness of the experimental, $A_{exp}(\lambda)$, and fitted, $A_{model}(\lambda)$ spectral curves also suggests the applicability of our model in this case. The sampling depth of our measurements is the fraction of millimeter corresponding to the signal originated from skin capillary loops [3].

Figure 4 demonstrates the monitoring of typical time behavior for blood oxygen saturation and relative hemoglobin concentration during artery occlusion calculated from our model. The finger occlusion was started at t=0 sec and released at t=700 sec. In normal conditions (before starting occlusion) the irregular oscillations in SO2 in the range of 50-70 % are observed (time interval between -600 and 0 sec). These oscillations are not random errors but real facts mainly due to the spatial non uniformity of SO2 in a skin layer and their temporal changes during the measurements. These temporal changes of oxygenation disguise small effects of laser induced changes at low light fluence rate (see bellow). The value of blood oxygen saturation in skin at rest (50-70%) at normal ambient temperature (20-22° C) agrees fairly well with that of reported by others [4-6]. It should be noted that the measurements done at lower ambient temperatures gave the values of blood oxygen saturation in skin at rest as low as 10-30 % with increasing temporal oscillation range. As can be seen from Figure 4 total hemoglobin deoxygenating in superficial skin layer is attained in 10 minutes after starting artery occlusion. The closeness of SO2 value at the end of occlusion to zero also demonstrates the accuracy of the model. After occlusion release we observe a sharp increase for both blood oxygen saturation and relative hemoglobin concentration due to the intensive blood circulation (reactive hyperemia), which after some time are restored to theirs previous values. The similar results have been observed also by other researchers [4,5].

Figure 5 demonstrates the blood oxygen saturation changes during PDT with sulphonated aluminum phthalocyanines as photosensitizer in mouse tumors [1,2]. We observe distinct vessel response to light irradiation in the presence of photosensitizer in blood. The sharp drop down of oxygen saturation in the case of short drug-light interval is due to vessel
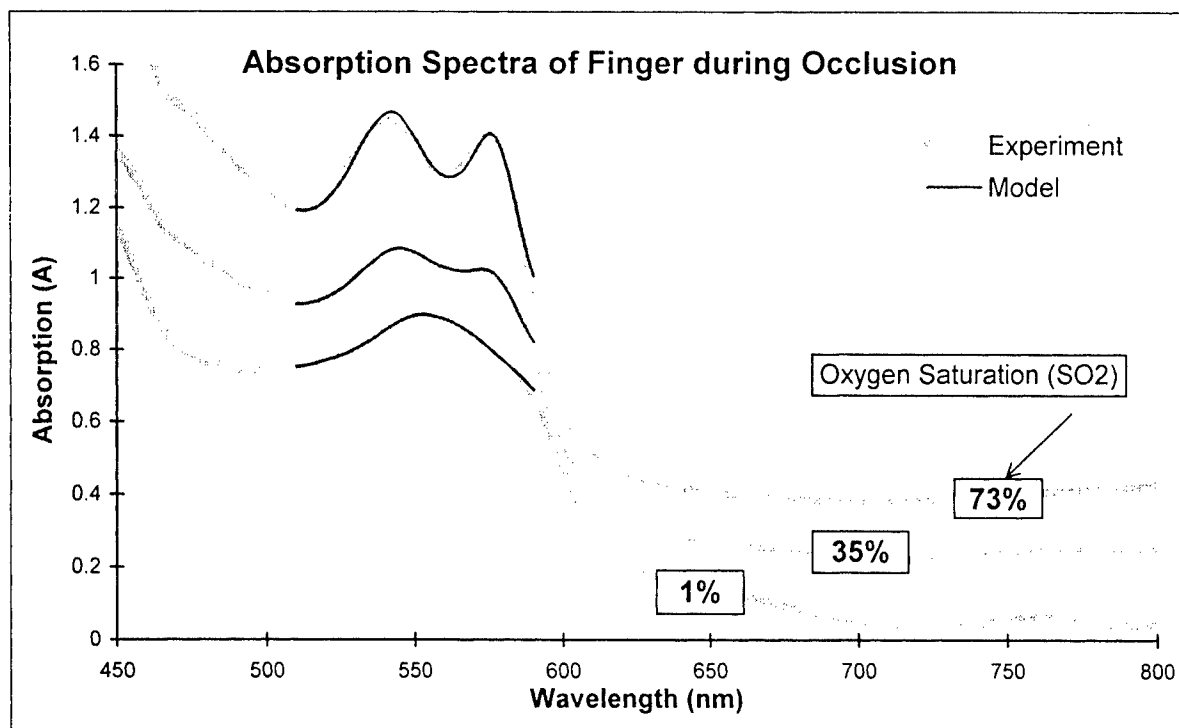
Figure 3. The absorption spectra of finger during occlusion at different time (thick gray) and fitted spectra A_model (thin black) in the range 510-590 nm. The corresponding blood oxygen saturation SO2 calculated from the model is shown in the Figure.
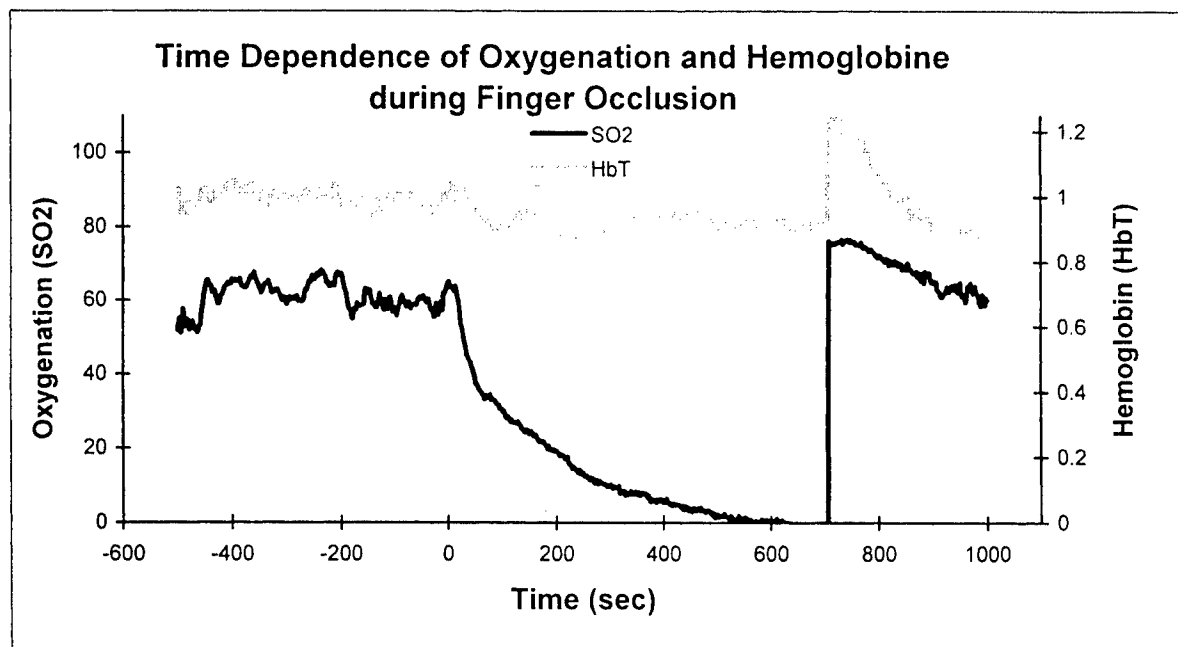
Figure 4. Time dependence of blood oxygen saturation (SO2) and total relative hemoglobin concentration (HbT) calculated from the model during finger occlusion. The occlusion was started at t=0 sec and released at t=700 sec.
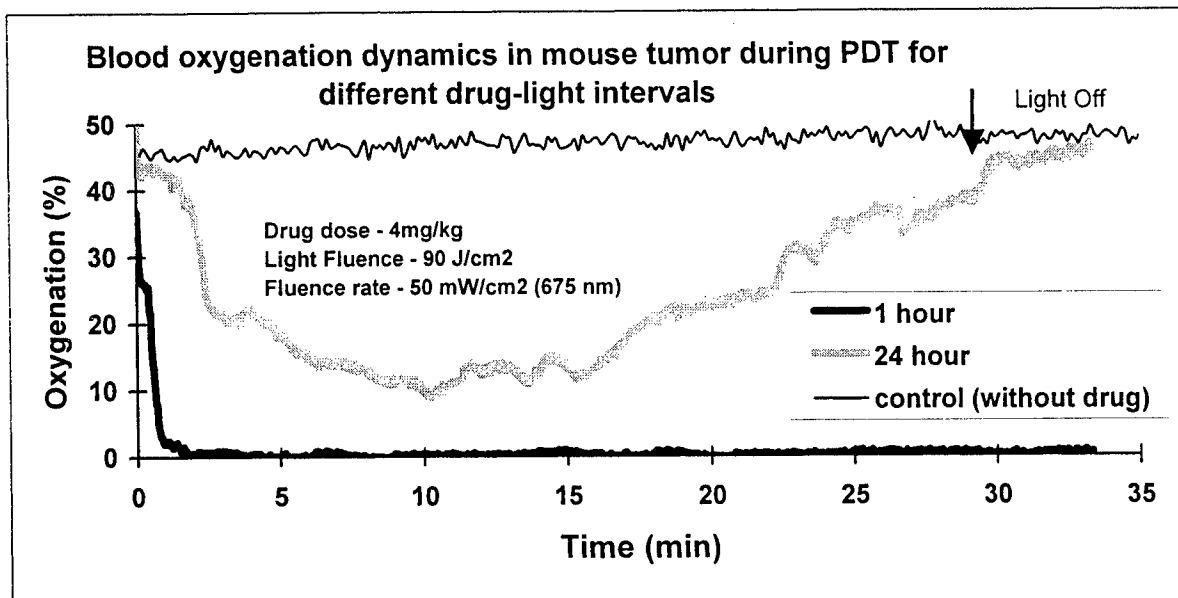
Figure 5. Blood oxygen saturation variations in mouse tumor during photodynamic therapy at different drug-light intervals (1 hour and 24 hours). Sulphonated aluminum phthalocyanine (Photosense) was used as photosensitizer. The evident vessel response is observed depending on drug concentrastion in capillaries. Irreversible capillaries destruction is obtained at short drug-light interval. No responce is observed in control mouse without photosensitizer.
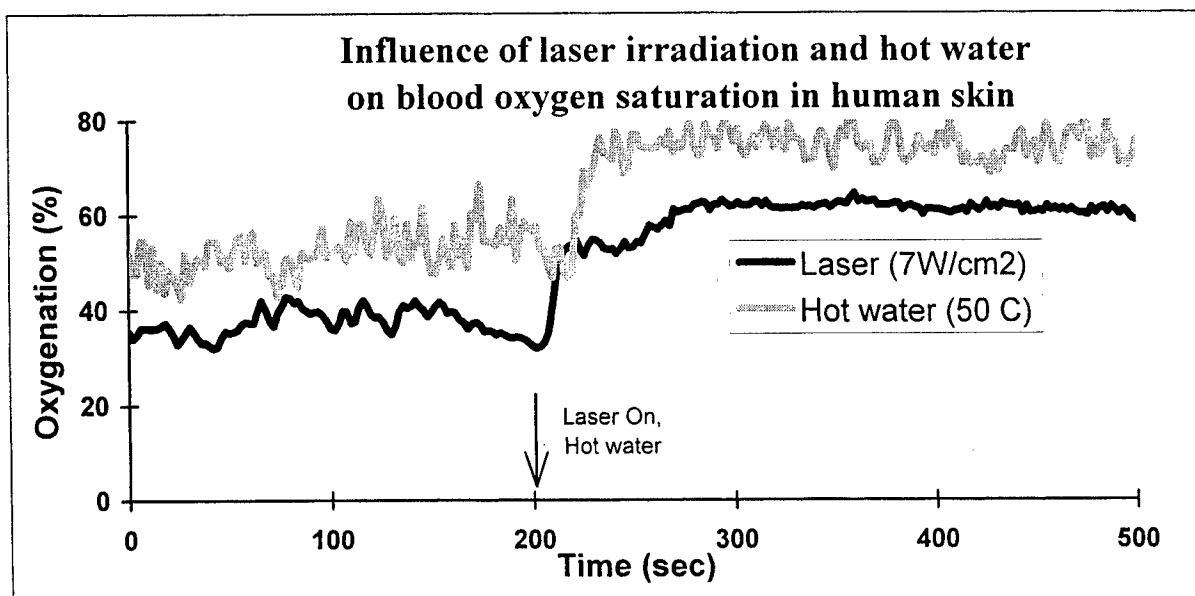
Figure 6. Comparison of oxygen saturation dynamics in human skin induced by laser irradiation (7W/cm^2, 675 nm) and hot water (50 C).
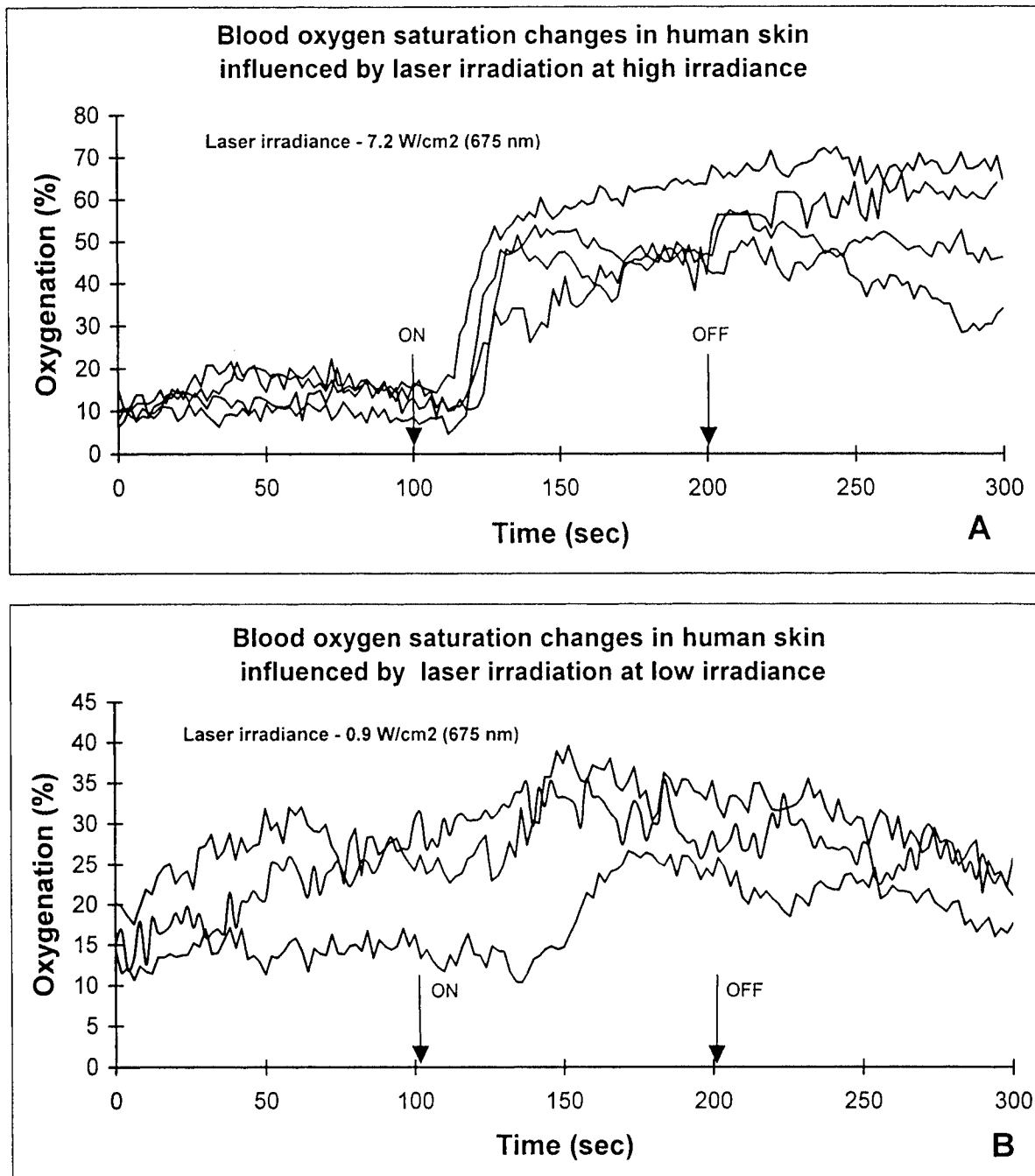
Figure 7. Blood oxygen saturation changes in human skin at low ambient temperature after laser irradiation at high (7.2 W/cm2 - upper frame) and low (0.9 W/cm2 - lower frame) irradiance . The laser was switched on at 100sec and switched off at 200sec. The evident sharp decrease of oxygenation is observed after some delay for all four trials at high laser irradiance. At low laser irradiance the decrease is less distinct.

occlusion together with enhanced oxygen consumption during PDT. It should be noted that in control animal (without photosensitizer) we observe no any vessel response at light fluence rates typically used in PDT (50-400 mW/cm^2).

The effect of laser irradiation alone on blood oxygen saturation in human skin appears when light fluence rate become more than 1 W/cm^2. One can observe sharp increase in oxygenation after some time delay as well as some stabilizing in time as shown in Figure 6. However, the similar behavior is observed when skin is heated by immersing hand into hot water. This evidence strongly suggests that heating is responsible for the observed laser induced blood oxygenation increase. These findings agree with that obtained in [7] where the influence of heating on skin oxygenation was studied in details.

Figure 7 shows the oxygenation dynamics in skin at low (0.9 W/cm^2) and high (7.2 W/cm^2) light fluence rates at several trials. This observation was done at low ambient temperature when the initial blood oxygen saturation is rather low (10-30 %) and its laser induced increase is more pronounced. At high light irradiance there is distinct increase of oxygenation up to 50-70 % with time delay 15-25 sec after switching on the laser. The restoration of oxygenation to initial value takes a rather long time period in this case and there is no tendency to oxygenation decrease even 200 seconds after switching off the laser. The changes in relative hemoglobin concentration were not substantial and reproducible and were masked by temporal variable background even at high light irradiances applied. The spatial area of increased oxygenation goes far beyond the irradiation spot and achieves more than two centimeters in diameter when irradiation spot was just half a centimeter. At low light irradiance (Figure 7B) the laser induced oxygenation increase is less pronounced and sometimes is completely disguised on the variable temporal background. The restoration of oxygenation to its previous value is observed about 200-300 seconds after switching off the laser.

It should be noted that absorption coefficient of deoxygenated hemoglobin is almost 10 times higher than oxygenated at wavelength of 675 nm used in our study. At low initial blood oxygen saturation the light absorption and consequently the heating rate will be higher resulting to more pronounced effect in this case. In this sense the heating with laser at wavelength in the range of 675 nm is different from the heating by water or heating with light in NIR range where the main light absorber is water.

Figure 8 shows the deoxygenation in skin after arterial occlusion with and without laser irradiation. It was found out that deoxygenation rate is higher in the presence of laser irradiation. The slope of deoxygenation curve after artery occlusion is proportional to metabolic oxygen consumption rate in tissue. It is quite reasonable that oxygen consumption rate is increased due to laser induced heating. The spatial non uniformity in deoxygenation was as in the previous case about two centimeters in diameter.
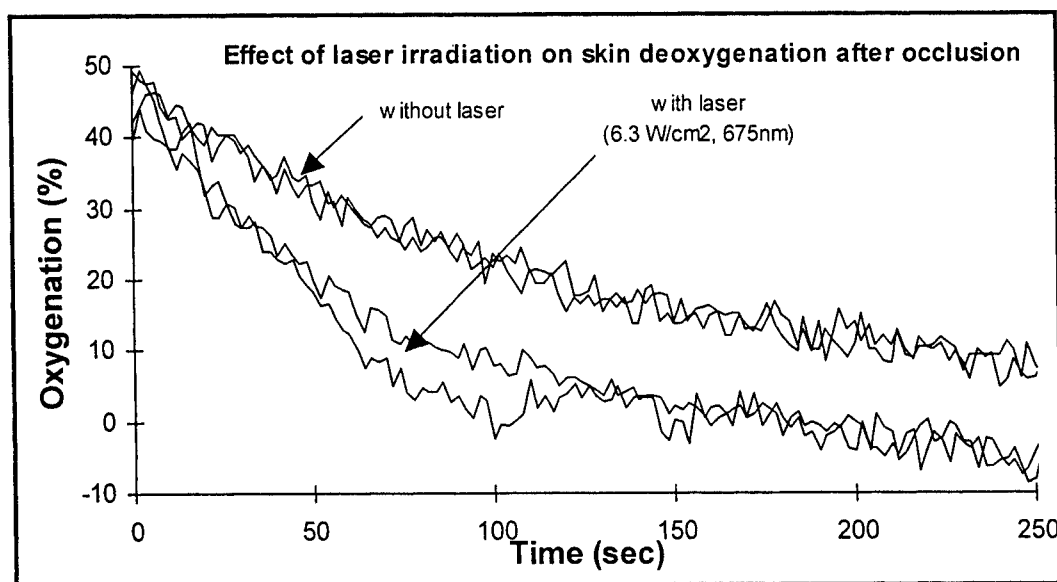
Figure 8. Deoxygenation dynamics in human skin after finger occlusion without laser irradiation (two upper curves) and with laser irradiation (two lower curves). Laser irradiation increases the oxygen consumption.

4. CONCLUSIONS

The changes in blood oxygen saturation may be evaluated by diffuse reflectance spectroscopy in visible range. The laser induced blood oxygen saturation increase in skin and increased oxygen consumption observed at rather high light fluence rates exceeding 1 W/cm^2 is due to the skin heating. At low light fluence rates applied for low intensity laser therapy (up to 100 mW/cm^2) no effect was observed suggesting that therapeutic effect in this case, if any, is not related to changes in microcirculation as was assumed by some authors.

ACKNOWLEDGMENTS

REFERENCES

1. A.A. Stratonnikov, G.A. Meerovich and V. B. Loschenov "Photobleaching of photosensitizers applied for photodynamic therapy", Proc. SPIE 3909, p.81-91 (2000).
2. Stratonnikov A.A., Douplik A.Y., Loschenov V.B. "Oxygen consumption and its transport in tissues during photodynamic therapy of tumors and whole blood" in Oxygen transport to tissues XXI, Ed. A. Eke and D.T. Delpy, Kluwer Academic/Plenum Publishers, NY, p. 515-524 (1999).
3. K.H. Frank, M. Kessler, K. Appelbaum, W. Dümmler, "The Erlangen micro-lightguide spectrophotometer EMPHO I", Phys. Med. Biol. 34, 1883-1900 (1989).
4. D.K. Harrison, S.D. Evans, N.C. Abbot, J. Swanson Beck, and P.T. McCollumn, "Spectrophotometric measurements of haemoglobin saturation and concentration in skin during the tuberculin reaction in normal human subjects" Clin. Phys. Physiol. Meas. 13(4), 349-363 (1992).
5. D.J. Wallace, B. Michener, D. Choudhary, M. Levi, P. Fennelly, D.M. Hueber, B.Barbieri, "Summary of the results of a 95 subject human clinical trial for the diagnosis of peripheral vascular disease using a near infrared frequency domain hemoglobin spectrometer", SPIE 3597, 300-316 (1999).
6. M. Oda, Y. Yamashita, T. Nakano, A. Suzuki, K. Shimizu, I. Hirano, F. Shimomura, E. Ohmae, T. Suzuki and Y. Tsuchiya, "Nearinfrared time-resolved spectroscopy system for tissue oxygenation monitor", SPIE 3597, 611-617 (1999).
7. Y. Kakihana, M. Kessler, A. Krug, H. Yamada, T. Oda and N. Yoshimira, "Dynamic changes in intracapillary hemoglobin oxygenation in human skin following various temperature changes" Microvascular Research 56, 104-112 (1998).

An approach toward characterizing the fraction of all oxidation events that attack a particular site within cells during PDT.

Steven L. Jacques, Paulo Bargo

Oregon Medical Laser Center,
Providence St. Vincent Medical Center, Portland, OR 97225

ABSTRACT

This paper considers the the fraction PDT-induced oxidizing radicals that react with a specific oxidizable target within a cell rather than with all possible oxidizable sites. There are many oxidizable sites within the cell, each with a different efficiency of oxidation (Y_ox_j) and a different in vivo concentration (C_iv_j). One measures the efficiency of oxidation of a single ith chemical species in vitro (Y_it_i), then measures the oxidation of the same species in vivo (Y_iv_i). The concentration of this ith species in vivo must be measured (C_iv_i). A convenient test chemical species is chosen, such as a photobleachable fluorophore. Then the in vivo yield is approximately:

$$Y\_iv\_i = (C\_iv\_i * Y\_it\_i) / sum\_all\_j(C\_iv\_j * Y\_iv\_j) \quad (Eq.1)$$

Rearranging to solve for the total oxidation:

$$sum\_all\_j(C\_iv\_j * Y\_iv\_j) = (C\_iv\_i * Y\_it\_i) / Y\_iv\_I \quad (Eq.2)$$

Once the sum_all_j() in Eq. 2 is specified, one can measure the in vitro oxidation efficiency and the in vivo concentration of any ith species and use Eq. 1 to predict the fraction of PDT-generated singlet oxygen that will attack that ith species in vivo. Of course, the above is only a first approximation toward a complex problem but is a beginning. This paper illustrates the experimental specification of the Y_ox_j for NADPH oxidation in a cuvette using the photosensitizer Photofrin.

1. INTRODUCTION

When photodynamic therapy (PDT) is used to generate oxidizing radicals such as singlet oxygen within cancer cells, how do those radicals attack the cell? Some radicals attack important sites which contributes toward cell death. Other radicals attack relatively unimportant sites that don't cause cell death. To understand how the attack by radicals is

partitioned amongst all possible oxidizable sites, we have been developing an experimental approach. In this paper, we report on a simple model system, the oxidation of NADPH in cuvette to illustrate the beginning steps in such an experimental scheme.
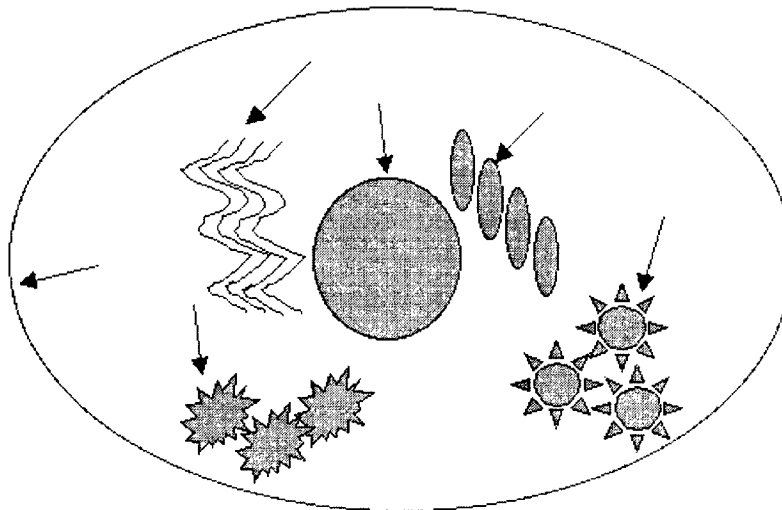
Fig. 1: Many oxidizable sites within a cell compete for the singlet oxygen generated by a light-activated photosensitizer during PDT.

Figure 1 schematically describes a cell with many different types of sites that can be oxidized by singlet oxygen radicals produced by PDT. The total number of oxidation events is specified by the number of oxygen radicals which are generated in the cell, N_o. These N_o radicals will attack various sites in the cell according to the local concentration (C) of a particular site in the cell and the efficiency of interaction (ϕ_I) for singlet oxygen reaction with that site.

$$N_{radicals} = f \sum_{j=1}^{N} C_j \phi_j$$

Eq. 1

where the number of types of oxidizable species or sites equals N, the concentration of the jth species is C_j, and the efficiency of singlet oxygen reaction with each jth species is ϕ_{Ij}. The factor f is a normalization factor, units of volume, that causes the summation to equal $N_{radical}$, the number of singlet oxygen radicals generated by the PDT. The number of oxidizing events directed against a particular i^{th} species is given:

$$N_{ox\,i} = \frac{C_i \phi_{Ii}}{\sum_{j=1}^{N} C_j \phi_{Ij}}$$

<div align="right">Eq. 2</div>

where C_i is the concentration of the ith species and ϕ_{Ii} is the efficiency of reaction of singlet oxygen with the ith species.

If one could specify the denominator of Eq. 2, one would have characterized the population of oxidizable sites with the cell. This denominator is a useful parameter to specify. If one then generates information about the concentration C_i and efficiency of reaction ϕ_{Ii} for an ith species, one can use Eq. 2 to predict the fraction of generated singlet oxygen that will attack the ith species in vivo.

This paper will report an experiment done in vitro to explore the efficiency of oxidizing NADPH with singlet oxygen, $\phi_{I\,NADPH}$. Our experiment suggests that the value of $\phi_{I\,NADPH}$ specified in vitro in a cuvette at high values of C_{NADPH} approaches a stable value which specifies the efficiency $\phi_{I\,NADPH}$. We speculate that indeed at higher concentrations, the ϕ_{Ii} for an ith species can be determined in vitro.

Assume that an in vitro experiment can specify ϕ_{Ii}. Then if one could estimate the value of C_i in vivo, one could predict the number of oxidation events, $N_{ox\,I}$, that attack that i^{th} species.

2. EXPERIMENTS

The experimental procedure is shown in Fig. 2. Light from a 488-nm argon ion laser was delivered via on optical fiber and a lens as a flat-field exposure to the bottom of a cuvette filled with 0.5 ml of NADPH and Photofrin in aqueous solution. After exposure to a known amount of light, a 50-ul aliquot was transferred into a final 2 ml volume in a second quartz cuvette for spectrophotometric assay. The absorbance at 340 nm was measured with a standard spectrophotometer which is a standard means of observing the oxidation of NADPH. Oxidation of NADPH to NADP causes a reduction in the 340-nm absorbance.
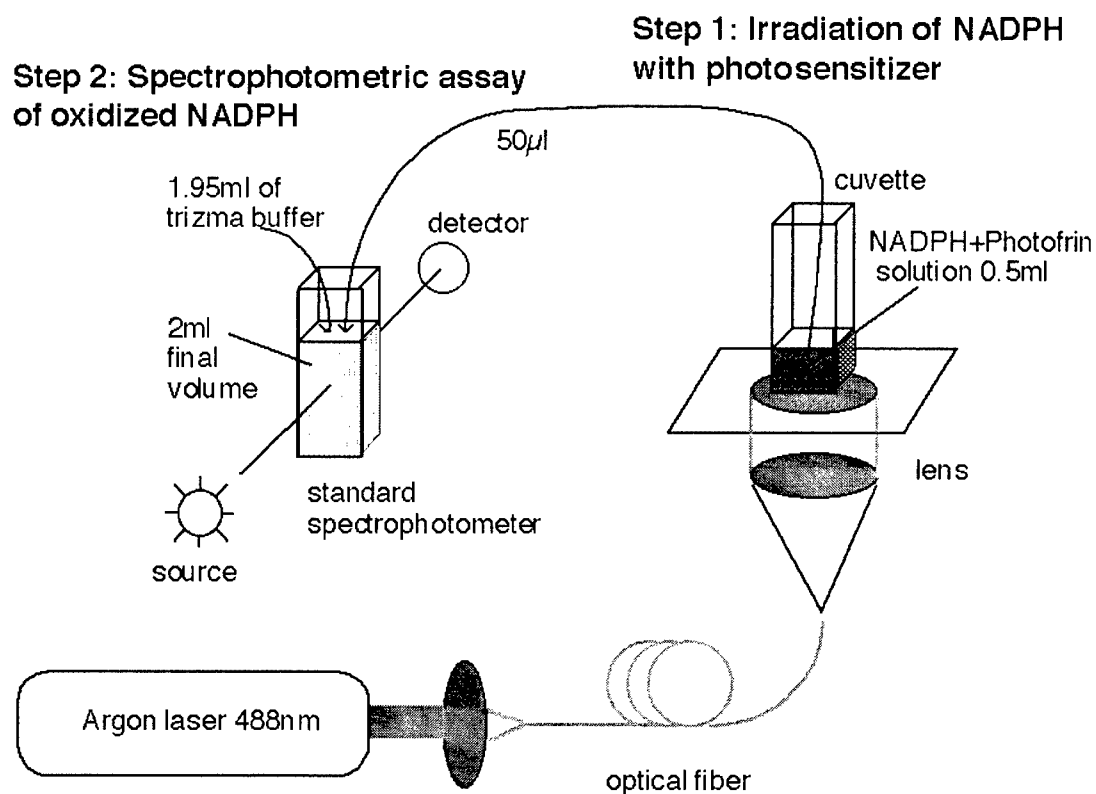
Fig. 2: Experimental setup. Argon ion laser irradiation of solution of NADPH and Photofrin causes oxidation of NADPH. Then spectrophotometric assay of absorbance at 340 nm indicates the oxidation of NADPH to NADP.

3. RESULTS

Figure 3 shows how the 340-nm absorbance of NADPH drops as oxidation to NADP proceeds with increasing amounts of delivered light. A solution with the photosensitizer Photofrin alone is shown with a constant value of about 0.06 absorbance units (OD). Addition of NADPH shows an increase at time zero in the OD to a value of about 0.20 OD. With increasing exposure time to the argon laser, the 340-nm OD decays to the baseline value due to the Photofrin. Also shown but not central to the theme of this paper is the inclusion of 5 mM azide to quench the singlet oxygen. The azide slowed the oxidation of NADPH, although it did not completely eliminate the oxidation.

Oxidation of NADPH by PDT

NADPH - 1mM

Photofrin - 50mM

Sodium Azide - 5mM
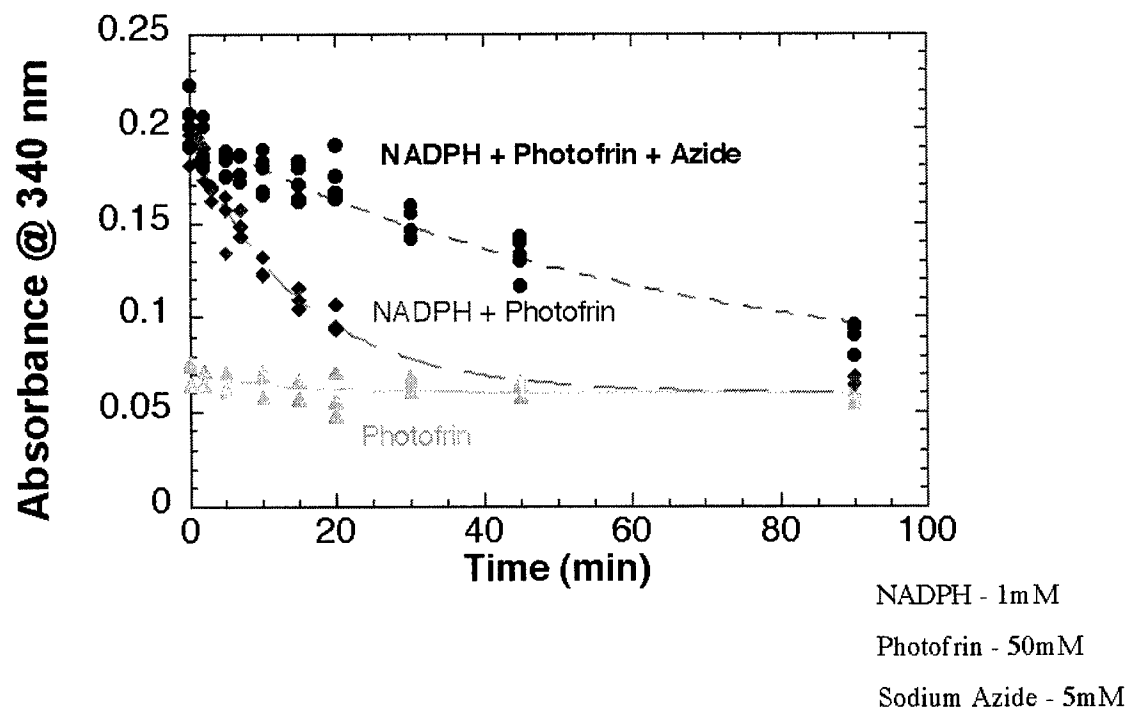
Fig. 3: Decay of NADPH absorbance due to increasing oxidation by PDT using Photofrin as a photosensitizer.

Number of Photons Absorbed by Photofrin

$$N_{abs} = P \cdot \tau \cdot b \cdot \left(1 - 10^{-A_{488}^{PF}}\right)$$

P = Irradiated Power (0.075 Watts)

τ = Time constant (seconds)

b = Conversion factor (2.5×10^{18} ph/J) @488nm

A_{488}^{PF} = Photofrin Absorbance @488nm

$$A_{488}^{PF} = \varepsilon_{488}^{PF} C_{irr} L_{irr}$$

ε_{488}^{PF} = Photofrin Extinction Coefficient 6.3 cm^{-1} (mg/ml)$^{-1}$

C_{irr} = Photofrin Concentration (50 μg/ml)

L_{irr} = Irradiated Path Length (0.5 cm^{-1})

Typical Absorbance kinetics as a function of exposure time

of PDT treatment
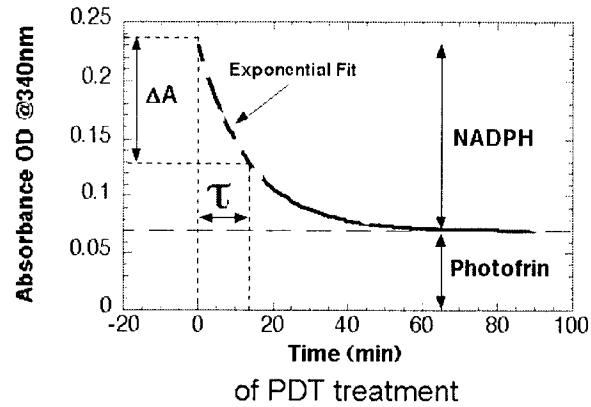
Fig. 4: The number of photons absorbed by Photofrin during argon ion laser irradiation, N_{abs}, is calculated from the experimental data.

Number of Oxidized NADPH Molecules

$$N_{ox} = \frac{\Delta A \cdot N_{av} \cdot V_{sp}}{\varepsilon_{nadph @ 340} \cdot L_{sp}} \frac{1}{f}$$

ΔA = Decay in Absorbance @ 340nm

N_{av} = Avogrado's Number
(6.02x10^{23} molec/mol)

V_{sp} = Diluted Sample Volume (2 ml)

$\varepsilon_{nadph@340}$ = extinction coefficient @340nm
(5.1 cm^{-1} mM^{-1})

L_{sp} = Cuvette Path length (1 cm)

$f = \dfrac{\text{Sample Volume}}{\text{Irradiated Volume}} = \dfrac{50\mu l}{500\mu l} = 0.1$

Typical Absorbance kinetics as a function of exposure time
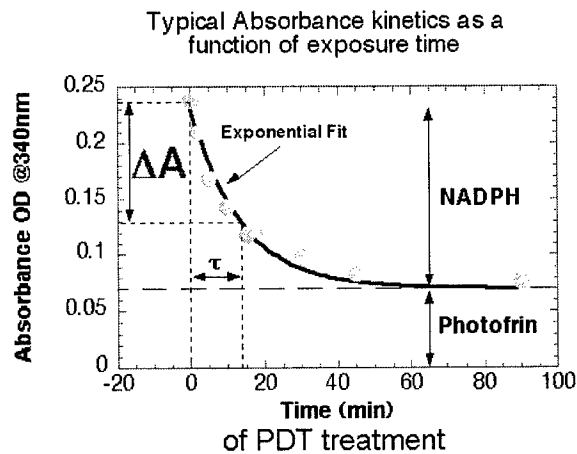
of PDT treatment

Fig. 5: The number of NADPH molecules oxidized by the PDT treatment, N_{ox}, is calculated from the experimental data.

The quantum yield for oxidation of NADPH by PDT is calculated:

$$\phi = \frac{N_{ox}}{N_{ab}}$$

Figure 6 shows how the value of ϕ varies as the concentration of NADPH in the cuvette is increased. At increasingly higher NADPH concentrations, the value of ϕ approaches a maximum value of about 0.005.

Quantum Yield of Oxidation (ϕ_{ox}) for different NADPH concentrations

$$\phi_{ox} = N_{ox} / N_{abs}$$

$$\phi_D = 1-\exp(-C/C^*)$$

which approximates diffusion theory model

$C^* \approx 0.6\text{mM}$

ϕ_{ox}
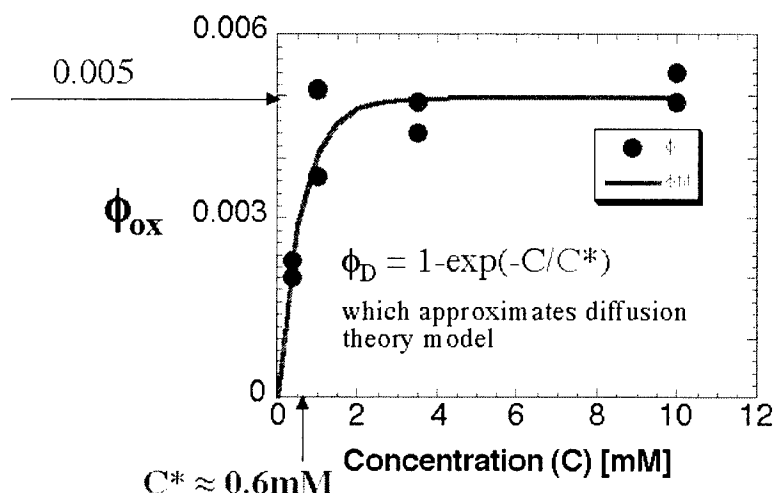
Concentration (C) [mM]

Fig. 6: The quantum efficiency for oxidizing NADPH with PDT-generated singlet oxygen increases to a maximum value of about 0.005 as the concentration of NADPH is increased well above 0.6 mM.

5. DISCUSSION

The quantum efficiency for oxidizing NADPH with PDT-generated singlet oxygen depends on several steps. Once a Photofrin molecule has been excited by photon absorption to its excited state, the molecule must convert to its triplet state (ϕ_T). Then the triplet state photosensitizer must exchange its excitation with triplet molecular oxygen to generate the singlet oxygen radical (ϕ_Δ). Then the singlet oxygen radical must diffuse to the NADPH (ϕ_D) before it can interact with the NADPH with a certain efficiency (ϕ_I). In summary,

$$\phi_{ox} = \phi_T\phi_\Delta\phi_D\phi_I \qquad\qquad \text{Eq. 3}$$

where

ϕ_T - quantum efficiency of Photofrin triplet state generation

ϕ_Δ - efficiency of singlet oxygen formation

ϕ_R - efficiency of reaction between singlet oxygen and NADPH

ϕ_D - efficiency of diffusion of singlet oxygen to encounter NADPH

ϕ_I - efficiency of singlet oxygen interaction with NADPH upon encounter

Egorov and Kamalov (1989) report a value for ϕ_T equal to 0.63 (1), and St-Denis and Fell (1971) report a value for ϕ_Δ equal to 0.32(2), both in aqueous solutions. Using these two values, assigning a value of unity to ϕ_D, and using our experimental value of 0.005 for ϕ_{ox}, we calculate a tentative prediction of the value of ϕ_I to be 0.025.

Efficiency of singlet oxygen interaction with NADPH (ϕ_I):

$$\phi_I = \frac{\phi_{ox}}{\phi_T \, \phi_\Delta \, \phi_D}$$

$$= 0.025$$

At high concentrations in vitro, the value of ϕ_D appears to approach unity. We speculate that in vivo where concentration of a particular oxidizable species is likely to be high, the value of ϕ_D will also approach unity. The above exercise with NADPH illustrates how to conduct a cuvette experiment to evaluate ϕ_I for an ith species. How does one use this information?

We are currently looking for a suitable fluorophore species which can be oxidized by PDT to cause a change in its fluorescence signature. Such a probe can be used to study the population of oxidizable sites within a cell. Let's refer to our probe as the kth

species. After determining ϕ_{Ik} from a cuvette experiment similar to the one above using NADPH, the probe will be put inside a cell. The probe's fluorescence will specify its concentration in vivo C_k. When the cell is treated by PDT, the rate of decay of our probe's fluorescence will specify the apparent $\phi_{ox\,k}$ here called ϕ_k. Then, ϕ_{Ik}, C_k, and ϕ_k will together specify the denominator of Eq. 2, the summation of all concentrations x efficiencies of interaction over all possible oxidizable species or sites. That denominator is a useful parameter that characterizes the ensemble of oxidizable sites within the cell.

for k^{th} species:

observe in cultured cells   from cuvette study

$$\text{if} \qquad \phi_k = \frac{C_k \phi_{Ik}}{\sum_{j=1}^{N} C_j \phi_{Ij}}$$

$$\text{then} \qquad \sum_{j=1}^{N} C_j \phi_{Ij} = \frac{C_k \phi_{Ik}}{\phi_k}$$

describes entire population of oxidizable
targets that compete for singlet oxygen

In summary, an experimental method has been outlined for characterizing the population of oxidizable targets which allows estimation of the fraction of PDT-generated singlet oxygen that attacks a particular target.

The heterogeneity of the cellular interior makes this a difficult problem to unravel. Measurements of local values of C_k and ϕ_k are a challenge given the

heterogeneity of the cellular interior. However a rational approach toward the problem is apparent.

Our next step is to identify a target fluorescent molecule for oxidation within cells by PDT, whose local concentration and oxidation can be monitored by fluorescence microscopy.

6. ACKNOWLEDGEMENTS

7. REFERENCES

1 S.U. Egorov, V.F. Kamalov, et al., Chem. Phys. Lett. 163:421-424, 1989.
2 C.E. St-Denis and C.D.J. Fell, Can. J. Chem. Eng., 49:885, 1971,

Depth-resolved degree of polarization of backscattered light and two-dimensional Mueller matrices of biological tissue measured by optical coherence tomography

Shuliang Jiao, Gang Yao, Lihong V. Wang[*]

Optical Imaging Laboratory, Biomedical Engineering Program,

Texas A&M University, 3120 TAMU, College Station, Texas 77843-3120

ABSTRACT

Mueller matrices provide a complete characterization of the optical polarization properties of biological tissue. A polarization-sensitive optical coherence tomography (OCT) system was built and used to investigate the optical polarization properties of biological tissues and other turbid media. The apparent degree of polarization (DOP) of the backscattered light was measured with both liquid and solid scattering samples. The DOP maintains the value of unity within the detectable depth for the solid sample while the DOP decreases with the optical depth for the liquid sample. Two-dimensional depth-resolved images of the full Mueller matrices of biological tissues were measured with this system. These polarization measurements revealed some tissue structures that are not perceptible with standard OCT.

Keywords: OCT, Mueller matrix, Stokes vectors, polarization, degree of polarization(DOP)

1. INTRODUCTION

Optical coherence tomography (OCT) is an important noninvasive medical imaging modality, which can reveal subsurface structures of biological tissue. High spatial resolution (~1 μm) and high scanning speed (video rate) have been achieved over the past few years.[1,2] Recently, polarization-sensitive OCT is emerging as a very attractive branch of OCT.[3-8] Polarization-sensitive OCT can provide more information about the optical properties of biological tissue. Results of these studies revealed the importance of polarization as a contrast mechanism. As is known in polarimetry, Stokes vectors and Mueller matrices[9] provide complete representations of the polarization properties of light and optical samples, respectively. By measuring the Stokes vectors of the light backscattered from biological tissue and calculating the Mueller matrix from the Stokes vectors, one can obtain a complete characterization of the optical polarization properties of the tissue. With the combination of Mueller-matrix measurements with OCT, one can obtain the Mueller matrix of a sample with OCT resolution. Yao and Wang[7] first reported the measurement of two-dimensional depth-resolved Mueller matrices of biological tissue with OCT. Jiao et al [8] further reported the experiment results with the same experimental setup. The results revealed some structures that were not observable in standard OCT. Therefore, Mueller matrices provide a unique approach to characterizing biological tissue.

In this paper we give a detailed account of our novel polarization-sensitive OCT system for characterizing the polarization properties of biological tissue and other turbid media with both depth and lateral resolution. A succinct relationship between the Stokes vectors and the Mueller matrix in our measurement approach was derived. We measured the Stokes vectors of backscattered light from solid biological tissue and liquid turbid media. The apparent degree of polarization was calculated from the Stokes vectors. The calculated results revealed the difference between solid and liquid in the degree of polarization as a function of the optical depth. An explanation for the mechanism contributing to this difference was speculated. We also measured 2D images of the full 4×4 Mueller matrix of a piece of rat bone.

2. STOKES VECTORS AND MUELLER MATRICES

In polarimetry, the Stokes vector S of a light beam is constructed based on six flux measurements with different polarization analyzers in front of the detector:

* To whom all correspondence should be addressed. Tel: 979-847-9040; Fax: 979-845-4450; Email: LWang@tamu.edu; URL: http://oilab.tamu.edu.

$$S = \begin{pmatrix} S_0 \\ S_1 \\ S_2 \\ S_3 \end{pmatrix} = \begin{pmatrix} I_H + I_V \\ I_H - I_V \\ I_P - I_M \\ I_R - I_L \end{pmatrix} = \begin{pmatrix} I_H + I_V \\ I_H - I_V \\ 2I_P - I_H - I_V \\ 2I_R - I_H - I_V \end{pmatrix},$$ (1)

where I_H, I_V, I_P, I_M, I_R, and I_L are the light intensities measured with a horizontal linear polarizer, a vertical linear polarizer, a +45° linear polarizer, a −45° linear polarizer, a right circular analyzer, and a left circular analyzer in front of the detector, respectively. Because of the relationships $I_H + I_V = I_P + I_M = I_R + I_L = I$, where I is the intensity of the light beam measured without any analyzer in front of the detector, a Stokes vector can be determined by four independent measurements, for example, I_H, I_V, I_P, and I_R.

From the Stokes vector, the degree of polarization (DOP), the degree of linear polarization (DOLP), and the degree of circular polarization (DOCP) are derived as:

$$DOP = \frac{\sqrt{S_1^2 + S_2^2 + S_3^2}}{S_0}, \ DOLP = \frac{\sqrt{S_1^2 + S_2^2}}{S_0}, \ DOCP = \frac{S_3}{S_0}.$$ (2)

The Mueller matrix (M) of a sample transforms an incident Stokes vector S_{in} into the corresponding output Stokes vector S_{out}.

$$\mathbf{S}_{out} = \mathbf{M} \mathbf{S}_{in},$$ (3)

The Mueller matrix can be experimentally obtained by measurements with different combinations of source polarizers and detection analyzers. We may express the 4×4 Mueller matrix as $\mathbf{M} = [\mathbf{M}_0 \ \mathbf{M}_1 \ \mathbf{M}_2 \ \mathbf{M}_3]$, where $\mathbf{M}_0$, $\mathbf{M}_1$, $\mathbf{M}_2$, and $\mathbf{M}_3$ are four column vectors of four elements each. The four output Stokes vectors corresponding to the four incident polarization states H, V, P, and R are denoted respectively by S_H, S_V, S_P, and S_R. These four output Stokes vectors are experimentally measured based on Eq. (1) and can be expressed as:

$$\begin{cases} \mathbf{S}_H = \mathbf{M} \mathbf{S}_{Hi} = \mathbf{M}_0 + \mathbf{M}_1 \\ \mathbf{S}_V = \mathbf{M} \mathbf{S}_{Vi} = \mathbf{M}_0 - \mathbf{M}_1 \\ \mathbf{S}_P = \mathbf{M} \mathbf{S}_{Pi} = \mathbf{M}_0 + \mathbf{M}_2 \\ \mathbf{S}_R = \mathbf{M} \mathbf{S}_{Ri} = \mathbf{M}_0 + \mathbf{M}_3 \end{cases}$$ (4)

The Mueller matrix can then be calculated from the output Stokes vectors:

$$\mathbf{M} = \frac{1}{2} [\mathbf{S}_H + \mathbf{S}_V, \mathbf{S}_H - \mathbf{S}_V, 2\mathbf{S}_P - \mathbf{S}_H - \mathbf{S}_V, 2\mathbf{S}_R - \mathbf{S}_H - \mathbf{S}_V]$$ (5)

In other words, at least four independent Stokes vectors for different source polarization states must be measured to determine a full Mueller matrix, where each Stokes vector requires four independent intensity measurements with different analyzers.

3. EXPERIMENTAL SETUP

A schematic of the OCT system for our studies is shown in Fig. 1. A superluminescent diode (SLD) laser with a center wavelength of 850 nm and a FWHM bandwidth of 26 nm is used as the light source. After passing through the polarizer P, the half-wave plate HW, and the quarter-wave plate QW, the light is split by a nonpolarization beam splitter (NBS). The sample beam is focused into the sample by an objective lens (L1) with an N.A. of 0.15. The reference beam passes through a variable-wave plate and is reflected back. The reflected beams from the reference and sample arms are coupled into a single-mode fiber and detected by a silicon photodiode. The minimal detectable signal of the system is −100 dB. A single depth scan through 1.5 mm takes 6 seconds in the current system. The depth resolution of this system is 10 μm. The focal spot size of the objective lens (L1) is 6.9 μm in air and is larger in tissue. The lateral resolution is expected to be around 10 μm.

We achieve four different incident polarization states H, V, P, and R by rotating the half-wave plate (HW) and the quarter-wave plate (QW) in the source arm. For each of these four incident polarization states, the variable-wave plate (VW) at the reference arm is adjusted to sequentially achieve the H, V, P, and R polarization states. A total of 16 polarization-

sensitive OCT images are acquired and processed to obtain the 16 Mueller matrix images [M_{ij}]. Alternatively, if the Stokes vector of the backscattered light is sought for a given incident polarization state, only four measurements need to be acquired by varying the reference polarization state. The Stokes vector is then calculated based on Eq. (1).
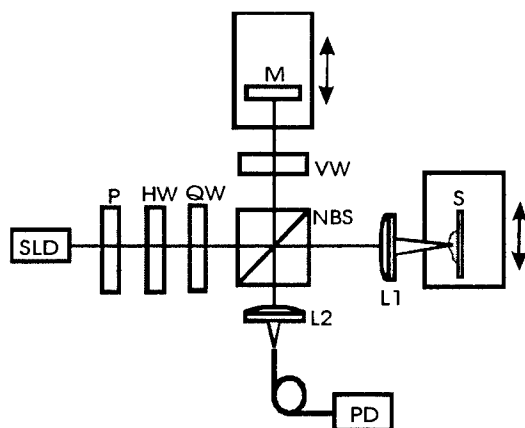
Fig.1 Schematic of the polarization-sensitive OCT system

Because the beam splitter is not an ideal polarization-independent optical element, the Mueller matrix of the beam splitter was measured for calibration. The Mueller matrices of simple optical elements measured with our setup agree with their known ideal matrices to within an error of 5% – 10% after calibration with the measured Mueller matrix of the beam splitter.

4. RESULTS AND DISCUSSION

We measured the Stokes vector S_H of a 5% *Intralipid* solution and a piece of bone tissue from a fish with the incident light in a state of horizontal linear polarization (*H*). The Stokes vectors were then used to calculate the DOP for the sample. The results are shown in Figs. 2 & 3, where the optical depth means the product between physical depth and the refractive index of the sample. Figure 2 shows the S_{H0} and DOP for the 5% *Intralipid* solution; Figure 3 shows the S_{H0} and DOP for the bone sample. In figure (3), the whole measurement depth of 500 μm are divided into 5 segments each of which is 100 μm in length and has 200 points. DOP is calculated for each point. The mean and the standard deviation for each segment are then calculated and plotted in the figure as the center value of each segment. All the data were averaged over 20 scans. Polynomial fitting was applied to the data for the *Intralipid* solution to reduce the fluctuation before calculating the Stokes vector.

The difference in the degree of polarization is striking between the liquid and the solid samples. For the liquid sample, the DOP decreases as the optical depth increases as shown in Fig. 2. For the solid sample, however, the DOP is approximately unity throughout the detectable range of optical depth apart from the fluctuation as shown in Fig. 3. The fluctuation of the DOP around unity for the solid sample is likely caused by the anisotropy of optical properties of the sample, which was not observed in the isotropic liquid samples. Anisotropy such as birefringence would cause the same physical feature to appear at different optical depths when it is measured with different analyzing polarization states. Conversely, the four quantities measured with different analyzing polarization states at a given optical depth may correspond to signals from slightly different physical depths. It would be challenging to accurately align the physical features among the one-dimensional depth-scan images of different analyzing polarization states. This slight misalignment causes the fluctuation of DOP.

The salient difference in degree of polarization between the liquid and solid samples indicates that a liquid medium acts upon our OCT signals differently from a solid medium. The variation of DOP with the optical depth and the solution concentration signifies that the apparent depolarization effect in liquid increases with the depth and the concentration. In principle, a DOP of less than unity means that the detected backscattered light is partially depolarized. Due to scattering, the completely polarized incident light is converted into non-uniformly polarized scattered light. If conventional intensity-based measurements were employed to detect the polarization property of this non-uniformly polarized light, the DOP would be less than unity and decrease with increasing scattering. The reduction of DOP is because that the light impinging upon different locations on the analyzers in front of the detector has different polarization states and adds in intensity after passing through the analyzers. The intensity signals of the light from different locations measured with orthogonal analyzers will partially offset each other in the calculation of the Stokes vector while the total intensity measured without analyzers is always the sum of the light from all of the locations.
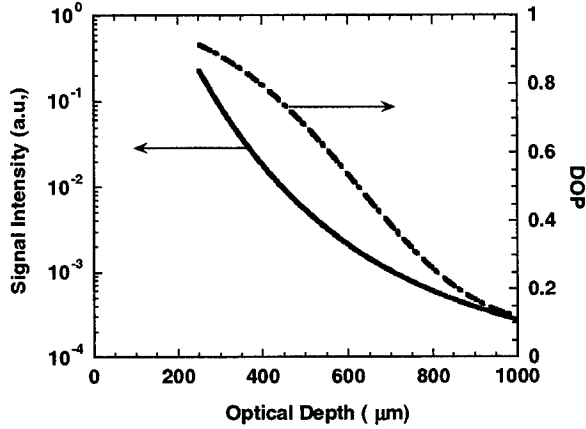
Fig.2 S_{H0} and DOP for 5% *Intralipid* solution.
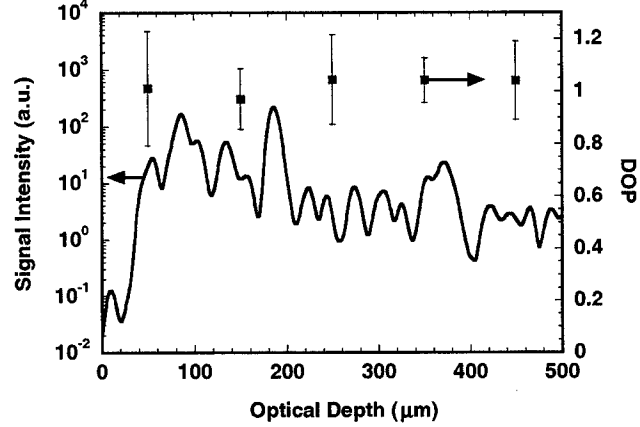
Fig.3 S_{H0} and DOP for a fish bone tissue.

However, OCT is an amplitude-based detection system by interference heterodyne. OCT detects the electric field of only the coherent part of the backscattered light. As is shown in Eq. (6), the electric field of the light from different locations of the detector is projected onto the analyzing polarization state E_r, then added in amplitude. Equivalently, the electric field of the light from different locations of the detector is summed in vector, and the vector sum E_s is then projected onto the analyzing polarization state. Because of this coherent detection scheme in OCT, a DOP of unity is maintained despite scattering as observed in the solid sample. Therefore, the conventional depolarization process in intensity-based measurements does not account for the decrease of DOP in the liquid media.

$$I = E_r \cdot E_{s1} + E_r \cdot E_{s2} + E_r \cdot E_{s3} + \dots$$
$$= E_r \cdot (E_{s1} + E_{s2} + E_{s3} + \dots)$$
$$= E_r \cdot E_s$$
$$E_s = E_{s1} + E_{s2} + E_{s3} + \dots \tag{6}$$

We speculate that the decrease of the apparent DOP in liquid is caused by the Brownian motion of the scattering particles and the signal averaging in the data acquisition. Brownian motion causes the polarization state of the backscattered light to fluctuate around an average state. Because our OCT system converts the interference fringes into an envelope of rectified fringes, only this positive envelope is detected and averaged.

To illustrate this point, we let I_H, I_V, I_P, and I_R denote the intensities of the average polarization state analyzed by horizontal linear polarization, vertical linear polarization, +45° linear polarization, and right circular polarization state, respectively. Let I_n denote the average intensity caused by the Brownian fluctuation, which is assumed to be the same for all of the four measurements with different analyzers for simplicity. The measured Stokes vector can be expressed as:

$$S' = \begin{pmatrix} I_H + I_V \\ I_H - I_V \\ 2I_P - I_H - I_V \\ 2I_R - I_H - I_V \end{pmatrix} + \begin{pmatrix} 2I_n \\ 0 \\ 0 \\ 0 \end{pmatrix} = S + S_n \tag{7}$$

The DOP of S is unity while the DOP of S_n is zero. The DOP of S' is

$$\text{DOP}(S') = \text{DOP}(S) \frac{S_0}{S_0 + 2I_n} = \frac{S_0}{S_0 + 2I_n} \tag{8}$$

As can be seen, the apparent DOP of the measured Stokes vector is less than unity. The increase of *Intralipid* concentration means an increase of random scattering that the light encounters per unit optical depth. An increase in optical depth means that the backscattered light encounters more scattering events. The increased scattering events would cause more fluctuation because each scattering event has Brownian motion. Therefore, the average intensity I_n would increase with both the optical depth and scatterer concentration in liquid, which would accordingly decrease the apparent DOP. This hypothesis

can be ultimately tested if our setup is improved such that the Stokes vector of a liquid sample can be measured in a sufficiently short time period.

We measured the 2D Mueller-matrix images of a piece of rat bone. The raw images and the images of the corresponding 16 Mueller-matrix elements are shown in Fig. 4. The four Stokes vectors corresponding to the four incident polarization states were first calculated using Eq. (2) and then were used to calculate the Mueller matrix. The image size is 1.0 mm in optical depth and 0.5 mm in the lateral dimension. The 1.0 mm optical depth may be converted to approximately 0.67 mm in physical depth assuming the index of refraction of the bone sample is 1.5. The image of the Mueller-matrix element M_{00} corresponds to a polarization-independent image as acquired by a nonpolarization OCT system. The other Mueller-matrix elements M_{ij} are pixel-wise normalized by M_{00} image. The polarization-independent element M_{00} reveals significantly less information than the other elements as clearly shown in the figure. Strong layered structures are clearly seen in some of the images such as M_{22}, M_{23}, M_{32} and M_{33}.
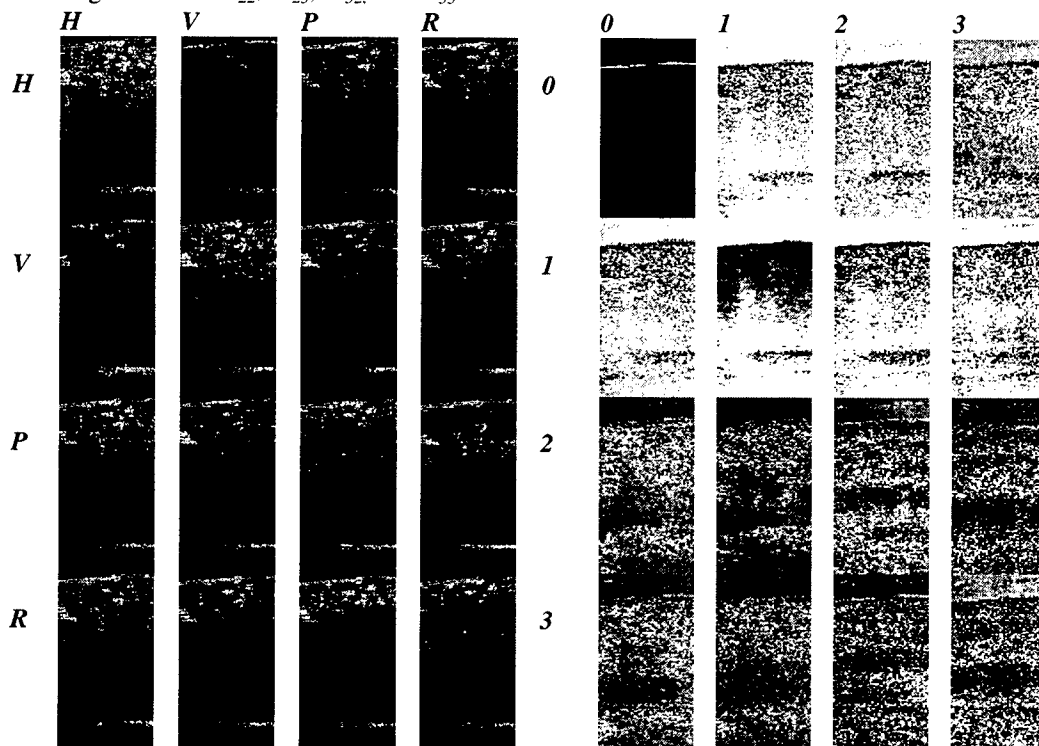
Fig. 4 The raw 2-D images and the 2-D images of the corresponding Mueller matrix of a piece of fish bone

5. CONCLUSION

In summary, we demonstrated a novel imaging technique that measures Stokes vectors and Mueller matrices with optical coherence tomography in biological tissue or other turbid media. With this technique we measured the DOP, DOLP, and DOCP of liquid and solid samples. The DOP maintains the value of unity within the detectable depth for the solid sample while the DOP decreases with the optical depth for the liquid sample. This different behavior of liquid is probably related to the Brownian motion of the scattering particles in liquid. The Brownian motion of the particles causes random variation of the polarization state of the incident light. The 2D images of the Mueller matrices revealed more information about the tissue samples than standard OCT. The Mueller-matrix imaging system has potential applications in both scientific research and clinical practice.

ACKNOWLEDGEMENTS

REFERENCES

1. W. Drexler, U. Morgner, F. X. Kärtner, C. Pitris, S. A. Boppart, X. D. Li, E. P. Ippen, and J. G. Fujimoto, "In vivo ultrahigh-resolution optical coherence tomography," Opt. Lett. 24, 1221 (1999).
2. A. Rollins, S. Yazdanfar, M. Kulkarni, R. Ungarunyawee, and J. Izatt, "In vivo video rate optical coherence tomography," Opt. Exp. 3, 219 (1998), www.osa.org.
3. M. J. Everett, K. Schoenenberger, B. W. Colston, Jr., and L. B. Da Silva, "Birefringence characterization of biological tissue by use of optical coherence tomography," Opt. Lett. 23, 228 (1998).
4. J. F. de Boer, S. M. Srinivas, A. Malekafzali, Z. Chen and J. S. Nelson, "Imaging thermally damaged tissue by polarization sensitive optical coherence tomography," Opt. Exp. 3, 212 (1998), www.osa.org.
5. J. M. Schmitt and S. H. Xiang, "Cross polarized backscatter in optical coherence tomography of biological tissue," Opt. Lett. 23, 1060 (1998).
6. J. F. de Boer, T. E. Milner and J. Stuart Nelson, "Determination of the depth-resolved Stokes parameters of light backscattered from turbid media by use of polarization-sensitive optical coherence tomography," Opt. Lett. 24, 300 (1999).
7. G. Yao and L. V. Wang, "Two dimensional depth-resolved Mueller matrix characterization of biological tissue by optical coherence tomography," Opt. Lett. 24, 537 (1999).
8. S. Jiao, G. Yao and L Wang, "Depth-resolved two-dimensional Stokes vectors of backscattered light and Mueller matrices of biological tissue measured with optical coherence tomography," Appl. Opt. 34, 6318(2000)
9. W. S. Bickel and W. M. Bailey, "Stokes vectors, Mueller matrices, and polarized scattered light," Am. J. Phys. 53, 468-478(1995).

Interpreting Mueller matrix images of tissues

Matthew H. Smith[*]

Department of Physics, The University of Alabama in Huntsville

ABSTRACT

In recent years, several investigators have begun to explore polarized light imagery as a potential diagnostic tool. For example, polarimetric images have show promise in identifying a variety of dermatological conditions. Because tissues tend to depolarize a large fraction (~85%) of incident light, the Mueller calculus lends itself well to these applications. A particular property of the Mueller matrix, the Depolarization Index, has demonstrated promise in discriminating between cancerous and benign moles. In this paper, we discuss the depolarizing aspects of tissues, however we primarily attempt to analyze the small fraction of light that has retained a polarization state. Analyzing the residual polarizing properties of a sample is challenging, and it requires a polar decomposition of the measured Mueller matrix into the basic properties of diattenuation, retardance, and depolarization. The diattenuation and retardance images contain information about the complex refractive index of the tissue, including any spatial variations in the index. We present measurements of the diattenuation and retardance of laser light reflected from skin as a function of incident angle and scattered angle.

Keywords: polarized light, polarimetry, diagnostic imaging, noninvasive diagnosis

1. INTRODUCTION

We have previously reported[1] Mueller matrix imagery of a variety of skin lesions. In that study, we verified the findings of other investigators[2] that indicated cancerous moles depolarize light less than surrounding tissues, whereas non-cancerous moles have the same depolarizing properties as the surrounding tissue. This effect is apparently caused by the presence of subsurface structures beneath cancerous moles that prevent light from penetrating the tissue as deeply as it would in normal skin.

In that study, we also examined a Lupus lesion, a raised rash or lesion on sun-exposed areas of the skin. Often times these scarring lesions form in a butterfly pattern across the nose and face, or smaller disc shaped lesions on the scalp, face, ears, neck and shoulders. Unlike the melanoma, the Lupus lesion was not visible in the depolarization images. When we examined the rest of the polarization parameters, however, we observed a striking effect in the *retardance* images. The Lupus lesions tended to alter the orientation of linear retardance. In this report, we provide a further analysis of that data from the Lupus lesions. We also present measurements of the retardance of the surface of skin as a function of scattered angle, and we show the unexpected observation of circular diattenuation on the margin of a vitiligo region. First, however, we describe our measurement technique.

2. EXPERIMENTAL TECHNIQUE

2.1 The Mueller Matrix Imaging Polarimeter

The Mueller Matrix Imaging Polarimeter[3] at The University of Alabama in Huntsville measures the full Mueller matrix of a sample. This is an imaging polarimeter, and thus a Muller matrix is measured for each pixel in an image of the sample. The MMIP was used to measure various skin regions of volunteers in an IRB approved protocol. Figure 1 is an illustration of the experimental setup. A HeNe laser (633 nm) was focused onto a spinning ground-glass disk, and light scattering from this point was collimated. The spinning disk acts as a spatial coherence scrambler, causing temporal variations in the laser speckle that are much faster than the integration time of our camera. The collimated beam passes through a *polarization generator* consisting of a fixed Glan-Thompson linear polarizer followed by a rotating quarter-wave linear retarder.

---

[*] SmithMH@uah.edu; phone 256-824-2853; fax 256-824-6077; http://www.osig.uah.edu; Department of Physics, OB-318, The Univ. of Alabama in Huntsville, Huntsville, AL 35899

82

Laser-Tissue Interaction XII: Photochemical, Photothermal, and Photomechanical, Donald D. Duncan, Steven L. Jacques, Peter C. Johnson, Editors, Proceedings of SPIE Vol. 4257 (2001)
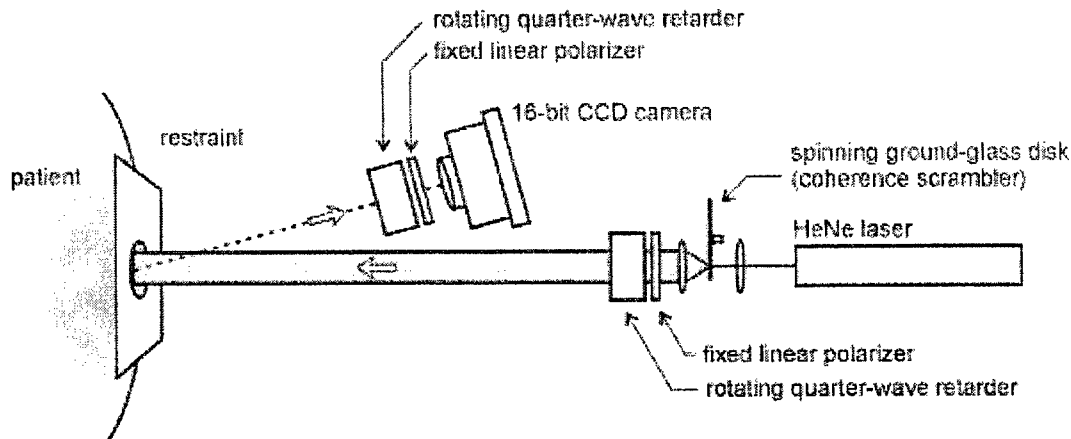
Figure 1. The Mueller matrix imaging polarimeter configured for skin reflectance measurements.

The region to be measured on a subject was pressed onto a restraint, and the collimated beam illuminated that area. The restraint was necessary because the measurement process requires about 45 seconds to complete, and any motion of the sample during acquisition causes image misregistration and subsequent false polarization signals[4].

The illumination beam was normal to the sample. The *polarization analyzer* can be positioned at any angle from 10° to 35° from the surface normal, and it collected any light that was reflected or scattered from the sample in that direction. The polarization analyzer consists of a rotating quarter-wave linear retarder followed by a fixed Glan-Thompson linear polarizer. A lens forms an image of the sample onto a TE cooled 16-bit CCD camera. The polarization generator and analyzer step through a sequence of 60 discrete measurements covering a wide range of input polarizations and measured output polarizations. On a pixel-by-pixel basis, a best-fit solution of these 60 measurements is used to calculate the 16 elements of the Mueller matrix for each pixel in the image. See Ref. 5 for a description of the mathematics required to calculate a Mueller matrix. The RMS error in our measured Mueller matrices is ~0.5%. This degree of accuracy is important when measuring tissue samples since such a large fraction of the incident light becomes depolarized.

2.2 Polar decomposition of Mueller matrices

A Mueller matrix is extremely powerful because it completely describes the polarization altering properties of a sample, however a raw Mueller matrix is difficult to interpret and provides little physical insight. As such, we perform a polar decomposition[6] of the Mueller matrix to yield the more familiar quantities of retardance (birefringence), diattenuation (dichroism), and depolarization

3. DEPOLARIZATION INDEX OF MOLES

The Depolarization Index (DI) is a parameter[5] that describes how completely a sample depolarizes incident polarized light. When DI = 0, no depolarization occurs. When DI = 1, the light reflected from (or transmitted through) a sample is completely depolarized. The DI is a value averaged across nearly all possible incident polarization states (linear, circular and elliptical). Figure 2 illustrates the depolarization index of an ordinary non-cancerous mole. We find that both the mole and the surrounding tissue depolarize approximately 90% of the incident light. The margins of the mole are not visible in the depolarization image. Figure 3 illustrates the depolarization index of a cancerous mole. We note that the cancerous mole depolarizes light significantly less than the surrounding tissue.
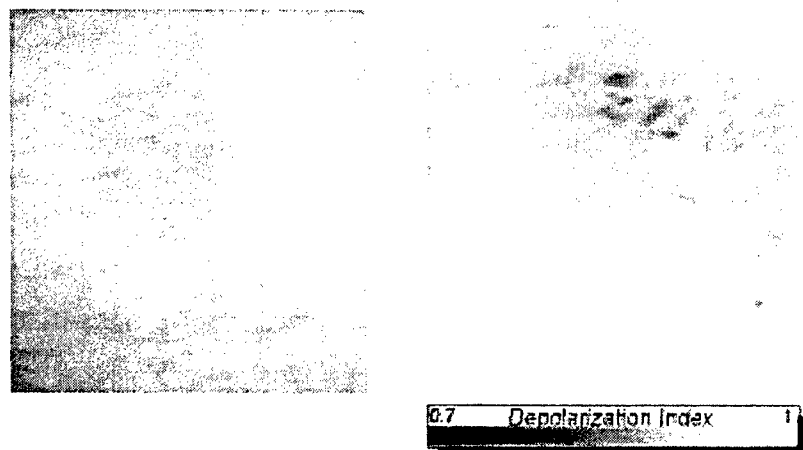
Figure 2. A benign mole (image on left) has depolarization properties (image on right) that are not significantly different than the surrounding tissue.
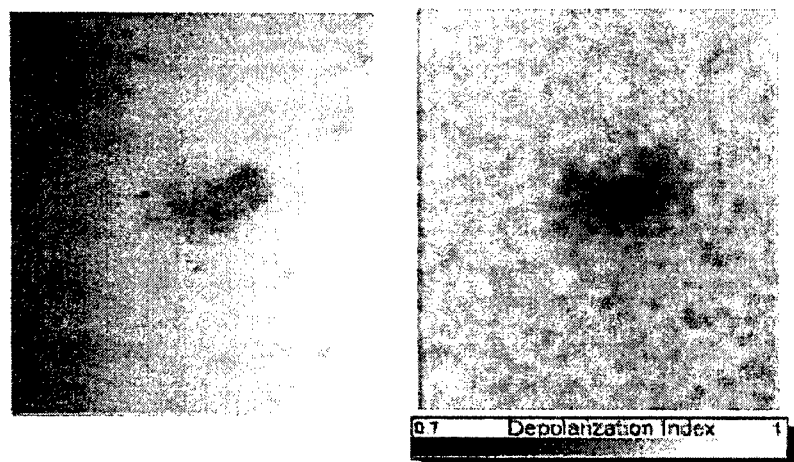
Figure 3. A malignant mole (image on left) depolarizes light significantly less than the surrounding tissue.

From this data it appears that the depolarization properties could be useful for identifying subsurface structures. However, it is important to note that not all of the incident light has been depolarized. We have become interested in how this small residual polarization is affected by various skin conditions. While the moles we measured did not exhibit interesting polarization effects, we *have* observed interesting polarization properties of several other dermatological conditions. Some example measurements are presented in the following sections.

4. ORIENTATION OF RETARDANCE IN LUPUS LESIONS

Figure 4 is an image of two Lupus lesions acquired at 633 nm. Because the lesions are red, they are difficult to see at this wavelength (hence the two arrows visible in the figure that were drawn on the subject with ball-point pen). We will examine three regions, labeled "normal skin", "Lupus lesion #1", and "Lupus lesion #2". Figure 5 shows the magnitude and orientation of linear retardance of the sample. Note that extracting the retardance from the measured Mueller matrix requires performing the polar decomposition described in Ref. 6. We find that the sample site exhibits a nearly uniform 17° of retardance oriented at 107° (where 90° is vertical). This residual retardance is likely created by our measurement geometry. We illuminated the sample at normal incidence and collected light at 30°, and vertically polarized light is in the s-state of reflection. Interestingly, we find that the orientation of the retardance varies significantly at the two Lupus lesions.
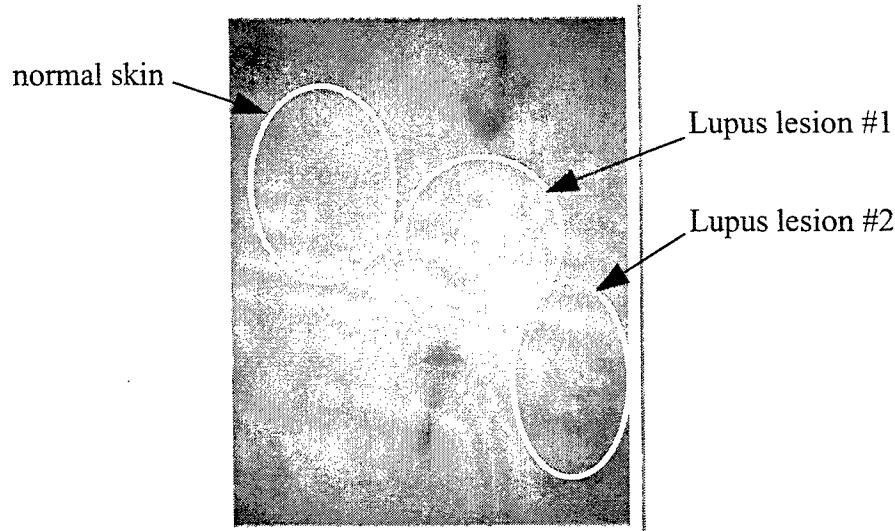
Figure 4. Two Lupus lesions were present in this measurement. We will examine these regions more carefully. We will also examine the region indicated as "normal skin."
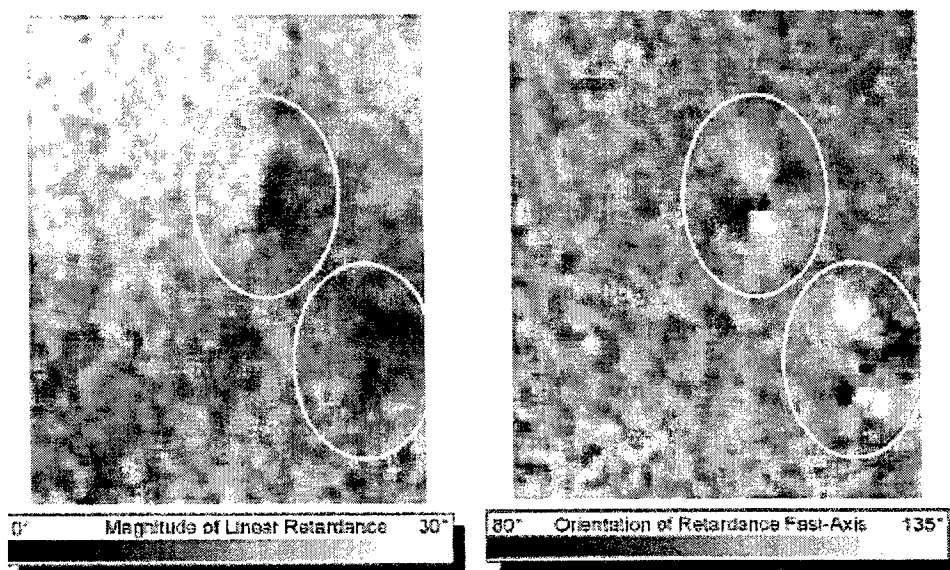
Figure 5. The entire skin region exhibits an average of 17° of retardance oriented nearly vertically (107° average). At the locations of the Lupus lesions, we observe a significant variation in the retardance orientation.

In order to isolate the effects of the Lupus lesions, we attempt to remove the overall 17° of retardance present in the image. We calculate the Mueller matrix for a 17° retarder oriented at 107°, take the inverse of this matrix, and perform a dot product with the Mueller matrices of each pixel in the image.

Figure 6 shows the region of normal skin with and without the residual retardance remove. In these images, the gray level indicates the magnitude of linear retardance and the white lines indicate the orientation of retardance. Note that once the residual retardance is removed, the orientation becomes randomized and the magnitude is nearly zero. Figures 7 and 8 show the two regions containing the Lupus lesions. In these images, we observe a significant retarding structure after the residual retardance is removed. We observe similar patterns when scar tissue is measured, and we expect that these patterns are caused by an underlying birefringent structure such as oriented collagen fibers.

original   residual retardance removed
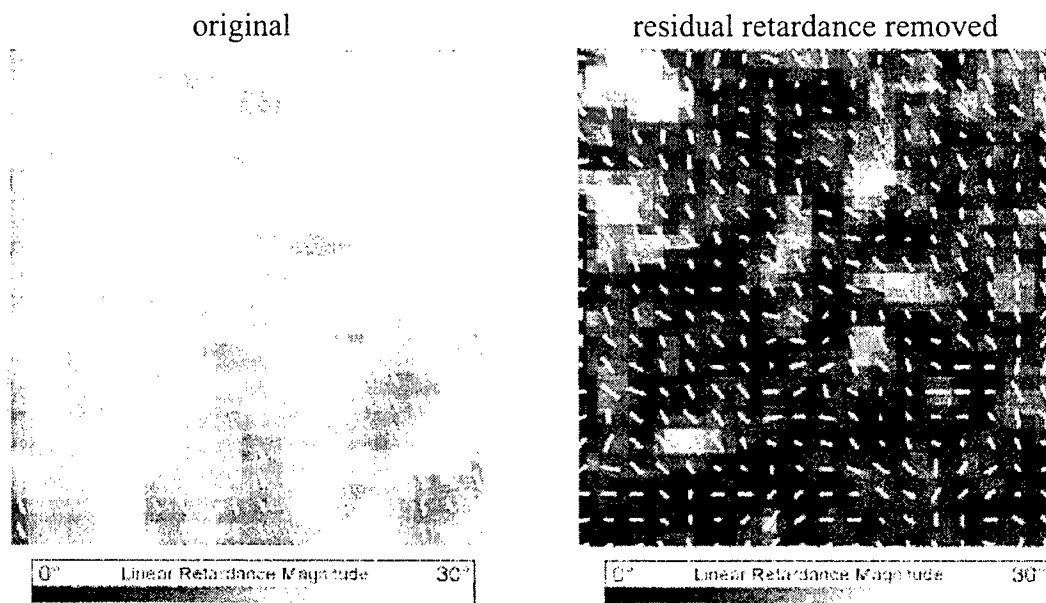
Figure 6. Retardance images of normal skin with and without the residual retardance removed. The white lines indicate the orientation of retardance. Only a random pattern remains after the near-uniform residual retardance is removed,

original   residual retardance removed
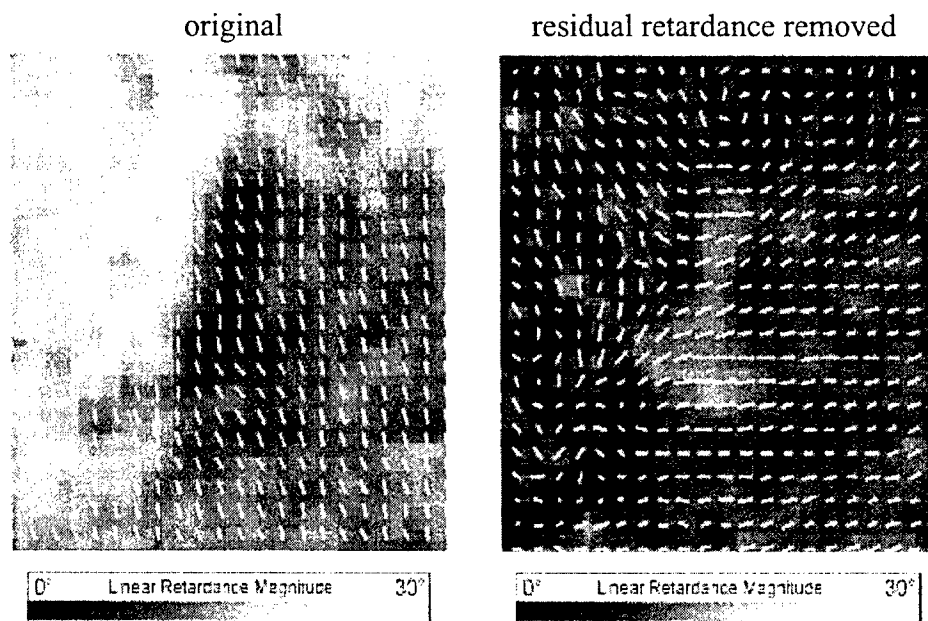
Figure 7. Retardance images of the region "Lupus lesion #1." The white lines indicate the orientation of retardance. After the residual retardance is removed, we still observe structured retardance at the location of the lesion.

original   residual retardance removed
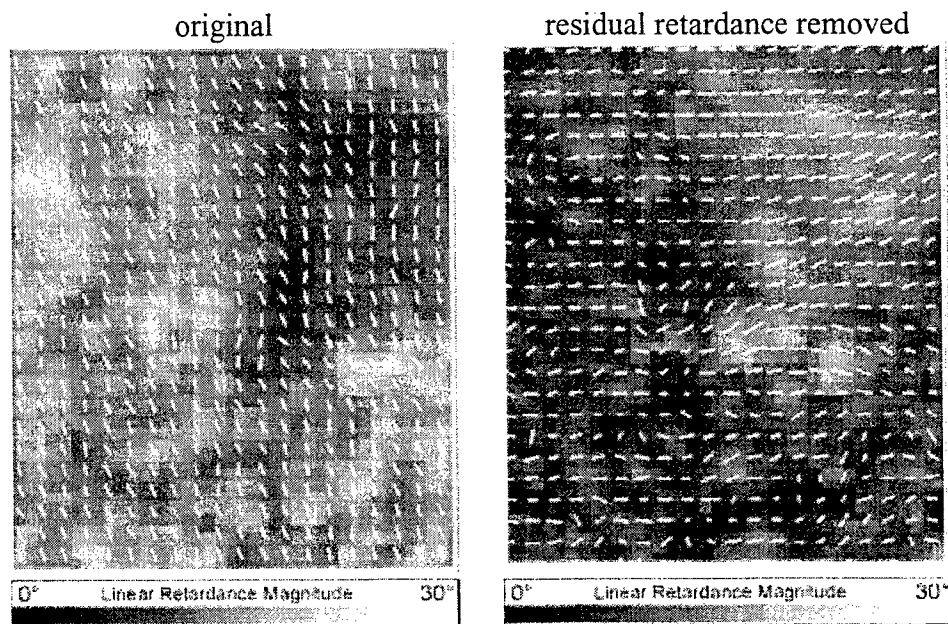
Figure 8. Retardance images of the region "Lupus lesion #2." The white lines indicate the orientation of retardance. After the residual retardance is removed, we still observe structured retardance at the location of the lesion.

5. VARYING COLLECTED ANGLE / VITILIGO REGION

We are interested in the cause of the residual retardance in our measurements. As such, we conducted an experiment in which we changed the angle of the collection camera (refer to Fig. 1) and measured retardance as a function of reflected angle. This data is shown in Fig. 9. The retardance varies monotonically with collection angle and appears to reach 180° (as expected) at normal incidence. Attempts at using ellipsometric equations to determine the refractive index of the skin from this data were unsuccessful. As such, we expect that this retardance is not simply caused by Fresnel reflection from the irregular skin surface.
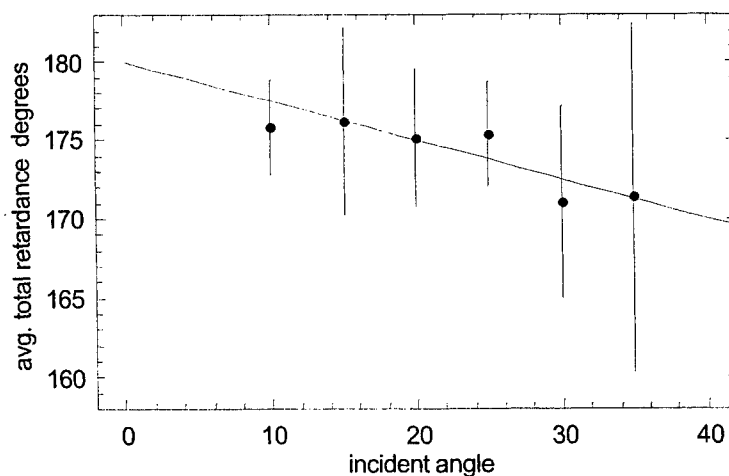
Figure 9. Average retardance of a skin region. The illumination beam was incident normal to the skin. The angle to the collection camera was varied from 10 to 36 degrees. A near monotonic variation in retardance with collection angle is observed. The error bars represent the standard deviation of all pixels in the image.

In this collection-angle experiment, we chose to measure a vitiligo region (an area of no pigmentation in a region of otherwise darkly pigmented skin) in order to determine if skin pigmentation affected the polarization properties. As seen in Fig. 10, the depolarization index correlated ($r^2 = 0.61$) with collected flux. Regions with high collected flux (corresponding to unpigmented vitiligo regions) depolarized ~91% of incident light. Regions of darkly pigmented skin (low intensity) only depolarized ~80% of incident light. We expect that heavily pigmented skin prevents light from penetrating the tissue as deeply as it would in unpigmented skin, thereby depolarizing the light less. We do not show the data here, but we found that there was no correlation between depolarization index and the collection angle.
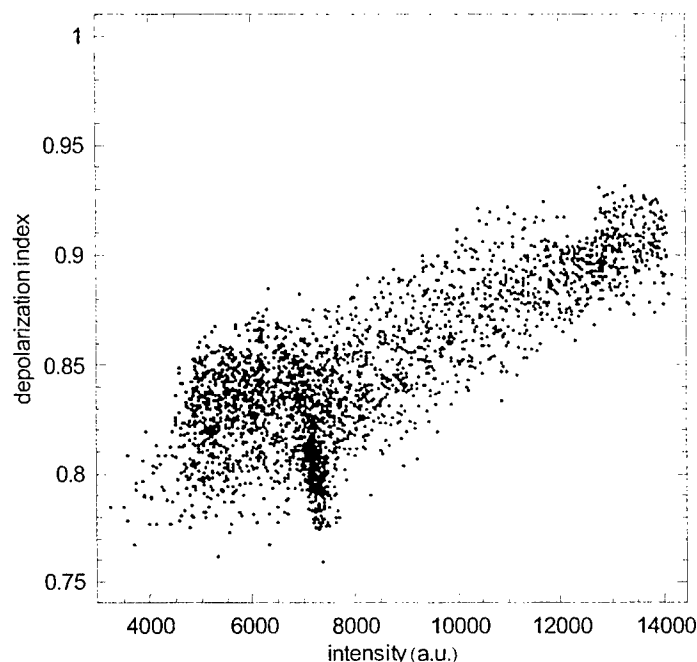
Figure 10. The depolarization index was found to correlate ($r^2 = 0.61$) with intensity. Here, high intensities correspond to regions of low pigmentation in a vitiligo region, and low intensities correspond to the surrounding darkly pigmented skin.

Our technique measures the full Mueller matrix of the sample, and we are therefore able to investigate *all* of a sample's polarization properties. In analyzing the collection-angle data from the vitiligo region, we uncovered an unexpected effect. On the border of the vitiligo region, where the pigmented skin and unpigmented skin meet, we observed significant quantities of *circular diattenuation*. Circular diattenuation is the preferential reflection of right circularly polarized light to left circularly polarized light, and is defined as $(I_{right} - I_{left})/(I_{right} + I_{left})$. The measured circular diattenuation increased as we increased the collection angle, and reached values as high as 25%. Figure 11 shows the maximum circular diattenuation as a function of collection angle. We currently have no explanation for this measured effect. We made several measurements of the region and verified that this was not an artifact of image motion. We do not show the data here, but strong circular retardance (~100°) was also measured at the margins of the vitiligo region.
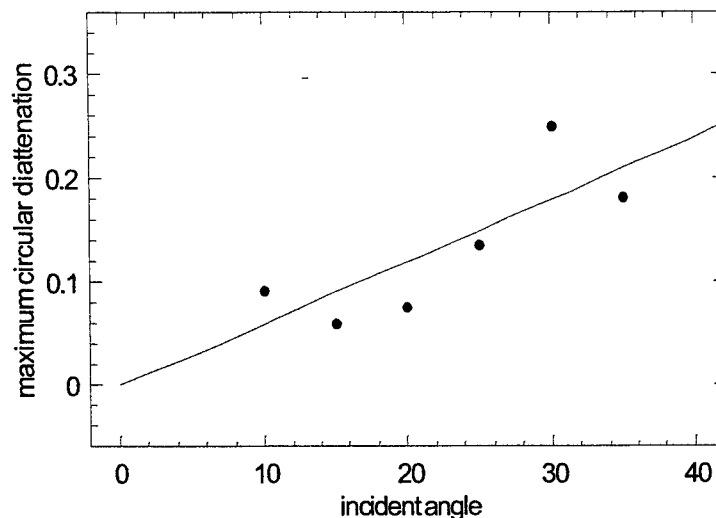
Figure 11. We observed significant levels of circular diattenuation on the margins of a vitiligo region. The maximum circular diattenuation increased as the collection angle was increased. We currently have no explanation for this effect.

6. DISCUSSION AND CONCLUSIONS

Human skin tends to depolarize 80% to 90% of incident polarized light. This depolarization depends on the pigmentation of the skin, with darkly pigmented skin depolarizing less. The depolarization can also be affected by subsurface structures such as cancerous moles. We have shown that the small fraction of light that retains a degree of polarization may contain a wealth of information that has previously been ignored. To interpret this information, we measure the full Mueller matrix of the sample and perform a polar decomposition in order to extract retardance information. We have shown that there is some measurable retardance between the s and p-planes when light reflects from tissue, and that this retardance does not appear to be defined simply by the complex Fresnel reflection coefficients. We have also shown that some skin lesions, such as Lupus lesions and scar tissue, appear to possess birefringent structures that can be mapped by measuring the orientation of linear retardance. Finally, we observed unexpected circular retardance and circular diattenuation at the edges of a vitiligo region that increased in magnitude as our collection angle was increased. We have no plausible explanation for these measured circular effects, but point out that the measurements were repeatable and not the result of instrumentation error. We hope that this work will inspire further investigations toward the application of imaging polarimetry to dermatology.

ACKNOWLEDGMENTS

REFERENCES

1. M. H. Smith, A Lompado, P. Burke, "Mueller matrix imaging polarimetry in dermatology," *Proc. SPIE* Vol. 3911, 210-216 (2000).
2. S. L. Jacques, K. Lee, "Imaging tissues with a polarized light video camera," *Proc. SPIE* Vol. 3863, 68-74 (1999).
3. J. L. Pezzaniti, R. A. Chipman, "Mueller matrix imaging polarimetry," *Opt. Eng.* **34**(6), 1558-1568 (1995).
4. M.. H. Smith, J. B. Woodruff, J. D. Howe, "Beam Wander Considerations in Imaging Polarimetry," *Proc. SPIE* Vol. 3754, 50-54 (1999).
5. R. A. Chipman, "Polarimetry," in the *Handbook of Optics*, vol. II, Chap. 22, (OSA/McGraw-Hill, 1994).
6. S. Lu and R.A. Chipman, "Interpretation of Mueller matrices based on polar decomposition," J. Opt. Soc. Am. A **13**,1-8 (1996).

Polarized light propagation and scattering in random media

Arnold D. Kim[a], Sermsak Jaruwatanadilok[b], Akira Ishimaru[b], and Yasuo Kuga[b]

[a]Department of Mathematics, Stanford University, Stanford, CA 94305, USA

[b]Department of Electrical Engineering, University of Washington, Seattle, WA 98195, USA

ABSTRACT

Using radiative transfer, we investigate linear and circular polarized light normally impinging a plane-parallel medium containing a random distribution of identically sized latex spheres in water. The focus of this study is to understand fundamental properties of polarized light scattering. In particular, we analyze backscattered and transmitted flux responses computed from direct numerical simulations. From these numerical computations, we observe that circular polarized light depolarizes at a slower rate than linear polarized light. In addition, circular polarized light shows a more noticeable dependence on the size of the scatterers than linear polarized light. Furthermore, the helicity flip observed in circular polarized backscattered light is a fundamental phenomenon manifested by low order scattering.

Keywords: Radiative transfer, Stokes parameters, polarization, Mie scattering

1. INTRODUCTION

To describe the effects of scattering on the polarization state of electromagnetic waves, the theory of radiative transfer generalizes to model the evolution of the Stokes vector of the specific intensity.[1,2] Because the inclusion of polarization presents significantly more complex mathematics, less theoretical work has been done on these problems. Recently, however, there has been a number of experimental and theoretical studies regarding polarized light propagation and scattering in random media for applications in tissue imaging.[3-7] Various experiments have demonstrated that depolarization requires longer length scales than those needed for diffusion. In that case, polarization characteristics of scattered waves provide another, and potentially more effective, way to discriminate between different kinds of optically thick media.

Since changes in polarization only occur from scattering, early transmitted responses co-polarized with the incident light have suffered very little scattering. Therefore, examining the polarization state of transmitted responses by scattering media provides a simple and effective way to discriminate between ballistic and snake photons from diffuse ones in optically thick media. This intuition has lead to a number of imaging and detection methods and techniques.[4-8] Many have also examined differences between linear and circular polarized incident light.[9-12] Except for very small scatterers, experimental evidence clearly suggests that circular polarized light transmitted through a scattering medium made up of spherical scatterers requires significantly more scattering to depolarize than linear polarized light. While this phenomenon is present in a variety of settings, this difference is most pronounced for spherical scatterers that are much larger than the wavelength of the incident light.[9,13,14] In contrast, experiments show that linear polarized light depolarizes more slowly than circular polarized light for actual tissue samples.[11,12]

Backscattered responses by polarized light also exhibit interesting phenomena. Backscattered circular polarized light maintains a significant degree of polarization.[15] In addition, backscattered circular polarized light exhibits a helicity flip.[15] In other words, the helicity channel from which you would expect more backscattering (i.e. the channel in which you would receive specular reflection from a perfectly conducting plate) in fact has less than the other helicity channel. The extent of these phenomena strongly depends on the sphere size. There has been some theoretical efforts to examine and predict the mechanisms of these phenomena,[15,16] although these efforts are not entirely exhaustive. Regardless, properties of circularly polarized backscattered light allow for an effective strategy to detect targets in scattering media.[17]

In this paper, we investigate the fundamental characteristics of polarized wave scattering in random media. Since there seems to be a broad variety of complicated phenomena present in these problems, our objective is to solve

90

Laser-Tissue Interaction XII: Photochemical, Photothermal, and Photomechanical, Donald D. Duncan, Steven L. Jacques, Peter C. Johnson, Editors, Proceedings of SPIE Vol. 4257 (2001)

a problem from which we ascertain an understanding of the very basic polarization characteristics in scattering media. To fulfill this objective, we solve the vector radiative transfer equation for a plane-parallel medium due to polarized (linear and circular) incident plane waves using direct numerical simulations. This plane-parallel medium has index-matched boundaries and contains a random distribution of identically sized latex spheres. We use Mie theory to compute the exact representation of the scattering operations. Although we are considering an ideal case where boundaries are index-matched and scatterers are identically sized spheres, we are most interested in examining fundamental multiple scattering effects on polarized waves. Therefore, we examine this simple setting to evaluate polarization without simplifying the scattering description.

We begin by reviewing the radiative transfer equations for plane-parallel problems with linearly and circularly polarized incident plane waves. Next, we present results from direct numerical computations of these vector radiative transfer equations. We compute these solutions using the Chebyshev Spectral Method.[18] From this data, we analyze transmitted and backscattered flux responses and the differences between linear and circular polarization. Finally, we conclude with a summary of our results regarding multiple scattering effects on polarized light.

2. VECTOR RADIATIVE TRANSFER

Consider a polarized plane wave normally impinging a plane-parallel medium containing a random distribution of identically sized spheres. The vector radiative transfer equation governing the diffuse modified Stokes vector $\bar{\mathbf{I}}$ for this problem[19,20] is

$$\mu \frac{\partial}{\partial \tau} \bar{\mathbf{I}}(\tau, \mu, \phi) + \bar{\mathbf{I}}(\tau, \mu, \phi) = \int_0^{2\pi} \int_{-1}^1 S(\mu, \phi, \mu', \phi') \bar{\mathbf{I}}(\tau, \mu', \phi') \, d\mu' \, d\phi' + \bar{\mathbf{f}}(\tau, \mu, \phi), \tag{1}$$

over the domain, $0 \leq \tau < \tau_o$. Here $\mu = \cos\theta$, $\tau = \rho\sigma_t z$, and $\tau_o = \rho\sigma_t d$ where ρ is the number density of scatterers and σ_t is the total scattering cross-section. Since we assume that all of the spherical scatterers have identical radii, σ_t is a constant. Furthermore, we assume that this incident wave provides the only source of radiation in the medium whose boundaries are index-matched so that

$$\bar{\mathbf{I}}(\tau = 0, \mu, \phi) = 0 \qquad \text{for} \quad 0 < \mu \leq 1 \tag{2a}$$

$$\bar{\mathbf{I}}(\tau = \tau_o, \mu, \phi) = 0 \qquad \text{for} \quad -1 \leq \mu < 0. \tag{2b}$$

The kernel of the integral operator in (1) is the Mueller matrix which gives the scattered Stokes vector observed in the (μ, ϕ) direction by an incident Stokes vector in the (μ', ϕ') direction from an individual scatterer.[2,21] The Mueller matrix is

$$S(\mu, \phi, \mu', \phi') = \sigma_t^{-1} \begin{bmatrix} |f_{11}|^2 & |f_{12}|^2 & \text{Re}(f_{11}f_{12}^*) & -\text{Im}(f_{11}f_{12}^*) \\ |f_{21}|^2 & |f_{22}|^2 & \text{Re}(f_{21}f_{22}^*) & -\text{Im}(f_{21}f_{22}^*) \\ 2\text{Re}(f_{11}f_{21}^*) & 2\text{Re}(f_{12}f_{22}^*) & \text{Re}(f_{11}f_{22}^* + f_{12}f_{21}^*) & -\text{Im}(f_{11}f_{22}^* - f_{12}f_{21}^*) \\ 2\text{Im}(f_{11}f_{21}^*) & 2\text{Im}(f_{12}f_{22}^*) & \text{Im}(f_{11}f_{22}^* + f_{12}f_{21}^*) & \text{Re}(f_{11}f_{22}^* - f_{12}f_{21}^*) \end{bmatrix} \tag{3}$$

where $\{f_{11}, f_{12}, f_{21}, f_{22}\}$ is the set of scattering amplitudes.[2] Throughout this paper, we refer to the submatrices of the Mueller matrix, $\{S_1, S_2, S_3, S_4\}$, where

$$S = \begin{bmatrix} S_1 & S_2 \\ S_3 & S_4 \end{bmatrix}. \tag{4}$$

For spherical scatterers, Mie theory provides the exact expressions for these scattering amplitudes.[2,21–24] The results of Mie theory are summarized by two complex amplitude functions:[23] s_1 and s_2, from which one is able to compute these scattering amplitudes and hence, the Mueller matrix.[20]

The source term $\bar{\mathbf{f}}(\tau, \mu, \phi)$ in (1) is the contribution from the reduced intensity corresponding to the incident plane wave. We consider two cases below: linearly and circularly polarized incident plane waves. R. L.-T. Cheung and A. Ishimaru give a full derivation for both cases,[20] so we only summarize the main results here.

2.1. Linearly Polarized Incident Plane Wave

To treat the azimuthal dependence in (1), let us consider a Fourier expansion of the Stokes vector

$$\bar{\mathbf{I}}(\tau,\mu,\phi) = \bar{\mathbf{I}}^{(0)}(\tau,\mu) + \sum_{n=1}^{\infty}\left[\bar{\mathbf{I}}_c^{(n)}(\tau,\mu)\cos(n\phi) + \bar{\mathbf{I}}_s^{(n)}(\tau,\mu)\sin(n\phi)\right]. \tag{5}$$

For normally incident, linearly polarized plane waves, we find that the mode zero and mode two Fourier modes of this series are the only ones that are non-zero.[20] This simplification is a manifestation of the azimuthal symmetry of the Mueller matrix constructed from Mie theory.

The equation for the Fourier mode zero term is

$$\mu\frac{\partial}{\partial\tau}\bar{\mathbf{\Psi}}_0(\tau,\mu) + \bar{\mathbf{\Psi}}_0(\tau,\mu) = \int_{-1}^{1}\mathbf{L}^{(0)}(\mu,\mu')\bar{\mathbf{\Psi}}_0(\tau,\mu')d\mu' + \bar{\mathbf{F}}^{(0)}(\mu)\exp[-\tau], \tag{6}$$

where

$$\bar{\mathbf{\Psi}}_0(\tau,\mu) = \left[\begin{array}{c} I_1^{(0)}(\tau,\mu) \\ I_2^{(0)}(\tau,\mu) \end{array}\right], \tag{7}$$

and

$$\bar{\mathbf{F}}^{(0)}(\mu) = \frac{1}{2\sigma_t}\left[\begin{array}{c} |A_{ll}(\mu)|^2 \\ |A_{rr}(\mu)|^2 \end{array}\right]. \tag{8}$$

The functions, A_{ll} and A_{rr} are proportional to the complex scattering amplitudes,[20]

$$A_{ll} = is_2^*/k, \qquad \text{and} \qquad A_{rr} = is_1^*/k. \tag{9}$$

The kernel of the scattering operator, $\mathbf{L}_1^{(0)}(\mu,\mu')$, is mode zero term of the Fourier series expansion of the S_1 submatrix,

$$\mathbf{L}_1^{(0)}(\mu,\mu') = \int_0^{2\pi} S_1(\mu,\mu',\phi'-\phi)d(\phi'-\phi). \tag{10}$$

The vector, $\bar{\mathbf{\Psi}}_0$, satisfies

$$\bar{\mathbf{\Psi}}_0(\tau=0,\mu) = 0 \qquad \text{for} \quad 0 < \mu \le 1 \tag{11a}$$
$$\bar{\mathbf{\Psi}}_0(\tau=\tau_o,\mu) = 0 \qquad \text{for} \quad -1 \le \mu < 0. \tag{11b}$$

The equation for the Fourier mode two term is

$$\mu\frac{\partial}{\partial\tau}\bar{\mathbf{\Psi}}_2(\tau,\mu) + \bar{\mathbf{\Psi}}_2(\tau,\mu) = \int_{-1}^{1}\mathbf{L}^{(2)}(\mu,\mu')\bar{\mathbf{\Psi}}_2(\tau,\mu')d\mu' + \bar{\mathbf{F}}^{(2)}(\mu)\exp[-\tau], \tag{12}$$

where

$$\bar{\mathbf{\Psi}}_2(\tau,\mu) = \left[\begin{array}{c} I_{1_c}^{(2)}(\tau,\mu) \\ I_{2_c}^{(2)}(\tau,\mu) \\ U_s^{(2)}(\tau,\mu) \\ V_s^{(2)}(\tau,\mu) \end{array}\right] \tag{13}$$

and

$$\bar{\mathbf{F}}^{(2)}(\mu) = \frac{1}{2\sigma_t}\left[\begin{array}{c} |A_{ll}(\mu)|^2 \\ -|A_{rr}(\mu)|^2 \\ -2\text{Re}(A_{ll}(\mu)A_{rr}^*(\mu)) \\ -2\text{Im}(A_{ll}(\mu)A_{rr}^*(\mu)) \end{array}\right]. \tag{14}$$

The kernel of the scattering operator is made up of four submatrices,

$$\mathbf{L}^{(2)} = \left[\begin{array}{cc} \mathbf{L}_1^{(2)} & \mathbf{L}_2^{(2)} \\ -\mathbf{L}_3^{(2)} & \mathbf{L}_4^{(2)} \end{array}\right], \tag{15}$$

where

$$
\mathbf{L}_1^{(2)}(\mu, \mu') \;=\; \int_0^{2\pi} S_1(\mu, \mu', \phi' - \phi) \cos\left[2(\phi - \phi')\right] d(\phi' - \phi), \tag{16a}
$$

$$
\mathbf{L}_2^{(2)}(\mu, \mu') \;=\; \int_0^{2\pi} S_2(\mu, \mu', \phi' - \phi) \sin\left[2(\phi - \phi')\right] d(\phi' - \phi), \tag{16b}
$$

$$
\mathbf{L}_3^{(2)}(\mu, \mu') \;=\; \int_0^{2\pi} S_3(\mu, \mu', \phi' - \phi) \sin\left[2(\phi - \phi')\right] d(\phi' - \phi), \tag{16c}
$$

$$
\mathbf{L}_4^{(2)}(\mu, \mu') \;=\; \int_0^{2\pi} S_4(\mu, \mu', \phi' - \phi) \cos\left[2(\phi - \phi')\right] d(\phi' - \phi). \tag{16d}
$$

The vector, $\bar{\mathbf{\Psi}}_2$, satisfies

$$
\bar{\mathbf{\Psi}}_2(\tau = 0, \mu) = 0 \qquad \text{for} \quad 0 < \mu \leq 1 \tag{17a}
$$

$$
\bar{\mathbf{\Psi}}_2(\tau = \tau_o, \mu) = 0 \qquad \text{for} \; -1 \leq \mu < 0. \tag{17b}
$$

After solving the mode zero and mode two boundary value problems, we construct the Stokes vector for the diffuse intensity,

$$
\bar{\mathbf{I}}(\tau, \mu, \phi) = \begin{bmatrix} I_1 \\ I_2 \\ U \\ V \end{bmatrix} = \begin{bmatrix} I_1^{(0)}(\tau, \mu) \\ I_2^{(0)}(\tau, \mu) \\ 0 \\ 0 \end{bmatrix} + \begin{bmatrix} I_{1_c}^{(2)}(\tau, \mu) \cos(2\phi) \\ I_{2_c}^{(2)}(\tau, \mu) \cos(2\phi) \\ U_s^{(2)}(\tau, \mu) \sin(2\phi) \\ V_s^{(2)}(\tau, \mu) \sin(2\phi) \end{bmatrix}. \tag{18}
$$

To calculate the Stokes vector corresponding to the polarization parallel and perpendicular to the polarization of the incident wave, we apply a rotation on (18),

$$
\begin{bmatrix} I_x \\ I_y \\ U_{xy} \\ V_{xy} \end{bmatrix} = \begin{bmatrix} \mu^2 \cos^2\phi & \sin^2\phi & -1/2\,\mu \sin 2\phi & 0 \\ \mu^2 \sin^2\phi & \cos^2\phi & 1/2\,\mu \sin 2\phi & 0 \\ \mu^2 \sin 2\phi & -\sin 2\phi & \mu \cos 2\phi & 0 \\ 0 & 0 & 0 & \mu \end{bmatrix} \begin{bmatrix} I_1 \\ I_2 \\ U \\ V \end{bmatrix}, \tag{19}
$$

where I_x is the intensity component polarized parallel to the incident polarization, or co-polarized intensity, and I_y is the intensity component polarized perpendicular to the incident polarization or cross-polarized intensity.

2.2. Circularly Polarized Incident Plane Wave

Let us consider a left-handed circularly polarized incident plane wave. By performing the same Fourier series analysis that we used for the linearly polarized incident wave, we find that only the mode zero Fourier mode is non-zero. Furthermore, we find that (1) reduces to two decoupled equations,

$$
\mu \frac{\partial}{\partial \tau} \bar{\mathbf{\Psi}}_0(\tau, \mu) + \bar{\mathbf{\Psi}}_0(\tau, \mu) = \int_{-1}^{1} \mathbf{L}_1^{(0)}(\mu, \mu') \bar{\mathbf{\Psi}}_0(\tau, \mu') d\mu' + \bar{\mathbf{F}}^{(0)}(\mu) \exp[-\tau], \tag{20}
$$

and

$$
\mu \frac{\partial}{\partial \tau} \bar{\mathbf{\Phi}}_0(\tau, \mu) + \bar{\mathbf{\Phi}}_0(\tau, \mu) = \int_{-1}^{1} \mathbf{L}_4^{(0)}(\mu, \mu') \bar{\mathbf{\Phi}}_0(\tau, \mu') d\mu' + \bar{\mathbf{G}}^{(0)}(\mu) \exp[-\tau]. \tag{21}
$$

Here (20) is identical to the mode zero equation for the linearly polarized incident wave. In (21), we define

$$
\bar{\mathbf{\Phi}}_0(\tau, \mu) = \begin{bmatrix} U^{(0)}(\tau, \mu) \\ V^{(0)}(\tau, \mu) \end{bmatrix}, \tag{22}
$$

$$
\bar{\mathbf{G}}^{(0)}(\mu) = \frac{1}{\sigma_t} \begin{bmatrix} -\mathsf{Im}(A_{ll}(\mu) A_{rr}^*(\mu)) \\ \mathsf{Re}(A_{ll}(\mu) A_{rr}^*(\mu)) \end{bmatrix}, \tag{23}
$$

and

$$
\mathbf{L}_4^{(0)}(\mu, \mu') = \int_0^{2\pi} S_4(\mu, \mu', \phi' - \phi) d(\phi' - \phi). \tag{24}
$$
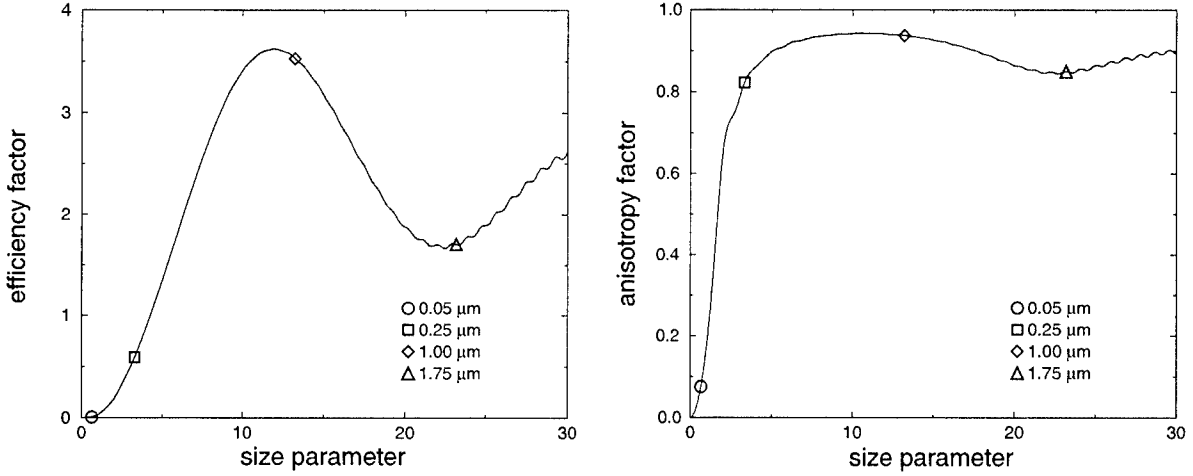
Figure 1. The efficiency factor, Q_{ext}, (left plot) and anisotropy factor, $\bar{\mu}$, (right plot) as a function of the size parameter, ka, for the polystyrene spheres used in the computational simulations calculated using the Mie scattering solution.

The vector, $\bar{\Phi}_0$, satisfies

$$\bar{\Phi}_0(\tau = 0, \mu) = 0 \qquad \text{for} \quad 0 < \mu \leq 1 \tag{25a}$$

$$\bar{\Phi}_0(\tau = \tau_o, \mu) = 0 \qquad \text{for} \quad -1 \leq \mu < 0. \tag{25b}$$

After solving (20) and (21), we determine the left-handed and right-handed circularly polarized intensities,[20]

$$I_{\text{lhc}} = (I_1 + I_2 + V)/2 \tag{26a}$$

$$I_{\text{rhc}} = (I_1 + I_2 - V)/2 \tag{26b}$$

Since we chose the incident wave to be left-handed circularly polarized, we define the transmitted co-polarized and cross-polarized intensities to be

$$I_{\text{co-pol}}^{(\text{trans})} = I_{\text{lhc}}^{(\text{trans})}, \quad \text{and} \quad I_{\text{x-pol}}^{(\text{trans})} = I_{\text{rhc}}^{(\text{trans})}.$$

Furthermore, since (26a) and (26b) are defined with respect to the direction of propagation, the backscattered co-polarized and cross-polarized intensities are

$$I_{\text{co-pol}}^{(\text{back})} = I_{\text{rhc}}^{(\text{back})}, \quad \text{and} \quad I_{\text{x-pol}}^{(\text{back})} = I_{\text{lhc}}^{(\text{back})}.$$

We choose to define the co-polarized backscattered intensity to correspond to the polarization state of a wave specularly reflected by a perfectly conducting plate. Recall that the incident plane wave that we consider is left-handed circularly polarized.

3. NUMERICAL RESULTS

We solved the vector radiative transfer equations for linearly and circularly polarized incident plane waves using the Chebyshev Spectral Method.[18] We chose this method because it yields stable and accurate solutions over a large range of optical depths, even for large anisotropy factors. The basis of this method is a Chebyshev spectral approximation of the spatial part of the intensity which results in a coupled system of integral equations. For all of these examples, we used 129 Chebyshev modes, and solved the system of integral equation using a Nyström method employing a 60-point Gaussian quadrature rule that used Legendre polynomial abscissa and weights.

After computing the transmitted and backscattered intensities, we computed the co-polarized and cross-polarized flux magnitudes,

$$\mathbf{F}_{\text{co-pol}} = \int_0^{2\pi} \int_{-1}^1 I_{\text{co-pol}}(\mu, \phi) \, \mu \, d\mu \, d\phi \tag{27a}$$

$$\mathbf{F}_{\text{x-pol}} = \int_0^{2\pi} \int_{-1}^1 I_{\text{x-pol}}(\mu, \phi) \, \mu \, d\mu \, d\phi, \tag{27b}$$

where $I_{\text{co-pol}}$ and $I_{\text{x-pol}}$ were evaluated at $\tau = 0$ for backscattering and $\tau = \tau_o$ for transmission. The azimuthal angle integrals were analytically calculated since the ϕ-dependence is simple due to the Fourier series expansion. The polar angle integrals were computed using the same Gaussian quadrature rule used to solve the integral equations.

For these numerical simulations, we considered latex spheres randomly distributed in water illuminated by an optical wave generated by a He-Ne laser. The wavelength of light from the He-Ne laser in air is $\lambda = 632.8$ nm. When light from this laser propagates in water whose refractive index is $n_{\text{water}} = 1.33$, its wave number is $k \approx 13.21 \, \mu m^{-1}$. The refractive index for these latex spheres in this problem is $n_{\text{spheres}} = 1.588$ so that the relative refractive index of these spheres in water is $n_{\text{relative}} = 1.19$.

In particular, we considered four different sphere radii: $a = 0.05$, 0.25, 1.00, and $1.75 \, \mu m$. Using the algorithm by Bohren and Huffman,[24] we calculated the efficiency and anisotropy factors for these spheres. A plot of these results appear in Fig. 1 and their size parameters, efficiency factors, and anisotropy factors appear in Table 1. We chose these four sphere sizes to sample the areas near and far from the Mie resonance regime.[22-24] Notice that there is no imaginary part in this relative refractive index so no absorption is present in the medium. Hence, a conservation of power calculation indicates the accuracy of our computations. For these computations, the conservation of power yielded maximum errors of $\sim 10^{-8}\%$ for the three smallest spheres and $\sim 10^{-4}\%$ for the largest sphere.

3.1. Transmission

In Fig. 2, we plot the transmitted flux responses as a function of optical depth for the four different scatterer sizes (rows) and for linear (left column) and circular (right column) incident polarization.

Since the $0.05 \, \mu m$ radius spheres are much smaller than the wavelength, we expect them to act like Rayleigh scatterers. Therefore, we expect transmitted responses to depolarize for these spheres much more quickly than responses from larger spheres. Our computations agree with this intuition. For both linear and circular incident polarizations, we find that waves depolarize and the difference between the co-polarized and cross-polarized fluxes are negligible for $\tau_o > 7$. Although the circular case decays slightly slower than the linear case, this difference is not significant.

For the larger spheres, we see that the transmitted flux responses do not fully depolarize at $\tau_o = 20$. Furthermore, we observe that the circularly polarized incident waves maintain a greater difference between its co-polarized and cross-polarized fluxes than linearly polarized incident waves. In Table 2, we summarize the differences between the co-polarized and cross-polarized fluxes. We observe that the largest flux differences occur for the near-resonant scatterers whose radii are $1.00 \, \mu m$. For that case, we observe that responses from linearly polarized waves exhibit a 2 dB difference while those from circularly polarized waves exhibit a 7 dB difference. For the non-resonant scatterers, we observe that the flux differences are small for linear polarized incident waves compared with those for circularly polarized ones. However, all of these flux differences exhibit a strong dependence on the sphere radius. Most

Table 1. Size parameters, efficiency factors, and anisotropy factors of the four different sphere radii used in our computations.

radius (μm)	ka	Q_{ext}	$\bar{\mu}$
0.05	0.66	0.00558	0.0752
0.25	3.31	0.590	0.823
1.00	13.23	3.526	0.938
1.75	22.15	1.705	0.850
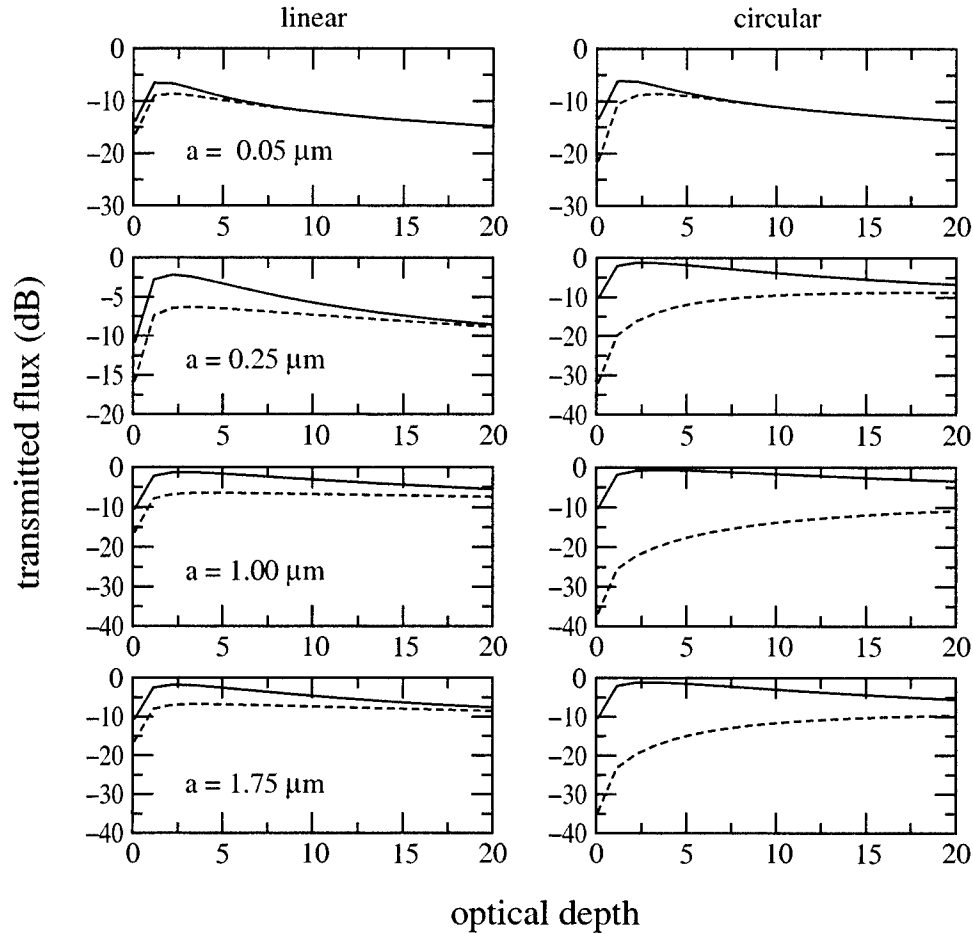
Figure 2. The diffuse transmitted flux responses for the linearly polarized waves (left column) and circularly polarized waves (right column). The plots on the first row from the top correspond to 0.05μm radius spheres; the second row corresponds to 0.25μm radius spheres; the third row corresponds to 1.00μm radius spheres; and the fourth row corresponds to 1.75μm radius spheres. The solid lines correspond to the co-polarized flux and the dashed lines correspond to the cross-polarized flux.

likely, this dependence is due to the large anisotropy factors of these scatterers. Transmitted flux quantities are weighted more heavily in forward directions. In addition, scattering in forward directions maintains a large degree of polarization compared with other directions. Hence, highly anisotropy scattering in which the angular spectrum is strongly peaked in the forward direction also exhibits a sizable degree of polarization.

3.2. Backscattering

In Fig. 3, we plot the backscattered flux responses as a function of optical depth for the four different scatterer sizes (rows) and for linear (left column) and circular (right column) incident polarization.

For $0.05\,\mu$m radius spheres, we observe that the backscattered flux responses exhibit ~ 1.5 dB differences between the co-polarized and cross-polarized flux for both linear and circular cases. The differences between the linear and circular cases are small and qualitatively similar. These fluxes saturate to a constant as the optical depth approaches infinity. For larger spheres, we observe that the flux responses due to linearly polarized incident waves are all qualitatively similar. While these flux responses do not completely depolarize, the differences between the co-polarized and cross-polarized flux are small. From Table 2, we observe that flux differences at $\tau_o = 20$ occur within fractions of a dB. This behavior persists for optical depths $\tau_o > 7$. Therefore, the backscattered flux responses by linearly polarized incident waves do not exhibit a strong dependence on different scatterer sizes. In contrast
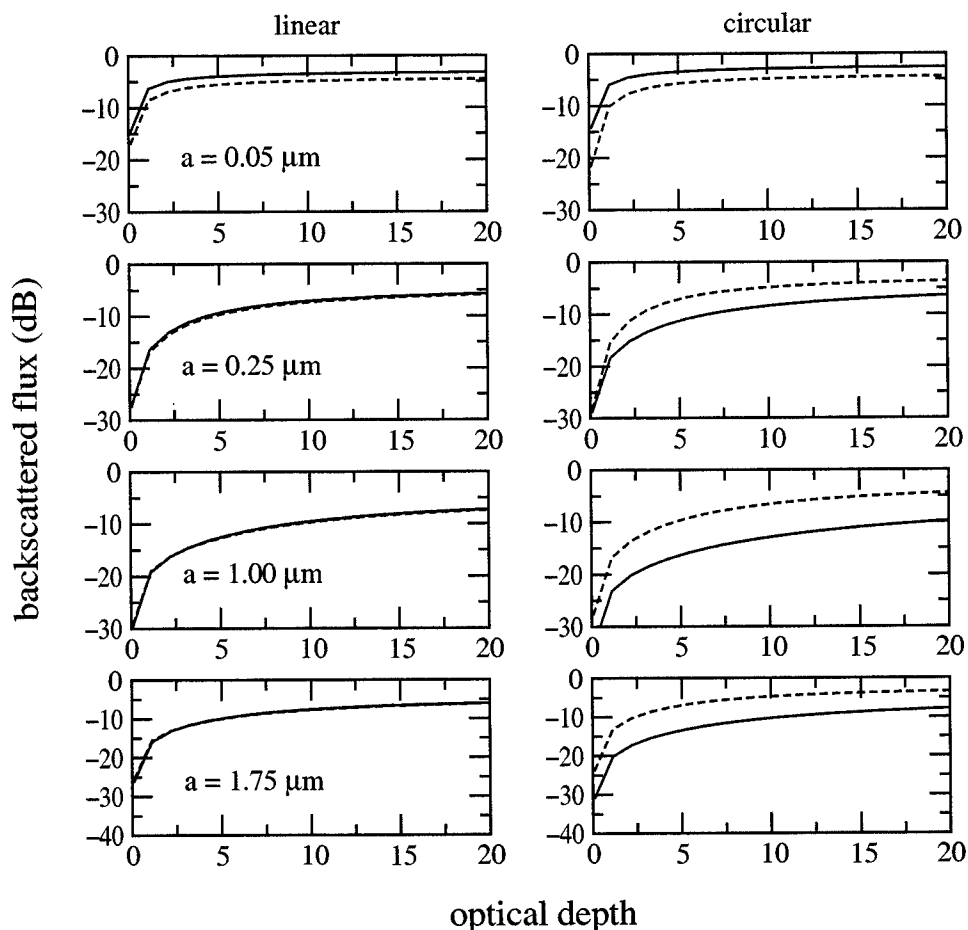
Figure 3. The diffuse backscattered flux responses for the linearly polarized waves (left column) and circularly polarized waves (right column). The plots on the first row from the top correspond to 0.05μm radius spheres; the second row corresponds to 0.25μm radius spheres; the third row corresponds to 1.00μm radius spheres; and the fourth row corresponds to 1.75μm radius spheres. The solid lines correspond to the co-polarized flux and the dashed lines correspond to the cross-polarized flux.

Table 2. Co-polarized and cross-polarized transmitted and backscattered flux differences at $\tau_o = 20$ for linearly and circularly polarized incident waves.

radius (μm)	transmitted		backscattered	
	linear (dB)	circular (dB)	linear (dB)	circular (dB)
0.05	6.5E-5	1.3E-5	1.2734	1.7711
0.25	0.2827	2.0571	0.1838	2.7555
1.00	1.9315	7.4400	0.1495	5.4003
1.75	0.9142	4.1145	0.1062	4.4135

to the linearly polarized incident wave results, the flux responses by circularly polarized incident wave show larger flux differences as well as a stronger dependence on the size of the scatterers. This flux difference is largest for near-resonant scatterers in which there is a $\sim 5\,$dB difference between the co-polarized and cross-polarized flux.

Another qualitative difference between the linear and circular cases is that for circularly polarized incident waves, a polarization "flip" occurs in which the cross-polarized flux is larger than the co-polarized flux. To investigate this phenomenon in more detail, we examine the first order scattering solution. In Fig. 4, we plot the degree of

polarization

$$m_{\text{circular}} = \frac{I_{\text{co-pol}} - I_{\text{x-pol}}}{I_{\text{co-pol}} + I_{\text{x-pol}}} \qquad (28)$$

computed from first-order scattering as a function of the cosine of the scattering angle. This figure shows the complicated angular dependence of the backscattered light. Furthermore, the values of the degree of polarization indicate changes in helicity from co-polarized ($m_c > 0$) to cross-polarized ($m_c < 0$). Since interpreting these angular spectra is not immediately intuitive, we computed the corresponding fluxes which appear in Table 3. From these flux computations, we observe that the three larger spheres show a helicity flip in which the cross-polarized flux is larger than the co-polarized flux. Hence, this polarization flip is present in first-order scattering and by observing the fluxes at larger optical depths, we see that this phenomenon becomes more pronounced.

4. CONCLUSIONS

In this paper, we numerically solved the vector radiative transfer equation to examine basic polarization phenomena as well as the differences manifested from linearly and circularly polarized incident waves. Through our numerical investigations of backscattering and transmission through a plane-parallel medium containing monodisperse spherical scatterers, we found that circularly polarized incident waves maintain larger differences between co-polarized and cross-polarized fluxes and stronger dependencies on the sphere size, even at large optical depths (except for nearly Rayleigh scattering), than linearly polarized incident waves. These differences are most pronounced for scatterers that lie within or near the Mie resonance regime.

Except for scatterers in the Rayleigh limit, we found that transmitted circularly polarized incident waves depolarize at a slower rate than linearly polarized ones. For larger spheres, we find that this difference is significant. In particular, for near-resonance scatterers, circularly polarized waves exhibit co/cross-polarized flux differences of approximately 7 dB while linearly polarized waves exhibit approximately 2 dB flux differences. In addition to depolarizing slower than linearly polarized waves, circularly polarized waves exhibit a stronger dependence on the size of the scatterers. In experimental studies of tissue samples, differences between circular and linear polarized light are not nearly as significant as those observed for spherical scatterers.[11,12] Furthermore, linear polarized light maintains a larger degree of polarization than circular polarized light in tissues. Since tissues exhibit markedly different polarization characteristics than phantoms made up of spherical scatterers, some more effort should be given to understanding the polarization characteristics of tissues.

Table 3. Fluxes of backscattered circularly polarized light by an optically thin medium ($\tau_o = 0.01$) of spherical scatterers computed using the first-order scattering solution.

radius (μm)	co-polarized flux (dB)	cross-polarized flux (dB)
0.05	-24.2310	-32.4692
0.25	-38.9421	-38.8451
1.00	-43.9701	-37.9167
1.75	-41.1327	-33.9478

In addition, we found that backscattering from circularly polarized incident waves exhibited a large degree of polarization for all of the scatterers that we have examined. For the $0.05\mu m$ and $0.25\mu m$ radii spherical scatterers, the co-polarized and cross-polarized flux difference is approximately $2 - 3$ dB at large optical depths. For the $1.00\mu m$ radius spherical scatterer, we find the largest difference between co-polarized and cross-polarized fluxes at approximately 5.4 dB over all optical depths that we considered. The $1.25\mu m$ radius spherical scatterer case yields an approximate flux difference of 4.4 dB at large optical depths. We observe that the helicity of circular polarized light flips upon backscattering by the three larger spheres. While this characteristic is present in first-order scattering, it becomes slightly more pronounced as the optical thickness increases. Theoretical descriptions of this helicity flip usually include multiple scattering arguments,[15,17] however, a detailed analysis of first-order scattering may reveal a more basic mechanism for this helicity flip.
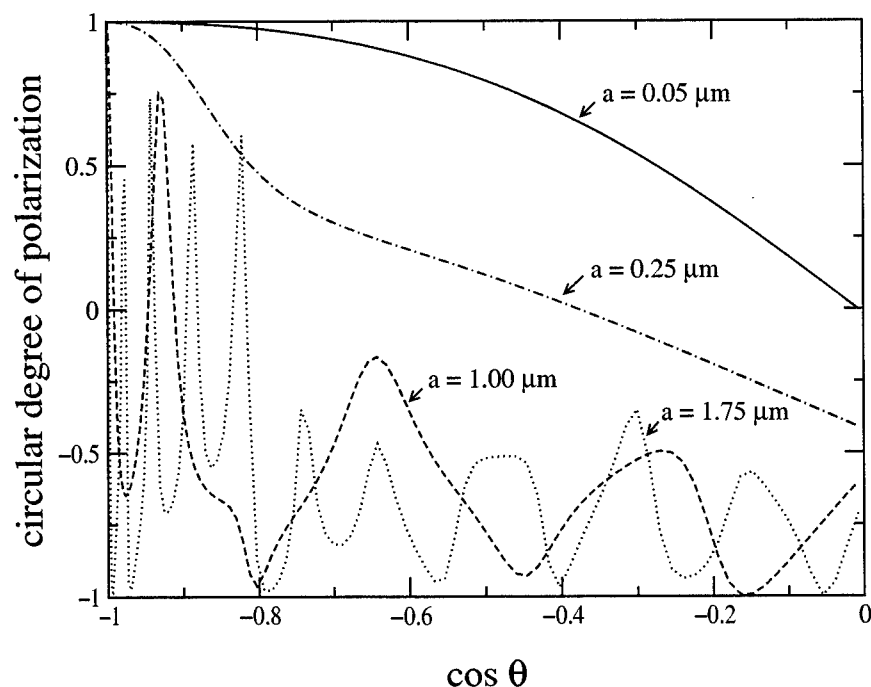
Figure 4. The degree of polarization for circular polarized light backscattered by an optically thin $(\tau_o = 0.01)$ slab containing spherical scatterers computed using the first-order scattering solution.

ACKNOWLEDGMENTS

REFERENCES

1. S. Chandrasekhar, *Radiative Transfer*, Dover, New York, 1960.
2. A. Ishimaru, *Wave Propagation and Scattering in Random Media*, IEEE Press, New York, 1997.
3. A. H. Hielscher, J. R. Mourant, and I. J. Bigio, "Influence of particle size and concentration on the diffuse backscattering of polarized light from tissue phantoms and biological cell suspensions," *Appl. Opt.* **36**, pp. 125–135, 1997.
4. S. G. Demos and R. R. Alfano, "Optical polarization imaging," *Appl. Opt.* **36**, pp. 150–155, 1997.
5. K. M. Yoo and R. R. Alfano, "Time resolved depolarization of multiple backscattered light from random media," *Phys. Lett. A* **142**, pp. 531–536, 1989.
6. J. M. Schmitt, A. H. Gandjbakhche, and R. F. Bonner, "Use of polarized light to discriminate short-path photons in a mutiply scattering medium," *Appl. Opt.* **31**, pp. 6535–6546, 1992.
7. S. L. Jacques, J. R. Roman, and K. Lee, "Imaging superficial tissues with polarized light," *Lasers in Surgery and Medicine* **26**, pp. 119–129, 2000.
8. M. Moscoso, J. B. Keller, and G. C. Papanicolaou, "Depolarization and blurring of optical images by biological tissues." to be published in J. Opt. Soc. Am. A.
9. E. E. Gorodnichev, A. I. Kuzoviev, and D. B. Gogozkin, "Diffusion of circularly polarized light in a disordered medium with large-scale inhomogeneities," *JETP Lett.* **68**, pp. 22–28, 1998.
10. D. Bicout, C. Brosseau, A. S. Martinez, and J. M. Schmitt, "Depolarization of multiply scattered waves by spherical diffusers: Influence of the size parameter," *Phys. Rev. E* **49**, pp. 1767–1770, 1994.
11. V. Sankaran, M. J. Everett, D. J. Maitland, and J. T. W. Jr., "Comparison of polarized-light propagation in biological tissue and phantoms," *Opt. Lett.* **24**, pp. 1044–1046, 1999.

12. V. Sankaran, J. T. W. J. K. Schönenberger, and D. J. Maitland, "Polarization discrimination of coherently propagating light in turbid media," *Appl. Opt.* **38**, pp. 4252–4261, 1999.

13. E. E. Gorodnichev, A. I. Kuzoviev, and D. B. Gogozkin, "Depolarization of light in small-angle multiple scattering random media," *Laser Physics* **9**, pp. 1210–1227, 1999.

14. E. E. Gorodnichev, A. I. Kuzoviev, and D. B. Gogozkin, "Propagation of circularly polarized light in media with large-scale inhomogeneities," *J. Experim. and Theoret. Phys.* **68**, pp. 22–28, 1998.

15. F. C. MacKintosh, J. X. Zhi, D. J. Pine, and D. A. Weitz, "Polarization memory of mutiply scattered light," *Phys. Rev. B* **40**, pp. 9342–9345, 1989.

16. K. J. Peters, "Coherent-backscatter effect: A vector formulation accounting for polarization and absorption effects and small or large scatterers," *Phys. Rev. B* **46**, pp. 801–812, 1992.

17. G. D. Lewis, D. L. Jordan, and P. J. Roberts, "Backscattering target detection in a turbid medium by polarization discrimination," *Appl. Opt.* **38**, pp. 3937–3944, 1999.

18. A. D. Kim and A. Ishimaru, "A Chebyshev spectral method for radiative transfer equations applied to electromagnetic wave propagation and scattering in a discrete random medium," *J. Comput. Phys.* **152**, pp. 264–280, 1999.

19. A. Ishimaru and R. L.-T. Cheung, "Multiple scattering effects on wave propagation due to rain," *Ann. Télécommunic.* **35**, pp. 373–379, 1980.

20. R. L.-T. Cheung and A. Ishimaru, "Transmission, backscattering, and depolarization of waves in randomly distributed spherical particles," *Appl. Opt.* **21**, pp. 3792–3798, 1982.

21. A. Ishimaru, *Electromagnetic Wave Propagation, Radiation and Scattering*, Prentice-Hall, Englewood Cliffs, New Jersey, 1991.

22. M. Kerker, *The Scattering of Light and Other Electromagnetic Radiation*, Academic Press, New York, 1969.

23. H. C. van de Hulst, *Light Scattering by Small Particles*, Dover, New York, 1981.

24. C. F. Bohren and D. R. Huffman, *Absorption and Scattering of Light by Small Particles*, John Wiley & Sons, New York, 1983.

Time resolved polarization imaging: Monte Carlo simulation

Gang Yao and Lihong V. Wang[*]
Optical Imaging Laboratory, Biomedical Engineering Program
Texas A&M University, College Station, TX 77843-3120

ABSTRACT

Monte Carlo method was used to simulate time resolved polarization imaging in turbid media. Mie theory was used to calculate the Mueller matrix of a single scattering event. In the simulation, the Stokes vector of each incident photon package was traced. The summation of the Stokes vectors of the traced photon packages gave the total output Stokes vector. The time integrated Mueller matrix of transmittance and reflectance light of a turbid media were calculated. The transmittance Mueller matrix and reflectance Mueller matrix have very different patterns. The time resolved two-dimensional images of degree of polarization (DOP) for transmitted light and reflected light were calculated. The patterns showed different features for linearly polarized incident light and for circularly polarized light. The DOP patterns were also related to the scattering properties of the sample. The time resolved two-dimensional DOP of the internal optical flux was also calculated. The DOP evolution was demonstrated vividly by the simulation results. The different patterns for linearly/circularly polarized light were compared. Linearly polarized light survived longer in turbid media with a small particle size. Circularly polarized light survived longer in turbid media with a larger particle size.

Keywords: Polarization, Mueller matrix, turbid media, time resolved Monte Carlo

1. INTRODUCTION

In recent years, polarization optics has been a very attractive topic in biomedical optics.[1-3] Except for the common optical contrast, polarized light can furnish the polarization contrast that is produced by specific tissue properties. For example, the collagen fibers can generate birefringence[4] and glucose molecule has dichroism.[5] These kinds of polarization contrast can not be revealed by non-polarized light. In addition to polarization contrast, polarization techniques have also been employed to discriminate weakly scattered light from multiply scattered light. It is widely recognized that the original polarization state is lost in multiply scattered light, but is partially preserved in weakly scattered light. By using polarization discrimination, we can perform imaging using multiply scattered photons or weakly scattered photons. Clearly, we can obtain more information if the optical polarization properties are utilized in the experiments.

The propagation of polarized light in turbid media is a complex process. Parameters, such as the size, shape, and density of the scatterers as well as the polarization state of the incident light, all play important roles.[6,7] A good understanding of this process is essential for improving the polarization-based techniques. Because the number of scattering events is related to the optical path length and the time of propagation, a time-resolved study is needed to understand the evolution of polarization in turbid media.

In our study, a time-resolved Monte Carlo[8] technique was used to simulate the propagation of polarized light in turbid media.[9] Mie theory was used to calculate the single scattering events.[10] Mueller matrix approach was applied because it is the most complete description of polarization phenomena.[11] In particular, we calculated the reflection Mueller matrices, the transmission Mueller matrices, and the evolution of the degree of polarization (DOP) in turbid media. We also studied the effects of the size of the scatterers and the polarization state of the source.

---

[*] To whom correspondence should be addressed.
Tel: (979) 847-9040; Fax: (979) 845-4450, Email: lwang@tamu.edu; URL: http://oilab.tamu.edu

2. METHODS

2.1 Stokes vector and Mueller matrix

The Stokes vector **S** of a light beam is constructed based on six flux measurements with different polarization analyzers in front of the detector:

$$S = \begin{pmatrix} I_H + I_V \\ I_H - I_V \\ I_P - I_M \\ I_R - I_L \end{pmatrix} \tag{1}$$

where I_H, I_V, I_P, I_M, I_R, and I_L are the light intensities measured with a horizontal linear polarizer, a vertical linear polarizer, a +45° linear polarizer, a −45° linear polarizer, a right circular analyzer, and a left circular analyzer in front of the detector, respectively. Stokes vector completely describes the polarization states of the light. Because of the relationships $I_H + I_V = I_P + I_M = I_R + I_L = I$, where I is the intensity of the light beam measured without any analyzer in front of the detector, a Stokes vector can be determined by four independent measurements, for example, I_H, I_V, I_P, and I_R:

$$S = \begin{pmatrix} S_0 \\ S_1 \\ S_2 \\ S_3 \end{pmatrix} = \begin{pmatrix} I_H + I_V \\ I_H - I_V \\ 2I_P - I_H - I_V \\ 2I_R - I_H - I_V \end{pmatrix} \tag{2}$$

From the Stokes vector, the degree of polarization (DOP), the degree of linear polarization (DOLP), and the degree of circular polarization (DOCP) are derived as:

$$\begin{cases} DOP = \dfrac{\sqrt{S_1^2 + S_2^2 + S_3^2}}{S_0} \\[4mm] DOLP = \dfrac{\sqrt{S_1^2 + S_2^2}}{S_0} \\[4mm] DOCP = \dfrac{|S_3|}{|S_0|} \end{cases} \tag{3}$$

The Mueller matrix (**M**) of a sample transforms an incident Stokes vector into the corresponding output Stokes vector.

$$S_{out} = MS_{in}, \tag{4}$$

where S_{in} and S_{out} are the incident and output Stokes vectors of the light beam, respectively. Obviously, the output Stokes vector varies with the state of the incident beam, but the Mueller matrix is determined by the sample. The Mueller matrix can fully characterize the optical polarization properties of the sample because we can obtain the output stokes vector of the incident light with any polarization states. The Mueller matrix can be experimentally obtained by measurements with different combinations of source polarizers and detection analyzers. Because a 4×4 Mueller matrix has 16 independent elements, at least 16 independent measurements must be measured to determine a full Mueller matrix.

2.2 Monte Carlo simulation

Several groups have used Monte Carlo techniques to simulate the steady-state backscattering Mueller matrix of a turbid medium.[12,13] Whereas an indirect method utilizing the symmetry of the backscattering Mueller matrix was

used in Ref.12, the direct tracing method [13] was used in our simulation. The turbid medium was assumed to have a slab structure, on which a laboratory coordinate system was defined (Fig. 1). A pencil beam was incident upon the origin of the coordinate system at time zero along the Z axis.
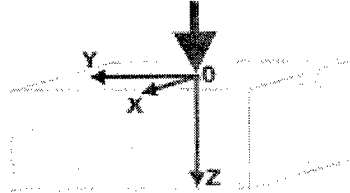
Fig. 1.   The laboratory coordinate system for the Monte Carlo simulation.

The basic Stokes-Mueller formalism and the simulation of propagation of polarized light in turbid media have been described earlier. The basic idea is to track the Stokes vector of each photon packet.

In the simulation, the Stokes vector and the local coordinates of each incident photon packet were traced statistically. At each scattering event, the incoming Stokes vector of the photon packet was first transformed into the scattering plane through a rotation operator and then converted by

$$\mathbf{S'} = \mathbf{M}(\theta)\mathbf{R}(\phi)\mathbf{S} , \tag{5}$$

where $\mathbf{S}$ is the Stokes vector before scattering, $\mathbf{R}(\phi)$ is the rotation matrix; $\mathbf{S'}$ is the Stokes vector of the scattered photon; θ is the polar scattering angle; ϕ is the azimuth angle; and $\mathbf{M}$ is the single-scattering Mueller matrix, given by the Mie theory as[10]

$$\mathbf{M}(\theta) = \begin{bmatrix} m_{11} & m_{12} & 0 & 0 \\ m_{12} & m_{11} & 0 & 0 \\ 0 & 0 & m_{33} & m_{34} \\ 0 & 0 & -m_{34} & m_{33} \end{bmatrix} . \tag{6}$$

The element m_{11} satisfies the following normalization requirement:

$$2\pi \int_0^\pi m_{11}(\theta)\sin(\theta)d\theta = 1 . \tag{7}$$

The joint probability density function (pdf) of the polar angle θ and the azimuth angle ϕ is a function of the incident Stokes vector $\mathbf{S} = \{S_0, S_1, S_2, S_3\}$:

$$\rho(\theta,\phi) = m_{11}(\theta) + m_{12}(\theta)[S_1 \cos(2\phi) + S_2 \sin(2\phi)]/S_0 . \tag{8}$$

In our method, the polar angle θ is sampled according to $m_{11}(\theta)$ and the azimuth angle ϕ is sampled with the following function:

$$\rho_\theta(\phi) = 1 + \frac{m_{12}(\theta)}{m_{11}(\theta)} \frac{[S_1 \cos(2\phi) + S_2 \sin(2\phi)]}{S_0} . \tag{9}$$

It is worth noting that a biased sampling technique was used in Ref.13. The Stokes vectors of all the output-photon packets were transformed to the laboratory coordinate system and then accumulated to obtain the final Stokes vector. The Mueller matrix of the scattering media can be calculated algebraically from the Stokes vectors of four different incident polarization states.[9] The degree of polarization (DOP) was calculated by Eq. 3.

To accelerate the computation we calculated the single-scattering Mueller matrix and the probability density functions of the scattering angles and stored them in arrays before tracing the photon packets. The path length of the photon packets was recorded to provide time-resolved information. For purposes of illustration, the scatterers were assumed to be spherical; the thickness of the scattering slab was taken to be 2 cm; the temporal resolution was 1.33 ps, corresponding to 0.4 mm in real space; the wavelength of light was 543 nm; the absorption coefficient was 0.01

cm^{-1}; the index of refraction of the turbid medium was unity, matching that of the ambient. The dimensions of the pseudo-color images in the following section are 4, 4, and 2 cm along the X, Y, and Z axes, respectively.

3. RESULTS

Figure 2 shows the reflection and the transmission Mueller matrices of a turbid medium with a scattering coefficient of 4 cm^{-1} and a radius of scatterers of 0.102 μm. The calculated Mueller-matrix elements were normalized to the m_{11} element to compensate for the radial decay of intensity. Each of the images is displayed with its own color map to enhance the image contrast. The size of each image is 4×4 cm^2.
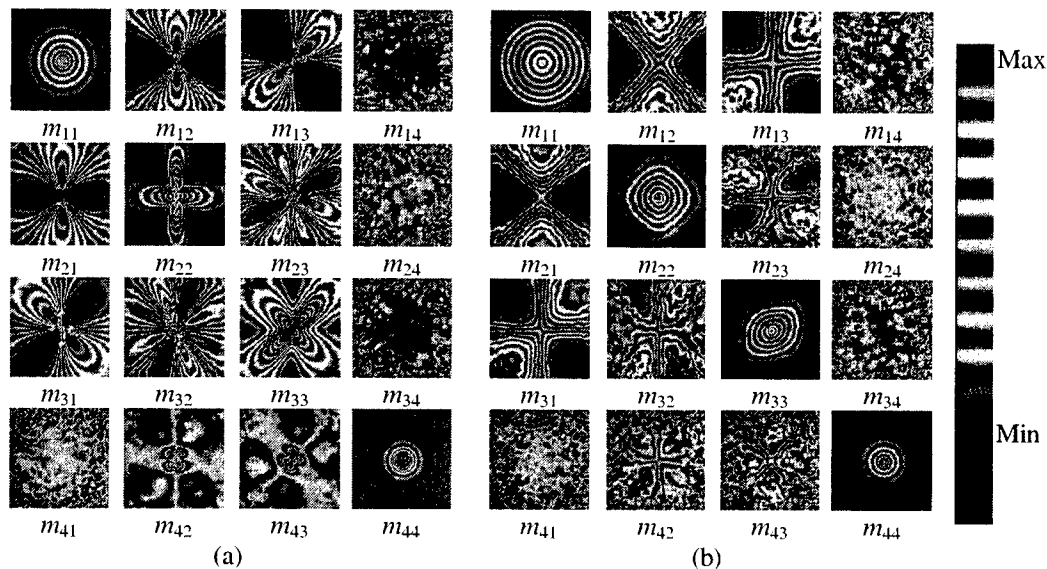
Fig. 2. (a) Reflection Mueller matrices and (b) transmission Mueller matrices of a slab of turbid medium.

The patterns of the reflection Mueller matrix are identical to those reported previously.[12,13] The symmetries in the patterns can be explained by the symmetries in the single-scattering Mueller matrix and the medium.[12] The transmission Mueller matrix has different patterns from the reflection Mueller matrix. One of the noticeable differences lies in elements m_{31} and m_{13}, which are anti-symmetric in the reflection Mueller matrix but symmetric in the transmission Mueller matrix. This difference is caused by the mirror effect in the reflection process of the scattered light.

Figure 3 shows the time-resolved DOP propagation in the turbid medium with right-circularly (R) and horizontal-linearly (H) polarized incident light. The scattering coefficient was 1.5 cm^{-1}, and the radius of the scatterers was 0.051 μm. The anisotropic factor $<\cos(\theta)>$ was 0.11. The transport mean free path was calculated to be 0.74 cm. In the simulation the Stokes vectors of the forward propagating photons were accumulated to calculate the DOP. As shown in the movies, the DOPs at the expanding edges of the distributed light remain near unity because these photons experience few scattering events. As the light propagates in the medium, the DOP in some regions decreases significantly. The DOP patterns are dependent on the single-scattering Mueller matrix and the density of scattering particles.

From Fig. 3 the DOP images have different patterns for the R- and the H-polarized incident light. As expected, such a difference appears in the DOP images of transmitted light as well. As shown in Fig. 4, the DOP images of the transmitted light are rotationally symmetric for circularly polarized incident light, whereas such symmetry does not exist for linearly polarized incident light. This difference is related to the dependence of the scattering probability on the incident Stokes vector (Eqs. 12 and 13). The Stokes vectors of the R- and the H-polarized light are $[1, 0, 0, 1]^*$ and $[1, 1, 0, 0]^*$, respectively. According to Eq. 13, the R-polarized light has a uniform pdf for the azimuth angle, whereas the H-polarized light has a non-uniform one. Hence, the single-scattering pattern depends

on the polarization state of the incident light. Because the change of DOP is related strongly to the single scattering events, it is understandable that the DOP images have different features for different incident Stokes vectors.
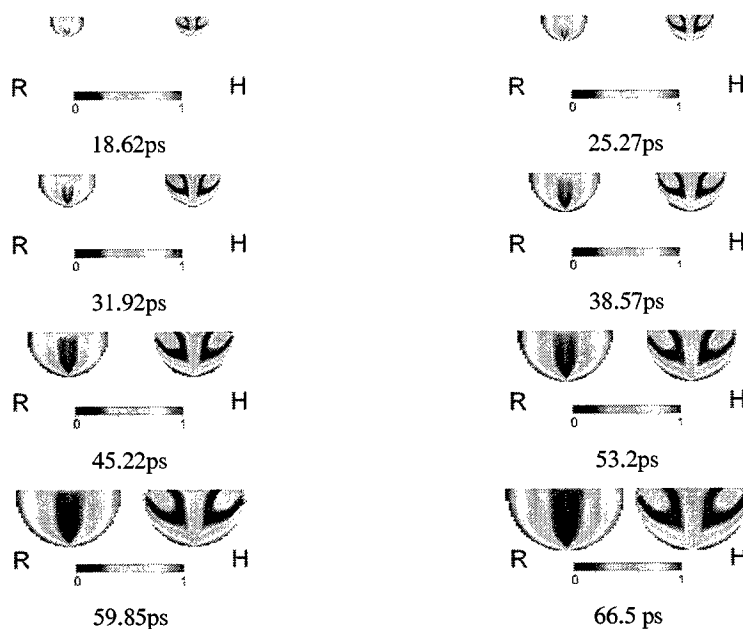
Fig. 3.   Time sequences of the DOP propagation in the slab(0.051 μm particle). The X axis is along the horizontal direction, and the Z axis is along the vertical direction. R: right-circularly polarized incident light. H: horizontal-linearly polarized incident light.
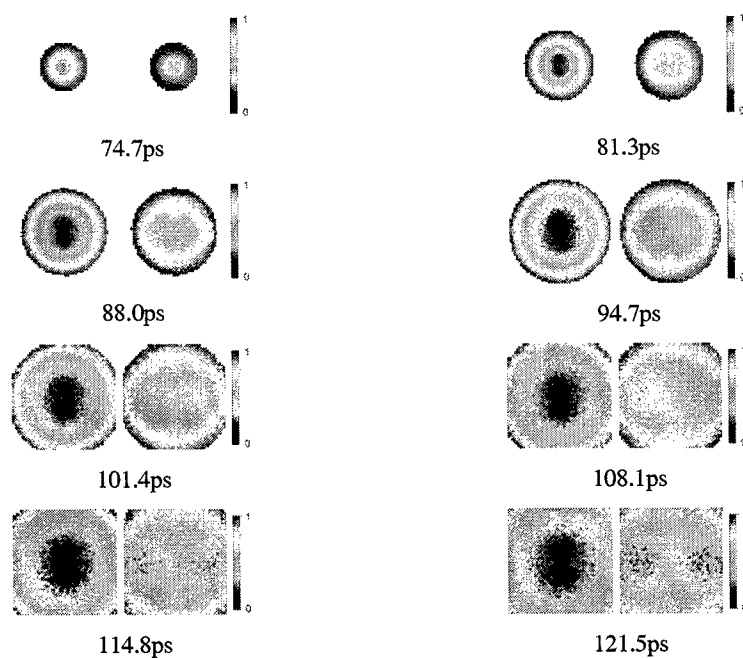
Fig. 4.   Time sequences of the DOP of the transmitted light with R-polarized (left side images) and H-polarized (right side images) incident light (0.051 μm particle). The X axis is along the horizontal direction, and the Y axis is along the vertical direction.
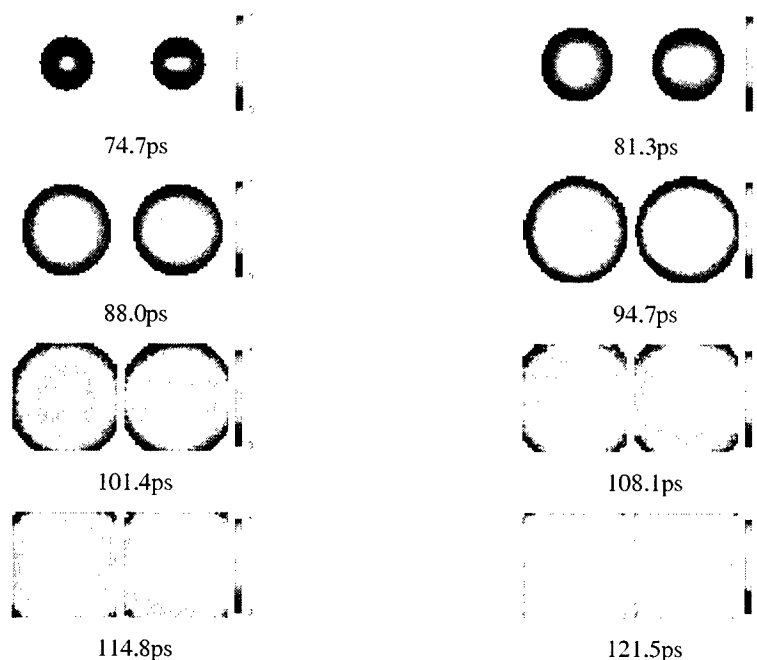
Fig. 5.   Time sequences of the weighted-averaged numbers of scattering events for R-polarized (left side images) and H-polarized (right side images) incident light. The numbers of scattering events are normalized to a maximum value of 7 for the plots. The X axis is along the horizontal direction, and the Y axis is along the vertical direction.
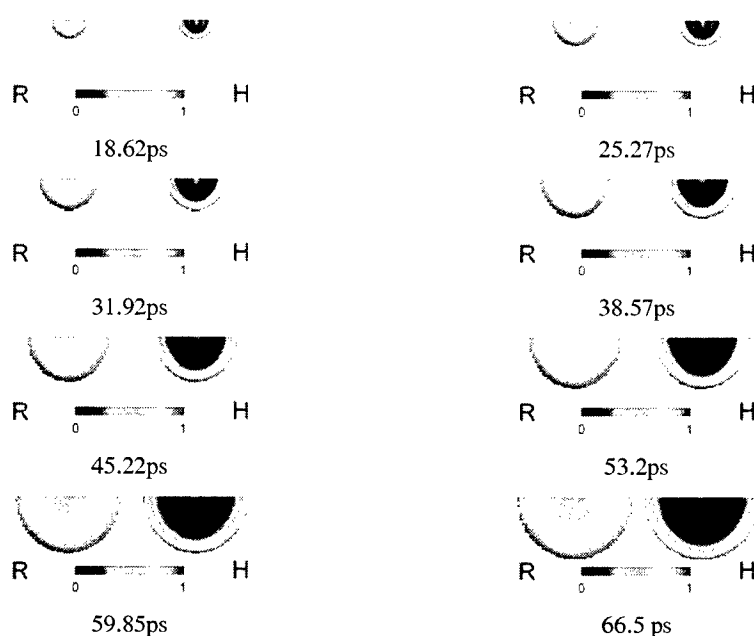
Fig. 6.   Time sequences of the DOP propagation in the slab(1.02 μm particle). The X axis is along the horizontal direction, and the Z axis is along the vertical direction. R: right-circularly polarized incident light. H: horizontal-linearly polarized incident light.

74.7ps   **81.3ps**

88.0ps   **94.7ps**

101.4ps   **108.1ps**

114.8ps   **121.5ps**
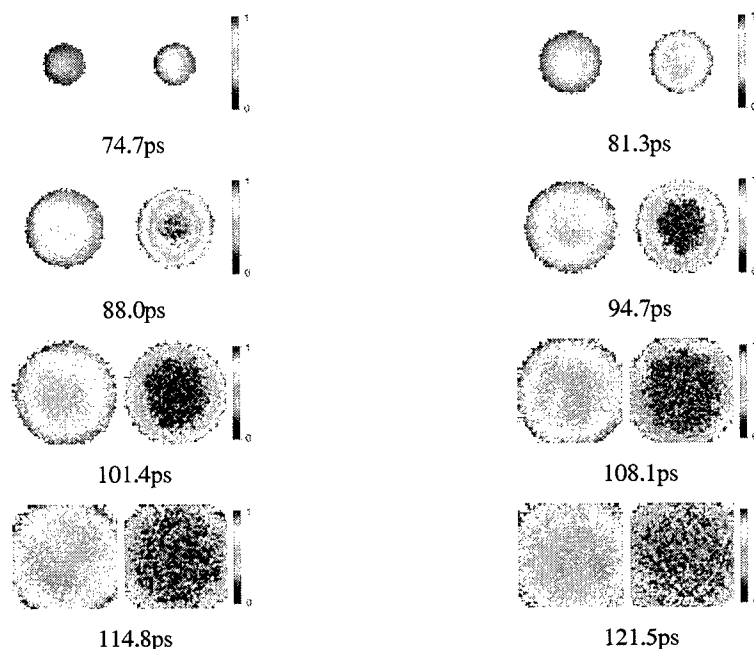
Fig. 7.   Time sequences of the DOP of the transmitted light with R-polarized (left side images) and H-polarized (right side images) incident light (1.02 μm particle). The X axis is along the horizontal direction, and the Y axis is along the vertical direction.

To demonstrate the dependence of the evolution of DOP on the number of scattering events, we recorded the time-resolved images of the average number of scattering events of the transmitted light (Fig. 5). The simulation parameters are the same as those for Figs. 3 and 4. As it can be seen, the transmitted photons experience more and more scattering events as time elapses. If we compare Figs. 5 and 4, it is clear that the patterns of DOP are related directly to the patterns of the scattering counts: the DOP decreases as the number of scattering events increases. Nevertheless, the number of scattering events does not solely determine the change of DOP. Two dark regions are clearly visible in Fig. 4(121.5ps), but they are inseparable in Fig. 5(121.5ps). The change of DOP must also depend on the nature of each scattering event, determined by the single-scattering Mueller matrix.

To study the effect of the size of the scatterers, we simulated the evolution of the DOP in a scattering medium with a different radius of 1.02 μm. The scattering coefficient of the medium was 14 cm^{-1}, and the anisotropic factor was 0.91. The transport mean free path was 0.76 cm, which was similar to the value for Figs. 3–5. The time-resolved propagation of the DOP in the medium is shown in Fig. 6. The DOP movie of the transmitted light is shown in Fig. 7.

Note the different patterns in Figs. 6–7 and Figs. 3–4. The key difference is that the DOP of R-polarized incident light was preserved much better than the DOP of H-polarized incident light for the large scatterers, as shown in Figs. 6–7. In contrast, the DOP of H-polarized incident light was preserved better than the DOP of R-polarized incident light for the small scatterers, as shown in Figs. 3–4. This observation is consistent with previous experimental and theoretical findings.
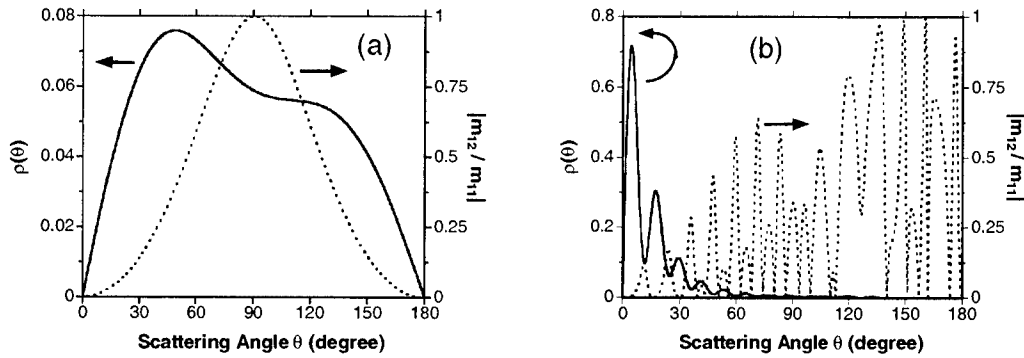
Fig. 8. Probability density function $\rho(\theta)$ and $|m_{12}/m_{11}|$ at a particle radius of (a) 0.051 μm and (b) 1.02 μm.

Another significant difference is that the DOP patterns for the large scatterers become rotationally symmetric even when the incident light is H-polarized. This phenomenon can be easily understood if we examine the probability distribution functions of the scattering angle for different particle sizes. The scattering angle θ is determined by m_{11}, and its probability density function $\rho(\theta)$ is $2\pi m_{11}\sin(\theta)$. The probability density function of the azimuth angle ϕ is a function of both ϕ and the incident Stokes vector, as defined in Eq. 9. The contribution of the ϕ-dependent term is proportional to $|m_{12}/m_{11}|$. The curves of $\rho(\theta)$ and $|m_{12}/m_{11}|$ are shown in Fig. 8. When the scatterer size is small, $\rho(\theta)$ is approximately homogeneous and the photon is likely to be scattered into 60°–120° [Fig. 8(a)]. At these angles, the $|m_{12}/m_{11}|$ ratio has large values and Eq. 9 depends strongly on ϕ. When the scatterer size is large, most of the photons are scattered into smaller angles [Fig. 8(b)]. The $|m_{12}/m_{11}|$ ratio is small at small scattering angles, which means that the homogeneous-distribution term is dominant in the probability distribution function of the ϕ angle. As a consequence, the scattering process becomes rotationally symmetric for the larger particle sizes.
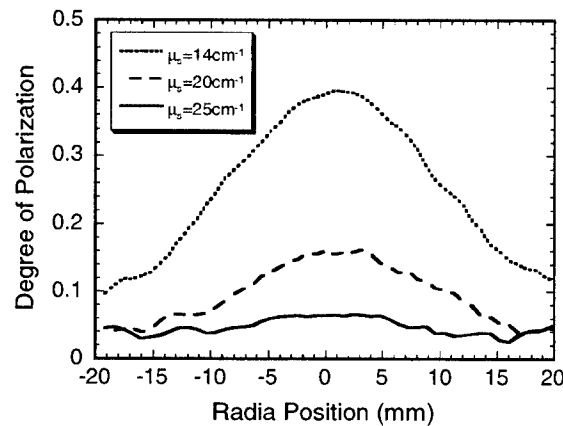
Fig. 9. Radial distribution of the DOP of the transmitted light for different scattering coefficients. The particle radius was 1.02 μm. The incident light was H polarized.

As observed in Figs. 4 and 7, the DOP at the center of the 2D time-resolved images is smaller than that in the outer area. However, the DOP decreases radially in the time-integrated images (Fig. 9), which is in agreement with previous experimental results.[7] This is because the photons exiting at early times have a limited span in space and hence have a dominant weight in the central area. These early exiting photons better preserve the DOP because they experience fewer scattering events than the photons exiting at later times. Consequently, a combination of

time-gating and polarization discrimination[14] has a better performance in rejecting multiply scattered photons than either technique alone. Figure 9 also reveals that the DOP decreases as the scattering coefficient increases. The radial distribution of the DOP becomes flat at a large scattering coefficient because of the increasing number of multiply scattered photons.[7]

4. SUMMARY

A Monte Carlo technique was employed to simulate the time-resolved propagation of polarized light in scattering media. Results are consistent with prior experimental findings. Hence, time-resolved simulation is a useful tool for understanding better the essential physical processes of polarization propagation in turbid media. Because of the nature of the Monte Carlo simulation, coherent phenomena, such as laser speckles, are not modeled. Nevertheless, the simulation method can be applied in the non-coherent regime or in the cases where the coherent effect is removed, such as ensemble-averaged measurements.[12]

REFERENCES

1   J. M. Schmitt, A. H. Gandjbakhche, and R. F. Bonner, "Use of polarized light to discriminate short-path photons in a multiply scattering medium," Appl. Opt. 31, 6535–6546(1992).
2   S. P. Morgan, M. P. Khong, and M. G. Somekh, "Effects of polarization state and scatterer concentration on optical imaging through scattering media," Appl. Opt. 36, 1560–1565(1997).
3   S. L. Jacques, J. R. Roman, and K. Lee, "Imaging superficial tissues with polarized light," Lasers in Surg. & Med. 26, 119–129(2000).
4   J. F. de Boer, S. M. Srinivas, A. Malekafzali, Z. Chen and J. S. Nelson, "Imaging thermally damaged tissue by polarization sensitive optical coherence tomography," Opt. Exp. 3, 212 (1998).
5   G. L. Coté, M. D. Fox, and R. B. Northrop, "Noninvasive Optical Polarimetric Glucose Sensing Using a True Phase Measurement Technique", IEEE Tran. Bio. Eng. 39, 752-56(1992).
6   D. Bicout, C. Brosseau, A. S. Martinez, and J. M. Schmitt, "Depolarization of multiply scattered waves by spherical diffusers: influence of the size parameter," Phy. Rev. E 49, 1767–1770(1994).
7   V. Sankaran, K. Schonenberger, J. T. Walsh, Jr., and D. J. Maitland, "Polarization discrimination of coherently propagation light in turbid media," Appl. Opt. 38, 4252–4261(1999).
8   L.-H. Wang, S. L. Jacques, and L.-Q. Zheng, "MCML – Monte Carlo modeling of photon transport in multi-layered tissue," Comput. Meth. Prog. in Biomed. 47, 131-146(1995).
9   G. Yao and L. V. Wang, "Propagation of polarized light in turbid media: an animated simulation study," Optics Express 7, 198-203(2000).
10 H. C. van de Hulst, Light Scattering by Small Particles (Dover, New York, 1981).
11 W. S. Bickel and W. M. Bailey, "Stokes vectors, Mueller matrices, and polarized scattered light," Am. J. Phys. 53, 468 (1995).
12 M. J. Rakovic, G. W. Kattawar, M. Mehrubeoglu, B. D. Cameron, L. V. Wang, S. Rastegar, and G. L. Coté, "Light backscattering polarization patterns from turbid media: theory and experiments," Appl. Opt. 38, 3399–3408(1999).
13 S. Bartel and A. H. Hielscher, "Monte Carlo simulation of the diffuse backscattering Mueller matrix for highly scattering media," Appl. Opt. 39, 1580–1588(2000).
14 X. Liang, L. Wang, P. P. Ho, and R. R. Alfano, "Time-resolved polarization shadowgrams in turbid media," Appl. Opt. 36, 2984–2989(1997).

Mueller Matrix description of collimated light transmission through liver, muscle and skin

Jessica C. Ramella-Roman, Steven L. Jacques

Oregon Medical Laser Center, Providence St. Vincent Medical Center
Oregon Graduate Institute of Science and Technology
Oregon Health Sciences University
Portland, Oregon 97225 USA

ABSTRACT

Propagation of polarized light through liver, muscle and skin was studied using the Mueller Matrix formalism. Collimated HeNe laser light was passed through a set of polarization elements to create one of four possible polarization states (horizontal (H), vertical (V) and 45-degree (P) orientations of linearly polarized light, and right circularly (R) polarized light). The beam passed through thin sections of tissue of varying thickness (0.2-0.9 mm thick). The unscattered, collimated, transmitted light passed through a second set of polarization elements to analyze for transmission of each of the 4 possible polarization states (H,V,P,R). Transmitted intensities for 16 possible combinations of source and detector polarization yielded a data matrix that was converted into a Mueller matrix describing the propagation properties of the tissue. The results were roughly consistent with all three tissue types behaving as ideal retarders whose birefringent values, dn = delta*wavelength/(2*pi*thickness), were in the range of 1x10^-3 to 5x10^-3 which is consistent with the literature. The order of the strength of birefringence was liver < muscle < skin. Although the above birefringence values may apply to muscle, the structured of liver and skin are not necessarily consistent with the ideal retarder model and further work is needed.

Keywords: Polarization, Mueller matrices, Stokes vectors, liver, muscle, skin

1. INTRODUCTION

Mueller calculus was first introduced in 1945 as a short-cut method of solving problems involving polarizers and retarders. The Mueller calculus employs matrices and vectors. The matrices are called Mueller matrices and specify optical components. The vectors are called Stokes vectors and define the status of polarization of the incident and transmitted beam of light. Multiplying the incident beam vector by the Mueller matrix of a sample yields the status of polarization of the transmitted beam [1,2]. If different kind of tissues can be modeled by their Mueller matrices then the status of polarization of light traveling through the tissues can be predicted.

Experiments were conducted on liver, muscle and skin samples of varying thickness, observing the on-axis, unscattered, collimated transmission. The results were converted into two parameters as a function of sample thickness: (1) the degree of linear polarization, and (2) the degree of circular polarization. These experimentally derived values were compared with theoretically predicted curves of the degrees of linear and circular polarization. The results were roughly consistent with tissue behaving as an idealized retarder whose birefringence was comparable to values from the literature.

2. MATERIALS AND METHODS

Apparatus for optical transmission measurements

The experimental apparatus is shown in Figure 1. A HeNe laser of emitting wavelength 632.8nm was chopped and passed through a linear polarizer (Ealing) oriented parallel to the optical table, i.e., horizontal (H). The polarized beam was passed through a half wave plate and a quarter wave plate (Meadowlark Optics) whose fast axes were manually rotated to sequentially generate sources of four different polarizing states: 0 degree (H), 90 degree (V) and 45 degree (P) orientations of linearly polarized light, and right circularly polarized (R) light. A sample of known thickness was located normal to the incident beam. A quarter wave plate and a polarizer in front of a silicon detector were sequentially rotated to enable the detector to detect 4 specific states of polarization: H, V, P, or R. The detector was positioned at 90 cm from the sample to

collect primarily the unscattered collimated component of the transmitted light. The data were collected with a lock-in amplifier (Stanford Research SR830) via a GPIB interface to a computer (G4, Macintosh).
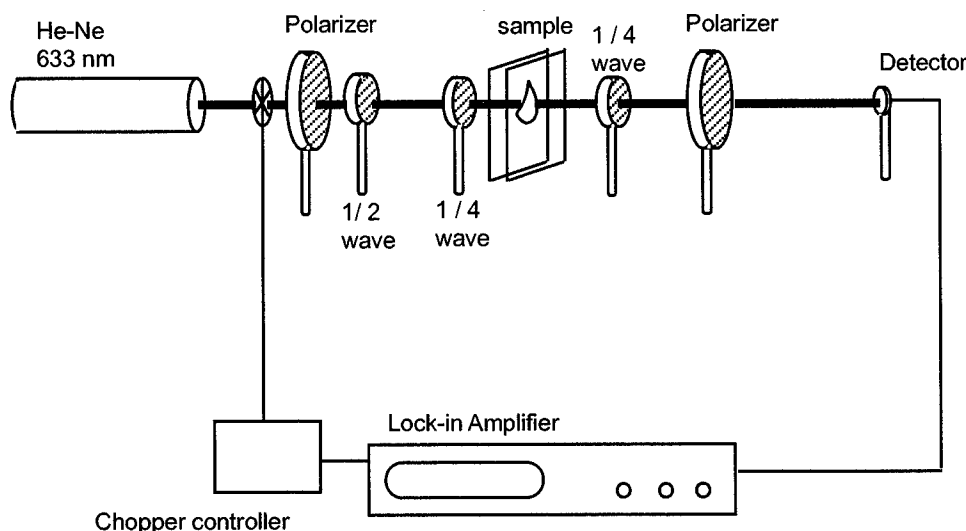
Fig. 1: Experimental apparatus

The status of polarization of linearly or circularly polarized light transmitted through a tissue sample was measured for each of the 16 combinations of source and detector polarization status. The Stokes Vector for linearly polarized light was multiplied by the experimentally specified Mueller Matrices. The resulting transmitted Stokes vector, [I Q U V], was used to calculate the degree of linear polarization,

$$\frac{(Q^2 + U^2)^{1/2}}{I} \quad (1)$$

and the degree of circular polarization,

$$\frac{(V^2)^{1/2}}{I} \quad (2).$$

Tissue preparation

Three different light-scattering tissues, calf liver, pig skin, chicken muscle, were measured. Fresh tissues samples from the abattoir were frozen then cut to the desired thickness (0.2-0.9 mm) and placed between glass slides. Sample thicknesses were measured by caliper while held between the glass slides, accounting for the slide thicknesses. The muscle fibers were oriented 45 degrees relative to the surface of the optical table. The skin was oriented with the laser beam normal to the skin surface such that the collagen fibers were perpendicular to the beam but the azimuthal angle of fibers was randomly distributed around the beam axis. normal to the fibers. Liver had no preferred orientation. Measurements of transmitted intensity were conducted on tissue samples of the various known thicknesses. Five locations on every sample were measured, giving five distinct Mueller matrices per sample.

2.1 Modeling and calibration

All optics components of the experimental set-up were modeled with their corresponding Mueller matrices based on separate experiments[3]. To generate one of the four needed detectors, the Mueller Matrices of opportunely oriented polarizer and quarter wave plate were used. In the same way for each of the four needed sources, the Mueller Matrices of an appropriately oriented quarter wave plate, half wave plate and linear polarizer were used. For example to generate a horizontal source and a horizontal detector, i.e. an HH measurement in the data matrix, the following train of matrices was used.

Transmitted Stokes vector = Polarizer * SAMPLE * 1/2 wave *Polarizer * Unpolarized beam

$$
\begin{bmatrix} I \\ Q \\ U \\ V \end{bmatrix} =
\begin{bmatrix} 1/2 & 1/2 & 0 & 0 \\ 1/2 & 1/2 & 0 & 0 \\ 0 & 0 & 0 & 0 \\ 0 & 0 & 0 & 0 \end{bmatrix}
\times
\begin{bmatrix} & & SAMPLE & \\ & & & \end{bmatrix}
\times
\begin{bmatrix} 1 & 0 & 0 & 0 \\ 0 & 1 & 0 & 0 \\ 0 & 0 & -1 & 0 \\ 0 & 0 & 0 & -1 \end{bmatrix}
\times
\begin{bmatrix} 1/2 & 1/2 & 0 & 0 \\ 1/2 & 1/2 & 0 & 0 \\ 0 & 0 & 0 & 0 \\ 0 & 0 & 0 & 0 \end{bmatrix}
\times
\begin{bmatrix} 1 \\ 0 \\ 0 \\ 0 \end{bmatrix}
\qquad (3)
$$

The experimental measurements corresponded to the intensity, I, which is the first element in the transmitted stokes vector.

The theoretical model of the apparatus consisted of sixteen different matrix multiplications like the above using different matrices to generate the needed sources and detectors. To generate and detect circular polarized light, a quarter-wave plate was needed as well and its corresponding Mueller Matrix was inserted.

Every matrix multiplication generated one Stokes vector. The first term (I) of every Stokes vector, corresponding to the intensity of the exiting beam, was arranged in a matrix form as shown in Figure 2. This matrix was called a *Data matrix*.

	H	V	P	R
H	HH	HV	HP	HR
V	VH	VV	VP	VR
P	PH	PV	PP	PR
R	RH	RV	RP	RR

Fig. 2: Data matrix (DM). Each element corresponds to the intensity of transmitted collimated light when the source was either H, V, P or R and the detector was either H, V, P or R.

From the Data matrix and using the transformation proposed by Yao and Wang[4], the Mueller matrix of the sample was obtained. The sample s Mueller matrix could be inserted as the sample within the calculation (Eq. 3) and Eq. 3 generated an [I Q U V] vector whose I value simulated the experimental measurement of transmitted power. Employing all possible HVPR combinations for source and detector, a data matrix was generated. Converting the data matrix to a Mueller Matrix successfully recovered the original Mueller matrix of the sample. Hence our analysis algorithm was shown to be operating properly.

Every optic component of the set up was tested to confirm manufacturing specifications. The error associated with every component was inserted in the model so that experimental error and expected error could be compared. Several tests using only air as a sample were conducted, Fig. 3. The first matrix on the left is the ideal Mueller Matrix for air which is an identity matrix because air does not have any polarizing property. Experimentally our Mueller Matrix for air deviated from its ideal behavior as shown in the matrix in the center due to the deviation from ideality of the various optical components in the system. The deviations of optical components from ideality were determined experimentally, yielding performance parameters consistent with the manufacturer s specifications, and these deviations were used to correct the air Mueller Matrix as shown in the third matrix in Fig. 3.

1	0	0	0
0	1	0	0
0	0	1	0
0	0	0	1

0.98	0.01	0.02	0.01
0.01	0.98	0.02	-0.01
0.07	-0.04	0.86	-0.08
0.02	-0.01	-0.04	0.89

0.97	0.00	0.00	0.00
0.00	0.97	0.00	-0.014
0.00	0.00	0.97	-0.015
-0.02	-0.00	-0.00	0.92

Fig..3: (Left) Ideal Mueller matrix of air. (Center) Experimental Mueller matrix for air
(Right) Corrected Mueller Matrix of air which accounts for the non-ideality of the optical components of the system
(still not perfect; work continues on calibration).

Other experiments using as a sample optical objects, linear polarizers, quarter wave plates and half wave plates, gave good results and helped calibrate the system.

Because our apparatus was not perfectly calibrated, as shown by the discrepancies of our MM_{air} for air shown in Fig. 3, our computer simulation determined the correction matrix, MM_{calib}, which allowed

$$\text{transmitted stokes vector} = MM_{detector}MM_{calib}MM_{air}MM_{source} \quad (4a)$$

to generate the Data Matrix of transmitted intensities expected for an air sample. Also a second correction matrix was determined which allowed

$$\text{transmitted stokes vector} = MM_{detector}MM_{air}MM_{calib}MM_{source} \quad (4b)$$

to generate the Data Matrix of transmitted intensities expected for an air sample. By placing MM_{calib} before or after MM_{air}, we were assigning the errors in our apparatus to either the source or the detector. The truth was probably somewhere in between but the goal was to identify the extreme possibilities and see how differently the two models behaved. We found that the predicted behavior was not strongly sensitive to whether Eq. 4a or 4b was used. Hence, although our system was not perfectly calibrated, the errors were not serious.

3. RESULTS

Beer s Law
Figure 4 shows the measured transmission through increasing thicknesses of liver, muscle and skin. The curve fits are the simple Beer s Law expression, $\exp(-\mu_t L)$ where L [cm] is the thickness of the slab and μ_t [cm^{-1}] is the total attenuation due to absorption and scattering. The values of μ_t are consistent with literature[5]. For the liver sample, the deviation from the ideal Beer s law behavior at large L (0.09 cm) was attributed to multiple scattering of light by the thicker samples. The intensity of the beam was specified from the experimental Data Matrix of the sample by summing the HH and HV values, which is equivalent to multiplying an incident linearly polarized Stokes vector by the corresponding Mueller Matrix and considering the intensity the first value of the transmitted Stokes vector.
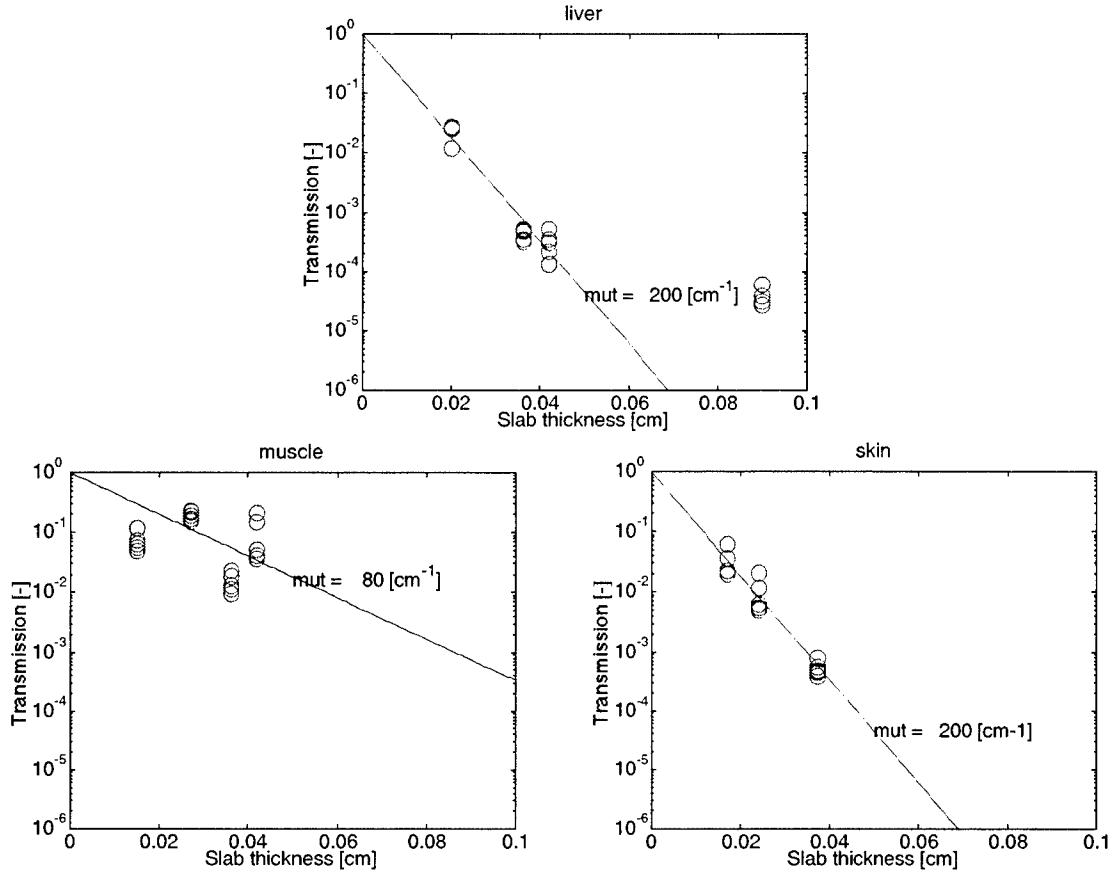
Fig. 4: Transmission (T) of a collimated HeNe laser beam through muscle, liver and skin samples of increasing thickness L, and the Beer s law curve fit, $T = \exp(-\mu_t L)$. The total attenuation coefficient, μ_t [cm^{-1}], for liver, muscle and skin, respectively, was 200, 80 and 200 cm^{-1}, which corresponded to mean free paths (mfp) of 50, 125, and 50 μm.

Degrees of linear and circular polarization

The Mueller Matrix for each site on each of the different tissue thicknesses for each of the 3 tissue types (liver, muscle, skin) was used to calculate the degrees of linear and circular polarization using Eqs. 1 and 2. These degree values were plotted versus the thickness of the particular tissue slab (Fig. 5). Thin sample thicknesses only slightly modified the polarization of the transmitted light. Thicker samples more strongly modified the polarization. The degree of linear polarization is initially unity and appears to drop and modulate as modified by the tissues. The degree of circular polarization is initially zero and appears to increase and modulate as birefringent tissue components convert some of the linearly polarized light into circularly polarized light.

We also prepared computer simulations of the expected behavior of the degrees of linear and circular polarization. The approach was to find the Mueller Matrix for a tissue section whose thickness was 1/20th of a mfp, here called MM$_o$, such that raising MM$_o$ to the jth power would mimic the behavior of a thicker tissue section whose thickness was L = j(mfp)/20:

$$MM_{tissue} = (MM_o)^j \qquad (5)$$

$$\text{where} \quad j = 20L/mfp = 20\;L_t$$

We found that the choice of MM$_o$ that satisfied Eq. 5 was not unique. So we chose a simple model for MM$_o$, an ideal retarder specified by its retardance and the orientation of its fast axis, in order to model the orientation and retardance of the birefringent fibers of a tissue. The Mueller matrix of a retarder can be expressed in terms of the orientation angle (ρ) between its fast axis and a reference axis (in our case, the horizontal axis that is parallel to our definition of the H linear

polarization source) and the imparted retardance or phase shift (δ) [7]. Liver has very little birefringence and was modeled with a retarder of low retardance. Muscle is rich in birefringent actin-myosin fibers which are all oriented in one direction. Skin is full of very birefringent collagen fibers but they are randomly oriented over the 1-mm spot size of the HeNe laser used in the experiments. Also shown in Fig. 5 are the predictions of the computer simulations where the degrees of linear and circular polarization were calculated from the MM_{tissue} of idealized liver, muscle, and skin samples of varying thickness.
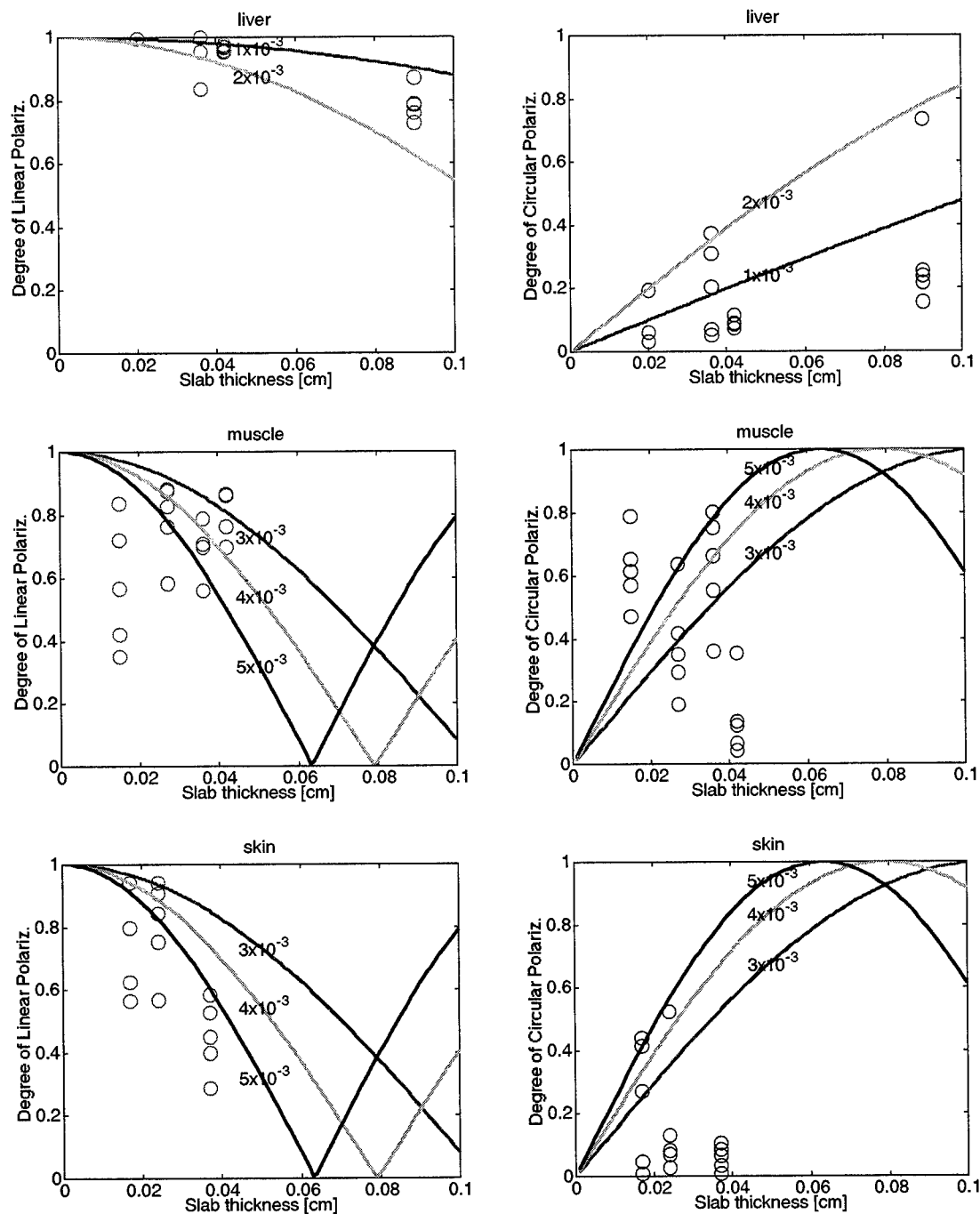
Fig. 5: Degrees of linear and circular polarization for tissue samples of increasing thickness. Circles indicate experimental data. Curves indicate theoretical curves based on the values of birefringence (Δn) indicated by labels.

The birefringence of a tissue is described as the apparent change in the refractive index (Δn) between the fast and slow axes of the tissue:

$$\Delta n = \delta \lambda / (2 \pi L) \qquad (6)$$

where δ is the retardance [radians], λ is the wavelength [cm], and L is the thickness of the tissue slab [cm]. Typical literature values for the birefringence of tendon, for example, are about 3.0×10^{-3}. In Fig. 5, the solid-line curves show the expected behavior for idealized retarders with birefringence values of 1×10^{-3} to 5×10^{-3} as denoted by labels in the figures. Although the theoretical curves only crudely approximate the experimental data, it is clear that the literature values of tissue birefringence are roughly consistent with the experimental results. The experimental results indicate that the order of the strength of birefringence is liver < muscle < skin. However, the differences are not very great.

A key feature of the experimental data was the large amount of variation in results even though the tissues were apparently homogeneous and evenly cut to a uniform thickness.

4. DISCUSSION

The ideal retarder model predicts periodic variation in the degrees of linear and circular polarization as a function of tissue thickness, as indicated by the theoretical curves in Fig. 5 for muscle and skin. These experiments did not use samples sufficiently thick to critically test for the existence of such periodicity. Hence, the retarder model should still be regarded as tentative.

5. CONCLUSIONS

Mueller matrices of three different tissue samples and several thickness were experimentally measured. For every tissue the Mueller Matrix for an incremental tissue thickness of $1/20^{th}$ mfp was specified and used to reconstruct the MM_{tissue} for thicker samples. The results were consistent with the birefringence values for tissues ranging between 1×10^{-3} to 5×10^{-3}, although our experimental data is still preliminary. More work is needed to improve the experimental technique and the quality of the data. Attention must be paid to the size of the probe laser beam, about 1 mm in our case, relative to the size of the microscopic domains of iso-birefringence, about 10-100 μm as reported in an accompanying paper at this conference.[8] Also, attention must be paid to the distribution of fiber orientation. While all the muscle fibers in a sample are approximately oriented in the same direction, collagen fibers in skin are nearly randomly oriented while roughly parallel to the skin surface.

REFERENCES

1. Born & Wolf *Principles of Optics* Sixth Edition (Cambridge University Press) 1980.
2. Collett *Polarized Light* (Marcell Dekker Inc) 1993.
3. Kerker M. *The scattering of light and other electromagnetic radiation* (Academic Press) 1969.
4. Yao and Wang, Two-dimensional depth-resolvedMueller matrix characterization of biologicaltissue by optical coherence tomography" Optics letters 24: 537-539, 1999.
5. WF Cheong. Appendix to Chapter 8: Summary of Optical Properties, in Welch AJ, van Gemert MJC, editors, *Optical-thermal response of laser irradiated tissue*, NewYork: Plenum Press, 1995.
6. Jacques SL, Roman R J, Lee K Imaging Superficial Tissues With Polarized Light Lasers Surg. Med. 26:119—129, 2000.
7. Sankaran V. Ph.D Thesis, Polarized Light Scattering by Tissue and Tissue Phantoms , 1999.
8. S. L. Jacques, A. Moody, J. Ramella-Roman, Characterizing microscopic domains of birefringence in thin tissues section , SPIE Proceedings 4257A-17, 2001.

Retinal Damage Thresholds for 40 Femtosecond Laser Pulses[§]

Benjamin A. Rockwell, Cynthia A. Toth,[+] David Stolarski,[‡] Gary Noojin,[‡]
Paul Kennedy, Jesse Shaver,[*] Gavin D. Buffington[*] and Robert Thomas[‡]

Air Force Research Laboratory, Human Effectiveness Directorate, Directed Energy Bioeffects Division,
Optical Radiation Branch, 8111 18th Street, Brooks AFB, TX, 78235-5215
[+]Duke University Eye Center, P.O. Box 3802, Durham, NC 27710
[‡]TASC, 4241 Woodcock Dr., Suite B-100, San Antonio, TX, 78228-1330
[*]Department of Physics, Fort Hays State University, Hays, KS 67601-3101

ABSTRACT

We have shown in previous work that the threshold for laser-induced breakdown is higher than the threshold for ophthalmoscopically visible retinal damage,[1] but they approach each other as pulse duration decreased from several nanoseconds to 100 femtoseconds. We discuss the most recent data collected for sub-50 fs laser induced breakdown thresholds and retinal damage thresholds. With these short pulse durations, the chromatic dispersion effect on the pulse should be considered to gain a full understanding of the mechanisms for damage. We discuss the most likely damage mechanisms operative in this pulse width regime and discuss relevance to laser safety.

Keywords: eye, safety, laser, nonlinear optics, retinal damage

1. INTRODUCTION

Several enabling laser technologies are allowing the proliferation of ultrashort laser systems in the visible (VIS) and near infrared (NIR) spectral regions (i.e. the retinal hazard regime). These wavelengths easily propagate through the eye and can result in retinal damage and functional vision loss if proper laser protective measures are not employed. In recent works by Cain, et al.[2,3] MVL threshold data for ultrashort single laser pulses show a decrease in the amount of pulse energy needed to cause observable retinal damage between 90 fs and 1 ns. We show here this trend continues for pulses shorter than 100 fs. Also, laser induced breakdown (LIB) has been extensively studied[4] for pulse durations above 100 fs to determine its influence on retinal damage thresholds. We extend this analysis to the shortest femtosecond regime.

In this paper we review the measured thresholds for minimum visible lesion (MVL) *in-vivo*[1] and laser-induced breakdown in an artificial eye for 40 fs pulses at 800 nm. We will consider visible and near infrared MVL studies and their impact on determining new damage mechanisms. We also calculate the trends expected for laser-induced breakdown as the input chirp of the pulse is altered. A review of all the MVL literature from the past few of decades indicates that the single-pulse MVL data exhibits three broad trends (see Figure 1). For exposures longer than 20 μs there is a region where near constant irradiance (W/cm^2) is required for retinal damage. For pulses from 1 ns to 20 μs, diffusion of heat is negligible during the exposure and the fluence

(J/cm^2) required for retinal damage is nearly constant. The third regime occurs for pulse durations shorter than one nanosecond where the data shows that it takes less energy to create retinal damage than for longer pulses. Recently, both the ANSI Z136.1 – 2000[5], ICNIRP and IEC laser safety standards have been updated to contain maximum permissible exposure limits for 100 fs – 1 ns exposures based largely on the work of the team of collaborators funded by the Air Force Office of Scientific Research. These exposure limits are also plotted in Figure 1 and reproduce the trends seen in the MVL data. For this present article, we will discuss the region of retinal damage for pulse durations below one hundred femtoseconds.
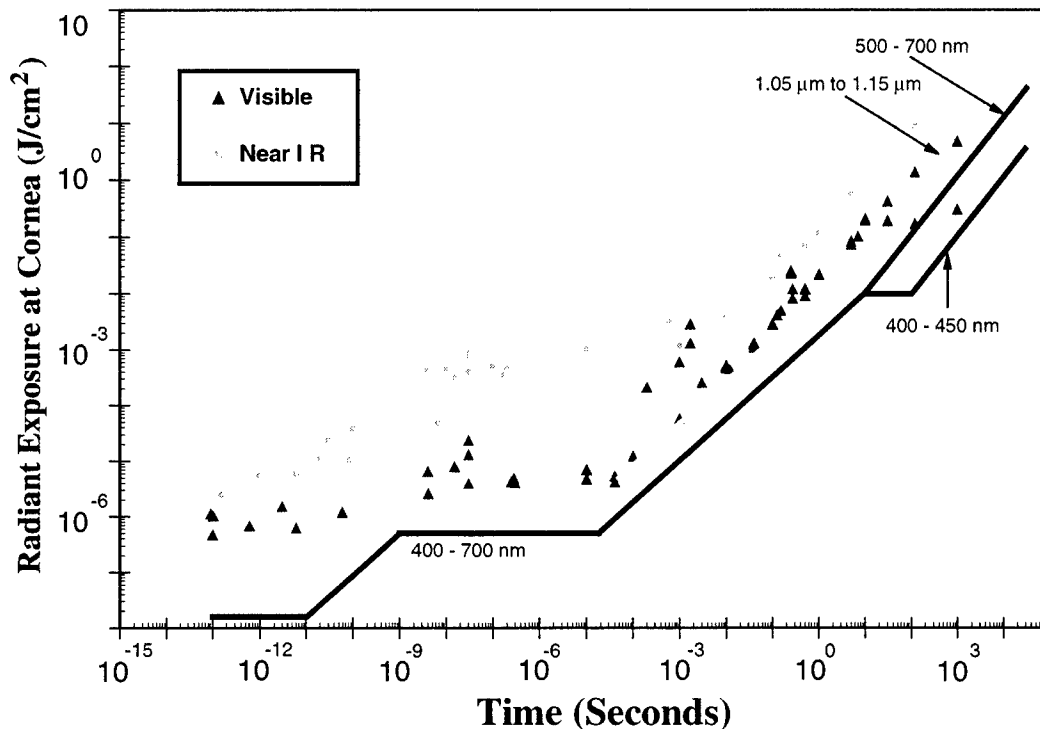
Figure 1. MVL data collected during the previous thirty years in addition to the maximum permissible exposure limits established in the ANSI Z136.1-2000. The data shows three trends as discussed in the text.

We also report the calculations of the effect of linear refractive index gradient, n(ω), on pulse broadening and the eventual change in laser-induced breakdown levels for laser pulses shorter than 100 fs. In this regime, the laser bandwidth required to support ultrashort pulse durations introduces contributions to the evolution of pulse characteristics during propagation. Electromagnetic waves are fully described by the time and space-dependent electromagnetic field. Semiclassical treatments of the propagation and interactions of such fields are governed by Maxwell's equations[6]. For an EM wave with a nominal wavelength of 810 nm, only 16 full cycles would be expected in a 40-fs pulse. In that timespan, light itself only travels in a vacuum 13 μm. Laser pulses in the sub-100 femtosecond range defy the intuitive notions held by those with some limited background in conventional laser physics, since the nearly monochromatic spectral profile of typical laser light is replaced by significant bandwidths, a consequence of the Heisenberg uncertainty principle[6]. Further, the slightly variant speed with which different wavelengths propagate through a particular medium, denoted in the nonzero derivatives of refractive indices with respect to frequency, causes a startling pulse distortion in time and space as an ultrashort pulse propagates through a plano-convex lens, or any dispersive medium and is generally termed group velocity dispersion (GVD) broadening. When propagating through a sample medium, the bandwidth-limited pulse (a bandwidth-limited Gaussian beam has no phase variation across the beam, requiring an infinite radius of

curvature at the phase front) develops a spectral phase with quadratic frequency dependence, resulting in "chirp." Since the spectrum of the pulse remains constant, the spectral components that lead to chirp must appear at the expense of temporal envelope shape, which necessarily becomes more broad[6].

However, a "pre-chirped" pulse, propagated into a dispersive medium, may be recompressed in time. A minimum pulse duration can be achieved at some depth within the material when the spectral phase chirp vanishes, having been compensated by the subsequent GVD. The excess bandwidth of a chirped pulse is converted into a narrowing of the temporal envelope by chirp compensation until the Fourier limit is reached[6].

2. ULTRASHORT LASER PULSE RETINAL DAMAGE AND LASER-INDUCED BREAKDOWN

We have published several studies on measurements of the MVL threshold for both the visible[2] and near-infrared[3] spectral regimes. Figure 1 shows our measured thresholds, which are included with data from many other groups over the past thirty years. Our experiments provide the majority of data for pulsewidths below one nanosecond, and concur with the limited, sub-nanosecond data points taken by other researchers. We have measured the MVL threshold to be dependent upon input chirp and to vary from 0.25 µJ to 0.17 µJ for flat phase and prechirped input pulses at 40 fs (band width limited).

When considering ultrashort retinal damage several phenomena should be considered that might influence the threshold or type of damage seen for these short pulses[4,7]. Because ultrashort laser pulses can possess significant peak powers and irradiance, nonlinear propagation effects need to be considered. For all pulse durations above one nanosecond, the propagation of laser light to the retina can be considered linear and the spot size can be calculated from the wavelength, aberrations and laser divergence. For ultrashort laser pulses, the retinal fluence and wavelength can be different than that resulting from linear propagation. The most significant nonlinear phenomena shown to influence the retinal damage threshold is laser-induced breakdown.
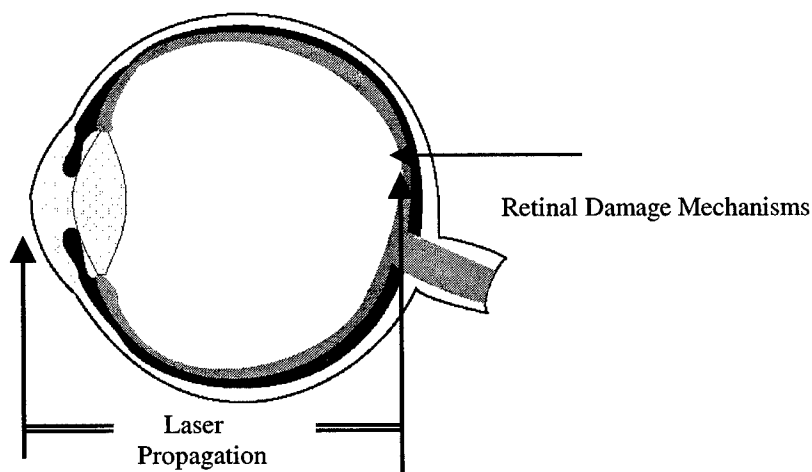
Figure 2. This figure highlights the need to consider both propagation and laser tissue interaction phenomena for ultrashort laser retinal damage.

The thresholds for laser-induced breakdown in the artificial eye have been measured[8,9] and compared for several different focusing geometries for pulse durations between 100 fs and 10 ns. We have also measured the threshold for LIB creation in-vivo[7,10,11] through the use of video imaging. Hence, it has been shown that the Cain artificial eye[8] mimics the focusing characteristics and LIB thresholds. Through these investigations, we have found that LIB is an MVL-threshold-level damage mechanism for 100 fs visible pulses and shorter, but occurs at superthreshold levels for longer pulse durations.

Table 1: LIB - Laser Induced Breakdown Thresholds with different pre-chirps on a 40 fs laser pulse.

Experimental Setup Number of Shots	LIB ED$_{50}$ (μJ)	Slope of Probit
LIB Threshold/Flat Phase Pulse 3 Sets, 200 shots each set	0.32	100
LIB Threshold/Chirped Pulse 3 sets, 200 shots each set	0.22	200

3. CALCULATION OF ULTRASHORT LASER PULSE LIB THRESHOLDS WITH GVD

By combining equations published by M. Kempe[12,13] and Jean-Claude Diels[6] with fitted parametric functions for optical path difference as a function of wavelength an overall equation incorporating temporal, chromatic, and spherical effects was produced. This equation was written into a comprehensive FORTRAN program and run on a multiprocessor parallel computer at Fort Hays State University. The code is easily adapted to different lens system's dispersive media, and pulse characteristics by changing the input parameters. Many lens systems, such as the eye may thus be modeled.

The electric field distribution can be written as

$$U(c, u; t) \propto \int_x^{x_c} d(\Delta\omega) A(\Delta\omega) \int_0^1 dr\, r\, J_0 \left[rc\left(1 + \frac{\Delta\omega}{\omega_0}\right)\right]$$
$$\times \exp(-r^2)\, \exp(-jur^2/2)\, \exp(-j\Delta r^4)$$
$$\times \exp\left\{-j(\Delta\omega)[t + \tau(\Delta\omega, r)r^2 + r^4 w/(2\omega_0)]\right\} \qquad (1)$$

where

$$A(\Delta\omega) = \frac{A_0\sqrt{\pi}T}{(1 + Q^2)^{1/4}} \exp\left\{j\Phi(\Delta\omega) - \frac{\Delta\omega^2 T^4}{4(1 + Q^2)}\right\} \qquad (2)$$

$$\Phi(\Delta\omega) = -\frac{1}{2}\tan^{-1}(Q) + \frac{QT^2}{4(1 + Q^2)}\Delta\omega^2 \qquad (3)$$

$$\tau(\Delta\omega, r) = \frac{\omega_0}{r\Delta\omega r^2}\left(A_2 + B_2 a^2 r^2\right) \qquad (4)$$

$$A_2(\Delta\omega) = \left[9.44 \times 10^{-2} + \Delta\omega(-1.71\ THz^{-1})\right] \times 10^{-6} m \qquad (5)$$

$$B_2(\Delta\omega) = 2.25\left[-4.25 \times 10^{-4} + \Delta\omega(6.27 \times 10^{-3}\ THz^{-1})\right] \times 10^{-6}\frac{m}{mm^2} \qquad (6)$$

J_0 - Zeroth order Bessel function of the first kind $j = \sqrt{-1}$
t - local time a - aperture r - normalized radial coordinate
T - pulse time ω_0 - central frequency $\Delta\omega = \omega - \omega_0$
$u = a^2 k_0 \left(\frac{1}{f_0} - \frac{1}{z}\right)$ $v = ak_0 r'/z$

The equation above is an amalgamation, adapted from published work in the field, as well as original experimental data collected. Equation (1) is based upon Eq. 3 in the formulation of Kempe[13] in his study of chromatic and spherical aberration on the focusing of ultrashort pulses into nondispersive, well-characterized systems. This equation forms the numerical backbone of the model, and was used in an unaltered state to test the initial versions of the code. Absent from our version is the parameter w, which Kempe included to allow specification of the beam intensity at the aperture edge relative to the optical axis. The dimensionless constant A in the second line of Equation (1) was determined for the Cain Cell at 810 nm. This constant is a parameter for spherical aberration, and was computed analytically based on the optical path difference (OPD) as a function of incident ray height. The value was found to be 1.6.

The first modification made was to add the proper structure to introduce an initial linear "pre-chirp" to the pulse. Equations (2) and (3) were adapted from material developed by Jean-Claude Diels[6], Eqs. 1.35 and 1.36. Equations (4), (5), & (6) represent the second incorporation of experimental data into the framework. The data were gathered for the Cain Cell, and incorporate into the model chromatic aberration effects in dispersive systems. The equations give the OPD for two rays of different wavelength which strike the lens at the same incidence.

4. GOALS OF THE RESEARCH GOALS OF THE CALCULATION

We have several goals for the calculations of pulse propagation in the eye for pulse durations shorter than 100 fs. These include:
1) Accurately model the propagation of Chirped Ultrashort Laser Pulses in any focusing geometry
2) Produce analytical expressions for temporal, spherical, and chromatic aberrations for geometries in which the pulse is focused into liquids or other dispersive media
3) Establish a robust numerical modeling and parallel computing resource for the calculation of electric field amplitude of the pulse in the focusing geometry
4) Incorporate material dispersion parameters and laser-induced breakdown data acquired in our laboratory
5) Determine trends in peak laser intensities to estimate laser-induced breakdown thresholds and augment experimental damage studies of:
    - Effects of Ultrashort Pulse Chirping on Damage Thresholds
    - Ocular Damage Mechanisms
    - Laser-Induced Breakdown Thresholds
6) Assess the importance of nonlinear effects in prediction of damage thresholds
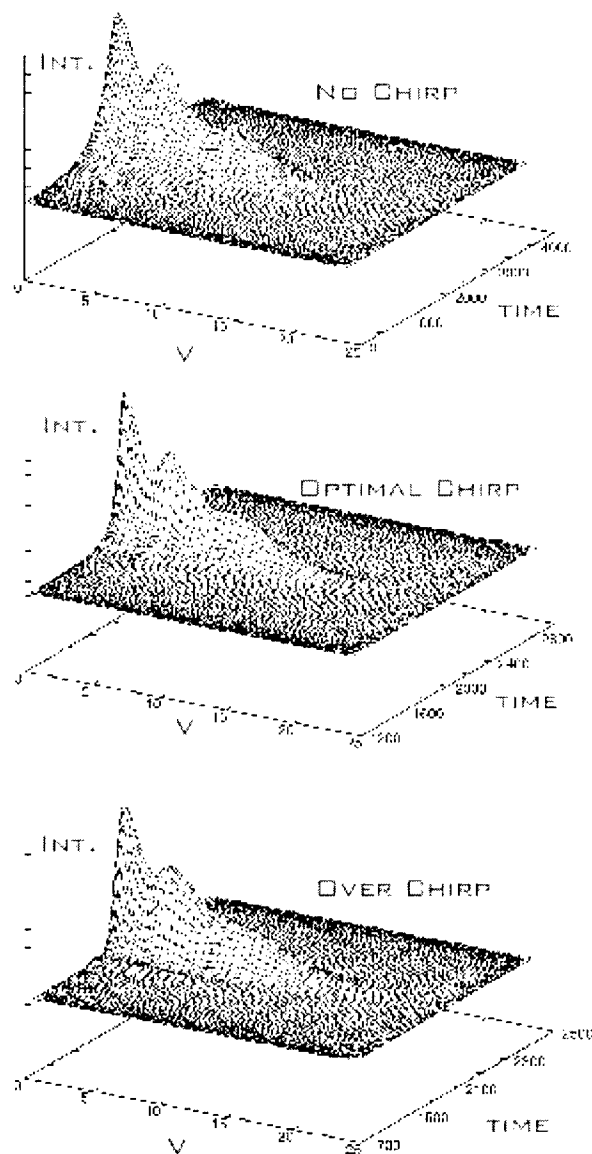
Figure 3. The peak intensity as a function of the radial component of the beam with time at focus.

5. SUMMARY

We have measured the retinal damage threshold and laser-induced breakdown thresholds for 40 fs, 800 nm laser pulses. We have also modeled these phenomena to allow the extension of damage trends across the entire retinal hazard regime for all pulse durations shorter than 100 fs. We have shown that the GVD models can predict minimum breakdown thresholds for chirped pulses in focal geometries which include dispersive media and that the relative thresholds can be computed without inclusion of non-linear effects for tight focusing geometries.

We plan to extend this analysis to evaluate the hazards from all ultrashort exposures to properties of the actual human eye. We also plan to examine whether the theoretical models developed here for LIB thresholds can determine if non-linear effects come into play when predicting absolute damage thresholds. This will allow for a

full extension of this work to evaluate the safe use of lasers in the retinal hazard regime for all pulse durations shorter than 100 fs.

There are numerous implications for laser safety from this work. The continued drop in MVL's below 100 fs suggests that the current laser safety standard[5] should be evaluated. There is explosive growth in the use of ultrashort laser pulses offers to applications across many fields of physics and industrial applications. The increased interest in using ultrashort laser pulses highlights the current deficiencies in the national laser safety standard. Our work is intended to define the interplay between the nonlinear-optical and melanin-mediated effects that determine the eventual MVL threshold.

6. ACKNOWLEDGMENTS

7. REFERENCES

[1]   *The animals involved in this study were procured, maintained, and used in accordance with the Federal Animal Welfare Act and the "Guide for the Care and Use of Laboratory Animals," prepared by the Institute of Laboratory Animal Resources - National Research Council.*

[2]   C. P. Cain, C. M. Toth, C. A. DiCarlo, C. D. Stein, G. D. Noojin, D. J. Stolarski, and W. P. Roach, "Visible retinal lesions from ultrashort laser pulses in the primate eye," *Investigative Ophthalmology and Visual Science*, vol. 36, pp. 879-888, 1995.

[3]   C. P. Cain, C. A. Toth, G. D. Noojin, V. Carothers, D. J. Stolarski, and B. A. Rockwell, "Thresholds for visible lesions in the primate eye produced by ultrashort near-infrared laser pulses," *Investigative Ophthalmology and Visual Science*, vol. 40, pp. 2343, 1999.

[4]   B. A. Rockwell, P. K. Kennedy, R. J. Thomas, W. P. Roach, and M. E. Rogers, "The Effect of Nonlinear Optical Phenomena on Retinal Damage," presented at Laser-Tissue Interaction VI, 1995.

[5]   ANSI, "Z136.1 American National Standard for Safe Use of Lasers,". Orlando, Florida: Laser Institute of America, 2000.

[6]   J.-C. Diels and W. Rudolph, *Ultrashort Laser Pulse Phenomena*. New York: Academic Press, 1996.

[7]   C. P. Cain, C. D. DiCarlo, B. A. Rockwell, P. K. Kennedy, G. D. Noojin, D. J. Stolarski, D. X. Hammer, C. D. Toth, and W. P. Roach, "Retinal damage and laser-induced breakdown produced by ultrashort pulse lasers," *Grafes Archives of Clinical Experimental Ophthalmology*, vol. 234, 1996.

[8]   C. P. Cain, G. D. Noojin, D. X. Hammer, R. J. Thomas, and B. A. Rockwell, "Artificial Eye for In-vitro Experiments of Laser Light Interaction with Aqueous Media," *Journal of Biomedical Optics*, vol. 2, pp. 88-94, 1997.

[9]   D. X. Hammer, R. J. Thomas, G. D. Noojin, B. A. Rockwell, P. K. Kennedy, and W. P. Roach, "Experimental Investigation of Ultrashort Pulse Laser-Induced Breakdown Thresholds in Aqueous Media," *IEEE Journal of Quantum Electronics*, vol. 32, pp. 670-678, 1996.

[10] C. P. Cain, C. D. DiCarlo, G. D. Noojin, R. E. Amnotte, B. A. Rockwell, and W. P. Roach, "In-Vivo Laser-induced Bubbles in the Primate Eye with Femtosecond Pulses," presented at Laser-Tissue Interaction VII, 1996.

[11]   C. P. Cain, C. A. Toth, C. D. Stein, G. D. Noojin, D. J. Stolarski, B. A. Rockwell, S. A. Boppart, and W. P. Roach, "Femtosecond laser threshold: retinal damage versus induced breakdown mechanisms," presented at Laser-Tissue Interaction V, 1994.

[12]   M. Kempe, U. Stamm, B. Wilhelmi, and W. Rudolph, *Journal of the Optical Society of America*, vol. B9, 1992.

[13]   M. Kempe and W. Rudolph, *Optics Letters*, vol. 8, 1993.

[14]   J. H. Shaver and G. D. Buffington, B. A. Rockwell, R. J. Thomas, C. P. Cain, G. D. Noojin, and D. J. Stolarski, "Effects of Dispersion & Aberrations in Ocular Focusing of Femtosecond Pulses & the Impact on Damage Mechanisms", Proceedings of the Boulder Damage Symposium 2000.

Reduction of protection from laser eyewear with ultrashort exposure

David J. Stolarski[a], Jacob Stolarski[b], Gary D. Noojin[a], Benjamin A. Rockwell[b], and Robert J. Thomas[a]

[a]Litton-TASC, San Antonio, TX, USA, 78228-1330

[b]Air Force Research Laboratory, AFRL/HEDO, Brooks Air Force Base, TX, USA, 78235-5215

ABSTRACT

We have measured the optical density of various laser eye protection samples as a function of increasing irradiance. We show that the protective quality of some eyewear degrades as irradiance increases. In previous studies this problem has been demonstrated in samples irradiated by nanosecond pulses, but the current study shows that the modern laser eye protection seems to be robust except for the irradiance possible with ultrashort laser pulse exposure. We discuss the most likely saturation mechanisms in this pulse duration regime and discuss relevance to laser safety.

Keywords: Laser eye protection, ultrashort laser pulse, laser safety

1. INTRODUCTION

The safe use of lasers necessitates the wearing of appropriate eye protection. Producers of laser eye protection have developed a variety of materials, approaches and designs to protect human eyes in a laser environment, while allowing adequate visible light transmission. Development of new laser configurations present eyewear manufacturers with new and challenging problems, such as ultrafast laser pulses, non-linear effects, high irradiance, and tunable wavelengths.

A reduction in optical density of laser eyewear has been noted in previous studies.[1-5] Taboada discusses "dynamic absorption effect" in his 1980 Technical Report[6] of a 1060 nm, picoseconds study of filters. Taboada also uses the term "self-induced transparency" that he gets from an earlier work by McCall and Hahn.[7] Koschinski et al,[8] in a study of a number of filter materials, describe "induced transmittance" brought about by nanosecond Nd:YAG pulses at 1064 nm and 532 nm, and femtosecond Ti:Sapphire pulses at 800nm, and provides an analysis methodology for determining saturable absorption parameters and thermal effects.

2. METHODS

The laser system used in this study was an Nd:YAG regenerative amplifier system that produced 100-ps or 5-ns pulses at 1064 nm or 532 nm. The pulse repetition frequency was 10 Hz. The energy was controlled with a waveplate/cube combination. The laser light was spatially filtered before entering the experimental setup. The experimental configuration is illustrated in Figure 1. The laser energy was measured using a Molectron radiometer. The input energy was determined by measuring the fraction of the input beam that was reflected from a beam splitter. The ratio of

Laser-Tissue Interaction XII: Photochemical, Photothermal, and Photomechanical, Donald D. Duncan, Steven L. Jacques, Peter C. Johnson, Editors, Proceedings of SPIE Vol. 4257 (2001)

125

the input beam splitter was verified before each experiment. This was accomplished by taking the ratio of split energy to the energy transmitted through the experimental setup without the sample in place. After the ratio for the experiment was measured, the detector behind the sample position was replaced with a silicon detector (Molectron J3-S10). The silicon detector was calibrated for each wavelength used in the study. Input pulse energies varied from approximately 10 µJ to 100 µJ.
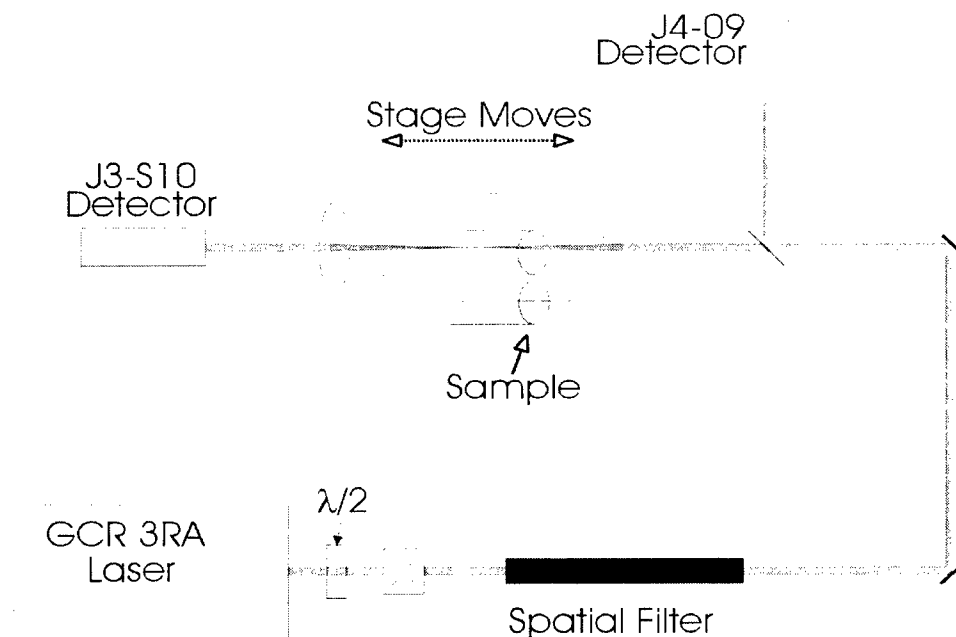
Figure 1. Experimental setup for the ultra-fast laser bleaching tests.

The effects of stray light from sources such as room lighting and scattered laser light were minimized by enclosing the apparatus in a dark housing. Effects of luminescence from samples were reduced by the use of appropriate interference filters inserted in front of the J3-S10 detector. These interference filters also reduced the effects of laser flash lamp emissions that could be co-linear with the laser.

Variable irradiances to the sample were accomplished by a translation stage moving the sample along the focused beam. The beam diameter measurement was made using a motorized stage and a CCD-based beam profiler. A camera was situated upon the stage in the same position as the sample. The beam diameter was measured at 5-mm increments along the optical axis as the camera traveled toward the focus of the 400-mm focal length lens and the corresponding beam diameters were recorded. This provided two orders of magnitude of experimental range, in addition to the adjustment of laser pulse energy. The sample and camera traversed a total of 245 mm.

To measure optical density (OD) the CCD camera was replaced by the eyewear sample on the translation stage. A LabVIEW program measured the energy of each laser shot and the amount of energy transmitted though the sample for that shot. The previously measured beam diameter data was then used to calculate the irradiance of the beam versus position of the stage. The software made use of a pulse energy filter designed to reacquire any data points where the laser energy fell outside of a predetermined energy window. The program also allowed the experimenter to average multiple shots at each position of the stage. After the program had

acquired the transmission of the sample versus position of the stage it would calculate the transmission versus peak power and versus energy. Then each data set would be plotted on the screen for review by the experimenter. The experimenter could then generate a printed report of the data.

A selection of eye protection filters common to laboratory applications were assembled for testing. Primarily, materials were selected which had a large optical density at either 532 nm or 1064 nm. Samples included dye-based polycarbonate filters and semiconductor doped glass filters. Table 1 outlines the sample identifiers and descriptions along with wavelengths at which optical density was measured. The table is coded to identify cases in which a measurable sample bleaching effect was observed, when no bleaching was observed, and in some instances the observation of increased absorption was observed.

In all cases, laser pulse energy was kept to a level at which laser-induced breakdown would not occur in the air, or would be observed at the sample surface. Prior to and after each measurement, the sample surface was examined with a microscope to determine if any thermal or other surface damage had occurred. None of the sample data presented here was acquired at damaging levels.

3. RESULTS
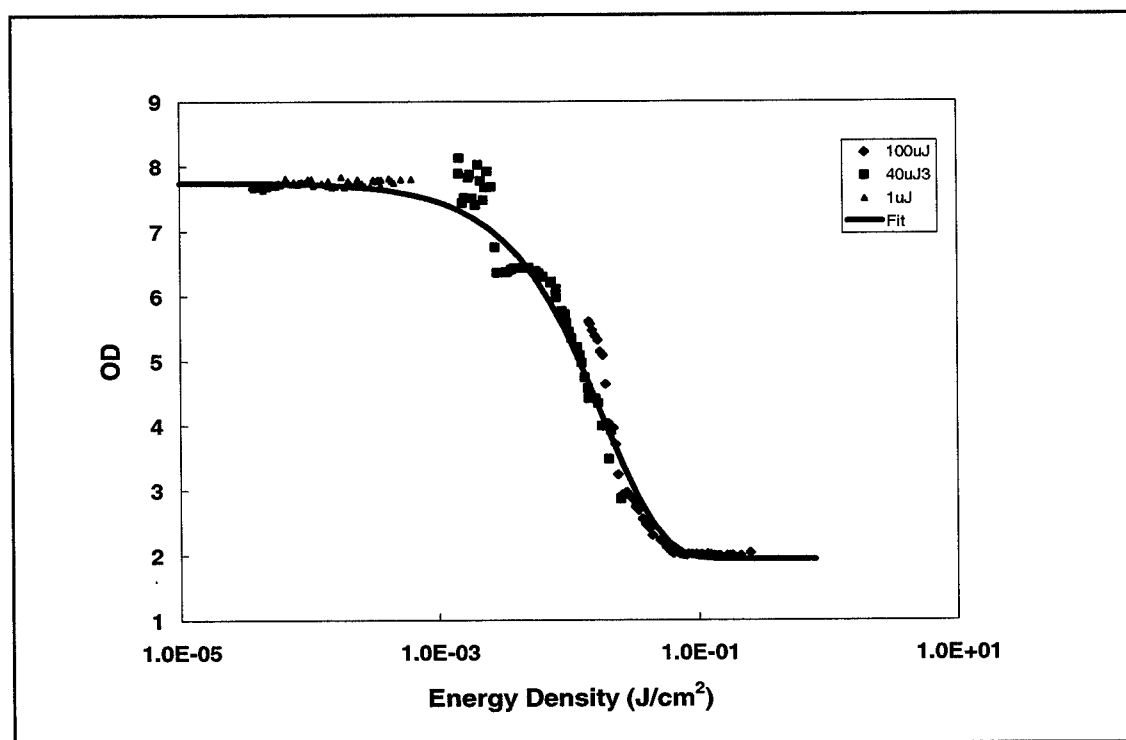
Figure 2. Induced optical transparency or "bleaching" of a semiconductor-embedded glass filter (Sample D).

Two typical sets of experimental data are presented in Figures 2 and 3. Figure 2 demonstrates a large decrease in optical density as a function of increasing irradiance for a semiconductor-doped glass filter. We see that this filter could be "bleached" or an induced

transparency generated from an OD of 5.2 to an OD of approximately 2.0 with 532-nm laser pulses. This effect was most clearly demonstrated with the 100-ps pulse duration. This was the most fully characterized sample during testing, with data collected for both 100-ps and 5-ns pulse durations. Note that the data demonstrates a "leveling-off" in the amount of bleaching that occurred, with a minimum OD being reached at approximately 0.1 J/cm^2.

Figure 3 demonstrates a sample in which a moderate increased absorption can occur with increasing laser irradiance. This sample was a polycarbonate filter and over a range of approximately 6 orders of magnitude of laser pulse energy density, exhibited an increase of approximately 1.5 OD in absorption. This occurred when the sample was exposed to a 100-ps duration laser pulse of 532 nm wavelength.
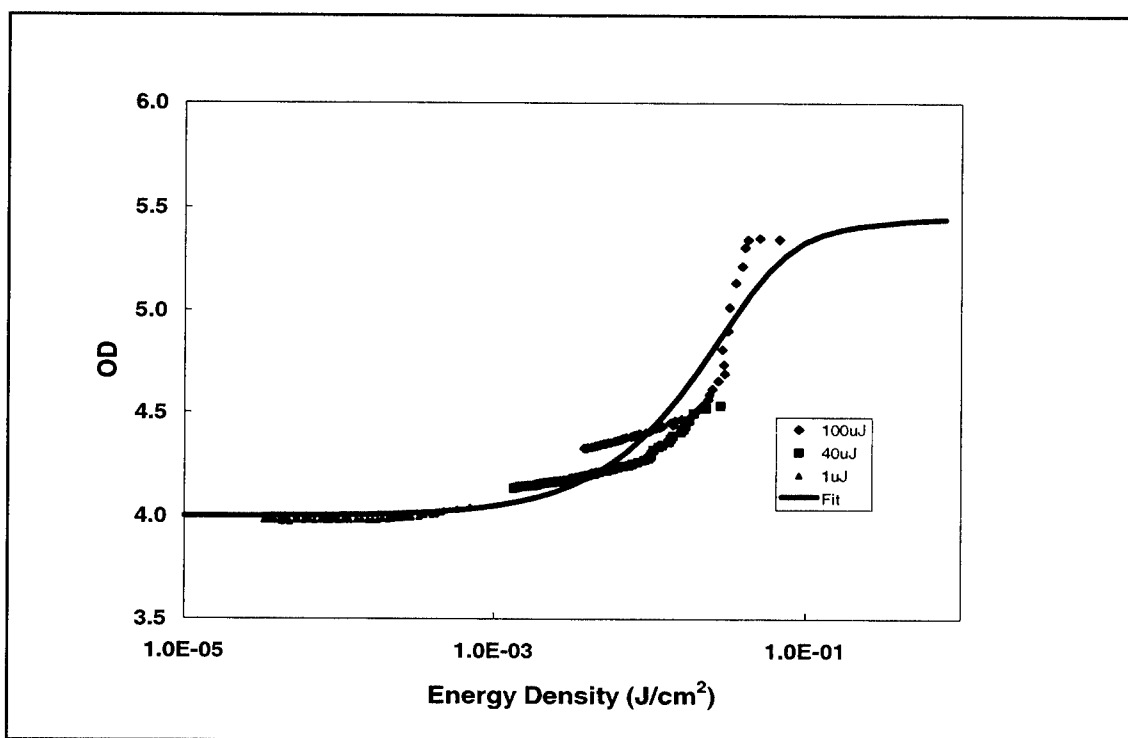
Figure 3. An example of increased optical absorption with increasing pulse energy density. (Sample A).

A scorecard of the samples examined in this study appears in Table 1. In this initial phase of testing, there are several observations to be made, and recommendations for the continuation of the work. We first note that some of both polycarbonate and semiconductor-embedded glass filters could be bleached. We also note that bleaching could not be achieved in all samples, even with irradiance values as high as 10^8 W/cm^2. Bleaching or decreased transmittance is reported in cases where a consistent change of greater than 0.5 OD was measured with little experimental uncertainty. Not all samples that did bleach could be bleached to the point where there was a leveling-off in optical density. We will see in our discussion that this is an important issue in determining accurate parameters that will describe the bleaching effects at other pulse durations or irradiance levels.

Table 1. A scorecard of sample effects from high irradiance laser pulses.

Code	5ns 532	5ns 1064	100ps 532	100ps 1064
SAMPLE A (P)	X		X	X
SAMPLE B (G)	X		X	
SAMPLE C (G)	X		X	
SAMPLE D (G)			X	
SAMPLE E (P)				X
SAMPLE H (G)				X
SAMPLE I (P)				X
SAMPLE J (G)		X		X
SAMPLE K (P)		X		X
SAMPLE L (P)		X		X
SAMPLE M (P)	X		X	
SAMPLE S (P)			X	
SAMPLE T (P)			X	
SAMPLE KG3 (G)		X		X

No Bleaching
Decreased Transmittance
Bleaching

4. DISCUSSION

In order to characterize the bleaching within any laser-absorbing filter, it is important to develop a working physical model that can be used to describe the processes acting in the experiment. Here, we will follow the work presented by Koschinski et. al.[8] This model presents a method in which laser absorption centers can be excited from a ground state as they absorb photons from the laser. Once in the excited state, they can relax back to the ground state with a time constant τ, or can be excited to yet a higher state by absorbing an additional photon. The transmittance of the sample is modeled by Beer's Law with the absorption coefficient, α, defined by Equation 1.

$$T = \frac{E(x - x_0)}{E(x_0)} = \exp[-\alpha \cdot (x - x_0)]$$
(1)

The distance x-x_0 is the thickness of the sample, E is the photon irradiance, and α is the absorption coefficient for the sample. The value of α is determined from Equation 2.

$$\alpha = N_0 \cdot \sigma_0 + N_1 \cdot \sigma_1$$
(2)

In Equation 2, N_0 and N_1 are the number of absorption centers in the ground state and first excited states, respectively. The recombination from higher states is assumed to be extremely fast, and the total number of absorption centers is therefore limited to $N = N_0 + N_1$. The σ_0 and σ_1 represent the cross section for the first and second absorption processes, respectively. Through an analysis of the generation rates of excited states and their relaxation, an expression for the number of absorption centers in the ground state is given by Equation 3.

$$N_0 = \frac{N\sigma_0}{\sigma_0 + \sigma_1 + \dfrac{1}{E \cdot \tau}} \exp\left[\left(-E(\sigma_0 + \sigma_1) - \frac{1}{\tau}\right)t\right] + \frac{N(E\sigma_1\tau + 1)}{E\tau(\sigma_0 + \sigma_1) + 1}$$
(3)

Here, t is the duration of the laser pulse, approximated as a square temporal envelope. The value of τ is the relaxation time constant from the first excited state back to the ground state of the absorption center. Data from experimental measurements can be modeled by substituting Equation 3 into Equation 2 and then using the fact that $N = N_0 + N_1$ to simplify. Transmittance is computed by placing Equation 2 into Equation 1.

The parameters in the model can be adjusted to fit the experimentally measured transmittance curves (or optical density curve), recalling that optical density is defined by Equation 4.

$$OD = -\log_{10} T \tag{3}$$

We find that the values of N and σ_0 act together to determine the transmittance or OD of the filter at low irradiance. They also are the primary determiners of the point at which bleaching begins, provided that the cross section values are significantly different, and that the time constant is sufficiently short. We also find that the values of N and σ_1 act together to determine the optical density at the highest irradiance limits. The time constant τ determines the intermediate slope between the two limits. Of course, the thickness of the sample also affects the absolute transmittance at both limits.

Table 2 lists values of fit parameters from selected data sets of the most fully characterized samples. Note that we did not have confidence in the excited state cross section values in samples where a leveling off in transmittance at the highest irradiances was not obtained. Table 2 shows an example of modeling parameters from bleaching data sets from picosecond and nanosecond pulses.

Table 2. Modeling Results for Selected Samples

Sample ID	Material Type	Sample Thickness (mm)	Wave-length (nm)	N (cm^{-3})	t (s)	τ (s)	σ_0 (cm^{-2})	σ_1 (cm^{-2})
A	Polycarb	3.0	532	6.60E+18	5.0E-9	3.35E-10	5.18E-18	1.80E-17
A	Polycarb	3.0	532	6.60E+18	1.0E-10	3.35E-10	4.65E-18	1.00E-17
B	Glass	1.0	532	3.10E+18	5.0E-9	9.60E-08	3.80E-17	2.60E-18
B	Glass	1.0	532	4.50E+18	1.0E-10	1.50E-08	2.65E-17	5.70E-18
D	Glass	3.0	532	3.40E+18	1.0E-10	8.00E-08	1.75E-17	2.50E-18
H	Glass	2.0	1064	6.50E+18	1.0E-10	9.80E-09	5.10E-18	1.60E-16

The data from Table 2 was used to generate graphs of the expected trends in bleaching effects with pulses of various durations. In Figure 4 we show the relative transmittance as a function of laser pulse energy density for pulses of 100 fs, 100 ps, 5 ns and 1 μs in sample A. This polycarbonate filter demonstrated a distinct decrease in transmittance with increasing pulse energy. The parameters from the data analysis of the 5 ns experimental data were applied to each pulse duration. Note that the material cross sections are set to the same values in each case, along with sample absorber density and relaxation time constant. Sample A demonstrated a relaxation time constant of approximately 300 ps, and an excited state absorption cross section greater than that of the ground state, as expected from the decrease in transmittance. The analysis indicates that pulses of microsecond duration will require approximately two orders of magnitude more

energy for the sample to exhibit the same bleaching effect. In the case of very short pulses, such as the 100-fs pulse duration plotted, the sample would be expected to show approximately the same amount of decreased transmittance as measured with the 100-ps pulse, an onset of approximately one order of magnitude less energy than seen in the 5-ns pulse case.
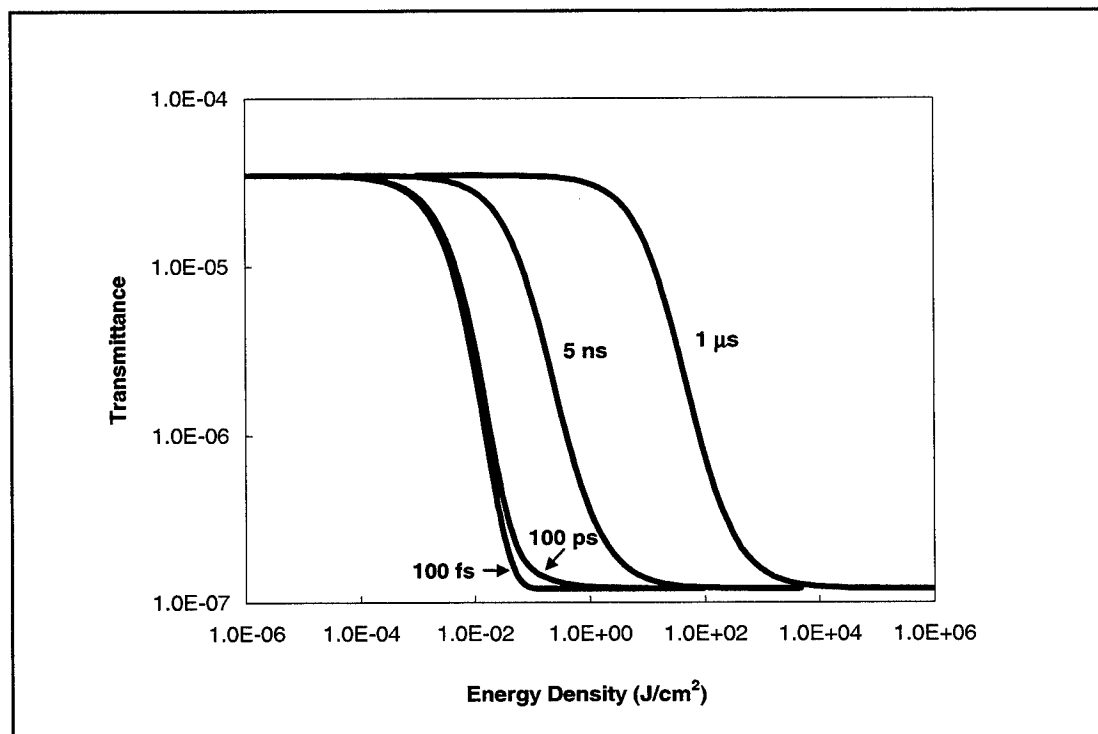
Figure 4. A comparison of the predicted effects of pulse duration on transmittance curves (Sample A).

Figure 5 illustrates data from sample B which showed significant bleaching. The increased transmittance resulted in analysis parameters that were anticipated. The cross section for the excited state absorption is smaller than that for the ground state. Also, the relaxation time constant turned out to be much longer than for sample A; nearly one nanosecond. This results in very little difference in bleaching as a function of pulse duration for pulses of the same energy. For pulse durations greater than about 10 ns, a significant increase in required pulse energy for bleaching to be seen occurs. The 100-ns curve shown indicates that an onset of bleaching at approximately 1×10^4 J/cm^2. This is most likely much larger than the surface damage threshold of the filter.

In both cases, the relative transmittance curves reflect the data that has been acquired. The parameters in Table 2 indicate that there may be small offset errors between data acquisition runs. This is evidenced in the fact that the products of N and σ_0 are not constant for differing pulse durations. The results are in good agreement for initial trials of the system. This observation also indicates that an additional level of certainty can be achieved in parameterization by conducting measurements with differing pulse durations and requiring the results to converge.
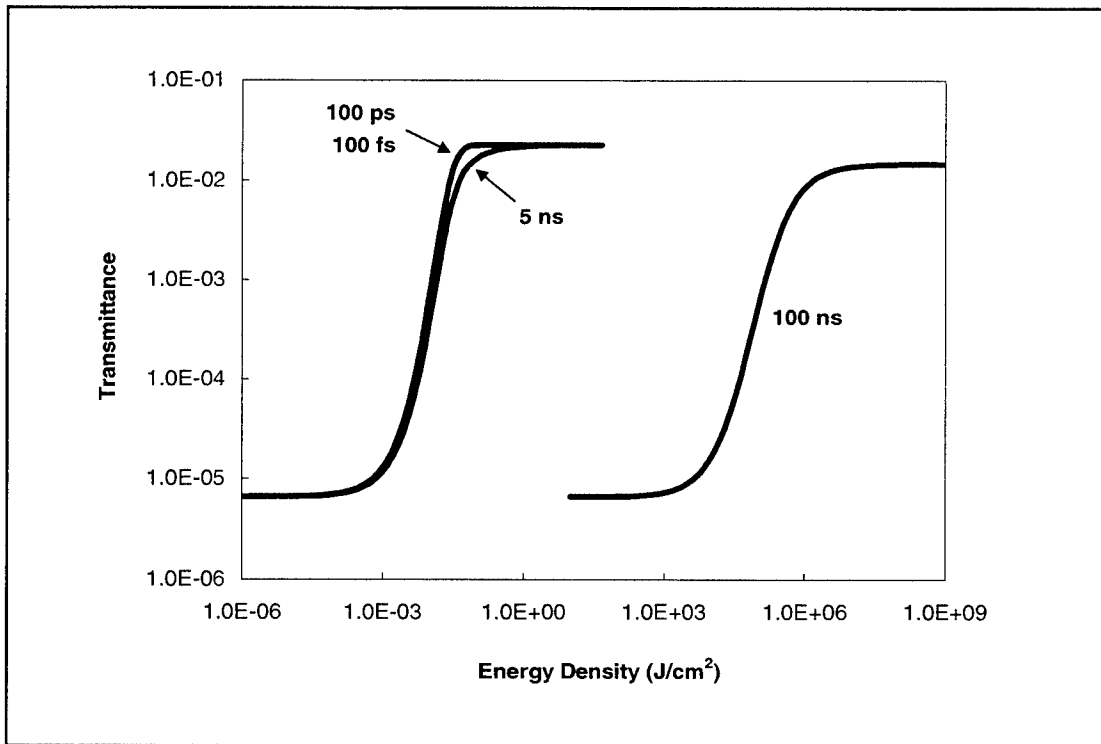
Figure 5. A comparison of the predicted effects of pulse duration on bleaching curves (Sample B).

The data and model presented here indicate that laser pulses as short at 100 ps can be characterized and modeled effectively. One question that remains is: for sub-picosecond pulses, is this model valid, and will it accurately predict the optical density of a given laser absorption filter for a given pulse duration, provided that the parameterization is available? An important assumption made in the modeling method is that relaxation time constants from higher level excited states will be extremely short compared to the duration of the laser pulse. This may not be true and a more detailed model may be required to accurately characterize filter samples below one picosecond.

Damage thresholds must also be addressed in order to determine if this methodology will be a satisfactory characterization method. As we have stated in the sections above, model parameters such as the excited state absorption cross section cannot be accurately determined, as an irradiance level for maximum photo-bleaching could not be reached. We were careful in all cases not to report data from damaged samples. In most cases, the approximate observed damage threshold is approximately 1 J/cm^2. Many samples showed only an initial bleaching effect before reaching this energy density.

5. CONCLUSIONS

Our preliminary data and analysis indicate that the effects of short pulse, high-irradiance exposures to laser filters are significant in many cases. We believe that this is an important issue to the laser safety community and that our continued efforts will provide a consistent methodology for the assessment of the suitability of these filters for use with ultrafast lasers. The results also indicate that it may be possible to identify a fixed set of parameters describing transmittance for any pulse duration and energy density in question.

Future work will extend the modeling effort and data collection to sub-picosecond pulses. Work will also continue to ensure the broadest possible range of energy and power densities that can be achieved in the laboratory.

ACKNOWLEDGEMENTS

REFERENCES

1. T. L. Lyon and W. J. Marshall, "Nonlinear properties of optical filters – implications for laser safety," Health Physics, 51 (1), pp 95-96, 1986.

2. P. M. Swearengen, W. F. Vance, and D. L. Counts, "A study of burn-through times for laser protective eyewear," Am. Ind. Hyg. Assoc. J., 49 (12), pp. 608-612, 1988.

3. P. Eriksen and P. K. Galoff, "Measurement of laser eye protection filters," Health Physics, 56 (5), pp. 741-742, 1989.

4. A. A. Robinson, W. J. Marshall, and S. G. Dudevoir, "Study of saturation in commercial laser goggles," SPIE Vol. 1207, Laser Safety, Eyesafe Laser Systems, and Laser Eye Protection, pp 202-213, 1990.

5. D. J. Lund and P. Edsall, "Another look at saturable absorbers for laser eye protection," SPIE Vol. 1207, Laser Safety, Eyesafe Laser Systems, and Laser Eye Protection, pp 193-201, 1990.

6. J. T. Taboada, "Picosecond laser pulse optical density of three 1060-nm filters," USAF School of Aerospce Medicine Technical Report SAM-TR-80-42, 1980.

7. S. L. McCall and E. L. Hahn, "Self-inuced transparency," Phys. Rev. 183, pp 457-483, 1969.

8. W. Koschinski, A. Schirmacher, and E. Sutter, "Induced transmittance of eye-protective laser filters," ILSC, pp. 612-621, 1997.

Revisiting the Internal Absorption Coefficient of the Retinal Pigment Epithelium Melanosome

Randolph D. Glickman[†,1,2], Steven L. Jacques[3], Rebecca T. Hall[2], and Neeru Kumar[1]

[1]Department of Ophthalmology and [2]Division of Radiological Sciences, The University of Texas Health Science Center at San Antonio, TX; [3]Oregon Medical Laser Center, Providence/St. Vincent's Hospital, Portland, OR.

ABSTRACT

Retinal pigment epithelial (RPE) cells of the vertebrate eye contain melanin packaged in structures called melanosomes. Previously, we reported that the bovine melanosome has a laser photodisruption threshold of 153.6 mJ/cm^2 at 25 °C and 532 nm (Glickman et al., Proc SPIE **2681**:460-467, 1996), and an internal absorption coefficient of 2237 cm^{-1} (Jacques et al., Proc. SPIE **2681**:468-477, 1996). Those values used an estimate of melanosome density inferred from studies of skin laser effects (Jacques et al., J. Invest. Dermatol. **88**:88-93, 1987). We now revisit that calculation using a density value obtained from density centrifugation analysis of bovine and baboon RPE melanosomes. Stepped-density gradients (60% to 80%) of the nonionic medium, Nycodenz, were formed, and samples of melanosomes were spun on the gradients in a swinging-bucket rotor at 10,000 rpm for 60 m. Bovine melanosomes formed two populations, one at the interface between 70% and 75%, and the other between 75% and 80%, corresponding to densities of ~1.38 and ~1.41 gm/cm^3, respectively. Baboon melanosomes migrated to within the same density region. Using a density value of 1.41 gm/cm^3, and assuming a water content of 52% for hydrated melanosomes, the internal absorption coefficient was calculated as 2339 cm^{-1}. Although this calculation uses an objective density measurement, the water content remains an estimate, and the actual value *in situ* may differ.

Keywords: density, laser photodisruption, melanin, Nycodenz, optical properties, RPE

1. INTRODUCTION

1.1 The retinal pigment epithelium and its pigment inclusions

Located underneath, or distal, to the neurosensory retina is the *retinal pigment epithelium* (RPE), a single layer of cells containing various pigment inclusions. The RPE cells have two primary roles. One is to provide nutrition and oxygen to the retinal neurons especially the photoreceptors of the retina, which are the most metabolically active cells of the retina and consume up to 60% of the total O$_2$ in the retina[1]. The other is to re-isomerize the visual pigments from the all-trans bleached state back to the unbleached 11-cis form. Specific binding proteins facilitate the transport of the bleached rhodopsin and cone pigments from the photoreceptors to the RPE cells where the re-isomerization occurs[2]. This is an essential process and prevents the photoreceptors from being depleted of 11-cis retinal, the chromophore of the visual opsin pigments. The RPE cells contain several other pigments that are not directly involved in visual transduction. These include melanin, lipofuscin, and melanolipofuscin. Lipofuscin and melanolipofuscin are age-related pigments and probably represent the accumulation of end-products of lipid and retinaldehyde metabolism[3]. They will not be considered further here, except to note that with age there is a relative decline of melanin granules and an increase in the lipofuscin granule content[4], and this is likely a marker of increased oxidative stress[5].

Melanin, itself, is a broadband absorber and may protect the retina from photic damage due to its ability to prevent light from reaching susceptible tissues[6], by binding heavy metals that might otherwise promote catalytic reactions[7], or by quenching and trapping free radicals produced by photochemical reactions[8,9]. Melanin may, in addition, reduce intraocular light scatter and improve retinal image contrast by absorbing light not absorbed by the retinal photoreceptors. Depending on local conditions,

however, melanin may serve to promote light damage. It has long been known that melanin is excited to a free radical during UV and visible light exposure[10,11]. Although the role of this free radical in vivo is not precisely known, excited melanin has been shown to promote the photo-oxidation of cellular components such as ascorbic acid, fatty acids, proteins, and possibly DNA[12-15], thereby contributing to retinal light damage.

1.2 Physical and optical properties of melanosomes

Within the RPE cell, melanin is packaged in cellular inclusions called melanosomes. While these structures do not have true lipid bilayer membranes, their contents are surrounded by a proteinaceous coat. These proteins, called melanoproteins, surround the melanosome and may also provide some internal structure, which apparently varies across species. For example, in the melanosomes of bovine RPE, the melanin does not appear to have a particular structure, appearing in the electron microscope as uniform and densely packed (Fig. 1). Two classes of melanosomes exist in the bovine RPE, one roughly spherical about 1 μm in diameter, and the other ellipsoid about 1μm by 3 μm. We have hypothesized that newly formed melanosomes are spherical, becoming more ellipsoid as they mature as the result of the addition of newly-synthesized melanin granules. It is possible that the internal structure may affect the actual density of the melanosome. The present investigation was conducted to determine the density of isolated RPE melanosome, using a direct physical measurement. These data are useful in deriving optical characteristics of the melanosomes, such as the internal absorption coefficient. Previously, we calculated the internal absorption coefficient of the RPE melanosome based on several laser-induced endpoints[16,17], but used density estimates from skin melanosomes[18,19]. We now revisit those calculations using new, experimentally determined density measurements of RPE melanosomes.
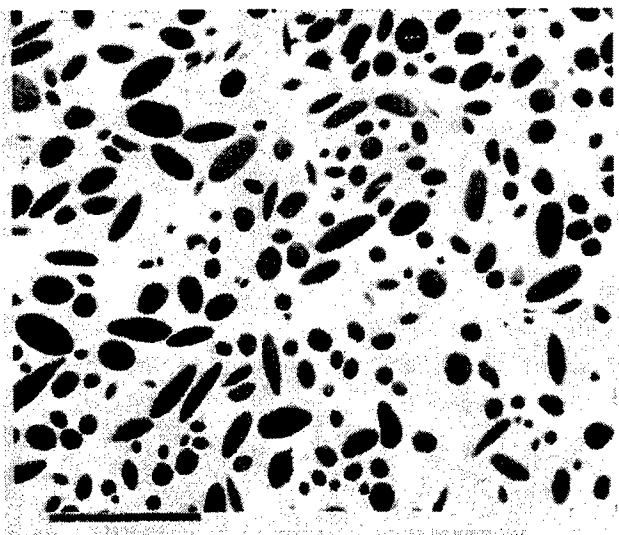
Figure 1: Transmission electron micrograph of crude preparation of bovine RPE melanosomes. Scale bar: 5 μm

2. METHODS

2.1 Isolated RPE melanosomes

RPE cells were isolated from freshly obtained bovine or baboon eyes. Bovine eyes were purchased from a local abattoir, and baboon eyes were kindly provided by the Southwest Foundation for Biomedical Research in San Antonio, Texas. The RPE cells were disrupted by ultrasonication, and the melanosomes were purified from other cellular material by successive centrifugations through sucrose[13]. Melanosome preparations were kept frozen at -20 °C until use.

2.2 Density Centrifugation and Analysis

Melanosome density was determined by *density gradient centrifugation*. The principle behind this method is that a particle in a gravitational or centrifugal field will migrate in the direction of the acceleration vector until its own density matches the density of the surrounding medium. At that point, there will be no net acceleration on the particle, and it will remain stationary in the medium. In practice, a medium of progressively varying density is made by mixing or forming a concentration gradient of a salt or other compound in the centrifuge tube. A common material used for density analysis in molecular biology is cesium chloride

(CsCl), however, as described below, the strong ionic nature and high tonicity of CsCl gradients interfered with an accurate density measurement of melanosomes. Therefore, a non-ionic material, Nycodenz, was used [systematic name 5-(N-2,3-dihydroxypropylacetamido)-2,4,6-triiodo-N,N'-bis(2,3-dihydroxypropyl)-isophthalamide][20]. In these experiments, a step gradient was formed in a 13.2-ml, thin-wall, polyallomer centrifuge tube (Beckman Instruments 331372) by placing about 1.7 ml of the most concentrated medium (80% w/v in the case of Nycodenz) in the bottom of the centrifuge tube, and then layering 1.7 ml aliquots of progressively less concentrated medium on top of each other, typically varied in concentration decrements of 5%. Melanosomes were defrosted, washed twice with 1 mM EDTA in 1 mM Tris buffer, pH 7.5, and re-suspended in the same solution. Melanosome samples in a volume of 50 µl were layered on the top of the concentration gradient, and the tubes placed in a swinging bucket rotor (Beckman Instruments SW-41T). The samples were centrifuged at 10,000 rpm (relative centrifugal force, RCF = 12,622 g) for 1 hr at 4 °C in a Beckman L7 ultracentrifuge. The melanosomes formed a stationary band at the interface between the layer in which the density of the medium was less than that of the melanosome, and the layer in which the density was greater than or equal to that of the melanosomes. The concentration of the medium at the relevant bands was confirmed by its refractive index as measured in an Abbé refractometer. This concentration was related to density by published formulas. In the case of Nycodenz, density was calculated from refractive index as follows:

$$density_{Nycodenz}(g/cm^3) = 3.242\eta_{20°C} - 3.323 \tag{1}$$

where $\eta_{20°C}$ is the refractive index of the Nycodenz solution at 20° C[20]. A similar procedure was used for CsCl gradients, except that the relationship between refractive index and density differs from Nycodenz, and was instead obtained from standard reference tables (Beckman Instruments Ultracentrifuge Reference Data) relating density to percent solution of CsCl by weight.

3. RESULTS

3.1 Density measurements with cesium chloride gradients
Because CsCl is the "classic" density gradient medium used in molecular and cell biology, initial measurements on RPE melanosomes were made using this material. When bovine melanosomes were centrifuged on a 30%-60% CsCl gradient, they stabilized at the 55% CsCl layer, corresponding to a density of $1.69 \pm .05$ g/cm^3. This value was higher than expected, and also higher than density calculations based on theory (Dr. James Gallas, University of Texas at San Antonio, personal communication). A possible reason for this discrepancy is that the melanosomes were dehydrated by the high tonicity of the CsCl gradient. For example, 55% CsCl corresponds to a molarity of 5.481. Considering that each molecule of CsCl yields two ions when fully dissociated, a 5-plus molar CsCl solution is many times the osmolarity of the typical intracellular environment, and represents an extremely hypertonic environment. A density medium of lower tonicity at the required density was used to reduce the effect of dehydration on the density measurements.

3.2 Density measurements with Nycodenz gradients
Nycodenz is a density gradient material introduced in the early 1980's because its non-ionic, non-sugar, and inert character, as well as relatively low toxicity, was an advantage for studies involving enzyme activity and cellular function. In addition, relatively dense solutions of the material are achieved with solutions of much lower molarity than with commonly used ionic media such as CsCl. This was expected to reduce the dehydration of melanosomes that may have caused the anomalously high density measurement with CsCl. Partially purified bovine melanosomes formed two bands after centrifugation on step gradients of 60% to 80% Nycodenz, one at the interface between 70% and 75%, and one between 75% and 80%. These bands corresponded to densities of 1.38 g/cm^3 and 1.41 g/cm^3, respectively (Figure 2, left-hand photograph). The molarities of 70%, 75%, and 80% Nycodenz were 0.853 M, 0.914 M, and 0.974 M, respectively. Thus the Nycodenz medium was much less hypertonic than the CsCl gradients previously used, with the result that the dehydration artifact was smaller.

The isolation procedure for the bovine melanosomes permitted the separation of two populations: one termed "heavy" and the other termed "light", based on their movement through a 30% sucrose solution during a velocity sedimentation step. These two populations could be separated on the basis of density, as already noted. After separating the heavy and light populations, an example of only the heavy melanosomes run on a Nycodenz gradient is shown in Figure 2, right-hand photograph). As can be appreciated in this photograph, most of the melanosomes segregate in the band between 75% and 80% Nycodenz, corresponding to 1.41 gm/cm^3. It is likely that the light and heavy melanosome populations correspond to the small spherical and larger ellipsoid melanosomes observed in electron microscopy.

Similar analysis has been performed with melanosomes isolated from baboon RPE cells. Using the same isolation procedure, a quantity of baboon melanosomes was prepared, and a 50 µl aliquot run on a Nycodenz step gradient. The results are shown in Figure 3. Instead of two distinct bands, most baboon melanosomes segregate at the interface between 70% and 75% Nycodenz (1.38 gm/cm^3), but there is also a more or less continuous distribution of melanosomes between 70% and 80%, suggesting that in the baboon RPE cell, most melanosomes are similar in size, but small populations exist of lighter or heavier melanosomes perhaps representing degenerating or aggregated particles. It may also be noted that the baboon melanosomes were harvested from animals aged 15-20 years, which represents a "middle age" for these primates that have a typical life span of 30 yrs, while the bovine melanosomes were from cows of a much younger age, probably less than two years of age at slaughter. Therefore some age-related changes in the morphology of the RPE cell may be a factor in the slightly different density characteristics of the baboon and bovine melanosomes.
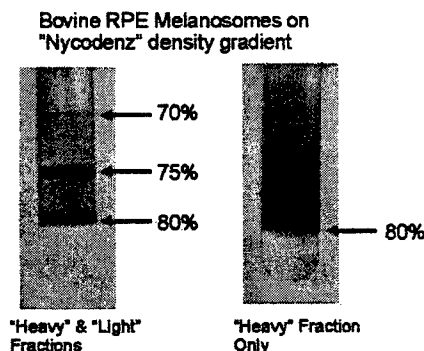
Figure 2: Bovine melanosomes separated on 60-80% Nycodenz gradients. Left photo: "crude" melanosome preparation. Right photo: "heavy" fraction only.
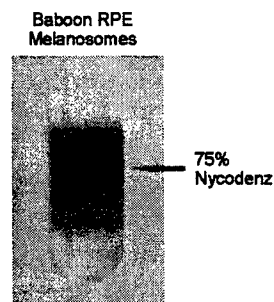
Figure 3: Baboon RPE melanosomes separated on a 60-80% Nycodenz gradient. Gradient steps as in Figure 2.

3.3 Estimation of internal absorption coefficient of RPE melanosome using the new density measurements
3.3.1 Visible endpoint
In the report by Jacques et al.[17], the internal absorption coefficient for the bovine RPE melanosome was calculated on the basis of several experimental endpoints. One was a "visible" endpoint, i.e. the laser radiant exposure required to produce a visual change or "clearing" of a suspension of melanosomes held between a glass microscope slide and a coverslip. The laser source was a frequency-doubled, Nd:YAG system (532 nm). The threshold laser exposure, H_{th}, was found to be a function of the initial temperature, T_i, of the melanosome preparation, and was the energy required to be deposited in the melanosome to raise it to a critical disruption temperature. The visible endpoint experiments indicated that the critical temperature was about 125 °C. From the slope of the relationship between T_i and H_{th}, the absorption coefficient was calculated as follows:

$$\mu_a = \frac{\rho C}{- dH_{th}/dT_i} \tag{2}$$

In equation (2), ρ represents the density of the melanosome (g/cm^3), and C represents its specific heat (cal/g•°C). From the visible endpoint experiments, dH_{th} was determined to be 0.190 J/cm^2 when T_i is 0 °C (dT_i = 125 °C). (Note: the slope of dH_{th}/dT_i is negative because as the initial temperature of the melanosome increases, the amount of energy required to raise the melanosome to the disruption point decreases; in equation (2), therefore the negative reciprocal of this quantity becomes positive). Converting to J/g• °C (1 cal = 4.186 J), and using a value of 3.4 J/cm^3•°C for the quantity, ρC, extrapolated from work with skin melanosomes[19], the melanosome absorption coefficient at 532 nm was calculated as

$$\mu_a = \frac{(3.4 J/cm^3 \cdot °C)(125°C)}{(0.190 J/cm^2)} = 2237 \ cm^{-1} \tag{3}$$

This calculation, i.e. equation (3), can now be refined using the melanosome density measurements from the Nycodenz density

gradient centrifugation experiments. The values for ρ of 1.38 g/cm³ for the "light" fraction, and 1.41 g/cm³ for the heavy fraction of melanosomes may be substituted into expression (2). The value of C, the specific heat, is taken from the work of Takata et al.[21], who found that a value of 0.37 cal/g•°C was generally representative of non-water constituents of tissue. The specific heat of hydrated tissue components varies according to its water content, w (equal to g water/g total), divided by the tissue density (ρ):

$$C = 0.37 + 0.63(w/\rho) \quad (cal/g\text{•}^oC) \tag{4}$$

According to Jacques and McAuliffe[19], the water content of skin melanosomes *in situ* was taken as 52% (w = 0.52). This value has been used for the following calculation of the RPE melanosome specific heat:

$$C_{heavy} = (4.186\,J/cal)(0.37 + 0.63(0.52/1.41)\,cal/cm^3\text{•}^oC) = 2.52 \quad J/cm^3\text{•}^oC \tag{5a}$$

$$C_{light} = (4.186\,J/cal)(0.37 + 0.63(0.52/1.38)\,cal/cm^3\text{•}^oC) = 2.54 \quad J/cm^3\text{•}^oC \tag{5b}$$

Substituting these values for C, and the density values measured for the heavy (1.41 g/cm³) and light (1.38 g/cm³) fractions of melanosomes, into equation (2), the internal absorption coefficient of RPE melanosomes at 532 nm has been recalculated as 2339 cm⁻¹ (heavy) and 2308 cm⁻¹ (light), respectively.

3.3.2 Oxidative endpoint

The second endpoint used for determining melanin optical properties was referred to as an oxidative endpoint[16]. This method exploited the fact that melanin was excited to a reactive free radical by absorption of light and laser radiation. This radical oxidized the nicotinamide cofactors, NADPH and NADH [22,23]. The redox state of these NAD cofactors was easily determined by spectrophotometry because their optical density at 340 nm was reduced in a systematic way by chemical oxidation. This reaction was utilized to measure the photoreactivity of RPE melanosomes, which was also discovered to be increased by laser disruption[14,16]. Isolated bovine RPE melanosomes were mixed with a constant aliquot of reduced NADPH. Exposing this mixture to a visible laser, for example, resulted in the exposure- and wavelength-dependent reduction of the sample's optical density at 340 nm[14]. Structural damage to the RPE melanosome, e.g. by acid hydrolysis or laser-induced damage, caused an increase in the rate of NADPH oxidation after a given laser exposure. The photodisruption threshold of the melanosome was estimated by determining the laser radiant exposure that caused an increased rate of NADPH oxidation by photoactivated melanosomes, compared to unexposed samples. Figure 4 (taken from Glickman et al.[16]) shows an experiment of this type in which the melanosome disruption threshold for doubled Q-switched Nd:YAG (532 nm) was determined. The experiment was conducted
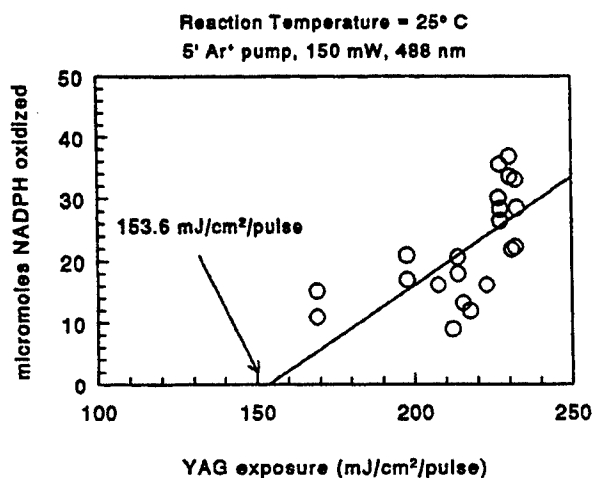
Figure 4: Photodisruption threshold for bovine melanosomes exposed to doubled Nd:YAG laser. Measurement of oxidative endpoint using NADPH oxidation as described in text. Figure from Glickman et al.[16].

by first exposing the melanosome+NADPH sample to the YAG laser at a given radiant exposure, then exposing it to the 488 nm output of an Argon ion CW laser for 5 min to drive the photochemical reaction, and finally measuring the optical density at 340 nm (after filtering out the melanosomes from the sample). The threshold for photodisruption was estimated by this method to be 0.154 J/cm², which is comparable to the *in vivo* retinal damage threshold for nanosecond visible pulses (on the order of several µJ) when equated for incident corneal energy, i.e. taking into account the focusing power of the eye's optics.

The data from the oxidative endpoint experiments were also used[17] to estimate the critical temperature for melanosome disruption, based on the relationship shown in equation 2, i.e. the equation was rearranged to solve for T_{th} as a function of the absorption coefficient (μ_a), threshold laser radiant exposure (H_{th}), and initial temperature (T_i). This yielded a very similar result to the visible endpoint, i.e. a critical disruption temperature of 126 °C. Therefore, using $T_{th} = 126$ °C, $H_{th} = 0.154$ J/cm², and a water content of 52%, the absorption coefficient at 532 nm for the heavy melanosomes (which were used in the experiment shown in Figure 4) was calculated at 2909 cm⁻¹, somewhat higher than the value based on the visible endpoint.

3.4 Effect of water content on melanosome absorption coefficient

Because the precise water content of the RPE melanosome has not been measured, the value of 52% used in the preceding calculations should be regarded as an estimate; however, it was of interest to consider the effect of different melanosome hydration states on the optical absorption coefficient. Using the threshold laser radiant exposure (H_{th}) and critical disruption temperature determined for the visible endpoint (0.19 J/cm² and 125 °C) and for the oxidative endpoint (0.154 J/cm² and 126 °C), equation (4) for specific heat (C) was solved for a hypothetical melanosome water content ranging from 30% up to 60%. This seemed to be a reasonable range to examine, based on observations on skin melanosomes[19]. The values for C, obtained over this range, were then used to recalculate absorption coefficient using equation (2). The results of these extrapolations are shown graphically in Figure 5. It is important to stress that this graph only shows the *theoretical* melanin absorption coefficient *with unchanging values of* H_{th} *and* T_{th}, *but increasing water content*, i.e. to maintain constant values for H_{th} and T_{th}, the effective absorption coefficient of melanin would have to be higher in order to overcome the effect of dilution. In reality, of course, as the hydration state of a given melanosome increases, the effective internal absorption coefficient will decrease because of melanin dilution, and the values for H_{th} and T_{th} will also vary[19].

Although "heavy" and "light" RPE melanosomes were easily distinguished on a Nycodenz density gradient, the actual difference in density was small, and there was a corresponding small difference in their relative absorption coefficients at 532 nm (Figure 5, heavy and light visible endpoint lines). The use of a different photodisruption endpoint, i.e. NADPH oxidation, resulted in a different experimental estimate of absorption coefficient, one which was more than 20% higher than that based on the visible
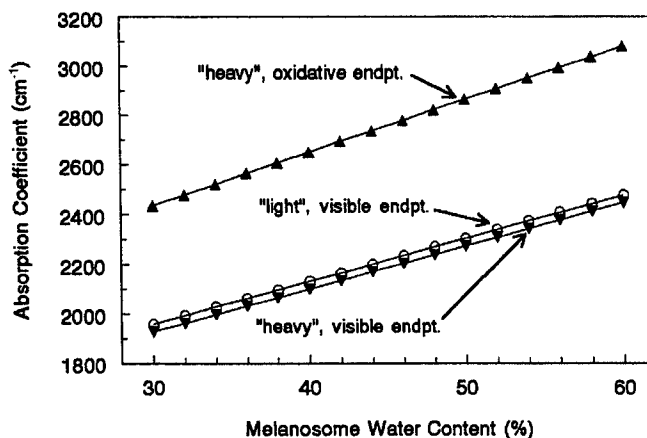
Figure 5: Theoretical melanin absorption coefficient as a function of varying amounts of water in melanosome, assuming **constant** H_{th} and T_{th}. "Heavy" and "light" refer to bovine melanosome fractions. See text for other details.

endpoint (Figure 5, compare oxidative and visible endpoints for the heavy melanosomes). This difference, however, probably reflected the higher variability in the oxidative endpoint measurements, rather than in some fundamental difference in the melanin property being measured. Both the visible and oxidative endpoints depended on melanosome disruption as the threshold change being detected. Overall, the estimates returned by the "optical" and "visible" endpoints were roughly similar.

4. DISCUSSION

4.1 Variability of estimates of the melanin absorption coefficient
There are relatively few published values for the absorption coefficient of skin or RPE melanosomes. The values reported range from a high of about 9600 cm^{-1} to a low of about 80 cm^{-1} at mid-visible wavelengths[17,19,24]. Some of this variation may be due to species variation, sample preparation, measurement technique, changes in the optical properties caused by the drastic measures required to solubilize melanin for routine spectrophotometric measurements, etc. Therefore, to avoid the complications of these extraneous factors, we have measured the melanin absorption coefficient indirectly, e.g. by laser-induced changes in the visual appearance of a melanosome suspension as well as changes in the photochemical properties of the melanosome. These two quite different approaches nevertheless yielded quite similar values for the absorption coefficient.

4.2 Refinements and limitations in the calculation of the melanosome absorption coefficient
The basis for the current analysis, previously described[17], assumes that the energy deposition from a laser pulse is absorbed in melanin, heating the internal water in the melanosome and causing explosive vaporization at some critical temperature. By measuring or determining the threshold laser energy required to produce melanosome disruption in preparations of melanosomes equilibrated at various initial temperatures, the absorption coefficient, μ_a, is calculated from the negative reciprocal slope of the relationship of threshold laser energy required for disruption vs the initial temperature ($-1/dH_{th}/T_i$). Our previous calculations of the melanosome absorption coefficient used a published, experimentally determined value for the specific heat of generic tissue (dried fat and meat)[21], but incorporated estimates of water content and melanosome density based on skin studies[18,19]. Our revisitation of the RPE melanosome absorption coefficient is updated with a value obtained from direct physical measurements for the density of two classes of bovine RPE melanosomes, although there is still the possibility of a small dehydration artifact introduced by the hypertonicity of the density gradient medium relative to the melanosome's interior. One approach to removing this artifact would be to devise a density gradient medium that is isotonic with respect to the typical mammalian cell interior, typically about 290 mOsm, however, an isotonic medium with sufficient density has not yet been identified. This issue also relates to the uncertainty about the actual water content of the melanosome in situ. As indicated in Figure 5, variations in melanosome water content will change the effective absorption coefficient appreciably. Until the in vivo hydration state of the melanosome in the RPE cell is determined, the calculated value of the melanosome absorption coefficient will remain subject to the qualification that it is based on an estimate of water content.

ACKNOWLEDGMENTS

REFERENCES

1. J. J. Weiter and R. Zuckerman, "The influence of the photoreceptor-RPE complex on the inner retina. An explanation for the beneficial effects of photocoagulation", *Ophthal.* **87**, pp. 1133-1139, 1980.
2. R. K. Crouch, G. J. Chader, B. Wiggert, and D. R. Pepperberg, "Retinoids and the visual process", *Photochem. Photobiol.* **64**, pp. 613-621, 1996.
3. R. Cubeddu, P. Taroni, D.-N. Hu, N. Sakai, K. Nakanishi, and J. E. Roberts, "Photophysical studies of A2-E, putative precursor of lipofuscin, in human retinal pigment epithelial cells", *Photochem. Photobiol.* **70**, pp. 172-175, 1999.
4. L. Feeney-Burns, E. S. Hilderbrand, and S. Eldridge, "Aging human RPE: morphometric analysis of macular, equatorial and peripheral cells", *Invest. Ophthalmol. Vis. Sci.* **25**, pp. 195-200, 1984.
5. A. E. Dontsov, R. D. Glickman, and M. A. Ostrovsky, "Retinal pigment epithelium pigment granules stimulate the photo-oxidation of unsaturated fatty acids", *Free Rad. Biol. Med.* **26**, pp. 1436-1446, 1999.
6. M. L. Wolbarsht, A. W. Walsh, and G. George, "Melanin, a unique biological absorber", *Appl. Opt.* **20**, pp. 2184-2186,

1981.

7. H. M. Swartz, T. Sarna, and L. Zecca, "Modulation by neuromelanin of the availability and reactivity of metal ions", *Annals of Neurology* **32 Suppl**, pp. S69-S75, 1992.

8. N. L. Sakina, A. E. Dontsov, G. G. Afanas'ev, M. A. Ostrovski, and I. I. Pelevina, "The accumulation of lipid peroxidation products in the eye structures of mice under whole-body x-ray irradiation [Russian]", *Radiobiologiia* **30**, pp. 28-31, 1990.

9. M. Porebska-Budny, N. L. Sakina, K. B. Stepien, A. E. Dontsov, and T. Wilczok, "Antioxidative activity of synthetic melanins. Cardiolipin liposome model", *Biochim. Biophys. Acta* **1116**, pp. 11-16, 1992.

10. H. S. Mason, D. J. E. Ingram, and B. Allen, "The free radical property of melanins", *Arch. Biochem. Biophys.* **86**, pp. 225-230, 1960.

11. W. Korytowski, B. Pilas, T. Sarna, and B. Kalyanaraman, "Photoinduced generation of hydrogen peroxide and hydroxyl radicals in melanins", *Photochem. Photobiol.* **45**, pp. 185-190, 1987.

12. R. D. Glickman and K.-W. Lam, "Oxidation of ascorbic acid as an indicator of photooxidative stress in the eye", *Photochem. Photobiol.* **55**, pp. 191-196, 1992.

13. R. D. Glickman, R. Sowell, and K.-W. Lam, "Kinetic properties of light-dependent ascorbic acid oxidation by melanin", *Free Rad. Biol. Med.* **15**, pp. 453-457, 1993.

14. R. D. Glickman, B. A. Rockwell, and S. L. Jacques, "Action spectrum of oxidative reactions mediated by light-activated melanin", in *Laser-Tissue Interaction VIII*, S. L. Jacques, Editor, Proc. SPIE Vol. **2975**, pp. 138-145, 1997.

15. M. Rozanowska, A. Bober, J. M. Burke, and T. Sarna, "The role of retinal pigment epithelium melanin in photoinduced oxidation of ascorbate", *Photochem. Photobiol.* **65**, pp. 472-479, 1997.

16. R. D. Glickman, S. L. Jacques, J. A. Schwartz, T. Rodriguez, K.-W. Lam, and G. Buhr, "Photodisruption increases the free radical reactivity of melanosomes isolated from retinal pigment epithelium", in *Laser-Tissue Interaction VII*, S. L. Jacques, Editor, Proc. SPIE Vol. **2681**, pp. 460-467, 1996.

17. S. L. Jacques, R. D. Glickman, and J. A. Schwartz, "Internal absorption coefficient and threshold for pulsed laser disruption of melanosomes isolated from retinal pigment epithelium" in *Laser-Tissue Interaction VII*, S. L. Jacques, Editor, Proc. SPIE **2681**, pp. 468-477, WA, 1996.

18. S. L. Jacques, D. J. McAuliffe, I. H. Blank, and J. A. Parrish, "Controlled removal of human stratum corneum by pulsed laser", *J. Invest. Dermatol.* **88**, pp. 88-93, 1987.

19. S. L. Jacques and D. J. McAuliffe, "The melanosome: threshold temperature for explosive vaporization and internal absorption coefficient during pulsed laser irradiation", *Photochem. Photobiol.* **53**, pp. 769-775, 1991.

20. D. Rickwood, T. Ford, and J. Graham, "Nycodenz: A new nonionic iodinated gradient medium", *Anal. Biochem.* **123**, pp. 23-31, 1982.

21. A. N. Takata, L. Zaneveld, and W. Richter, "Laser-induced thermal damage in skin", USAF School of Aerospace Medicine Report SAM-TR-77-38. Brooks AFB, TX, p 22, 1977.

22. M. H. van Woert, "Oxidation of reduced nicotinamide adenine dinucleotide by melanin", *Life Sci.* **6**, pp. 2605-2612, 1967.

23. E. V. Gan, H. F. Haberman, and I. A. Menon, "Oxidation of NADH by melanin and melanoproteins", *Biochim. Biophys. Acta* **370**, pp. 62-69, 1974.

24. L. Goldman, "The skin", *Archives of Environmental Health* **18**, pp. 434-436, 1969.

Using Optical Coherence Tomography to Elucidate the Impact of Fixation on Retinal Laser Pathology

Michelle N. McCall[a], Curtis J. Harkrider[a], Vincent Deramo[a], Sarah F. Bailey[a], Katrina P. Winter[a], Benjamin A. Rockwell[c], Dave Stolarski[d], Cynthia A. Toth[a,b]

a. Duke University Medical Center, Department of Ophthalmology, Durham, NC 27710
b. Duke University, Department of Biomedical Engineering, Durham, NC 27710
c. Air Force Research Laboratory, Brooks AFB, TX 78235-5215
d. Litton-TASC, San Antonio, TX 78228

ABSTRACT

Purpose: The direct comparison of *in-vivo* OCT images with fixed tissue sections assumes the fixation of tissue has no effect on the size and configuration of final pathology images such as light micrographs. Fixation artifact has been a concern in numerous studies of the pathology of retinal laser lesions. [1-3] We tested this hypothesis.

Methods: The Humphrey OCT model 2000 with a custom mirror and lens assembly was used to scan tissue phantoms and both fresh and fixed *ex-vivum* tissue samples. The optical configuration was determined by optimization of the contrast and signal strength on tissue phantoms. Fresh porcine retinas were scanned using this optimal configuration, then fixed using either glutaraldehyde or formalin. OCT images were taken of the tissue at various stages during the fixation process. Additionally, we examined fixed retinal tissue containing retinal laser lesions as a part of our study of ultrashort-pulsed laser effects on the macacca mulatta retina. Histologic sections were prepared and evaluated.

Results: In this presentation, we describe our optical setup and image optimization process and assess the effects of glutaraldehyde and formalin processing on OCT image quality. The OCT images of glutaraldehyde-fixed laser lesions are compared with similar images of laser lesions *in-vivo*. Fixation artifacts appeared on OCT at 2 to 24 hours. Opacification of the lumen of large vessels was seen at 2 hours with both glutaraldehyde and formalin, while fixation induced retinal detachment appeared at 24 hours. Overall, there was a greater delineation of the laser lesions by OCT at 24 hours when compared to at 1 or 2 hours of fixation. This appeared to be, in part, due to the focal separation of tissue layers induced by fixation.

Conclusions: Fixation induced changes in OCT scans of retinal tissue are present as early as 2 hours after immersion in fixative. Although both glutaraldehyde and formalin fixation preserve much of the tissue structure, these method of fixation have a significant effect on OCT imaging of both normal retinal tissue and laser lesions.

1. INTRODUCTION

Optical coherence tomography (OCT) is an imaging technique that uses low-coherence interferometry to localize the signal from a specific depth in tissue. This allows high-resolution visualization of structures in tissue similar to that offered by histological examination. However, instead of physically cutting the tissue into sections, the "visual slice" of tissue can be viewed *in situ* or even *in vivo* without damaging or disturbing the tissue in any way. While stained histologic sections give image contrast by variation in light absorption and color, OCT image contrast is a function of tissue scattering properties. In past studies, when the targeted tissue has been lased, there have been artifacts discovered in the histologic sections that are not visible on the OCT images. Birgruber et al. speculated that fixation of laser retinal lesions caused retinal swelling and mechanical ruptures due to incomplete fixation and thermal induced changes. OCT can be

compared to light micrographs to identify and analyze the preparational artifacts incurred during processing[3]. OCT and light microscopy analyze and describe tissue structure and disease processes differently[4]. Marshall et al reported that fixation with 2.5% Gluteraldehyde in 0.1M Sodium Cacodylate (pH7.4) produces no significant change in the OCT images of the retina. They did not describe how this was tested. In this study we evaluated the impact of specimen preparation with two fixation techniques on the final appearance of the tissue on OCT.

2. PURPOSE

We compared in-vivo and ex-vivum OCT images with light micrographs to identify the impact of fixation on OCT appearance of tissue components and laser lesion size and configuration. We also compared OCT imaging to light micrographs of these lesions.

3. METHODS

3.1   Experimental Systems

Ex-Vivum Laser Setup
After testing the laser intensity in the peripheral retina, cw argon laser was directed through a 1.47x Mainster wide field lens, to the retina of 8 fresh, enucleated porcine eyes purchased from a slaughterhouse.

Laser treatment was applied one disk diameter from the optic nerve in a 4x4 grid pattern as diagrammed below. Seven of these lesions were 200 micron, 550-600mW, moderate, white marker lesions while nine of the lesions were 50 micron, 230-290mW, mild to moderate, gray-white lesions. The lesion rows were shot approximately 1 mm apart. There was no change in energy between lesions within each group.

```
★ ✳ ✳ ✳              ★ ✳
★ ✳ ✳ ✳      ◯       ★ ✳
★ ✳ ✳ ✳   Optic Nerve   ★ ✳
★ ★ ★ ★              Test shots
      Grid
```
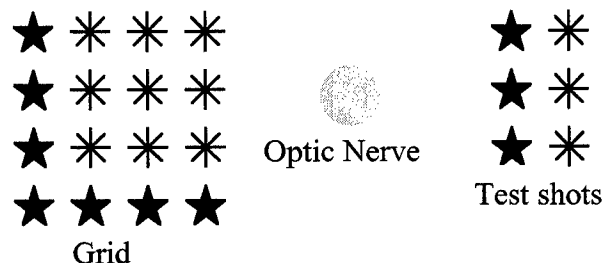
In-Vivo Laser Setup
The animals involved in this study were procured, maintained, and used in accordance with the Federal Animal Welfare Act and the "Guide for the Care and Use of Laboratory Animals," prepared by the Institute of Laboratory Animal Resources, National Research Council.[5]

Ultrashort laser pulses had been delivered to the retina of mature macacca mulatta in a 5x5 grid in the macula and the paramacula. Ten marker lesions per grid were delivered at 2.8W for 4ms approximately 200 microns apart. Sixteen lesions in each grid were created with the ultrashort laser set at 810nm wavelength with 55fs chirped pulsewidth and with energy ranging from 0.1μJ to 0.4μJ.

OCT System Setup
The OCT scans were performed used a Humphrey OCT Model 2000. The Humphrey OCT system is designed for performing *in-vivo* scans of the human fundus and therefore incorporates the imaging properties of the human eye into the optical design. After enucleation, cornea and lens of the porcine eyes gradually become opaque. While OCT can still be performed, the images are much clearer if the anterior chamber and lens are removed prior to scanning. To compensate for the anterior chamber removal, a 50-diopter glass lens was placed anterior to the eyecup. Additionally, a gold-plated flat mirror was used to redirect the beam on to the bench top, as shown in figure 1.

The mirror was positioned at an approximately 45-degree angle and the external lens was aligned to minimize distortion of a bar target. The eyecup was then placed underneath the external lens and raised up until the liquid in the eye contacted the posterior surface of the external lens. The reference arm length of the OCT was adjusted to coincide with the total optical path length of the sample arm such that we were scanning the retina. The objective lens of the Humphrey scanners was focused to maximize the back reflection of the retinal layers. The polarization control was also adjusted to give maximum signal. The scan beam was steered over the laser lesions using the x-,y-transverse galvanometer controls. The scan power of the superluminscent diode source was 750 μW at a center wavelength of 845 nm.
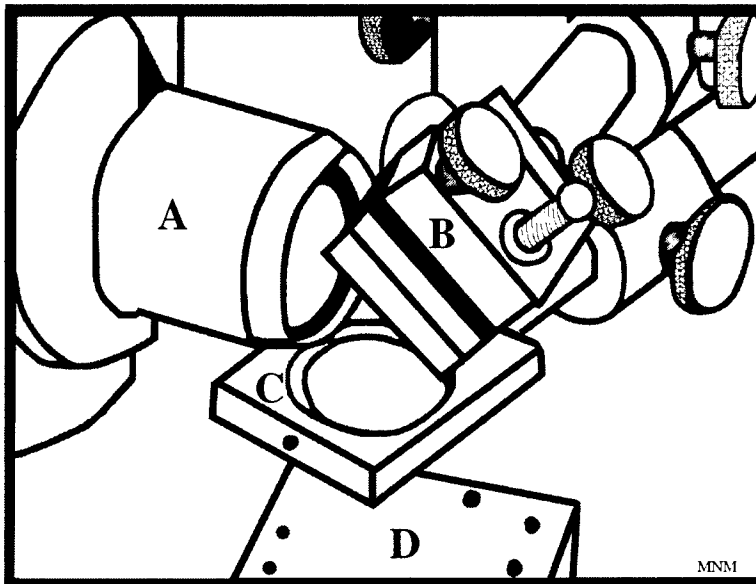
Figure 1. Arm adapter for Humphrey OCT system.
A. Humphrey OCT lens system; B. Gold-plated flat mirror;
C. 50-Diopter Glass Lens; D. Stage

3.2   Porcine Tissue Preparation/Examination

Fresh porcine eyes were obtained from a local abattoir. The eyes were prepared and laser lesions created within 3 hours of enucleation. After laser delivery, the anterior chambers were removed and OCT scans were done before fixation. Four eyes were placed in 10% neutral buffered formalin and 4 eyes in 2% gluteraldehyde. The right and left eyes of each group were alternated so that each fixation group had 2 right and 2 left eyes. The vitreous was removed 45 to 60 minutes post fixation. Prior to scanning, the eyecups were filled with buffer. Sodium Calcodylate buffer was used for gluteraldehyde fixed tissue. Phosphate Buffered Saline was used in formalin fixed tissue. OCT scans were performed initially, at 2 hours, and 1 day for both fixative groups. Scans were alternated to prevent bias. Light micrographs were obtained from 2 eyes from each group. The eyes fixed in formalin were embedded in paraffin, microtomed in 5-micron sections, and stained with Hematoxylin and Eosin. Gluteraldehyde fixed eyes were embedded in Spurr's resin, microtomed in 0.5-micron sections, and stained with Toluidine Blue.

3.3   Primate Tissue Preparation/Examination

Enucleated globes had been incised and immersed in 3% Glutaraldehyde and 0.1M sodium cacodylate buffer immediately after euthanasia. After 10 minutes, the anterior segment had been removed and the posterior eyecup placed back into the fixative. After approximately one month in fixative, the globes were removed from the Gluteraldehyde fixative and filled with 0.1M sodium cacodylate buffer for OCT scanning.

4. RESULTS

Fixation did not preclude OCT imaging. Retinal images were obtained from all specimens at all timepoints. Sodium cacodylate buffer solution appeared to create a diffuse fine speckle artifact in the solution over the tissue. This fine speckled artifact was very infrequently seen in the neutral buffer solution over formalin fixed lesions. The fine reflectance pattern in the overlying cacodylate buffer solution may have diminished the very fine resolution of OCT imaging of glutaraldehyde fixed lesions.

Fixation artifacts appeared within the retinal tissue on OCT at 2 to 24 hours. Both glutaraldehyde and formalin fixation increases the overall reflectivity of retinal tissue in the 1 to 2 hour post-fixation range. More striking, however, was the opacification of the lumen of large vessels with secondary increased shadowing from the vessels as was seen at 2 hours with both gluteraldehyde and formalin fixation. In addition, fixation induced retinal detachment appeared at 24 hours with both fixatives.

There was a greater delineation of the laser lesions by OCT at 24 hours of fixation when compared to 1 or 2 hours of fixation. This increase in delineation over time, appeared to be due to variations in the fixation effects on laser treated tissue in contrast to the surrounding tissue. This delineation of laser lesions occurred with both types of fixation.

While retinal lesions of 50 microns in size and greater were clearly identified by this modified OCT imaging system, the transverse resolution of the Humphrey OCT system with the added reflective mirror-arm was not sufficient to measure laser lesions smaller than 50 microns.
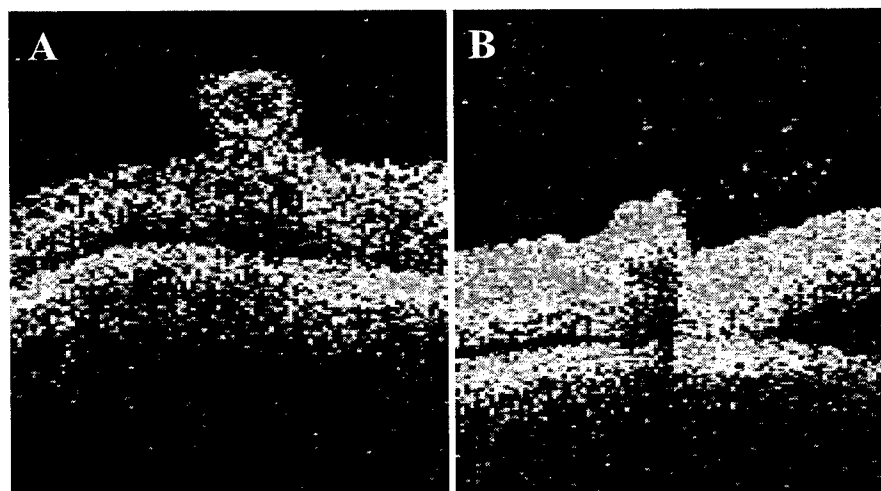
Figure 2. Retinal tissue over time. Tissue fixed in 10% Neutral Buffered Formalin.
A. Initial tomograph; B. 24 hour tomograph.
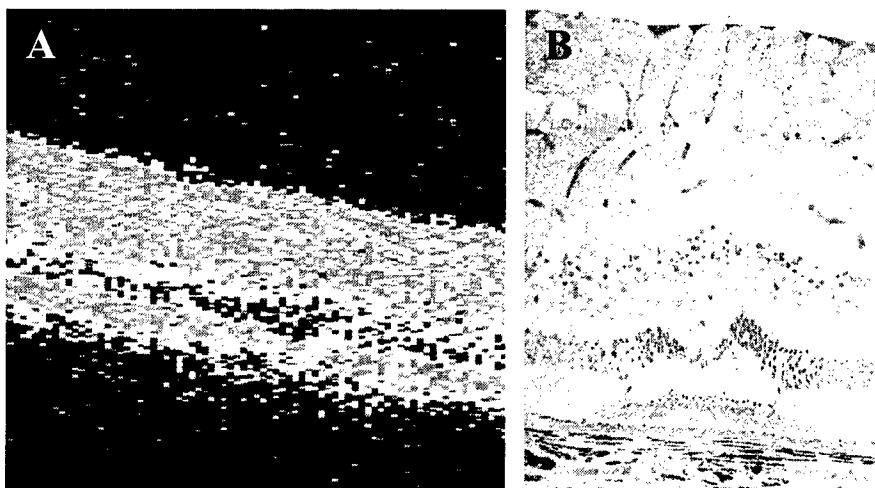
Figure 3. Gluteraldehyde fixed 50μm, 230-290mW, moderate, gray-white
lesion: A. 24 hour tomograph; B. Light micrograph stained with Toluidine blue.
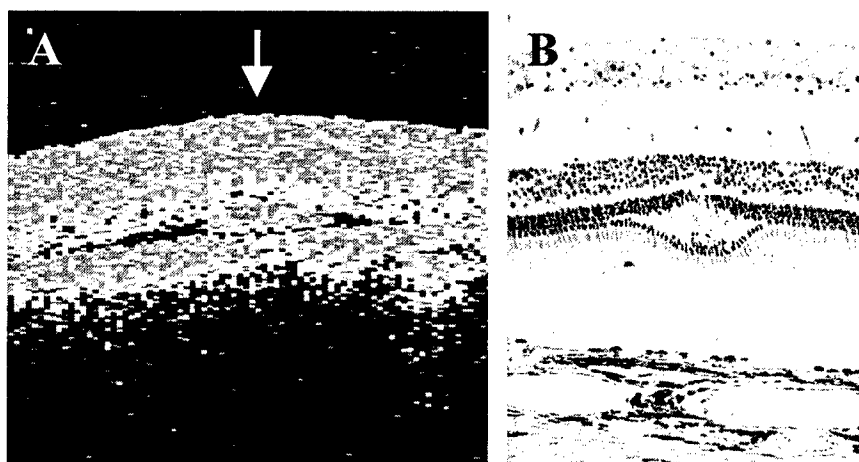
Figure 4. Formalin fixed 50μm, 230-290mW, moderate, gray-white
lesion: A. 24 hour tomograph; B. Light micrograph stained with H&E.

5. DISCUSSION

The OCT imaging of glutaraldehyde or formalin-fixed normal retinal tissue and laser-treated retinal tissue changed with the duration of fixation. Several fixation effects were probably responsible for the change in the retinal appearance on OCT over time. Fixation-induced changes in reflectivity of retinal structures due to chemical changes in proteins and cell membranes is the most likely cause for the overall increase in tissue reflectivity. The fixation-induced changes in serum proteins, probably caused the notable change in OCT scans of large (> 100 micron) vessels in this study. Fixation of tissue may be associated with variable shrinkage of different tissue layers and thus with separation of layers. This appeared in the retinal tissue as a detachment on OCT at 24 hours.

Several fixation-induced effects were probably also responsible for the more pronounced imaging of the laser lesion at 24 hours when compared to after one hour of fixation. These effects include: fixation induced retinal detachment, possible difference in fixative effect on tissue proteins that were treated with thermal laser versus untreated and possible difference in laser treated versus surrounding tissue contraction due to fixation.

The smallest laser lesions were found on light micrographs of the fixed tissue but could not be imaged with the modified OCT system. The longitudinal resolution of the OCT image is determined by the temporal coherence of the superluminescent diode source. The coherence length, measured to be about 15 microns in water, is inversely proportional to the spectral bandwidth of the source. The transverse resolution is limited by the large spot size of the scanning beam. There is a trade-off between depth-of-focus and transverse resolution. Since the Humphrey system can scan about a 3mm depth without focal adjustment, the Rayleigh range is estimated to be 1.5mm. Given the 845-micron wavelength, this limits the $1/e^2$ spot diameter to approximately 40-microns at best focus. This means structural detail in the lateral direction smaller than 40-microns cannot be resolved with the Humphrey scanning optics. It is important to note that the optical system design includes the optics of the human eye. Since our samples do not include the anterior chamber or crystalline lens, refractive power must be added using an external lens. A 50 Diopter plano-convex lens is used to focus the beam on to the retina of the ex-vivum samples. The plano side of the lens is placed in contact with the buffer solution inside the globe of the eye. While this increases the back focal distance of the lens, the lens-liquid contact does not change the optical power of the lens. Given the large f-number of the optical system (about f/40), the aberrations introduced by the external lens are inconsequential.

When selecting parts for the OCT arm adapter, we chose to use a protected-gold mirror coating instead of standard protected-aluminum. At the measured wavelength of the Humphrey OCT, 845nm, aluminum has a drop in reflectivity. Therefore, we used a protected-gold mirror because it has better than 97% reflectivity at 845nm, compared to 85% for protected aluminum. This increases the signal to noise ratio over that of the aluminum mirror by allowing more light to reach the sample.

6. CONCLUSION

OCT imaging of fixed tissue can be affected by the fixation. Thus caution must be used in interpreting OCT imaging studies utilizing fixed tissue. Although the structure may be maintained, there are fixation-induced artifacts that may impact interpretation of the images. With increased time in fixative, argon laser lesions, for example, become more prominent in OCT imaging in contrast to adjacent tissue .

OCT scanning of fixed retinal tissue may be used to localize laser lesions for sectioning. The current OCT setup did not allow imaging of laser lesions of < 50 microns in diameter, but was quite good at imaging larger lesions. This imaging could be used to aid in orienting retinal tissue for sectioning.

7. REFERENCES

1. Lorenz, B. Morphologic changes of chorioretinal argon laser burns during the first hour post exposure. Lasers in the Life Sciences 1988; 2(3): 207-226.
2. Margo, C.E., Lee, A. Fixation of whole eyes: the role of fixative osmolarity in the production of tissue artifact. Grafe's Arch Clin Exp Ophthalmol 1995; 366-370.
3. Birngruber, R, Hee, M.R., Boppart, S.A., Fujumoto, J.G., Swanson, E.A., Toth, C.A., Di Carlo, C.D., Cain, C.P., Noojin, G.D., Roach, W.P. In-Vivo imaging of the development of linear and non-linear retinal laser effects using optical coherence tomography in correlation with histopathological findings.
4. Toth, C.A., Narayan, D.G., Boppart, S.A., Fujuimoto, J.G., Birgruber, R., Cain, C.P., DiCarlo, C.D., Roach, W.P. A comparison of retinal morphology viewed by optical coherence tomography and by light microscopy. Arch Ophthalmol 1997; 115: 1425-1428.
5. C.P. Cain, C.A. Toth, C.D. DiCarlo, C.D. Stein, G.D. Noojin, D.J. Stolarski, and W.P. Roach, "Visible retinal lesions from ultrashort laser pulses in the primate eye." Investigative Ophthalmology & Visual Science. 36(5):879-888, 1995.
6. Chauhan & Marshall. Interpretation of optical coherence tomography images of the retina. IOVS 40(10): 2332-42;1999.

ACKNOWLEDGMENTS

Laser Induced Retinal Shock Waves and Bubbles and Their Dependencies on The Thermo-Mechanical Properties of Melanosomes

Bernard S. Gerstman and Jinming Sun
Department of Physics, Florida International University, Miami, FL 33199
(gerstman@biophys.fiu.edu)

ABSTRACT

We have developed a detailed theoretical model that allows for the prediction of the shockwave strength and bubble size that are expected to result in the retina as a result of a laser pulse of any pulse duration or energy. The results of the calculations for the shockwave and bubble size depend on the absorption coefficient and unknown thermo-mechanical properties of the absorbing melanosomes. We discuss how the shock strength and bubble size depend on melanosome parameters such as absorption coefficient, thermal coefficient of expansion and bulk modulus. We also describe experiments that could be performed to measure these coefficients in spite of the difficulty presented by the small size of the melanosomes.

Key Words: laser, retina, damage, shock, bubble, vaporization, melanosome, thermal, mechanical

1. INTRODUCTION

Bubble formation and shock wave generation by photoacoustic means have been the focus of recent works by a variety of authors.[1-7] A main reason for this interest is that pulsed lasers are used on an increasing basis in medical and commercial applications. A true quantitative understanding of the various physical processes involved in the interaction of laser light with biological tissue is crucial for setting safety standards[8] and for maximizing the benefit and minimizing the risk in intraocular laser surgery.[9,10] The subject is also interesting from the standpoint of applied physics and material science for investigations of stress damage in polymers.[11] From the standpoint of fundamental physics, the subject is a highly non-linear problem with close connections to systems found in acoustics, hydrodynamics, and bubble dynamics.[12]

There have been many interesting experiments probing bubble motion after laser deposition in a solid absorber.[1-4] However, the small size of biologically important absorbers, such as the micron size melanosomes that dominate absorption in the retina, lead to experimental difficulties in providing a clear and complete picture of pressure effects and bubble dynamics. It is known that purely thermal effects can be understood in terms of transit times across the absorber.[13] The thermal transit time across a micron size particle such as a melanosome is approximately 10^{-6} seconds (1 µsec) and for laser pulses of shorter duration than this transit time, the thermal effects should be independent of the pulse duration. Analysis of bubble generation[14] appears to support this concept of thermal confinement. It was shown recently[15] that pressure generation within the melanosome does not exhibit independence of pulse duration for durations shorter than pressure transit times, i.e. stress confinement is not valid within the melanosome. Therefore, exploding a melanosome through tensile stress generation requires less and less energy as the pulse duration is

shortened. Unanticipated results such as this show the necessity of a full treatment of the system based upon the fundamental principles of physics, i.e. a "first principles" treatment We have carried out such an investigation[15,16] and summarize the results in this paper.

2. PHYSICAL MODEL

The biophysical phenomena that we are interested in, shock waves and bubbles, emanate from the strongest absorbing particles in the retina. The absorbers are melanosomes that are approximately one micrometer (1 μm) in size that are located in the retinal pigment epithelium cells. The melanosomes are unevenly spaced on the order of a few microns apart. The cellular fluid that the melanosomes are immersed in is treated as water.[14] We treat shock wave and bubble generation in a single melanosome as independent of events occurring in other melanosomes. The justification for this is straightforward. All melanosomes are illuminated by the same laser pulse and therefore generate their shockwaves and bubbles simultaneously. Therefore, the shockront and bubble generated by any single melanosome have had time to become fully formed and propagate away from their melanosome before the shockfront or bubble from any other melansome have had enough time to impact the first one. This allows us to use a model in which we investigate only a single melanosome immersed in water. In order to simplify the calculations, we assume that the melanosome is spherical. (Future work will need to be carried out to determine the effect of reducing the symmetry of the melanosome to the more realistic elliptical shape.)

The fundamental equations describing the system are explained in Refs. 15 and 16, and are summarized here. Laser energy absorption in the melanosome is assumed to be uniform with the rate of energy absorption $\dot{I}_e$ in (Joules/gram·second) given as[14]

$$\dot{I}_e = \frac{3I_o}{4a\tau_o\rho_o}\left[1 - \frac{1}{2a^2\alpha_L^2}\left(1 - e^{-2a\alpha_L}(1 + 2a\alpha_L)\right)\right] \tag{1}$$

where I_o is the laser fluence in J/cm^2, τ_o is the laser pulse duration in seconds, a is the melanosome radius is cm, ρ_o is the static melanosome density (1.35 g/cm^3) and α_L is the melanosome's absorption coefficient for the laser light.

The response of the material, including the large scale expansion of the medium if it vaporizes, is determined by calculating P,V,T,S. The calculation is done assuming spherical symmetry. We start the calculation by setting up a radial system of grid points r_I (400/μm is found to be a good compromise between accuracy and speed). Each grid point is initially equally spaced in the radial direction. Due to small scale expansion and contraction due to pressure gradients, or large scale expansion of the medium due to vaporization, the position of the grid points can change. The position of mass unit i which is originally at r_i, is given at any later time t by u(i,t). Newton's equation of motion both inside the absorber and outside can be expressed as

$$\rho\ddot{u} = -\nabla_u P \tag{2}$$

where ρ is the time varying density at the position u, and P is the time varying pressure at u.

Conservation of mass in spherical geometry gives the following relation between the initial position r of a mass point and its corresponding position u at a later time

$$\rho_o r^2 = u^2 \rho \frac{\partial u}{\partial r} \qquad (3)$$

Energy conservation in the absorber is expressed as

$$\dot{I}_e = T\dot{s} - \frac{\lambda}{\rho}\nabla_u^2 T = c_v \dot{T} + B\alpha T\dot{v} - \frac{\lambda}{\rho}\nabla_u^2 T \qquad (4)$$

where $\dot{s}$ is the time rate of change of the specific entropy, λ is the thermal conductivity of the absorber, c_v is the specific heat of the absorber, B is the bulk modulus of the absorber, α is the thermal coefficient of expansion of the absorber and v is the specific volume ($v=1/\rho$). The equivalent equation for the medium is

$$T\dot{s} - \frac{\lambda}{\rho}\nabla_u^2 T = 0 \qquad (5)$$

where $\dot{I}_e \equiv 0$ because the medium is transparent. The simplification leading to the right side of Eq. (4) for the absorber is based upon the assumption that the absorber does not change phase and that since it remains in the solid phase its B and α remain constant. For the medium which can vaporize to form bubbles, this simplification is not applicable.

Finally, the equation of state (EOS) for the absorber is also simple because of the assumption about constant B and α and is

$$\frac{\dot{v}}{v} = -\frac{\dot{P}}{B} + \alpha \dot{T} \qquad (6)$$

using the mathematical identity $\dot{v} = \partial v / \partial t + u \cdot \nabla_u v$, Eq. (6) becomes

$$\nabla_u \cdot \dot{u} = -\frac{\dot{P}}{B} + \alpha \dot{T} \qquad (7)$$

For the aqueous medium, an EOS as simple as Eq. (7) is not possible for the same reasons explained after Eq. (5). In order to take into account the phase changes of the medium we use an EOS based upon the NBRS Steam Tables of water.[17]

With the governing equations (1-7) we can now calculate P,V,T including shock waves and bubble formation for a laser of any duration and energy absorbed by any solid absorber with any absorption strength, and any thermo-mechanical properties B and α. The numerical algorithm used in the computations is described in Ref. 16.

3. DEPENDENCIES OF SHOCK WAVES AND BUBBLES ON B AND α OF THE ABSORBER

Figure 1 displays the results of a single calculation. It demonstrates that we can determine all the relevant thermodynamic response of the system with a single calculation. Figure 1a shows the propagation of the shock front in the medium and Fig. 1b shows the expansion of the bubble from

the surface of the melanosome. The times listed on the graphs are the observation times after the start of the laser pulse. We note that at early times (t<0.4 ns) the shock front is moving through the aqueous medium at speeds significantly greater than the speed of sound in water which is 1500 m/s. As the strength of the shock front decreases, we see that its speed of propagation also decreases. In addition, we note that the shock front is always propagating outwards much faster than the bubble wall is expanding and therefore the main shock front has disappeared out into the medium before the bubble begins to grow. However, there is a train of trailing shock fronts due to residual "ringing" of the melanosome that are still in the vicinity of the melanosome at the same time that the bubble is growing and this necessitates the full thermodynamic treatment that includes the non-linear coupling between pressure and volume changes.

For this example, we used the following values for the laser properties: τ_o=100 psec, I_o=3.5 J/cm^2. The melanosome values used were a=1 μm, α_L=10,000 cm^{-1}, ρ_o=1.35 g/cm^2, c_v=2.51 J/(g·K), thermal conductivity λ=5.56x10^{-3} J/(cm·K·s), α=2.98x10^{-5} K^{-1}, B=39.4 GPa. The values for α and B for melanosome are not known and the values that we chose are taken fron graphite based on its chemical similarity. However, the true values of α and B for melanosomes may be very different and we know show how the results of our calculations for shockwaves and bubble size will change depending on the actual size of α and B.

3.1 Dependence on Melanosome's Absorption Coefficient α_L

The greater the absorption coefficient of the melanosome, the greater fraction of incident laser energy will be absorbed. Therefore, greater α_L implies that a smaller I_o is required in order to get the same pressure and bubble generation. The following table uses eq. (1) to show how the fluence scales inversely with the absorption coefficient.

Table I

α(cm^{-1})	I_o(J/cm^2)
1,000	1.000
5,000	0.260
10,000	0.175

3.2 Dependence on Melanosome's Thermal Expansion Coefficient α

Upon absorption of laser energy the temperature rises are effectively instantaneous, limited in repsonse time only by atomic molecular scale processes like electron-phonon coupling. These temperature rises then lead to pressure buildup which are relieved by the expansion of the melanosome. The most extreme case is when the temperature rises so fast that the melanosome has no time to expand. This corresponds to ΔV=0 in eq. (6) and a maximum pressure rise of

$$\Delta P_{max}= B\alpha\Delta T_{max} \tag{8}$$

Since the pressure buidup and expansion of the melanosome create the pressure changes in the medium, Eq. (8) demonstrates that the strength of the shock front in the medium should depend strongly on α. Figure 2a shows this dependence. All curves were generated using the same laser

pulse. The values for the melanosome parameters are the same as used in Fig. 1 except for the variations in α. Figure 2a shows that the strength of the shockfront immediately outside the melanosome scales linearly with α. At locations further out from the melanosome, the linear dependence on α no longer holds because of the non-linear decay of the shock front as it propagates away from the melanosome.

The dependence of the pressure on α displayed in Fig. 2a is as expected from eq. (8). The results displayed in Fig. 2b are more surprising. In Fig. 2b we show that the size of the bubble also depends on the value of the thermal expansion coefficient α. This is surprising because it was assumed[14] that bubble formation is a result only of thermal transfer of energy causing vaporization. The dependence of bubble size on α shows that the mechanical pulsating of the melanosome also plays a role in bubble formation.

3.2 Dependence on Melanosome's Bulk Modulus B

Equation 8 shows that the pressures generated will depend on the bulk modulus of the melanosome. By itself, eq. 8 implies a linear relationship. However, the presence of P in the equation of motion, eq. 2, causes the pressure to depend in a non-linear fashion on B, and to have a more complicated dependence than α. This nonlinear dependence is displayed in Fig. 3. The shorter the pulse duration, the greater the effect on the pressure generation when using a different value of B.

4. PROPOSED EXPERIMENTS TO MEASURE α AND B

Figures 2 and 3 show how the response of the melanosome depends on the thermal expansion coefficient and bulk modulus of the melanosome. The small (micrometer) size of the melanosome makes it difficult to carry out experimental measurements directly on the melanosome itself. However, it is possible to make measurements in the surrounding medium that will give these parameters, as explained in detail in Ref. 15.

Because of a mismatch in the mechanical impedance between the melanosome and the surrounding medium, pressure waves traveling from the center of the melanosome will be partially reflected at its surface back towards the center. After reflecting off the center, a second pressure wave will travel out towards the surface and generate a second pressure wave in the medium. This melanosme "ringing" process will continue to send pressure signals into the medium, with a time delay between the signals of $\tau_c = a/c$, where 'a' is the melanosome radius and $c = \sqrt{B/\rho_o}$ is the speed of sound inside the melanosome. Therefore, instead of making a measurment directly on the melanosome, if an acoustic transducer can be placed in the medium several microns away from a melanosme of known size and used to measure the time between pressure peaks in the medium, this will give c and therefore B of the melanosome. Once B is known, a measurement of the amplitude of the pressure signal in the medium will allow the determination of α.

5. SUMMARY

We have described in this paper our first principles calculations for the thermo-mechanical repsonse of a melanosome in the retina upon absorption of laser light. This allows us to predict the

size and strength of all potentially biologically damaging responses such as tensile stresses, shock waves, vaporization, temperature rises, etc. This model is applicable to any spherical absorber in any medium.

We have shown how the melanosome response depends strongly on its absorption coefficient and thermal expansion coefficient, and less strongly on its bulk modulus. We have also described experiments that might allow the measurement of these parameters in spite of the micrometer size of the absorbers.

ACKNOWLEDGEMENTS

REFERENCES

1.	A. Vogel, S. Busch and U. Parlitz, J. Acoust. Soc. Am. **100**, 148, 1996.

2.	M. Frenz, G. Paltauf and H. Schmidt-Kloiber, Phys. Rev. Lett., **76**, 3546, 1996.

3.	O. Yavas, P. Leiderer, H. K. Park, C. P. Grigoropoulos, C.C. Poon, W.L. Leung, N. Do, and A.C. Tam, Phys. Rev. Lett., **70**, 1830, 1993.

4.	M. Strauss, *et. al.*, Proc. SPIE **2975**, 261, 1997.

5.	E.J. Chapyak, R.P. Goodwin and A. Vogel, Proc. SPIE **2975**, 335, 1997.

6.	C.P. Lin and M.W. Kelly, Appl. Phys. Lett. **72**, 2800, 1998.

7.	C.P. Lin, M.W. Kelly, S.A.B. Sibaya, M.A. Latina, and R.R. Anderson, IEEE J. Sel. Top. Quantum Electron. **5**, 1, 1999.

8.	D. H. Sliney and W.A. Palmisano, AIHA Jour. **20**, 425, 1968.

9.	B.S. Gerstman, Proc. SPIE **2975**, 180, 1997.

10.	T. Juhasz, S.H. Hu, L. Turi, and Z, Bor, Lasers Surg. Med. **15**, 91, 1994.

11.	D.E. Hare, J. Franken, and D.D. Dlott, Chem. Phys. Lett. **244**, 224, 1995.

12.	W. Lauterborn and E. Cramer, Phys. Rev. Lett. **47**, 1445, 1981.

13.	C.R. Thompson, B.S. Gerstman, S.L. Jacques, and M.E. Rogers, Bull. Math. Biol. **58**, 513, 1996.

14.	B.S. Gerstman, C.R. Thompson, S.L. Jacques, and M.E. Rogers, Lasers Surg. Med. **18**, 10, 1996.

15. J.M. Sun and B. Gerstman, Phys. Rev. E, **59**, 5772, 1999.

16. J.M. Sun, B.S. Gerstman, and B. Li, J. Appl. Phys., **88**(5), 2352, 2000.

17. L. Haar, J.S. Gallagher, and G.S. Kell, *NBS/NRC Steam Tables* (Hemisphere, New York), 1984.

Figure 1: Example of (a) shock front propagation and (b) bubble expansion for τ_L=0.1ns, I_o=3.5 J/cm^2, α_{mel}=10,000 cm^{-1}. Times listed on graphs are observation times. Notice that :

speed of pressure waves (>1500 m/s) >> Speed of bubble (<100 m/s)
⇒ Main shock front is long gone before bubble wall arrives (residual ringing)

(a)

(b)
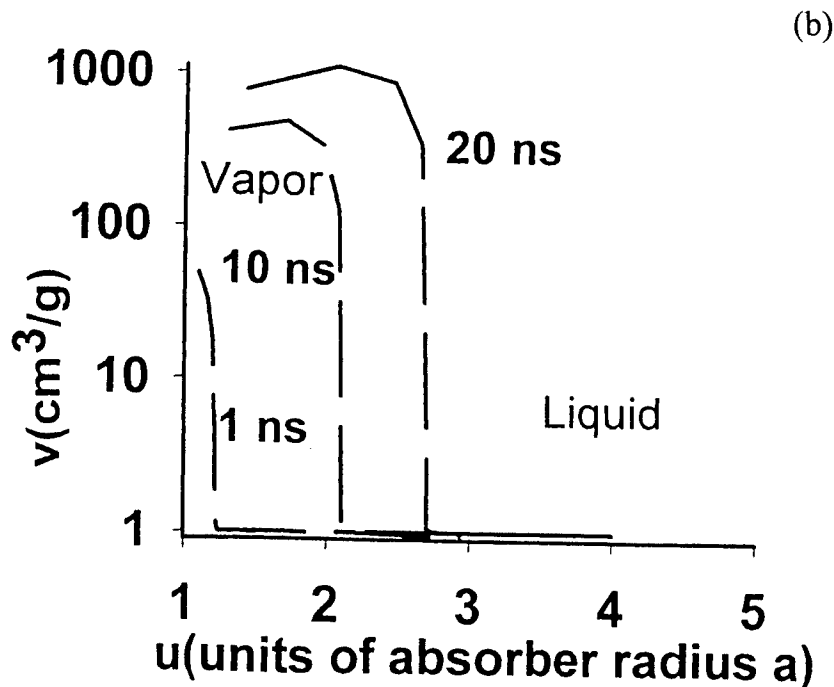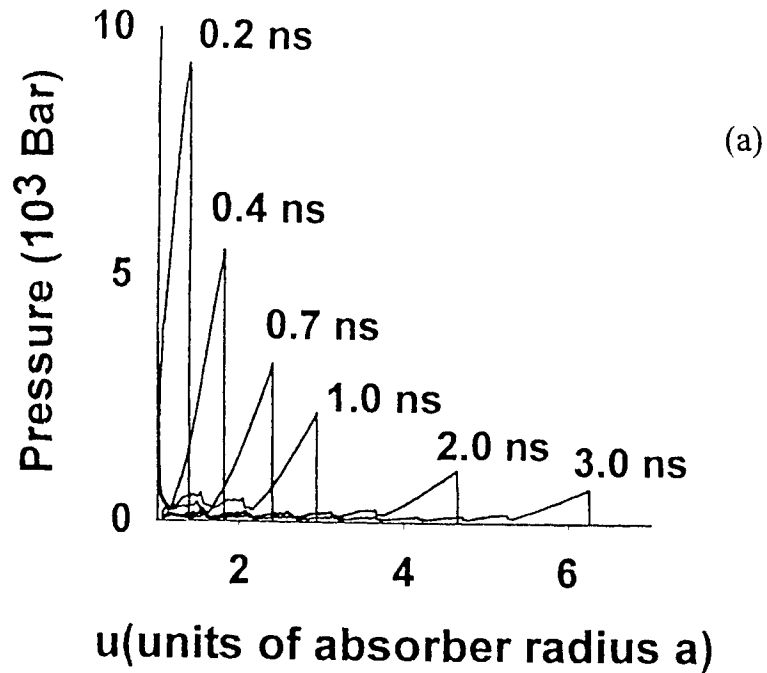
Figure 2: Effects of Coefficient of thermal expansion $\alpha_{thermal}$
(a) Initial shockfront pressure varies linearly

τ_0=0.1 ns I_0=0.875 J/cm^2

———·· α=2.98 10^{-5} K^{-1}

······ α=6 10^{-5} K^{-1}

——— α=1.2 10^{-4} K^{-1}
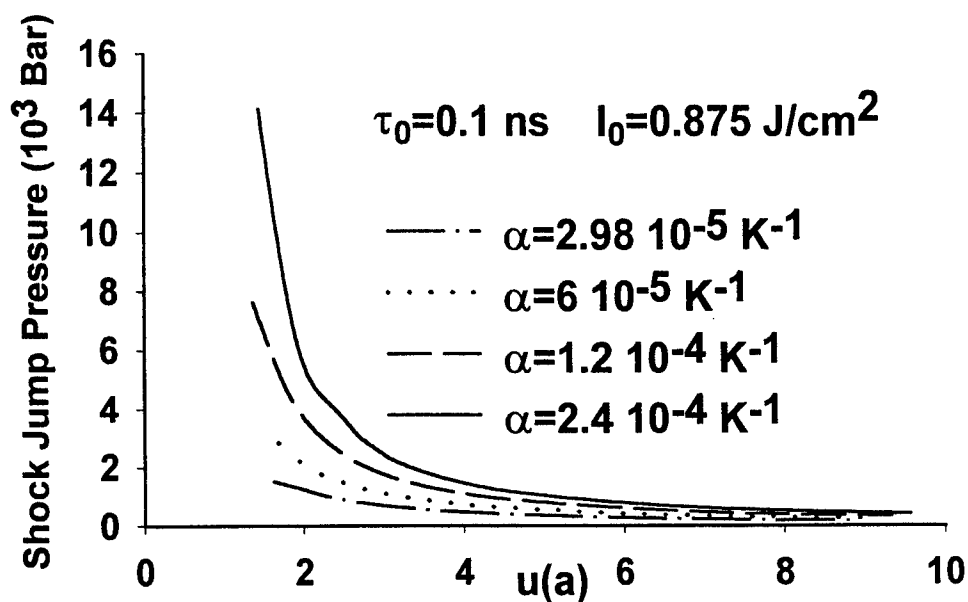
——— α=2.4 10^{-4} K^{-1}

(b)Maximum size of bubble R_{max} depends weakly on α

▼ α=2.98 10^{-5} K^{-1}

▲ α=6 10^{-5} K^{-1}

■ α=1.2 10^{-4} K^{-1}
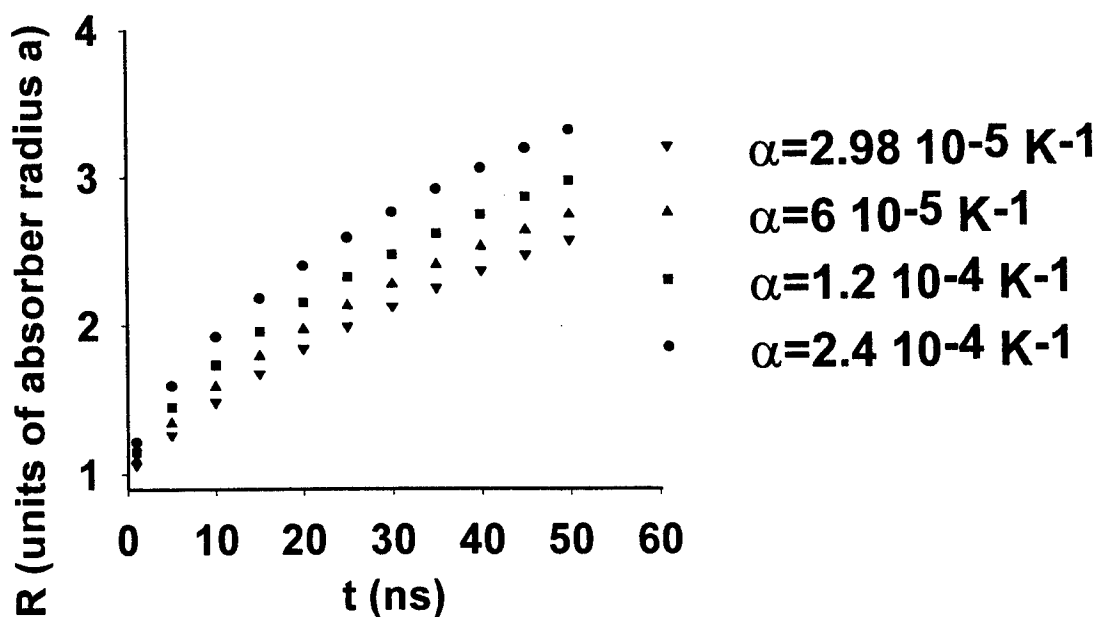
● α=2.4 10^{-4} K^{-1}

Figure 3: Effect of Different Bulk Modulus B on Shockwave

Shockfront pressure jump expected at u=2μm
(1μm outside melanosome)

Fluence $I_o = 0.12$ J/cm^2, $\alpha_{abs} = 10,000$ cm^{-1}, $\alpha_{thermal} = 2.4 \times 10^{-4}$K
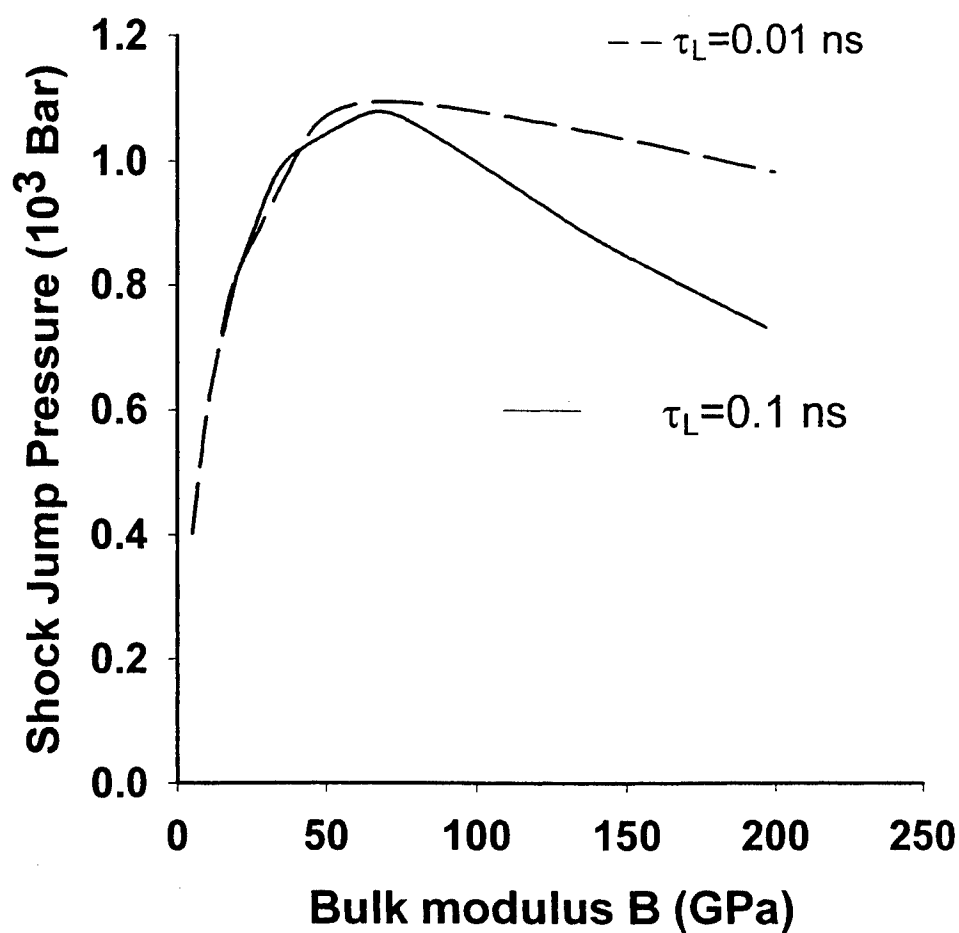
Pulsewidth-Dependent Nature of Laser-Induced DNA Damage in RPE Cells

Rebecca M. Hall[1], Randolph D. Glickman[1,2], Benjamin A. Rockwell[3], Neeru Kumar[2], and Gary D. Noojin[4]

[1]Division of Radiological Sciences, and [2]Department of Ophthalmology, University of Texas Health Science Center at San Antonio, San Antonio, TX; [3]US Air Force Research Laboratory, Brooks AFB; [4]TASC Inc., San Antonio, TX.

ABSTRACT

Ultrashort pulse laser radiation may produce cellular damage through unique mechanisms. Primary cultures of bovine retinal pigment epithelial (RPE) cells were exposed to the output of a Ti:Sapphire laser producing 30 fs (mode-locked) pulses, 44 amplified fs pulses, or continuous wave exposures at 800 nm. Laser exposures at and below the damage threshold were studied. DNA damage was detected using single cell gel electrophoresis (comet assay). Unexposed (control) cells produced short "tails" with low tail moments. In contrast, all laser-exposed cells showed some degree of DNA fragmentation, but the size and shape of the resulting comets differed among the various modalities. CW-exposed cells produced generally light and relatively compact tails, suggesting fewer and larger DNA fragments, while mode-locked laser exposures (30 fs pulses) resulted in large and diffuse comets, indicating the DNA was fragmented into many very small pieces. Work is continuing to define the relationship of laser pulsewidth and intensity with the degree of DNA fragmentation. These results suggest that DNA damage may result from multiple mechanisms of laser-cell interaction, including multiphoton absorption.
Keywords: comet assay, DNA, laser bioeffect, multiphoton, RPE cell, ultrashort pulse

1. INTRODUCTION

The specific aim of this research was to determine if ultrashort laser pulses interact with biological cells through multiphoton processes producing UV-like effects such as DNA damage. Denk et al.[1], and Soini et al.[2], have suggested that ultrashort pulse laser emissions may interact with tissue through a distinct, non-linear mechanism, i.e. multiphoton absorption. When the laser emissions are delivered in an ultrashort pulse, e.g. in the short picosecond or femtosecond domain, these long-wavelength photons are up-converted to a shorter wavelength photon by multi-photon absorption in a suitable chromophore.

An 800 nm laser was used for these experiments. If UV-like effects were to occur, the 800 nm laser radiation would have to undergo some sort of interaction in the tissue resulting in the critical wavelengths necessary to interact with DNA. Two types of interactions with DNA could have resulted. First, if a 260 nm wavelength photon resulted, there could be a direct interaction with the nucleic acids in DNA, which have a strong absorption band between 240 and 280 nm. An indirect interaction with an unidentified chromophore was also possible. Peak et al.[3] demonstrated an absorption band between 340 and 360 nm associated with DNA breakage.

In the present investigation, primary cultures of bovine RPE cells were exposed to various outputs of a Ti:Saphire 800 nm laser. Then DNA damage was assayed using the comet assay. The single cell gel assay is similar to electrophoresis, however, it is more sensitive and able to detect DNA damage at the cellular level. The assay was used to detect single and double strand breaks. The sensitivity provided by the comet assay was necessary because it is difficult to achieve a high radiant exposure over a large area. A smaller exposure area permits a higher energy density, however, only a limited number of cells can be confined to a small surface area. Regular electrophoresis requires millions of cells and was not applicable in this situation. Thus, the comet assay, which only requires a few thousand cells was employed[4].

The comet assay was first introduced in 1984 by Ostling and Johanson[5]. This is a unique assay because it allows the direct determination of DNA damage in individual cells. The assay has been modified several times since its introduction. In this experiment the protocol of Vijayalaxmi et al was used[6]. Cells are suspended in agarose and deposited on a frosted microscope slide. The DNA is then lysed and unwound, exposing single strand (SD) and double strand (DS) breaks. Then, during electrophoresis, "comets form as broken ends of negatively charged DNA molecules become free to migrate in the

electric field toward the anode"[4]. As with standard electrophoresis, the smallest fragments migrate the fastest, while the larger fragments migrate more slowly. The extent of the DNA damage can be qualitatively measured from the comet pattern itself, using two parameters, tail length and tail moment. The tail length is defined as the distance of DNA migration from the body of the nuclear core, and the tail moment is defined as the product of the tail length and fraction of total DNA in the tail[4].

2. METHODS AND MATERIALS

2.1 Cell preparation

Cell preparation was carried out as follows. The experiments were carried out using RPE cells isolated from bovine or baboon eyes. The bovine eyes were obtained at a local slaughterhouse. The baboon eyes were obtained from the Southwest Foundation for Biomedical Research (SWFBR) in San Antonio from animals in their primate colony undergoing necropsy (the animals were sacrificed for SWFBR projects). RPE cells isolated from the eyes were grown in standard cell culture conditions with serum-supplemented Delbecco's Minimal Essential Medium, under 5% CO_2, incubated at 37°C. These cells are primary RPE cells. Therefore, they retained most of their pigmentation. The cell cultures were maintained in the Retinal Physiology Laboratory at the UTHSCSA, and transported to Brooks AFB (about a 35 min drive) on the day of experimental laser exposure.

2.2 Laser system

The laser system used for these experiments is located in the AFRL Laser Laboratory at Brooks AFB, Texas, where all laser exposures were carried out. The laser source was a Ti:Saphire regenerative amplifier system (Spectra Physics, Mountain View, CA.) with an associated pump laser and a sub 35fs Tsunami mdelocked laser used as the seed for the regenerative amplifier. The laser system was capable of out putting energies in the range of hundreds of µJ per pulse. The output was attenuated with a ½ wave plate and polarization cube combination to achieve the desired exposure levels. The beam was focused to a spot size of 0.5 mm or less (nominal spot size 1.96×10^{-3} cm^2). The cells were exposed to the following 800nm laser outputs:

    (1) 44 fs amplified regenerative pulses (1 sec train at 10 Hz; 60 and 120 µJ/pulse)
    (2) 30 fs mode-locked pulses (0.25 sec envelope delivering pulses at 80 MHz; 61 and 164 mW average power)
    (3) Continuous wave (CW) exposures (>0.25 sec; 61 and 164 mW)

Cells at edge of well may not have been exposed
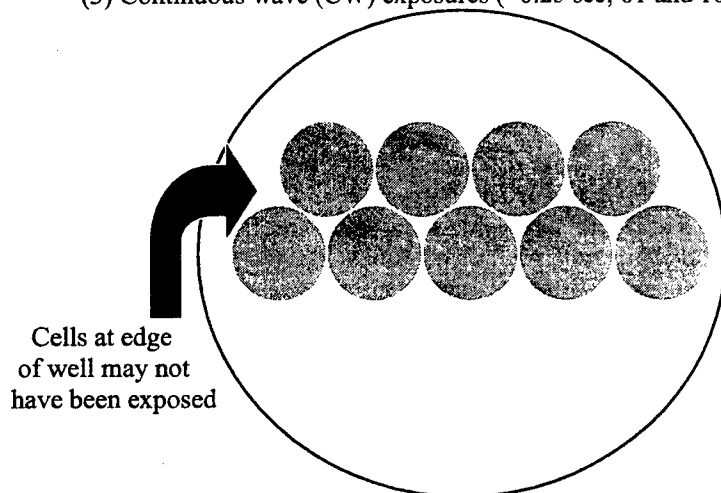
Figure 1: Example of exposure pattern of cells in circular well

Figure 1 shows the raster scan type exposure pattern used to expose the cells. The cells were grown in circular wells. The circular wells were placed under the laser, which moved along throughout the exposure until the area of entire well was

covered. However, there may have been a few cell at the edge of the circular wells which may not have been exposed, as shown in Figure 1.

2.3 Comet Assay

The technique described by Singh et al.[7] and modified by Vijayalaxmi et at.[6] was used for this investigation, with some minor adjustments. The steps are as follows:

a) Slide Preparation: Following laser exposure, cells were sandwiched between two layers of 0.5% agarose on a frosted microscope slide. This was done in the following way. The microscope slide was coated with 110 µl of 0.5% agarose solution. A cover slip was placed on the slide so the agarose would dry to form a flat surface. The cover slip was removed and the slide coated with approximately 5,000 RPE cells suspended in low melting point agarose (LMPA). The cover slip was again placed on the slide, and the slide placed on a flat ice pack to accelerate drying. When the layer of agarose was sufficiently hardened, the coverslip was removed. The slide was then coated with a final layer of 75 µl of 0.5% LMPA. Again, the cover slip was placed on the slide, and the slide was placed on a flat ice pack to accelerate drying. When the cover slip was removed, a flat surface of agarose was revealed.

b) Lysis: The cells were then lysed in situ with a lysis buffer containing: 2.5 M NaCl, 100mM EDTA, 10mM Tris (pH 10.0), 1% sodium lauryl sulfate, 1% Triton-X 100, and 10% DMSO. The slides were placed in a glass jar with lysis solution. The slides were incubated in the lysis solution for one hour at 4°C.

c) Electrophoresis: The slides were placed in a horizontal electrophoresis chamber, as shown in Figure 3. The chamber was filled with an alkaline buffer (300 mM NaOH and 1 mM EDTA, pH 13.0) such that the solution covered the slides. The cells were incubated in the alkaline buffer for 40 minutes to allow DNA to unwind. The electrophoresis was then carried out at 25V and 300 mA for 40 minutes. In electrophoresis molecules are separated according to size by an agarose gel. When a current is run through the electrophoresis chamber, the DNA, which is negatively charged, migrates toward the positive electrode, with the agarose acting as a sieve, allowing the small molecules to migrate the fastest and large molecules to migrate the slowest. This is demonstrated in Figure 2.

Negative pole
(cathode)
—

Positive pole
(anode)
+
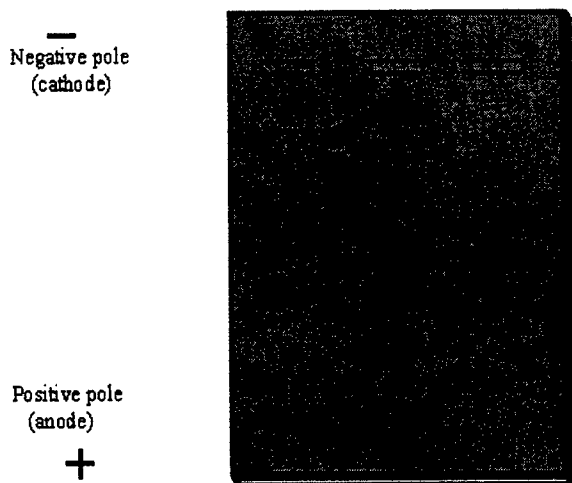
Figure 2: In electrophoresis large molecules migrate slowest, while smaller molecules migrate faster
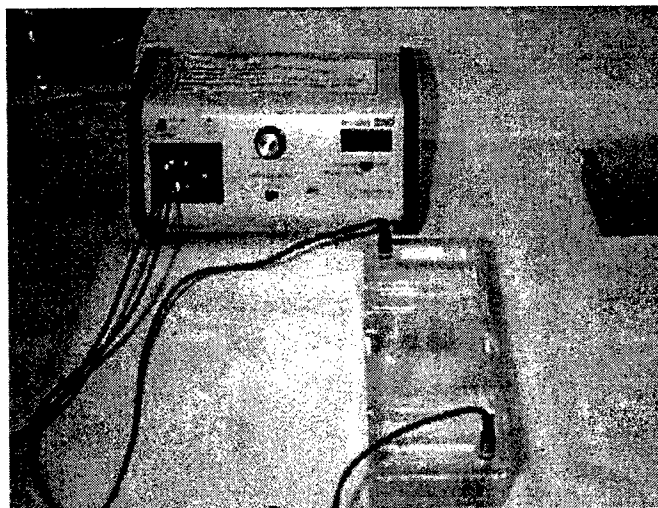
Figure 3: Minielectrophoresis system used for the comet assay

d) Neutralization: Upon completion of electrophoresis slides were removed from the electrophoresis chamber and neutralized with a Tris buffer, pH 7.5.

e) Staining: slides were stained with SYBER Green I (Molecular Probes), a nucleic acid stain (1 µl/10 ml) in a Tris Buffer for 30 minutes. SYBER Green I is less toxic than ethidium bromide, has a greater fluorescent yield, and is excited by visible light (excitation band 480-500 nm), with emission in the green range of the spectrum. Thus, SYBER Green I is an ideal stain for the comet assay.

f) Viewing: A drop of fluorescence-grade mounting medium (Sigma Chemical, St Louis. MO) was placed over the gel area, and the slides examined with a fluorescence microscope with fluorescein filters. Images were taken with an Optronix integrating CCD camera, captured by a PC-based frame-grabber at 400 x 600 resolution, and stored for later analysis.

g) Image Analysis: Comet Images were analyzed with the Scion Image program (the PC version of NIH Image) using the analysis macro of Helma and Uhl[8]. The comet macro itself was downloaded from http://mailbox.univie.ac.at/christoph.helma/comet/. Their analysis system is based on the scientific image-processing program NIH image, and is written in its Pascal-like macro language. To use the macro, the image file of interest was selected and loaded as shown in Figure 4. The image was rotated such that the head of the comet faced the left of the screen and the tail faced the right of the screen. The comet macro defaults to a threshold value to distinguish the comet from the background, but this value may be adjusted using the LUT tool of the program. The manually adjusted values are retained automatically and used for further measurements to enable uniform conditions within an experiment[8]. The comet is then outlined with the "wand" tool, and this selection is either accepted or rejected. Next, the measure command was applied. The macro copies the selected cell to another window and calculates the area and DNA content (based on the fluorescence intensity) of the whole comet including head and tail. Finally the properties of the comet are calculated according to equations 1 – 4. This process is demonstrated in Figure 5. The basic comet properties are defined by the macro as follows. Tail length (L_T) is the distance between the right end of the head and the end of the DNA migration. The head area (A_H) is the area covered by the cell nucleus, and is calculated from the head radius (H_R) as shown in Figure 5. Tail area is the area covered by the tail. Comet DNA in the tail (DNA_T) is calculated by multiplying the intensity (I_T) by the area of the tail (A_T). The tail moment (M_T) is defined as the product of the tail length (L_t) and fraction of DNA in the tail ($\%DNA_T$)[8].

Figure 4: The first step in using the analysis macro is to convert to import the image into NIH-Image, set the threshold, and rotate the comet such that the head is left. The outline wand tool is then used to select a particular comet.
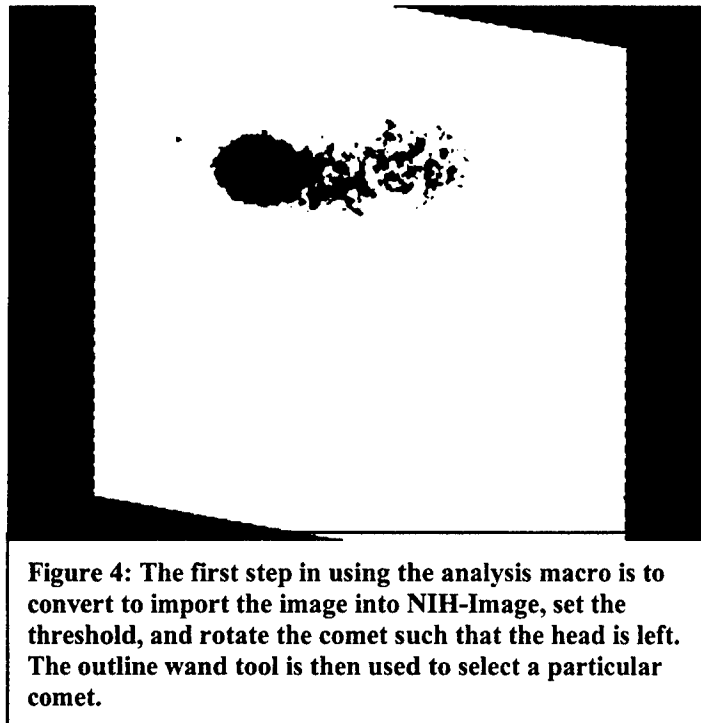
The following formulas were used by the macro to calculate comet properties:

$$(1)\ DNA_{H} = A_H * I_H$$

$$(2)\ DNA_{T} = A_T * I_T$$

$$(3)\ \%DNA_{T} = 100 * \left[\frac{DNA_T}{(DNA_T + DNA_H)} \right]$$

$$(4)\ M_{T} = L_T * \%DNA_T$$

STATUS:
No Code
1 0
RESULTS:
Tail Length % Migrated DNA Tail Moment
    166   66.3   11012.60
Type "K" to keep the measurement
Type "D" to discard this measurement and make a new one

Figure 5: Scion Image Analysis macro determines the size and location of the comet head and them calculates, comet moment and tail length (H$_r$)=Radius of comet head, L$_T$=Length of comet tail).
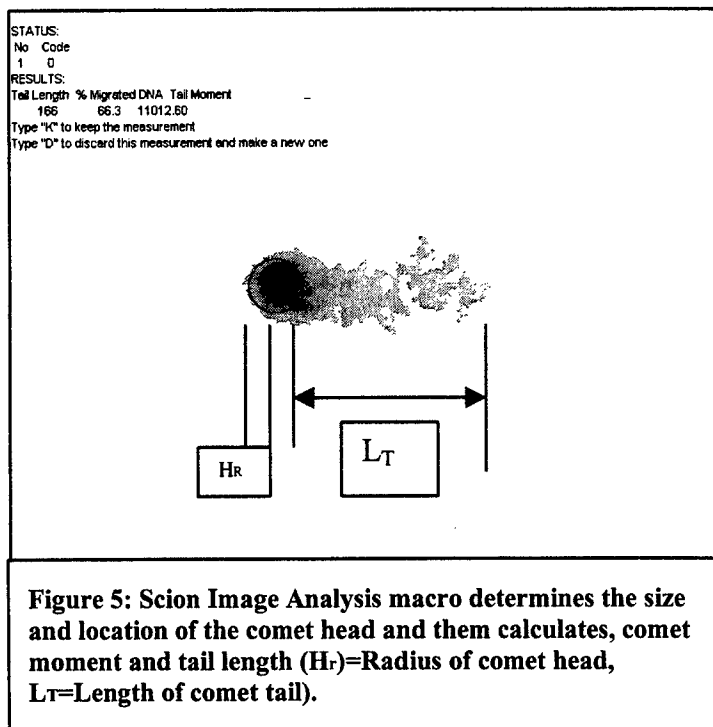
3. RESULTS

3.1 Sample images

Presented below are images of comets produced by unexposed cells (Figure 6) as well as continuous wave (Figure 7) and 30-fs modelocked (Figure 8) exposed cells.

Figure 6: Example of control Cells
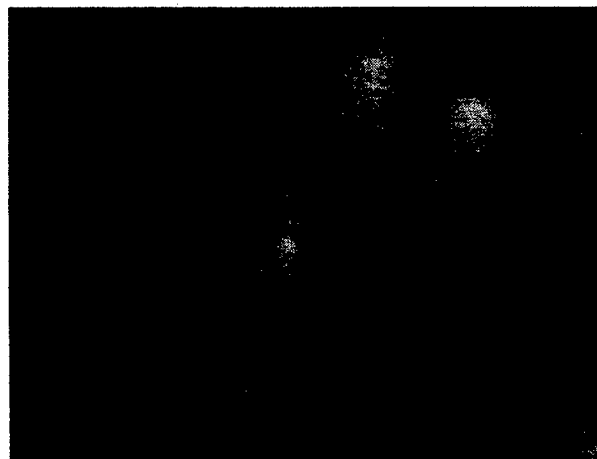
Figure 7: Example of CW Exposed Cells

Figure 8: Example of 30 fs mode locked laser exposed cells
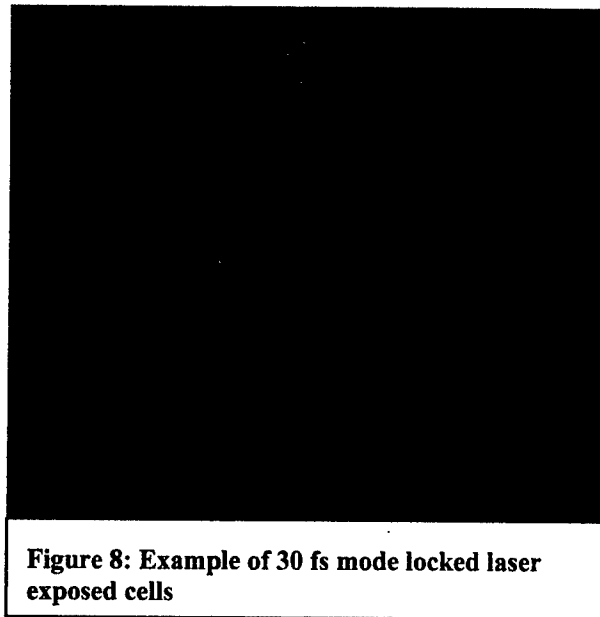
3.2 Comet data

Presented below is the DNA content in each comet (column labeled "DNA"), comet moments ("Moment"), comet lengths ("Length") for the control cells (received no laser exposure) the 44-fs amplified regenerative pulsed exposed cells, the 30-fs mode-locked pulse exposed cells, and the continuous wave (CW) exposed cells. Tables 1, 2, 3, and 4 provide a summary of the comet parameters calculated using Scion Image. The data in the tables are in pixel units. The data were analyzed using the Bonferoni multiple comparison test. Unexposed RPE cells demonstrated the least DNA damage. All laser exposed cells showed some degree of DNA fragmentation. Longer comet tails and larger moments were seen among the group exposed to 30 fsec IR laser, which were found to be statistically different from the CW and from the 44 fsec groups ($p < 0.001$).

	Control Length	Control Moment	Control DNA
Mean	18.44	836.77	41.48
s.d.	13.95	782.07	8.68

Table 1: Results for Control Cells

	CW Length	CW Moment	CW DNA
Mean	71.57	3976.54	48.82
s.d.	48.43	3767.58	14.44

Table 2: Results for Continuous Wave Exposed Cells

	30 fs modelocked length	30 fs modelocked moment	30 fs modelocked DNA
Mean	142.36	10658.71	67.63
s.d.	92.29	9069.4	12.41

Table 3: Results for 30 fs mode-locked exposed cells

	44 fs Regenerative Pulse Length	44 fs Regenerative Pulse Moment	44 fs Regenerative Pulse DNA
Mean	60.47	3545.69	57.48
s.d.	17.85	1434.29	8.61

Table 4: Results for 44 fs Regenerative Pulse exposed cells

4. DISCUSSION

All the laser exposed cells showed a greater amount of fragmentation compared to the control cells. The size and shape of the comets varied among the different modalities. In general, the unexposed cells had shorter comets and lower comet moments, i.e. 18.44 and 836.77, respectively. The CW exposed cells generally had light and compact comets with average length of 71.57 and an average moment of 3,976. This suggests that the CW exposure resulted in a few large fragments rather than many small fragments. The 30-fs mode locked laser exposed cells showed the most diffuse comets, with a tail length of 142 and a tail moment of 10,659. This indicates that the laser interacted extensively with the DNA in the cells causing many single and double strand breaks, resulting in numerous small fragments. Finally, the 44-fs regenerative pulse exposed cells demonstrated DNA damage comparable to that of the CW exposure group. This was an unexpected response because the 44-fs regenerative pulses delivered the greatest energy per pulse. It was presumed that the highest radiant exposure would result in the largest amount of DNA damage. It is suspected that the majority of the cells exposed to the 44-fs regenerative pulses were simply obliterated by the extremely high energy density and the comets were due to cells remaining on the edge of the exposure window. However, this was a preliminary investigation, and further work must be done to confirm this speculation. Overall, the present results suggest that ultrashort laser pulses may affect RPE cell DNA by interaction with an as yet unidentified chromophore through a multiphoton process. The nature of the chromophore and mechanism of the multiphoton excitation will be primary goals of our upcoming research. Future work will include a detailed investigation of the dose response between laser exposure parameters and cellular responses. Cells will be exposed to each pulsewidth at several energy densities. Also, the scope of the pulsewidths under investigation will be increased to include microsecond and nanosecond pulses to determine if the amount of DNA damage is dependent on pulse width

Ultrashort pulse laser systems are now commercially available and used in biomedical applications such as two-photon excitation of fluorophores in confocal laser scanning microscopes. Two or three-photon excitation is increasingly being used in confocal scanning microscopy for excitation of fluorophores[1] because of the presumed safety for living specimens[9] and because of the reduced photo-bleaching effects of long-wavelength light[10] (due to its lower photon energy compared to short-wavelength visible or UV). A CW laser source emitting near 800 nm is insufficient to excite a fluorophore (with an excitation wavelength near 400 nm), since its wavelength is too far from the excitation wavelength. However, an 800 nm laser with an ultrashort pulse of 200 femtoseconds will excite the fluorophore with about the same efficiently as a 400 nm laser[10]. In theory collateral damage is minimized because of the lower photon energy of the 800 nm laser. This premise is an active area of research, with some reports finding cellular damage to ultrashort NIR laser exposure because of presumed multiphoton absorption[11,12]. Other reports have indicated that ultrashort sources can be used safely with living specimens during prolonged observation periods[9]. Mulitphoton effects may need to be considered in the context of laser safety standards applicable to these increasingly popular ultrashort pulse laser systems, and may also affect the viability of living specimens observed with confocal laser scanning microscopes using 2 photon excitation.

ACKNOWLEDGEMENTS

REFERENCES

1. W. Denk, J.H. Strickler, and W.W Webb, "Two-photon laser scanning fluorescence microscopy." *Science* **248**,pp73-76.1990
2. E. Soini , N.J. Meltola, A.E. Soini, J. Soukka , J.T. Soini, and P.E. Hanninen "Two-photon fluorescence excitation in detection of biomolecules." *Biochem. Soc. Trans.* **28**,pp70-74.2000
3. M.J. Peak, J.G. Peak, and B.A. Carnes, "Induction of direct and indirect single-strand breaks in human DNA by far- and near-ultraviolet radiations: action spectrum mechanisms." *Photochem. Photobiol..* **45**, pp381-387
4. D. Fairbairn, P. Olive, and K. O'Neill, "The Comet Assay: A Comprehensive Review." *Mut. Res.* **339**, pp37-59.1995
5. O. Ostling, and K. Johanson, "Microelectrophoretic Study of Radiation Induced DNA Damages in Individual Mammalian Cells." *Biochem.Biophys.Res.Commun.***123**, pp 291-298. 1984
6. T. Vijayalaxmi, and G. Strauss, "Assessment of Radiation-Induced DNA damage in Human Blood Lymphocytes using the Single-Cell Gel Electrophoresis Technique." *Mut.Res.* **271**, pp 243-252. 1992
7. N.Singh, M. McCoy, R. Tice, and E. Schneider, "A Simple Technique for Quantitation of Low Levels of DNA Damage in Individual Cells." *Exp.Res.* **175**, pp 184-191. 1988
8. C. Helma and M. Uhl, "A public domain image-analysis program for the single-cell gel-electrophoresis (comet) assay." *Mut. Res.* **466** pp9-15. 2000
9. J.M. Squirrell, D.L.Wokosin, J.G.White, and B.D. Bavister "Long-term two-photon fluorescence imaging of mammalian embryos without compromising viability." *Nature Biotech.* **17**, pp763-767.199
10. K. Konig, P.T.C.So, W.W. Mantulin, B.J. Tromberg,and E.Gratton "Two-photon excited lifetime imaging of autofluorescence in cells during UVA and NIR photostress." *J. Microsc.* **183**, pp197-204. 1996
11. K. Konig, H. Liang, M.W.Berns, and B.J.Tromberg "Cell damage by near-IR microbeams." *Nature* **377**, pp20-21.1995
12. K. Konig, H. Liang, M.W.Berns, and B.J.Tromberg "Cell damage in near-infrared multimode optical traps as a result of multiphoton absorption." *Optics Lett.* **21**, pp 1090-1092.1996

Interaction of laser-produced cavitation bubbles with an elastic tissue model

Alfred Vogel[1*], Emil A. Brujan[2**], Peter Schmidt[1], Kester Nahen[1]

1) Medizinisches Laserzentrum Lübeck, Germany
2) Department of Hydraulics, Univ. Politechnica, Bucharest, Romania

ABSTRACT

We investigated the interaction of a laser-induced cavitation bubble with an elastic tissue model by high-speed photography with up to 5 Mill. frames/s. The elastic material consisted of a transparent polyacrylamide (PAA) gel whose elastic properties can be controlled by modifying the water content to mimic various biological tissues. The elastic modulus E of the PAA sample was varied between 0.017 and 2 MPa. The dimensionless bubble-boundary distance γ (distance between laser focus and sample boundary, scaled by the maximum bubble radius) was for each value of E varied between $\gamma = 0$ and $\gamma = 2.2$. In this parameter space, we determined the jetting behavior, jet velocity, jet penetration into the PAA sample and bubble-induced removal of PAA material. The jetting behavior varies between unidirectional jets towards or away from the boundary, and formation of an annular jet which results in bubble splitting and subsequent formation of two very fast axial jets flowing simultaneously towards the boundary and away from it. General principles of the formation of annular and axial jets are discussed which allow to interpret the complex dynamics. The liquid jet directed away from the boundary reaches a maximum velocity between 300 m/s and 600 m/s (depending on E) while the peak velocity of the jet directed towards the boundary ranges between 400 m/s and 960 m/s. The peak velocities near an elastic material are 10 times higher than close to a rigid boundary. The liquid jet penetrates PAA samples with an elastic modulus in the intermediate range $0.12 < E < 0.4$ MPa. In this same range of elastic moduli and for small γ-values, PAA material is ejected into the surrounding liquid due to the elastic rebound of the sample surface that was deformed during bubble expansion. The surface of the PAA sample is, furthermore, lifted during bubble collapse when a region of low pressure develops between bubble and sample. For stiffer boundaries, only an axial liquid jet towards the boundary is formed, similar to the bubble dynamics next to a rigid wall. For softer samples, the liquid jet is directed away from the boundary, and material is torn off the PAA sample during bubble collapse, if the bubble is produced close to the boundary. These processes play an important role for the efficiency and side effects of pulsed laser surgery inside the human body.

Key words: Laser ablation, photodisruption, cavitation, elastic materials, polyacrylamide, tissue model, jet, jet penetration, cavitation-enhanced ablation, ablation efficiency.

1. INTRODUCTION

Gibson[1] observed more than 30 years ago that under certain conditions the liquid jet formed during bubble collapse near an elastic boundary as well as the bubble migration are both directed away from the boundary. Since jet impact and the high pressures developed during bubble collapse near a rigid boundary were known as majors factors causing cavitation erosion, the use of compliant boundaries was considered as a means of preventing erosion. This conclusion was also supported by Gibson & Blake[2] who examined the behavior of spark-generated bubbles in the vicinity of rigid boundaries with rubber coatings. Blake & Gibson[3] observed that, for some range of coating properties, no re-entrant jet towards or away from the boundary is developed during bubble collapse. In this case, the bubble collapses from the sides forming an hour-glass shape which can eventually lead to bubble splitting. However, no details of the motion after the bubble splitting were presented by these authors and in later, related studies by Shima et al.[4], Duncan, Milligan & Zhang[5], Shaw et al.[6], and Kodama & Tomita[7].

In recent years, the interaction between cavitation bubbles and elastic boundaries has become very important in the context of medical laser applications. Whenever short laser pulses are used to ablate or disrupt biological tissue in a liquid environment, cavitation bubbles are produced which interact with the tissue. This situation is encountered, for example, in

intraocular photodisruption[8], laser angioplasty, laser thrombolysis, myocardial laser revascularization and arthroscopic cartilage ablation. The interaction between cavitation bubbles and tissue during pulsed laser ablation and photodisruption may cause collateral damage to sensitive tissue structures in the vicinity of the laser focus[9], and it may also contribute in several ways to ablation and cutting: by disruption caused during bubble expansion, by jetting towards the boundary, by tensile stress exerted during bubble collapse, or by the elastic-plastic response of the deformed tissue. In any case, a characterization of the interaction is of interest for an optimization of the surgical procedure.

The present study addresses both the cavitation erosion in a technical environment and the cavitation effects in pulsed laser surgery, with emphasis on the medical laser application. We investigated the behavior of laser-induced bubbles in a large range of distances to boundaries with different elastic properties to obtain a better understanding of the complex jetting dynamics and the possible cavitation damage to nearby surfaces. Investigations covering a large part of the (E,γ) space are of interest for medical laser applications, because not only mechanical tissue properties but also the distance between bubble center and tissue boundary may vary strongly in clinical practice. This is obvious in the case of intraocular photodisruption, because it relies on the generation of an optical breakdown at the laser focus which is largely independent of the linear absorption properties of tissue. Breakdown can thus be produced at almost any location within the eye. It applies also for pulsed laser ablation in a liquid environment using mid IR laser pulses. In this wavelength range, ablation is based on the high linear absorption of water, and bubbles will be produced at a distance from the target if the tip of the fiber transmitting the pulses is not in contact with the tissue.

A more detailed account of the investigations is given in References [10] and [11].

2. METHODS

Bubbles with 1.5 mm radius were created by focusing Q-switched Nd:YAG laser pulses of 8 mJ pulse energy in a glass cuvette filled with distilled water (figure 1). The bubbles interacted with transparent polyacrylamide (PAA) gel samples whose elastic properties were controlled by modifying the water content of the sample. The samples were 20 mm thick and the surface area exposed to the bubble was 15×15 mm^2. The elastic modulus, E, was varied between 0.017 MPa and 2.03 MPa by changing the PAA water content from 95% to 50%. This range corresponds to the elastic properties of various human tissues, such as renal parenchyma (0.06 MPa[7]), articular cartilage (0.4 - 1.1 MPa[12]), arteries (1.2-5 MPa[12]), and cornea (3-5 MPa[13]). The dimensionless bubble-boundary distance γ (defined as distance between laser focus and boundary, scaled by the maximum bubble radius R_{max}) was for each value of E varied between $\gamma = 0$ and $\gamma = 2.2$. In this parameter space, we investigated the jetting behavior, jet velocity, bubble migration and the bubble-induced alterations of the PAA sample. For this purpose, the bubble boundary interaction was recorded by high-speed photography with framing rates between 50000 f/s and 5 Mill. frames/s using an image converter camera with CDD readout. Diffuse illumination was used to visualize the bubble interior, while parallel illumination provided optimal contrast for the observation of the boundary deformation, shock wave emission upon bubble collapse, and liquid jet penetration into the sample.
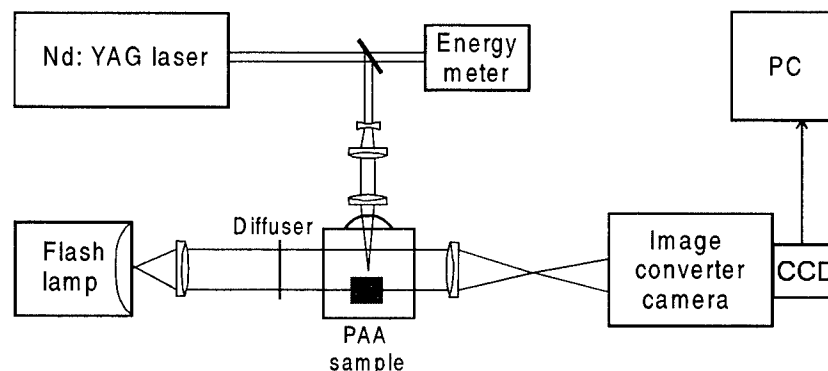
Figure 1: Experimental set-up for the investigation of the interaction of a laser-induced bubble with an elastic boundary (PAA sample).

3. RESULTS AND DISCUSSION

3.1 Characteristic features of bubble dynamics

The dynamics of bubbles near PAA samples with 80% water content ($E = 0.25$ MPa) exhibits many characteristic features of the interaction between cavitation bubbles and elastic materials in a particularly clear form. When the bubble is situated relatively far away from the boundary ($\gamma \approx 1.14$, figure 2), it retains much of its spherical symmetry during expansion and early collapse phases. In the late collapse stage, however, a 'cone-shaped' bubble region develops at the side next to the boundary (second row, frame 5). The fast collapse of this high-curvature region of the bubble subsequently produces a high-speed axial liquid jet directed away from boundary. The bubble motion is characterized by a migration of the bubble away from the boundary, most pronounced during the collapse phases. This behavior was also observed previously by Gibson[1], Gibson & Blake[2], and Shima et al.[4].
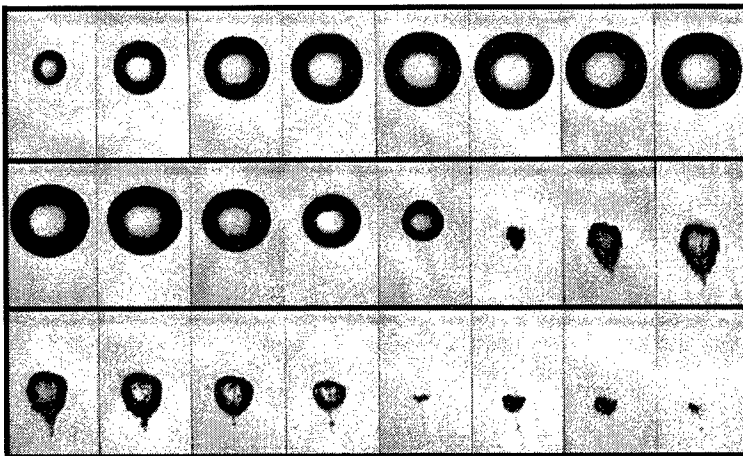
Figure 2: Interaction of a laser-produced bubble with an elastic boundary, $E = 0.25$ MPa, $\gamma \approx 1.14$. The boundary is located at the top of each frame. Framing rate 50,000 f/s. Frame width 3.5 mm.
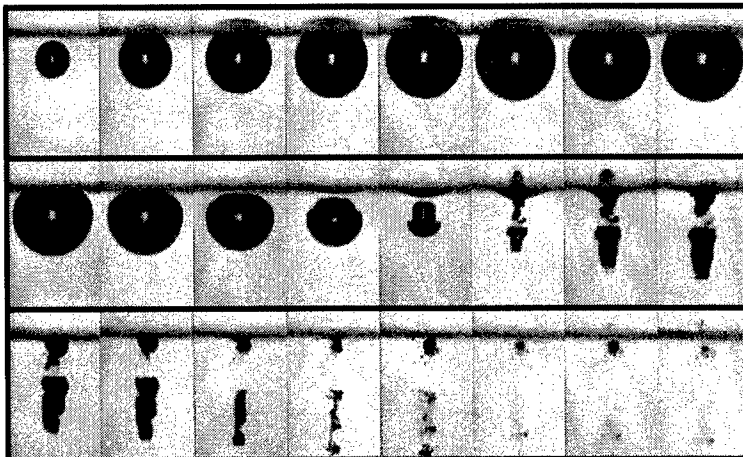
Figure 3: Interaction of a laser-produced bubble with an elastic boundary, $E = 0.25$ MPa, $\gamma \approx 0.62$. Framing rate 50,000 f/s.
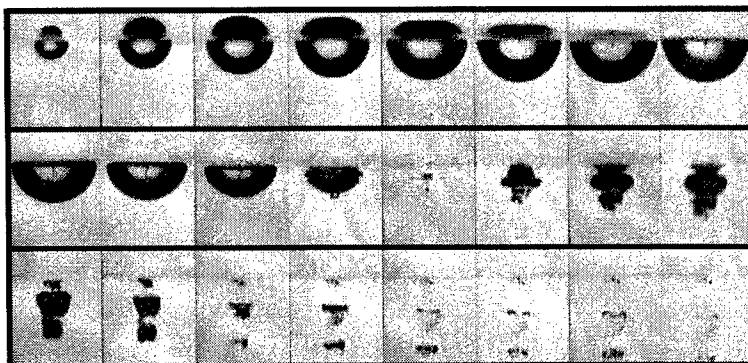
Figure 4: Interaction of a laser-produced bubble with an elastic boundary, $E = 0.25$ MPa, $\gamma \approx 0.04$. Framing rate 50,000 f/s.

When the bubble is produced closer to the boundary ($\gamma \approx 0.62$, figure 3), it touches and compresses the PAA sample during its expansion phase. Due to the rebound of the elastic material, the bubble becomes flattened in a direction parallel to the boundary. The boundary stays almost motionless for some time and becomes afterwards elevated by the tensile forces exerted during bubble collapse (see the 'hump' in frame 5, second row). The oblate bubble (first frame, second row) collapses from the sides leading to the production of an annular flow which is most pronounced around the surface of the bubble closer to the boundary. Therefore, a mushroom-like shape of the bubble develops in a later stage of the collapse. The annular flow from the bubble sides results in bubble splitting during the final stage of collapse with a part of the bubble migrating towards the boundary and another part migrating away. Bubble splitting is accompanied by a redirection of the annular jet flow and the formation of two axial jets flowing in opposite direction. The jet directed towards the boundary is so fast (810 m/s, see figure 6, further below) that it penetrates into the sample. The penetration depth is 0.53 mm when measured from the undisturbed surface, and 0.9 mm when measured from the peak of the hump.

For $\gamma \le 0.5$, the rebound of the elastically deformed PAA boundary is accompanied by the formation of a PAA jet which threads the cavitation bubble. Figure 4 shows the case when the bubble is generated almost at the surface of the boundary ($\gamma \approx 0.04$). Following a strong compression, a hemispherical cavity is formed in the PAA sample. The sample rebounds early during the growth phase of the bubble and a very strong PAA jet develops which, finally, penetrates the bubble wall opposite to the boundary. The maximally expanded bubble is no longer an oblate spheroid, as observed at larger γ-values, but has now an approximately hemispherical shape. The mushroom-like shape of the bubble is not very pronounced, no bubble splitting occurs, and the bubble migrates away from the boundary during rebound. Consequently, a damage of the boundary caused by the penetration of a liquid jet is no longer observed. Formation of a jet emanating from the elastic material was recently predicted in numerical simulations by Chapyak & Godwin[14]. Liquid jet penetration into the elastic boundary has previously not been reported in the literature.

The picture series with 50000 frames/s provide a good overview of the variety of phenomena which occur at different stand-off distances between bubble and boundary. However, the temporal resolution is not sufficient to resolve the final collapse phase where bubble splitting and the formation of axial jets away or towards the boundary occur. This phase is, therefore, shown in figure 5 with 1 million frames/s.
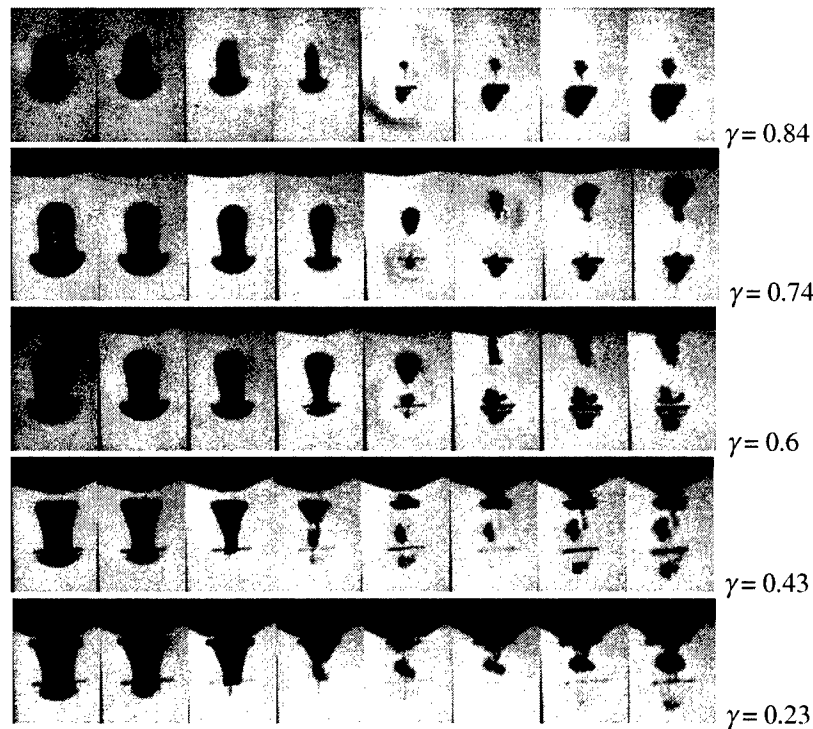
Figure 5: Interaction of a laser-produced bubble with an elastic boundary, $E = 0.25$ MPa. Framing rate 1 Mill. f/s. Frame width 1.4 mm.

At $\gamma = 0.84$, the "foot" of the mushroom-shaped bubble, which is located next to the boundary, collapses earlier than the "cap". This is indicated by the larger diameter of the shock wave emanating from the collapsing foot. As a consequence, a liquid jet directed away from the boundary is formed. At $\gamma = 0.74$, the cylindrical part of the cavity necks during the final stage of bubble collapse as a result of the annular liquid flow induced in an earlier stage of the collapse. At closure of the neck, the bubble splits in two. The cavity situated far away from the boundary now collapses first and is accompanied by liquid jet formation directed away from the boundary. The cavity nearest to the boundary acquires an almost triangular shape subsequent to the bubble splitting and is then hit by the shock waves emitted during the rebound of the second cavity. Therefore, it collapses with a high-speed liquid jet and a strong translational motion directed towards the boundary. When the value of the stand-off parameter γ is reduced to 0.6, the behavior is similar, but the liquid jet towards the boundary is even faster. With smaller γ, no shock wave is emitted by the cavity oscillating far from the boundary. The reason for the absence of a shock wave is that the cap of the mushroom-like shape of the bubble ends its collapse before the splitting phenomenon has occurred. Consequently, the gas and vapor content of the cap is pushed into the larger volume of the rest of the bubble (mushroom foot). The pressure rise inside the collapsing cap and in the region of the bubble neck is, therefore, relatively low during the whole collapse period, resulting in a weaker force driving the liquid jet towards the boundary.

Figure 6 shows the maximum velocity of the liquid jets directed towards and away from the elastic boundary, derived from the framing series taken with 1 million frames/s. The velocities are strikingly high: up to 800 m/s were measured for the liquid jet towards the boundary at $\gamma = 0.6$. Photographic series taken with 5 Mill. frames/s yielded a peak velocity as high as 960 m/s[10] for $\gamma = 0.6$. This value is ten times higher than the jet velocity reached near a rigid boundary at a similar γ- value[11].
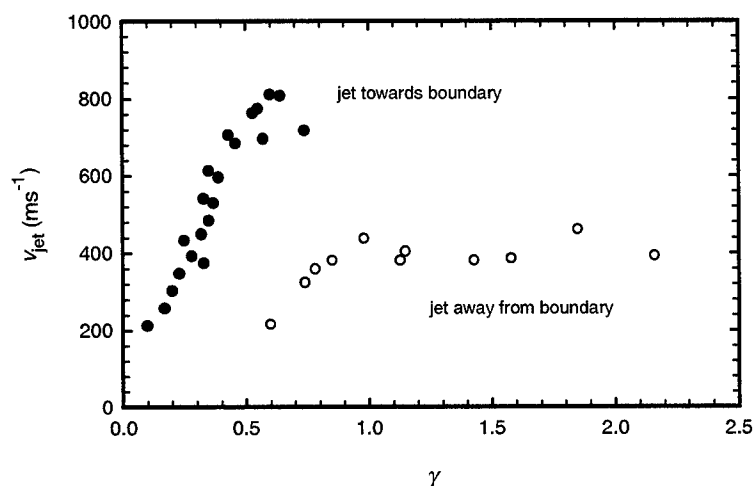
Figure 6: Maximum jet velocities

3.2. Underlying principles: Axial and annular jets

To better understand the complex behavior and the origin of the fast jets, it is helpful to analyze the principal mechanisms involved in the various kinds of jet formation. A jet develops if one part of the bubble collapses faster than the other parts. Slight differences in the collapse velocity are amplified/enhanced during bubble collapse by geometrical 'focusing' of the asymmetric flow. When one or both poles of the bubble collapse faster than the other parts, needle-like jets develop. When the equatorial region collapses faster, an annular, disk-like flow towards the bubble center develops which leads to bubble splitting and to the formation of two needle-like jets flowing in opposite direction perpendicular to the equatorial plane. The type of jet formation that occurs or dominates depends on the initial and boundary conditions.

Under *symmetric boundary conditions* (infinite static fluid, no buoyancy), jet formation arises when the bubble shape is aspherical. A bubble having the form of a prolate spheroid develops two 'axial' jets directed towards the center, but an oblate spheroid develops an 'annular' jet[15]. When the fluid rushing in from the bubble equator meets in the bubble center, the bubble splits in two parts and two jets flowing in opposite direction towards the poles develop[16]. In both cases the jets originate from those parts of the bubble wall with the largest curvature.

When the bubble oscillates under *asymmetric boundary conditions*, it is usually exposed to pressure gradients. This leads to a faster collapse of the bubble section(s) exposed to a higher pressure, and to jet formation even for an initially spherical bubble. Which type of jet forms, depends on the complexity of the boundary conditions. In simple cases when there is only one force acting on the bubble, an axial jet is formed. In more complex situations, when opposing effects act on the bubble motion, an annular jet can be formed if the strength of both effects is approximately equal.

Examples for *axial jets* from unidirectional pressure gradients are: (i) jet through a buoyant bubble, (ii)jet formed when a shock wave hits a bubble, (iii) jet towards a rigid wall or away from a free surface. Situations with opposing forces where *annular jets* form are: (i) bubble between two rigid walls, (ii) buoyant bubble above a plate, (iii) bubble in an axissymmetric stagnation flow towards a rigid wall, (iv) a bubble near an elastic deformable boundary.

What are the opposing forces acting on a bubble near an elastic boundary? As in the case of a rigid wall, the bubble oscillation is associated with a pressure gradient towards the wall due to the low pressure region between bubble and wall developing during collapse. Unlike the rigid wall, however, the material is deformed during bubble expansion, it rebounds, and thus creates a flow and pressure gradient directed away from the wall. The counteracting forces lead to a flattening of the bubble, and the collapse of the oblate bubble then results in an annular jet, bubble splitting, and the formation of two axial jets in opposite direction. When the opposing forces are not equally strong, the bubble splits into unequal parts, and the jet originating from the larger bubble part is stronger than the other jet in opposite direction. The velocity of the dominant needle-like jet becomes very high, because the region from which the fluid flow is focused into the jet is large, and the jet has a small diameter. In the limit, however, where one force is much stronger than the other, only one axial jet is formed.

For large γ-values, we observed an axial jet flow directed away from the boundary (figure 2). This indicates, according to the above analysis, that the flow induced by the rebounding PAA sample is stronger than the Bjerknes attractive force caused by the low pressure between bubble and boundary. With decreasing γ-value, the strength of the Bjerknes force increases faster than the flow from the boundary. The highest jet velocity is achieved for γ-values around $\gamma = 0.6$, where an asymmetric annular jet leads to the formation of a strong axial jet towards the elastic boundary. Various factors contribute to the high jet velocity: (i) The fluid flow is focused from a very large solid angle into a very thin jet, (ii) the redirection of the annular ring into an axial jet is mediated by the shock waves emitted upon the collapse of the mushroom cap and neck (see figure 5), (iii) the jet is not only redirected by the shock wave but also further accelerated, because the bubble part next to the boundary has a conical shape which allows for a continuous shock-wave-driven focusing of the annular flow into the axial jet until it reaches the opposite bubble wall[17].

3.3 Influence of the elastic modulus

Figure 7 gives an overview of the jetting behavior as a function of the elastic modulus of the boundary E and the normalized bubble-boundary distance γ. In the region between 85% and 70% water content, corresponding to an elastic modulus of 0.12
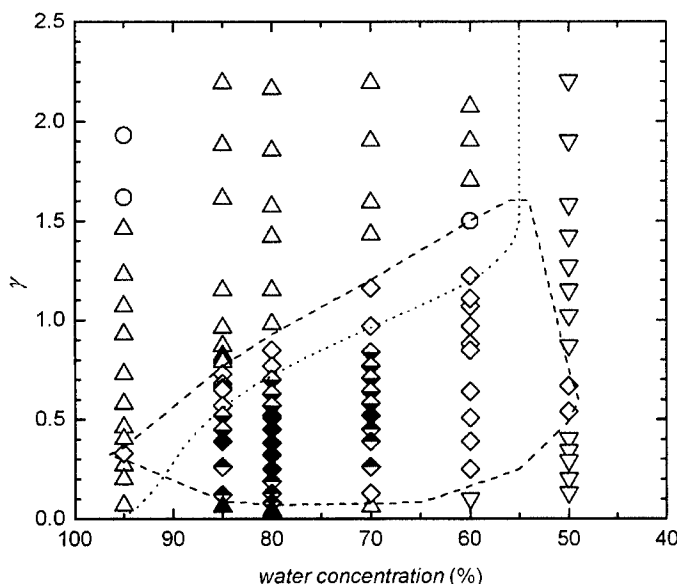
Figure 7: Jetting behaviour of bubbles near PAA samples with different water content and elastic modulus, respectively: 95% ↔ 0.02 MPa, 85% ↔ 0.12 MPa, 80% ↔ 0.25 MPa, 70% ↔ 0.4 MPa, 60% ↔ 1.0 MPa, 50% ↔ 2.0 MPa. Symbols: o no jet formation, Δ liquid jet away from the boundary, ∇ liquid jet towards the boundary, ◊ liquid jets away from and towards the boundary, ◈ liquid jets away from and towards the boundary, with jet penetration into the PAA sample, ◉ liquid jets away from and towards the boundary, and jet-like ejection of PAA material, ◆ liquid jets away and towards the boundary, with liquid jet penetration into the boundary and jet-like ejection of PAA material, ▲ liquid jet away from the boundary and jet-like ejection of PAA into the liquid. The dashed line surrounds the bubble splitting region, and the dotted line denotes the state where the 'centre of gravity' of the two-bubble system does not migrate.

MPa $< E <$ 0.4 MPa, the elastic response of the deformed boundary is particularly strong. The rebound of the boundary after its deformation during bubble expansion leads to the formation of a jet flow directed away from the boundary - either as a unidirectional jet or as one component of a pair of jets flowing in opposite directions. An unidirectional liquid jet directed away from the boundary is only observed for very large and very small γ-values. In the intermediate γ-range, bubble splitting occurs and, besides the jet away from the boundary, a fast jet directed towards the boundary is formed. A characteristic feature of the bubble-splitting-region is the extremely high velocity of the jets (figures 6 and 8). The high jet velocity results in a penetration of the PAA samples with a water content between 70% and 85%.

With larger elastic modulus (E = 2.03 MPa, at 50% water content), the bubble dynamics starts to resemble the behavior near a rigid wall[18]: the PAA is so stiff that the jet is always directed towards the boundary. With a smaller elastic modulus (E = 0.017 MPa, at 95% water content), the behavior becomes more similar to the dynamics in an infinite liquid. The elastic response of the boundary is, however, still strong enough to cause formation of a liquid jet directed away from the boundary.

Figure 8 presents the maximum jet velocity in the direction away from and towards the elastic boundary as a function of E and γ. It is interesting to note that for the more compliant samples with smaller elastic modulus (higher water content) the maximum jet velocities are reached at smaller γ-values than for the stiffer samples. The reason is that compliant surfaces allow the formation of an oblate spheroidal bubble at smaller γ-values than stiff boundaries. As already mentioned, this bubble shape is essential for the development of an annular jet flow which is followed by the formation of fast axial jets.

The highest velocities of the liquid jet towards the boundary are reached near the PAA sample with 80% water content. The weaker elastic rebound of the PAA samples with lower water content (85% and 95%) causes a less pronounced flattening of the oblate spheroid and, therefore, a weaker annular jet. For stiffer samples, a more hemispherical shape is assumed by the expanded bubble. As a result, the liquid flow towards the boundary is both for very soft and very stiff samples not as strongly focused as that encountered when the bubble oscillates near the PAA sample with 80% water content, and the maximum velocities of the jets are therefore smaller.
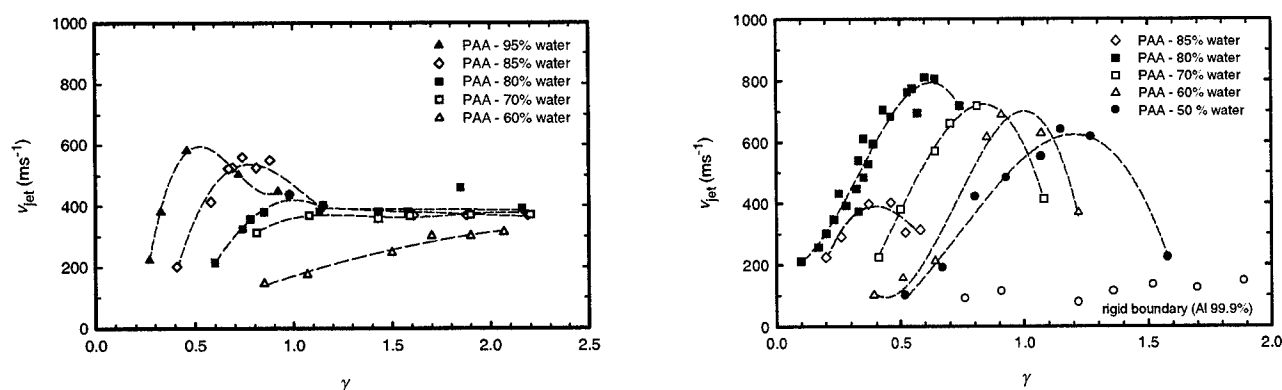
Figure 8: Jet velocity as a function of E and γ for jets directed away from the material surface (a) and for jets flowing towards the elastic boundary (b). The E-values for each PAA water content are given in the caption of figure 7.

3.4 Bubble boundary interaction

A specific feature of the cavitation bubble interaction with an elastic boundary is that not only the bubble but also the boundary changes shape, and that these changes are interdependent. Three different mechanisms may contribute to cavitation erosion and to cavitation-enhanced ablation of elastic materials: (i) Liquid jet penetration into the material (figure. 9), (ii) Formation of a jet consisting of elastic material directed into the surrounding liquid caused by the elastic rebound of the deformed boundary (figure 10). (iii) Elevation and tearing of the material surface during bubble collapse (figures 11, 3). The latter mechanism of material erosion is due to the low pressure between the collapsing cavitation bubble and the PAA surface and must be clearly distinguished from the PAA ejection arising from the elastic rebound of the boundary itself. Elevation of the material surface has previously been reported also by Grimbergen et al.[19], and Godwin et al.[20] pointed out the role of bubble dynamics for an enhancement of pulsed laser ablation.
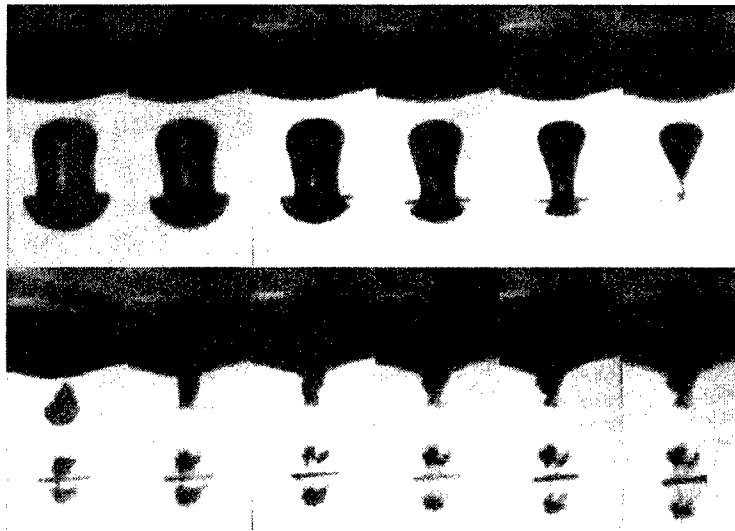
Figure 9: Liquid jet penetration into a PAA sample during the final stage of bubble collapse. $E = 0.25$ MPa, $\gamma = 0.55$. Framing rate 1 Mill. frames/s, frame width 1.4 mm. The jet impact occurs in the second frame in the second row, the penetration becomes visible in the last two frames.
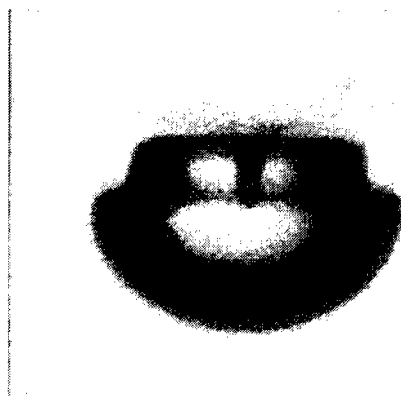
Figure 10: Jet consisting of PAA material directed into the surrounding liquid. $E = 0.25$ MPa, $\gamma = 0.45$. The PAA sample is only faintly visible in the top third of the frame because of the diffuse illumination required to show the jet inside the bubble. The jet is formed during the mid phase of bubble collapse when the sample surface rebounds that was deformed during bubble expansion. The mushroom shape of the bubble indicates that bubble splitting resulting in two liquid jets flowing in opposite direction will occur in a later collapse phase (see Fig.3) . Frame width 3.5 mm.

a)

b)
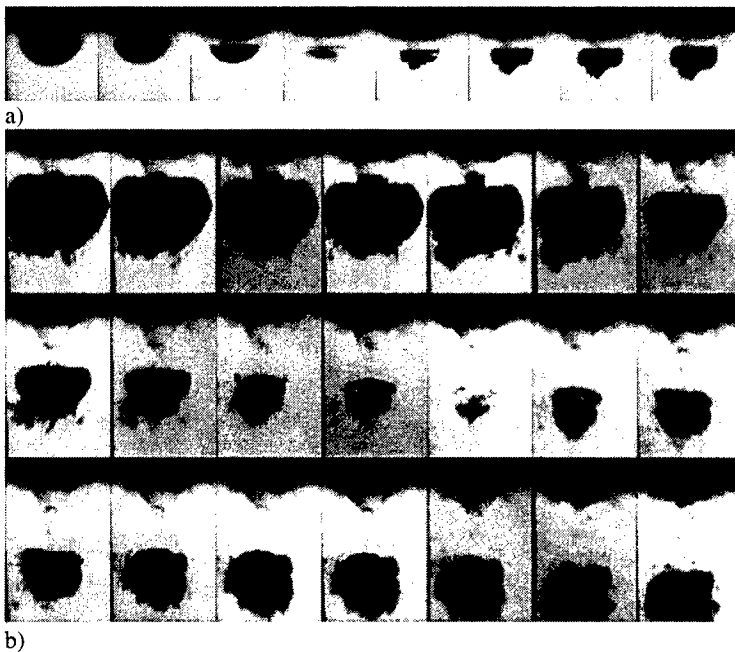
Figure 11: Interaction of the collapsing cavitation bubble with a soft PAA sample ($E = 0.017$, 95% water content, $\gamma = 0.07$). (a) first collapse, taken with 1 Mill frames/s, (b) second collapse, taken with 200,000 frames/s. It is clearly visible that PAA material is torn off the sample due to the low pressure collapsing bubble and boundary. Frame width 1.4 mm.

The regions in the (E,γ) parameter space for which the three mechanisms liquid jet penetration, jet-like PAA ejection, and elevation and tearing of the material surface were observed are indicated in figure 12.
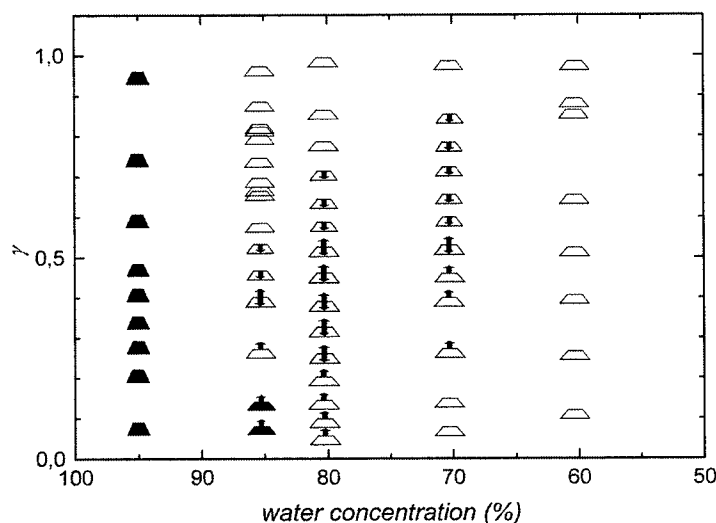
Figure 12: Mechanisms of cavitation erosion and cavitation-enhanced ablation of elastic materials, and the regions in the (E,γ)-parameter space where they can occur. The E-values for each PAA water content are given in the caption of figure 7. Trapezoid: uplifting of the boundary surface during bubble collapse (the filled symbols indicate that material is torn off from the PAA sample), arrow up: jet-like ejection of boundary material into the liquid, arrow down: liquid jet penetration into the boundary.

Liquid jet penetration after single laser exposures was observed within the bubble splitting region for PAA samples with a water content between 70% and 85%. PAA jet formation occurred with the same PAA samples at $\gamma < 0.6$. PAA material was torn off during bubble collapse near samples with 85% and 95% water content. The most pronounced liquid jet penetration and PAA jet ejection over the largest γ- range was observed when the bubble oscillates near the PAA sample with 80% water content ($E = 0.25$ MPa). For this case, quantitative data on the depth of the liquid jet penetration and the height of the PAA jet are given in figure 13.
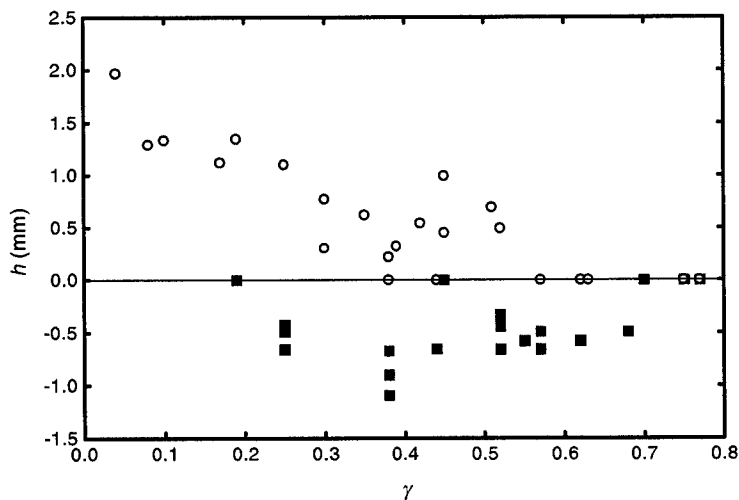
Figure 13: Penetration depth of the liquid jet into a PAA sample with 80% water content (filled symbols) and height of the PAA jet (open symbols). Both values are measured with respect to the undisturbed surface of the elastic boundary.

Figure 14 shows an example of the interaction of a laser-produced bubble with real tissue. The lesion was caused by the collapse of a laser-induced bubble near the corneal endothelium. When the cornea experiences small deformations, its elastic modulus is $E = 0.3 - 0.5$ MPa[13], similar to PAA with 80 % water content ($E = 0.25$ MPa). The dimensionless distance between bubble and cornea was $\gamma = 0.45$, which corresponds to the bubble splitting regime where very fast jets are formed. A central rupture in Descemet's membrane (the next layer below the corneal endothelium) is visible which was most likely caused by the impact of the high velocity liquid jet towards the elastic boundary formed after bubble splitting. Around the
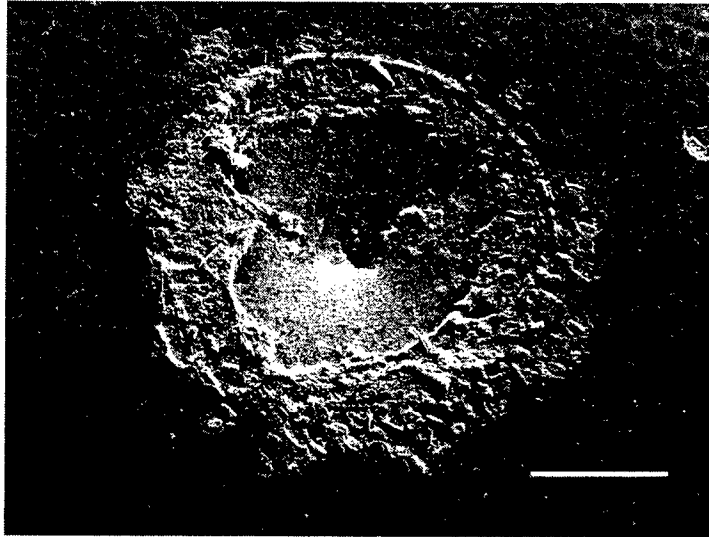
Figure 14: Scanning electron micrograph of the lesion produced by the interaction of a laser-induced cavitation bubble with a cornea specimen. The direction of the laser light was parallel to the surface of the cornea, the laser focus was located at the endo-thelial side of the cornea at a dimensionless distance $\gamma = 0.45$. The white bar represents 100 μm. Figure adapted from Reference [9].

central crater there is a zone where the endothelial cell layer is removed, and further outside another zone where the cells are still present, but damaged. These effects are probably caused by the shearing forces arising during the radial jet flow on the corneal surface after its impact, and by the tensile stress acting on the cornea during the elevation of its surface upon bubble collapse.

3.5 Conclusions

We conclude that cavitation erosion cannot be prevented by covering rigid structures with elastic materials. On the contrary: in a fairly large region of the (E,γ) parameter space, erosion is even more pronounced than for rigid boundaries. This is the case for those parameters where the bubble boundary interaction leads to annular jets which are followed by bubble splitting and the formation of very fast axial jets. The maximum jet velocities observed were 960 m/s towards the boundary and 600 m/s away from the boundary. Such high velocity jets penetrated the PAA sample even through a water layer of 0.35 mm thickness (at $E = 0.25$ MPa, $\gamma = 0.6$).

In short-pulsed laser surgery, liquid jet penetration, the jet-like ejection of boundary material, and the tensile stress from the collapsing bubble can contribute to the desired ablation or cutting effect, but these processes may also cause unwanted collateral damage if fine effects merely consisting in tissue evaporation are desired.

ACKNOWLEDGEMENT

REFERENCES

1. D. C. Gibson, "Cavitation adjacent to plane boundaries," *Proc. 3rd Australasian Conf. on Hydraulics and Fluid Mechanics*, Sydney, pp. 210-214, 1968.

2. D. C. Gibson and J. R. Blake, "Growth and collapse of cavitation bubbles near flexible boundaries," *Appl. Sci. Res.* **38**, 215-224, 1982.

3. J. R. Blake and D. C. Gibson, " Cavitation bubbles near boundaries," *Ann. Rev. Fluid Mech.* **19**, 99-123, 1987.

4. A. Shima, Y. Tomita, D. C. Gibson, and J. R. Blake, "The growth and collapse of cavitation bubbles near composite surfaces," *J. Fluid Mech.* **203**, 199-214, 1989.

5. J. H. Duncan, C. D. Milligan, and S. Zhang, "On the interaction between a bubble and a submerged compliant structure," *J. Sound Vibr.* **197**, 17-44, 1996.

6. S. J. Shaw, Y. H. Jin, T. P. Gentry, and D. C. Emmony, "Experimental observations of the interaction of a laser-generated cavitation bubble with a flexible membrane," *Phys. Fluids* **11**, 2437-2439, 1999.

7. T. Kodama and Y. Tomita, "Cavitation bubble behaviour and bubble-shock wave interaction near a gelatin surface as a study of in vivo bubble dynamics," *Appl. Phys.* B **70**, 139-149, 2000.

8. A. Vogel, "Nonlinear Absorption: intraocular microsurgery and laser lithotripsy," *Phys. Med. Biol.* **42**, 895-912, 1997.

9. A. Vogel, P. Schweiger, A. Frieser, M. N. Asiyo, and R. Birngruber, "Intraocular Nd:YAG Laser surgery: light tissue interaction, damage range, and reduction of collateral effects," *IEEE J. Quantum Electron.* **26**, 2240-2260, 1990.

10. E. A. Brujan, K. Nahen, P. Schmidt, and A. Vogel, "Dynamics of laser-induced cavitation bubbles near an elastic boundary," *J. Fluid Mech.* **433,** 251-281, 2001.

11. E. A. Brujan, K. Nahen, P. Schmidt, and A. Vogel, "Dynamics of laser-induced cavitation bubbles near elastic boundaries: Influence of the elastic modulus," *J. Fluid Mech.* **433**, 283-314, 2001.

12. F. A. Duck, *Physical Properties of Tissue*, Academic Press, London, 1990

13. D. A. Hoeltzel, P. Altmann, K. Buzard, and K. I. Choe, "Strip extensiometry for comparison of the mechanical properties of bovine, rabbit, and human corneas," *Trans. ASME E: J. Biomech. Engng* **114**, 202-215, 1992.

14. E. J. Chapyak and R. P. Godwin, "Physical mechanisms of importance to laser thrombolysis," *SPIE Proc.* **3245**, 12-18, 1998.

15. R. B. Chapman and M. S. Plesset, "Nonlinear effects in the collapse of a nearly spherical cavity in a liquid," *Trans. ASME* D: *J. Basic Eng.* **94**, 142-145, 1972.

16. J. R. Blake, M. C. Hooton, P. B. Robinson, and R. P.Tong, "Collapsing cavities, toroidal bubbles and jet impact," *Phil. Trans. R. Soc. Lond.* A **355**, 537-550, 1997.

17. G. Birkhoff, D. P. Macdougall, E. M. Pugh, and G. Taylor, "Explosives with lined cavities," *J. Appl. Phys.* **19**, 563-582, 1948.

18. A. Vogel, W. Lauterborn, and R. Timm, "Optical and acoustic investigations of the dynamics of laser-produced cavitation bubbles near a solid boundary," *J. Fluid Mech.* **206**, 299-338, 1989.

19. M. C. M. Grimbergen, R. M. Verdaasdonk, and C. F. P. van Swol, "Correlation of thermal and mechanical effects of the holmium laser for various clinical applications," *Proc. SPIE* **3254**, 69-79, 1998.

20. R. P. Godwin, E. J. Chapyak, S. A. Prahl, and H. Shangguan, "Laser mass ablation efficiency measurements indicate bubble-driven dynamics dominates laser thrombolysis," *Proc. SPIE* **3245**, 2-11, 1998.

Effects of IR wavelength on ablation mechanics: A study of acoustic signals

Stephen R. Uhlhorn, David Mongin
Mark A Mackanos and E. Duco Jansen

Vanderbilt University
Department of Biomedical Engineering
Nashville, TN 37235, USA

ABSTRACT

The effects of wavelength on infrared (IR) laser ablation with a free electron laser were studied by analyzing the acoustic signals produced during ablation of gelatin and tissue samples. The acoustic signals resulting from surface ablation of the samples were recorded with a piezoelectric microphone and the acoustic energy contained in the signal was calculated for samples of varying mechanical strength. Gelatin samples of different mechanical strengths were made by varying the water concentration in the gels to 70% and 90% wt./vol. The gels were irradiated at wavelengths of $\lambda = 2.94$, 2.80, and $6.45\,\mu$m with the measured acoustic energy normalized to the incident laser pulse energy. The results showed that while there was a statistically significant difference in the average acoustic energy measured for both concentrations of gelatin at $\lambda = 2.94$ and $2.80\,\mu$m, there was no difference in the average acoustic energy for the two concentrations of gelatin at $\lambda = 6.45\,\mu$m. This supports the model of mechanical weakening of the sample by breaking the amide II molecular bonds in proteins, originally proposed by Edwards et al.[1]

Keywords: Free electron laser, IR, tissue, ablation, acoustics

1. INTRODUCTION

Our overall goal in this research is to investigate the relative role of wavelength and pulse structure of a free electron laser (FEL) in soft tissue ablation. This laser has been used to study soft tissue ablation for several years now, and it is currently being used in clinical trials for neurosurgical cases. Despite all this, the mechanism of tissue ablation using the FEL is poorly understood.

The Vanderbilt University FEL is a continuously tunable source of pulsed mid-IR radiation with a wavelength tuning range of $\lambda = 2 - 10\,\mu$m. This make the FEL well suited for tissue ablation since most tissues are composed mostly of water, which is highly absorbing in the mid-IR spectrum. The FEL has been used to study many wavelengths in this region of the spectrum and there is evidence that by targeting the laser to protein absorption bands, namely the amide II, the laser can ablate tissue with high yield and minimal collateral damage. Edwards et al.[1] proposed that the absorption of laser radiation at $\lambda = 6.45\,\mu$m can break the amide II bonds which help hold the protein backbone together. This will weaken the mechanical strength of the tissue since the tissue matrix is composed of amide II bond containing proteins such as collagen.

The irradiation of an absorbing medium can cause acoustic transients to be generated by thermoelastic expansion and ablative recoil of the medium. The energy contained in the emitted pressure wave can be used as an indicator of the strength of the ablation event. For laser wavelengths where water is the primary absorber, the acoustic energy from ablation would be expected to increase in materials that have a higher relative water content. Recent studies have been published by Nahen et al.[2-4] where they reported a factor of 3–10 increase in the acoustic energy recorded during the ablation of a gelatin sample with 90% water content compared to a gelatin sample with 70% water content using a free-running Er:YAG laser at $\lambda = 2.94\,\mu$m. They attributed the extremely large difference in the acoustic energies recorded from the two different gels to the difference in the mechanical strength, where the gel with 90% water content was much softer and could eject material more easily than the harder gel with only 70% water.

Further author information: (Send correspondence to S.R.U.)
S.R.U.: E-mail: stephen.uhlhorn@vanderbilt.edu
E.D.J.: E-mail: duco.jansen@vanderbilt.edu
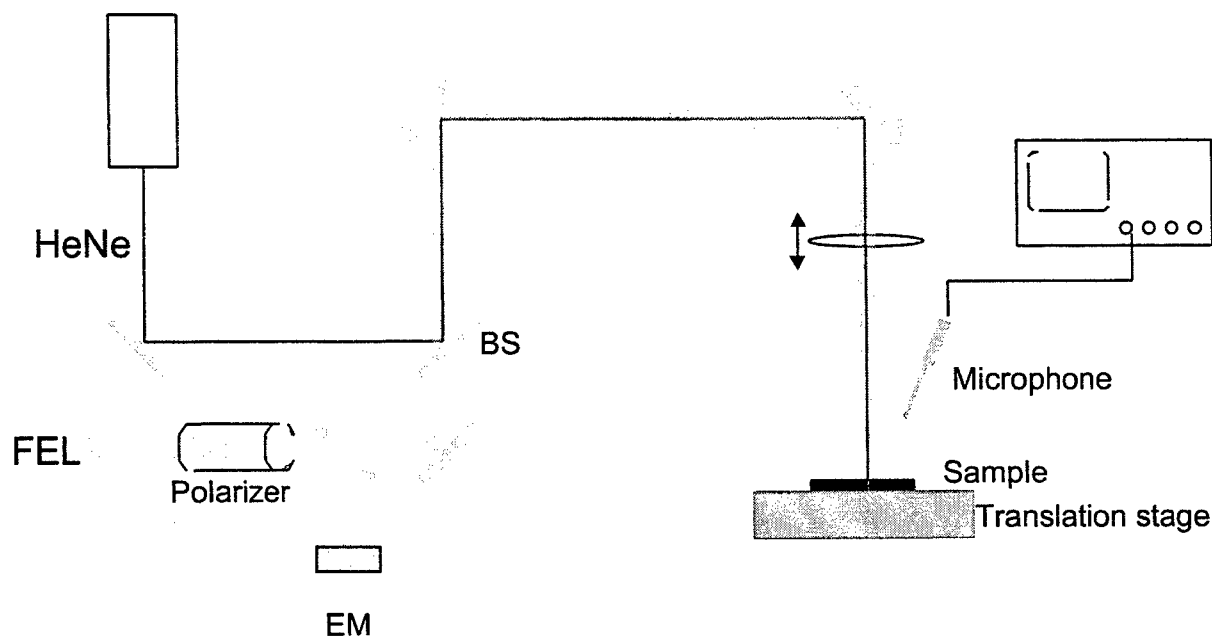
Figure 1. Experimental setup for recording acoustic signals. EM: energy meter; BS: beam splitter

Based on the results seen by Nahen et al., we should be able to observe a difference in the acoustic energy recorded at different wavelengths depending on whether or not the mechanical strength of a sample containing protein is indeed compromised by amide II bond-breaking. We expect to see a difference in acoustic energy in samples with different mechanical strengths when they are irradiated with wavelengths where only water absorption plays a role, e.g.— $\lambda = 2.94$ and $2.80 \, \mu m$. On the other hand, at wavelengths where amide II bond breaking is proposed, this difference in acoustic energy which is caused by differences in tissue mechanical properties should be eliminated since the $\lambda = 6.45 \, \mu m$ wavelength weakens the structural mechanical properties by means of the amide II bond breaking. Thus, our hypothesis is that tissue ablation using a free electron laser, and the associated collateral damage is attributable to both the wavelength and pulse structure.

2. METHODS

Gelatin samples of different mechanical properties were prepared by making the water concentration in the samples 70% and 90% wt./vol. Additionally, rat skin samples were used as well. The spot diameter of the laser was held at 1.0 mm and the repetition rate of the laser was 2 Hz. The samples were placed on a translation stage and moved at a constant speed of 3 mm/s so that there was no overlap of subsequent pulses. Two sets of experiments were performed. In the first, the incident energy was adjusted to twice the ablation threshold of water. In the second, the pulse energy was varied from 0–20 mJ, which corresponds to 0–25.6 mJ/mm² for the 1.0 mm spot size. The acoustic transducer was an amplified piezoelectric microphone with a frequency response of 5 kHz to 1MHz (PCB, 132A42). For each sample and wavelength studied, the average of 30 acoustic traces was recorded on an oscilloscope and the calculated acoustic energy, $E_{ac} = \int_0^t p^2(t) \, dt$, was normalized to the incident laser pulse energy.

The experimental set up appears in Fig. 1. The FEL is attenuated with a polarizer to adjust the incident energy, and a portion of the beam is picked off with a CaF_2 window and monitored with an energy meter. The laser beam was focused onto the sample with a CaF_2 lens ($f = 200$ mm). The acoustic signals were recorded with the microphone positioned 3 mm from the sample surface at $\approx 30°$ off of the beam axis and a He-Ne laser was coupled into the beam path for alignment purposes.

3. RESULTS

The results for all wavelengths studied are summarized in Fig. 2. The normalized acoustic energy for all wavelength and samples is plotted as a function of wavelength. The samples were irradiated at twice the threshold fluence for
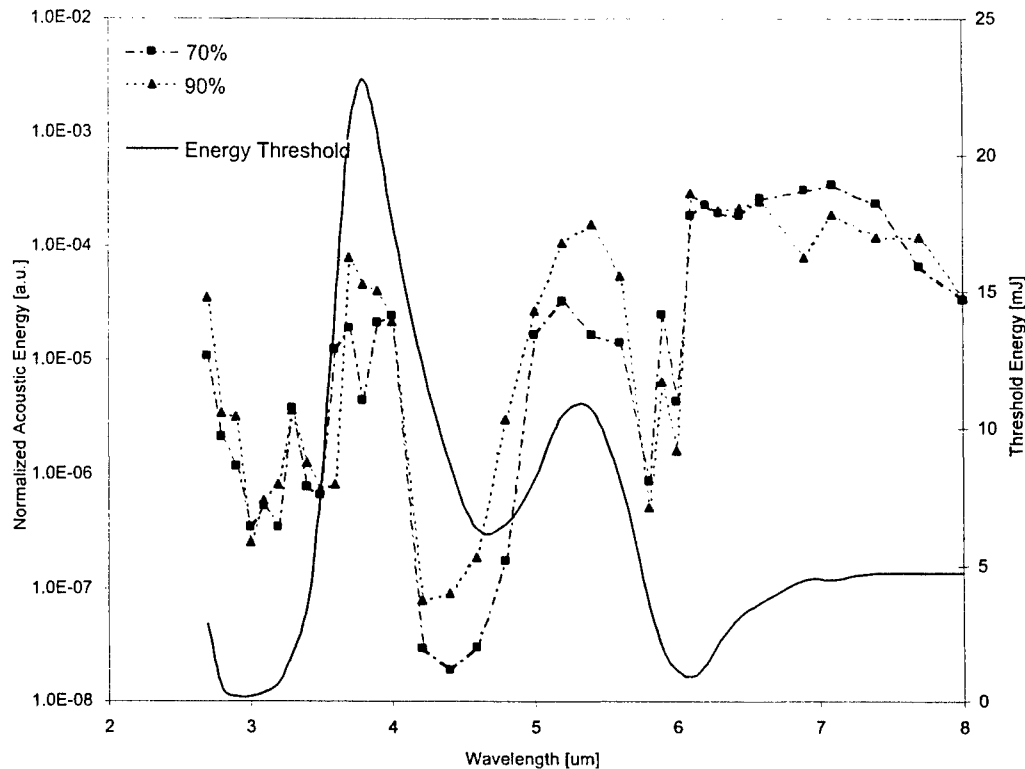
Figure 2. Normalized acoustic energy for all wavelengths studied using 70% and 90% water content gelatin and rat skin samples at 2X threshold fluence for water ablation. Each data point is the normalized acoustic energy for the average of 30 signals. These data points are plotted with the ablation threshold energy for water.

water absorption, which is plotted with the data. From the plot, we can see that the acoustic energy for each sample roughly follows the water ablation threshold curve, i.e.—the absorption coefficient. Another observation is that for most wavelengths, the emitted acoustic energy is different for the 70% and 90% water gelatin samples, while in the region between $\lambda = 6.0 - 6.45\,\mu m$ the acoustic energy appears to be the same for both gelatin samples.

Of all the wavelengths studied, three are of special interest, $\lambda = 2.94$, 2.80, and 6.45 μm. At $\lambda = 6.45\,\mu m$, the gelatin samples have a strong absorption peak from the amide II bonds in addition to the water absorption. At $\lambda = 2.94\,\mu m$, which is the Er:YAG laser line, the gels do not demonstrate any protein absorption, only water absorption, however the absorption coefficient is about an order of magnitude greater than at $\lambda = 6.45\,\mu m$. We included $\lambda = 2.80\,\mu m$ in the studies because it has the same absorption coefficient as $\lambda = 6.45\,\mu m$, but is strictly governed by water absorption.

The acoustic energy for each sample at several incident energies for $\lambda = 2.94\,\mu m$ is seen in Fig. 3. In it, we see that there is a statistically significant difference ($p < 0.001$) in the measured acoustic energy from the 70% and 90% water content gelatin samples which was consistent for input energies used between 5 and 25 mJ. At very low fluences (2 and 0.5 mJ), there was not a significant difference. For all energies with a significant difference in average acoustic energy the gelatin sample with 90% water (the softer gel) had produced more acoustic energy than the gelatin with 70% water (the harder gel). This trend is in agreement with what was expected, however we did not observe the extremely large differences in acoustic energy that Nahen et al. observed.

Repeating the previous experiment at $\lambda = 2.80\,\mu m$ (Fig. 4) gave similar results. At most incident laser energies there was a statistically significant difference in the average acoustic energy recorder for the 70% and 90% water gels. Again, the softer gel (90% water) produced a larger acoustic energy emission than the harder gel (70% water).

At $\lambda = 6.45\,\mu m$ (Fig. 5, we observed a different result. For all incident laser energies, there was no statistically
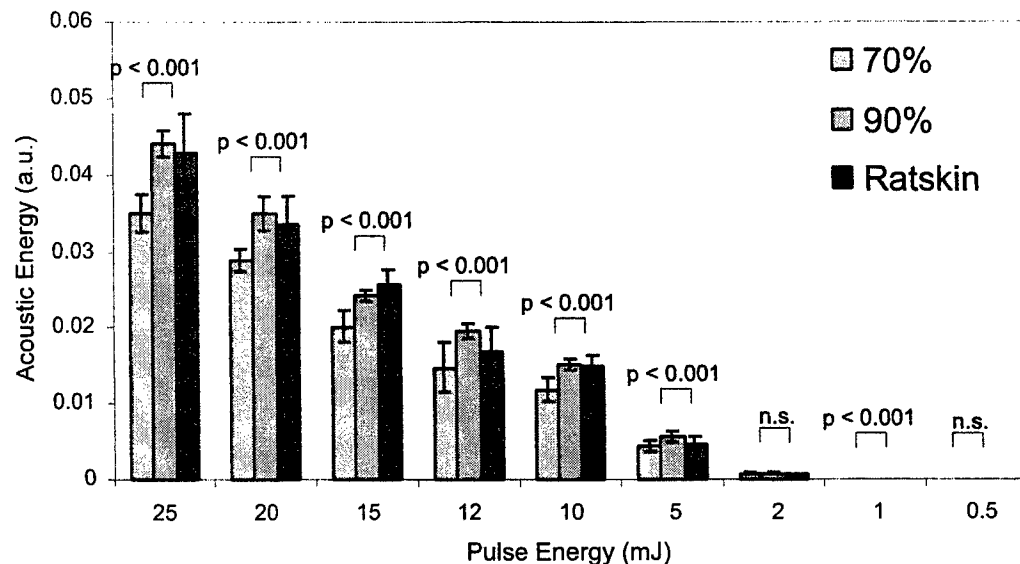
Figure 3. Average normalized acoustic energy at $\lambda = 2.94\,\mu m$ for 70% and 90% water content gelatin and rat skin samples. Most incident energies showed a statistically significant difference ($p < 0.001$) in the average acoustic energy for the 70% and 90% water gels. n.s.: no statistical significance
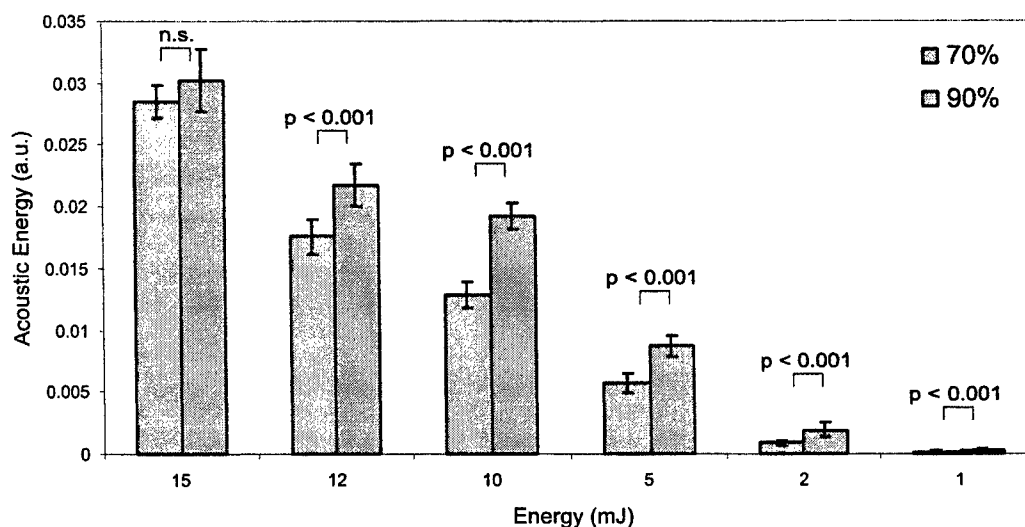
Figure 4. Average normalized acoustic energy at $\lambda = 2.80\,\mu m$ for 70% and 90% water content gelatin. Most incident energies showed a statistically significant difference ($p < 0.001$) in the average acoustic energy for the 70% and 90% water gels. n.s.: no statistical significance
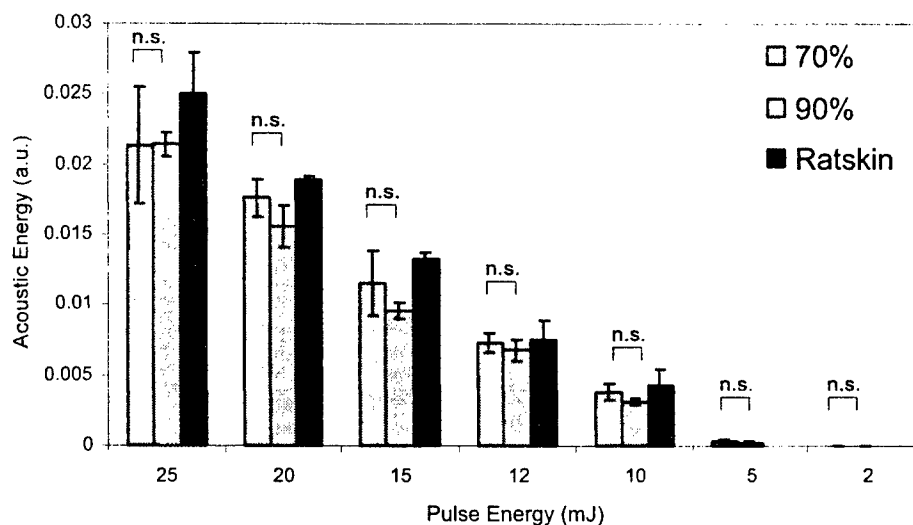
Figure 5. Average normalized acoustic energy at $\lambda = 6.45\,\mu m$ for 70% and 90% water content gelatin and rat skin samples. All incident energies showed no statistically significant difference in the average acoustic energy for the 70% and 90% water gels. n.s.: no statistical significance

significant difference in the average acoustic energy emitted from the 70% and the 90% water gels. This agrees well with our hypothesis that if the mechanical strength of the protein matrix is compromised by amide II absorption, the differences in emitted acoustic energy for gels with different mechanical strengths should be mush smaller for $\lambda = 6.45\,\mu m$, than for other wavelengths where protein absorption is not a factor.

4. CONCLUSIONS

From the results presented, several conclusions can be drawn. The region between $\lambda = 6.0 - 6.45\,\mu m$ shows no difference in the average acoustic energy emitted during FEL ablation of gelatin samples with different mechanical strengths. Furthermore, by comparing the results from $\lambda = 2.80$, 2.94 and 6.45 μm, we can see that while there are significant differences in the acoustic energy emitted from the two gels with different concentrations at $\lambda = 2.80$ and 2.94 μm, there is no difference at $\lambda = 6.45\,\mu m$. This supports the model of amide II molecular bond-breaking at $\lambda = 6.45\,\mu m$. At $\lambda = 2.80$ and 2.94 μm, there is no absorption by the protein component of the samples and consequently, no effect on the mechanical strength.

The differences in emitted acoustic energy observed at water absorbing wavelengths ($\lambda = 2.94\,\mu m$) between the two gelatin samples were significant, but not as great as those observed by Nahen et al. One possible explanation for this the FEL pulse structure. The FEL pulse structure consists of a train of very fast (1 ps) micropulses that have been shown to generate large stress transients[5] which may be capable of affecting the mechanical strength of the sample.

ACKNOWLEDGMENTS

REFERENCES

1. G. Edwards, R. Logan, M. Copeland, L. Reinisch, J. Davidson, B. Johnson, R. Maciunas, M. Mendenhall, R. Ossoff, J. Tribble, J. Werkhave, and D. O'Day, "Tissue ablation by a free-electron laser tuned to the amide II band," *Nature* **371**, pp. 416–419, 1994.

2. K. Nahen and A. Vogel, "Investigations on acoustic on-line monitoring of ir laser ablation of burned skin," *Lasers in Surgery and Medicine* **25**(1), pp. 69–78, 1999.

3. K. Nahen and A. Vogel, "Acoustic signal characteristics during ir laser ablation, and their consequences for acoustic tissue discrimination," in *Laser-Tissue Interaction XI: Photochemical, Photothermal, Photomechanical*, vol. 3914, SPIE, 2000.

4. K. Nahen, W. Eisenbeiß, and A. Vogel, "Acoustic on-line moitoring of ir laser ablation of burnt skin," in *Biomedical Optoacoustics*, vol. 3916, SPIE, 2000.

5. S. R. Uhlhorn, R. A. London, A. J. Makarewicz, and E. D. Jansen, "Hydrodynamic modeling of tissue ablation with a free-electron laser," in *Laser-Tissue Interaction XI: Photochemical, Photothermal, Photomechanical*, vol. 3914A, SPIE, 2000.

Minimization of thermo-mechanical side effects in IR ablation by use of Q-switched double pulses

Alfred Vogel[*], Peter Schmidt, and Barbara Flucke

Medizinisches Laserzentrum Lübeck, 23562 Lübeck, Germany

ABSTRACT

Holmium laser pulses ($\lambda = 2.1$ µm) are often used for medical laser applications inside the human body, because they can be transmitted through low-OH quartz fibers, and they are relatively well absorbed in water and biological tissues. However, large thermal damage zones were observed after application of free-running holmium laser pulses for arthroscopic surgery. The aim of our study is to reduce thermal damage without introducing additional mechanical damage and without impairing the hemostatic action of the laser radiation. For that purpose we use double pulses from a custom-made acousto-optically Q-switched thulium laser ($\lambda = 2.0$ µm) that can emit pulses with energies of up to 150 mJ. The penetration depth of the thulium laser radiation (170 µm) as well as the thermal damage zone are only half as large as that of the holmium laser. The use of Q-switched pulses creates stress confinement conditions leading to a more efficient ablation than with free running pulses. For a given ablation depth, the residual heat deposited in the tissue is therefore smaller than with free-running pulses and, hence, also the thermal damage zone. This reduction of thermal damage is possible even though the free-running pulses already fulfil the condition for thermal confinement. The thermal damage zone was only 100 µm for the Q-switched thulium pulses but 200 µm for the free-running pulses. The degree of thermal damage was, in addition, much more severe for the free-running pulses. Q-switched pulses lead to an explosive ablation of the target material. In a liquid environment, this gives rise to the formation of cavitation bubbles and to mechanical damage of the surrounding tissue. To reduce the cavitation effects, we release a pre-pulse with small energy (40 mJ) before each ablation pulse of up to 150 mJ. The pre-pulse produces a small cavity that is then filled by the ablation products of the main pulse. The ablation pulse is emitted about 100 µs after the pre-pulse when the bubble is maximally expanded. This way, no additional cavitation effects are induced, and the transformation of laser energy into mechanical energy is minimized. The pre-pulse creates, furthermore, a channel through which the laser light is transmitted, avoiding absorption losses in the liquid between fiber tip and target. The ablation efficiency was 2-3 times better for the Q-switched pulses than for the free-running pulses.

Key words: Thulium laser, Q-switched pulses, double pulses, arthroscopy, cartilage, thermal damage, cavitation, mechanical effects, ablation efficiency

1. INTRODUCTION

Holmium laser pulses ($\lambda = 2.1$ µm) are often used for medical laser applications inside the human body, because they can be well transmitted through low-OH quartz fibers, and they are relatively well absorbed in water and biological tissues. However, thermal damage zones of up to 800 µm were observed after application of free-running holmium laser pulses for arthroscopic surgery.[1, 2] The aim of our study is to reduce thermal damage without introducing additional mechanical damage and without impairing the hemostatic action of the laser radiation. For that purpose we employ a thulium laser ($\lambda = 2.0$ µm) instead of a holmium laser, because the penetration depth of the thulium laser radiation (170 µm)[3] is only half as large as that of the holmium laser. The smaller penetration depth leads to a smaller thermal damage zone. A further reduction of the thermal damage is achieved by using Q-switched pulses instead of free-running pulses.[4] For Q-switched pulses, stress confinement conditions[5, 6] are fulfilled which lead to a more efficient ablation than with free running pulses.[7] For a given ablation depth, the residual heat deposited in the tissue is therefore smaller than with free-running pulses and, hence, also the thermal damage zone. This reduction of thermal damage is possible even though the free-running pulses already fulfill the condition for thermal confinement.

Q-switched laser pulses lead to an explosive ablation of the target material. In a liquid environment, this gives rise to the formation of cavitation bubbles which may cause mechanical damage in the surrounding tissue.[8] To reduce the hazardous cavitation effects as much as possible, we release a pre-pulse with small energy before each ablation pulse with larger

---

energy. The principle of this technique, which has been described in detail in a previous publication,[9] is illustrated in Figure 1. The pre-pulse produces a small cavity which is then filled by the ablation products of the main(=ablation) pulse. The ablation pulse is released about 100 µs after the pre-pulse when the bubble is maximally expanded. When the energy ratio of the pulses is optimally chosen, the ablation products raise the pressure in the bubble to ambient pressure, but not higher. This way, no additional cavitation effects are induced, and the transformation of the energy of the ablation pulse into mechanical energy is minimized. As a result, tissue tearing and other mechanical side effects are minimized as well.

(a) Pre-pulse alone
   (small energy)

(b) Ablation pulse alone
   (large energy)

(c) Pre-pulse + ablation pulse
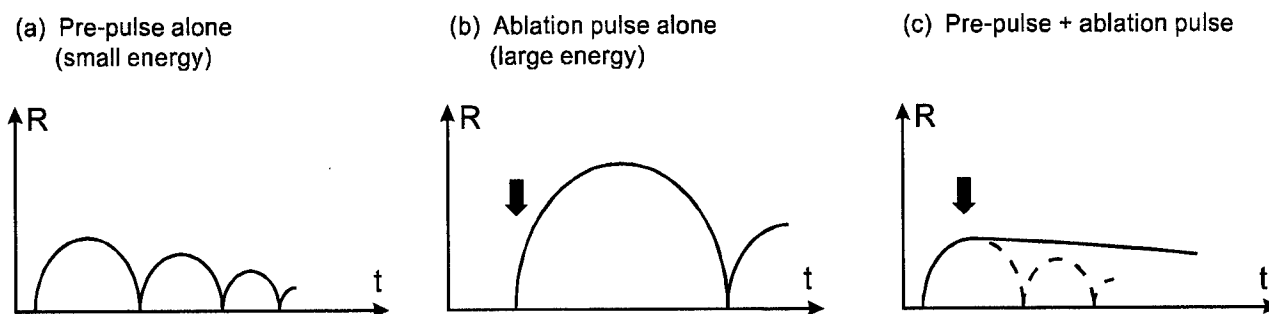
Figure 1: Illustration of the reduction of cavitation effects achieved by employing double pulses. The schematic drawings show the radius vs time curve of the cavitation bubble oscillation for single pulses with small energy (a) and large energy (b), as well as for double pulses consisting of a pre-pulse with small energy and an ablation pulse with large energy (c). The ablation pulse is released when the bubble created by the pre-pulse has reached its maximum size.

The transiently empty space created by the pre-pulse is not only a prerequisite to reduce the mechanical side effects originating from the ablation pulse, but it also facilitates the energy deposition in the tissue to be ablated. If the fiber tip is located at a certain distance from the tissue surface, as usually the case in clinical practice, a considerable fraction of the laser light will be absorbed in the water between fiber tip and application site. The pre-pulse bubble forms a channel through which the laser light is transmitted, thus avoiding absorption losses in the liquid.

2. METHODS

2.1 Generation of Q-switched double pulses

The double pulses were obtained from a custom-made acousto-optically Q-switched thulium laser (λ = 2.0 µm) which was based on the clinical holmium laser system BLM 1000 produced by Baasel Lasertech. The Cr,TmHo:YAG rod was replaced by a 127 mm long Cr,Tm:YAG rod with 4 mm diameter (0.6% Cr, and 6% Tm). An acousto-optic Q-switch (Gooch & Housego) was introduced into the 70 cm long resonator next to the highly reflecting mirror. The acousto-optic Q-switch was specified for 50 W HF power applicable in permanent operation, but we used 100 W HF power in a pulsed operation mode (during and shortly after the flash lamp discharge) to achieve a diffraction efficiency of 40%. A sapphire window with a total reflectivity of 16% was used as output coupling mirror. The low reflectivity of the sapphire window limits the laser power in the resonator at a given laser pulse energy and is thus an efficient means to protect the optical elements in the resonator. With this system, we could produce laser pulses with energies of up to 150 mJ and a duration of 70 ns.

The technique used for the generation of double pulses is illustrated in Figure 2. The Q-switch was opened for the pre-pulse when the inversion in the laser medium was high enough to produce a pulse of the desired energy. It was opened a second time 60-150 µs later to release the ablation pulse when the bubble created by the pre-pulse was maximally expanded. To achieve the maximum desired energy of the ablation pulse at this time, the flash lamp voltage was adjusted accordingly. To create ablation pulses with smaller energy, the duration of the flash lamp discharge was reduced without altering the voltage. This technique allowed for the generation of double pulses with variable time separation and energy ratio. We could achieve an energy ratio of up to 1:10 between pre-pulse and ablation pulse, with an ablation pulse energy of 150 mJ.

The second pulse in a sequence of two successive pulses is usually longer (up to 150 ns) than a single pulse of equal energy. The prolongation of the pulse duration is probably a consequence of the interaction of the pre-pulse with the medium shortly before the main pulse is released. This interpretation is supported by the fact that the pulse prolongation is more pronounced for higher pre-pulse energies.

The Q-switched pulses could be transmitted through a low-OH quartz fiber with a core diameter of 600 µm.
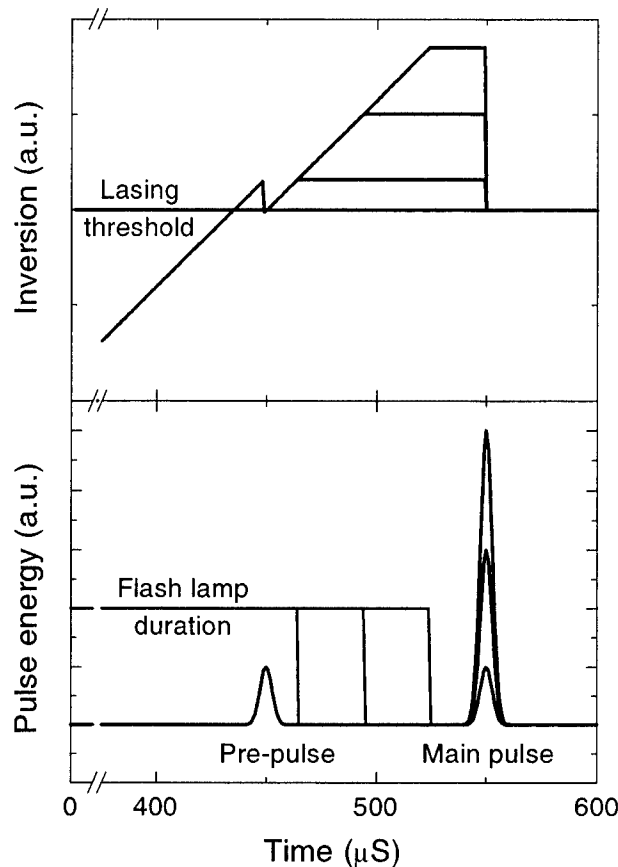
Figure 2: Illustration of the technique used for the generation of double pulses with variable energy ratio and pulse separation (see text).

2.2 Irradiation of tissue samples

We used hyaline cartilage from porcine knee joints obtained from a local slaughterhouse to demonstrate the tissue effects of Q-switched thulium double pulses in comparison to free running thulium pulses. The knees were used within 24 hours after slaughtering and stored on ice or at 4°C in the refrigerator until the experiment was performed. Circular specimens were obtained using a 9 mm trepan. They were irradiated under an angle of 30° with a distance of 500 μm between fiber tip and sample surface to simulate clinical conditions. The fiber had a core diameter of 600 μm, and the irradiated spot size was 800 μm. The specimens were translated by 100 μm after each laser exposure such that a cut was produced after applying a series of pulses.

2.3 Flash photography of cavitation bubble dynamics

The dynamics of the cavitation bubbles produced at the fiber tip was investigated by time resolved photography. Photographs were taken with 4.5x magnification on Kodak TMax 100 film using a Zeiss macro-objective (F=4.5, f = 63 mm). The bubbles were back-illuminated with a parallel beam from a xenon flash lamp (High Speed Photosystems, Wedel, Germany) with 150 ns flash duration.

2.4 Histologic determination of the thermal damage range

Immediately after irradiation, the specimens were immersed in liquid nitrogen, and 6-8 μm thick sections were prepared using a cryo-microtome (Leica/Reichert Jung Frigocut 2800 E, Bensheim, Germany). The sections were air-dried at 37°C for several days. They were stained with hematoxiline after Weigert, light green, and safranin-O.[10] After dehydration in a series of graded alcohols and xylol they were mounted and inspected by light microscopy.

2.5 Determination of ablation rates by OCT

The ablation rates were determined by measuring the cross section of the cut in the cartilage specimen using optical coherence tomography (4Optics, Lübeck, Germany).

3. RESULTS AND DISCUSSION

3.1 Reduction of cavitation effects by double pulses

The pulse energy for generation of the pre-pulse has to be sufficiently high to guarantee bubble generation in 100% of the cases. The bubble must, furthermore, be large enough to completely create a channel between the fiber tip and the tissue surface. Tissue ablation by the main pulse will be considerably reduced if liquid remains on the tissue surface after the pre-pulse. Both requirements are fulfilled for laser pulse energies of 35-40 mJ (Fig. 3).
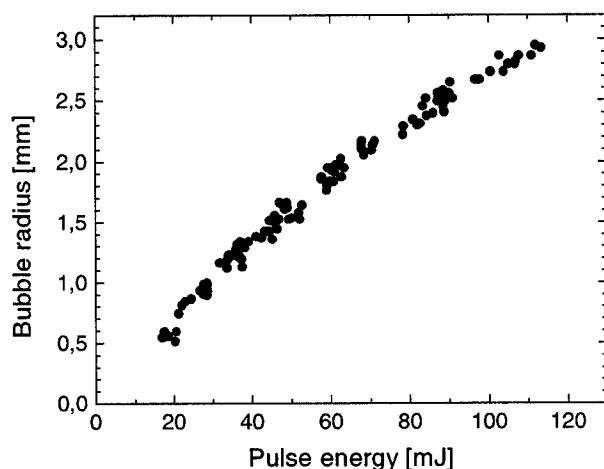
Figure 3: Maximum cavitation bubble radius plotted as a function of laser pulse energy. To produce a channel between the fiber tip and a tissue surface at 1 mm distance, a minimum bubble radius of 1 mm is required. This radius can be achieved at pulse energies of 35-40 mJ.

Figure 4 shows the cavitation bubble at maximum expansion when the cartilage specimen was irradiated by single pulses of 40 mJ and 100 mJ, respectively, and by a double pulse consisting of a 40 mJ pre-pulse and a 100 mJ ablation pulse. The ablation pulse was released 120 μs after the pre-pulse. It is obvious that the double pulse technique reduces the cavitation effects. The ablation pulse does not lead to an enlargement of the cavitation bubble beyond the size reached after the pre-pulse. The volume of the bubble produced by the double pulse (Fig. 4c) amounts to only 1/9 of the value that is reached when the 100 mJ ablation pulse is applied alone (Fig. 4b).
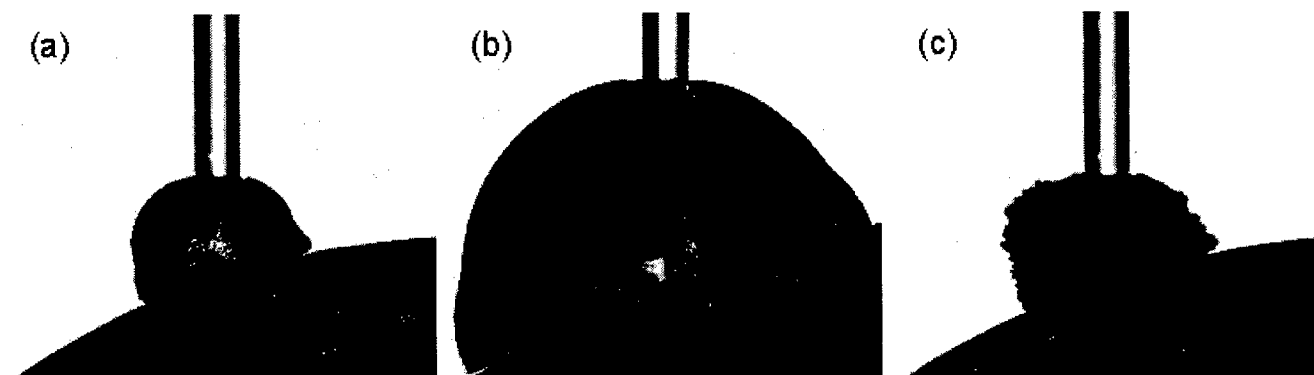
Figure 4: Reduction of cavitation effects by use of double pulses. The distance between fiber tip and the surface of the cartilage sample was 500 μm. (a) Cavitation bubble after a single QS-pulse with 40 mJ pulse energy. (b) Bubble after a single 100 mJ laser pulse. (c) Cavitation bubble after application of double pulses. A pre-pulse of 40 mJ was followed by an ablation pulse of 100 mJ which was released when the bubble produced by the pre-pulse was maximally expanded (after 100 μs). All pictures show the bubble at the stage of maximum expansion. Frame width: 5.5 mm.
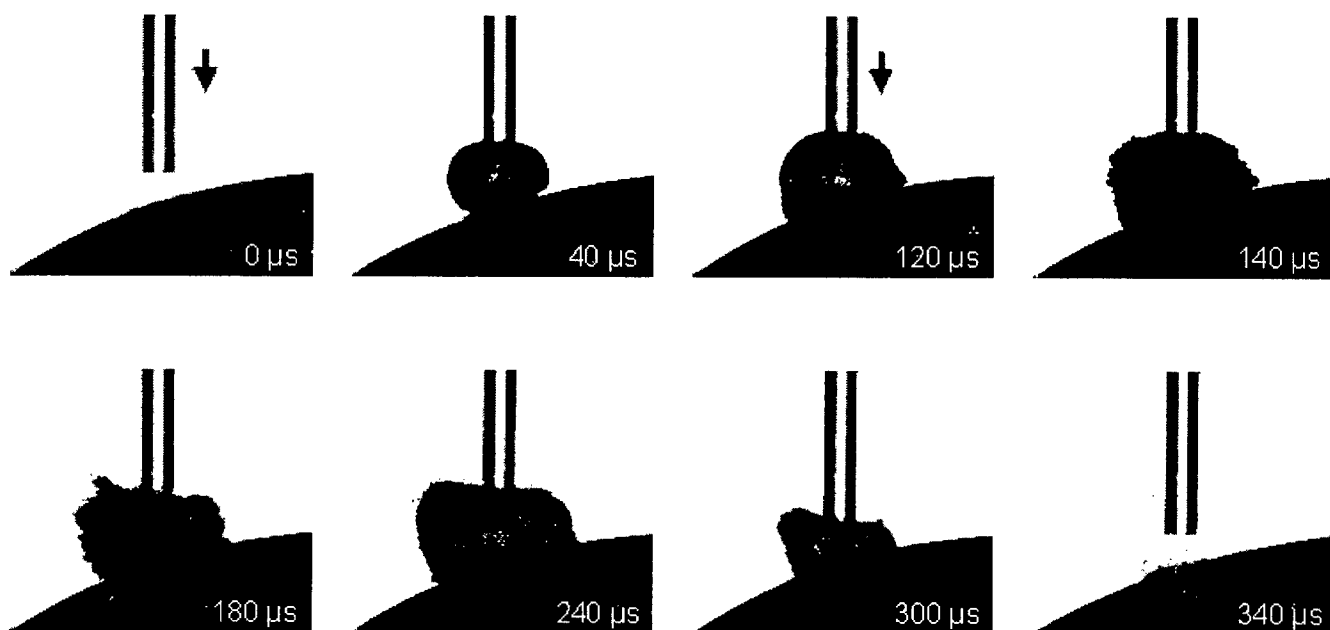
Figure 5: Cavitation bubble dynamics induced by a Q-switched double pulse of 40 mJ + 100 mJ. The arrows mark the times at which the pre-pulse and the ablation pulse are released (time separation 120 μs).

Figure 5 shows the dynamics induced by the double pulse. The bubble formed by the pre-pulse creates an empty space between fiber tip and tissue surface. The bubble wall is deformed by the impact of ablation products which are ejected from the tissue surface after release of the main pulse. The collapse phase lasts twice as long as the expansion phase of the bubble, probably owing to the ablation products filling the bubble.

3.2. Thermal damage zone after Q-switched double pulses and free-running pulses from a thulium laser

Figure 6 shows histologic sections of cartilage tissue after application of a Q-switched double pulse (40 mJ + 100 mJ, Fig. 6a) and of a free-running thulium laser pulse (600 mJ, Fig. 6c). The ablated mass is similar in both cases, but the thermal damage zone is twice as large and more severe with the free running pulse ($\approx$200 μm) than with the Q-switched double pulse ($\approx$100 μm). In the inner zone of the lesion produced by the free-running pulse, cells are completely absent and the connective tissue is stained more intense than healthy tissue. Such severe damage is not observed with Q-switch pulses. The lesion produced by the QS-double pulse looks similar to the outer zone of the lesion from the free-running pulse. Here, the cell nuclei are condensed, and the connective tissue is stained less intense than the healthy tissue.

The thermal confinement condition is fulfilled both for the Q-switched and the free-running pulses, since the thermal relaxation time $\tau_R = \delta^2/4\kappa$ is about 50 ms ($\delta = 170$ μm is the optical penetration depth, and $\kappa = 0.15$ mm^2/s is the thermal diffusivity of water at 37°C). The reduction of thermal damage achieved by use of Q-switched pulses can thus not be explained by less thermal diffusion with the shorter pulse duration. It is, in fact, caused by the higher ablation efficiency of the Q-switched pulses (see section 3.3 below). The higher ablation efficiency is coupled with less residual heat in the tissue at equal ablated mass and, therefore, with less thermal damage.
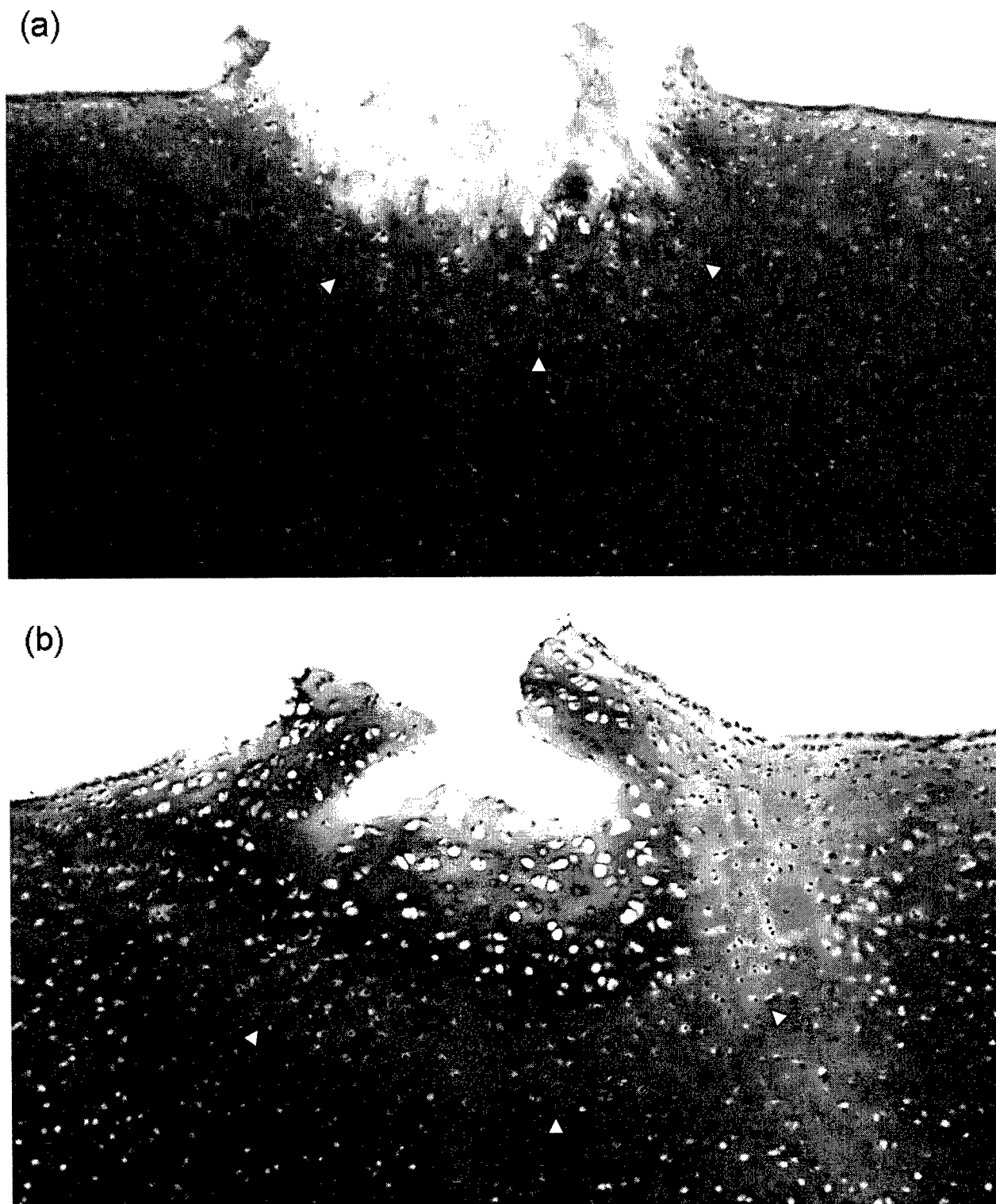
Figure 6: Histologic sections of laser effects in cartilage produced (a) by Q-switched double pulses (40 mJ + 120 mJ) and (b) by free-running pulses with 600 mJ. The pulse energies were selected such as to compare laser effects with a similar amount of ablated material. The thermal damage zone is much larger after the free-running pulse than after the QS-double pulse, and the damage is more severe. In the inner zone of the lesion produced by the free-running pulse, cells are completely absent and the connective tissue is stained more intense than healthy tissue. The outer zone looks similar to the lesion produced by the QS-double pulse (arrowheads). Here, the cell nuclei are condensed, and the connective tissue is stained less intense than the healthy tissue.

3.3 Ablation rates of Q-switched double pulses and free-running pulses from a thulium laser

The efficiency of cartilage ablation under water achieved with Q-switched double pulses is 2-3 times higher than with free-running pulses, and the ablation threshold is much lower (Fig. 7a, Table 1). This result can be explained by the fact that the stress confinement condition $\tau_L < \delta / c$ is fulfilled for Q-switched pulses but not for free-running pulses (τ_L is the laser pulse duration, δ is the optical penetration depth, and $c = 1500$ m/s is the sound velocity in water). Since the duration of the Q-switched ablation pulses (70-150 ns) is in the order of the time for stress waves to propagate a distance equal to the optical penetration depth (115 ns for $\delta = 170$ μm), thermoelastic stresses build up during the pulse. The compressive, tensile and shear stresses resulting from the thermoelastic expansion of the heated tissue lead to local ruptures of the tissue matrix.[7] These tears facilitate the material ejection driven by the explosive vaporization of the tissue water. That lowers the ablation threshold and increases the ablation efficiency.
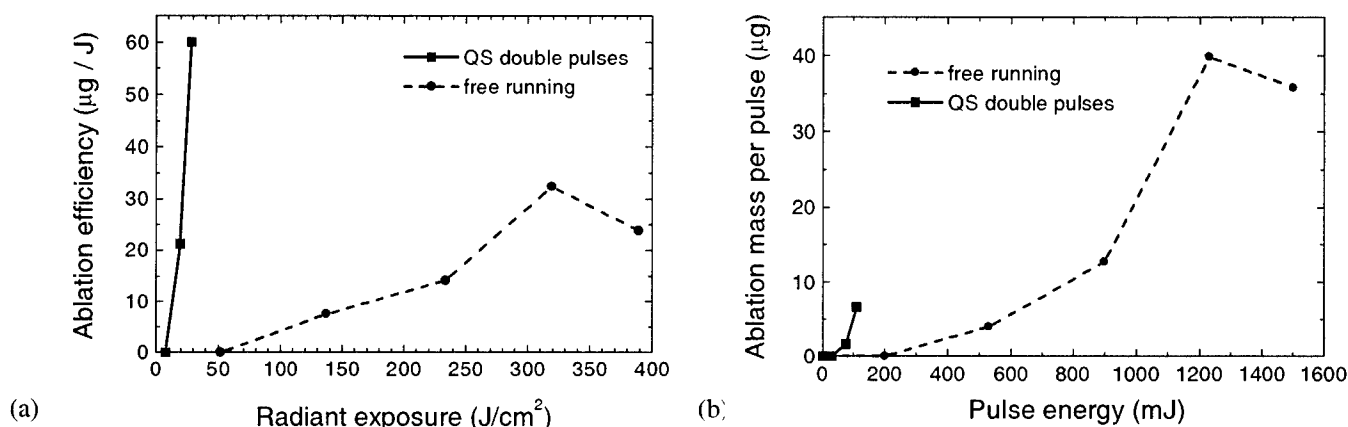
Figure 7: Ablation efficiency (a) and ablated mass per pulse (b) for cartilage ablation under water using QS-double pulses and free running pulses. The distance between fiber tip and tissue surface was 500 μm.

Even though the ablation efficiency is higher for the Q-switched pulses, the ablated mass per pulse is still higher with free-running pulses because larger pulse energies are available in this mode of operation (Fig. 7b). It should be noted, however, that one should not make use of pulse energies beyond 1 J in clinical practice to avoid excessive thermal damage. In the energy range below 1 J, free-running pulses ablate little more material than Q-switched double pulses. Another point worth mentioning is that the energy range available with Q-switched pulses has not yet been fully exploited in the first ablation experiments reported here. We have used only 100 mJ pulses, while the maximum pulse energy is 150 mJ. We expect that with 150 mJ pulse energy the ablated mass will be comparable to the mass removal with 1 J free-running pulses.

Laser	Ablation threshold (J/cm²)		Ablation efficiency (μg/J)	
	air	water	air	water
Thulium, Q-switched	10	14	102	60
Thulium, free-running	50	70	60	25

Table 1: Comparison of ablation thresholds of QS-double pulses and free-running pulses in water and air. The values for water refer to a distance of 500 μm between fiber tip and tissue surface. The ablation efficiencies refer to the highest pulse energies investigated.

Table 1 presents a comparison of the ablation thresholds and efficiencies in water and air for both operation modes of the laser. Thresholds are higher and efficiencies are lower in water than in air, because ablation is impaired by the water layer between fiber tip and tissue surface. The ablation efficiency drops 60% of the value in air for free-running pulses but only 40% for the double pulses. The impairment of ablation is less pronounced for the Q-switched double pulses because the release of a pre-pulse is a very efficient way to create an absorption-free channel to the ablation site.

3.4 Conclusions

Thermo-mechanical side effects in IR ablation can be minimized by use of Q-switched double pulses. Extent and severity of thermal damage is much less with Q-switched pulses than with free-running pulses. The thermal effects are, on the other hand, probably still strong enough to support hemostasis: a thermal damage zone of 85 μm is sufficient for hemostatic effects in skin,[11] and the damage zone observed in our experiments with Q-switched thulium pulses is ≈100 μm.

The use of double pulses guarantees that the reduction of thermal effects is not coupled with an increase of mechanical damage. The pre-pulse creates a small bubble which is then filled by the ablation products of the main pulse without being further enlarged. The cavitation effects of Q-switched double pulses with appropriate energy ratio are, therefore, much weaker than of single pulses.

Ablation with Q-switched thulium pulses occurs under stress confinement conditions and is, therefore, 2-3 times more efficient than with free-running pulses.

ACKNOWLEDGEMENT

REFERENCES

1. K. B. Trauner, N. S. Nishioka, T. Flotte, and D. Patel, "Acute and chronic response of articular cartilage to holmium:YAG laser irradiation," *Clin Orthopaed Rel Res* **310**, 52-57, 1995.

2. C. T. Vangsness, T. Watson, V. Saadatmanesh, and K. Moran, "Pulsed Ho:YAG laser menisectomy: effect of pulsewidth on tissue penetration rate and lateral thermal damage," *Lasers Surg Med* **16**, 61-65, 1995.

3. K. P. Köstli, M. Frenz, H. P. Weber, G. Paltauf, and H. Schmidt-Kloiber, "Optoacoustic measurements of water, bone and cartilage with an infrared-OPO," *Proc. SPIE* **3601**, 310-318, 1999.

4. M. Frenz, H. Pratisto, F. Könz, E. D. Jansen, A. J. Welch, and H. P. Weber, "Comparison of the effects of absorption coefficient and pulse duration of 2.12-μm and 2.79-μm radiation on laser ablation of tissue, " *IEEE J Quant Electron* **32**, 2025-2036, 1996.

5. R. S. Dingus and R. J. Scammon, "Grüneisen-stress induced ablation of biological tissue," *Proc. SPIE* **1427**, 45-54, 1991.

6. S. L. Jacques, "Laser-tissue interactions. Photochemical, photothermal, and photomechanical," *Lasers Gen. Surg.* **72**, 531-558, 1992.

7. I. Itzkan, D. Albagli, M. L.Dark, L. T. Perelman, C. von Rosenberg, and M. Feld, "The thermoelastic basis of short pulsed laser ablation of biological tissue," *Proc. Natl. Acad. Sci. USA* **92**, 1960-1964, 1995.

8. A. Vogel, E. A. Brujan, P. Schmidt, and K. Nahen, "Interaction of laser-produced cavitation bubbles with an elastic tissue model," *Proc. SPIE* **4257** (this issue), 2001.

9. A. Vogel, R. Engelhardt, U. Behnle, and U. Parlitz, "Minimization of cavitation effects in pulsed laser ablation - illustrated on angioplasty. *Appl Phys B* **62**, 173-182, 1996.

10. B. E. Gerber, T. Asshauer, G. Delacretaz, T. Jansen, and T. Oberthür, "Biophysikalische Grundlagenuntersuchungen zur Wirkung der Holmium-Laserstrahlung am Knorpelgewebe und deren Konsequenzen für die klinische Applikationstechnik," *Orthopädie* **25**, 21-29, 1996 (in German).

11. H. A. Green, Y. Domankevitz, and N. S. Nishioka, "Pulsed carbon dioxide laser ablation of burned skin: in vitro and in vivo analysis. *Lasers Surg. Med.* **10**, 476-484, 1990.

Mechanical Behavior of Cartilage During Laser Irradiation

Sergio Diaz [a], Enrique Lavernia [b], and Brian J. F. Wong, M.D. [a]

[a] Beckman Laser Institute and Medical Clinic, UC Irvine, CA 92612
[b] Chemical and Biochemical Engineering and Materials Science, UC Irvine, CA 92612

ABSTRACT

Internal stress $\sigma(t)$, diffuse transmitted light intensity $I(t)$ from a He-Ne probe laser ($\lambda = 632.8$ nm), and radiometric surface temperature $T_s(t)$ were measured during the photothermal heating of porcine septal cartilage using a pulsed Nd:YAG laser ($\lambda = 1.32$ μm). Rectangular specimens, 1-4 mm thick, were secured to a tensile force testing rig and laser irradiated. Force measurements during heating showed significant variations in the rate of deformation, which were found to be strongly dependent on tissue orientation; revealing the anisotropic nature of its thermo-mechanical properties. These findings suggests that the collagen and proteoglycan networks lie in a preferential orientation within the extracellular matrix, which must be addressed before this procedure can be used on a wider basis.

Keywords: Cartilage reshaping, stress relaxation, plastic surgery, laser heating, thermal and mechanical behavior.

1. INTRODUCTION

Laser assisted reshaping of cartilage is a new surgical procedure designed to allow in-situ treatment of deformities in the head and neck with less morbidity than traditional surgical procedures.[1] During laser irradiation, mechanically deformed cartilage undergoes accelerated stress relaxation that permits tissue to be reshaped into new stable configurations. Clinically, this reshaped cartilage can then be used to reconstruct the framework of structures within the head and neck, such as the ear, nose, larynx, and trachea. Heat introduced into cartilage by a laser causes its proteins to partially denature and undergo a phase transformation, which makes the cartilage relax and become malleable.[2] Since reshaping can be performed using minimally invasive techniques, with less morbidity than traditional reconstructive procedures, *laser-assisted cartilage reshaping* has the potential to radically alter the practice of aesthetic and reconstructive cranio-maxillo-facial surgery. The principal advantages of using laser radiation to generate thermal energy in tissue are the precise control of both the space-time temperature distribution and time-dependent thermal denaturation kinetics resulting in minimization of cellular injury.

Optimization of the reshaping process requires characterization of the temperature dependent stress relaxation and correlation of these changes with observed alterations in cartilage physical properties (e.g., elastic modulus, thermal diffusivity, and optical scattering coefficient). While numerous animal and human studies have demonstrated clinical feasibility,[3,4] the fundamental biophysical mechanisms accompanying laser reshaping are largely unknown. It has been suggested that the underlying mechanism of laser reshaping is primarily associated with a phase transformation of cartilaginous bound water to free water taking place at a temperature of $T_w \cong 70$ °C.[5] However, the precise details of this mechanism are still under investigation. It is still necessary to determine how a phase transition in the state of water allows irreversible tissue stress relaxation. Preliminary studies using diffuse light scattering measurements and calorimetry have identified changes in cartilage tissue thermal and optical properties that are consistent with the phase transformation hypothesis.[1,6]

Because protein denaturation (and subsequent cell death) is time- and temperature- dependent, it is necessary that the physical and molecular processes accompanying this phase change be characterized in order to allow prediction of desired morphological changes in the tissue for a given laser dosimetry. The purpose of this study was to perform a preliminary characterization of the thermal, mechanical, optical, and morphological changes in porcine cartilage (PC) during sustained high power Nd:YAG laser ($\lambda = 1.32$ μm) irradiation. Thermo-mechanical effects were observed by measuring changes in tissue tension (F) during laser irradiation. Surface temperature of the PC specimen (T_s) was obtained by measuring infrared emissions radiometrically. Structural alterations in the tissue matrix were indirectly monitored by measuring the changes in diffusely transmitted light (I) from a second probe laser beam (HeNe, $\lambda = 632.8$ nm) during photothermal heating with the Nd:YAG laser.

2. MATERIALS AND METHODS

Tissue preparation

The septal cartilages from fresh domestic pigs were obtained from a local packing house (Farmers John, CA) and harvested as described by Wong et al.[7] Several cartilage grafts from each septal cartilage were obtained and cut into rectangular slabs measuring 25 mm x 10 mm with thickness of 1 to 4 mm. Two specimen orientations were used during preparation of the grafts: a) longitudinal, where the specimen's length lies parallel to the length of the septal cartilage, and b) transverse, where the specimen's length lies perpendicular to the length of the septal cartilage, as shown in Fig. 1. Uniform specimen thickness was accomplished by removing the outermost layers of the intact full-thickness septal cartilage using a commercial rotary food slicer (model 620, Chef's Choice Int., EdgeCraft Corp, Avondale, PA) until the desired thickness was reached. Then a Perspex semi-cylindrical end-tab was glued (cyanoacrylate) to each end of the slab. After the glue dried (~ 10 minutes), the specimens were immersed in saline solution for rehydration prior to mechanical testing.
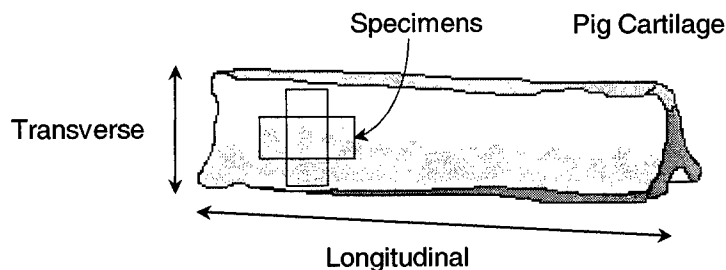
Figure 1. Sketch of porcine septal cartilage showing test specimen geometry and orientations.

Biophysical measurements

Two C-shaped clamps were used to connect the semi-cylindrical end-tabs holding the specimen to the experimental apparatus, as illustrated in Fig. 2. One of the clamps was connected to a thin-beam load cell while the other was secured to a stationary stand. A micropositioner attached to the load cell was used to adjust an initial force (30-50 g) across the stretched specimen. Laser irradiation resulted in time-dependent expansion or contraction of the specimen dimension accompanied by a decrease or increase in F, respectively.

A temperature controlled feedback loop was used to terminate laser irradiation while heating the tissue. PC specimens were irradiated until surface temperature reached 70 °C using an Nd:YAG laser ($\lambda = 1.32$ µm, 50 Hz PRR, Laser Aesthetics, Auburn, CA) at one of several laser powers (1–10 W). The total irradiation time was therefore dependent on the laser power density used as well as the specimen thickness. The laser energy was delivered using a 400-µm core-diameter silica multimode optical fiber terminating in a collimating lens. Laser spot size (4.8 mm diameter) and power were measured with thermal paper and a pyroelectric meter (Model 200/10, Coherent, Auburn CA), respectively.

Radiometric surface temperature (T_s) was estimated by using a thermopile sensor (response time of 120 ms (95%), spectral sensitivity 7.6-18 µm, Laser Aesthetics), and calibrated as described by Anviari et al.[8] A load cell with peak capacity of 217g (LCL-217G, Omega Engineering, Inc., Stamford, CT) was used to measure the tension (F) across the tissue. The signal from this load cell was amplified and low-pass filtered (3 db cutoff at 30 Hz) with a low-noise preamplifier (model SRS 560, Stanford Research Systems, Sunnyvale, CA). Diffusely transmitted light from the HeNe probe laser ($\lambda = 632.8$ nm, 15mW, Melles Griot) incident on the irradiated surface of the specimen was collected by an optical fiber (400-µm silica core fiber, Sidefiber 1800H, Ceramoptic, Longmeadow, MA; with adapter modification from SMA 905 to FC, Rifocs, Santa Barbara, CA) in close approximation (1-5 mm) to the non-irradiated surface, with near normal orientation. The collected light was measured with a silicon photoreceiver (model 2001 FC, New Focus, Mountain View, CA). HeNe laser intensity was amplitude modulated (9 kHz) and synchronously detected with a lock-in amplifier (model SR 850, Stanford Research Systems). An analog to digital converter (AT-MIO-16XE-50, National Instruments, Austin, TX) was used to record T_s, F, and I using software written in LabVIEW (National Instruments) running on a personal computer.
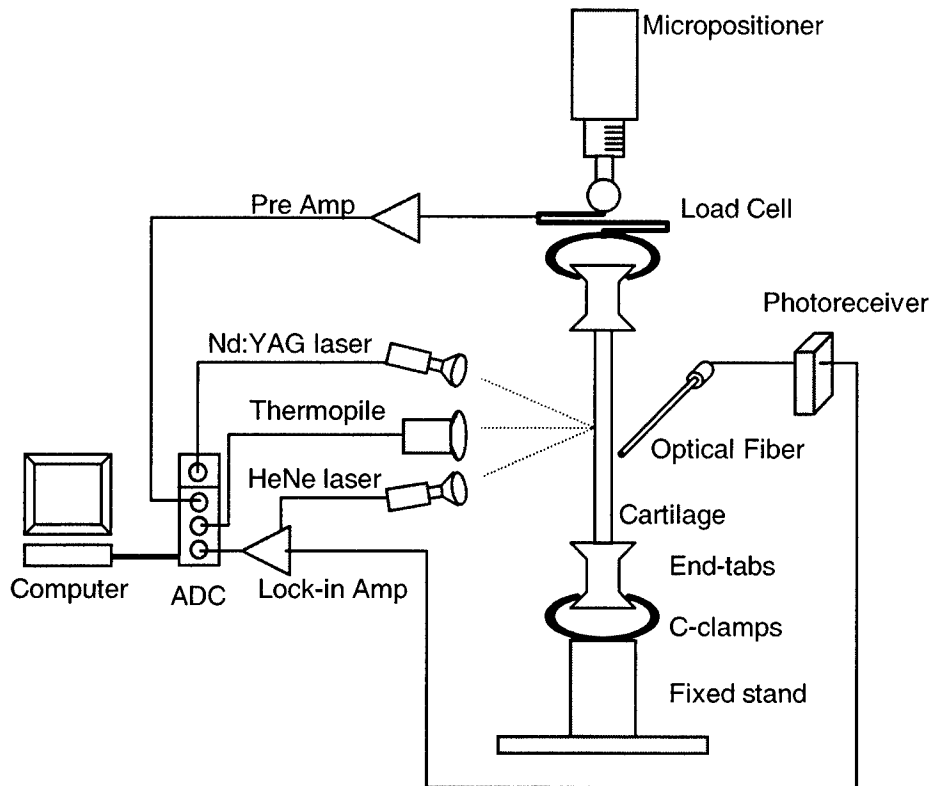
Figure 2. Schematic of experimental setup.

3. RESULTS

Figures 3a and 3b shows changes in T_s, F, and I during laser irradiation at 5 W and 3 W, respectively. T_s initially increases at the onset of the irradiation with a high heating rate. This heating rate gradually decreases due to heat loss to the surrounding environment. This behavior is more pronounced at low power (1-3 W) than at high power (5-10W) where the heating rate does not change noticeably by the time 70 °C is reached. With termination of laser irradiation, T_s cools to ambient temperature. Diffusely transmitted light intensity changes during irradiation; it decreases to a minimum and subsequently rises back to and above its initial value. Figures 3a and 3b illustrate I as a function of time, showing in each case a minimum at 4.35 s, and 13.65s corresponding to temperatures of 44.0 °C and 54.11 °C, respectively. The occurrence of this minimum in I has been suggested to coincide with the onset of mechanical stress relaxation, the presence of a phase transition, and the initiation of tissue denaturation.[9] However, volumetric changes due to water loss and thermoelastic expansion effects could also account for variations in this parameter.

Tensile force varies significantly as temperature rises from ambient to 70 °C, and its behavior appears to be highly dependent on tissue orientation; an observation that based on the available literature, has not been previously reported. Figures 4a and 4b illustrate the variation in F for two 3-mm thick PC specimens with longitudinal and transverse orientations, respectively. As temperature increases, F in the specimen with longitudinal orientation decreases at an initial temperature-force rate, which gradually becomes more pronounced and accelerates after approximately 5 s of laser irradiation. This reduction in F is likely to be due to the thermal expansion of the specimen, however this expansion appears to occur at two different strain rates. With termination of laser irradiation, F increases to a new equilibrium value (lower than the initial baseline). In contrast, in transversely oriented specimens, F initially decreases as temperature rises, reaches a minimum, and then subsequently increases continuously until irradiation is terminated (Fig. 4b). With thermal relaxation, F asymptotically decreases to a new equilibrium value.
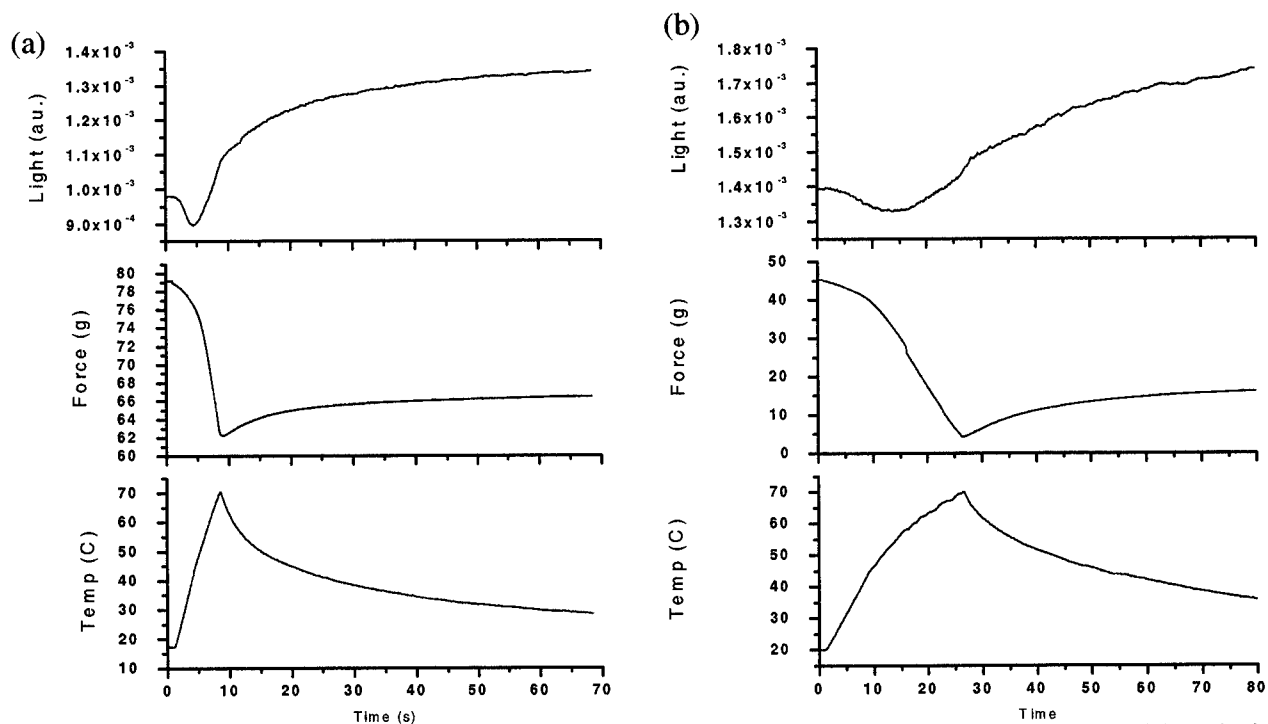
Figure 3. Simultaneous measurements of T_s, F, and I at two irradiation power levels: (a) 5W and (b) 3W. Plots obtained from a 3-mm thick porcine cartilage specimen cut with longitudinal orientation.
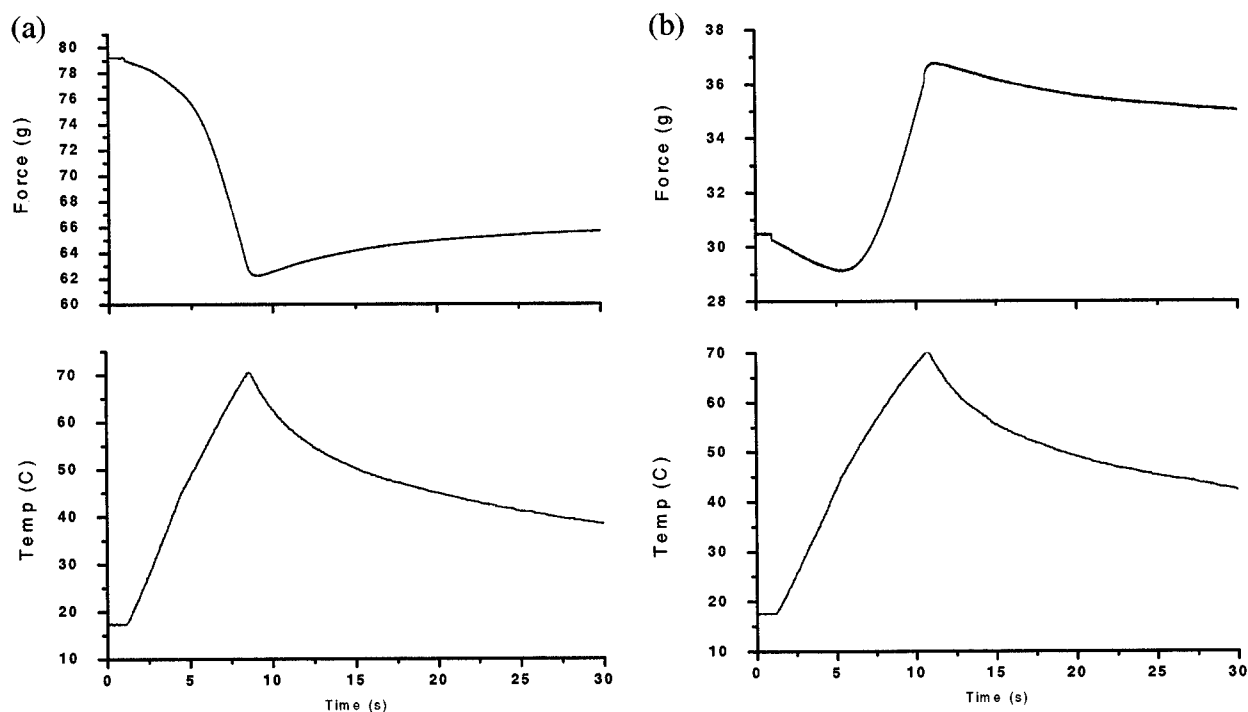
Figure 4. Simultaneous measurements of T_s and F during laser irradiation (5W) of (a) 3-mm thick specimen with longitudinal orientation, and (b) 3-mm thick specimen with transverse orientation.

Before irradiation, the specimen surface is soft and appears opaque-white to translucent-white depending upon the thickness of the specimen. It is malleable and tends to return to its original shape when deformed. Following irradiation, focal volume reduction in the laser target site is observed and the irradiated regions on the surface feel stiffer and brittle; the tissue is more translucent here than in the non-irradiated areas. Also, small droplets of water form around the target site during heating. With termination of laser irradiation the specimen appears desiccated throughout, but following immersion in saline (1-3 hours), the native appearance returns, except in the laser target location where changes remain.

4. DISCUSSION

In this study, we performed a preliminary characterization of the various biophysical changes in porcine cartilage that accompany laser heating. Measurements of tensile force (F) along with radiometric surface temperature (T) and diffuse transmitted light intensity (I) provided insight into the fundamental mechanisms that govern laser-mediated cartilage reshaping. A temperature feedback control system was used to limit the duration of laser irradiation, since temperatures in excess of 65 °C can reduce tissue viability, particularly if heating is sustained for long time intervals. This is the approximate denaturation temperature for collagen. [10]

The changes in transmitted light intensity observed during photothermal heating may result from several mechanisms including changes in the refractive index of the material due to variations on temperature, stress distribution, and water content or alterations in the optical properties due to tissue denaturation and fine structure alterations. Previous measurements of light scattering kinetics in cartilage during irradiation have identified an increase of diffusely scattered light when the stress across tissue specimens reaches a maximum and then abruptly drops. [11,12] Sobol et al. suggested that the presence of this peak in light scattering during irradiation is due to nucleus formation of a new phase (water droplets, micropores) that increases the number of scattering foci. [2] Such behavior in light scattering may represent a bound-to-free water phase transition. The plots of I (diffusely transmitted light) shown in Fig. 3 illustrate a reduction in signal intensity, which is consistent with the observation of an increase in backscattered light during irradiation. However, in these plots, the temperature at which the minimum for I occurs is much lower than 60-70 °C (considered as a threshold for protein denaturation, or the temperature at which a phase transition of water in tissue takes place). Hence, while at this point our results on I are not conclusive, they still demonstrate a consistent pattern that may be associated with molecular changes accompanying photothermal heating.

Changes in internal stress σ (σ is proportional to F) and the corresponding strain rate $d\varepsilon/dt$ appear to be thermally mediated, involving volumetric change due to thermal expansion. In addition, thermal expansion in porcine cartilage appears to be surprisingly anisotropic. Thermal expansion in longitudinally oriented PC specimens is higher than that of specimens where the orientation is perpendicular to this longitudinal axis. This observation suggests that either the collagen network or the proteoglycan molecules within the matrix (or both) are preferentially arranged with in the PC septum. The non-linear behavior of F depicted in Fig. 4 may be explained in terms of the differential thermal expansion along the width and length of the specimen. Dimensional change along the longitudinal direction dominates in both force-time histories, which is illustrated by the continuous reduction of F in Fig. 4a and by the change in sign of the strain rate (from decreasing to increasing force) in Fig. 4b. Though of lesser magnitude, expansion in the transverse direction of each PC specimens also influences the force-time plots by reducing the strain rate in the initial stages of heating in Fig. 4a (t< 5 s) and by initial decrease in the tensile force in Fig. 4b.

5. CONCLUSIONS

Laser irradiation can be used to reshape cartilage into complex geometries, and has the potential to alter the practice of head and neck reconstructive surgery. While the molecular basis for this complex phenomenon is not completely understood, experiments are underway in our laboratory to better understand the underlying physical mechanisms.

The experiments performed in this study focused on detecting dimensional changes in porcine cartilage specimens due to the onset of stress relaxation during photothermal heating. The initiation of accelerated stress relaxation may in turn indicate the onset of the bound-to-free water phase transformation. However, the volumetric change of the specimen

observed in this work is the result of a combination of effects that include water loss and thermo elastic expansion, where the latter appear to dominate the overall dimensional change in the specimen.

Our use of an optical fiber to deliver light and probe the tissue was motivated by the need to develop a non-contact method to control the reshaping process. The flexibility and reduced dimensions are attractive advantages that make this a practical technique to incorporate into a clinical instrument. However, further refinement of this technique is needed to more fully understand the relationship between light scattering and parameters such as geometry changes due to thermal expansion (variations in tissue-probe distance), stress distributions near the laser target, and tissue biophysical property alterations during heating.

ACKNOWLEDGMENTS

REFERENCES

1. Wong B. J. F., Milner T. E., Anvari B., Sviridov A., Omel'chenko A., Bagratashvili V. V., Sobol E. N., Nelson J. S. *Measurement of radiometric surface temperature and integrated back-scattered light intensity during feedback controlled laser-assisted cartilage reshaping*. Lasers in Medical Science 1998; 13:66-72.

2. Sobol E, Sviridov A, Omel'chenko A, Bagratashvili V, Kitai M, Harding SE, Jones N, Jumel K, Mertig M, Pompe W, ovchinnikov Y, Shekhter A, and Svistushkin V. *Laser reshaping of cartilage*. Biotechnology and genetic engineering reviews 2000,17:539-564.

3. Wang Z, Pankratov MM, Perrault DF, Shapshay SM. *Laser-assisted cartilage reshaping: In vitro and In vivo Animal studies*. Proceedings SPIE 1995, 2395; 296-302.

4. Sobol EN, Sviridov AP, Bagratashvili VN, Omel'chenko AI, Ovchinnikov YM, Shekhter AB, Svistishkin VM, Shinaev AN. *Laser reshaping of nasal septum cartilage: clinical results for 40 patients*. Proceedings SPIE, 3907, (to be published) 2000.

5. Sobol E. N. Phase transformations and ablation in laser-treated solids. In: New York: John Wiley, 1995: 316-322.

6. Wong B. J. F., Milner T. E., Kim H. K., Telenkov S., Chew C., Kuo T. C., Smithies D. J., Sobol E. N., Nelson J. S. *Critical Temperature Transitions in Laser Mediated Cartilage Reshaping*. Proceedings SPIE 1998; 3245:161-172.

7. Wong BJF, hao KKH, Kim HK, Chu EA, Dao X, Gaon M, SunCH, Nelson JS. *The porcine and lagomorph septal cartilages: Models for tissue engineering and morphologic cartilage research*. Submitted to the American Journal of Rhinology, 2000

8. Anvari B, Milner TE, Tanenbaum BS, Kimel S, Svaasand LO, Nelson JS. *Selective cooling of biological tissues: application for thermally mediated therapeutic procedures*. Phys Med Biol 1995; 40:247-252.

9. Choi J, Tanenbaum BS, Milner TE., Dao XV., Nelson JS. *Thermal, mechanical, optical, and morphological changes in bovine nucleous pulposus induced by Nd:YAG laser irradiation*. Lasers in Surgery and Medicine 2000; 1-7.

10. Allain JC, Le Lous M, Cohen-Solal L, Bazin S, and Maroteaux P. *Isometric tension developed during the hydrothermal swelling of rat skin*. Connective Tissue Res. 1980; 7, 127-133.

11. Sviridov A, Sobol E, Bagratashvili N, Omelchenko A, Jones N and Lowe J. *Dynamics of optical and mechanical properties of cartilage at laser heating*. Society of Photo-Optical Instrumentation Engineers, Proceedings 2923, 114-117.

12. Wong B. J. F., Milner T. E., Kim H. K., Nelson J. S., Sobol E. N. *Stress relaxation of porcine septal cartilage during Nd:YAG ($\lambda = 1.32$ mm) laser irradiation: mechanical, optical, and thermal responses*. Journal of Biomedical Optics 1998; 3:409-414.

Photo thermal Stimulation of Chondrocyte Proliferation in ex-vivo Cartilage Grafts

Mai Thy Truong[1,2], David Gardener[3], Nidhi Pandhoh[2], Brian Wong[1,2,4]

[1]Department of Otolaryngology- Head and Neck Surgery, [2]the Beckman Laser Institute and Medical Clinic, and [3]Department of Developmental and Cell Biology, University of California, Irvine, [4]Whitaker Center for Biomedical Engineering University of California, Irvine

Abstract

In vivo, laser radiation has been shown to stimulate cartilage repair and proliferation, which is of clinical relevance as light can be delivered using minimally invasive techniques. However, dosimetry and temperature dependence of this phenomenon have neither been determined nor have these findings been conclusively demonstrated *ex vivo*. In this study, we detected the presence of proliferating chondrocytes in intact laser irradiated rabbit septal cartilage using a novel whole mount Bromodeoxyuridine (BrdU) assay, and determined the dependence of this phenomenon on laser dosimetry. Cartilage specimens were irradiated with light from an Nd:YAG laser (λ=1.32μm, 3-16 sec, 10-45 W/cm^2) and placed in tissue culture with BrdU for 7-9 days. BrdU (a thymidine analogue) is incorporated into DNA during replication. Specimens were then fixed and treated with an enzyme-linked double antibody system providing a color change to indicate the presence of BrdU in dividing cells. The samples were analyzed in whole mount and with conventional histology. Proliferation was clearly identified for laser exposures greater than 6 seconds at (25 W/cm^2), and was observed only on the periphery of the laser spot. This study clearly demonstrates that laser heating of *ex vivo* cartilage tissue results in chondrocyte proliferation. Inasmuch as this phenomenon was observed in tissue culture, the non-specific cellular and humoral responses present in an intact organism were eliminated. Cell division likely results from either changes in the fine structure of the tissue matrix or direct stimulation of chondrocyte metabolism.

Keywords: Chondrocyte, proliferation, laser stimulation, bromodeoxyuridine (BrdU) Nd:YAG, cartilage

1. Introduction

1.1 Previous Studies investigating the effect of laser stimulation on cell proliferation

Many researchers have investigated laser interactions with tissues. Whether a laser can photo-thermally stimulate cells to proliferate has been the focus of many studies. Previous *in vivo* and *in vitro* studies have given conflicting results, some reports suggesting that laser energy can stimulate DNA synthesis and metabolic process, while other reports have concluded that laser energy results in necrosis and cell death. These reports all vary in the types of lasers used, the energy parameters, tissue models, and the methods used to assay for proliferating cells.

In a study by Spivak et al, the authors used bovine and canine cartilage in vitro to investigate the effect of low level Nd:YAG laser irradiation. The authors concluded that laser irradiation decreased the rate of DNA synthesis, but actually increased matrix synthesis, indicating that laser irradiation may be increasing chondrocyte metabolism and repair while having no effect on cell proliferation. The authors analyzed cell proliferation through histological comparison of laser irradiated samples to controls. Matrix synthesis was analyzed by looking at proteoglycan synthesis[4].

In another study by Smoot et al, the authors found that CO_2 laser energy decreased chondrocyte viability in the vicinity of laser irradiation. In this study, the authors used rabbit ear cartilage *in vitro* and analyzed for cell viability using radioactive sulfur uptake studies, comparing the density of cells that took up radio-labeled sulfur to the density seen in controls[2].

Finally, in a study by Sobol et al, the authors looked at using a Holmium:YAG laser to irradiate rabbit spinal disk cartilages *in vivo*. One month after irradiation, the authors assayed for cell proliferation by OCT(Optical Coherence Tomography) and then by conventional histology comparing irradiated tissue to non-irradiated controls two months later. In this study, the authors concluded that the laser stimulated new growth of fibrous or cartilaginous tissues[3].

However, in looking at the question of whether a laser can stimulate cells to proliferate, an *in vitro* study is ideal in that *in vivo* studies cannot eliminate reparative processes to trauma that may occur in an intact animal. Also, many of these techniques used to assay for cell proliferation did not directly correlate the location of cell replication to the region of laser irradiation to determine a direct causal effect. Finally, it may be that a wide range of laser parameters must be explored in each model, as the tissue response may be very sensitive to laser dosimetry and subtle changes my result in necrosis or proliferation.

1.2 *In vitro* investigation of the effect of Nd:YAG laser stimulation
In this study, we wanted to determine whether a laser can stimulate chondrocyte proliferation by developing an assay that was both *in vitro*, to eliminate any intact animal response, and whole mount, to be able to directly compare new growth regions to the light distribution of heating. We also wanted to identify the optimal laser parameters that stimulated growth and investigate if whether there was a dose response.

1.3 Bromodeoxyuridine (BrdU) antibody detection system
To assay for proliferating cells we looked at a Bromodeoxyuridine (BrdU) Secondary antibody detection system. BrdU is a thymidine analog incorporated into DNA during DNA synthesis. In this assay, anti-BrdU monoclonal antibody is used to identify cells with incorporated BrdU. The advantage of using this technique over radioactive studies to assay for cell proliferation is that, first; there is no need for radioactivity, which can be expensive and dangerous. Detection of anti-BrdU monoclonal antibody is from an alkaline phosphatase, enzyme-linked secondary antibody. When exposed to substrate, alkaline phosphatase provides a yellow to purple color reaction. The color detection is both robust and amplified. A second advantage to an enzyme-linked secondary antibody detection system is that specimens can be analyzed in whole mount. This provides a better way to correlate regions of new proliferation with laser irradiated areas in the tissue. This BrdU detection system has been used to assay for DNA synthesis and cell division in many tissues, including the limb bud, lymphatic endothelial cells, myoblast cells in graft tissue and neurons in the hippocampus[1].

To apply this BrdU secondary antibody detection system to chondrocytes, many technical considerations had to be considered. First, the slow intrinsic rate of proliferation in chondrocytes may be below the level of detection of this assay. Second, the cartilage matrix in the experimental model may be too thick to allow for the proper diffusion of antibodies of the assay. Also, there may be a high intrinsic level of alkaline phosphatase in the experimental model, creating an intense background that may mask any true positive signals. Finally, there may be non-specific binding of primary anti-BrdU antibodies and/or secondary antibodies to sites in the tissue eliminating specificity to BrdU. All of these considerations had to be addressed in the use of the BrdU secondary antibody detection system to assay for chondrocyte proliferation.
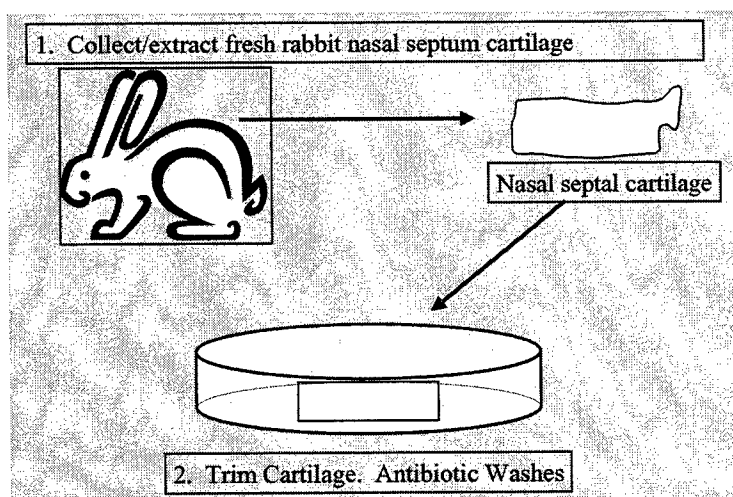
Figure 1. Schematic of Experimental Setup

2. Materials and Methods
In this study, fresh rabbit nasal septal cartilage was extracted from rabbit heads obtained from a local abattoir within 12 hours postmortem. Skin and soft tissues were removed from the upper side of the head through the bilateral nasal side. Bilateral nasal bone osteotomies were performed along the line of incision. The nasal septal cartilage was removed from the site and perichondrium and connective tissue was removed from the surface of the cartilage manually. Nasal cartilage was trimmed with a razor blade to a standard size and stored in saline at room temperature before experimentation.

Cartilage samples were prepared for culture with antibiotic washes and irradiated before culture (Fig 1). Cartilage samples were irradiated with a Newstar Nd:YAG (λ=1.32μm) operating at approximately 300 μsec pulse duration, 50Hz pulse repetition rate, and variable pulse energy (Fig 2).
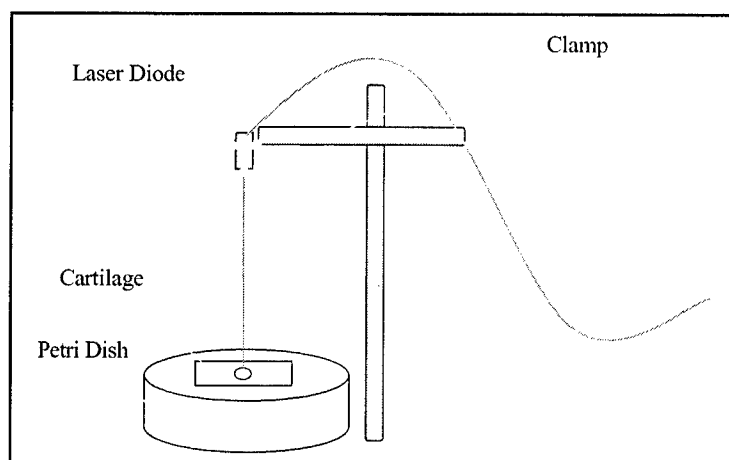
Figure 2. Schematic of laser irradiation of rabbit nasal septal cartilage.

After Nd:YAG laser irradiation, rabbit nasal septal cartilage samples were cultured at 37°C incubation with Complete Growth Media (Sigma) in 500μM concentration of BrdU for 7-9 days, exchanging growth media daily. After culture, samples were fixed in Carnoy's fixative (60% ethanol, 30% cholophorm, 10% acetic acid), overnight. After fixation, samples were re-hydrated in a Tris Buffered Saline with Tween solution(TBST), denatured in 4N HCl in a 37°C water bath for 30 minutes and then neutralized in a 0.1M borate solution. After numerous washes in TBST and water, the samples were treated with a "Blocking Solution" (0.1% bovine serum albumin, 5% non-fat dry milk in TBST) overnight to decrease potential background levels from non-specific binding of the antibodies to antigenic sites in the tissue.

Next, samples were exposed to the primary antibody, a monoclonal mouse IgG directed against BrdU(Roche), overnight. After two hours of washes at room temperature in TBST, the samples were exposed to the secondary antibody, an alkaline phosphatase conjugated sheep anti-mouse IgG, overnight(Sigma). After two hours of further washes in TBST, the samples were exposed to substrate, nitro-blue tetrazolium chloride, 5-bromo-4chloro-3 indolyphosphate toludine salt (NBT/BCIP) for two hours (Fig. 3).
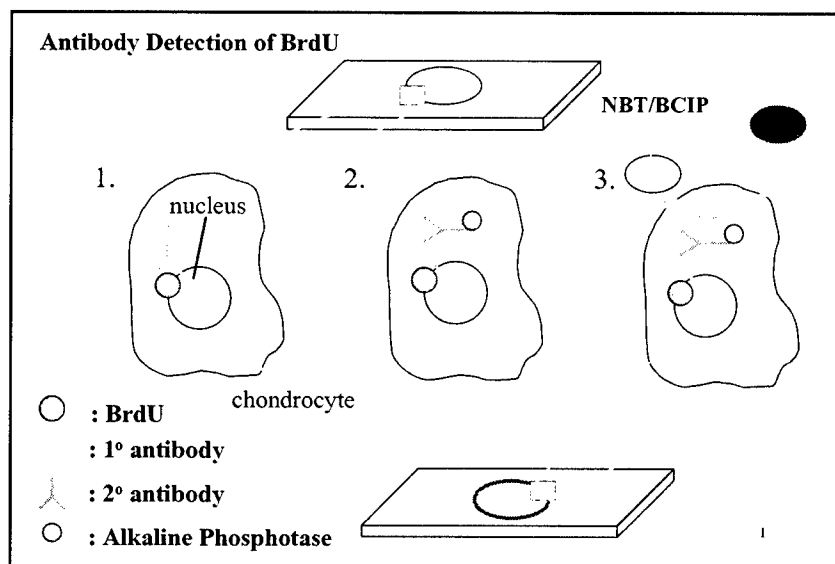
Figure 3. Enzyme-linked, secondary antibody BrdU detection system. Laser irradiated samples were exposed to primary antibody, a monoclonal mouse IgG directed against BrdU, overnight. Following washes in TBST, samples were exposed to secondary antibody, alkaline phosphatase conjugated sheep anti-mouse IgG. Finally, samples were exposed to substrate (NBT/BCIP) and allowed for color reaction detection.

3. Results

3.1 Control Specimens

To determine background levels of signal in this assay, two controls were run of samples that were not irradiated with an Nd:YAG laser, but were cultured with and without BrdU in the culture media. Samples that were cultured in the absence of BrdU did not show any positive signal for BrdU when exposed to the enzyme-linked secondary antibody system (Fig 4A). This demonstrated that our experimental model, rabbit septal nasal cartilage, did not display any endogenous alkaline phosphatase activity or any non-specific antigenic sites that would mask a specific signal against BrdU.

Samples that were cultured in the presence of BrdU without laser stimulation allowed for analysis of background levels of chondrocyte proliferation and BrdU uptake (Fig 4B). In these samples, no positive BrdU signals were found under dissection microscope in the cartilage, however, any perichondrium remaining on the cartilage gave a positive signal for BrdU uptake. This is not a surprising finding as it was expected that the supportive connective tissue would be highly proliferative and uptake BrdU. Positively stained perichondrium was easily differentiated from the underlying cartilage under dissection microscope based on depth of field and cell morphology.
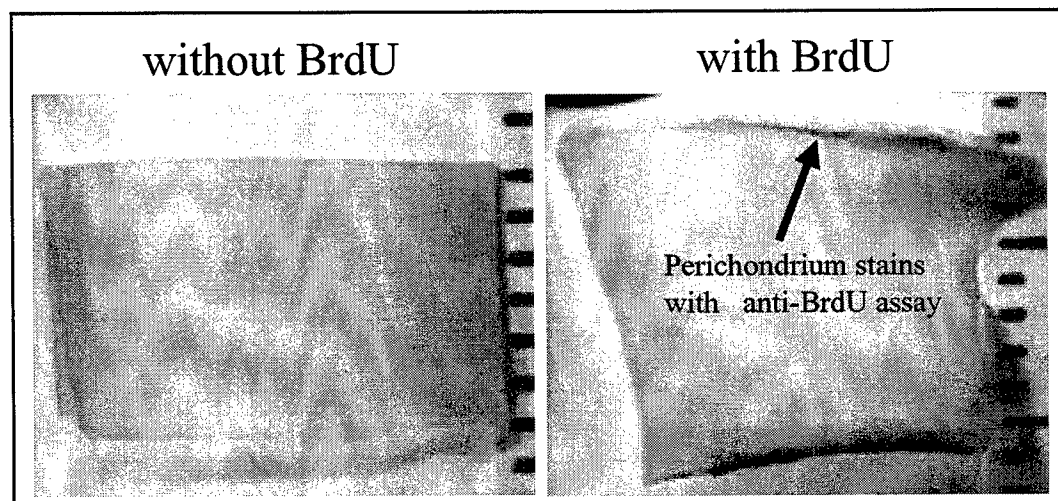
Figure 4A   **Figure 4B**

Figure 4A, 4B. Non-laser irradiated control specimens cultured with or without BrdU. **4A.** Rabbit nasal septal cartilage cultured without BrdU in the culture media demonstrated no specific signal for BrdU. **4B.** Rabbit nasal septal cartilage cultured with BrdU demonstrated positive signals for BrdU uptake in the perichondrium, the supportive connective tissue surrounding the cartilage.

Next, we looked at control samples that were Nd:YAG laser irradiated and cultured in BrdU, but exposed to only the primary or only the enzyme-linked secondary antibody. Specimens were irradiated for 8 seconds exposures with the laser operating at 6W. These controls allowed for analysis of the cartilage after laser irradiation to investigate if irradiation created any changes that would permit non-specific binding sites for either antibody used in the assay. Laser irradiated samples exposed only to the primary antibody showed no positive signal for BrdU uptake (Fig. 5A). This control demonstrated that the secondary antibody is necessary for detection of BrdU uptake.

Laser irradiated samples exposed only to the secondary antibody also showed no positive signal for BrdU uptake(Fig. 5B). This control was used to determine whether the secondary antibody is specific only for the primary antibody and is not binding to any other endogenous sites in the cartilage that would give false positive signals. These controls allowed for the conclusion that the enzyme-linked secondary antibody detection assay was specific for presence of BrdU uptake in rabbit nasal septal cartilage.

Exposed to Primary Antibody only   **Exposed to Secondary Antibody Only**
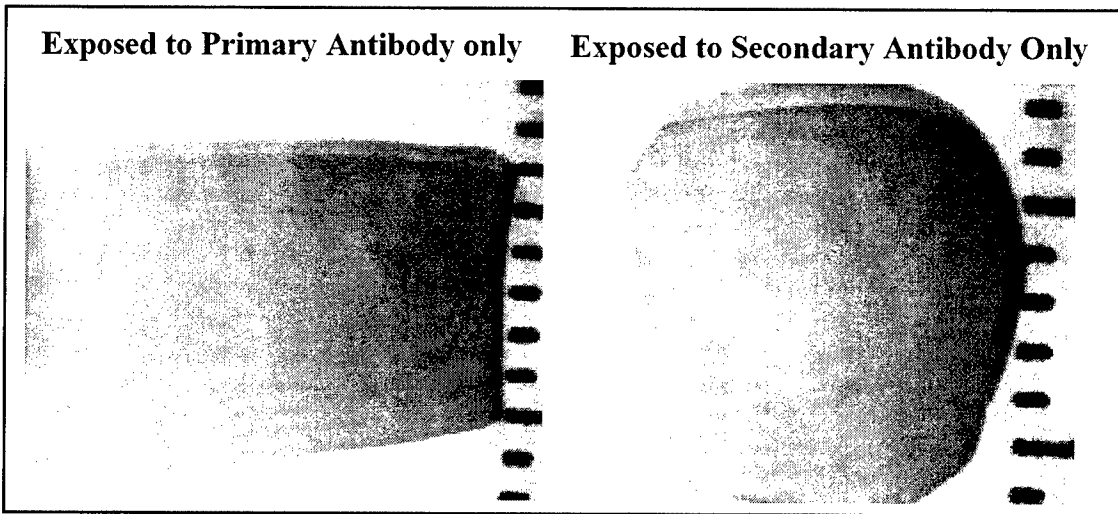
Figure 5A   Figure 5B

Figure 5A, 5B. Laser irradiated control specimens exposed to only primary or only secondary antibodies. **5A.** Laser irradiated rabbit nasal cartilage exposed to only the primary antibody demonstrated no specific signal for BrdU uptake. **5B.** Laser irradiated rabbit nasal cartilage exposed to only secondary antibody demonstrated no specific signal for BrdU uptake.

3.2 Laser irradiated rabbit nasal septal cartilage exposed to BrdU secondary antibody detection system.

Rabbit nasal septal cartilages were irradiated at 3 W, 6W and 10 W for variable exposure durations. Samples were cultured for seven days in the presence of BrdU and culture media and assayed for the presence of BrdU with the enzyme linked secondary antibody system. Samples were then analyzed for the presence of a positive signal under dissection microscope and results were tabulated (Table 1).

Table 1. Laser irradiated rabbit nasal septal cartilage was assayed for the presence of BrdU uptake by enzyme linked secondary antibody system. Samples were irradiated at 3W, 6W and 10W for variable pulse exposure durations, τ (seconds). Specimens that were unclear by dissection microscopy to whether or not there was truly a positive signal for BrdU uptake were put aside for further histological analysis.

Specimens irradiated at 6W beyond 4 seconds demonstrated positive signals for BrdU uptake. Positive signals were seen as purple signals on the periphery of the laser irradiated spots (Fig 6). In the sample featured in figure 6, dissection microscopy was used to determine how cellular the positive signal appeared (Fig 7A, 7B). Other positive signals were observed in other samples, with variable intensity of signal along the periphery of the laser irradiated spot (Fig 8A, 8B).

	τ	BrdU +	BrdU-	BrdU +/-?	#
3W	12 sec	0	4	0	4
	16 sec	0	2	0	0
6W	4 sec	0	3	0	0
	6 sec	5	1	2	8
	8 sec	7	2	2	11
	12 sec	3	1	0	4
	16 sec	6	4	0	10
10W	3 sec	0	4	0	4
	4 sec	0	1	1	2
	5 sec	0	4	0	4
total					47

Table 1
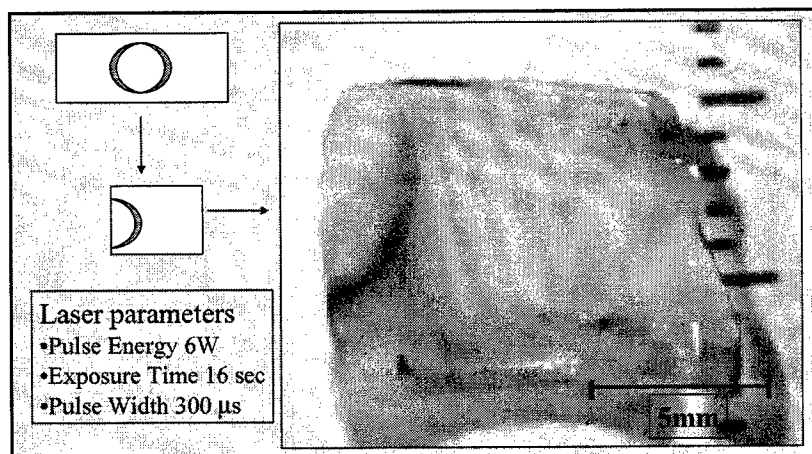
Figure 6. Laser irradiated rabbit nasal cartilage assayed for BrdU uptake. This specimen was irradiated for 16 seconds with the laser operating at 6W, and divided into halves for half to serve as a control (not shown). A positive BrdU signal can be seen in the periphery of the laser irradiated spot.
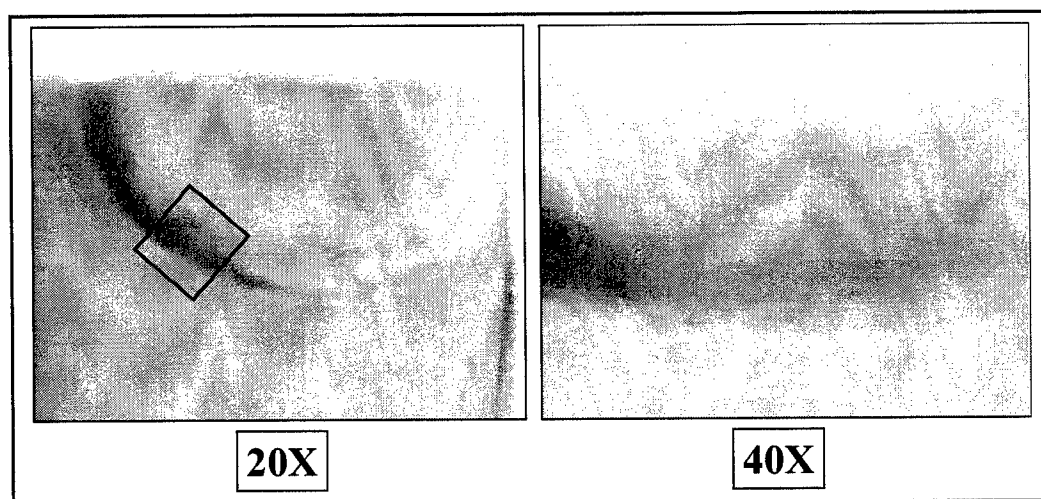
Figure 7A   Figure 7B

Figure 7A, 7B. Laser irradiated rabbit nasal cartilage analyzed under dissection microscopy. The same specimen irradiated for 16 seconds at 6W was analyzed under dissection microscopy at 20X(**7A**) and 40X(**7B**) to assess for the cellularity of the BrdU signal.

Figure 8A, 8B. Examples of laser irradiated rabbit nasal cartilage assayed for BrdU uptake. These samples were both irradiated for 16 seconds at 6W. Chondrocytes staining positive for BrdU uptake can be seen along the periphery of the laser irradiated spot. Positively stained perichondrium is also present demonstrating that this supportive tissue is also proliferating and had taken up BrdU from the growth media.
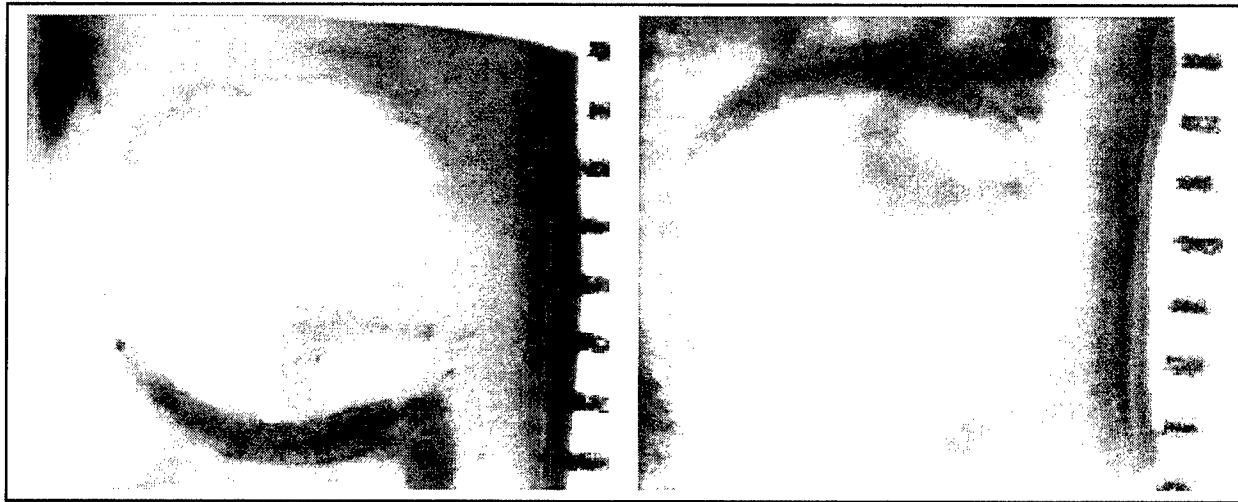
| Figure 8A | Figure 8B |

4. Conclusions

In this study, we demonstrated that an enzyme-linked secondary antibody system could successfully detect BrdU uptake in proliferating chondrocytes in rabbit nasal septal cartilage, *in vitro*. This whole mount assay allows for the direct correlation of laser irradiated areas to regions of proliferation detected. We also found that Nd:YAG laser irradiation of cartilage demonstrated cell proliferation in response to laser stimulation. Proliferation was only observed at a pulse energy of 6W and a pulse exposure of at least 6 seconds. This "window" may reflect a proper delivery of laser energy that allows for a proliferative response. However, a culture of only seven to nine days with BrdU may not be long enough to see a proliferative response with other laser parameters.

Future studies include histological analysis of positive BrdU signals to confirm the cellularity of the signal and further analysis of optimal laser parameters that stimulate cell proliferation. Investigation of the mechanism of this proliferative response can be pursued to determine whether a reparative process is responsible for stimulating proliferation, and if the process is mediated by chondrocytes alone or if the matrix plays a critical role. Finally, studies to see if a similar proliferative response can be evoked through other mechanical stressors, such as heat from a water bath, may give insight to the underlying mechanism stimulating the proliferation of chondrocytes.

5. Acknowledgments

6. References

1. K Ohsugi, DM Gardiner, SV Bryant. "Cell Cycle Length Affects Gene Expression and Pattern Formation in Limbs," *Developmental Biology* 189, 13-21 (1997).
2. EC Smoot, B Bergman, S Lyons. " Effect of the Carbon Dioxide Laser on Viability of Ear Cartilage in a Rabbit Model." *The Journal of Craniofacial Surgery*, vol. 6, no. 2, March 1995.
3. EN Sobol, NN Vorobieva, AP Sviridov, AI Omelchenco, AV Baskov, AB Shekhter, VA Baskov, FI Feldchtien, VA Kamensky, RV Kuranov. "Laser induced activation of regeneration processes in spine disc cartilage," Proceedings SPIE 2000;3907:504-509.
4. JM Spivak, DA Grande, A Ben-Yishay, DS Menche, MI Pitman. " The Effect of Low-Level Nd:YAG Laser Energy on Articular Cartilage in vitro," Arthoscopy: The Journal of Arthoscopic and Related Surgery, Vol. 8(1)36-43, 1992.

Determination of Optimum Laser Parameters for Cartilage Reshaping in Porcine Septum Using Nd:YAG Laser (λ=1.32 μm)

Elizabeth Johansen[1,2], Matt Burden[1,2], Brian J.F. Wong[2,3,4]

[1]Department of Engineering, Harvey Mudd College
[2]Beckman Laser Institute and Medical Clinic, University of California Irvine
[3]Department of Otolaryngology- Head and Neck Surgery, University of California Irvine
[4]The Whitaker Center for Biomedical Engineering, Samueli School of Engineering,
University of California, Irvine

ABSTRACT

In this study, a computer-controlled instrument was designed and constructed in order to systematically evaluate the effect of laser dosimetry on shape change during laser-mediated cartilage reshaping. Porcine nasal septal cartilage specimens, stripped of pericondrium were cut (25 X 5 X 2 mm) using a custom guillotine microtome and bent into a cylindrical shape (7.38 mm bend radius) using a jig constructed from aluminum tubing and high tension wire. Each specimen was irradiated (Nd:YAG laser λ=1.32 μm, 6-10 W, 2-16 s pulse duration, 31-51 W/cm^2) in five distinct regions using a pattern that maximized cooling between laser exposures. Real-time measurements of tissue optical properties and surface temperatures were recorded during each laser exposure as these features correlate with the onset of stress relaxation and shape change. After irradiation, each specimen was re-hydrated in saline solution (15 minutes), removed from the jig, and photographed with a digital camera. The radius of curvature of the specimen was compared to the radius (7.38 mm) of the reshaping jig. Optimal reshaping (greatest degree of curvature) was observed at 6W, with an irradiation time of 16s, or alternately at 10W, with an irradiation time of 8s.

Keywords: stress relaxation, cartilage, Nd:YAG laser, shape change, plastic surgery

1. INTRODUCTION

The objective of this preliminary investigation was to develop a method to systematically evaluate the effect of laser dosimetry on shape change during Nd:YAG laser cartilage reshaping[16-17, 19, 21-23, 25-26, 33-38]. In order to accomplish this goal, a matrix comparing laser dosimetry with resultant specimen curvature must be developed. This data ultimately must be associated with a similar matrix likewise comparing dosimetry and tissue viability to determine the therapeutic window within which the cartilage is effectively reshaped, but not thermally damaged (Fig. 1).
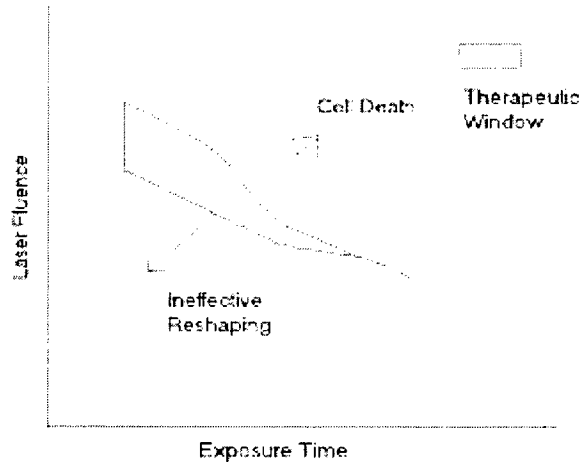
Figure 1. Figurative graph illustrating therapeutic window.

This study focuses exclusively on developing an experimental method to define the lower boundaries of this therapeutic window. A cartilage reshaping device was constructed for use in this study which is described elsewhere in these proceedings (see Burden et al, SPIE 2001 proceedings, #4244E66).

2. MATERIALS AND METHODS

In order to minimize interference between the retaining structures holding the cartilage specimen in deformation and the Nd:YAG and probe laser light, a novel device was constructed to hold the cartilage in deformation during laser irradiation (Fig. 2).

Figure 2. The jig holding a piece of cartilage in deformation.

The jig was constructed using a 6"-long, 0.5" diameter aluminum tubee with a wall thickness of 2mm. A 1"-long segment was removed from the midsection of the tube along the longitudinal direction creating a near-circumferential defect. The cartilage was held in deformation by positioning the graft between two sets of wire scaffolds. Five 0.2mm gauge, steel, high-tension wires were stretched along the length of the tube in order to span the removed segment. A second set of wires, maintained under tension, formed the outer layer. The cartilage was placed between the two wire layers by first laying it on the bottom set of wires and then sequentially securing the top set of wires over the cartilage. This second set of high-tension wire was secured by hooking the ends of the wire (connected to an elastic band and then to a metal clip) to the end of the tube.

Finally, the end of the jig was attached to a rotating motor using a plastic connecter piece 1" in length. The jig permits irradiation of nearly the entire outer surface of the cartilage specimen. The back surface of the specimen is similarly free of obstructive retention clamps or platforms thus allowing detection of diffusely transmitted, scattered, probe, laser light using an optical fiber inserted longitudinally into the jig.

Actual specimen reshaping was accomplished using a device described elsewhere in detail within these proceedings (see Burden et al, SPIE 2001 proceedings #4244E66).
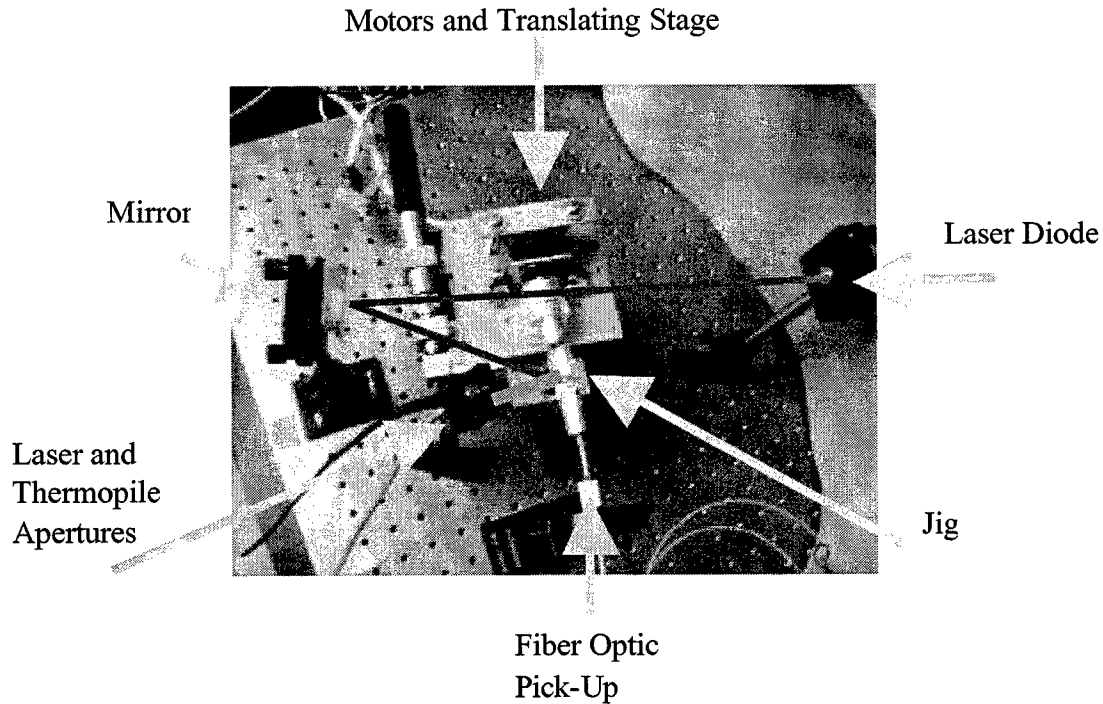
Figure 3. Diagram of experimental setup.

An Nd:YAG laser was used (λ=1.32 μm, spot diameter = 5mm) at two different power settings (6W and 10W), and five different pulse durations (2, 4, 6, 8, and 16 s). Three specimens were irradiated using each combination of pulse duration and power.

All cartilage specimens were cut to the same dimensions (25x5x2.03mm) using a custom guillotine microtome[5]. The grafts were then mounted to the reshaping jig and secured. The sequence in which the entire surface of the cartilage specimen would undergo irradiation was selected to allow for maximum thermal relaxation between adjacent regions of the specimen, and henceforth minimize overheating due to heat conduction (Fig. 4) [36].
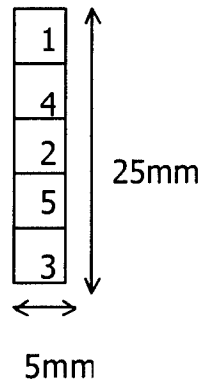
Figure 4. Diagram of maximum cooling pattern.

During each experimental trial, the software controlling the instrument (implemented in LabView [National Instruments, Austin, TX] recorded temperature and transmitted light signals and saved these in an Excel-formatted file for each of the five laser target sites on the sample. After irradiation, the sample was re-hydrated in saline solution for fifteen minutes while secured on the jig [33]. The specimens were then removed from the jig and photographed using a digital camera (Fig. 5).
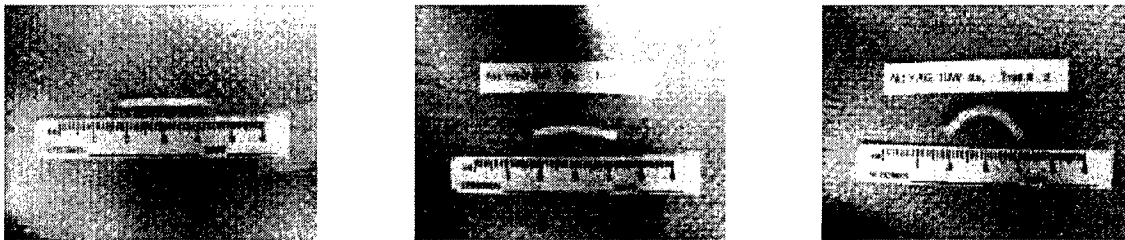
Figure 5. (left) A cartilage sample before irradiation. (middle) A cartilage sample after 2 seconds irradiation on each spot, Nd:YAG at 6W. (right) A cartilage sample after 8 seconds of irradiation on each spot, Nd:YAG at 10W.

The resultant shape was measured by determining the effective radius around which the sample was bent and comparing that to the radius of the jig, using modification of the technique developed by Gray, Kimball et al (Lasers in Surgery and Medicine, 2001 in press). Digital micrometry was used to determine the specific geometric measurements of each reshaped specimen. The effective radii (r) of the subtended circle for each reshaped cartilage specimen was determined using the following equation (numerically evaluated using Excel, Microsoft, Redmond, WA):

(1)   distance between ends = 2r sin (sample length / 2r)

The calculated effective radius was then compared to the radius of the jig (7.38mm). Data were averaged for each power setting and pulse duration pair.

3. RESULTS AND DISCUSSION

The average radii values for the two different power settings were graphed versus pulse duration in order to compare them to the 7.38mm target radius (Fig. 6).

Average Radius v. Pulse Duration
Porcine Cartilage
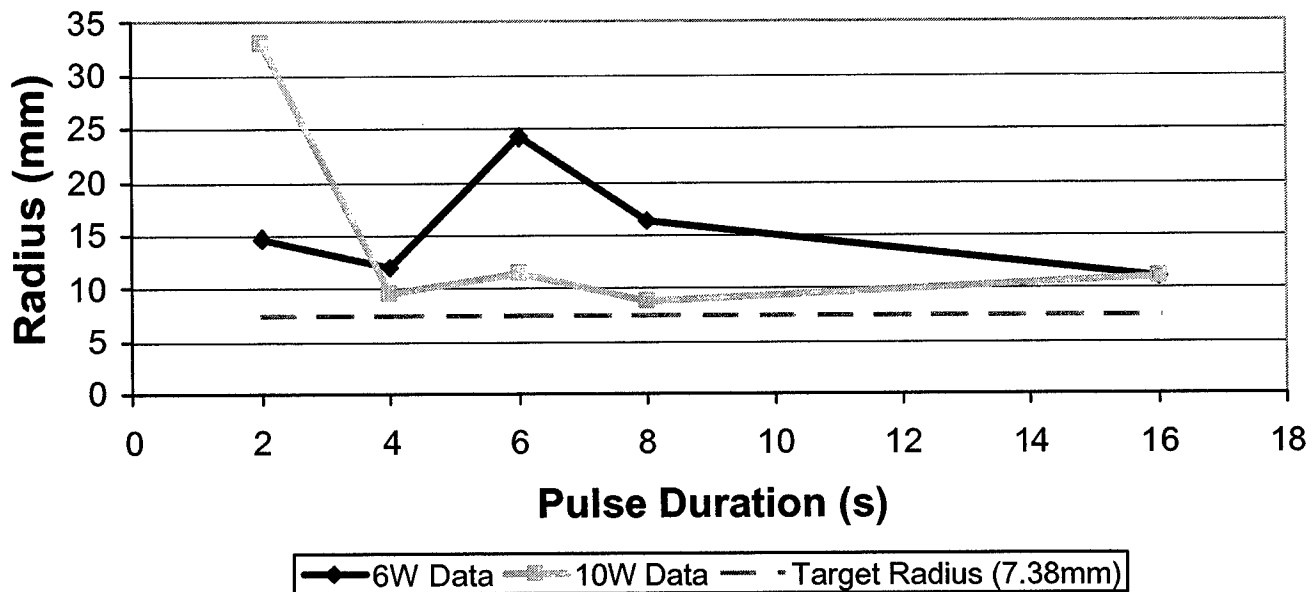
Figure 6. Graph of average sample radius versus pulse duration.

4. CONCLUSIONS

Optimal cartilage shaping, defined as creating a shape as close as possible to jig shape, was achieved with a pulse duration of 16s at 6W (10.99mm), and 8s at 10W (8.73mm). Future investigations will use the methods outlined here to more fully explore the laser dosimetry parameter space, in particular with a greater number of samples and at different wavelengths. Finally, to define the therapeutic window, investigations will need to be performed which compare tissue viability and shape change.

6. REFERENCES

1.   Bagratashvili VV, Sobol EN, Sviridov A, Popov VK, Omel'chenko A, Howdle SM. Thermal and diffusion processes in laser-induced stress relaxation and reshaping of cartilage. J. Biomechanics 1997;30:813-817.

2.   Dorf RC. Modern Control Systems. (Third Edition ed.) Reading, MA: Addison-Wesley Publishing Co., 1983.

3.   Helidonis E, Sobol EN, Kavvalos G, et al. Laser Shaping of Composite Cartilage Grafts. American Journal of Otolaryngology 1993;14:410-412.

4.   Helidonis ES, Sobol EN, Velegrakis G, Bizakis J. Shaping of Nasal Septal Cartilage with the Carbon Dioxide Laser- a Preliminary Report of an Experimental Study. Lasers in Medical Science 1994;9:51-54.

5.   Karamzadeh AM, Rasouli A, Tanenbaum BS, Milner TE, Nelson JS, Wong BJF. Laser-Mediated Cartilage Reshaping With Feedback-Controlled Cryogen Spray Cooling: Biophysical Properties And Viability. Lasers Surg Med 2001;28:1-10.

6.   Lai W, Hou J, Mow V. A triphasic theory for the swelling of hydrated charged soft biological tissues. In: Mow V, Ratcliffe A, Woo S-Y, ed.^eds. Biomechanics of diarthroidal joints. New York: Springer-Verlag, 1990:283-312. vol 1,2).

7.   Lai W, Hou J, Mow V. A Triphasic Theory for the Swelling and Deformation Behaviors of Articular Cartilage. Journal of Biomechanical Engineering 1991;113:245-258.

8.   Omel'chenko AI, Bagratashvili NV, Dmitriev AK, Sobol EN. Acoustic Control of Laser Shaping of Cartilage. Laser Spectrometry and Optical Diagnostics: Novel Trends and Applications in Laser Chemistry, Biophysics, and Biomedicine 1999;3732:312-319.

9.   Omel'chenko AI, Bagratashvili VN, Sobol EN, Dmitriev AK. Mechanical Examination of Cartilage Reshaped under laser radiation. Advanced Materials 1999;3:56-63.

10.   Omel'chenko AI, Sobol EN, Sviridov AP, et al. Opto-acoustic monitoring of laser corrections of the shape of porcine ear. Russian Journal of Quantum electronics 2000;11:823-826.

11.   Ovchinnikov YM, Nikiforova GN, Svistushkin VM, et al. Changes in the cartilage shape under the action of laser irradiation. Vestnik Otorinolaringologii 1995;3:5-10.

12.   Ovchinnikov Y, Svistushkin V, Shekhter A, et al. Holmium laser in chondrology: potentials and prospects. Vestnik Russian Academy of Medical Sciences 2000;7(36-39).

13.   Ovchinnikov YM, Gamov VP, Shekhter AB, et al. Possibilities of the use of surgical laser irradiation in spontaneous formation of cartilage tissue in ENT plastic surgery. Vestnik Otorinolaringologii 1996;3:21-22.

14.   Ovchinnikov Y, Svistushkin V, Shekhter A, et al. Non-invasive correction of nasal septum - laser surgery opportunity. *Vrach* 1999;12:35-36.

15.   Stefanovic-Racic M, Taskiran D, Georgescu HI, Evans CH. Modulation of chondrocyte proteoglycan synthesis by endogenously produced nitric oxide. Inflamm. Res. 1995;44:S216-S217.

16.   Sobol EN, Bagratashvili VV, Omel'chenko A, et al. Laser Shaping of Cartilage. Proceedings SPIE 1994;2128:43-49.

17.   Sobol E, Sviridov A, Omeltchenko A, et al. Laser Reshaping of Cartilage. Biotechnology & Genetic Engineering Review 2000;17:539-64.

18.   Sobol EN, Vorobjeva N, Sviridov AP, et al. Laser-induced activation of regeneration processes in spine disc cartilage. Proceedings SPIE 2000;3907:504-509.

19.   Sobol E, Sviridov A, Bagratashvili V, et al. Laser Reshaping of Nasal Septum Cartilage: Clinical Results for 40 Patients. Proceedings SPIE 2000;3907:in press.

20.   Sobol E, Omel'chenko A, Mertig M, Pompe W. Scanning force microscopy of the fine structure of cartilage irradiated with a CO2 laser. Lasers in Medical Science 2000;15:15-23.

21.   Sobol EN, Kitai M, Jones N, Sviridov A, Milner TE, Wong BJF. Heating and structure alterations in cartilage under laser radiation. IEEE Journal of Selected Topics in Quantum Electronics 1999;35:532-9.

22.   Sobol EN, Kitai M, Jones N, Sviridov A, Milner T, Wong B. Theoretical Modelling of Heating and Structure Alterations in Cartilage under Laser Radiation with Regard of Water Evaporation and Diffusion Dominance. Proceedings SPIE 1998;3254:54-63.

23.   Sobol EN, Sviridov AP, Omel'Chenko A, Bagratashvili V, Bagratashvili N, Popov VK. Mechanism of laser-induced stress relaxation in cartilage. Proceedings SPIE 1997;2975:310-315.

24.   Sobol EN. Personal Communication. 1996:

25.   Sobol EN, Sviridov A, Bagratashvili VV, et al. Stress Relaxation and Cartilage Shaping under Laser Radiation. Proceedings SPIE 1996;2681:358-363.

26.   Sobol EN, Bagratashvili VV, Sviridov A, et al. Phenomenon of Cartilage Shaping using Moderate Heating and its Application in Otorhinolaryngology. Proceedings SPIE 1996;2623:560-564.

27.   Sobol EN, Bagratashvili VV, Sviridov A, et al. Cartilage Reshaping with Holmium Laser. Proceedings SPIE 1996;2623:556-559.

28.   Sobol EN. Phase transformations and ablation in laser-treated solids. New York: John Wiley, 1995:316-322.

29.   Sviridov A, Sobol EN, Bagratashvili VV, et al. In Vivo Reshaping of Pig Ear Cartilage Under Holmium Laser Radiation. Proceedings SPIE 1998;in press.

30.   Sviridov A, Sobol EN, Jones NS, Lowe J. Effect of Holmium laser radiation on stress, temperature and structure alterations in cartilage. Lasers in Medical Science 1998;13:73-77.

31.   Sviridov A, Sobol EN, Bagratashvili V, et al. In vivo study and histological examination of Laser Reshaping of Cartilage. Proceedings SPIE 1999;3590:222-228.

32.   Sviridov A, Sobol E, Bagratashvili V, et al. In Vivo Alteration In Shape Of Porcine Ear Cartilage Under Holmium Laser Radiation. Russian Journal of Laser Medicine 1999;3:12-18.

33.   Wong BJF, Milner TE, Kim HK, Nelson JS, Sobol EN. Stress relaxation of porcine septal cartilage during Nd:YAG? ? ? = 1.32 mm) laser irradiation: mechanical, optical, and thermal responses. Journal of Biomedical Optics 1998;3:409-14.

34.   Wong BJF, Milner TE, Anvari B, et al. Measurement of radiometric surface temperature and integrated back-scattered light intensity during feedback controlled laser-assisted cartilage reshaping. Lasers in Medical Science 1998;13:66-72.

35.   Wong BJF, Milner TE, Kim HK, et al. Characterization of Temperature Dependent Biophysical Properties During Laser Mediated Cartilage Reshaping. IEEE J Selected Topics Quantum Electronics 1999;5:1095-1102.

36.   Wong BJF, Milner TE, Harrington A, et al. Feedback Controlled Laser Mediated Cartilage Reshaping. Archives of Facial Plastic Surgery 1999;1:282-287.

37.   Wong BJF, Milner TE, Kim HK, et al. Proteoglycan Synthesis in Porcine Nasal Cartilage Grafts Following Nd:YAG (? ? ? ? ? ? ? ? m) Laser Mediated Reshaping. Photochemistry and Photobiology 2000;71:218-224.

38.   Wong BJF, Chao K, Kim HK, et al. The Porcine and Lagomorph Septal Cartilages: Models for Tissue Engineering and Morphologic Cartilage Research. American Journal of Rhinology 2001;in press.

39.   Youn J-I. Laser-Mediated Cartilage Reshaping: Thermal, Optical, and Quasi-Elastic Light Scattering Studies [Master's Thesis]. Austin, TX: The University of Texas at Austin, 1999. 87 p.

40.   Youn J-I, Telenkov SA, Kim E, et al. Optical and Thermal Properties of Nasal Septal Cartilage. Lasers in Surgery and Medicine 2000;27:119-28.

Thermally Induced Birefringence Changes in Cartilage Using Polarization Sensitive Optical Coherence Tomography

Jong-In Youn[1], Gracie Vargas[1], Mathieu G. Ducros[2], Sergey A. Telenkov[1], Brian JF Wong[3], and
Thomas E. Milner[1]

[1]Biomedical Engineering Graduate Program, The University of Texas at Austin, Austin, TX 78712
[2]Ecole Polytechnique Federale de Lausanne, 1015 Lausanne, Switzerland
[3]Beckman Laser Institute and Medical Clinic, The University of California at Irvine, Irvine, CA 92715

ABSTRACT

Thermodynamic induced changes in birefringence of nasal septal cartilage following Nd:YAG laser irradiation were investigated using a polarization-sensitive optical coherence tomography (PSOCT) system. Birefringence in cartilage is due to the asymmetrical collagen fibril structure and may change if the underlying structure is disrupted due to local heat generation by absorption of laser radiation. A PSOCT instrument and an infrared imaging radiometer were used to record, respectively, depth-resolved images of the Stokes parameters of light backscattered from *ex vivo* porcine nasal septal cartilage and radiometric temperature changes following laser irradiation. PSOCT images of cartilage were recorded before (control), during, and after laser irradiation. From the measured Stokes parameters (I, Q, U, and V), an estimate of the relative phase retardation between two orthogonal polarizations was computed to determine birefringence in cartilage. Stokes parameter images of light backscattered from cartilage show significant changes due to laser irradiation. From our experiments we differentiate dehydration and thermal denaturation effects and observe the birefringence changes only in the dehydration effect. Therefore, a dynamic measurement of birefringence changes in cartilage using PSOCT as a feedback control methodology to monitor thermal denaturation is problematic in non-ablative surgical procedures such as laser assisted cartilage reshaping.

Keywords: Birefringence, Cartilage, Polarization Sensitive Optical Coherence Tomography, Stokes Parameters

1. INTRODUCTION

Cartilage is a fundamental tissue that provides structural support, withstands loads, and allows the bones to move smoothly against one another [1-3]. Various types of cartilage are composed of similar chemical structures such as water, collagen and proteoglycans [3]. Collagen in cartilage provides tensile stiffness and strength while proteoglycan aggregates give resistance to compressional deformation [1]. The negatively charged sulfate (SO_3^-) and carboxyl (COO^-) groups are fixed along the proteoglycan molecules and responsible for the mechanical properties of cartilage [1]. When pressure is applied to cartilage, water is forced away from the sulfate and carboxyl groups, and these negatively charged groups become closer and the repulsive Coulomb's force acts against further compression [1]. Release of pressure allows the proteoglycan molecules to relax and water to return to the charged domain [1].

In conventional cartilage reconstructive surgery, an autologous cartilage graft is used to replace deformed or damaged cartilage, but may result in associated problems with damage to normal healthy tissue due to carving or suturing [4]. In 1993, Sobol and his colleagues introduced laser-assisted cartilage reshaping, demonstrating that under the effect of photothermal heating, mechanically deformed cartilage undergoes a temperature dependent phase transformation, resulting in accelerated stress relaxation [4]. The advantage of this technique is that local laser irradiation may be used to change the shape of cartilage without ablating tissue [4]. Clinically, laser reshaped cartilage tissue can be used to recreate the underlying cartilaginous framework of structures in the head and neck such as ear, larynx, trachea, and nose. Therefore, optimization of the laser-assisted cartilage reshaping process requires identification of the biophysical transformations responsible for stress relaxation in cartilage accompanying laser heating. Sobol and colleagues used CO_2 and Ho:YAG laser light to investigate the phase transformation of cartilage during laser irradiation by analyzing light scattering [4]. They found that under shaping conditions, overheating of the cartilage surface to 130°C during CO_2 laser radiation causes micro structural changes, while a Ho:YAG laser allows treatment of thicker cartilage specimens without overheating and destruction of superficial layers [4-6]. Wong and colleagues have investigated changes in internal stress and integrated backscattered light intensity as a potential mechanism to control laser dosimetry during cartilage reshaping using a Nd:YAG laser [7-9]. Furthermore, they also attempted to determine the critical temperature transition in laser assisted cartilage reshaping [7-9]. Youn et al. measured thermal diffusivity and conductivity at three temperatures (27, 37 and 50°C) and spectral absorption and

reduced scattering coefficients in the 400 – 1400 nm spectral range using a spectrophotometer with porcine nasal septal cartilage [10].

Polarization sensitive optical coherence tomography (PSOCT) has been used to characterize the polarization state of light backscattered as a function of the optical path length in birefringent biological tissues such as muscle, skin and cornea [11,12]. De Boer et al. demonstrated the application of PSOCT to biological materials and determined the optical axis in rodent muscle and in vivo rodent skin [11]. They concluded that the coherent detection of the interference fringe intensity in orthogonal polarization channels allows determination of the depth-resolved Stokes parameters [11]. In another study, Ducros et al. used PSOCT to observe birefringence in the rabbit eye and measured the thickness of the birefringent retinal nerve fiber layer that was in relatively good agreement with values determined from histology [12].

Limited studies have been reported investigating birefringence in cartilage. Yarker et al. measured birefringence of the deep zone of pig tibial plateau cartilage using polarized light microscopy and provided information on collagen fibril orientation in the tissue [13]. Kiraly et al. also investigated birefringence changes in the articular cartilage collagen network and proteoglycans due to the deterioration of joint disease [14]. They exposed tissue plugs to cyclic loading and observed that birefringence increased in the superficial zone and decreased in the deep zone using quantitative microscopic methods [14].

Since PSOCT is emerging as a new technique to determine birefringence in biological materials, we attempted to measure thermodynamic induced changes of birefringence in cartilage for application to laser assisted cartilage reshaping. In cartilage, the asymmetrical collagen fibril structure gives a difference in refractive indices between two orthogonal axes and may change if the underlying structures are disrupted due to local heat generation by absorption of laser radiation. Although mechanisms underlying laser assisted cartilage reshaping are incompletely understood, thermodynamic measurements of birefringence changes in cartilage may find laboratory and clinical applications to characterize internal dynamics of macromolecules such as collagen and proteoglycans during laser irradiation. Moreover, active monitoring of birefringence changes in cartilage may find application as a feedback control methodology in non-ablative laser assisted cartilage reshaping procedures.

2. MATERIALS AND METHODS

2.1. Cartilage Harvest

The nasal septal cartilage extraction procedure was approved by Animal Resource Center of the University of Texas at Austin (Protocol #: 99020101). A fresh porcine head was obtained from a local abattoir and cartilage was extracted 2-h postmortem before the experiment. The prepared porcine head was placed on an operating table and explored for an incision line. The skin was removed from the upper side of the head through the bilateral nasal side. Bilateral nasal bone osteotomies were performed along the line of incision by using a standard carpenter's hammer and chisel. The hard bone was removed from the site, being careful not to damage the nasal septal cartilage, and the specimen was removed by using a chisel. After the extraction, soft tissue including perichondrium was peeled away from the cartilage specimen and the sample was rinsed in tap water for approximately 15 minutes to remove hemocytes. By using a scalpel, the cartilage specimens were sliced in rectangular parallelepiped shapes ($28 \times 31 \times 5$ mm^3) and placed on a sample plate. Samples were stored in physiological saline solution at 4 °C just prior to experimentation.

2.2. Experimental Methods

To investigate the thermodynamic induced birefringence changes following laser irradiation, a polarization sensitive optical coherence tomography (PSOCT) system [12] combined with a Nd:YAG laser as a heating source and infrared imaging radiometer was used (Fig.1). Light from a super luminescent diode (SLD) (0.8 mW, λ=859 nm, FWHM=18 nm) is linearly polarized along the horizontal and then divided into reference and sample paths by a nonpolarizing beam splitter (BS). In the reference path, after reflection from a reference mirror moving at 5 Hz and passage through a polarizer at 45°, the reference light is linearly polarized at 45 ° to the horizontal. In the sample path, a quarter wave plate (QWP) transforms the light incident onto the sample into a right circularly polarized state. Interference fringes between the light backscattered from a reference mirror and sample are split into two orthogonal polarization components by a polarizing beam splitter (PBS). The vertical and horizontal polarization components are detected by photodiodes D1 and D2, respectively.

We used a Nd:YAG laser (6W, λ=1.32 μm, D=4 mm, Pulse duration=6 s) as a heating source and an infrared imaging radiometer to measure temperature changes during laser irradiation. Infrared blackbody emission from the cartilage sample is reflected by a dichroic mirror positioned between the focusing lens and sample and detected by an InSb IR imaging radiometer (Merlin, Indigo Systems Inc., 320 × 240 pixels) (Fig.1).

Coherent detection of the amplitude and phase of the interference fringes in orthogonal polarization channels allows image information of the Stokes parameters (I, Q, U, V), the degree of polarization, P, as well as an intensity based image similar to

that conventional OCT provides [11]. The parameter I represents total intensity of light backscattered from the cartilage sample, Q represents the difference between intensities of light linearly polarized at 0° and 90°, normalized to total intensity. Similarly, parameters U and V represent the differences between intensities of light linearly polarized at +45° and –45°, right circularly polarized and left circularly polarized, respectively [12].
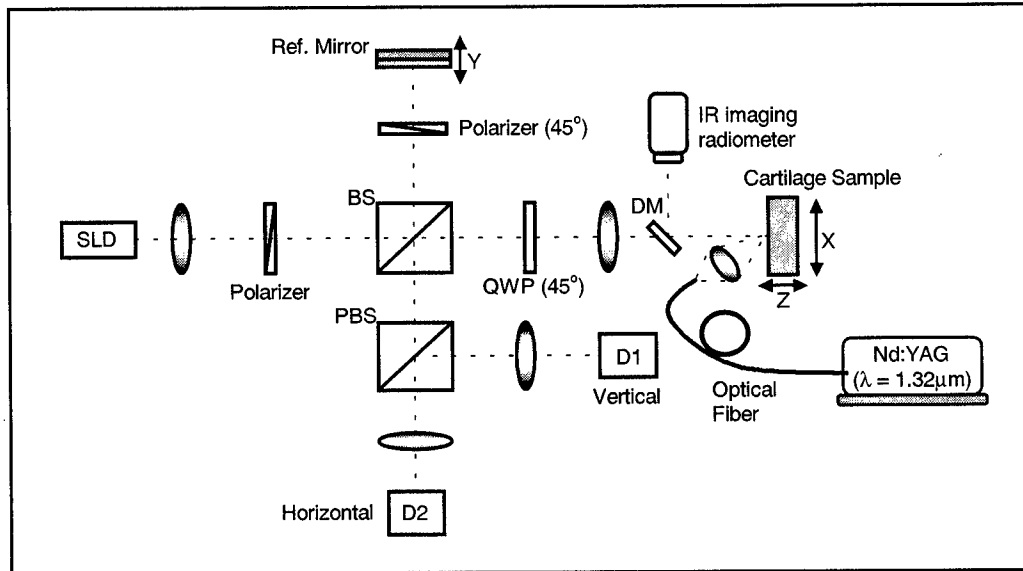
Figure 1. Schematic diagram of PSOCT instrument combined with a heating laser source ($\lambda = 1.32\mu m$) and an infrared imaging radiometor. SLD: Super Luminescent Diode, BS: nonpolarizing Beam Splitter, PBS: Polarizing Beam Splitter, QWP: Quarter Wave Plate, DM: Dichroic Mirror

$$Q = \frac{I_{0°} - I_{90°}}{I} \qquad U = \frac{I_{45°} - I_{-45°}}{I} \qquad V = \frac{I_{rc} - I_{lc}}{I}$$

$$P = \sqrt{Q^2 + U^2 + V^2}$$
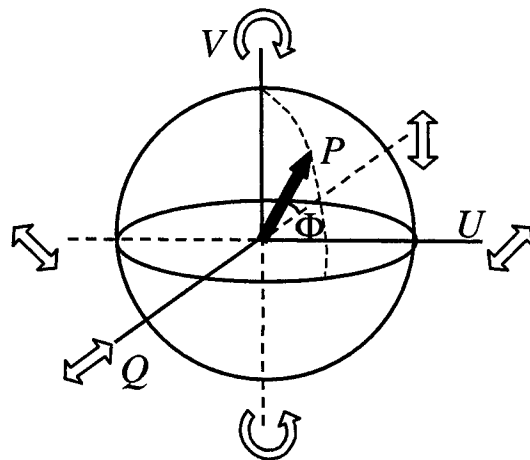
Figure 2. Schematic illustration of Poincaré sphere representation [15]. Parameter Φ is the angle between the Stokes vectors of incident light (Q=U=0, V=1) and light backscattered from the user-specified region inside the cartilage sample denoted as P vector. In this representation, Φ represents the phase retardation between two orthogonal polarization components of light backscattered from the sample relative to incident light.

The computed Q, U, V Stokes parameters represent the polarization state of light backscattered from the sample, transmitted through QWP and incident onto the detectors. For example, the Stokes parameters for the light specularly reflected from the surface of the sample are $Q = -1$, $U = 0$, and $V = 0$.
From this knowledge, we calculated phase retardation, Φ:

$$\Phi = \arccos\ (-Q) \tag{Eq. 1}$$

In the Poincaré sphere representation (Fig.2) [15], parameter Φ is the angle between the Stokes vectors on the Poincaré sphere of light backscattered from inside the cartilage specimen and the front surface of the sample ($Q = -1$, $U = V = 0$). In this representation, Φ represents the phase retardation between vertical and horizontal polarization components of light backscattered from the user-specified region inside the cartilage sample relative to incident light. We obtain information about birefringence changes by calculating phase retardation, Φ, at each pixel representing a discrete position in the cartilage. When the backscattered light is unpolarized or when the intensity is lower than the system noise level, Φ varies uniformly between $0°$ and $180°$ and averages $90°$.

The cartilage specimen was sliced into six rectangular parallelepiped shapes and the prepared sample was placed in the sample path of the PSOCT system. A red aiming beam aligned with the imaging beam was used to insure the PSOCT, IR imaging and laser heating positions were coincident. Two PSOCT images (2 mm wide $\times$ 1.0 mm deep) centered on the irradiated area were acquired before and after Nd:YAG laser irradiation. In the PSOCT images recorded during laser irradiation, successive depth scans at 5 scans per second were recorded at a constant lateral position at the center of the irradiation beam over a period of 10 seconds. Simultaneously radiometric temperature was measured using an infrared imaging radiometer at a 60 Hz frame rate. After recording measurements, a calibration procedure was performed for the radiometer using a blackbody source with a thermocouple attached to the surface.

3. RESULTS AND DISCUSSION

Figure 3 shows recorded PSOCT images scanned spatially (2 mm width $\times$ 1.4 mm depth) for phase retardation, Φ, before and after laser irradiation. Incident light that is right circularly polarized at the air-tissue interface and polarization state of light propagating through the sample varies in depth and lateral position. Although the light incident onto the sample is right circulary polarized, polarization state of the data is seen as vertically polarized light because the light passes through the quarter wave plate and is displayed at the photodiodes. As seen in Figure 3, the Φ image changes before and after laser irradiation. An S-shaped structural feature in Figure 3(A) is not apparent following laser irradiation (Figure 3(B)) indicating that the scattering properties of cartilage have changed and the birefringence decreases following laser irradiation. Moreover, surface shrinkage (~75μm) was observed after laser irradiation.
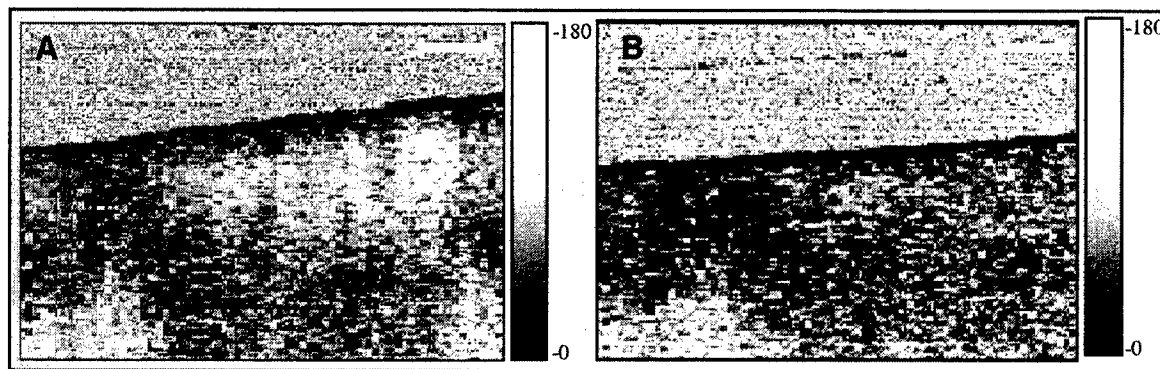
Figure 3. The phase retardation (Φ) images (2mm $\times$ 1.4mm), i.e. (Eq. 1), in the cartilage sample (A) before laser irradiation, and (B) after laser irradiation. Scale bar is 300μm.

The Φ image recorded during laser irradiation is shown in Figure 4(A) and compared with the radiometric temperature changes during laser irradiation (Figure 4(B)). The x-axis represents time, while the y-axis represents depth. The left side of the image corresponds to the beginning of the laser irradiation. Upon heating the cartilage sample, structural optical property changes are observed at approximately the 20th A-scan or about 4 seconds (~75°C) after beginning laser irradiation. When the radiometric temperature reaches 65°C – 75°C, protein systems in tissue begin to undergo thermal denaturation and the observed changes signal the initial stages of thermal denaturation of collagen and other macromolecules within cartilage [16]. When the thermal denaturation of collagen or other macromolecules occurs, the helixes may unwind and then recoil as the tissue is allowed to cool [16]. The birefringence changes accompanying laser irradiation may be used to identify the biophysical transformation responsible for stress relaxation in cartilage.
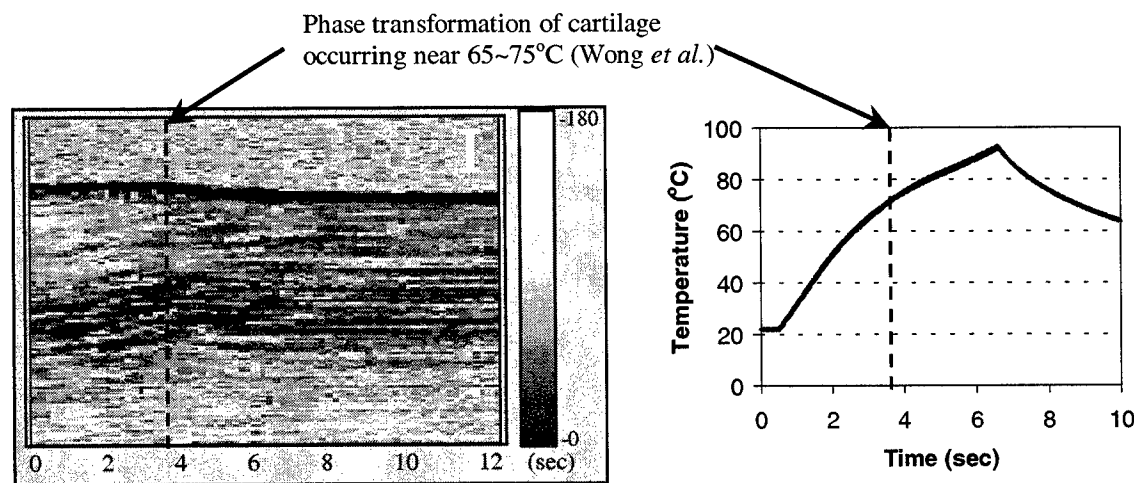
Figure 4. The phase retardation (Φ) images in the cartilage sample and radiometric temperature changes following laser irradiation. Scale bar is 200μm.

Figure 5 shows plots of the Stokes parameters, Q, U, and V (Figures 5 (A) and (B)), degree of polarization, P (Figure 5(C)) and phase retardation, Φ (Figure 5(D)) of light backscattered from the cartilage sample before and after laser irradiation. For these results, we reregistered and averaged the 200 A-scans for each Stokes parameter and then plotted versus depth. The data we obtained contained a noise due to speckle, averaging 200 A-scans of each parameter reduced this noise.
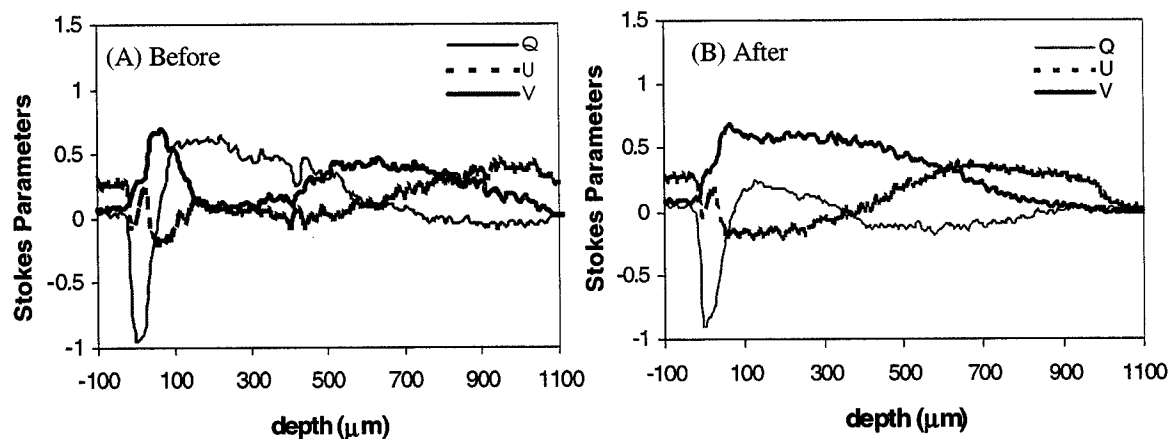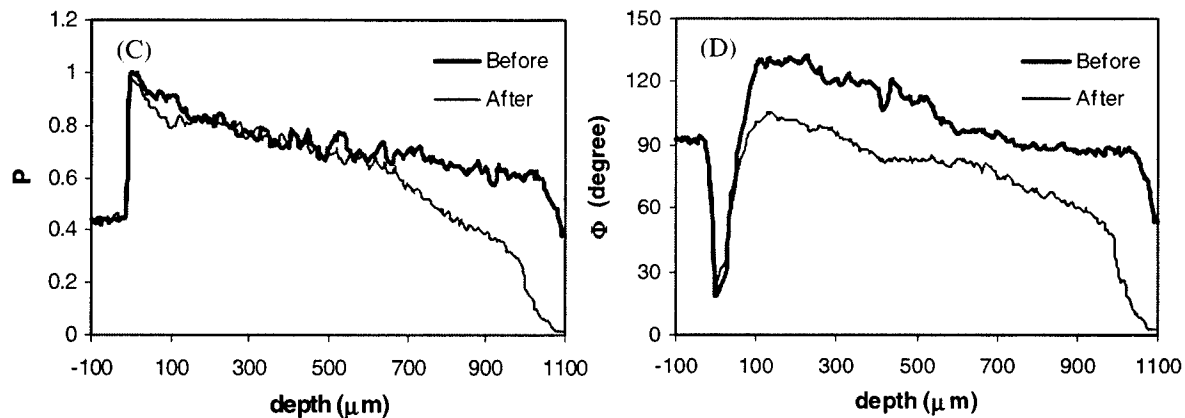
Figure 5. Plots of Stokes Parameters of (A) before and (B) after laser irradiation, (C) degree of polarization, and (D) phase retardation versus depth before and after laser irradiation showing that the birefringence of the cartilage sample decreases following laser irradiation.

In Figure 5(A), the Stokes parameters before laser irradiation versus depth, the polarization state of light backscattered from the cartilage sample begins linearly polarized vertically below the air-tissue interface and transforms to right circularly polarized light at approximately 70μm in depth. As the incident light passes 100μm in depth, the light is linearly polarized horizontally and then transforms to linearly polarized at approximately 500μm. After laser irradiation (Figure 5(B)), the light begins linearly polarized vertically below the air-tissue interface and becomes right circularly polarized at about 90μm deep. As incident light passes through deeper depths (~600μm), backscattered light transforms to a linearly polarized state at +45° to the horizontal. As seen in Figures 5(A) and (B), the polarization state of light propagating in the cartilage sample changes after laser irradiation. Degree of polarization decreases at deeper depths, meaning the light becomes depolarized, after propagating into and out of the sample (Figure 5(C)). Phase retardation, i.e, the birefringence in cartilage is observed to decrease at the surface and all depths following laser irradiation (Figure 5(D)).
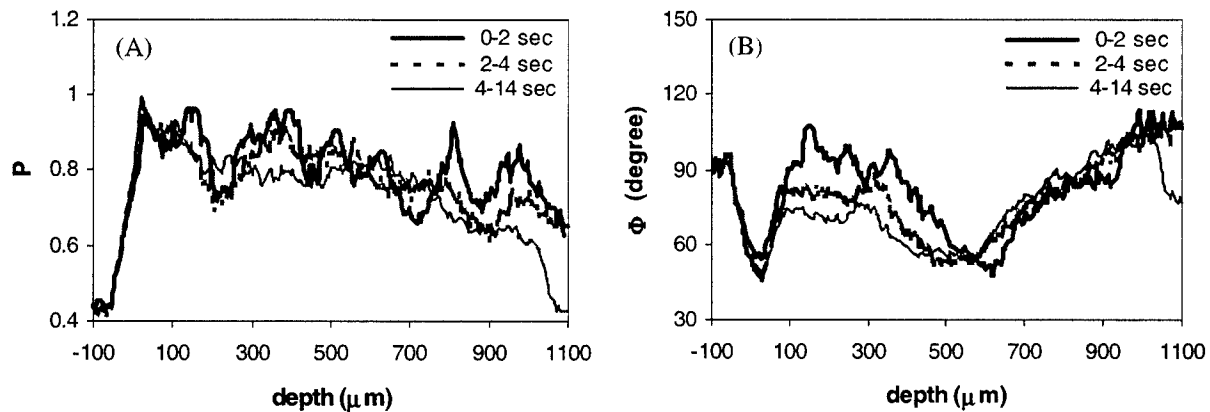
Figure 6. Plots of (A) degree of polarization and (B) phase retardation versus depth during laser irradiation showing that the degree of polarization and phase retardation values decrease following laser irradiation.

In figures 6(A) and (B), the plots of degree of polarization and phase retardation respectively over depth during laser irradiation are presented to investigate the thermodynamic induced changes in birefringence. Inasmuch as data during laser irradiation was scanned in time at a fixed position, we grouped recorded A-scans into three groups: (1) early laser irradiation (10 A-scans, 0-2 seconds, 20°C ~ 50°C) (2) transition (10 A-scans, 2-4 seconds, 50°C ~ 78°C) (3) post transition (40 A -scans, 4-12 seconds). Pulse duration of Nd:YAG laser as a heating source was 6 seconds and the PSOCT imaging process started simultaneously with laser irradiation. From both plots, degree of polarization and phase retardation are observed to decrease following laser irradiation. These results show that birefringence of the cartilage sample changes following laser

irradiation. Since the depth-resolved Stokes parameters and images give structural information through the backscattered light and induced changes in the polarization states accompanying laser irradiation, this active monitoring of birefringence changes in cartilage may find application as a feedback control methodology in laser assisted non-ablative cartilage reshaping.

To understand the origin of the observed birefringence decrease following laser irradiation, two effects should be considered; dehydration and thermal denaturation. In dehydration, when water is evaporated from cartilage due to laser irradiation, the fibrils move closer together and the volume fraction of fibrils is increased that causes decrease in birefringence [17,18]. In thermal denaturation, the birefringence decreases since fibrils occupy a larger volume due to unraveling of the underlying structures [17,18]. We investiagated these two effects by conducting experiments using a glycerol and heated saline at about 63 °C. From the experiments, no birefringence changes observed in cartilage in heated saline over the time. Therefore, the observed birefringence changes following laser irradiation were considered to be only due to the dehydration effect.

4. CONCLUSIONS

Thermodynamic induced changes in birefringence of porcine nasal septal cartilage (extracted 2-h postmortem) following Nd:YAG laser irradiation were investigated using a polarization sensitive optical coherence tomography (PSOCT) system combined with an infrared imaging radiometer. We observed surface shrinkage following laser irradiation using PSOCT imaging, and an S-shaped structural feature could be differentiated using a phase sensitive contrast variable on the Stokes parameters of backscattered light. We analyzed the data using lateral adjacent A-scans averaging to reduce the noise due to speckle effects and system noise. Phase retardation was observed to decrease following laser irradiation indicating that the scattering properties of cartilage vary and the birefringence decreases following laser irradiation. Since the birefringence changes following laser irradiation were significantly due to dehydration, the use of PSOCT as a feedback control methodology is problematic to minimize nonspecific thermal injury and preserve chondrocyte viability in laser assisted cartilage reshaping.

5. ACKNOWLEDGEMENTS

6. REFERENCES

1. LY Woo and JA Buckwalter, "Injury and repair of the musculoskeletal soft tissue", American Academy of Orthopaedic Surgeons, 1987.
2. AI Caplan, "Cartilage", *Scientific American Journal*, vol. 251, pp84-94, 1984
3. H Gray, "Gray's anatomy", Gramercy Books, 1997.
4. EN Sobol, "Phase Transformations and Ablation in Laser-treated Solids", John Wiley & Sons, 1995.
5. EN Sobol, V Bagratashvili, A Sviridov, A Omel'chenko, M Kitai, N Jones, V Zenger, N Nasedkin, M Isaev, V Karlov, and A Schechter, "Study of cartilage shaping with holmium laser ", *Proceedings of SPIE*, vol. 2623, pp544-547, 1996
6. EN Sobol, V Bagratashvili, A Sviridov, A Omel'chenko, A Schechter, N Jones, S Howdle, and E Helidonis, "Phenomenon of cartilage shaping using moderate laser heating and its application in otorhinolaryngology", *Proceedings of SPIE*, vol. 2623, pp548-552, 1996
7. BJF Wong, TE Milner, HK Kim, S Telenkov, C Chew, T kuo, DJ smithies, EN Sobol, and JS Nelson, "Critical temperature transitions in laser medicated cartilage reshaping", *Proceedings of SPIE*, vol. 3425, pp161-172, 1998
8. BJF Wong, TE Milner, B Anvari, A Sviridov, A Omel'chenko, VV Bagratashvili, EN Sobol, and JS Nelson, "Thermo-optical response of cartilage during feedback controlled laser-assited reshaping", *Proceedings of SPIE*, vol. 2970, pp380-391 , 1997
9. BJF Wong, TE Milner, B Anvari, A Sviridov, A Omel'chenko, VV Bagratashvili, EN Sobol, and JS Nelson, "Measurements of radiometric surface temperature and integrated backscattered light intensity during feedback controlled laser-assisted cartilage reshaping", *Lasers in Med. Sci.*, vol. 13, pp66-72, 1998
10. JI Youn, S Telenkov, E Kim, NC Bhavaraju, BJF Wong, JW Valvano, and TE Milner, "Optical and thermal properties of nasal septal cartilage", *Lasers in Surg. and Med.*, vol. 27, pp119-128, 2000
11. JF de Boer, TE Milner, and JS Nelson, "Determination of the depth resolved stokes parameters of light backscattered from turbid media using polarization sensitive optical coherence tomography", *Optics Letters*, vol.24, 1999, pp300-302.

12. MG Ducros, JF de Boer, HE Huang, LC Chao, Z Chen, JS Nelson, TE Milner, and HG Rylander III, "Polarization sensitive optical coherence tomography of the rabbit eye", *IEEE J. of selsected topics in quantum elec.*, vol.5, no.5, pp1159-1167, 1999

13. YE Yarker, RM Aspden, and DWL Hukins, "Birefringence of articular cartilage and the distribution of collagen fibril orientations", *Connective Tissue Research*, vol. 11, pp207-213 , 1983

14. K Kiraly, M Hyttinen, J Parkkinen, J Arokoski, T Lapvetelainen, K Torronen, I Kiviranta, and HJ Helminen, "Articular cartilage collagen birefringence is altered concurrent with changes in proteoglycan synthesis during dynamic in vitro loading", *The Anatomical Record*, vol. 251, pp28-36, 1998

15. C Brosseau, "Fundamentals of polarized light: A statistical optics approach", John wiley & Sons, 1998

16. BJF Wong, TE Milner, HH Kim, JS Nelson and EN Sobol, "Stress Relaxation of Porcine Septal Cartilage During Nd:YAG ($\lambda = 1.32$mm) Laser Irradiation: Mechanical, Optical, and Thermal Response", J. of Biomed. Opt., 3(4), pp409-414, 1998

17. WL Bragg, AB Pippard, "The Form Birefringence of Macromolecules", Acta Cryst, vol. 6, pp865-867, 1953

18. DJ Maitland, JT Walsh Jr., "Quantitative Measurements of Linear Birefringence During Heating of Native Collagen", Laser Surg Med, vol. 20, pp310-318, 1997

Wavelength Dependent Scattering of Light during Nd:YAG Laser Heating of Porcine Septal Cartilage

Reshmi Basu[a], Brian J.F. Wong[a,b,c], and Steen J. Madsen[d]

[a]Beckman Laser Institute and Medical Clinic, University of California at Irvine, Irvine, CA 92715

[b]University of California, Irvine Medical Center, Department of Otolaryngology/Head and Neck Surgery, Orange CA 92868

[c] Whitaker Center for Biomedical Engineering, University of California at Irvine, Irvine, CA 92715

[d]University of Nevada, Las Vegas, Department of Health Physics, Las Vegas, NV 89154

ABSTRACT

Heat alters the bulk physical properties of cartilage tissue, including the optical scattering and absorption coefficients. The purpose of this investigation was to measure wavelength dependent scattering of light using three different probe lasers (λ=488 nm, 670 nm, 808 nm) during Nd:YAG laser (λ= 1.32μm, 50 Hz pulse repetition rate) heating of porcine septal cartilage. An integrating sphere was used to collect diffusely backscattered light from these probe lasers and three lock-in amplifiers were used to discriminate between the different signals. Peak signal intensity of the backscattered light was observed at different temperatures depending on the probe laser wavelength and specimen thickness. The observed changes are unlikely due to axial thermal gradients created during Nd:YAG laser heating and do not correlate with the fluence distribution of the three probe laser wavelengths evaluated. The observed wavelength dependent differences suggest that tissue matrix alterations during heating are due to macromolecular conformation changes that occur on the scale of the wavelength of the probe laser light. As changes in the bulk properties of cartilage can be inferred by using simple non-contact techniques such as light scattering, the characterization of the wavelength dependence of these phenomena will become increasingly important.

Keywords: cartilage, laser mediated cartilage reshaping, Nd:YAG laser, optical properties, plastic surgery, otolaryngology

1.0 INTRODUCTION

1.1 Cartilage Molecular Structure

Cartilage is a macromolecular tissue composed of 80% water. Chondrocytes are the constitutive cells of this tissue, and produce and maintain the extracellular matrix, which consists of a network of proteoglycan aggregates and collagen type II fibers. These macromolecular proteoglycan aggregates are formed from repeating hyaluronic acid groups to which are attached numerous protein chains. These chains (composed of chondroitin sulfate and keratan sulfate) contain a large number of fixed negative charges. The interaction of these negatively charged groups with free cations and hydrogen bonding result in charge shielding and maintenance of electric neutrality. Proteoglycans are approximately 300-400 nm in length with a width of about 80 nm [1].

The collagen type II fibers in the matrix range from 5-200 nm in diameter and are assembled from rod-like subunits called tropocollagen each about 300 nm long and 1.5 nm in diameter. In turn, tropocollagen consists of three polypeptide α-chains that are twisted to form a triple helix. Collagen exhibits several orders of organization, from the primary structure of the α-chains to the quaternary structure of the collagen fibers [1].

Water within the matrix is divided into two compartments; "bound" water non-covalently interacts with proteoglycan-collagen macromolecules, and "free" water passes readily through the extracellular matrix [3]. When force is applied to cartilage, negatively charged molecular groups come in close approximation resulting in Coulombic repulsion that resists further compression. Cartilage tends to return to its original shape when the applied force is removed and equilibrium is re-established.

1.2 Clinical Use of Laser Mediated Cartilage Reshaping

The use of laser irradiation to reshape cartilage via thermally induced stress relaxation was introduced by Sobol et al. in 1993 [4-11]. Laser reshaping may replace traditional surgical techniques to alter cartilage shape, and thereby minimize recovery times and reduce complications. It is important to understand the mechanisms underlying reshaping in order to develop safe energy parameters and a reliable feedback technique to optimize and monitor this process and reduce the risk of thermal necrosis. Detecting changes in tissue optical properties during laser heating can be performed using non-contact probe laser techniques which are often simpler than measuring changes in stress or surface temperature [15]. But, optimization of this technique requires characterization of the wavelength dependence of the optical properties.

1.3 Optical Properties of Cartilage during Laser Irradiation

Previous studies demonstrated that laser irradiated cartilage undergoes a phase transformation, resulting in accelerated stress relaxation and shape change [6], and this is accompanied by alterations in the biophysical properties of the cartilage tissue such as thermal conductivity, optical scattering, and elastic modulus [10-12]. Measurement of changes in tissue optical properties is of particular interest, as light can be used to rapidly probe tissue to substantial depths using simple non-contact techniques. In previous studies, time and temperature dependent changes in diffuse reflectance or integrated backscattered light intensity [I(t)] generated by visible wavelength lasers (632.8 to 670 nm) was recorded during laser heating. The fractional change in integrated backscattered light intensity, $\Delta I(t)/I_0$, was calculated by measuring the change in I(t) relative to the baseline I_0 recorded prior to the onset of Nd:YAG laser irradiation [10,11].

$\Delta I(t)/I_0$, from a HeNe probe laser (λ=632.8 nm) has been observed to increase, plateau, and then decrease during laser heating of cartilage [10,11]. The plateau region occurred when the cartilage front surface temperature reached approximately 60-70°C. The peak value for $\Delta I(t)/I_0$ occurred at $t=\tau_l$, which in general was shorter than τ, the laser pulse duration. τ_l increased following successive irradiation of the same specimen [13]. While the precise molecular mechanisms of this process are not fully understood, several mechanisms have been proposed, including: 1) a bound-to-free water transition in the cartilage matrix at the critical temperature; 2) collagen or proteoglycan denaturation; 3) local mineralization of proteoglycan subunits by positive Na or Ca ions; and/or 4) reorganization or alteration of weak van der Waals or hydrogen bonds between proteoglycan subunits [3, 14].

In this investigation, diffusely reflected light from three probe lasers (λ= 488 nm, 670 nm, and 808 nm) and surface temperature (using IR radiometry) were recorded during the Nd:YAG laser heating of cartilage with the objective of determining whether light scattering during laser heating is sensitive to wavelength and temperature.

2.0 MATERIALS AND METHODS

2.1 Cartilage Specimens

Fresh porcine heads were obtained from a local abattoir (Clougherty Packing Company, Vernon, CA), and the septal cartilage was harvested as previously described [11]. Specimens measuring 10 × 20 mm were cut with a razor. Immediately prior to irradiation, each specimen was cut to a specific thickness varying from 1 mm to 3 mm using a guillotine microtome designed by our laboratory [15].

2.2 Cartilage Irradiation

Cartilage specimens were irradiated with light from an Nd:YAG laser (λ= 1.32μm, 50 Hz pulse repetition rate, NewStar Lasers, Auburn, CA), which was delivered by a 400μm core-diameter silica multimode optical fiber terminating in

an anti-reflection coated collimating lens. Laser spot size (6mm) was estimated by measuring the burn diameter using thermal paper (Zap-It, Kentek, Pittsfield, NH). Laser power (6.60W) was measured using a pyroelectric meter (Model 201, Coherent Commercial Products). Each specimen was irradiated three times with a pulse duration of 15 seconds. The specimens were allowed to cool for four minutes between each successive irradiation.

2.3 Optical and Thermal Properties during Laser Irradiation

Cartilage specimens were placed in front of one port of the integrating sphere (Spectralon, 6", Labsphere, North Sutton, NH) (Figure 1). Collimated light from a red diode laser (λ=670 nm, 5 mW, ThorLabs, Newton, NJ), an infrared diode laser (λ= 808 nm, 5 mW, Lasermate Co., Walnut, CA), and an argon-ion-pumped dye laser (λ= 488 nm, 1.5 W, Coherent Innova 90-5 Ar Laser, Coherent 599 DCM dye laser, Palo Alto, CA) was directed toward the *non-irradiated surface* of the specimen, coincidentally centered behind the central region of the Nd:YAG laser spot. A 1-mm aperture was used for each laser to reject scattered laser light and maintain uniform beam size. Backscattered light from the three lasers was measured using a silicon photoreceiver (Model 2001, New Focus, Mountain View, CA).

The output of each laser was amplitude modulated at a different frequency to allow simultaneous collection of three signals. The red and infrared diode lasers were amplitude modulated internally at 9 kHz and 9.7 kHz, respectively, using reference signals generated by two lock-in amplifiers (Model SR830 DSP and Model SR850 DSP, Stanford Research Systems, Sunnyvale, CA). The argon ion laser light was amplitude modulated (2.9 kHz) using a mechanical chopper (Model SR540 Chopper Controller, Stanford Research Systems, Sunnyvale, CA) and synchronously detected by a third lock-in amplifier (Model SR530, Stanford Research Systems, Sunnyvale, CA).

Radiometric surface temperature on the Nd:YAG laser irradiated surface of the cartilage specimen was estimated using a thermopile infrared detector. The Nd:YAG laser and the thermopile infrared detector were integrated into a handpiece unit and were concentrically focused. The thermopile infrared detector was calibrated as described previously [10].

Figure 1. Schematic of instrumentation used to simultaneously measure radiometric surface temperature and backscattered light from probe lasers of three different wavelengths during Nd:YAG (λ=1.32µm) laser heating of porcine septal cartilage.

3.0 RESULTS

Figure 2 shows cartilage radiometric surface temperature $S_c(t)$ and the fractional change in integrated backscattered light intensity $\Delta I(t)/I_0$ for all three probe lasers (488 nm, 670 nm, and 808 nm).. For each probe laser wavelength, $\Delta I(t)/I_0$ was observed to increase, plateau and then decrease with plateaus observed prior to the termination of the laser irradiation. The maxima in $\Delta I(t)/I_0$ for all three wavelengths occurred when $S_c(t)$ was approximately 60-70°C. $\Delta I(t)/I_0$ from the 488 nm, 670 nm, and 808 nm probe lasers reached peaks when $S_c(t)$ was approximately 60°C, 63°C, and 70°C

Figure 3a-c illustrate that the peaks in $\Delta I(t)/I_0$ for sequential irradiation of a single specimen (2.94 mm thick) behave similarly for all three probe laser wavelengths.. Integrated backscattered light intensity, in all cases, increased, peaked, and then decreased. However, τ_l increased with each successive irradiation. **3a** shows three peaks in $\Delta I(t)/I_0$ from the 488 nm probe laser which were observed after approximately 5, 7.5, and 9 seconds of laser exposure corresponding to the first, second, and third laser irradiation, respectively (all peaks occurred prior to the onset of laser irradiation). Similar findings were observed using the 670 nm probe laser (**Figure 3b**) with peaks observed after 5, 10.5, and 11.5 seconds of laser heating. In **Figure 3c** (808 nm probe laser) the peaks occurred after 7.5, 13, and 14.5 seconds.

Prolongation of τ_l was observed with increasing probe laser wavelength. This trend was observed with increasing specimen thickness (0.95 mm, 2.13 mm, and 2.95 mm) with the peaks in $\Delta I(t)/I_0$ from the 488 nm probe laser occurred first, followed by peaks generated by the 670 nm and 808 nm probe lasers, respectively. **Figure 4a-c** illustrates this trend and corresponds to the second laser irradiation of each specimen. **4a** shows three peaks in $\Delta I(t)/I_0$ during heating of a specimen 0.95 mm thick. $\Delta I(t)/I_0$ from the 488 nm probe laser peaked at 8 seconds; $\Delta I(t)/I_0$ from the 670 probe laser peaked at 10.5 seconds; $\Delta I(t)/I_0$ from the 808 nm probe laser peaked at 13.5 seconds. **4b** and **4c** show similar results for specimens 2.13 mm and 2.95 mm thick, respectively. In **4b**, the peaks occurred at 7.5, 8.5, and 9 seconds for the 488, 670, and 808 nm probe lasers. In **4c**, the peaks occurred at 9.5, 11, and 14 seconds for the three laser wavelengths.
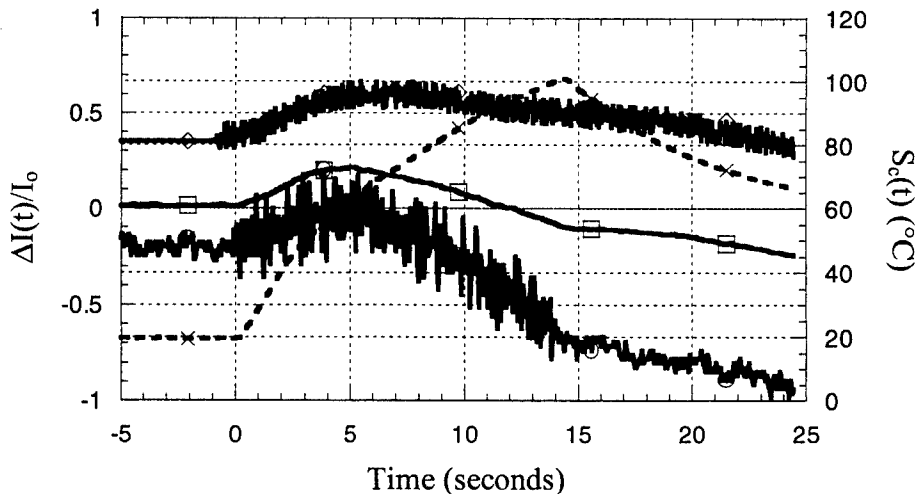
Figure 2. Simultaneous measurement of radiometric surface temperature [$S_c(t)$ (°C)] and fractional change in integrated backscattered light intensity [$\Delta I(t)/I_0$] for three probe lasers (488 nm, 670 nm, and 808 nm). (O—O—$\Delta I(t)/I_0$, 488 nm; □—□—$\Delta I(t)/I_0$, 670 nm; ◇—◇—$\Delta I(t)/I_0$, 808nm; ×—×—$S_c(t)$).
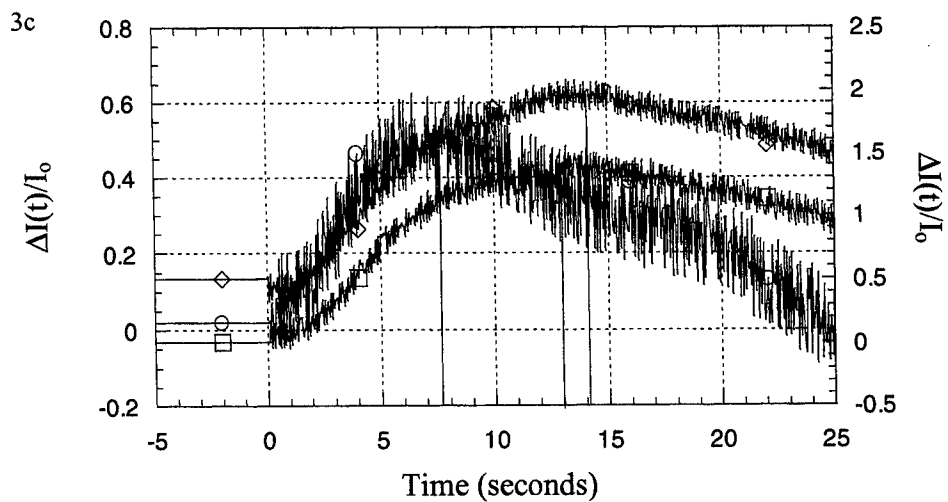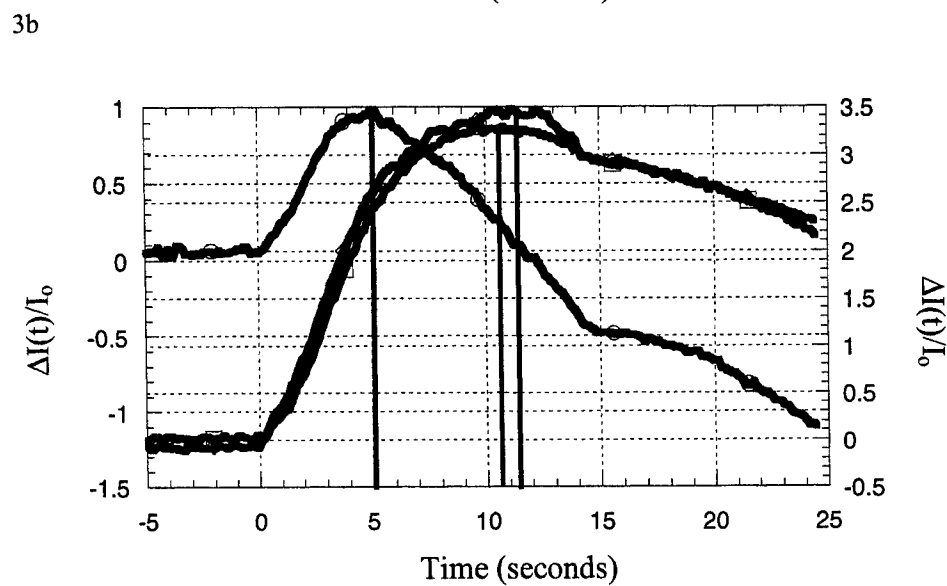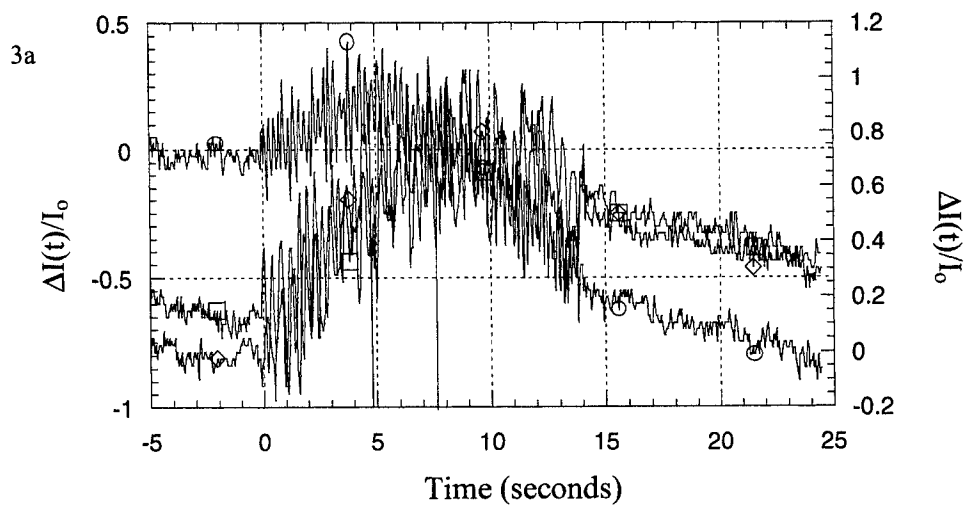
Figures 3a-c. τ_l increased with sequential laser irradiation. (O—O—$\Delta I(t)/I_o$, pulse 1, □—□—$\Delta I(t)/I_o$ pulse 2 ◇—◇—$\Delta I(t)/I_o$, pulse 3).
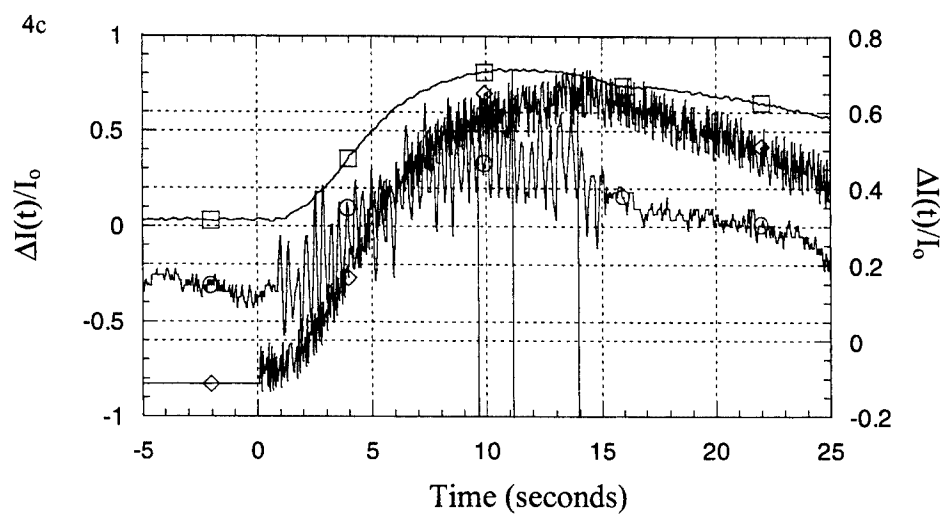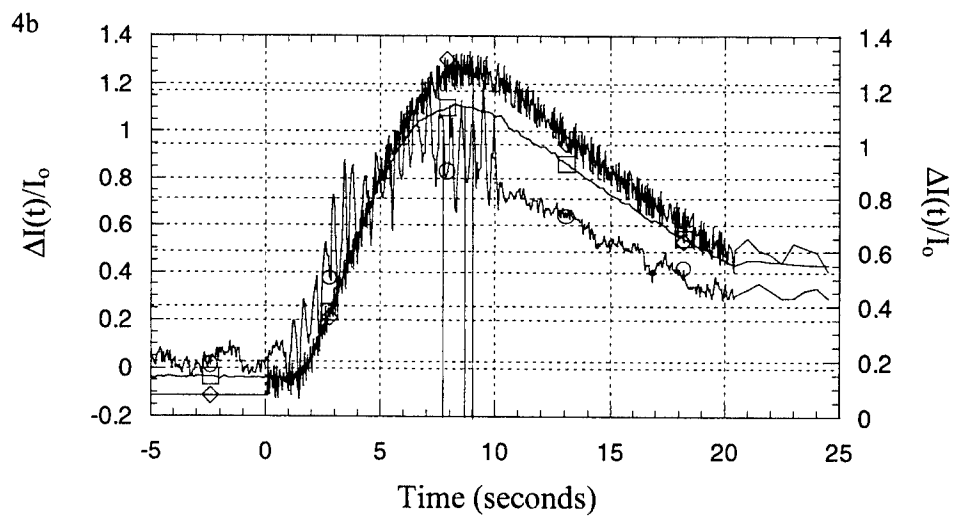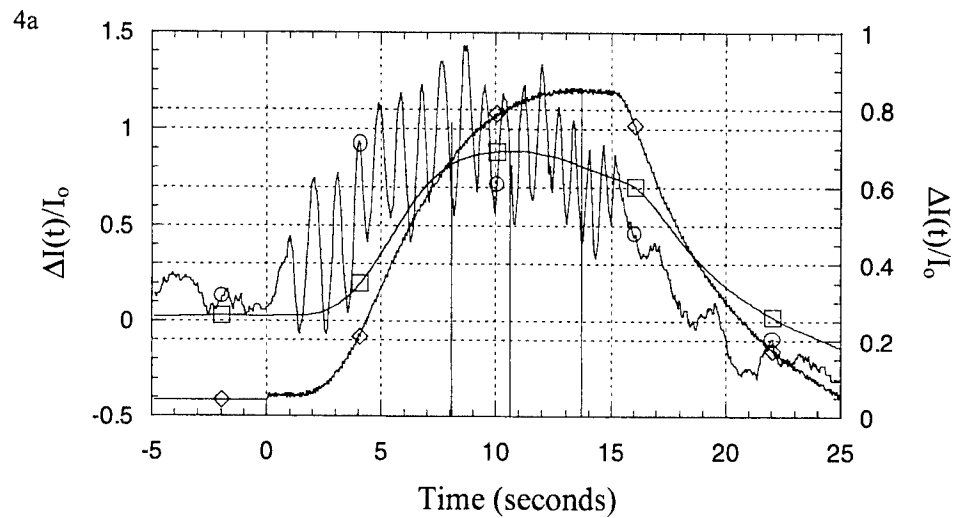
Figures 4a-c. τ_l lengthened with increasing probe laser wavelength. (O—O—$\Delta I(t)/I_o$, 488 nm, □—□—$\Delta I(t)/I_o$, 670 nm, ◇—◇—$\Delta I(t)/I_o$, 808 nm).

4.0 DISCUSSION

Previous studies have shown that the peak in signal intensity from laser light in the red spectral region occurs when the surface temperature reaches 60-70°C and is synchronous with the onset of stress relaxation [10-12,16]; the results illustrated in **Figure 2** suggest this observation is independent of laser wavelength through the visible and near-infrared spectra.

Similarly our findings confirm previous observations that the peak in diffuse reflectance occurs at successively higher temperatures with each sequential laser exposure [13, 22]. (**Figure 3**). This observation may in part be explained by considering the axial temperature distribution in cartilage generated by Nd:YAG laser heating. During the first laser exposure, light from the Nd:YAG laser heats primarily the outermost layers of the specimen, causing changes in the tertiary structure of matrix macromolecules with subsequent alteration of tissue optical properties. Subsequent laser exposures must then deliver radiant energy to deeper tissue layers because the more superficial layers have already been thermally altered. Hence, the irradiation time must be longer and the plateau in $\Delta I(t)/I_0$ is observed at higher temperatures [13].

The time dependent behavior in diffuse reflectance was similar for all three probe beam wavelengths; peaks occurred in the same temperature range during the first irradiation and higher temperatures with each successive laser exposure. However, some subtle differences were observed. The specific temperature at which the peak in $\Delta I(t)/I_0$ occurred demonstrated slight probe laser wavelength dependence. The signal generated by the argon laser (488 nm) peaked first, followed by observation of the peak from the 670 nm and then the 808 nm probe laser (**Figure 4**).

Several possible mechanisms have been proposed to account for the observed changes in light scattering and stress relaxation. 65°C is often cited as the critical temperature for the denaturation of collagen and related proteins [17] and it is likely that heat alters the tertiary structure of collagen with possible loss of its helical geometry. The peaks in $\Delta I(t)/I_0$ may coincide with unwinding of these helices; the scattering peaks would be expected to occur when the distance between individual collagen molecules matched the probe laser light wavelength. Alternatively, Sobol has suggested that alterations in the proteoglycan structure are responsible for stress relaxation [3]. He suggested that with heating, proteoglycan chains and subunits undergo spatial redistribution (while under a mechanical load) and move a specific distance resulting in the release of mechanical stress. The peak in $\Delta I(t)/I_0$ may occur when the distance between proteoglycan aggregates reaches a particular length equal to the probe beam wavelength. In either case, spatial separation of macromolecular structure accompanying heating and redistribution of stress may account for the observed changes in tissue optical properties.

The wavelength dependence of optical scattering during heating (**Figure 4a-c**) must be interpreted within the context of the optical penetration depth (δ) of the three probe wavelengths, and of the Nd:YAG laser (λ = 488 nm, 670 nm, 808 nm and 1.32 µm, respectively). Optical penetration depth is given by:

$$\delta = [3\mu_a(\mu_a + \mu_s')]^{-1/2} \qquad (1)$$

where μ_a=absorption coefficient and μ_s'=reduced scattering coefficient [18]. At 488 nm, δ=3.24 mm (μ_a=0.026 mm^{-1}, μ_s'=1.191 mm^{-1}); at 670 nm, δ=5.40 mm (μ_a=.020 mm^{-1}, μ_s'=0.552 mm^{-1}); at 808 nm, δ=7.29 mm (μ_a=0.015 mm^{-1}, μ_s'= 0.403 mm^{-1}); and at 1.32 µm, δ=3.18 mm (μ_a=0.093 mm^{-1}, μ_s'=.262 mm^{-1}) [19].

The peak position of $\Delta I(t)/I_0$ may be related to the volume of cartilage probed by the lasers. As probe laser light was aimed at the back surface of laser irradiated cartilage specimens (relative to the Nd:YAG laser), the deeper penetrating probe wavelengths will interact with the more superficial tissue layers (relative to the laser heated surface) that are undergoing photothermal modification. The shallower penetrating wavelengths probe deeper tissue layers (again relative to the laser heated surface) and hence the phase transformation will require a longer laser irradiation interval or additional time for heat conduction to occur. It is expected, then, that τ_l decreases with increasing probe laser penetration depth ($\delta_{488} < \delta_{670} < \delta_{808}$). Our observation that τ_l increases with probe laser wavelength (**Figures 4a-c**) does not fit these expectations, and may be explained by considering the geometrical structure of the specimens.

In this study we observed that τ_l increases with probe laser wavelength in both thick and thin specimens. Since no appreciable thermal gradient exists in thin specimens [23], uniform heating in the axial direction occurs. Further, axial fluence distribution in thin specimens is nearly uniform for the three probe laser wavelengths used. If observed wavelength dependent changes in τ_l were due primarily to the light distribution of the probe laser, then τ_l would be the same for each wavelength. Exactly the opposite was observed.

Therefore, we postulate that the observed wavelength dependence of τ_l may be due to changes in the fine structure of the cartilage tissue matrix or macromolecules. Alterations in fine structure responsible for the observed light scattering

signals may involve dehydration or, as mentioned above, changes in protein conformation due to loss of tertiary structure in proteoglycans and/or collagen

In future studies, we plan to heat cartilage in saline within a Rose chamber and measure the wavelength dependence of diffuse scattering as a function of temperature [12]. By heating in saline, dehydration effects are eliminated. Laser irradiation of thick cartilage specimens results in non-uniform heating of the tissue [20], causing asynchronous stress relaxation in different regions of the tissue. Slow heating of cartilage within a Rose chamber will allow the creation of uniform temperature profiles independent of specimen thickness and provide another method to determine whether the trend in τ_l is due to changes in cartilage fine structure or due to effects of light transport and heat distribution and dehydration.

It may also be worthwhile to measure the temperature dependence of diffusely scattered light in cartilage specimens under conditions where either the proteoglycans or collagen has been selectively modified. For example, if the cartilage specimens remain at room temperature for 24 hours before conducting the experiment, then proteoglycan degradation will occur. In contrast, collagen molecules are extremely stable with half-lives several orders of magnitude longer than the proteoglycans. Hence, changes in light scattering during the laser heating of this degraded tissue will be more sensitive to alterations in intact proteoglycan structure. Alternately, highly specific enzymes may be used to selectively digest various matrix components [20].

The measurement of integrated backscattered light alone, though, cannot provide any direct information on the structural changes causing the observed optical properties. Techniques such as electron or atomic force microcopy [21] may provide more detailed information on the subtle alterations in tissue molecular structure that occur during reshaping.

It is important to characterize the wavelength dependence of optical properties before they can be used for feedback control during laser reshaping. For example, if the peak in $\Delta I(t)/I_o$ is used to identify a phase transition and subsequently terminate laser heating, then slight differences in laser exposure due to wavelength dependent differences in τ_l may critically impact chondrocyte viability [24]. Inasmuch as temperature dependent diffuse reflectance during laser heating is wavelength dependent, selection of probe laser wavelength is critical with respect to the design of a feedback controlled laser system for reshaping cartilage in patients.

5.0 CONCLUSION

Characterizing the wavelength dependence of optical properties such as diffuse reflectance may lead to optimization of feedback control techniques during laser cartilage reshaping as well as provide insight into the molecular basis of this process. The temperature at which peak optical scattering occurred was observed in increasing order of probe laser wavelength. These findings suggest that the changes in fine structure that occur during heating are on the order of the wavelength of the probe beams and that wavelength is an important factor when using optical scattering for feedback purposes during clinical reshaping of cartilage. Further studies are needed to determine the specific nature of these structural alterations.

ACKNOWLEDGEMENTS

REFERENCES

1.   D. Comper, "Physiochemical aspects of cartilage extracellular matrix," in *Cartilage: Molecular Aspects*. B. Hall, S. Newman, Eds. Boca Raton: CRC Press, 1991.

2.   L. Stockwell, *Biology of Cartilage Cells*, p. 32, Cambridge, Great Britain, 1979.

3. E. N. Sobol, M. S., Kitiai, N. Jones, A. P. Sviridov, T. Milner, and B. J. F. Wong, "Heating and Structural Alterations in Cartilage Under Laser Radiation," *IEEE J. of Selected Topics Quantum Electronics*. **35(4)**, pp. 532-539, 1999.

4. C. Helidonis, E. N. Sobol, G. Kavvalos, et al., "Laser Shaping of Composite Cartilage Grafts," *American Journal of Otolaryngology*. **14**, pp.410-412, 1993.

5. A. Helidonis, E. N. Sobol, G. Velegrakis, and J. Bizakis, "Shaping of Nasal Septal Cartilage with the Carbon Dioxide Laser—a Preliminary Report of an Experimental Study," *Lasers in Medical Science*. **9**, pp. 51-54, 1994.

6. E. N. Sobol, V. Bagratashvili, A. Omel'chenko, et al., "Laser Shaping of Cartilage," *Proceedings of SPIE*. **9**, pp. 51-54, 1994.

7. E. N. Sobol, V. Bagratashvili, A. Sviridov, et al., "Cartilage Reshaping with Holmium Laser," *Proceedings of SPIE*. **2623**, pp. 556-559, 1996.

8. E. N. Sobol, V. Bagratashvili, A. Sviridov, et al., "Phenomenon of Cartilage Shaping using Moderate Heating and its Application in Otorhinolaryngology," *Proccedings of SPIE*. **2623**, pp. 560-564, 1996.

9. E. N. Sobol, A. Sviridov, V. Bagratashvili, et al., "Stress Relaxation and Cartilage Shaping under Laser Radiation," *Proceedings of SPIE*. **2681**, pp. 358-363.

10. B. J. F. Wong, T. E. Milner, B. Anvari, et al., "Measurement of radiometric surface temperature and integrated backscattered light intensity during feedback controlled laser-assisted cartilage reshaping," *Lasers in Medical Science*. **13**, pp. 66-72, 1998.

11. B. J. F. Wong, T. E. Milner, H. K. Kim, J. S. Nelson, and E. N. Sobol, "Stress relaxation of porcine septal cartilage during Nd:YAG ($\lambda= 1.32$ μm) Laser Irradiation: Mechanical, Optical, and Thermal Responses," *J. of Biomedical Optics*. **3(4)**, pp. 1-6, 1998.

12. B. J. F. Wong, T. E. Milner, H. K. Kim, et al., "Characterization of Temperature Dependent Biophysical Properties During Laser Mediated Cartilage Reshaping," *IEEE J. of Selected Topics Quantum Electronics*. **5**, pp. 1095-1102, 1999.

13. T. C. Kuo, H. K. Kim, T. E. Milner, J. S. Nelson, E. N. Sobol, and B. J. F. Wong, " The effect of partial denaturation on Nd:YAG laser mediated stress relaxation of porcine septal cartilage," *Proceedings of SPIE*. **3914**, pp.75-85, 2000.

14. E. N. Sobol, A. P. Sviridov, A. I. Omel'chencko, V. Bagratashvili, M. S. Kitai, and V. K. Popv, "Mechanism of laser-induced stress relaxation in cartilage," *Proceedings of SPIE*. **2975**, pp. 310-315, 1997.

15. B. J. F. Wong, T. E. Milner, A. Harrington, J. Ro, X. Dao, E. N. Sobol, J. S. Nelson, "Feedback Controlled Cartilage Reshaping," *Arch Facial Plast Surg*. **1**, pp. 282-287, 1999.

16. E. N. Sobol, *Phase Transformations and Ablation in Laser-treated Solids*, pp. 316-322, Wiley, New York, 1995.

17. J. C. Allain, M. Le Lous, L. Cohen-Solal, S. Bazin, and P. Maroteaux, "Isometric tensions developed during the hydrothermal swelling of rat skin," *Connect. Tissue Res*. **7**, pp. 127-133, 1980.

18. S. J. Madsen, E. A. Chu, B. J. F. Wong, "The Optical Properties of Nasal Cartilage," *IEEE J. of Selected Topics Quantum Electronics*. **5 (4)**, pp. 1127-1133, 1999.

19. J. Youn, S. A. Telenkov, K. Kim, N. C. Bhavaraju, B. J. F. Wong, and J. W. Valvano, and T. E. Milner, "Optical and Thermal Properties of Nasal Septal Cartilage," *Lasers in Surgery and Medicine*. **27**, 2000.

20. A. M. Karamzadeh, A. Rasouli, B. S. Tanenbaum, T. E. Milner, J. S. Nelson, and B. J. F. Wong, "Laser-Mediated Cartilage Reshaping with Feedback-Controlled Cryogen Spray Cooling: Biophysical Properties and Viability," *Lasers in Surgery and Medicine.* **28**, pp. 1-10, 2001.

21. E. Sobol, A. Omel'chenko, M. Mertig, and W. Pompe, "Scanning Force Microscopy of the Fine Structure of Cartilage Irradiated with CO_2 Laser," *Lasers in Medical Science.* **15**, pp. 15-23, 2000.

22. C. Chew, B. J. F. Wong, T. E. Milner, H. Kim, A. Gomez, S. Nelson, and E. Sobol, "Feedback controlled cartilage reshaping with Nd:YAG laser: effect of pH variation," *Proceedings of SPIE.* **3245**, pp. 206-216.

23. A. M. Karamzadeh, B. J. F. Wong, X. Dao, B. S. Tanenbaum, T. E. Milner, J. S. Nelson, "Temperature Distributions in Nd:YAG (λ=1.32µm) Laser-Irradiated Cartilage Grafts Accompanied by Cryogen Spray Cooling," *Proceedings of SPIE.* **3601**, pp. 422-433.

24. B. J. F. Wong, T. E. Milner, H. K. Kim, K. Chao, C. Sun, E. Sobol, and J. S. Nelson, "Proteoglycan Synthesis in Porcine Nasal Cartilage Grafts Following Nd:YAG (λ=1.32 µm) Laser Mediated Reshaping," *Photochemistry and Photobiology.* **71 (2)**, pp 218-224, 2000.

The effect of osmolarity on shape retention following laser-mediated cartilage reshaping

Amir M. Karamzadeh[1], Darren S Gray[2], Joey A Kimball[3], and Brian JF Wong[1,4,5*]

[1]Beckman Laser Institute and Medical Clinic, University of California Irvine, 1002 Health Sciences Road East, Irvine, CA 92612

[2]Department of Biomedical Engineering, The Johns Hopkins University School of Medicine, 720 Rutland Avenue,Baltimore, MD, 21205

[3]Departments of Physics and Engineering, Harvey Mudd College, Claremont, CA

[4]Department of Otolaryngology- Head and Neck Surgery, University of California Irvine, 101 The City Drive, Orange, CA 92668

[5] The Whitaker Center for Biomedical Engineering, Samueli School of Engineering University of California Irvine, Irvine, CA 92612

ABSTRACT

Laser reshaping of mechanically deformed cartilage specimens accelerates stress relaxation and results in permanent shape change. The mechanism of laser-mediated cartilage reshaping is still unknown, but clearly depends upon the complex molecular interactions between the physio-chemical environment and matrix proteins (collagen, and proteoglycans). It is well known in articular tissues that the mechanical properties of cartilage are sensitive to changes in tissue pH and osmolarity. The objective of this study was to determine the effect of osmolarity on shape change during laser reshaping in morphologic cartilage tissues. Porcine nasal septal cartilage specimens were cut (20 x 5 x 1.5 mm) and immersed in osmotically graded NaCl (0.2NS, 0.8NS, 1.0NS, 1.2NS and 5NS) or Phosphate buffered (0.2NS, 0.9NS, 1.0NS, 1.1NS, and 5NS) solutions for 12 hours to establish equilibrium. Then, specimens were bent into semicircular shapes, secured with clamps, and irradiated with an Nd:YAG laser (λ= 1320nm, 5W, 15 secs, 5mm spot size) along the region of maximum curvature. Resultant bend angle was measured. Shape retention was calculated by comparing resultant curvature with pre-irradiation measurements. Non-irradiated, untreated (negative controls) cartilage retained less than 46% of the original bend. There was no difference in shape retention with respect to varying osmolarity (changed tissue water content) in either group. Resultant bend angles varied from 84° to 194° corresponding to shape retention varying from 42% to 72% in specimens which were immersed in either NaCl or Phosphate buffered solutions. While laser heating of deformed specimens does result in significant reshaping, the alterations in osmolarity do not seem to effect this process significantly over the range of values evaluated in this study.

KEYWORDS: Osmolarity, Mechanical Properties, Cartilage, Laser-Mediated Cartilage Reshaping, Nd:YAG Laser, Shape Retention

1.0 INTRODUCTION

1.1 Laser Mediated Cartilage Reshaping

Reshaping native cartilage tissue into new stable conformations remains a challenge for reconstructive surgeons. The clinical guidelines for preparing autogenous cartilage grafts for nasal reconstructive and aesthetic surgery were defined by Gilles (1920)[1], Gibson (1958)[2], and Fry (1967)[3-5]. The standard surgical techniques have not changed in more than 30 years.

A novel method, introduced by Sobol in 1993, uses laser irradiation to permanently reshape cartilage by accelerating mechanical stress relaxation[6-7]. An increasing amount of experimental data continues to support laser-mediated cartilage reshaping as a more effective method of altering cartilage graft morphology in situ compared with conventional surgical techniques[8-14].

1.2 Osmolarity

The mechanism of laser-mediated cartilage reshaping is still unknown, but clearly depends upon the complex molecular interactions between the physio-chemical environment and matrix proteins (collagen, and proteoglycans). It is well known in articular tissues that the mechanical properties of cartilage are sensitive to changes in tissue pH and osmolarity [15-17].

1.3 Objectives

Little is known of the effect of altering the electrochemical environment of cartilage on the outcome of laser-mediated reshaping. The objective of this study is to determine whether manipulating the tissue osmolarity will serve to enhance the laser reshaping process.

2.0 MATERIALS AND METHODS

2.1 Specimen Preparation

Porcine nasal septal cartilage was removed from the crania of domestic pigs obtained from a local packing house approximately 48 hours after euthanasia as previously described[8] . While in storage at the packinghouse, specimens were maintained in a commercial refrigerator at 4° C. Mucosa and perichondrial tissues were removed from the underlying cartilage that was then cut into slabs (20 x 5 x 1.5 mm) using a custom built guillotine microtome. Samples where then immersed in osmotically graded NaCl (0.2NS, 0.8NS, 1.0NS, 1.2NS and 5NS) or Phosphate buffered (0.2NS, 0.9NS, 1.0NS, 1.1NS, and 5NS) solutions for 12 hours (at 4°C) to establish equilibrium.

2.2 Laser Irradiation and Reshaping

Prior to laser reshaping, specimens were bent into a semicircular shape and secured with a jig composed of two plastic clamps (**Figure 1**), and mounted on a single axis micropositioning stage for alignment with the laser.
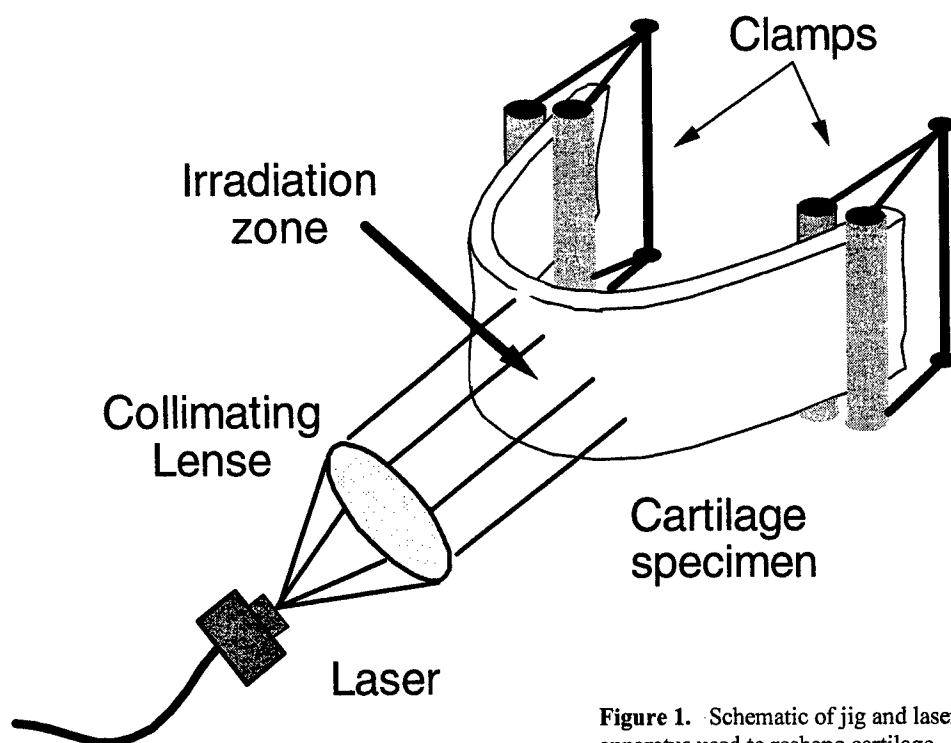
Figure 1. Schematic of jig and laser apparatus used to reshape cartilage

The distance (L_j) between the two ends of the specimen was measured with a micrometer (**Figure 2**). Next, specimens were irradiated for 15 s with light from a Nd:YAG laser (λ=1.32 μm, 50 Hz PPR, 5W, 6 mm spot diameter, New Star Lasers, Auburn, CA) delivered via a multimode silica optical fiber terminated with an anti-reflection coated collimating lens. These laser parameters are similar to those used in previous investigations by our group[11-13]. The laser beam was directed at the center of the specimen along the lines of maximum force and deformation (**Figure 1**). Immediately following laser heating, the specimen and the securing clamps were immersed in saline solution at ambient temperatures for fifteen minutes. Lastly, clamps were released, and the distance between the two ends of the specimen was measured. Control specimens underwent identical bending procedures, omitting laser irradiation thus allowing estimation of the isolated effect of mechanical deformation on shape change.

2.3 Cartilage Deformation Analysis/ Bend Angle Measurement

The specimen deformation (cartilage bend angle) was calculated using a model which assumed that each specimen was reshaped into an arc representing a segment of a circle. For example, the bend angles of a semicircle and complete circle would be a 180° and 360° respectively. Using this model, the distance between the ends of a cartilage slab is equal to the length of the chord joining the ends of aforementioned arc (**Figure 2**). Where:

$$L = \frac{2 \bullet L_i \bullet \sin(\theta/2)}{\theta}$$

L is the distance between the ends of the bent sample, L_i is the initial length of the sample before clamping, and θ is the bend angle in radians. L was measured immediately prior to laser irradiation (while bent and secured with the clamps) and immediately after laser irradiation and rehydration (see measurement setup **Figure 2**).
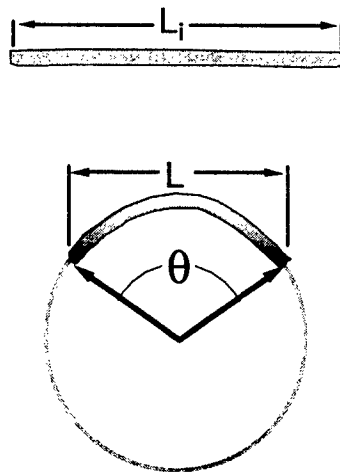
Figure 2. Diagram of specimen measurements and bend angle

The bend angle corresponding to each set of measurements was numerically determined using the above equation implemented in Excel (Microsoft Corporation, Redmond, WA).

The percentage of shape retention was determined by comparing the bend angle still secured to the clamps with the bend angle following release. For example, if a sample was bent and secured at a bend angle of 180° and then after heating and clamp release relaxed to 90°, its percent shape retention would be as 50%. Two-sample t-tests with unequal variances (Welsh approximation to the Behrens Fisher Distribution) were used to determine significance levels for differences between measurements.

3.0 RESULTS

Resultant bend angles varied from 84° to 194° corresponding to shape retention varying from 42% to 72% in specimens which were immersed in either NaCl or Phosphate buffered solutions (**Figure 3**). There was no significant difference in reshaping outcome between osmotically graded NaCl and Phosphate buffered solutions or between the different osmotic solutions within each group (**Figure 3**).
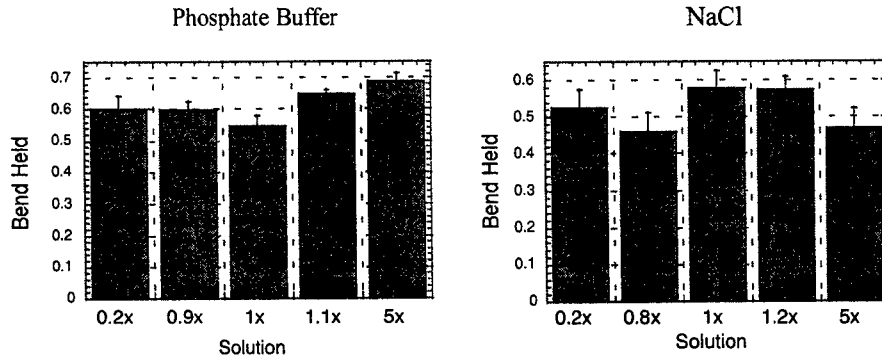
Figure 3. Bar Graphs illustrating the relationship between osmotic concentration of the bathing solution and percent shape (bend) following laser irradiation.

Non-irradiated, untreated (negative controls) cartilage retained less than 46% of the original bend. **Figure 4** illustrates an example of a control specimen before and after laser mediated reshaping.
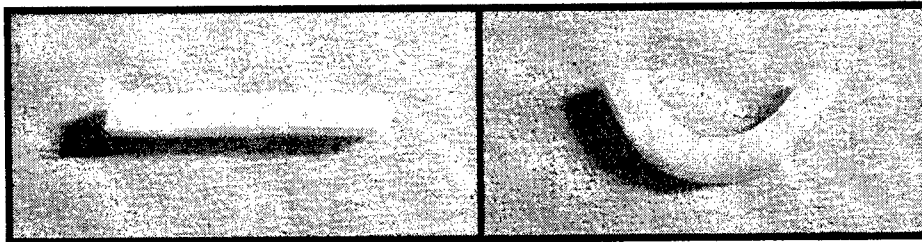
Figure 4. Photograph of a cartilage specimen before and after laser reshaping

4.0 DISCUSSION

Cartilage is a dense connective tissue, best described as a gel of non-diffusible macromolecules reinforced by collagen fibers. It is composed of 60-80% water and a small portion of cells (chondrocytes) within the extracellular matrix (ECM). The proteoglycan (glycosaminoglycan) portion of the ECM contains a high density of fixed negative charges. Because cartilage is avascular, it depends on the diffusive transport of water, ions, and nutrients for both function and survival. In accordance with the Donnan equilibrium theory, the distribution of ions between the cartilage and the bathing media will never be equal. In order to maintain electrical neutrality, the osmolarity of the fluids in the cartilage matrix will be greater than in the surrounding media. The combination of the excess mobile ions and immobile macromolecules gives rise to osmotic pressure. Variations of the ionic concentration of the equilibrating media alters the Donnan contribution (mobile ions) to the osmotic pressure.

The osmotic pressure of the bathing environment has been shown to alter the mechanical properties of articular cartilage. Creep indentation tests performed by Bar (1926) and Hirsch (1944) indicate that articular cartilage acts as a visicoelastic solid[15]. In these early experiments, application of a step load through a rigid indenter resulted in a deformation (indention) of the cartilage. This initial shape modification was followed by a time dependent creep to an asymptotic value of deformation. Interestingly, after removal of the test load, the cartilage retained its deformed state. Later, Elmore demonstrated that the incomplete deformational recovery observed by Bar and Hirsch was an artifact due to the dehydrational effects of testing the cartilage in air[15]. When these experiments were repeated in Hanks balanced salt solution (HBSS), Elmore et al obtained complete recovery after removal of the load. Further, this study indicated that the magnitude of indentation and deformation was strongly dependent on the ionic concentration of the test environment. Hypertonic solutions increased deformation, while hypotonic solutions significantly decreased the deformation. In a series of experiments designed to appreciate the relationship between the ionic concentration of the environment and the mechanical response of rabbit articular cartilage, Pearson and Black (1979), reported that a functional relationship exists between shear moduli, retardation time spectra and ionic concentration[15]. Specifically, hypotonic solutions significantly increased the shear moduli. These studies were further supported by Hall (1983) which also found a inverse relationship between shear modulus of articular cartilage and ionic strength of the bathing solution[16].

Under physiologic conditions, mechanical resistance to cartilage reshaping is due to the large molecular forces between water and proteoglycan molecules. In laser laser-mediated cartilage reshaping shape change is likely dependent on a temperature sensitive bound-to-free water phase transition. Under moderate laser heating, internal stress relaxation occurs when water bound to the proteoglycans is liberated. If this process occurs without damaging the matrix macromolecules then stable shape change occurs.

By changing the osmotic pressure in the surrounding media, the water content of the tissue should be altered. The objective of this study was to assess whether changes in tissue water content will have an effect on reshaping outcome following laser irradiation. The results illustrated in **Figure 3** fail to show an association between osmotic variation and shape retention. One would expect that exposure to hypertonic environment would drive water out of the tissue—facilitating the bound-to-free water phase transition required to establish stable reshaping. The opposite would be expected when exposed to hypotonic solutions. It is possible that the matrix components may have undergone some degree of biologic degradation, though the half-lives of the constitutive matrix proteins may be as long as several days. Borghetti (1995) and coworkers describe the adaptive chondrocyte response to osmotic stress[17]. They found that in culture, chondrocytes adapt quickly to osmotic stress with respect to maintaining intact osmoregulatory systems, protein synthesis, amino acid transport and proliferation rates. Conversely, at the highest osmolarity (0.58osM) there were detrimental biochemical and morphological effects observed. Specifically, at these higher ionic conditions, long-term exposure resulted in loss of cellular phenotypic stability demonstrated by chondrocytes taking on a fibroblast-like shape.

The assessment of shape change or deformation in cartilage using closed-form analytic or numerical solutions is difficult and has prompted the use of simplified techniques employed in this study and others. For example, Adams et al photographed rib cartilage specimens over time and assessed warping by measuring "longitudinal angle" on anterior and lateral views[18]. Their angular measurement was an estimate of the native shape change that occurs when rib cartilage is cut and interlocked forces relax. Gunter estimated warping my simply measuring the angular deviation of one end of the specimen from a line tangent to the other end[19] . Murakami et al indirectly measured curvature in both native and cut porcine ears by using an analog strain gauge to estimate the force required to straighten a specimen[20] . Harris estimated warping by measuring the angle produced by drawing two tangent lines to the end of rectangular human rib cartilages[21].

In this study, photothermal heating was concentrated in the central region of the specimen where deformation and force are greatest, and, as expected, this is where maximum shape change was observed. To simplify the analysis, we modeled the cartilage shape change using a circular model, which we believe is a reasonable method to correlate an easily determined linear measurement with the actual deformation. Shape change after laser heating could be compared to either the shape of the specimen while it is secured in the jig just prior to heating or the original flat shape of the specimen. Our analysis compared the secured shape prior to irradiation to the final shape attained after heating because our apparatus created a variable initial bending angle (188° to 229°). Calculations based on percent shape retention normalizes for this variation.

5.0 CONCLUSIONS

This is the first investigation that quantitatively examined the effects of alterated osmotic environments on shape change after laser mediated cartilage reshaping. While laser heating of deformed specimens does result in significant reshaping, the alterations in osmolarity do not seem to significantly effect (enhance) this process over the range of values evaluated in this study. Use of this technology in surgery will require continued refinements of the physical parameters of the laser delivery systems as well as the biological environment of the cartilage grafts. All the experiments that showed the effects of altered osmotic pressure on mechanical properties were done using *articular* cartilage. In this study, porcine septal cartilage was evaluated for shape change following laser irradiation. Future study is required to assess the effects of ionic strength on the mechanical properties of septal cartilage as well as other donor sites such as the auricle, trachea, and rib. These studies may enhance our understanding of the biomechanics of cartilage and no doubt enhance this technology before clinical implementation.

ACKNOWLEDGEMENTS

REFERENCES

1. Gillies HD, *Plastic Surgery of the Face*, Oxford University Press, London, 1920

2. Gibson T, Davis W, "The distortion of autogenous cartilage grafts: its cause and prevention," *British Journal of Plastic Surgery,* **10**, pp 257-74, 1958

3. Fry H, "Cartilage and cartilage grafts: the basic properties of the tissue and the components responsible for them," *Plastic and Reconstructive Surgery*, **40**, pp 426-439,1967

4. Fry H, Robertson W, "Interlocked Stresses in cartilage," *Nature*, **251**, pp 53-54, 1967.

5. Fry H, "Interlocked stresses in human nasal septal cartilage," *British Journal of Plastic Surgery*,**19**, pp 276-278, 1966.

6. Helidonis E, Sobol EN, Kavvalos G, et al, *"Laser Shaping of Composite Cartilage Grafts,"* *American Journal of Otolaryngology,*14, pp 410-412, 1993.

7. Sobol EN, Bagratashvili VV, Omel'chenko A, et al, *"Laser Shaping of Cartilage,"* Proceedings *SPIE*, **2128,** pp 43-49, 1994.

8. Wong BJF, Milner TE, Kim HK, Nelson JS, Sobol EN, "Stress relaxation of porcine septal cartilage during Nd:YAG (λ = 1.32 mm) laser irradiation: mechanical, optical, and thermal responses," *Journal of Biomedical Optics,* **3**, 409-14, 1998.

11. Wong BJF, Milner TE, Harrington A, et al, *"Feedback Controlled Laser Mediated Cartilage Reshaping,"* Archives of Facial Plastic Surgery, **1**, pp 282-287, 1999.

12. Karamzadeh AM, Rasouli A, Tanenbaum BS, Milner TE, Nelson JS, Wong BJF, *Laser-Mediated Cartlage Reshaping With Feedback-Controlled Cryogen Spray Cooling: Biophysical Properties And Viability*, Lasers in Surgery and Medicine, 2000;in press.

13. Wong BJF, Milner TE, Kim HK, et al, "Critical Temperature Transitions in Laser Mediated Cartilage Reshaping. Proceedings," Proceedings SPIE, **3245**, pp 161-172, 1998.

14. Wong BJF, Milner TE, Anvari B, et al, *"Measurement of radiometric surface temperature and integrated back-scattered light intensity during feedback controlled laser-assisted cartilage reshaping.,"* Lasers in Medical Science, **13**, pp 66-72, 1998.

15. Parsons JR, Black J, *"Mechanical behaavior of articular caritlage: quantitative changes with alteration of ionic environment. Journal of Biomechanics,"* **12**, pp 765-773, 1979

16. Myers RM, Mow VC, *Biomechanics of cartilage and its response to biomechanical stimuli. In: Hall B, ed. Cartilage, structure, function, and biochemistry* p 313-37: v1, New York: Academic Press, 1983.

17. Borghetti P, Della Salda L, De Angelis E, et al, *"Adaptive cellular response to osmotic stress in pig articular chondrocytes,"* Tissue Cell, **2**, pp 173-83, 1995

18. Adams WPJ, Rohrich RJ, Gunter JP, Clark CP, Robinson JBJ, *"The rate of warping in irradiated and nonirradiated homograft rib cartilage: a controlled comparison and clinical implications,"* Plastic and Reconstructive Surgery, **103**, 265-70, 1999.

19.   Gunter JP, Clark CP, Friedman RM, *"Internal stabilization of autogenous rib cartilage grafts in rhinoplasty: a barrier to cartilage warping,"* Plastic and Reconstructive Surgery,**100**, pp 161-9, 1997.

20.   Murakami WT, Wong LW, Davidson TM, *"Applications of the biomechanical behavior of cartilage to nasal septoplastic surgery,"* Laryngoscope, **92**, pp 300-9, 1982.

21.   Harris S, Pan Y, Peterson R, Stal S, Spira M, *"Cartilage warping: an experimental model,"* Plastic and Reconstructive Surgery, **92**, pp 912-5, 1993.

Histology of Porcine Nasal Cartilage Grafts Following Nd:YAG (1320 nm) Laser Mediated Reshaping: Effects of Sequential Irradiation

Hong K. Kim, B.S[a], Brian J.F. Wong, M.D.[b], Hilary P.Benton, Ph.D.[c], Lih-Huei L. Liaw, M.S.[a], J. Stuart Nelson, M.D., Ph.D.[a], and Thomas E. Milner, Ph.D.[d]

[a]The Beckman Laser Institute and Medical Clinic, University of California Irvine,
[b]University of California Irvine Medical Center, Department of Otolaryngology - Head and Neck Surgery and Whitaker Center for Biomedical Engineering, University of California Irvine
[c]Department of Anatomy, Physiology, and Cell Biology, School of Veterinary Medicine, University of California Davis
[d]Biomedical Engineering Program, Department of Electrical and Computer Engineering, University of Texas at Austin

Abstract

Mechanically deformed morphologic cartilage grafts undergo temperature dependent stress relaxation during sustained laser irradiation resulting in stable shape changes. In this study, porcine nasal septal cartilage specimens were evaluated histologically following laser mediated reshaping using H&E. Cartilage specimens were irradiated with light emitted from a Nd:YAG laser (25 W/cm2, l=1.32 mm) while recording simultaneously radiometric surface temperature, internal stress, and backscattered light intensity from a probe laser. Each specimen received one, two, or three sequential laser exposures. The duration of each exposure was determined from real-time measurements of characteristic changes in backscattered light intensity that correlate with accelerated stress relaxation. A five-minute time interval between each laser exposures allowed the cartilage specimen to return to thermal equilibrium. Specimens were then fixed in formalin, serially dehydrated in ethanol, embedded in paraffin, and sectioned with a microtome for histologic examination using light microscopy. Large variation in native tissue histology was observed among individual tissue samples, and vascular were identified in several specimens. Large lacunae with shrunken chondrocytes were identified along with cells with pyknotic nuclei, although these histologic observations did not correlate with the degree of laser exposure. These observations are discussed.

Keywords: cartilage, tissue reshaping, Nd:YAG, histology, stress relaxation, porcine

Introduction

Cartilage specimens mechanically deformed under a constant load, undergo accelerated stress relaxation during laser heating resulting in plasticity and sustained shape change (Figure 1). Since cartilage is a composite amorphous polymeric material, its heating results in a phase transformation within the tissue matrix governed by heat and mass transfer processes. Cartilage
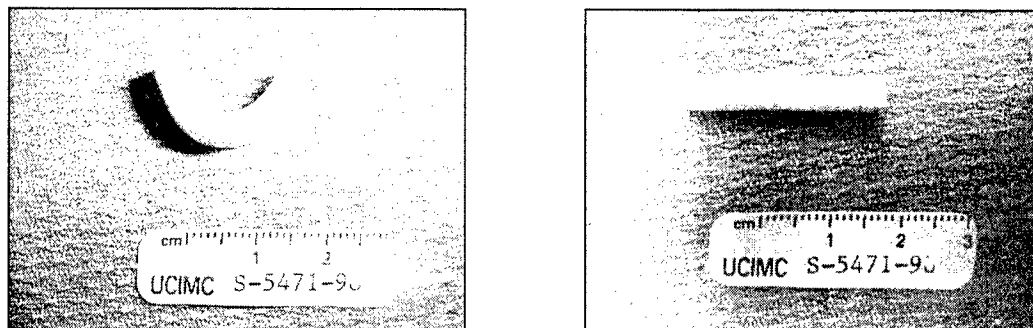
Figure 1: Porcine nasal septal cartilage after reshaping

undergoes the same temperature dependent phase transformations (melts, crystallization, glass transition etc.) as those that occur in synthetic polymers. Since laser reshaping can be performed using fiber optic delivery systems and minimally

Surface temperature

i

ii

Internal stress

iii

Back scattered probe laser light

↑ **Laser on**   ↑ **Laser off**

Figure 2: Biophysical changes in Cartilage during laser irradiation

invasive techniques, *laser mediated cartilage reshaping* has the potential to broadly change the practice of facial plastic surgery. While other heat sources can reshape cartilage, the principal advantages of using laser radiation for the generation of thermal energy are 1) minimization of cellular injury through the precise control of both the space-time temperature distribution and time-dependent thermal denaturation kinetics, 2) exact spatial localization, and 3) simplicity of delivery systems.

Biophysical Changes in Cartilage During Laser Heating

Figure 2 illustrates Laser-Mediated Cartilage Reshaping and accompanying time-dependent changes in easily measured physical properties. A flat cartilage specimen (**a**) is held in a reshaping jig (**b**) during Nd:YAG laser irradiation to create a new curved shape (**c**) while surface temperature (**i**), internal stress (**ii**), and backscattered HeNe laser light (*diffuse reflectance*) (**iii**) are recorded. When surface temperature reaches approximately 60-70oC (arrow) a change in the slope of the temperature curve is observed suggesting a change in tissue thermal properties. With the onset of laser irradiation, internal stress initially increases, and then at 65oC, internal stress begins to rapidly decrease (large arrow) as reshaping begins (**ii**). Alterations in measured backscattered light (**iii**) from a probe HeNe laser mirror corresponding changes in internal stress.

Objectives

The purpose of this study was to determine the effect of sequential Nd:YAG laser (l=1.32 mm) irradiation on porcine nasal septal cartilage by recording surface temperature, internal stress, and diffuse reflectance and examining specimens using light microscopy. Laser dosimetry is similar to that used in several previous laser reshaping studies.

Overview of Experiment (Figure 3)

The nasal septal cartilage was extracted from the crania of freshly sacrificed domestic pigs (100 kg) and cut into 25 x 10 x 2 mm slabs). Cartilage specimens secured to the experimental apparatus (**Figure 4**) and irradiated with light emitted from an Nd:YAG laser (25 W/cm2) while radiometric surface temperature, internal stress, and backscattered light intensity from a probe laser were simultaneously recorded.

A lock-in detection technique was required to measure the very small changes in diffuse reflectance. Each specimen received one, two, or three sequential laser exposures. The duration of each exposure was determined from real-time measurements of characteristic changes in backscattered light intensity that correlate with accelerated stress relaxation. A five-minute time interval between each laser exposures allowed the cartilage specimen to return to thermal equilibrium. Specimens were then fixed in formalin.

Septal cartilage

cartilage slab (25 x 10 x 2 mm)

Laser irradiation with measurement of:

Temperature
Stress
Diffuse reflectance

one laser exposure

two laser exposures

three laser exposures

Figure 3: Overview of Experiment

Figure 4: Experimental

Histologic Processing

After fixation, specimens were serially dehydrated using graded ethanol solutions and subsequently embedded in paraffin. The microsections were at 6 μm thickness were obtained, and then stained with hematoxylin and eosin, and examined microscopically at 4, 20, and 60 x. Images were recorded using a digital camera.
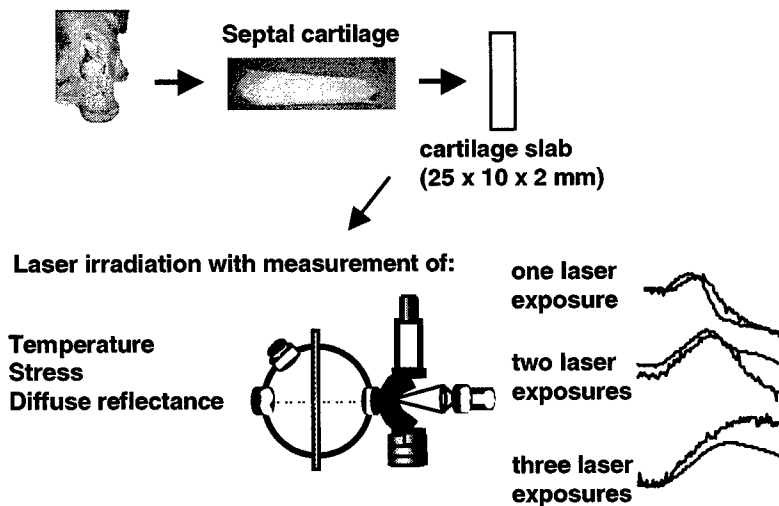
Physical Measurements

During laser-mediated cartilage reshaping, characteristic changes in optical and mechanical properties are observed which accompany the reshaping process. Two examples of these changes are illustrated in **Figures 5** and **6**. In each figure diffusely reflected light from a HeNe probe laser (lower set of curves) and internal stress (upper set of curves) were recorded during sequential laser exposures. The curves in each plot are color coded with **black**, ⋯ , and ⋯ corresponding to the waveforms obtained during the **first**, second, and third laser exposure respectively. The laser exposure time for each pulse is noted in the legend beneath each plot. For clarity, radiometric surface temperature measurements are not included in these figures; a representative series of heating curve is illustrated in **Figure 7**.

Figure 5

Figure 6

The time intervals from the onset of laser irradiation to observed peaks in diffuse reflectance and internal stress increased with each successive laser exposure (**Figure 5** and **6**). We designate the time from the onset of laser irradiation to the observation of a peak in diffuse reflectance τ_I. Similarly, the corresponding time interval for the observation of peak in internal stress is designated τ_σ. Because laser exposure was terminated when the peak in diffuse reflectance was observed on the lock-in amplifier signal monitor, laser irradiation terminated slightly after occurrence of the actual peaks in either diffuse reflectance or internal stress.

For the first and second laser exposures, peaks for diffuse reflectance and internal stress occurred synchronously ($\tau_I = \tau_\sigma$); following the third laser exposure, the peak for diffuse reflectance occurred just prior to peak internal stress. These are the most commonly observed findings, but several other patterns were observed which are illustrated in the accompanying plots.

Figure 7
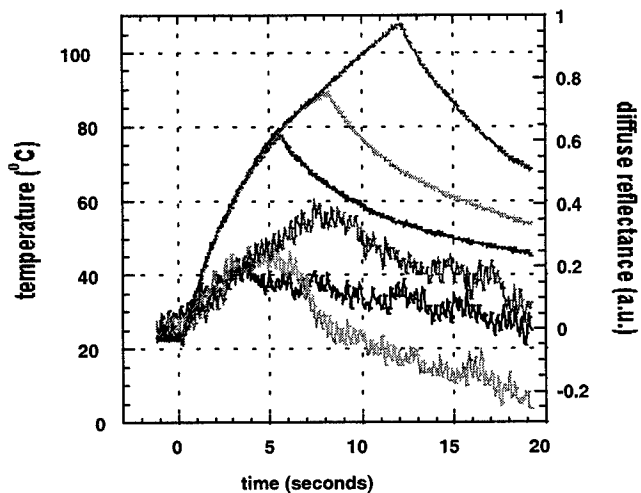
Figure 8
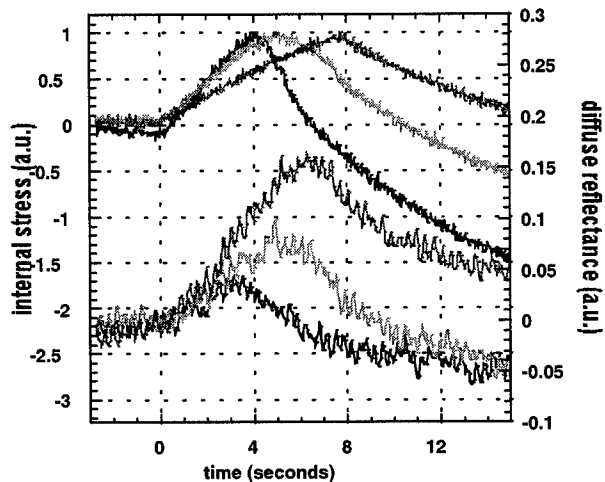
The most common observation following the third laser exposure is a sharp transition in internal stress resulting in a "tented" waveform shape. This sharp transition occurs precisely when laser irradiation is terminated (**Figure 8**). In native cartilage tissue, this "tenting" is most often observed after the third laser exposure where nearly half of the specimens exhibiting this pattern.
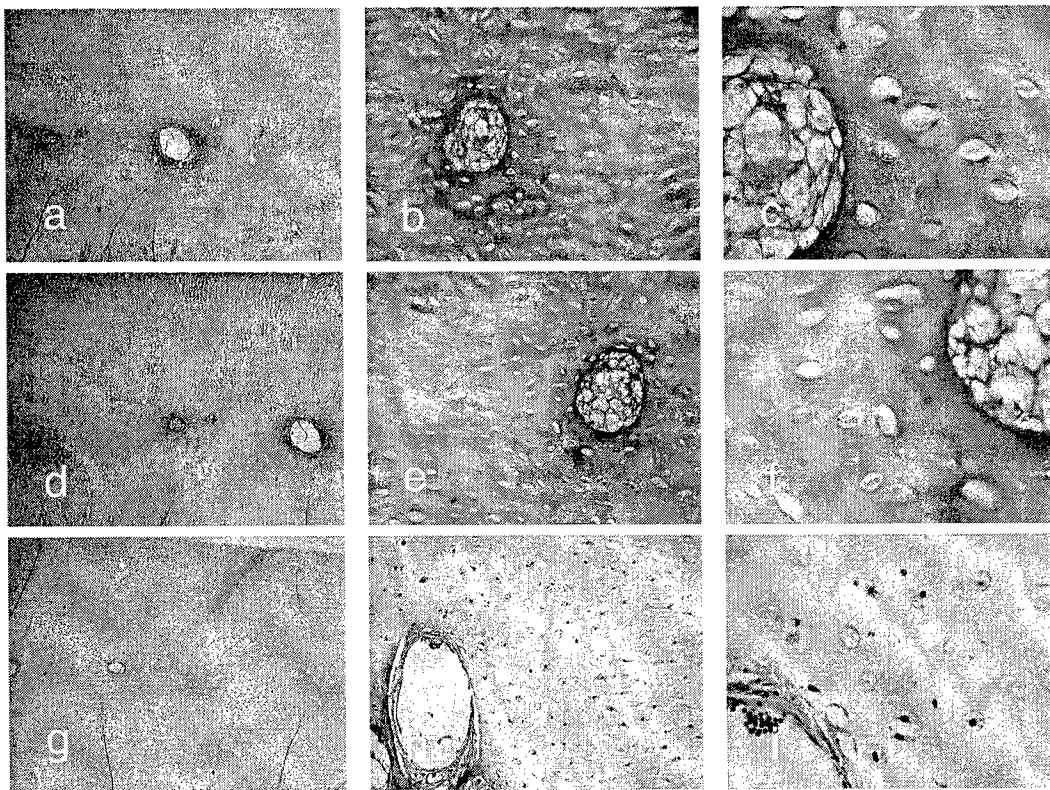
Figure 9: Control specimens at 4,20, 60 x
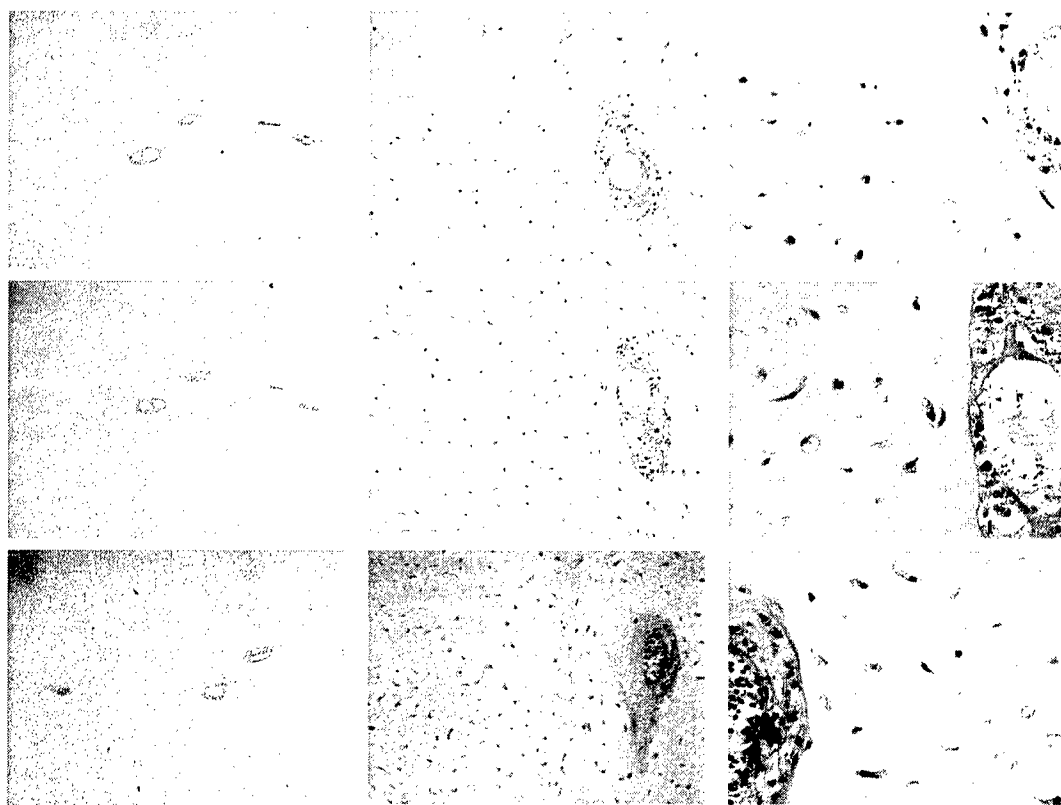
Figure 10: Laser irradiate specimens at 4,20, 60 x magnification

Histologic Findings

Large variation in native tissue histology was observed among individual tissue samples, and vascular were identified in several specimens. Large lacunae with shrunken chondrocytes were identified along with cells with pyknotic nuclei, although these histological observations did not correlate with the degree of laser exposure. **Figure 9** and **Figure 10** are montages of native (control) and irradiated cartilage specimens respectively. **Figures 10 a-c** are images at 4, 20, and 60 power magnification of specimens irradiated once with the laser (controls are in **Figure 9 a-c**). Similarly, **d-f** and **g-i** correspond to the two and three laser exposures, respectively.

Discussion

Physical Measurements

The prolongation in τ_I and τ_σ observed in these experiments may be partially explained by the differences in light distribution of the two lasers which we illustrate using a simple two-layer tissue model (**Figure 11**). The first laser exposure heats the most superficial layers of tissue, which undergo a phase transition that results in changes in diffuse reflectance and internal stress, which as noted the previous figures. In this simplified model, only the superficial layer undergoes thermal alteration and the deep layer is largely unmodified. A second laser exposure would again result in deposition of Nd:YAG laser light primarily in the superficial tissue layer, a region where the phase transition (e.g. shape change, stress relaxation) has already occurred. In order to heat the deeper layers to this critical temperature a longer laser exposure time is required.

With the second laser pulse, both τ_I and τ_σ are prolonged. This also occurs with a third laser pulse as well, though often diffuse reflectance and internal stress are "decoupled" as evidenced by observation of the "tenting" phenomenon. The "tenting" phenomenon is characterized by an increases internal stress during the laser pulse followed by and abrupt "cut-off" with termination of laser irradiation. After extensive heating (e.g. three laser pulses) in the two-layer model, both superficial and deep layers have been adequately heated to the critical temperature required to accelerate stress relaxation. No further stress relaxation occurs. We postulate, that the increase in internal stress during laser heating is likely due entirely to thermo elastic expansion. An alternative explanation for this observation is that thermal modification of the entire tissue specimen is not required to achieve adequate stress relaxation. As the cartilage is irradiated on its convex surface, irradiation of the superficial layers of cartilage may be enough to release interlocking forces: in essence creating a tissue effect analogous to

scoring of the cartilage on one surface which has been observed to cause warping of the cartilage towards the opposite surface.

Histology
This study was a preliminary investigation and the preparation quality in each specimen was highly variable. A significant shrinkage was observed in several samples (large lacunae and very sick looking cells pulled away from the surrounding matrix. Some cells almost appear pyknotic suggesting apoptosis. We did not observe any clear correlation with between these histological observations and degree of irradiation, or for that matter between experimental and control groups. This may be due to artifact introduced by a variable fixation process. Interestingly, blood vessels were observed in this cartilage specimen, which is not observed in humans or rodents. Future histologic investigations will standardize the fixation process and include metachromatic stains such as alcian blue or safranin O which would allow critical assessment of the matrix and hence proteoglyan loss. Hematoxylin and Eosin primarily assess the collagen components of the extracellular matrix.
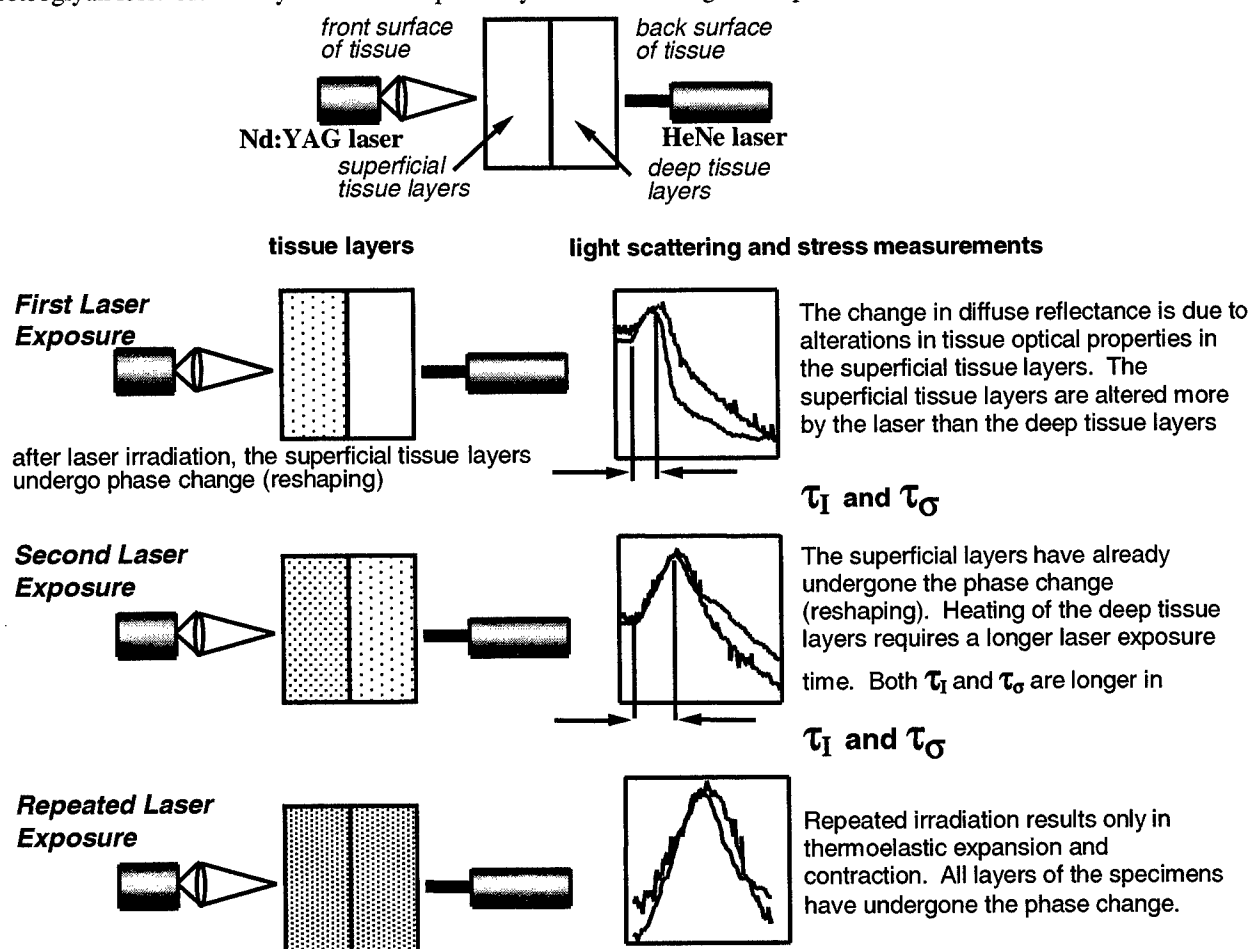
Figure 11: Heat transfer and light distribution in cartilage during reshaping

Conclusion

Thermal mediated non-ablative tissue modification is an emerging field of interest, particularly with the advent of low-cost laser and radiofrequency (RF) devices. Since heat alters protein conformation, it alters both the fine structure and bulk properties of the matrix that may also lead result in tissue remodeling. While industrial non-ablative laser applications are commonplace in semiconductor, alloy, ceramic, and polymer processing, lasers use in medicine predominantly has been to ablate and destroy tissue. Laser mediated cartilage reshaping is a new non-ablative laser application that changes tissue shape by creating subtle alterations in the matrix structures. This preliminary investigation focused on describing the histologic changes in laser irradiated cartilage tissue after reshaping.

Reference

1. Bagratashvili, VN; Sobol, EN; Sviridov, AP; Popov, VK; Omel'chenko, AI; Howdle, SM. **Thermal and diffusion processes in laser-induced stress relaxation and reshaping of cartilage.** Journal of Biomechanics, 1997 Aug, 30(8):813-7.

2. Helidonis E, Volitakis M, Naumidi I, Velegrakis G, Bizakis J, Christodoulou P. **The Histology of Laser Thermo-Chondro-Plasty.** American Journal of Otolaryngology. 1994;15:423-428.

3. Helidonis E, Sobol EN, Kavvalos G, et al. **Laser Shaping of Composite Cartilage Grafts.** American Journal of Otolaryngology 1993;14:410-412.

4. Karamzadeh A, Wong BJF, Milner TE, Wilson M, Liaw L-H, Nelson JS. **Angiogenic Response in the Chick Chorioallantoic Membrane Model to Laser-Irradiated Cartilage.** Proceedings SPIE 1999;in Press.

5. Min, YG; Kim, YK; Kim, HS. **The Histology of Autologous Auricular Cartilage Implanted into the Nasal Septum.** Clinical Otolaryngology, 1996 Aug, 21(4):339-42. (UI: 97044231)

6. Pullin JG, Collier MA, Das P, et al. **Effects of Holmium:YAG Laser Energy on Cartilage Metabolism, Healing, and Biochemical Properties of Lesional and Perilesional Tissue in a Weight-Bearing Model.** Arthroscopy 1996;12:15-25.

7. Sobol EN, Bagratashvili VV, Omel'chenko A, et al. **Laser Shaping of Cartilage.** Proceedings SPIE 1994;2128:43-49.

8. Sviridov A, Sobol EN, Jones NS, Lowe J. **Effect of Holmium laser radiation on stress, temperature and structure alterations in cartilage.** Lasers in Medical Science 1998;13:73-77.

9. Wong BJF, Milner TE, Anvari B, et al. **Measurement of radiometric surface temperature and integrated back-scattered light intensity during feedback controlled laser-assisted cartilage reshaping.** Lasers in Medical Science 1998;13:66-72.

10. Wong BJF, Milner TE, Kim HK, Nelson JS, Sobol EN. **Stress relaxation of porcine septal cartilage during Nd:YAG (•=1.32 mm) laser irradiation: mechanical, optical, and thermal responses.** Journal of Biomedical Optics 1998;3:409-14.

11. Wong BJF, Milner TE, Kim HK, et al. **Characterization of Temperature Dependent Biophysical Properties During Laser Mediated Cartilage Reshaping.** IEEE J Selected Topics Quantum Electronics 1999;5:1095-1102.

12. Wong BJF, Milner TE, Kim HK, et al. **Proteoglycan Synthesis in Porcine Nasal Cartilage Grafts Following Nd:YAG (•=1.32 mm) Laser Mediated Reshaping.** Photochemistry and Photobiology 2000;in Press.

13. Wong, BJ; Si, MS; Cho, C; Liaw, LH; Neev, J. **XeCl laser surgery of the vocal cords: a histologic comparison with CO2 laser in a porcine model.** Otolaryngology - Head and Neck Surgery, 1998 Mar, 118(3 Pt 1):371-5.

14. Wong BJF, Milner TE, Harrington A, et al. **Feedback Controlled Laser Mediated Cartilage Reshaping.** Archives of Facial Plastic Surgery 1999;1:282-287.

Dynamic changes in the elastic modulus of lagomorph nasal septal cartilage during Nd:YAG (λ=1.32 μm) laser irradiation

Kenneth K.H. Chao[1,2], Matt A. Burden[3], Brian J.F. Wong[2,4,5]

[1] School of Medicine, University of Texas Health Science Center at San Antonio
[2] Beckman Laser Institute, University of Irvine
[3] Departments of Engineering, Harvey Mudd College
[4] Department of Otolaryngology- Head and Neck Surgery, University of California Irvine,
[5] The Whitaker Center for Biomedical Engineering, Samueli School of Engineering, University of California, Irvine

ABSTRACT

The elastic modulus of rabbit nasal septal cartilage was measured during Nd:YAG laser (λ=1.32 μm, 10 seconds, 21.22 W/cm^2) radiation. Cyclical force versus displacement curves were generated in cantilevered specimens (9.5 mm x 3.0 mm x 1.0 mm) using a calibrated thin beam load cell and a single axis motorized micropositioner (velocity = 0.3 mm/sec). The laser and a thermopile were positioned above the secured specimen. Samples were irradiated three times with 30 second cooling intervals between each sequential laser exposure. Surface temperature reached a maximum of 65°C. Measurements were recorded before, during, and after each laser irradiation, and then following complete rehydration in normal saline (NS) for 1 hour at 25°C. Following each laser exposure, the sample was sprayed with normal saline delivered via an atomizer to prevent desiccation. Elastic modulus was calculated using a model assuming linear elastic behavior. The modulus in native tissue was 6.08 ± 0.17 Mpa, and this decreased during and after each successive laser exposure (5.41 ± 0.39 Mpa, 4.94 ± 0.46), (5.05 ± 0.104 Mpa, 4.17 ± 0.46 Mpa), (4.23 ± 0.53, 3.71 ± 0.60 Mpa), for the first, second, and third laser exposures, respectively. Following rehydration for one hour in normal saline, the modulus returned to near-baseline values (5.33 ± 0.40 Mpa). The results suggest that molecular changes that occur in the cartilage tissue matrix during laser cartilage reshaping are not accompanied by irreversible changes in the matrix molecules.

Keywords: Laser, cartilage, reshaping, elastic modulus, otolaryngology

1. INTRODUCTION

Traditional aesthetic and reconstructive surgery of the nose, pinnae, and trachea requires cutting, suturing, and morselizing cartilage that can result in tissue waste and donor site morbidity. These techniques are also invasive and may be associated with post-operative complications. Furthermore, the physical manipulation of the tissue may alter graft resilience and weaken the tissue. In 1993, Sobol demonstrated that it was possible to reshape cartilage with a laser. Photothermal heating accelerates stress relaxation in cartilage tissue thus allowing the creation of complex curvilinear shapes while minimizing many of the limitations associated with classic surgical techniques[1]. In this study, the elastic modulus of lagomorph nasal septal cartilage was measured during real-time laser irradiation during cyclic displacement as a constant velocity. The information will provide insight into the ability of the cartilage to maintain its baseline physical properties and resilience while under photothermal stress similarly experienced during laser-mediated cartilage reshaping.

2. MATERIALS AND METHODS

2.1 Specimen preparation

Nasal septal cartilages were extracted from the crania of freshly euthanized New Zealand white rabbits (2.04 - 2.27 kg, B & B Rabbit Company, Fontana, CA) using a modification of a method used to obtain septal cartilage from pigs[3]. A rectangular slab measuring 9.5 mm x 3.0 mm with a thickness of 1.00-1.20 was cut with a razor from the central region of each septum perpendicular to the caudal-cephalic axis and freed of perichondrial tissue (Figure 1). This region of the septum is extremely uniform in thickness. A total of 10 cartilage slabs were extracted from 5 animals. Each slab was analyzed once.
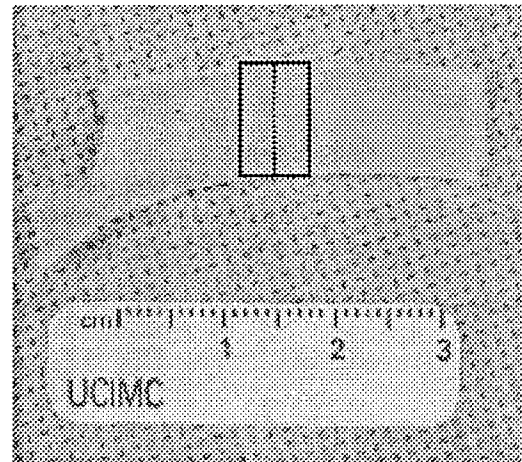
Figure 1. Rabbit nasal septal cartilage. Box shows the area cut into 9 mm x 3 mm x 1 mm rectangular slabs to be used for experimental analysis.
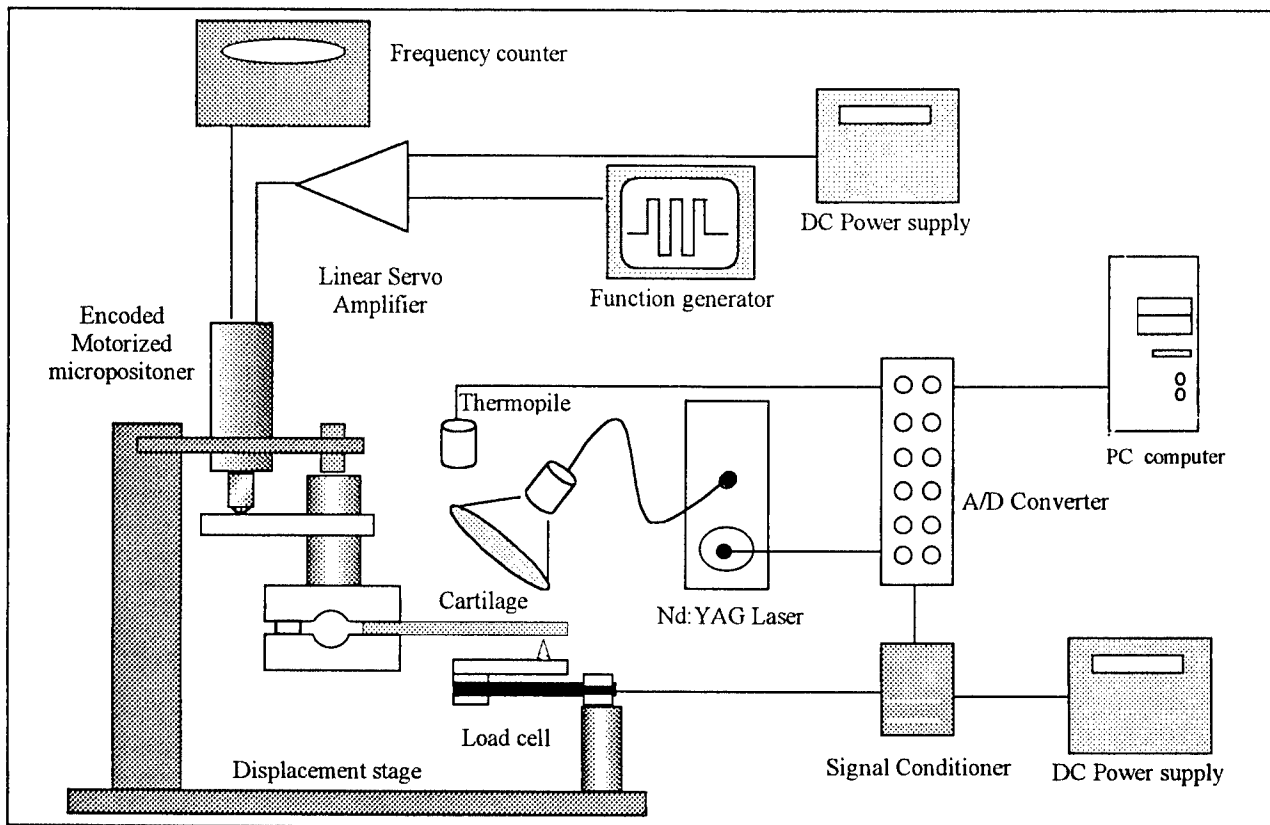
Figure 2. Diagram of experimental setup

2.2 Measurement of physical properties

Figure 2 illustrates the schematic of the experimental setup used to measure force and displacement during oscillatory flexure and repeated laser irradiation. A 2 mm segment at one end of the specimen slab is gently clamped between two aluminum blocks attached to a single axis translation stage powered by an encoded micropositioner (Model 18009 Oriel Corp, Stratford, CT). This stage is secured to a three-axis micropositioner that adjusts the initial specimen position in order to maintain consistent geometry for each individual measurement. The distal end of the cartilage graft is rested on a point attached to a calibrated full-bridge, thin-beam load cell (Model LCL 227G, Omega Engineering Inc, Stamford, CT) coupled to a modular signal conditioner (Model OM5-WBS-2-C, 300 – 10 k Ohms, 10 kHz bandwidth, Omega Engineering Inc).

The point contacts the graft approximately 1 mm away from the distal edge, leaving 6 mm of the slab between the edge of the translational stage and the tip of the screw (Figure 3). The apex of the point is slightly blunted so it does not pierce the cartilage during displacement. To calibrate the load cell, the cell was attached to a single axis micropositioner and displaced against a digital balance (Model 100A, Denver Instrument Co, Arvada CO) at increments of 0.01 mm. Forces vs. voltage plots per displacement were then obtained. Once secured, the distal end of the specimen is displaced at a constant velocity of 0.299 mm/sec for a total distance of 0.75mm by the motorized vertical axis translation stage. The drive voltage to the motor was supplied by a custom linear servo amplifier with a driving square waveform of 0.2 Hz produced by a function generator (Model DS 345, Stanford Research Systems, Sunnyvale, CA). A frequency counter (Model 34401A Hewlett Packard, Stanford, CA) was used to monitor the encoder output of the micropositioner (corresponding to motor velocity) and a DC offset was used to adjust motor velocity accordingly to produce uniform speed in both directions. Each slab was flexed for a total of 30 cycles.
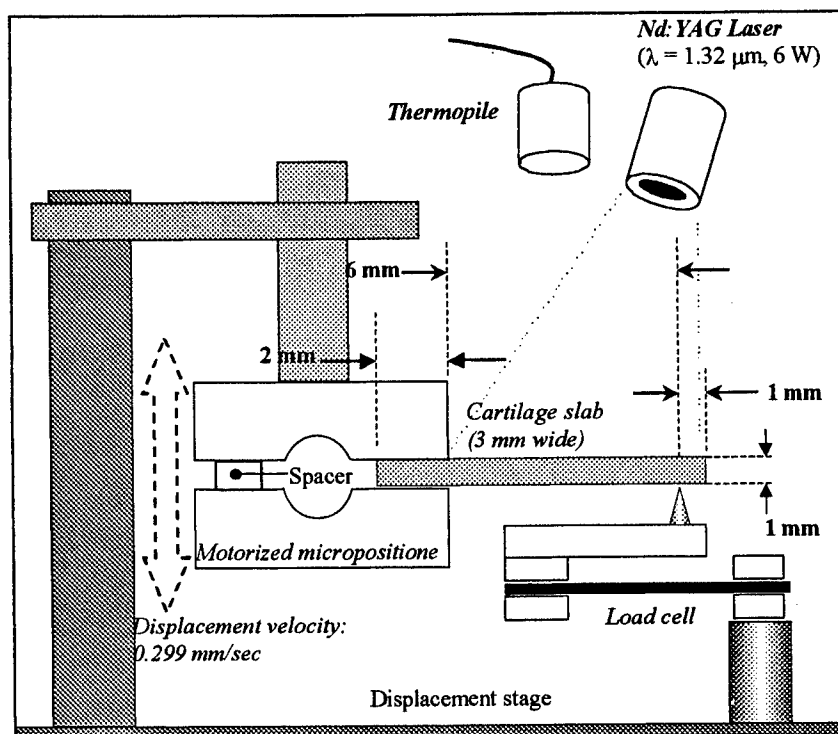
Figure 3. Close-up of cartilage slab on displacement apparatus. Specimen is placed in a conformation where 6 mm is held between the micropositioner and support point.

2.3 Laser parameter and tissue irradiation

An integrated module consisting of a calibrated thermopile and a collimated lens connected by a 600 μm core-diameter silica multimode optical fiber to an Nd:YAG laser (6 W, λ = 1.32μm, 6 mm spot diameter, 21 W/cm^2 NewStar Lasers, Auburn, CA) was placed 40 mm away directly above the slab. Due to finite geometric constraints, the light from the laser reached the surface of the graft at a 30° angle. Spot size was estimated by measuring the burn diameter created on irradiated thermal paper (Zap-It, Kentek, Pittsfield, NH). Laser power was calibrated with a pyroelectric meter (Model 10 A-P, Ophir, Jerusalem, Israel). The resultant spot size was large enough to cover the whole cartilage slab. Samples were irradiated for ten seconds followed by a 30 second cooling interval between each of the three successive laser exposures. In order to compensate for water vaporization (and specimen dehydration) during laser heating, two fine atomized sprays of normal saline (approximately 0.07-0.10 c.c. each) were delivered after termination of each laser exposure. Initial tests without post-irradiation rehydration led to excessive photothermal evaporation of water in the cartilage and caused the samples to dehydrate and shrivel. The resultant shrinkage caused the cartilage to lose contact with the load cell support, thereby leading to experimental failure because accurate force measurements could not be measured. Adequate hydration maintained geometric consistency and allowed for accurate force readings. After the third irradiation, the specimen was rehydrated in normal saline for 1 hour at 25°C and then resecured to the mechanical testing apparatus with the same approximate orientation and the measurements were repeated.

Signals from the load cell and thermopile were amplified, low-pass filtered and digitized with a modular signal conditioner (OM5-WBS, Omega Engineering Inc) and collected using an analog to digital converter (AT-MIO-16XE-50, National

Instruments, Austin, TX) and a personal computer running software written in LabVIEW (National Instruments). The resultant force recorded is used to calculate the modulus value using the equation for elastic flexure of a cantilevered beam with a load concentrated at the free end:

$$E = \frac{\Delta P}{\Delta Y} \frac{L^3}{3I}$$

where E = Young's modulus of elasticity, ΔP is the force, ΔY is the maximum displacement of the specimen, L is length of specimen, I is the moment of inertia (moment equation for a plank of width d and length b is $bd^3/12$). The modulus was calculated using four force measurements during each irradiation sequence. Only four specimen displacement cycles occurred during the 10s laser exposure time so the values were averaged. The modulus was calculated before, after, and during each laser irradiation sequence.

3. RESULTS
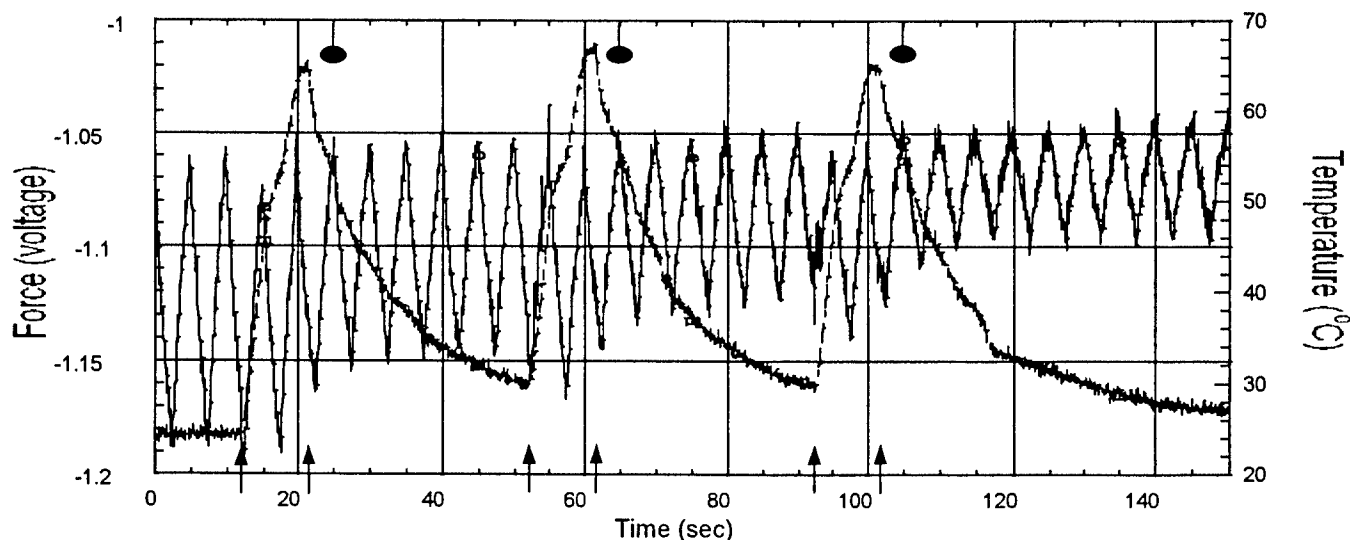
Figure 4. Force and temperature measurements during cyclic displacement of the cartilage slab. Paired arrows indicate time of onset and termination of laser irradiation. Oval points represent rehydration with normal saline mist.

Representative force (expressed as voltage values) and surface temperature measurements as a function of time are depicted in Figure 4 during laser heating. Measurements obtained during the initial 10 seconds provide baseline modulus values. The onset and cessation of each laser exposure is indicated by the paired arrows. This is accompanied by an increase in surface temperature. The peak surface temperature reached during laser irradiation was 65°C, which is above the temperature threshold required to accelerate stress relaxation as observed noted in previous studies[23]. Each laser exposure time was 10 seconds. A dramatic reduction in force was observed immediately following the cessation of laser irradiation. The resultant modulus then appeared to remain constant throughout the remainder of the 30-second cooling interval prior to the next irradiation. A normal saline spray was applied to the specimen 2-3 seconds after irradiation to prevent overt desiccation. No significant changes in the force-displacement waveforms were noted during delivery of the spray. Force-time curves in samples rehydrated in normal saline for 1 hour appeared qualitatively similar to baseline waveforms (pre-irradiation) (Figure 5). Displacement (and hence modulus) can be calculated knowing the velocity of the load cell. Of the ten samples tested, four specimens were inadequately rehydrated with saline spray leading to loss of contact with the load cell. Figure 6 and 7 summarize the average elastic modulus of nasal septal cartilage (N=6) before, during, and after three

laser exposures. The modulus prior to laser exposure was 6.08 Mpa ± 0.17 Mpa (1.1% error), and decreased sequentially with each subsequent laser irradiation. After a one-hour rehydration in normal saline at 25°C, the elastic modulus returned to approximately 90% of baseline value.

Figure 5. Force vs. time curves of laser-irradiated cartilage following one-hour rehydration in normal saline.
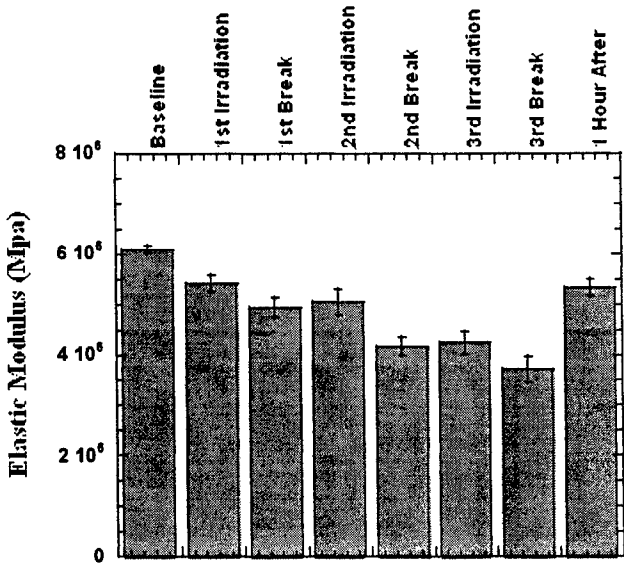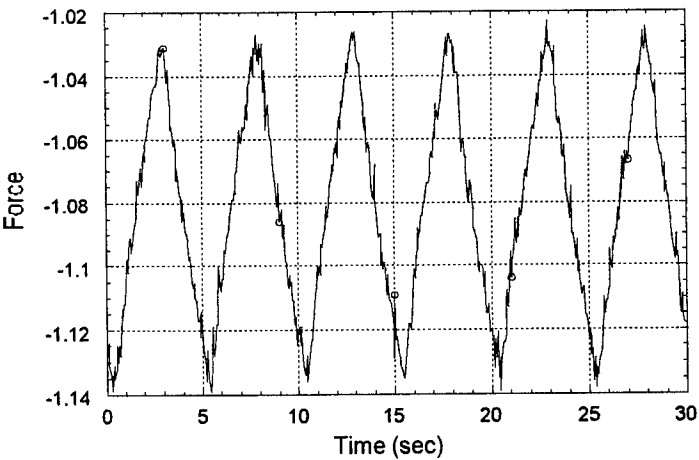
	Average (N=6)	Standard Deviation	Percent Error
Baseline	6,081,559.38	171,047.92	1.1%
1st Irradiation	5,408,026.64	391,428.38	3.0%
1st Break	4,938,057.12	459,083.16	3.8%
2nd Irradiation	5,057,057.41	609,109.71	4.9%
2nd Break	4,168,159.57	460,319.08	4.5%
3rd Irradiation	4,229,712.35	549,081.41	5.3%
3rd Break	3,710,364.71	598,400.84	6.6%
1 hour after	5,326,199.43	401,628.82	3.1%

Figure 6 (left) and 7 (right). Average elastic modulus of rabbit cartilage grafts before, during, and after three sequential laser exposures. Error bars indicate percent error.

4. DISCUSSION

The results of this experiment showed that the elastic modulus of rabbit nasal septal cartilage decreases after multiple laser exposure and returns to near baseline value after submersion in normal saline. The elastic modulus represents a measure of the stiffness of a body or its ability to resist deformation within the proportional limit of the material[2]. The greater the modulus the less the sample will deform under a unit stress.

Cartilage is complex macromolecular tissue consisting of a meshwork of collagen, PTG subunits, and ionic/hydrophilic bonds. These intricate lattices of interlocking bonds maintain the elasticity and strength of the tissue. During cyclic displacement, the cartilage undergoes reflexive mechanical changes. As the specimen is pushed down on the load cell support, the upper portion becomes concave while the lower portion becomes convex. This imparts changes in the internal mechanical stress within the matrix. The area of concavity becomes increasingly compressed as the matrix subunits against each other. On the other side, the area of convexity exhibits increased tension as the matrix is stretched apart. The amount of interlocking bonds within the cartilage needed to counteract these influences determines the resultant force displayed by the graft onto the load cell.

Any changes in the constitutive elements of the matrix (enzymatic digestion, heat, pH changes, similarity) will alter the bulk properties of the tissue. In 1993, Sobol first proposed that photothermal heating of cartilage caused accelerated stress relaxation of the tissue. This, he hypothesized, resulted from several processes including 1) being bound to free water transition, 2) from local mineralization of tissue caused by the interaction of free Na^+ or Ca^{+2} with charged carboxyl or sulfate groups residing on proteoglycans, 3) from alteration of weak non-covalent bonds between collagen, PTG subunits, 4) from local polymerization of PTG aggregates, and 5) from denaturation of collagen framework[7].

With the loss of interlocking bonds, they are more susceptible to compression and stretch. Thus cyclic flexure becomes easier to perform, as shown by the drop in elastic modulus after each irradiation. The results of this experiment demonstrated that sequential laser irradiation of rabbit nasal septal cartilage produces a stepwise reduction in the tissue elastic modulus (Figure 6) with an overall decrease of approximately 30%. After the samples are rehydrated in normal saline, the modulus returns to approximately 90% of baseline value. The mechanisms supporting complete denaturation or covalent interactions thus appear less likely, and that water and weak molecular interactions may play the dominant role.

Photothermal energy was delivered uniformly to the cartilage slabs because the small size of the rabbit specimens matched the laser spot diameter created by the collimating lens. In addition, the tissue samples used were very thin (1.00-1.20 mm thickness), allowing spatially uniform heat generation in the specimen. Because absorption of light at 1.32 μm is low in cartilage, very small axial temperature gradients were also anticipated, particularly in thin specimens[9, 10]. Hence, rapid bulk heating was accomplished with minimal thermal gradients in either axial or radial directions.

To prevent excessive dehydration of the cartilage from photothermal evaporation, fine mists of normal saline were delivered from an atomizer shortly after termination of laser irradiation. When cartilage was insufficiently hydrated the tissue shriveled, resulting in loss of contact with the load cell as well as loss of the linear beam geometry. The effect would make force measurements impossible and elastic modulus calculation inaccurate. Fine mists of NS allowed the cartilage to retain its gross structural dimensions and to maintain its contact with the load cell. No changes in load cell voltage output were observed during the application of saline spray. Despite these efforts, four of the ten samples were inadequately rehydrated. A computer controlled saline spray delivery system is presently being incorporated into the present apparatus and will be used in future to studies in order to optimize this hydration process.

A 10 seconds firing duration was selected based on previous studies on feedback-controlled irradiation showing that accelerated phase transformation occurs after 6-12 seconds of laser exposure[24]. A series of three laser exposures were selected, as it is unlikely in clinical practice that surgeons would only irradiate specimens once to effect a shape change. Although post-irradiative cartilage viability was not assessed in this study, previous experiments using the similar or longer firing durations have shown that cartilage viability is preserved[25]. Our group is presently performing studies correlating laser dosimetry, mechanical properties, and tissue viability in rabbit septal tissue.

Previous studies on laser-mediated cartilage reshaping have focused on assessing feedback-control parameters and post-irradiation viability. The mechanical properties of cartilage affected by photothermal heating, however, have not been

extensively explored. Gaon investigated the elastic modulus of porcine nasal septal cartilage, but the samples were irradiated on a resting stage before placing the slab on the displacement apparatus[6]. No measurements of these physical properties during real-time laser irradiation during dynamic flexure were assessed. In addition, the mechanical properties of rabbit septal cartilages have not been studied at all. Lagomorph's specimens exhibit tissue modalities similar to human tissue and can be used as appropriate animal models for nasal septal cartilaginous surgery [26].

5. CONCLUSION

The elastic modulus represents a measure of the stiffness of a material, or its ability to resist deformation within the proportional limit of the material[2], and allows us to quantitatively characterize the effects of laser irradiation on the bulk material properties of nasal septal cartilage. The results of this study showed that successive irradiation of rabbit nasal septal cartilage caused a sequential reduction in the elastic modulus, but this effect was almost completely reversed following rehydration in saline. This suggests that the molecular changes that occur in the cartilage tissue matrix during laser cartilage reshaping are not accompanied by irreversible changes in the matrix molecules (e.g. denaturation, covalent bonding). Histological and molecular studies will be needed to fully verify the gross observation of these mechanisms. While optical and biological changes associated with laser-mediated cartilage reshaping have been extensively studied, few investigations have examined the mechanical properties accompanying these changes. To date, this is the first study to measure dynamic changes in the elastic modulus of cartilage during laser heating. Further studies into improving tissue hydration during laser irradiation, especially in thin tissues, as well as using different parameters such as dynamic mechanical thermal analysis (DMTA) to measure the modulus and damping properties of the tissue are currently underway in our laboratory.

ACKNOWLEDGEMENTS

REFERENCES

1. Bagratashvili VV, Sobol EN, Sviridov A, Popov VK, Omel'chenko A, Howdle SM. "Thermal and diffusion processes in laser-induced stress relaxation and reshaping of cartilage", *Journal of Biomechanics* 30:813-817, 1997.
2. Eshbach O. "Sec 5: Mechanics of deformable bodies", *Handbook of Engineering Fundamentals, 2nd Ed*:1-82, John Wiley, New York, 1952.
3. Wong BJF, Milner TE, Anvari B, Sviridov A, Omel'chenko A, Vagratashvili V, Sobol EN, Nelson JS. "Thermo-optical response of cartilage during feedback controlled laser-assisted reshaping", *Proceedings SPIE* 2970:380-391, 1997.
4. Wong BJF, Milner TE, Anvari B, Sviridov A, Omel'chenko A, Bagratashvili VV, Sobol EN. Nelson JS. "Measurement of radiometric surface temperature and integrated back-scattered light intensity during feedback controlled laser-assisted cartilage reshaping", *Lasers in Medical Science* 13:66-72, 1998.
5. Fry H. "Interlocked stresses in human nasal septal cartilage", *British Journal of Plastic Surgery* 19:276-2, 1966
6. Fry H, Robertson W. "Interlocked Stresses in cartilage", *Nature* 251:53-54, 1967
7. Gaon M, Wong B. "Measurement of the elastic modulus of porcine septal cartilage specimens following Nd:YAG laser treatment", *Proceeding SPIE*, 3907:370-379, 2000.
8. Sobol EN, Sviridov A, Omel'chenko A, Bagratashvili VV, Kitai M, Harding SE, Jones N, Jumel K, Mertig M, Pompe W, Ovchinnikov Y, Shechter A, Svistushkin V. "Laser reshaping of cartilage", *Biotechnology and Genetic Engineering Reviews* 17:539-564, 2000.
9. Karamzadeh AM, Wong BJF, Milner TE, Dao X, Tanenbaum BS, Nelson JS. "Temperature distributions in Nd:YAG (λ=1.32 μm) laser-irradiated cartilage grafts accompanied by cryogen spray cooling", *Proceedings SPIE* 3601:422-433, 1999.
10. Karamzadeh AM, Rasouli A, Tanenbaum BS, Milner TE, Nelson JS, Wong BJF. "Laser-mediated cartilage reshaping

with feedback-controlled cryogen spray cooling: biophysical properties and viability", *Lasers in Surgery and Medicine* [in press], 2000.

11. Wong BJF, Milner TE, Kim HK, Chao KKH, Sun CH, Sobol EN, Nelson JS,. "Proteoglycan Synthesis in Porcine Nasal Cartilage Grafts Following Nd:YAG (λ = 1.32μm) Laser-Mediated Reshaping", *Photochemistry and Photobiology* **71**(2):218-24, 2000.

12. Wong B, Chao KKH, Kim HK, Chu E, Dao X, Gaon M, Sun CH, Nelson JS. "The Porcine and Lagomorph Septal Cartilages: Models for Tissue Engineering and Morphologic Cartilage Research", *American Journal of Rhinology* [submitted for publication], 2000.

13. Fry H. "Cartilage and cartilage grafts: the basic properties of the tissue and the components responsible for them", *Plastic and Reconstructive Surgery* **40**:426-439, 1967.

14. Lai W. "A triphasic theory for the swelling and deformation behaviors of articular cartilage", *Journal of Biomechanical Engineering* **113**:24-258, 1991.

15. Helidonis ES, Sobol EN, Kavvalos G, Bizakis J, Christodoulou P, Velegrakis G, Segas J, Bagratashvili VV. "Laser shaping of composite cartilage grafts", *American Journal of Otolaryngology* **14**:410-412, 1993.

16. Helidonis ES, Sobol EN, Velegrakis G, Bizakis J. "Shaping of nasal septal cartilage with the carbon dioxide laser- a preliminary report of an experimental study", *Lasers in Medical Science* **9**:51-54, 1994.

17. Helidonis ES, Volitakis M, Naumidi I, Velegrakis G, Bizakis J, Christodoulou P. "The histology of laser thermo-chondro-plasty", *American Journal of Otolaryngology* **15**:423-428, 1994.

18. Sobol EN, Bagratashvili VV, Omel'chenko A, Sviridov A, Helidonis ES, Kavvalos G, Christodoulou P, Naoumidi I, Velegrakis G, Ovchinnikov Y, Shechter A. "Laser shaping of cartilage", *Proceedings SPIE* **2128**:43-49, 1994.

19. Sobol EN, Sviridov A, Bagratashvili VV, Omel'chenko A, Ovchinnikov Y, Shechter A, Downes S, Howdle S, Jones N, Lowe J. "Stress relaxation and cartilage shaping under laser radiation ", *Proceedings SPIE* **2681**:358-363, 1996.

20. Sobol EN, Kitai M, Jones N, Sviridov A, Milner TE, Wong BJF. "Theoretical modeling of heating and structure alterations in cartilage under laser radiation with regard of water evaporation and diffusion dominance", *Proceedings SPIE* **3254**:54-63, 1998.

21. Sobol EN, Kitai M, Jones N, Sviridov A, Milner TE, Wong BJF. "Heating and structure alterations in cartilage under laser radiation", *IEEE Journal of Selected Topics in Quantum Electronics* **35**:532-9, 1999.

22. Wong BJF, Milner TE, Kim HK, Nelson JS, Sobol EN. "Stress relaxation of porcine septal cartilage during Nd:YAG (λ = 1.32 μm) laser irradiation: mechanical, optical, and thermal responses", *Journal of Biomedical Optics* **3**:409-14, 1998.

23. Wong BJF, Milner TE, Kim HK, Telennov S, Chew CF, Kuo TC, Smithies DJ, Sobol EN, Nelson JS. "Critical temperature transitions in laser mediated cartilage reshaping", *Proceedings SPIE* **3245**:161-172, 1998.

24. Wong BJF, Milner TE, Kim HK, Telenkov S, Chew CF, Sobol EN, Nelson JS. "Characterization of temperature dependent biophysical properties during laser mediated cartilage reshaping", *IEEE Journal of Selected Topics Quantum Electronics* **5**:1095-1102, 1999.

25. Wong BJF, Milner TE, Harrington A, Ro J, Dao X, Sobol EN, Nelson JS. "Feedback controlled laser mediated cartilage reshaping", *Archives of Facial Plastic Surgery* **1**:282-287, 1999.

Finite Element Analysis of Thermal Residual Stress and Temperature Changes in Cartilage During Laser Radiation

Yongseok Chae[*a,b], Sergio Diaz [a,b], Enrique J. Lavernia [b], Brian J.F. Wong [a]

[a] Dept. of Otolaryngology –Head and Neck Surgery, Beckman Laser Institute and Medical Clinic;
[b] Dept. of Chemical and Biochemical Engineering and Materials Science, Univ. of California Irvine

ABSTRACT

In this study, the rheological and phase behavior of porcine nasal cartilage were determined using dynamic mechanical thermal analysis (DMTA), differential scanning calorimetry, and thermogravimetric analysis and the principles of thermal analysis (TA). The results were then incorporated in a finite element analysis used to estimate thermal residual stress and temperature distributions during laser irradiation. The finite element analysis was conducted by using a commercially available code ABAQUS (Hibbitt, Karlsson & Sorensen, Inc, USA) to solve the fully coupled thermo-mechanical equations. Arrhenius kinetics were used to obtain the activation energy associated with the phase transition as determined using DMTA and the results were compared with the energy of the phase transformation calculated using DSC. Laser-induced stress relaxation produced an increase in the von Mises stress within the simulation. The values generated during photo thermal heating were calculated assuming cartilage as an isotropic linear viscoelastic material. The advantages and limitations of this approach technique are discussed, in particular with relevance to optimizing this procedure for use in clinical settings.

Keywords: Finite Element Analysis, Cartilage Reshaping, Phase Transition, ABAQUS, Thermal Residual Stress, von Mises Nd:YAG irradiation, Differential Scanning Calorimetry, Thermogravimetric Analyzer, Dynamic Mechanical Thermal Analyzer

INTRODUCTION

In 1994, Sobol and Omel'chenko introduced a novel method of reshaping cartilage using laser irradiation to accelerate mechanical stress relaxation and permanently modifying graft morphology[1]. Subsequent measurements of tissue optical, mechanical and thermal properties during photothermal heating identified characteristic changes in tissue optical properties that occurred within a critical temperature range of 60~70°C, which marks the beginning of stress relaxation[2-12]. Helidonis et al[13], Sobol[14] and Sobol et al. [1,3] described stress relaxation and cartilage reshaping during laser radiation and suggested that the process involves a temperature sensitive, bound to free water phase transition[15-17]. Using calorimetry, they demonstrated that the laser reshaping was caused by thermal energy and the temperature of the phase transformation was 350K. By integrating the heating curve, energy requirement of this phase transition was estimated to be between 1,200-1,800 J/cm^3. We hypothesized that this represented the energy change during the transition of water from a bound to a free state[1,14].

Cartilaginous tissues contain specialized cells called chondrocytes and an extracellular matrix (ECM) consisting of collagen fibers (20–25 %) and proteoglycan aggregates (5~15%) and water (65~85%). The special mechanical properties of cartilage that allow it to be classed with hard tissues are associated with the presence in it of internal stresses, as well as with the high stresses that developduring mechanical deformation. The ECM is a hydrated gel containing proteoglycans that rely on the diffusive transport of water through the cartilage for both function and to maintain its nutrition. Laser mediated cartilage reshaping is accompanied by changes in the mechanical, thermal, and optical properties of the tissue[1,4,6,7,14] without dramatic structural alterations in the tissue as observed using conventional light microscopy.. The structural integrity of the tissue is preserved provided laser dosimetry remains within specific limits.

Photothermal heating of mechanically deformed cartilage accelerates stress relaxation and results in sustained shape change. The shape retension was measured in Nd: YAG laser reshaped porcine septal cartilage [28]. Photothermal heating results in accelerated stress relaxation and as a result the tissue becomes pliable, allowing the creation of complex curvilinear shapes while minimizing many of the shortcomings associated with current surgical methods. Sobol has proposed that laser reshaping results from a phase transition of cartilaginous bound to free water occurring at about T = ~65°C [1,4,14]. Heating above this temperature value may result in irreversible thermal injury. Classically, thermal alteraton of soft tissues is

reversible up to a temperature of about 45°C. Around 60°C, the proteins denature and coagulate [20]. Over 100C, the tissue water and organic molecules evaporate, resulting in local tissue shrinkage by dehydration, cell contraction, carbonization and vacuolization. Photothermal heating can be used to thermally modify the physical properties of materials while precisely controlling the spatial and temporal generation heating. In order to optimize laser-mediated cartilage reshaping for use in clinical practice, heat generation must be finely controlled, as loss of cell viability may result in tissue necrosis complete graft resorbtion.

A quantitative understanding of heat conduction and mechanical stress generated during the laser irradiation of mechanically deformed porcine nasal cartilage specimens is necessary to optimize reshaping. Laser reshaping may best be phenomenologically described by a thermoviscoelastic model where mechanical properties are a function of the temperature field variables, and hence are inherently nonlinear[18]. Heat and stress are coupled because the thermal history of the material effects the constituitive stress field relationships and time-dependent volumetric changes alter thermal behavior. Coupled thermoviscoelastic equations, which include temperature dependent mechanical properties, are very difficult to solve analytically. The relaxation energy of phase transition (activation energy) was characterized using TGA and DMTA and the energy of phase transition was determined using DSC, electrically high sensitive instrument.

The finite element method (FEM) has been extensively used to evaluate the behavior of biomaterials[24]. FEM can be used as a tool to evaluate the thermal stress behavior and thermal response of nonlinear biomaterials, and it can be extended to complex geometries and loading arrangements which are closer to real physiologic situations. The displacement finite element method is based on force and momentum equilibrium states maintained in an average sense over a finite number of divisions in the volume elements of interest. ABAQUS (Hibbitt, Karlsson & Sorensen Inc. USA), commercial finite element software package, was used because it allows simulation of coupled temperature-displacement relationships.

This study presented a finite element analysis for the three dimensional non-linear analysis of soft hydrated tissues such as cartilage under laser irradiation conditions. The deformable element within ABAQUS was used to evaluate the stress/strain field and temperature distribution in cartilage developing in slab during laser irradiation. The resulting first-order nonlinear system of equations is described in time using an implicit finite difference scheme, and solved using the Newton Raphson method. A significant contribution of this work is the implementation and testing of a single phasic description with a transversely isotropic viscoelastic material. Our objective was to develop and evaluate finite element formulations to simulate the nonlinear transversely isotropic monophasic behavior of biological soft hydrated tissues, in particular cartilage.

THEORY

Conduction of heat in an isotropic solid

We consider only isotropic material whose structure and thermal/mechanical properties in the neighborhood of any point are the same relative to all directions through the point. For a homogeneous isotropic material whose thermal conductivity is dependent of the temperature within which heat is generated, the governing heat equation is

$$\nabla^2 T - \frac{1}{k}\frac{\partial T}{\partial t} = -\frac{Q(x,y,z,t)}{K} \qquad \text{where } k = \frac{K}{\rho C} \qquad (a)$$

The constant k is the diffusivity of the material, and K is the thermal conductivity expressed as functions of temperature T. ρ is the material density and C is the specific heat at temperature T. Heat production per unit time and unit volume is Q. In this study Q is the rate of laser energy density varying with a penetration depth. The initial conditions include $T(0,t) = T(d,t)$, $Q(x,y,z,t) = \mu I(x,y,z,t)$ where μ is the absorption coefficient at the wavelength of the laser and I is the laser irradiance in W/cm^2.

Boundary or Surface Conditions

In the mathematical theory of heat conduction, the flux across the surface is proportional to the temperature difference between the surface and the surrounding material, such that the flux is given by $H(T - T_0)$ where H is the coefficient of surface heat transfer or the surface conductance. The boundary condition is

$$K\frac{\partial T}{\partial n} + H(T - T_0) = 0 \qquad \text{(b)}$$

Thermoviscoelasticity

In considering the means of solving isothermal, linear thermoviscoelastic boundary value problems, a linear theory of thermoviscoelasticity was derived under quasi-static equilibrium conditions. Accordingly, a consistent thermodynamical derivation of a general linear theory of thermoviscoelasticity is given. This derivation is based on two fundamental thermodynamic postulates, the balance of energy and the entropy production inequality. The local balance of energy equation from infinitesimal theory is given by

$$\rho r - \rho\left[A^* + T^*S + TS^*\right] + \sigma_{ij}\varepsilon_{ij} - Q_{i,i} = 0 \qquad \text{(c)}$$

where r is the heat supply function per unit mass, A is the Helmholtz free energy per unit mass, T is the absolute temperature, S is the entropy per unit mass, and Q_i are the Cartesian components of the heat flux vector measured per unit area per unit time. The related local entropy production inequality is given by

$$\rho TS^* - \rho r + Q_{i,i} - Q_i(T_{,i}/T) \geq 0 \quad \rho TS^* - \rho r + Q_{i,i} - Q_i(T_{,i}/T) \geq 0 \qquad \text{(d)}$$

The above equation is often referred to as the Clausius-Duhem inequality. The stress depends not only upon strain, but also upon the past history of strain, which allows stress to be expressed as a functional of strain history. The free energy not only depends upon the strain history, but also depends upon the temperature history. The value of the stress tensor depends upon the complete past history of the components of the strain tensors is expressed as

$$\sigma_{ij}(t) = F_{ijkl}(0)\varepsilon_{kl}(t) + \int_0^t F_{ijkl}(t - \tau)\frac{d\varepsilon_{kl}(\tau)}{d\tau}d\tau \qquad \text{(e)}$$

where the stress vector σ is defined in terms of the resultant force F acting on the surface element δa through

$$\sigma_i = \lim_{\delta a \to 0}\frac{F_i}{\delta a} \qquad \text{(f)}$$

The strain history $\varepsilon_{ij}(t)$ is continuous and the function is assumed to be linear. The symmetry of the stress and strain tensors imply the following relations $F_{ijkl}(t) = F_{jikl}(t) = F_{ijlk}(t)$. The strain history is specified by the displacement component, u_i in the strain displacement relations.

$$\varepsilon_{ij} = \frac{1}{2}(\frac{\partial u_i}{\partial X_j} + \frac{\partial u_j}{\partial X}) \qquad \text{(g)}$$

The basic hereditary integral formulation for linear isotropic viscoelasticity is:

$$\sigma(t) = \int_0^t 2G(\tau - \tau')e dt' + I\int_0^t K(\tau - \tau')\phi dt' \qquad \text{(h)}$$

where e and ϕ are the mechanical deviatoric and volumetric strains. K is the bulk modulus and, G is the shear modulus, which are functions of the reduced time τ and τ'.

A commonly used shift function is the Williams-Landell-Ferry (WLF) equation, which has the following form:

$$\tau = \int_0^t \frac{dt'}{A_T(T(t'))} , \qquad -\log A_T = \frac{C_1(T - T_g)}{C_2 + (T - T_g)} \qquad \text{(i)}$$

where C_1 and C_2 are constants and T_g is the phase transition temperature.

The time dependent relaxation function $K(t)$ and $G(t)$ is defined individually in terms of a series of exponentials known as the Prony series:

$$K(\tau) = K_\infty + \sum_{i=1}^{nK} K_i e^{-\tau/\tau_i^K} = K_0 \left(k_\infty + \sum_{i=1}^{nK} k_i e^{-\tau/\tau_i^K} \right) \tag{j}$$

$$G(\tau) = G_\infty + \sum_{i=1}^{nG} G_i e^{-\tau/\tau_i^G} = G_0 \left(g_\infty + \sum_{i=1}^{nG} k_i e^{-\tau/\tau_i^K} \right) \tag{k}$$

where K_∞ and G_∞ represent the long term and K_0 and G_0 are the instantaneous small strain shear and bulk moduli. ABAQUS assumes that the relaxation times $\tau_i = \tau_i^K = \tau_i^G$ are the same so that from here on.

Basic Finite Element Equations in Abaqus

With the equilibrium statement, the virtual work equation

$$\int_v \sigma : \delta D dV = \int_{V^0} \tau^c : \delta \varepsilon dV^0 = \int_s \delta v \bullet t dS + \int_v \delta v \bullet f dV \tag{l}$$

where "true" or Cauchy stress matrix σ at a point of S is defined by $t = n \bullet \sigma$ and n is the unit outward normal to S at the point. δD and δv are compatible :

$$\delta D = \frac{1}{2} \left(\frac{\partial \delta v}{\partial x} + \left[\frac{\partial \delta v}{\partial x} \right]^T \right) \tag{m}$$

where δv is compatible with all kinetic constrains and τ^c and ε any conjugate pairing of material stress and strain measures.

The minimum potential energy approach to the finite element formulation of displacement problems gives the following general matrix equation;

$$F_1 = K_s d \tag{n}$$

where F_1 is the global load vector, K_s is the global stiffness matrix and d is the global displacement vector. The application of Galerkin's method to the thermal problems processes the following matrix equation;

$$K_c T + CT + F_h = 0 \tag{o}$$

where K_c is the conductivity matrix, T is the temperature vector, C is the heat capacity matrix, F_h is the heat flow vector and T is the derivative of temperature vector with respect to time. The heat capacity, conductivity and stiffness matrices in equations are generated using a full Gaussian integration scheme, and the coupled system is solved using Newton's method.

FINITE ELEMENT ANALYSIS

Geometry and Element

A rectangular specimen (20 mm long, 10 mm wide, 5 mm thick) is shown in Figure.1 which has one plane of symmetry . All of the surfaces of the specimen are assumed to be exposed to an ambient atmosphere. The body of the specimen is modeled with 32 second-order plane stress hybrid reduced integration elements C3D8HT. These 8-node quadrilaterals allowed fully coupled temperature-displacement analysis. The problem is also solved with the first order fully coupled temperature-displacement C3D8HT elements in a 21 x 41 x 6 mesh.
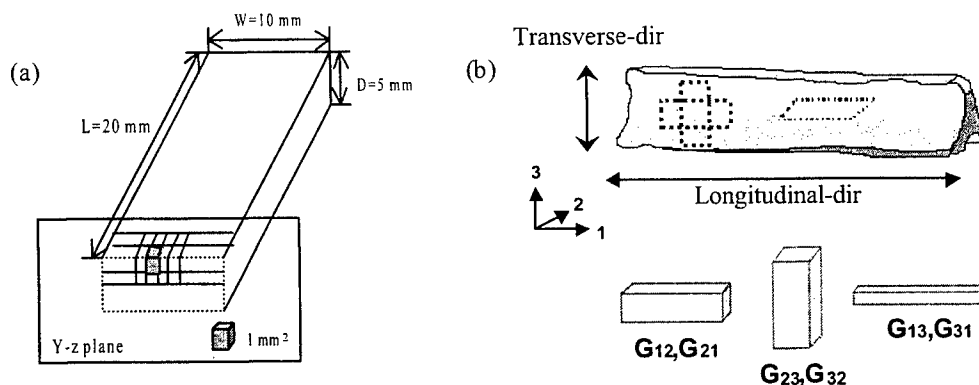
Fig 1.   (a) Cartilage Specimen for Finite Element Analysis in 3-D and Heating Zone of Laser Radiation
(b) Sample Specimen of Cartilage from Different Location

Numerical Analysis

The model is an elementary nonlinear simulation of three-dimensional heat transfer and stress analysis. The material definition of the specimen is assumed to be independent of orientation. The thermal and mechanical properties (density, thermal conductivity) were obtained from the literature [13,19] and incorporated into this transversely isotropic viscoelastic model. Experimental data obtained using dynamic thermal and mechanical tests were also incorporated into this model. The thermal material properties are arbitrarily defined in consistent units with thermal conductivity, specific heat and density obtained from the experimental data. The thermo-viscoelastic material behavior is defined using the temperature-time shift principle and the Williams-Landell-Ferry approximation. The coefficient of thermal expansion is assumed to be a linear function of temperature. In addition to the displacement degrees of freedom, incompatible deformation modes are added internally to the elements that possess negligible interfacial strength in absence of mechanical interlocking and interaction between phases.

The energy source was simulated using the measured temperature profile produced by laser irradiation (see below). For the purposes of this simulation, energy was deposited only at the surface of the specimen with subsurface heating occurring only via heat conduction. The thermal load was applied to a rectangular region of interest on the surface of the slab (the heating zone) for 9.5 sec using several heating rates (10°C/sec, 7°C/sec and 4°C/sec). The thermal boundary condition consists of uninsulated external surfaces; hence heat flux occurs on all surfaces. The simulation runtime was 9.5 sec. The surface elements are defined by the surface film, which defines the heat transfer properties of the superficial elements of the simulation. Each element is identified by a film type (linear or non-linear) and element type (defined by the software). In this model, uniform heat flow through the exposed surfaces was estimated using convection coefficients based on tabulated values (Table 1) ref. These convection coefficients were used to model heat transfer under both natural air convection and forced convection of superheated air.

The viscous behavior was modeled assuming time dependent shear and bulk moduli , and the material behavior was expanded in a single term Prony series in terms of the corresponding instantaneous modulus.

Table 1.   Heat Transfer Coefficients on the Surface of Cartilage During Laser Irradiation.

	Convective Heat Transfer Coefficient
Heating Points (Free convection of air)	21 W/m^{2}K
Other Surfaces (Forced convection of steam air)	90 W/m^{2}K

MEASUREMENT OF THERMAL AND MECHANICAL BEHAVIOR

1. Thermal Analysis

1.1 Thermogravimetric Analysis

Cartilage specimens (1-5 mg) were placed in tared platinum pans (PE No.0319-0024, Perkin-Elmer, Norwalk, CT) and analyzed over a temperature range of 25-100°C using a thermogravimetric analyzer (TGA7, Perkin-Elmer) which contained a precise electronic microbalance with an accuracy of $\pm$ 1.0 mg. Samples were heated at a rate of 1 to 7°C/min up to 80°C in N_2 flow (50ml/min) environment with N_2 also as serving the inert reference. The sample was 2.5-3.0 mm in diameter and 1.5-2.0 mm in thickness. Using a clean and dry crucible, the base line of the thermobalance was determined. The cartilage samples were heated and the mass-loss curve recorded.

1.2 Differential Scanning Calorimetry

The samples (1-5 mg) were placed into aluminum pans (PE No.0219-0041, Perkin-Elmer) and evaluated over a temperature range of 25~100°C using a differential scanning calorimeter (DSC7, Perkin Elmer). The thinly sliced samples (0.5 mm) were hermetically sealed in highly conductive pans and thus reducing the internal resistance of the sample. Heat flow was recorded and the enthalpy was calculated from the area beneath the peak on the heat flow temperature plot (thermogram). Volatile sample pans were used, as the vapor pressure generated during heating of the specimen was considerable, particularly near the temperature of phase transition. Measurements were performed at a rate of 1 to 7°C/min within the temperature range of 30-80°C.

1.3 Dynamic Mechanical Thermal Analysis

The loss tangent and the dynamic modulus were measured using a dynamic mechanical thermal analyzer (DMTA) form manufactured by Polymer Laboratories Ltd (MA, USA). The instrument included a temperature programmer and a testing head all under computer control, running thermal analysis software written by Polymer Laboratories (PL V5.11, PL Thermal Science, Mundelein, IL). The specimens were secured to the testing head using a jig that allowed single cantilever deformation. The specimen was constrained at each end by a clamping bar arrangement, one end being fixed to a rigid frame and the other end being driven by an electromagnetic vibrator via a composite drive shaft. This arrangement produces displacement in a fixed-guided cantilever beam configuration. The resulting sinusoidal force and displacement values were recorded and analyzed by the software to calculate loss tangent and dynamic modulus.

The strain amplitude was varied from 260 x 10^{-7} to 260 x 10^{-3} m (ε_0, the maximum specimen surface strain amplitude) to examine its effect on damping over time intervals of 1-30 min; the tests were conducted at 1 Hz and under various isothermal conditions. The oscillation frequency was varied from 0.01 to 5 Hz at ε_0 = 260 x 10^{-7}. The temperature dependent phenomena were evaluated by changing the heating rate from 1-7°C/min through an interval of 25°C to 80°C. The temperature was monitored with a platinum resistor placed next to the specimen. During heating, the sample was deformed at 5 discreet frequencies (0.1,0.3,1.0,3.0 and 5.0 Hz) in sequence.

1.4 Schematic Laser System and Irradiation

Figure 2. is a schematic of the experimental arrangement used to measure surface temperatures during laser irradiation. An integrated module consisting of a calibrated thermopile and a collimated lens connected by a 400μm core-diameter silica multimode optical fiber to an Nd:YAG laser (6W,λ=1.32μm, 6mm spot diameter, 21W/cm^2 NewStar Lasers, Auburn, CA) was placed 40 mm away directly above the specimen. The spot size was estimated by measuring the burn diameter created on irradiated thermal paper (Zap-It, Kentek, Pittsfield, NH). Laser power was calibrated using a pyroelectric meter (Model 10A-P, Ophir, Jerusalem, Israel).

Flat cartilage specimens were secured in a two piece steel frame (2 x 2 cm) and positioned in the path of the Nd:YAG laser beam. Data were acquired using a 16-bit AD converter (AT-MIO-16XE-50, National Instruments, Austin, TX) and Windows workstation running software written in Lab View (National Instruments).
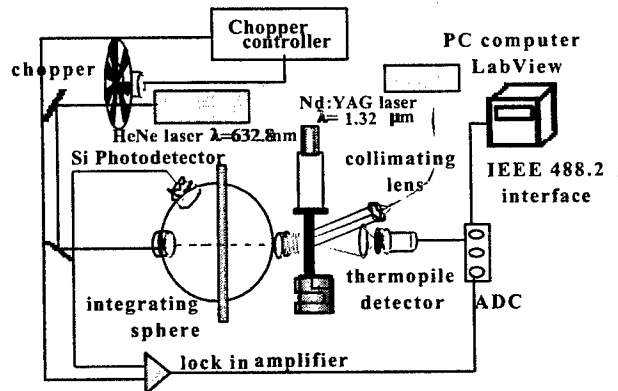
Fig 2. Schematic Laser System and Measurement of Surface Temperature Under Laser Radiation

Table 1. Heat Transfer Coefficients on the Surface of Cartilage During Laser Irradiation.

	Convective Heat Transfer Coefficient
Heating Points (Free convection of air)	21 W/m^{2}K
Other Surfaces (Forced convection of steam air)	91 W/m^{2}K

1.5 Cartilage Specimen Preparation

Porcine nasal septal cartilages from freshly sacrificed domestic pigs were obtained from a local abattoir (Lizzy's Custom Processing, Chino, CA) and harvested. The cartilage was removed within approximately 24 hours after euthanasia as previously described [30]. Each septal cartilage was cut into rectangular slips measuring 25 x 10mm with thicknesses of 1.5, 2.0, 2.5 to 3.0mm using a custom guillotine microtome. Specimens were stored in saline solution at 4°C until experiments and further divided into three groups. Specimens were divided into transverse, longitudinal directions and parallel direction to the bottom layer for analysis of direction variations, as shown in figure 1(b).

RESULTS AND DISCUSSION

An understanding of the thermal and mechanical stress generated during heating of cartilage specimens is important to optimize laser-mediated cartilage reshaping and the finite element method provides a means to obtain better insight into this behavior. This study developed a finite deformation simulation, which allowed the quantitative evaluation of temperature dependent changes in the physical properties of cartilage (and potentially other soft tissues), which is important particularly in light of possible clinical implementation of this technology.

Differential Scanning Calorimetry and Thermogravimetric Analysis

Thermogravimetric analysis provides information about the thermal stability and composition of a material. TGA decomposition kinetics method (ASTM Standard E1640) uses the data from experiments run at several heating rates to calculate kinetic parameters including activation energy using an Arrhenius kinetics model;

$$\frac{d\alpha}{dt} = f(\alpha)[Z\exp(-\frac{E_a}{RT})] \text{ and } E_a = -(\frac{R}{b})\left(\frac{d(\ln b)}{d(1/T)}\right) \tag{p}$$

where α is the fraction of weight lost, $f(\alpha)$ is a function of α not dependent on temperature, Z is the pre-exponential factor, E_a is the activation energy, R is the universal gas constant, t is time and T is temperature. By plotting the log-heating rate against the inverse temperature of a particular weight loss for several heating rates, the activation energy was estimated from the slope of the best curve fit. The rate of water evaporation from the cartilage specimens and the relaxation energy of cartilage specimen were determined using TGA. The TGA thermal decomposition curves for cartilage are shown in Figure 3.

Dehydration occurred during the 1st stage of heating, which was followed by a phase transition in the 2nd stage. The logarithm of the heating rate, although constant for any particular experiment, was retained in the equation (p) to permit correlation of TG curves carried out at different heating rates. From the 2nd stage, the relaxation energy of cartilage was calculated with 1.5×10^4 J/mole using equation (p) with data from the weight loss curve, Figure 4(b).
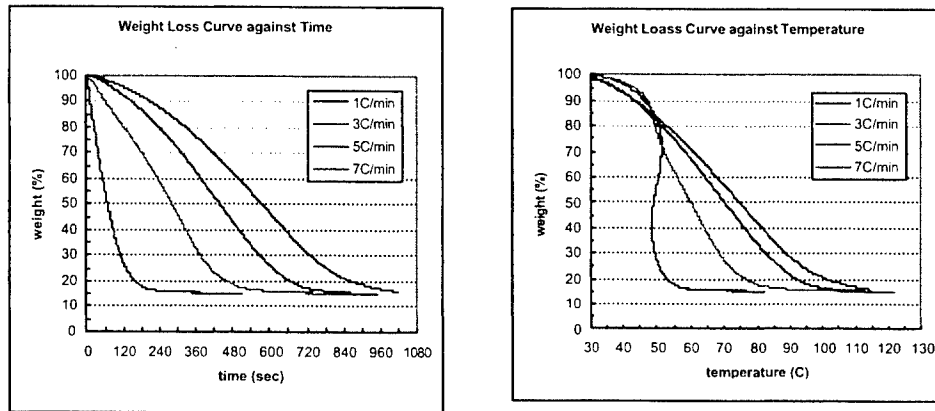
Fig 3.   Weight Loss Curve at various Heating Rate   (a) Mass Loss vs Temp   (b) Mass Loss vs Time

Compared with the activation energy for water diffusion, 1.7×10^4 J/g [13], the experimental relaxation energy of cartilage was larger than the energy of water evaporation possibly due to the resistance to diffusion within the matrix and the occurrence of a phase transition which alters molecular structure of the ECM. Using DSC, the reaction was found to be exothermic.
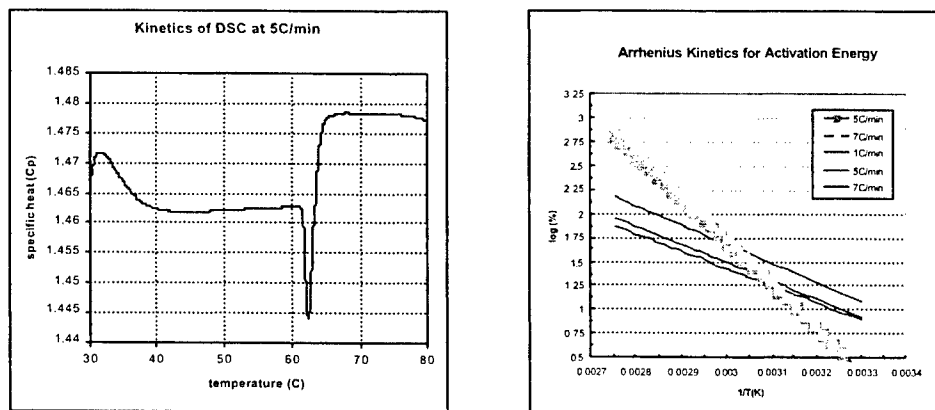
Fig 4.   Specific Heat Curve (a) Plot of Weight Loss against 1/T (b) Arrhenius Kinetic for Activation Energy

DSC measures heat flow, dH/dt in mJ/sec as a function of temperature relative to an inert reference and it is often used to characterize phase transitions. The heat flow curve for a cartilage specimen heated at 5 °C/min is illustrated in Figure 4(a) and the phase transition was identified using the baseline method for the evaluation phase transition behavior (7 Series/Unix Software, Part No. 0993-8706, Perkin-Elmer). The baseline is proportional to the heat capacity (Newton's law of heating). . The temperature of the phase transition was about 63.0-65°C and the activation energy of phase transition was

1.4-1.7 J/g and exothermic. The specific heat values derived using DSC as a function of temperature are listed in Table 2. Thermal conductivity values were obtained from Youn[19] (2000).

Table 2. Thermal Properties of Cartilage at various Temperatures

Temperature (K)	Specific Heat (J/gK)	Thermal Expansion (1/K)	Thermal Conductivity (W/mK)
303.15	1.4682	9.4733E-6	0.4801
305.45	1.4714	-	-
310.25	1.4640	-	-
323.15	1.4620	-	0.5007
334.55	1.4622	-	-
335.65	1.4443	-	-
338.55	1.4778	-	-
339.65	1.4783	-	-
347.85	1.4784	2.01523E-5	-

Thermal Mechanical Analysis and Temperature-Time Superposition

Dynamic Mechanical Thermal Analysis measures the modulus and damping (energy dissipation) properties of a material deformed under periodic stress. Figure 5. shows the difference between transversely and longitudinally oriented specimens in terms of shear modulus. The shear modulus of G_{13} (or G_{31}) was 9-12 MPa and the shear modulus (G_{23} or G_{21}, G_{21} or G_{21}) of longitudinally and transversely oriented specimens were 6-7 MPa. The transverse direction was slightly higher than the longitudinal direction by 5-10 %. These values decrease over time as calculated using the approximation to the Prony expansion. The values of shear modulus approached 1.5-2.0 MPa after a long time (> 20 min). Over short time intervals, the shear modulus was higher than values obtained over longer time intervals (t > 20 min.). This relaxation was observed (Figure 6) illustrating the viscous behavior of cartilage and the material performance was accurately evaluated in time domain.
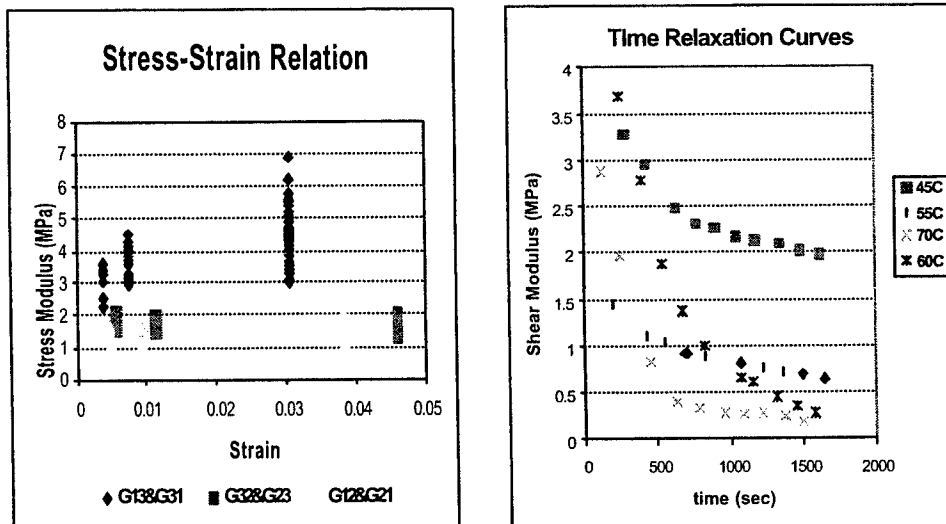
Fig 5. Stress-Strain Relation at Sample Position
Fig 6. Time Relaxation Curve of Shear Stress at various Temperatures (Prony Eq.)

The specimens were analyzed at oscillations of 0.1, 0.3, 1.0, 3.0 and 5.0 Hz allowing the generation of a set of master curves. For this experiment, a temperature of 337.15 K was selected as the phase transition temperature, as shown in Figure 7. Prediction of mechanical properties were estimated using the principle of time-temperature super position

principle, which states that the viscoelastic properties of materials are interdependent of both time and temperature and that there is an equivalency between the effects of time and temperature. Thus data collected at one temperature can be superimposed on data at a different temperature by shifting one of the curves along the time axis. The degree of time shifting of the shear modulus with respect to a reference can be described by Williams-Landel-Ferry (WLF) equation and Arrhenius activation model. The WLF equation is typically used to describe the time/temperature behavior of materials in the phase transition region. Above the phase transition temperature (337.15 K), the fractional free volume increases linearly with respect to temperature. We found that $C_1 = -4.7899\text{E-}7$ and $C_2 = 86.63$ (calibration constants for WLF equation) when Tg $=337.15$ K (Figure 7). The mechanical properties of cartilage at various temperatures were derived using comparable elasticity relations from Sokolnikoff [25] (viscoelatic Poisson's ratio [13] v=0.42) and DMTA measurements (Table 3).

Table 3. Mechanical Properties of Cartilage at various Temperature.

Temperature (K)	Modulus (MPa)			Poisson Ratio (v)
	Young (E)	Shear (G)	Bulk (K)	
303.24	8.9953	3.1673	18.740	0.42
312.50	8.0134	2.8216	16.694	0.42
319.20	6.9074	2.4322	14.390	0.42
328.70	5.6055	1.9737	11.678	0.42
335.01	4.6293	1.6300	9.6444	0.42
345.15	2.7396			

In the Arrhenius relation, E_a is the activation energy associated with the relaxation transition using;

$$\Delta H_a = 2.303 R C_1 C_2 T^2 / (C_2 + (T - T_g)) = R \times \frac{d \ln A_T}{d(1/T)} \qquad (q)$$

Fig 7. Time-Temperature Superposition Curve in Frequency Domain (WLF Eq.)

Based on the slope of ln A_T versus 1/T, the relaxation energy of cartilage specimen material was determined to be approximately 15 x 10^4 J/mole. This activation energy value obtained using DMTA is nearly 1.5 times that o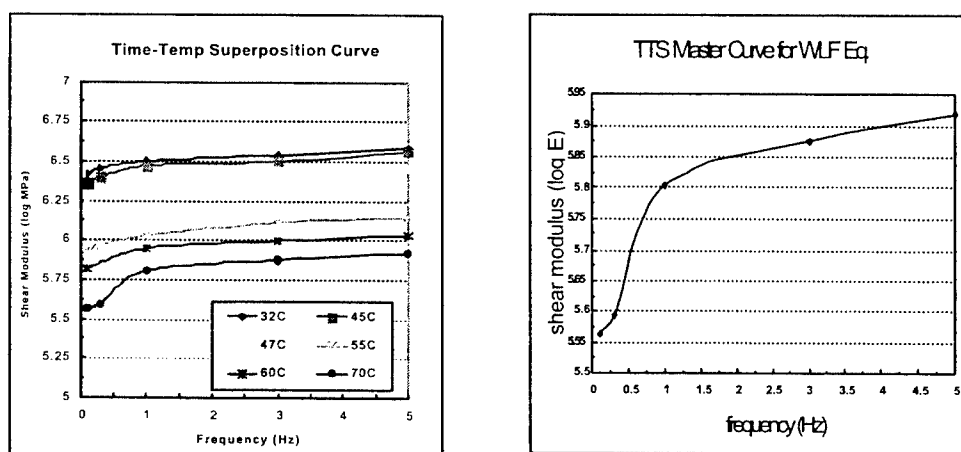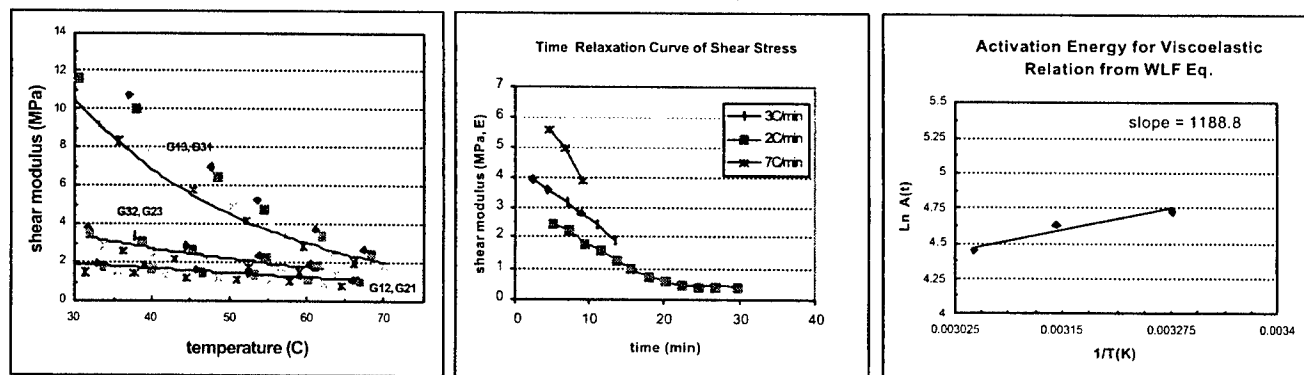btained using TGA . From the calculated value, the energy density required to induce the phase transformation accompanying shape change in cartilage may be estimated.

Analysis of Phase Behavior and Phase Transition Energies

The thermal and mechanical relaxation behavior of porcine nasal septal cartilage was examined using differential scanning calorimetry and dynamic mechanical thermal analysis. Calorimetry identified a slope change in heat flow at 63~65°C indicating the onset of a phase transition with a transition energy of 1.4~1.7 J/g for a 5°C/min heating rate. The specific heat was calculated by 7 Series/Unix Software at various temperatures and it was used in the simulation. From DSC curve we could find the effect of water evaporation below the point of the phase transition. Using TGA and DMTA, the relaxation energy of cartilage specimen was calculated and shown to be dependent on the orientation and the size of cartilage specimen, temperature and dehydration. The temperature of phase transition of DSC was compared with that of TGA and DMTA. The temperature from DSC was lower than those of TGA and DMTA.

Young's modulus was estimated using DMTA at various temperatures with shear and bulk moduli estimated using linear elasticity relations and relaxation data. The values in the transverse direction (z-axis, or short axis of the specimen) were larger than those in the longitudinal direction (x-axis) and the value of axial direction (in depth) was greatest. The relaxation energy was estimated to be 90-100 kJ/mole, which was 10 times larger than both the evaporation heat of free water, and the calculated experimental values obtained using DSC. The phase transition energy measured using DMTA and TGA was greater than estimates obtain using DSC The temperature time shift was estimated using DMTA and the master curve showed time and temperature dependence. The WLF calibration constants C_1 = - 4.7899E-7 and C_2 = 86.63 at Tg =337.15 K was calculated from the DMTA measurements.

DMTA may overestimate the relaxation energy as it incorporates the effect of water evaporation and effects of the mechanisms used to secure the specimen in a fixed position (clamps, jigs, etc.), as well as the effect of air damping. Derived measurements of relaxation energy using DMTA, must therefore account for these effects. Similarly, the phase transition energy calculated using TGA depends upon the specimen surface area. The second stage of the mass loss curve (about 25-40% mass loss) may suggest a phase transition state, as water evaporation is the hallmark of the first stage (100-75% mass loss), and the distinction may be due to the bound-water content in the sample. We assumed that the second stage of the mass loss curve was dominated by a phase transition. This value (90 kJ/mole) is smaller than the energy of phase transition determined using DMTA (~120 kJ/mole).

DMTA, DSC and TGA provided a means to obtain an estimate of the energy density required to reshape cartilage and may allow prediction of optimum laser power.. In our experiments, heating cartilage (2.0 mm thick) at a rate of 3-5°C/min or above 7°C/min produced excessive dehydration reducing the efficiency of thermal energy to induce a phase transition.

Numerical Simulation

Since the stress and temperature distributions in cartilage during laser irradiation and mechanical loading are interdependent, the thermo viscoelastic problem is fully coupled, i.e. solution of thermal and mechanical equations must be performed simultaneously. The estimated von Mises stresses and temperature profile are shown in Fig 10. It shows the von Mises' equivalent stresses and temperature distribution within cartilage slab and the equivalent stress at the irradiation site as a function of depth measured along the z direction from the top to bottom. The residual stress predictions within cartilage were based on infinitesimal and Lagrangian strain theory.

It is thought that the von Mises stress initially increases due to thermal expansion and then decreases due to structural relaxation after the phase transition. The highest stresses occur at a point 1.0 mm beneath the surface after 5 sec at 305~307K. This finding suggests that it is reasonable to approximately model the influence of residual stress distribution by simply assuming variations in thermal and mechanical properties. From the von Mises equivalent stress, the relaxation time was calculated for the specific thickness of cartilage specimen and the stress was strongly dependent of the thermal and mechanical properties of cartilage and temperature. Figure 10 shows the contours diagram of von Mises and temperature distribution in the three dimensional cartilage. From this finite element analysis we estimated the temperature and von Mises stress distribution in cartilage specimen assuming a linear isotropic thermoviscoelastic material and using experimental data

for thermal and mechanical properties. . After 9.5 seconds of heating, the model estimated the temperature 1.0 mm beneath the surface to be about 310K and the stress was reduced by 50%. The von Mises stress at the cartilage surface was 5.5 x 10^4 Pa and the stress at a depth 1.0 mm was 1.6 x 10^4 Pa after 8 sec. The von Mises stress of all points increased with time and reached maxilla after 9.5 sec.
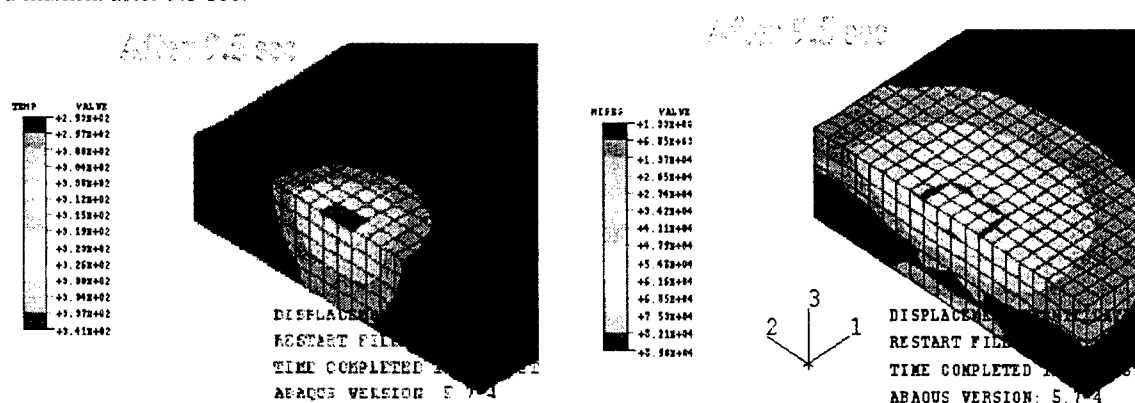
Fig 10. (a) Temperature (NT 11) contours for cartilage speciemn after 9.5 sec (Abaqus 5.7)
(b) Von Mises contours for cartilage specimen after 9.5 sec (Abaqus 5.7)
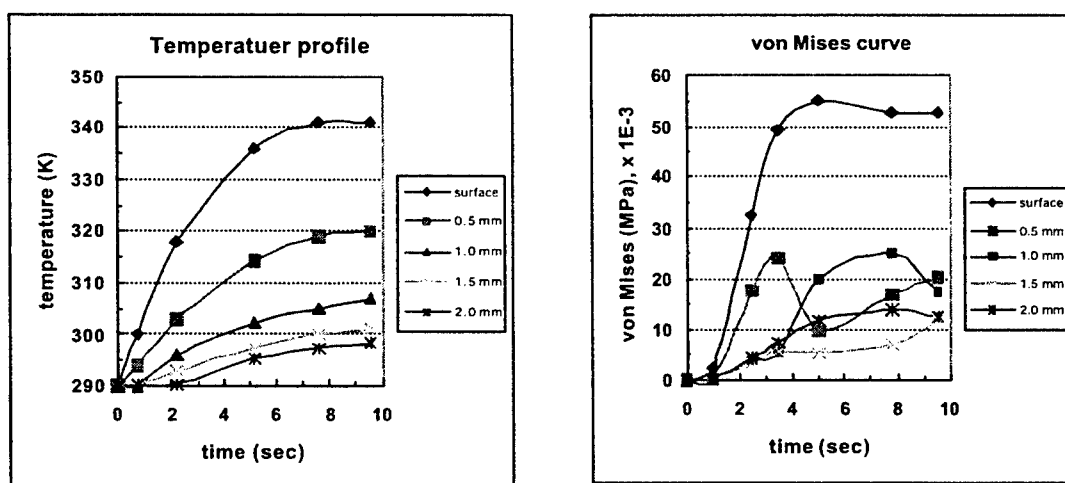
Fig 11. (a) Von Mises Equivalent Stress along the Different Depth under Heating Zone
(b) Temperature Changes on the Different Depth under Heating Zone

Conclusions

The thermal and mechanical properties of cartilage were estimated at various temperatures along with the relaxation energy using TGA, DSC, and DMTA. The physical properties obtained were incorporated into a finite element model assuming linear isotropic homogeneous behavior. The shear modulus was dependent on specimen orientation and demonstrated orthotropic or anisotropic mechanical behavior; this dependency alters the results of the simulation because the orthotropic and anisotropic properties were applied as the instantaneous elasticity in the stress displacement analysis.

In addition, measurement of thermal properties should account for heterogeneity of cartilage, which is a composite material; we assumed heat transfer was a linear process. In reality, the differential rates of heating occur in this tissue. The small changes in thermal properties, which were dependent on the specimen orientation, were not incorporated into this simulation as linear isotropic behavior was assumed. The water content of cartilage decreased during heating (TGA, DMTA) and this loss altered the mechanical properties. This loss is dependent on the ambient environmental conditions in which heating occurs and also upon the initial state of cartilage specimen. Water content affects the relaxation behavior.

The present finite element simulation coupled temperature-dependent viscoelastic behavior in the time domain as the inherent inhomogeneity, anisotropy and non-linearity of cartilage, make analytic solutions to modeling the stress distribution in loaded cartilage intractable. In this finite element analysis, cartilage was assumed to be a linear isotropic and homogeneous viscoelastic material, and we simulated a heat source using experimental temperature profile of laser irradiated cartilage with a fixed laser spot size.

At present we have not attempted to determine any of the material coefficients (i.e. the nonlinear permeability and solid matrix anisotropic viscoelastic coefficients) of cartilage, but plan to do so in the future using transient creep, tension and compression measurements. This study assumed linear viscoelastic material properties as a first approximation to the behavior of true biomaterials, which in reality are multiphasic. The biomechanical and thermal properties of cartilage do vary substantially with temperature. Future investigations must include the incorporation of the nonlinear and anisotropic properties (e.g. finite deformation). However the present finite element model provides a starting point for the development of more complex simulations of multiphasic behavior, which may ultimately lead to the optimization the laser mediated cartilage reshaping on other temperature-dependent phenomena in living tissues. Determination of the physiological stress distribution is problematic, as analytical solutions require a large number of assumptions on tissue behavior. The use of finite element techniques allows sensitivity analysis of the impact of these various assumptions on material behavior and provides a useful complimentary approach to experimental and clinical studies.

ACKNOWLEDGEMENTS

REFERENCES

1. Sobol E, B.V., Omel'chenko A, *Laser Shaping of Cartilage*. Proceedings SPIE, 1994. **2128**: p. 43-49.
2. Sobol E, B.V., Sviridov A, *Cartilage Reshaping with Holminum Laser*. Proceedings SPIE, 1996. **2623**: p. 556-559.
3. Sobol E, B.V., Sviridov A, *Phenomenon of Cartilage Reshaping using Moderate Heating and its Application in Otorhinolaryngology*. Proceedings SPIE, 1996. **2623**: p. 560-564.
4. Sobol E, S.A., Bagratashvili V, *Stress Relaxation and Cartilage Reshaping under Laser Radiation*. Proceedings SPIE, 1996. **2681**: p. 358-363.
5. Wong, B.J.F., *et al. Feedback controlled laser mediated cartilage reshaping*. 1998.
6. Wong, B.J.F., *et al., Stress relaxation of porcine septal cartilage during Nd:YAG (lambda =1.32 mu m) laser irradiation: mechanical, optical, and thermal responses*. Journal of Biomedical Optics, 1998. **3**(4): p. 409-14.
7. Sviridov A, S.E., Jones NS, Lowes J, *Effect of Holmium Laser Radiation on Stress, Temperature and Structure Alterations in Cartilage*. Laser in Medical Science, 1998. **13**: p. 73-77.
8. Wong BJF, M.T., Anvari B, *Measurement of Radiometric Surface Temperature and Integrated Back-Scattered Light Intensity During Feedback Controlled Laser Assisted Cartilage Reshaping*. Laser Medicine Science, 1998. **13**: p. 66-72.
9. Wong, B.J.F., *et al., Characterization of temperature-dependent biophysical properties during laser mediated cartilage reshaping*. IEEE Journal of Selected Topics in Quantum Electronics, 1999. **5**(4): p. 1095-102.
10. Bagratashvili, V.N., *et al., Thermal and diffusion processes in laser-induced stress relaxation and reshaping of cartilage*. Journal of Biomechanics, 1997. **30**(8): p. 813-17.
11. Edgard S.A, R.L., Spilker, *Finite Element Formulations for Hyperelastic Transversely Isotropic Biphasic Soft Tissues*. Computational Methods of Applicated Mechanical Engineering, 1998. **151**(513-538).
12. Madsen SJ, C.E., Wong BJF, *The Optical Properties of Porcine Nasal Cartilage*. IEEE Journal of Selected Topics in Quantum Electronics, 1995. **5**: p. 112-113.
13. Richard S., Shu C., *Handbook of Bioengineering.*,1987, USA; McGraw-Hill
14. Sobol E.N., *Phase Transformations and Ablation in Laser Treated Solids*. 1995, Canada: John Wiley & Sons. Inc.
15. Sobol E.N., A.P. Sviridov, and V.N. Bagratashvili. *Mechanisms of laser ablation of hard tissues*. 1995.
16. Sobol E.N. and M.S. Kitai, *Calculation of the kinetics of heating and structural changes in the cartilaginous tissue under the action of laser radiation*. Kvantovaya Elektronika, Moskva, 1998. **25**(7): p. 651-4.
17. Bagratashvili, V.N., *et al., Thermal and diffusion processes in laser-induced stress relaxation and reshaping of cartilage*. J Biomech, 1997. **30**(8): p. 813-7.
18. R.M. Christensen, *Theory of Viscoelasticity - An Introduction*, 1971, London Academic Press

19. Jong-In Y, Naresh B., Eunha K. Sergey T.,Brian W.,Thomas E.M ., *Optical and Thermal Properties of Nasal Septal Cartilage*, Laser and Surgery in Medicine, 2000, **27**: p119-128

20. Gutknecht N, K.S., Moritz A, Mitteermayer C, Lampert F., *Effects of Nd:YAG laser irradiation on monolayer cell cultures*. Lasers Surgery Medicine, 1998. **22**: p. 30-36.

21. Zienkiewicz O.C., T.R., *Basic Formulation and Linea Problems*. The Finite Element Method. Vol. 1. 1988, London: McGraw-Hill.

22. Zienkiewicz O.C., T.R., *Solid and Fluid Mechanics. Non-linear Problems*. The Finite Element Method. Vol. 2. 1988, London: McGraw-Hill.

23. Huiskes, R. and E.Y. Chao, *A survey of finite element analysis in orthopedic biomechanics: the first decade*. J Biomech, 1983. **16**(6): p. 385-409.

24. Mow VC, A.G., Rosenwasser MP, *Development of finite element models for diarthrodial joints In computational Methods in Bioengineering*. Vol. 9. 1988, New York: American Society of Mechanical Engineers.

25. Sokolnikoff I.S.,*Mathematical Theory of Elasticity*, 2nd ed. McGraw-Hill, New York, 1956

26. Wong B.J., Milner T.E., Kim H.K., Chao K., Sun C.H., Sobol E.N., Nelson J.S., *Proteoglycan Synthesis in Porcine Nasal Cartilage Grafts Following Nd:YAG ($\lambda=1.32\mu m$) Laser Mediated Reshaping*, Photochemistry and Photobiology, 2000, **71**(2); p.218-24

27. A.M. Karamzadeh, A. Rasouli, Tanenbaum, T.E. Milner, J.S. Nelson, B.J.F. Wong, Laser Mediated Cartilage Reshaping with Feedback Controlled Cryogen Spray Cooling; Biophysical Properties and Viability, Laser Surg Med, 2001, **28**: p 1-10

28. D.S. Gray, J.A. Kimball, B.J.F. Wong, *Shape Retention in Porcine Septal Cartilage Following Nd:YAG ($\lambda=1.32\mu m$) Laser MediatedReshaping*, in press

29. Rasouli Alexandre, Kim Charlton C, Basu Reshmi, Wong Brian J., *Use Flow Cytometry to Assess Chondrocyte Viability after Laser Reshaping of Cartilage*, Proceeding of SPIE, 2000, **3907**; p.328-338

30. Brian J.F. Wong, Kenneth K.H. Chao, Hong K. Kim, Eugene A. Chu, Xavier Dao, Mark Gaon, Chung-Ho Sun, J. SSStuart Nelson, *The Porcine and Lagomorph Septal Cartilage; Models for Tissue Engineering and Morphologic Cartilage Research*, in press

Study of the Luminous Plasma and Plume Produced on Interaction of a XeCl Laser and Biological Tissues

Andrea K Murray[*], Mark R Dickinson (Laser Photonics Group, Dept. of Physics and Astronomy, Univ. of Manchester, Manchester, M13 9PL, UK)

ABSTRACT

Above the ablation threshold the removal of tissue is characterised by a luminous plasma, followed by a plume of non-luminous debris. Both the plasma and the plume are capable of shielding the ablation site, attenuating the beam and decreasing the ablation rate significantly at high numbers of pulses (n) and high fluence. The ablation of several biological tissues by a XeCl excimer laser at 308 nm has been studied. The laser pulse length is 200 ns, around a factor of 10 longer than previously reported studies. In order to study the plume's effect on the ablation rate it has been captured using an Imacon 468 camera capable of 1×10^8 frames per second. We have calculated the evolutionary speed and the extent of the plasma and ensuing debris with respect to pulse repetition rate (PRR), n and energy for a range of tissues. Probe beam experiments have also been carried out to confirm these results. With this data we can determine the amount of time that the tissue is shielded on the time scale of the incoming pulses and use the results to help explain the ablation rate measurements. A maximum velocity of 2.58×10^4 m/s was found for dentine and the tissue was found to be shielded for a maximum of 120 μs by the luminous plasma and 10 ms by the non-luminous plume.

Laser ablation, dentine, enamel, high speed photography, plasma velocity

1. INTRODUCTION

Many laser wavelengths have been studied for medical applications, from ophthalmology[1] to angioplasty[2] to dentistry[3]. In the majority of cases IR lasers are used due to their high ablation rates, useful for cutting and removing tissues or for their haemostatic effects. The main disadvantage to their use is a temperature rise in the surrounding tissue which can cause thermal damage and necrosis of cells around the target site[4]. Strong water absorption peaks at IR wavelengths makes cooling of the tissue difficult, especially as the crater depth increases and water fills the hole, preventing radiation reaching its base. UV lasers are preferred to IR lasers because they are able remove tissue that travels away from the ablation site carrying with it energy which would otherwise have remained in the peripheral tissue as heat. This 'cold' ablation causes little or no thermal damage and as the absorption of water is low between 300-700 nm water can be used for cooling.

For both IR and UV lasers incident on tissue[5][6] it has been found that above the ablation threshold the ablation rate per pulse rises proportionally with increasing fluence until a saturation fluence is reached whereby it levels off. A decrease in the ablation depth per pulse is found with increasing numbers of pulses at constant fluence. These effects have been observed for several biotissues and materials ablation[7] and are believed to be caused by a number of factors. One reason may be that as the crater increases in depth its walls absorb more of the incoming energy, decreasing the ablation capabilities of the pulse. The increased depth could also be responsible for hindering the escape of ablated debris, hence stopping incidence of the next (or the end of the original) laser pulse on the base of the hole. The plume of tissue produced upon ablation is ejected from the surface of the tissue. Initially this takes the form of a luminous plasma, travelling away from the surface of the tissue and towards the incoming pulse. The removed tissue may block advancing pulses, attenuating the available energy for further ablation.

In an attempt to understand the decrease in ablation depth per pulse for varying parameters an Imacon 468 high speed camera has been used to capture the dynamics of the luminous plasma. A XeCl excimer laser (200+ ns, 308 nm) has been used to study the plume produced upon ablation of both hard and soft tissues over a range of energies, pulse repetition rates and numbers of pulses.

---

[*] andi@fs4.ph.man.ac.uk; phone +44 (0)161 275 4292; fax +44 (0)161 275 4293

As the plume begins to fade it is no longer visible to the camera therefore a second experiment, attenuation of a beam probe, was carried out to determine whether the plume remained to block the beam as its brightness decreased or whether its density also decreased to allow a new pulse to permeate through to the tissue.

2. METHOD

A XeCl excimer laser system (LAIS Dymer 200+), lasing at 308 nm, with a pulse width of ~200 ns was used. The maximum available energy per pulse was ~150 mJ, monitored by an in-built digital energy meter. The pulses were delivered in continuous-pulsing mode at PRRs between 5 and 25 Hz in steps of 5 Hz. The cumulative number of pulses was recorded on a digital display panel for reference. The laser was also operable via an external trigger providing additional PRRs or a single pulse option.

The high speed digital camera capturing the plume of tissue was an Imacon 468 whose maximum speed was 1×10^8 frames per second. In total 8 frames each from a separate CCD module were taken and transferred to a PC and monitor. Each of the available frames could be independently controlled for exposure duration and gain sensitivity. Each inter-frame time
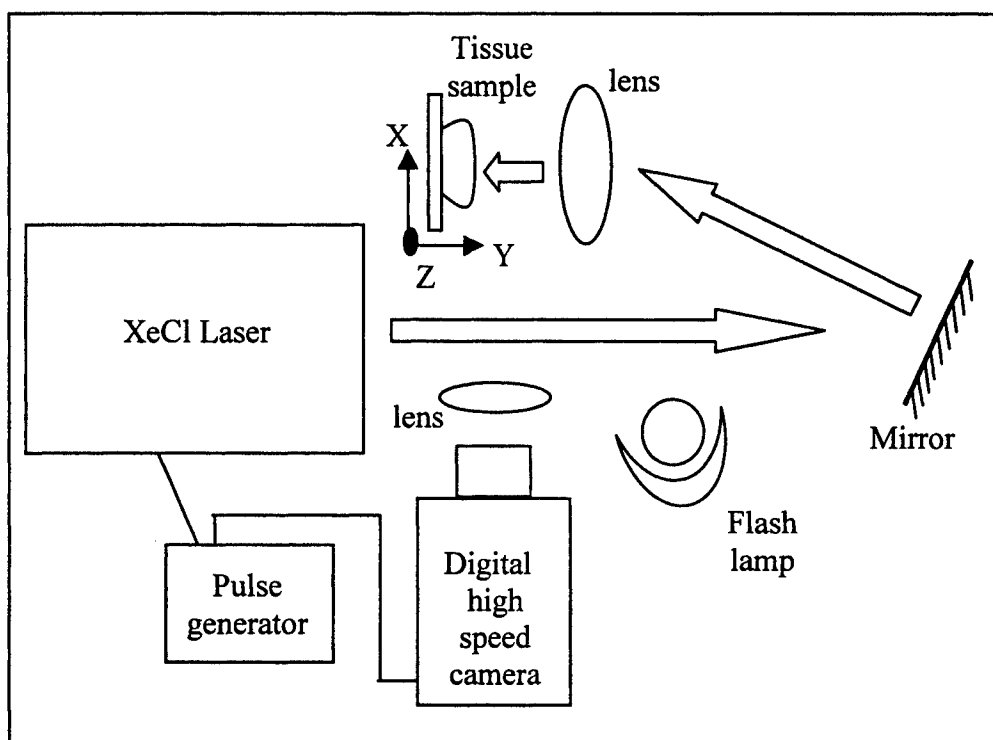
Figure 1: Experimental set-up for digital high speed photographs of the plume of debris created upon ablation.

was also independent and the delay time between trigger and first exposure was variable. The minimum temporal resolution of the system was 10 ns. The frames were available immediately on the monitor following the exposure, allowing confirmation that the plume had been captured and giving an instant time scale for the ablation event so that further frames could be taken. At the onset of ablation the plasma provides enough light for the event to be easily observed but as the luminosity decreases a flash lamp was used to illuminate the plume. For each frame the exposure time and gain was set for optimum observation of the plume.

Dentine and enamel samples were taken from healthy, human molars stored in 10% neutral buffered formalyn and removed just before use. Samples were parallel-sided slices of ~1-2 mm in thickness, cut by a diamond saw. Chicken flesh and bone

were obtained fresh from the butcher on the day of the experiment, stored refrigerated and allowed to reach room temperature before use. The flesh was cut into thin slices and the bone was cut normal to its length into samples ~2 cm long.

During ablation the samples were placed on a translation stage with the flat surface to be lased perpendicular to the direction of the beam (figure 1). The laser beam was focussed down on to the tissue using a fused silica lens of focal length 2.5 cm, minimum achievable spot size was $0.50 \pm 0.05x\ 10^{-3}\ cm^2$. Since the ablation depth of the crater was much smaller than the depth of focus of the system the samples were not translated along the beam towards the lens to compensate for the ablated surface moving out of the focal plane during the production of any single crater. The ablated surface was assumed to be in the focal plane at all times. A lens was placed between the camera and the plume to magnify the images. The size of these images were calibrated using images of the teeth slices, whose exact width was known. The plume of debris was found to increase in length as the leading edge moved away from the tooth but the left hand end remained at the edge of the sample. The leading edge was used to determine velocities by measuring its distance from the trailing edge i.e. the difference in the length of the plumes gave the velocity.
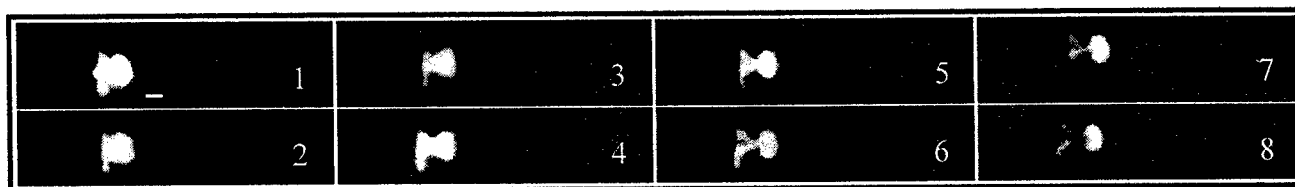

Figure 2: A typical luminous ablation plume on dentine. The laser is incident on the tissue from the right hand side of the frame and the flat surface of the tooth lies at the base of the plume on the left hand side. From the first frame (1) the plume can be seen to develop into a mushroom-like cloud. The velocity of the plume was measured for the forward leading edge. For this set of frames the exposure time for each frame was 10 ns, the inter-frame time was 3 us and the energy was 20 mJ. The bar represents 1 mm.
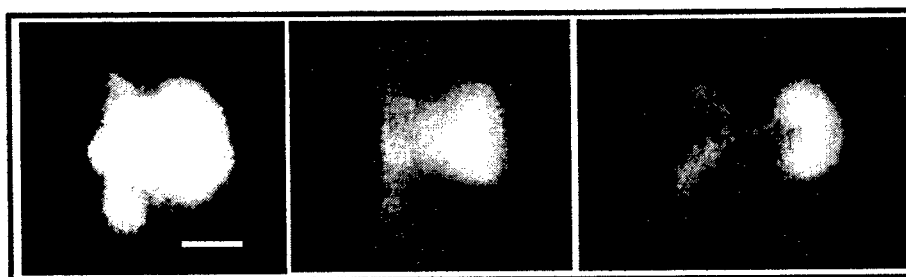
Figure 3: Frames 1, 3 and 8 of figure 2 enlarged. The bar represents 1mm.

The aim of the study was to determine how the luminous plume was affected by varying several parameters of the laser and how it differed for several tissues. This was achieved by varying the energy, pulse repetition rate (PRR), number of pulses individually whilst keeping all other variables constant. To compare ablation of the four tissues, plumes were studied at a constant energy for each tissue (22 mJ), each plume was the product of a single pulse. Initially a set of frames was taken to determine the overall length of time that the plasma remained visible, then further sets were taken to capture the first few nanoseconds of the event. The inter-frame time was then increased in steps to follow it through to its conclusion. To compare the effects of numbers of pulses, PRR and energy dentine was used. For laser energies of 7.5, 11, 15, 20 and 31 mJ frames were taken for plumes after one pulse was incident, individual pulses were produced using a pulse generator. PRRs of 1, 2, 5, 10 and 20 Hz were compared for plumes after 100 pulses at a constant energy of 23 mJ. The pulse generator was used to provide repetition rates lower than those available from the laser to give a broader range of frequencies. The plume was also observed for 1 to 1000 pulses incident on the dentine at a rate of 5 Hz and energy of 24 mJ.

For each variable a number of properties of the plume were studied: The physical size of the plume, length (along the axis of motion) and width (perpendicular to the axis), the delay time between the incidence of laser radiation and ablation, the

time for which the plume remains in front of the sample blocking oncoming pulses and the evolution of the velocity over time. The velocity of the plume was determined using the leading edge of the plume which moved away from the surface of the tissue whilst the trailing edge remained at the surface of the sample. A typical example of a plume (from dentine) is present in figures 2 and 3. The time between the incoming laser pulse incident on the sample and the beginning of the
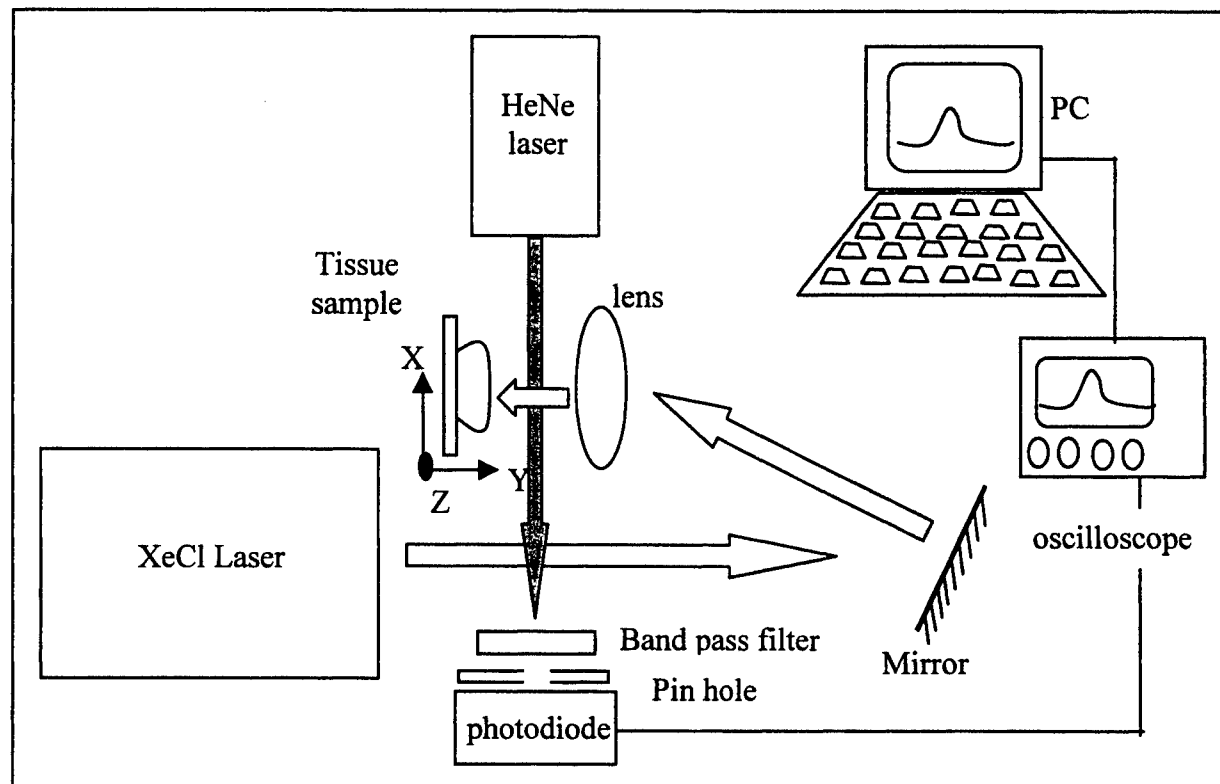
Figure 4: Experimental set-up for probe beam attenuation to determine the relative density of the plume produced upon ablation and its lifetime.

ablation event was particularly difficult to determine due to the inaccuracy of the pulse generator. The time delay between triggering the laser and the camera was found to be up to 50 ns. This meant that unless the whole event both before the incidence of the laser to the beginning of the ablation event was captured within the 8 frames the error on the start time would be several hundred percent. Consequently incidence data was not available for all data.

As the plasma's luminosity decreased and it was no longer visible to the camera, it was unclear whether its density also reduced and the plume dispersed thus no longer blocking the crater from the incident pulses. After two flash lamps had been unsuccessful in illuminating the non-luminous plume an alternative method was carried out. Attenuation of a probe beam was carried out to determine how the density of the plume varied with time. A probe HeNe laser beam, (Figure 4) perpendicular to the XeCl laser and the direction of the plume was placed across the plume's path. The HeNe beam was passed through a high band pass filter, pinhole, was detected by a reverse-bias silicon photodiode (RS OSD 5.8-7Q), sent to a Gould oscilloscope (DSO 4096) and then stored on a PC for later analysis. As the plume passed through the probe beam diffraction and refraction occurred due to the distortion of the air. By monitoring the time that the HeNe beam was distorted we were able to determine the presence of the plume after its luminosity had decreased.

3. RESULTS

Upon enlargement of the frames the resolution of individual particles was not possible. The debris deposited on a slide in the path of the plume was found to conglomerate therefore the size of debris originating in the ablation process has yet to be determined.

3.1 Effect of energy on the properties of the plasma

Table 1: Properties of the plasma for differing pulse energies

Energy incident on tissue mJ	Average distance travelled mm	Average width mm	Time between incidence and ablation μs	Maximum velocity mm/μs
31 set 1	3.50	1.50	0.01	25.74
31 set 2	2.80	1.90-2.20	0.03	24.31
20	1.38	1.20	0.03	21.45
15	0.79	1.20-1.60	0.01	14.39
11	0.53	1.40-2.00	-	14.30
7.5	0.02	0.40	0.01	28.60

No data was collected for the dependence on pulse energy of the time for which the tissue was blocked by the plasma.

3.1.1 The effect of pulse energy on the velocity of the plasma

The distance travelled by the plume front (the plume length) varies logarithmically with time as shown in figure 5. A line of best fit has been used for clarity. It can be seen that at high energies the luminous plume reaches further than at lower energies. For two sets of data taken at the same energy there is a difference in the velocities possibly due to pulse to pulse energy variation or inhomogeneities of the tissue samples. As the energies become closer the data points begin to overlap, the scattering of the data again due to tissue variations. Figures 6 and 7 show lines of best for an exponential decrease in velocity with time. As pulse energy is increased the velocity of the plume is found to increase as would be expected by kinetic energy arguments. The initial velocity of the plume in the first 10-50 ns is supersonic but ever decelerating. The logarithmic saturation effect on the distance travelled over time is a consequence of the frictional forces acting on the plume to slow it down.

The maximum velocity of the plume was found to increase, in general, with increasing energy as shown in figure 8. The exception to this rule was at pulse energy of 7.5 mJ, which had the highest maximum velocity of 28.6 mm/μs equal to 2.8 x 10^4 m/s.
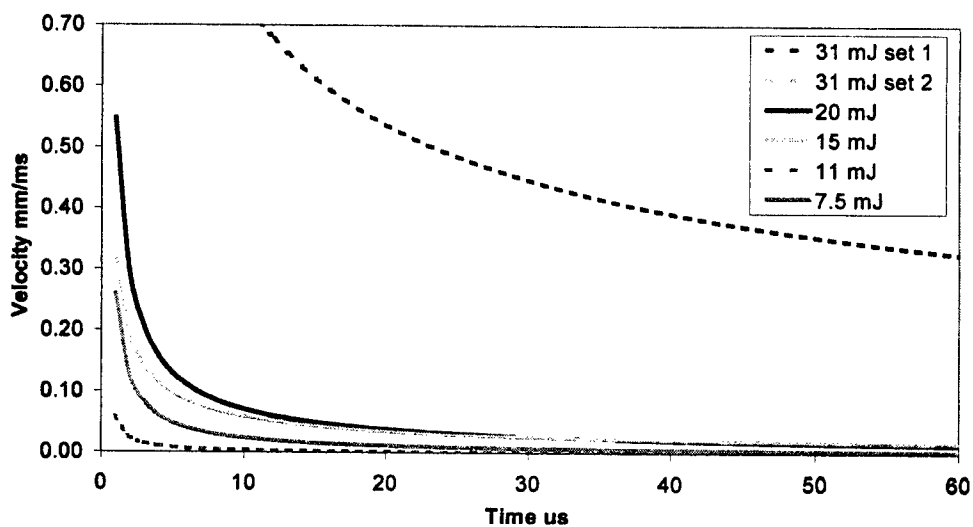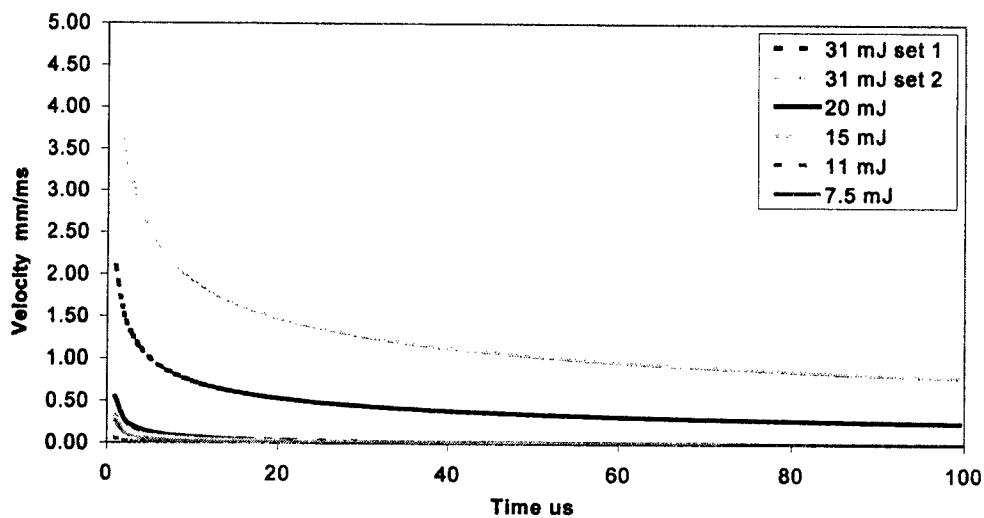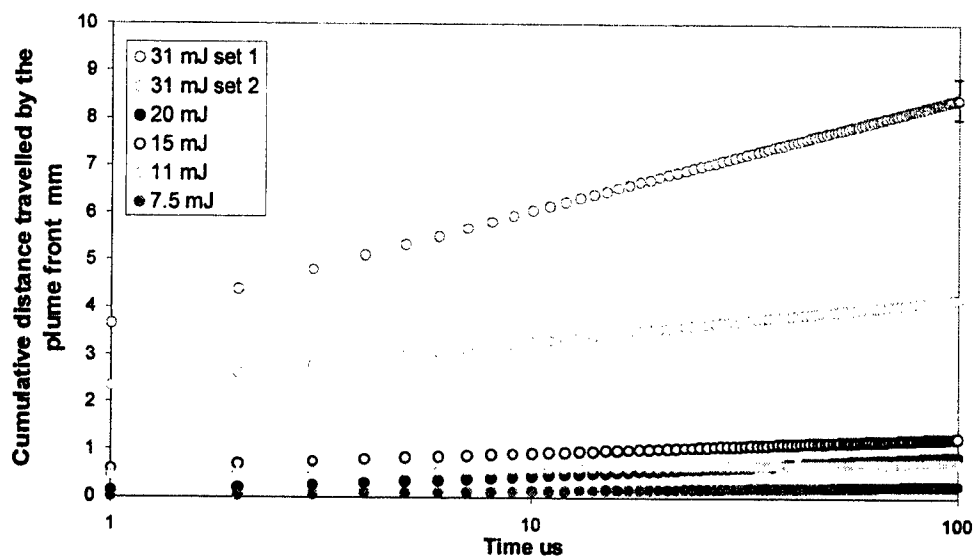
Figures 5, 6 & 7: Figure 5 (top) shows the cumulative distance travelled by the front edge of the plasma over (logarithmic) time for different energies. Graphs 6 and 7 (middle and bottom) show the variation of velocity of the plasma over time for differing energies incident on the dentine.
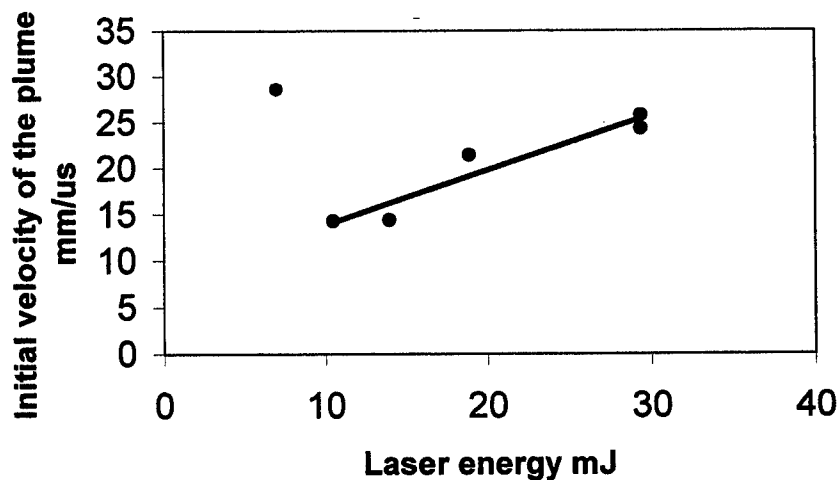
Figure 8: The relationship between the initial velocity (first 10-20 ns) of the plume
and the incident pulse energy on the tissue.

3.1.2 Dimensions of the plasma with varying energy

The measurement of the width of the plume was taken once the maximum width had been reached. After this point the width of the plume did not change, this is the measurement that was monitored. The width of the plume was found to be proportional to the energy as is shown in figure 9. The length of the plume was also found to be larger with increasing pulse energy.
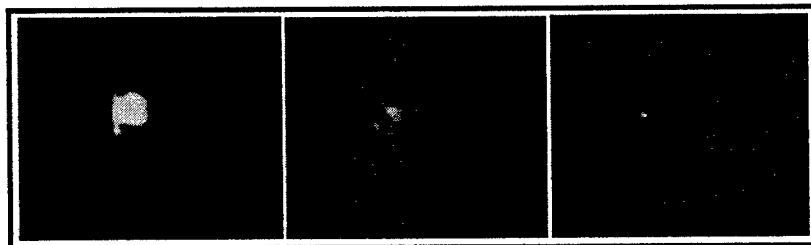
Figure 9: Comparison of ablation plasma at energies of 20, 15, 7.5 mJ
respectively, all with the same magnification as in figure 2.

3.13 Time between incidence of the laser and the ablation event as a function of pulse energy

The time between the laser pulse's incidence on the tissue and the ablation event beginning was found to be independent of the pulse energy. The ablation was found to occur 10 ns after incidence of the pulse with the constraint of the time resolution of the system (10 ns) giving 100 % errors. This implies that the beginning of the pulse causes an ablation plasma which may block the rest of that same pulse from reaching the surface.

3.2 Effect of PRR on the plasma

Table 2: Properties of the plasma with varying PRRs

PRR pulses per second	Average length (distance travelled by plume front) mm	Average width mm	Average Duration μs	Maximum velocity mm/μs
1	1.60-1.86	1.50	42.0	0.26
2	1.86	1.50	68.0-94.0	0.29
5	1.70	1.50	81.0-94.0	0.11
10	1.86	1.50	81.0-94.0	0.23
20	2.72	1.50	94.0-120.0	0.29

3.2.1 Velocity of the plasma with varying pulse frequency
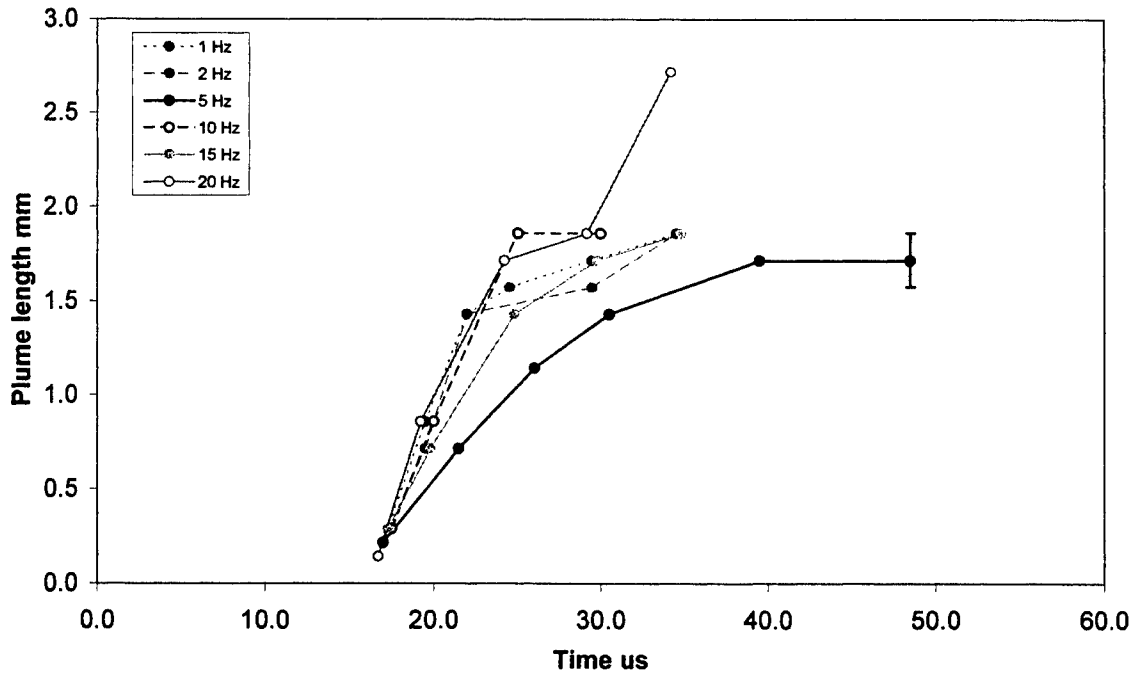
Figure 10: The variation of plume length over time for several PRRs

The velocity of the plume front was not found to be dependent on the PRR. The relationship between length of the plume over time is demonstrated in figure 10. As can be seen from the gradients of these data points increasing the PRR has a random effect on each set of data. Any variation of the gradient due to differing pulse frequency can be attributed to content variability of the tissue.

3.2.2 The effect of PRR on the size and longevity of the plasma

Both the width and the length of the plume were found to be independent of the incident pulse rate. The plumes due to high pulse repetition rates were found to shield the tissue for longer than low pulse frequencies.

3.3 Plasma changes as the number of pulses increases

Table 3: Properties of the plasma with increasing numbers of pulses

Number of pulses	Average length (disance travelled by leading edge) mm	Average width mm	Average Duration µs	Maximum velocity mm/µs
1	3.29	2.86	45.0	0.30
11	2.57	2.57	29.0	0.14
40	1.72	2.15	13.0	0.14
300	1.43	1.72	21.0	0.11
700	0.57	1.14	8.5	0.12
1000	0.57	0.86	4.6	0.23

3.3.1 Velocity of the plasma as number of pulses increase

As figure 11 shows the velocity of the plasma was found in general to decrease with increasing numbers of pulses. As with the variation in energy the results are not so clear cut as to be able to find a definite difference in velocity with two sets of data close together in number of pulses however for numbers of pulses between 1 and 50 the velocity is greater than for 100 to 1000.
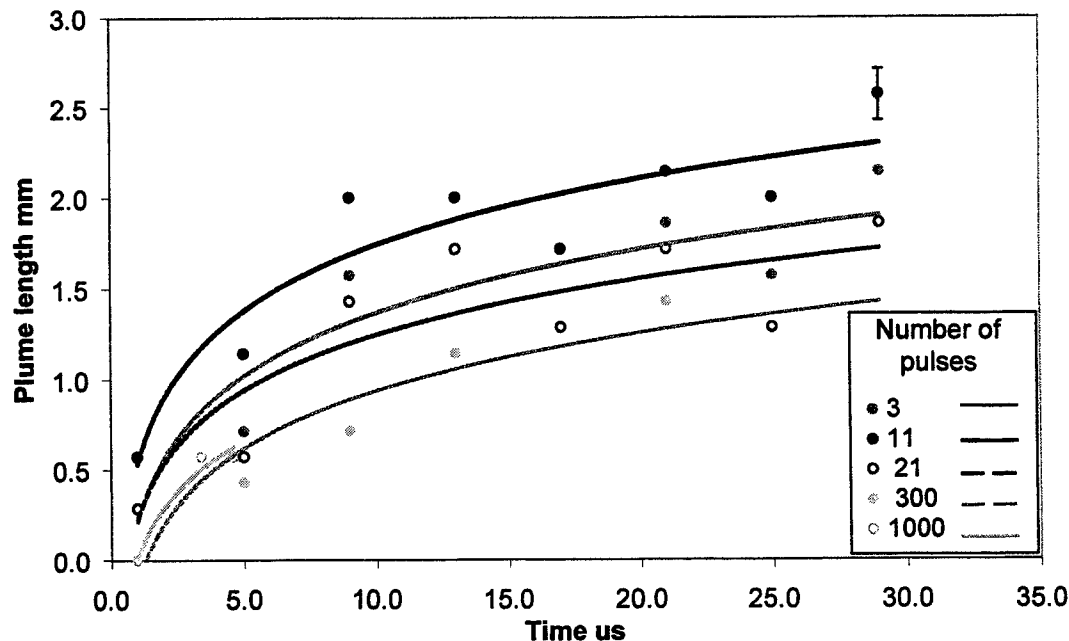
Figure 11: The cumulative plume length over time for differing numbers of pulses

3.3.2 The effect of increasing the number of pulses on size, lifetime and temporal incidence threshold of the plasma

The size of the plume was found to decrease, both in length and width with increasing numbers of pulses as shown in figure 12. The duration of the luminous plasma also decreased with increasing numbers of pulses. The time between the incidence of the laser pulse and the beginning of ablation was found to be unchanged by the number of pulses.
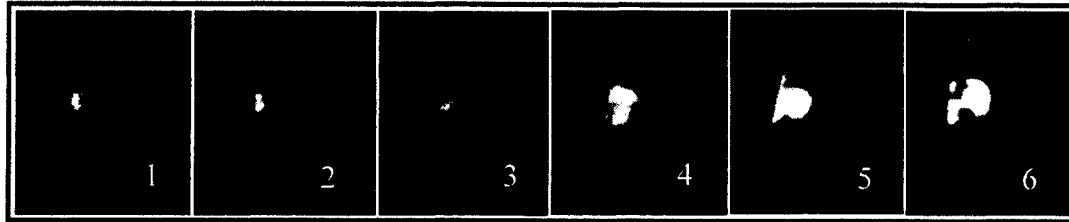
Figure 12: Ablative plumes due to increasing numbers of pulses. Frame 1) represents the 1000th pulse, 2) 600 pulses, 3) 300 pulses, 4) 50pulses, 5) 9 pulses and 6) one pulse.

3.4 DEPENDENCE OF THE PROPERTIES OF THE PLASMA ON TISSUE TYPE

Table 4: Properties of the plume for different tissues

Tissue	Average length (distance travelled) mm	Average width mm	Average Duration of the visible plasma μs	Maximum velocity mm/μs
Dentine	1.50-1.75	1.58	30.0-45.0	0.28
Enamel	0.30-1.00	0.72	30.0-45.0	0.13
Chicken bone	0.30-0.75	0.72	0.5-3.0	3.58
Chicken flesh	0.50-0.75	0.57	0.5-3.0	1.43

3.4.1 Variation of the velocity of the plasma from different tissues
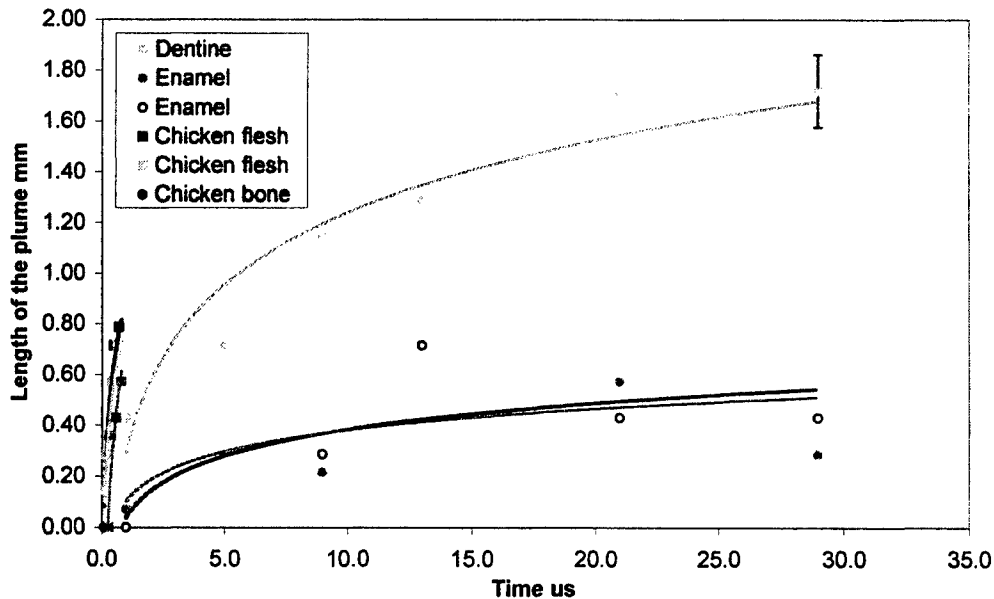
Figure 13: Cumulative length of the plasma with time for different tissues

The distances reached by the luminous plasmas from enamel, chicken bone and chicken flesh were similar however these chicken tissue plasmas reached these distances a factor of ten faster than those of dentine and enamel, thus the velocity of the chicken bone and flesh were much larger. Upon closer inspection it was found that chicken bone plasma travelled faster than chicken flesh and dentine faster than enamel. Figures 13 and 14 show how the distance travelled by the front edge of the plasma varies over time, figure 14 is on a smaller time scale than 13.

3.4.2 Size and lifetime of the plasma from different tissues
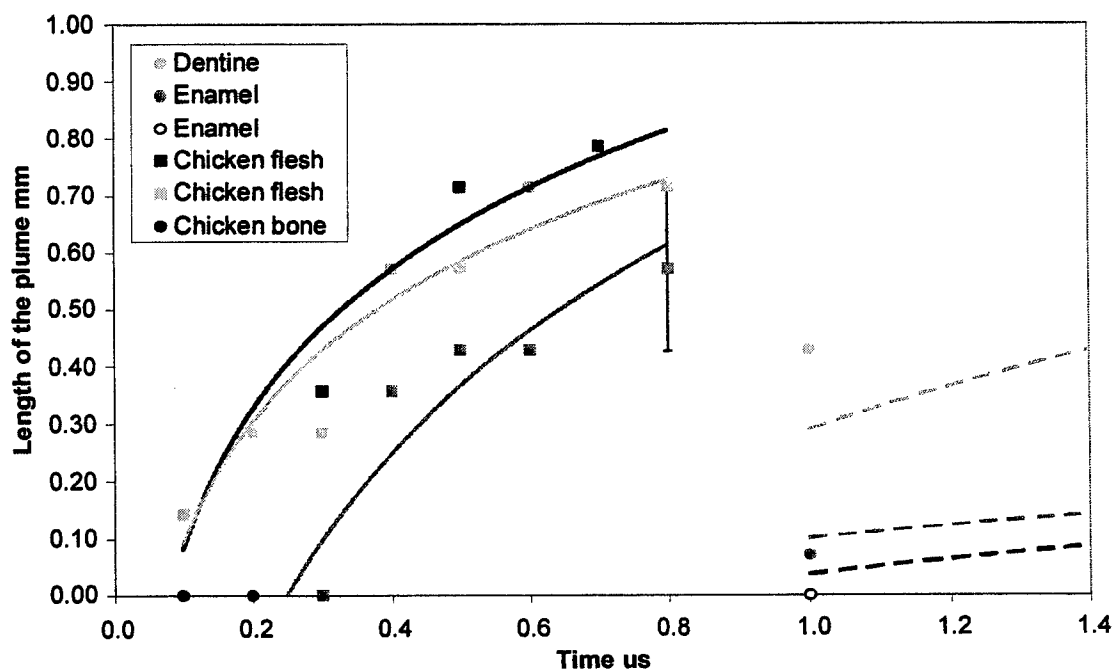
Figure 14: Cumulative length of the plasma with time for different tissues. An expansion of the lower end of the scale of figure 13. The lines on the right hand side of the plot are those of enamel and dentine.

For all four tissues the plumes were found to decrease in width in the order of dentine, enamel, chicken bone and chicken flesh. Length measurements are similar but with the two chicken tissues being almost the same. The plumes of dentine and enamel, chicken flesh and bone were found to last up to 45 μs and 1 μs respectively.

3.5 ATTENUATION OF THE PROBE BEAM
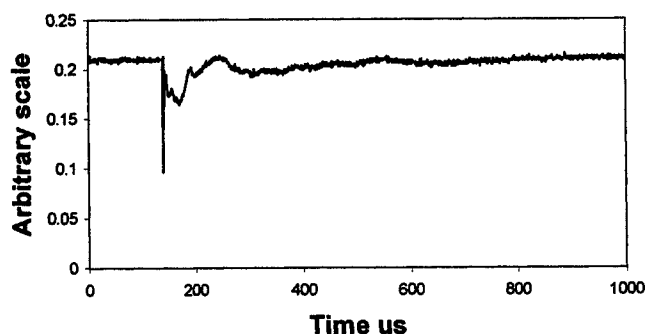
Figure 15: An oscilloscope trace of the diffraction of a HeNe beam caused by the disturbance in air due to the plume of debris

Using oscilloscope traces similar to that in figure 15 (at an pulse energy of ~150 mJ) the plasma and plume were determined to last for 10 ms. This would block oncoming pulses at repetition rates above 100 Hz but would not affect the PRRs available for this laser system.

4. DISCUSSION AND CONCLUSIONS

The study of the luminous plasma produced on ablation of tissue by a long pulsed XeCl excimer laser has shown that in its initial stages, below 10 ns (the maximum time resolution of the system) the debris is ejected from the sample supersonically at velocities up to 2.58×10^4 m/s. The laser was incident in the horizontal plane and yet gravity had no noticeable effect on the plume. Whilst in its luminous stage the plasma can shield tissue for up to 120 μs. Initially the plasma first forms a thin jet from the tissue surface. The base of the jet remains at the surface of the sample while the leading edge surges forward, back towards the direction of the laser pulse. After about 500 ns the plasma begins to slow down due to the friction caused by the surrounding air molecules. As this happens the plume begins to form a mushroom like shape and the velocity of the already decelerating plasma drops quickly. This corresponds to a logarithmic saturation effect in the distance/time graphs found. This slower movement continues for several μs depending on the laser parameters before the plume loses its luminous properties and can no longer be visually tracked. It should be noted that the maximum velocity obtained corresponds well with both IR[8] and UV[9] laser studies previously carried out on tissues at shorter pulse lengths.

It was found that for increasing pulse energies the velocity of the plasma increased. The scattering of the data points due to the variation of the tissue components meant that at close energies the data occasionally overlapped. For two sets of data which were taken at the same energy a variation in velocity occurred, probably for the same reason or because of pulse to pulse differences. The width of the plume and the distance that the leading edge travelled from the sample also increased with energy. The time between the incidence of the laser pulse and the ablation event occurring was found to be independent of pulse energy, this implies that the time for ablation to occur is a set value, and above threshold it will be fixed but characteristic of tissue.

The pulse repetition rate had no effect on velocity, the width of the plume or how far it travelled (the plume length) however higher pulse frequencies produced plumes which lasted for longer, up to 120 μs. In previous experiments[10] it has been found that increasing PRR causes a rise in ablation rates however these two facts contradict each other. Longer shielding would imply less energy getting through the debris to the tissue leading to a lower ablation rate.

An increase in the number of pulses was found to decrease the luminous time of the plasma, perhaps due to more of the energy from the beam being absorbed in deeper holes or debris trapped inside, thus less ablation occurs and less energy escapes to make the plasma luminous. Both the distance travelled i.e. the length of the plasma and its width decreased with increasing numbers of pulses and a general decrease in velocity accompanies increasing numbers again possibly due to absorption of the incoming pulse energy in the hole, shielding plasma and trapped debris.

Ablation of different tissues demonstrated that those with a high water content, chicken bone and flesh had a much higher ablation plume velocity than enamel and dentine. The luminous plumes of the two chicken tissues lasted a factor of 10 less than those of dentine and enamel and yet reached the same distance as the enamel plumes. The dentine and enamel plumes were found to be much larger than those of both chicken flesh and bone.

The attenuation of the probe beam gave a lifetime for the plume of ~10 ms. This implies that the plume could continue to shield the tissue after the luminous phase is over. It can be assumed that the same parameters which affect the luminous part of the ablation plume will have similar effects on the non luminous stage.

ACKNOWLEDGEMENTS

REFERENCES

1. S.L. Jacques, D.J. McAuliffe, I.H. Blank, and J.A. Parrish, "Controlled Removal of Human Stratum Corneum by a Pulsed Laser," Journal of Investigative Dermatology **88**, pp. 88-93, 1987.

2. T.K. Bohley, F. Aparicio, G.S. Derrickson, R.A. Golobic, K.P. Grace, I. Trefil, and G.A. Murray, "An excimer system for coronary angioplasty," *Laser Surgery: Advanced Characterisation, Therapeutics, and Systems II*, 1200, pp. 480-486, 1990.

3. U. Keller, and R. Hibst, "Lasers in dentistry clinical applications today and tomorrow," *Dental Applications of Lasers*, 2080, pp. 2-7, 1993.

4. G.J. Pearson, and A.V. McDonald, "Invited Review Use of Infra-red and Ultra-violet Lasers in the Removal of Dental Hard Tissue," Lasers in Medical Science **9**, pp. 227-237, 1994.

5. J.A. Izatt, D Albagli, M Britton, J.M. Jubas, I Itzkan, and M.S. Feld, "Wavelength Dependence of Pulsed Laser Ablation of Calcified Tissue," Lasers in Surgery and Medicine **11**, pp. 238-249, 1991.

6. J. Neev, D.V. Raney, W.E. Whalen, J.T. Fujishige, P.D. Ho, J.V. McGrann, and M.W. Berns, " Dentin Ablation with Two Excimer Lasers: A Comparative Study of Physical Characteristics, " Lasers in Life Sciences **5**, pp. 129-153, 1992.

7. H. Hame, R. Voss, T. Papioannou, W. Grundfest, and R. Johnson, "The effect of the 308 nm excimer laser on tooth dentin," *Laser Surgery: Advanced Characterisation, Therapeutics, and Systems II*, 1200, pp. 452-458, 1990.

8. J.T. Walsh, and T.F. Deutsch, "Measurement of Er-YAG laser ablation plume dynamics," Applied Physics B **B52**, pp. 217-224, 1991.

9. Y. Uchida, J. Yamada, H. Furuhashi, and Y. Uchida, "Characteristic Properties of Ablation Plasma Plumes from Materials Produced by an Excimer Laser," Reports of the Institute of Fluid Science **10**, pp. 203-208, 1997.

10. A. K. Murray, and M.R. Dickinson, " An investigation into the interaction of a XeCl excimer laser with hard tissue," *Laser Tissue Interaction: Photochemical, Photothermal, and Photomechanical XI*, 3914, pp. 137-143, 2000.

Shielding by the ablation plume during Er:YAG laser ablation

Kester Nahen and Alfred Vogel

Medical Laser Center Lübeck, Peter-Monnik-Weg 4, D-23562 Lübeck, Germany

ABSTRACT

Free running Er:YAG lasers are used for a precise tissue ablation in various clinical applications as, for example, laser skin resurfacing. The ablated material is ejected from the tissue surface in the direction of the incident laser beam. We investigated the influence of the shielding by the ablation plume on the energy deposition into the irradiated sample because it influences the ablation dynamics and the amount of ablated material. The shielding was investigated for gelatin with different water content, skin, and water. Laser flash photography combined with a dark field Schlieren technique was used to visualize the gaseous and liquid ablation products. The distance traveled by the ablating laser beam through the ablation plume was evaluated from the photographs for various times after the beginning of the laser pulse. The temporal evolution of the transmission through the ablation plume was probed using a second free running Er:YAG laser beam directed parallel to the sample surface. The ablation dynamics shows two phases: Vaporization and material ejection. The photographic observations give evidence for a phase explosion to be the driving mechanism for the material ejection. The transmission is only slightly reduced by the vapor plume, but it decreases by 25–50 % when the ejected material passes the probe beam. The laser energy deposited into the sample amounts to only 61 % of the incident energy for gelatin samples with 90 % water content and 86 % for skin samples. The shielding must therefore be considered in modeling the ablation dynamics and determining the dosage for clinical applications.

Keywords: Infrared photoablation, ablation dynamics, ablation plume, shielding, phase explosion

1. INTRODUCTION

The free running Er:YAG laser has gained interest in the last few years because of its potential for a precise tissue removal. One clinical application which takes advantage of this potential is laser skin resurfacing.[1] Since laser systems delivering pulse energies of up to 2 J are now available, it is possible to use large spot diameters at radiant exposures which are large enough to achieve substantial ablation rates. The frequent use of free running Er:YAG lasers motivated us to study the ablation dynamics of the IR laser tissue interaction in order to establish a basis for an acoustic online control of the ablation process.[2–4] Our photographic investigations of the ablation dynamics showed that the material removal is caused mainly by material ejection and not only by vaporization.[3] The material is ejected perpendicular to the sample surface and thus into the direction of the incident laser beam.[3] It is the aim of the present study to quantify the attenuation of the laser beam by the ejected material. Although the dynamics of free running Er:YAG laser ablation of soft tissue has been studied in the past, no experimental investigation of the interaction of the incident laser beam with the ejected material has been performed so far.

Izatt et al. proposed a debris attenuation model to explain a discrepancy between the ablation depths measured during HF laser ablation of bone and the predictions of a simple steady state model.[5] This model, which is based on the assumption of a constant extinction coefficient of the ablation plume, yields reasonable results for pulse durations of less then 1 µs. Majaron et al. extended the simple debris attenuation model for pulse durations of up to 1 ms by assuming a time dependent extinction coefficient.[6] The extinction coefficient depends on the rate of material ejection which, in turn, is influenced by the interaction between the incident laser beam and the ablated debris. Majaron et al. used their model to explain the unexpected small ablation depths observed for the free running Er:YAG laser ablation of hard biological tissues. Hibst et al. explain discrepancies between measured ablation rates of dental hard substances and predictions of a steady state model also by shielding effects.[7] The analysis of the shielding by the ablation plume performed by Izatt et al.[5] and Majaron et al.[6] are based on measurements of the ablation depth and on simple models of the ablation dynamics. Extinction coefficients are derived under the assumption that these models are sufficient to fully describe the ablation dynamics. To overcome these limitations we directly measured

---

E-mail: Kester Nahen: nahen@mll.mu-luebeck.de, Alfred Vogel: vogel@mll.mu-luebeck.de;
Phone: +49-451-500-6504; Fax: +49-451-505486

the absorption by the ablation plume at the wavelength of the ablation laser. The present study presents, to the best of our knowledge, the first experimental results on the shielding during free running Er:YAG laser ablation of soft tissue.

To find out how strongly the ablation plume influences the energy deposition into the sample we first measured the temporal evolution of the absorption coefficient of the ablation plume. For that purpose a probe beam delivered by a free running Er:YAG laser was sent through the ablation plume. In a second step, we evaluated the pathlength of the ablation laser beam through the plume from photographs of the ablation dynamics. These experimental results enabled us to calculate the temporal evolution of the energy deposition into the sample as well as the total amount of deposited energy.

2. METHODS

2.1. Laser System

We used a free running Er:YAG laser (Dermablate MCL 29 D1, Asclepion Meditec, Jena, Germany) with a pulse duration of $200\,\mu s$ and a maximum pulse energy of 2 J to ablate various sample materials (Sec. 2.2). The beam diameter at the sample surface was 5 mm. Radiant exposures of $4.6\,\mathrm{J\,cm^{-2}}$ and $7.8\,\mathrm{J\,cm^{-2}}$ were used for the experiments. The ablation threshold for skin is $0.8\,\mathrm{J\,cm^{-2}}$.

2.2. Irradiated Samples

We irradiated water, gelatin with 70 % and 90 % water content (by weight), and skin. The ablation of water was investigated because water is the main chromophore at the Er:YAG laser wavelength of $2.94\,\mu n$. A comparison with the results obtained for skin clarifies the role of the tissue matrix for the ablation dynamics. Gelatin samples with different water content were used to study the influence of the mechanical properties of the sample on the ablation dynamics.[3]

2.3. Photographic Investigation of the Ablation Dynamics

Laser flash photography of the ablation dynamics was performed using a shadowgraph and a dark field Schlieren arrangement. The photographs served to determine the pathlength of the incident laser beam through the ablation plume and allowed to distinguish between parts of the plume consisting of vapor and particulate matter. The shadowgraph arrangement makes objects visible which absorb the illumination light or refract it out of the aperture of the imaging optics. The shadowgraph technique was, therefore, used to study the material ejection during the ablation process. The dark field Schlieren arrangement visualizes not only light absorbing and strongly refracting objects but also week phase objects as, for example, gaseous ablation products, which cannot be seen on shadowgraph photographs. The experimental setup of the dark field Schlieren arrangement was described in detail in Ref. 2. For the illumination of the photographs we used a frequency doubled Q-switched Nd:YAG laser with a pulse duration of 6 ns (Continuum YG 671-10, Santa Clara, CA).

We obtained picture series of the ablation process by taking photographs with different time delays between the ablation laser pulse and the illumination laser pulse. From the picture series we evaluated the pathlength traveled by the ablation laser beam through the ablation plume. The position of the front of the gaseous ablation products and of the ejected material were analyzed separately.

To study the processes at the sample surface, we took photographs in top view. The sample surface was illuminated by a collimated laser beam delivered from the frequency doubled Nd:YAG laser. Illumination beam and camera were both oriented under an angle of 35° to the ablation-laser beam. The illumination light was specularly reflected by the undisturbed sample surface into the direction of the camera. All changes of the surface leading to reflecion or scattering of the illumination light out of the aperture of the camera objective lead to a darkening of the respective surface location.
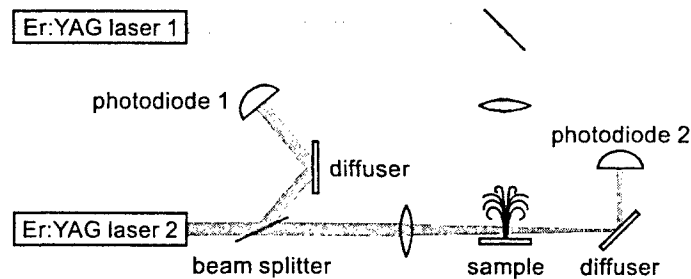
Figure 1. Experimental setup used for the investigation of the ablation plume transmission at the Er:YAG laser wavelength.

2.4. Measurement of the Ablation Plume Transmission

The temporal evolution of the absorption coefficient of the ablation plume was investigated using the experimental setup depicted in figure 1. To measure the absorption coefficient at the wavelength of the Er:YAG laser used for ablation (laser 1) we sent the beam of a second free running Er:YAG laser (laser 2) through the ablation plume and measured the pulse shape of probe beam before and after the transit through the plume. The probe beam had a diameter of 2 mm at the ablation site. The beam path was oriented parallel to the sample surface, with 2.5 mm distance between the beam axis and the sample surface. To detect the shape of the incident pulse a part of it was deflected by an inclined quartz plate in the beam path, sent on a diffuser (SRM-990 Spectralon, Labsphere, North Sutton, NH), and detected by a GaAs photodiode (J125AP-R02M, EG&G Judson, Montgomeryville, PA; rise time 10 ns). The other part of the probe beam passed through the ablation plume and was focused on a second diffuser. The pulse shape was detected by a second GaAs photodiode of the same type as photodiode 1. The probe beam was directed on a diffuser to achieve a spatial integration over all components of the beam traversing through different parts of the ablation plume. The focusing enabled to achieve this integration while using a short distance between the photodiode and the diffuser. This way, strong signals and a good signal to noise ratio could be obtained. The distance between the photodiode and the diffuser was chosen in a way that light which was scattered by the ablation material under an angle of more than 10° did not contribute to the photodiode signal. Both photodiodes were operated at the same output voltage to minimize the influence of their characteristic curves on the output signal. The diameter of the probe beam (2 mm) was significantly smaller than the diameter of the ablation laser beam (5 mm). The pathlength of rays passing through the ablation plume on the beam axis and at the edges of the probe beam were thus nearly the same. The total radiant exposure in the probe beam was $0.22 \, \mathrm{J \, cm^{-2}}$ which is one order of magnitude smaller than the ablation threshold for water with regard to a $200 \, \mu s$ long laser pulse. The radiant exposure of each part of the ablation plume passing the probe beam is even much smaller, since the ejected material interacts with the probe beam only for about $20 \, \mu s$ because of the high particle velocity of about $100 \, \mathrm{m \, s^{-1}}$.[3] An influence of the probe beam on the ablation plume can, therefore, be ruled out. Our photographic investigations showed that the size of the particulate ejecta is large compared to the optical penetration depth of about $1 \, \mu m$. Scattering does therefore not considerably contribute to the extinction of the laser beam. The absorption coefficient of the ablation plume was calculated by relating the probe beam transmission to the pathlength of the beam within the plume (for further details see sections 3.2.1 and 3.2.2).

The probe beam was produced using a laboratory laser system equipped with a pulse forming network (CB17OJ-15, LISA Laser Products, Katlenburg, Germany) capable of generating long pulses with $440 \, \mu s$ durations. The transmission T of the ablation plume could thus be measured during the whole ablation laser pulse duration of $200 \, \mu s$. The probe pulse was triggered $80 \, \mu s$ before the beginning of the ablation laser pulse. The photodiode signals measured in front of and behind the ablation site during this time interval with $T = 1$ were used as a reference for the calculation of the ablation plume transmission.

The transmission of the ablation laser beam to the target as well as the energy deposited into the sample were calculated from the absorption coefficient of the ablation plume and the temporal evolution of the pathlength of the ablation beam through the plume. A detailed description of the analysis is given in sections 3.2.3 and 3.2.4.

3. RESULTS AND DISCUSSION

3.1. Ablation Dynamics

The ablation dynamics observed during the irradiation of gelatin, skin, and water have some characteristic features in common. The characteristic sequence of events will be described for the case of gelatin with 70 % water content, and for water. A comparison between the ablation dynamics for gelatin samples with 70 % and 90 % water content can be found in Ref. 3.

Figure 2 gives an overview of the ablation dynamics for gelatin with 70 % water content during the first $100\,\mu s$ of the laser pulse. The ablation laser beam is incident from the top. The radiant exposure was $4.6\,\mathrm{J\,cm^{-2}}$ at a spot diameter of 5 mm. The pictures were taken with the dark field Schlieren arrangement (Sec. 2.3). The sample surface appears as a horizontal white line. The Schlieren photographs first show a vapor plume which starts to form about $10\,\mu s$ after the beginning of the laser pulse. The vapor plume is generated by the heating of a superficial sample layer leading to normal vaporization.[8] The vapor plume expands predominately into the direction of the incident laser beam. The vapor front reaches a height of approximately 5 mm after $100\,\mu s$. After about $30\,\mu s$, the sample surface starts to rise across the whole irradiated area. This is probably a consequence of the formation of vapor bubbles inside the sample. The surface is still intact after $100\,\mu s$ because the tensile strength of the gelatin counteracts the vapor pressure inside the bubbles. When the vapor pressure exceeds the ultimate tensile strength, the sample surface tears, and material is ejected. This part of the ablation process, which starts about $120\,\mu s$ after the beginning of the laser pulse, is shown in figure 3. The particle front travels with a high velocity into the direction of the incident laser beam. The particle density near the sample surface reaches its maximum after about $180\,\mu s$. The density then decreases towards and after the end of the laser pulse (pulse duration $200\,\mu s$).

Our photographic observations support the thermo-mechanical micro-explosion model developed by Majaron et al..[9] The micro-explosion model describes the formation of vapor bubbles inside the irradiated sample which finally leads to a tearing of the matrix and material ejection. The predicted ablation threshold is, therefore, related to the ultimate tensile strength of the sample material.
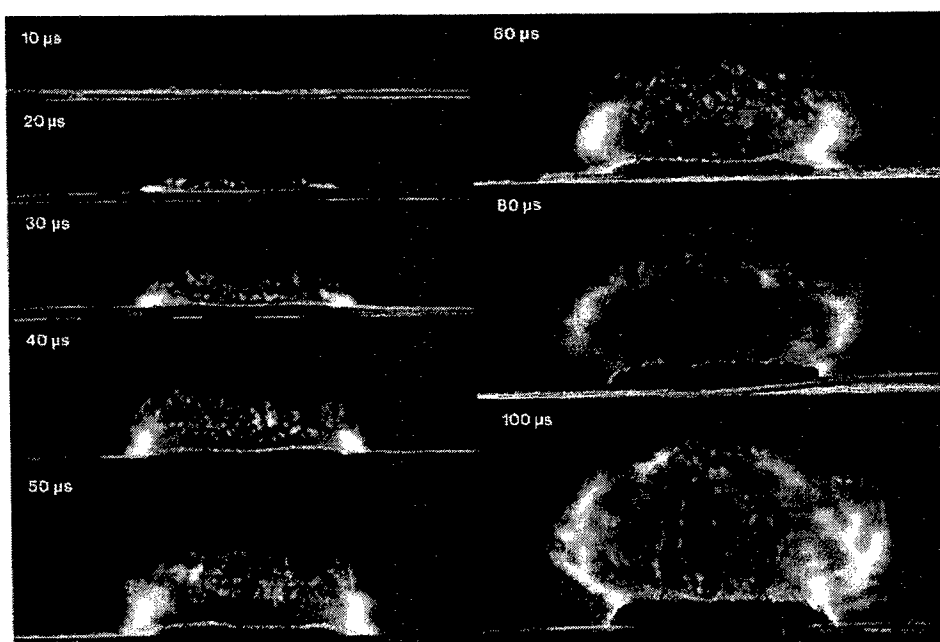
Figure 2. Initial phase of Er:YAG laser ablation of gelatin with 70 % water content (radiant exposure $4.6\,\mathrm{J\,cm^{-2}}$, spot diameter 5 mm, ▬ = 1 mm). The pictures were taken 10–$100\,\mu s$ after the beginning of the laser pulse using a dark field Schlieren arrangement. The ablation starts with the formation of a vapor plume. The water vapor becomes visible because its refractive index differs from the surrounding air. After $30\,\mu s$ the sample surface starts to rise, because of the formation of vapor bubbles inside of the sample. The surface is still intact after $100\,\mu s$ because the tensile strength of the gelatin counteracts the vapor pressure.
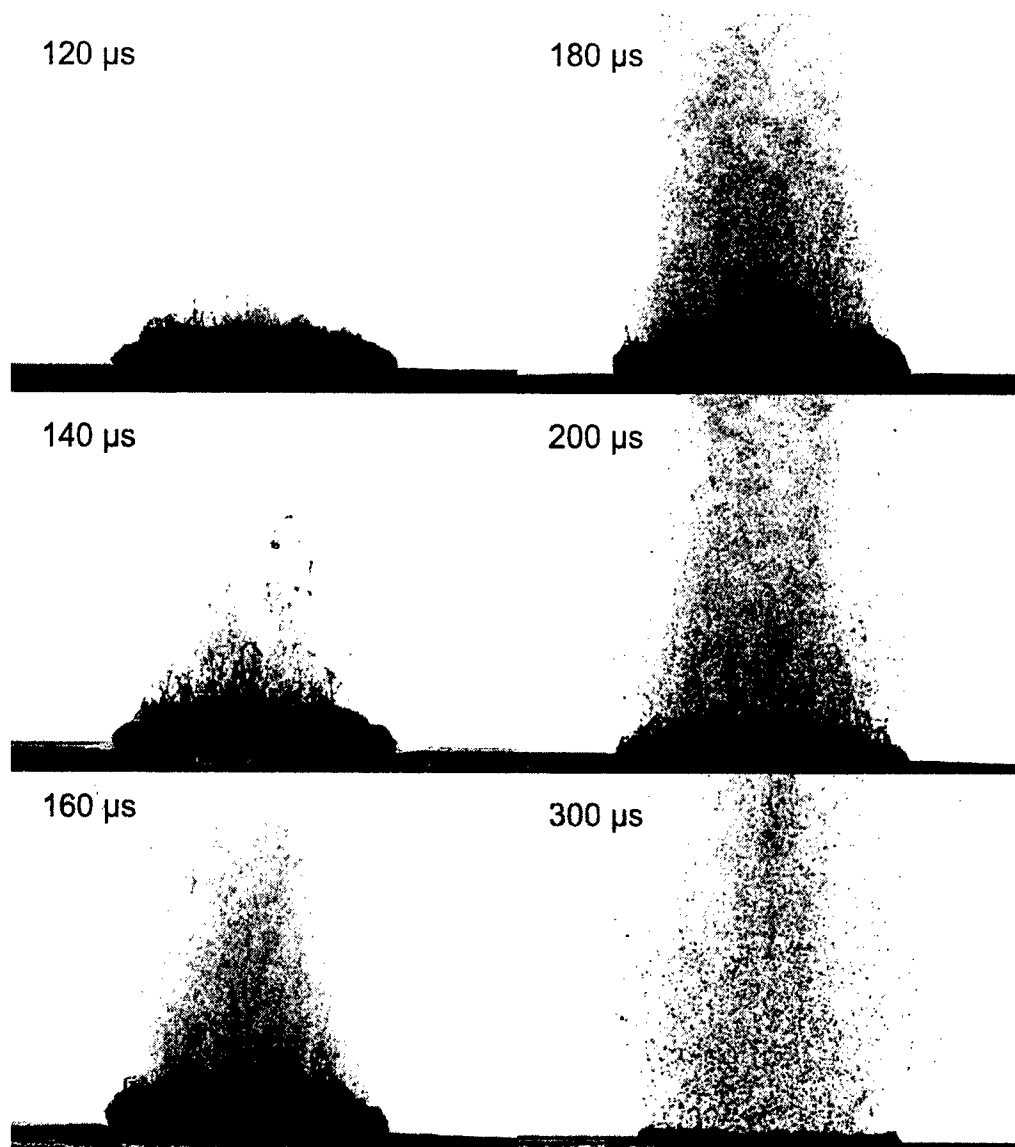
Figure 3. Dynamics of Er:YAG laser ablation of gelatin with 70 % water content in the second half and after the end of the laser pulse (laser parameters see Fig. 2, ┠━┨ = 1 mm). The pictures were taken using a shadowgraph technique to show the material ejection starting approx. 120 μs after the beginning of the laser pulse.

The photographs of Figs. 2 and 3 suggest that the vapor formation as well as the particle ejection take place across the whole irradiated spot. This result contradicts the scenario described by Zweig et al.[10] who assume that material ejection is driven by a gradient of the vapor pressure in the plume above the sample surface. The pressure gradient leads to a radial acceleration of the material ablated in the central part of the irradiated spot and thus to material ejection in directions parallel to the sample surface. The ejection would occur mainly at the edges of the irradiated spot. What we observe, however, is an ejection perpendicular to the sample surface. This observation can only be explained by material ejection taking place across the whole irradiated spot. To remove all doubts about this interpretation, we took the photographs of the sample surface during laser ablation presented in figure 4. A white disk appears at the ablation site 20 μs after the beginning of the laser pulse. At this time vapor is formed above the surface (Fig. 2), and the sample surface is roughened by surface instabilities caused by the interaction between the vapor plume and the gelatin.[11,12] After 100 μs, an irregular dark structure is visible across the whole ablation laser beam diameter which corresponds to the risen surface area visible on the dark field and shadowgraph pictures (Fig. 2 and 3). 200 μs after the beginning of the laser pulse particulate ejecta above the ablation site (Fig. 4). The
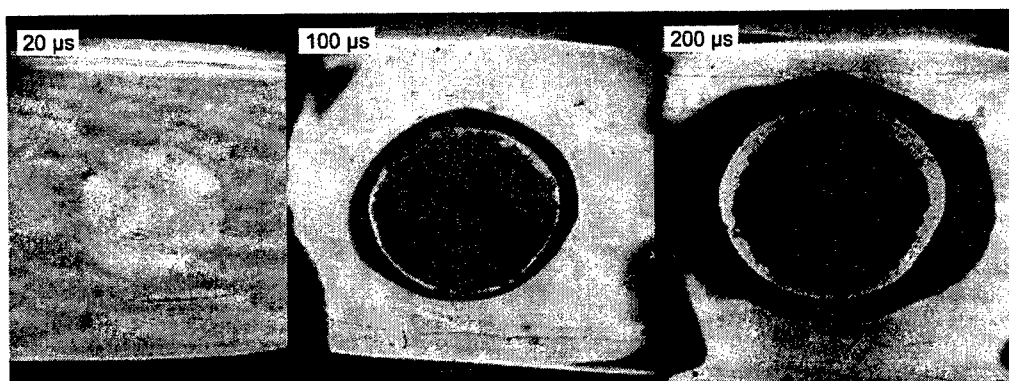
Figure 4. Top view of the ablation site during the irradiation of gelatin samples with 70 % water content (radiant exposure 4.6 J cm^{-2}, horizontal: ├────────┤ = 5 mm, vertical: ├────────┤ = 5 mm).

dark dots below the ablation site are mirror images of the ejected particles. The homogeneous roughening of the sample surface observed after 100 μs confirms that the material ejection takes place across the whole beam diameter, in contrast to the model of Zweig et al..[10]

Our photographic investigations of the ablation dynamics for the irradiation of gelatin and skin showed that the material removal is caused mainly by the ejection of sample material and not only by vaporization. The photographs in figure 5 and 6 show that this is also true for water, even though water does not possess an elastic matrix counteracting the formation and growth of vapor bubbles. The ablation starts with the formation of a vapor plume (Fig. 5) like in the case of gelatin (Fig. 2). After 30 μs the white line demarcating the water surface in the dark field pictures starts to show some irregularities. A comparison with the photographs taken with the shadowgraph arrangement (Fig. 6) reveals that at this time water droplets start to be ejected perpendicular to the sample surface. The droplet density reaches its maximum approximately 60 μs after the beginning of the laser pulse and decreases thereafter already during the laser pulse. The ejection of water droplets during Er:YAG laser irradiation of pure water can be explained by the hypothesis that the water is superheated and that this superheating leads to a phase explosion. A phase explosion is characterized by a rapid transition of a superheated metastable liquid into a system containing the two separate phases of gas and liquid in equilibrium states.[13,14] The transition occurs when the temperature of the liquid reaches the spinodal limit ($\approx$ 90 % of the critical temperature[15]) and homogeneous nucleation sites are generated very rapidly. The phase transition leads to a strong expansion of the vapor phase, because water has a volumetric expansion coefficient of 1696.[16] The water droplets formed during the phase explosion are accelerated by the expanding vapor and ejected from the sample surface with a very high velocity. To check if the spinodal limit of superheated water can be reached during Er:YAG laser irradiation we calculated the temperature evolution at the sample surface. The solution of the inhomogeneous heat diffusion equation given by Freund et al.[17] was calculated numerically. The calculations predict that the spinodal temperature of water (302 °C, at atmospheric pressure)[14] is reached about 25 μs after the beginning of the laser pulse. The shadowgraph pictures in figure 6 show that material ejection starts after 30 μs, i. e. shortly after the spinodal limit has been reached according to the calculations. This provides additional evidence for the interpretation that a phase explosion is the mechanism responsible for droplet ejection during water ablation.

The observation of a phase explosion during Er:YAG laser irradiation of water suggests that a phase explosion may also contribute to the material ejection observed during the ablation of gelatin and skin samples, because they mainly consist of water. The elastic matrix may, however, delay the onset of the material ejection with respect to the onset observed for water if the material strength is higher than the vapor pressure at the spinodal point. The matrix counteracts the vapor expansion inside the sample until the ultimate tensile strength of the matrix is reached and the ablation starts (Fig. 2).

With regard to our investigations of the transmission of the ablation plume we can summarize the results of our photographic observations of Er:YAG laser ablation dynamics as follows: A subablative phase where a superficial sample layer is heated is followed by a phase of vaporization, and, later on, by material ejection. For the calculation of the laser beam transmission to the target, the ablation plume must therefore be divided into a vapor plume and a part consisting of vapor mixed with particulate matter.
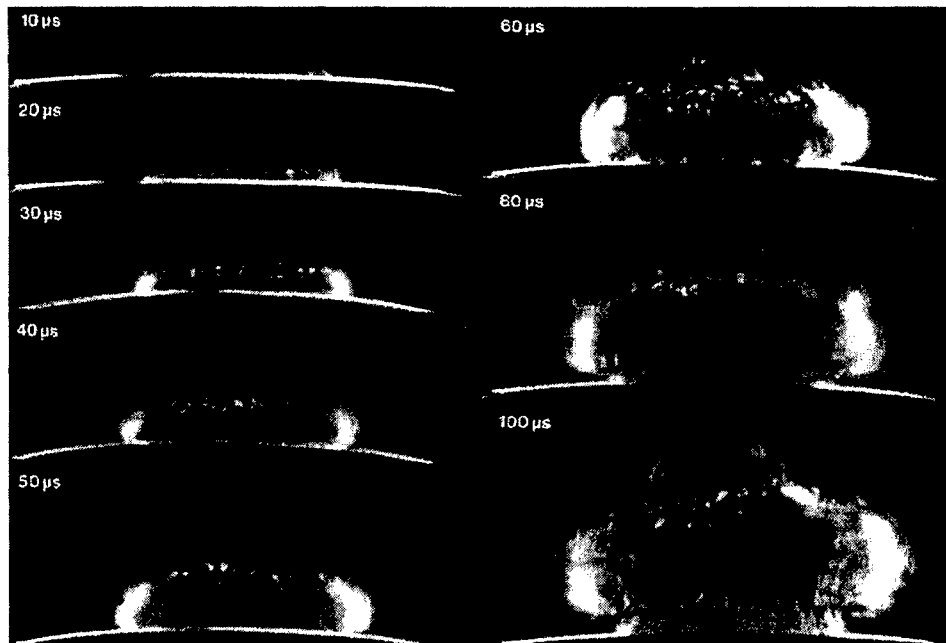
Figure 5. Initial phase of the Er:YAG laser ablation dynamics of water (radiant exposure $4,6\,\mathrm{J\,cm^{-2}}$, spot diameter 5 mm, ├──┤ = 1 mm). The photographs were taken 10–100 μs after the beginning of the laser pulse using the dark field Schlieren arrangement. The water surface appears as a white line. The surface has a curvature because the cuvette was over-filled to be able to see the ablation site. The ablation starts with the formation of a vapor plume. After 30 μs, the white line demarcating the water surface starts to show some irregularities. The water surface disappears completely on the picture taken after 80 μs. After 100 μs, water droplets are visible close to the water surface.
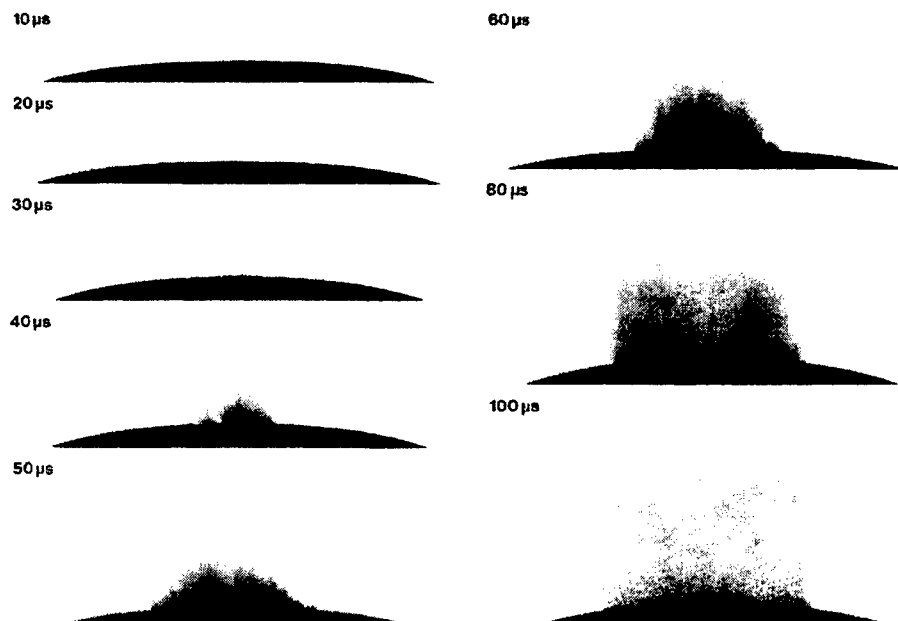
Figure 6. Initial phase of the ablation dynamics for the Er:YAG laser irradiation of water (laser parameters see Fig. 5, ├──┤ = 1 mm). The photographs were taken using the shadowgraph arrangement to make the ejection of water droplets visible. The droplet ejection starts 30–40 μs after the beginning of the laser pulse. The droplets are ejected perpendicular to the sample surface. The droplet density reaches its maximum approximately 60 μs after the beginning of the laser pulse and decreases thereafter already during the laser pulse.

3.2. Shielding by the Ablation Plume

To obtain the temporal evolution of the energy deposition into the sample and to calculate the total amount of deposited energy we first determined the temporal evolution of the transmission of the ablation plume. For that purpose we calculated the absorption coefficient of the plume for the different phases of the ablation dynamics from the measured transmission of the probe laser beam (Sec. 3.2.1 and 3.2.2). We then calculated the transmission of the ablation laser beam through the plume from the absorption coefficients of the different parts of the plume and the pathlength of the laser beam through these parts (vapor, and particles mixed with vapor) until it reaches the sample surface (Sec. 3.2.3). The temporal evolution of the position of the vapor front and particle front were taken from the photographs of the ablation dynamics. Finally, the transmission data for the ablation laser pulse were used to calculate the transmitted pulse shape (Sec. 3.2.3) and the deposited energy (Sec. 3.2.4).

3.2.1. Temporal evolution of the probe beam transmission

The temporal evolution of the probe beam transmission was calculated from the ratio of the photodiode signals measured in front of and behind the ablation plume (Sec. 2.4). Figure 7 shows the shape of the ablation laser pulse (a) and the shapes of the probe laser pulse incident into and transmitted through the ablation plume (b) for the ablation of a gelatin sample. The probe laser pulse begins 80 μs before the ablation laser pulse. To normalize the pulse shapes of the incident and transmitted beam relative to each other, we used the photodiode signal measured in a time interval of 30 μs just before the beginning of the ablation laser pulse. The mean value of the ratio of the photodiode signals during this time interval served as normalization factor. The pulse shapes shown in figure 7 (b) are already normalized. Figure 7 (c) depicts the temporal evolution of the probe beam transmission which was obtained by dividing the normalized signals of figure 7 (b). Figure 7 presents the result of a single measurement. For further evaluation, we generally averaged the transmission data from 15 single measurements. The standard deviation of the averaged transmission was less than 7 % for every point in time.
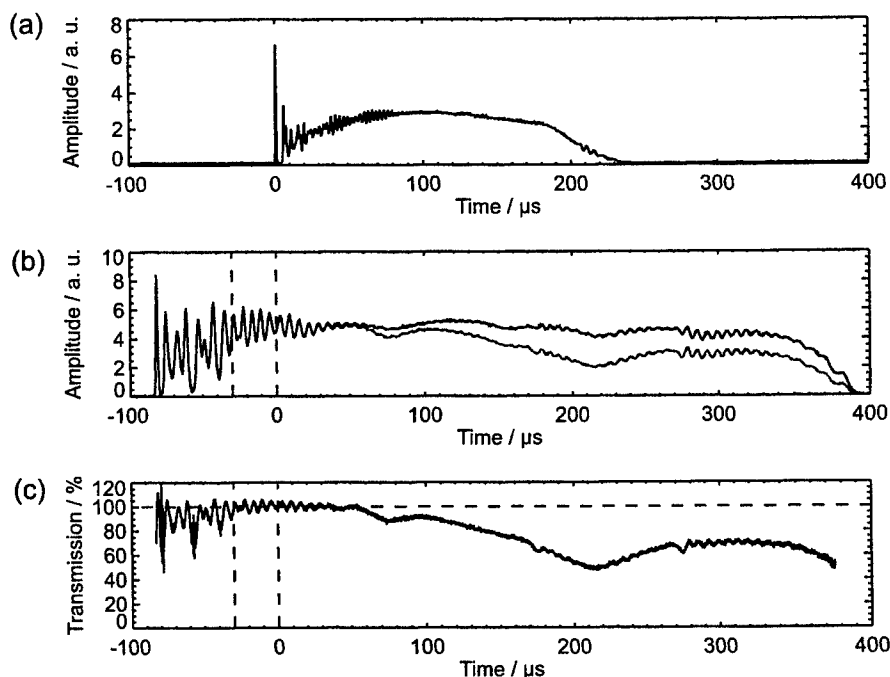
Figure 7. Illustration of the method used for the calculation of the probe beam transmission through the ablation plume. The figure shows a typical result for a single measurement performed during Er:YAG laser ablation of a gelatin sample with 90 % water content (radiant exposure 4.6 J cm^{-2}). (a) ablation laser pulse, (b) incident probe laser pulse (upper curve) and transmitted probe laser pulse (lower curve), (c) transmission curve calculated from the pulse shapes in (b). The vertical lines in (b) and (c) demarcate the time interval which was evaluated to normalize the signals in (b) relative to each other.
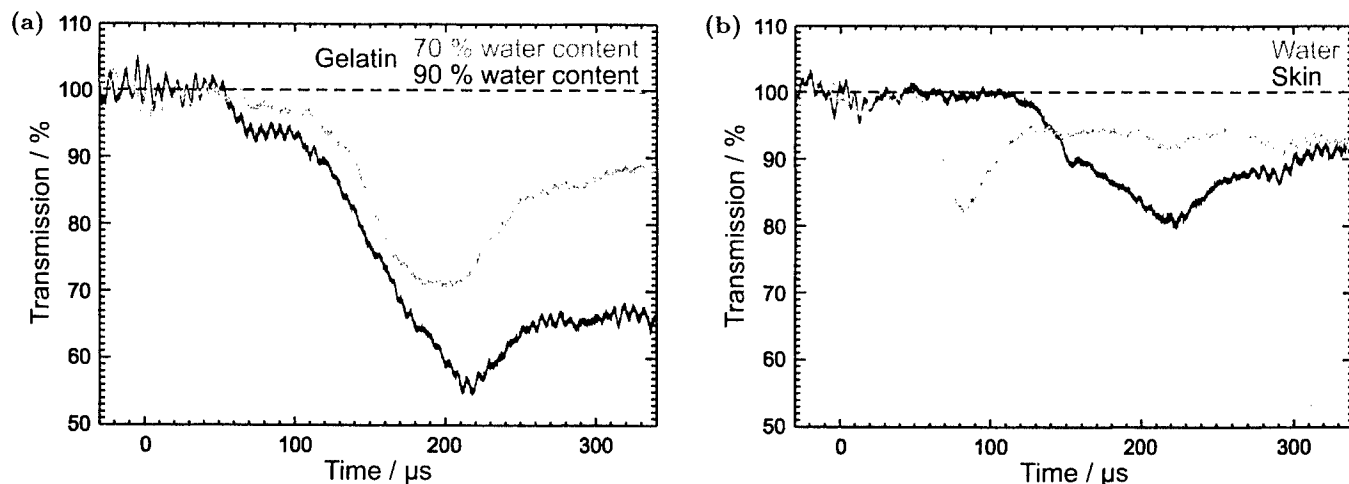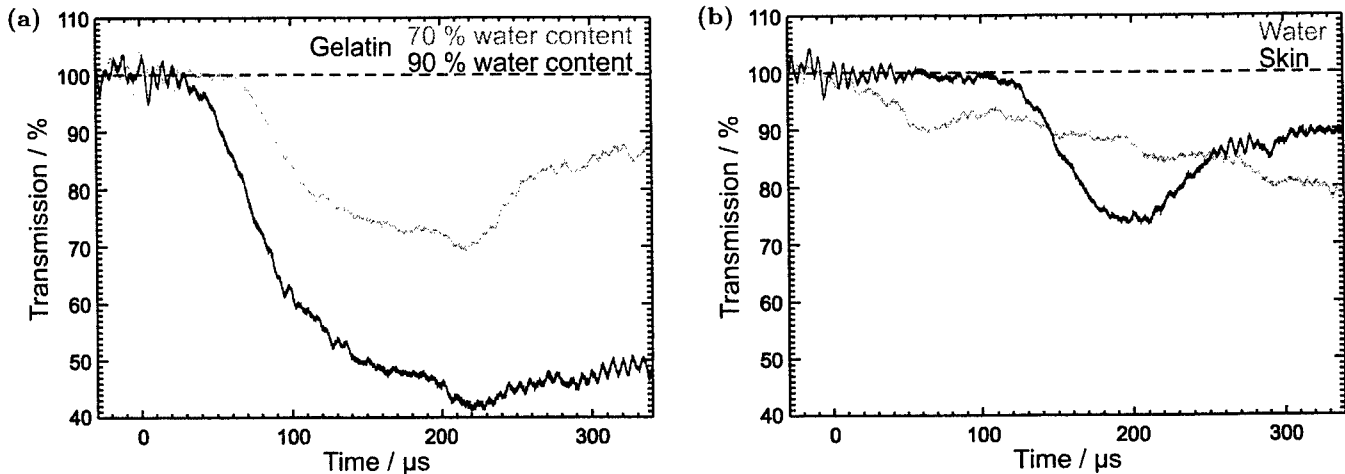
Figure 8. Temporal evolution of the probe beam transmission through the ablation plume (a) for gelatin with 70 % and 90 % water content, and (b) for water and skin. The radiant exposure of the ablation laser pulse was 4.6 J cm^{-2}, the beam diameter 5 mm, and the pulse duration 200 μs (FWHM). Time zero corresponds to the beginning of the ablation laser pulse. The curves are averaged over 15 events.

The temporal evolution of the probe beam transmission is shown in figures 8 and 9 for the ablation of gelatin, water, and skin with radiant exposures of 4.6 J cm^{-2} and 7.8 J cm^{-2}. Time zero corresponds to the beginning of the ablation laser pulse. The temporal evolution of the probe beam transmission can be understood by comparing the transmission curves with the photographs of the ablation dynamics shown in section 3.1.

For the ablation of gelatin with a radiant exposure of 4.6 J cm^{-2}, the transmission starts to decrease 60 μs after the beginning of the laser pulse and remains constant thereafter for about 30 μs (Fig. 8 (a)). During this time interval the gaseous ablation products pass through the probe beam. A further decrease of the transmission starts 100 μs after the beginning of the laser pulse. This decrease is caused by the ejection of solid and liquid ablation products. Until the end of the laser pulse, the transmission decreases to 71 % and 56 % for gelatin with 70 % and 90 % water content, respectively. The transmission for water and skin (Fig. 8 (b)) is always higher than for gelatin. The transmission curve for skin exhibits a considerable decrease of transmission only at very late times. This corresponds to a late onset of material ejection observed photographically. During the ablation of water, the transmission decreases very rapidly after about 60 μs but increases again already during the laser pulse. Afterwards, the transmission stays on a constant level for the rest of the pulse. The transient decrease of the transmission portrays the ejection of water droplets caused by a phase explosion. This explanation is supported by the pictures in figure 6 which show that the water droplets begin to pass through the probe beam approximately 60 μs after the beginning of the laser pulse (considering that the distance between probe beam axis and sample surface is 2.5 mm). The decrease of the probe beam transmission occurs at the same time. The photographs show, furthermore, that the droplet density at the probe beam axis is maximal after about 80 μs when the transmission curve reaches its minimum value. After the phase explosion, water droplets are still ejected, but with a smaller density. This explains why the transmission increases again and remains at a constant level after 120 μs.

Figure 9 presents the probe beam transmission for ablation with a radiant exposure of 7.8 J cm^{-2}. The transmission curves for gelatin samples with 70 % and 90 % water content drops to 70 % and 42 %, respectively, at the end of the laser pulse. The decrease starts earlier and the minimum transmission is lower than in the case of 4.6 J cm^{-2} radiant exposure . This can be explained by a larger amount of ejected material and by an earlier onset of material ejection. The higher radiant exposure induces a faster temperature and pressure rise inside the sample, and thus a faster onset of the phase explosion or rupture of the material matrix, respectively. It is interesting to note, however, that these changes with radiant exposure only apply to water and gelatin. During skin ablation with a radiant exposure of 7.8 J cm^{-2}, the transmission decreases not earlier than with a radiant exposure of 4.6 J cm^{-2}. The tissue matrix seems to sustain the increased pressure much better than the gelatin. During ablation of water with the higher radiant exposure, the transmission decrease starts earlier but is less pronounced than with a radiant exposure of 4.6 J cm^{-2}. This difference can be explained by the influence of heat diffusion inside the sample. For 7.8 J cm^{-2} the phase explosion occurs already early during the laser pulse when only a very thin water layer at the sample surface is

Figure 9. Temporal evolution of the probe laser beam transmission through the ablation plume, (a) for gelatin with 70% and 90% water content, and (b) for water and skin. The radiant exposure of the ablation laser pulse was 7.8 J cm^{-2}, the beam diameter 5 mm, and the pulse duration 220 μs (FWHM). The curves are averaged over 15 events.

heated to the spinodal temperature. Therefore, the phase explosion incorporates only a small water volume, and the number of ejected water droplets is small. In contrast, at a radiant exposure of 4.6 J cm^{-2}, the phase explosion takes place with a delay of 60 μs. At that time, heat diffusion has led to superheating of a much larger sample volume which causes the ejection of a large number of water droplets.

3.2.2. Absorption coefficients of the ablation plume

The absorption coefficient of the ablation plume was determined separately for the vaporization phase and the phase of material ejection. The mean transmission T during each phase was used to calculate the mean absorption coefficient α. The values for vapor are denoted T_v and α_v, respectively, and the values for the mixture of vapor, liquid, and solid ablation products are denoted T_{vp} and α_{vp}. The time intervals used to determine the absorption coefficients during each phase were taken from the photographs of the ablation dynamics. For the determination of α_{vp}, the transmission was considered only until the end of the ablation laser pulse, because this time interval is relevant for the shielding properties of the ablation plume.

The absorption coefficients were calculated from the transmission data using Beer's law

$$\alpha = -\frac{\ln T}{d}. \tag{1}$$

Here d is the pathlength through the ablation plume which was set equal to the ablation spot diameter of 5 mm. The transmission values and absorption coefficients are listed in table 1 for a radiant exposure of 4.6 J cm^{-2}, and in table 2 for 7.8 J cm^{-2}. For the phase of material ejection we used not only the mean transmission but also the minimum transmission for further evaluation. The minimum transmission provides an upper estimate of the absorption coefficient of the ablation plume and thus yields a lower estimate of the laser energy deposited into the sample.

The absorption coefficients of the vapor plume ranged between 0.016 and 0.124 cm^{-1}. The highest value of the absorption coefficient was at both radiant exposures obtained for the ablation of gelatin samples with 90% water content. No general dependence between the absorption coefficient of the vapor plume and the radiant exposure could be identified. Our experimental data lie within the range of values for the absorption coefficient of water vapor at the Er:YAG laser wavelength given in the literature. Young[18] quoted a value of 0.0075 cm^{-1} for a temperature of 100 °C at atmospheric pressure (0.1 MPa), and a value of 1.8 cm^{-1} for the temperature and vapor pressure at the spinodal point, 302 °C and 9.7 MPa, respectively. The results of our measurements (0.016–0.124 cm^{-1}) lie at the lower end of this range. The highest value is more than one order of magnitude smaller than the absorption coefficient of vapor at the spinodal limit. This result surprises at first because a phase explosion was observed at the end of the vaporization phase which can only occur at temperatures close to the spinodal point. The discrepancy

	vapor		vapor and particles			
			mean transmission		minimum transmission	
sample	$\frac{T_v}{\%}$	$\frac{\alpha_v}{cm^{-1}}$	$\frac{T_{vp}}{\%}$	$\frac{\alpha_{vp}}{cm^{-1}}$	$\frac{T_{vp}}{\%}$	$\frac{\alpha_{vp}}{cm^{-1}}$
water	98,6	0,028	91,8	0,171	82,2	0,392
gelatin 90 %	94,0	0,124	74,7	0,591	55,9	1,163
gelatin 70 %	97,0	0,061	82,8	0,377	71,1	0,682
skin	98,5	0,030	88,1	0,253	81,1	0,419

Table 1. Transmission T and absorption coefficient α of the ablation plume at a radiant exposure of $4.6\,\mathrm{J\,cm^{-2}}$.

	vapor		vapor and particles			
			mean transmission		minimum transmission	
sample	$\frac{T_v}{\%}$	$\frac{\alpha_v}{cm^{-1}}$	$\frac{T_{vp}}{\%}$	$\frac{\alpha_{vp}}{cm^{-1}}$	$\frac{T_{vp}}{\%}$	$\frac{\alpha_{vp}}{cm^{-1}}$
water	98,5	0,030	91,4	0,180	85,0	0,325
gelatin 90 %	97,5	0,051	61,7	0,966	42,0	1,735
gelatin 70 %	99,2	0,016	78,8	0,477	69,5	0,728
skin	98,4	0,032	81,7	0,404	74,0	0,602

Table 2. Transmission T and absorption coefficient α of the ablation plume at a radiant exposure of $7.8\,\mathrm{J\,cm^{-2}}$.

can be explained by the expansion of the vapor plume occurring until the vapor front reaches the location of the probe beam. The adiabatic expansion leads to a reduction of temperature and pressure inside the plume and thus to a lowering of the absorption coefficient.

For a radiant exposure of $4.6\,\mathrm{J\,cm^{-2}}$ the mean absorption coefficient of the ejected material mixed with vapor is 5–8 times larger than the values obtained for vapor (Tab. 1). For a radiant exposure of $7.8\,\mathrm{J\,cm^{-2}}$, the difference between the two parts of the ablation plume is even larger, it ranges between a factor of 6 and 30 (Tab. 2). The absorption coefficient calculated based on the minimum transmission values for the ejected material are 10–50 times larger than the values obtained for vapor. We can thus conclude that the absorption of the laser beam in the ablation plume is mainly caused by the ejected material.

The absorption coefficients of the ejected material depend on the ablated sample material. They increase in the following order: water, gelatin with 70 % water content, skin, and gelatin with 90 % water content. This order was observed for both radiant exposures investigated. The absorption coefficient measured during water irradiation is smallest because the ejected water droplets are much smaller than the gelatin droplets and tissue fragments which are ejected during the ablation of the other samples. The particularly high absorption during the ablation of gelatin samples with 90 % water content can be explained by the fact that the ablated material consists of a large number of relatively thick strings of liquefied gelatin (Figs. 6 and 7 in Ref. 3). In the case of gelatin with 70 % water content, in contrast, only small droplets and fragments of gelatin are ejected (Fig. 3). During the ablation of skin small tissue fragments are ejected which are similar in size and density to the ejecta produced during the ablation of gelatin with 70 % water content.[19] The resulting absorption coefficient of the ablation plume is, therefore, similar in both cases.

3.2.3. Temporal evolution of the transmission of the ablation laser beam

To calculate the temporal evolution of the energy deposition into the sample we have to know the absorption coefficients of the different parts of the ablation plume and the temporal evolution of the pathlength of the ablation laser beam through these parts. The pathlength was obtained from the photographs of the ablation dynamics (Sec. 3.1) by measuring the position of the fronts of the vapor plume z_v and the particulate ejecta z_{vp} at different times after the beginning of the laser pulse. We defined that part of the ablation plume as "front" of the particulate ejecta which looked like the plume at the location of the probe beam when the mean value of the transmission T_{vp} was measured. From the discrete measurement data continuous position time curves were calculated by cubic spline interpolation.[20] The position time curves are denoted by $z_v(t)$ for the vapor front and $z_{vp}(t)$ for the particle front.

The temporal evolution of the transmission, $T(t)$, of the ablation laser pulse through the ablation plume was calculated using the following set of equations for the different phases of the ablation dynamics:

$$T(t) = \begin{cases} e^{-\alpha_v z_v} & : \quad z_v > 0 \quad \wedge \quad z_{vp} = 0 \\ e^{-\alpha_v (z_v - z_{vp})} e^{-\alpha_{vp} z_{vp}} & : \quad z_v > z_{vp} \quad \wedge \quad z_{vp} \neq 0 \\ e^{-\alpha_{vp} z_{vp}} & : \quad z_v < z_{vp} \end{cases} \qquad (2)$$

The first line describes the transmission through the vapor plume before the onset of material ejection. The second line corresponds to the transmission through the plume after material ejection has started. The first term herin describes the transmission through the vapor plume above the particle front, and the second term describes the transmission through the particle plume mixed with vapor. The third line in equation 2 is valid only if the particle front overtakes the vapor front.

The figures 10 and 11 contain sets of three plots for each type of sample and radiant exposure showing the position vs. time curves of the vapor and particle front, $T(t)$, and a comparison between the shapes of the incident pulse and the pulse at the sample surface. $T(t)$ was calculated using equation 2 with the absorption coefficients of table 1 and 2 and the position time curves of figures 10 and 11. For the particle plume we used values of the absorption coefficient that were obtained from the mean probe beam transmission during the phase of material ejection. The transmitted pulse shape at the sample surface was calculated by multiplying the incident laser pulse shape by $T(t)$.

The plots in figures 10 and 11 show that the transmission of the ablation laser pulse does not decrease significantly before the material ejection starts. The absorption coefficient of the vapor plume is too small to cause a significant extinction of the laser beam. The temporal evolution and the extent of the transmission reduction are, therefore, governed mainly by the material ejection. Three factors play a role: (i) the onset of material ejection, (ii) the absorption coefficient α_{vp} of the particle plume, and (iii) the velocity of the particle front. A higher velocity of the ejected material leads to a longer pathlength of the incident light through the ablation plume and thus to a stronger shielding effect, if α_{vp} and the onset of material ejection are the same. The overall transmission reduction is most pronounced for gelatin with 90 % water content because the material ejection starts earlier than for the other samples and the absorption coefficient of the particle plume is larger (Tabs. 1 and 2). The shielding is stronger at a radiant exposure of $7.8\,\mathrm{J\,cm^{-2}}$ then at $4.6\,\mathrm{J\,cm^{-2}}$ because the ejected particles are faster and α_{vp} is larger at the higher radiant exposure. The transmission reduction starts relatively late for gelatin with 70 % water content and, in particular, for skin because material ejection is here initially inhibited by the tissue matrix. For a radiant exposure of $7.8\,\mathrm{J\,cm^{-2}}$, the transmission drops, nevertheless, to about 50 % until the end of the laser pulse because the particles are ejected very fast. The shielding effects during ablation of water are relatively weak throughout the whole laser pulse even though material ejection occurs fairly early. This can be explained by the small size of the ejected droplets and their small number density after the end of the phase explosion (Sec. 3.2.1). The absorption coefficient of the particle plume is, therefore, considerably smaller than for all other samples.

3.2.4. Deposited energy

The fraction of the laser pulse energy deposited into the sample was determined by calculating the ratio of the time integral over the deposited and incident laser pulse shapes. The results are listed in table 3. For each sample, an upper and lower estimate of the deposited energy is given based on the absorption coefficients of the ejected material derived from the mean and minimum transmission of the probe beam during the phase of material ejection (Tabs. 1 and 2).

	upper estimate		lower estimate	
sample	$F=4.6\,\mathrm{J\,cm^{-2}}$	$F=7.8\,\mathrm{J\,cm^{-2}}$	$F=4.6\,\mathrm{J\,cm^{-2}}$	$F=7.8\,\mathrm{J\,cm^{-2}}$
water	93 %	88 %	84 %	79 %
gelatin 90 %	87 %	74 %	81 %	61 %
gelatin 70 %	93 %	83 %	90 %	77 %
skin	97 %	89 %	95 %	86 %

Table 3. Fraction of the laser pulse energy deposited into the sample. The upper and lower estimate given are based on the absorption coefficients of the ejected material calculated from the mean and minimum transmission of the probe laser beam during the phase of material ejection (Tabs. 1 and 2).
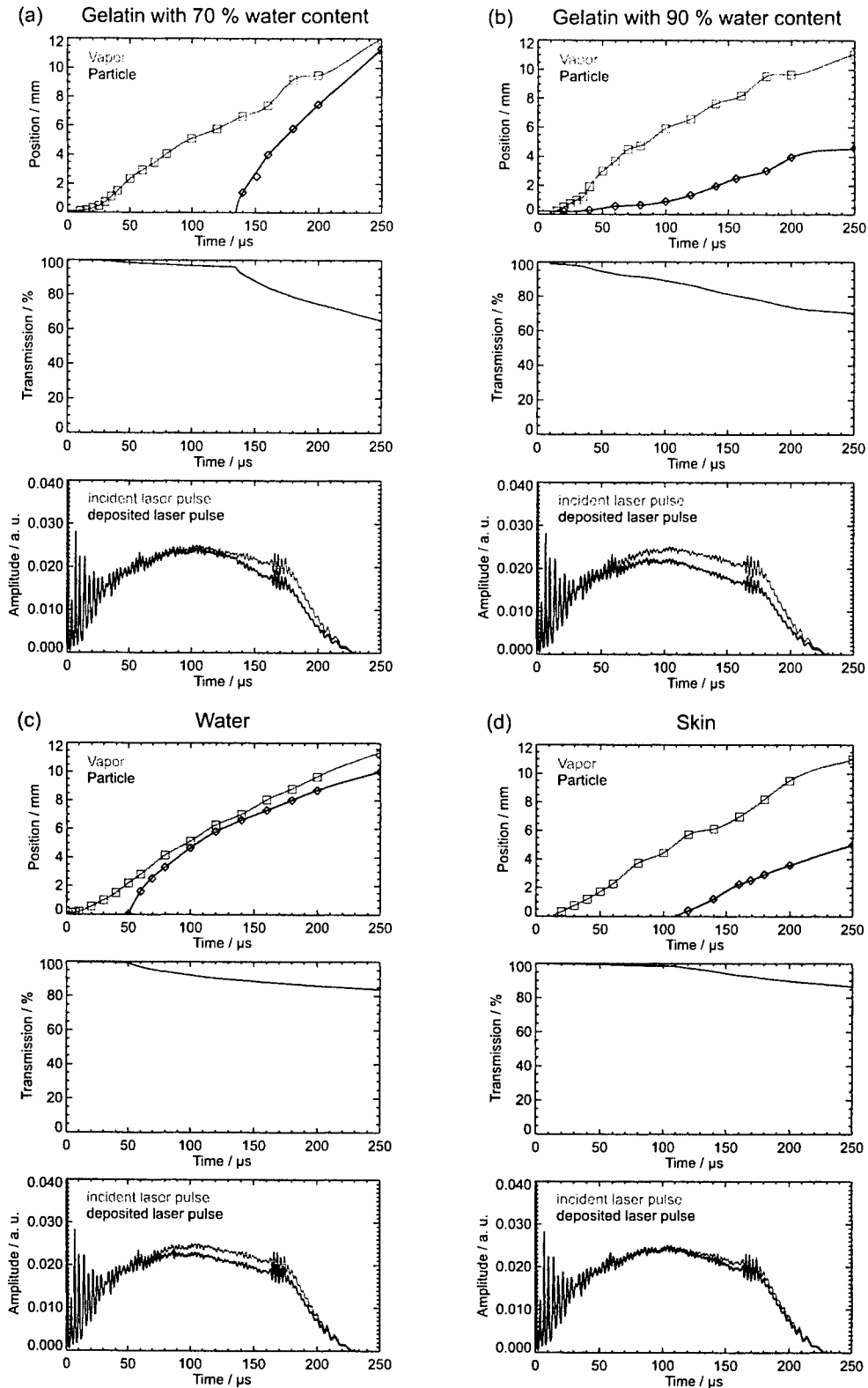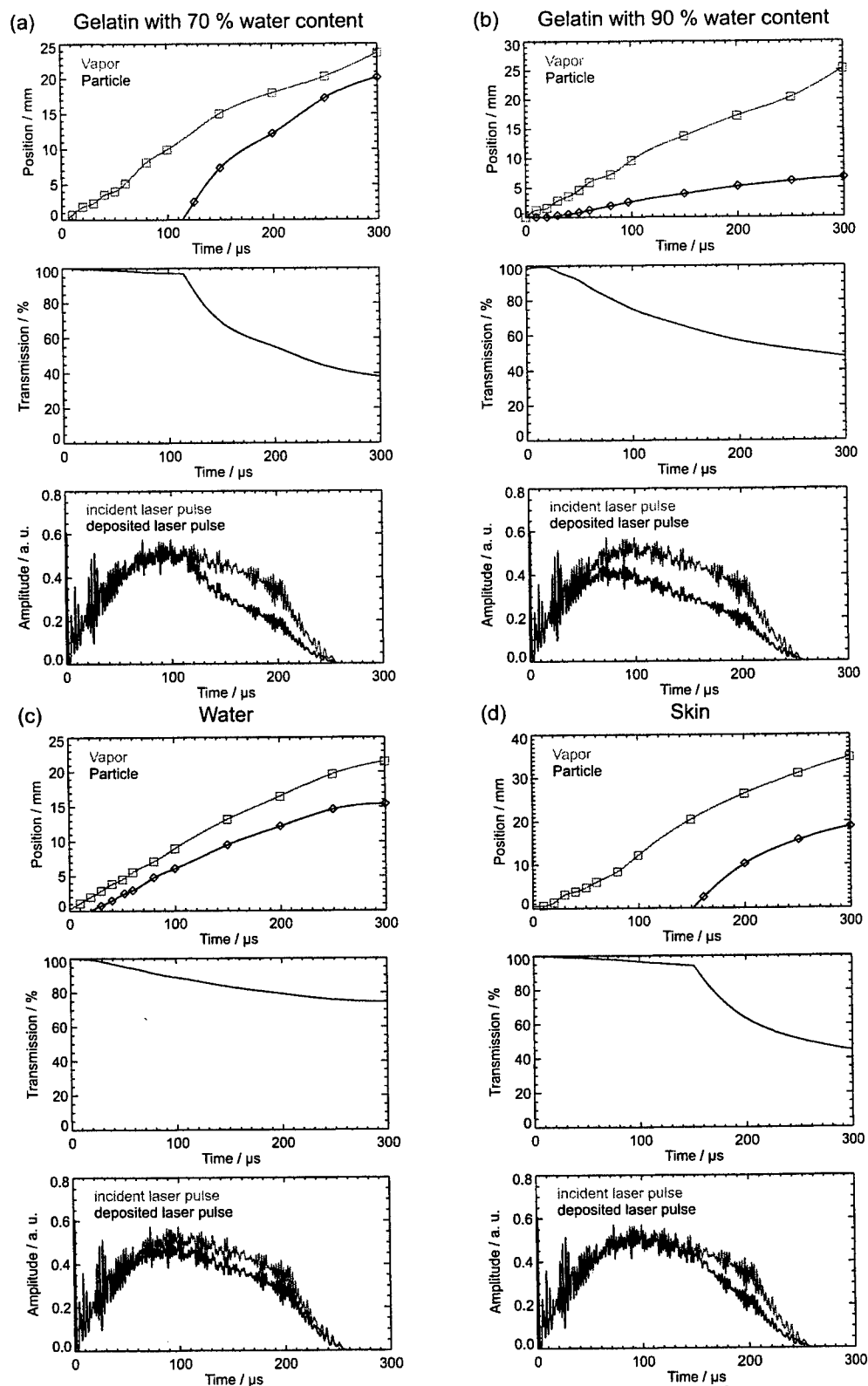
Figure 10. Transmission of the ablation plume for a radiant exposure of $4.6 \, \mathrm{J \, cm^{-2}}$, (a) for gelatin samples with 70 % water content, (b) for samples with 90 % water content, (c) for water, and (d) for skin. Each set of plots shows the position of the vapor front and the particle front as a function of time (top), the transmission of the ablation plume calculated using equation 2 (middle), and a comparison of the incident ablation laser pulse with the calculated pulse shape at the sample surface (bottom).

Figure 11. Transmission of the ablation plume for a radiant exposure of $7.8 \, \mathrm{J \, cm^{-2}}$, (a) for gelatin samples with 70 % water content, (b) for samples with 90 % water content, (c) for water, and (d) for skin. Each set of plots shows the position of the vapor front and the particle front as a function of time (top), the transmission of the ablation plume calculated using equation 2 (middle), and a comparison of the incident ablation laser pulse with the calculated pulse shape at the sample surface (bottom).

The fraction of transmitted laser pulse is lowest for the ablation of gelatin samples with 90 % water content. For a radiant exposure of 7.8 J cm^{-2}, only 61–74 % of the incident laser pulse energy are deposited into the sample (lower and upper estimates in Tab. 3). The low transmission is caused by the early onset of material ejection and the relatively high absorption coefficient of the ejected material. For water, gelatin samples with 70 % water content and skin the upper estimates for the fraction of transmitted pulse energy range between 83 % and 89 %, and the lower estimates between 77 % and 86 % (at 7.8 J cm^{-2}).

We can conclude that for the radiant exposures investigated up to 39 % of the laser pulse energy are absorbed in the ablation plume. The parameters used in our study are typical for large area ablations as applied, for example, in skin resurfacing.[1] Much higher radiant exposures are employed for cutting and drilling of tissue.[21,22] In these cases, shielding will play an even stronger role because the fraction of the pulse energy transmitted to the target decreases with increasing radiant exposure (Tab. 3). The estimates given for the absorption coefficient of the ejected material are based on measurements of the plume transmission performed at a distance of 2.5 mm from the sample surface. The particle density of the ejected material has already decreased until the particle front reaches the probe beam location, as can been seen from the photographs (Fig. 6). The values of the absorption coefficient and of the deposited energy given here are, therefore, still a lower estimate of the real values.

Consideration of the shielding effects is certainly relevant for the discrimination of the dosage for clinical laser applications, but it is even more important with respect to a theoretical understanding of the ablation process. The shielding by the ablation plume has, for example, to be considered for the calculation of ablation enthalpies. Data on ablation enthalpies found in the literature have to be reanalyzed because the influence of the ablation plume on the energy deposition was ignored in previous investigations. Future models for free running Er:YAG laser ablation of soft tissue should also take the material ejection during the laser pulse and the shielding by the ablation plume into account.

4. CONCLUSIONS

The shielding by the ablation plume during free running Er:YAG laser ablation of soft tissue has been experimentally investigated for the first time. The influence of the ablation plume on the energy deposition into the sample was studied for the ablation of water, gelatin samples, and skin. A probe beam delivered by a free-running Er:YAG laser was directed through the ablation plume to measure the absorption coefficients of the gaseous as well as of the liquid and solid ablation products. To achieve a better understanding of the temporal evolution of the probe beam transmission, it was compared with the ablation dynamics which was investigated by high speed photography. The photographic investigations revealed that material ejection during the ablation process is the key feature governing the shielding by the ablation plume. A particularly interesting observation was that an explosive material ejection occurs even during the irradiation of pure water, i. e. without the influence of a tissue matrix. The ejection of water droplets mixed with vapor can only be explained by a phase explosion. The presence of a tissue matrix can delay the phase explosion but will not completely change the driving force for material ejection, because the tissue water is the most important absorber at the Er:YAG laser wavelength. Our results demonstrated thus for the first time, that the material removal by free running Er:YAG laser pulses is driven by a phase explosion. This kind of a phase transition does, hence, not only occur during Q-switched IR laser ablation as suggested by Venugopalan et al..[23]

The shielding leads to a considerable reduction of the energy deposition in the sample. For gelatin samples with 90 % water content, for example, only about 61 % of the laser pulse energy are deposited into the sample at a radiant exposure of 7.8 J cm^{-2}. Even for skin, where we observed the lowest attenuation of the ablation pulse, only 86 % of the laser energy are deposited into the sample. The material ejection and shielding by the ablation plume must be considered in theoretical models for the ablation dynamics, calculations of the ablation enthalpy and in the dosimetry for clinical applications of free running Er:YAG lasers.

ACKNOWLEDGMENTS

REFERENCES

1. T. S. Alster, "Clinical and histological evaluation of six Erbium:YAG lasers for cutaneous resurfacing," *Lasers Surg. Med.* **24**, pp. 87–92, 1999.

2. K. Nahen and A. Vogel, "Investigations on acoustic on-line monitoring of IR laser ablation of burned skin," *Lasers Surg. Med.* **25**, pp. 69–78, 1999.

3. K. Nahen and A. Vogel, "Acoustic signal characteristics during IR laser ablation, and their consequences for acoustic tissue discrimination," in *Laser-Tissue Interaction XI*, vol. 3914, pp. 166–176, SPIE, 2000.

4. K. Nahen, W. Eisenbeiß, and A. Vogel, "Acoustic online monitoring of IR laser ablation of burnt skin," in *Biomedical Optoacousctics*, vol. 3916, pp. 218–226, SPIE, 2000.

5. J. A. Izatt, N. D. Sankrey, F. Partovi, M. Fitzmaurice, R. P. Rava, I. Itzkan, and M. S. Feld, "Ablation of calcified biological tissue using pulsed hydogen fluoride laser radiation," *IEEE J. Quantum. Electron.* **26**, pp. 2261–2270, 1990.

6. B. Majaron, D. S. und M. Lukac, M. Skaleric, and N. Funduk, "Heat diffusion and debris screening in Er:YAG laser ablation of hard biological tissues," *Appl. Phys. B* **66**, pp. 479–487, 1998.

7. R. Hibst and U. Keller, "The mechanism of Er:YAG laser induced ablation of dental hard substances," in *Dental Applications of Lasers*, vol. 1880, pp. 156–162, SPIE, 1993.

8. A. Miotello and R. Kelly, "Critical assessment of thermal models for laser sputtering at high fluences," *Appl. Phys. Lett.* **67**, pp. 3535–3537, 1995.

9. B. Majaron, P. Plestenjak, and M. Lukac, "Thermo-mechanical laser ablation of soft biological tissue: modeling the micro-explosions," *Appl. Phys. B* **69**, pp. 71–80, 1999.

10. A. D. Zweig and H. P. Weber, "Mechanical and thermal parameters in pulsed laser cutting of tissue," *IEEE J. Quantum Electron.* **QE-23**, pp. 1787–1793, 1987.

11. S. I. Anisimov and V. A. Khokhlov, *Instabilities in laser-matter interaction*, CRC Press, 1995.

12. D. Bäuerle, *Laser processing and chemistry*, Springer, 2000.

13. P. Debenedetti, *Metastable liquids*, Princeton Academic Press, 1996.

14. V. P. Skripov, *Metastable liquids*, Israel Program for Scientific Translations, Jerusalem, Wiley, New York, 1974.

15. M. M. Martynyuk, "Phase explosion of a metastable fluid," *Combust. Explos. Shock Waves* **13**, pp. 178–191, 1977.

16. D. R. Lide, ed., *CRC Handbook of Chemistry and Physics*, p. 6:18. CRC Press, Boca Raton, 1995.

17. D. E. Freund, R. L. McCally, R. A. Farrall, and D. H. Sliney, "A theoretical comparison of retinal temperature changes resulting from exposure to rectangular and gaussion beams," *Lasers in the Life Sciences* **7**, pp. 71–89, 1996.

18. J. S. Young, "Evaluation of nonisothermal band model for H_2O," *J. Quant. Spectrosc. Radiat. Transfer.* **18**, pp. 29–45, 1977.

19. K. Nahen, *Akustische Online-Kontrolle der Infrarot-Photoablation biologischer Gewebe*. PhD thesis, Technisch-Naturwissenschaftliche Fakultät der Medizinischen Universität zu Lübeck, 2001.

20. W. H. Press, B. P. Flannery, S. A. Teukolsky, and W. T. Vetterling, *Numerical Recipes in PASCAL*, Cambridge University Press, 1989.

21. M. Frenz, V. Romano, Y. D. Zweig, and H. P. Weber, "Instabilities in laser cutting of soft tissue," *J. Appl. Phys.* **66**(9), pp. 4496–4503, 1989.

22. H. Pratisto, M. Frenz, H. J. Altermatt, A. Arnold, K. Ehrenberger, D. Felix, and H. P. Weber, "Experimental in vivo fenestration of guinea pig cochlea using 2.79 μm laser radiation," *Lasers Med. Sci.* **12**, pp. 123–130, 1997.

23. V. Venugopalan, N. S. Nishioka, and B. B. Mikic, "Thermodynamic response of soft biological tissue to pulsed infrared-laser irradiation," *Biophysical Journal* **70**, pp. 2981–2993, 1996.

Nanosecond-time-response temperature measurements using radiation thermometry during 193 nm and 247 nm pulsed light irradiation: Comparison of corneal surface temperature histories

Miya Ishihara[1], Tsunenori Arai[1], Shunichi Sato[2], Yuji Morimoto[1], Minoru Obara[3], Makoto Kikuchi[1],

[1] Department of Medical Engineering, National Defense Medical College,
[2] Division of Biomedical Information Sciences, National Defense Medical College Research Institute
[3] Department of Electrical Engineering, Faculty of Science and Technology, Keio University

ABSTRACT

We have developed the fast time-response measurement of thermal radiation with 15ns rise time to monitor the corneal surface temperature during ArF excimer laser ablation. In this study, we aim to investigate the influence of the relation between the corneal penetration depth and sampling depth of the measurement system on the measured temperature using 193 nm and 247 nm pulsed lights which have different penetration depths of cornea. When the sampling depth was defined as the penetration depth of cornea at the thermal radiation wavelength, we obtained about 3 μm of the sampling depth by pulsed photothermal radiometry (PPTR). In the case of the 247 nm light irradiation, where the corneal absorption coefficient at 247nm was approximately equal to that for the thermal radiation, we found that the measured temperature rises were same as the estimated temperature rises based on the photothermal process. In contrast, in the case of the 193 nm light irradiation, where the absorption coefficient at 193 nm was larger than that for the thermal radiation, we found that the measured temperature rises were lower than the estimated temperature rises.

Keywords: Temperature, thermal radiation, time-response, PPTR (pulsed photothermal radiometry), absorption coefficient, ArF excimer laser, sampling depth

1. INTRODUCTION

We have developed the corneal temperature measurement system by using detection thermal radiation with 15 ns response time which has been shorter than the ArF excimer laser pulse duration [1]. The measured temperature value may be affected by its spatial resolution along to depth (sampling depth). To apply this measurement to ablation quality and quantity monitoring, the sampling depth of the thermal radiation temperature measurement should be determined.

In this study, we measured the temperature rises of two different wavelengths, which had remarkably different penetration depths [2] in order to evaluate influence of the relation between the penetration depth and sampling depth on the measured temperature rise. We used pulsed lights of 193nm and 247nm in wavelength. Since the sampling depth of the system was thought to be the depth where the thermal radiation mainly came from, it was defined as the inverse of the absorption coefficient (penetration depth) of cornea for the thermal radiation. The absorption coefficient of cornea for the thermal radiation was obtained by applying the time course of the measured thermal radiation intensity to the PPTR (pulsed photothermal radiometry) theory [3]. We compared the measured temperature rise with the estimated temperature rise which was calculated from the absorbed laser energy density in the layer defined by the penetration depth of cornea at the irradiation wavelength [4].

2. BACKGROUND THEORY

We employed the PPTR theory established by Tam et al. to determine the absorption coefficient for thermal radiation. The time course of the measured thermal radiation power was applied to PPTR of which signal amplitude is described as follow [3].

$$S(t) = A \frac{\beta}{\beta^2 - \alpha^2} \{ \beta exp(\alpha^2 Dt) erfc\sqrt{\alpha^2 Dt} - \alpha exp(\beta^2 Dt) erfc\sqrt{\beta^2 Dt} \} \tag{1}$$

* Miya Ishihara; kobako@cc.ndmc.ac.jp; phone +81-42-995-1596, fax +81-42-996-5199 Dept. of Medical Engineering, National Defense Medical College, 3-2 Namiki, Tokorozawa, Saitama, JAPAN, 359-8513

where, S(t) is the blackbody thermal radiation power, A is the constant depending on the electronic gain, α is the absorption coefficient for irradiation pulsed light, β is the absorption coefficient for thermal radiation, D is the thermal diffusivity and t is the time. The thermal diffusivity (D) was assumed to be that of water of 0.0013 cm²/s [5].

3. MATERIALS AND METHODS

<1> Derivation of the absorption coefficient for the cornea at 193 nm and 247 nm

In order to apply the time course of the thermal radiation to the PPTR formula (Eq.(1)) to obtain the sampling depth of the measurement system, the absorption coefficient at irradiation light wavelength for cornea should be derived as a fixed parameter in Eq.(1). For this derivation, the dependence of the ablation depth per pulse on laser fluence was applied to the Beer' law blow off model which can be expressed by Eq.(2) [6].

$$d = \frac{1}{\alpha} * ln\left(\frac{F}{F_{th}}\right) \tag{2}$$

where, d is the ablation depth per pulse, F is the fluence, α is the absorption coefficient, and F_{th} is the threshold fluence. For obtaining the ablation depth per pulse, experiments were performed as follows. Fresh porcine corneas were used as samples. As light sources for the ablation, an ArF excimer laser (wavelength: 193 nm, pulsewidth: 15 ns (FWHM)) and an OPO (optical parametric oscillator) (pulsewidth: 8 ns (FWHM)) were employed. The output wavelength of the OPO was adjusted at 247 nm. The light beams were focused onto the corneal surface by a 200-mm focal length silica lens. The beam spot sizes were 2.4 mm² for the 193 nm light and 0.75 mm² for the 247 nm light, respectively. The corneal samples were irradiated with laser fluence ranging from 50 to 500 mJ/cm² with the repetition rate of 10 Hz. The number of shots was fixed at 300. After the irradiation, the samples were fixed with a 4% glutaraldehyde phosphate buffer solution. The fixed samples were cut at the center of the ablation hole and the ablation depth was measured along the vertical section of the ablation hole by a microscope. The ablation threshold, which should be assigned to Eq.(2), was determined as the minimum fluence at which the ablation hole was visible.

<2> Derivation the absorption coefficient of the cornea for thermal radiation

The thermal radiation measurement generated by the 247 nm light irradiation was performed in addition to the 193 nm using a 150 MHz cut-off frequency photovoltaic MCT detector and a series of two 100 MHz-bandwidth amplifiers [1]. In order to apply the measured thermal radiation to the PPTR formula, which does not include ablation effect, the thermal radiation was measured at the laser fluences below the ablation threshold. The absorption coefficients at the thermal radiation wavelength were obtained when the time course of the thermal radiation generated by the 193nm and 247nm light irradiation were applied, respectively to Eq.(1).

4. RESULTS

<1> Absorption coefficients at 193nm and 247nm for cornea

The ablation thresholds were obtained at 65 mJ/cm² and 100 mJ/cm² for the 193 nm and 247 nm light irradiation, respectively. The ablation depth per pulse increased with the laser fluence. At the maximum laser fluence in the experiment (500 mJ/cm²), the ablation depths are 0.9 μm and 6.8 μm for the 193 nm and 247 nm light irradiation, respectively. We obtained the corneal absorption coefficients of 20000 cm⁻¹ and 3200 cm⁻¹ for 193 nm and 247 nm light, respectively.

<2> Determination of the absorption coefficient of the cornea for the thermal radiation

The transient thermal radiation signals from the corneal surface generated by 193 nm and 247 nm light irradiation at the fluence below the ablation threshold are shown in Fig.1(a) and (b). When these waveforms were applied to the PPTR formula (Eq.(1)) with the obtained absorption coefficients of cornea at 193 nm and 247 nm as a fixed parameter, the absorption coefficients for thermal radiation were obtained with a correlation coefficient of over 0.9. The obtained absorption coefficients were summarized together with the absorption coefficients of cornea at 193 nm and 247 nm in Table 1.
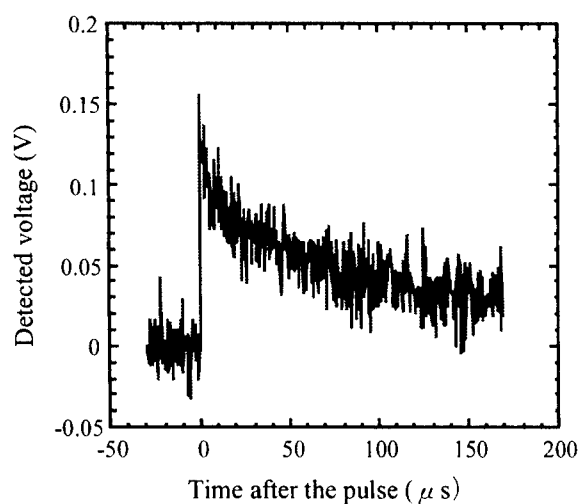
Fig.1 (a) The transient thermal radiation signal from the corneal surface generated by the ArF excimer laser
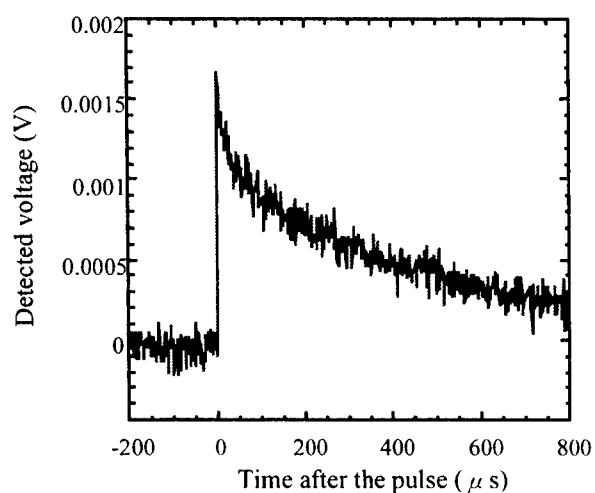(Fluence: 35 mJ/cm², averaged over 30 shots)

Fig.1 (b) The transient thermal radiation signal from the corneal surface generated by the 247 nm light
(Fluence: 35 mJ/cm², averaged over 50 shots)

Table 1. The summary of the absorption coefficient at the light source wavelength and the thermal radiation wavelength

Light source	193 nm	247 nm
Abs. Coef. (α)	20000 cm⁻¹	3200 cm⁻¹
Abs. Coef. (β)	3000 cm⁻¹	4000 cm⁻¹

Abs. Coef. (α): absorption coefficient at the light source wavelength
Abs. Coef. (β): absorption coefficient at the thermal radiation wavelength

5. DISCUSSION

<1> Sampling depth of the measurement system

We defined the sampling depth of the measurement system as the corneal penetration depth of the thermal radiation. The sampling depth was obtained as around 3 μm from the calculation by the PPTR formula (Eq.(1)). The estimated thermal radiation spectrum detected in our experiment was ranged from 4 to 13 μm. This estimated spectral range was based on Planck's law of radiation, the transmitted spectra through the optical components, and sensitivity spectrum of the MCT detector. Since the absorption coefficient of water, the major content of cornea, at this spectral range is 400-1800 cm⁻¹ [7], the corresponding penetration depth is 5.6-25 μm. We think there is a discrepancy between the obtained sampling depth and the estimated penetration depth for the thermal radiation. The explanation of this event has not been obtained.

<2> Comparison of the measured temperature and the estimated temperature based on the photothermal process

We compared the measured temperature rise with the estimated temperature rise to study the relation between the corneal penetration depth at irradiation light wavelengths (193 nm and 247 nm) and the obtained sampling depth [4],[8]. The measured temperature rise was obtained from the peak voltage of the measured thermal radiation signal with the calibration studied in our previous experiment [1]. The estimated temperature rise was calculated by the following equation [4].

$$\Delta T = \frac{\mu_a F}{\rho c} \qquad (3)$$

where, ΔT is the temperature rise (℃), μ_a is the absorption coefficient at irradiation light wavelength (cm⁻¹), F is the laser fluence (J/cm²), ρ is the density (g/cm³) and c is the specific heat (J/g/℃). The absorption coefficients of 20000 cm⁻¹ for the 193 nm and 3200 cm⁻¹ for the 247 nm were used. The values for ρ and c were assumed as those of water ($\rho = 1.0$ g/cm³, c=4.2J/g/℃) [8]. This equation could be applied only for the sub-ablative condition, so that the input laser fluences (F) in Eq.(3) were kept less than the obtained ablation thresholds. The calculated temperature rises are compared with the measured temperature rises as a function of laser fluence in Fig.2. In Fig.2, in the case of 247 nm irradiation, the calculated temperature rises are coincident to the measured temperature rise (R>0.9). In contrast, for the 193 nm irradiation, the measured temperature rises are much lower than the calculated temperature rises. Therefore, when the absorption coefficient at the irradiated light wavelength is approximately equal to the absorption coefficient for the thermal radiation, as in the case of 247 nm irradiation, our temperature measurement system indicates the estimated temperature rises using the absorption coefficient at irradiation light wavelength. On the other hand, when the absorption coefficient at the irradiated light wavelength is larger than the absorption coefficient of the thermal radiation, as in the case of 193 nm irradiation, the measurement system indicates underestimation of the estimated temperature rises.
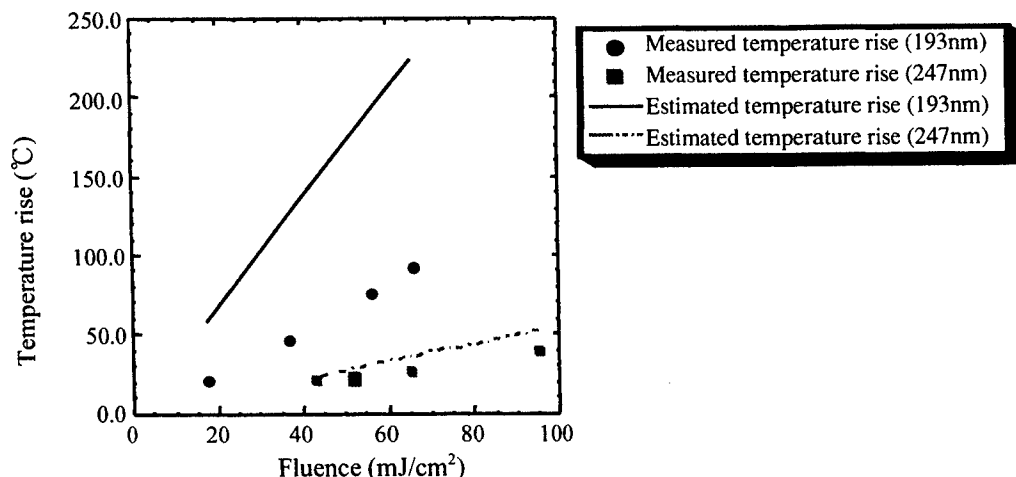

Fig.2 The comparison of the measured temperature rises generated by 193nm and 247nm irradiation with the estimated temperature rises as a function of the fluence.

One possible reason of the disagreement of the measured temperature rise with the estimated temperature rise in the case of 193nm light irradiation, in contrast with the agreement in the 247 nm light irradiation, may be due to various consumption way of the absorbed 193nm light energy. As the photon energy of 193nm light is 6.4 eV [9], the absorbed light energy seems to be spent not only for temperature rise but for cut of protein bonding by photochemical reaction [9] and fluorescence (peak wavelength; 350nm) observed during light irradiation [10] and so on. The estimated temperature becomes lower when a part of the light energy which is consumed only by temperature rise is input in Eq.(3). Accordingly, the estimated temperature may be close with the measured temperature rise. Therefore, in the case of 193 nm light irradiation, the disagreement of the measured temperature rise with the estimated temperature rise seemed not to be significantly caused by the relation between the corneal penetration depth and the obtained sampling depth. We supposed that the measured temperature rise seems to be affected by the absorption coefficient at 193nm.

6. CONCLUSION

We investigated the influence of the relation between the absorption coefficient for the irradiation light and sampling depth on the measured temperature using the irradiation of 193 nm and 247 nm pulsed lights which have different absorption coefficients of cornea. As the sampling depth was defined as the penetration depth at the thermal radiation wavelength, we obtained about 3 μm of the sampling depth by pulsed photothermal radiometry (PPTR). In the case of the 247 nm light irradiation, where the absorption coefficient at 247nm was approximately equal to that at the thermal radiation wavelength, we found that the measured temperature rises were same as the estimated temperature rises based on the photothermal process. In contrast, in the case of the 193 nm light irradiation, where the absorption coefficient at 193 nm was larger than that for the thermal radiation, we found that the measured temperature rises were lower than the estimated temperature rises. In the case of 193 nm light irradiation, the disagreement of the measured temperature rise with the estimated temperature rise seemed not to be significantly caused by the relation between the corneal penetration depth and the obtained sampling depth.

7. REFERENCES

1. M. Ishihara, S. Sato, T. Arai, M. Obara, M. Kikuchi, SPIE Proc, 3914, 122-126, 2000
2. C.A. Puliafito, R.F. Steinert, T.F. Deutsch. F. Hillenkamp, E.J. Dehm, C.M. Adler, Opthal., 92, 741-748, 1985
3. A.C. Tam, B. Sullivan, Appl. Phys. Lett. 43, 333-335, 1983
4. B.Choi, J.A.Pearce, A.J. Welch, Phys.Med.Biol., 45, 1-17. 2000
5. C.H. Schmitz, T.G. Hantzko, S. Lohmann, H. Lubatschowski, W. Ertmer, SPIE Proc, 2923, 12-19, 1996
6. G.H. Pettit, M.N. Ediger, Appl. Opt., 35, 3386-3391, 1996
7. G.M Hale, M.R. Querry, Appl. Opt., 12, 555-563, 1973
8. D.J. Smithies, T.E.Milner, B.S.Tanenbaum, D.C.Goodman, J.S.Nelson, Phys.Med.Biol., 43, 2453-2463, 1998
9. M.S Kitai, V.L. Popkov, V.A. Semchishen, A.A. Kharizov, IEEE J. of Q.E., 27, 302-307, 1991
10. H. Nakano, M. Ishihara, T. Arai, S. Sato, M. Kikuchi, M. Obara, JJSLSM, 21, 309-317, 2000

Highly resolved tracing of Q-switched mid-IR laser induced vaporization

Tobias Brendel and Ralf Brinkmann

Medical Laser Center Luebeck, Peter-Monnik-Weg 4, 23562 Luebeck, SH, Germany

ABSTRACT

We investigated Q-switched, TEM_{00} thulium laser induced bubble formation at a silica-water interface in the abscence of a speckle pattern. An optical bubble detection unit of high sensitivity was developed to observe on-line the bubble formation onset. Additional fast flash photographs revealed a heterogeneous bubble onset close by the silica surface, at a maximum distance of 8 μm from the surface. Under control of the optical detection unit, threshold radiant exposures for bubble formation were determined. Strong threshold variation was observed, when replacing a silica surface by another. By performing a series of 45 threshold measurements on different silica surfaces of same 60/40 (scratch and dig) quality, threshold radiant exposures in a range between 26 mJ/mm^2 and 95 mJ/mm^2 were found, with equal distribution of the 45 threshold values over this range. With help of the "gas entrapping crevice" model we present a first interpretation of our results. They show, in conclusion, that accurate predictions of the bubble onset solely as a function of irradiation parameters cannot be made.

Keywords: infrared lasers, ablation, speckle, bubble formation, cavitation, vaporization

1. INTRODUCTION

Pulsed laser sources in the mid-IR, i.e. in the 2 μm spectral range are established tools for laser-assisted surgery. This is chiefly based on the strong absorption of 2 μm optical radiation in water, which is the main constituent of most biological tissues. Mid-IR laser radiation therefore allows efficient tissue ablation and in addition it is transmittable by standard low OH multimode waveguides. The latter property opens up the field of minimally invasive laser surgery for sources such as the holmium laser (Cr:Tm:Ho:YAG, $\lambda = 2.12\,\mu$m) or the thulium laser (Cr:Tm:YAG $\lambda = 2.01$ μm) by inserting the flexible waveguides into small luminal catheters.

In many minimally invasive approaches the ablation process at the catheter tip proceeds in an environment of absorbing liquid. On this condition, tissue ablation can be accompanied by bubble formation and the generation of strong acoustic transients. Both processes contribute to the overall damage that is caused in the tissue and in particular the formation of bubbles comprises a number of additional damage mechanisms. Moreover, the precision of a laser-surgical invasion is determined by the maximum bubble extent and not by the dimensions of the irradiated zone.

For these reasons, the mechanisms of bubble formation have been object of extensive research.[1-4] With the application in mind, the investigations were mostly performed at a submerged fiber tip, assuming a homogeneous irradiance over the entire fiber tip area. However, the irradiation profile is modulated by a *speckle pattern* at the end of a multimode fiber guiding coherent laser light. And recent works have pointed out that this modulation has significant influence on the bubble formation process.[1,3]

(Send all correspondence to T.B.)

T.B.: brendel@mll.mu-luebeck.de; phone +49 451 5006517

R.B.: brinkmann@mll.mu-luebeck.de; phone +49 451 5006507

fax +49 451 505486; www.mll.mu-luebeck.de

The speckle pattern originates from a mutual interference of all fiber modes caused by their different path lengths within the fiber. The spatio-temporal evolution of the speckle pattern is thus dependent on the given fiber settings as well as on on the operation mode of the laser.[1] In consequence. the actual irradiation conditions at a fiber tip are hard to define for a given setup and vary with every experimental setup.

The goal of this study was to investigate the onset of bubble formation at a silica-water interface on well-defined irradiation conditions. For this, a Q-switched thulium laser ($\lambda = 2.01\,\mu$m) was adjusted to emit in gaussian ground mode (TEM_{00}), allowing precise determination of the radiant exposure applied. To avoid any speckle formation the laser beam was solely mirror guided. We developed an optical bubble detection unit of high sensitivity to accurately measure the threshold radiant exposures for bubble formation. In company with CCD images series of the silica-surface during irradiation. these experiments revealed the influence of the silica surface constitution to the bubble formation process.

2. MATERIAL AND METHODS

2.1. Experimental setup

All experiments were performed with a self-built, Q-switched. flash-lamp pumped thulium laser ($\lambda = 2.01\,\mu$m) which was adjusted to emit in gaussian ground mode (TEM_{00}). The Q-switched operation was realized by a standard rotating mirror setup, yielding maximum pulse energies of 40 mJ at a pulse duration of 300 ns (FWHM).

The bubble formation was studied in a filled cuvette with an entrance aperture which was closed by the surface of a fused silica dove prism, yielding the water-silica-interface of interest (see Fig. 1). The thulium laser radiation was sent through the prism into the liquid. For sufficiently high radiant exposures the laser output beam radius $\omega \simeq 1$ mm was reduced by means of a convex IR lens. A relatively long focal length of 200 mm was chosen to produce a quasi-parallel beam over the absorption depth of $\simeq 200\,\mu$m for the 2.01 μm laser radiation in water. To vary the pulse energy with minimum influence on the beam profile two 8 mm thick quartz plates were used, attenuating the polarized laser radiation by angle-dependent reflectance losses.

When the laser pulse was applied a magnified, axial image of the silica-water interface was recorded by a CCD camera through a glass window in the cuvette's side. By imaging a microscopic test rule the spatial resolution of the optic was determined to be better than 10 μm for a total field size of 0.8 x 1 mm. The moment of taking the image was controlled by the onset of the flash lamp lighting (flash duration: 14 ns). To achieve a bright and homogenenous lighting of the interface the flash lamp light was coupled into a Koehler illumination setup (adapted from microscopy).

2.2. Bubble Detection

The bubble detection unit basically consists of two parts (see Fig. 1): A p-polarized probing HeNe laser beam that is incident under 45° to the silica-water interface and a photomultiplier tube (PMT), monitoring the reflected light from the interface. Ambient light is blocked by a 633 nm bandpass filter at the entrance aperture of the PMT. With this arrangement, the growth of a bubble at the silica surface is observed by the PMT as an intensity rise. This is owing to the higher refractive index for water (n $\simeq 1.33$) than for the vapor inside a bubble (n $\simeq 1$), resulting in a higher reflectance for a silica-vapor interface than for a silica-water interface.

The detector sensitivity takes considerable advantage of the 45° incidence of the probing laser beam: On that incidence a liquid-vapor transition at the interface effects a reflectance rise of four orders of magnitude (see Table 1). This pronounced contrast results from two facts: For the silica-water interface the 45° incidence is close to the Brewster angle and the reflectance is correspondingly small. On the other hand. total reflection is obtained for the
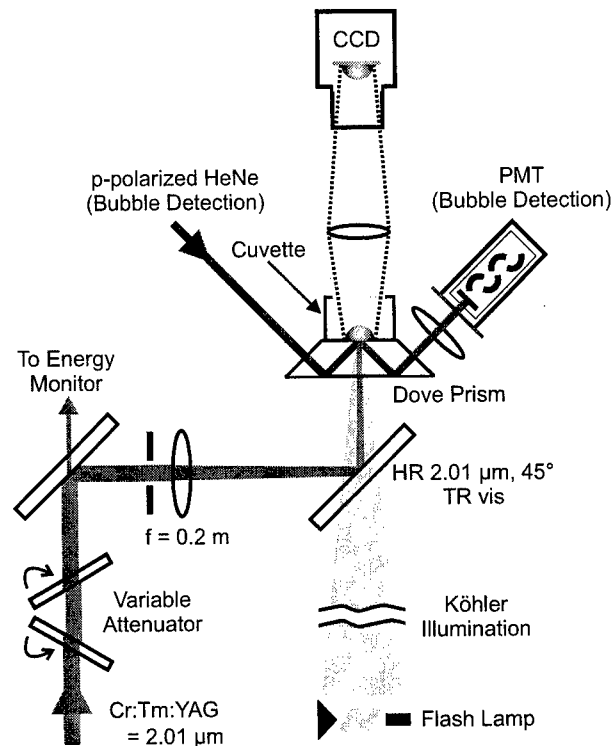
Figure 1. Experimental setup.

silica-vapor interface since the critical angle is exceeded. For comparison: At normal incidence the reflectance rise is given by a factor of 17.

As a result of diffraction effects the propagation of beams being reflected from very tiny bubble structures is no longer parallel but divergent. The divergence can be expressed in terms of Airy disk radii. E.g., the Airy disk radius of an initially 5 μm radial structure amounts to 6.2 mm at a distance of 80 mm where the PMT's photocathode is located. The photocathode measures 5 mm in radius, thus a part of the reflected probing light would be lost for detection. To avoid this, a convex lens was placed behind the dove prism collecting all the reflected probing light from tiny bubble structures, as well. Before the probing beam entered the dove prism it was sent through a lens-pinhole-lens optical low pass with subsequent beam expansion, yielding a homogeneous and parallel gaussian beam of radius $\omega_p = 1.5$ mm. In doing so, the alignment of the probing beam to the thulium spot of $\omega = 315\,\mu$m became considerably simple.

interface	Refractive Indices	Reflection Coefficient (45°, p-polarized)
silica-water	1.457 and 1.332 (T=20°C)	$R_p \simeq 10^{-4}$ (Brewster's angle: 42.4°)
silica-vapor	1.457 and $\simeq 1$	$R_p = 1$ (critical angle: 43.3°)

Table 1. Refractive indices and resulting reflection coefficients at the interface for 45° incidence and p-polarized HeNe laser light.

The PMT output was amplified by an integrated 5.8 Mhz current amplifier, yielding an output sensitivity $S = 4.4\,V/\mu$W. The peak irradiance I_0 of the probing beam was $I_0 = 2P/\pi\omega_p^2 = 0.57$ mW/mm^2 for $\omega_p = 1.5$ mm and a beam power $P = 2$ mW. The residual reflection of 0.01% at the silica-water interface produced a signal offset of 900 mV which was filtered out electronically. Since this cannot be done without increasing the noise level a signal rise ΔU of 50 mV was necessary to clearly determine the appearance of a bubble. With these data a rough calculation of

the detector sensitivity and lateral detection range can be made: Given a distance r from the center of the probing beam, a signal rise of 50 mV is produced by a bubble with radius

$$r_b(r) = \sqrt{\frac{\Delta U}{\pi S I_0}} \exp(r^2/\omega_p^2).$$

(1)

With the data given above, a radius $r_b \simeq 0.8\,\mu$m is calculated for the center of the probing beam ($r = 0$), and by regarding the inverse of Eq. (1) a distance $r = 1.3$ mm is found for an assumed bubble radius $r_b = 5\,\mu$m.
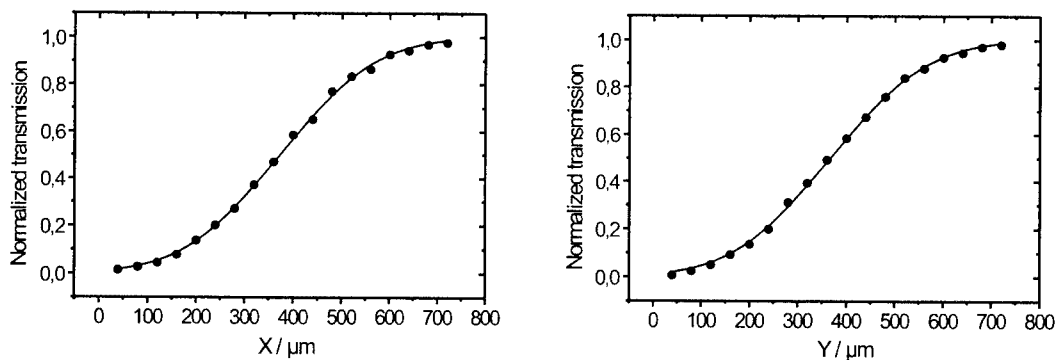
2.3. Measurement of Thulium Beam Profile

Given the pulse energy E, a radial gaussian beam profile $H(x,y)$ [mJ/mm^2] is fully described by the beam radius ω, according to

$$H(x,y) = H_0 \exp\left(-\frac{2\,(x^2 + y^2)}{\omega^2}\right), \text{ with } H_0 = \frac{2E}{\pi\omega^2}.$$

(2)

We determined ω experimentally by means of the "knife edge" technique.[5] At this, a knife edge is passed through the laser beam (perpendicular to the beam axis) and the residual transmission $T(x)$ is measured as a function of the knife edge position x. The obtained data points $T(x)$ are integral values of the beam profile in direction of the knife edge movement and thus follow the expression

$$T(x) = \frac{1}{2}\left[1 + \text{erf}\left(\frac{\sqrt{2}(x - x_0)}{\omega}\right)\right].$$

(3)

Here, $T \in [0...1]$ is the normalized transmission, x_0 is an auxiliary variable with $T(x_0) = 0.5$, and "erf" is the error function.

Figure 2. Horizontal and vertical knife edge measurement of the gaussian beam profile right behind the prism surface. Values of $\omega_x = 314(\pm 5)\,\mu$m and $\omega_y = 316(\pm 5)\,\mu$m were obtained from numerical fits of Eq. (3) to the data (straight lines). Each data point is a mean value over 4 single laser pulses.

For our experiment, we uncoupled the cuvette from the dove prism and performed the knife edge measurement right behind the prism surface at which the bubble formation was to be investigated. In order to consider a possible beam ellipticity, we performed measurements both in horizontal and vertical direction. Fig. 2 depicts the experimental results. Numerical fits of Eq. (3) to the data showed high accuracy and revealed a non-elliptical beam profile with a mean radius of 315 μm. With this value all further calculation of the radiant exposure was performed.

2.4. Thresholds for Bubble Formation

Thresholds for bubble formation were investigated in purified, degassed water under control of the optical bubble detector. They were determined from at least 120 laser pulses of different pulse energy, where it was noted which (peak) radiant exposure H_0 was applied and if the optical detector recorded a bubble or not. Then, radiant exposure intervals of suited width ΔH were defined and the corresponding bubble formation probability for each interval was evaluated. A statistical analysis of the resulting probability distribution was performed by means of a standard Probit algorithm, yielding an ED 50 value for bubble formation. This value was defined to be the treshold value for bubble formation.

In a preliminary study we investigated the effects of *cavitation erosion* due to continued bubble generation at the silica surface. For this, we measured the bubble formation threshold repeatedly (10 times) at the same surface spot. Since no change of the threshold value occured in this experiment, it can be concluded, that a single threshold measurement remains unaffected by erosive effects. However, the erosion advances with the number of generated bubbles, and therefore we frequently changed the dove prisms in our experiments. In doing so, we noticed a strong variability of the bubble formation thresholds with changing surfaces. To better quantify this observation we performed a series of N=45 threshold measurements, where all parameters were kept constant apart from the surface. These measurements were performed at the surfaces of 4 new silica dove prisms with a standard 60/40 (scratch and dig) surface quality.

2.5. Temperature Calculations

The absorption of pulsed laser radiation in water causes a temperature rise and a thermoelastic stress transient. Both effects are moderated by heat diffusion and acoustic wave propagation out of the absorption zone. The achieved temperature and stress amplitudes are therefore not only a function of the total pulse energy deposited but also of the pulse duration in relation with the dimensions of the absorption zone.

For the given case, the absorption zone is defined laterally by the gaussian beam radius $\omega = 315\,\mu$m and axially by the penetration depth $\delta \simeq 150\,\mu$m (at 20°C) of the 2.01 μm radiation in water. On account of $\delta < \omega$, a thermal relaxation time $\tau_r \simeq \delta^2/\kappa > 150$ ms (where, $\kappa = 1.43 * 10^{-7}$m^2/s is the thermal diffusivity in water) and an acoustic transit time $\tau_{ac} = \delta/c = 93$ ns (where $c = 1480$m/s is the speed of sound in water at 20°C) are calculated, yielding the characteristic time scales for the regimes of thermal and stress confinement. Comparing these data with the pulse duration of 300 ns, it follows, that the energy deposition is thermally but not stress confined. On this condition, the stress evolution is strongly dependent on the temporal power profile of the laser pulse. The temperature change with time is given in thermal confinement by

$$\frac{\partial T}{\partial t} = \frac{\mu(T)}{\rho\,C_p}\,I(t), \tag{4}$$

where ρ and C_p are the density and heat capacity (at constant pressure) of the liquid. $I(t)$ [W/mm^2] denotes the applied irradiance. Experimentally, the Q-switched laser pulses showed a gaussian-like course, yielding (with τ expressing the full width at half maximum)

$$I(t) = HI_0 \exp\left[-\ln 2\left(\frac{2t}{\tau}\right)^2\right], \text{with } I_0 = \left(2\,\tau\sqrt{\frac{\pi}{\ln 2}}\right)^{-1} \tag{5}$$

to fulfill the normalization condition $\int_{-\infty}^{\infty} I(t)\,\mathrm{d}t = H$. When Eq. (4) is integrated to obtain $T(t)$ the notable temperature dependence of $\mu(T)$ has to be taken into account (the temperature dependencies of ρ and C_p are neglectable). Jansen et al.[6] derived a linear function $\mu(T) = a + bT$ for water in the temperature range of 20°C to 100°C. For our requirements, we measured $\mu(T)$ with improved accuracy in the same temperature range. As

a result, we also found a linear function. but with different values for a and b. namely $a = 6.99 \pm 0.02$ mm^{-1} and $b = -0.0254 \pm 3 \ast 10^{-4}$ (°C mm)$^{-1}$.[7] The temperature dependence of μ turns Eq. (4) into a linear differential equation for the objective function $T(t)$. It is solved analytically by separation of variables. giving the final expression[1]

$$T(t) = \frac{1}{b} \left[\mu(T_0) \exp\left(\frac{b}{\rho C_p} \int_{-\infty}^{t} I(\tilde{t}) \, d\tilde{t} \right) - a \right] \tag{6}$$

for the evolution of T, starting at a temperature T_0.

3. RESULTS AND DISCUSSION

3.1. Spatial Localization of Bubble Onset

The spatial localization of the bubble onset with respect to the silica surface was investigated by comparison of the surface-confined optical detector signal with a series of CCD images. A representative image of the early bubble formation stage is shown in Fig. 3 (left). revealing a remarkable heterogeneous bubble onset. This was similarily observed at the end of a submerged fiber tip[1,3] and correlated to the presence of the speckle pattern, providing nucleation sites by hot spots. This correlation does not hold in our experiment, however. nucleation sites given by micro-bubbles are always present in a liquid and in particular on a solid surface. Thus, the bubble onset is also heterogeneous in the abscene of a speckle pattern. Now. to perform the image-to-detector comparison, a series of laser pulses of equal radiant exposure (and pulse duration) was applied and for each a CCD image was taken at a different point of time within the irradiation period. To secure a stable and clear bubble onset a radiant exposure of more than twice the bubble formation threshold was chosen, namely $H_0 = 115$ mJ/mm^2. For this, at first the bubble formation threshold was determined to be 55 mJ/mm^2 in this experiment (see next subsection for details).

The results are shown on the right in Fig. 3. In this graph, each circle on the temporal laser pulse profile marks one of 22 CCD images taken. An open circle indicates, that no bubble was observed at this point of time while for a closed circle it was. The corresponding detector response is shown in the graph, as well. The detector signal proved to be highly reproducible over all laser pulses, hence the plotted curve can be compared to the entire image series.
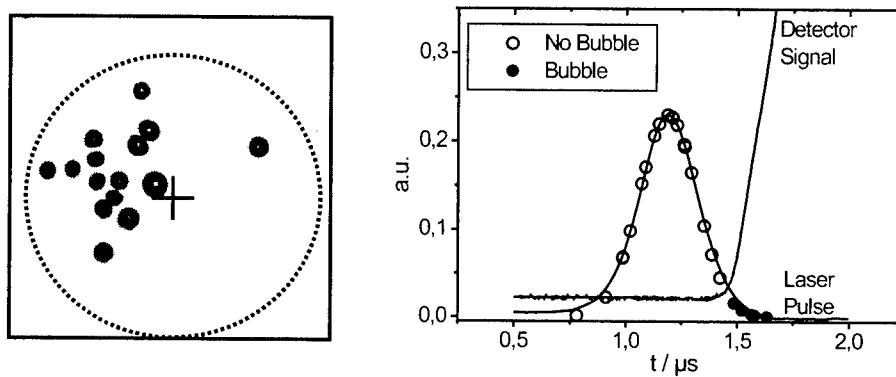
Figure 3. Left: CCD image of an early bubble formation stage (240 ns after the end of the laser pulse). The position of the thulium beam is indicated by the cross and the dotted circle, marking the center of the beam and the gaussian beam radius $\omega = 315 \, \mu$m, respectively. **Right:** Comparison of bubble formation onset as found by CCD images (circles) and detector signal.

The comparison reveals, that the bubble onsets as observed by a rising detector signal and by the image series coincide within a time window of $\simeq 60$ ns. To turn this value into a distance information of the bubble onset with

respect to the silica surface, we first estimated the inital bubble radius velocity from the time between the last image without bubble and the first image with bubble and the maximum bubble size on the latter image. In doing so, a bubble radius velocity of 125 m/s was determined which is in the range of previous results.[2] A bubble growing over 60 ns with this velocity reaches a radius of 8 μm, such that the localization of the bubble onset can be confined to this distance.

3.2. Thresholds for Bubble Formation

In Fig. 4 a typical bubble formation threshold measurement is shown. It consists of N = 120 exposures in the range of 10 mJ/mm^2 to 46 mJ/mm^2, being divided into 6 intervals of width $\Delta H = 6$mJ/mm^2 (according to the width of the bars). The plotted curve represents the Probit analysis of the data, yielding an ED50 value of 30 mJ/mm^2, which is marked by an arrow. Note, that the data is plotted over the peak radiant exposure H_0. Now, the 45 threshold measurements with varying surface are summarized in Fig. 5. They reveal an overall threshold range of

$$26 \text{ mJ/mm}^2 \leq H_0 \leq 95 \text{ mJ/mm}^2,$$

thus the minimum and maximum value differ by a factor of almost 4. Moreover, it can be derived from Fig. 5 that the distribution of the threshold data shows no significant "center of mass". A threshold value of particular interest is $H_0 = 60$ mJ/mm^2, because for this radiant exposure a water temperature of 100°C is reached. Any threshold above this value thus represents a regime of *boiling retardation*, which can develop if the number of nucleation sites is not sufficient to completely transfer the deposited latent heat into the vaporization process. Moreover, for sub-μm nucleation sites surface tension turns out to significantly rise the working pressures and with it the vaporization threshold. With respect to our experiment a maximum temperature of 130°C for $H_0 = 95$ mJ/mm^2 was achieved in this way (according to Eq. (6)).
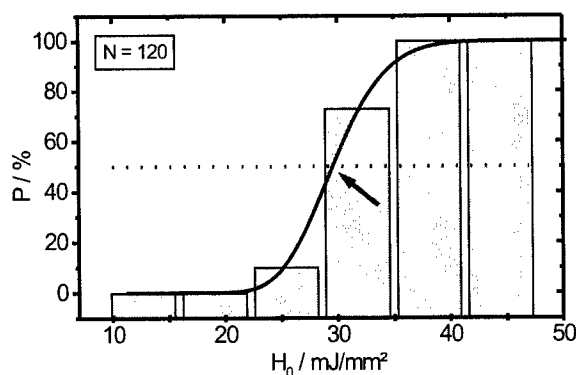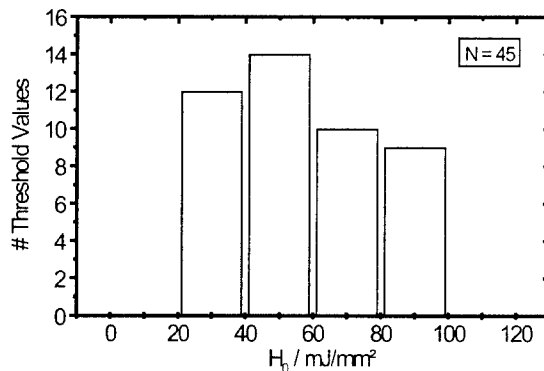

Figure 4. Example of a bubble formation threshold measurement. The straight line denotes the Probit analysis of the data, yielding an ED50 value of 30 mJ/mm^2 (arrow), which is to be defined as threshold value.

A bubble formation below $H_0 = 60$ mJ/mm^2 is most likely addressed to tensile stress induced cavitation. Although stress confinement is not fulfilled in our experiment, sufficient tensile stresses for cavitation can be calculated. Based on a sophisticated 3-d thermoelastic stress model with consideration of the temporal shape of the laser pulse (that is going to be presented in detail in a future publication) tensile stresses of -30 bar are already found for the lowest threshold radiant exposure $H_0 = 26$ mJ/mm^2.

Both mechanisms for bubble formation, vaporization and cavitation, are initiated by the same type of nucleation site, namely by micro gas cavities.[8] As a consequence, the onset of both effects is dependent on the number and size of nucleation sites for the reasons described above. In the last section we determined the bubble onset to occur

16
14   N = 45
12
10
Threshold Values
8
6
4
2
0
0   20   40   60   80   100   120
H_b / mJ/mm²

Figure 5. Variation of the bubble formation threshold with varying silica surface. Plotted are the number of counted threshold values over radiant exposure intervals of width $\Delta H = 20$ mJ/mm² (denoted by the width of the bars).

close by the silica surface, at a maximum distance of $8\,\mu$m. Moreover, since we used purified and degassed water, it is most likely, that mainly the surface provides nucleation sites in our experiments. In the theory of liquid-vapor phase change phenomena this is a noted effect and it is modeled by gas entrapping surface crevices.[8] At this, gas is entrapped when the liquid front sweeps over the surface during the filling of the cuvette. Since these crevices can be replenished in our experiments by the vapor of a forming bubble, a permanent existence of gas-filled crevices cannot be avoided. However, number and size of the crevices may vary over the regarded surface region, yielding varying nucleation conditions, as well. We assume this to be the underlaying mechanism for the observed threshold scatter with varying surfaces in our experiment.

4. CONCLUSIONS

The process of Q-switched thulium laser induced bubble formation at a silica-water interface was investigated under well-defined irradiation conditions. An optical bubble detector of high sensitivity was developed and employed to observe the bubble formation process. By comparison with CCD image series, a hetereogeneous bubble onset was observed and located close by the silica surface, at a distance of $\leq 8\,\mu$m. Under control of the optical detector, thresholds for bubble formation were investigated and a strong threshold variation with varying surfaces was observed. For standard optical quality surfaces threshold values between 26 mJ/mm and 95 mJ/mm were measured. As underlying mechanism microscopic, gas trapping crevices in the surface are assumed, yielding varying nucleation conditions as a function of the crevice distribution on the surface. While these effects are noted in the theory of liquid-vapor phase change phenomena, they have not been described in the context of pulsed laser ablation, yet. In consequence of the strong threshold scatter, accurate predictions of the bubble onset solely as a function of irradiation parameters cannot be made.

ACKNOWLEDGEMENT

REFERENCES

1. R. Brinkmann and C. Hansen, "Beam-profile modulation of thulium laser radiation applied with multimode fibers and its effect on the threshold fluence to vaporize water," *Appl. Opt.* **39** 19, pp. 3361-3371, 2000.

2. R. Brinkmann, and C. Hansen, "The Analysis of Cavitation Bubble Dynamics by Optical On-line Monitoring," in *Laser-Tissue Interaction and Tissue Optics IV*, Guy P. Delacretaz et al., eds., *Proc. SPIE* **3195**, pp. 273–279, 1998.

3. M. Frenz, F. Koenz et al. , "Starting mechanisms and dynamics of bubble formation induced by a Ho:Yttrium aluminium garnet laser in water," *J. Appl. Phys.* **84** 11, pp. 5905-5912, 1998.

4. D. Jansen, T. van Leeuwen et al. , "Partial vaporization model for pulsed mid-infrared laser ablation of water," *J. Appl. Phys.* **77** 12, pp. 1-8, 1995.

5. A. E. Siegman, M. W. Sasnett et al. , "Choice of Clip Levels for Beam Width Measurements Using Knife-Edge Techniques," *IEEE J. Quantum. Electron.* **27** 4, pp. 1098-1104, 1991.

6. D. Jansen, T. van Leeuwen et al. , "Temperature Dependence of the absorption coefficient of water for midinfrared laser radiation," *Lasers Surg. Med.* **14**, pp. 258-268, 1994.

7. B. I. Lange and T. Brendel, Medical Laser Center Luebeck, Germany. To be published.

8. V. P. Carey, *Liquid-vapor phase change phenomena: an introduction to the thermophysics of vaporization and condensation processes in heat transfer equipment*, Hemisphere Publishing Corporation, Washington, 1992.

Channeling in myocardium tissue through nanosecond pulsed laser photodisruption at visible and near-infrared wavelengths

Makoto Ogura*[a], Shunichi Sato**[b], Tunenori Arai***[c], Miya Ishihara***[c],
Satoko Kawauchi***[c], Takemi Matsui****[d], Akira Kurita****[d], Makoto Kikuchi***[c],
Hitoshi Wakisaka**[b], Hiroshi Ashida**[b], Minoru Obara*[a]

[a]Faculty of Science and Technology, Keio Univ. ; [b]Div. of Biomedical Information Sciences, National Defense Medical College Research; [c]Dept. of Medical Engineering, National Defense Medical College; [d]Div. of Biomedical Engineering, National Defense Medical College Research

ABSTRACT

We investigated *in vitro* the mechanism of myocardium tissue ablation with nanosecond pulsed laser at the visible and near-infrared wavelengths. In experiments, porcine myocardium tissue was used as sample. It was found that the ablation rate at 1064 nm was larger than that at 532 nm in spite of lower absorption coefficient at 1064 nm than that at 532 nm for the tissue. During ablation the laser-induced optical emission intensity was measured and it was correlated with the ablation depth. Ablated tissue samples were fixed and stained, and histological analysis was performed with an optical microscope and a polarization microscope. For the 1064-nm laser-ablated tissues thermal damage was very limited, although damage that was presumably caused by mechanical effect was observed. The optical emission intensity during the 1064-nm laser ablation was higher than that during the 532-nm laser ablation at the same laser intensity. And for the 1064-nm laser ablation the ablation threshold was nearly equivalent to the optical emission. Based on these experimental results, we concluded that with the 1064-nm laser light, the tissue removal was achieved through a photodisruption process. Application of 1064-nm, nanosecond pulsed laser photodisruption to transmyocardial laser revascularization(TMLR) was discussed.

Keywords: laser ablation, myocardium tissue, transmyocardial laser revascularizaiton(TMLR), Q-switched Nd:YAG laser, visible, near-infrared, thermal damage, laser-induced plasma, photodisruption

1. INTRODUCTION

Recently, transmyocardial laser revascularization (TMLR), that is the laser surgery for treating serious ischemic heart diseases, has been introduced. In this treatment laser beam irradiates ischemic myocardium tissue to create blood flow channels, and this could improve blood perfusion in the myocardium.[1] However, no comprehensive study has been performed to reveal the optimum laser condition for this treatment. We have been studying ablation mechanism of myocardium tissue, where an emphasis has been placed on the effects of the laser wavelengths. In a previous study, we made *in-vitro* experiments with porcine myocardium tissue in the spectral region from ultra-violet to near-infrared by using a Q-switched Nd: YAG laser,[2] and it was found that the ablation efficiency decreased as the laser wavelength became longer.
But the ablation efficiency for 1064-nm laser irradiation was comparable to that for 355-nm laser irradiation. During the 1064-nm laser irradiation the intense laser-induced plasma which accompanied strong optical and acoustic emissions was observed. It was thought that the laser-induced plasma might influence the ablation mechanism essentially.
In this paper, we report the influence of the laser-induced plasma on the ablation characteristics for the porcine myocardium tissue at the visible and near-infrared wavelengths. Based on the experimental results of the ablation efficiency, laser-induced plasma intensity, and tissue damage, we discuss the ablation mechanism for the two laser wavelengths. And application of nanosecond pulsed laser photodisruption to TMRL is duscussed.

2. EXPERIMENTAL

A Q-switched Nd:YAG laser was used as a light source for ablation. Laser outputs at 1064 nm (the fundamental band) and 532 nm (the second harmonics) were used. The pulse durations were 6.0 – 7.0 ns and 4.0 – 5.0 ns respectively. The laser repetition rate was kept constant at 10 Hz.

*contact. makogura@obara.elec.keio.ac.jp; Obara Lab., Keio Univ., 3-14-1 Hiyoshi, Kouhoku-ku, Yokohama-shi, Japan 223-8522

Figure 1 shows the experimental arrangement. The laser output beam was focused with an uncoated quartz lens (f = 200 mm) and irradiated the tissue sample with a constant spot area of 7.85×10^{-3} cm^2 that was equivalent to an area of a 1-mm diameter circle. Porcine myocardium tissue was used as sample.
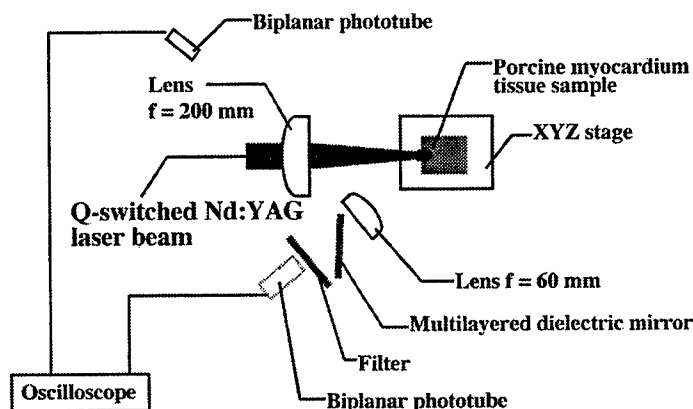

Fig. 1: Experimental arrangement.

The temporal profile of the laser-induced optical emission, which was collimated with an uncoated quartz lens (f = 60 mm) to enhance the signal intensity, was measured with a biplanar phototube.

The side view of the laser-induced optical emission was taken with a CCD camera.

Ablation depth was measured, tissue samples fixed with a 2% glutaraldehyde phosphate buffer solution. The ablated tissues fixed with a 10% formalin solution were observed with an optical microscope and a polarization microscope to evaluate the laser-induced damage in the tissue.

3. RESULT & DISCUSSION

3.1. Ablation characteristics

Figure 2 shows the dependence of the ablation depth on the laser intensity at 1064 nm and 532 nm. At each laser intensity 10 laser pulses were irradiated the tissue sample to obtain the ablated hole deep enough for accurate measurement. It is shown that the ablation rate for the 1064-nm laser irradiation is larger than that for the 532-nm laser irradiation. Although it is thought that the absorption coefficient at 1064 nm is smaller than that at 532 nm for the tissue, the ablation threshold for the 1064-nm irradiation is about 0.8 GW/cm^2, which is a half of that for the 532-nm irradiation. Strong optical and acoustic emissions were also observed during the 1064-nm laser irradiation.
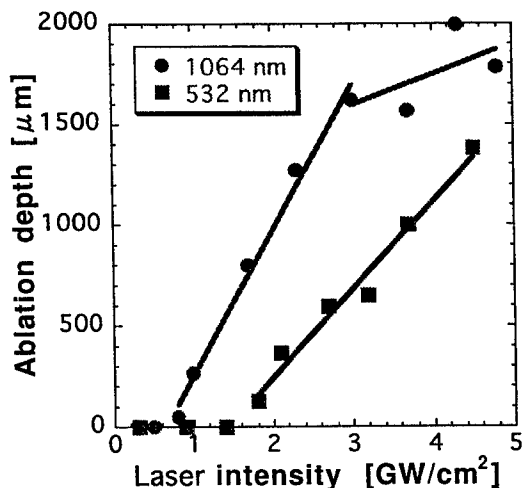

Fig. 2: The dependence of the ablation depth on the laser intensity for 10 laser pulses (n > 3).

Figure 3 (a) and (b) show histological images of the ablated tissue obtained with a polarization microscope. The thermal damage thickness for the 1064-nm laser-ablated tissue seems to be very limited. Although it is known that the penetration depth for the 1064-nm light is deeper than that for the 532-nm light, thermal damage thickness for the 1064-nm laser-ablated tissue is smaller than that for the 532-nm laser-ablated tissue. For the 1064-nm laser irradiation, a few hundreds micrometer thick damage that is presumably caused by acoustic effect could be seen (not shown).

(b)
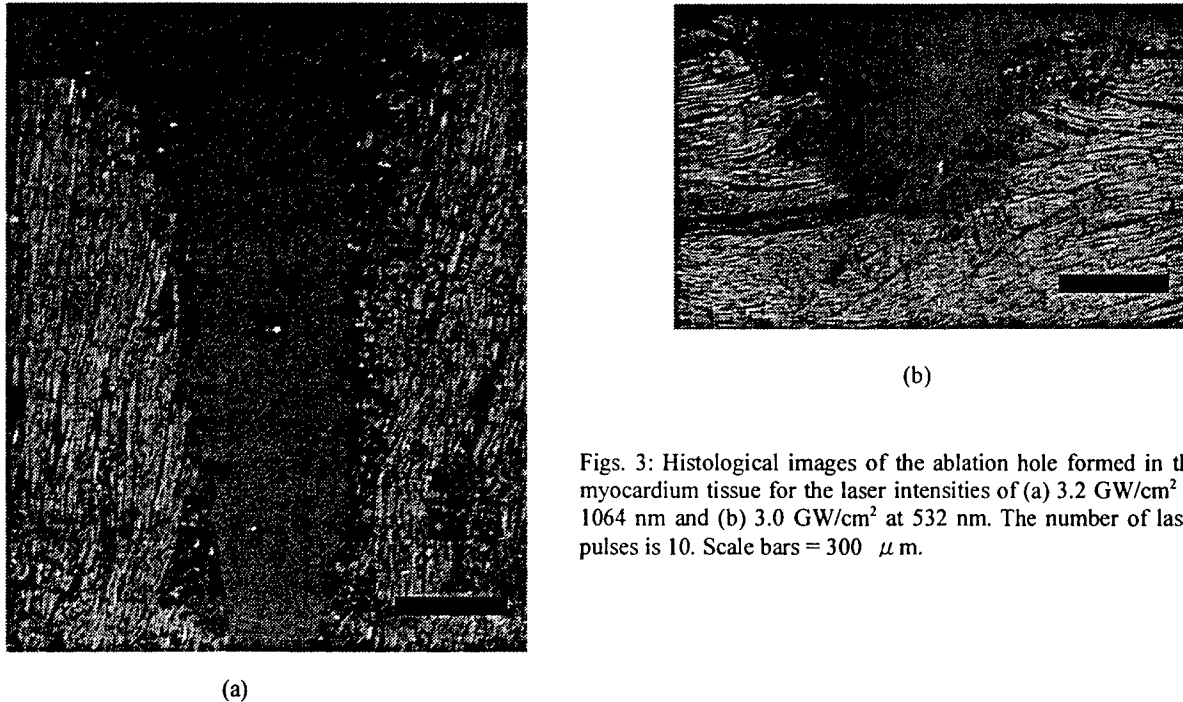
Figs. 3: Histological images of the ablation hole formed in the myocardium tissue for the laser intensities of (a) 3.2 GW/cm^2 at 1064 nm and (b) 3.0 GW/cm^2 at 532 nm. The number of laser pulses is 10. Scale bars = 300 μ m.

(a)

These observations indicate that the tissue removal is not achieved through a simple photothermal process. To understand the mechanism of the 1064-nm laser ablation, we paid attention to the strong laser-induced optical emission observed during laser irradiation.

3.2. Mechanism of the 1064-nm laser ablation

Figure 4 shows the temporal profiles of the laser pulse and the laser-induced optical emission at a 1064-nm laser intensity of 3.1 GW/cm^2. In this case, the laser-induced optical emission could be detected for as long as 400 ns. We think that this optical emission is dominated by plasma (optical breakdown) because of two reasons. Firstly, the optical emission accompanied strong acoustic emission. And secondly, the optical emission intensity rises rapidly and its peak appears during the laser pulse.[3] Recombination time for typical particles in plasma is a few picosecond.[3, 4] Therefore, the optical emission remained after the laser pulse is thought to be originated from the ablated particles, not direct optical breakdown.

Figures 5 (a) and (b) show the dependence of the peak intensity of the laser-induced optical emission on the laser intensity for the 1064-nm and the 532-nm laser irradiations respectively. The peak intensity of the laser-induced optical emission for the 1064-nm irradiation is four times larger than that for the 532-nm irradiation at the same intensity of 4.2 GW/cm^2.

For the 1064-nm irradiation, the laser-induced optical emission could be observed from a relatively low laser intensity of 0.8 GW/cm^2. It should be noted that this intensity (0.8 GW/cm^2) corresponded to the ablation threshold of the tissue. Both in ablation depth and optical emission an inflection point is seen at a laser intensity of about 3.0 GW/cm^2.

The CCD image (side view) of the optical emission for the 1064-nm laser ablation showed that the optical emission was generated not only on the tissue surface but also in the tissue (not shown).

From all of the observation described above, we consider that the tissue removal by the 1064-nm laser light is achieved through a photodisruption process.

There have been reported that in the plasma-mediated ablation with high-intensity lasers, the strong acoustic wave is generated and the pressure amplitude exceeds hundreds of bar.[5, 6, 7] It is supposed that in our case, a strong acoustic wave is generated by plasma formation and it might cause mechanical damage in the tissue under some experimental condition.
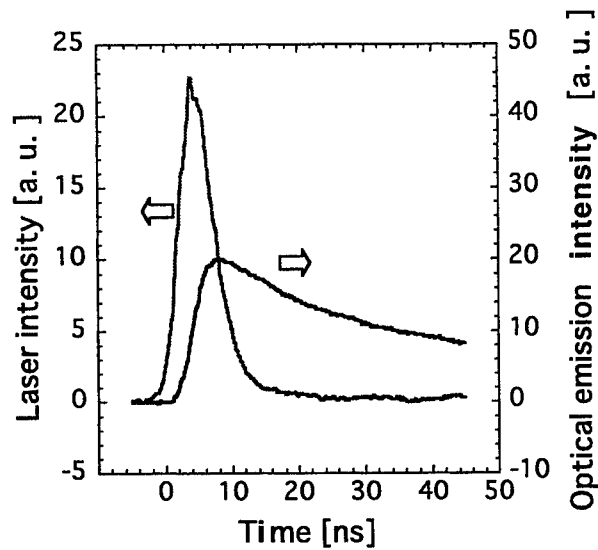
Fig. 4: Temporal profiles of the laser induced-optical emission and the laser pulse
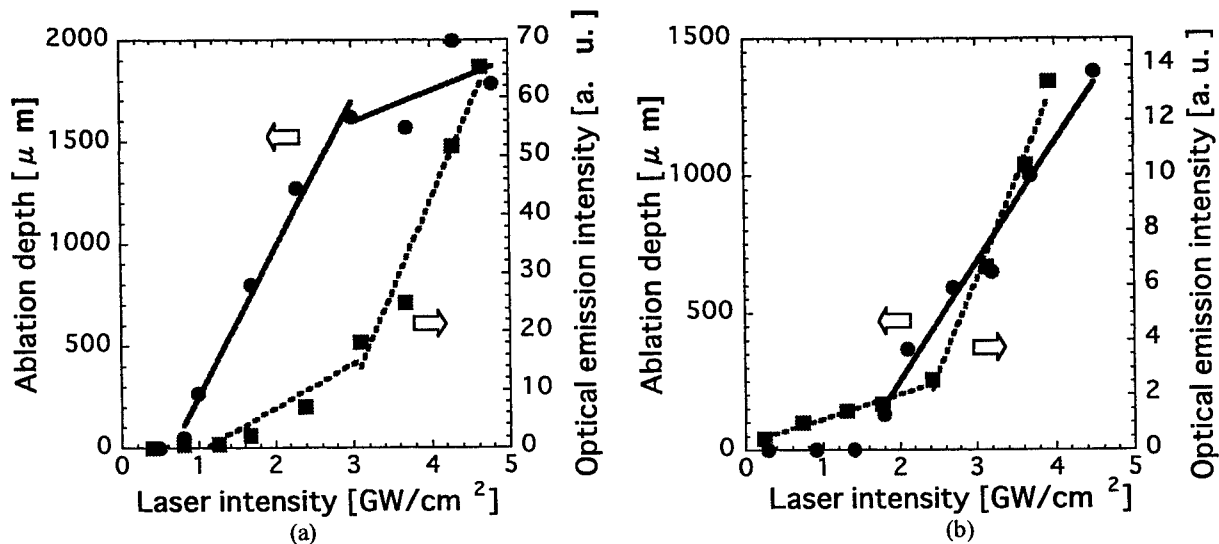for a laser intensity of 3.1 GW/cm² at 1064 nm. (Averaged for 10 pulses)

Fig. 5: Dependence of the ablation depth and the peak intensity of the laser-induced optical emission on the laser intensity at
the laser wavelengths (a) 1064 nm and (b) 532 nm. (n > 3)

3.3. Mechanism of the 532-nm laser ablation

In the case of the 532-nm laser ablation, the laser-induced optical emission is observed even under the ablation threshold, and an inflection point is observed at a laser intensity of 2.5 GW/cm². In the ablation depth, however, no inflection point is seen. It is found that the temporal profile of the optical emission for intensities lower than 2.5 GW/cm² is similar to that of laser pulse. This indicates that the laser-induced optical emission is dominated by fluorescence. On the other hand, at intensities higher than 2.5 GW/cm², the temporal profile of the laser-induced optical emission was similar to that for the 1064-nm laser ablation shown in fig. 4.

It is considered, therefore that the tissue removal is achieved through a photothermal process at < 2.5 GW/cm², while a photodisruption process may occur at > 2.5 GW/cm², too.

With nanosecond laser pulse the main mechanism of plasma formation is the avalanche ionization via the inverse bremsstrahlung, and the avalanche ionization rate is proportional to the laser wavelength.[4] Therefore, the optical breakdown threshold for the 532-nm laser is higher than that for the 1064-nm laser.

3.4. Application to TMLR

Our experiments described above show that the 1064-nm ablation is characterized by 1) high ablation rate (channeling speed), 2) limited thermal damage, and 3) damage presumably due to acoustic effect. For clinical application, however, ablation rate (channeling speed) for myocardium tissue should be further improved. This can be achieved by increasing the repetition rate of the laser. But higher repetition rate may cause additional thermal damage and mechanical damage in the tissue. The evaluation of tissue damage is one of the most important issues to consider the applicability of the Q-switched Nd:YAG laser to TMLR. In spite of these uncertain factors, we conclude that the 1064-nm Q-switched Nd:YAG laser would be a potential candidate for a laser source to be applied to TMLR, because of high ablation efficiency with limited thermal damage, possible fiber-based beam delivery, and the reliability and compactness of the laser device.

4. SUMMARY

We investigated *in vitro* the mechanism of myocardium tissue ablation with nanosecond pulsed laser at 532 nm and 1064 nm. It was found that the ablation rate at 1064 nm was larger than that at 532 nm, although the absorption coefficient at 1064 nm is smaller than that at 532 nm. For the 1064-nm light-ablated tissues, thermal damage was very limited, while damage presumably due to mechanical effect was observed. The peak intensity of the laser-induced optical emission with the 1064-nm light was higher than that with the 532-nm light at the same laser intensity, and a correlation was observed between the peak intensity of the laser-induced optical emission and the ablation depth for the 1064-nm laser ablation. In the case of the 532-nm laser ablation, the laser-induced optical emission was observed at > 2.5 GW/cm^2, which was higher than the ablation threshold of 1.6 GW/cm^2. Based on these results, we conclude that the tissue removal is achieved through a photodisruption process with the 1064-nm laser light. And with the 532-nm laser light the tissue removal is achieved by a photothermal process at < 2.5 GW/cm^2, while it may be achieved both by a photothermal process and by a photodisruption process at > 2.5 GW/cm^2. The 1064-nm Q-switched Nd:YAG laser would be a potential candidate for a laser source to be applied to TMLR, because of high ablation efficiency with limited tissue damage, possible fiber-based beam delivery, and the reliability and compactness of the laser device.

REFERENCE

1. T. Krabatsch, F. Schaper, et al., "Scientific Basis of TMR - Mechanisms under the discussion", *SPIE*, 3681, pp. 19-26, 1998.
2. S. Sato, H. Ashida, et al., "Plasma-mediated tissue ablaiton with nanoecond laser pulses in the spectral region from ultraviolet to near-infrared:*In-vitro* study with porcine myocardium tissue", *SPIE*, 4161, pp. 12-17, 2000.
3. A. A. Oraevsky, S. Letokhov, et al., "Temporal Characteristics and Mechanism of Atherosclerotic Tissue Ablation by Nanosecond and Picosecond Laser Pulses", *Lasers in the Life Science*, 5(1-2), pp. 75-93, 1992.
4. J. Noack, A. Vogel, "Laser-Induced Plasma Formation in Water at Nanosecond to Femtosecon Time Scales:Calculation of Thresholds, Absorption Coefficients, and Energy Density", *IEEE J. of QUANTUM ELECTRONICS*, 35, pp. 1156-1167, 1999.
5. E. Reichel, A. Eherer, et al., "Interaction of short laser pulses with biological structures", *OPTICS AND LASER TECHNOLOGY*, pp. 40-44, 1987.
6. H. Schoeffmann, E. Reichel, et al., "Time-resolved investigations of laser-induced shock wave in water by use of polyvinykudenefluoride hydrophones", *J. Appl. Phys.* 61(1), pp. 46-51. 1988.
7. V. Venugopalan, B. B. Mikic, et al., "Thermodynamic Response of Soft Biological Tissues to Pulsed Infrared-Laser Irradiation", *Biophysical J.* 70, pp. 2981-2993, 1996.

ROLE OF DESICCATION IN PULSED LASER ABLATION
AT THE 2.94 μm WAVELENGTH: EXPERIMENTS AND MODELING

Laurel R. Jones, Steven L. Jacques

Oregon Graduate Institute of Science and Technology, Beaverton OR 97006
Oregon Health Sciences University, Portland OR 97225

ABSTRACT

A difficulty with using an OPO laser to reshape the cornea by ablation is the tendency for ablation to stop prematurely. We report on using an OPO laser (2.94 um wavelength, 5 ns pulse duration, 7 mJ pulse energy, approx. 0.5-mm $1/e^2$-radius Gaussian beam) to ablate a 20% acrylamide gel as a model for the cornea. Experiments demonstrated that ablation proceeds at an average rate of ablation of 3-4 μm/pulse then stops at about 1 mm depth. A computer model was developed to simulate the ablation and desiccation processes. Using a range of operating parameters, the model could achieve ablation rates of 2.8-3.5 μm/pulse and cessation of ablation after 0.25-2.1 mm. A key factor is the absorption coefficient of desiccated gel which was measured experimentally to be about 1700 cm^{-1}. In conclusion, desiccation from residual heat after an ablative pulse creates a dried layer that attenuates subsequent pulses. If the threshold energy density required for ablation is too high, then too much residual energy remains after each pulse and the consequent dried layer halts the ablation process.

1. INTRODUCTION

1.1 OPO Laser and unexpected ablation stoppage

During experiments on ablation of the cornea with an OPO laser, a difficulty was encountered in that the ablation process stopped spontaneously, unexpectedly, and prematurely despite continued irradiation. The laser was sent to this research team to discover why that phenomenon occurred.

2. EXPERIMENTAL SETUPS

2.1 Acrylamide gel model for cornea

Acrylamide gel (5 g acrylamide, 0.125 g NN-methylene BIS-acrylamide, 0.01g NH_4 persulfate, 0.1 ml TEMED, 20 ml H_2O) at approximately 80% water content by mass was used in these experiments. Such a gel only approximated the roughly 74% water content expected for the cornea. The gel was transparent and non-scattering.

Thin Gels (800, 450, and 300 micron): Thin samples were used in ablation experiments where ablation succeeded in penetrating the gels. 800-micron gels were prepared using a mold consisting of an oval from a plastic engineering templates sandwiched between two glass slides. The template was 800 μm thick. An additional thickness (~80 μm) was imposed by double-stick

Laser-Tissue Interaction XII: Photochemical, Photothermal, and Photomechanical, Donald D. Duncan,
Steven L. Jacques, Peter C. Johnson, Editors, Proceedings of SPIE Vol. 4257 (2001)

317

tape adhering the template to the glass slides. The gel mixture solidified while held in the mold. Upon solidification, there was a slight decrease in thickness, which offset the extra thickness from the tape. Micrometer measurements showed that the gels averaged 800 μm +/- 5%. The 300 and 450 μm samples were prepared using a sandwich of two glass microscope slides separated, respectively, by two or three layered sets of 150-μm cover slips acting as spacers, clamped by binder clips. The gel was introduced between the slides using capillary action and a pipette.

Thick Gels (> 1cm): Thick gels were used in ablation experiments to observe where ablation eventually stopped despite continued laser irradiation. The gels were prepared ranging from 0.75 to 1.5 cm thick, using a 50-ml beaker as a mold. They were very carefully removed so that the sides of the flat cylinders remained transparent, serving as a window for observing the progress of the ablation from the side of the gel.

Very Thin Desiccated Gels (150 μm): Very thin desiccated gels were used in experiments to determine the optical properties of the gel when fully dry. Gels were prepared as for the 300 and 450 μm samples above using a single layer of the 150-μm cover slips. After preparation, one slide was removed and the gel was allowed to desiccate completely on the remaining slide. The final thickness was measured by caliper to be 30 μm, which is roughly consistent with full desiccation of a 150-μm gel initially at 80% water content.

2.2 Laser and experimental setup

The laser was a Q-switched Nd: YAG -pumped OPO laser (special prototype: IR Vision, Inc., San Clemente, CA) operating at 2.94 μm wavelength. The pulse duration was 4.5 ns. The pulse energy ranged from 6-8 mJ, and was reduced systematically by adding glass slides as attenuators (transmission through one slide is 0.65). The beam was passed through a BaF lens (23-cm focal length) to achieve a maximum focal spot of about 1-mm diameter. The gels were placed at this position of maximum focus. The energy delivered to the gel in each experiment was measured with a joulemeter (model EM400: Molectron Inc., Beaverton, OR) positioned behind the sample holder before the gel was put in place. (See Fig. 1.)

The laser was operated at repetition rates of 0.91, 4.55, 9.09, 22.72, 45.45 Hz as measured on an oscilloscope monitoring a photodiode that measured the laser's flashlamp. These rates corresponded to 91% of the stated repetition rates on the laser control panel (1, 5, 10, 25, and 50 Hz).
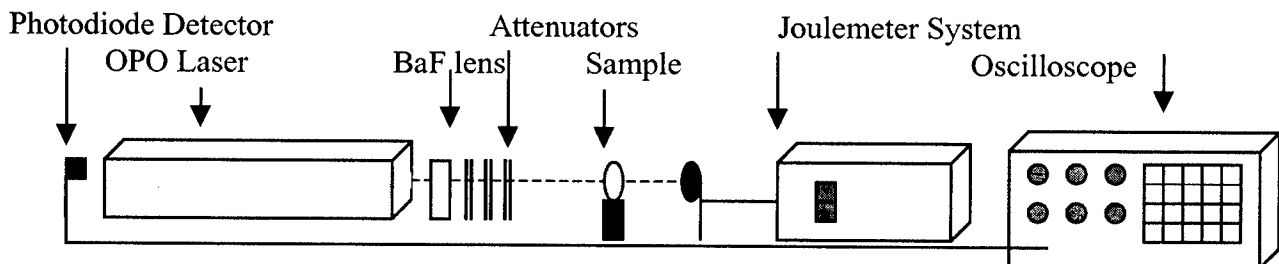

Fig. 1: Experimental setup for laser ablation of samples (polyacrylamide gels).

2.3 Experimental protocols

The gels were irradiated with a large number of laser pulses at the various repetition rates, f [Hz], and various radiant exposures per pulse, H [J/cm^2].

Thin Gels: The 300, 450, and 800-μm samples were ablated until full perforation was achieved. The number of pulses to perforate the samples, N_p, was specified by count for slow repetition rates (1-5 Hz) and by time, using a stopwatch for faster rates (10-50 Hz). Perforation was determined by observing the onset of transmission of laser energy through the ablation hole in the gel as monitored by the joulemeter behind the gel. The attenuators were used in these experiments also, to vary pulse energies and determine their respective rates of ablation.

Thick Gels: The 1-cm gels were ablated until ablation ceased and continued irradiation did not achieve any further depth. The gels were carefully broken along the axis of the ablation hole and the depth of ablation was measured with a caliper. Attenuators were used in these experiments to determine ablation stoppage points for different pulse energy levels.

Very Thin Desiccated Gels: These gels were irradiated with a single laser pulse and the transmitted energy (U_{gel}) detected by the joulemeter behind the gel. Reference transmitted energy (U_{ref}) was measured through a clear glass slide without gel. The ratio U_{gel}/U_{ref} equaled the transmission, T, through the gel. The absorption coefficient of the gel was calculated: μ_a = - ln(T)/d where d was the 30 μm gel thickness. This procedure was repeated on 24 spots on two gels.

Measuring Qth: A gel sample about 3mm thick was placed in front of the laser and irradiated with a single pulse. The glass microscope slides, 1mm thick, were used as attenuators to regulate the pulse energy. A signal analyzer was used to record acoustic waveforms caused by the laser pulse through the gel. The joulemeter recorded the beam energies. 5 waveform samples each were taken with 0 to 6 attenuators in place. Ablation threshold pulse energy was determined by observing the resulting waveforms to see whether ablation had taken place. This was also confirmed by integrating the waveforms to determine whether the integrals went to zero.

3. ABLATION AND DESICCATION THEORY

The simple ablation "blow-off" theory is a useful way to model ablation. It is based on Beer's Law, which states that the ratio of the energy delivered to a certain depth to that deposited on the surface is an exponential function of the depth multiplied by the substance's coefficient of absorption and/or scattering. If a certain amount of energy is delivered at a specific depth, vaporization occurs there, blowing off the material above it as does a volcano when the vaporized and molten material beneath erupts through the surface layers of rock. This theory has been expanded herein to include desiccation phenomena as well. If the energy delivered is not sufficient to cause ablation but sufficient to evaporate water, the surface desiccates, leaving behind a layer of partially or fully dried material. This dry material has an absorption coefficient significantly lower than that of water, creating an insulating layer that hinders the ablation process. Eventually, the desiccated layer thickens to the point where ablation stops completely.

This Ablation/Desiccation model has the advantage over the Finite Difference Model in that the simulation is significantly less time consuming, and hence was used for the modeling processes described herein.

3.1 Theory

The ablation depth per pulse is calculated using the simple blow-off theory as:

$$z_{abl} = \ln(H/H_{th})/\mu_a \qquad (1)$$

z_{abl} [cm] is the thickness of tissue removed per pulse and μ_a is the apparent absorption coefficient of the medium despite the reality involving a dynamic μ_a that varies throughout the process.

This equation is derived from Beer's Law, $H = H_0 e^{-\mu_a z}$, where H is the fluence in the gel [J/cm^2] at a depth z and H_0 is the incident radiant exposure. Manipulating this, we get $H/H_0 = e^{-\mu_a z}$. The ratio on the left side is unitless, and so $e^{-\mu_a z}$ can be used equally well to represent ratios in units of energy, power per unit volume or per unit length, or just energy in Joules. Thus, $e^{-\mu_a z}$ can represent Q/Q_0, W/W_0, I/I_0, E/E_0, etc. where $z = z_{abl}$ and μ_a is the absorption coefficient. We are not concerned here with scattering. The cornea is transparent.

From this equation, we assume that there is a threshold radiant energy density deposited, Q_{th} (measured in Joules/cm^3) above which ablation will automatically occur. This was modeled in our program by taking a differential depth and, if the amount of energy deposited was greater than Q_{th}, ablation occurred, and that differential volume was removed, i.e. the volume went to zero. Then the next volume element below that was examined to determine whether or not enough energy was available to remove that also.

We expanded this model to include a threshold Q for desiccation, called Q_{des}. This is smaller than Q_{th} by about an order of magnitude. It is the product of the temperature in °C, the density of water, $\rho = 1$ g/cm^3, and the specific heat of tissue (slightly lower than water) C = 4.18 J/g/°C.

If the deposited Q was above Q_{des}, but below Q_{th}, desiccation of the "tissue" (acrylamide gel in our model) occurred.

4. MODELING/ANALYSIS

4.1 Matlab Program Description

The program used to simulate the experimental results was written in Matlab, a matrix-oriented C-based programming language. This program was written to be capable of modeling ablation in one or two dimensions, although only one dimension was used, as the two dimensional model was too time and memory consuming.

A fixed radius and depth were defined for the simulated sample, and these were divided into a specific number of equal subdivisions, dr for the radial dimension, dz for the depth. Initial water concentration was defined to be 80%, matching the water concentration in the Acrylamide

gel used experimentally. Consequently, the initial volume was divided into 80% water and 20% dry volume for each "voxel" i.e. volume element. The dimensions of the voxel were A*dz, A being the area, pi*dr^2 for the one-dimensional case used.

Mass of water was defined in terms of the density of water, rho = 1g/cm^3 multiplied by 80% of the volume of one voxel, modified during the program to reflect desiccation of the water in the voxel

The program was set to generate a simulated laser pulse, which deposited a given amount of energy into the surface voxel in the center of the beam. It then ran in an iterative loop through all the z depth increments for each voxel in the center of the beam pulse. The beam deposited energy into the voxel under consideration, and the energy level [J] was determined. The absorption coefficient was then determined based on this condition. Beer's law was used, modified by a function we derived from the experiments reported by Walsh and Cummings (1994) [1] wherein they showed how temperature affects the absorption coefficient and hence the ablation rates of water at mid-infrared wavelengths.

If the energy was greater than a threshold energy Q_{th}, and the amount of water remaining in the voxel was greater than a certain amount, Wth, needed for ablation, the voxel was ablated away. The volume and water content of that element was set to zero and the next element considered.

Otherwise, if the deposited energy was less than that needed for ablation, but greater than the desiccation threshold, the water in that voxel was evaporated away, but the dry volume remained, and the next element considered. The new ablation front was calculated after each reiteration. The ablation/desiccation front was plotted on a graph, along with the incremental difference in microns per pulse ablated or desiccated.

The program was set to run either until it reached the maximum depth of the sample or until ablation stopped. It could also be set to run until both ablation and desiccation stopped, if desired.

This program was designed so that the energy per pulse, the absorption coefficients μ_a for pure water or dry volume, the threshold energy density for ablation or desiccation, and the threshold amount of water needed for ablation were all readily variable by the user. These were changed one at a time and simulated systematically to determine the effects of the various perturbations on the results.

5. EXPERIMENTAL RESULTS

5.1 Ablation that stops in thick gels

In the thick samples, the ablated holes were approximately 1 mm in diameter and initially just over 1-mm depth (see Table 1). As ablation continued, exceeding 1 mm depth, the ablation hole quickly narrowed to about 0.25 mm, eventually tapering to a narrow spike that persisted into the sample to about 4 mm in depth relative to the original surface. The mechanism underlying this

tapered hole phenomenon is not understood. One possibility might be related to high pressures and liquefaction of the bottom of the ablation hole, perhaps following the suggestion of Zweig [2].

Table 1: Depth of ablation hole (Not including spike)

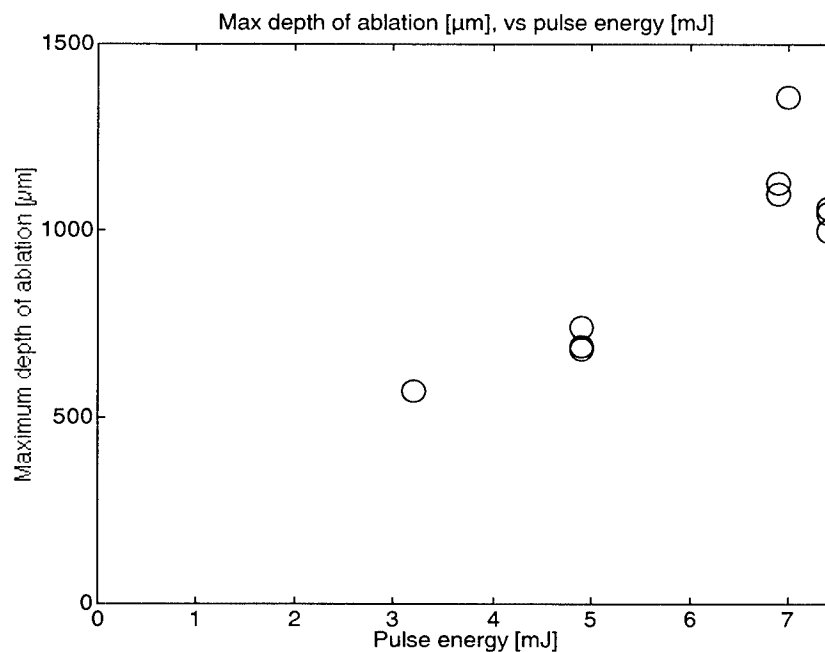| Exp. #	pulse energy	depth of hole
1	NA	1.35-1.37 mm
2	6.9 mJ	1.13 mm
3	6.9 mJ	1.10 mm
4	7.4 mJ	1.05 mm
5	7.4 mJ	1.00 mm
6	7.4 mJ	1.06 mm
7	4.9 mJ	0.74 mm
8	4.9 mJ	0.68 mm
9	4.9 mJ	0.69 mm
10	3.2 mJ	0.57 mm

NA = not available

Fig. 2: Maximum depth of ablation achieved by laser pulses with different pulse energies (data from Table 1). The depth of primary hole when ablation eventually stops after about 5-10 min exposure to a 50-Hz repetition rate for pulses. After 30,000 pulses (10 min x 50 Hz), the depth of ablation was measured against various pulse energy levels as plotted here.

5.2 Ablation that perforates thin gels

In the 800-μm gels, the number of pulses required for perforation, N_p, was measured as a function of repetition rate. The ablation rate was calculated as $(800 \ \mu m)/N_p$ [μm/pulse]. Figure 2 shows the number of pulses until perforation (Fig. 2A) and the ablation rate (Fig. 2B) versus the repetition rate [Hz]. The experiment was repeated at three different pulse energies: $U_p = 6.6$, 6.8, and 7.8 mJ. Lower pulse energies did not perforate the samples. There was little systematic dependence on the repetition rate.

However, the ablation rate did depend on the pulse energy, as shown in Fig. 3. The mean – standard deviation for all the ablation rate data at a given pulse energy (6.6, 6.8, or 7.8 mJ) is shown on the y-axis in units of [cm/pulse]. The x-axis shows the radiant exposure per pulse, $H_o = U_o/area$ where area of the 1-mm-dia. spot is 0.0079 cm^2.
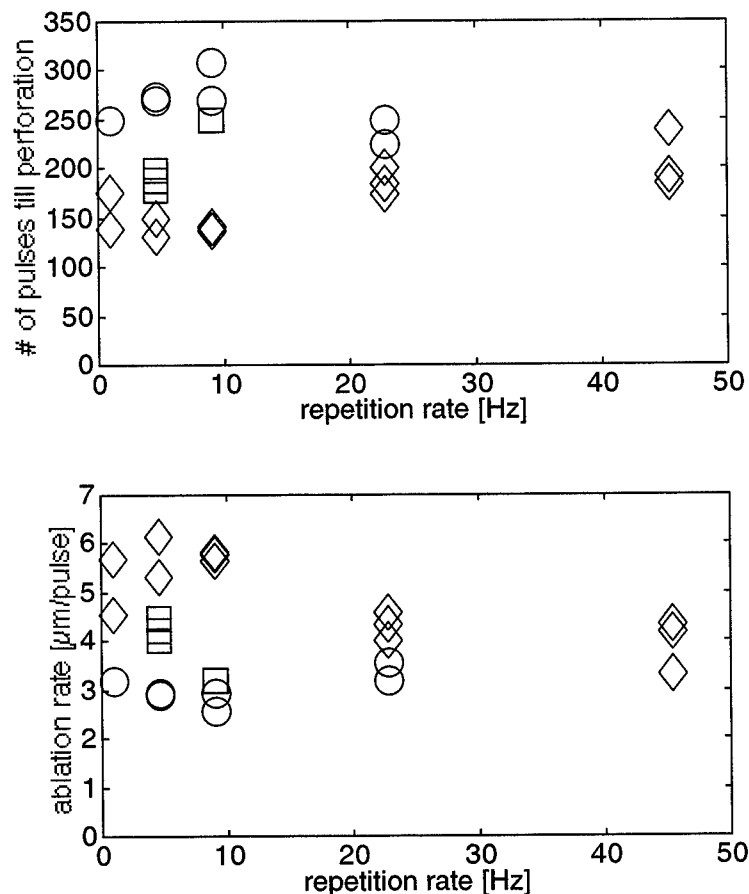
Fig. 3: (A) Number of pulses until perforation vs. repetition rates for 800-μm-thick samples. (B) Average ablation rate [μm/pulse] versus repetition rate [Hz] based on the (800 μm)/(number of pulses at perforation). Experiment was conducted at three pulse energies [mJ]: 6.6 mJ (circle), 6.8 (squares), 7.8 (diamonds).

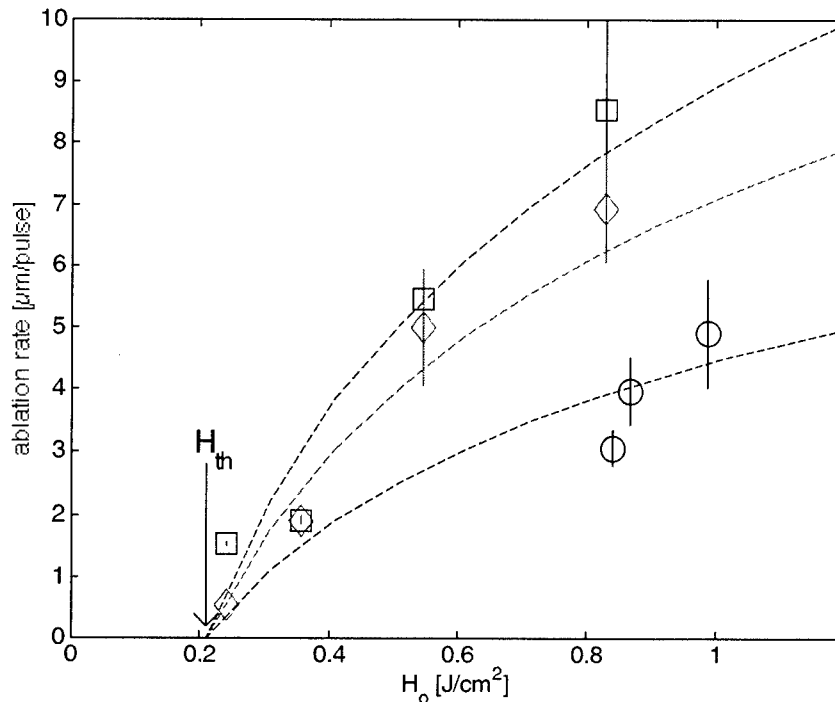Fig. 4: Ablation rate [μm/pulse] versus radiant exposure [J/cm²] per pulse. Squares indicate rates for 300 μm, diamonds for 450 μm, and circles for 800 μm. The threshold is 0.21 J/cm² where the apparent absorption coefficient is about 1750, 2200, and 3500 respectively for each of the three depths according to the Beer's law fit curves (dotted lines). The value of dry gel absorption coefficient is about 1710 cm^{-1}, which suggests that the water content required for ablation is varies with depth from nearly zero to around 11.5-12%. The absorption coefficient of water at the operating wavelength of the experimental laser is around 12700. (1710 * .88 + 12700 *.12 = 3028.8)

In the thinner samples, ablation rates ranged from 2.5 to 6.2 microns per pulse, depending on pulse energy levels, which varied in the laser from 6-8 mJ. The three series shown here were done at three separate times with the laser running at different pulse energy levels, not controllable by the operator. The slight dependence on repetition rate turned out to be due to the higher repetition rates running at slightly higher pulse energy levels.

5.3 Measured dry μ_a.

The measured value for dry μ_a averaged 1710 for the first experimental run. Combining this with a second experimental session later, the overall mean was 1712.4 with a standard deviation of 55.57.

5.4 Measured Q_{th}:

From the slope of the graph of average integrals at each beam energy level and by the waveform shapes themselves, it was determined that the threshold radiant exposure needed for ablation was about 0.21 Joules/cm^2. This puts Q_{th} at about 2200 J/cm^3.
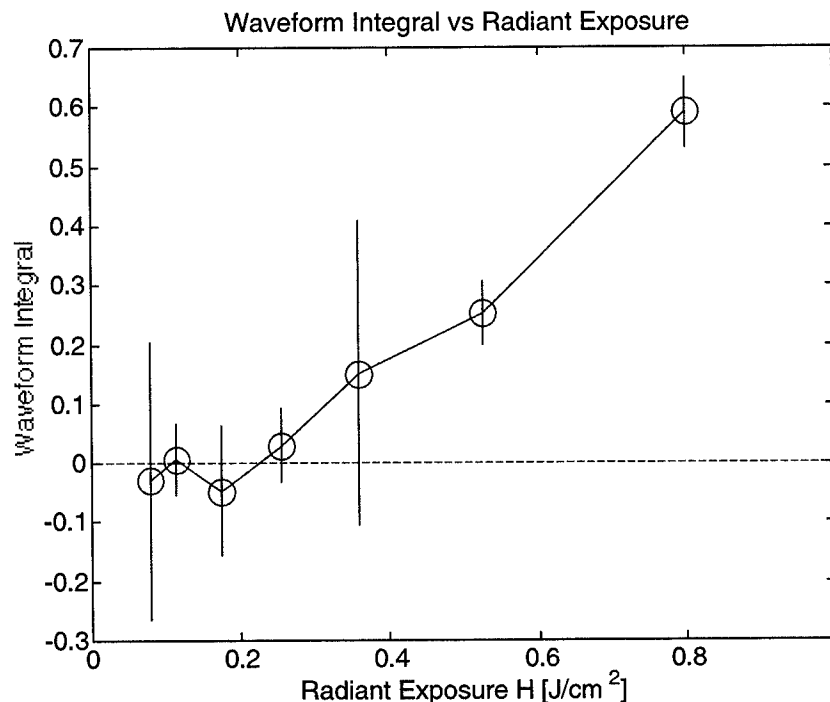

Fig. 5: Ablation indicated by excess compressive pressure. The transmitted pressure was integrated over time. Without ablation, the integral was zero. With ablation, the integral was positive indicating an excess of positive compressive positive pressure. This measurement enabled the determination of Q_{th}.

6. MODELING RESULTS

Figure 6 shows the model results from a sample simulation. Where the ablation stops, the ablation rate line goes to zero, but desiccation continues. Similarly, the ablation front stops increasing (flat line) while the desiccation front keeps going for awhile longer before flattening out.

In the ablation model, when pulse energy was increased, all else being equal, the final ablation depth increased also. The higher the pulse energy, the more material was removed per pulse, hence the rate of ablation also increased. When the radiant energy density ablation threshold was varied, the final depth decreased with an increase in this threshold, which is reasonable since more energy is needed for ablation with a higher energy per volume is required. On the other hand, an increase in the threshold radiant energy density required for desiccation caused an increase in the final ablation front. This also makes sense in that the more energy

required to cause desiccation, the less desiccation will occur and the deeper the ablation front will go before it is stopped by the dry surface layer around the ablated cavity. Varying the percentage concentration of water required for ablation from zero to 10 percent did not significantly affect the ablation depth except at very low water thresholds (0-2.5%). Above 10%, the final ablation depth decreased slightly. This shows that the amount of water needed for ablation only marginally affects the ablation depth. If almost no water is needed at all, the ablation will go a little further. It is a minor effect compared to the other variables.
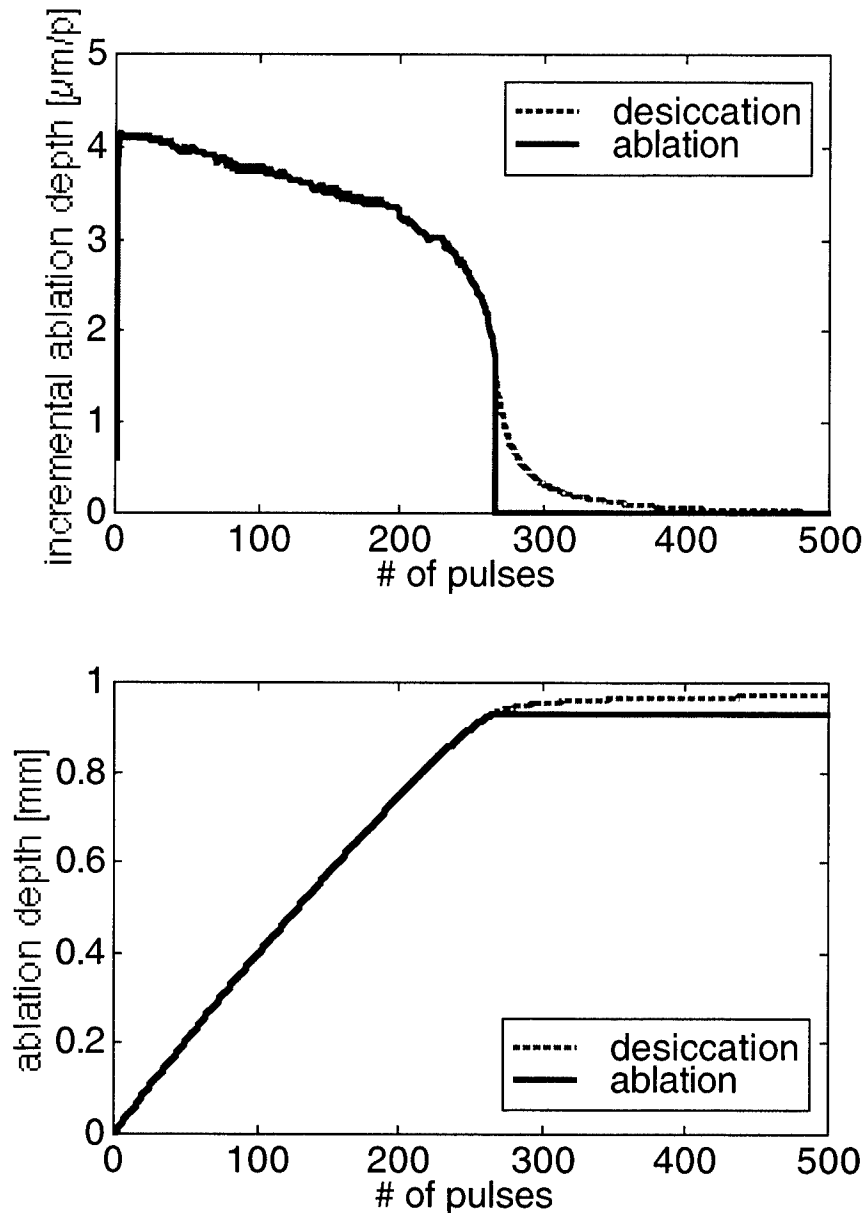

Fig. 6: The rate of ablation and the movement of the ablation front versus number of laser pulses delivered. The simulation parameters illustrated here were $\mu_a$dry = 2000 cm^{-1}, water content threshold = 0.5%, Q_{des} = 271.7, Q_{th} = 2415.

The model was not able to simultaneously achieve the ablation rates and depths that were found experimentally. This effect of ablation depths achieved being greater than that predicted by theory has been described by J.T Walsh and J.P Cummings. While their function for the absorption coefficient of water was used in the simulation, it is evident that further study of the parameters affecting ablation is in order.
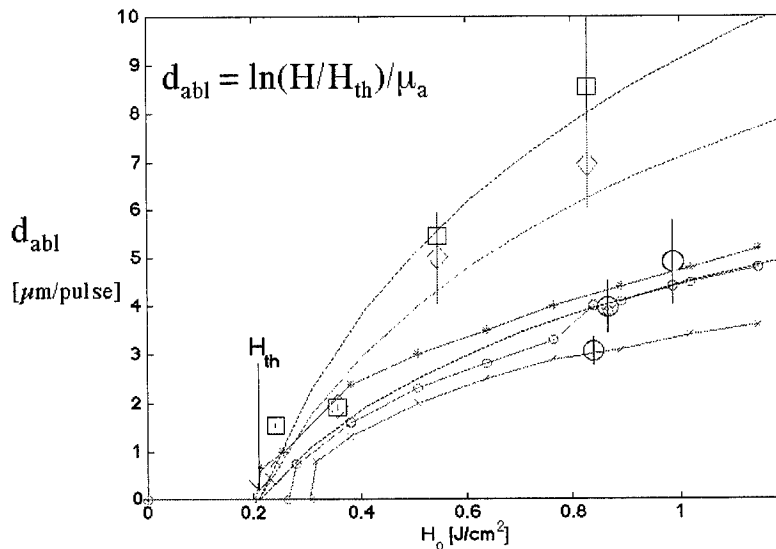

Fig 7: Experimental. Data for 300, 450, and 800 μm thick gels. The computer simulation generated the three lower lines with small symbols corresponding to the thickest gel (800 μm) for three values of Qdes. Qth = 1850 J/cm^3. Qdes = 292.6 J/cm^3; Qdes = 271.7 J/cm^3; Qdes = 250.8 J/cm^3. The differences in absorption (μ_a) are presumably due to dessication of the thinner gels during the experiment which lowered μ_a:

300 μm Gel (Squares)	$\mu_a = 1710$ cm^{-1}
450 μm Gel (Diamonds)	$\mu_a = 2200$ cm^{-1}
800 μm Gel (Circles)	$\mu_a = 3500$ cm^{-1}

Superimposed Model fit curves at 800 μm perforation closely model 800 μm curve.

Max depth of ablation [μm] vs pulse energy [mJ]

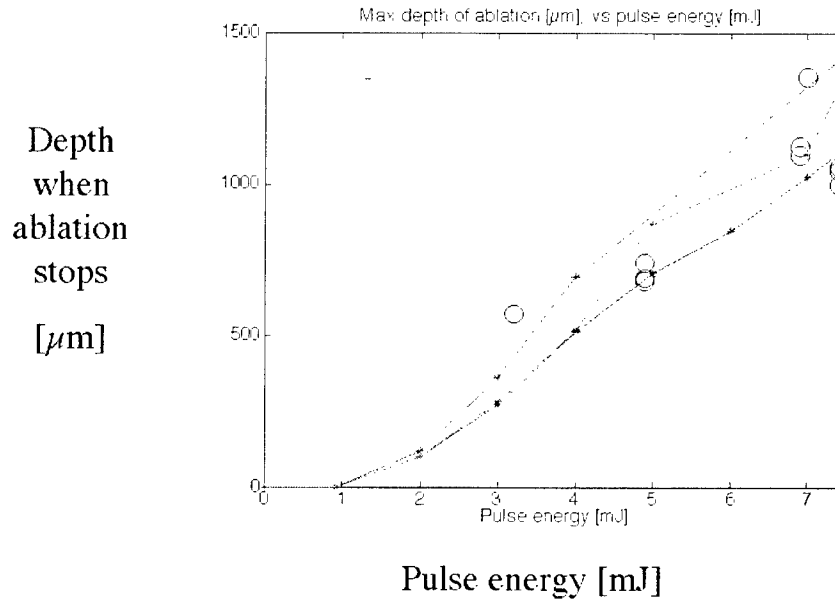Depth
when
ablation
stops

[*μ*m]

Pulse energy [mJ]

Fig. 8: Experimental data and model for depth at which ablation stops versus pulse energy. The computer simulation generated the three lines corresponding to the thickest gel (800 μm) for three values of Qdes. Qth = 1850 J/cm^3. Qdes = 292.6 J/cm^3; Qdes = 271.7 J/cm^3; Qdes = 250.8 J/cm^3

7. CONCLUSIONS

The evidence indicates that desiccation does indeed play a role in stopping the ablation process. Its effects are more pronounced at lower pulse energies, higher ablation threshold energies or lower desiccation threshold energies. It does not appear to be greatly affected by threshold water content for ablation for amounts greater than zero. It would be reasonable to conclude that lower pulse energies would cause more desiccation since more pulses would be required to ablate to a given depth. Meanwhile, since Qdes is lower than Qth, more desiccation occurs per ablation event. Similarly, a higher Qth would cause more desiccation because it would take more time to build to the threshold and meanwhile desiccation is occurring. A lower Qdes would cause more desiccation in that it would take less energy to invoke the desiccation process. Experiments also clearly demonstrated that ablation rates drop rapidly after the first few hundred microns of ablation depth. Further experiments not described herein confirm that desiccation of the surface or within the ablation cavity does indeed stop ablation for pulse energies up to 2.5 times the threshold ablation energy.

8. REFERENCES

1   J. T. Walsh, J. P. Cummings, Effect of the Dynamic Optical Properties of Water on Midinfrared Laser Ablation, *Lasers in Surgery and Medicine* 15:25-305, 1994

2   A. D. Zweig, Infrared tissue ablation: consequences of liquefaction, *Proc. SPIE* Vol. 1427, p. 2-8, Laser-Tissue Interaction II, Steven L. Jacques; Ed., 1991

In situ tomographic observation of tissue surface during laser ablation

Masamitsu Haruna*, Ryuh Konoshita*, Masato Ohmi*, Naomi Kunizawa* and Mayumi Miyachi*
School of Allied Health Sciences, Faculty of Medicine, Osaka University
1-7, Yamada-Oka, Suita, Osaka 565-0871, Japan

ABSTRACT

In laser ablation of tissues, tomography of the tissue surface is necessary for measurement of the crater depth and observation of damage of the surrounding tissue. We demonstrate here OCT images of craters made by UV laser ablation of different tissues. The maximum depth of a crater is found among several OCT images, and then the ablation rate is determined. The conventional OCT of the spatial resolution of 15μm was used in our experiment, but OCT of the resolution of the order of 1μm is required because the ablation rate is usually a few microns per pulse. Such a high-resolution OCT is also demonstrated in this paper, where the light source is a halogen lamp. Combination of laser ablation and OCT will lead to in situ tomographic observation of tissue surface during laser ablation, which should allows us to develop new laser surgeries.

Key words: laser ablation, optical coherence tomography (OCT), tissue optics

1. INTRODUCTION

Laser ablation is essentially effective for precise surgical operations such as the refractive surgery of cornea [1] and the surgery of vascular [2], because it can remove tissues layer by layer. On the other hand, the tissue ablation is used as a diagnostic tool, where trace elements are detected from tissue by the time-gated spectroscopy of plume [3-6]. Very recently, the authors demonstrated Ca detection of human hair and nail, leading to screening of osteoporosis [7, 8]. For further development of laser ablation in the medical use, it is necessary to characterize the tissue ablation in more detail. An important issue is to measure the crater depth of the tissue surface for determination of the ablation rate. Up to now, the measurement has been made by observation of the cross section of the tissue surface, using a microscope or SEM, after cutting and polishing of a tissue sample [9]. This sort of process is cumbersome and destructive. On the other hand, shape of the tissue surface may change gradually with time after irradiation of laser pulses. The deformation of tissue surface is due to dehydration. The surrounding tissue may also suffer serious damage from laser ablation if the laser fluence is too high. Therefore, in situ observation of the cross section of the tissue surface is strongly required.

A very promising candidate for such an in situ observation is the so-called optical coherence tomography (OCT) [10]. In the past decade, there has been keen interest in the OCT for a new class of medical imaging. The OCT is potential for monitoring of the surface change during tissue ablation. At present, in the practical OCT, a super luminescent diode (SLD) is used as the light source for the low coherence interferometer, providing the spatial resolution of 10μm or more along the depth. This kind of OCT is useful for the laser-ablation imaging, but the spatial resolution of nearly 1μm is often required for precise measurement of the crater depth because the ablation rate becomes below 10μm in order to minimize damage of the surrounding tissue. Such a ultra-high resolution OCT is realized by the white light interferometer.

In this paper, we demonstrate a series of OCT images of the tissue surface irradiated by UV laser pulses, where several different tissues were used as a sample, including human nail, tooth, gallstone, rat femur and stomach wall, etc. The ablation rate was then determined for each tissue sample although the resolution of OCT is around 10μm. Furthermore, we present ultra-high resolution OCT images for tissue ablation where a halogen lamp is used as the light source of the interferometer.

*Correspondence: Email: haruna@sahs.med.osaka-u.ac.jp

2. TISSUE ABLATION AND OCT OF TISSUE SURFACE

In laser ablation of tissues, the Q-switched Nd:YAG laser is used as the light source which supplies laser pulses of 9ns at the fourth harmonic of 266nm with the repetition rate of 10Hz. The UV laser pulse is loosely focused on a tissue sample where a focused spot size is around 150μm in diameter. The laser pulse energy is typically 17mJ. The tissue sample is placed on a translation stage to shift the ablation position after irradiation of a certain number of laser pulses, and then several craters of different depths align on the sample surface. Subsequently, the tissue sample is placed in the signal arm of the Michelson interferometer where the light source is a 850-nm SLD whose output power is 3mW. The coherence length of the SLD is 15μm which determines the resolution of OCT along the optical axis. In the interferometer, the visible He-Ne laser is also aligned with the SLD light to find the position of laser ablation on the sample. The SLD light is focused on the sample by a 20× objective, and the reference mirror is scanned back and forth, shifting the sample by a step of 5μm, to form an OCT image.

3. DETERMINATION OF THE ABLATION RATE FROM OCT IMAGES

UV laser pulses were focused on the surface of rat femur to make several craters, where the crater depth was different from each other depending upon the laser-pulse shot number. The diameter of the crater increases greatly with the shot number of laser pulses. OCT images were formed with a spacing of 20μm to find the maximum depth of the crater, where the image size is $1 \times 1mm^2$ with a pixel size of $5 \times 5\mu m^2$. The maximum depth is thus found clearly. The crater depth increases with the laser-pulse shot number N, as shown in Fig. 1. The measurement accuracy of the crater depth is $\pm 20\mu m$, which is almost twice as long as the coherence length of the SLD due to surface roughness of rat femur. The crater diameter also increases with N, and becomes nearly 400μm on the surface in the case of N=120. No damage appears in the surrounding tissue. The measured carter depths are plotted with respect to N, as shown in Fig. 2. All data fit a straight line determined by the least squares method. This fact indicates that there are less dregs on the bottom of the crater. The slope of the straight line yields the ablation rate of 2.7μm/pulse when the laser pulse energy is 17mJ.
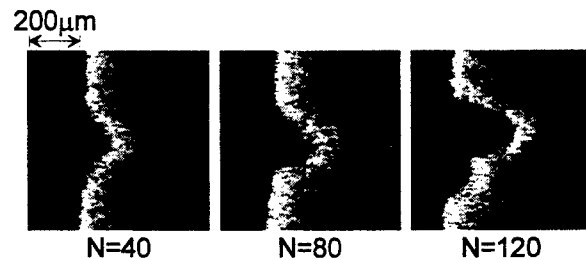

Fig.1   A series of OCT images of craters in UV laser ablation of rat femur, where N is the laser-pulse-shot number.
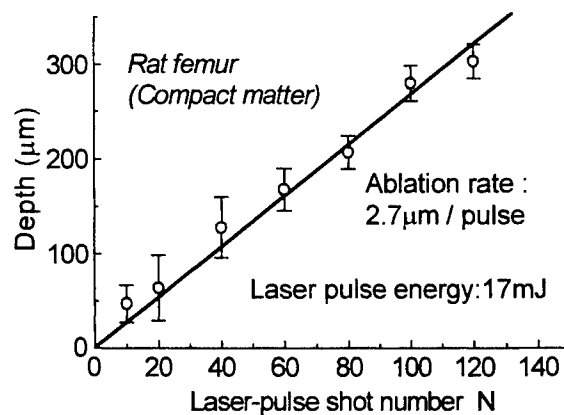

Fig.2   Determination of the ablation rate.

4. OCT IMAGES OF CRATERS FOR DIFFERENT TISSUES

OCT images of craters were obtained for different tissues including human nail, tooth and gallstone, and rat stomach wall, where the laser pulse energy was always 17mJ. In the case of human nail, we can find some cracks in the surrounding area due to a shock wave, as shown in Fig. 3(a). The cracks become more serious as the laser-pulse shot
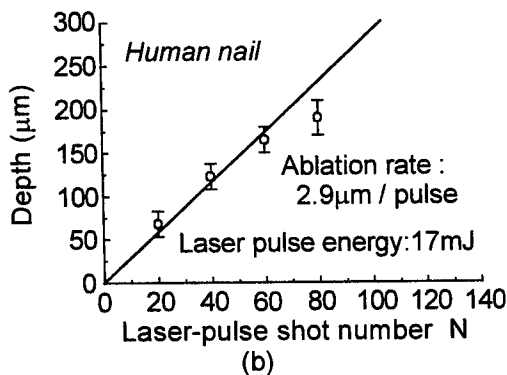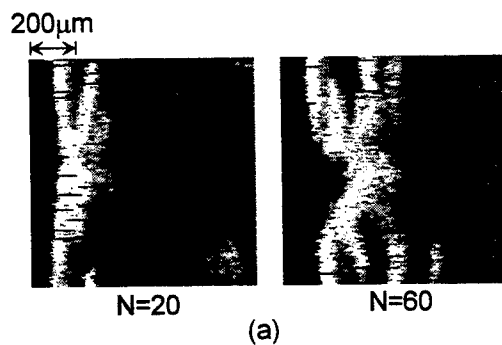
Fig.3 Laser ablation of human nail. (a) OCT images of craters, and (b) the ablation rate.
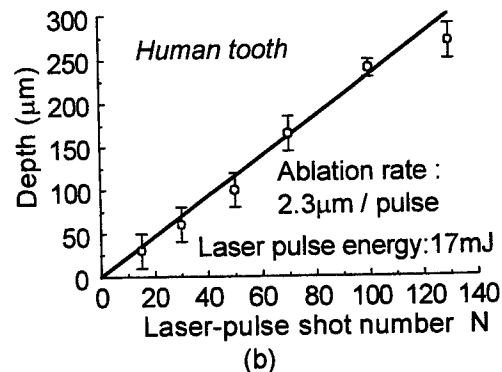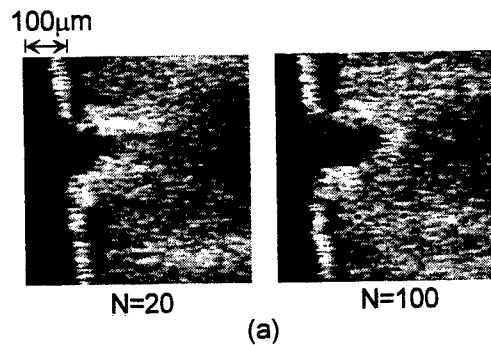

Fig.4 Laser ablation of human tooth.

number N exceeds 60. The crater is deformed by the cracks when N=80, and thereby, the crater depth tends to be smaller than the actual depth. It is found in Fig. 3(b) that the ablation rate of human nail is 2.9μm/pulse. On the other hand, in the case of human tooth, there is no damage in the surrounding tissue even when N=100, as shown in Fig. 4(a). The crater diameter is 140μm which is considerably smaller than the crater of the rat femur (see Fig. 1). The ablation rate of human tooth is as low as 2.3μm/pulse. It is thus easy to drill deeply a small hole in enamel of human tooth because the enamel is rather hard. As a sample of soft tissue, UV laser ablation was made for rat stomach wall. In this case, thermal deformation of craters occurs in each shot of the laser pulse, as shown in Fig. 5. Probably, the laser pulse energy is too high to suppress heat generation on the tissue surface.

From the experiment results described above, one can find that OCT is really useful for monitor of the crater shape and damage of the surrounding tissue. At present, however, the spatial resolution of the OCT is 10μm or more along the optical axis although the ablation rate is 2 to 3μm for hard tissue. High resolution OCT of the order of 1μm is then required for precise measurement of the crater depth.
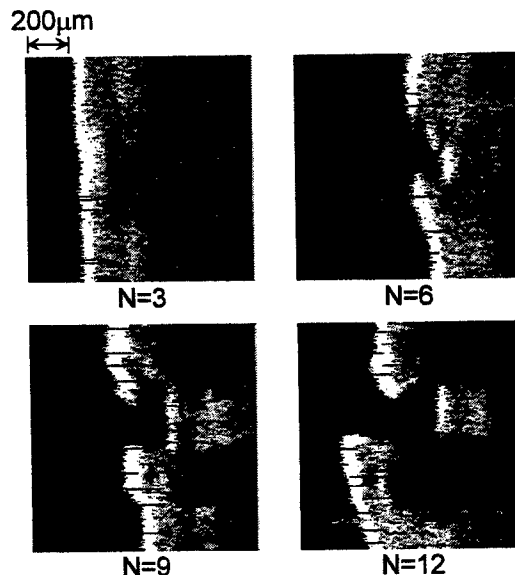

Fig.5 Laser ablation of rat stomach wall.

5. HIGH RESOLUTION OCT FOR LASER ABLATION

A possible candidate is a halogen lamp for the light source of high resolution OCT. In the experiment, the light from a highly bright halogen lamp of 400W is launched into a graded-index (GI) fiber of 65μm core diameter for extraction of light having the same coherence as the fiber-guided modes, and the light output from the fiber is only 100μW. The coherence of such a fiber output light is not a little imperfect because of the multimode fiber. In other words, a certain amount of fiber output is obtained at the sacrifice of the spatial coherence of light. The fiber output light is then used as the light source of the Michelson interferometer, where the reference mirror is placed on a translation stage with a 0.1-μm step. The translation speed of the stage is up to 40mm/s for OCT. An IR absorption filter is placed in front of a beam splitter to obtain a symmetrical spectrum around the wavelength of 650nm. The overall spectrum of the fiber output light exhibits the FWHM of 119nm at the center wavelength of 657nm, considering the spectral responsibility of the photodiode. In this sort of ultra-low coherence interferometer, the problem is broadening of the envelop of interference fringes due to unbalance of chromatic dispersion between the sample and reference arms. The unbalance of chromatic dispersion is compensated by placing the same objective lenses in the two arms. The coherence length Δl_c of 1.3μm is thus obtained in our interferometer, where Δl_c is almost one tenth of that of a SLD.

Using the ultra-low coherence interferometer, as described above, OCT imaging was made for human tooth, as shown in Fig. 6, where the laser-pulse shot number N is only five. It is here noted that the scale along the depth is magnified 10 times with respect to the axis parallel to the surface; thereby, a slant angle of the image becomes abnormally large. The bottom of the crater is not clear because the ultra-low coherence light from a halogen lamp is only 100μW; nevertheless, the crater depth is found to be 11μm in the OCT image of Fig. 6.
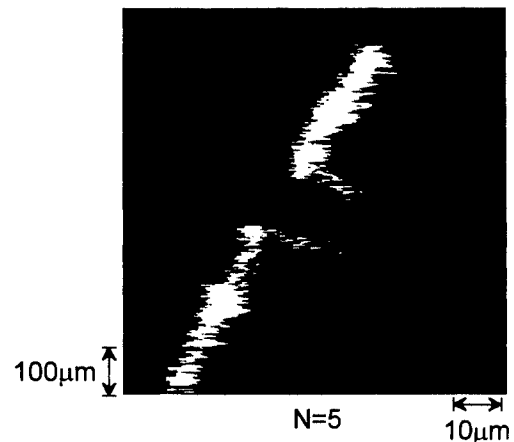

Fig.6 High-resolution OCT image of a crater of human tooth, where N is only 5.

6. CONCLUSION

We have presented OCT images of craters in UV laser ablation of different tissues. It is seen that OCT is useful for measurement of the crater depth and monitor of damage of the surrounding tissue. The ablation rate is thus determined easily without any destructive processes. A change of the crater shape can also be observed in detail with monitor of damage of the surrounding tissue. Our effort is now directed at combination of laser ablation and OCT, resulting in situ tomography of tissue surface during laser ablation. This unique technique will provide new laser surgeries.

ACKNOWLEDGMENTS

REFERENCES

1. for example, C. A. Puliafito, R. F. Steinnert, T. F. Deeutsch, F. Hillenkamp, E. J. Dehm, and C. M. Adler, "Excimer laser ablation of the cornea and lens," Opthalmol. **92**, No. 6, pp. 741-748 (1985).
2. for example, J. M. Isner, P. G. Steg, and R. H. Clarke, "Current status of cardiovascular laser therapy, 1987," IEEE J. Quantum Electron. **23**, No. 10, pp. 1756-1771 (1987).

3. S. Anderson-Engels, J. Johansson, and S. Svanberg, "Fluorescence diagnosis and photochemical treatment of diseased tissue using lasres: Part I," Analyt. Chemist. **61**, No. 24, pp. 1367A-1373A (1989).

4. P, Teng, N. S. Nishioka, R. R. Anderson, and T. F. Deutsch, "Optical studies of pulsed-laser fragmentation of biliary calculi," Appl. Phys. **B42**, pp. 73-78 (1987).

5. L. I. Deckelbaum, J. J. Scott, M. L. Stretz, K. M. O'Brien, and G. Baker, "Detection of calcified atherosclerotic plaque by laser-induced plasma emission," Lasers Surg. Med. **12**, pp. 18-24 (1992).

6. A. A. Oraevsky, S. L. Jacques, G. H. Pettit, F. K. Tittel, and P. D. Henry, "XeCl laser ablation of atheorisclerotic aorta: luminescence spectroscopy of ablation products, " Lasers Surg. Med., **13**, pp. 168-178 (1993).

7. M. Haruna, M. Ohmi, M. Nakamura, and S. Morimoto, "Calcium detection of human hair and nail by the nanosecond time-gated spectroscopy of laser-ablation plume," SPIE **3917**, pp. 87-92 (2000).

8. M. Ohmi, M. Nakamura, S. Morimoto, and M. Haruna, "Nanosecond time-gated spectroscopy of laser-ablation plume of human hair to detect calcium for potential diagnoses," Opt. Rev. **7**, pp. 353-357 (2000).

9. R. Esenaliev, A. Oraevsky, S. Rastergar,C. Frederickson, and M. Motamedi, "Mechanism of dye-enhanced pulsed laser ablation of hard tissue: Implications for density," IEEE J. Select. Topics in Quantum Electron. **2**, pp. 836-846 (1996).

10. J. G. Fujimoto, B. Bouma, G. J. Tearney, S. A. Boppart, C. Pitris, J. F. Southern, and M. E. Brezinski, "New technology for high-speed and high-resolution optical coherence tomography," pp. 95-107 in R. R. Alferno ed., Advances in Optical Biopsy and Optical Mammography, published by The New York Academy of Sciences (1998).

Theoretical study of variable function (cutting/coagulating) laser surgical system using continuous wave 3 μm, 2 μm cascade Ho³⁺:ZBLAN fiber laser

Kyota Naruse*[a], Tsunenori Arai**[b], Satoko Kawauchi**[b], Tetsumi Sumiyoshi***[c],
Shoichi Kiyoshima****[d], Miya Ishihara**[b], Shunichi Sato*****[e], Makoto Kikuchi**[b],
Hitoshi Sekita***[c], Minoru Obara*[a]

[a]Faculty of Science and Technology, Keio University;
[b]Department of Medical Engineering, National Defense Medical Collage;
[c]Cyber Laser Inc.; [d]Research Center of Computational Mechanics, Inc.;
[e]Division of Biomedical Information Sciences, National Defense Medical Collage Research Institute

ABSTRACT

We theoretically investigated variable-function (cutting/coagulating) characteristics of the continuous wave 3 μm, 2 μm cascade Ho³⁺:ZBLAN fiber laser using three-dimensional heat-conduction calculation with finite element method. We have modified a commercial-available simulator in order to calculate heat conduction and thermal ablation process in soft tissue. In this calculation we considered specific heat rise due to the thermal denaturation of protein and volume shrinkage caused by temperature elevation. Beam profile, beam traveling speed, output power, and absorption coefficient were employed to describe the laser beam. The configuration of cutting groove and temperature distribution were calculated by varying the power ratio of the two wavelengths. Coagulation layer was defined as the region that was over 60°C for 1 second because we found that birefringence loss in porcine myocardium observed by a polarizing microscope occurred on this temperature history. When we increased the power ratio of 2 μm radiation to the total power of 0.9 W from 0% to 100% at the traveling speed of 0.5 mm/s, the incision depth decreased from 1.45 mm to 0.25 mm, while the coagulation layer thickness increased from 0.17 mm to 0.70 mm. We experimentally performed laser cutting on the same condition by our calculation using extracted porcine myocardium and compared this experimental results with the calculated results. We demonstrated that the incision depth and coagulation layer thickness estimated by our calculation indicated good agreement with the experimental results within 20% differences regarding the function variability by 3 μm/2 μm light mixing.

Keywords: heat conduction calculation, finite element method, thermal denaturation, thermal ablation, variable function

1. INTRODUCTION

Since laser surgical systems generally operate at a certain fixed wavelength, it is difficult to vary their tissue interaction. CO_2 laser ($\lambda = 10.6$ μm) and Nd:YAG laser ($\lambda = 1.06$ μm) are widely used for cutting and coagulation of soft tissue respectively. However, there is not a practical variable-function laser surgical scalpel system that can vary cutting/coagulating characteristics.

Water is dominant constituent in soft tissue, so that the absorption of soft tissue in infrared spectral region can be approximated as that of water. A spectral absorption curve for water is shown in Fig.1. Absorption coefficient at 3 μm is 10000 cm⁻¹, which is the highest peak in infrared. Therefore a laser scalpel operating at 3 μm may have a strong cutting capability. On the other hand, 2 μm radiation which has medium absorption coefficient (20
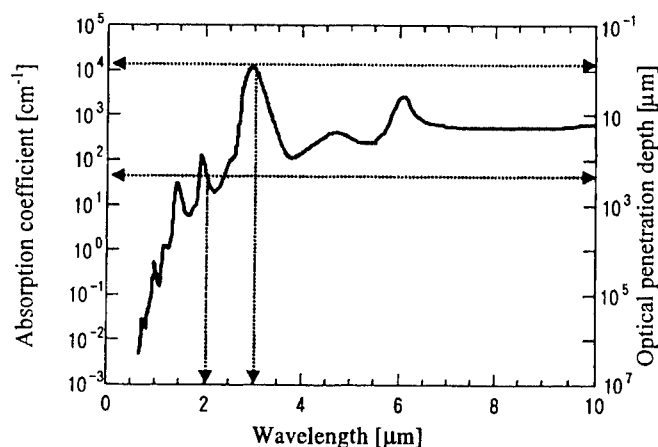

Fig.1: Spectral absorption curve of water.

cm^{-1}) is appropriate for appending coagulation layer to the cutting groove to stop bleeding.

Er:YAG laser and Ho:YAG laser are employed as a laser surgical system operating at 3 μm and 2 μm respectively. Er:YAG laser has been used in dentistry as in treating dental caries and cleaning tartar. Ho:YAG laser has been popular in orthopedics to perform percutaneous laser disc decompression (PLDD). These pulsed lasers produce great stress wave generated by water vapor bubble expansion on the laser exposure front so that they are suitable for hard tissue treatment[1]. If they are employed for cutting soft tissue, tissue dissection may occur as complications. A continuous wave laser is generally more applicable to soft tissue treatment than a pulsed one.

Therefore a continuous wave laser instrument operating at 3 and 2 μm simultaneously has a strong possibility of achieving variable function by varying the power ratio of the two wavelengths. We have developed a continuous wave Ho^{3+}:ZBLAN fiber laser operating at these two wavelengths simultaneously[2]. We have investigated the variable function using this fiber laser. In this paper we quantitatively estimated the variable function using the three-dimensional heat-conduction calculation with finite element method in order to explain the variable function theoretically. The theoretical results were compared with the experimental results that we had already attained by focusing the laser on extracted porcine myocardium using the power ratio adjustment of the two wavelengths[3].

2. METHODOLOGY

2.1 Heat conduction calculation

We modified a commercially available three-dimensional heat-conduction simulator, Quick Therm^{TM} (Research Center of Computational Mechanics Inc., Tokyo, Japan) based on finite element method in order to estimate cutting/coagulating characteristics. Our heat conduction equation at each element node can be written as

$$\frac{\rho C V}{\Delta \tau}(T_i - T_p) = K_{ij}(T_i - T_j) + Q \qquad (1)$$

where T_i is the temperature at a certain node i, T_p is the previous temperature at i, T_j is the temperature at the adjacent node to i, Q is the laser heat source term, ρ is the mass density, C is the specific heat, V is the volume, τ is the time, and K_{ij} represents the heat conduction matrix.

We considered a 4 mm^2 square finite-element model in cross-sectional plane and divided into 32×32 elements. The elements exposed to the laser beam where the large temperature gradients occurred were partitioned into the half sizes of the surrounding elements in order to achieve improved resolution for calculation

Fig.2: Cross section of the finite-element model.

(Fig.2). We used the mass density of 10^6 g/m^3, the heat conduction of 0.6 W/m°C, and the absorption coefficient at 3 μm and 2 μm of 10000 cm^{-1} and 20 cm^{-1} respectively. These values are from water that mainly composes soft tissue.

The laser beam was defined as a Gaussian shape heat flux. The beam spot radius, $\omega(z)$, is given by

$$\omega(z) = \omega_0 \sqrt{1 + z^2 / z_0^2} \qquad (2)$$

where ω_0 is the beam waist, z_0 is the Rayleigh range, and z is the position along the laser beam. The light intensity, $I(z)$, given by the Beer's law is written as
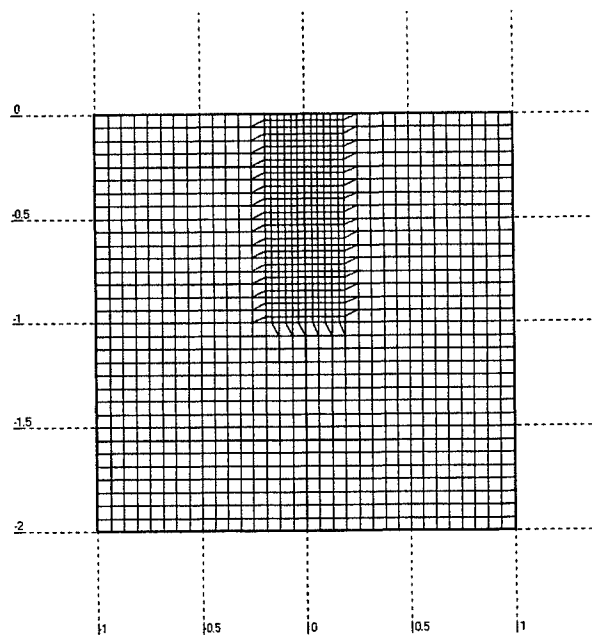
$$I(z) = I_0 \exp(-\mu_a z) \tag{3}$$

where I_0 is the incident light intensity, μ_a is the absorption coefficient, and $z = 0$ represents the model surface. Because in soft tissue the absorption coefficient in infrared is much larger than the scattering coefficient, the total attenuation coefficient is nearly equal to the absorption coefficient. The laser beam was traveled perpendicular to Fig.2. We used the beam waist of 30 µm, the Rayleigh range of 330 µm, the output power of 0.9 W, and the beam traveling speed of 0.5 mm/s.

The specific heat of soft tissue rises by means of thermal denaturation of protein[4]. To determine the specific heat at various temperatures, we compared experimental and theoretical temperature cross-sectional distribution in myocardium tissue. We decided 4.2 J/g°C under 45°C and 12 J/g°C over 45°C. We represented the volume shrinkage caused by temperature elevation. Based on the preliminary experimental results using porcine myocardium and a plane heater, -20% line strain over 90°C was considered in our calculation. Thermal ablation was regarded to start at 100°C, the boiling point of water. The elements reaching this temperature were removed with water evaporation heat of 2300 J/g.

2.2 Continuous wave 3 µm, 2 µm cascade Ho^{3+}:ZBLAN fiber laser

The energy level diagram of Ho^{3+} is shown in Fig.3. Sumiyoshi et al. have successfully demonstrated high power and high efficiency operation at 2.93 and 2.06 µm with a cascade Ho^{3+}:ZBLAN fiber laser pumped by a 1.15 µm fiber Raman laser radiation[2]. We adopted an optical fiber as a laser medium, which could achieve high-density excitation of the laser ion and attain excellent cooling characteristics with its large surface area. The fiber is a 2.5 m long multimode ZBLAN (ZrF_4-BaF_2-LaF_3-AlF_3-NaF) fiber doped with 2500 ppmw Ho^{3+} in the 10 µm diameter core. The ZBLAN glass has high transmissivity from 0.2 µm to 7.0 µm.
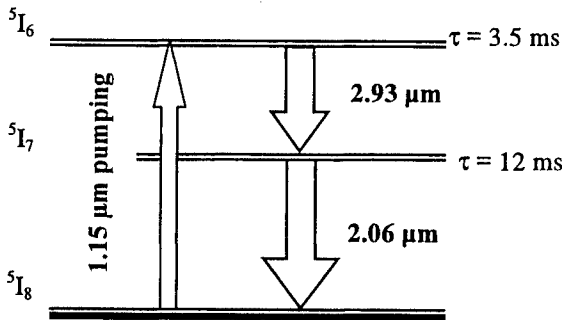

Fig.3: The energy diagram of Ho^{3+} and the cascade oscillation by the 1.15 µm pumping.
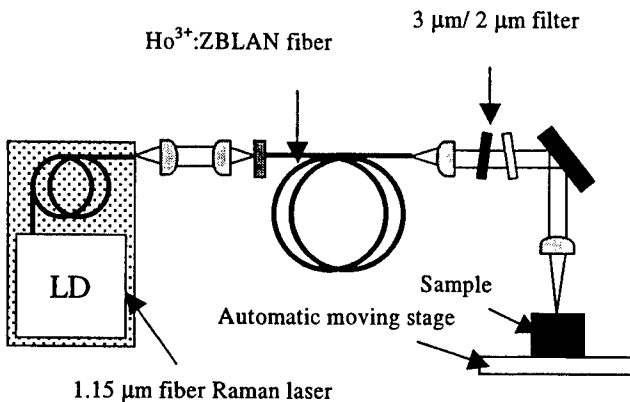

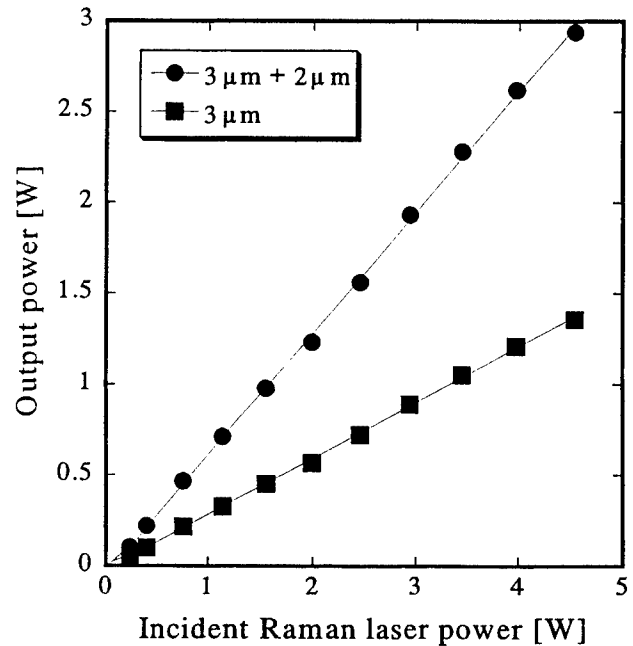Fig.4: Schematic diagram of experimental setup.

Fig.5: Cascade laser output power as a function of incident Raman laser power.

The schematic diagram of experimental setup is shown in Fig.4. As the 1.15 μm light source, we employed a fiber Raman laser with an output power of 5 W. The output beam from this laser was focused on the end surface of the ZBLAN fiber and cascade oscillation at 3 and 2 μm was obtained. The power ratio of the 3 μm to the 2 μm radiation is approximately 1:1. The output beam from the ZBLAN fiber was collimated with a 20 mm F.L. Ge lens. We could arrange 3 μm/2 μm power ratio using dielectric multi-layered filters which had different transmissions for 3 μm and 2 μm. These power-arranged beam was turned down with an Au mirror and focused with a 70 mm F.L. Ge lens. An automatic moving stage was employed to make line incision.

The cascade laser output power as a function of incident Raman laser power is shown in Fig.5. No saturation is observed in the output power dependence on the incident pump power. The highest combined output power and slope efficiency obtained were 3.0 W and 65% respectively (1.4 W, 30% for 3 μm laser, 1.6 W, 35% for 2 μm laser).

3. RESULTS

We estimated cutting/coagulating characteristics on the condition described in section 2.1 changing the power ratio of 2 μm radiation from 0% to 100%. The configuration of cutting groove and maximum temperature distribution calculated by this estimation are shown in Fig.6. The deepest cutting groove and smallest temperature elevation spread were obtained by the pure 3 μm radiation. When we increased the power ratio of the 2 μm radiation, the incision depth decreased and the temperature elevation distributed widely. We defined the coagulation layer as the region that was over 60°C for 1s because we experimentally found that birefringence loss in porcine myocardium observed by a transmission polarizing microscope occurred on this temperature history. When we increased the power ratio of the 2 μm radiation from 0% to 100%, the incision depth decreased from 1.45 mm to 0.25 mm, while the coagulation layer thickness increased from 0.17 mm to 0.70 mm. We successfully demonstrated the controllability of cutting/coagulating characteristics by the power ratio change of the 3 μm and 2 μm radiation using our heat-conduction calculation. It took about 20 minutes for the PC with a CPU of 333 MHz and with a RAM of 192 MB to estimate one figure in Fig.6.

We compared the calculated results with the previous experimental results on the same condition by our calculation. We used porcine myocardium blocks taken from the left ventricular wall that contained uniform rich muscle fibers. In the experiment the power ratio of the 2 μm radiation was set to 0%, 29%, 50%, 71%, and 96% using dielectric multi-layered filter exchange. With a hematoxylin-eosin (H.E.) stained specimen of the irradiated myocardium blocks, the incision depth was measured under the view of a light microscope and the coagulation layer thickness was measured by a polarizing microscope observation (Fig.7). The birefringence region indicates irreversible thermal denaturation of protein[5]. The incision depth and coagulation layer thickness as a function of the power ratio of the 2 μm radiation are shown in Fig.8 and Fig.9, respectively. Each experimental plot represents the mean values of four measurements. The incision depth and coagulation layer thickness estimated by our calculation indicated good agreement with the experimental results within 20% differences regarding the function variability by 3 μm/2 μm light mixing.

4. DISCUSSION

Comparing the calculated results with the experimental results, it is found that incision depth in the experiment tends to be smaller than the calculated results on 3 μm-radiation dominant conditions. We considered that one reason for this difference might be the prevention of laser light transmission by oozing fluid in the bottom of the cutting groove which comes from the thermally shrunk tissue. Another reason might be the prevention of laser light transmission by an ablation plume. There is discrepancy between measured and calculated coagulation layer thickness on 3 μm-radiation dominant conditions. We think that the waste energy absorbed into oozing fluid or the plume might make the coagulation layer thicker.

We modified the commercially available heat-conduction simulator in order to estimate the laser tissue interaction. We considered the specific heat rise, tissue coagulation, and volume shrinkage. They were caused by the temperature elevation. The specific heat of soft tissue rises by means of thermal denaturation of protein. To determine the specific heat at various temperatures, we compared the temperature in porcine myocardium measured by a thermography with the temperature calculated by the simulator. Assuming the specific was constant, the calculated temperature was about twice as high as the
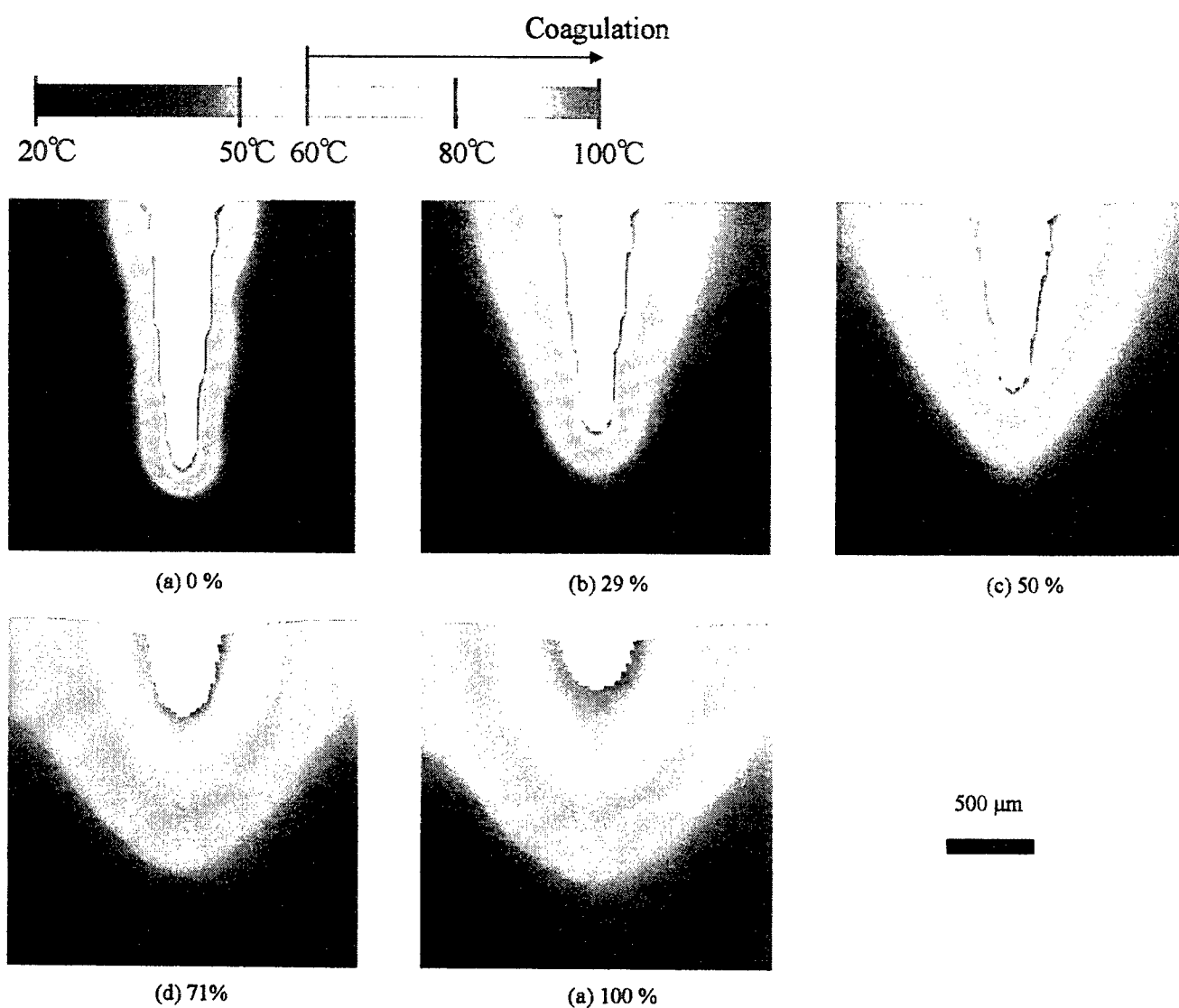
Fig.6: Images of cutting grove and maximum temperature distribution obtained by our calculation.
The power ratio of the 2 μm radiation was (a) 0%, (b) 29%, (c) 50%, (d) 71%, and (e) 100%, respectively.
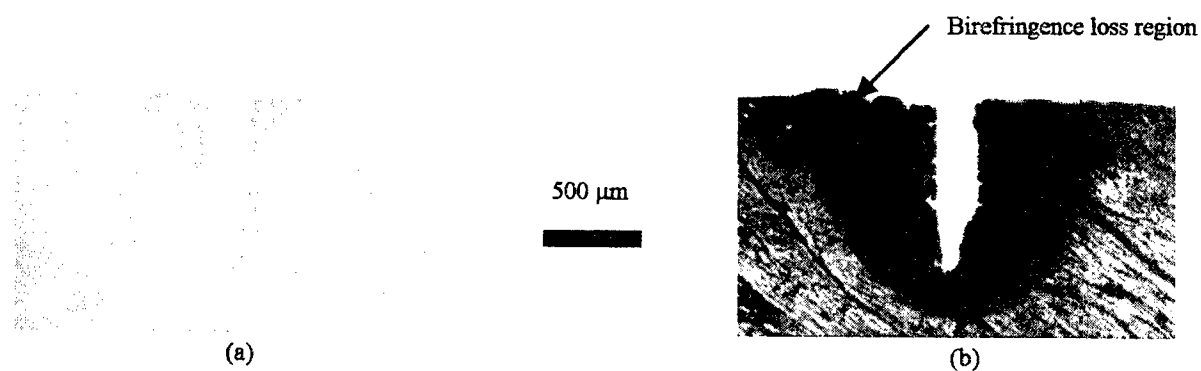

Fig.7: H.E. stained specimen observed by a light microscope (a) and a polarizing microscope (b).
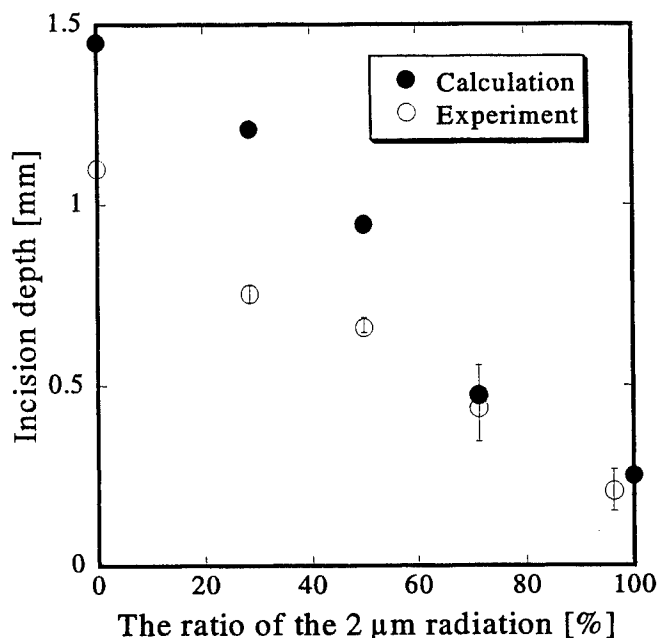The power ratio of the 2 μm radiation was 50%.

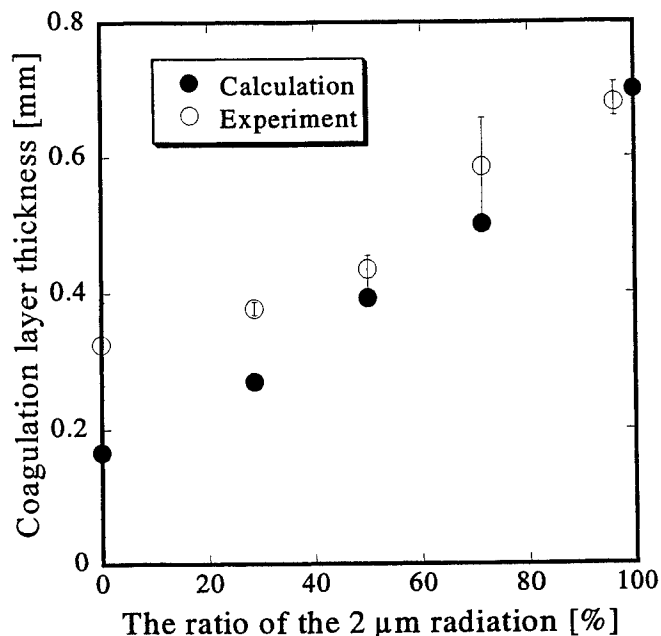Fig.8: Incision depth as a function of the ratio of the 2 μm radiation to the total power.

Fig.9: Coagulation layer thickness as a function of the ratio of the 2 μm radiation to the total power.

measured temperature. When we defined the specific heat of 12 J/g°C over 45°C, the calculation indicated good agreement with the experiment. That was why we employed the variable specific heat over 45°C. To attain the judgment criteria for a coagulation layer, we investigated the temperature history in the birefringence loss region. By comparing the birefringence loss region observed by a polarizing microscope with the temperature history given by a thermography, we defined a coagulation layer as the region that was over 60°C for 1s. We considered tissue volume shrinkage mainly caused by water evaporation. We experimentally found the thermally shrunk region corresponded to the deep stained region in the H.E. stained specimen observed by the light microscope. We measured the line strain in a porcine myocardium block heated by a defocused CO_2 laser beam. We determined -20% line strain occurred over 90°C. We can not find any theoretical studies describing the tissue volume shrinkage.

We determined these parameters based on the experiment. We found various reports regarding the theoretical study of laser tissue interaction with finite element method[6-9]. We do not know heat conduction calculation based on the experimental results. Rastegar et al. have estimated the ablation process considering scattering effect[7]. We do not consider scattering. The scattering effect plays an important role in estimating laser tissue interaction. However the scattering effect may be neglected in infrared because the absorption coefficient in infrared is much larger than the scattering coefficient. If we estimate laser tissue interaction in visible region, it must be necessary to consider the scattering effect.

5. CONCLUSION

We have quantitatively estimated the variable-function characteristics of the continuous wave 3 μm, 2 μm cascade Ho^{3+}:ZBLAN fiber laser using our modified heat conduction simulator based on the finite element method. We have explained the variable function theoretically. The irradiating conditions of the dual-wavelength laser for practical use can be predicted by our simulator. We think that laser tissue interaction by other infrared lasers might be quantitatively estimated by our method.

REFERENCES

1. Leeuwen TG, Jansen ED, Motamedi M, Welch AJ, and Bors C, "Bubble formation during pulsed laser ablation: mechanism and implications", *Proceedings of SPIE*, 1882, pp.13-22, 1993
2. Tetsumi Sumiyoshi, Hitoshi Sekita, Tsunenori Arai, Shunichi Sato, Miya Ishihara, and Makoto Kikuchi, "High power continuous wave 3 and 2 μm cascade Ho^{3+}:ZBLAN fiber laser and its medical applications", *IEEE Journal of Selected Topics in Quantum Electronics*, 5, No.4, pp.936-943, 1999
3. Tsuneri Arai, Tetsumi Sumiyoshi, Kyota Naruse, Miya Ishihara, Shunichi Sato, Makoto Kikuchi, Tadashi Kasamatsu, Hitoshi Sekita, and Minoru Obara, "Laser tissue interaction of a continuous wave 2 μm, 3 μm cascade oscillation fiber laser: sharp incision with controlled coagulation layer thickness", *Proceedings of SPIE*, 3914, pp.252-259, 2000
4. Ming-Sing Si, Thomas E. Miliner, Bahman Anvari, and J. Stuart Nelson, "Dynamic heat capacity changes of laser-irradiated type 1 collagen films", *Lasers in surgery and Medicine*, 19, pp.17-22, 1996
5. Sharon Thomsen, "Mapping of thermal injury in biologic tissues using quantitative pathologic techniques", *Proceedings of SPIE*, 3594, pp.82-95, 1999
6. Tami N. Glenn, Sohi Rastegar, and Steven L. Jacques, "Finite element analysis of temperature controlled coagulation in laser irradiated tissue", *IEEE Transactions on Biomedical Engineering*, 43, No.1, pp.79-87, 1996
7. Sohi Rastegar, Massoud Motamedi, Ashley J. Welch, and Linda J. Hayes, "A theoretical study of the effect of optical properties in laser ablation of tissue", *IEEE Transactions on Biomedical Engineering*, 36, No.12, pp.1180-1187, 1989
8. Avi Ravid, and Abraham Katzir, "Theoretical model simulating CO_2 laser ablation of biological tissue due to steam pressure generation", *Proceedings of SPIE*, 3195, pp.287-295, 1998
9. Alexander N. Yakunin, Yury N. Scherbakov, Valery V. Tuchin, Sergei R. Utz, and Ilya V. Yaroslavsky, "Temperature distribution in biotissue under cw low intensity laser irradiation", *Proceedings of SPIE*, 1646, pp.161-171, 1992

Time-domain Optical and Thermal Properties of Blood Undergoing Laser Photocoagulation

John F. Black[a] and Jennifer Kehlet Barton[b#]

[a]Research and Development Department, Coherent Medical Group, 2400 Condensa Street MS C10, Santa Clara, CA 95051
[b]Division of Biomedical Engineering, The University of Arizona, 1230 E. Speedway Blvd., Tucson, AZ 85721-0104

ABSTRACT

We have examined the temporal characteristics of the optical properties of blood undergoing laser-induced photocoagulation during long pulse (10 ms) 532-nm irradiation. The time-domain optical properties were probed at 532 nm, 594 nm, 633 nm and 1064 nm using a newly developed pump-probe technique in a double integrating sphere apparatus. During the 10 ms illumination period, blood evolves from liquid to a liquid blood/coagulum mixture to a system at the liquid/vapor transition in an essentially adiabatic manner. As with previous studies, a sharp rise in the 532 nm signal remitted from the sample can be linked to the onset of coagulation and a concomitant increase in scattering caused by microscopic coagulum particles. We also observe a subsequent decay in this remittance and, at sufficiently high radiant exposures, acoustic and visual transients indicating the onset of microvaporization. Probing the sample at the other wavelengths, we show that the optical properties of the system display highly complex behavior in multiple time frames. We believe that this rich behavior results from the interplay of:

(i)   a time/temperature-dependent red-shift in the absorption spectrum of the oxy-hemoglobin chromophore,
(ii)   coagulation dynamics occurring on at least two distinct time and length scales, and,
(iii)   the creation of at least one new chemical species possessing a different absorption spectrum to that of oxy-hemoglobin.

The thermal properties of the system were measured in a time- and spatially-resolved manner using a newly developed technique, and modeled using finite-element analysis incorporating the effects of time-dependent changes in the absorption coefficients of the blood, and phase changes representing coagulation and the liquid/vapor transition. Cross-correlating the optical and thermal studies, we show that the temporal properties of the 532 nm and 633 nm remittance signals can potentially be used to develop a sensitive real-time probe of the onset of coagulation, which in turn will lead to accurate dosimetry during clinical procedures. We also show that the three features of the coagulation highlighted above have profound implications for the design of lasers for vascular therapeutic applications.

Keywords: Light scattering, dosimetry, thermal analysis, oxy-hemoglobin, met-hemoglobin, Nd:YAG laser.

1. INTRODUCTION

Laser-induced photocoagulation of blood and other biological tissues is a widely used technique in ophthalmology, surgery and dermatology. Applications range from treatment of diabetic retinopathy to tumor thermotherapy to port wine stains and other cutaneous vascular disorders. Despite the widespread applicability and use of this technique, definitive clinical endpoints to the procedure are often lacking, leading to subjective treatment parameter spaces and an intrinsic barrier to communication of good technique. During treatment, it is desirable that the minimum energy necessary to achieve a therapeutic result be applied to the target area. This minimum energy may be well below the energy necessary to produce an observable change in the tissue. Interactive feedback from the treatment site, and a quantifiable end point, could allow the tailoring of the photocoagulation pulses to produce good clinical results without unnecessary collateral damage. Finally, with the advent of capable machine vision systems and precision scanning mechanisms, a real-time diagnostic with feedback

---

To whom correspondence should be addressed. Phone (520) 621-4116, Fax (520) 621-8076, Email: barton@u.arizona.edu.

could allow the development of handpieces and slit-lamps capable of autonomous treatment of large areas with increased speed and accuracy.

Several groups have studied the optical properties of retinal tissues undergoing laser-induced chemical and mechanical changes.[1,2] In general, the target in retinal photocoagulation is the Retinal Pigmented Epithelium (RPE). Heat diffusion from the RPE following laser photocoagulation causes a visible whitening of the surrounding tissue, and leaves a distinct lesion. The radiant exposure required to produce these lesions varies widely from person to person, resulting in inconsistent treatment for standard parameter sets. Confocal reflectometry has been successfully applied to the real-time observation of these RPE lesions, and to real-time feedback control of the laser, resulting in standardized lesion densities.

To the best of our knowledge, we are not aware of any application of real-time reflectometry to the laser coagulation of dermal vascular lesions. This may be because until recently, light sources for this purpose had pulse durations too short to allow true feedback control, or perhaps because the highly scattering nature of the dermis gives rise to a large non-resonant background complicating the measurement. We present results here showing that the time-dependent optical properties of blood undergoing laser photocoagulation have characteristic features that may allow for real-time feedback of the progress of coagulation.

2. EXPERIMENTAL

2.1 In-vitro Model – Optical Measurements.

A commercial long-pulse green laser (VersaPulse Cosmetic Laser, Coherent Medical Group, Santa Clara, CA) was used to provide the 532 nm laser pulses. At a 3 mm diameter spot, the laser could operate at radiant exposures up to 16 Jcm^{-2} with a 10 ms pulsewidth. Laser pulse energies were monitored using a power meter (PM30V1 volume-absorbing head, EM5200 readout; Molectron Detector Inc., Portland, OR). The long-pulse 532 nm laser was transmitted to the experiment using a fiber-optic cable and the output recollimated using an imaging system. Incident pulse temporal waveforms and energies were monitored using a photodiode.
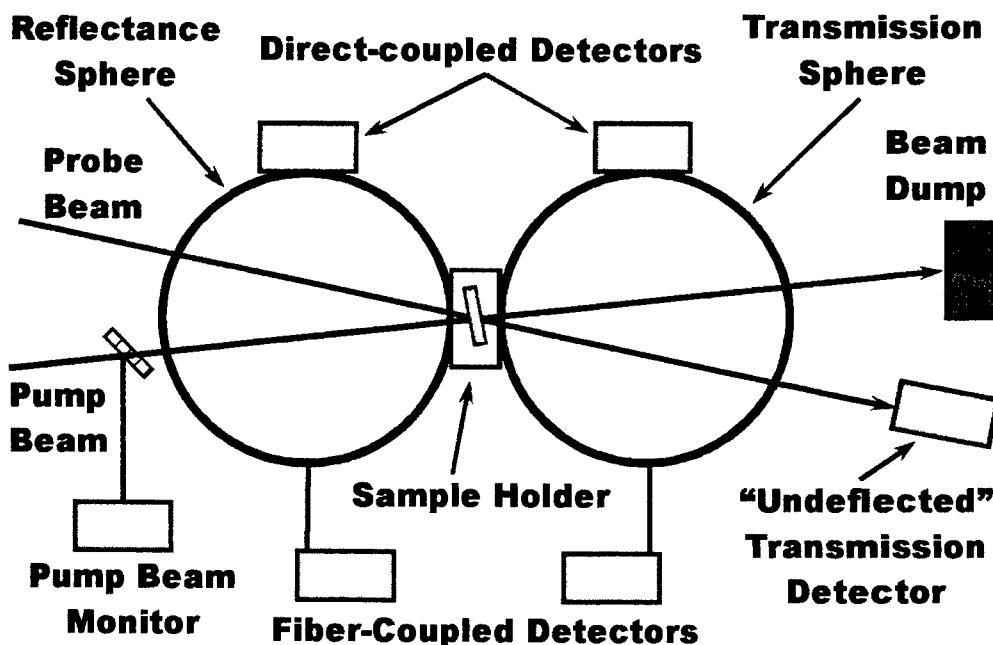
Figure 1: Experimental apparatus for the *in vitro* portion of this work.

Blood samples were obtained from two apparently healthy Caucasian volunteers. The samples were kept refrigerated, and used within 72 hours after extraction. Samples were diluted where necessary using isotonic saline. Washed suspensions of red blood cells were prepared by taking whole blood samples and repeatedly centrifuging and washing the samples in isotonic saline. Macerated red-blood-cell (RBC) suspensions were prepared by taking the plasma-free RBC suspensions

formed in the previous step and lysing by diluting with deionized water. Where a "clear" solution of oxy-Hb was needed, the macerated mixture formed in the previous step was subjected to centrifugation and the supernatant extracted. For the two-color pump-probe experiments, appropriate samples were loaded into demountable cuvettes of various thicknesses from 0.1 – 1 mm (20/O-G Series, Starna Cells, Atascadero, CA), which were then placed into the central sample compartment of a standard double integrating sphere experiment.[3] The experimental arrangement is shown in Figure 1. Two integrating spheres (RT-60-SF, Labsphere, North Sutton, NH) were coupled using a specially designed sample holder angled to retro-reflect the front-surface Fresnel reflection from the cuvette back through the laser beam launch port. This modification proved necessary as the diffuse reflectivity of the samples was found to be on the order of 0.1 – 0.5%. Detecting such small signals in the presence of a Fresnel reflection from the cuvette wall would have severely complicated the experiment. Each blood sample was used once only to avoid complications resulting from localized microvaporization nucleated by residual coagulum particles. In practice it was also found that the diffuse reflectivity of a sample containing coagulum particles was substantially higher than that of unmodified blood.

To probe the transient optical properties at 633 nm, a 15 mW HeNe laser (Melles-Griot 05-LHP-151; Irvine, CA) was launched through a port adjacent to the 532 nm launch port. The optical properties at 594 nm and 1064 nm were probed by replacing the 633 nm HeNe with either a 5-mW 594 nm HeNe Laser (Trius Engineering, Durant, OK) or a 150 mW 1064 nm DPSS laser (STAR-150, Coherent Laser Group, Santa Clara, CA) respectively. The beam from this laser was overlapped with the spot from the 532 nm laser at the image / sample plane between the two spheres. Scattered light in the spheres was sampled by fiber-optic patch cables leading to monitoring photodiodes (PDA-55 and Det-110, Thorlabs, Newton, NJ). The diodes were equipped with interference filters or low-pass cut-off filters to isolate the wavelength of interest and, where necessary, neutral-density filters. In some case, the low signals from the experiment predicated direct coupling of the diodes to the spheres. In this configuration, and to ameliorate the angle-of-incidence specificity found in interference filter wavelength response, a wide-area photodiode with variable gain (Model 2031; New Focus, Santa Clara, CA) using primarily long-pass absorbing glass filters and only one interference filter close to the diode active area was employed.

Total transmission measurements were made with a high-albedo scattering plug in the probe laser exit port of the rear sphere. "Undeflected" transmission measurements were made by removing the plug, placing a detector outside the rear sphere and measuring the collimated transmission plus forward scattered light contained within a solid cone of approximately 2.8 degrees half-angle. While making these "undeflected" transmission measurements, we also monitored the signal in the integrating sphere. We denote these latter measurements as "deflected" transmission, as they constitute a measure of the energy deflected out of the normal path of the probe beam. The light intensity in the reflectance sphere was calibrated using Fresnel reflections from AR-coated and uncoated windows in the sample position. The transmission of the AR-coated and uncoated windows was measured separately in a spectrophotometer (Cary 50, Varian Instruments, Palo Alto, CA). The transmission sphere was calibrated by using neutral density filters in the sample position. The outputs of the sphere photodiodes and also the photodiodes monitoring the source laser power were sent to an oscilloscope (TDS224, Tektronix Inc., Beaverton, OR). Waveforms were captured and processed using commercial software (Tektronix WaveStar™ and IGOR™; Wavemetrics, Lake Oswego, OR).

2.2 In-vitro Model – Thermal Measurements.

We wish to make temperature measurements in a manner which is (a) non-perturbative to the sample, (b) spatially selective in the z-axis (where z is the propagation direction of the pump laser), (c) time-resolved, and (d) "real-time" in nature in that the results can be easily related to a temperature. Thermocouples and high-speed IR cameras do not simultaneously meet all these requirements.[4,5] We have chosen instead to make time-domain measurements of the thermal properties of the system using a technique similar to that of Martinelli et al.[6] based on the change in reflectivity of a solid-liquid interface given a dynamically changing refractive index in the liquid phase. For p-polarized light, the reflection coefficient at the solid-liquid interface is given by:

$$r(\theta, n_2) = \frac{n_2^2 \cos\theta - n_1 \sqrt{\left(n_2^2 - n_1^2 \sin^2\theta\right)}}{n_2^2 \cos\theta + n_1 \sqrt{\left(n_2^2 - n_1^2 \sin^2\theta\right)}},$$

where θ is the angle of incidence, n_1 is the refractive index of the solid substrate and n_2 is the refractive index of the liquid. The observable reflectivity is the square of this quantity. It is straightforward to show that setting the angle of incidence to be the Brewster angle for the two "cold" refractive indices, extraordinarily large changes in reflectivity can result from a change in the refractive index of the liquid. We have chosen however to work at 45 degrees, partly for experimental convenience.

This angle is less sensitive in terms of its absolute response to changes in n_2, but is also less sensitive to systematic errors such as the intrinsic divergence of the laser beam or in measuring the angle of incidence at the sample. The two configurations used in this experiment are shown in Figure 2.
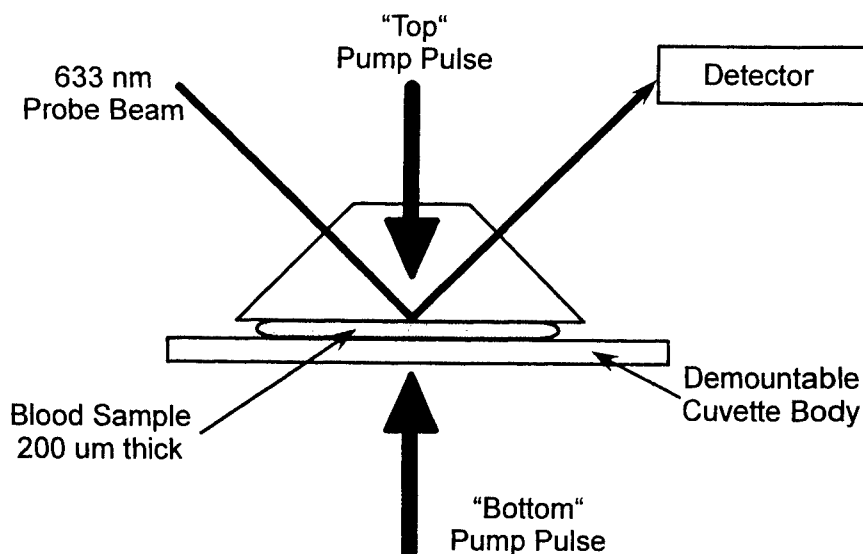
Figure 2: The TIR thermal probe experimental schematic.

The sample holder is formed using a right-angle prism (K32-332, Edmund Scientific, Barrington NJ) which has been polished to approximate a dove prism. As shown, the 532 nm pump beam may interact with the sample at normal incidence from either the "top" or bottom" surfaces of the cuvette while allowing the probe beam to interact with the interface at angles around 45 degrees. This experimental arrangement eliminates complications that would be caused by a second, more intense reflection that would result from using, for example, a flat-sided cuvette. It is important that the pump beam be parallel to the sample surface normal to avoid asymmetric heating of the sample. A He-Ne laser (Melles-Griot 05-LHP-151) impinges on the sample at 45 degrees (+/- 0.3) in p-polarization. The reflected beam propagates for approximately 1 meter and then impinges on a detector (Thorlabs PDA55) placed behind a 632.8 nm interference filter and a pinhole. The signal from the diode is fed to an oscilloscope (Tektronix TDS224) and recorded contemporaneously with the 532 nm remittance from the sample.

The starting refractive index of whole (centrifuged) blood plasma was measured using a refractometer (Atago R5000, Cole-Parmer Instrument Company, Chicago, Il) and found to be 1.3500 +/- 0.0005. The refractive index of isotonic saline was measured to be 1.3345 +/- 0.0005, consistent with book values.[7] The experiment was performed using a 2x dilution of whole blood, giving a starting refractive index of 1.3423. Since the starting composition of blood plasma is 91% water[5], and our dilution only increases this percentage, we have assumed that the functional form of $\frac{dn_2}{dT}$ is the same as that for pure water.[8]

The change in the refractive index of the prism substrate as a function of temperature is a factor of ten smaller than that for water and we have neglected it in the analysis to follow.[6] We will explore the validity of this simplification in future work.[9] By recording the time-domain reflectivity at the interface, we therefore monitor the time-domain refractive index of the sample. This can then be inverted in a most straightforward manner to give the temperature at the sample/glass interface at any given moment. We measure the temperature at two places in the sample with spatial selectivity; these measurements then becoming the boundary conditions for subsequent calculations on the sample. The **only** free parameter in the inversion is the functional form of the refractive index of water vs. temperature. This technique for temperature measurement has the advantage of being non-perturbative (unlike the insertion of a thermocouple), insensitive to the presence of a large pump laser pulse (unlike a thermocouple), spatially selective (unlike an IR camera or thermocouple) and real-time (unlike an IR camera).

2.3 In-vitro Model – Thermal Model.

The details of the finite element model of the *in vitro* system will be the subject of a more detailed publication.[9] Briefly, the cuvette/blood/laser interaction is modeled assuming cylindrical symmetry about the center of the incoming beam. The model makes explicit consideration of:

i) the cuvette wall material (thermal diffusivity) and thickness,
ii) sample thickness, starting absorption coefficient, and (linear) changes in absorption as a function of temperature,
iii) the liquid/steam phase change and the latent heat of vaporization at the liquid/steam transition point,
iv) laser pulse energy and temporal pulse duration (square wave pulse).

The model computes the time-domain temperature profiles on a grid in two dimensions (r and z). The model was developed and solved using SINDA/ATM, a commercially available package based on the FEMAP modeling engine and the SINDA/G thermal solver. The standard parameters used in the simulation are shown in table 1 below.[7,9]

Quantity	Value	Unit	Quantity	Value	Unit
BK-7 Thermal Conductivity	1.114	$W.m^{-1}.K^{-1}$	Water Latent Heat of Vaporization	2257	$kJ.kg^{-1}$
BK-7 Density	2.51	$kg.dm^{-3}$	Phase change onset temperature.	90	deg. C
BK-7 Specific Heat	858	$J.kg^{-1}.K^{-1}$	Phase change end temperature.	100	deg. C

Table 1. Standard parameters used in the thermal model.

For a cuvette with BK-7 walls, the simulations show a nearly uniform (top-hat) radial temperature profile across the radius of the pump laser beam as a function of time (1.35 mm radius top-hat *vs.* 1.5 mm radius laser beam). Our use of a small (< 1mm diameter) probe beam centered on the pump beam in both the optical and thermal pump-probe experiments described in sections 2.1 and 2.2 can therefore be expected to yield results representative of the system as a whole. The situation is far more complicated if a sapphire cuvette is used. Due to its higher thermal diffusivity, the window acts as an efficient heat sink and, concomitantly, heating is much less uniform and the top-hat profile approximation breaks down. We have observed this non-uniformity while observing this system with a high-speed (2.5 kHz) thermal imaging camera using a sapphire cuvette. Future IR camera work will use windows made from magnesium fluoride, which is transparent in the 3 – 5 μm camera window and which has the advantage (over sapphire) of very poor thermal diffusivity. For all the work described here, BK-7 cuvettes were used.

3. RESULTS

Figure 3 shows a representative plot of the time-resolved transmission and remittance at 532 nm of a whole blood dilution (2x dilution in isotonic saline) being irradiated at 10 Jcm^{-2} using the 532 nm laser. The traces are the diffuse reflected 532 nm light, the deflected transmission, and the total transmission at 532 nm. The traces have been normalized to the 532 nm laser power and low-pass filtered in the plotting program using a 15-point second-order Savitsky-Golay routine to remove 20 kHz ripple from the VPC flashlamp power supply. Figure 4 shows the remitted 532 nm signal, the deflected transmission, and the total transmission at 532 nm for a "clear" solution of oxy-Hb (effective hct ~ 24.5%, 14 Jcm^{-2}). Figure 5 shows a representative plot of the time-resolved undeflected (collimated) transmission at 594 nm for a 2x whole blood dilution (9 Jcm^{-2}, hct = 24.5%). Figure 6 shows a representative plot of the time-resolved undeflected transmission at 594 nm for a solution of oxy-Hb (effective hct ~ 24.5%, 14 Jcm^{-2}). Figure 7 shows the total transmission and diffuse reflectance at 633 nm of a dilution of whole blood (10 Jcm^{-2}, hct = 24.5%). Figure 8 shows a representative plot of the time-resolved transmission at 633 nm for a solution of oxy-Hb (eff. hct ~ 24.5%, 12 Jcm^{-2}). Figure 9 shows a representative plot of the time-resolved transient total transmission and diffuse remittance at 1064 nm of a blood sample (10 Jcm^{-2}, hct = 24.5%). The low-pass filtering (and where necessary, normalization) of figures 4 – 9 is the same as that for figure 3. All the data shown are from 200-micron pathlength cuvettes. The "clear" solution samples tended not to give worthwhile remittance data (very low signals) for the CW probe lasers. The 532 nm laser is much more powerful and in this case gave useful data. The error analysis of those plots with calibrated ordinates suggests potential accuracies of +/- 10% of the value for large (double-digit) values of R and T. The error level could rise to as much as +/- 25% of the value for small (0.1 – 1%) values of R and T.

Figure 10 shows a representative plot of the initial time-domain total internal reflection (TIR) data measured on the top (front, pump laser) and bottom sides of the "cuvette", superimposed on the 532 nm remittance signal in the TIR thermal probe experiment. Figure 11 shows the inversion of the front-surface reflectivity data of figure 10 into time/temperature

space, and for comparison, the results of a simulation at $z = 0$ using the thermal model described above and the experiment-specific parameters in Table 2. Also shown is the peak sample temperature for the same simulation parameters. This peak sample temperature occurs approximately 30 microns into the sample from the "front" surface ($z = 0.03$ mm). As a caveat to the data in figures 10 and 11, we should point out that the experiment and model are at a relatively early stage of development, and there is clearly some refinement to take place (the time lag and shape differences between the experiment and theory for example). However we will show later that an independent measurement of a critical temperature point in the photocoagulation dynamics is in encouragingly good agreement with our preliminary data. We believe therefore that we currently have a good qualitative picture of the time-domain thermal properties of the sample in our experiments.

Quantity	Value	Unit	Quantity	Value	Unit
Pump Pulse Width	10	ms	Starting absorption coefficient @ 532 nm	115	cm^{-1}
Radiant Exposure	10	$J.cm^{-2}$	Degradation of μ_a at elevated T	20%	Over 20 – 100 C

Table 2. Specific parameters used for the simulation shown in figure 11.
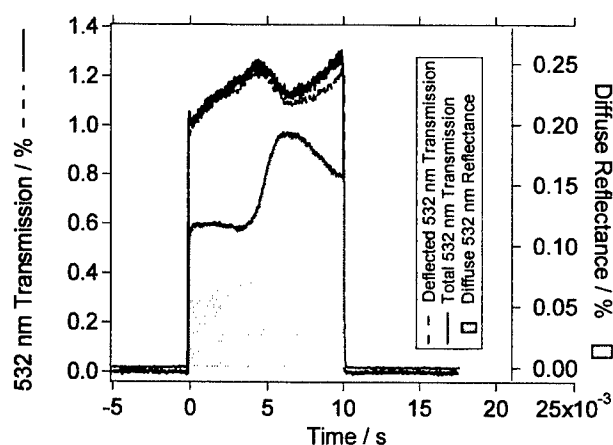
Fig. 3: 532 nm Probe – Whole Blood Dilution (hct = 24.5%, 10 Jcm^{-2})
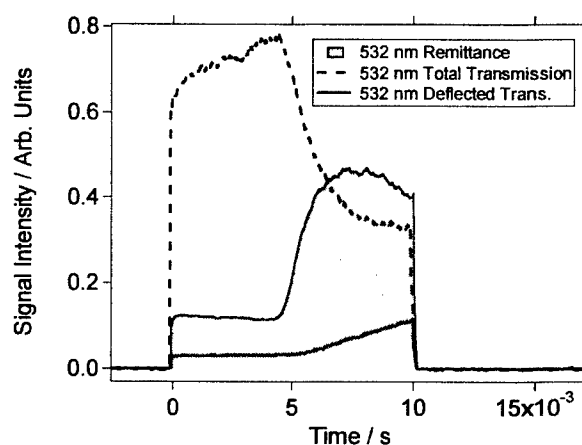
Fig. 4: 532 nm Probe – Oxy-Hb Solution (hct ~ 24.5%, 14 Jcm^{-2})
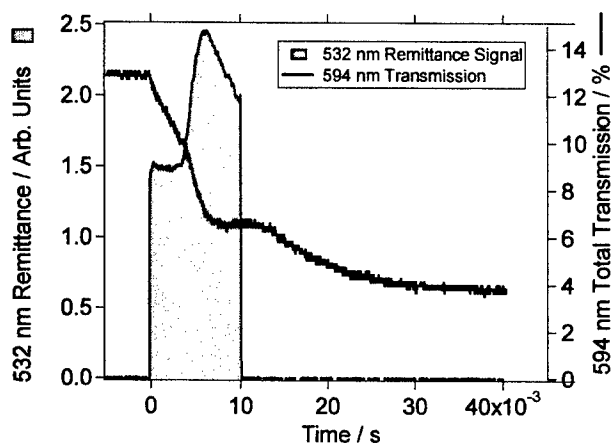
Fig. 5: 594 nm Probe – Whole Blood Dilution (hct = 24.5%, 9 Jcm^{-2})
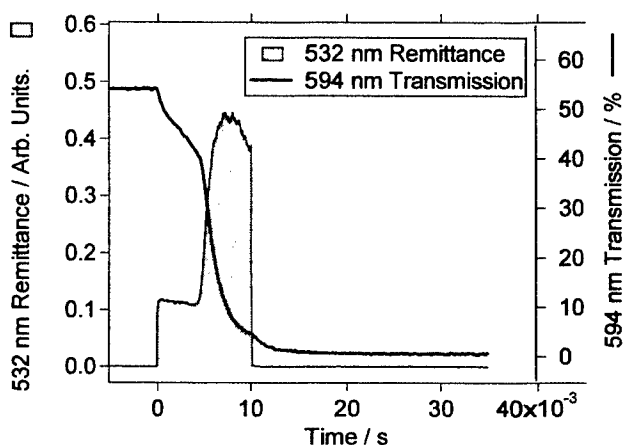
Fig. 6: 594 nm Probe – Oxy-Hb Solution (hct ~ 24.5%, 14 Jcm^{-2})
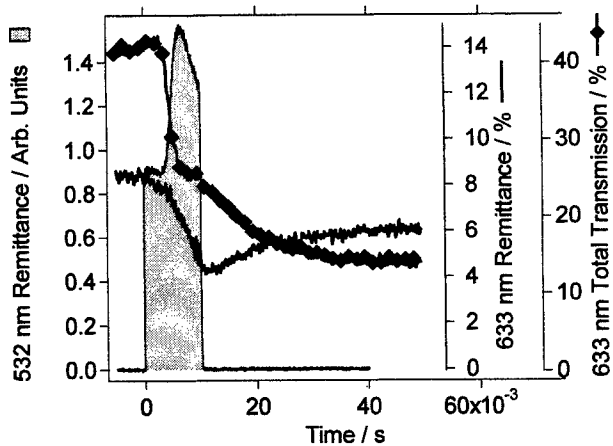
Fig. 7: 633 nm Probe – Whole Blood Dilution
(hct = 24.5%, 10 Jcm^{-2})

Fig. 8: 633 nm Probe – Oxy-Hb Solution
(hct ~ 24.5% eqv. 12 Jcm^{-2})

Fig. 9: 1064 nm Probe – Whole Blood Dilution
(hct = 24.5%, 10 Jcm^{-2})

Fig. 10: 633 nm TIR Thermal Probe
(hct = 21%, 10 Jcm^{-2})

Fig. 11: Calculated and Measured Temperature Profiles
(hct = 21%, 10 Jcm^{-2}, other params. per table 2)

4. DISCUSSION

Overview

While the shapes, slopes and asymptotes of the reflection and transmission plots for each wavelength are all very different, they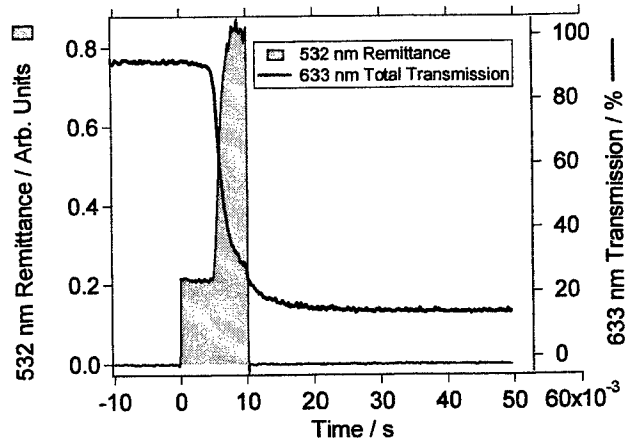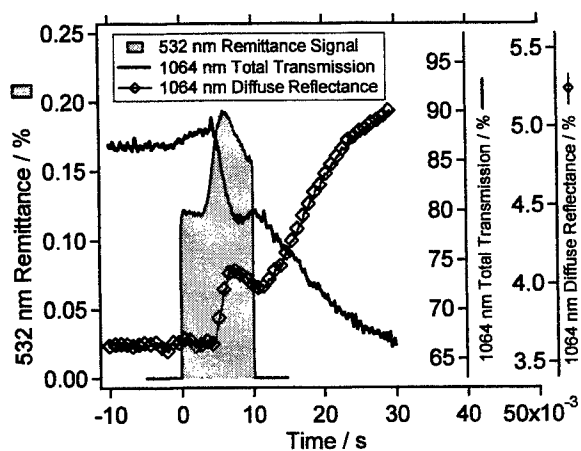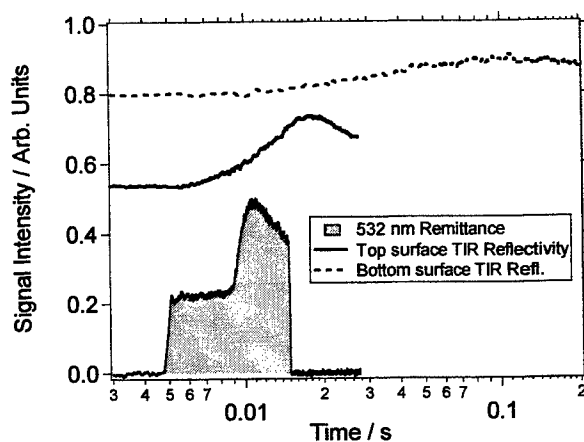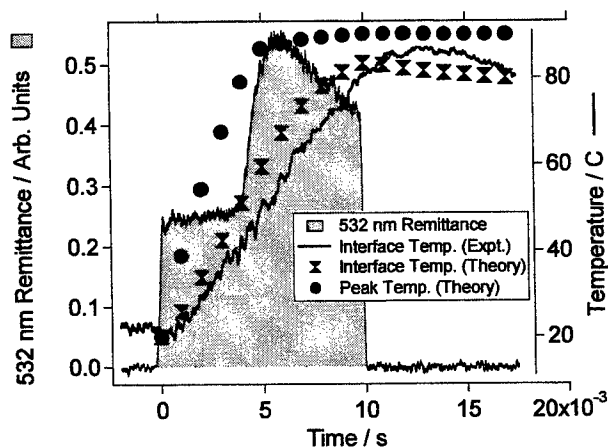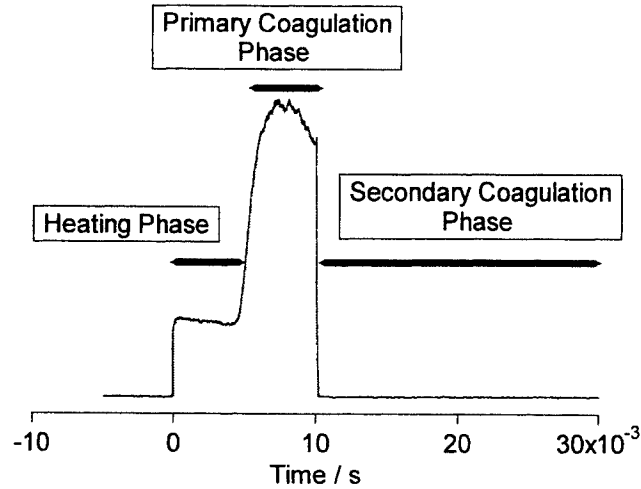 all have one thing in common, namely 3 distinct temporal phases. We have categorized these as (i) the heating phase, (ii) the primary coagulation phase, and (iii), the secondary coagulation phase, shown schematically in figure 12.

**Figure 12:** Schematic representation of the three phases of coagulation

4.1 Heating Phase

The data from the measurements most sensitive to scattering (reflectance, deflected transmission) do not change appreciably during the heating phase. Furthermore, the total transmissions of the weakly absorbed probe wavelengths (633 nm, 1064 nm) do not change significantly during this phase. The transmissions of the 532 and 594 beams change substantially however, in both whole blood dilutions and solutions of oxy-Hb. The transmission of the 532 nm beam increases, while that of the 594 beam decreases. The transmission changes start from the moment the green pulse impinges on the sample, and continue monotonically until the start of what we have termed the primary coagulation phase, where the slopes change abruptly and become non-linear. We can say with confidence that the major mechanism responsible for the slope changes at 532 and 594 nm is not photodissociation of oxy-Hb to give deoxy-Hb, although cursory examination of the absorption coefficients at 532 nm and 594 nm in Table 3 would not rule this out.[10-16] Referring to the table, this deoxygenation reaction would also cause a large decrease in transmission at 633 nm and an increase in transmission at 1064 nm. We observe neither effect in figures 7 and 9. The observations also cannot be explained by a reaction that converts oxy-Hb to met-Hb. In this situation, the 633 nm transmission would decrease immediately, and the 1064 nm transmission would *decrease*. Again, we see no evidence for this in figures 7 and 9.

Absorption Coefficient (cm⁻¹)	532 nm	594 nm	632 nm	1000 nm	1064 nm
Oxy-Hb (Aqueous Solution)[12]	115	23	1.4	2.6	-
Oxy-Hb (Blood)[15]	-	-	-	-	3[†]
Oxy-Hb (Blood)[16]	118	21	1.7	3.2	-
Oxy-Hb (Blood)[14]	-	-	-	-	2.4
Deoxy-Hb (Aqueous Solution)[12]	86	58	11	0.6	-
Oxy-Hb (Blood)[15]	-	-	-	-	0.4[†]
Deoxy-Hb (Blood)[16]	(110)	61	15	0.64	-
Met-Hb (Aqueous Solution)[12]	70	35	41	8	-

Table 3: Absorption coefficients (cm⁻¹) of oxy-, deoxy-, and met-hemoglobin compiled from various sources.[12,14-16] All values have been scaled to hct = 24.5%. † denotes an estimated value.

If we define the heating time as the time from the onset of the pump pulse to the onset of coagulation (figure 12), we have found that the heating time is inversely proportional to the radiant exposure.[17] This implies a constant energy deposition to get the sample to the onset of coagulation and therefore that the sample temperature at the onset of coagulation is approximately constant for a range of radiant exposures. A similar observation was made by Verkryusse et al.[18] The thermal modeling suggests that from the onset of heating to this point in the pump pulse, the temperature in the sample rises smoothly. A possible explanation for the 532 and 594 nm transmission data therefore is that we are seeing a red-shift in the absorption spectrum related to the temperature of the sample. This explanation would be consistent, by extrapolation, with earlier data from 20 – 300 K[19] and 20 – 40 degrees C.[20,21] Referring to figure 13, an absorption spectrum for oxy-Hb from 500 –700 nm, in the event of a red-shift the 532 nm absorption coefficient would be expected to drop, and the 594 nm coefficient would be expected to increase.[10-12]
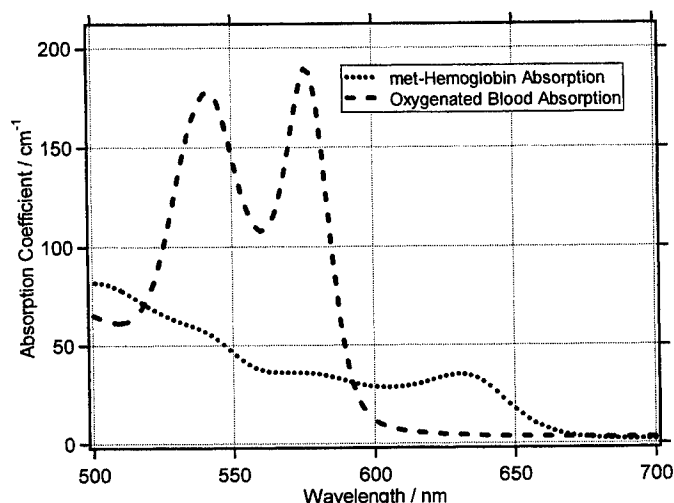
Figure 13: Optical absorption spectra of a dilution of whole blood (hct = 24.5%) and a scaled spectrum of met-Hb.

We cannot infer much beyond this. Previous authors have noted that in addition to a red shift, the *shape* of the absorption spectrum of oxy-Hb also changes with temperature.[19-21] Despite a knowledge of the real-time system temperature, we cannot reliably extract a functional form for the absorption at a given wavelength as a function of temperature based on just two probe points. However the two effects could be deconvoluted by probing the system with a white light continuum, coupled to our temperature measurement technique. Suitable probe wavelengths could then be found to allow real time monitoring of the temperature of a blood sample based purely on spectroscopic means, a highly desirable goal.

What we can say here however is that the selection of optimum wavelengths for therapeutic vascular lasers, or a comparison of commercial devices for marketing purposes, cannot be accomplished through *a priori* consideration of the *room-temperature* oxy- and deoxy-Hb absorption spectra. Figure 6 for example shows that at 594 nm, a solution of oxy-Hb becomes *almost completely* opaque (T < 2%), implying an effective attenuation coefficient on the order of 400 cm^{-1} for whole blood at high (80 – 100 degrees C) temperature at this wavelength. This corresponds to an order-of-magnitude increase in the system μ_a at 594 nm under the influence of heating, yielding a value close to the maximum found for blood at room temperature (430 cm^{-1} at 577 nm[14]). Verkryusse et al. have also found a large increase in absorption coefficient at 586 nm with respect to temperature in experiments in a different time-domain.[18] The increase in μ_a at this wavelength found by Verkryusse et al. also supports the hypothesis of a substantial red-shift in the absorption spectrum. Red-shift-induced changes on this side of the oxy-Hb absorption spectrum will reduce the effective penetration depth of the laser light into the blood in the vessel, and will increase the effective penetration depth on the 530 nm side of the spectrum. These factors must be taken into account in the selection of a vascular laser wavelength.

4.2 Primary Coagulation Phase

At some time in the 532 nm pump pulse, at a point related to the radiant exposure of 532 nm light and on the sample preparation, the behavior for all the probe wavelengths diverges dramatically. The diffuse 532 nm remittance from a dilution of whole blood (fig. 3) rises sharply and then decays, while the deflected and total 532 nm transmissions show a slight dip

and then resumes its increase. For a solution of oxy-Hb, the 532 nm remittance signal also rises (fig. 4), but the transmissions show divergent behavior, with the deflected transmission rising monotonically and the total transmission signal falling sharply. At 594 nm for a dilution of whole blood, the negative slope in the collimated transmission signal steepens, and then plateaus (fig. 5). The situation at 594 nm for a solution of oxy-Hb in isotonic saline is even more dramatic (fig. 6). (We were unable to record a remittance signal at 594 nm because of lack of laser power in the probe beam, and because there is some contamination from broad-band (white-light) flashlamp emission in the 532 nm pulse, as found by Pfefer et al.[5] Although this light is not sufficiently strong to have any therapeutic effect, it complicates severely the measurement of weak remittance signals at other wavelengths.)

At 633 nm, for a dilution of whole blood, the total transmission decreases sharply and then seems to stabilize (fig. 7). The 633 nm remittance also decreases, but less sharply than the transmission. We have shown elsewhere that the form of the 633 nm transmission signal is similar for both the deflected and undeflected detection modes, indicating that absorption is the primary contributor to the observed attenuation, but that an increase in μ'_s also plays a (secondary) role.[10,11] The total transmission signal at 633 nm for a solution sample shows an even steeper decline at the onset of coagulation, before an eventual plateau (fig. 8). At 1064 nm, the transmission decreases and then stabilizes, akin to the 633 nm measurements, but the remittance (backscatter) rises and then stabilizes towards the end of the 532 drive pulse (fig. 9). Again, we have shown elsewhere that the temporal waveforms of the undeflected and deflected transmission signals at 1064 nm are practically identical, indicating that the primary mechanism involved in the attenuation is absorption.[10,11] Monte Carlo calculations show that for these dilutions and assuming constant absorption coefficients, the reduced scattering coefficient at 1064 nm would have to increase by approximately 15x to cause a significant decrease in the transmitted signal.[17]

It would be simple to state that the rise in 532 nm remittance is due to increased back-scatter from microscopic particles formed through "coagulation", however this is defined. The actual situation is more complicated than this however. The rise in 532 nm remittance is present in:

a) whole blood diluted with isotonic saline (hct = 24.5%)
b) plasma-free suspensions of RBC's,
c) macerated suspensions of plasma-free RBC's (hct ~ 24.5%), and
d) solutions of oxy-hemoglobin.

Based on the above observations, we feel that what we have termed the "primary coagulation" phase is *not* associated with the melting of RBC's and macroscopic coagulation of the plasma and cell membrane proteins. We also feel that the phase transition from biconcave disc to spheroid in the RBC's identified by Nilsson et al.[22] is not a major contributor to the rise in backscatter in this situation. Addressing specifically the 532 nm remittance signal, we believe that this must originate from the denaturation of the actual hemoglobin protein itself (or some other **solvated** component of the red blood cell cytoplasm), and the subsequent formation of microscopic particles which give rise to increased Mie scattering. The work of Tan et al. is particularly interesting in this respect, although the experimental timescales are quite different.[23] They describe seeing the development of small (80 – 1000 Angstrom) features *inside* the RBC cytoplasm following low-level irradiation of blood with a pulsed dye laser. When we probe solution samples at 594 and 633 nm (figures 6 and 8), the forms of the transmission and reflectance waveforms are similar to those obtained from suspensions of intact RBC's, although the absolute magnitudes and slopes differ, in some cases appreciably. We take this as a further indication that in the primary coagulation phase the optical properties of the sample are evolving at the molecular or cell cytoplasm level, rather than on a more extended length scale.

The development of a coagulum in the system will obviously affect the transmission of the various probe beams. The different types of transmission experiments performed (undeflected or collimated transmission, deflected transmission and total transmission) allow us to derive some further conclusions about the time evolution of the system. Figure 3 shows the deflected and total transmissions of a sample of intact RBC's under irradiation at 532 nm. Figure 4 shows the deflected and total transmissions of the 532 nm drive pulse along with the sample remittance for a *solution* of oxy-Hb at approximately equivalent hct. The relative scales of the total and deflected transmission are correct in figure 4. The two samples show quite disparate behavior. In figure 3, we see that for a whole blood dilution, the deflected and total transmission measurements are practically identical in form and magnitude, indicating that in this sample absorption is the dominant mechanism contributing to attenuation. What we believe is happening is that the development of a coagulum increases the effective pathlength of the photons in the sample, giving rise to an increased propensity for absorption and the corresponding dip in the transmission function. The rise in the remittance signal corresponds to the development of microscopic scattering centers, and is precisely synchronous with the drop in transmission.

For the solution sample, the deflected signal rises monotonically following the onset of primary coagulation, whereas the total transmission decreases, initially quite rapidly, before leveling out at the end of the pulse. The evolution of a coagulum in an otherwise clear solution will tend to scatter energy out of the probe beam and into the collection range of the second sphere. The increase in "deflected" transmitted signal reflects this increase in wide-angle scattering. The evolution of the coagulum also increases the effective pathlength in the solution, in turn increasing the probability for photon absorption. So we might expect the total transmission to drop as this increase in pathlength turns on.

All the analysis presented above (in this section) is based on the notion that the sample evolves from one stage to the next in "quantum" steps. However the situation is actually far more complicated. It is quite likely for example that during the primary coagulation phase, the 532/594 nm remittance and deflected transmission signals are being influenced by the underlying red shift of the absorption curve of hemoglobin in uncoagulated areas of the sample. The same will be true for the other probe wavelengths. The thermal model shows that we can expect a "wave" of coagulation to sweep from the front of the cuvette to the back as heat diffuses axially in the sample. Depending on the time from the start of irradiation, the transmitted photons may therefore have traversed a region of coagulating sample and then a region of hot, but uncoagulated sample, and then a region of cool sample. The remitted photons may have traversed these regions twice. Our results therefore necessarily represent a superposition of all the different zones in the cuvette.

There are also other factors affecting the optical properties during the primary coagulation phase. At 633 nm for example, the transmission and remittance signals both decrease at coagulation (fig. 7). In other work we have shown that the undeflected transmission decreases faster than the deflected transmission, indicating that although scattering is increasing during the coagulation phase, the dominant mechanism at 633 nm at this stage is a rapid and substantial increase in the absorption coefficient of the system.[10,11] While it is technically conceivable that this is just an extension of the red-shift of the hemoglobin absorption curve, we have presented evidence that the rapid change is in fact primarily due to the creation of a new chemical species, met-Hb, through some as-yet-undetermined mechanism.[10,11] The absorption data at 1064 nm are also consistent with the generation of met-Hb coupled with an increase in effective pathlength resulting from an increase in μ'_s. It is encouraging to note from figures 10 and 11 that there is no "kink" in the TIR thermal probe signal at the point of coagulation (and when met-Hb is generated). This suggests that increased absorption at this wavelength does not perturb the measurement through attenuated total internal reflection. It also suggests that the coagulation proceeds in a manner that is (to within our experimental error) net thermoneutral, i.e. little or no energy is expended or released at coagulation.

Our hypothesis of met-Hb generation is substantiated by recent work using MRI detection of this highly paramagnetic species.[24] Farahani et al. measured the temperature correlation to the decrease of the longitudinal spin relaxation time T_1 (an observable corresponding to the generation of MRI-active paramagnetic species) and to the increase in absorption of blood samples at 630 nm (indicative of met-Hb generation). They found that a critical temperature of 60 C was required to produce these signatures. Referring to our figure 11, we see that the rise in 532 nm remittance, which we also have correlated to the onset of met-Hb generation[10,11], occurs at an average sample temperature of around 60 – 70 C. The two values, determined by independent methods, are encouragingly similar. The observations of Farahani et al. also suggest an intriguing experiment to determine exactly where a vessel is damaged in vivo when it is struck by a laser pulse. If the laser pulse produces met-Hb, it will generate this species with spatial selectivity only in regions where the critical temperature was exceeded. Time-domain high-field MRI could then be used to get a snap-shot of the vessel, identifying the regions of met-Hb generation, and, by implication the zones of laser-induced focal necrosis. Such knowledge would be invaluable to the refinement of laser parameters for vascular therapies.

Based primarily on the solution phase experiments, we can tentatively say that the short-length scale molecular/cytoplasm coagulation, and any associated chemical changes, are largely complete by the end of the 532 nm pump pulse in those regions of the sample which are over the critical temperature. Our evidence for this is the leveling-out of all the CW probes at the end of the pump pulse in the solution experiments. The different wavelengths are sensitive to different aspects of the changes in the sample. For example the 633 nm probe is most sensitive to the chemical conversion of oxy-Hb to met-Hb. The 1064 nm probe on the other hand is sensitive to the product of increased absorption (through met-Hb generation) and the increased pathlength resulting from scattering. The 594 nm probe is sensitive to the red-shift in the oxy-Hb spectrum, increased scattering, and the generation of met-Hb. The near-extinction of the 594 nm probe beam, and the substantial attenuation of the 633 nm probe yield changes in the system absorption coefficients of a magnitude that cannot be explained through invocation of any one of the three processes we believe to be occurring in the sample.

Finally in this section, we should point out that although the data for the primary coagulation phase can be interpreted in a consistent manner postulating short-range coagulation and the generation of met-Hb, this is probably an incomplete

description. We cannot rule out other processes which could affect the signals but which are happening at a level that is swamped by the other mechanisms. As an example, we cannot rule out thermal dissociation of the oxy-Hb to generate deoxy-Hb at the critical temperature. In isolation, this process would have a clear spectral signature.[10,11] However the absorption coefficients dictate that if we have substantial met- generation and also deoxy- generation occurring together, we are likely to see only the met-Hb channel using our particular combination of probe wavelengths.

III) Secondary Coagulation Phase

A notable aspect of this work is the observation that the optical properties of the whole-blood system continue to evolve even after the drive laser pulse is removed (Figures 5, 7, 9). At all wavelengths where we have CW probe lasers (594, 633 and 1064 nm), both the transmissions and remittances are affected. The general features at the three wavelengths are similar. The transmissions drop, while the remittances increase. The rates of change at 633 and 1064 nm of the two measurables are almost mirror images of one-other (figures 7 and 9), indicating that perhaps the same mechanism is behind the changes in the two. The optical properties in the secondary coagulation phase seem to stabilize approximately 30 – 50 milliseconds after the end of the 10 ms pump pulse. We have followed the signals out to approximately 100 ms, beyond which point convection in the sample starts to perturb the measurements. These "secondary coagulation" features are *not* present when the target is a solution of oxy-hemoglobin, as opposed to a dilution of whole blood (figures 6 and 8). They are present, but quite diminished, if the target is a suspension of erythrocytes which have been repeatedly washed in isotonic saline and then centrifuged to remove the components of the blood plasma.

We infer from the above observations that the secondary phase of coagulation is dominated by the gradual accretion of a macroscopic coagulum composed of the denatured hemoglobin already formed, the cell membranes of ruptured erythrocytes and thermally denatured plasma proteins (fibrin etc.).[5] We believe that the dominant influence on the optical properties comes from the change in μ'_s of the system resulting from the emergence of this macroscopic coagulum. When the time-domain thermal properties of the system are examined, it becomes clear that the heated "disc" of blood remains hot long after the laser pulse terminates.[9] This can be seen in the data of figure 10 also, particularly for the "bottom" surface where the reflectivity continues to rise out to approximately 100 ms. This indicates that the temperature at the interface is rising as a result of heat diffusion from the front (top) surface of the cuvette. It is then perhaps not surprising that the system continues to evolve. The reader is referred to a timely article in the "popular" scientific press for a possible aggregation mechanism.[25]

Finally for this section, we note that the optical properties again represent a superposition state of the system as the "wave" of coagulation sweeps from front to back. The inferences we have drawn are based on the notional "quantizing" of the system, but we believe that the overall picture is qualitatively correct. Verkryusse *et al.* noted the same problem in their analysis of the time-domain optical properties of photocoagulating blood at 586 nm.[18]

Implications for Laser Photocoagulation of Cutaneous Blood Vessels

There are a number of implications for laser therapy of cutaneous blood vessels resulting from the present study. Firstly, it is clear that the efficacy of one wavelength over another cannot be predicted by simple consideration of the "cold" hemoglobin absorption spectra. In the event of a red-shift, absorbances can change dramatically, particularly when using wavelengths on the red side of the oxy-Hb spectrum from say 590 – 600 nm. As a corollary to this, it may be that the optimum wavelengths to ameliorate the effects of the red shift and maintain roughly constant absorption (factoring in the absorption of epidermal melanin) are around 565 nm, in the middle of the "camels-hump" feature.[12] Alternatively it might be considered advantageous to have a wavelength whose penetration depth increases as a function of temperature, so that the energy deposition becomes weighted towards the center of the vessel. In this case, wavelengths from 520 – 540 nm may prove useful.

Secondly, our observations of two distinct time frames for coagulation, namely a "molecular" time frame and a more long-range macroscopic time frame, may have profound implications for the design of vascular therapeutic lasers, specifically the range of delivered pulse widths. The observation that the macroscopic coagulation occurs on a time scale of several tens of ms even in just a 200-micron thickness of blood means that designers must now consider fluid flow in the vessel, and heat diffusion out of the vessel as factors in generating a flow-stopping coagulum. It is possible that the use of temporally shaped pulses, or staggered delivery of multiple pulses will prove to be enhancements to current devices.

We have shown previously that by using two pulses at different wavelengths in combination, vessels may be successfully closed using radiant exposures that would be sub-therapeutic in isolation.[10,11] We have interpreted our results as a sequential

process in which the first (532 nm) pulse causes a chemical change in the blood yielding met-Hb, which in turn makes the blood more opaque to the second (1064 nm) pulse. The technique offers several potential advantages over current single color therapies. The advantages of the two-color, two-pulse technique may be subtler than previously anticipated however. We have not fully explored the optimum delay between the two pulses. It may be that longer delays will be better, as we can take advantage of the scattering properties of the secondary coagulum to increase the effective path-length of the sample for the second pulse. It also seems intuitively correct to try to seal the vessel when the macroscopic coagulum has evolved into something resembling an embolus or thrombus. The ability to delay the second pulse to effect this sealing may prove to be advantageous.

Finally for the two-photon technique, the observation that the critical temperature for met-Hb generation could be as low as 60 degrees C is very encouraging. This temperature rise will clearly require a lower radiant exposure than that needed to generate the 90+ degree intra-luminal temperatures hitherto necessary for vessel closure.[5] Lower radiant exposures will translate immediately to improved safety (lower incidence of epidermal side effects), and a possible extension of the range of Fitzpatrick skin types that may be treated.[26] It will also lead to several advantages in the design of the laser itself.

Accurate Dosimetry

We note that with the 532 nm and 633 nm remittance waveforms, we have two traces that show changes of opposite sign upon coagulation. Specifically, when the 532 nm remittance increases, the 633 nm remittance decreases. This suggests that by monitoring the two wavelengths simultaneously and watching for this divergent behavior, a sensitive real-time probe of the onset of coagulation is possible. Such a device is important for at least two reasons. Firstly, from the point of view of dosimetry, it is desirable that the minimum dose to achieve a therapeutic end-point be delivered.[27] Doing this limits the possibility of collateral damage due to heat diffusion[28] and, for the case of yellow-green wavelengths for vascular lesions, ameliorates complications associated with absorption by epidermal melanin.[26]

Secondly, our two-color, two-pulse photocoagulation technique[10,11] relies on appropriate temporal sequencing of the two pulses. One of the practical keys to the technique will be to optimize the timing of the two laser pulses. A real-time monitor of the onset of the primary coagulation phase could "start the clock" for the second pulse and allow autonomous delivery. This could in turn lead to a reduction in the parameter space to be explored by the physician and therefore potentially a reduced learning curve. One advantage of the technique described above is that the optimum probe wavelength (630 – 640 nm) is convenient in a practical sense (HeNe lasers, semiconductor diode lasers), and while not performing a monitoring role, the red probe laser could be the system aiming beam, and potentially a vessel-finding tool.[29]

5. CONCLUSIONS

We have shown that the time-domain 532 nm remittance waveforms of blood undergoing laser photocoagulation can be decomposed into 3 distinct stages, specifically a heating phase, a phase containing the onset of coagulation and a phase during which we believe that the particle size distribution of the coagulum evolves. The optical properties of the samples show highly complicated behavior resulting from substructure to these phases. Our observations have several important implications for the design of therapeutic vascular lasers. Finally we have shown that monitoring the 532 nm and 633 nm remittance signals from photocoagulating blood has some potential to create a real-time diagnostic for the onset of coagulation, which will in turn allow accurate dosimetry.

6. REFERENCES

1. J. H. C. Inderfurth, R. D. Ferguson, M. B. Frish, and R. Birngruber, "Dynamic reflectometer for control of photocoagulation on the retina", *Lasers Surg. Med.* **15**, pp 54 – 61, 1994.
2. C. H. G. Wright, S. F. Barrett, R. D. Ferguson, H. G. Rylander, and A. J. Welch, "Initial *in vivo* results of a hybrid retinal photocoagulation system", *J. Biomed. Opt.* **5**, pp 56 – 61, 2000.
3. J. W. Pickering, S. A. Prahl, N. van Wieringen, J. F. Beek, H. J. C. M. Sterenborg, and M. J. C. van Gemert, "Double-integrating-sphere system for measuring the optical properties of tissue", *Appl. Opt.* **32**, pp. 399 – 410, 1993.

4. J. W. Valvano and J. Pearce, "Temperature Measurements", *in Optical-Thermal Response of Laser Irradiated Tissue*, eds. A. J. Welch and M. J. C. van Gemert, pp 489 – 534, Plenum Press, New York, 1995.

5. T. J. Pfefer, B. Choi, G. Vargas, K. M. McNally, and A. J. Welch, "Mechanisms of laser induced thermal coagulation of whole blood *in vitro*", *Proc. SPIE* **3590**, pp 20 – 31, 1999.

6. M. Martinelli, M. Gugliotti, and R. J. Horowicz, "Measurement of refractive index change at a liquid-solid interface close to the critical angle", *Appl. Opt.* **39**, pp 2733 – 2736, 2000.

7. D. R. Lide (Editor in chief), *CRC Handbook of Chemistry and Physics*, **8**, pp 77, CRC Press, Boca Raton, 1998-1999.

8. NIST Database #10, NIST STEAM, National Institute of Standards and Technology, US Department of Commerce, 2000.

9. D. Popok and J. F. Black, *in preparation*.

10. J. K. Barton, G. Frangineas, H. Pummer, and J. F. Black, "Cooperative phenomena in two-pulse, two-color laser photocoagulation of cutaneous blood vessels", *submitted to Photochemistry and Photobiology*.

11. J. F. Black, J. K. Barton, G. Frangineas, and H. Pummer, "Cooperative phenomena in two-pulse, two-color laser photocoagulation of cutaneous blood vessels", *Proc. SPIE* **4244**, Paper 4244A-02, 2001.

12. W. G. Zijlstra, A. Buursma and O. W. van Assendelft, *Visible and Near Infrared Absorption Spectra of Human and Animal Haemoglobin*, VSP Publishing, Utrecht, 2000.

13. A. Roggan, M. Friebel, K. Dorschel, A. Hahn and G. Muller, "Optical properties of circulating human blood in the wavelength range 400 – 2500 nm", *J. Biomed. Opt.* **4**, pp. 36 – 46, 1999.

14. M. J. C. van Gemert, A. J. Welch, and A. P. Amin, "Is there an optimal treatment for port wine stains", *Lasers Surg. Med.* **6**, pp. 76 – 83, 1986.

15. T. Halldorsson, "Alteration of optical and thermal properties of blood by Nd:YAG laser irradiation", *Proceedings of the 4th Congress of the International Society for Laser Surgery*, Tokyo, Japan, Nov. 23 – 27, 1981.

16. S. Prahl, Optical absorption spectra of hemoglobin, http://omlc.ogi.edu/spectra/hemoglobin/index.html

17. J. K. Barton and J. F. Black, *unpublished data*.

18. W. Verkryusse, A. M. K. Nilsson, T. E. Milner, J. F. Beek, G. W. Lucassen, and M. J. C. van Gemert, "Optical absorption of blood depends on temperature during a 0.5 ms laser pulse at 586 nm", *Photochem. Photobiol.* **67**, pp. 276 – 281, 1998.

19. L. Cordone, A. Cupane, M. Leone, and E. Vitrano, "Optical absorption spectra of deoxy- and oxyhemoglobin in the temperature range 300 – 20 K", *Biophys. Chem.* **24**, pp 259 – 275, 1986.

20. P. L. San Biagio, E. Vitrano, A. Cupane, F. Madonia, and M. U. Palma, "Temperature induced difference spectra of oxy and deoxy hemoglobin in the near-IR, visible and Soret regions", *Biochem. Biophys. Res. Comm.* **77**, pp 1158 – 1165, 1977.

21. J. M. Steinke and A. P. Shepherd, "Effects of temperature on optical absorbance spectra of oxy-, carboxy- and deoxy-hemoglobin", *Clin. Chem.* **38**, pp 1360 – 1364, 1992.

22. A. M. K. Nilsson, G. W. Lucassen, W. Verkryusse, S. Andersson-Engels, and M. J. C. van Gemert, "Changes in optical properties of human whole blood *in vitro* due to slow heating", *Photochem. Photobiol.* **65**, pp 366 – 373, 1997.

23. O. T. Tan, J. G. Morelli, D. Whitaker, J. Boll, and G. Murphy, "Ultrastructural changes in red blood cells following pulsed irradiation *in vitro*", *J. Invest. Derm.* **92**, pp 100 – 104, 1989.

24. K. Farahani, R. E. Saxton, H-C. Yoon, A. A. F. De Salles, K. L. Black, and R. B. Lufkin, "MRI of thermally denatured blood: Methemoglobin formation and relaxation effects", *Magnetic Resonance Imaging* **17**, pp 1489 – 1494, 1999.

25. T. C. Halsey, "Diffusion-limited aggregation: A model for pattern formation", *Physics Today*, pp 36 – 41, Nov. 2000.

26. E. F. Bernstein, S. Kornbluth, D. B. Brown and J. Black, "Treatment of spider veins using a 10 millisecond pulse-duration frequency-doubled neodymium YAG laser", *Dermatol. Surg.* **25**, pp. 316 – 320, 1999.

27. J. K. Barton, G. Vargas, T. J. Pfefer, and A. J. Welch, "Laser fluence for permanent damage of cutaneous blood vessels", *Photochem. Photobiol.* **70**, pp. 916 – 920, 1999.

28. D. J. Smithies, P. H. Butler, W. A. Day, and E. P. Walker, "The effect of illumination time when treating port wine stains", *Lasers Med. Sci.* **10**, pp 93 – 104, 1995.

29. A. Kienle, L. Lilge, I. A. Vitkin, M. S. Patterson, B. C. Wilson, R. Hibst, and R. Steiner, "Why do veins appear blue: A new look at an old problem", *Appl. Opt.* **35**, pp 1151 – 1160, 1996.

Skin Exposures from 1318 nm Laser Pulses

Thomas E. Johnson[1], B. K. Ketzenberger[1], K.B. Pletcher[1], Steven P. Wild[2], W.P. Roach[1]

[1]Departments of Preventive Medicine and Biometrics
[2]Department of Laboratory Animal Medicine
Uniformed Services University of the Health Sciences
4301 Jones Bridge Road, Bethesda MD, 20814

ABSTRACT

Our work addresses laser tissue interaction for skin exposures from 1318 nm laser pulses. Single pulse data from 0.5 milli-second exposures, along with the mechanisms of photon energy absorption in tissue are investigated. We offer preliminary ED_{50} data and its implication within the realm of laser tissue interaction for discussion. A comparison will be made between the skin reaction of the Yucatan mini-pig (highly pigmented model) and Yorkshire pig (lightly pigmented model). This study represents the first systematic histological investigation of skin reaction to 1318 nm laser pulses.

Keywords: Skin, ED_{50}, 1318 nm, Yucatan pig, Yorkshire pig

INTRODUCTION

The interaction of 1318 nanometer (nm) wavelength lasers with skin to our knowledge has never been systematically investigated. Current laser safety standards[1] for the skin are lower than those for the cornea in this wavelength regime. It is not known if this standard is overly protective or not sufficiently protective. Additionally, it is unknown if increased skin pigmentation has a significant effect on laser injury at this wavelength. Our study seeks to determine the skin ED_{50}, establish if skin pigmentation is a factor in 1318 nm injury by using Yorkshire pigs and Yucatan mini-pigs, and develop models to predict skin damage[2].

MATERIALS AND METHODS

The laser utilized for exposures is a Nd:YAG with an intra-cavity filter suppressing the 1064 nm wavelength resulting in 1318 nm emission. The laser, model ERB-G 1-2-3 was built by Lasersight Technologies of Orlando, Florida. Pulses of 500 microseconds were used for all exposures. The laser is

arranged as detailed in Figure 1. Energy is measured by sampling the 1318 nm photons from the beam

combiner. Approximately 1% of the beam energy is reflected into the energy meter. The energy detector

is a Molectron J25 (S/N 0357I99) connected to a Molectron EPM 2000 (S/N 8785). The pulse duration

is measured from photon reflection from the subject using a germanium photo-detector (Thor Labs

model PDA 255) connected to a Tektronics TDS 644B oscilloscope (S/N B010655). During each

exposure the pulse duration is recorded electronically as a waveform and analyzed. The beam is focused

on the subject using a CVI 100 mm focal length lens with anti reflective coating. A co-linear HeNe

laser (633 nm) is used to locate the exposure site and another HeNe laser (633 nm) to locate the

appropriate focusing site on the subject. Spot size was determined using a knife-edge and Photon IR

camera and software as 0.0239 cm $1/e^2$ diameter at the Rayleigh range of 101 mm from the lens holder.

Rayleigh range was verified by performing multiple knife-edge measurements.
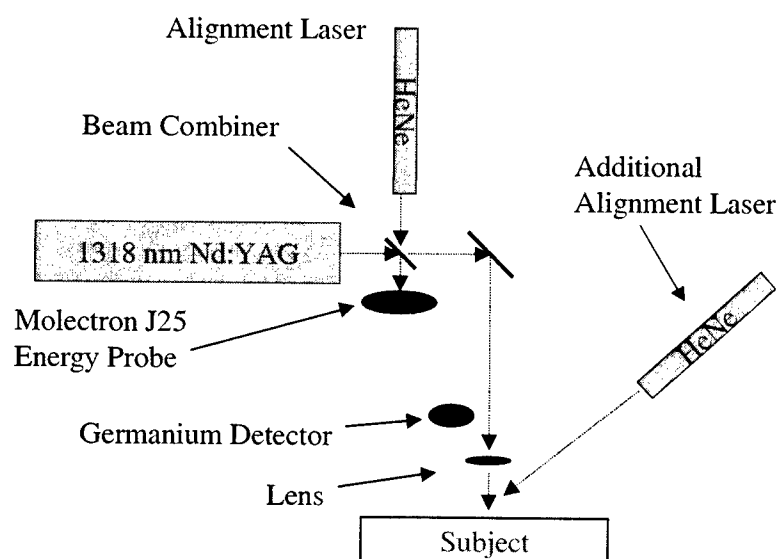
Figure 1, Schematic of Skin Exposure Arrangement

Probit analysis was performed using the methods described by Finney[3]. Complete statistical analysis

has not yet been performed. Two species, Yorkshire pigs and Yucatan mini-pigs, will eventually be

used for this study. Five different animals of each species are estimated to be required to minimize

subject to subject variation, although 95% fiducial limits were obtained when using EZ-Probit (version

1.0, TASC, San Antonio TX) on a single animal. Examination of the data using SAS and SPSS will be

performed upon completion of exposure of a second subject.

A total of 67 locations were exposed on the left flank of a female Yucatan mini-pig weighing

approximately 92 kg (207 lbs). Evaluation of the exposure sites was performed using the techniques

described in Rico et al[3] acutely, one hour and at 24 hours post exposure. Two of the 67 exposure

locations were unreadable at 24 hours. A total of 67 lesions were used for acute and one hour data

analysis. Sixty-five lesions were used for the 24-hour data analysis.

RESULTS

Acute and one hour post exposure analysis showed identical threshold results. Fifteen exposure sites

differed from the acute and one hour results. We noted 15 of the injury sites differed from the acute and

one hour readings. For example, a total of seven locations were not read as injured at 24 hours, but were

recorded as injury sites at acute and one hour end points. Eight locations that had not shown injury

acutely and at one hour were recorded as injuries at 24 hours. The acute and one hour ED_{50}'s were

determined to be 786 J/cm^2 and the 24-hour ED_{50} was found to be 776 J/cm^2. Detailed results are shown

in Table 1.

Table 1, ED$_{50}$ Results

Results[*]	ED50, J/cm^2	Upper Fiducial Limit at 95% confidence, J/cm^2	Lower Fiducial Limit at 95% confidence, J/cm^2
Acute and 1 Hour	786	800	763
24 Hour	776	794	740

[*] Note that results are preliminary, not statistically significant, unverified.

There were 41 injury sites and 26 no-injury sites acutely and at the one hour point, and 42 injury sites and 23 no-injury sites at the 24 hour point. A graph of the acute and 24 hour results is given in figure 2 and 3.
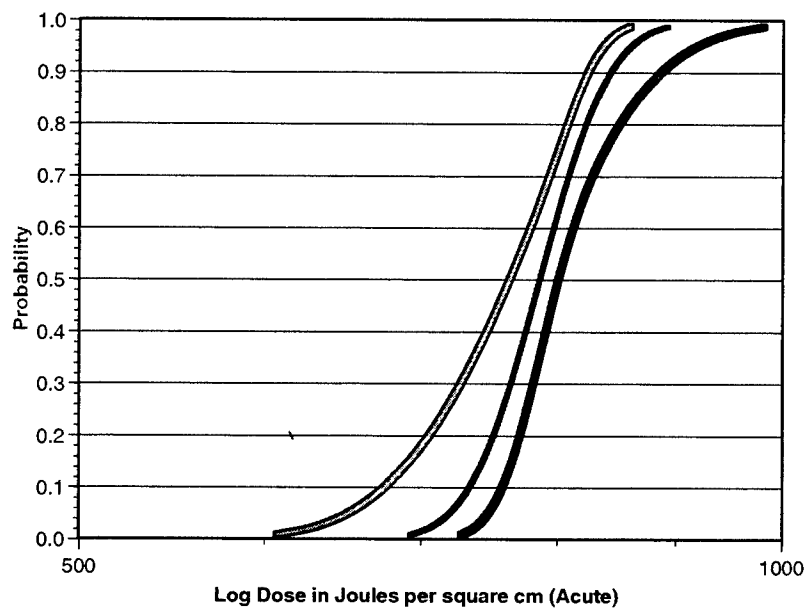

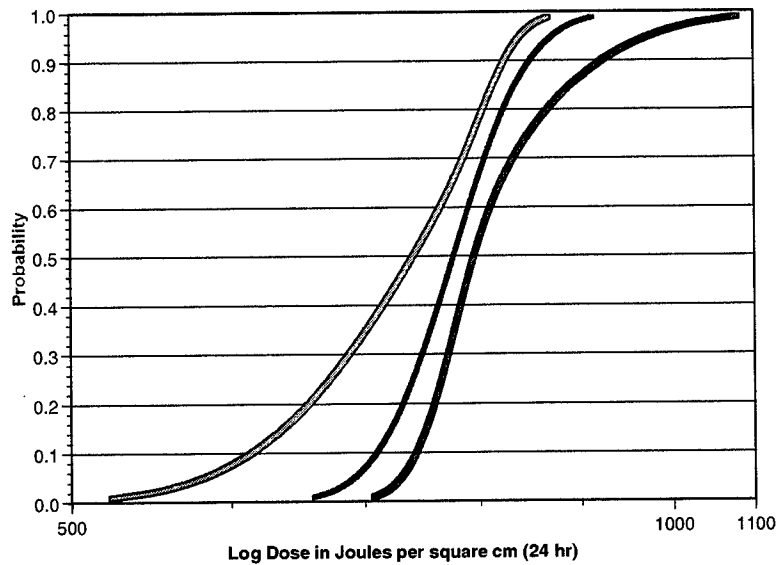Figure 2, Acute and One Hour Probit Curves

Figure 3, 24-Hour Probit Curve

DISCUSSION

Literature was examined for information on ED_{50} levels for skin. Only two studies at wavelengths

adjacent to 1318 nm were found in peer-reviewed literature (See Table 2). No skin studies were found at

1318 nm, but several have been performed on the cornea and retina at this wavelength[4,5,6].

Extrapolation from cornea data to skin is generally not advisable, as the structure and function of each

tissue is different. The layers that comprise the skin are different in composition, thickness, and optical

properties in comparison to the cornea. The assumption that skin requires a lower MPE than the cornea

in the mid-IR regime is not always true[7]. It appears that the use of the cornea to describe skin damage,

or the use of skin to describe corneal damage is not prudent based on the data in table 2.

Table 2, Selected Mid-IR Tissue Studies

Wavelength	Time	ED_{50}, J/cm^2	Spot Size, mm	Model	Target	Author
1318, 1338	5 s	212	1.4	Rhesus monkey	Cornea	Stuck[4]
1318, 1338	0.25 ms	45	0.4	Rhesus monkey	Cornea	Stuck[4]
1318, 1338	0.25 ms	10.67 J (45 J/cm^2)	5.5	Rhesus monkey	Cornea	Lund[5]
1318	CW	1.374 J	1	Dutch Belted	Cornea	Zuchlich[6]
1318	CW	0.56 J	1	Rhesus monkey	Cornea	Zuchlich[6]
1356	CW	0.224 J	0.7	Dutch Belted	Cornea	Zuchlich[6]
1356	CW	0.335 J	0.7	Rhesus monkey	Cornea	Zuchlich[6]
1318	0.5 ms	776	0.24	Yucatan mini-pig	Skin	This work

The absorption coefficient of 1318 nm light in water was calculated based on data from Query (in cm^{-1}) of 1.98 cm^{-1} using a logarithmic interpolation[8]. It is important to note that the absorption coefficient is changing rapidly from 1300 nm = 1.35 cm^{-1} to 1349 nm = 3.77 cm^{-1}. This gives a theoretical 1/e penetration depth of 0.35 cm for 1318 nm in water. Our investigation will examine histologic sections of tissue to determine if skin penetration is in accordance with that predicted by skin absorption, as theorized by some.

Only one Yucatan mini-pig has been exposed to date. Although fiducial limits were obtained, all of the data presented is not statistically significant and should be considered preliminary. The ED_{50}

initially determined here is surprisingly high. At this time we have not been able to perform additional experiments to further explore what seems to be an anomalous result. There are many difficulties associated with this study that are still being resolved and explored. The small spot size necessitated to induce lesions requires careful examination of the skin in order to determine the presence of a lesion. An additional factor that makes lesion identification difficult is the highly pigmented skin of the Yucatan mini-pig. Our preliminary data is not statistically significant, but it appears that unusually high energies may be required at this wavelength to induce lesions. It is difficult to compare the results of this study with other skin studies as water absorption, thought to be the primary absorber in skin, changes rapidly with wavelength in this regime. We consider the information presented here to be very preliminary as only one subject has been exposed thus far, and a complete analysis of these results is not yet complete.

CONCLUSION

This paper presents the first preliminary results of an investigation into skin hazards from 1318 nm laser pulses. As yet, statistically significant results have not been obtained, but an initial estimate of the ED_{50} for Yucatan mini-pigs is made. As this study progresses, a comparison of both Yucatan mini-pig and Yorkshire pig ED_{50}'s will be performed in an effort to elucidate the method of interaction of 1318 nm laser light with tissue. The difference between the ED_{50} of the Yorkshire pig and the Yucatan mini-pig were important at 1540 nm. Based on these results we postulate that the assumption that only water absorbs the 1318 nm laser energy may not be completely correct. Water and another absorbing medium, such as melanin, we theorize to be the primary absorber of energy. Future results will direct the progress of this theory.

ACKNOWLEDGMENTS

REFERENCES

1. American National Standard for Safe Use of Lasers, American National Standards Institute, ANSI Z136.1-2000.

2. The animals involved in this study were procured, maintained and used in accordance with the Animal Welfare Act and the "Guide for the Care and Use of Laboratory Animals" prepared by the Committee on Care and Use of Laboratory Animals of the Institute of Laboratory Animal Resources, National Research Council. The Uniformed Services University of the Health Sciences has been fully accredited by the Association for the Assessment and Accreditation of Laboratory Animal Care, International since 1982.

3. D. J. Finney, *Probit Statistical Analysis*, Cambridge University Press, 1971.

4. B.E. Stuck, D. J. Stuck, E. S. Beatrice, "Ocular effects of laser radiation from 1.06 to 2.06 u," Health Phys. **40** pp. 835-846, 1981.

5. D.J. Lund, M.B. Landers, G.H. Bresnick, J.O. Powell, J.E. Chester, C. Carver, "Ocular Hazards of the Q-switched Erbium Laser" Investigative Opthamology, Volume 9, Number 6, p.463-470, June 1970.

6. J.A. Zuchlich, D.A. Gagliano, F. Cheney, B.E. Stuck, H. Zwick, P. Edsall, D.J. Lund, "Ocular Effects of Penetrating IR Laser Wavelengths," Laser Tissue Interaction VI, Steven L. Jacques, Ed. SPIE, Vol. 2391, pp 112-125, 1995.

7. P.J. Rico, T. E. Johnson, M. A. Mitchell, B. H. Saladino, W. P. Roach, "ED_{50} Determination and Histological Characterization of Porcine (Sus scrofa domestica) Dermal Lesions Produced by 1540 nm Laser Radiation Pulses" Comparative Medicine, December, 2000.

8. Query, M. R., D. M. Wieliuczka, and D. J. Segelstein. 1991. Water (H_2O): handbook of optical constants of solids II. Academic Press, Orlando, FL.

Porcine Dermal Lesions Produced by 1540 nm Laser Radiation Pulses

W. P. Roach and Thomas E. Johnson

Department of Preventive Medicine and Biometrics
Uniformed Services University of the Health Sciences, 4301 Jones Bridge Road,
Bethesda, Maryland 20814

ABSTRACT

Completion of recent studies within our group indicates a breed-based difference in dermal response to 1540 nm 0.8 millisecond laser pulses. Laser exposure to Yucatan Mini-Pigs (highly pigmented skin) and Yorkshire pigs (lightly pigmented skin) demonstrate statistical differences between the ED_{50}'s of the two breeds. Laser delivery is accomplished using an Er:Glass system producing 1540 nm of light at millisecond exposure times and in the range of 5 to 95 J/cm^2. Dermal lesion development was evaluated for acute, 1 hour, and 24-hour post exposure presentation. Our data contradicts the theory that water absorption is the sole mechanism of dermal tissue damage observed from 1540 nm laser exposures, as skin chromophores appear to play a role in lesion development.

Keywords: exposure, laser, skin, pigs, Yorkshire, Yucatan, 1540 nm, "eye-safe

1. INTRODUCTION

This research effort was aimed at studying the effects of 1540 nanometer (nm) laser tissue interaction. Two in-vivo porcine skin models, Yorkshire Pig and Yucatan Minipig, were considered. During the study the median effective dose (ED_{50}) for 1540 nm laser exposures was determined, along with the suitability of each model to be used in the future for correlation of laser exposure to humans. Histological characterization of injured and non-injurious samples from each pig model was considered.

Interest in this work has centered upon providing the biological database for determining the Maximum Permissible Exposure limits for 1540 nm exposure to humans. Our research focuses on the region of 1000 to 2000 nm owing to the increased use and development of lasers operating in these regions both in the military and in the communications industry.

Previous findings have suggested the presence of a different mechanism of laser-tissue skin injury in the two breeds examined.[1] We have shown conclusively that a photo-thermal mechanism appears to induce the skin lesions in the Yorkshire pig. However, a photo-thermal and photochemical mechanism appears to be involved in laser induced lesion formation in the Yucatan Mini-Pig. We believe this will change the overall view of a water-mediated injury mechanism theory for near infrared exposure in skin and especially that of 1540 nm.

2. MATERIALS AND METHODS

2.1 Exposure procedure, sample collection and preparation

As previously indicated by Rico et al.[1], six female Yorkshire pigs and seven female Yucatan Mini-Pigs were used in this study. The age of the animals ranged from 5 to 9 months in both breeds and their weight varied from 25 to 60 kilo-grams (kg). The Uniformed Services University of the Health Sciences' Animal Care and Use Committee approved all procedures performed.[2]

Prior to laser exposure and biopsy collection, all solid food was withheld for 24 hours. Pigs were pre-anesthetized with Tiletamine/Zolazepam IM and general anesthesia was induced and maintained with Propofol in accordance with approved animal use protocol.[3] Animals were kept warm throughout the experimental procedure by using a surgical table with a thermal support system. Buprenorphine was given for analgesia prior to anesthesia recovery after laser exposure and biopsy procedures.

Laser beam delivery was accomplished using an Er:Glass system producing 1540 nm of light with a 0.8 millisecond exposure times, with a variable range of energy densities from 7 to 90 J/cm^2. The complete laser system set up is depicted in Figure 1.

The workings of this particular set up are described in detail elsewhere.[4] The plane of laser exposure is located about 20.4 cm away from the focusing lens for an elliptical exposure area of 0.003 cm^2 for the Yorkshire pigs and Yucatan Mini-Pigs.
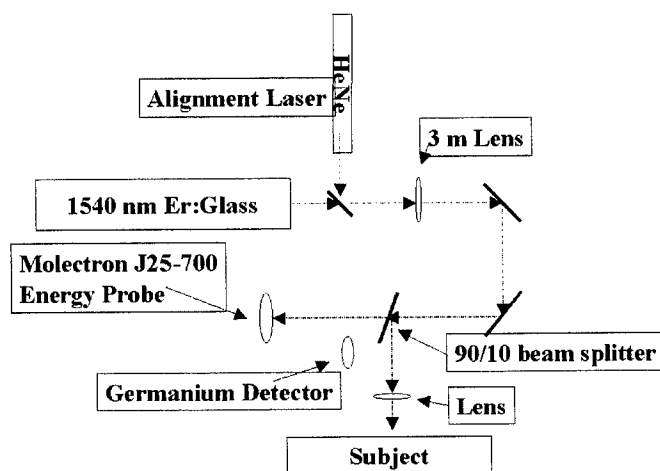
Figure 1: Simple schematic of current laser set up for 1540 nm delivery to *in vivo* skin models.

Skin exposures were delivered by single laser pulse to the flank of each animal. An area of approximately 2.5 cm^2 bound each exposure site. Square boundaries were clearly marked with black ink for easy identification. Areas exposed with given energy density for Yorkshire pigs and for Yucatan Mini-Pigs were examined acute, 1 hour and 24 hours post exposure. Three independent evaluations were performed for each exposure site for the presence or absence of a laser induced skin lesions. All samples were fixed in 10% formalin, blocked in paraffin, cut to 5 micrometers (μm), stained with hematoxylin and eosin (H&E), and mounted for histological evaluation.

2.2 Sample evaluation

24 hr lesions were evaluated using SAS Probit analysis to an ED_{50}, estimated dose of 50% injury, at 95% fiducial limits.[5] H&E stained slides were evaluated to determine epidermal lesion extent and type of tissue and cellular damage produced.

Special stains were used to further characterize the tissue damage at the basal and dermal layers. Histologic evaluation findings of skin biopsies collected at 24 hr post exposure were used to correlate observations between microscopic to gross lesions. Rico et al. have described the process of sample evaluation in detail.[1,4]

3. RESULTS

At this time quantitative data to compare and contrast the laser induced skin lesions from the different pig breeds is not yet complete, although there are some qualitative observations that can be reported. In our study the greatest readily apparent differences between the two breeds are the acute appearance of erythematous skin lesions after laser exposures in the Yucatan Mini-Pigs and the delayed formation of erythematous skin lesions in Yorkshire pigs. Yucatan Mini-Pigs required increased energy densities (J/cm^2), therefore a higher ED_{50}, to induce a lesion as compared to Yorkshire pigs. Histologic observation of lesions revealed that injury developed at or near the basal layer of the epidermis, causing underlying dermal tissue damage in each breed of pig. Histologic results are outlined in detail by Rico et al.[1,4] We note that laser exposure affects the tissues of the dermal layer near the stratum basale of the epidermis by producing coagulative necrosis in both animal models.

The ED_{50} determination of each breed of pig conducted at the 24-hour endpoint. Probit analysis was accomplished using SAS[5]. Resulting Probit curves are shown in Figure 2 and Figure 3. The ED_{50} at 95% Fiducial Limits are computed at the $1/e^2$ area and given in Table 1.
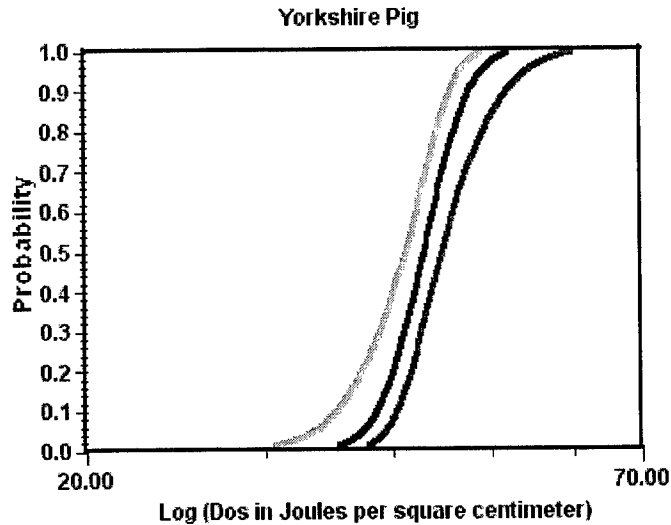
Yorkshire Pig

Figure 2: Probit Analysis for Yorkshire pigskin exposure to 1540 nm single laser pulses.
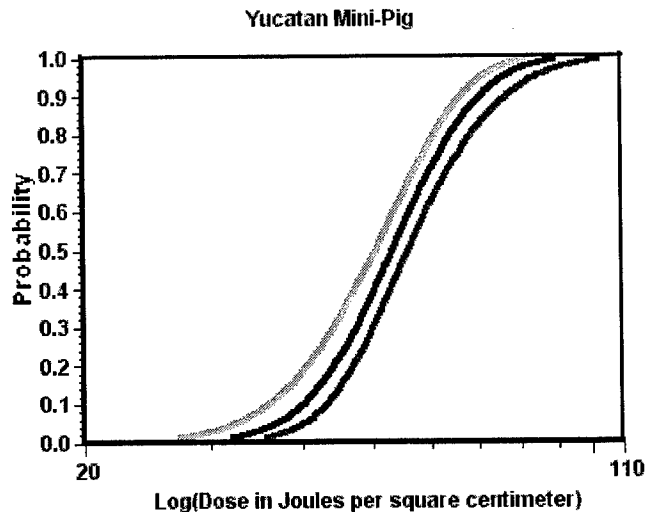
Yucatan Mini-Pig

Figure 3: Probit Analysis for Yucatan Mini-Pig skin exposure to 1540 nm single laser pulses.

Table 1. Summary of Probit analysis of 1540 nm exposures at 24 hr

Subject	No. of Subjects	No. of Data	Lower FL (J/cm^2)	ED_{50} (J/cm^2)	Upper FL (J/cm^2)
Yorkshire	6	180	41.3*	43.1*	44.8*
Yucatan	7	242	50.7*	53.5*	56.2*

* Values are calculated at the $1/e^2$ incident average beam area of 0.003 cm^2 for the Yorkshire pigs and 0.003 cm^2 for the Yucatan Mini-Pigs.

4. DISCUSSION

The method of laser tissue interaction for 1540 nm wavelength laser induced skin lesions are still under investigation. There is a statistically significant difference at the

95% fiducial limits between the ED_{50} values found between the two breeds. As seen in Table 1. above, the lower 95% fiducial limit (50.7 J/cm^2) for the Yucatan Mini-Pig does not encompass the upper 95% fiducial limit (44.8 J/cm^2) for the Yorkshire pig. Also, the narrow range of response centered about the ED_{50} for the two models demonstrates the highly predictable nature of skin injury upon exposure to 1540 nm laser light.

The results indicate two major differences in lesion formation after 1540 nm laser exposure in these two animal models. First, laser lesion formation was seen more readily at the acute end point of examination in the Yorkshire pigs when compared with the Yucatan Mini-Pigs. Second, the ED_{50} value found in the Yucatan Mini-Pig indicates a higher dose than that found for the Yorkshire pig.

5. CONCLUSIONS

Current theory[8, 9] places water absorption with a raise in temperature as the sole mechanism for dermal tissue damage using this exposure duration and 1540 nm light. Our data supports the theory that water absorption is not the sole mechanism of dermal tissue damage observed from 1540 nm laser exposures. Skin melanin appears to play a significant role in lesion development. It may be that melanin acts, as it does for UV exposure in skin, as a protective aid for 1540 nm laser exposure.

ACKNOWLEDGMENTS

REFERENCES

1. P.J. Rico, T.E. Johnson, M.A. Mitchell, B.H. Saladino, and W.P. Roach,"ED_{50} Determination and Histological Characterization of Porcine (Sus scrofa domestica) Dermal Lesions Produced by 1540 nm Laser Radiation Pulses", Comparative Medicine, November 2000, in press.

2. The animals involved in this study were procured, maintained and used in accordance with the Animal Welfare Act and the "Guide for the Care and Use of Laboratory Animals" prepared by the Committee on Care and Use of Laboratory Animals of the Institute of Laboratory Animal Resources, National Research Council. The Uniformed Services University of the Health Sciences has been fully accredited by the Association for the Assessment and Accreditation of Laboratory Animal Care, International since 1982.

3. W.P. Roach, T.E. Johnson, T.A. Eggleston, and M. Mitchell, "Risk Assessment of the "Eye Safe Laser" Wavelength for Cornea and Skin (Rabbits, Pigs)" Animal Use Protocol, G387HQ, April 1996.

4. P.J. Rico, M.A. Mitchell, T.E. Johnson, and W. P. Roach "ED_{50} determination and histologic characterization of porcine dermal lesions produced by 1540 nm laser radiation pulses", Proceedings of SPIE, Vol. 3907-E-56, (2000).

5. D. J. Finney, *Probit Statistical Analysis*, Cambridge University Press, 1971.

6. The statistical analysis software was provided by SAS/STAT Probit Procedure, SAS Institute, Cary, NC 27513, 1994.

7. T.A. Eggleston, W.P. Roach, M. Mitchell, and T.E. Johnson, "Comparison of *In Vivo* Skin Models for Near Infrared Laser Exposure", Comparative Medicine, #J-99-106, August 2000.

8. ANSI, *American National Safety Standard for Safe Use of Lasers (ANSI Z136.1-2000)*, Laser Institute of America, Inc., Orlando, 2000.

9. A. V. Lukashev, S. E. Sverchkov, V. P. Solovyev, B. I. Denker, V. V. Engovatov, and P. P. Pashinin, "Investigation of laser damage on skin by 1540 nm Er-glass laser," *Final Report*, General Physics Institute, Russian Academy of Sciences, 1995.

Combined Interstitial Laser Therapy for Cancer Using Microwave Radiometric Sensor and RODEO MRI Feedback
Part 1. Microwave Radiometry

Vladimir P. Zharov[a], Sergey G. Vesnin[b], Steven E. Harms[c], James Y. Suen[d], Alexander V. Vaisblat[b], N.Tikhomirova[b]

[a]Philips Classic Laser Laboratory, University of Arkansas for Medical Sciences (UAMS), Little Rock, [b]RES, Ltd, Moscow, [c]Arkansas Cancer Research Center, [d]Department of Otolaryngology of UAMS.

ABSTRACT

The concept of complex laser treatment of localized cancer is recently suggested with the focus on optimization, increasing efficiency and selectivity of Interstitial Laser Therapy (ILT) with interactive imaging and temperature feedback. This treatment is based upon a combination of ILT, photoacoustic (PA) and photodynamic therapy (PDT) with microwave radiometric remote control of the temperature in the treated zone. The features of this concept for primary breast and head and neck cancer are: 1) the application of microwave thermometry for non-invasive real-time overheating control during ILP; 2) direct intralesional injection of a photosensitizer and dye enhancer through a tiny needle, followed by PA and ultrasonic impregnation and partly cancer cells damage; 3) combination ILT and PDT therapies; 4) post-operative PDT of the tumor by positioning LED arrays around breast; 5) using RODEO MRI for control of location of the tumor, needle and fiber and to monitor tissue changes during complex laser treatment. This paper focuses more on development of microwave radiometry temperature control. The previous experiments are presented concerning the study of remote microwave radiometric sensor for diagnostic purpose including the results of the clinical trials that have been conducted among over 1000 patients.

Key words: Laser, microwave, temperature control, breast cancer, diagnostic.

1. INTRODUCTION

Presently the earlier detection and treatment of breast cancer is one of the most important problems. In many countries this disease is the main course of women death. Specialists believe that early detection of breast cancer by the clinical method is later biologically. So it is expedient to use screening in conjunction with other non-invasive investigative methods.

One of the promising modality for breast treatment is Interstitial Laser Therapy (ILT) .But it is has still some problems: no real –time temperature control during ILT; high temperature gradient around fiber tip; creating a nonuniform thermal lesion; potential complications after possible overheating and charring like burning, infections, inflammations; tumor spread from water vaporization; residual disease from inadequate ILT.

Recently we developed of new approach of combined laser interstitial laser therapy with microwave radiometric sensor and RODEO MRI feedback with following features: design of a microwave thermometry-based laser temperature control system utilizing modified existing technology; comparison of the data provided by the microwave thermometry and MRI to obtain comprehensive information about temperature and changing properties of tissue during thermal treatment; design magnetic susceptibility coating for visualization of fiber on MRI; development of breast tumor treatment that combines interstitial photothermal and photodynamic therapies in order to reduce the temperature needed for thermal destruction of tumor; a study of the role of laser-induced photoacoustic and ultrasound waves in tumor cell damage; use of laser-acoustic techniques to enhance the diffusion of photosensitizing and photoabsorbing agents ;post-operative, non-invasive phototreatment of the breast by positioning Light Emitting Diode (LED) arrays around the breast to photoactivate the immune system and to complete the photodynamic destruction of residual cancer cells.

This paper focuses more on development of microwave radiomery temperature control. Microwave radiometry [1-10] is based on measuring the intensity of natural electromagnetic radiation from a patient's tissue. This intensity is proportional to the temperature of tissue. The change in temperature (thermal abnormality), that is a basis of the earlier detection of breast cancer, may be caused by increased cancer cell metabolism. It should be noted that thermal changes precede to the anatomical changes that can be detected by traditional methods such as ultrasonography, mammography and palpation. Thus microwave radiometry is a very promising method for the breast cancer detection at an earlier stage.

The one of the first work discussing the use of microwave radiometry for the breast cancer detection was published in 1977 [1]. This subject was further also discussed in the literature [2-13]. At the same time the method has not been used widely in medicine practice. In 1997 RES, Ltd. developed the RTM-01-RES microwave computer-based radiometer which is using now for temperature control during ILT . The system includes a microwave sensor to invasively measure the temperature of internal tissue and a non-contact infrared sensor to the measure skin temperature. This paper focuses on previous clinical trials of RTM-01-RES held in 4 oncological centers on 1000 patients, and showed, that the sensitivity of RTM-01-RES in detection of breast cancer is 90%, specificity 76-81%.

2. FEATURES of MICROWAVE RADIOMETRY

Microwave radiometry allows to measure natural electromagnetic radiation from a patient's internal tissue at microwave frequencies. The intensity of the radiation is proportional to the temperature of tissue. So we can say that microwave radiometry allows to measure internal temperature of tissue and display it on the monitor of the computer. The main difference between well known infrared thermography and microwave radiometry is that the former allows to read and display skin temperature, when the latter indicates internal temperature. Microwave radiometry measures natural electromagnetic radiation from the patient's tissue, it is absolutely harmless and safe both to the patients and to the medical personnel. So the method can be used successfully for screening for the monitoring treatment.

The specific heat generation in the tumor is proportional to the grow rate of the tumor. So fast growing tumors are "hotter" and they are more contrast in thermograms [2]. Thus microwave radiometry is an unique method that allows to detect first of all fast growing tumors. Using microwave radiometry (RTM-Diagnosis) in conjunction with other tradition methods allows to select patients with fast growing tumors.

The important feature of microwave radiometry is that it can distinguish proliferative mastopathy and fibroadenoma from non-proliferative mastopathy and fibroadenoma. So the method can select patients who risk to have breast cancer.

The device is a modulated null-radiometer with a slipping circuit for compensating reflection between the biological object and the antenna. The used wavelength is 26 cm. The functional scheme is illustrated in Fig. 1.
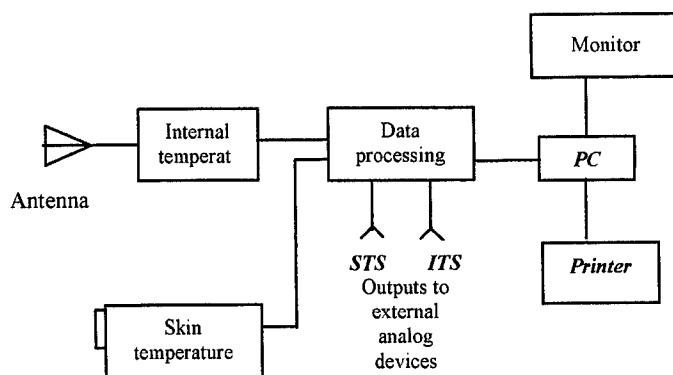

Fig.1 Functional scheme of RTM-01-RES

When the temperature is measured, the antenna contacts the patient's skin at the projection of the examined organ. The antenna receives microwave radiation from the examined organ as noise at microwave frequencies and the signal is amplified in ITS (internal temperature sensor). The signal amplified in ITS is transmitted to the DPU (data processing unit), where it is processed.

The voltage from the skin temperature sensor (STS) is transmitted to the DPU too. The skin temperature sensor is non-contact infrared frequencies receiver. The modes are switched by the buttons located on the front cover of the data

processing unit. The internal and skin temperature values are displayed on the 3-digit temperature indicator as degrees Celsius with discreteness of 0.1.Data processing unit produces serial digital signals for interfacing with PC.

The internal temperature is measured by contacting the antenna with a patient's skin at the point of the investigated organ or its part projection.

Noise signal power at microwave frequencies received by the antenna is

$$P = \varepsilon K T B, \qquad (1)$$

where K- the Boltzmann constant; T – averaged internal tissue temperature (Kelvins); B – microwave frequency band of the receiver (Hz); ε – emittance. When frequency band B is 100 MHz (10^8Hz) and the tissue temperature is 310K, this power is 4×10^{-13} W. The power is proportionate to a body temperature, so it can be measured in degrees, if other conditions are constant.

There is a switch behind the antenna. It is switched from close to open position 1000 times per second. When the switch is closed the signal transfers through circulator branches (path) to the device radiometry region. When the switch is open heated resistor noise transmit to circular leg. This noise is reflected from the switch and transmitted from circulator legs *to* the radiometer input. Signals are amplified and their power (temperature) values corresponding to close and open switch positions are compared. Voltage that is proportional to the temperature differential between tissue and heated resistor heats the resistor until these temperatures are equal. Thus instead of measuring the internal temperature we measure the temperature of the heated resistor, so that the device is simplified.

The schematically described procedure compensates reflection form skin surface. Noise power of a bioobject with temperature T_p achieves the border between the bioobject surface and the antenna, then the antenna receives it reduced by 1-r (r-coefficient reflection) according to Kirchov's low*. Some noise T_p x r is reflected and absorbed in the bioobject. Noise with the temperature T_p as mentioned above achieves the border from the receiver input. Some noise with temperature T_p (1 - r) is absorbed in bioobject, and the rest of noise is reflected with the temperature T_p x r. The sum of signal temperatures in the antenna input is T_p. So the reflection at the border is compensated even if the temperature of bioobject are different.
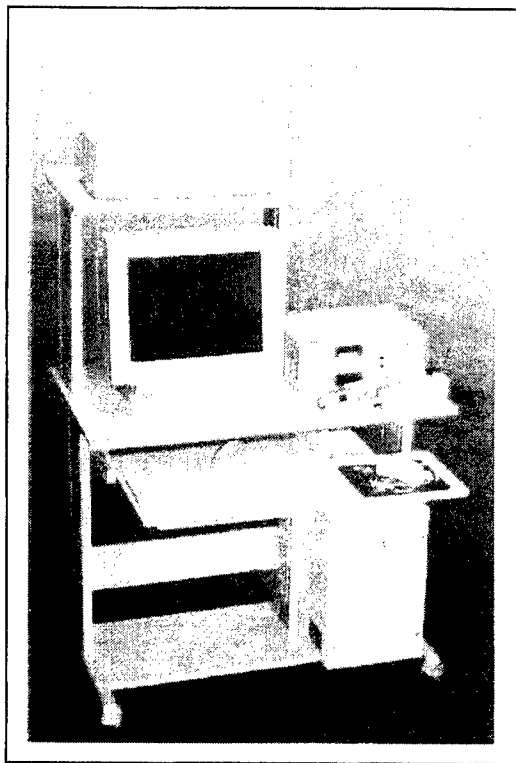
Fig. 2. RTM-01-RES
computer based
microwave radiometer

The skin temperature is measured by a noncontact method. The skin temperature sensor consists of an optical system that forms a surveyed surface shield, a mechanism that breaks ray flow from the compared body heated to the temperature T_1 and a radiometric part.
A spot diameter on a patient's skin under study depends on the distance between the antenna and skin.

When the distance is ten centimeters the diameter is 1.5 cm. When the distance is one centimeter the spot diameter is about 0.5 cm. These distances are set with help of special facilities.
The skin temperature and compared body temperature are compared with help of the mechanical breaker that operates 24 times in a second. The results of measurement are transmitted as direct voltage to the switch and then to analog-digital converter (ADC).
External view of RTM-01-RES is showed in fig 2. The system includes a microwave sensor to invasively measure the temperature of internal tissue and a non-contact infrared sensor to the measure skin temperature. Information about the skin temperature allows to obtain more reliable results. RTM-01-RES has no organs of regulation and control. The device does not require calibration. Instrument tests on long and continuous operation have shown that RTM-01-RES radiometer keep not only differential but also an absolute accuracy measurement of the internal tissues temperature.

The main device specifications are the following:

Table 1

Items	Specifications
Thermal abnormality (i.e. a lower or higher temperature) is detected at a depth of, cm	3 -7 (depending on water content tissue type)
Accuracy of measuring the averaged internal temperature, when a temperature is 32 - 38 °C, °C	± 0,2
Time required for measuring internal temperature at a point, seconds	10
Antenna diameter, mm	39
Accuracy of measuring the skin temperature, °C	± 0,2
Time required for measuring skin temperature at a point, when the temperature is 32 - 38 °C, seconds	1
Device mass, kg	4
Power consumption, Watt	20

In some works [9-10] discussing microwave radiometry temperature data are displayed as a diagram, when the names of the measured points go along the horizontal axis and the internal temperature values are along the vertical axis. This method allows to analyze temperature differentials between corresponding points on the left and right breasts. However it is difficult to analyze the temperature at various locations on one entire breast by this method. Therefore temperature data are also displayed as a temperature field, which is used in infrared thermography In the temperature field each temperature value is displayed by its own color on the monitor (Fig.3).
In the temperature field cold areas of the breast are displayed by "cold" colors (i.e. blue) and hot ones are reflected by "warm" colors (red and pink).Imaging thermal data as a internal temperature field show temperature abnormalities, that, in particularly, correspond to location of cancer. The presented on Fig. 3A data just s example image for healthy person without significant asymmetry between left and right breast. The Fig.3B shows a significant asymmetry due with local cancer when nipple heat of right and left are compared. The thermal differential is about 1 C. Analysis of great number of such termograms has showed that different cancer types have different temperature image features.
Note that for medical personnel it is easier to analyze temperature data displayed as a thermogram or a temperature field than numerical values of the measured temperature.
The feature of RTM-01-RES is an expert computer system for the breast cancer detection. The expert system analyzes several parameters, including thermal asymmetry, dispersion of the temperature within the breast, etc.
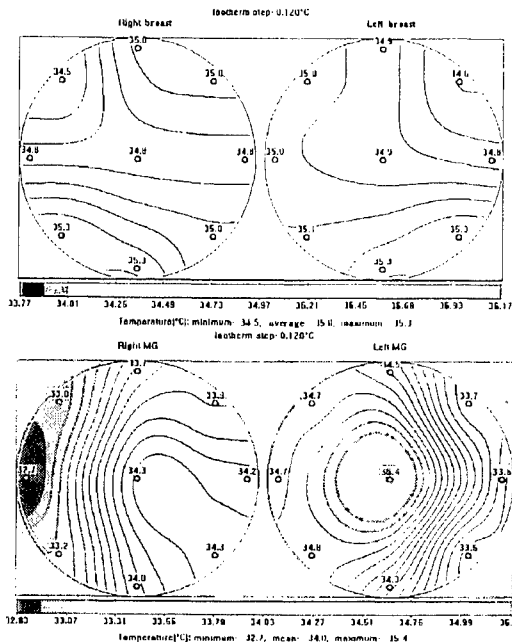
Fig. 3A Thermogram of a normal healthy patient.

Fig. 3B Thermogram with breast bnormalatiesa.

3. CLINICAL TRIALS OF MICROWAVE THERMOMETRY

The clinical trials were held under the direction of leader Russian specialists at four Moscow medical centers. They are the following: The Branch #1 of the Mammology Health Center; The Municipal Hospital #40;The Russian Oncological Institute under the Science Center of the Russian Academy of Medicine Sciences; The Oncology Health Center of the Moscow Committee of Health.

The purpose of the clinical trials was to estimate the ability of the RTM-01-RES system to detect breast cancer and monitor the treatment of benign tumors. At the Oncology Health Center of the Moscow Committee of Health specialists estimated ability of RTM-01-RES to select risk patients. The risk patients are patient that should be undergo complex diagnosis. RTM-diagnosis was carried out independently from clinical, X-ray and other examinations. The results of RTM-diagnosis were compared with results reported by histology. They were blind clinical trials (a doctor did not know results reported by other methods). The results of the clinical trials are displayed in Fig. 4.
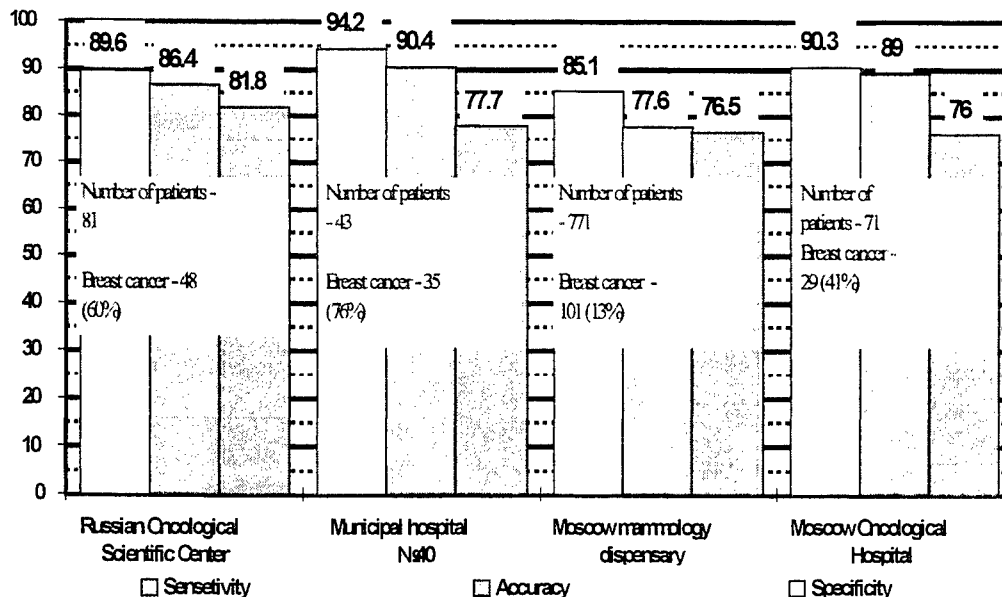

Fig. 4 The result of clinical trials of microwave radiometer (diagnostic of breast cancer).

The Fig. 4 shows that all data are coordinated. The sensitivity of the method is 85-94%, the specificity is 76-81%, and the accuracy is 77-90%. These results are comparable with results of mammography.

The investigation has also shown that RTM-Diagnosis can distinguish mastopathy and fibroadenoma with proliferation from mastopathy and fibroadenoma without proliferation. Therefore it can select patients who may get cancer under unfavorable conditions. These patients should have an complex examination in specialised health centers. The results are represented in Table 2.

Table 2

Disease	Number of examined patients	Ultrasound	Mammography	RTM-Diagnosis
Mastopathy and fibroadenoma with proliferation	11	2 – cancer 4- mastopathy 5- fibroadenoma	4 – cancer 6 – mastopathy 1- fibroadenoma	9- Thermogram shows RTM-features of risk group 2-There are no RTM-features of risk group
Mastopathy and fibroadenoma without proliferation	18	12- mastopathy 4- fibroadenoma 2 – not performed	14 – mastopathy 2 – fibroadenoma 1 – cancer 1 – not performed	3 – Thermogram shows RTM-features of risk group 15–There are no RTM-features of risk group

The table 2 shows that RTM-Diagnosis distinguish mastopathy and fibroadenoma with proliferation from mastopathy and fibroadenoma without proliferation enough well. Thus one of the advantages of RTM-Diagnosis is to select patients with fibroadenoma and mastopathy with proliferation. Other diagnostic techniques can not do this as they detect anatomical changes in the breast. RTM-Diagnosis provides a doctor with information on active processes in the breast.

4. RESUME

The clinical trials and experience of using RTM-01-RES at the leader oncological centers have shown that microwave radiometry is an effective method for the earlier breast cancer detection. As it is harmless, it allows to select patients with abnormal thermograms at an earlier stage. These patients should undergo the complex breast examination. The sensitivity for the method is comparable with the sensitivity for mammography and ultrasound. The method is very promising to be used for diagnosing young women, as mammography is not effective for this group. Also microwave radiometry is useful for monitoring the treatment of benign diseases. . It will be important to compare data obtaining by microwave and MRI technique.
Mammology is not a single area where microwave radiometry can be used. The system can be also used in urology for diagnostics prostate cancer , gynecology, for diagnosis of thyroid diseases and very promising for temperature control during different therapies including ILT. Right now spatial resolution is not so high to measure spatial temperature distribution and system allow just to control average temperature at functional diagnostics. The possible improvements are concluded in development of multi-frequency and multi-channel schemes to provide possibility to measure of spatial temperature distribution with good spatial resolution.

LITERATURE

1. A.Barrett, P.C.Myers, N.L.Sadowsky. Detection of breast cancer by microwave radiometry. Radio Sci., 12, №68, pp. 167-171,1977

2. K.L Carr. Microwave Radiometry: Its Importance to the Detection of Cancer. IEEE MTT, 37 № 12 ,pp1862-1869, 1989.

3. V.M.Poliakov, A.S.Shmalenuk. Microwave thermography and perspectives of its development. Microwave Electronics, 8, №1640, 1991.

4. K.M.Ludeke, B.Schick, J.Kohler. Method and argument for measuring the physical temperature of object of microwaves. United States Patent, 4 235 107, Int. Cl.3 G01J5/52, 1980.

5. Y.Leroy. Microwave radiometry and thermography: Present and prospective in Biomedical Thermography. New York: Alan R. Liss, pp.485-499, 1982.

6. P.C.Myers, N.L.Sadowsky, A.H.Barret. Microwave thermography: principles, methods and clinical applications. J. Microwave Power, 14, № 2, pp.105-113, 1979.

7. A.Mamouni, P.H.Gelin, Y.Leroy. Modelling of radiometric signals for medical applications. Proc. 18-th Europ. Microwave Conf.: Stockholm-88, pp. 832-637, 1988

8. E.A.Cheever, K.R. Foster. Microwave radiometry in living tissue: what does it measure? IEEE Trans Biomed Eng, Jun, pp. 563-568,1982

9. V.S. Troitskiy. To theory of contact radiometric measurements of internal temperature in body. High Education Institutes' News, Radio physics seria, 24, №9, p. 1054,1981.

10. Book of reports from the all-union conference "Methodical issues of detecting temperature of biological objects with radio-physic methods" (Zvenigorod - 84), 1985

11. A V.Vaisblat. Medical radiometer. Patent of the Russia Federation №2082118 with priority on 11 Jule 1994.

12. L. M.Burdina, A.V.Vaisblat, S.G.Vesnin, M.A.Konkin, A.V.Lashchenkov, N.G.Naumkina, N.N.Tihomirova. Detection of breast cancer with microwave radiometry. Mammology, №2, pp. 3-12, 1998.

13. L. M.Burdina, A.V.Vaisblat, S.G.Vesnin, N.N.Tihomirova. Possibility to diagnose breast cancer by measuring natural electromagnetic radiation from tissues (radiometry). Mammology, №2, pp. 17-22,1997.

Optical imaging of Hsp70 gene expression following thermal laser injury

Josh T. Beckham, Jennifer A. Baran, Agnella D. Izzo, E.Duco Jansen

Department of Biomedical Engineering
Vanderbilt University, Nashville, TN 37235, USA

ABSTRACT

In the past the effects of laser irradiation upon tissue have been assessed based on structural and macroscopic characteristics such as temperature, pressure and tissue mass removal. However, the effects of laser irradiation on a cellular level are not well understood and it is postulated that cellular injury caused by laser treatment may affect the efficacy of the laser procedure [1]. In this research we have used an alternative method of detecting injury by targeting the heat shock protein (Hsp70). A stable cell line was generated containing the luciferase reporter gene attached to the heat shock protein (Hsp70). After thermal injury luciferase is produced in tandem with the heat shock protein to emit bioluminescence at 563 nm. The luminescence was quantified with a photon counting ICCD camera system. The heat shock to bring about Hsp70 transcription was created by immersing the cells in a water bath or by irradiating the cells with a Holmium:YAG pulsed laser (λ= 2.1 μm, τ_p = 250 μs). For the laser experiments, radiant exposures varied from 5 to 30 mJ/mm^2 and the number of pulses varied at 15,25, and 35. The peak expression of luciferase was found to be 3 to 4 hours post heat shock for lower exposures but increases to between 6 and 9 hours if higher radiant energies are used. An experiment was also done to assess to what extent the celluar response to heat followed the Arrhenius rate process.

Keywords: bioluminescence, luciferase, heat shock protein, hsp70, laser, tissue

1. INTRODUCTION

Assessment of effects of laser radiation on biological tissue has traditionally been limited to macroscopic effects and histopathological endpoint analysis. The irradiation parameters (wavelength, spot diameter) and treatment parameters (pulse duration and radiant exposure) are important factors in determining the outcome of the laser procedure. In the past, these parameters have been chosen with limited insight into the injury that may occur on a cellular level. A better understanding of the cellular mechanisms, pathways activated, and effects involved will further facilitate the selection of laser parameters which may significantly enhance the treatment provided by laser irradiation by reducing undesirable side effects and by potentially provinding new pathways for therapeutic intervention[1].

Use of the luciferase reporter gene coupled the heat shock protein (Hsp70) offers two distinct advantages. First, the cellular effects pertaining to the heat shock protein can be examined. Secondly, the cells do not have to be sacrificed since the bioluminescence can be detected externally. Therefore, there is the opportunity to track the response of the cells over time as they continue to live.

A mammalian heat shock 70 promoter – luciferase reporter (hsp70-luc) system was utilized in this study to determine the transcriptional regulation of the stress inducible heat shock protein 70. In response to stress, cells synthesize *heat shock proteins*, which function as molecular chaperones, offering protection to the cell in repairing existing damage and preventing further damage. A firefly luciferase reporter gene, *Photinus pyralis*, was inserted downstream of the heat shock promoter in the DNA of the cells and provided a means to assay promoter activity. The luciferase reporter gene is expressed upon activation of the promoter (i.e., by utilizing an external stimulus), and emits light at a wavelength of 563 nm (the yellow-green region of the spectrum). The observed changes in reporter gene activity can be used to infer the amount of cellular stress caused by the laser irradiation and can be correlated with various laser irradiation protocols.

Bioluminescence is a unique reaction in which light is produced through a chemical reaction. The origin of this light emission differs from fluorescent and phosphorescent emissions due to the fact that a chemical reaction, rather than the absorption of light, supplies its excitation energy. The luciferase enzyme found in the common North American firefly,
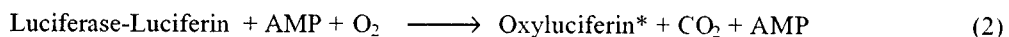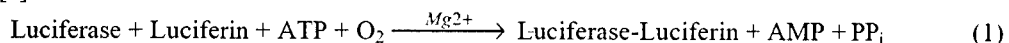
Photinus pyralis, catalyzes the oxidation reaction of the substrate luciferin in the presence of ATP, Mg^{2+}, and molecular oxygen [2].

$$\text{Luciferase} + \text{Luciferin} + \text{ATP} + O_2 \xrightarrow{Mg2+} \text{Luciferase-Luciferin} + \text{AMP} + PP_i \qquad (1)$$

$$\text{Luciferase-Luciferin} + \text{AMP} + O_2 \longrightarrow \text{Oxyluciferin*} + CO_2 + \text{AMP} \qquad (2)$$

$$\text{Oxyluciferin*} \longrightarrow \text{Oxyluciferin} + h\nu \qquad (3)$$

In this reaction, the oxidation of luciferin forms oxyluciferin in its electronically excited state [3]. Oxyluciferin returns to the ground state while emitting light of wavelength 563 nm. For each molecule of luciferin oxidized, a single photon is emitted [4]. The quantum yield of this bioluminescent reaction is 0.88, which is the highest known efficiency of any chemiluminescent reaction [2]. Kinetic studies of the luciferase reaction *in vitro* indicate a peak-intensity reached within seconds following the addition of luciferin. In the presence of excess luciferin, the light emitted is proportional to the concentration of luciferase protein [5].

2. MATERIALS AND METHODS

Cell Culture Conditions

A mouse NIH-3T3 cell line (epithelial cell line, American Tissue Culture Collection, Manassas, VA) was used in this study. Two DNA plasmids were transfected; pGL3Basic-Hsp70a1luc and a pcDNA3.1(+) vector. The pGL3Basic-Hsp70a1luc consisted of a mouse hsp70 promoter with a firefly luciferase gene inserted upstream. The pcDNA3.1(+) vector was a used as a selection marker to generate a stable cell line (i.e., a permanent cell line that has incorporated both plasmids into the cell's genome). This vector contained a neomycin resistance gene, which provided antibiotic resistance to cells cultured in DMEM supplemented with 1mg/ml Geneticin (G418, GIBCO BRL, Gaithersburg, MD). Cells were cultured and heat shocked in Dulbeccos Modified Eagle Medium (DMEM, GIBCO BRL, Gaithersburg, MD) supplemented with 10% Fetal Bovine Serum (FBS, GIBCO BRL, Gaithersburg, MD).

Water Bath Heat Shock Experiments

The cells were plated in 6-well (i.d. = 35 mm) and 96-well (i.d. = 6 mm) tissue culture plates (Costar, Fischer Scientific, Sewanee, GA) with 4×10^5 cells per well in 2 ml culture medium and 4×10^4 cells per well in 200 µl culture medium respectively. The cells were returned to the 37 °C CO_2 incubator for an overnight incubation. Upon confluence, the tissue culture plates were sealed with parafilm and placed in a 43 °C water bath for 15, 30, or 45 minutes.

Arrhenius Water Bath Experiments

Experiments were done using the water bath to assess the heat shock protein's response in relation to the Arrhenius damage integral. The equation for the integral is shown:

$$\Omega = A \int e^{\frac{-E}{RT}} dt$$

The Ω is the tissue damage, A is the frequency factor - i.e. damage rate(1/sec), E is the activation energy, R is the gas constant and the integral is over the time of the heat application. The Arrhenius relationship predicts that for a four degree increase in temperature the exposure time should be reduced by one order of magnitude in order to achieve the same amount of damage. If the time and temperature conditions change in accordance with these parameters, then the damage to the cells should be the same. Consequently, the luciferase response is expected to be consistent for each sample in this experiment. The cells in six well plates were heat shocked at different time/temperature combinations along the theoretical Arrhenius damage curve and Hsp expression was measured by means of an ICCD camera.

Laser Irradiation Experiments

Cells in 96-well tissue culture plates were placed in a modified 37 °C Lab Line incubator (VWR, West Chester, PA), which allowed laser delivery to individual wells through an optical fiber. A pulsed Holmium:YAG laser (λ= 2.1 µm, τ_p = 250 µs, Schwartz Electro Optics 1-2-3, Orlando, FL) was used in all experiments and was coupled into a 600 µm optical fiber

(NA = 0.39). The distal end of the fiber was placed under each well, such that the spotsize was equal to the diameter of the well (6.4 mm), allowing the laser to irradiate the entire bottom of the well. Figure 1 illustrates the laser experimental set-up.

Media

Cells

Beam

Fiber
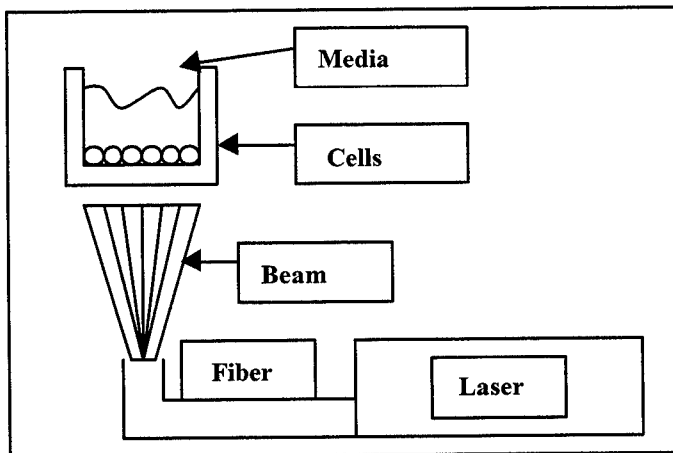
Laser

Figure 1. Schematic of laser experiment setup using the Ho:YAG laser.

Calculations for determining the radiant exposure necessary to achieve a temperature of 43 °C in a single pulse in the bottom of a well (outer diameter =6.4 mm) of a 96-well tissue culture plate were done. This temperature was chosen because it has been shown that a 5-6 °C elevation above optimal growth temperature of 37 °C causes significant induction of the heat shock response in water bath heat shock experiments [6]. The radiant exposure required to initiate a temperature rise of 6 °C in the bottom of the well (i.e. $T_{initial}$ = 37 °C and T_{final} = 43 °C) in a single laser pulse was determined to be 12 mJ/mm^2 (391 mJ) for a spot size of 6.4 mm. The calculations accounted for absorption and reflection losses at the bottom of the well.

In the experiments, radiant exposure, total number of pulses delivered, and the repetition rate of the laser were varied. Since 12 mJ/mm^2 was required to initiate a 6 °C temperature rise in the bottom of the well, radiant exposures between 5 and 30 mJ/mm^2 (150-950 mJ) per pulse were evaluated. The number of pulses delivered to each well was varied from 15, 25, and 35 total pulses.

Temperature Measurements During Ho: YAG Irradiation

In a single laser pulse, the temperature-time response is a sharp peak consisting of a rapid heating phase with a rise time equal to the pulse duration (τ_p), followed by a relaxation phase determined by the thermal diffusion time ($\tau_{thermal}$). As successive laser pulses are delivered, the temperature-time response will consist of numerous heating and relaxation phases in series, with each successive laser pulse beginning at a higher initial temperature than the one before, as shown in Figure 2 The peak temperature rise in a single pulse at the bottom of the well of a 96-well can be calculated when the radiant exposure is known. Additionally, the average temperature rise ($\Delta T_{avg\ rise}$) in the irradiated volume for multiple laser pulses can be calculated when the radiant exposure for a single pulse is given and the volume of the culture medium is known. Each well in the plate is surrounded by air and thus can be considered as a fairly well isolated system. The average temperature rise for consecutive laser pulses is determined by multiplying the average temperature rise for a single laser pulse by the total number of pulses delivered [7].

Temp

Time

Figure 2. Schematic of profile of temperature rise within each laser irradiated well.
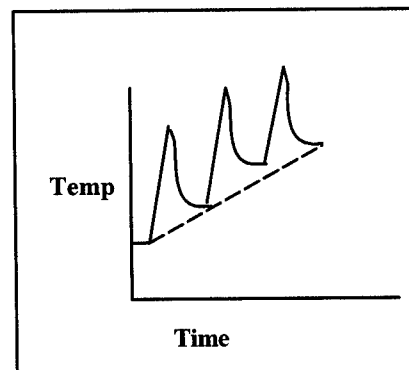
The temperature rise during Ho:YAG irradiation was measured in a single well of a 96-well plate. A mini hypodermic thermocouple probe (Chromega/Alomeaga, teflon insulation, diameter 254 μm, Omega Engineering Inc, Stamford, CT) was placed on the side of the well slightly above the bottom. The thermocouple was attached to a data acquisition card (DAQcard A1-16E4) and a LAB VIEW program was used to record temperature-time measurements. For the temperature measurement, laser parameters similar to cell exposure experiments were varied and measurements were recorded and the sampling rate was 50 Hz.

The thermal diffusion time ($\tau_{thermal} = \delta^2/4\alpha$), where δ = penetration depth and α = thermal diffusivity (mm^2/s), for the culture medium was determined to be 185 ms. This calculation assumed properties of water for the culture medium and a penetration depth of 300 μm for the Ho:YAG laser at room temperature. Given a pulse duration of 250 μs for the Ho:YAG laser, thermal diffusion can not take place during the laser pulse itself. However, significant heat diffusion takes place between pulses since there is a 500 ms interval. However, even though diffusion is significant from the directly irradiated part of the culture well to cooler areas, the well by itself , which is made up of polystyrene and is surrounded by air, is a well insulated system.

Figure 3. Stable transfected cells (Hsp70-Luc) exposed to Holmium:YAG laser radiation. Repetition rate 2Hz, 35 pulses, 6 mm diameter spotsize, pulse energy: 155 - 615 mJ, radiant exposure 5.48 - 21.7 mJ/mm^2. Imaged 3 hours post laser exposure. Note that the top row is not expressing luciferase despite receiving the highest radiant exposure. A viability assay showed that this radiant exposure for 35 pulses lead to cell death.
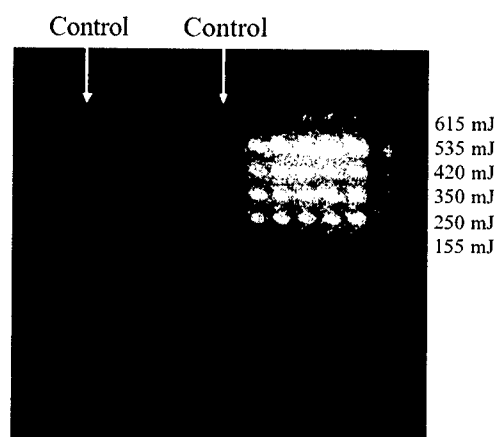
Luciferase Imaging

Following heat shock, the substrate needed for the enzymatic reaction of luciferase, firefly potassium salt – i.e. Luciferin (4,5-Dihydro-2-[6-hydroxy-2-benzothiazolyl]-4-thiazolecarboxylic acid potassium salt ($C_{11}H_7N_2O_3S_2K$), Biosynth AG, Switzerland), was added in excess to the culture medium at a concentration of 15 μg per ml of media. Luciferase activity was measured at various time points following heat shock using an intensified photon counting camera system (Hamamatsu Photonics Systems, Bridgewater, NJ). Photon counting images were taken for an integration time of three minutes. For every time point new luciferase was added. The light intensity of each well in the 96-well plate was determined quantitatively and used as a measure of hsp70 expression following exposure to varying experimental parameters. A typical image generated by the Argus 50 is shown in Figure 3.
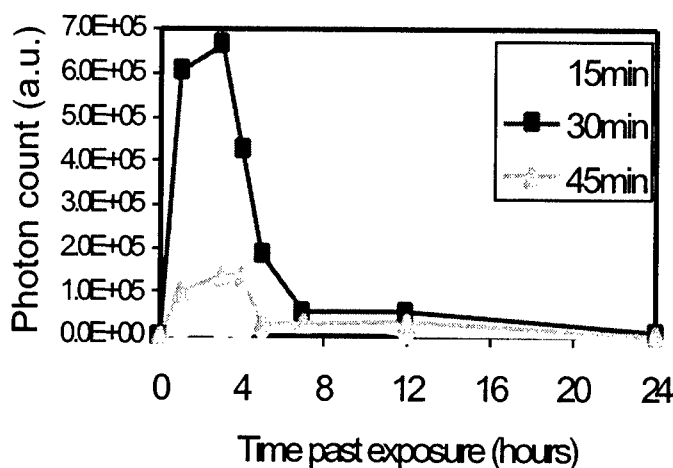
Figure 4. Hsp70 response of 3T3 cells after water bath heat shock at 43 degrees for 15, 30, and 45 minutes. Imaged through ICCD camera.

3. RESULTS

Water Bath Experiments

1. Response of Cells Following Water Bath Heat Shock

Figure 4 illustrates stable cells heat shocked in the water bath for 15, 30 and 45-minutes in 6-well plates. Peak expressions for the 30-minute heat shock occurred 3 hours after heat shock. The 45-minute heat shock had peak expression at 4 hours after heat shock. The relative peak intensity for the 30-minute heat shock was found to be 5 fold greater than the peak intensity for the 45-minute heat shock. The 15-minute heat shock in a 6-well plate had minimal luciferase activity.

2. Arrhenius Response

The hsp70 response of the cells to the Arrhenius experiment is shown in Figure 5 for the following parameters.

Temp (C)	Time (min)
37	N/A
41	102.52
43	30.00
44	16.98
45	9.39
46	5.22
47	3.00

Table 1. Time and temperature settings for Arrhenius water bath heat shock

Figure 5. Hsp70 response of 3T3 cells after Arrhenius heat shock in water bath

Arrhenius Hsp70 Water Bath Expression
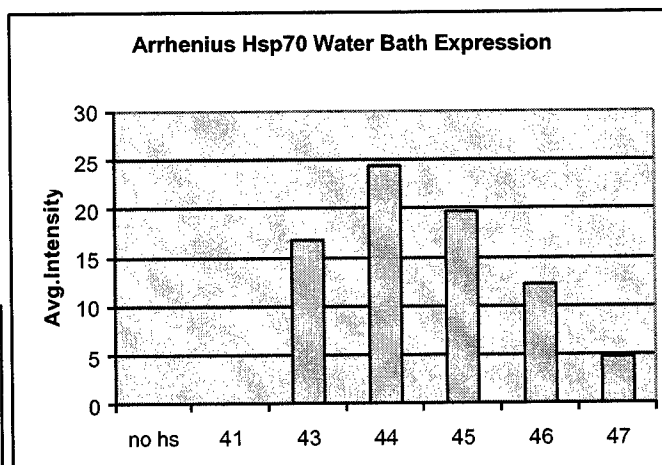
Holmium:YAG Laser Experiments

1. Temperature Measurements

The effect upon temperature of increasing the radiant exposure was evaluated by varying the radiant exposure from 5 to 30 mJ/mm^2 (spot size = 6.4 mm, 150 - 950 mJ) per pulse for a constant total number of pulses at a repetition rate of 2 Hz. These radiant exposures corresponded with an average temperature rise ($\Delta T_{avg\ rise}$) in the irradiated volume between 3.1 to 19.6 °C for 25 pulses delivered. The calculated and measured maximum temperature rises for a set number of pulses, were approximately equal at low radiant exposures, 5 mJ/mm^2, and began to deviate as the radiant exposure was increased, with the measured temperature being less than the calculated.

To examine the effect upon temperature from increasing the number of pulses, the same increasing radiant exposure experiment was done for 35 pulses. However, the radiant exposure was not increased above 20 mJ/mm^2 (650 mJ) because above this exposure cell death occurred. The maximum $\Delta T_{avg\ rise}$ for 35 pulses delivered was higher for each radiant exposure and ranged from 4.3 to 18.2 °C.
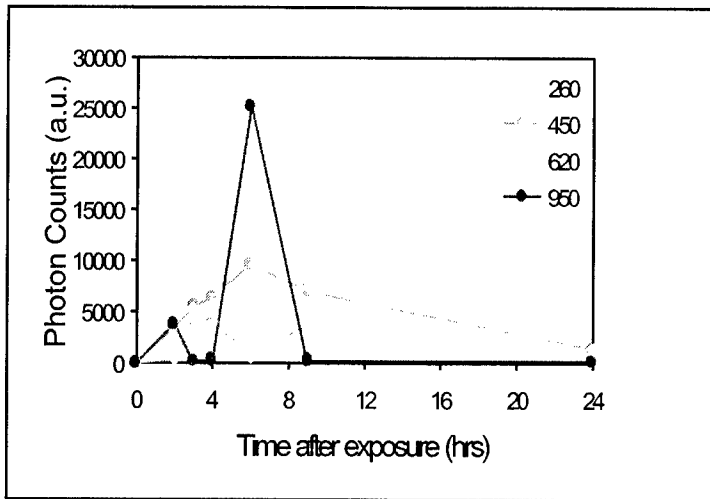
2. Hsp70 Expression

As the radiant exposure was increased at a constant repetition rate, there was a corresponding increase in the intensity of luciferase activity measured from the ICCD camera until a maximum radiant exposure was reached. For the 25 and 35 total pulses delivered, expression of hsp70 reached a maximum at 17 mJ/mm^2 (550 mJ) and 11 mJ/mm^2 (350 mJ) respectively, and steadily declined thereafter for increased radiant exposures. Also, for each radiant exposure an increase in the number of pulses resulted in an increase in the hsp expression.

Peak expression of luciferase activity at 11 mJ/mm^2 (350 mJ) for 35 pulses corresponded with a maximum measured temperature rise of 8.9 °C ± 1.0. This was a little lower than the calculated value of 10.1 °C. For 25 pulses, the temperature rise achieved at maximum luciferase expression, with a radiant exposure of 17 mJ/mm^2 (550 mJ), was 10.4 °C ± 0.9. The calculated value was also higher in this case at 11.3 °C.

In comparison to cells irradiated in a 96-well plate (200 µl of medium), cells irradiated under identical laser parameters but in a 6-well plate (2 ml of medium) showed significantly less hsp70 expression.

3. Time Course of hsp70 Expression Following Ho: YAG Laser Irradiation

Figure 6. Hsp70 time course response of 3T3 cells after laser heat shock at 2,3,4,6,9, and 24 hours. 25 pulses at 2Hz. Radiant energy of 260 mJ - 950 mJ

Hsp70 expression was measured at various time points following Ho:YAG laser irradiation. Figure 6 illustrates hsp70 expression at 2, 3, 4, 6, 9, and 24 hours following irradiation at radiant exposures of 8, 14, 19, and 30 mJ/mm^2 (spot size = 6.4 mm, 260, 450, 620, and 950 mJ), with 25 pulses delivered at a repetition rate of 2 Hz. The radiant exposures corresponded with an average temperature rise ($\Delta T_{avg\,rise}$) for 25 pulses delivered of 5.2, 9.3, 13.0, 19.6 °C. Maximum hsp70 expression for a radiant exposure of 8 mJ/mm^2 occurred at 4 hours . The peaks of hsp70 expression for radiant exposures of 14, 19, and 30 mJ/mm^2 occurred 6 hours following laser exposure. A radiant exposure of 30 mJ/mm^2 (950 mJ) produced the most response with a two fold increase in hsp 70 expression when compared to other radiant exposures.

To test the effect of increasing the number of pulses on the time course of hsp70 expression, an experiment was also performed for 35 pulses delivered at 2 Hz. Hsp70 expression was observed at 2, 3, 4, 6, 9, and 24 hours after irradiation for radiant exposures of 8, 14, and 20 mJ/mm^2 (spot size = 6.4 mm, 250, 460, and 640 mJ). The radiant exposures corresponded with an average temperature rise ($\Delta T_{avg\,rise}$) for 35 pulses delivered of 7.2, 13.0, 18.2 °C. For 35 total pulses at a 2 Hz repetition rate, maximum hsp70 expression occurred at 4 hours following laser irradiation for 8 mJ/mm^2, and 9 hours for 14 mJ/mm^2 (460 mJ) and 20 mJ/mm^2 (640 mJ).

4. DISCUSSION

Kinetic Analysis of hsp70 Induction Following Heat Shock

Kinetic analysis of hsp70 following a 43 °C water bath heat shock revealed a delay in peak expression of hsp70 as the duration of the heat shock was increased. This may indicate that an increase in thermal stress results in a delay in the activation of mechanisms that facilitate repair of the cell. However, the 15-minute heat shock in a 6-well plate was not consistent with this trend. The luciferase activity for this time exposure was comparable to control plate (i.e., background) levels. This may indicate that a 15-minute heat shock is below the threshold for inducing the hsp70 promoter.

Arrhenius Experiments

The cells' response to equivalent heat damages with varying temperature and times in accordance to the Arrhenius damage model was not consistent to the uniform response that would be expected. This discrepancy is evident in the samples where the temperature was low. These temperatures were below the critical temperature for the hsp70 response to be initiated. Consequently, there was weaker hsp expression. The luciferase expression values tend to drop off as the temperature increased and exposure time decreased. It is possible that at these parameters, cells are dying off and no longer

producing hsp70. Additionally, we compared expression at a fixed time point (3 hours post heatshock). From our water bath and our laser experiments, it is however apparent that more severe levels of heat shock delay the time of peak expression. Hence the measurement at 3 hours may not be representative for true maximum hsp70 expression under all conditions. Further analysis of cell survival at these temperatures is needed in order to properly examine the cells' Arrhenius response.

Kinetic Analysis of hsp70 Following Ho:YAG Laser Irradiation

A kinetic analysis of cells following Ho:YAG laser irradiation demonstrated a delay in maximum hsp70 expression at higher radiant exposures. The kinetic results following laser irradiation were similar to the kinetic response of hsp70 following water bath heat shock. At higher radiant exposures, the cells' experienced higher maximum temperatures. As a result, a delay in maximum hsp70 occurred. This response may be an indication that an increase in thermal stress caused a delay in the activation of the hsp70 response to initiate repair of the cell. A delay in maximum hsp70 expression was also seen when the number of pulses was increased.

Also, when the number of pulses was raised, a reduction in the radiant exposure value at which peak hsp70 expression occurred was observed. This shift was due to the longer time at which the cells were subject to elevated temperatures due to the additional pulses. Thereby, a greater amount of heat damage could be achieved at lower radiant exposures when there was more time for irradiation.

In addition, cells that were irradiated in a 96-well plate experienced significantly more heating of the overall culture media than cells exposed in a 6-well plate with ten times the amount of media (i.e. the average temperature of the well was significantly higher due to the smaller thermal mass in the smaller wells. However, the peak temperatures that the cells are subjected to remain the same between the 6 well and 96 well since the surface irradiation per square millimeter is the same. Thus, this data suggests that the cells' response to an increase in radiant exposure (peak temperature) was less significant than the response to increase in overall temperature of the well for a longer period of time.

Since the laser irradiation was performed from underneath the cell culture plate, thus through the bottom of the plate, a concern was direct heating of the cells by virtue of laser absorption in the plastic of the well bottom. This could provide additional heating of the cells since they are growing right on the bottom of the culture plate. Potentially this could affect our results in particular since the thermal conductivity of the plastic is relatively small (k for polystyrene = 0.03 W/m K). The thickness of the well plate was measured to be 1.15 mm and the absorption coefficient was determined to be 0.29 mm^{-1} which is approximately one order of magnitude less than the absorption coefficient of water for the Ho:YAG wavelength (3 mm^{-1}). The net result is that 28% of the incident energy is absorbed in the plastic of the bottom of the well while the remaining 72% is transmitted and absorbed in the cells and culture media. Mainly due to the 10-fold difference in absorption coefficient between the cells and media versus the plastic of the well bottom, the contribution of this direct heating of the well plate to the hsp70 pattern is assumed to be minimal.

The Effect of Increasing the Radiant Exposure and the Total Number of Pulses

An increase in the radiant exposure revealed a corresponding increase in the expression of hsp70 . This response was in agreement with literature, in which following exposure to stress, there is a dramatic increase in synthesis of hsp70 to ensure cell survival [8]. Hsp70 reached maximum expression at a *critical radiant exposure*, which was found to depend on the total number of pulses delivered. (This term is defined as the radiant exposure under specific laser conditions, which caused maximum expression of hsp70 to occur). The critical radiant exposure corresponded with 17 mJ/mm^2 at 2 Hz-25 pulses, and 11 mJ/mm^2 for 3 Hz-35 pulses. At radiant exposure above the critical radiant exposure, there was a decrease in the levels of hsp70.

As the radiant exposure and total number of pulses was increased, there was a corresponding rise in the maximum temperature and the duration of time above physiological temperature. As the thermal stress was increased, the cells responded by an increase in the synthesis of hsp70 until the critical radiant exposure was reached. Above the critical radiant exposure the severity of the thermal stress may have become too great for the cells. The decrease in the expression of hsp70 may be an indication of the deactivation of biochemical pathways, including important repair mechanisms, which ultimately lead to cell death.

5. CONCLUSIONS

The hsp-luciferase cell line provided a unique way to assess hsp70 gene expression through noninvasive monitoring of luciferase expression. It was shown that there exists a threshold temperature below which the heat shock protein is not expressed. Above this threshold, the response to increasing exposure to elevated temperatures rises until a critical level where stress-induced damage can not be repaired and lethal cellular injury may be present, including apoptosis and necrosis [9]. For low irradiations, the peak expression of hsp was about four hours. When higher radiant exposures were used,

though, the expression was delayed beyond four hours. It appears from this research that the cellular heat shock response is more dependent on the time of exposure than the actual peak temperatures obtained. However, it was also seen that either the cells or the hsp expression mechanism does not strictly follow an Arrhenius relationship to the heat damage. A more comprehensive study needs to be done that includes a live/dead assay to assess survivability of the cells so the heat shock response can be normalized to the number of cells alive.

ACKNOWLEDGMENTS

REFERENCES

1. Welch, A., et al., Laser thermal ablation. Photochemistry and Photobiology, 1991. 53(6): p. 815-823.

2. Gould, S. and S. Subramani, Firefly luciferase as a tool in molecular and cell biology. Analytical Biochemistry, 1988. 175: p. 5-13.

3. Hastings, J., Chemistries and colors of bioluminescent reactions: a review. Gene, 1996. 173: p. 5-11.

4. Nguyen, V., M. Morange, and O. Bensaude, Firefly Luciferase Luminescence Assays Using Scintillation Counters for Quantitation in Transfected Mammalian Cells. Analytical Biochemistry, 1988. 171: p. 404-408.

5. Brasier, A., J. Tate, and J. Habener, Optimized use of the firefly luciferase assay as a reporter gene in mammalian cell lines. BioTechniques, 1989. 7(1116-1122).

6. Mizuno, S., et al., Stress dose-dependent suppression of heat shock protein gene expression by inhibting protein synthesis during heat shock treatment. Cell structure and function, 1997. 22: p. 7-13.

7. van Gemert, M., J.C. and A.J. Welch, Approximate solutions for heat conduction: time constants, in Optical-Thermal Response of Laser-Irradiated Tissue, A.J. Welch and M. van Gemert, J.C., Editors. 1995, Plenum Press: New York. p. 411-443.

8. Baler, R., W.J. Welch, and R. Voellmy, Heat shock gene regulation by nascent polypeptides and denatured proteins: hsp70 as a potential autoregulatory factor. Journal of Cell Biology, 1992. 117(6): p. 1151-1159.

9. James, M., Monitoring of holmium: YAG laser induced heat shock protein 70 expression using the bioluminescent luciferase reporter gene, in Biomedical Engineering. 1998, Vanderbilt University: Nashville. p. 50.

Cavitation-induced drug delivery in tumors for cancer chemotherapy: Phantom studies

Irina Larina[1], Christian Bartels[1], Kirill Larin[1,2], Rinat Esenaliev[1,2]*

[1]Center for Biomedical Engineering, [2]Department of Physiology and Biophysics,
University of Texas Medical Branch in Galveston, TX 77555

ABSTRACT

One of the major problems of cancer chemotherapy is slow diffusion of anti-cancer drugs in the interstitium and their poor penetration from blood through tumor capillary wall and cancer cell membrane. To enhance delivery of the drugs in cancer cells we proposed to use interaction of exogenous microparticles with laser or ultrasonic radiation. This interaction results in cavitation near the particles upon certain irradiation conditions. Our previous pilot studies demonstrated feasibility of enhanced delivery of model and real anti-cancer drugs in tissues in vitro and in vivo if laser pulsed or ultrasonic radiation is applied. In this work we performed studies in tissue phantoms in order to find optimal parameters that can be used for safe and efficient delivery of anti-cancer drugs in tumors. Water solutions and gelatin were used as tissue phantoms with well-controlled parameters. Cavitation in the phantoms was studied by using optical and ultrasound techniques. Results of our studies indicate that efficient cavitation-driven drug delivery can be achieved with no or minimal damage to normal tissues.

Keywords: cavitation, laser, ultrasound, tumor, anti-cancer drug

1. INTRODUCTION

Many promising drugs have been developed and proposed for cancer therapy. Some of these drugs perfectly work in cell cultures, but fail to work in tissues in vivo due to poor penetration from blood to cancer cells [1-5]. In order to reach a cancer cell, the drugs have to pass three barriers: blood vessel wall, interstitial space between blood vessel and this cell, and cancer cell membrane [1-5].

The time of diffusion of a molecule across a distance (L) is proportional to this distance squared divided by diffusion coefficient (D):

$$t_{diff} \sim L^2 / 4D$$

Average distance between capillaries in tumor is about 200 μm. As a result, the time of diffusion of anticancer drugs from blood to cancer cells distant from blood vessels is higher than half-life time of these drugs.

The most specific and efficient anti-cancer agents are usually macromolecules: monoclonal antibodies, cytokines, antisense oligonucleotides, gene-targeting vectors, et. al. The rate of diffusion for macromolecules is especially low. As a result, the drugs degrade sooner than they can reach the cells distant from blood vessels.

Recently we proposed to use interaction of microparticles with pulsed laser radiation or ultrasound to break these barriers and enhance drug delivery [6, 7]. Interaction of microparticles with radiation at certain conditions can result in cavitation that can rupture blood vessel wall and cancer cell membrane, produce microconvection in the interstitium, and push drug molecules inside the cells.

*Correspondence: Email: rinat.esenaliev@utmb.edu; Telephone: (409)-772-8144; Fax: (409)-772-0751

The microparticles can selectively be accumulated in tumor blood vessels by two mechanisms. The first mechanism is so-called 'passive' delivery. If a microparticle suspension is injected in blood, microparticles with certain diameter can selectively accumulate in tumor due to increased leakage of tumor blood vessels [8]. The second way to accumulate microparticles in tumor is by coating them with antibodies specific to tumor blood vessel walls.

Cavitation can be induced by interaction of microparticles with pulsed laser radiation or with ultrasound. Formation and collapse of laser- or ultrasound-induced microbubbles results in rupture of tumor blood vessel wall and cancer cell membrane and produce microconvection that can enhance drug delivery. Interaction of strongly absorbing particles with pulsed laser radiation results in local heating and water evaporation on the surface of the particles. Evaporation results in formation of microbubbles [6, 7, 10].

The other way to produce cavitation is by using ultrasound. Microbubbles are formed by negative pressure of ultrasonic wave, while positive pressure of ultrasound produces collapse of the microbubbles.

It is known that microparticles lower cavitation threshold because they serve as cavitation nuclei. This phenomenon was demonstrated at the frequencies of 0.757, 0.989, 2.3, and 2.5 MHz in water suspensions of polystyrene microspheres [11].

Therefore, one can expect that threshold of laser- and ultrasound-induced cavitation in the presence of microparticles is lower than that without microparticles.

The aims of this study were to confirm that microparticles lower threshold of laser- and ultrasound-induced cavitation in tissue phantoms and to determine optimal parameters of laser and ultrasonic radiation and microparticle concentration, which can be used for efficient and safe drug delivery in tumors.

2. MATERIALS AND METHODS

Laser-induced cavitation. Experimental setup to study interaction of microparticles with pulsed laser radiation is presented in Figure 1. First harmonic (λ = 1064 nm) of a Q-switched Nd:YAG laser with 10 ns pulse duration was used to induce cavitation in the sample. Microbubble formation was detected by changes in scattering of He-Ne laser light, which was delivered using optical fibers. Scattered light was measured by a photodetector, recorded by a scope and stored by a computer for processing. An interferometric filter at the front
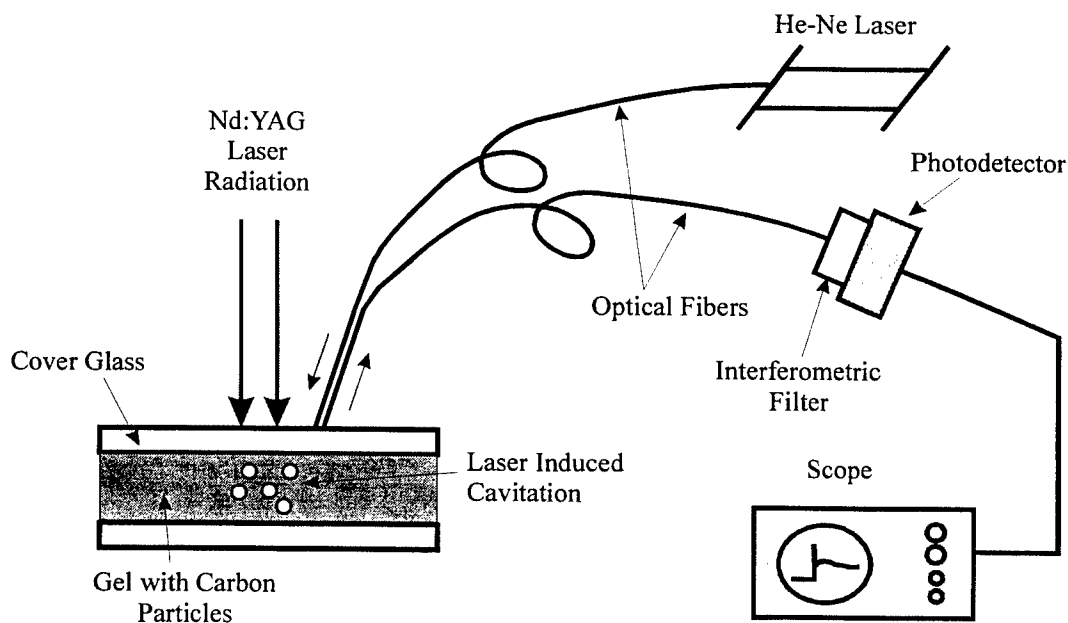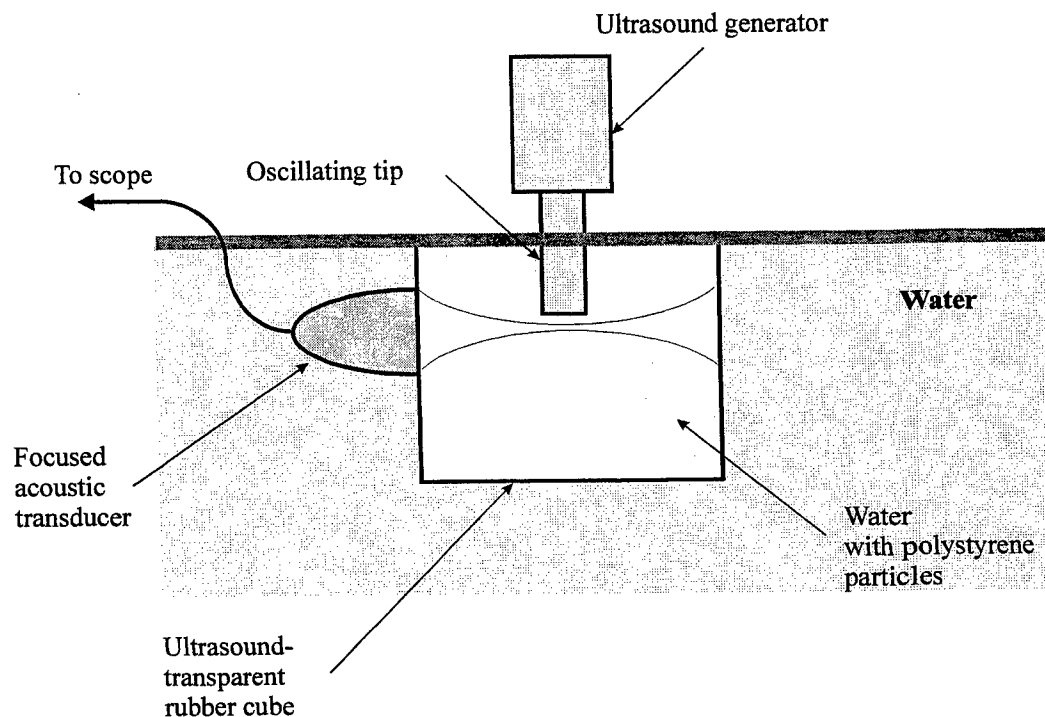

Figure 1. Experimental setup to study cavitation produced by laser irradiation.

of the photodetector was used to attenuate stray light and scattered Nd:YAG laser radiation. We used 10% gelatin as a phantom medium simulating tissue properties. Gel samples were covered with microscopic slides to avoid dehydration of the surface. Cavitation was studied in gel with and without carbon particles, which have high absorption in the near infrared spectral range. We used carbon particles with the diameter of 200 nm at the concentration of 0.1%.

Ultrasound-induced cavitation. Figure 2 shows experimental setup, which was used to study ultrasound-induced cavitation. Ultrasound generator Sonics VCX 500 (Sonics & Materials Inc.) with oscillating tip produced ultrasonic wave with the frequency of 20 kHz in a sample. Ultrasound-induced cavitation was detected by a focused acoustic transducer Panametrics BCU-58-6W. The frequency of 20 kHz was eliminated in transducer signals by a high-pass filter. The filtered signals were recorded by a scope and stored by a computer. Water with polystyrene microspheres with the diameter of 100 nm at different concentrations was used as a tissue phantom in experiments on ultrasound-induced cavitation. The phantom in ultrasound-transparent rubber cube (10x10x10 cm) was embedded in a water tank with the dimensions of 25x50x30 cm to avoid reflections from borders and interferention of ultrasonic waves. The tank bottom was covered with polyvinilchloride tubes with different diameters to provide attenuation of the waves and minimize their reflection from the bottom. The water used as a phantom medium was distilled, boiled for 5 minutes and left overnight to eliminate air bubbles, which can lower cavitation threshold.

3. RESULTS AND DISCUSSION

Laser-induced cavitation. Figure 3 shows photographic picture of gel with carbon particles after irradiation by one Nd:YAG laser pulse. Bubbles produced by heating of carbon particles are clearly seen. No bubbles were seen in gel without carbon or in gel with carbon below cavitation threshold.

**Figure 2.** Experimental setup to study ultrasound-induced cavitation.
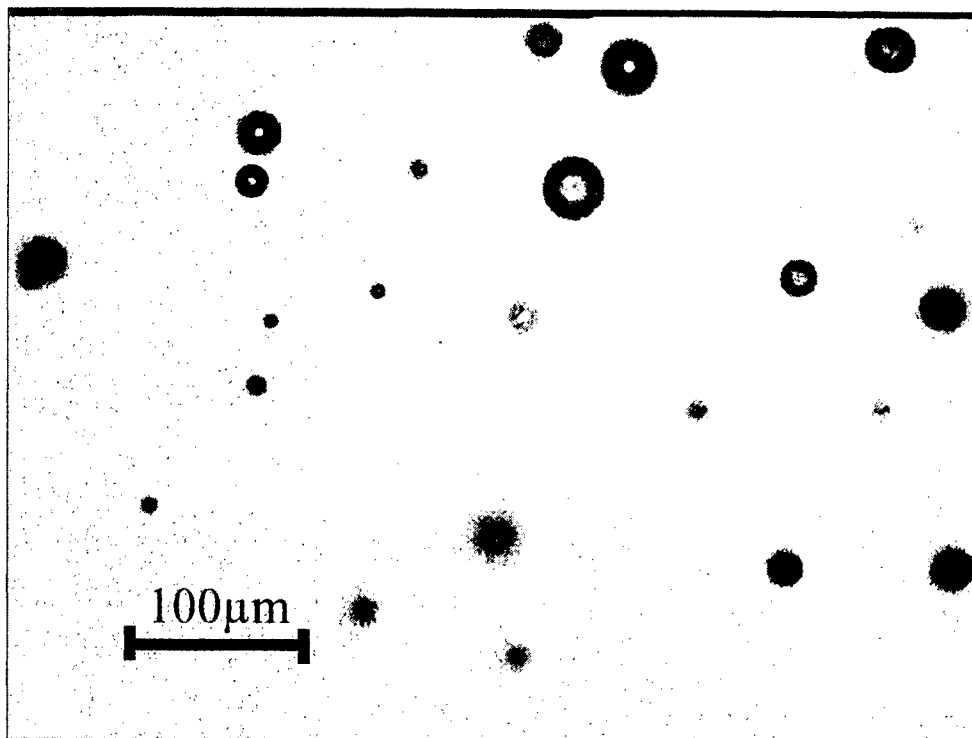
Figure 3. Photograph of gel with carbon particles taken 1 minute after a single shot Nd:YAG laser irradiation. Laser fluence was 0.56 J/cm^2.

Typical photodetector signals at different laser fluence are shown in Figure 4. Sharp peak is produced by pulsed Nd:YAG laser radiation. Signal before the Nd:YAG laser pulse is background scattering. At low laser fluence, signal after the laser pulse has the same amplitude as signal before the laser pulse. At higher laser fluence, the photodetector signal after the laser pulse is higher due to the formation of microbubbles, which scatter He-Ne laser light. Signal from the bubbles increases with laser fluence because more bubbles are produced. Moreover, the formed bubbles are bigger. The photodetector signal slowly decreases with time because some bubbles collapse, while other bubbles stay for a longer time.

To estimate cavitation threshold in gel with and without carbon microparticles, we integrated the photodetector signal after the Nd:YAG laser pulse. Figure 5 represents the integrated photodetector signal, which characterizes the level of cavitation, as a function of laser fluence. Each laser pulse was directed to a new place on the sample and every point in the figure is an average value of 12 pulses. The fluence of about 0.2 J/cm^2, where integrated photodetector signal from gel with carbon starts to grow, is cavitation threshold. No cavitation was produced in gel without carbon at least up to 20 J/cm^2. Therefore, the presence of carbon microparticles lowers threshold of laser-induced cavitation at least by two orders of magnitude.

In our previous studies [7] we determined the threshold of laser-induced cavitation in water suspensions of carbon particles. The threshold of cavitation in water with carbon is about 0.02 J/cm^2. Cavitation threshold in blood with carbon particles is expected to be close to that in water. Threshold value in the interstitium is close to that of gel. Therefore, the threshold of laser-induced cavitation in tumor with accumulated carbon particles should be between 0.02 and 0.2 J/cm^2. Tissue ablation threshold is about 40 J/cm^2 at the wavelength of 1064 nm. Therefore, laser radiation with fluence in the range between 0.2 and 40 J/cm^2 can enhance drug delivery in tumors with no or minimal damage to normal tissues.

Ultrasound-induced cavitation. Figure 6 shows typical acoustic transducer signals recorded below and above the cavitation threshold in the sample. The transducer signals have no peaks without cavitation. If cavitation is produced, the transducer signals have multiple peaks. These peaks are induced by collapsing
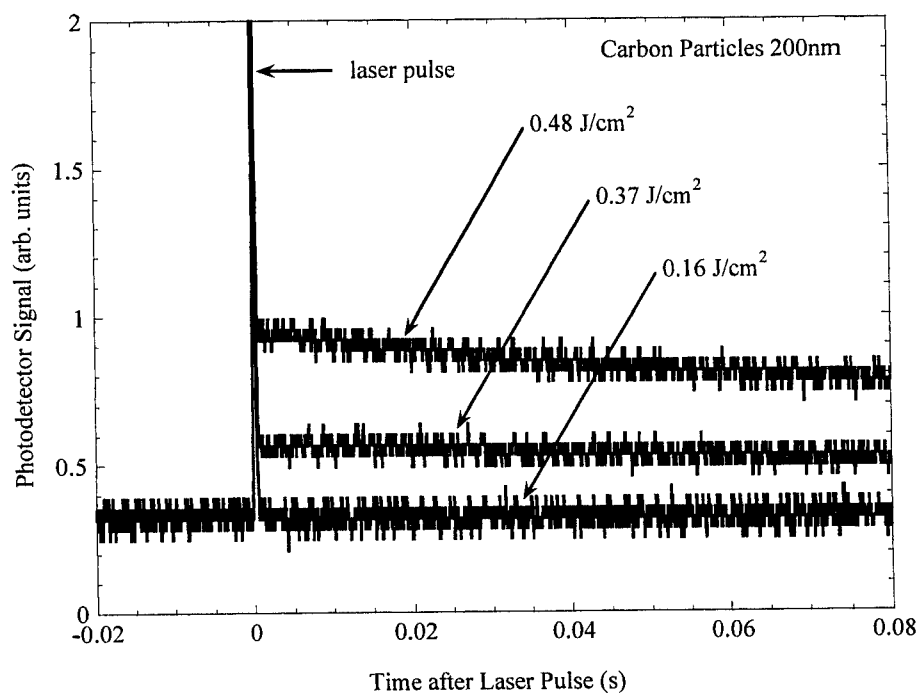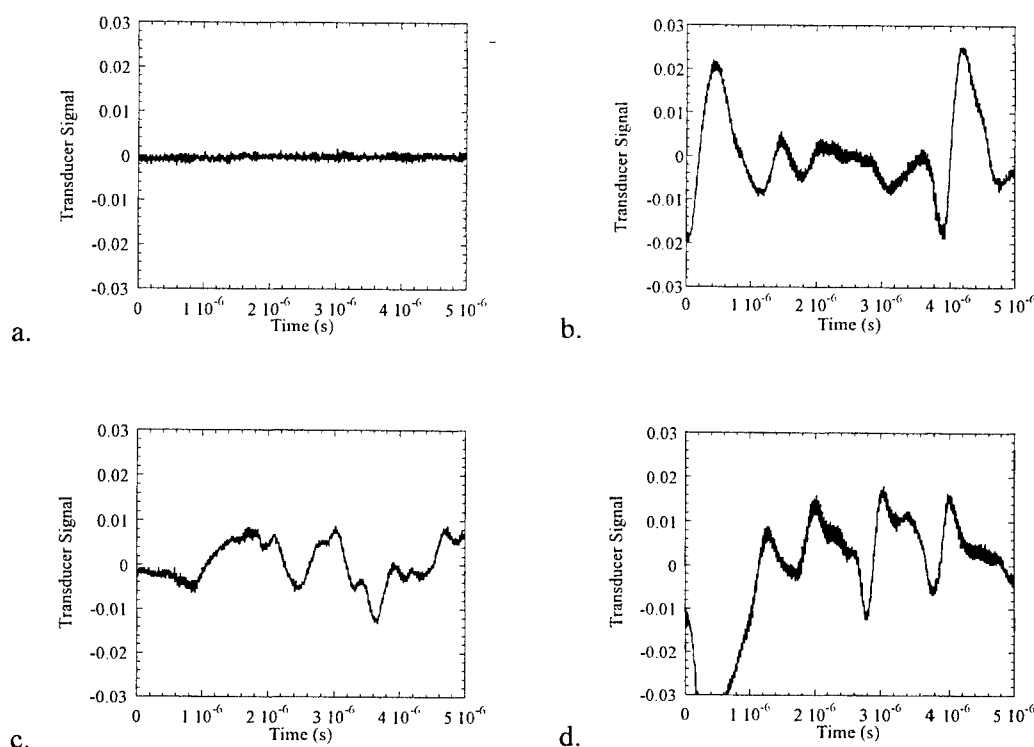
Figure 4. Typical photodetector signals recorded from gel with carbon particles at different laser fluences.
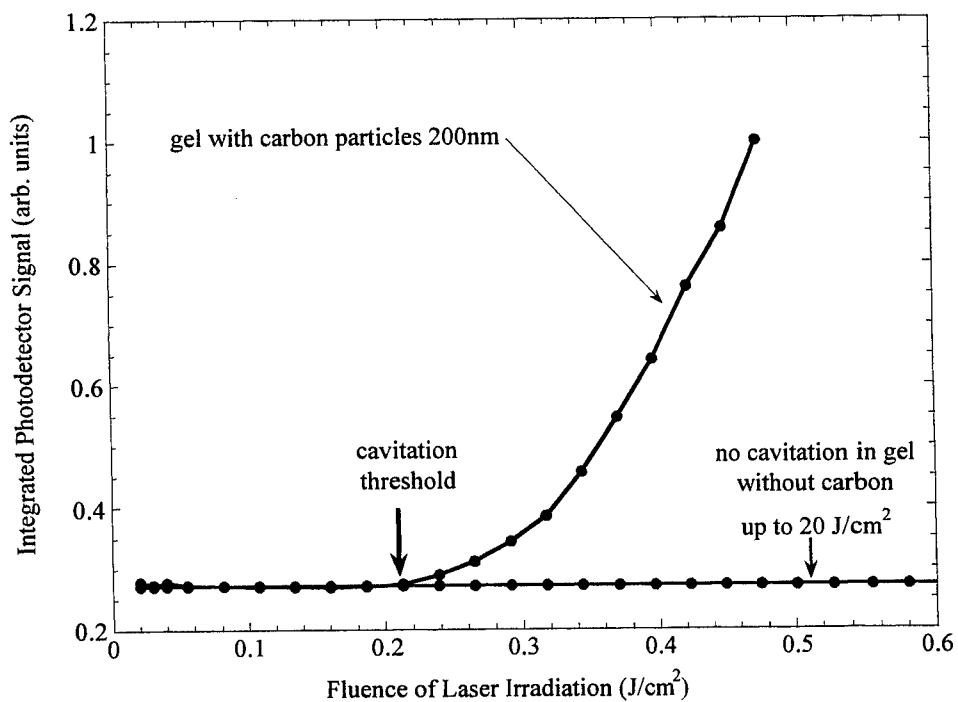
Figure 5. Level of laser-induced cavitation in gel with and without carbon particles as a function of laser fluence.

Figure 6. Typical transducer signals (in Volts) (a) without cavitation, and (b)-(d) with cavitation.

microbubbles. Integrated transducer signal was used to characterize level of cavitation in the sample. Figure 7 represents the integrated signal as a function of vibration amplitude of ultrasound generator tip at different concentrations of polystyrene microspheres. Absolute value of pressure amplitude should be measured in near-field conditions by a specially designed acoustic detector calibrated at 20 kHz. However, the upper limit of the pressure amplitude can be theoretically estimated by using the value of the tip vibration amplitude in the plane wave approximation. These estimations give the pressure amplitude upper limit of 10 bars at vibration amplitude of about 10.5 μm. However, the real pressure can be substantially lower. Every point in the graph is an average value of 12 measurements. The integrated signal is very small at small vibration amplitude. There is a sharp increase of integrated transducer signal at certain amplitude, which corresponds to the threshold of ultrasound-induced cavitation. Cavitation threshold measured in pure water was at about 7.5 μm. Polystyrene particles lower cavitation threshold down to about 3.5 μm.

Ultrasound-induced cavitation threshold is presented in Figure 8 as a function of microparticle concentration. Cavitation threshold decreases with the increase of microparticle concentration and reaches a saturation level at concentrations higher than 0.075% (w/w).

The estimated threshold of ultrasound-induced cavitation in blood is about 11.5 μm. The threshold in the interstitium is even higher. Therefore, tip vibration with the amplitude from 3.5 to 11.5 μm will produce cavitation selectively around microparticles. If polystyrene microspheres accumulated in tumor, ultrasound irradiation at this level can be used for efficient and safe drug delivery from blood to cancer cells. Based on results of these experiments, we used tip vibration amplitude of 10.9 μm in our animal studies [13].
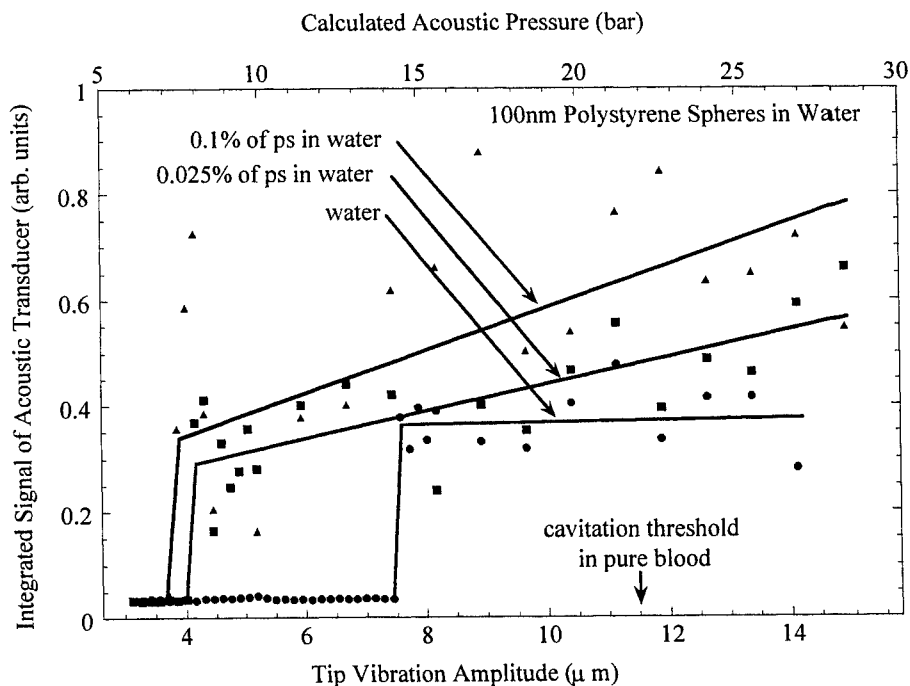
Figure 7. Level of ultrasound-induced cavitation as a function of vibration amplitude. Circles, squares, and triangles are data points for pure water and water with 0.025% and 0.1% concentrations of polystyrene particles, respectively. Pressure was calculated from tip vibration amplitude in plane wave approximation.
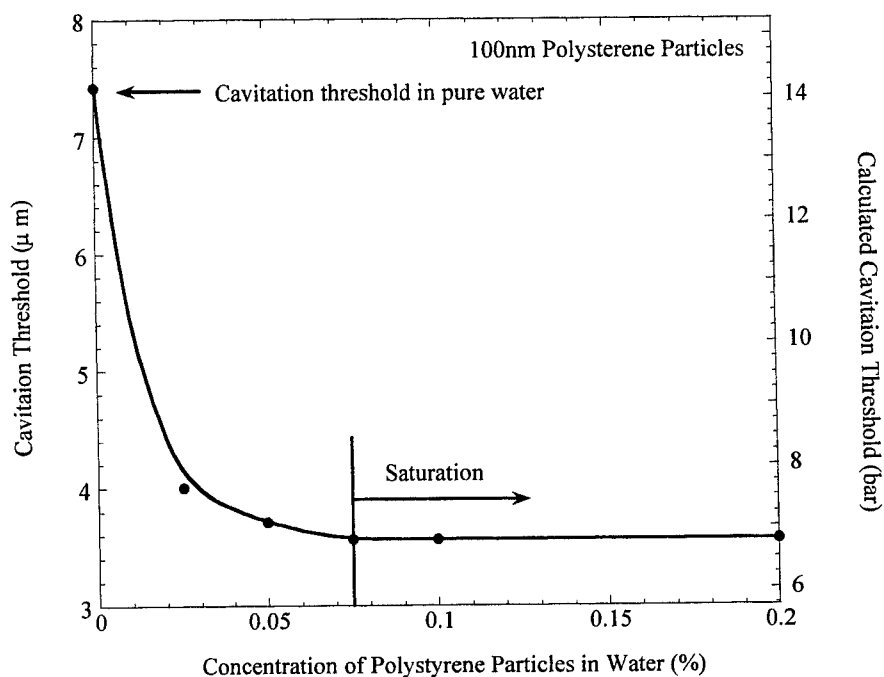
Figure 8. Threshold of ultrasound-induced cavitation as a function of polystyrene particle concentration. Pressure was calculated from tip vibration amplitude in plane wave approximation.

4. CONCLUSION

Our studies demonstrated that threshold of cavitation induced by laser or ultrasound irradiation can be significantly lowered by microparticles. Threshold values of cavitation induced by pulsed laser and ultrasound radiation with and without particles were found. Optimal irradiation parameters and particle concentration were determined. These parameters can be applied in animal studies for safe and efficient drug delivery. Our results suggest that laser- or ultrasound-induced cavitation can sufficiently enhance penetration of drugs from blood to cancer cells and improve efficacy and safety of cancer chemotherapy.

5. ACKNOWLEDGMENT

6. REFERENCES

1. Jain R.K. Delivery of Novel Therapeutic Agents in Tumors: Physiological Barriers and Strategies. Journal of the National Cancer Institute, v.81(8), pp. 571-576, 1989.
2. Jain R.K. Delivery of Molecular Medicine to Solid Tumors. Science, v. 271, pp. 1079-1080, 1996.
3. Curti B.D. Physical Barriers to Drug Delivery in Tumors. In: Chabner B. A. and Longo D. L., et al. "Cancer Chemotherapy and Biotherapy", pp. 709-719, 1996.
4. Gerlowski L.E., Jain R.K. Microvascular permeability of Normal and Neoplastic Tissues. Microvasc. Res., v. 31, pp. 288-305, 1986.
5. Jain R.K. Barriers to drug delivery in solid tumors. Scientific American, pp. 58-65, July 1994.
6. Esenaliev R.O. Interaction of radiation with microparticles for enhancement of drug delivery in tumors. In "Laser-Tissue Interaction", ed. S.L. Jacques, SPIE Publishing, Bellingham, WA., v. 3601, 1999, pp. 166-176.
7. Esenaliev R., Larina I., Larin K., Motamedi M., Evers M. Mechanism of Laser-Induced Drug Delivery in Tumors. In "Laser-Tissue Interaction", ed. S.L. Jacques, SPIE Publishing, Bellingham, WA., v. 3914, pp. 188-196, 2000.
8. Hobbs S.K., Monsky W.L., Yuan F, Roberts W.G., Griffith L., Torchilin V.P., Jain R.K. Regulation of transport pathways in tumor vessels: Role of tumor type and microenvironment. Proc. Natl. Acad. Sci. USA. Vol. 95, pp. 4607-4612, 1998.
9. Hopper R.W., Uhlmann D.R. Mechanism of Inclusion Damage in Laser Glass. J. Appl. Phys., v. 41 (10), pp. 4023-4037, 1970.
10. Esenaliev R.O., Karabutov A.A., Podymova N.V., Letokhov V.S. Laser Ablation of Aqueous Solutions with Spatially Homogeneous and Heterogeneous Absorption. Appl. Phys. B, v. 59, pp. 73-81, 1994.
11. Holland C.K., Apfel R.E., Thresholds for transient cavitation produced by pulsed ultrasound in a controlled nuclei environment. J. Acoust. Soc. Am., Vol. 88(5), pp. 2059-2069, Nov. 1990.
12. Deng C.X., Xu Q., Apfel R.E., Holland C.K. Inertial cavitation produced by pulsed ultrasound in controlled host media. J. Acoust. Soc. Am., Vol. 100(2), pp. 1199-1208, August 1996.
13. Esenaliev R., Larina I., Ivanova Y., Ashitkov T., Evers M. Cavitation-induced Drug Delivery in Tumors for Cancer Chemotherapy: Animal Studies. In "Laser-Tissue Interaction", ed. S.L. Jacques, SPIE Publishing, Bellingham, WA, v. 4257, 2001, in press.

Cavitation-induced Drug Delivery in Tumors for Cancer Chemotherapy: Animal Studies

Rinat Esenaliev[1,2*], Irina Larina[1], Yuliana Ivanova[1],
Taras Ashitkov[1], Robert Thomas[3], Mark Evers[3]

[1]Center for Biomedical Engineering, [2]Department of Physiology and Biophysics,
[3]Department of Surgery
University of Texas Medical Branch, Galveston, TX 77555

Recently we proposed to use laser- and ultrasound-induced cavitation to enhance delivery of anti-cancer agents from blood into tumor cells through tumor capillary wall, interstitium, and cancer cell membrane. Cavitation threshold can be lowered by using microparticles (with certain optical and acoustic properties) which can accumulate in tumors after injection in blood. Lower cavitation threshold allows for local and pronounced cavitation in tumors and, therefore, may provide safe and efficient delivery of anti-cancer drugs in cancer cells without damage to normal tissues by laser or ultrasound radiation. In this paper, we studied enhanced penetration of model macromolecular (rhodamine-dextran) and real anti-cancer (5-FU) drugs and efficacy of cancer therapy with the use of this technique in nude mice bearing human colon tumors KM20. Our studies showed enhanced penetration of the drugs in irradiated tumors and significant improvement of cancer therapy when radiation was applied in combination with polystyrene particle and 5-FU injections. Complete tumor regression of irradiated tumors was obtained when optimum conditions were used. Our results suggest that this technique can potentially be used for efficient and safe cancer chemotherapy.

Keywords: Cancer therapy, interstitium, cavitation, colon tumor, ultrasound

1. INTRODUCTION

Blood vessel wall, interstitial space, and cancer cell membrane are physiological barriers to delivery of drugs (especially macromolecular agents) from blood into cancer cells [1-3]. Recently, we proposed to use laser- and ultrasound-induced cavitation to enhance delivery of anti-cancer agents from blood into tumor cells through these physiological barriers [4]. This technique is based on interaction of exogenous micro- and nanoparticles with laser or ultrasonic radiation. The interaction of the particles with laser or ultrasonic radiation may result in cavitation when the particles and radiation with certain parameters are used. The laser-induced cavitation can be achieved by local heating of strongly absorbing particles by pulsed laser radiation [4, 5]. The ultrasound cavitation is produced by negative (tensile) pressure of ultrasonic waves and the particles serve as cavitation nuclei which lower cavitation threshold [4, 6]. The laser- or ultrasound-induced cavitation results in perforation of tumor blood vessel walls and cancer cell membranes and produces microconvection in the interstitial space.

In this paper, we studied (1) penetration of model macromolecular (rhodamine-dextran) and real anti-cancer (5-FU) drug and (2) efficacy of cancer therapy with the use of ultrasound-induced cavitation.

*Correspondence: Email: rinat.esenaliev@utmb.edu; Telephone: (409)-772-8144; Fax: (409)-772-0751

2. MATERIALS AND METHODS

Athymic nude male mice (average weight of 30 g) were used in this study. The mice were housed in the Nude Mouse Facility of the Animal Research Center of UTMB. The animal protocol for these studies was approved by the Institutional Animal Care and Use Committee of UTMB.

Suspension of human colon cancer cells KM20 (2 x 10^6 per site) was injected s.c. in the dorso-scapular area on the left and right sides of each mouse. Experiments were initiated when tumors reached the size of 5 to 10 mm (usually two weeks after the injection). One tumor was irradiated by ultrasound for 10 minutes, while the other tumor served as control. Vibration amplitude of the oscillating tip of our ultrasound system, pulse duration, and pulse repetition rate were 10.9 μm, 0.1 s, and 2 Hz, respectively. These parameters provide efficient cavitation in tissue phantoms with polystyrene particles [6]. Since KM20 colon tumors grow quickly and are capable of producing metastases, they are often used in colon cancer studies. Moreover, they are highly resistant to chemotherapy and served as a good tumor model in our experiments.

Polystyrene particles (10% w/w suspension in water) with the diameter of 100 nm were used as cavitation nuclei. The suspension of polystyrene particles was injected in the tail vein of nude mice one day prior to irradiation to allow extravasation of the particles in tumor blood vessels. In some experiments we used rhodamine-dextran (M.W. = 20 kDa) and polystyrene particles (dia. = 100 nm) colored with fluorescent dye (FITC) to study migration of the macromolecules and particles in the interstitium. Anti-cancer drug 5-Fluorouracil (5-FU) was used to study tumor necrosis and in the cancer therapy experiments. 5-FU is currently used for colon cancer chemotherapy in patients and nude mice. The drug was injected i.p. prior to irradiation at the dose of 90 mg/kg which is the optimum doze for cancer therapy in nude mice.

Length and width of each tumor were measured with a caliper. Tumor volume, V, was calculated by the formula: $V = L \times W^2 / 2$, where L and W is the length and the width of the tumor, respectively. This formula is commonly used for the calculation of tumor volume in cancer therapy studies. The tumor volume is presented as a function of time (in days) after the first treatment (irradiation).

3. RESULTS AND DISCUSSION

Figure 1 shows regular (a) and fluorescent microscopy of a control tumor obtained with green (b) and red (c) filter to visualize distribution of fluorescent polystyrene particles and rhodamine-dextran, respectively. A tumor blood vessel is visible in the central part of the top picture with regular microscopy. Fluorescent microscopy of the same site of the tumor revealed accumulation of the particles and rhodamine-dextran in the vessel. One can see some penetration of rhodamine-dextran in the interstitium. Regular (Fig. 2, a) and fluorescent (Fig. 2, b and c) microscopy of an irradiated tumor showed increased penetration of the particles and rhodamine-dextran from blood into the interstitium.

Histological examination of tumor slices stained with H&E revealed necrosis only in small areas of control tumors induced by 5-FU (Fig. 3, left). Irradiation of tumors resulted in dramatic tissue necrosis in large areas (Fig. 3, right) due to enhanced delivery of the anti-cancer drug in tumor cells.

Complete regression of irradiated tumors was obtained after one or two treatments when ultrasound was applied after the injection of polystyrene particles and 5-FU (Fig. 4). Arrows indicate days of treatment. The volume of the control tumors increased despite 5-FU injections. This response is typical for colon tumors due to their high resistance to chemotherapy [7, 8]. Combination of ultrasound
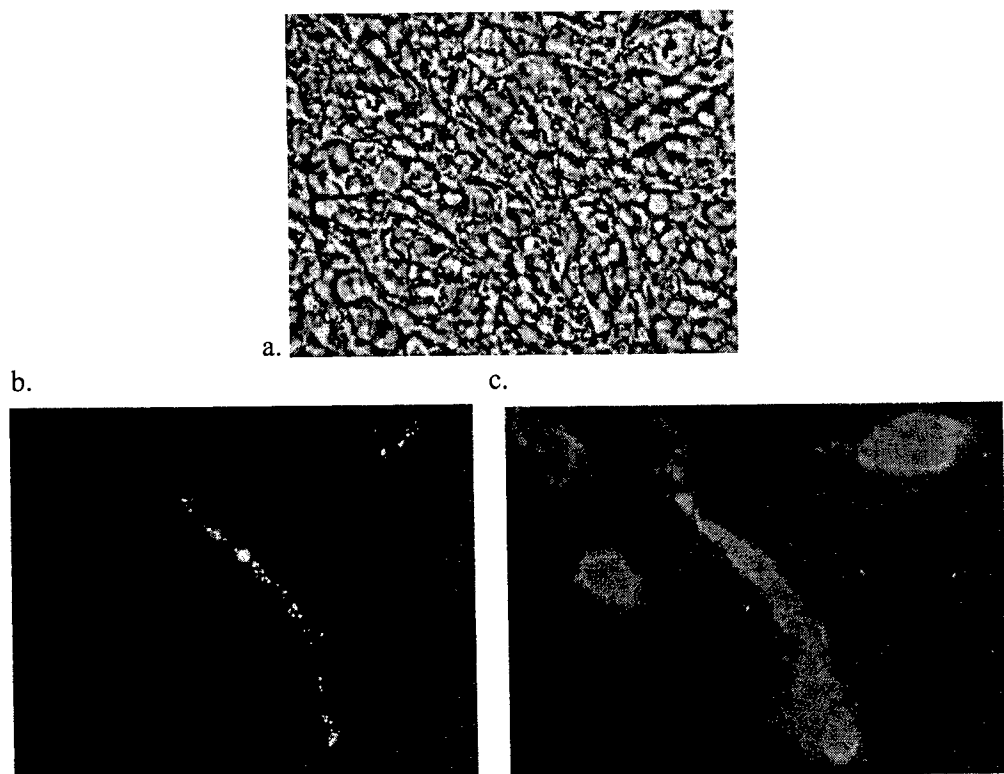
Figure 1. Regular (a) and fluorescent microscopy of a control tumor obtained with green (b) or red (c) filter.
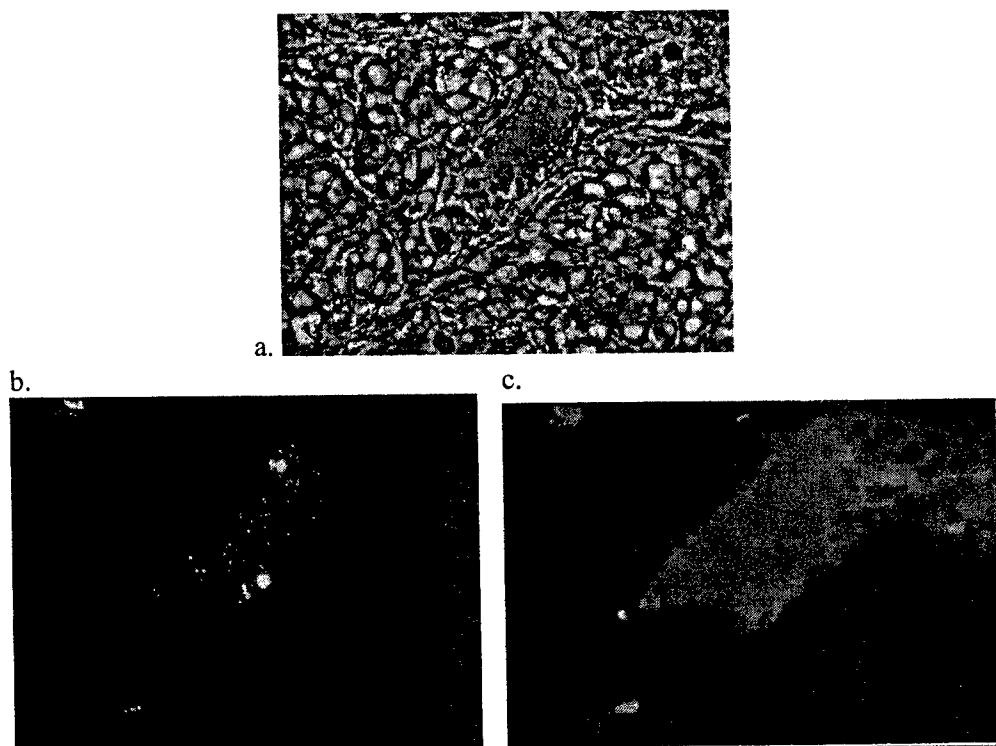

Figure 2. Regular (a) and fluorescent microscopy of an irradiated tumor obtained with green (b) or red (c) filter.

with polystyrene particle and 5-FU injections produced enhanced delivery of 5-FU into cancer cells as well as damage to tumor blood vessels in the irradiated tumors. This resulted in death of all cancer cells in the tumors. Detailed studies of efficacy of cancer therapy with the application of this drug delivery technique will be presented in [9].
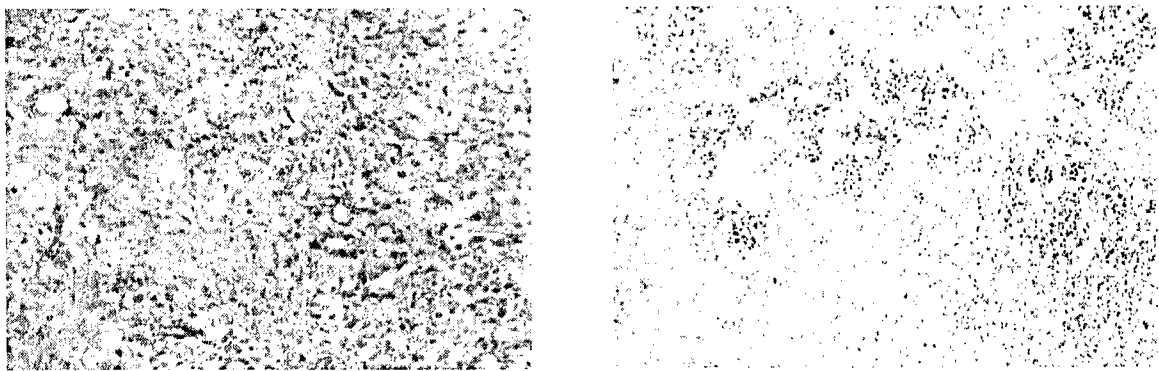
Figure 3. Control (left) and irradiated (right) tumor histology with standard H&E staining.
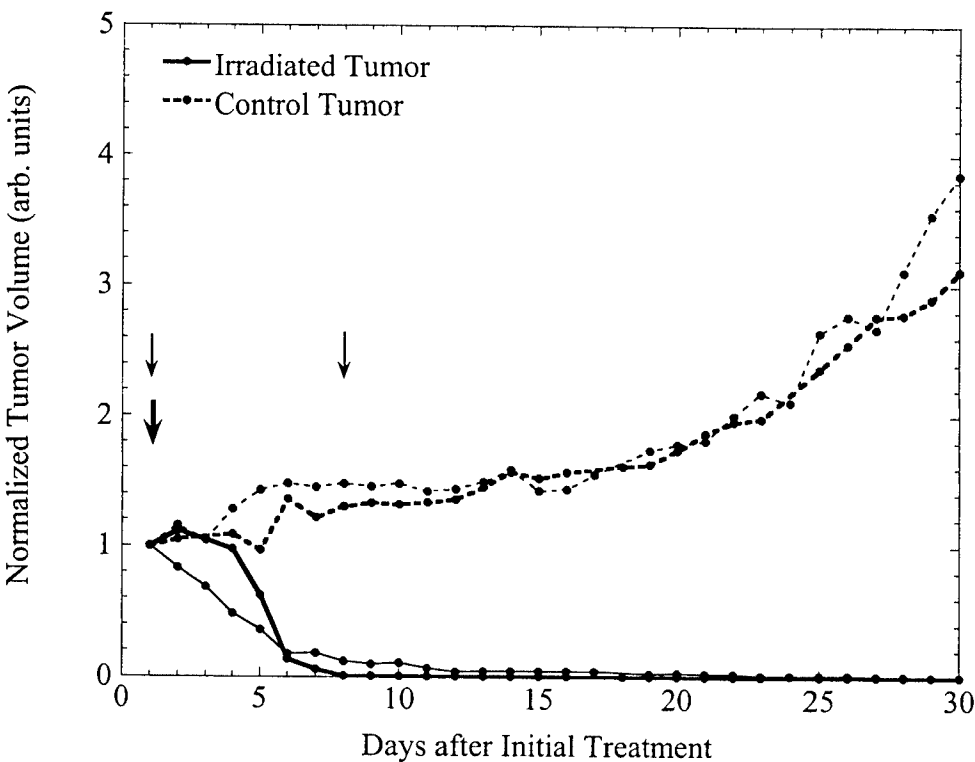
Figure 4. Complete regression of irradiated tumors due to enhanced delivery of 5-FU.

4. CONCLUSION

Our *in vivo* studies in nude mice with human colon tumors demonstrated that:

1. Cavitation enhances delivery of macromolecular anti-cancer drugs and nanoparticles in the interstitium of tumors;

2. Cavitation-enhanced delivery of anti-cancer drug 5-FU results in tumor necrosis;

3. Complete tumor regression can be obtained by using the cavitation-enhanced drug delivery technique.

These studies suggest that efficacy of cancer chemotherapy can substantially be improved if this drug delivery technique is applied.

ACKNOWLEDGMENT

REFERENCES

1. Jain R.K. Delivery of Novel Therapeutic Agents in Tumors: Physiological Barriers and Strategies. Journal of the National Cancer Institute, v.81(8), pp. 571-576, 1989.
2. Jain R.K. Delivery of Molecular Medicine to Solid Tumors. Science, v. 271, pp. 1079-1080, 1996.
3. Curti B.D. Physical Barriers to Drug Delivery in Tumors. In: Chabner B. A. and Longo D. L., eds. "Cancer Chemotherapy and Biotherapy", pp. 709-719, 1996.
4. Esenaliev R.O. Interaction of radiation with microparticles for enhancement of drug delivery in tumors. In "Laser-Tissue Interaction", ed. S.L. Jacques, SPIE Publishing, Bellingham, WA., v. 3601, 1999, pp. 166-176.
5. Esenaliev R., Larina I., Larin K., Motamedi M., Evers M. Mechanism of laser-induced drug delivery in tumors. In "Laser-Tissue Interaction", ed. S.L. Jacques, SPIE Publishing, Bellingham, WA., v. 3914, 2000, pp. 188-196.
6. Larina I.V., Bartels C., Larin K.V., Esenaliev R.O. Cavitation-induced Drug Delivery in Tumors for Cancer Chemotherapy: Phantom Studies. In "Laser-Tissue Interaction", ed. S.L. Jacques, SPIE Publishing, Bellingham, WA., v.4257, 2001, in press.
7. Van Ginckel R. Distelmans W. De Brabander M. Callens M. Janssens B. Jagers E. Wouters L. De Coster R. Janssen PA. Levamisole plus 5-fluorouracil inhibits the growth of human colorectal xenografts in nude mice. European Journal of Cancer. 28A(6-7):1137-9, 1992.
8. Britten CD. Hilsenbeck SG. Eckhardt SG. Marty J. Mangold G. MacDonald JR. Rowinsky EK. Von Hoff DD. Weitman S. Enhanced antitumor activity of 6-hydroxymethylacylfulvene in combination with irinotecan and 5-fluorouracil in the HT29 human colon tumor xenograft model. Cancer Research. 59(5):1049-53, 1999.
9. Esenaliev R.O., Larina I.V., Ashitkov T.V., Evers B.M. Efficacy of cancer chemotherapy with ultrasound-enhanced drug delivery. Cancer Research, in preparation.

Model system for investigating laser-induced subcellular microeffects

Gereon Hüttmann, Jesper Serbin, Benno Radt, Björn I. Lange and Reginald Birngruber

Medical Laser Center Lübeck, Peter-Monnik-Weg 4, D-23562 Lübeck, Germany

ABSTRACT

Background: Laser induced protein denaturation is of fundamental interest for understanding the mechanisms of laser tissue interaction. Conjugates of nanoabsorbers coupled to proteins are presented as a model system for investigating ultrafast protein denaturation. Irradiation of the conjugates using repetitive picosecond laser pulses, which are only absorbed by the nanoabsorbers, could result in effects with a spatial confinement of less than 100 nm.

Materials and Methods: Experiments were done with bovine intestinal alkaline phosphatase (aP) coupled to 15 nm colloidal gold. This complex was irradiated at 527 nm wavelength and 35 ps pulse width with a varying number of pulses ranging from one up to 10^4. The radiant exposure per pulse was varied from $2 \, mJ/cm^2$ to $50 \, mJ/cm^2$. Denaturation was detected as a loss of protein function with the help of the fluorescence substrate 4MUP.

Results and Discussion: Irradiation did result in a steady decrease of the aP activity with increasing radiant exposures and increasing number of pulses. A maximal inactivation of 80% was reached with 10^4 pulses and $50 \, mJ/cm^2$ per pulse. The temperature in the particles and the surrounding water was calculated using Mie's formulas for the absorption of the nanometer gold particles and an analytical solution of the equations for heat diffusion. With $50 \, mJ/cm^2$, the particles are heated above the melting point of gold. Since the temperature calculations strongly depend on changes in the state of matter of the particles and water, a very sophisticated thermal model is necessary to calculate exact temperatures.

It is difficult to identify one of the possible mechanisms, thermal denaturation, photochemical denaturation or formation of micro bubbles from the dependance of the inactivation on pulse energy and number of applied pulses. Therefore, experiments are needed to further elucidate the damage mechanisms.

In conclusion, denaturing proteins irreversibly via nanoabsorbers using picosecond laser pulses is possible. The confinement of the heat to the nanoabsorbers when irradiating with picosecond pulses suggests that the denaturation of proteins could be possible with nanometer precision in cells with this approach. However, the mechanism of protein inactivation, which is part of present investigations, is crucial for the precision of such nanoeffects.

Keywords: Laser medicine, nanoparticles, colloidal gold, protein denaturation

1. INTRODUCTION

Lasers are used in a large variety of medical applications because of their ability to modify or destroy tissue with high precision. Two different ways may be used to restrict the laser-induced damage to the target volume. The laser beam can either be focused directly to the target tissue, or a selective absorption in the tissue can be used to restrict damage to the target volume (Fig. 1). When focusing the laser beam, the precision of the laser induced effects is limited by the size of the laser focus, which can be in the order of a micron, if optics with a high numerical aperture are used.[1,2] For applications in real tissues even this precision may not be achieved. Typical examples for this kind of laser application are laser cutting or laser ablation. Using differences in tissue absorption, the temperature can be raised selectively in the stronger absorbing structures. These high temperatures give the opportunity for a destruction of the absorbing structures. The precision of these effects can be comparable to the size of the absorber,

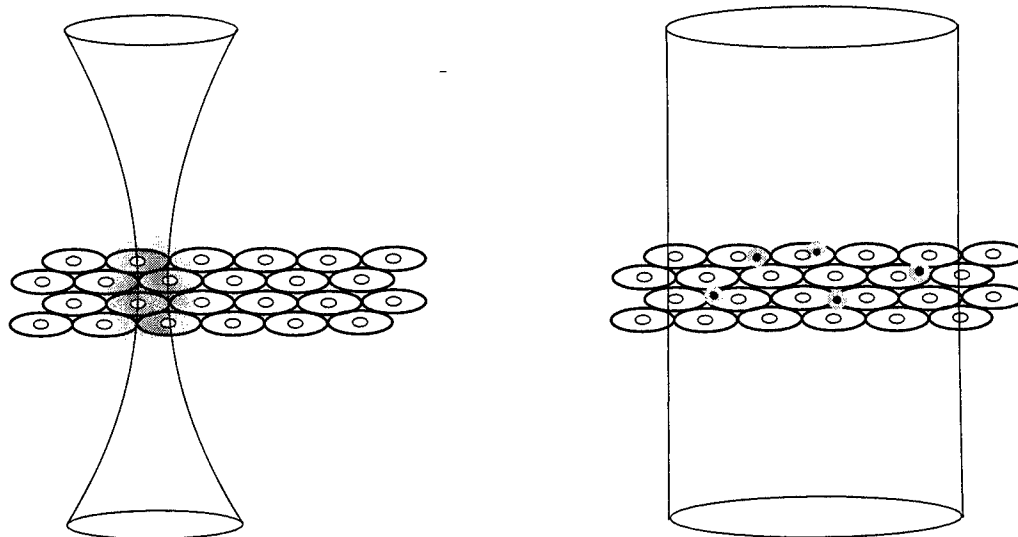Further author information: (Send correspondence to Gereon Hüttmann)
Gereon Hüttmann: E-mail: huettmann@mll.mu-luebeck.de
Benno Radt: E-mail: radt@mll.mu-luebeck.de
Jesper Serbin: E-mail: js@lzh.de
Brörn I. Lange: E-mail: lange@mll.mu-luebeck.de
Reginald Birngruber: E-mail: bgb@mll.mu-luebeck.de

Figure 1. Localized tissue damage can be induced either by tight focusing of the laser beam (left) or by using increased absorption in the target structures (right).

if the collateral damage, caused by heat diffusion, shock-waves, or mechanical destruction can be limited to the near vicinity of the absorbing structures. In order to limit heat diffusion, the pulse width of the laser irradiation has to be shorter than the thermal relaxation time of the heated volume. This principle of high precision laser effects, which was proposed by Parrish and Anderson,[3] is often called selective thermolysis. Several clinical applications of lasers rely on this principle, e. g. laser epilation,[4] the phototherapy of port wine stains with pulsed lasers,[5,6] or the selective photocoagulation of the retinal pigment epithelium with microsecond laser pulses[7] in which single melanin containing cells can be destroyed selectively.

At the moment it is not clear whether also cell organels or even single macromolecules like proteins or DNA can be selectively destroyed by photothermolysis. The generation of high temperatures in nanometer volumes is possible since strongly absorbing particles, which can create temperatures of several thousend Kelvins on their surface, are available with diameters in the nanometer range. The main problem, when going to smaller structures, is the reduction of the laser pulse width, which is necessary to stay in the thermal confinement. This decreases the duration of increased temperature in the tissue. Since thermal damage depends on temperature and time,[8,9] the reduction in time has to be compensated for by an increased temperature. A high temperature and a very fast temperature increase can cause mechanical disruption by evaporation of water or shock waves, which may then destroy the precision of the laser-induced effects. Since thermal damage for multiple temperature expositions adds up, the necessary peak temperature can be reduced using multiple pulses. The additivity of laser induced damage was shown in a large variety of experiments, e. g. laser induced damage of the retina[10,11] or thermal damage of vascular tissue.[12] Extrapolation of rates of thermal damage of proteins and tissues to very high temperatures shows the possibility of selective thermal damage of biological structures near strongly absorbing nanometer-sized particles.[13]

Several groups have investigated the possibility of sub-cellular thermal damage. Jori et al. postulated the possibility of using single strongly absorbing molecules to create thermal damage in cells.[14] In this work, however, the increase of the damage temperature with decreasing heating time was not taken into account. If this is considered, molecules will rather undergo photochemistry than cause a sufficient temperature increase, as calculations have shown.[13] This was also supported by experiments in which malachite green was used to inactivate proteins under irradiation with nanosecond laser pulses.[15] Although these experiments were designed for a thermal inactivation, it was later shown that radical formation destroyed the proteins.[16] In recent experiments, phototoxic effects of Cu(II)-hematoporphyrin and a Ni(II)-naphthalocyanine were observed in cell culture and tumor bearing mice, when irradiated with Q-switched pulses.[17,18] The observations that the substances do not produce singlet oxygen and that with cw irradiation no cytotoxic effects were observed, led to the supposition of photothermal damage of the cells under nanosecond irradiation.

The aim of this work was to investigate the possibility of protein inactivation on an ultrashort time scale by the irradiation of protein-gold conjugates with picosecond laser pulses. For the experiments, conjugates made of colloidal gold with a diameter of 15 m and alkaline phosphatase (aP) were chosen, because they were commercially available. Alkaline phosphatase is commonly used for a variety of enzymatic assays, and therefore simple and sensitive assays for probing its activity exist. These conjugates were irradiated with a mode-locked frequency-doubled Nd:YLF laser. After irradiation the residual activity of the proteins was measured by a fluorescence assay.

2. MATERIALS AND METHODS

2.1. Samples and measurement of the protein activity

The conjugates of 15 nm gold particles with bovine intestinal alkaline phosphatase were purchased from ICN Biomedical Inc. Although the conjugates can be stored at 4°C for several weeks, a certain amount of proteins separates from the gold particles during storage, because the proteins are not covalently bound to the particle surface. Therefore, in the beginning of each experiment, unbound proteins were removed by centrifugation at 10000 rmp for 45 min. The loose pallet was carefully transferred with a pipette to a new vial, where they were resuspended in phosphate buffer. After this procedure the aP activity of unbound protein was less than 25% of the activity of the aP-gold conjugates. Additionally, the activity of the bound and free aP was measured before and after irradiation.

The activity of aP was measured with 4-MUP (4-Methylumbelliferylphophatase, Calbiochem), which was used in a concentration of 10 mMol/l in DEA (Diethanolamine, Fluka). Through cleavage of the phosphate group from 4-MUP, a new derivative of the dye (4-MU) is produced, which fluorescence excitation/emission maxima are shifted from 323 nm/385 nm to 370 nm/445 nm. The aP-activity was measured in 2 mm wells with a fluorescence spectrometer (Fluoromax, Spex), which was equipped with a quartz fiber bundle in order to transmit excitation and fluorescence light between the spectrometer and the samples, which were excited at 370 nm. The fluorescence was measured at 445 nm. Since at these wavelength the fluorescence of 4-MUP is very small a conversion of 4-MUP to 4-MU through the catalytic action of aP results in an increase of the measured fluorescence signal with time. Using different concentrations of aP, it was checked that under our experimental conditions the slope of the fluorescence increase was in a linear relationship to the concentration of active aP.
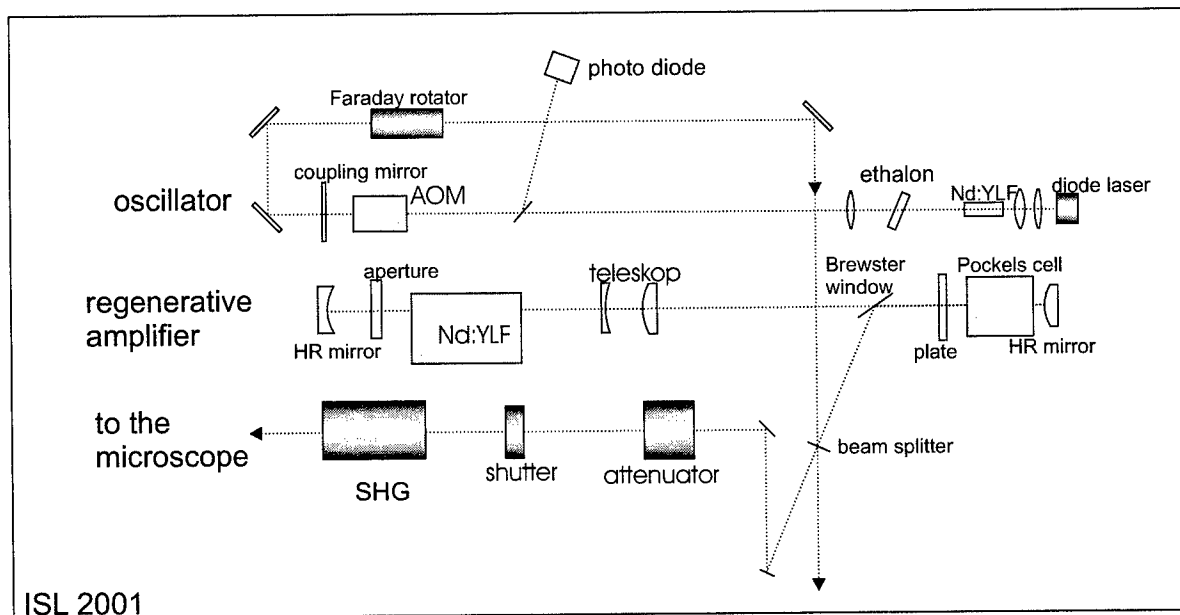
2.2. Irradiation of the samples

The samples were irradiated with a mode-locked Nd:YLF laser (ISL 2001 MPL, Intelligent Laser Systems Inc.) which was originally build for ophthalmic laser applications, but then modified for these experiments. The system consists of a cw pumped oscillator, which generates an continuous train of picosecond pulses with 167 MHz repetition rate, and a regenerative amplifier (Fig. 2a). The oscillator, which is actively mode-locked by an acousto-optic modulator, emits at a wavelength of 1057 nm. After passing a Faraday rotator, a small fraction of the picosecond pulses were fed into the amplifier. With an Electro-Optic Pockels, cell a single picosecond pulse is selected, which is then amplified in the cavity of the regenerative amplifier in approximately 100 round trips. When the inversion in the active medium is depleted, the Pockels cell is switched again and the pulse is ejected from the cavity. The amplifier can generate pulses with an energy of up to 1 mJ at a rate of 1 kHz. Due to the high quality of the cavity and the large number of round trips in the regenerative amplifier, a large amplification factor in the order of 10^6 can be achieved even though the active medium is pumped only by an cw arc-lamp. The large number of round trips also gives a very good discrimination against higher transverse modes. This and the low pump intensity compared to a flash lamp pumped system give a stable output energy with 5% standard deviation together with a Gaussian intensity distribution.[19]

With a $\lambda/2$-plate and a polarizer, the pulse energy can be attenuated to the desired level. A 15 mm LBO crystal (Casix) was used for frequency doubling of the infra-red radiation. LBO was chosen because of it's high damage threshold and the possibility of non-critical phase matching. The resulting large acceptance angle allows an efficient doubling even with slightly divergent beams. The crystal was heated in an self-buildt oven to 167°C. With a slight focusing of the output beam, a doubling efficiency of over 40% was achieved.

The pulse width of the oscillator was measured with a self-built autocorrelator using an Michelson interferometer and a 4 mm LBO crystal. The full width at half maximum of the autocorrelation trace was 75 ps. Assuming a Gaussian pulse profile, the pulse width can be estimated to 53 ps. During the frequency doubling the pulse is shortened by a factor of $\sqrt{2}$. Therefore, at 527 nm the pulse width was around 35 ps.

The samples were irradiated in wells with a diameter of 2 mm, which were custom-made in a 25 mm x 75 mm slide of optical glass (Hellma). Each of the 18 wells took a sample volume of 3.5 μl. The glass slide was positioned under a

a)

b)
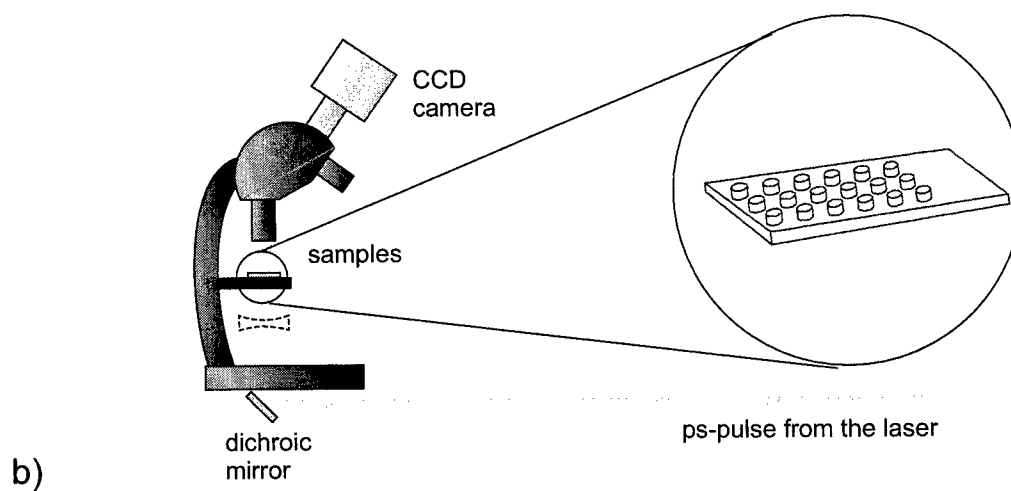
Figure 2. Set-up for the irradiation of the aP-gold conjugates. a) Mode-locked frequency-doubled Nd:YLF-laser, which generated the picosecond pulses b) Microscope, which was used for positioning of the samples during the irradiation.
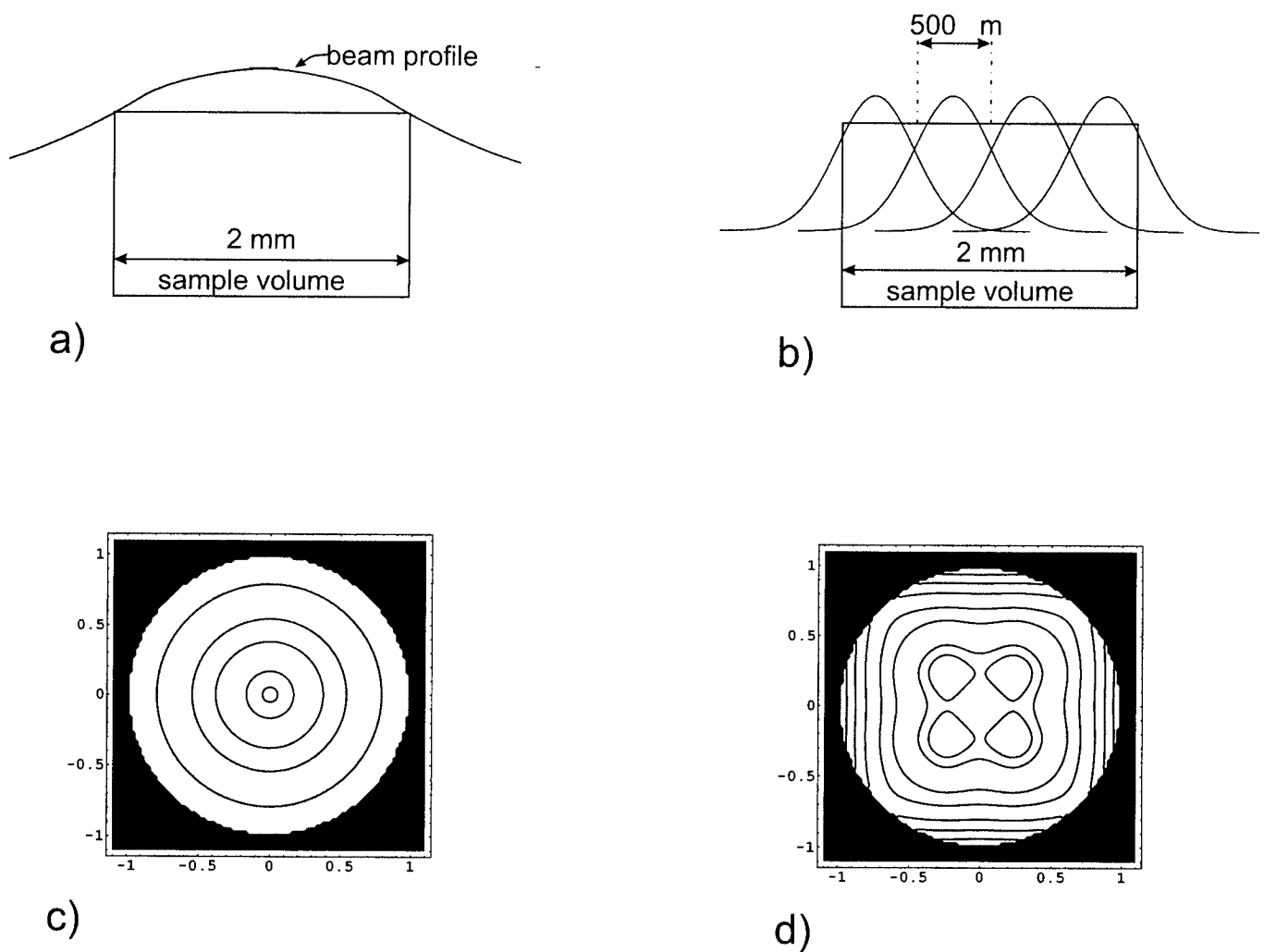
Figure 3. Distribution of the radiant exposure inside the sample volume. a), c) Irradiation with the expanded beam. b), d) Scanned irradiation with a 0.5 mm beam. c) and d) show a contour plot of the total radiant exposure. The contour lines were drawn at 50%, 60%, 70%, 80%, 90%, 95%, 99%, and 99.9% of the maximum.

microscope, the illumination system of which was replaced by a dichroic mirror in order to guide the irradiation beam to the sample and separate frequency-doubled light from the infrared irradiation (Fig. 2b). For the irradiation, the laser beam was either expanded using a diverging lens or the unexpanded laser beam was scanned over the sample area. In the first case, 30% of the beam passed through a 2 mm aperture, which means that, assuming a gaussian beam profile, the irradiance at the rim of the 2 mm samples was 70% of the maximal irradiance in the center (Fig. 3a and b). The radiant exposure averaged over the area of 2 mm was $2 \, \text{mJ/cm}^2$ at maximal pulse energy. In order to achieve a higher exposure, the unexpanded beam, which had a diameter of approximately 0.5 mm, was directed to a field of 4x4 spots in the sample, which had a distance of 0.5 mm from each other (Fig. 3b). With this approach, a nearly homogeneous total radiant exposure of up to $50 \, \text{mJ/cm}^2$ per pulse was achieved (Fig. 3d). The average radiant exposure was measured by either placing a 2 mm or a a 0.5 mm aperture in front of a pyroelectric energy meter (PE10, Ophir). The radiant exposure was then calculated by dividing the measured pulse energy by the area of the aperture.

2.3. Temperature calculations

The temperature at the surface and in the surroundings of gold particles in water was calculated using Mie's formular for the efficiency factor of absorption Q_{abs} and an analytical solution of the differential equations for heat diffusion. For 15 nm particles, which are small compared to the wavelength, the ratio of the absorption cross-section and the geometric cross-section of the particle (Q_{abs}) can be calculated with an accuracy of a few percent by a simple approximation[20]:

$$Q_{abs} = -\frac{8\pi R}{\lambda} \operatorname{Im}\left(\frac{m^2 - 1}{m^2 + 2}\right).$$ (1)

λ is the wavelength of the irradiating light in water, R the radius of the particle. m, which is the index of refraction of gold divided by that of the surrounding water, was taken as $0.59 - i\,1.67$.[20] With Equation (1), the power density A of absorbed light inside a particle, which is irradiated with the irradiance I, can be calculated:

$$A = I\frac{Q_{abs}\pi R^2}{4/3\pi R^3}.$$ (2)

During the irradiation, part of the thermal energy diffuses into the water. This was accounted for with help of a solution for the differential equations for macroscopic heat diffusion which describes the temperature in and around a sphere, that is embedded in an infinite medium. In this solution, it is assumed that starting at time zero heat is produced homogeneously with a rate A inside of the particle.[21] Thermal conductivity K and thermal diffusivity κ in the sphere can differ from the respective values of the surrounding medium. At the surface, a steady change of the temperature is assumed when passing from inside to outside. With these assumptions, the temperature inside (T_1) and outside (T_2) the particle can be calculated from following formulas:

$$T_1(t,r) = \frac{R^2 A}{K_1}\left[\frac{1}{3}\frac{K_1}{K_2} + \frac{1}{6}\left(1 - \frac{r^2}{R^2}\right) - \frac{2Rb}{r\pi}\cdot\int_0^\infty \frac{\exp(-\frac{y^2 t}{\gamma_1})}{y^2}\frac{(\sin y - y\cos y)\sin(\frac{ry}{R})}{\left[(c\sin y - y\cos y)^2 + b^2 y^2 \sin^2 y\right]}dy\right]$$ (3)

$$T_2(t,r) = \frac{R^3 A}{rK_1}\left[\frac{1}{3}\frac{K_1}{K_2} - \frac{2}{\pi}\int_0^\infty \frac{e^{\frac{-y^2 t}{\gamma_1}}}{y^3}\frac{(\sin y - y\cos y)\left[by\sin y\cos \sigma y - (c\sin y - y\cos y)\sin \sigma y\right]}{\left[(c\sin y - y\cos y)^2 + b^2 y^2 \sin^2 y\right]}dy\right]$$ (4)

with

$$b = \frac{K_2}{K_1}\sqrt{\frac{\kappa_1}{\kappa_2}}, \quad c = 1 - \frac{K_2}{K_1}, \quad \sigma = \left(\frac{r}{R} - 1\right)\sqrt{\frac{\kappa_1}{\kappa_2}}, \quad \gamma_1 = \frac{R^2}{\kappa_1}.$$

The parameters inside the sphere are denoted by the suffix 1, the parameters of the medium by suffix 2.

Equations (3) and (4) give the time-dependent temperature for an unlimited long pulse. Since the differential equations for heat diffusion are linear in time, a solution for a rectangular laser pulse with the pulse width τ can be constructed by subtracting two solution $T(t,r)$, which are separated in time[22]:

$$T_\sqcap(t,r) = T(r,t) - T(r,t-\tau)$$ (5)

3. RESULTS

3.1. Irradiation of the conjugates

With the expanded beam, no inactivation of the irradiated aP-gold conjugates was observed, even when the samples were irradiated with 10^4 pulses. As an example, Fig. 4a shows the increase of the 4-MU fluorescence of ten samples, of which five were irradiated with 10^4 pulses at $2.1\,mJ/cm^2$. From the fluorescence intensity of each sample, the slope was calculated, which is proportional to the activity of the aP in the samples (Fig. 4b). No significant reduction of the aP activity after irradiation was observed at that radiant exposure. When a higher radiant exposure was used
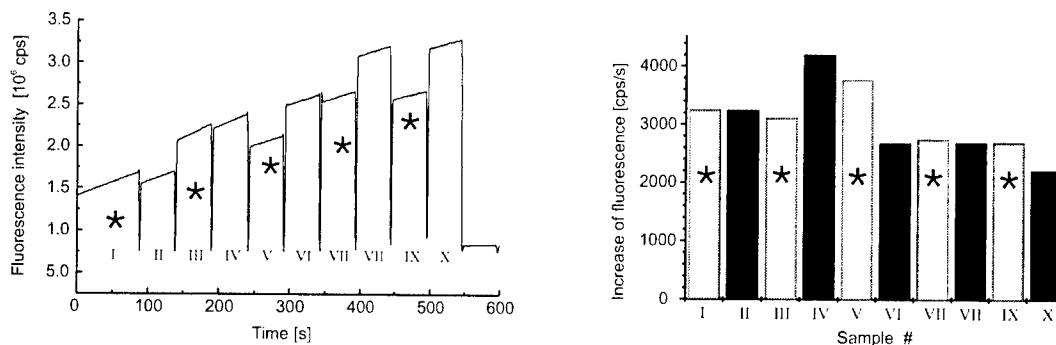
Figure 4. Activity of alkaline phosphatase after irradiation with 10^4 pulses at $2.1\,\mathrm{mJ/cm^2}$.

a) 4-MU fluorescence of ten samples measured over 70 s. Only five samples marked by a star (∗), were irradiated; the other non-irradiated samples served as a control.

b) Slope of the fluorescence of the tens samples, which is proportional to the aP activity.
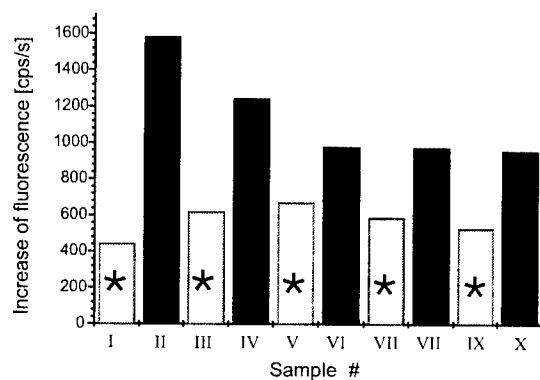
Figure 5. Activity of aP after irradiation with 16×10^4 pulses at $50\,\mathrm{mJ/cm^2}$. Irradiated samples are marked by a star (∗), the remaining samples are controls.
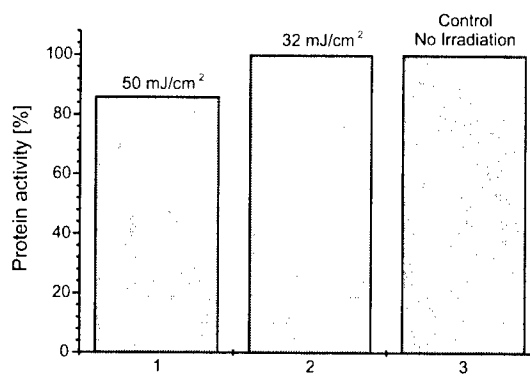
Figure 6. Activity of uncoupled alkaline phosphatase in solution, after irradiation with 10^4 pulses at different radiant exposure.
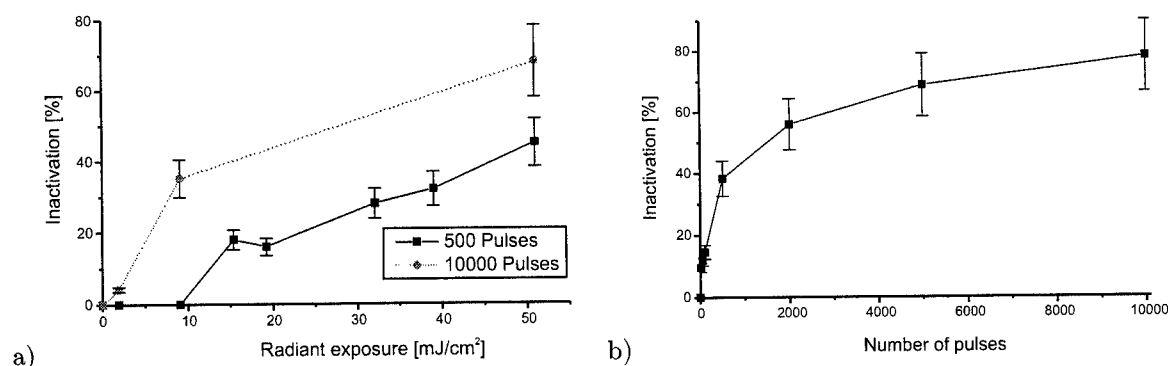
Figure 7. Inactivation of aP bound to the gold particles.
a) Dependence of the inactivation on the radiant exposure for 500 and 10^4 pulses.
b) Dependence of the inactivation on the number of pulses at a radiant exposure of $50 \, \text{mJ/cm}^2$.

by scanning the sample with the 0.5 mm laser beam in 16 fields, the activity of the aP in the samples was markedly reduced (Fig. 5). When in a control experiment a solution of unbound alkaline Phosphatase was irradiated under the same conditions, only a slight reduction of the aP activity was observed (Fig. 6).

The inactivation of aP (IA) was defined by the loss of activity due to the irradiation divided by the protein activity without irradiation:

$$IA = \frac{A_{Con} - A_{Irr}}{A_{Con}} \tag{6}$$

A_{Con} and A_{Irr} are the slopes of the 4-MU fluorescence of control samples which were not irradiated, and the irradiated samples samples, respectively. Even though unbound aP was removed from the samples before irradiation by centrifugation, there was always a certain amount of unbound protein in the sample, that could not be inactivated by the picosecond irradiation. In order to correct the measured inactivation for this error, a fraction of the sample solution was spun down before the experiments were conducted, and the activity of the sediment A_{Sed} and the supernatant A_{Sup} were measured. The inactivation IA was than corrected by the factor $(A_{Sed} - A_{Sup})/A_{Sed}$.

Protein activity was measured for different radiant exposures and different numbers of pulses and the corrected inactivation was calculated from these measurements. With single pulses, no inactivation was observed up to a radiant exposure of $50 \, \text{mJ/cm}^2$. With 500 pulses, the protein activity was reduced with a radiant exposure above $10 \, \text{mJ/cm}^2$ (Fig. 7a). After irradiation with $50 \, \text{mJ/cm}^2$, proteins were inactivated by nearly 40%. After an irradiation with 10^4 pulses the effect was even stronger. $10 \, \text{mJ/cm}^2$ gave nearly 40% inactivation, and with $50 \, \text{mJ/cm}^2$ the activity was reduced by almost 70%. The dependance of the inactivation on the number of pulses was measured for $50 \, \text{mJ/cm}^2$ (Fig. 7b).

3.2. Temperature calculation

The temperature distribution inside and in the surroundings of a 15 nm gold particle immersed in water was calculated for a 50 ps rectangular laser pulse at different times after the beginning of the pulse (Fig. 8). Since the thermal diffusivity of gold is nearly 900 times larger than that of water, the temperature inside the particle stays constant across the radius during the cooling: The temperature in the center exceeds the temperature at the rim only by a few percent. In contrast, the temperature decreases quite rapidly in the surrounding of the particle. At the distance of 10 nm from the particle surface, the temperature reaches less than 5% of the temperature of the surface. 10 nm is the approximate size of aP, which is bound to the surface of the gold particles. Therefore, a strong temperature gradient along the proteins is expected. After the end of the laser pulse, the particle rapidly cools down within hundreds of picoseconds (Fig. 8b). 400 ps after the beginning of the pulse the surface has only 10% of the maximal temperature which is reached at the end of the pulse.
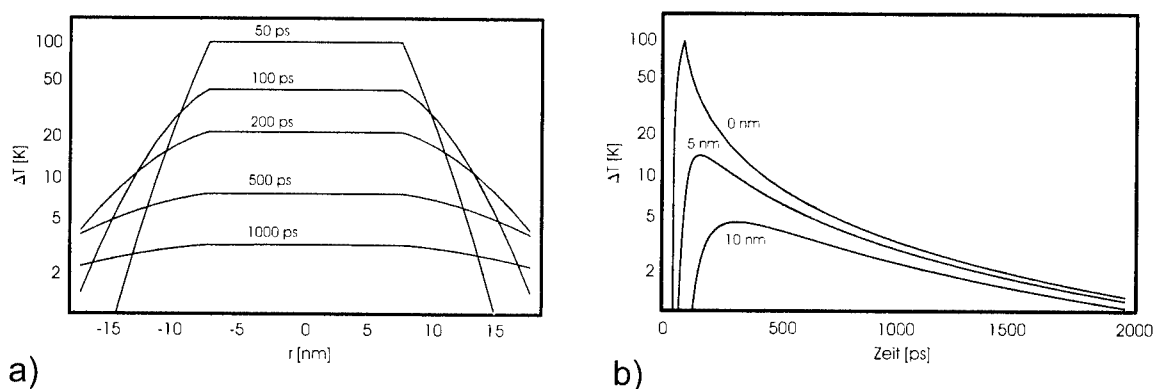
Figure 8. a) Temperature distribution inside and around a 15 nm gold particle when irradiated with 1 mJ/cm² at various times after the beginning of the irradiation. b) Change of the temperature with time at the surface, in 5 nm and 10 nm distance from the surface.

4. DISCUSSION

Aim of these experiments was to investigate whether it is possible to inactivate proteins which are bound to nanometer-sized gold particles by picosecond laser irradiation. Ultra short pulses were used in order to prevent heat diffusion to the surrounding water. Due to the high absorption of the gold particles, extremely high temperatures can be reached at the surface of the particles with pulses of 50 ps width. The temperature is increased by approximately 100 K with every mJ/cm² radiant exposure. These temperatures are localized in a volume with a diameter of 35 nm and last only a few hundred picoseconds. Under these conditions, a reduction of the activity of proteins which were bound to the gold particles was observed, when the samples were irradiated with multiple pulses. With 500 pulses, inactivation started above 10 mJ/cm² and increased more or less linearly with the radiant exposure. With 10^4 pulses, an inactivation of 40% was observed even below 10 mJ/cm². As multiple pulses were used, the degree of inactivation increased with the number of pulses. Therefore, a certain additivity of the effect was observed. Assuming all pulses act independently from each other, an exponential dependence of IA on the number of pulses is expected:

$$IA(N) = 1 - e^{-\alpha N}. \tag{7}$$

α gives the probability that a protein is damaged by one pulse. The measured increase of the inactivation with the number of pulses used for irradiation roughly shows this relationship.

The dependence of the inactivation on the radiant exposure is determined by the damage mechanism. Possible mechanisms are a thermal inactivation, mechanical destruction due to shock waves or evaporation of the water and photochemistry. In principle, a thermal inactivation of aP could be possible with in 10 ps. From inactivation experiments of aP solutions which were heated in a water bath, a frequency factor $A_0 = 1.85 \times 10^{23}$ and activation energy $E_a = 161$ kJ/mol were obtained as parameters for the Arrhenius equation, which describes the thermal damage rate k_{TD} at temperatures below 100°C:[23]

$$k_{TD} = A_0 e^{-\frac{E_a}{RT}}. \tag{8}$$

R is the universal gas constant. If the Arrhenius equation is extrapolated to damage rates of 10^{11} 1/s, a temperature of 410°C is expected to be necessary for a thermal protein inactivation within 10 ps. According to the temperature calculations (Fig. 8), these temperatures are achieved at the surface with an radiant exposure of 4.5 mJ/cm², whereas at a distance of 10 nm at least 90 mJ/cm² is necessary to reach 410°C. Even if the extrapolation of the Arrhenius equation into the picosecond range gave valid data, the extreme temperature gradient over the protein with an extend of 10 nm makes it very difficult to compare the results of the experiment with the Arrhenius theory.

In general, a sharp increase of the inactivation with increasing radiant exposure is expected for a thermal damage mechanism, since the damage rates depend exponentially on the temperature. This was not observed in the experiments. When the laser beam is scanned in the volume, the sharp increase of the inactivation is washed out, because,

although the average radiant exposure is quite homogeneous, the damage rates vary strongly in the sample, being highest at the maxima of the 16 beam position. If not the the surface temperature, but the temperature in some distance from the particle were responsible for the thermal protein damage, this would also lower the slope of the inactivation curves.[23]

With the mathematical model form Sect. 3.2, a particle temperature of nearly 5000°C is calculated at a radiant exposure of 50 mJ/cm². This is well above the boiling point of gold. However, as gold melts at temperature of 1064°C, the absorbed energy is partly needed as latent heat for the melting process. With 15.5 kJ/mol, the latent heat is large enough to heat solid gold particles by 620 K. After melting, density, heat capacity, and thermal conductivity do not change very much.[24,25] However, the complex index of refraction changes, and this will lower the absorption by 50%.[26] A simple estimation, which takes these effects into account, a particle temperature of 1700°C at 50 mJ/cm². These calculations do not account for the change of the properties of water with increasing temperature. As soon as water is evaporated, a gas bubble may be formed which insulates the particle from the surrounding water. In this case, the temperature could rise significantly since in the absence of heat conduction 1 mJ/cm² causes a temperature increase of 285 K instead of 100 K. This vapor bubble may also destroy the proteins or detach them from the surface of the particles.

It may also be possible that the aP lost its activity due to photochemical processes. Two different mechanisms are possible. Under irradiation with the picosecond pulses electrons, which oxidize the Amino acids in the aP, may be injected from the gold particles into water.[27] The second photochemical mechanism uses a direct 2-photon excitation of the protein. Aromatic amino acids decompose with a quantum efficiency η_{PD} of a few percent if excited with cw-irradiation at 254 nm.[28] For an irradiation with N the damage rate k_{PD} can be estimated with following equation:

$$k_{PD} = N\,\eta_{PD}\,\sigma_{2ph}\left(\frac{E}{\tau\frac{h\,c_0}{\lambda}}\right)^2 .\tag{9}$$

Assuming a 2-photon absorption cross-section σ_{2ph} of 10^{50} cm²s/photons,[29] a radiant exposure $E = 50$ mJ/cm², and a quantum efficiency for photodamage of 5%, the damage rate caused by the 2-photon absorption is $7 \cdot 10^7$ 1/s. This is approximately three orders of magnitude too slow in order to destroy the proteins during the pulse width τ which was 35 ps. A destruction of free proteins in solution is therefore not expected with these laser parameters. However, the electric field of the irradiation can be increased by several orders of magnitude at the surface of metallic particles. This effect causes increased Raman emission, known as the SERS effect. Also, an increase of the 2-photon absorption from molecules at the surface from metallic particles was observed.[30] Therefore, the proteins could also be destroyed by a "surface enhanced" 2-photon photochemistry.

In conclusion, protein inactivation is possible via nanoparticles and picosecond laser pulses. The confinement of the heat to the nanoabsorbers when irradiating with picosecond pulses suggests that a denaturation of single proteins in cells could be possible with this approach. However, the mechanism of protein inactivation which is part of present investigations is crucial for the precision of these nanoeffects.

ACKNOWLEDGMENTS

REFERENCES

1. N. Ponelies, J. Scheef, A. Harim, G. Leitz, and K. O. Greulich, "Laser micromanipulators for biotechnology and genome research," *J. Biotechnol.* **35**, pp. 109–120, 1994.
2. K. Schütze, I. Becker, K. F. Becker, S. Thalhammer, R. Stark, W. M. Heckl, M. Böhm, and H. Pösl, "Cut out or poke in — the key to the world of single genes: Laser micromanipulation as a valuable tool on the look-out for the orign of disease," *Genet. Anal.* **14**, pp. 1–8, 1997.
3. R. R. Anderson and J. A. Parrish, "Selective photothermolysis: Precise microsurgery by selective absorption of pulsed radiation," *Science* **220**, pp. 524–527, 1983.
4. C. Dierickx, M. B. Alora, and J. S. Dover, "A clinical overview of hair removal using lasers and light sources," *Dermatol. Clin.* **17**, pp. 357–666, 1999.

5. M. J. C. Van Gemert, A. J. Welch, J. W. Pickering, and T. O. T., "Laser treatment of port wine stains," in *Optical-Thermal Response of Laser-Irradiated Tissue*, A. J. Welch and M. J. C. Van Gemert, eds., pp. 789–829, Plenum Press, New York, 1995.

6. M. Landthaler, U. Hohenleutner, and T. A. el Raheem, "Laser therapy of childhood haemangiomas," *Br. J. Dermatol.* **133**, pp. 275–281, 1995.

7. J. Roider, F. Hillenkamp, T. Flotte, and R. Bringruber, "Microphotocoagulation: Selective effects of repetitive short laser pulses," *Proc. Natl. Acad. Sci. U.S.A.* **90**, pp. 8643–8647, 1993.

8. F. H. Johnson, H. Eyring, and B. J. Stover, *The theory of Rate Processes in biology and medicine*, Wiley, New York, 1974.

9. J. Pearce and S. Thomsen, "Rate process analysis of thermal damage," in *Optical-Thermal Response of Laser-Irradiated Tissue*, A. J. Welch and M. J. C. Van Gemert, eds., pp. 561–606, Plenum Press, New York, 1995.

10. G. A. Griess, M. F. Blankenstein, and G. G. Williford, "Ocular damage from multiple-pulse laser exposures," *Health Phys.* **39**, pp. 921–927, 1980.

11. W. T. Ham Jr., H. A. Mueller, M. L. Wolbarsht, and D. H. Sliney, "Evaluation of retinal exposures from repetitively pulsed and scanning lasers," *Health Phys.* **54**, pp. 337–344, 1988.

12. J. Roider, J. Traccoli, N. Michaud, T. Flotte, R. Anderson, and R. Birngruber, "Selektiver Gefäßverschluß durch repetierende kurze Laserpulse.," *Ophthalmologe* **91**, pp. 274–279, 1994.

13. G. Hüttmann and R. Birngruber, "On the possibility of high-precision photothermal microeffects and the measurement of fast thermal denaturation of proteins," *IEEE J. Select. Topics Quantum Electron.* **5**, pp. 954–962, 1999.

14. G. Jori and J. D. Spikes, "Photothermal sensitizers: possible use in tumor therapy," *J. Photochem. Photobiol. B.* **6**, pp. 93–101, 1990.

15. D. G. Jay, "Selective destruction of protein function by chromophore-assisted laser inactivation," *Proc. Natl. Acad. Sci. U.S.A.* **85**, pp. 5454–5458, 1988.

16. J. C. Liao, J. Roider, and D. G. Jay, "Chromophore-assisted laser inactivation of proteins is mediated by the photogeneration of free radicals," *Proc. Natl. Acad. Sci. U.S.A.* **91**, pp. 2659–2663, 1994.

17. M. Soncin, A. Busetti, F. Fusi, G. Jori, and M. A. Rodgers, "Irradiation of amelanotic melanoma cells with 532 nm high peak power pulsed laser radiation in the presence of the photothermal sensitizer cu(ii)-hematoporphyrin: a new approach to cell photoinactivation," *Photochem. Photobiol.* **69**, pp. 708–712, 1999.

18. A. Busetti, M. Soncin, E. Reddi, M. A. Rodgers, M. E. Kenney, and G. Jori, "Photothermal sensitization of amelanotic melanoma cells by Ni(II)-octabutoxy-naphthalocyanine," *J. Photochem. Photobiol. B.* **53**, pp. 103–109, 1999.

19. M. Saeed, D. Kim, and L. DiMauro, "Optimization and characterization of a high repitition rate, high intensity Nd:YLF regenerative amplifier," *Appl. Opt.* **29**, pp. 1752–1757, 1990.

20. H. C. van de Hulst, *Light scattering by small particles*, Dover Publications Inc., New York, 1981.

21. H. Goldenberg and C. J. Tranter, "Heat flow in an infinite medium heated by a sphere," *Brit. J. Appl. Phys.* **3**, pp. 296–298, 1952.

22. R. Roider and R. Birngruber, "Solution of the heat conduction equation," in *Optical-thermal response of laser-irradiated tissue*, J. Welch, A and M. J. C. van Gemert, eds., pp. 385–409, Plenum Press, New York, 1995.

23. J. Serbin, *Wechselwirkung von Gold-Protein-Konjugaten mit ultrakurzen Laserpulsen.* PhD thesis, Technical University München, 2000.

24. R. C. Weast, M. J. Astle, and W. H. Beyer, *CRC Handbook of Chemistry and Physics*, CRC Press, Boca Raton, Florida, 68 ed., 1987.

25. D. R. Lide and H. P. R. Frederikse, *CRC Handbook of Chemistry and Physics*, CRC Press, Boca Raton, New York, London, Tokyo, 76 ed., 1995.

26. U. Kreibig and M. Vollmer, *Optical Properties of Metal Clusters*, vol. 25 of *Springer Series in Material Science*, Springer, Berlin, Heidelberg, 1995.

27. J. Z. Zangh, B. A. Smith, A. E. Faulhaber, K. J. Andersen, and T. J. Rosales, "Femtosecond studies of colloidal metal nano-particles: Dependence of electronic energy relaxation on the liquid-solid interface and particle size.," in *Ultrafast Processes in Spectroscopy*, O. Svelto, ed., pp. 561–565, Plenum Press, New York, 1996.

28. D. N. Nikogosyan and G. Helmut, "Laser-induced photodecomposition of amino acids and peptides: Extrapolation to corneal collagen," *IEEE J. Select. Topics Quantum Electron.* **5**, pp. 1107–1115, 1999.

29. Y. W. Xu, J. R. Zhang, Y. M. Deng, L. K. Hui, S. P. Jiang, and S. H. Lian, "Fluorescence of proteins induced by two-photon absorption," *J. Photochem. Photobiol. B.* **1**, pp. 223–7, 1987.

30. G. Peleg, A. Lewis, O. Bouevitch, L. Loew, D. Parnas, and M. Linial, "Giant optical non-linearities from nanoparticle-enhanced molecular probes with potential for selectively imaging the structure and physiology of nanometric regions in cellular systems," *Bioimaging* **4**, pp. 215–224, 1996.

Effect of Fiber Optic Probe Design on Fluorescent Light Propagation in Tissue

T. Joshua Pfefer[a], Kevin T. Schomacker[a], and Norman S. Nishioka[a,b] *

[a]Wellman Laboratories of Photomedicine and [b]Gastrointestinal Unit, Massachusetts General Hospital, Harvard Medical School, Boston, Massachusetts 02114 USA

ABSTRACT

Fiber optic probes used to deliver and collect light for biomedical fluorescence spectroscopy applications have varied widely in design. Critical design parameters include fiber diameter, tissue-fiber tip spacing, and illumination-collection fiber separation distance. While device design has been shown to influence spectral distributions, previous studies have not thoroughly addressed how probe geometry affects the spatial origin of detected fluorescence or how probe design might be customized for specific tissue sites or applications. We have developed a Monte Carlo model of laser-induced fluorescence and investigated the effect of design parameters on light propagation using gastrointestinal tissue optical properties. The distribution of emission locations for detected fluorescence were calculated. Initial results indicated that average fluorescence emission depth and total signal intensity are highly dependent on fiber size and tissue-fiber spacing. The implications of these results for the optimization of probes used in the detection of neoplasia are discussed.

Keywords: fluorescence spectroscopy, numerical modeling, fiber optic probe, Monte Carlo

1. INTRODUCTION

Laser-induced fluorescence (LIF) spectroscopy has shown potential in the detection of cancer and dysplasia[1] as well as in monitoring treatments such as photodynamic therapy,[2] photocoagulation[3] and ablation.[4] While both imaging and "single-point" approaches to fluorescence can be effective, the latter enables easier quantitative measurement of LIF signals. The flexibility and small size of optical fibers have enabled clinical LIF with non-imaging probes in a wide variety of sites including the colon,[5] esophagus,[6] bladder,[7] cervix,[8] and lungs.[9]

A number of different probe designs have been implemented in LIF studies, from single-[5,10] and double-fiber[11,12] designs to multi-fiber probes with different fiber sizes, excitation/collection fiber arrangements and spacer sizes.[8,13] While fundamental tissue optics mechanisms involved in fiber-based LIF are well understood, the manner in which these mechanisms affect fluorophore detection for different illumination-collection geometries has not been studied thoroughly.

The influence of fiber geometry on LIF has been investigated to a limited degree in previous experimental studies. The effect of changing fluorescence collection geometry from a single to multiple-fiber style was shown to increase blood absorption effects in LIF spectra taken *in vitro*.[14,15] Other studies have investigated the effect of fiber probe design on photosensitizer fluorescence measurement for concentration determination and dosimetry monitoring during photodynamic therapy (PDT)[16] as well as near IR reflectance spectroscopy.[17]

Theoretical modeling with the Monte Carlo (MC) method has helped to improve understanding of light propagation during diagnostic procedures.[18,19] MC modeling has been used to reconstruct autofluorescence spectra[20-22] in order to investigate variations in fiber separation distance[22] and tissue morphology.[21] Using a multi-layered approach to simulating light transport, DaCosta et al.[23] investigated spectral variations as a function of colonic polyp type and fiber optic probe design (multifiber contact probe and imaging).

An alternative way to present LIF data – one which is more useful when the goal is to target specific fluorophores or chromophores – involves identifying the origin of detected fluorescence signals. This approach has been used to investigate light propagation in arterial tissue with analytical modeling and experiments[4] as well as for presenting MC modeling results for normal and atherosclerotic aorta.[18]

In the present study, we have investigated the influence of fiber optic probe design parameters on the depthwise distribution of remitted fluorescence using a computational model. Our goal was to identify trends and effects which might be exploited to optimize probe design for specific applications.

2. METHODS

Computational modeling of laser and fluorescent light propagation was performed using custom-designed software based on the three-dimensional, non-weighted photon Monte Carlo technique.[24,25] This approach involves the use of stochastic relations which describe the random walk of "photons" through tissue. Geometric parameters, tissue optical properties and randomly generated numbers are used in these equations to determine the location and angle of photon launch, step size, trajectory changes at scattering and emission sites, reflection and refraction at changes in index of refraction, and absorption. As the number of photons simulated increases, the results converge on a solution. A more detailed description of the MC technique and its implementation is available in the literature.[24]

Photons were emitted at random, uniformly-distributed locations across the fiber surface and over a range of angles within the acceptance angle (12.5° corresponding to a numerical aperture of 0.22). Absorption of an excitation photon was always followed by the emission of a fluorescence photon, thus providing a homogeneous quantum yield of unity throughout the tissue. Final termination of a photon was brought about by absorption of a fluorescence photon, or by escape of a photon (excitation or fluorescence) at a tissue boundary.

A cylindrical tissue region 5.0 mm in diameter and 2.5 mm in depth was simulated. Fluorescence photon absorption/emission events were recorded using 100x100 (radial x axial dimensions) grids of 25x25 μm elements. Extending the tissue boundaries beyond this size had no significant affect on results. The optical properties used in this study (Table 1) were based on two clinically relevant sets of illumination/collection wavelengths. The wavelength pair 337/450 nm is pertinent to fluorescence-based discrimination of colonic polyps.[5] The wavelength pair 400/630 nm is similar to those used in the detection of high grade dysplasia in the esophagus,[6] as well as the detection and monitoring of porphyrins, which have been noted in a variety of cancers[26,27] and are used extensively in photodynamic therapy (eg. protoporphrin IX and hematoporphyrin derivatives).[28] As illustrated in Figure 1, a homogeneous tissue region was simulated and the model allowed for arbitrary specification of spacer thickness (S) and illumination/collection geometry based on concentric rings (Di, Dc, L).

For each wavelength pair, nine probe geometries were simulated: five single-fiber optical probes without spacers and four single-fiber probes with spacers. A summary of probe geometries tested is listed in Table 2. In order to balance accuracy and computation time, a total of 100,000,000 excitation photons were launched in each simulation. Computation time was approximately 10 hours on a 600 MHz personal computer (Micron Millennia Max, Micron PC, Inc., Meridian, Idaho). Monte Carlo software was developed and executed using C++ (Microsoft Visual C++ 6.0, Microsoft Corporation, Redmond, Washington).
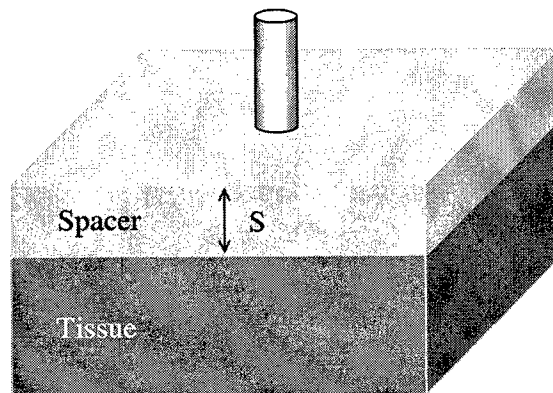
Figure 1. Schematic of the fiber-tissue system simulated. The two primary variables were fiber diameter (D) and transparent spacer thickness (S).

Table 1. Optical properties used in simulations, as estimated from published measurements of colonic and esophageal tissues.[21,29,30]

Wavelength Pairs	μ_a (mm^{-1})	μ_s (mm^{-1})	g	n
Excitation (337 nm)	1.3	20	0.9	1.37
Emission (450 nm)	0.4	10	0.9	1.37
Excitation (400 nm)	1.6	14	0.9	1.37
Emission (630 nm)	0.03	7	0.9	1.37

Table 2. Summary of probe geometries and simulation results. A total of 100,000,000 excitation photons were launched in each simulation. Data for 400 nm is graphed in Fig. 2.

| Probe type | D_i (μm) | S (mm) | 337 nm | | 400 nm | |
			# Photons Detected	80% Probe Depth (μm)	# Photons Detected	80% Probe Depth (μm)
SF100c	100	0	111603	175	151533	200
SF200c	200	0	165382	225	218824	250
SF400c	400	0	244303	300	312800	325
SF600c	600	0	305396	325	382306	375
SF1000c	1000	0	396113	375	489397	450
SF200nc1	200	1.0	65226	275	82413	300
SF200nc5	200	5.0	7912	425	9559	475
SF600nc5	600	5.0	64967	425	79210	475
SF1000nc5	1000	5.0	156296	425	193377	500

3. RESULTS

The outcomes of the eighteen simulations are presented here in various forms to elucidate different light propagation effects. Summaries of the results are provided in Table 2 and Figure 2. This data includes the total number of fluorescence photons detected and the 80% source depth – the depth by which 80% of detected fluorescence was emitted. While Table 2 shows results for both wavelength pairs, the graphical data presented here focuses on the 400/630 nm data. The trends noted in this study were nearly identical for both wavelengths and therefore complete data sets are not presented. There was a strong increase in both the detected signal intensity and the 80% probe depth with fiber size. Spacer presence and thickness tended to decrease the number of photons detected and increase the detection depth.
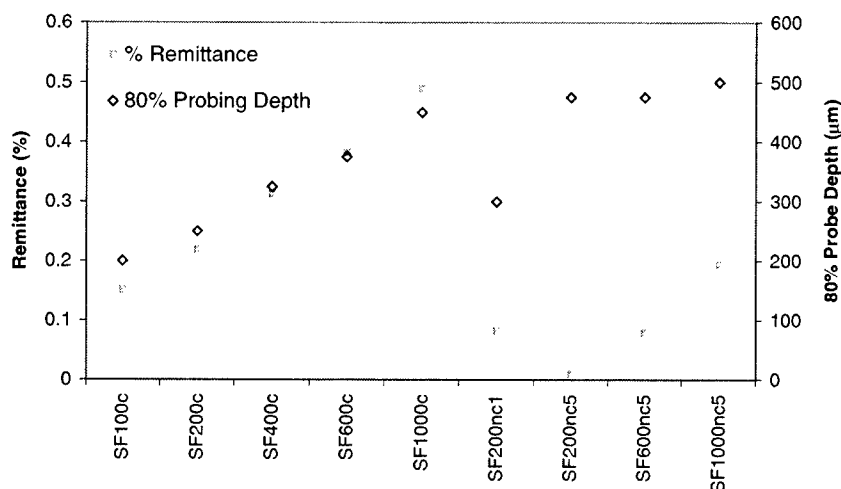
Figure 2. Summary of results for 400/630 nm simulations. Graph includes percent remittance (squares; number of fluorescence photons detected divided by total number of excitation photons launched), and 80% probe depth (diamonds; 80% of detected fluorescence was emitted from this depth or shallower).

The axial distribution of detected fluorescence emission locations is displayed for probes of 0.1 to 1.0 mm diameter in direct tissue contact. These results (Figure 3) are displayed in two different ways: (a) the number of photons emitted from each depth; and (b) the data in (a) normalized to the total number of photons detected. . In general, increased fiber size caused an increase in the fluorescence detected from all tissue depths (Figure 3a) while reducing the change in fluorophore sensitivity with depth (Figure 3b).

Normalized emission distributions (similar to data format in Fig. 3b) are shown in Figure 4 to illustrate the effect of fiber spacer thickness (s = 0, 1.0, 5.0 mm) on selectivity for three fiber diameters (0.2, 0.6, 1.0 mm). For all fiber diameters, the

presence of a spacer decreased the relative sensitivity to the most superficial fluorophores, producing a more homogeneous distribution. This effect was most pronounced on the smallest diameter fiber, whereas with a 5.0 mm spacer, all three geometries showed nearly identical distributions.

An illustration of the effect of fiber separation distance is shown in Figure 5 for a 0.1 mm diameter illumination fiber. This graph represents data collected in a different way than previous graphs. When remission at *any* radial location occurred within the acceptance angle, the photon was binned in a two-dimensional matrix according to the radial remission location and the depth of the emission event. Therefore, each curve represents the axial distribution of fluorescence emission locations detected within the specified 0.05-mm-thick concentric ring. Fluorescence detected within the illumination zone was relatively intense and highly sensitive to superficial fluorophores. The first ring outside the illumination fiber (0.05-0.10 mm) also shows relatively high fluorescence levels, yet is optimally sensitive to subsurface fluorophores, with a peak sensitivity at approximately 0.125 mm. The outer rings show distributions which are more homogeneous and reduced in overall intensity and peaks which become progressively deeper.

(a)

(b)
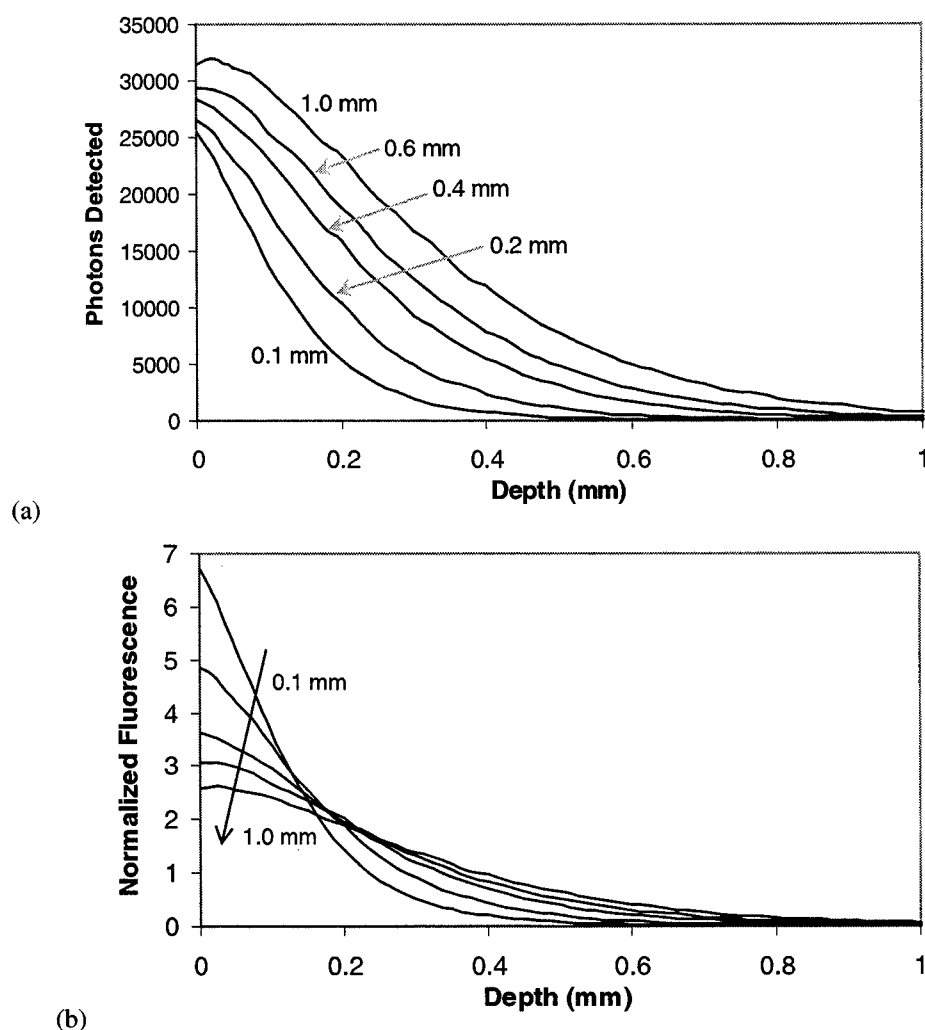
Figure 3. Effect of fiber diameter (0.1 mm to 1.0 mm) on source of detected fluorescence: (a) distribution of fluorescence generation locations for all detected photons; and (b) distribution of fluorescence generation locations normalized to area under curve.
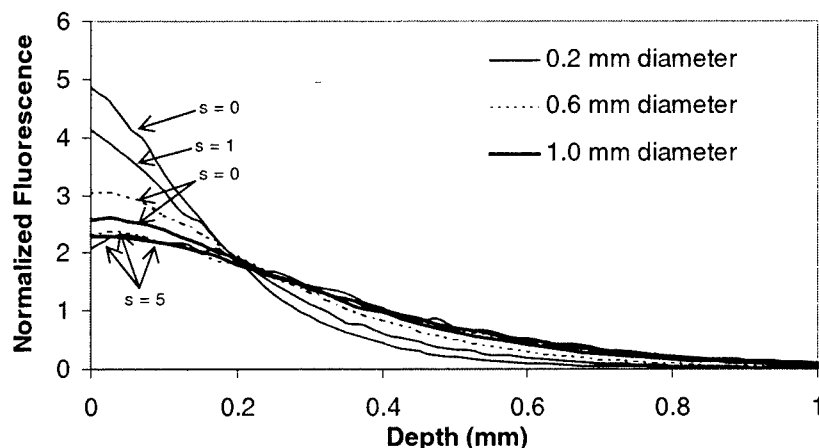
Figure 4. The effect of beam diameter and spacer thickness (s) on the distribution of emission locations for detected fluorescence photons.
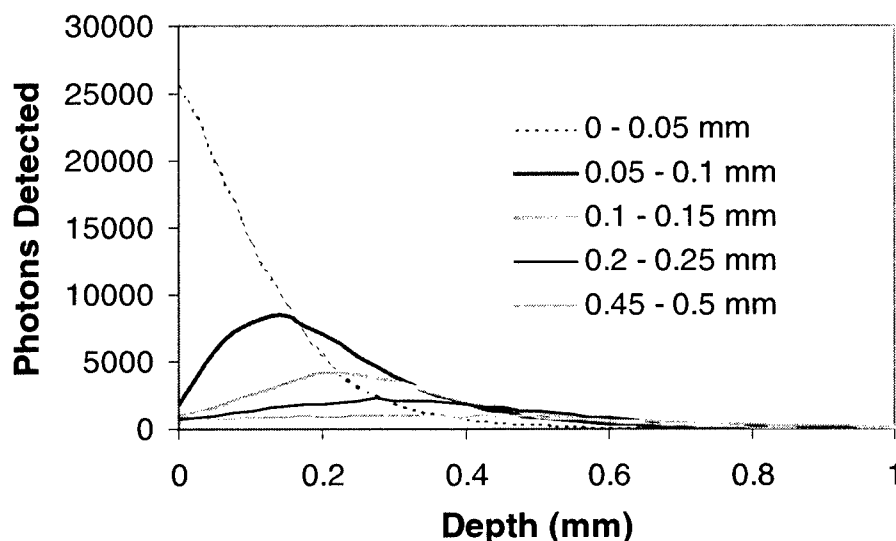
Figure 5. The effect of collection ring location on emission depth distribution for excitation with a 0.1 mm diameter fiber.

4. DISCUSSION

Construction and testing of a large number of optical probes is neither cost- nor time-efficient. Computational modeling provides an efficient way to "experiment" with probe design and identify potentially useful designs or trends. In this section we analyze the results of the MC simulations and discuss their potential exploitation for optimization of LIF-based diagnostic systems. Although this study is primarily focused on gastrointestinal applications such as surveillance for dysplasia in Barrett's esophagus and monitoring of esophageal PDT, a homogeneous tissue geometry was used to provide insight into optical effects which are relevant to a wide variety of applications and tissue sites.

Variations due to excitation/emission wavelength were, for the most part, limited to relatively minor changes in signal intensity and penetration depth. The wavelength pair 337/450 nm produced lower signals and 80% probe depths than 400/630 nm. This was likely due to an absorption level greater than one order of magnitude higher for 337/450 nm. Trends with fiber diameter and spacer distance were similar at both wavelengths. It should be noted, however, that a quantum yield of unity was assumed for all simulations, thus disregarding differences in fluorescence efficiency – which is typically several times higher for 337 than 400 nm excitation.[31]

Variations in fiber diameter had a strong impact on both signal intensity and fluorophore selectivity. The level of fluorescence detected, both from superficial and deeper regions increased with fiber size. However, the increase was greater in deeper regions, thus leading to a more homogeneous probing of tissue fluorophores. In fact, the 80% probing depth of a 1.0 mm fiber was more than twice that of a 0.1 mm fiber. The reason for these changes is that the deeper the location of fluorescence photon emission, the further its remission location tends to be from the excitation photon entry location. A

small diameter fiber is selective for excitation-emission photon pairs that travel a small lateral distance before remission and thus are emitted from superficial regions. Larger diameter fibers, however, can detect photons which have traveled longer distances, and thus show increased sensitivity to deeper fluorophores.

While fiber-tissue separation – by solid spacer or in air – has been implemented in previous studies, we are not aware of any study which analyzes of the effect of this parameter. Our results illustrate that for single fiber probes, spacers increase the homogeneity of sensitivity and average probing depth, but decrease the LIF signal intensity. These effects are linked to the following facts: that a spacer causes an increase in spot size (eg. from 0.2 mm to about 2.4 mm) at the tissue surface, thus improving sensitivity to photons emitted from deeper regions; and that a spacer causes a reduction in the collection efficiency for fluorescence emitted from superficial regions immediately below the fiber. When 5 mm spacers were used, the signal intensity increased dramatically with fiber size – due to the increased detection area – yet the 80% probe depth (~0.5 mm) changed little – because of the reduction in collection efficiency for superficially emitted fluorescence.

The use of separate fibers for illumination and collection significantly altered the tissue volume probed. A multifiber geometry appears to produce subsurface peaks, and as excitation-collection fiber separation distance increases, the depthwise distribution becomes more homogeneous. The primary reason for the transition from surface to subsurface peak in sensitivity is that a large amount of fluorescence is generated in superficial regions directly below the fiber and remitted from the tissue at a location near their point of entry. These photons are efficiently collected by contact, single fiber probes. Spacerless multi-fiber probes do not detect these photons efficiently, but tend to be selective for photons which travel some finite lateral distance away from the entry location.

5. CONCLUSIONS

We have developed and implemented a computational model of laser/fluorescent light propagation to investigate the effect of fiber optic probe design parameters on spatial sensitivity to tissue fluorophores. For the single fiber probe designs studied, an increase in fiber diameter or spacer thickness led to an increase in probing depth and homogeneity of spatial sensitivity. By separating the illumination and collection fibers, the selectivity to emission from different layers can be changed. Based on the trends noted in this study, optimization of probe geometry may be possible through customization of designs to tissue regions/layers of interest. Fiber probes may also be used to provide information about the depthwise distribution of tissue fluorophores. *In vitro* and *in vivo* studies are needed to validate these trends in the lab and evaluate their true utility in a clinical context. In addition to identifying potentially useful optical effects, this study has also demonstrated the power of numerical models in facilitating the optical device design process.

REFERENCES

1. G. Wagnieres, W. Star and B. Wilson, "*In vivo* fluorescence spectroscopy and imaging for oncological applications," *Photochem. Photobiol.*, 68, pp. 603-632, 1998.
2. W. Star, "Light dosimetry *in vivo*," *Phys. Med. Biol.*, 42, pp. 763-787, 1997.
3. J. Tang, F. Zeng, H. Savage, P. Ho and R. Alfano, "Laser irradiative tissue probed *in situ* by collagen 380-nm fluorescence imaging," *Lasers Surg. Med.*, 27, pp. 158-164, 2000.
4. A. Gmitro, F. Cutruzzola, M. Stetz and L. Deckelbaum, "Measurement depth of laser-induced fluorescence with application to laser angioplasty," *Appl. Opt.*, 27, pp. 1844-1849, 1988.
5. K. Schomacker, J. Frisoli, C. Compton, T. Flotte, J. Richter, N. Nishioka and T. Deutsch, "Ultraviolet laser-induced fluorescence of colonic tissue: basic biology and diagnostic potential," *Lasers Surg. Med.*, 12, pp. 63-78, 1992.
6. M. Panjehpour, B. Overholt, T. Vo-Dinh, R. Haggitt, D. Edwards and F. r. Buckley, "Endoscopic fluorescence detection of high-grade dysplasia in Barrett's esophagus," *Gastroenterology*, 111, pp. 93-101, 1996.
7. F. Koenig, F. J. McGovern, H. Enquist, R. Larne, T. F. Deutsch and K. T. Schomacker, "Autofluorescence guided biopsy for the early diagnosis of bladder carcinoma," *J Urol.*, 159, pp. 1871-1875, 1998.
8. N. Ramanujam, M. Mitchell, A. Mahadevan, S. Warren, S. Thomsen, E. Silva and R. Richards-Kortum, "*In vivo* diagnosis of cervical intraepithelial neoplasia using 337-nm-excited laser-induced fluorescence," *Proc. Natl. Acad. Sci.*, 91, pp. 10193-10197, 1994.
9. J. Hung, S. Lam, J. LeRiche and B. Palcic, "Autofluorescence of normal and malignant bronchial tissue," *Lasers Surg. Med.*, 11, pp. 99-105, 1991.
10. D. Braichotte, G. Wagnieres, R. Bays, P. Monnier and H. van den Bergh, "Clinical pharmacokinetic studies of photofrin by fluorescence spectroscopy in the oral cavity, the esophagus, and the bronchi," *Cancer*, 75, pp. 2768-2778, 1995.
11. H. Zeng, C. MacAulay, D. I. McLean and B. Palcic, "Spectroscopic and microscopic characteristics of human skin autofluorescence emission," *Photochem. Photobiol.*, 61, pp. 639-645, 1995.

12. P. Heil, S. Stocker, R. Sroka and R. Baumgartner, "*In vivo* fluorescence kinetics of porphyrins following intravesical instillation of 5-aminolaevulinic acid in normal and tumour-bearing rat bladders," *J Photochem Photobiol B: Biol*, 38, pp. 158-163, 1997.

13. T. Vo-Dinh, M. Panjehpour, B. Overholt, C. Farris and F. Buckley, "Laser-induced differential fluorescence for cancer diagnosis without biopsy," *Appl. Spectros.*, 51, pp. 58-63, 1997.

14. R. Richards-Kortum, A. Mehta, G. Hayes, R. Cothren, T. Kolubayev, C. Kittrell, N. Ratliff, J. Kramer and M. Feld, "Spectral diagnosis of atherosclerosis using an optical fiber laser catheter," *Am. Heart J.*, 118, pp. 381-391, 1989.

15. M. Keijzer, R. Richards-Kortum, S. Jacques and M. Feld, "Fluorescence spectroscopy of turbid media: autofluorescence of the human aorta," *Appl. Opt.*, 28, pp. 4286, 1989.

16. B. Pogue and G. Burke, "Fiber-optic bundle design for quantitative fluorescence measurement from tissue," *Appl. Opt.*, 37, pp. 7429-7436, 1998.

17. G. Kumar and J. Schmitt, "Optimal probe geometry for near-infrared spectroscopy of biological tissue," *Appl. Opt.*, 36, pp. 2286-2293, 1997.

18. A. Welch, C. Gardner, R. Richards-Kortum, E. Chan, G. Criswell, J. Pfefer and S. Warren, "Propagation of fluorescent light," *Lasers Surg. Med.*, 21, pp. 166-178, 1997.

19. E. Okada, M. Firbank, M. Schweiger, S. Arridge, M. Cope and D. Delpy, "Theoretical and experimental investigation of near-infrared light propagation in a model of the adult head," *Appl. Opt.*, 36, pp. 21-31, 1997.

20. H. Zeng, C. MacAulay, D. McLean and B. Palcic, "Reconstruction of *in vivo* skin autofluorescence spectrum from microscopic properties by Monte Carlo simulation," *J Photochem. Photobiol. B*, 38, pp. 234-240, 1997.

21. G. Zonios, R. Cothren, J. Arendt, J. Wu, J. Van Dam, J. Crawford, R. Manoharan and M. Feld, "Morphological model of human colon tissue fluorescence," *IEEE Trans. Biomed. Eng.*, 43, pp. 113-122, 1996.

22. S. Avrillier, E. Tinet, D. Ettori, J. Tualle and B. Gelebart, "Influence of the emission-reception geometry in laser-induced fluorescence spectra from turbid media," *Appl. Opt.*, 37, pp. 2781-2787, 1998.

23. R. DaCosta, L. Lilge, J. Kost, M. Cirroco, S. Hassaram, N. Marcon and B. Wilson, "Confocal fluorescence microscopy, microspectrofluorimetry, and modeling studies of laser-induced fluorescence endoscopy (LIFE) of human colon tissue," Proc. SPIE 2975, pp. 98-107, 1997.

24. L. Wang, S. L. Jacques and L. Zheng, "MCML - Monte Carlo modeling of light transport in multi-layered tissues," *Comput. Methods Programs Biomed.*, 47, pp. 131-146, 1995.

25. S. L. Jacques and L. Wang, "Monte Carlo modeling of light transport in tissues," in *Optical-Thermal Response of Laser-Irradiated Tissue*, A. J. Welch and M. J. C. van Gemert, eds., Plenum Press, 1995.

26. M. Inaguma and K. Hashimoto, "Porphyrin-like fluorescence in oral cancer," *Cancer*, 86, pp. 2201-2211, 1999.

27. D. Harris and J. Werkhaven, "Endogenous porphyrin fluorescence in tumors," *Lasers Surg. Med.*, 7, pp. 467-472, 1987.

28. D. Robinson, H. de Bruijn, N. van der Veen, M. Stringer, S. Brown and W. Star, "Fluorescence photobleaching of ALA-induced protoporphyrin IX during photodynamic therapy of normal hairless mouse skin: the effect of light dose and irradiance and the resulting biological effect.," *Photochem. Photobiol.*, 67, pp. 140-149, 1998.

29. R. Bays, G. Wagnieres, D. Robert, D. Braichotte, J. Savary, P. Monnier and H. van den Bergh, "Clinical determination of tissue optical properties by endoscopic spatially resolved reflectometry," *Appl Opt*, 35, pp. 1756-1766, 1996.

30. R. Marchesini, E. Pignoli, S. Tomatis, S. Fumagalli, A. Sichirollo, S. Di Palma, M. Dal Fante, P. Spinelli, A. Croce and G. Bottiroli, "*Ex vivo* optical properties of human colon tissue," *Lasers Surg Med*, 15, pp. 351-357, 1994.

31. R. Richards-Kortum, R. P. Rava, R. E. Petras, M. Fitzmaurice, M. Sivak and M. S. Feld, "Spectroscopic diagnosis of colonic dysplasia," *Photochem. Photobiol.*, 53, pp. 777-786, 1991.

Deep Penetration of Light into Biotissue

Edward D. Bearden[a], James D. Wilson[a], Vladimir P. Zharov[b], and Curtis L. Lowery[c]
[a] University of Arkansas at Little Rock, Applied Science Department, Little Rock, AR 72204 USA
[b] University of Arkansas for Medical Sciences, Philips Classic Laser Biomedical Laboratory
[c] University of Arkansas for Medical Sciences, Department of Obstetrics and Gynecology

ABSTRACT

The results of a study of deep (several centimeters) light penetration into biological tissue are presented in order to estimate its significance to potentially photosensitive structures and processes including the fetal eyes. In order to accomplish this goal, samples of various tissues (fat, muscle, and uterus) from surgical patients and autopsies were examined with a double integrating sphere arrangement to determine their optical properties. The results were implemented in a Monte Carlo modeling program. Next, optical fiber probes were inserted into the uterus and abdominal wall of patients undergoing laparoscopic procedures. The fibers were couples to a photomultiplier tube with intervening filters allowing measurements of light penetration at various wavelengths. To determine the feasibility of stimulation *in utero*, a xenon lamp and waveguide were used to transilluminate the abdomen of several labor patients. Light in the range of 630 to 670 nm where the eye sensitivity and penetration depth are well matched, will likely provide the best chance of visual stimulation. Fetal heart rate, fetal movement, and fetal magnetoencephalography (SQUID) and electroencephalography (EEG) were observed in different studies to determine if stimulation had occurred. Since internal organs and the fetus are completely dark adapted, the amount of light required to stimulate in our opinion could be on the order of 10^{-8} Watts.

Keywords: Fetal stimulation, scattering, visible light, evoked potential, optical penetration

1. INTRODUCTION

The majority of the body of research concerning visible light and its interaction with human tissue has focused on penetration to depths of only a few millimeters. The primary focus of the work presented here is to determine the feasibility of transilluminating the maternal abdomen for the purpose of visually stimulating the fetus for assessing physiological and neurological well being. However, the procedures and problems encountered would be applicable in other studies of deep penetration. There is a potential for a variety of uses of deeply penetrating light. For instance, photothermal and photochemical treatment of diseases of internal organs and breast cancer. However, much of this work has involved wavelengths outside the visible range.[1] Ramanujam *et al.* have studied fetal brain oximetry using near infrared wavelengths.[2,3] In the attempt to stimulate the fetus with visible light, the power of the incident light must be sufficient to penetrate multiple tissue layers but not cause any damage to the maternal tissue or the fetal eyes. The results of a similar study which was performed on rats and guinea pigs showed that a significant amount of light was transmitted through the abdominal and uterine walls. However, the depths encountered in that study were in the range of 5 mm or less.[4]

There has been little work published in the area of deep penetration with visible or near infrared light. Extensive and accurate measurements of the abdominal penetration *in vivo* are difficult to perform and limited due to medical-legal implications. These limitations required the supplemental use of theoretical calculations and the measurements of *ex vivo* tissue.
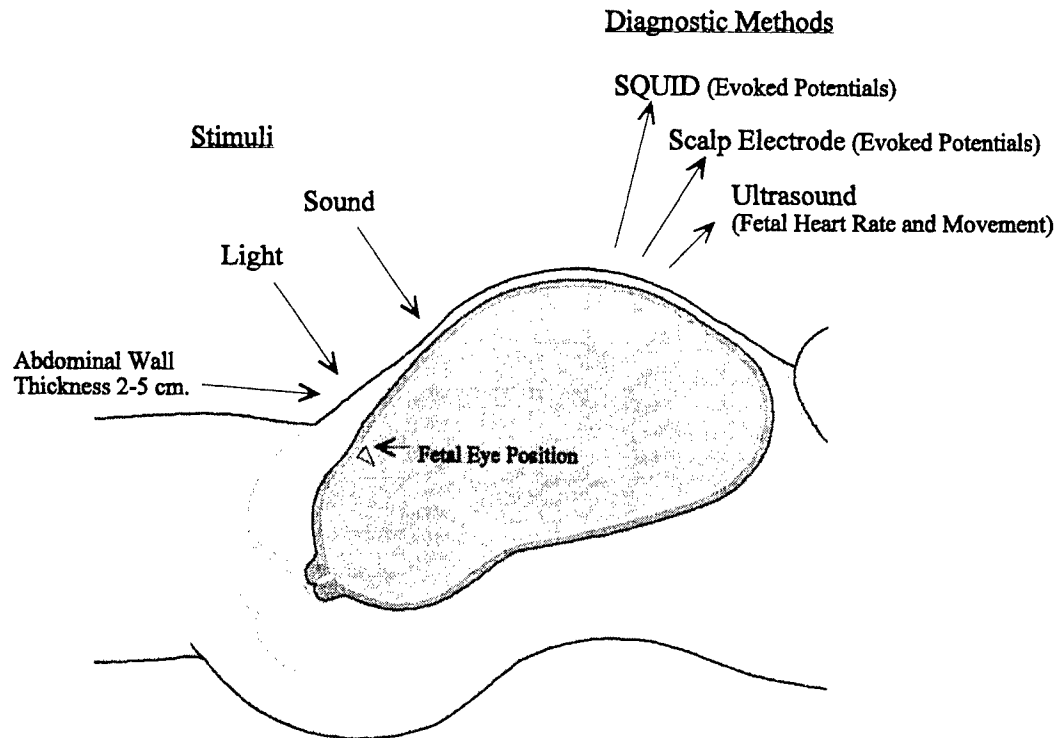
Figure 1. Principle fetal stimulation and diagnostic responses. Using sound and light to stimulate the fetus, physiological and neurological responses may be used as diagnostic tools.

To assess the feasibility of deeply penetrating light for use as a visual stimulus, both direct and indirect measurement methods were employed. Optical fibers with an isotropic scattering tip were used to measure the fluence rate of light in the abdomen and in the uterus. In addition, a xenon light source was used to transilluminate the abdomen of pregnant patients in labor and the response of the fetus was monitored.

For the theoretical calculations of light transport, the Monte Carlo method was used. It was necessary to establish the optical parameters of the abdominal tissues at visible wavelengths. Some published data were available, however, there were some values that were not found. The scattering coefficient, absorption coefficient, and anisotropy factor for adipose, abdominal muscle, and uterus were calculated using measurements from a double integrating sphere apparatus. In addition, the optimal wavelength(s) to use for visual stimulation in the given environment was assessed based upon penetration data and responsivity of the eyes.

2. MATERIAL AND METHODS

2.1 *In Vivo* Study.

In order to implement the Monte Carlo simulations for modeling transport of the light into the abdomen, it was necessary to determine the optical properties of the abdominal tissues. These properties were measured with a double integrating sphere arrangement. Two six inch diameter integrating spheres (Labsphere model IS-060) were used. The light sources used were available lasers (543.5nm HeNe, 632nm HeNe, 640nm diode, 674nm diode). While these sources did not provide continuous wavelength data for a detailed spectrum of optical properties, they were sufficient to provide an idea of the properties at wavelengths which were previously unreported. This data should be useful for other studies of visible light-tissue interactions. Abdominal muscle and adipose tissue samples were excised during autopsies. Uterine tissue samples were excised from non-cancerous uteruses immediately following hysterectomies. Skin samples were not analyzed in this study; published data and estimates of the optical properties were used. The tissue samples were chilled and then sliced in varying thicknesses from 200 µm to 1 mm and sealed between microscope slides. The tissue was not frozen or placed in

chemical solutions in an attempt to keep the mechanical structure and chemistry of the tissue close to its natural state. This increased the difficulty of tissue slicing and preparation. However, care was taken to insure that samples were reasonably consistent in thickness and blood content and were not compressed between the microscope slides other than the amount that was necessary to insure good contact with the slide. Tissue samples with holes, tears, or other anomalies were discarded. Microscope slide covers were used for spacing to maintain a constant distance between the slides and prevent compression. Saline (0.9%) was injected between the slides to insure that no air pockets were present. The slides were placed between the two spheres in the beam path of the laser, reflection and transmission data were recorded. This was repeated two additional times after moving the sample so that the beam was incident on a different location of the tissue each time. The three reflection and transmission measurements of each sample were averaged and the inverse adding doubling algorithm used to calculate the absorption and scattering coefficients and anisotropy factor of the tissue.[5,6] The standard deviations for the values were somewhat large, but this was consistent with the results of other studies.[7] Published values for the optical properties of skin were used.[8] Amniotic fluid was also taken into consideration. The parameters for 0.9% saline were used to simulate amniotic fluid.

Tissue Optical Properties Calculated in This Study.

543 nm	Adipose	Muscle	Uterus	632 nm	Adipose	Muscle	Uterus
μ s	110	103	198	μ s	134	119	154
μ a	1.03	3.81	13	μ a	2.57	2.06	0.91
g	0.66	0.82	0.85	g	0.72	0.63	0.81
640 nm	Adipose	Muscle	Uterus	674 nm	Adipose	Muscle	Uterus
μ s	148	116	140	μ s	160	128	137
μ a	2.17	2.08	0.70	μ a	2.18	1.91	0.60
g	0.77	0.60	0.89	g	0.72	0.67	0.87

Table 1. Abdominal and uterine tissue properties calculated using the inverse adding doubling algorithm. Absorption and scattering values are given in units of cm^{-1}. Values are averages of the data. Variances were large but consistent with other published data.

2.2 Theoretical Approach

The calculated properties were used in a Monte Carlo simulation program (MCML) to model the amount of light penetration at various tissue depths and configurations.[9] The use of theoretical calculations will supplement the *in vivo* measurements to provide an idea of the penetration depths and the distribution of light in the abdominal tissue layers. The Monte Carlo method was chosen because of its wide acceptance and reliability. Other methods such as diffusion theory and path integral are under consideration for alternative methods of modeling. Diffusion theory is of particular interest due to its calculation speed and accuracy at greater depths.

A first step was to determine the range of wavelengths to use. For the purposes of visual stimulation, the range would have to be from approximately 400 nm to 700 nm, with 500 to 550 nm being ideal range to use because it is in this range that the human eye has peak response. However, previous work supported by current measurements indicates that the longer wavelengths penetrate tissue more effectively. Thus there is an inverse relationship between eye sensitivity and depth of penetration. The penetration data in the literature suggested that the optimal wavelength would be in the range of red light (620-700 nm). To verify this tendency, qualitative light penetration measurements of ex-vivo tissue samples were made using a xenon light source (Pentax LX500-A), a monochromator, and an optical power meter (Newport model 835). Well hydrated tissue samples were sliced to thicknesses of less than 1 mm and mounted between microscope slides. (The tissue preparation was the same as that for the samples in the previous section). The monochromator was adjusted to provided an output bandwidth of less than 5 nm. An adjustable aperture was used to create a 3 mm beam. The samples were placed between the power meter detector head and the aperture. Power measurements with and without the intervening samples were made at 10 nm increments. The variations in the output spectrum of the xenon source and effects of the glass slides were taken into consideration. Figure 1 shows the trend of greater penetration through the tissue as wavelength increases. For comparison, the scotopic (dark adapted) luminous efficiency of the human eye is plotted.[10] The scotopic efficiency curve and the tissue transmission curves intersect in the range of 525 to 550 nm. The normalization process and thinness of the samples contribute to this. The wavelength at which the intersections occur will increase as the thickness of the tissue increases. As the tissue becomes thicker, the attenuation grows exponentially. For tissue thicknesses approaching what would be encountered *in vivo*, the optimal wavelength approaches the upper limits of visual efficiency (see Figure 3).

Scotopic Eye Efficiency and Tissue Transmission Data (Normalized)
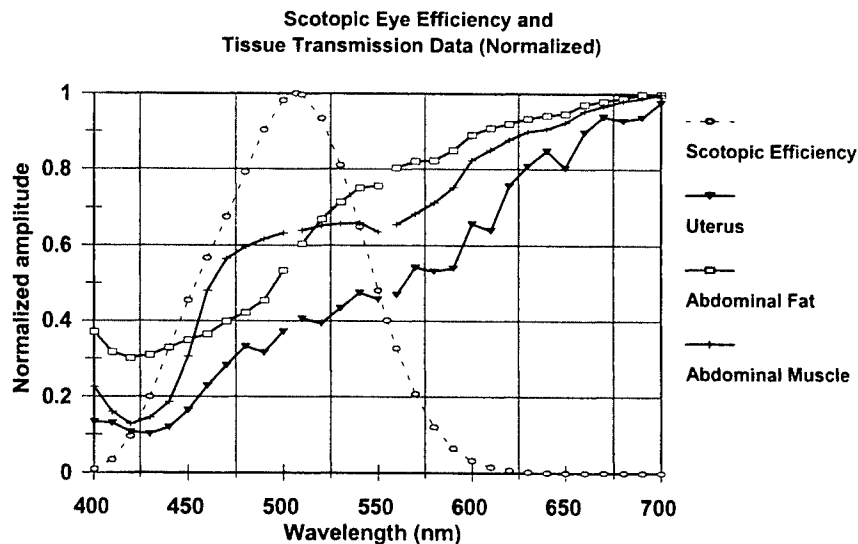
Figure 2. Comparison of the luminous efficiency of the human eye and the transmission of light through three types of tissue. Values have been normalized over the range of 400 to 700 nm. Average tissue thickness was approximately 0.5 mm.

**Scotopic Eye Efficiency and
Tissue Transmission Data (Normalized)**
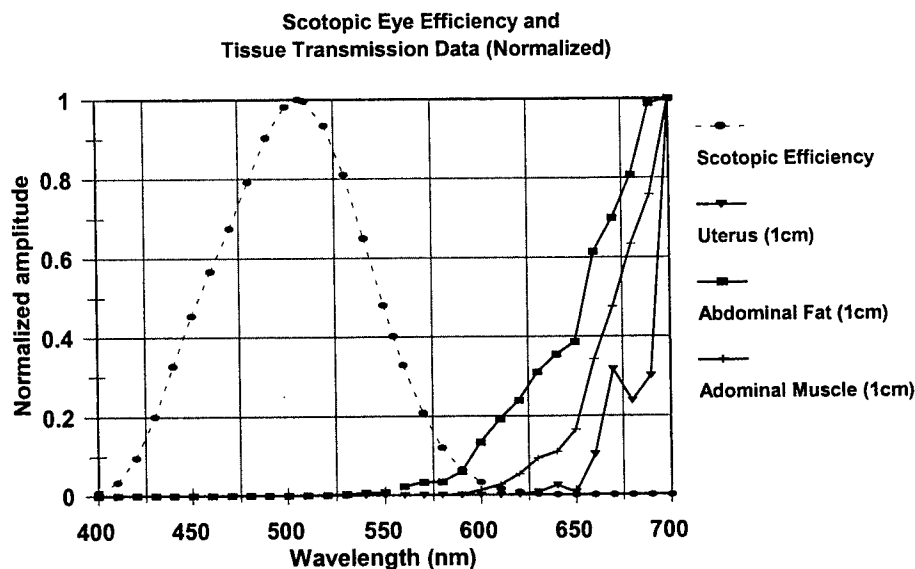
Figure 3. Similar comparison of luminous efficiency and transmission through tissue with tissue thicknesses at 1 cm. Transmission values were again normalized over the visible range.

2.3 Direct Measurements (*In Vivo*)

Clinical *in vivo* measurements were carried out on five patients who were undergoing routine laparoscopic gynecological procedures. After anesthesia was administered, a small (diameter <600 micrometers) optical fiber with an isotropic scattering tip was placed inside the uterus through a uterine manipulator. The intrauterine position of the fiber was estimated using the uterine manipulator and uterine sounds. The fiber was placed inside a polyimide tube which served as a protective sheath in the event that the tip separated from the fiber or the fiber itself was fractured. Although polyimide is not transparent, it was chosen because of its durability and resistance to crimping. (Initially, the protocol was designed to be carried out during amniocentesis where the probes would be inserted through the amnio needle. However, it was determined that this procedure would unnecessarily increase the risk to both patient and fetus due to the extended amount of time which the needle would be located near the fetus.) Another similarly sheathed fiber was inserted into the peritoneal cavity through a laparoscope tube and positioned immediately under the abdominal wall. The position of the fiber tip in the abdominal cavity was located by using the laparoscope. The optical fibers were calibrated in a manner similar to the procedure described in the paper by Marijnissen and Star.[11]

The optical fibers were coupled to a photomultiplier tube (Hamamatsu Model 955) through an interference filter (550, 632, 640, 650, 671, 730, and 800 nm center wavelengths were used individually). The output signal of the PMT was connected to a discriminator/amplifier (Pacific Precision Instruments). The discriminator output was then read via a frequency counter. The light from the xenon source was directed onto the patient's abdomen through a five foot length of a half inch diameter liquid core waveguide (Ray Visions, Inc.). The measured power output through the waveguide ranged from 3 to 5 mW over a 10 nm range (the bandwidth of the interference filters). Results indicated that there is measurable light penetrating the abdominal wall to depths as great as 4 cm, with longer wavelengths penetrating better. However, only inconsistent signals have been detected *in utero*. The distance between the source and the intrauterine detector was on average greater than 6 cm. This is greater than the distance that would be normally encountered between the source and the eyes of the late term fetus. Thus the relaxed, thicker state of the tissues in this study should be an overestimate of the density and thickness of abdominal tissues in a female in the third trimester of pregnancy.

In addition to the above measurements, light penetration was observed in the uterus alone. Ten uteruses were examined following hysterectomy. The optical fiber and sheath were inserted into the uterus through a large gage needle (Cook, 20GXXTW). The depth of the probe tip ranged from 0.5 cm to 2cm. The light guide was held at a constant distance from the surface of the uterus, approximately perpendicular to both the surface and the probe.

The results showed that visible light can penetrate appreciably into the uterus to depths of 2 cm. The attenuation at this depth was on the order of 10^{-4}. Wide variations were evident in all measurements. Much of this could be attributed to the imprecise positions and orientations of the light source and fibers relative to each other. In addition, significant differences

in patients' abdominal and uterine tissues also contribute to the inconsistent results.

These measurements were not rigorous or exhaustive. Rather, the measurements demonstrate that deep penetration is practical and achievable without the use of high power light sources which could be thermally damaging.
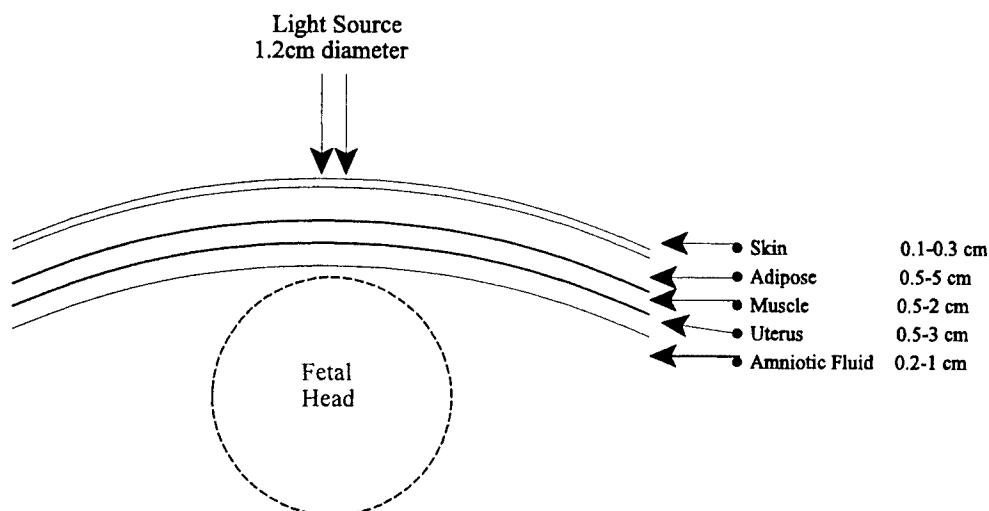

Figure 4. Generalized anatomical geometry of the female abdomen used for modeling.
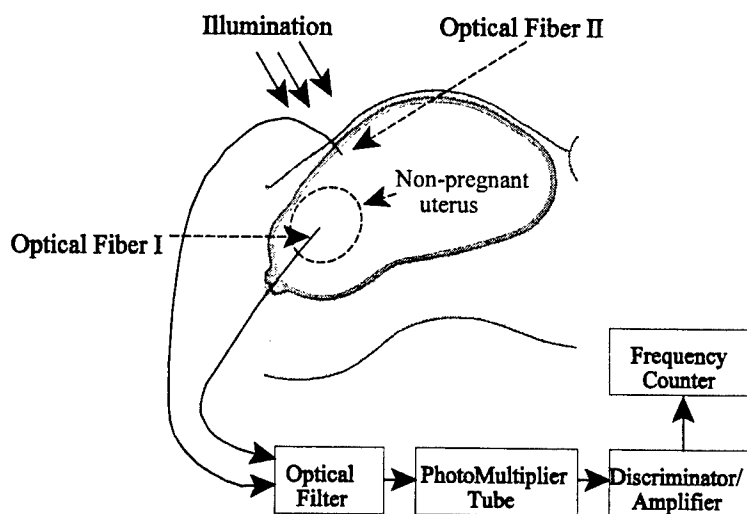A range of tissue thicknesses reflects the differences in the pregnant versus non-pregnant abdomen.

Figure 5. Diagram of instrumentation for measuring attenuation across abdominal and uterine tissue. Non-pregnant patients undergoing routine laparoscopic procedures were recruited for this study. Abdominal wall thickness ranges from 1.5 cm to 4.0 cm. Distance from light source at abdominal surface to intrauterine probe was estimated to be greater than 5 cm. The probes were enclosed in a protective sheath of polyimide.
Optical fiber I was inserted into the uterus through a uterine manipulator. Fiber II was inserted through the laparoscopic port.
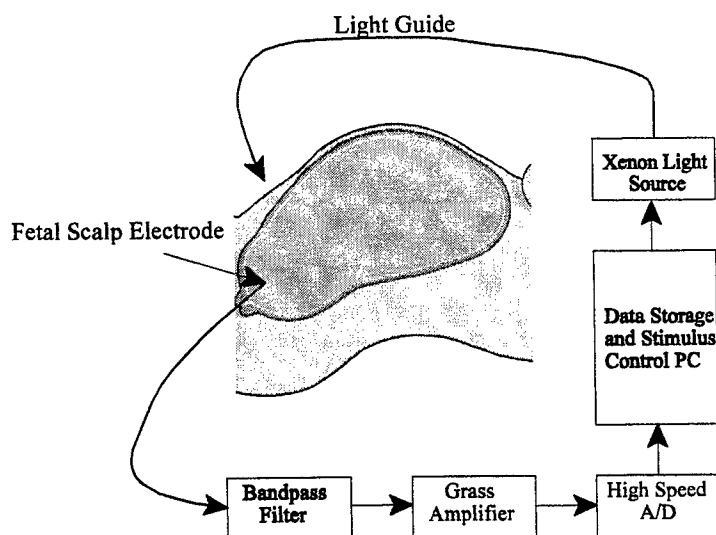
Figure 6. Process for collecting Visual Evoked Potential (VEP) data. Stimulus is a 25 ms. pulse triggered at 0.5 Hz by the PC. The responses from 250 flashes are averaged and the waveform analyzed for VEP patterns.

2.4 Indirect Measurements (*In Vivo*)

To assess the practicality of fetal stimulation, two studies were conducted with late third trimester patients. In the first, the xenon light source and waveguide were used to present white light onto the abdomen of pregnant patients. An ultrasound imaging device was used to locate the eyes of the fetus and to measure the distance from the surface of the maternal abdomen to the fetal eyes. The light was shown on the abdomen in the area of the fetal eyes for 30 seconds and then removed for two minutes. This process was repeated ten times. The fetal heart rate (FHR) was monitored by Doppler ultrasound and the patients asked to report any fetal movement. The results were mixed showing some increase in FHR and fetal activity immediately following the introduction of the light. However, this occurred in only half of the patients. In the patients where a change in FHR was noted, the presence and duration of the increased heart rate tended to diminish after the first few cycles. This could be the result of habituation which has been seen in a similar study of sound stimulation of the fetus.[12]

For the second study, six labor patients with scalp electrodes were recruited. The light source was modified so that an internal shutter was computer controlled to produce a 25 ms flash. The position of the fetal eyes was determined by ultrasound imaging and the light was placed accordingly on the maternal abdomen. The average distance from waveguide to fetal eyes was 3.3 cm. The source was flashed 250 times at 0.5 Hz. To determine if stimulation occurred, the fetal EEG was measured via a fetal scalp electrode (FSE) and analyzed for visual evoked potential (VEP). For comparison, baseline EEG data was collected for the same amount of time during which no light stimulus was present. The preliminary results are encouraging. In the four of the patients tested, a response consistent with VEP in newborns has been observed. No signal was discernible from the remaining two patients. In one case, this may be attributable to a noisy environment and contractions. The signal to noise ratio of the VEP signal has been consistently low. It is believed that this is due to the small amount of light reaching the fetal eyes. Since the exposure time of the light for VEP measurements is short, the amount of incident light may be increased without damage to maternal tissues or the eyes of the fetus. An alternative light source consisting of narrowband, high output LED's which may be operated in a pulse mode to produce above 300 mW is being investigated.

It is important to note that in both of the above studies, the open or closed state of the fetal eyes may be determined with the ultrasound imaging device. However, since the ultrasound imager is not used during the procedures, the position of the eyelids during this time is uncertain. Obviously, this could have a significant effect on the amount of light which reaches the eyes.

3. DISCUSSION

Anecdotal evidence and published work indicate that the dark adapted human eye can detect on the order of 10^{-16} W at 507 nm (green).[13,14] This corresponds to approximately 100 photons per second entering the pupil. Correcting for less sensitivity in the longer red wavelengths, this may be as high as 10^6 photons per second at 680 nm. Assuming that the source incident on the abdomen is on the order of 10^{-3} W and that the power of red light required to stimulate the fetal eyes is on the order of 10^{-12} W, if the attenuation of red light is less than nine orders of magnitude, stimulation should be possible. The results of the direct measurements made during laparoscopy show that it is possible to transmit light through the 1 to 4 cm. thick abdominal wall with three to five orders of magnitude attenuation. These results are consistent with those of Wan *et al.* which indicated three to five orders of attenuation over the range of 600 to 700 nm.[15] The attenuation will of course increase as the abdominal wall thickness increases. While trans-illuminating the abdomen, no consistent amount of light has been detected in the uterus. However, separate measurements on the uterus indicate that appreciable transmission at visible wavelengths is possible to depths of 2 cm. The failure to measure light in the intact uterus may be attributed to imprecise location and orientation of the optical fiber probe. In addition, the patients involved in this part of the study were not pregnant, thus the intervening tissue layers could be significantly thicker and the attenuation much higher. Where direct measurements have failed, theoretical calculations should aid in determining penetration depth and light distributions.

The results of the fetal stimulation studies have been mixed. When presented with a constant light source, fewer than half of the fetuses in the study exhibited a consistent change in heart rate or movement. It was unclear if the changes that were observed were as a direct result of the light or indirect effects from changes in maternal tissue (e.g. thermal effect). The use of VEP measurements provides a more objective method of determining if direct visual stimulation occurred. The data has been collected through a fetal scalp electrode which monitors a single location on the fetal head. The preliminary results of this study have shown what appears to be evoked potentials in a majority of the participating patients. Additional electrode sites would likely provide a more accurate and detailed signal. However, since it is not practical to place multiple scalp electrodes on the fetus, a study using a superconducting quantum interference device (SQUID) array is underway. In that study, the patient is seated, leaning forward with her abdomen pressed against into a molded form which is embedded with an array of sensors capable of sensing magnetic fields on the order of 10^{-15} Tesla. An array of high power LED's located around the abdomen will be used in this study. The total power of the light source will be higher than that used in this paper with the intent of increasing the signal to noise ratio of the VEP. In addition, the geometry of the light source array should increase the probability of a source being located above the fetal eyes should the fetus change positions during the study. This arrangement will allow maximum illumination of the abdomen without thermal injury.

The SQUID Array for Reproductive Assessment (SARA) is located in the University of Arkansas for Medical Sciences. It is a dedicated fetal MEG system and part of a project led by Dr. Curtis Lowery.

4. CONCLUSIONS

We believe that based upon theoretical calculations, and direct and indirect *in vivo* measurements, it should be possible for visible light to penetrate deeply (> 4 cm) into biotissue. The primary goal of the research presented here is to determine if it is feasible to stimulate the fetus with a transabdominal light source. Stimulation of the fetus appears to be possible without damaging the maternal tissue. For tissue geometries that would be encountered in the pregnant female abdomen, the optimal wavelength will be in the range of 600 to 700 nm. The optimal wavelength will tend to be longer for penetration through thicker abdominal walls. A pulsed, narrow band light source on the order of 10^{-3} W incident on the maternal abdomen may be sufficient to stimulate the fetus. Since the duration of exposure to light is short (20 to 25 ms), the source power may be safely increased by an order of magnitude or more with the expectation of increased fetal response. In addition, a more objective and sensitive method of assessing fetal response to light is necessary. SQUID based technology should be well suited for this task.

5. ACKNOWLEDGMENTS

5. REFERENCES

1. Steven L. Jacques, "Laser-Tissue Interactions", *Cancer Bull.*, pp. 211-218, 1989.
2. Steven L. Jacques, Nimmi Ramanujam, Gargi Vishnoï, Regine Choe, and Britton Chance, "Modeling photon transport in transabdominal fetal oximetry.", *J. Biomedical Optics*, pp. 277-282, 2000.
3. Nirmala Ramanujam, et al.,"Antepartum, Transabdominal Near Infrared Spectroscopy: Feasibility of Measuring Photon Migration Through the Fetal Head In Utero.", *J. Maternal Fetal Medicine*, pp. 275-288, 1999.
4. Steven L. Jacques, David R. Weaver, and Steven M. Reppert, "Penetration of Light into the Uterus of Pregnant Mammals.", *Photochem. and Photobiol.*, pp. 637-641, 1987.
5. S. A. Prahl, M. J. C. van Gemert, and A. J. Welch, "Determining the optical properties of turbid media by using the adding-doubling method.", *Appl. Opt.*, pp. 559-568, 1993.
6. J. W. Pickering, *et al.* "A double integrating sphere system for measuring the optical properties of tissue," *Appl. Opt.*, pp. 399-410, 1993.
7. Wai-Fung Cheong, Scott A. Prahl, and Ashley J. Welch, " A Review of the Optical Properties of Biological Tissues.", *IEEE J. Quantum Electronics*, pp. 2166-2185, 1990.
8. C.R. Simpson, M. Kohl, M. Essenpreis, and M. Cope, "Near infrared optical properties of ex-vivo human skin and subcutaneous tissues measured using the Monte Carlo inversion technique.", *Phys Med Biol* pp. 2465-2478, 1998.
9. Lihong Wang, Steven L. Jacques, and Liqiong Zheng, "MCML- Monte Carlo modeling of light transport in multi-layered tissues", *Computer Methods and Programs in Biomedicine*, pp. 131-146, 1995.
10. Alex Ryer, Light Measurement Handbook, p 27, 1997.
11. J. P. A. Marijnissen and W. M. Star, "Calibration of isotropic dosimetry probes based on scattering bulbs in clear media.", *Phys. Med. Biol.*, pp. 1191-1208, 1996.
12. Hari Eswaran, , "Auditory Evoked Potentials and Magnetic Fields in the Human Fetus.", Doctoral Dissertation, University of Arkansas at Little Rock, Applied Science Department, 1999.
13. S. Hecht, S. Schlaer, and M.H. Pirenne, "Energy, quanta and vision.", *J. Opt. Soc. Am.*, pp. 196-208, 1942.
14. D.A. Baylor, T.D. Lamb, K.W. Yau, "Response of retinal rods to single photons.", *J. Physiology, pp.* 613-634, 1979.
15. San Wan, John A. Parrish, R. Rox Anderson, and Michael Madden, "Transmittance of nonionizing radiation in human tissues.", *Photochem. and Photobiol.*, pp. 679-681, 1981.

Acousto-optical Elastography

Sean J. Kirkpatrick
Oregon Medical Laser Center and
Oregon graduate Institute of Science and Technology
Portland, OR 97225
USA

Donald D. Duncan
The Johns Hopkins University
Applied Physics Laboratory
Laurel, MD 20723 USA

Introduction

It is well known that the mechanical properties of pathological tissues vary from that of healthy tissue. For example, many disease processes such as tumors of the breast and prostate manifest themselves as stiff, hard nodules relative to the surrounding tissue. Subsurface skin tumors present themselves as objects with distinct mechanical properties relative to the surrounding normal tissue. The displacement of fibrillar papillary dermis by the softer, cellular mass of a growing melanoma is one such example of this. This feature frequently allows their detection through manual palpation. However, standard soft tissue palpation is not only qualitative, but also highly subjective. Furthermore, it provides information on a rather large spatial scale, thus the ability to detect small tumors by palpation is limited.

To overcome some of the limitations of manual palpation, a number of imaging modalities for visualizing the distributions of tissue stiffness *in vivo* have been devised and are reviewed in the literature[1]. Examples of such methods include vibration amplitude sonoelastography[2], vibration phase gradient sonoelastography[2], elastography[3], spectral tissue strain measurement[4], and various methods employing MRI data[5]. Critical issues such as imaging low-contrast elastic modulus distributions in tissue[1], out-of-plane displacements, and image decorrelation[6] are still being addressed in these methods. Elastographic imaging has seen experimental applications in such diverse areas as intravascular elastography for identifying plaque composition, determining the elastic moduli of healthy and diseased breast and prostate tissue under compression, for breast cancer detection and for demonstrating the difference in the stiffness between the renal cortex and the renal sinus[7]. Ultrasonic and MRI elastographic imaging thus has an extremely wide array of applications. A relatively recent review of existing elastographic methods and applications can be found in the literature.[1,2,7]

Coherent optical radiation-based elastography offers the potential for increased spatial resolution (i.e. smaller lesions may be detected) and better strain resolution (low-contrast elastic modulus distributions may be visualized) than other elastographic methods. However, this increased spatial and strain resolution is gained at the cost of decreased probing depth, as coherent optical methods are limited to the outer few millimeters of tissue. Furthermore, optical elastography is limited in that only relatively small areas or volumes of tissues may be probed at any one time. Never the less, optical methods can still be useful in the early detection of neoplastic changes because many of these early changes occur in the mucosa and submucosa of the affected organs. Herein, we present an imaging elastography system, acousto-optical elastography (AOE), for quantifying the local strain response of biological tissues to an imposed stress.

In AOE, a contact electroacoustic transducer is placed adjacent to a region of interest (ROI) of the tissue and is driven with a sinusoidal or triangular waveform at low frequency. The ROI is then sequentially illuminated with a low power laser from two equal, but opposite illumination angles, θ_s. The backscattered speckle pattern is by a linear array CCD camera equipped with a telecentric lens (Fig. 1). The system is intentionally misfocused by a distance L_o in order to observe any speckle translation due to the acoustic loading. A perfectly focused imaging system would produce a "boiling" speckle pattern, as

opposed to a translating pattern and our goal was to track the translating speckle pattern as a function of the imposed acoustic stress.
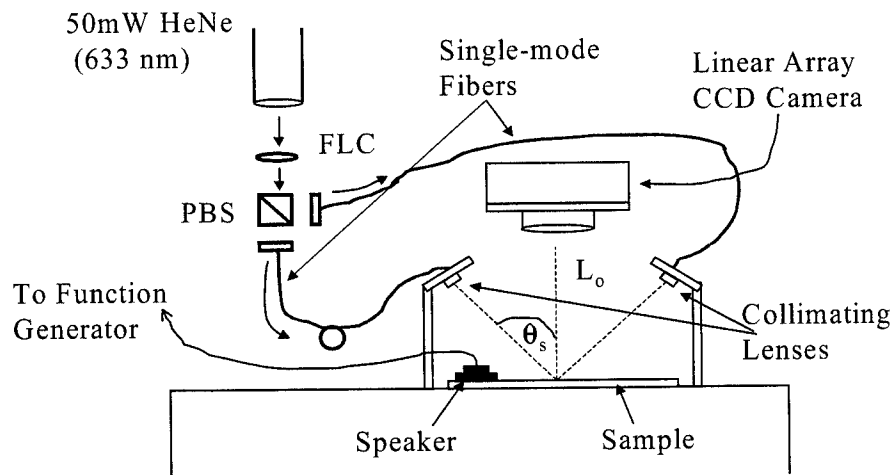
Figure 1. Acousto-optical elastography set-up. The sample is strained by the acoustic pressure generated with the speaker. The surface strain due to the Rayleigh (surface) waves is measured by tracking the laser speckle pattern shift with the mis-focused telecentric imaging system.

Methods

The speckle patterns sequentially generated by illuminating first through $+\theta_s$ and then through $-\theta_s$ (via the ferroelectric crystal and the polarizing beam splitter) where observed with the linear array CCD camera equipped with an $f/2.8$ telecentric lens and the 1-D "images" were stacked into separate stacked speckle histories as shown in Fig. 2. Stacked speckle histories are time-position representations of a series of 1-D views of the backscattered speckle stacked into a 2-D array where time (or record number) is along the y-axis and position on the CCD (pixel) is along the x-axis.
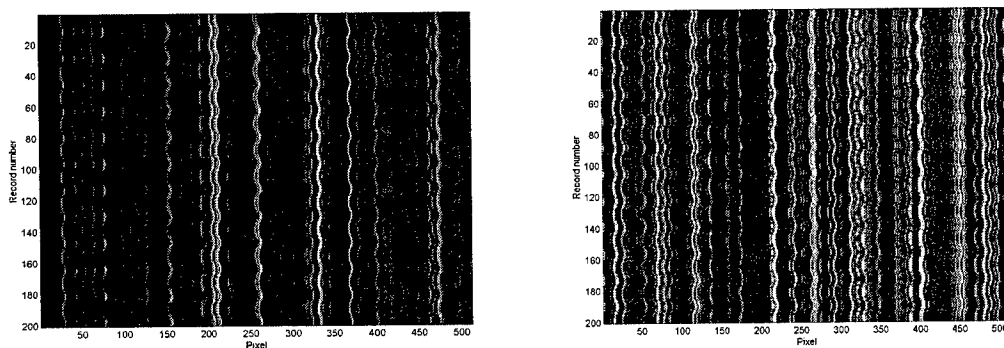
Figure 2. Stacked speckle histories from two equal, but opposite illumination angles.

Our goal was to use the translating laser speckle to infer the strains in the tissues. To accomplish this, we take advantage of the earlier works of Yamaguchi[9] and Duncan et al.[8]. Based on the derivations given in these works, the strain in the plane of the laser beams and CCD array, ε_{xx}, is inferred according to the formula

$$\varepsilon_{xx} = \frac{\delta(+\theta_S) - \delta(-\theta_S)}{-2L_O \sin\theta_S},$$ (1)

where $\delta(\pm\theta_s)$ are the measured shifts in the speckle patterns for each illumination angle. The crux of the problem, then, is to estimate $\delta(\pm\theta_s)$. A variety of processing schemes present themselves, such as the transform method[8], maximum likelihood methods, and correlation approaches. Experimental concerns dictate which processing algorithm is preferred and each method has advantages and disadvantages. The transform method is very robust and effectively disassociates the low frequency speckle behavior from that of higher frequency noise[8]. Maximum likelihood methods excel where the speckle motion is small, but they are sensitive to noise in the data. Correlation techniques are straightforward and computationally efficient, but have relatively poor sensitivity and are very susceptible to speckle decorrelation. Herein, we used a maximum likelihood approach to quantify the speckle shifts[10].

A strip of white PVC (polyvinyl chloride) plastic was used as a tissue phantom in the first set of experiments. Our goal was to measure the attenuation of the strain response of the PVC (and thereby the decrease in the acoustic pressure) as the point of strain measurement, r, was moved further and further away from the acoustic source (Fig. 3).
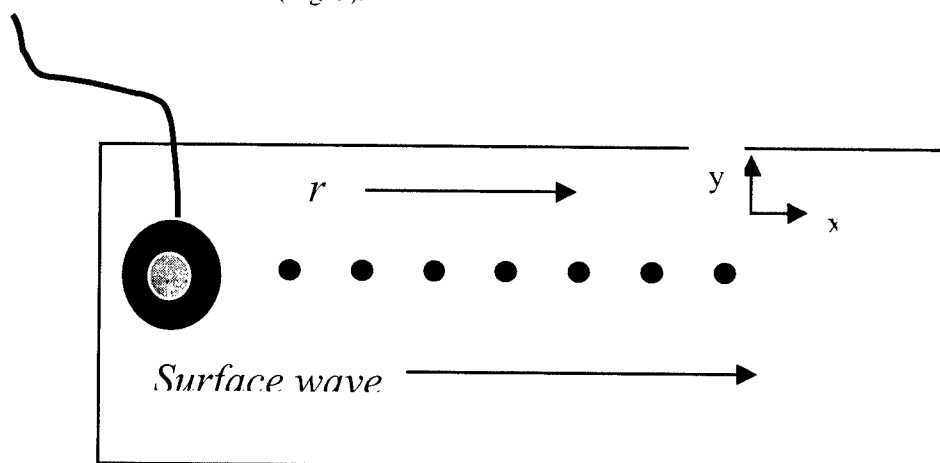
Figure 3. Representation of locations for strain measurement relative to speaker location in the PVC phantom.

Similar tests were performed on pork muscle (perpendicular to fiber orientation) and pork fat strips. The parameters for the tests are given in Table 1.

Table 1

Parameter	Value
Wavelength, λ	633 nm
Source angle, θ_s	40^0
Observation distance, L_o	0.1 m
Camera integration time, T_i	30 ms
Sample interval	0.12 s
Acoustic waveform	Sinusoid @ 0.5 Hz

Results

The optical arrangement provided good speckle histories from which we were immediately able to calculate the speckle shift as a function of record number (Fig. 4).
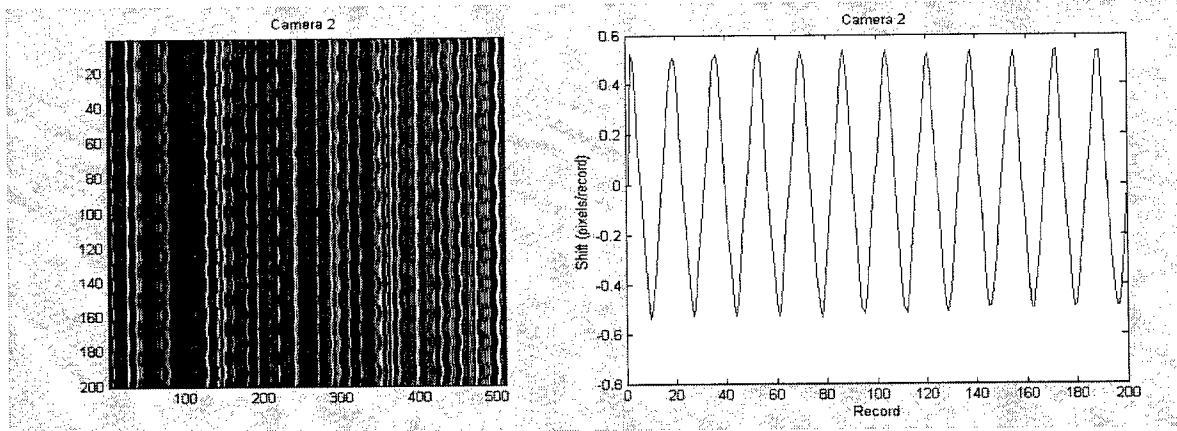
Figure 4. One stacked speckle history (+θ$_s$) from the PVC tissue phantom (left) and the corresponding speckle shift as a function of record number (right).

By evaluating the speckle histories from both +θ and -θ, cumulative strains and instantaneous strain rates can be calculated using Eq. 1 (Fig. 5).
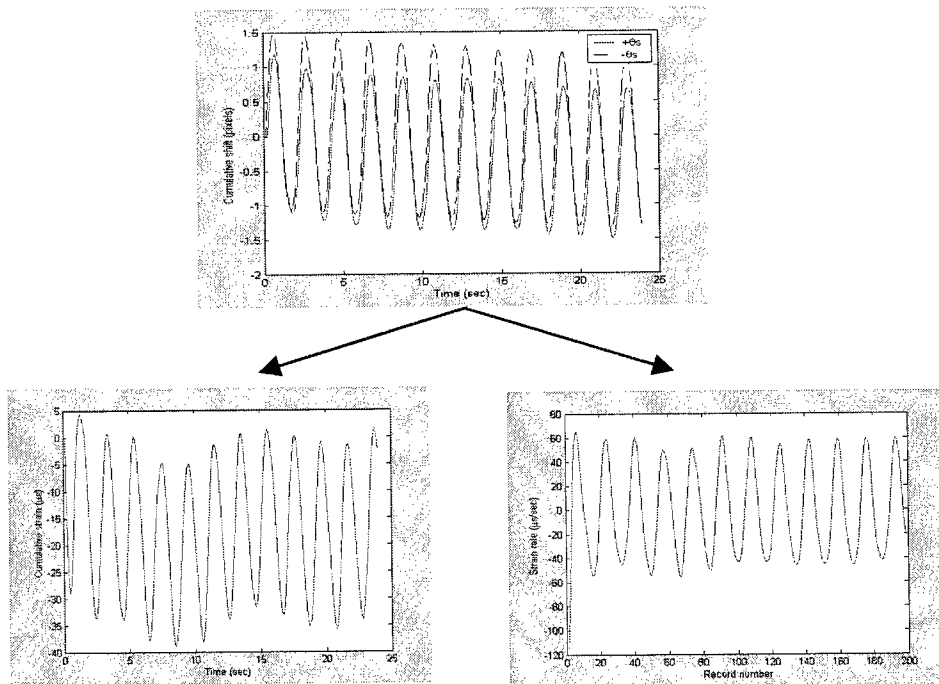
Figure 5. Cumulative strain as a function of time (bottom left) and instantaneous strain rates as a function of record number (bottom right) for one of the PVC tissue phantom measurements.

By measuring the peak-to-peak strains in the PVC tissue phantom as a function of distance from the acoustic source, we found an exponential decrease in the magnitude of the strains as the measurement point was moved from 1 to 9 cm along the x-axis of the specimen (Fig. 6.)
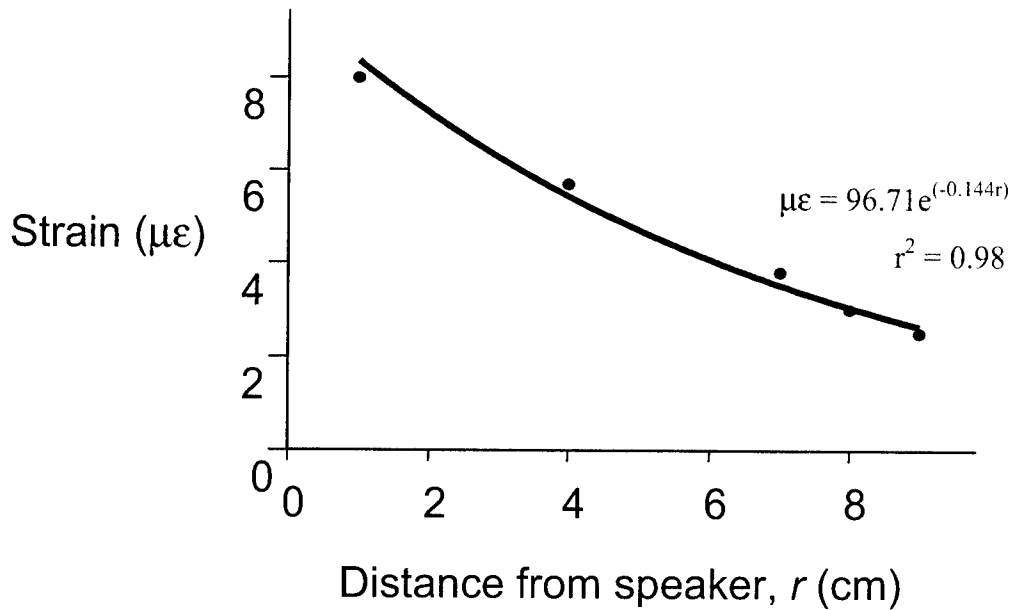
Figure 6. Decrease in peak-to-peak strains as a function of distance from the acoustic source in the PVC tissue phantom.

Similarly, for the pork muscle (circles in Fig. 7) and fat (triangles in Fig. 7), an exponential decrease in the strain magnitude was also observed (Fig. 7).
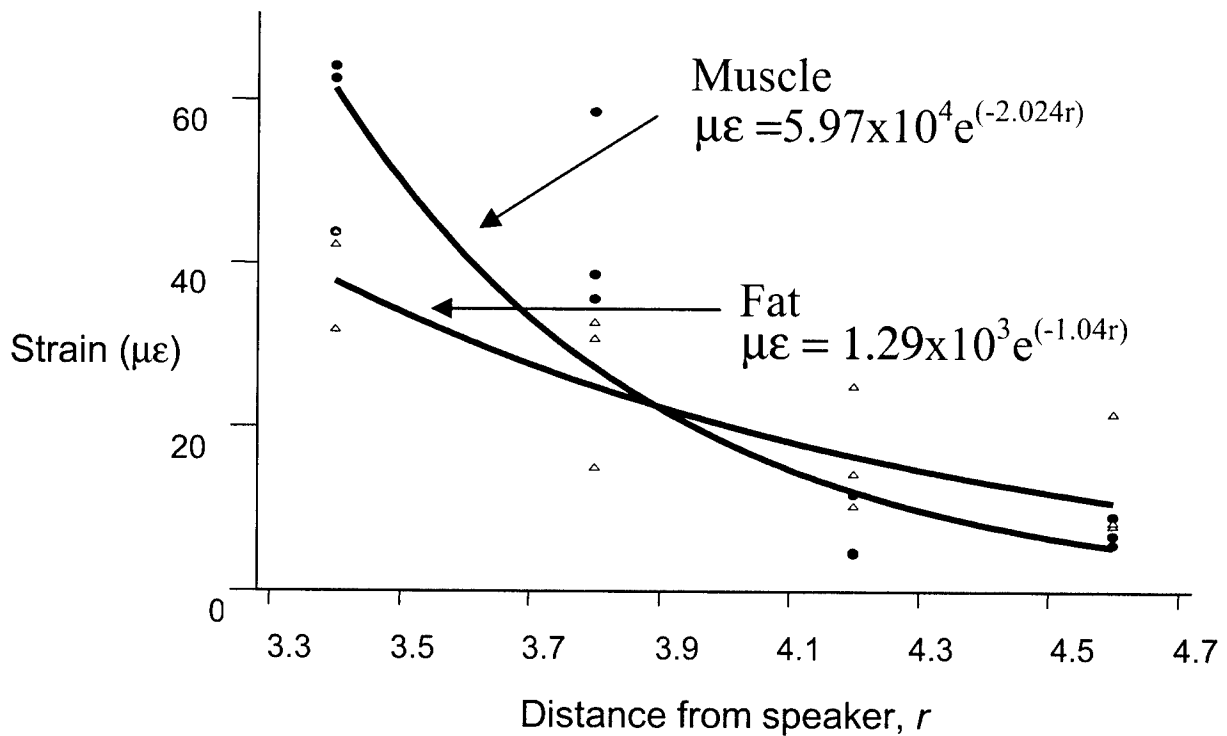
Figure 7. Decrease in strain in tissue as a function of distance from speaker.

An alternative view of the data is to make assumptions about the shear modulus, G, of the PVC and the tissues and calculate the decrease in the shear stress (acoustic pressure) as a function of lateral distance from the speaker. The tensile modulus, E, was measured for all three materials and a simple assumption that $3G=E$ was made. The values of G were taken to be; PVC = 3.3e8 Pa, Muscle = 1.45e7 Pa, Fat = 1.65e4 Pa. The resulting decrease in shear stress as a function of distance is shown in Fig. 8.
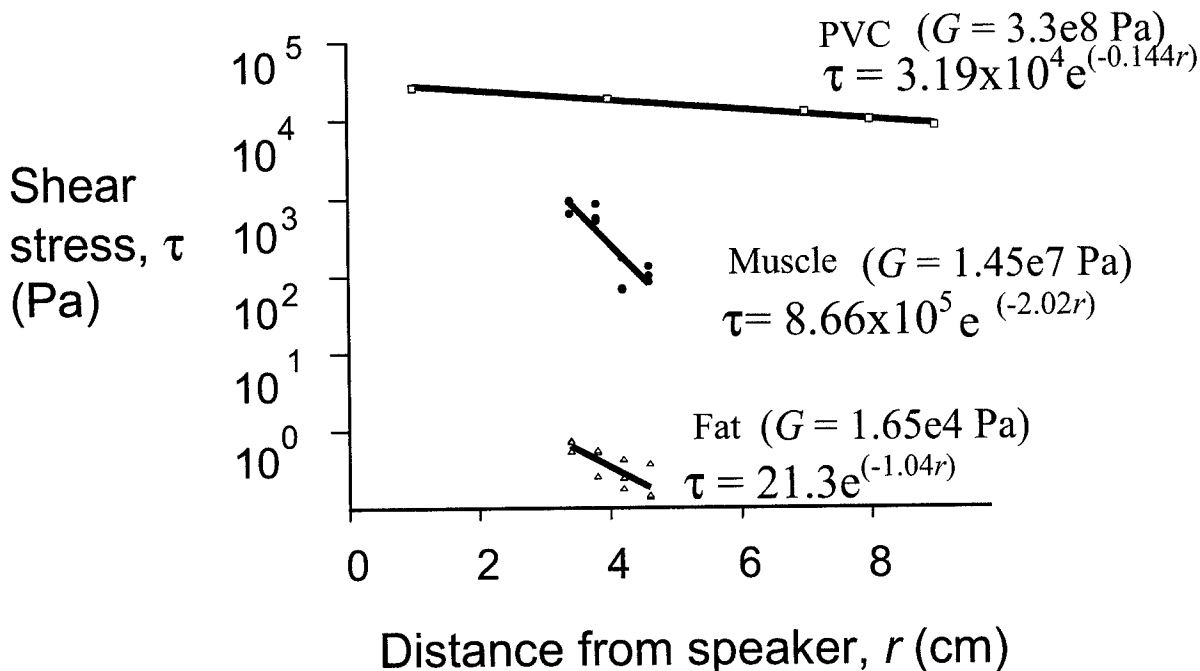
Figure 8. Decrease in surface shear stress as a function of distance from speaker.

Conclusions

We have demonstrated an acousto-optical method for evaluating the strain response of materials, including two biological tissues, muscle and fat, to an infra-sound perturbation. The decrease in the strain response of the materials as a function of lateral distance from the speaker is a measure of the viscous nature of the materials. In a theoretically purely elastic material, there would be no decrease in the acoustic pressure as a function of lateral distance from the speaker. This technology may find applications in non-invasively evaluating the mechanics of tissue *in vivo* as well as in locating defects immediately below the surface in engineered structures.

Acknowledgements

References

1. Gao, L., Parker, K.J., Lerner, R.M., and Levinson, S.F., Imaging of the elastic properties of tissue – a review, *Ultasound in Med & Biol.*, 22(8), 959-977 (1996).

2. Lerner, R.M., huang, S.R., and Parker, K.J., "Sonoelasticity images derived from ultrasound signals in mechanically vibrated tissues, *Ultrsound in Med & Biol.*, 16(3), 231-239 (1990).
3. Ophir, J., Cespedes, I., Ponnekanti, H., yazdi, Y., Li, X., elastography: A quantitative method for imaging the elsticity of biological tissues, *Ultrason Imaging*, 13, 111-134 (1991).
4. Talhami, H.E., Wilson, L.S., and Neale, M.L., spectral tissue strain: A new technique for imaging tissue strain using intravascular ultrasound, *Ultrasound in Med & Biol.*, 20(8), 759-772 (1994).
5. Muthupillai, R., Rossman, P.J., Lomas, D.J., Greenleaf, J.F., Riederer, S.J., and ehman, R.L., Magnetic resonance imaging of transverse acoustic strain waves, *MRM*, 36, 266-274 (1996).
6. Konofagou, E. and Ophir, J., A new elastographic method for estimation and imaging of lateral displacements, lateral strains, corrected axial strains and poisson's ratios in tissues, *Ultrasound in Med. & Biol.*, 24(8), 1183-1199 (1998).
7. Kallel, F., Ophir, J., Magee, K., and Krouskop, T., Elastographic imaging of low contrast elastic modulus distributions in tissue, *Ultrsound in Med & Biol.*, 24(3), 409-425 (1998).
8. Duncan, D. D., Kirkpatrick, S. J., Mark, F. F., and Hunter, L. W. Transform method of processing for speckle strain rate measurements, *Appl. Optics*, 33, 5177-5186 (1994).
9. Yamaguchi, I. Speckle displacement and decorrelation in the diffraction and image fields for small object deformation, *Opt. Acta.*, 28, 1359-1376 (1981).
10. Duncan, D.D. and Kirkpatrick, S.J. processing algorithms for tracking speckle shifts in optical elastography of biological tissues, *J. Biomed. Opt* (in press) 2001.

Quantitative Analysis of Blood Vessel Geometry

Michael G. Fuhrman[*a], Othman Abdul Karim[a], Sujal Shah[a],
Steven G. Gilbert[b], Richard Van Bibber[b]
[a]TISSUEINFORMATICS.INC.;[b]SNBL USA BIOSUPPORT, LTD

ABSTRACT

Re-narrowing or restenosis of a human coronary artery occurs within six months in one third of balloon angioplasty procedures. Accurate and repeatable quantitative analysis of vessel shape is important to characterize the progression and type of restenosis, and to evaluate effects new therapies might have. A combination of complicated geometry and image variability, and the need for high resolution and large image size makes visual/manual analysis slow, difficult, and prone to error. The image processing and analysis described here was developed to automate feature extraction of the lumen, internal elastic lamina, neointima, external elastic lamina, and tunica adventitia and to enable an objective, quantitative definition of blood vessel geometry. The quantitative geometrical analysis enables the measurement of several features including perimeter, area, and other metrics of vessel damage. Automation of feature extraction creates a high throughput capability that enables analysis of serial sections for more accurate measurement of restenosis dimensions. Measurement results are input into a relational database where they can be statistically analyzed and compared across studies. As part of the integrated process, results are also imprinted on the images themselves to facilitate auditing of the results. The analysis is fast, repeatable and accurate while allowing the pathologist to control the measurement process.

Keywords: restenosis, blood vessel measurement, quantitative microscopic image analysis

1. INTRODUCTION

Accurate and repeatable analysis of the shape of blood vessels is important to a variety of researchers for several reasons. Geometrical analysis is required to determine the extent of damage caused by atherosclerotic plaques, to determine the progression of restenosis and the formation of aneurysms, to determine the consequences of novel drug or device therapeutics on blood vessel structure, and to aid in the design and manufacture of engineered blood vessels. Software tools to characterize the geometry of blood vessels and to automate the analysis and archiving of the extracted information have been developed. The measurement process that will be described was developed using images of porcine vessels exhibiting restenosis-like response to balloon angioplasty.

Manually outlining the contours of feature boundaries of dozens of vessel specimens a week is a very tedious process. Given the variability of blood vessel shape, the manual process cannot be replicated exactly from one time to the next simply because the boundaries are not smooth and will be drawn differently each time. The process is similar to tracing the boundary of a shoreline on a map while deciding whether to outline every small inlet. The diameter of a vessel can span hundreds of microns, while micron resolution is required to detect and outline features such as the internal elastic lamina. As a result, vessel geometry must be analyzed at several resolution scales requiring zooming and panning across an image.

Two other time-consuming parts of the process include calculating the required parameters and archiving the results in a way that they can be easily retrieved along with the images. Image processing algorithms are capable of identifying and computing boundary perimeters and areas, both with and without manual intervention. However, more effort is needed to determine whether there is any detectable difference between various treatments for restenosis. As will be seen, there is variability in the shape of injured vessel cross sections. The data needs to be organized and retrievable both for audit and statistical analysis.

[*]mfuhrman@tissueinformatics.com; 1-412-488-1100; http://www.tissueinformatics.com; Tissueinformatics.Inc, 711 Bingham Street, Pittsburgh, PA 15203

Since the measurements may not completely characterize vessel geometry, the images need to be easily retrieved along with the numerical results. Measurement and analysis, database management, retrieval and statistical analysis of data, and data visualization need to be integrated to provide a process a researcher can use to answer questions quantitatively and efficiently.

2. RESTENOSIS DEFINED

It is useful to briefly define restensosis, the impact it has on blood vessel geometry, and the visual appearance of the different features. In particular, we would like to point out the source of the textural differences between the types of tissue. Figure 1 highlights the features that will be discussed. These include the lumen, internal elastic lamina, external elastic lamina, tunica intima, neointima, tunica media, and tunica adventitia.

The pathobiology of restenosis is a multi-factorial process[1]. The process exhibits the characteristics of an inflammatory response to injury. Cytokines and adhesion molecules produced in this response recruit macrophages/monocytes and other inflammatory cells into the tunica media[2]. This recruitment is an attempt to "heal" or remodel the wound. The macrophages produce metalloproteinases, protein-degrading enzymes, which break down the extracellular matrix proteins (e.g., collagen) compromising the structural integrity of the underlying endothelium[3]. When this happens, the underlying extracellular matrix is exposed to circulating coagulation factors and platelets. In particular, platelet adhesion causes the release of platelet-derived growth factor, which in turn stimulates the proliferation of the medial smooth muscle cells into the tunica intima.

The slides were stained with a combination of Verhoeff's elastin and Masson's Trichrome[4] stains, which stain elastin and collagen respectively. The internal elastic lamina and external elastic lamina stain black, collagen stains blue, and smooth muscle stains red. In our porcine model, the smooth muscle cells invading the tunica intima lack the connective tissue that is stained black. It therefore stains differently than the tunica media and tunica adventitia. As a result, the neointima tissue is differentiated texturally from the tunica media and tunica adventitia. Image processing can enhance the boundaries between these tissues. In the images studied, angioplasty has also resulted in the rupture of the internal elastic lamina in one or more places.

3. IMAGE CAPTURE

The images were captured from the standard video output of a Sony DKC-5ST CCD camera mounted on a Nikon Eclipse E600 microscope with a planar apo-epifluorescence objective (20X). Each image is an assembly of a montage of images with height by width dimensions of 300 μm x 403 μm. The image resolution is 0.65 μm / pixel. A background image of a tissue-free area of the slide is captured before imaging each tissue sample to normalize for any changes in color or intensity of the incident light over time. The imaging system is also calibrated by imaging a microscopic grid to more precisely determine pixel resolution. Feature extraction and segmentation is dependent on accurate color and texture differentiation. Therefore, imaging of tissue is performed after making sure the background image intensity is not saturated.

The left side of Figure 1 shows a cross-section of a normal artery. Note that the intensity of the image is saturated. The light intensity had been adjusted to permit an operator to comfortably view the image. This affects the quantitative repeatable measurement of color and therefore has an adverse effect on automated feature extraction. The right side of Figure 1 shows an image after analysis where the internal elastic lamina was fractured. Features of interest are the lumen, the internal elastic lamina, any fracture of the internal elastic lamina and the distance between the fractured ends, the tunica intima, the neointima, and the vessel perimeter defined by the inside edge of the external elastic lamina. The feature boundaries have been outlined in the image, and the measurement results were imprinted on the image itself. The analysis is discussed in Section 5.
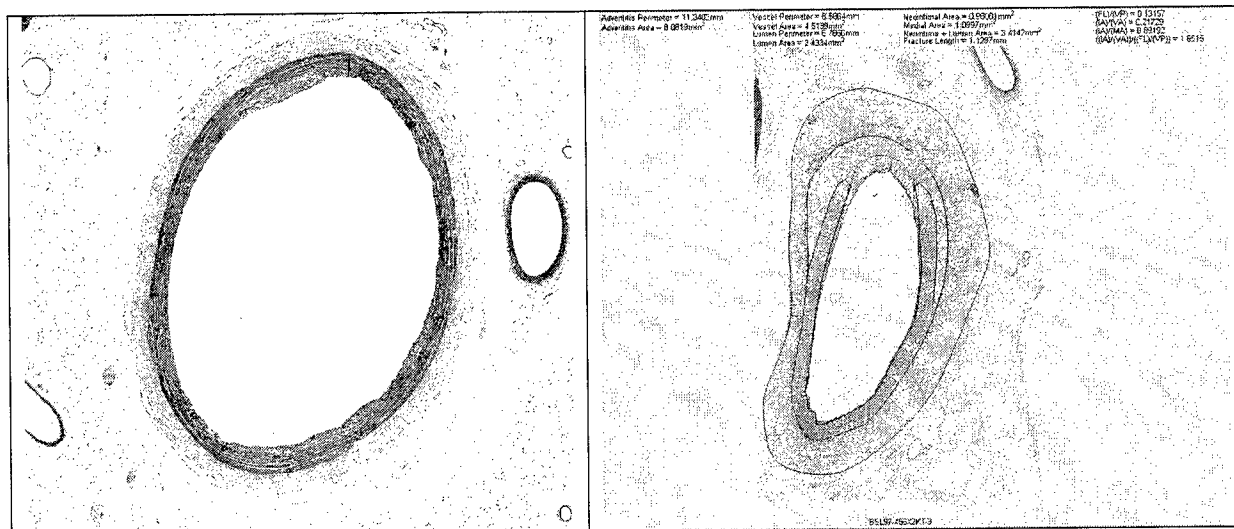
Figure 1: The image on the left is of a normal artery showing the lumen, tunica media and tunica adventitia. The internal elastic lamina surrounds the thin layer of endothelial cells around the lumen, and cannot be seen in this image without zooming to micron resolution. The image on the right shows the internal elastic lamina, a fracture of the internal elastic lamina and the distance between the fractured ends, the neointima, and the vessel perimeter defined by the inside edge of the external elastic lamina. This image of an analyzed vessel was saved with results imprinted directly on the image for auditing purposes.

4. FEATURE EXTRACTION

The vessels that have been studied have all been injured by balloon angioplasty. The damage consists of one or more fractures of the internal elastic lamina, and subsequent restenosis-like response of the vessels by the proliferation of smooth muscle cells within the vessel boundary. These vessels do not have the geometry of a normal vessel with defined symmetric layers. Images of several vessels showing the variability in the shape of injured vessels that have been processed are shown in Figure 2.
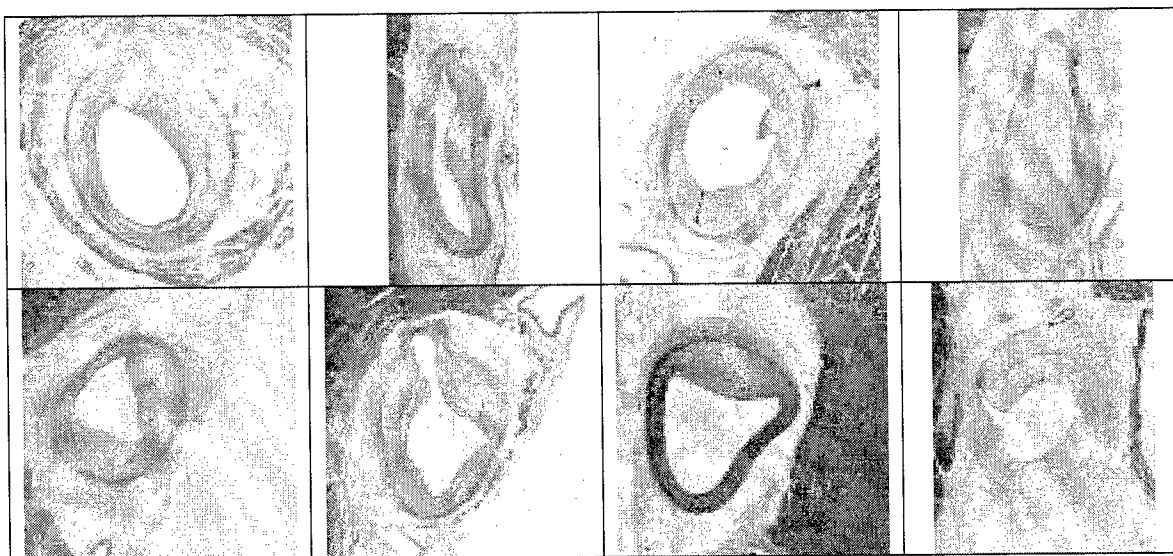
Figure 2: Assortment of blood vessels showing range of variability in vessel geometry following injury.

Features are extracted using three attributes: intensity, color, and morphology. The lumen and external elastic lamina are extracted first. The internal elastic lamina is then extracted using the constraint that it is located between these layers. Dark areas of the internal elastic lamina and the external elastic lamina are

close in color. The Verhoeff's elastin stain absorbs all three color channels, in particular green light, so these regions appear black. The resulting color vector of these features is unique enough within the image to segment these regions.

Since there is no tissue within the area of the lumen, this area is unstained. The lumen area and boundary are extracted automatically using an optimal threshold determined from the intensity histogram of the grayscale image. The lumen is generally the largest object in the image with an intensity above the threshold that does not touch the edge of the image. However, there may be other blood vessels or tears in the tissue. If so, the user can be asked to indicate a point within the lumen to identify it as the object of interest. Extraneous islands of tissue within the lumen are filtered out using a morphological filling operation[6] to create one large connected lumen area.

The external elastic lamina is at the boundary between the tunica adventitia and the tunica media. To extract this feature, the user is asked to sample the color of a dark pixel within the tunica adventitia near the boundary. This pixel will have been stained by Verhoeff's elastin stain and should correspond with the external elastic lamina. The expression

$$D = \sqrt{(R - R_{EEL})^2 + (G - G_{EEL})^2 + (B - B_{EEL})^2}$$ (1)

is evaluated for every pixel in the image. R, G, and B refer to the red, green, and blue color channels. The subscript "EEL" refers to the external elastic lamina. D is the three-dimensional Euclidean distance in color space between the color of the sampled pixel in the tunica adventitia and each pixel in the image. Pixels within a threshold distance in this color space of the 3-D color of darkly stained tissue in the tunica adventitia are segmented from the image.

The pixels are connected into a contiguous region using several dilation operations. After these operations, the resulting region will be the largest single connected object in the image. The pixels that were the source for creating this large region, and are a subset of this region, are identified as belonging to the external elastic lamina. The inside boundary of the external elastic lamina is identified as being those points that are closest to the lumen. These points are identified as points on the vessel perimeter. The external elastic lamina may be incomplete and open because of the angioplasty procedure. The resulting gaps can be spanned with a section of an ellipse or a spline curve with minimal interaction from the user.

The internal elastic lamina is normally just beyond the thin endothelial layer bounding the lumen. The observed width is approximately 4 μm across. In an injured vessel, neointimal tissue proliferates between the internal elastic lamina and the lumen. In addition, the fractured ends of the internal elastic lamina separate away from each other. In addition to one or two major fractures, the internal elastic lamina is often comprised of short disconnected segments.

The stained internal elastic lamina does not have any particularly unique geometrical properties or color although it does stain darker than its surrounding tissue. To extract this feature the user is asked to sample the color of a pixel comprising the lamina, and the program identifies and highlights all other pixels in the image of similar color. For each of the highlighted pixels D, as expressed by Equation 1, is less than a threshold value. Other connective tissue in the media and tunica adventitia is also stained, so this process must be followed by several morphological operations to extract the internal elastic lamina. To filter out extraneous objects, regions with a maximum width, minimum perimeter, and minimum area are extracted from the objects of specified color within the image[5]. Further morphological operations are used to connect segments into continuous larger sections. These larger objects between the lumen and the external elastic lamina are selected to belong to the internal elastic lamina.

The perimeter of the lumen, the internal elastic lamina, and the external elastic lamina are extracted with minimal effort. The results are shown in Figure 3. The coordinates of these features can now be extracted easily even at low resolution for further processing.
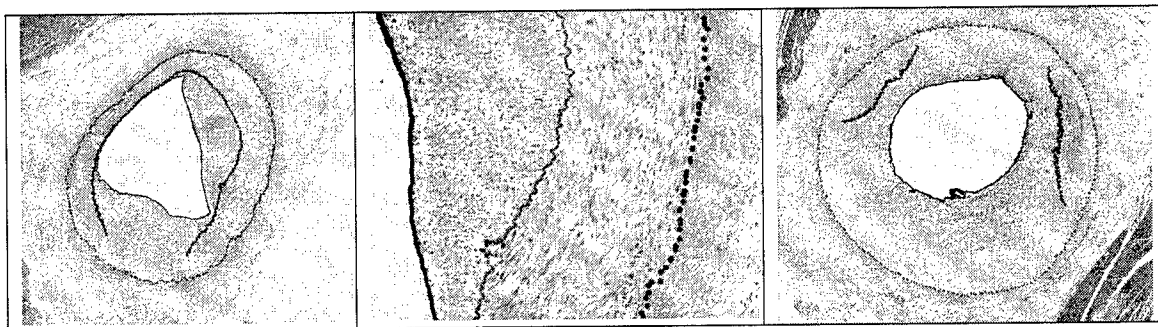
Figure 3: Points on the lumen boundary, the internal elastic lamina, and the inside edge of the external elastic lamina, are automatically extracted for further processing. The image on the left shows the case of a single fracture, the image on the right shows a double fracture.

Two subjective measurements remain. The first is to determine the best way to draw a smooth curve between the fractured ends of the internal elastic lamina in order to determine the size of the separation. Each fractured end is a measurable distance away from both the lumen and the external elastic lamina. At each end these distances have specific ratios. As a curve is generated between one fractured end and the other, the condition that this ratio varies linearly from its value at one end to the other is enforced. Examples are shown in Figure 4.
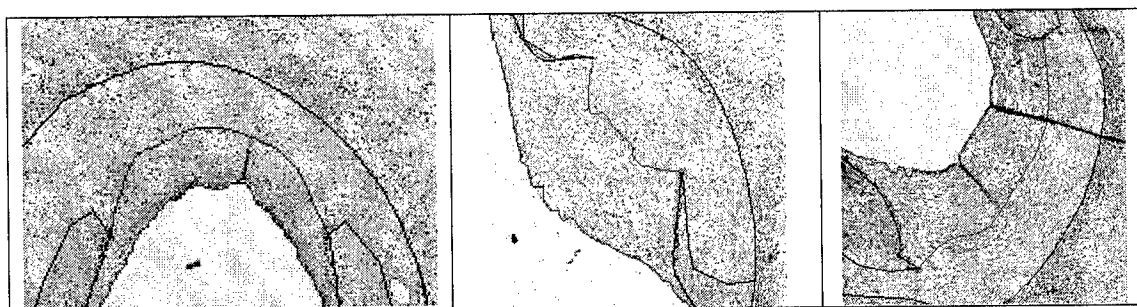
Figure 4: Images showing a contour that was automatically generated that connects the two ends of the broken internal elastic lamina. The size of the fracture as measured by the length of the contour is one of the parameters used to assess the restenosis-like response.

The second subjective measurement is the detection of the boundary between the neointima and the tunica media. This boundary may not be well defined. Instead, its visual appearance can vary slowly and continuously through the tissue.

The neointima is composed of smooth muscles cells with little of the darkly stained connective tissue that is present in the tunica media. Modifying the image histogram[7] can enhance image contrast. The intention is to determine if the image can be analyzed at a lower resolution without the need to pan and zoom, thereby increasing the speed and reducing the tedium of the measurement process. Three pairs of images are shown in Figure 5 to show the increased contrast generated by creating images with exponential histograms within each color image plane to accentuate regions with different texture.
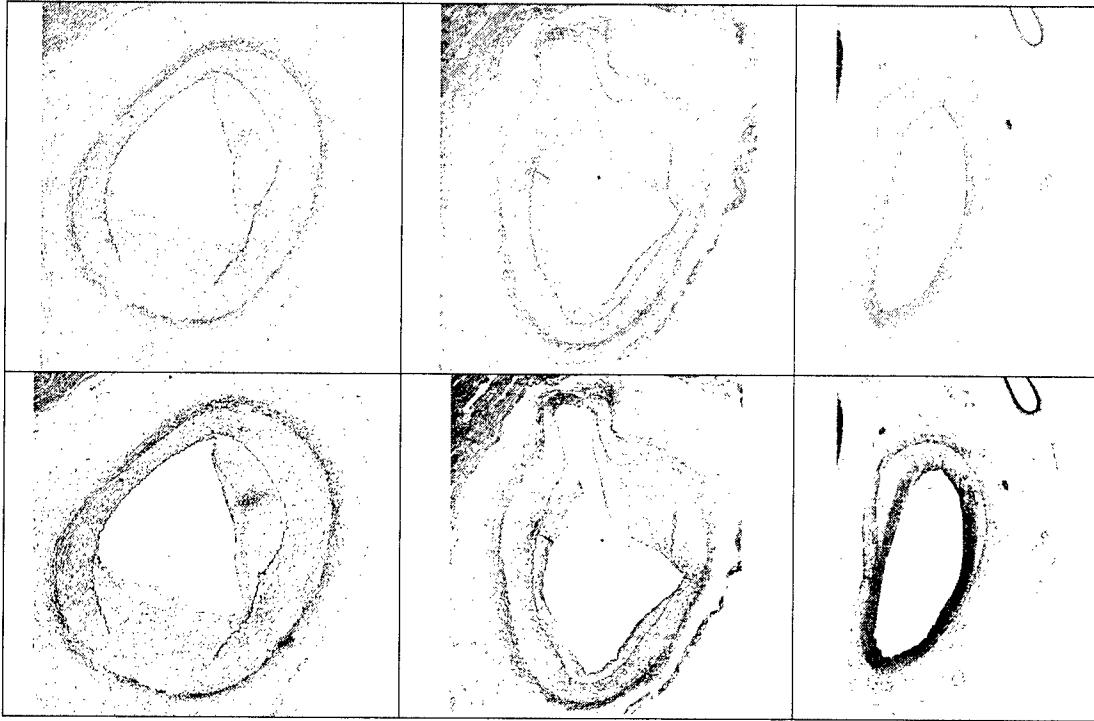
Figure 5: The images in the top row were modified to have exponential histograms. The enhanced images are shown in second row. They were created to provide higher contrast between tunica media and neointima.

5. MEASUREMENT AND ANALYSIS

In the last section, it was described how feature extraction has been automated to an extent. In addition, the image-processing capabilities of the analysis software have been augmented with tools common to computer-aided design (CAD) to further enhance and automate the measurement and analysis process. Tools that are common to CAD include the ability to pick points and group them, the ability to fit polynomial curves or splines to groups of points, and the ability to merge curve segments in an ordered fashion so they bound regions of interest.

The process for assembling points into groups through which curves will be fit is as follows. The user first identifies the feature of interest that is being extracted to the program, which in turn expects the user to extract the feature using a standard procedure. The user then manually traces feature boundaries. If the points chosen along the path defined by the user are within a threshold distance of the extracted points, the extracted points are used to compute a boundary curve. If the chosen points veer from the automatically extracted points, the boundary is modified to follow the chosen points. When the threshold is set to zero an outline of the feature is created without using any of the automatically extracted points, aside from the guidance they provided.

Tools are provided to enable a user to identify boundary segments in an order that circumscribes the boundaries of features of interest as opposed to circumscribing the entire feature in one procedure. When doing this, the beginning and end of the boundary segments need to be identified in a specific order to connect the boundary segments together. Additional tools are provided to enable the user needs to make corrections if the automatically extracted boundaries need adjustment.

Measurement and analysis has been developed independently of feature extraction to determine the following:

1. Perimeter of the tunica adventitia.
2. The vessel perimeter. (Circumscribed inside edge of the external elastic lamina.)

3. Vessel area. (Area within the vessel perimeter.)
4. Lumen perimeter.
5. Lumen area.
6. Fracture length: arc length between fractured ends of internal elastic lamina drawn roughly equidistant between the external elastic lamina and the edge of the lumen.
7. Neointimal area: circumscribe the neointima being careful to exclude the lumen.
8. Medial area: computed as the vessel area minus the combined lumen and neointimal area.

A set of ratio computed from these measurements provide more information for evaluating the extent of restenosis:

1. Fracture length / vessel perimeter.
2. Neointimal area / vessel area.
3. Neointimal area / medial area.
4. Ratio #2 divided by ratio #1: (neointimal area / vessel area) / (fracture length / vessel perimeter).

Determination of the vessel perimeter and lumen perimeter are usually automatic. If not, they can be defined manually. The neointima is bounded by the fractured internal elastic lamina, by a segment of the external elastic lamina, and by segments of the media boundary as shown in Figure 6. The neointima shares a segment of the vessel perimeter. That particular segment should not need to be outlined twice, once as part of the vessel perimeter and once as part of the neointima boundary, as is done when the features are outlined manually without aid from the computer. It is for this reason the software is able to merge existing curve segments.
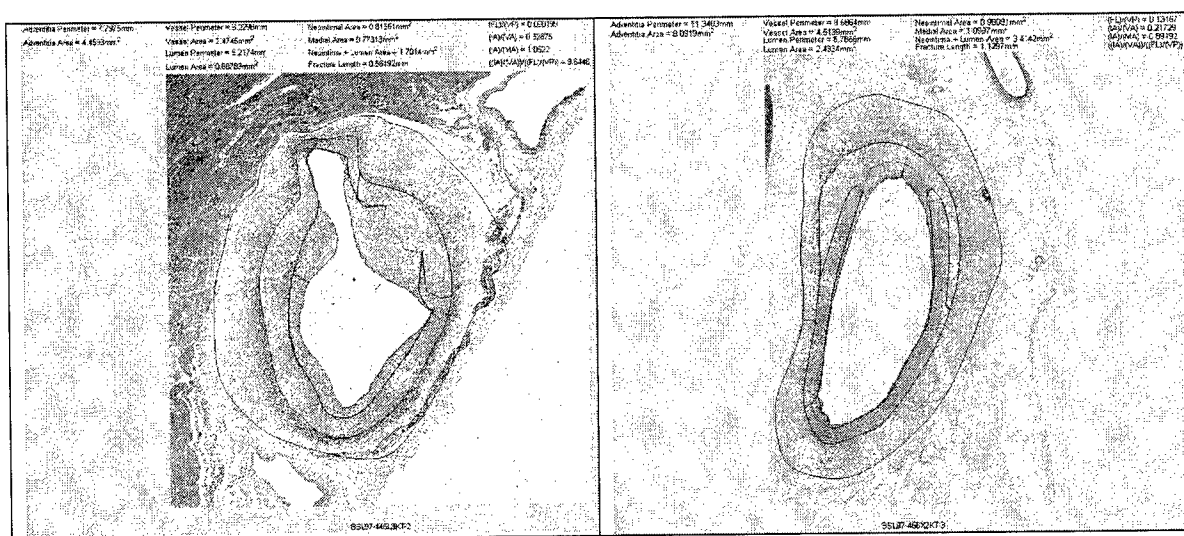
Figure 6: Images of analyzed vessels are saved with results imprinted directly on the images for auditing purposes. The data is input into a relational database for comparative analysis.

6. DATABASE

More often than not, images and data are stored separately. The data may be kept in spreadsheets where it is not easily accessible, efficiently analyzed or shared. Similarly, the images are accessible separately through the operating system. In principle, the images and data can be merged using hyperlinks. From a practical standpoint, a more robust database that manages the input and retrieval of data and images is needed to compare studies taking place at different times, with different protocols, and with measurements made by different systems. The database needs to have sufficient and accurate information to enable the user to normalize the results to make meaningful comparison between studies.

The analysis of individual tissue sections is not of much value unless the results can be compared within and across experimental studies. As an example, consider the following therapeutic approaches being examined to prevent restenosis:

1. Brachytherapy or transient exposure to either beta or gamma radiation[8] has been shown to reduce restenosis from 45% to 12%.
2. New stent design[9], which preserves the endothelium or cells lining the lumen, appears critical.
3. Distal protection devices placed downstream of the stent collect debris to prevent embolisms or blood clots from causing ischemia or infarctions.
4. Stent coatings that prevent neointimal proliferation[10].
5. Novel catheters that minimize vascular perturbation and enhance diagnostics and therapeutics.
6. Photodynamic chemotherapy that reduces inflammation[11,12,13,14].
7. Diet and lipid/cholesterol lowering regimens.

Ideally, information from all studies such as these would be input into a shareable database that could be queried in a way that enables researchers to draw conclusions and make predictions.

The images and the output of the analysis results that have been presented have been input into a relational database that provides query tools, advanced analysis tools, data visualization capabilities, and web access. Genetic, mechanical, and clinical information can also be extracted from the tissue for the purpose of correlating this additional information with the structural information extracted through image processing. A perpetual, shared, database that can be queried for statistical analysis provides a resource where data and images are organized that is important for quantitatively comparing the differences in effects seen between studies.

7. SUMMARY

A measurement and analysis system that was developed to be a tool for pathologists to quantitatively evaluate blood vessel shape while reducing the tedium involved in making manual measurements has been described. The entire process is composed of several steps. Though not discussed in this paper, image capture requires the assembly of a montage[15] of multiple images, each of which requires focusing[16] before image capture. After assembling the image, features of interest including the lumen, neointima, internal elastic lamina, tunica media, external elastic lamina, and tunica adventitia are identified and the boundaries of these features are extracted. Extraction of these features normally requires extensive zooming and panning to outline areas of interest. The extracted features are then analyzed to characterize the geometry of the vessel. Finally, the data must be put in some format for retrieval. Depending on the level of existing automation this process can take as much as an hour.

The emphasis in this paper has been on feature extraction and geometric analysis. Structures such as the lumen, internal elastic lamina and external elastic lamina are first segmented using a combination of grayscale, color, and morphological operations. The boundaries of the extracted features are overlaid on the image enabling a pathologist to use the computed coordinates, or to outline features of interest manually. The process of feature extraction takes approximately 1 minute on an 800 Mhz Pentium III processor with 1Gbyte of memory for a 10 Mbyte region of interest, and requires minimal user interaction. The subsequent generation of the boundaries of interest using the extracted points or manually selected points takes approximately 2 minutes. The analysis time is minimal.

The benefit of this process is the pathologist still decides where feature boundaries are located but is relieved of the need to work intensively with the images. Finally, the results are automatically input into a relational database for statistical analysis and comparison with accumulated results and the results of other studies. This process effectively merges computer aided design, image processing and analysis to relieve the tedium of both the measurement process and the archiving of results.

REFERENCES

1. Orford, JL, Selwyn, AP, Ganz, P, Popma, JJ, and C. Rogers. The comparative pathobiology of atherosclerosis and restenosis. *Am J Cardiol* **86**(4B): 6H-11H, Aug 24, 2000.
2. Qiao, JH, Tripathi, J, Mishra, NK, *et al.* Role of macrophage colony-stimulating factor in atherosclerosis: Studies of osteopetrotic mice. *Am J Pathol* **150**: 1687-99, 1997.
3. Galis, ZS, Sukhova, GK, Lark, MW, and P Libby. Increased expression of matrix metalloproteinases and matrix degrading activity in vulnerable regions of human atherosclerotic plaques. *J Clin Invest* **94**: 2493-403, 1994.
4. Carson, F., Histotechnology, ASCP Press, Chicago, 1997.
5. User Guide, Matrox Imaging Library, Matrox Electronic Systems Ltd., 1999.
6. User Guide, Image Processing Toolbox, The Mathworks Inc., 1997
7. Pratt, W., Digital Image Processing, p. 275, Wiley Interscience, New York, 1991.
8. Tierstein, PS. Gamma versus beta radiation for the treatment of restenosis (Editorial). *Herz* **23**: 335-6, 1998.
9. Rogers, C, Tseng, DY, Squire, JC, and ER Edelman. Balloon-artery interactions during stent placement: A finite element analysis approach to pressure, compliance, and stent design as contributors to vascular injury. *Circ Res* **84**: 378-83, 1999.
10. Fischell, TA. Polymer coatings for stents. Can we judge a stent by its cover? (Editorial). *Circulation* **94**: 1494-5, 1996.
11. Pollock, ME, Eugene, J, Hammer-Wilson, M, and MW Berns. Photosensitization of experimental atheromas by porphyrins. *J Am Coll Cardiol* **9**: 639-46, 1987.
12. Michaels, JA. The accumulation of porphyrins in atheroma: Potential for diagnosis and treatment? *J Photochem Photobiol B* **2**: 134-7, 1988.
13. Allison, BA, Crespo, MT, Jain, AK, Richter, AM, Hsiang, YN, and JG Levy. Delivery of benzoporphyrin derivative, a photosensitizer, into atherosclerotic plaque of Watanabe heritable hyperlipidemic rabbits and balloon-injured New Zealand rabbits. *Photochem Photobiol* **65**: 877-83, 1997.
14. Hsiang, YN, Crespo, MT, Richter, AM, Jain, AK, Fragoso, M, and JG Levy. *In vitro* and *in vivo* uptake of benzoporphyrin derivative into human and miniswine atherosclerotic plaque. *Photochem Photobiol* **57**: 670-4, 1993.
15. Dani, P., Chaudhuri, S. Automated Assembling of Images: Image Montage Preparation, Pattern Recognition, Vol 28, No. 3, pp. 431-435, Elsevier Science, Ltd., 1995
16. Yeo, T., Ong, S., Jayasooriah, Sinniah, R., Autofocusing for tissue microscopy, Image and Vision Computing, Vol 11, No. 10, pp. 629-639, Butterworth-Heinemann Ltd., 1993

In vitro imaging of bone tissue and monitoring of tissue viability by optical coherence tomography

Xiangqun Xu, Ruikang K Wang[*], Alicia El Haj

Centre for Science & Technology in Medicine, School of Medicine, Keele University/North Staffordshire Hospital Trust, UK

ABSTRACT

Optical coherence tomography (OCT) has developed as a promising medical diagnostic imaging technology for non-invasive *in situ* cross-sectional imaging of biological tissues. We present this technique to image bone tissue and to monitor the redox state of mitochondria enzyme Cytochrome oxidase (CytOx) in bone for applications in tissue engineering. Superluminescent diode (SLD) with its peak emission wavelength (λ = 820nm) on the absorption band of oxidized form of CytOx was used in the experiments. The results demonstrate that the OCT system is capable of imaging the calvaria of newborn rats tomographically with a resolution at 9 microns, which could only be previously obtained by the conventional excisional biopsy. The thickness of periosteum of various calvarias from different ages of rats can be accurately determined by the system.

The backscattered power–versus–depth profile from the liquid phantoms (naphthol green B with intralipid) and tissue specimens (periosteum of calvaria from newborn rats) are used to quantify the absorption changes of the sample. Absorption coefficients of naphthol green B could be quantified accurately by the linear relationship between attenuation coefficients from the slopes of the reflected signals and naphthol green B concentration. The results also show that the attenuation coefficient decreases in periosteums as CytOx being reduced by sodium dithionite, demonstrating the feasibility of this method to monitor the redox state of tissues studied.

1. INTRODUCTION

Optical coherence tomography (OCT) has developed as a promising medical diagnostic imaging technology for non-invasive *in situ* cross-sectional imaging of biological tissues. By combining the advantages of white-light interferometry and confocal microscopy, OCT achieves sufficient sensitivity to probe weakly backscattering structures beneath the surface of biological tissues. The axial resolution of OCT is determined by the bandwidth of the low-coherence light source, and image with resolution 10-100 times better than standard ultrasound imaging have been achieved. The technique has been shown to be suitable for non-invasive two-dimensional tomographic imaging of the microstructures of tissues [1,2]. Recently, this technique has been used to determine analyte concentration in a scattering media [3] and to measure optical properties of tissues [4], and to derive spectroscopic information from tissue phantom [5] and tissues [6].

Mitochondria cytochrome c oxidase (CytOx) is a terminal enzyme in the respiratory chain. The reaction that this enzyme catalyses is linked to the generation of ATP in cells. In the presence of oxygen and absence of substrate, the enzyme is fully oxidized. Changes in CytOx redox state could be useful markers for the oxygenation state of the tissue due to its redox changes in response to oxygen availability at the cellular level. Monitoring the redox state of CytOx could thus provide an insight into cellular activity and viability of tissues.

CytOx has a broad absorption band that is found in the near infrared region. This band absorbs with a maximum at 830nm in oxidized CytOx and is bleached on reduction. The technique of Near-Infrared Spectroscopy (NIRS) shows great promise for minimally invasive assessment based on the fact that near infrared absorption signals, which change with oxygenation, arise from only haemoglobin and CytOx in tissues. NIRS has been studied for monitoring regional blood volume change, extracellular (Hb oxygenation) and intracellular tissue oxygenation (CytOx redox state) [7, 8]. However, conventional NIRS

---

[*] Correspondence to: Dr R Wang, r.wang@keele.ac.uk

with large area pickup optode is not capable of discriminating redox change of CytOx as a function of depth in the tissue, and its spatial resolution is severely limited too.

In the present study, cross sectional images with high resolution of rat calvarias and discrimination of various thickness periosteums of calvarias are achieved by the OCT system. The feasibility of optical coherence technique for detection of the redox state of CytOx in tissue is demonstrated for the first time.

2. METHODS AND MATERIALS

2.1 OCT System

Figure 1 shows a schematic of the low coherence interferometry system, known as optical coherence tomography (OCT) system, based on a fibre optic implementation of a Michelson type interferometer [9]. In this system, incident light from a broadband light source is coupled into a fibre, and is split by an optic-fibre coupler. Half of the light is directed towards a moving mirror. This path is known as the reference arm of the interferometer. The remaining light is guided towards the sample with a focusing optics. When light reflected from the reference arm is recombined with light that has returned from the sample arm to detector, these two beams interfere only if the optical path lengths of the two beams are matched to within the coherence length of the light. The coherence length of light source is analogous to the pulse duration for the

Figure 1, Schematic of the OCT system used in the experiments

measurement of echo delay time. It thus determines the axial resolution of the OCT system. Therefore, the higher axial resolution can be achieved with the choice of the shorter coherence length, i.e. broader spectrum bandwidth of the light source.
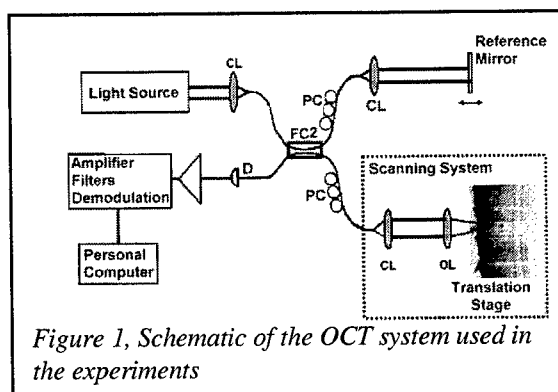
The OCT system used in this study employs a broadband light source, delivering an output power of 1 mW at the central wavelength of 820nm with a bandwith of 25nm. The light source yields 12 μm axial resolution in free space that determines the imaging axial resolution of the system. In-depth monitoring of the reflectance, or imaging, was performed by directing low coherence light at a certain point of the sample and detecting the reflections from various depths in the sample by the use of an optic-fibre integrated scanning system. Polarisation fibres are used to provide the maximum obtainable resolution for the given spectral width of the source. The beam spot size was measured at 16μm, limited by the numerical aperture of the lens used to deliver the light onto the sample, and the optical frequency of the incident light as that in conventional microscopy. The system has a measured signal to noise ratio at 97dB.

2.2 Materials

Liquid phantoms were first constructed to demonstrate the feasibility of the OCT system to quantify the absorption changes in the tissue. The liquid phantom consists of intralipid solution mixed with different concentrations of Naphthol green B, an effective absorber for the near infrared light. 1% intralipid solution was prepared to make the phantoms with the concentration of Naphthol green B ranging from 0 to 0.2%.

To simplify experimental model, periosteum of calvaria from young adult rats was chosen as experimental tissue due to its relatively transparent and blood-free nature. Calvarias were harvested from fresh postmortem calvarias of young adult Wistar rats. All the experiments were performed within 2 hours of their removal.

2.3 Measurements

The samples were mounted on a translation stage at the sample arm and were placed perpendicular to the probing beam. The amplitude of reflected light as a function of depth within the sample is obtained by scanning the reference mirror with a constant velocity (Figure 1). The cross-section images of the calvarias examined were obtained by enabling the movement of translation stage on which the samples were mounted.

For absorption measurement, repeated scans at one spatial point of the sample were performed. The result is the measurement of optical backscattering or reflectance, R(z), versus axial ranging distance, or depth, z. The reflectance depends on optical properties of tissue, i.e. the absorption (μ_a) and scattering (μ_s) coefficients, or total attenuation

coefficient (μ_t), $\mu_t = \mu_a + \mu_s$. The relationship between R(z) and μ_t is, however, very complicated due to the high scattering nature of biological tissue. But for the relatively transparent tissue, reflected power will be negatively proportional to $2\mu_t z$ in exponential scale according to the single scattering model that is valid for optical depth less than 4, i.e. [10]:

$$R(z) = I_0 * T(z) * \exp(-2\mu_t z) \qquad (1)$$

Where I_0 is the optical power launched into the tissue sample and T(z) is the reflectivity of the tissue at the depth of z. The factor of 2 in the exponential accounts for the light passing through the tissue twice after is backscattered. It should be noted that optical depth is a measure of depth in terms of number of mean free path length i.e. $\mu_s z$. T(z) is linked to the local refractive index and backscattering property of the tissue [11]. However, for a homogenous turbid medium, it can be considered to be constant. Therefore, μ_t can be obtained theoretically from the reflectance measurements at two different depths, z1 and z2:

$$\mu_t = \frac{1}{2(\Delta Z)} \ln(\frac{R(Z1)}{R(Z2)}) \qquad (2)$$

where $\Delta z = |z_1 - z_2|$. As noise is inevitable in the measurement, a final result should thus be obtained by the use of least square fitting technique in order to improve the accuracy of the determined value of μ_t.

Eighty repeated scans for one spatial point of each liquid phantom were performed, and reflected powers were averaged to minimize noise.

Fresh calvaria was spread in phosphate-buffered saline (PBS) for monitoring oxidized form of CytOx. Firstly, thirty depth scans were taken at one spatial point of the sample and the averaged reflectance as a function of depth profile was obtained and treated as the control. After measuring of reflected signals as a function of depth from one spatial point of the specimen with oxidized CytOx, 1% sodium dithionite PBS solution was then applied to reduce CytOx in the specimen. Scans started immediately at the same point of the sample after introducing the reducing agent. Every ten scans were averaged to obtain each reflectance profile of the tissue specimen with redox change of CytOx as a function of reduction time, respectively.

For monitoring of the redox state of CytOx of tissue, extracting the absorption coefficient changes will be the main concern. It is possible to determine the absorption coefficient difference between the tissue with oxidised and reduced CytOx if two measurements for attenuation coefficients are made, i.e. one at the oxidised and another at reduced states:

$$\Delta\mu_a = \mu_t(oxidized) - \mu_t(reduced) \qquad (3)$$

This equation is established under the condition that the scattering changes in the tissue after its CytOx shifts can be negligible, though this assumption remains to be explored.

The functional monitoring of the absorption changes during the redox shift of CytOx of the tissue can also be made possible by the use of the OCT system through repeated scans over a period of time.

3. RESULT AND DISCUSSION

3.1 Two-dimensional images of rat calvarias by the OCT system
Optical-coherence tomograms of the backscattered power measured within a two-dimensional region of adult and newborn rat calvarias at 820nm are shown in Figure 2. The periosteum, cartilage and other features of the calvaria from adult rat, 10-day rat and newborn rat are sharply differentiated. From the images, increase in thickness of periosteum with rat age was clearly seen. The thickness of periosteum layer from the newborn rat was measured at approximately 30μm. Some brighter regions of the image from variations in the density or orientation of structure of calvaria can be seen clearly. Such results demonstrate that the OCT is capable of tomographically imaging the calvaria with high resolution, which could only previously be obtained by the conventional excisional biopsy. However the cellular structure within the specimens can not be differentiate because axial and lateral resolutions of both systems used in this study exceed the widths of the cell layers in the tissue samples.

3.2 Absorption coefficients measured by the OCT system

3.2.1 Liquid phantom

Naphthol Green is an effective absorber for the short near infrared (NIR) light (700-850nm), which is highly water-soluble and introduces minimal scattering in the solution [12]. Intralipid is often used as a scattering agent in tissue models. Thus in the first set of experiments, the different concentrations of the dye solution mixed with intralipid were prepared and used as phantoms to simulate absorption changes in the tissue with CytOx redox shift. Figure 3 shows reflectance versus depth profiles measured with OCT at 820nm from (a) 1% and 2% intralipid solution only and (b) the samples consisting of several different concentrations from 0.0025% to 0.2% of naphthol green B with 1% intralipid in water. It can be clearly

Figure 2, False colour OCT images at 820nm from Rat calvaria (a) adult, (b) young and (c) baby, respectively, where P represents periosteum, C the cartilage, and S the suture.

seen from Figure 3 that the backscattered signals recorded from all liquid phantoms appear straight on the semi-logarithmic plot and the reflected signals fell off exponentially with depth. The decay rates were increased as the increase of scatter concentration (a) and absorber concentration (b) of samples. According to single scattering model, the slopes of the reflectance signals versus depth from the sample represent the total attenuation at that wavelength. The slopes were

determined by fitting the backscattered power curves, plotted on a logarithmic scale as a function of the samples depth. The attenuation of the sample containing 2% intralipid (μ_t ~1.23/mm) is higher than that of the sample of 1% intralipid (μ_t ~0.61/mm) because of the more scatterer. The attenuation of the sample containing 0.20% naphthol green B (μ_t

Figure 3, Reflectance signals from liquid phantom at 820 nm, (a) intralipid suspensions (scatter), (b) naphthol green B with 1% intralipid (absorber with scatter)

~1.18/mm) is higher than that of the sample of 0.08% naphthol green B (μ_t ~0.76/mm) because of more absorption.

The total attenuation coefficients of different concentration naphthol green B solution mixed with 1% intralipid were calculated from curve slopes based on single scattering model using least square curve-fitting method. Figure 4 shows the relationship between the total attenuation coefficient of sample solutions containing absorber of various concentrations and naphthol green B concentration for dye content of 0 to 0.2%. The attenuation coefficients (μ_t) demonstrate a linear increase with the concentration of the dye. The coefficient appears to be an accurate measure of absorber concentration, even in very low content down to a green B concentration of 0.0025%. By subtracting scattering coefficient of 1% intralipid, absorptivity of the dye was estimated to be 3.70mm^{-1}/%.

Figure 4, Total attenuation coefficients of naphthol green B with 1% intralipid measured by optical coherence quantitation at 820nm

Such results demonstrate the capability of the OCT to quantify accurately the absorption of a sample.

3.2. 2 Bone tissues

As evident from Figure 2, the uniform intensity in the OCT image produced by the periosteum demonstrates that the structure of periosteum is macroscopically homogeneous. Indeed, periosteum is a relatively transparent tissue without blood perfusion. The absorption changes at 820nm from haemoglobin can therefore be excluded to simplify experimental model. Calvarias from young adult rats were harvested freshly and submerged in PBS solution. The reflected signal versus depth from one spatial point of a specimen with oxidized form CytOx was plotted in Figure 5 (a) as an example, where backscattered signals from $41\mu m$ to $105\mu m$ and from $105\mu m$ to $150\mu m$ in optical depth in the profile correspond to reflections from periosteum layer and cartilage layer of the calvaria respectively. The optical depth range corresponds to the measured displacement (z) of the reference mirror in air. The effective sample thickness is given by $d = z/n_s$, where n_s is the mean refractive index of the sample (assumed equal to 1.35 for periosteum and cartilage used in this study). The thickness of the periosteum and cartilage of the calvaria was determined to be $\sim47.4\mu m$ and $34\mu m$ respectively. The other distinct peaks in the measured profile were produced by each discontinuity in the refractive index in the sample. As predicted by the single-backscatter model in the ideal case of tenuous and relatively transparent tissues, the slope of reflectance from periosteum represent the total attenuation (absorption of CytOx at 820nm and scattering) of the periosteums with oxidized form of CytOx. Total attenuation was estimated to be 4.11 mm^{-1} by using least square method.

Figure 5, Reflectance vs depth profiles at 820nm by OCT of calvaria with (a) oxidized and (b) reduced CytOx after 5 minutes
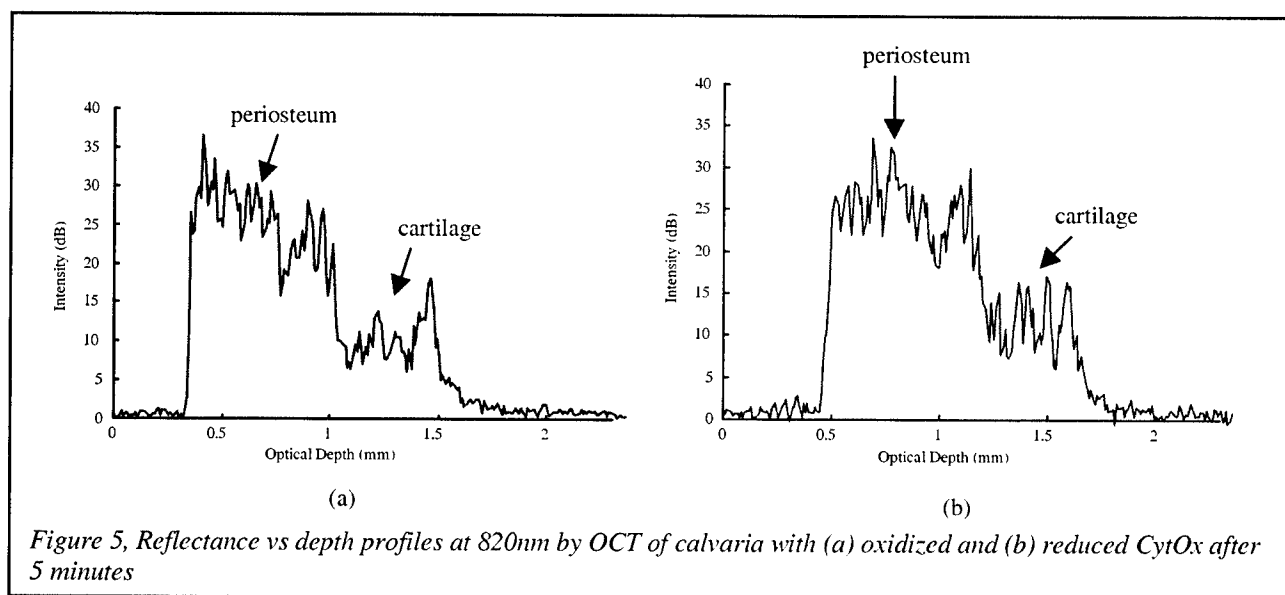
To demonstrate the capability of OCT system to extract the information of redox state, experiments were conducted by chemically reducing CytOx in tissues with sodium dithionite. The total attenuation was measured as the function of reduction time. As an example, the reflectance-vs-depth (average of ten scans) at the same spatial point after CytOx was reduced for 5 min was shown in Figure 5 (b). The result shows that the attenuation coefficient ($1.93mm^{-1}$) in the periosteum is markedly decreased as CytOx is reduced. About 53% decrease of attenuation coefficients in the periosteum was clearly observed with redox change of CytOx after 5 min reduction due to less absorption of reduced CytOx. Provided that the change of the scattering coefficients in the tissue with the redox shift of its CytOx is negligible, the difference in absorption ($\Delta\mu_a$) between the oxidized and reduced form of CytOx was estimated to be $2.18mm^{-1}$ from the difference in total attenuation between them.

The results suggested that OCT might be capable of monitoring redox change of CytOx in periosteum of calvaria by applying single scattering model. Single-backscattering approximation that neglects multiple scattering is applied to interpret reflectance profiles recorded from tenuous and relatively transparent tissues for optical depth less than 4. For optical depth more than 4, multiple scattering from tissue becomes dominant. Multiple scattering leads to spreading of a light beam and loss of directionality. Therefore the backscatter signals from tissues measured by OCT system are very complicated, which are dependent on the backscattering coefficient, total scattering coefficient, the mean scattering angle

(scattering anisotropy) and absorption coefficient within the sample [10]. From Figure 5, we can see it is not possible to get total attenuation coefficient of cartilage layer of calvaria, which is in the deeper optical depth, by using single scattering model due to multiple scattering.

4. CONCLUSIONS

We have presented optical coherence tomography technique to image bone tissue and to monitor the redox state of mitochondria enzyme Cytochrome oxidase (CytOx) in bone for applications in tissue engineering. The results have demonstrated that the OCT system is capable of imaging the calvaria of rats tomographically with a resolution approaching 9 microns, which could only be previously obtained by the conventional excisional biopsy. Various thickness periosteums of calvarias from different age rats can be determined accurately by the system. The thickness of periosteum layer from the newborn rat was measured at approximately 30 microns.

The backscattered power-versus-depth profile from the liquid phantoms (naphthol green B with intralipid) and tissue specimens (periosteum of calvaria from newborn rats) were used to quantify the absorption changes of the sample. Absorption coefficients of naphthol green B were accurately quantified by the linear relationship between attenuation coefficients from the slopes of the reflected signals and naphthol green B concentration. The absorptivity of the dye was estimated to be $3.70mm^{-1}/\%$.

The results also show that the attenuation coefficients decreased in periosteums as CytOx was reduced by sodium dithionite. The difference in absorption between the oxidised and reduced form of CytOx was estimated to be $2.18mm^{-1}$ for the periosteum of young adult rat calvaria. This suggests the feasibility of optical coherence tomography for monitoring the redox state of tenuous and relatively transparent tissues.

ACKNOWLEDGEMENTS

REFERENCES

1. Tearney G J., Brezinski M E., Bouma B E., et al 1997 *In vivo* endoscopic optical biopsy with optical coherence tomography. *Science, 276:2037-2039*
2. Wang R K., Elder J B., Smith V. 2000 High resolution tomographic imaging of human gastro-intestinal tissues with optical coherence tomograph. *Proc. SPIE, 4224, 294-299*
3. Sathyam U S., Colston B W., Da Silva L B., et al 1999 Evaluation of optical coherence quantitation of analytes in turbid media by use of two wavelengths. *Applied Optics 38 (10): 2097-2104*
4. Schmitt J M., Knüttel A., and Bonner R.F. 1993 Measurement of optical properties of biological tissues by low-coherence reflectometry. *Applied Optics32 (30): 6032-6042*
5. Schmitt J.M., Xiang S.H., and Yung K.M. 1998 Differential absorption imaging with optical coherence tomography. *J. Opt. Soc. Am A 15 (9): 2288-2296*
6. Morgner U., Drexler W., Kärtner F.X., Li X.D., et al 2000 Spectroscopic optical coherence tomography. *Optics Letters 25 (2): 111-113*
7. Jöbsis FF. 1977 Noninvasive, infrared monitoring of cerebral and myocardial oxygen sufficiency and circulatory parameters. *Science 198: 1264-126*
8. Deply D T., Cope M. 1997 Quantification in tissue near-infrared spectroscopy. *Philosophical Transactions of the Royal Society of London Series B- Biological Sciences 352 (1354): 649-659*
9. Wang R.K. 1999 Resolution improved optical coherence-gated tomography for imaging through biological tissues. *J. Modern Optics 46(13): 1905-1912*
10. Schmitt J M., Knüttel A., Gandjbakhche A., et al 1993 Optical characterization of dense tissues using low-coherence interferometry. *SPIE 1889: 197-211*
11. Wang R K. 2000 Modelling optical properties of soft tissue by fractal distribution of scatters. *Journal of Modern Optics 47: 103-120*
12. Iizuka M.N., Sherar M.D., Vitkin A.I. 1999 Optical phantom materials for near infrared laser photocoagulation studies. *Lasers in Surgery and Medicine 25: 159-169*

Optical BRDF and BSDF Measurements of Human Incisors From Visible to Mid-Infrared Wavelengths

D.W. Blodgett and S.C. Webb
Air-Defense Systems Department
The Johns Hopkins University Applied Physics Laboratory
Laurel, MD 20723

ABSTRACT

The optical bi-directional reflectance distribution functions (BRDF) and bi-directional scattering distribution functions (BSDF) of human incisors were measured from -180° to 180° using a scatterometer at 632.8 nm, 1.064 μm, and 3.39 μm. Results from these measurements show that multiple scattering events dominate the optical characteristics of the tooth at the measurement wavelengths in the visible and near-IR. Results from the 3.39 μm wavelength indicate that very little scatter or absorption occurs. This allowed us to obtain an estimated absorption coefficient of about 0.7 cm^{-1}, which is much smaller than previously reported for the visible and near-IR wavelengths.

Keywords: dental hard tissue, tissue optics, scatterometer

1. INTRODUCTION

The optical characteristics of dental hard tissues are important for the development of new diagnostic, imaging, and therapeutic techniques. The presence of oral diseases, such as caries and non-caries lesions, periodontitis, and oral and maxillofacial tumors, is associated with a change in the structure of the dental hard tissue. One means of early detection of these diseases is the development of high-resolution imaging and diagnostic techniques. Current techniques include X-ray radiography, computed tomography (CT), magnetic resonance imaging (MRI) and spectroscopy (MRS), and conventional ultrasound [1]. However, each of these methods has problems resolving sub-millimeter tissue structure in clinical practice. Recently, researchers have begun investigating the use of light for characterizing the internal structure of dental hard tissue.

Some of the earliest work in optical diagnostics of dental hard tissues involved monitoring differences in the emission spectra of carious and noncarious tissue using an Argon laser (488 and 514.5 nm). Alfano et al. and others illuminated hard dental tissue with monochromatic light at 530 nm and noted a shift in the emission spectra to > 540 nm for carious regions [2-4]. Researchers have also taken advantage of the relatively high transparency between 560 and 575 nm of dental hard tissue to monitor the pulpal blood flow and oxygenation [5,6]. Preliminary work has also been performed to develop optical techniques for measuring dental deformation [7].

For surgery and therapeutic applications, the Nd:YAG laser (1.064 μm) has shown much promise. Researchers have developed a fiberoptic, direct contact delivery system that can not only cut, but also sterilize and seal soft tissue at very low optical power. One specific area of success for the Nd:YAG laser in dental research is the removal of carious lesions without damage to the surrounding tooth enamel and minimum associated discomfort [8]. The 9-11 μm region is another spectral region of interest in dental research. The carbon-dioxide (CO_2) laser, which operates in this waveband, has met with success in fusing enamel, dentin, and apatite. This fusion has led to the inhibition of subsequent lesion progression and markedly improved the bonding strength of a composite resin to dentin [8,9].

More recently, much interest has been generated in the use of optical coherence tomography (OCT) for high-resolution imaging of dental structures. In general, OCT makes use of the intensity of reflected or backscattered light as a function of position within the object to construct a three-dimensional image [10-12]. Blodgett and Baldwin have also done preliminary work in the use of optical generation and detection of ultrasound in dental structure [13]. In each of these optical diagnostic, imaging, and therapeutic techniques, an understanding of the interaction of the light and the dental tissue is critical.

When considering laser interaction with any material, there are four basic mechanisms that occur: reflection, absorption, transmission, and scatter. In the case of dental hard tissue, these basic mechanisms are manifested as: (1) light reflection and propagation at the enamel boundary; (2) light propagation in the enamel; (3) light reflection and propagation at the enamel-dentin junction; (4) light propagation in dentin; and (5) light reflection and propagation at the pulp-dentin junction. The importance of each of these five mechanisms depends on the wavelength of light being used by the optical diagnostic technique. Shown in Fig. 1 are results from a spectrophotometric analysis of a) enamel and b) dentin, comparing absorbance,

reflectance, and transmittance from 250 nm to 2,500 nm [8]. These figures show that both enamel and dentin are relatively transparent through the visible spectrum with absorption peaks near the ultraviolet (UV) (<200 nm) and near-infrared (2 μm).

(a)   (b)   (c)
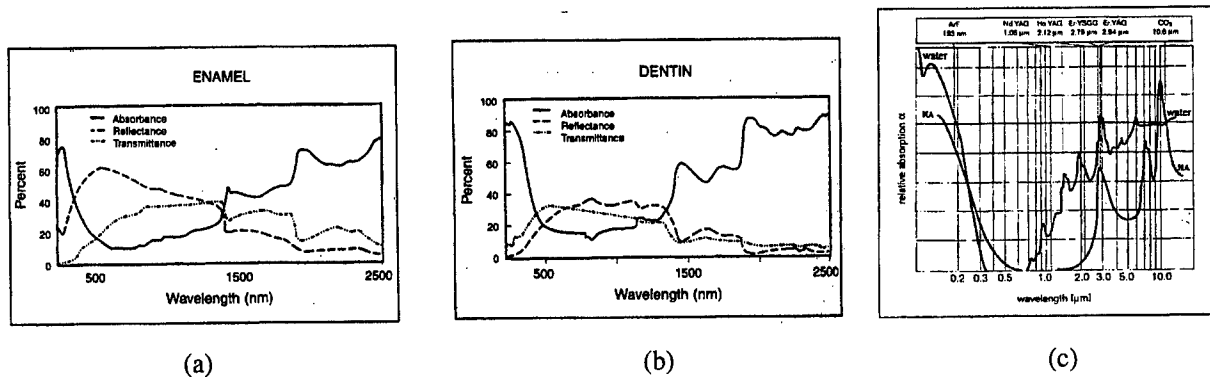
Fig. 1. Comparison of spectrophotometric analysis for a) enamel and b) dentin and c) relative absorption of hydoxyapatite and water [8].

Dental enamel is the hard protective substance that covers the crown of the tooth. It is the hardest biologic tissue in the body and designed to resist fractures during mastication (chewing). Enamel is composed of about 96% inorganic mineral in the form of hydroxyapatite and 4% water and organic matter [8,14]. A comparison of the relative absorption of hydroxyapatite and water is shown in Fig. 1c. It is apparent from this figure that dominant regions of absorption occur in the UV (<200 nm), 2.9 μm, 7.5 μm, and 10 μm. Hydroxyapatite is a crystalline calcium phosphate that is also found in bone, dentin, and cementum. Enamel is composed of rods that extend from their origin at the dentino-enamel junction to the outer surface of the tooth [8,14]. The rod itself resembles a keyhole in shape, allowing individual rods to form a strong interlocking structure (see Fig. 2a). The head of the rod measures about 5 μm across while the tail is only about 1 μm. Each rod is filled with crystals, whose orientation varies along the rod. At the head of the rod, these crystals are approximately parallel to the rod axis while near the tail of the rod, the crystals are oriented almost perpendicular to the rod axis (see Fig. 2b). The variation in the orientation of the crystals causes a certain anisotropy of the optical constants.
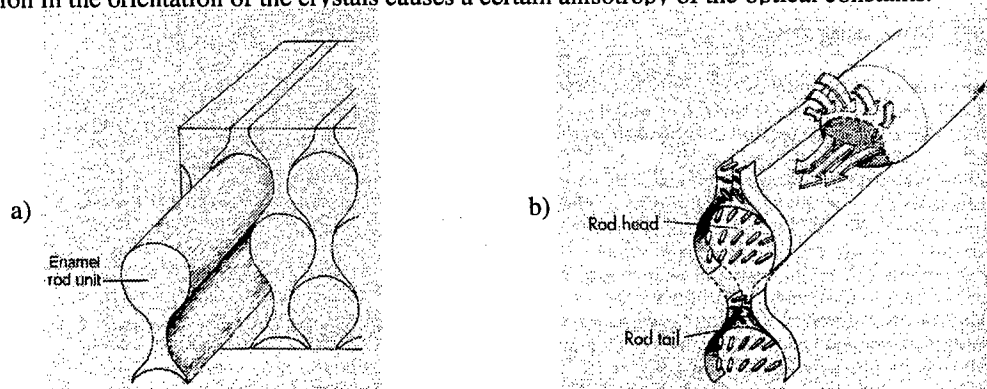
Fig. 2. Examples of a) interlocking of individual enamel rods and b) variation in crystal orientation [14].

Dentin is the hard tissue that constitutes the body of the tooth. Unlike enamel, which is almost white in color, dentin appears almost yellowish. Dentin is a living tissue that is not normally exposed to the oral environment. Like bone, dentin is composed primarily of an organic matrix of collagen fibers (20%), inorganic hydroxyapatite crystals (70%), and about 10% water [14]. With 20% less mineral than enamel, dentin is softer and slightly elastic. It is this change in structural composition that contributes to the different spectrophotometric properties. Dentin itself is classified as primary, secondary, and tertiary on the basis of the time of its development and the histologic (microscopic) characteristics of the tissue. Primary dentin is the major component of the crown and root while secondary dentin forms only after tooth eruption (i.e. when the teeth begin to function) and borders the pulp. Finally, tertiary or reparative dentin occurs in response to the presence of a trauma to the pulp. The structure of dentin is composed of S-shaped tubules that run from the dentino-enamel junction to the dentino-pulp junction (see Fig. 3). Each of these tubules is about 1-3 μm in diameter and surrounded by a matrix of needle-shaped, hydroxyapatite crystals in a protein matrix of composed mostly of callogen [15].

The third component of a tooth is the pulp, which is the soft connective tissue located in the central portion of each tooth. It is composed of both a crown (coronal part) and root (radicular part). Pulp contains specialized connective tissue composed of thin-walled blood vessels, nerves, and nerve endings enclosed within the dentin.
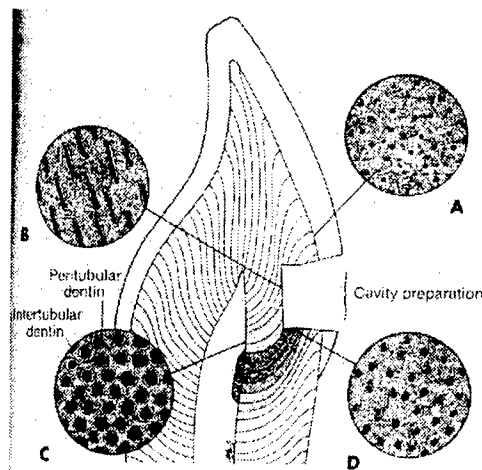
Fig. 3. Diagram of dentin showing S-shaped curvature of dentin tubules [14].

In the visible spectrum, light scattering is the dominant factor in determining the color and appearance of dental enamel and dentin. In fact, it is this dependence on scattering that allows for the quantification of enamel caries [16]. When a collimated beam irradiates the enamel of a tooth, the beam becomes partially reflected and scattered in the backwards direction, while the rest is either absorbed in the surface layer or penetrates more deeply into the enamel. The reflected light is propagated in a direction close to the specular direction angle with an angular spectrum determined by the enamel surface curvature and the surface macroroughness (several dozen micrometers). These two factors make the angular spectrum of the reflected beam very dependent on the location where the beam is incident on the enamel (tooth) surface. The scattered component of the backward propagating light is due to both macro- and microroughness of the enamel. The macroroughness component is due to surface irregularities that are large with respect to the incident wavelength and result in a nonuniform distribution. Scattering due to microroughness (i.e. features smaller than the wavelength of the incident beam) has a smooth, homogeneous, angular distribution that can be accurately described by Lambert's law. These factors, combined with the fact that a tooth is a multilayered system, make accurate modeling of the optical properties very difficult.

In an effort to better understand the behavior of light in a tooth, several research groups have been investigating the nature of optical scatter in both enamel and dentin. Spitzer and ten Bosch determined that the hydroxyapatite crystals are mainly responsible for the scatter in enamel [16]. In a later study by ten Bosch and Coops [17], the relation between light scattering (between 400 nm and 700 nm) and enamel hardness was investigated. Results indicated that tooth color is predominately determined by the properties of the dentin. The contributions of scattering from the enamel can only be seen in the blue range (about 400nm). In an effort to better understand the nature of scatter in the visible spectrum, Zijp and ten Bosch made angular dependence measurements of Helium-Neon (HeNe) scattered light transmitted through bovine and human dentine [18,19]. For these measurements, special dentin sections, 10-20 μm thick were prepared to reduce multiple scattering. The samples were polished with 1200-mesh sanding paper and then ultrasonically cleaned to reduce any smear on the surface. Placing the sections in water during the measurements helped reduce reflections at the dentino-water interface. Results from these studies showed that the tubules are the most important scatterers in dentin. The authors also determined a scattering coefficient of 1200 cm^{-1} and a scattering anisotropy parameter of about 0.4.

Fried and fellow researchers [15] made similar measurements on dental enamel and dentin using a rotating goniometer at 543, 632.8, and 1053 nm. As with Zijp and ten Bosch, thin samples (30-2000 μm) were cut, polished, and cleaned to remove any smear on the surfaces. To further reduce the effects of surface scatter, the samples were placed in an index matching fluid during the measurements. This allowed the authors to improve the measured accuracy of the bulk optical properties of the dental enamel and dentin. They estimated scattering coefficients of 280 cm^{-1} at 543 and 632.8 nm and 260 cm^{-1} at 1053 nm, which are substantially smaller than those calculated by ten Bosch and Coops [18,19]. The absorption coefficient calculated by Fried and coworkers was 3-4 cm^{-1} and was wavelength independent in the measured spectral regime.

In this paper, in-vitro optical bidirectional reflectance distribution functions (BRDF) and bi-directional scattering distribution functions (BSDF) of human incisors were measured using a scatterometer at 632.8 nm, 1.064 μm, and 3.39 μm. Results from these measurements will prove useful in developing future in-vivo optical diagnostic and imaging techniques.

2. EXPERIMENTAL CONFIGURATION

A scatterometer was used to determine the BRDF and BSDF of the incisors at wavelengths of 632.8 nm, 1.064 μm, and 3.39 μm [20]. A diagram of the experimental setup is shown in Figure 4. The detector is mounted on one end of a motorized swing arm, and the other end of the arm is fixed at the sample. The scatterometer measures the incremental angular dependent scatter over the back hemisphere. For the first set of experiments, we used a polarized 30 mW HeNe laser operating at 632.8 nm, and a large area Si detector with a notch filter. All measurements were made in the plane of incidence from $\theta_r = -180°$ to $180°$. The second set of experiments were conducted using a 300 mW CW Nd:YAG laser and a large area Si detector. The final set of experiments was conducted using a 2 mW infrared (IR) HeNe laser (3.39 μm) with a large area InSb detector. For each experiment, the laser beam was chopped to allow for coherent detection with a lock-in amplifier. This improved measurement SNR by removing unwanted background noise.
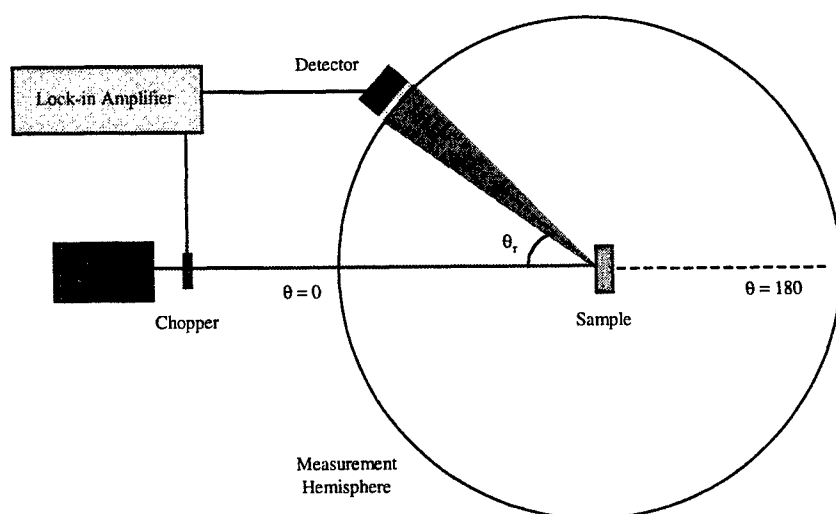
Fig. 4. Experimental configuration for BRDF and BSDF measurements.

In these experiments, we assume that the BRDF and BSDF are the same for all ϕ_r for a particular θ_r, which implies that the reflectance is rotationally symmetric about the specular direction. This geometry is illustrated in Figure 5, where the reflective surface lies in the xy plane, and the light is incident from the z-direction. As the sample is rotated from normal incidence to oblique angles, the illuminating spot changes from a circle to an ellipse, with its long axis in the plane of incidence. The reflectance from this elliptical spot is no longer independent of ϕ_r. However, this effect is minimal for small angles of incidence ($\theta_i < 45°$).
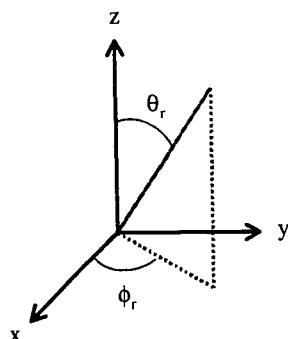
Fig. 5. Experimental geometry for scatterometer measurements.

Depending on the surface characteristics of a material, the BRDF can have specular and diffuse components. A specular reflection is at a specific angle from a very smooth surface ($\theta_r = -\theta_i$), while a diffuse reflection is scattered at different angles from a rough surface. A completely diffuse, or Lambertian, phase function is independent of the angle of incidence, and varies as the cosine of the reflected angle. In general, as the wavelength of the incident light increases, the

reflection becomes more specular, because the longer wavelength is no longer sensitive to small structural variations on the surface of the material. The change in the BRDF as a function of wavelength can be indicative of the size of the structure in the material. Finally, the measured reflection characteristics also depend on the beam profile of the laser. Figure 6 shows a comparison of the functional forms of the various BRDF components that can be observed.
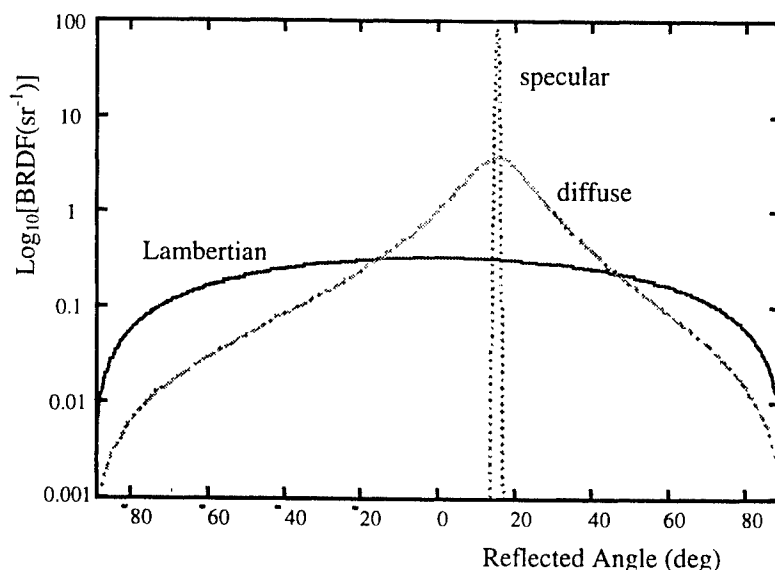
Fig. 6. Comparison of functional forms of Lambertian, specular, and diffuse materials.

3. RESULTS

For each wavelength, the BRDF and BSDF were measured with the laser at a -15° angle of incidence on the labial (front) surface of the tooth. This allowed for the near-specular component of the backscatter to be measured without being blocked by the detector. To help remove any artifacts in the measurements due to the tooth curvature, the tooth was aligned such that the incident beam was near-normal to the labial surface. In between measurements, the teeth were stored in a water solution prior to each test, but the surface of the tooth was dry during the measurements. The measured BRDF/BSDF of an incisor at 632.8 nm is shown in Fig. 7. In this figure, the BRDF is nearly Lambertian, with a small diffuse or specular component near 15°. A diffuse component is expected due to the large number of scattering events that occur from enamel (rods measure 1-5 μm across) and dentin (tubules measure 1-3 μm in diameter) structure that is larger than the wavelength of the incident light. The BSDF measurement shows that a small amount of the incident light makes it completely through the tooth. It is unclear from this data how many ballistic photons (i.e. photons that undergo no scattering) contribute to this transmitted component due to the relatively wide instrument function. The large angular extent of the instrument function, which is simply a measure of the beam profile, is due to the large area detector used in these experiments. We chose large area detectors to help average out the effects of speckle and to improve the SNR under the low light conditions [20].
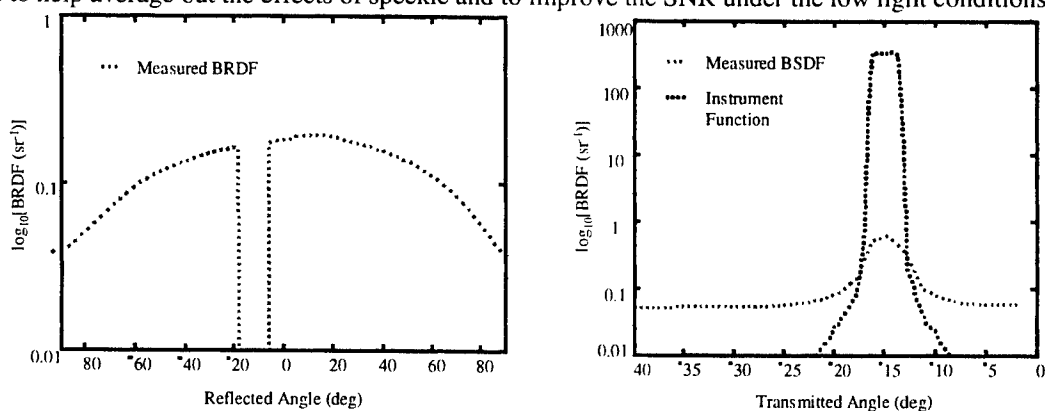
Fig. 7. BRDF and BSDF measurements at 632.8 nm.

Figure 8 shows similar plots for an incisor illuminated by 1.064 μm light. Here the reflectance is purely Lambertian while the forward-scattered light (BSDF) is almost identical to that measured at a wavelength of 632.8 nm. The similarities between figures 7 and 8 are expected due to the similar optical properties of the dental hard tissue at these wavelengths (see Fig. 1) and the relative size differences between the dental hard tissue structures and the incident wavelengths.
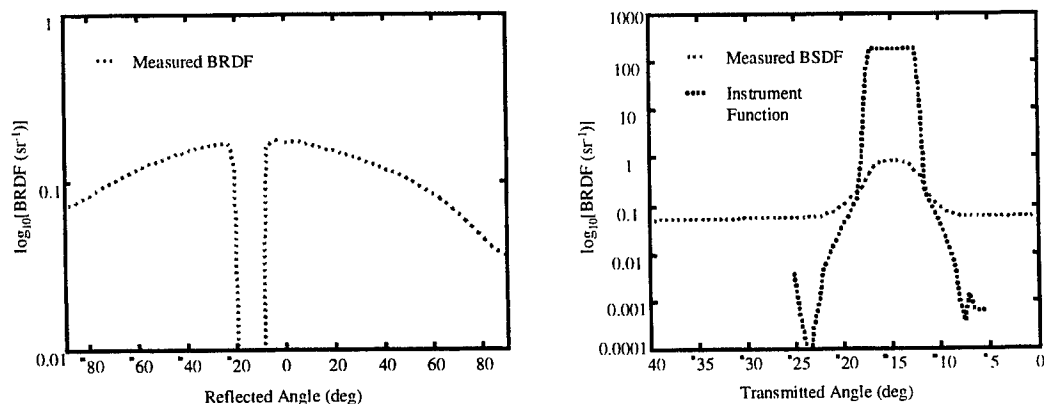
Fig. 8. BRDF and BSDF measurements at 1.064 μm.

The most surprising results were found for the BRDF/BSDF measurements at an incident wavelength of 3.39 μm (see Figure 9). The magnitude of the back scattered light is almost an order of magnitude lower than that for the two previous measurements and the angular extent of the forward-scattered light almost perfectly matches that of the instrument function. This implies that there is very little absorption or scattering occurring within the tooth, which is not expected since there is supposed to be a marked increase in absorption in the hydroxyapatite at 3.39 μm (see Fig. 1). Due to the lack of scattering, we were able to estimate the absorption coefficient at 3.39 μm as

$$\alpha = \frac{\log\left(\dfrac{I_{instrument}}{I_{sample}}\right)}{t_{sample}} \approx 0.7 \, cm^{-1}, \tag{1}$$

where $I_{instrument}$ and I_{sample} are the peak values of the instrument and sample BSDF measurements and t_{sample} is the sample thickness. This value is significantly smaller than the 3-4 cm^{-1} reported by Fried for dentin and enamel [15] at visible and near-IR optical wavelengths.
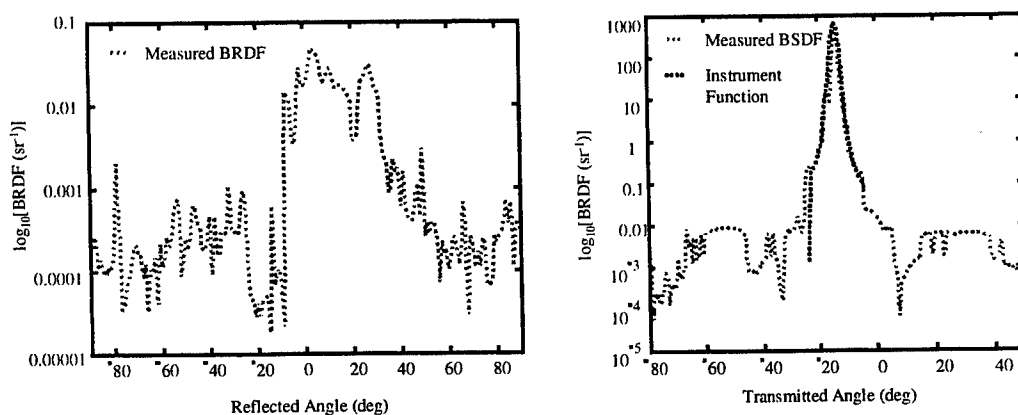
Fig. 9. BRDF and BSDF measurements at 3.39 μm.

4. CONCLUSIONS

In-vitro measurements of the BRDF and BSDF of human incisors are reported at optical wavelengths of 632.8 nm, 1.064 μm, and 3.39 μm. As expected for the visible and near-IR measurements, the optical properties of the incisors are

dominated by multiple scattering events within the tooth structure. The measured BRDF/BSDF were nearly identical at 632.8 nm and 1.064 μm. The most interesting result was found at 3.39 μm, where very little scatter or absorption was found. We estimate an absorption coefficient of about 0.7 cm⁻¹, which is far smaller than that previously reported by Fried and his coworkers [15] at the visible and near-IR wavelengths. This result is interesting since the absorption coefficient of hydroxyapatite is supposed to increase as the optical wavelength increases from the visible to the infrared. This apparent "optical window" may prove useful in developing new pulp diagnostic techniques.

REFERENCES

1. S.R. Matteson, S.T.Deahl, M.E. Alder, and P.V. Nummikoski, "Advanced imaging methods," *Crit. Rev. Oral Biol. Med.* **7**, pp. 346-395, 1996.
2. R.R. Alfano and S.S. Yao, "Human teeth with and without dental caries studied by visible luminescence spectroscopy," *J. Dent. Res.* **60**, pp. 120-122, 1981.
3. J.J. ten Bosch, H.C. van der Mei, and P.C.F. Borsboom, "Optical monitor of in vitro caries," *Caries Res.* **18**, pp. 540-547, 1984.
4. V.K. Kutsch, "Caries illumination with an argon laser: a clinical trial," *ISLD Third International Conference on Lasers in Dentistry*, p. 22, 1992.
5. J. Schmitt, R.L. Webber, and E.C. Walker, "Optical determination of dental pulp vitality," *IEEE Trans. Biom. Engr.* **38**(4), pp. 346-352, 1991.
6. O.S. Kyosti, V. Kainulainen, V. Sarkela, K. Alaniska, and H. Kopola, "Information of circulation from soft tissue and dental pulp by means of pulsatile reflected light," *Oral Surg. Oral Med. Oral Path*, **84**, pp. 315-320 1997.
7. J. Kokaj, Y. makdisi, and K. Bhatia, "Dental deformation measurement using coherent optical techniques," *Optik*, **107**(1), pp. 11-19, 1997.
8. L.J. Miserendino and R.M. Pick, *Lasers in Dentistry*, Quintessence Books, Chicago, 1995.
9. J.D.B. Featherstone, and D.G.A. Nelson, "Laser effects on dental hard tissues," *Adv. Dent. Res.* **1**(1), pp. 21-21, 1987.
10. F.I. Feldchtein, G.V. Gelikonov, V.M. Gelikonov, R.R. Iksanov, R.V. Kuranov, N.D. Gladkova, M.N. Ourutina, J.A. Warren, and D.H. Reitze, "In vivo OCT imaging of hard and soft tissue of the oral cavity," *OSA* **3**(6), pp. 239-270, 1998.
11. J.M. Schmitt, S.X. Xiang, and K.M. Yung, "Differental absorption imaging with optical coherence tomography," *J. Optic. Soc. Am. A*, **15**(9), pp. 2288-2296, 1998.
12. M.J. Everett, K. Schoenenberger, B.W. Colston, L.B. Da Silva, "Birefringence characterization of biologic tissue by use of optical coherence tomography," *Opt. Lett.* **23**(3), pp. 228-230, 1998.
13. D.W. Blodgett and K.C. Baldwin, "Laser Ultrasonic Techniques for Assessment of Tooth Structure," *SPIE BIOS*, 2000.
14. J.K. Avery, *Essentials of Oral Histology and Embryology: A Clinical Approach*, Mosby, St. Louis, 2000.
15. D. Fried, R.E. Glena, J.D.B. Featherstone, and W. Seka, "Nature of light scattering in dental enamel and dentin at visible and near-infrared wavelengths," *App. Optics* **43**(7), pp. 1278-1285, 1995.
16. D. Spitzer and J.J. ten Bosch, "The absorption and scattering of light in bovine and human dental enamel," *Calc. Tiss. Res.* **17**, pp. 129-137, 1975.
17. J.J. ten Bosch and J.C. Coops, "Tooth color and reflectance as related to light scattering and enamel hardness," *J. Dent. Res.* **74**(1), pp. 374-380, 1995.
18. J.R. Zup and J.J. ten Bosch, "Angular dependence of HeNe-laser light scattering by bovine and human dentine," *Archs oral Biol.* **36**(4), pp. 283-289, 1991.
19. J.R. Zup and J.J. ten Bosch, "Theoretical model for the scattering of light by dentin and comparison with measurements," *App. Optics* **32**(4), pp. 411-415, 1993.
20. J.C. Stover, *Optical Scattering: Measurement and Analysis*, SPIE Press, Bellingham WA, 1995.

Tracking speckle motion with directional wavelets

I. Patrickeyev, Institute of Continuum Mechanics, Perm, Russia

S. Kirkpatrick, Oregon Health State University, Oregon, USA,

D.Duncan, The Johns Hopkins Applied Physics Laboratory, Laurel, MD USA.

Keywords: speckles, wavelets

INTRODUCTION

Speckle-based strain measurements in biological tissues can be useful for many applications. In using the speckle strain gauge the goal is to observe and track speckles that are translating in both time and space as a result of an applied load [1]. Usually, speckle images are processed with the FFT [5] or the Radon transform [6]. Here we have attempted to apply the novel technique of the Directional Continuous Wavelet Transform (DCWT) for image processing. This method yields two kinds of image decompositions 1) in terms of dilation scale and rotation angle (scale-angle representation) or 2) in terms of time and rotation angle (time-angle representation). In our study these properties of DCWT have been used to track the dynamics of speckle motions.

1. IMAGES AND METHODS

Two images of the speckle motion (one for each illumination angle) have been obtained by Sean Kirkpatrick *et al* [1].

These images were processed with the wavelet transform. This mathematical method has been extensively used in the last decade in many fields of research [2,3]. It has the advantage that the analysis can be performed locally, in contrast to the Fourier transform, which is based on the infinitely elongated harmonics. We have used this feature for determining the motion direction as a function of time. Since speckle tracks are oriented, it seems reasonable to use *directional* wavelets for solving the problem. The directions of speckle motions have been determined through image processing with the Cauchy wavelet (the choice of this wavelet is dictated by its good angular selectivity [3]. Here the scale is the size of the wavelet matrix side (in pixels). If the matrix is enlarged, the wavelet becomes more expanded and sensitive to larger details of an image.

For comparison, both images were also processed with the Radon transform.

2. RESULTS

In all halftones figures dark areas correspond to small values, bright – to large values. Most of the results are presented only for CAM2 image (because for CAM1 image the results are similar).

The original images are shown in Fig.1. The space (the pixel number of CCD) is plotted on the horizontal axis and the time (in milliseconds) on the vertical axis.

The scale-angle representation of the energy distribution with respect to one of the images (CAM2) is shown in Fig.2. The scale in pixels (=wavelet dilation parameter)

is plotted on the horizontal axis and angle in degrees (=wavelet rotation parameter) on the vertical axis. It is clearly seen that the energy at small scales is localized near two angles: 45 and 135 degrees, corresponding to the directions of the local speckle motion.

Integrating of the energy over the angle gives the scale spectrum, presented in Fig.3. There is one maximum in the small-scale region, which corresponds to the width of the speckle track.

The total angle spectrum is obtained as a result of integrating over a scale [2]. In contrast to the total angle spectrum it is possible to use profiles of the phase-plane (this approach conserves the locality). Three profiles at fixed scales are presented in Fig.4. The most interesting result is represented by curve at fixed small scale (profile marked by "scale=7pix"). It has two peaks, corresponding to the directions of local speckle motions. On the contrary, at fixed large scale the curve has two peaks corresponding to the 90 and 180 degrees, i.e. to the direction of image edges (profile mark by "scale=31pix"). The curve at intermediate scale shows "rearrangement" of directions (profile marked by "scale=15pix").

The Radon transform coefficients for both images are plotted in Fig.5. These curves are similar to the directional CWT profile at small values of the dilation parameter (Fig.4, "scale=7pix"). This similarity is not a surprise, because the Radon transform can be considered as a limiting case of the directional CWT [2,4], the so-called "singular" wavelet transform.

The time-angle representation of the energy distribution at the fixed dilation parameter (scale = 7) is shown in Fig.5. This scale corresponds to the "mean width" of a stripe in the image. The angle (wavelet rotation parameter) is plotted on the abscissa and

the time (in milliseconds) on the ordinate. Four moments corresponding to reversal of applied load are clearly seen.

3. DISCUSSION

This work is the first attempt to apply Directional Continuous Wavelet Transform for speckles image processing. All results are preliminary.

We suppose that the proposed approach may excel in the case where there is a non-uniform strain field (this will result in the speckle histories having different slopes in different locations). It could be useful for better estimation of the Young's modulus (or other mechanical characteristics of testing material) as a function of time or space.

REFERENCES

1. S.Kirkpatrick, M.Cipolla "High resolution imaged laser speckle strain gauge for vascular application", *Journal of Biomedical Optics*, January, 2000, pp.62-71.

2. M.Holschneider, "Wavelets: an analysis tool", Oxford, 1995.

3. J.-P.Antoine, R.Murenzi "Two-dimensional directional wavelets and the scale-angle representation", *Signal processing*, vol.52, 1996, pp.259-281.

4. I.Patrickeyev, P.Frick "Lymphocyte nucleus reconstruction via wavelet tomography", *Journal of Biomedical Optics*, July, 1999, pp.376-380.

5. D.Duncan, S.Kirkpatrick, F.Mark, L.Hunter "Transform method of processing for speckle strain-rate measurements", *Applied Optics*, V.33, No.22, August 1994, pp.5177-5186.

6. D.Duncan, S.Kirkpatrick "Noncontact microstrain measurements in orthodontic wires", *Journal of Biomedical Materials Research*, V.29, 1995, pp.1437-1442.
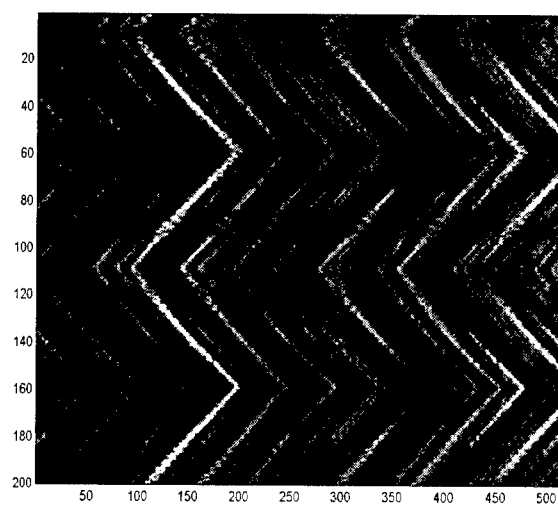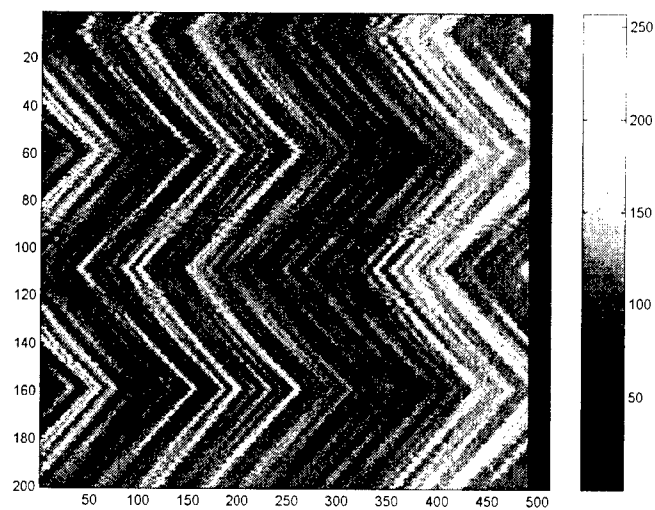
Fig. 1. CAM1 (top) and CAM2 (bottom) speckle images. Space (the pixel number of CCD) is along the horizontal axis and the time (in milliseconds) is along the vertical axis
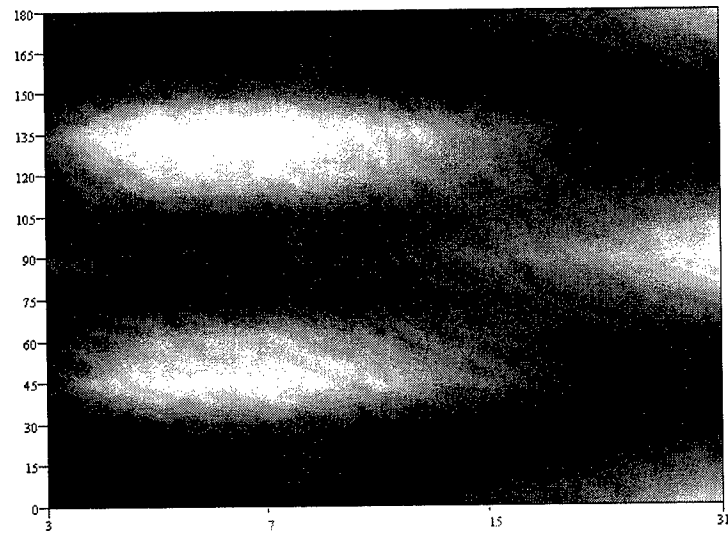
Fig.2. Energy distributions of CAM2 image. The scale (wavelet dilation parameter) is along the horizontal axis and angle in degrees (wavelet rotation parameter) is along the vertical axis.
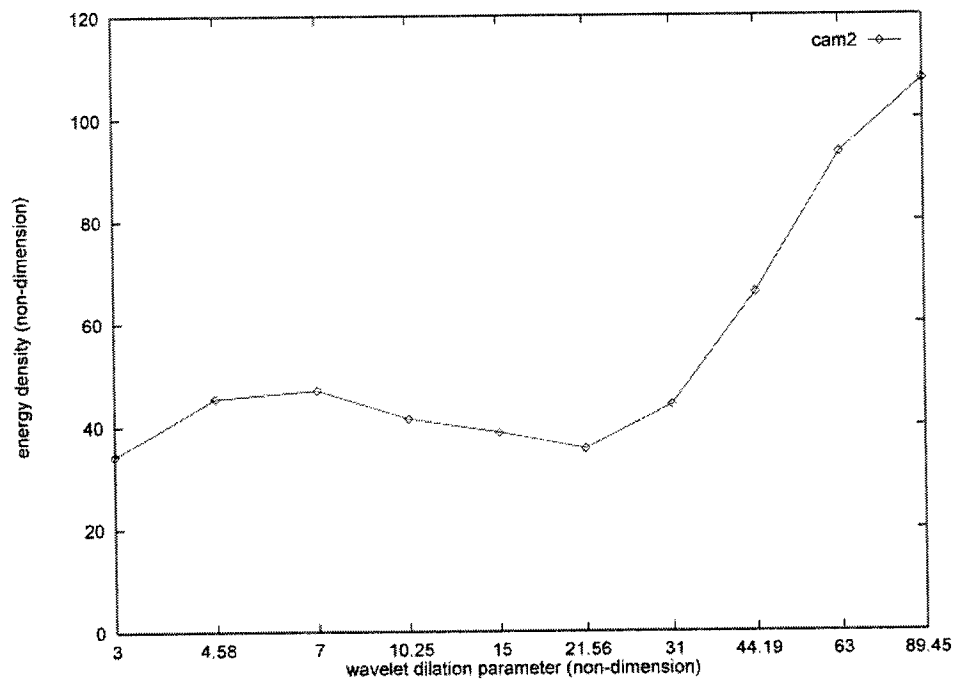
Fig.3. Scale spectrum of CAM2 image
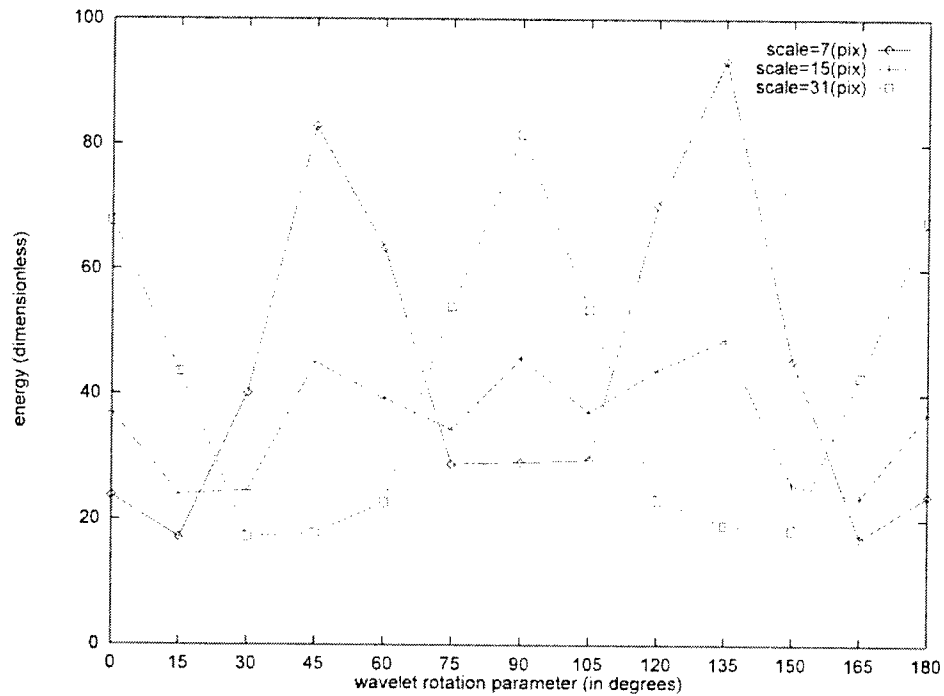
Fig.4. Profiles of phase plane of CAM2 image for three fixed values of dilation parameter, which corresponds to scale equal to dilation 7,15 and 31
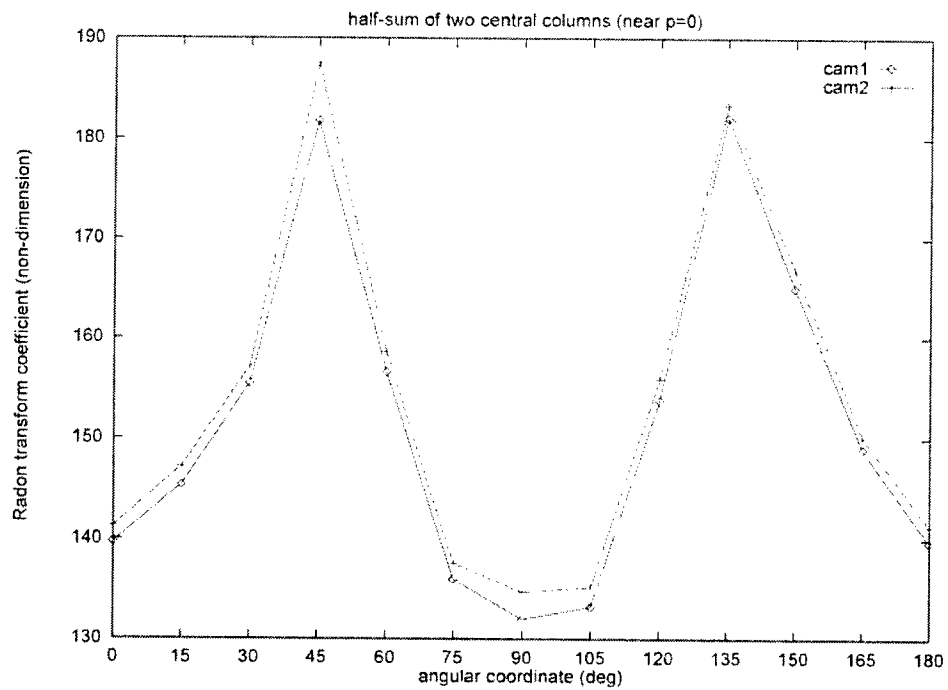
Fig.5 Radon transform coefficients for both CAM1 and CAM2 images.
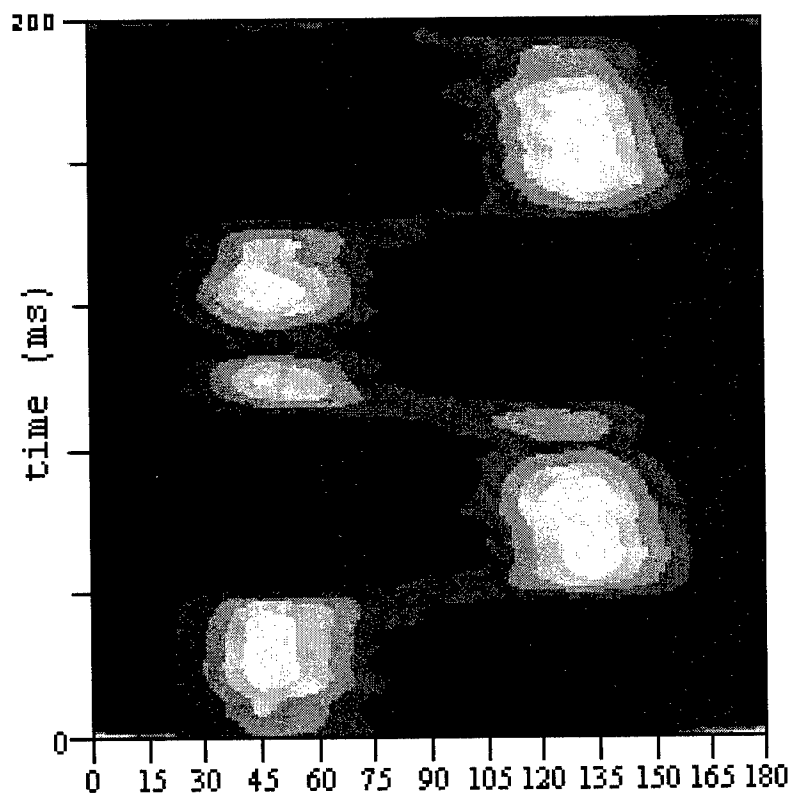
Fig.6. Time-angle representation of energy distribution of CAM2 image. The angle in degrees (wavelet rotation parameter) is along the horizontal axis and the time (in milliseconds) in the vertical axis

Characterizing microscopic domains
of birefringence in thin tissue sections

Steven L. Jacques, Alex Moody, Jessica C. Ramella Roman

Oregon Health Sciences University
Oregon Medical Laser Center, Providence St. Vincent Medical Center
Oregon Graduate Institute of Science and Technology
Portland, Oregon 97225 USA

ABSTRACT

A tissue engineering problem that we anticipate will become increasingly of interest is how to grow protein layers and filaments in preferred orientations. For example, the polymerization of monomers into an oriented structure which may exert influence on adherent cells. In this paper, we report on an optical solution using polarized light measurements to probe the structure and orientation of fibers. In particular in this initial study, we measure the fast-axis orientation and retardance of micro-domains in thin sections of liver, muscle, and skin tissues using a polarizing microscope. The size of microdomains of iso-retardance is in the range 10-100 μm, which suggests that optical measurements with laser beams that are on the order of 1-mm in diameter or with imaging cameras with pixels sizes on the order of 100 s of μm will average over several microdomains and consequently complicate interpretation of measurements.

Keywords: Polarization, fiber orientation, liver, muscle, skin

1. INTRODUCTION

A tissue engineering problem that we anticipate will become increasingly of interest is how to grow protein layers and filaments in preferred orientations. For example, the polymerization of monomers into an oriented structure which may exert influence on adherent cells. Polarized light has been used by other investigators to study fiber orientations, such as assessing the orientation of collagen fibers in scars of the skin. At the Oregon Medical Laser Center, Dr. Kenton Gregory and colleagues are polymerizing elastin monomers to create elastin polymers for artificial tissue patches. The project needs a means of monitoring the orientation of such protein layers and filaments.

We have been developing polarized light imaging to locate the margins of skin tumors so as to guide surgical excision. Our work has led us to look at the microscopic domains of tissues such as liver, muscle, and skin using the standard polarization microscope.

In this paper, we initiate a study on use of an optical solution using polarized light measurements to probe the structure of oriented fibers. In particular in this initial study, we measure the fast-axis orientation and retardance of micro-domains in thin sections of liver, muscle, and skin tissues using a polarizing microscope.

2. MATERIALS AND METHODS

Tissue sections of calf liver, chicken breast muscle, and pig skin were prepared by freezing the tissue then cutting about 200-400 μm thicknesses of tissue. The samples were placed on glass slides with coverslips and viewed through a polarization microscope. As shown in Fig. 1, linearly polarized light illuminated the sample from below. Bandpass filters selected a wavelength of illumination and this paper reports on 540 nm green light. The orientation of the linearly polarized light source could be rotated manually. The analyzing linearly polarizer in front of a CCD camera was in a fixed position. The angle θ between the source and analyzer linear polarizers was varied from 0 to 90 degrees as a set of 9 images were acquired, each at a 10 degree interval.

As in Fig. 2, the transmission of light at each pixel in the set of 9 images was used to plot transmission versus angle θ. A fitting routine fit the plot to the function $A\sin^2(\theta) + B\cos^2(\theta) + \text{offset}$ versus θ. The shift, Δθ, was determined as shown in Fig. 3.
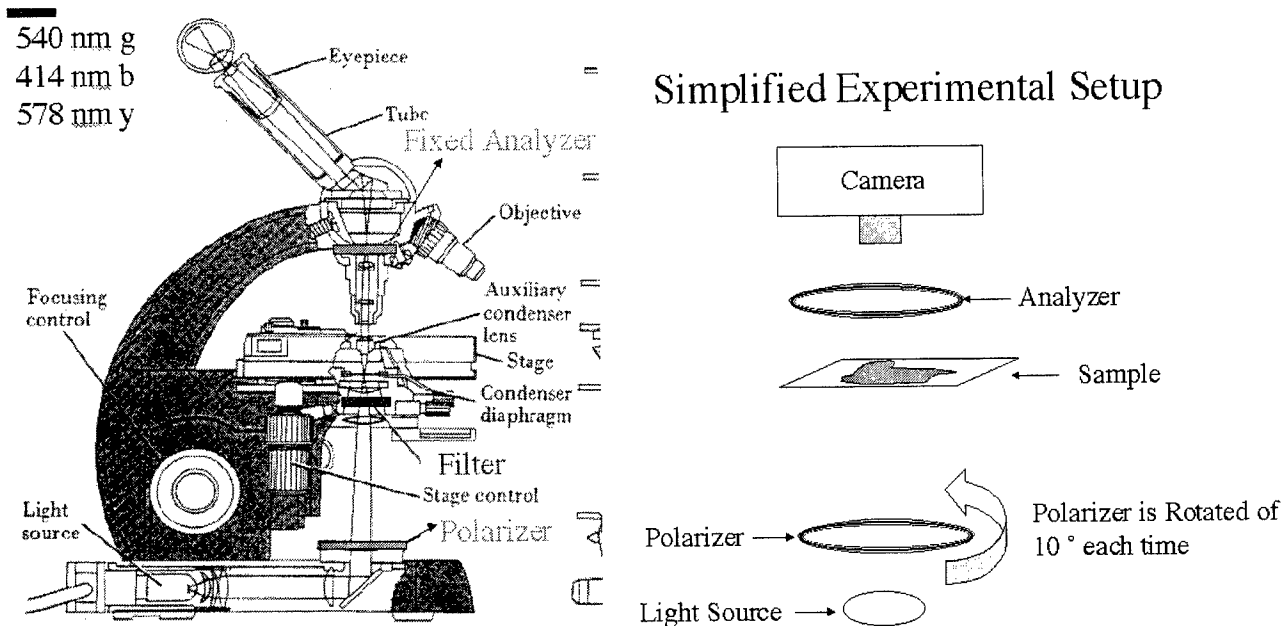
Fig. 1: Transmission images with source linear polarizer oriented in 10-degree increments.
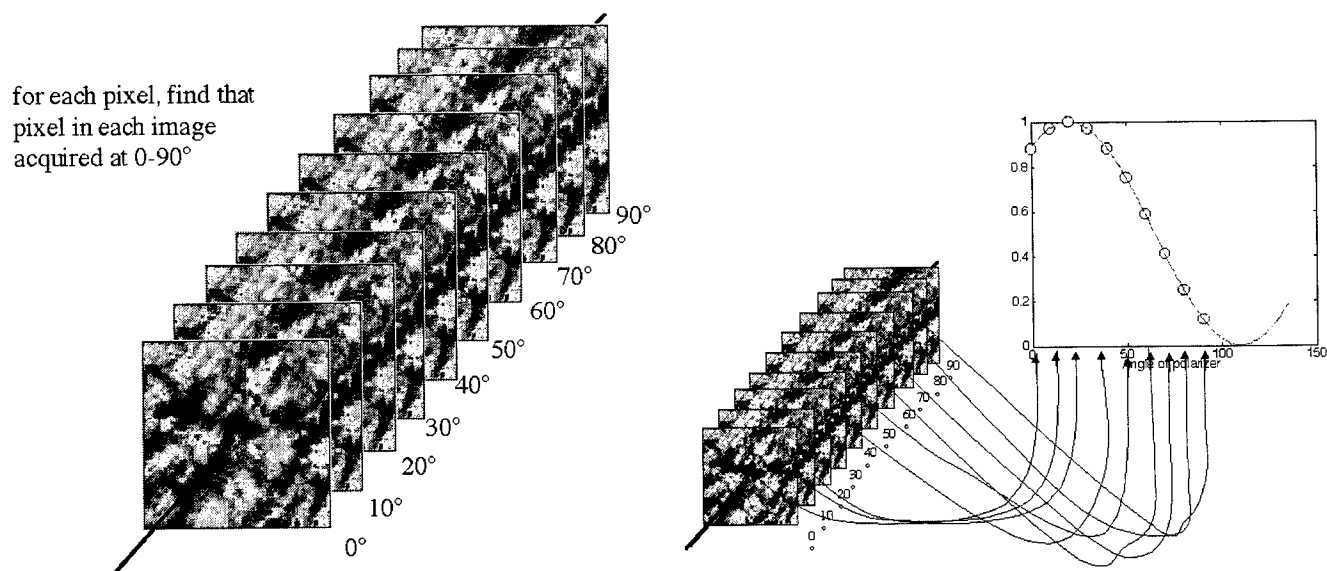
Fig. 2: The nine corresponding pixels in nine transmission images are
analyzed versus angle between source and analyzer polarizer.
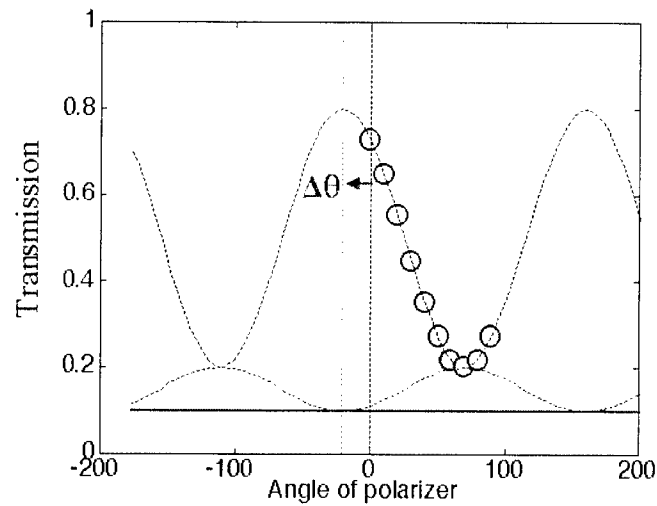
Fig. 3: The transmission versus angle data was fit as $Asin^2(\theta) + Bcos^2(\theta)$ + offset versus θ.
The shift $\Delta\theta$ was determined.

3. RESULTS

Typical results are shown in Fig. 4. The transmission image is shown on the left. The retardance image is shown on the right. The range of retardance values in this case, muscle, varied from zero to 60 degrees. Figure 5 shows typical results for liver, muscle, and skin. The size of iso-retardance domains is on the order of 10-100 m.
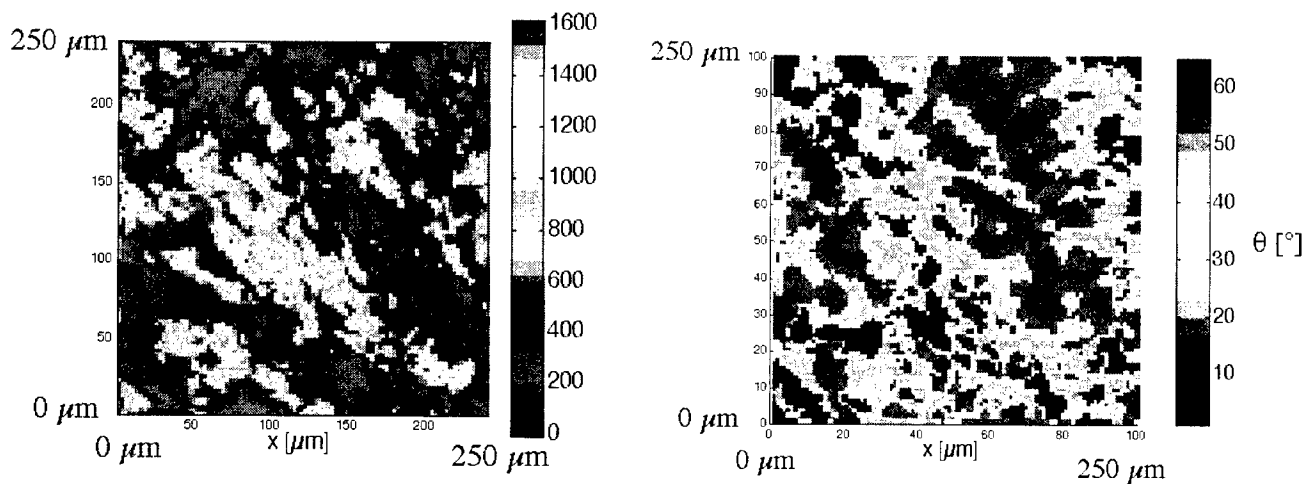
Fig. 4: (Left) Transmission image. (Right) Map of the retardance, $\Delta\theta$ [degrees].
The size of iso-retardance domains is on the order of 10-100 m.

Liver

Muscle

Skin
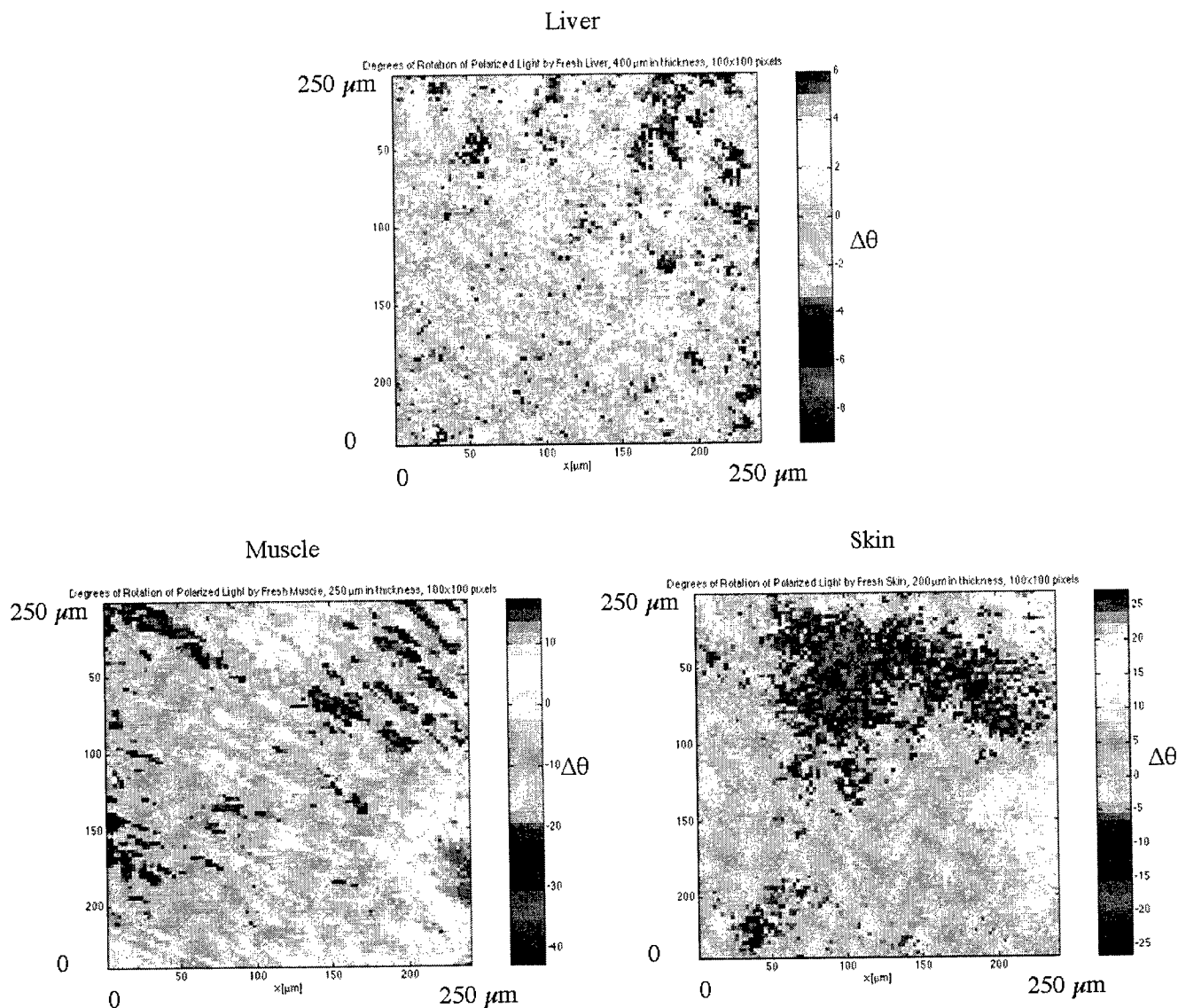
Fig. 5

4. DISCUSSION

Birefringence is reported as the apparent difference in refractive index, Δn, between the fast and slow axes of oriented fibers:

$$\Delta n = \delta\lambda/(2\pi d)$$

where δ is retardation, d is tissue thickness, and λ is the wavelength of light. Values from the literature for tendon are:

$\Delta n = 3.7 \times 10^{-3}$ deBoer (1997)
$\Delta n = 3.0 \times 10^{-3}$ Maitland (1996)
$\Delta n = 2.8 \times 10^{-3}$ Chang (1974)
$\Delta n = 3.0 \times 10^{-3}$ Naylor (1953)

In this paper we report values of $\Delta\theta$ = 10-20 degrees for a couple hundred μm thickness of pig skin which corresponds to a birefringence of Δn = 1.7 x 10^{-3} to 3.4 x 10^{-3} at 543 nm wavelength.

5. CONCLUSION

Microscopic domains of birefringence can be characterized by optical polarization measurements. Of course, polarization microscopy is not a new technique. However, motivated by problems encountered in Tissue Engineering, we are implementing polarization methods to document efforts by our tissue engineering colleagues at the Oregon Medical Laser Center, and elsewhere, to prepare oriented polymerization of proteins.

The size of microdomains of iso-retardance is in the range 10-100 μm, which suggests that optical measurements with laser beams that are on the order of 1-mm in diameter or with imaging cameras with pixels sizes on the order of 100 s of μm will average over several microdomains and consequently complicate interpretation of measurements.

ACKNOWLEDGEMENTS

3D IMAGING OF LUNG TISSUE BY CONFOCAL MICROSCOPY AND MICRO-CT

Andres Kriete [1], Andreas Breithecker [2], Wigbert Rau [2]

[1] Institute of Anatomy and Cell Biology
Image Processing Laboratory (IPL), University of Giessen
Aulweg 123, 35385 Giessen, Germany

[2] Department of Diagnostic Radiology, University Clinic Giessen
Klinikstr.36, 35385 Giessen, Germany

ABSTRACT

Two complementary techniques for the imaging of tissue subunits are discussed. A computer guided light microscopic imaging technique is described first, which confocally resolves thick serial sections axially. The lateral area of interest is increased by scanning a mosaic of images in each plane. Subsequently, all images are fused digitally to form a highly resolved volume exhibiting the fine structure of complete respiratory units of lung. A different technique described is based on microtomography. This method allows to image volumes up to 3x3x3 cm at a resolution of up to 7 microns. Due to the lack of strong density differences, a contrast enhancement procedure is introduced which makes this technique applicable for the imaging of lunge tissue. Imaging, visualization and analysis described here are parts of an ongoing project to model structure and to simulate function of tissue subunits and complete organs.

Keywords: Lung tissue, tissue preparation, 3-D imaging, confocal microscopy, X-ray microtomography

1. INTRODUCTION

There is a long history of experimental difficulties in the investigation of the lung tissue, because no technique was available so far to give a highly resolved, three-dimensional insight into the structural complexity. Several conditions have generally to be fulfilled for the investigation of lungs:

- the preparation technique should fixate the lung fully inflated
- it should preserve the fine structure and give sufficient contrast
- the imaging technique should be powerful enough to penetrate a block of tissue containing complete tissue subunits such as respiratory units (acini)
- a resolution should be available to resolve structural details down to the size of the alveoli .

Correspondence: E-Mail: andres.kriete@anatomie.med.uni-giessen.de, URL: www.med.uni-giessen.de/ipl

For mouse and rat, the size of a respiratory unit, also called pulmonary acinus, is in the range of 1000-2000 microns in diameter. Depending on the degree of inflation, the diameter of alveoli is in the range of 40 to 100 microns with a mean around 70 microns. To resolve the lung parenchyma a resolution of 5-7 microns or better is required. For human lungs these values have to be multiplied approximatly by a factor of 5. So far, investigations of acini were based on cast models, for human lung [1] as well as for rat and mouse [2,3]. Unfortunately, these preparations don't give any insight into the internal structural organization but restrict to a description of the outer form and a quantification of global parameters, such as volume. One investigation of one half of an human acinus is given in the literature, based on a very time consuming manual performed reconstruction of serial sections with a wax plate technique [4].

The only alternative way is to mechanical cut a block of tissue into a set of serial sections and to investigate these with traditional light or electron microscopical techniques. Because of such requirement, a complete 3-D computer based investigation at a high level of resolution of an acinus is not reported until recently [5,6]. We describe this computer-guided image acquisition procedure in confocal microscopy, which allows a substantial increase of the usual available field of view and an extended imaging in axial direction by scanning aligned thick serial sections. This guarantees for highly resolved volume containing complete respiratory units. As an alternative technique, X-ray microtomography is discussed to image bulks of specimen at high resolution without requiring tedious sectioning and alignment techniques.

2. PREPARATION AND MORPHOLOGY OF LUNG TISSUE

Lungs from mouse and rat and mice were inflated under a pressure of 20 cm H_2O with Buoin's solution (containing Pikrin acid) and dehydrated. Embedded in paraffin, mechanical sections of 70 micron thickness can be cutted with a microtome. These sections can be stained with Haemalaun and Eosin (HE). Lung tissue, in its native form, gives rise to autofluorescence which stems from elastic fibers. The H+E staining is a histochemical staining procedure, the Eosin is an acid stain which links to the basic structures of the tissue. Eosin Y is identical with a Fluorescein stain (tetrabrom) and gives rise to additional fluorescence beside the red color visible at the cytoplasm and tissue. The cell nuclei, stained blue by the acid stain Haemalaun, links to the phosphoric groups of the nuclei, consequently cell nuclei containing chromatin do not emit fluorescent light and remain dark in such preparations. For high resolution imaging of lunge tissues of larger, in particular human lungs, we have developed a technique which allows a fixation of lungs fully inflated [*]. Lungs undergo a process of ventilation with hot Formalin gas (see Figure 2). Evaporation over a period of 24 hours fixates the lung preserving the fine structure. For microtomography, small blocks of tissue were cutted out and were placed in solutions of $AgNO_3$. This heavy metal, previously used in electron microscopy, introduces higher densities differences to the tissue.

The subject of investigation is a tissue subunit called acinus, which is the fundamental ventilatory unit in the design of the respiratory part of lung. All structures in the acinus participate, to a lesser or higher degree, in the gas exchange, whilst all structures proximate to the acinus are of air conducting nature only. Differences about this definition mainly address the gradual, transitional alveolarization in the bronchioles being different in various species and the corresponding intra-individual developmental schemes [3]. These units are built up by alveolar ducts, which are larger acinar pathways completely ensheated with alveoli, and all other substructures attached to that compose the hexagonal acinus in total. Alveolar ducts end in alveolar sacs which are the blind-ending terminations.

---

* Investigations of the human lung were approved by the ethic commission at the University of Giessen.

3. OPTICAL IMAGING

For optical imaging, an upright Zeiss confocal laser scan microscope with a HeNe laser was used (Zeiss LSM 410). Fluorescence was detected above 545 nm from the lung parenchyma. Microscopical investigation was started at a low magnification of a 2.5 or 5 x magnifying lens. The 5x lens (Planapo 0.15) has a field of view of 4 mm^2. At this magnification prominent structures like bronchii, arteries and veins and larger alveolar ducts were visible. About 40 histological sections of 80 micron thickness were scanned, and the limited aperture of the 5x lens was not high enough to give rise to any 'confocal' effect. This pre-scan at a limited resolution had the goal to determine the area of interest containing a likelihood to completely cover a pulmonary acinus and to generate a framework for detailed analysis. Subsequently, the area of interest was scanned with higher magnifying lenses, such as 20x and 40x, which, by their higher aperture, confocally resolved the thick serial sections. An example is given in Figure 1. The field of view was increased by imaging adjacent subvolumes to areas of 1-2 mm^2 in size. Digital image processing was used to fuse all images obtained, and typically 800-1500 images had to be taken.

The disadvantages brought along with this procedure are obvious: It is not only a time consuming approach, but what is required is a precise alignment and correction of the cutted and eventually distorted histological sections. Furthermore, in view of the limited field of view of optical lenses a mosaic of images has to be taken to cover a sufficient field of view. The demands for the resolution required are still higher in this case. The problem is the occurrence of 'artificial' holes or pores between larger volumetric subtleties. Frequently the volumes of adjacent ductus or even the airspaces between two adjacent acini are just separated by a thin parenchyma. If the fusion was not correct and a slightly misalignment remains, visual interpretation but in particular automatic digital area or volume searching algorithms tend to break through these artificial pores. These passages may link structures together which may be misinterpreted as collateral ventilations.
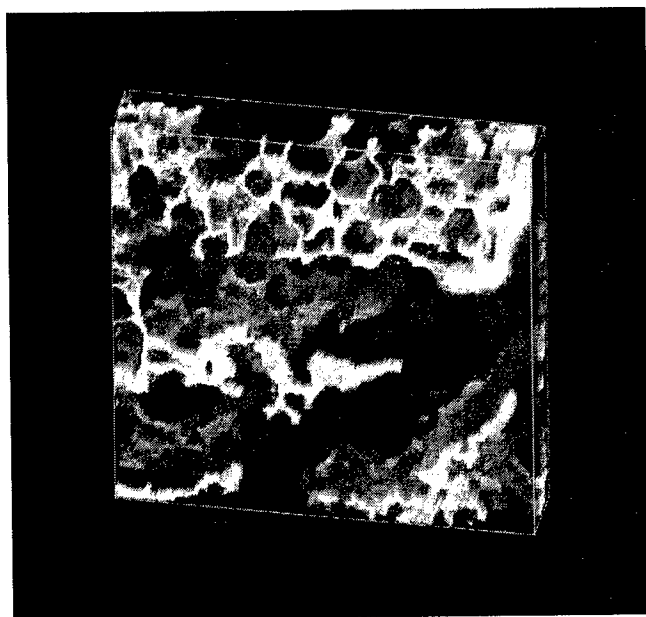
Fig. 1: 3D reconstruction of confocal images out of a sequence of serial sections. Displayed is a part of a respiratory unit with alveolar ductus and alveoli.

4. MICRO - CT

Microfocus tubes are new sources in X-ray imaging which emit polychromatic radiation, so one cannot use X-ray lenses as in the case of synchrotron radiation. However, the microfocus spotsize, which governs the resolution, is sufficiently small and one can project the object over a large distance before reaching the detector to achieve a magnification [7]. Our system (Skyscan 1072, Skyscan, Belgium) is equipped with a sealed microfocus tube of 7 micron spotsize, 20-80 kV, combined with a 12 bit cooled CCD detector with 1 K resolution. Reconstructions are generated from projections as the block rotates on a precision specimen holder. Typical 3-D images of lung tissue contained volumes of 5-15 mm in diameter at 10-50 micron resolution, or larger volumes at the cost of lower resolution. First biological applications in microtomography focussed on the investigations on bone microarchitecture [8], because differences in density give rise to high contrast. Our preparations show, that it is also possible to image fine structure of lung, including the alveoli, when the contrast is enhanced by a heavy metal stain (see Figure 4). Contrast differentiation can be used to segment specific subtleties of the volume, such as veins (Figure 5).

Fig.2: System for fixation of human lungs with Formalin gas.
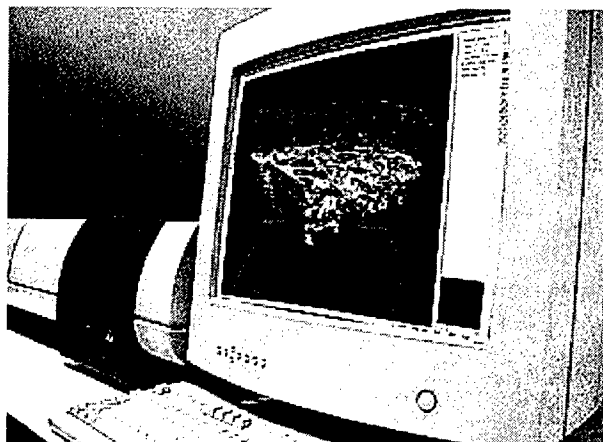
Fig.3: Desktop microtomographic system (Skyscan).
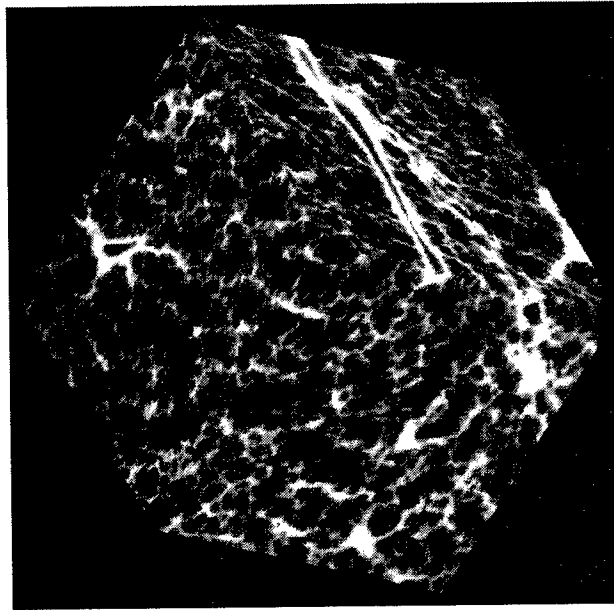
Fig.4: Human lung tissue scanned with a microtomographic system. At a resolution of 40 microns the alveoli get resolved, the contrast is enhanced by a silver staining technique. The side length of the cube is about 5 mm.
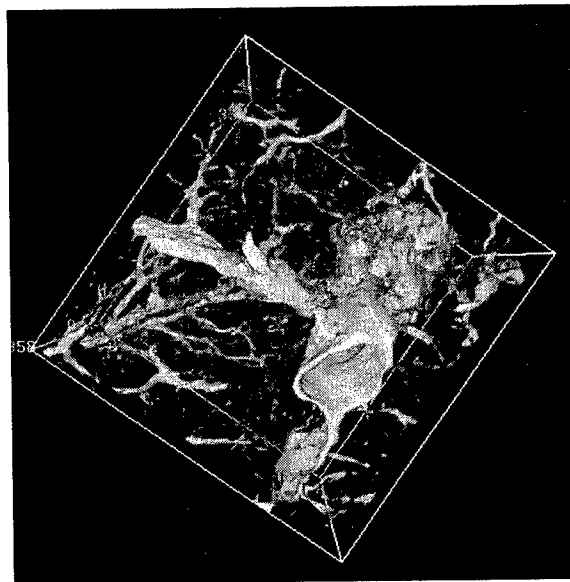
Fig.5: Due to contrast differences substructures like this vessel can be visualized in microtomography.

5. VISUALIZATION, ANALYSIS AND SIMULATION

For further investigation complete data volume of tissue substructures were visualized and quantified. Scientific visualization applied to 3-D microscopy leverages accurate and reliable concepts in computing and graphics to precisely interpret microstructures. Therefore, visualization and analysis are not mutually exclusive. This is quite obvious in the term 'analytical graphics' [9]. In particular, any processing step to extract and identify volumetric substructures prior to a quantitative analysis may be controlled by a 3-D reconstructed view. In addition, a number of visualization applications give evidence of integrated analytical tools to render specific volumetric subtleties. In order to fulfill such analytical tasks, visualization benefits from proven sets in digital image processing to enhance, filter, segment and code pictorial information, as required here to analyze the content of the acinar volume. As an inherent part of visualization the idea of topology was applied to measure the branching pattern and volumes of an acinus. Image sequence were binarized and contoured. Due to the high contrast, no special image processing steps were necessary, but shift of the mean gray level in the images required an interactive control of the gray level threshold. Subsequently, the images were traced for structure boundaries, that means the demarcation between the lungs parenchyma and the airspaces was marked. These closed polygons were analyzed with a contour visualization program on a graphic workstation [10] and the topology of the branching pattern was quantified (see Figure 6).
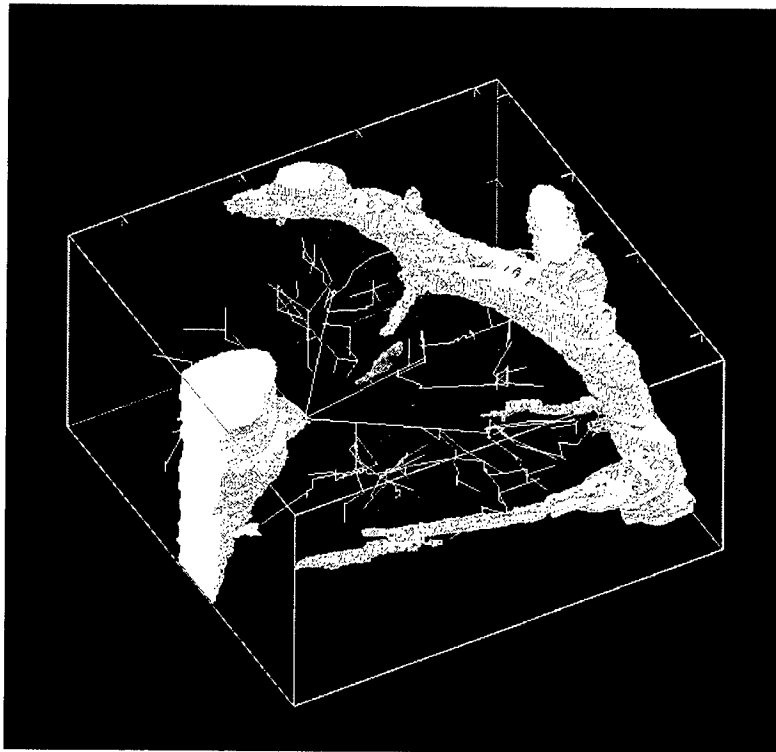
Fig.6 : 3D segmented structure of a complete respiratory unit. Two systems of branching   bronchioli are displayed. The branching pattern of the ductus which has its origin at the left bronchioli is visualized as embedded geometric lines. Diameter of this acinus is about 1 mm.

With the help of the parameters measured, a computer model of the acinus was designed to prepare functional simulations [5,6]. The structural dynamics of ventilatory units during inhalation and expiration was also included. The model of acini was incorporated into a computer model of the bronchial tree of lung, and functional simulations concerning the gas flow and gas uptake were performed by invoking computational physics. Since mass-transport equations for these kind of objects can no be calculated in a direct, analytical fashion, the equations had to be solved iteratively, in respect to time and space. Concerning time, this means that the process of inhalation and expiration had to be subdivided into many individual single time steps. Concerning space, the structure had to be subdivided into individual segments in the sense of a finite-element model. The number of time-steps required is governed by the precision and robustness of the equations used.

6. DISCUSSION

Optical imaging is limited by scattering and absorption, which restricts the useful range of operation to tissues which have 50-100 microns in thickness. Sophisticated techniques, such as double-photon excitation, have been developed which increase the area of light microscopic operation. Nevertheless, optical techniques can not deal with large blocks of tissue in the mm-range, among these are specimen from inner organs. Serial sectioning is the chief alternative to deal with such a problem. It was suggested and demonstrated for single acinar pathways of the respiratory system, that confocal imaging applied to thick sections and digital image processing might be promising [11]. We described a computer-guided image acquisition procedure in confocal microscopy, which allows a substantial increase of the available field of view and an extended imaging in axial direction by scanning aligned thick serial sections. This registration technique guarantees for the necessary axial and lateral alignment and resolution of volumes containing complete respiratory unit. The computational expense for alignment and fusion was however high.

Recently there has been significant improvement of X-ray microscopes. The new devices do not require synchroton sources which are not available for many researchers. Instead, the steady improvement of X-ray source technology has led to the development of compact, sealed X-ray microfocustubes that have a long lifetime. Due to the small focus sizes resolutions up to 5 micron can be obtained. X-rays can penetrate bulks of tissue, but special preparations for artificial contrast enhancement are necessary for tissue, since contrast in X-ray imaging depends on density differences. For lung tissue we introduced a heavy metal staining technique, which allowed to image the fine tissue and resolve the parenchyma including alveolar walls. The application of this kind of preparation for other kind of tissue is subject of future research. The distinct advantage of this imaging technique is that the complete volume is available in precise registration.

New forms of numerical and physically based simulations allow for a tight coupling with graphical visualizations. For such a thorough computer modeling of biological systems, the inherent structural hierarchy has to be considered, since the macroscopic structures are built-up from microscopical ones, and microscopical structures are based on macromolecular arrangements. No imaging techniques are known, which transfer these hierarchies directly into a numerical data format accessible by computers. However, a comprehensive computer model can combine the representation of organelles, individual cells, tissues and organs.

The combination of structural investigation of form with computational physics is an initial step towards physiological interpretation of biological structures, a concept which is generally applicable and of interest for many organs and tissues. For the lung, an appropriate computer model describing the biological structure can be used to simulate function, such as the oxygen uptake. The fusion of form and function may also open a new road for interpretation of the morphogenesis. For tissue engineering it has to be discussed in how far generic physical mechanisms such as adhesion, tension, viscosity and convection may interact with genetic mechanisms and have an impact on morphogenesis and pattern formation. The computer assisted imaging, analysis and simulations discussed may help to elucidate related questions.

7. ACKNOWLEDGEMENTS

8. REFERENCES

1. B.Haefeli-Bleuer, E.R.Weibel, "Morphometry of the human pulmonary acinus". *Anat.Rec.* 220. 401-414, 1988

2. M. Rodriguez, S. Bur, A. Favre, E.R. Weibel, "Pulmonary acinus: geometry, and morphometry of the peripheral airway system in rat and rabbit". *Am.J.Anat.* 180, pp. 143-155, 1987

3. K.-P. Valerius, *Bauprinzipien der Säugetierlunge*. Thesis, Univ. of Giessen, 1992

4. E.A. Boyden, The structure of the pulmonary acinus in a child of six years and eight months", Am.J.Anat. 132: pp 275-300, 1971

5. A. Kriete, *Form and function of mammalien lung: analysis by scientific computing*. Advances in Anatomy, Embryology and Cell Biology, 145, 1998

6. A. Kriete, "Hierarchical data representation of lung to model morphology and function. in: K.-H. Höhne, R. Kikinis, "Visualization in Biomedical Computing" Springer, NY, pp 399-404, 1996

7. A. Sasov, "Microtomography". J.Microscopy, 147, pp. 169-192, 1987

8. P.Ruegsegger, B.Koller, R.Müller, "A microtomographic system for the nondistructive evaluation of bone architecture". *Calcif.Tissue Int.* 58, pp. 24-29, 1996

9. A. Kriete, T. Pepping "Volumetric data representations in microscopy: applications to confocal and NMR-microimaging". in A.Kriete (Ed.): *Visualization in Biomedical Microscopies*. VCH-Verlag, Weinheim, pp 329-360, 1992

10. A. Kriete, T. Schwebel, "3DTOP – a software package for the topological analysis of image sequences". *J.Struct.Biology* 116, pp. 150-154, 1996

11. E.H Oldmixon, K. Carlsson "Methods for large data volumes from confocal scanning laser microscopy of lung." *J. of Microscopy*, Vol. 170,3, pp 221-228, 1993

OPTICAL ANISOTROPY OF BIOTISSUES

aGeorgy V. Simonenko[1], bTatyana P. Denisova, aNina A. Lakodina,
aAlexander V. Papaev, aValery V. Tuchin

aSaratov State University
bSaratov Medical State University

ABSTRACT

To create a model of development of atherosclerosis and other "major" human diseases the structural and functional peculiarities of bradytrophic tissues were studied in series of investigations. Sclera, cornea, tendon, cartilage and some other tissues belong to bradytrophic tissues, which nutrition is the result of the diffusion of extravasal liquid. In this fragment of research isotropic properties of cartilage tissue were established before optical enlightenment, induced by tissue immersion, and after it. The sample of sarcoma (muscular tissue's tumor) is also isotropic. By its optical properties and enlightenment dynamics sarcoma is very like cartilage tissue. The enlightenment rate in the indicated tissues significantly higher than in sclera.

Keywords: cartilage, sarcoma, polarization properties, optical enlightenment.

1. INTRODUCTION

In spite of the broad spreading of the atherosclerosis and other "major" human diseases and a great many of the studies in that field the model of forming and interaction of those diseases is absent yet.[1] The studies of structural and functional peculiarities of bradytrophic tissues occupy one of the major places in the comprehension of atherosclerosis formation.[2] To the bradytrophic tissues belong sclera, cornea, tendon, cartilage and other tissues with slow metabolism. The nutrition of such tissues is the result of the diffusion of extravasal liquid.

An experimental research of polarization and optical properties (and their comparing) of different kinds of tissues was performed as the first stage of the study. The previous investigations of polarization properties of such tissues as sclera, cornea, muscular tissue showed that enlightened (due to application of immersion technique) samples of sclera, well exsanguinate (bloodless) muscular tissue and cornea has optical properties very look like uni-axial and bi-axial crystals.[3-6] To continue that research we studied the enlightenment rate and polarization properties of cartilage and malignant tumor (sarcoma of thigh muscular tissues) as examples of less organized tissues.

MATERIALS AND METHODS

To investigate the enlightenment of the scattering tissue samples and their polarization properties the experimental set-up described in Ref. 5 was used. In the Fig. 1 present the photo of experimental installation. Horizontal thin sections of the articulate surfaces of cow femur were used as the samples of cartilage. Thin sections of thigh sarcoma of young man (received during the operation) were used as the samples of malignant tumor.

To investigate the optical properties of tissues the method of reduction of tissue scattering due to immersion of osmotically active liquid with a higher refractive index than tissue interstitial media was used.[3-7] To enlighten the tissues (to reduce their scattering properties) we have used 60% trazograph solution (X-ray contrasting drug). The samples were of 1 cm x 1 cm in size, their thickness was of 0.5 –0.7 mm. The surrounding (room) temperature during all studies was kept at about 22°C. Trazograph solution was warmed up to 36 – 40°C and with the help of pipette was drifted on the surface of tissue sample, after all it diffused into the preparation.

RESULTS AND DISCUSSION

The graph for enlightenment of cartilage sample is shown in the Fig. 2, where the following value is used as characteristic of enlightenment

---

[1] SimonenkoGV@info.sgu.ru

$$\text{Contrast} = (T(t)-T_{min})/T_{min},$$

where $T(t)$ is the current sample brightness, T_{min} is the minimal sample brightness. The mean brightness of a sample was evaluated on the basis of the images obtained with the help of the digital CCD camera and the program MS Photo Editor. The program allows to evaluate medial brightness of the image or its discharged part by quantity of pixels having a given intensity level.
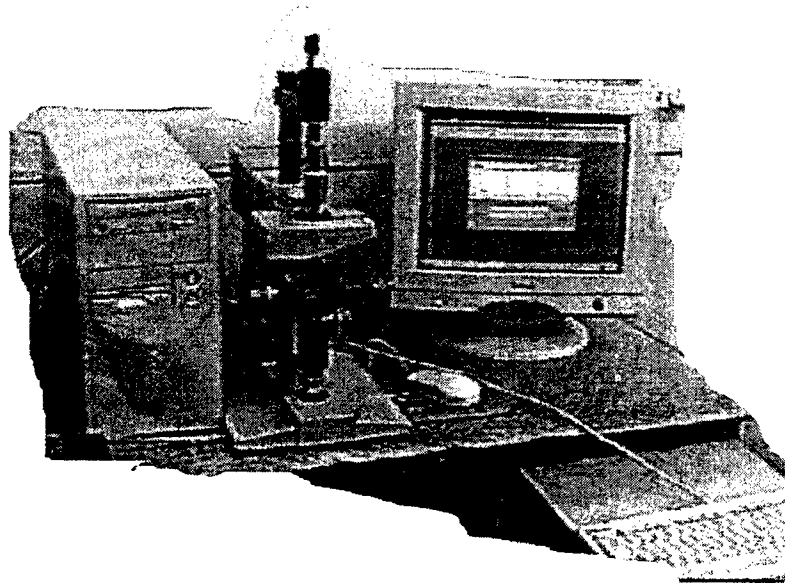
Fig. 1 The photo of experimental installation

From figure 2 is clear, that the process of enlightenment was of high rate and the sample enlightens through about 1 minute. But the enlightenment rate of sclera sample, for example, is significantly lower (8-10 min for the sample of 0.7-1.0 mm in thickness).[3-6] Such difference in the rate of clarification of a cartilaginous tissue and sclera is stipulated by the several reasons. First, the solution of trazograph, with which the sections of a cartilaginous tissue were clarified, had temperature of a body of the man that essentially improves rate of a clarification. Second, the sections of a cartilaginous tissue were explored which are deprived of outer shells, while dynamics of a clarification of a sclera of an eye was explored on the whole samples having an outer shell. Third, sclera and cartilaginous tissue have some differences in structure.

For examination of an optical anisotropy of thin sections of a cartilaginous tissue the method of color coordinates was utilized, in which the color coordinates of a CIE 1930 XYZ and dominant wavelength λ_{dom} of light are acted.[8] This method grounded on dependence of color of a sample showing anisotropic properties, from quantity of an anisotropy of refractive indexes of a sample. In the case, when the sample shows isotropic properties, its color is determined by color of the light source. In Tab. 1 the quantities of a dominant wavelength of light are shown at different orientation of a sample of a tissue regarding the polarizers (polarizers are crossed). As follows from this table, the rotational displacement of a sample does not give any serious change of value of the dominant wavelength. It speaks that the thin section of the clarified cartilaginous tissue shows isotropic properties, in a direction perpendicular to shear surface. The similar behavior is watched in changes of a clarification of a thin section of a cartilaginous tissue, that is at a clarification of an explored sample the dominant wavelength of light remains to a stationary value in time, while the induced transmission of a sample varies. These both facts speak that the thin sections of a cartilaginous tissue show isotropic properties in a direction, perpendicular to shear surface.

Table 1. Dependence of the dominant wavelength of the thin section of a cartilaginous tissue at a different angle orientation of the polarizers (φ)

φ, degrees	0	15	30	45	60	75	90
λ_{dom}, nm	572	573	573	575	573	577	574
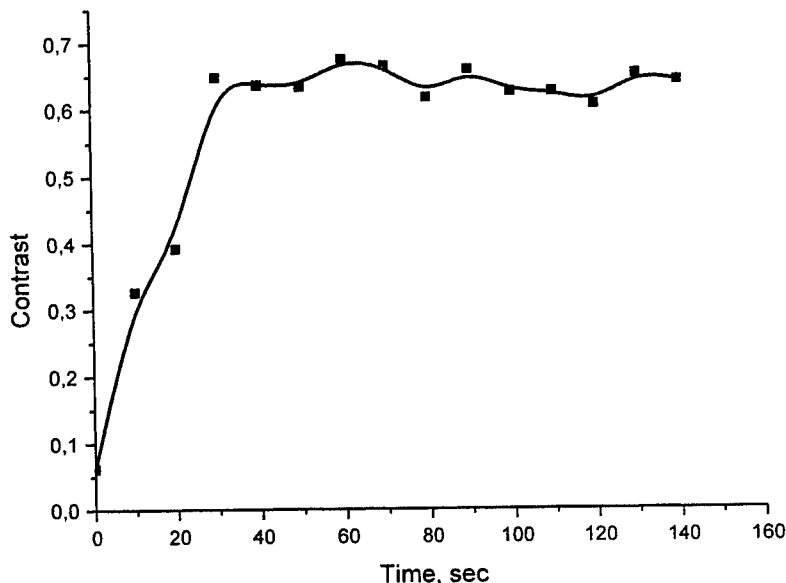
Fig. 2 Dynamics of enlightenment of cartilage tissue

Let us consider optical properties of normal and sarcoma muscle tissue. We have noted the visual difference of sarcoma tissue from the healthy one. The first difference is that the thin (up to 1 mm) sample of bloodless muscular tissue poorly scatter the light. It's properties are the same as a uni-axial crystal. The sample of tumor tissue of the same thickness is a scattering system, and as was shown in our investigations has isotropic optical properties. In the Tab. 2 the dominant wavelength for the clarified sample of a section of a sarcoma of a muscle is shown at different positions of a sample regarding the polarizers (polarizers are crossed). As the dominant wavelength not dependent from an angle of orientation of a sample respective to polarizers is seen from this table, that speaks about exhibiting of an isotropic optical behavior of the given sample. For comparison in the Fig. 3 the photos of thin sections of an able-bodied muscle tissue are shown at different orientation of a muscle tissue in respect to the polarizers. These images show a high degree of normal muscle tissue optical anisotropy. At changes of a clarification of a sample of a thin section of a sarcoma of the muscle apparent in crossed or parallel polarizers, the dominant wavelength does not vary on time, while the induced transmission of a sample varies strongly. Thus it is possible to make a deduction that the thin section of a sample of a sarcoma of a muscle tissue shows isotropic properties, as against an able-bodied tissue.

Table 2. Dependence of the dominant wavelength of the thin section of a sarcoma at a different angle orientation of the polarizers (φ)

φ, degrees	0	15	30	45	60	75	90
λ_{dom}, nm	578	577	576	579	578	578	578

The enlightenment dynamic graph of sarcoma is presented in Fig. 4. As it is clear from the graph, the enlightenment dynamics of sarcoma is more like the enlightenment dynamics of cartilage. The drop of Contrast (t) while t>120sec is nearly connected with trazograph flowing out from the sample due to its porous structure. This makes tumor tissue again more scattering tissue. Polarization studies of the tumor tissue were performed with the help of polarization microscope connected to computer. The observation of enlightening and scattering samples of sarcoma showed their optical properties typical to isotropic samples.

Basing on the upper said, we can propose that sarcoma is very like cartilage tissue by its optical properties, but has some special features. They are: enlightenment maximal value reaching is next to 100 sec, that on 70 sec longer then in cartilage. The enlightenment maximal value reaching is more smoother then the same process in cartilage tissue.
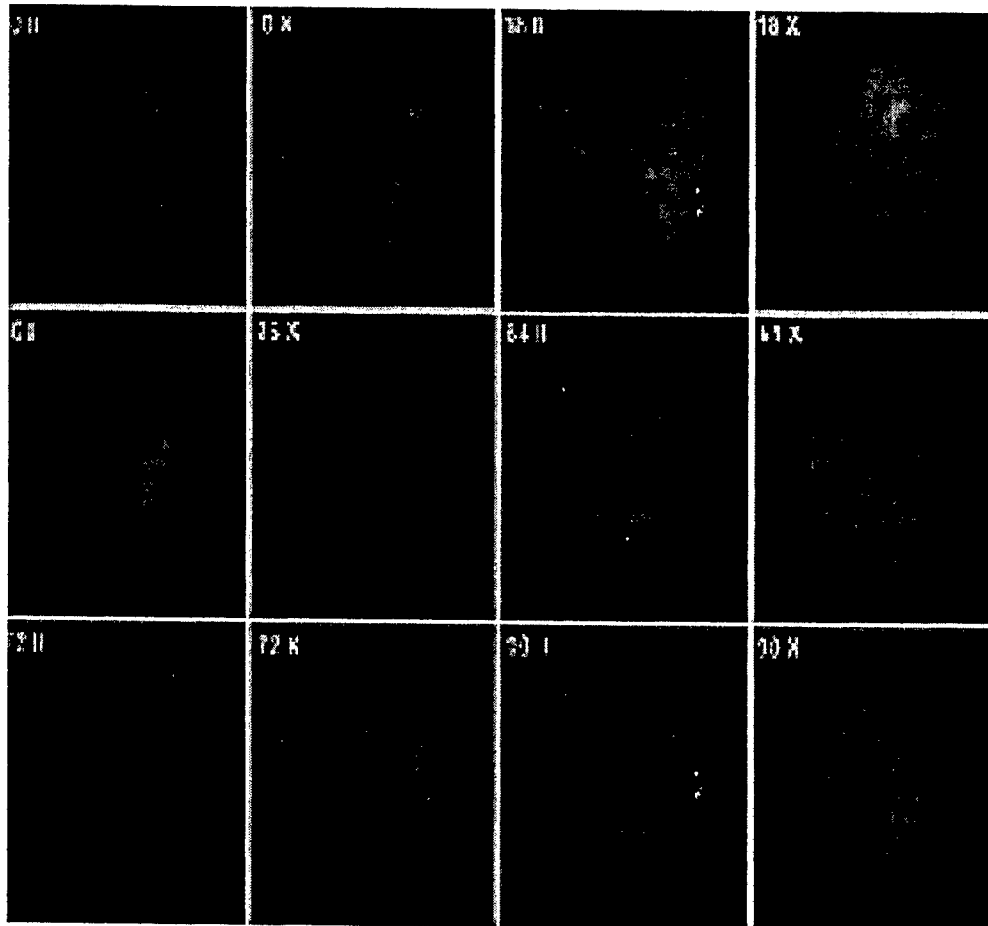
Fig. 3. Images of the normal muscle tissue obtained by the polarization microscope at different rotating positions of a sample between the crossed and parallel polarizers. The orientation of the sample of a muscle is shown in the corner of each image | | - parallel polarizers; x - crossed polarizers

All the bradytrophic and mesenchymal tumors (to whom belongs sarcoma) have the same sources of the ontogenesis – mesenchyme. Mesenchyme is the beginning of connective tissues, vessels, muscles, the tissues of locomotor system, serous membranes. Observed likeness between cartilage and mesenchymal malignant tumor based on studied parameters can be explained by the same descend and the structural relationship in spite of the principal different status in human organism.

CONCLUSION

The lead examination has established isotropic properties of thin (0.5–0.7 mm) section of a cartilaginous tissue both up to a clarification, and after it. Besides fixed, that the sample of a sarcoma of a muscle tissue also shows properties of isotropic material, and it essentially distinguishes it from an able-bodied muscle tissue.

ACKNOWLEDGMENTS
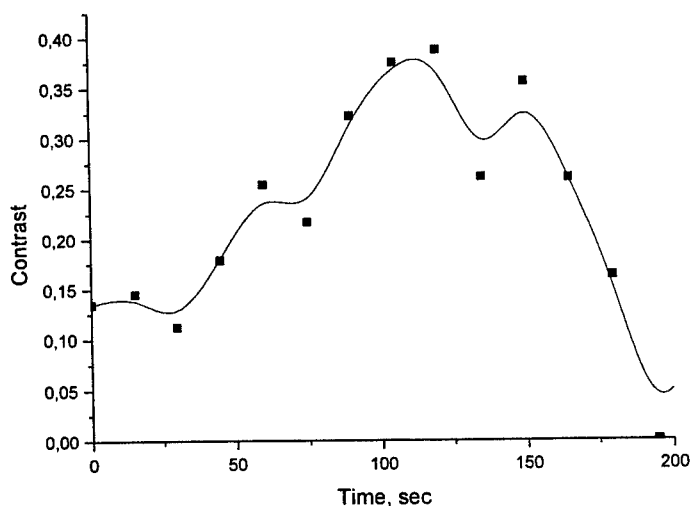
Fig. 4. Dynamics of enlightenment of tumor (sarcoma) muscle tissue

REFERENCES

1. V.M. Dilman, *The four models of the medicine*, Leningrad, Medicine, 1987.
2. B.V. Ilyinskiy, *Prevention, early diagnostic and care of atherosclerosis*, Moscow, Medicine, 1977.
3. I.L. Maximova, D.A. Zimnyakov, and V.V. Tuchin "Modeling of an optical characteristics of a sclera of an eye. Part 1," *Optcs and Spectroscopy* **89**, №1, c. 78 – 86, 2000.
4. G.V. Simonenko, T.P. Denisova, N.A. Lakodina, and V.V. Tuchin "Measurement of an optical anisotropy of biotissues" *Proc. SPIE* **3915**, pp. 152-157, 2000
5. G.V. Simonenko, V.V. Tuchin, N. A. Lakodina Measurement of the optical anisotropy of biological tissues with the use of a nematic liquid crystal cell. *J. Optical Technology* **67**, N 6, pp. 70 - 73, 2000.
6. V.V. Tuchin, "Tissue image contrasting using optical immersion technique," *Proc. SPIE* **4224**, 2000.
7. V.V. Tuchin, *Tissue Optics: Light Scattering Methods and Instruments for Medical Diagnosis*, SPIE Press, **TT38**, Bellingham, USA, 2000, 352 p.
8. G. A. Agoston, *Color theory and its application in art and design*, Springer – Verlag, New York, 1979

Addendum

The following papers were announced for publication in this proceedings but have been withdrawn or are unavailable.

[4257-06]   **Comparison of the effects of cationic and anionic porphyrins in tumor under illumination of argon ion laser**
C. A. Melo, V. C. Carvalho, V. S. Bagnato, J. R. Perussi, Univ. de São Paulo (Brazil)

[4257-10]   **Photobleaching of endogenous fluorochromes in human skin by laser irradiation**
A. A. Stratonnikov, V. S. Polikarpov, V. B. Loschenov, General Physics Institute (Russia)

[4257-28]   **Laser-induced alteration in fine structure of cartilage**
E. N. Sobol, A. I. Omel'chenko, A. P. Sviridov, Institute of Laser and Information Technologies (Russia); W. Pompe, M. Mertig, Technical Univ. of Dresden (Germany); N. Jones, Univ. of Nottingham (UK)

[4257-51]   **Nonlinear confocal imaging of biological tissues**
B.-M. Kim, P. C. Stoller, Lawrence Livermore National Lab. (USA); K. M. Reiser, Univ. of California/Davis Medical Ctr. (USA); A. M. Rubenchik, Lawrence Livermore National Lab. (USA); J. P. Eichler, Lawrence Livermore National Lab. (USA) and Univ. of Applied Science (Germany); L. B. Da Silva, Lawrence Livermore National Lab. (USA)

[4257-55]   **Fluence rate and radiance distributions in biological tissue**
H. Li, S. Xie, Fujian Teachers Univ. (China); Z. Lu, Zhejiang Univ. (China)

[4257-57]   **Diffuse properties from a semi-infinite surface of biological tissue**
H. Li, Fujian Teachers Univ. (China) and Zhejiang Univ. (China); S. Xie, Fujian Teachers Univ. (China); Z. Lu, Zhejiang Univ. (China)

[4257-59]   **Bone marrow stromal cells: cell therapy and tissue engineering for bone repair**
R. Cancedda, Istituto Nazionale per la Ricerca sul Cancro (Italy) and Univ. di Genova (Italy); R. Quarto, Istituto Nazionale per la Ricerca sul Cancro (Italy); A. Muraglia, Univ. di Genova (Italy); M. Mastrogiacomo, Istituto Nazionale per la Ricerca sul Cancro (Italy) and Univ. di Genova (Italy); M. Galotto, Istituto Nazionale per la Ricerca sul Cancro (Italy); S. M. Kutepov, Ural Scientific Research Institute of Traumatology (Russia) and Orthopaedics (Russia); M. Marcacci, Istituti Ortopedici Rizzoli (Italy)

[4257-65]   **Maximum entropy algorithm for the detection and localization of embedded inhomogeneties using photon density waves**
D. G. Fischer, NASA Glenn Research Ctr. (USA)

[4257-67]   **Fully automated three-dimensional microscopy system**
R. L. Kerschmann, Resolutions Sciences Corp. (USA)

Author Index